THE JOURNAL
OF
CHEMICAL PHYSICS

VOLUME 35, NUMBER 4 OCTOBER, 1961

Hydrogen Bonding Interaction between Adsorbate Molecules and Surface Hydroxyl Groups on Silica

MICHAEL R. BASILA

Gulf Research & Development Company, Pittsburgh, Pennsylvania

(Received January 30, 1961)

The interactions of the surface hydroxyl groups on amorphous silica with two series of adsorbates, the methylbenzenes and the chloromethanes, have been studied. A correlation is demonstrated between the frequency shifts of the surface hydroxyl stretching vibration and the ionization potential of the adsorbate. A similar correlation is found for the interaction of the hydroxyl group of a carbinol with the methylbenzene series. The importance of charge-transfer interaction in hydrogen bonding, which is indicated by these correlations, is discussed.

INTRODUCTION

IT is well known that the infrared spectra of porous glass or amorphous silica exhibit a sharp band in the region 3730–3750 cm^{-1} which is due to the OH stretching fundamental of surface silanol groups, and that shifts in the frequency of this band occur when molecules are adsorbed on the surface. Eischens and Pliskin,[1] in their comprehensive review, have summarized the work published up to 1957, both on the OH stretching fundamental and first overtone vibrations. However, the early data are confusing, and it is not possible to form a clear picture of the nature of the interaction which causes the shift in the OH stretching frequency. Subsequent work published by McDonald[2,3] and Folman and Yates[4,5] has clarified the picture somewhat.

McDonald[2,3] has studied the interaction of several different molecules, i.e., Ar, Kr, Xe, N_2, O_2, CH_4, CF_4, H_2O, CH_3OH, $(C_2H_5)_2O$, benzene, and cyclohexane with the surface silanol groups on amorphous silica (Cabosil). He has tentatively assigned several of the broad bands observed in the spectrum of the unperturbed surface. Folman and Yates[4,5] have studied the surface silanol groups on porous glass and the interaction of CH_3Cl, SO_2, $(CH_3)_2CO$, and NH_3 with these groups. The nature of the interaction between surface silanol groups and adsorbate molecules has been shown to be hydrogen bonding.[1–5]

In this laboratory, the frequency shifts of the surface silanol OH stretching fundamental which occur when a member of the methylbenzene or chloromethane series is adsorbed on amorphous silica have been studied. This study of the frequency shifts produced by a series of closely related molecules was made to provide further insight into the nature of the interaction between the adsorbate and the silanol OH. The results indicate the importance of charge-transfer interactions.

RESULTS AND DISCUSSION

Frequencies

The spectrum of the silica surface prior to adsorption, which is shown in Fig. 1, is essentially the same as that obtained by McDonald.[2,3] There is a strong, sharp band centered at 3743 cm^{-1} which has a long tail on the low-frequency side. McDonald[2,3] has assigned this sharp band to the fundamental OH stretching vibration of the surface silanol groups. He has also assigned bands in the 3680–3660 cm^{-1} region (the region of the tail) to weakly hydrogen bonded surface silanol groups, the bonding occurring between adjacent surface silanol OH groups or between a surface silanol and a siloxane oxygen.

It is of interest to examine further the large tail of the 3743 cm^{-1} band. In Fig. 2, the interaction of diethylamine with the silica surface is shown. This example was chosen because the interaction is unusually strong. The resulting 990-cm^{-1} shift of the 3743-cm^{-1} band toward

[1] R. P. Eischens and W. A. Pliskin, *Advances in Catalysis* (Academic Press Inc., New York, 1958), Vol. X, pp. 1–56.
[2] R. S. McDonald, J. Am. Chem. Soc. **79,** 850 (1957).
[3] R. S. McDonald, J. Phys. Chem. **62,** 1168 (1958).
[4] M. Folman and D. J. C. Yates, Proc. Roy. Soc. (London) **A246,** 32 (1958).
[5] M. Folman and D. J. C. Yates, J. Phys. Chem. **63,** 183 (1959).

Copyright © 1961 by the American Institute of Physics

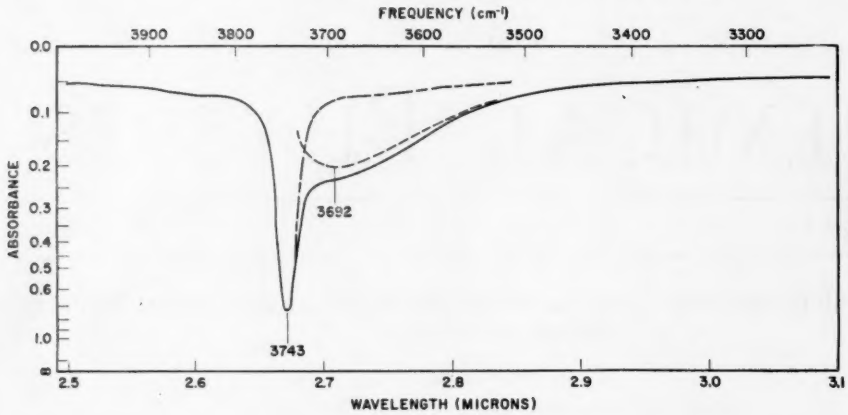

FIG. 1. Spectrum of Cabosil wafer degassed at 450°C. Dashed lines indicate the mechanical separation of the overlapping bands.

lower frequency allows the region of interest, i.e., 3550–3750 cm^{-1}, to be examined without intereference from strongly overlapping bands. It is clear from the spectra of Fig. 2 that the band at 3670 cm^{-1} is the source of the low-frequency tail on the 3743-cm^{-1} band since it remains quite intense even though the 3743-cm^{-1} band has completely disappeared. This 3670-cm^{-1} band can also be observed when diethyl ether is adsorbed on silica as shown in Fig. 7 (a) in McDonald's paper.[3] This band undoubtedly corresponds to the weakly hydrogen bonded ($\Delta\nu_{OH}\sim 80$ cm^{-1}) silanol groups which McDonald has already assigned.

Since both diethylamine and diethyl ether interact strongly with the surface silanol OH groups, it is surprising that the 3670-cm^{-1} band remains after all the free OH, i.e., the groups producing the 3743-cm^{-1} band, have interacted. It would be expected that the weak interaction which is characterized by the 3670-cm^{-1} band would be overcome by the much stronger interaction with diethylamine or diethyl ether. Apparently, the silanol groups producing the 3670-cm^{-1} band are relatively inaccessible. However, they are probably available for interaction under the right conditions. This is indicated by the diminished intensity of the 3670-cm^{-1} band of curve A, Fig. 2, as compared with curve B.

The foregoing observations would be explained if these groups were partially occluded in cavities near the surface but still available for interaction if the adsorbate molecules are able to diffuse into the cavity. Additional evidence is provided by some recent studies[6] on the exchange of deuterium with the bound hydrogen on silica and silica-alumina samples. The results indicate that a small fraction of the hydrogen which exchanged was not located on the surface, but was presumably located in the bulk of the material.

McDonald's results show that, after high-temperature prolonged evacuation, the resulting surface OH band is quite symmetrical. If one assumes that the band centered at 3743 cm^{-1} is symmetrical, the contour of the underlying band can be obtained by a mechanical separation. The results of this separation are given in Fig. 1. It is interesting to note that the band which appears at 3670 cm^{-1} in Fig. 2, curve A, has a peak near cm^{-1} in Fig. 1. The shift of the 3692 cm^{-1} band to 3670 cm^{-1} upon adsorption of a strongly interacting adsorbate is in the right direction since the most weakly hydrogen bonded silanol groups in the cavity should be the first to interact. However, it is also possible that this small shift is produced by the errors inherent in the mechanical separation.

It has been shown by McDonald[2] that the shift $\Delta\nu_{OH}$ in the frequency of the OH stretching fundamental which occurs when molecules are adsorbed varies with the degree of surface coverage. For example, when N_2 is adsorbed on silica at -190°C, the shift observed at an N_2 pressure of 4.85 mm is 27 cm^{-1} as compared with a shift of 34 cm^{-1} when the N_2 pressure is 47.3 mm.[2] McDonald[3] has suggested that this dependence on surface coverage indicates that at low coverage each adsorbate molecule interacts with several surface hydroxyl groups.

An alternate possibility is that the interaction is one-to-one at low coverage, but that, as the surface becomes more crowded, each hydroxyl suffers additional perturbations from its neighboring adsorbate molecules. In either case, it is necessary to establish a standard method for comparing frequency shifts. One possibility is an extrapolation of a plot of $\Delta\nu_{OH}$ vs f, where f is the fraction of the free OH groups which are interacting with the adsorbate. The method for obtaining values of f is discussed in the following section. Plots of this type for the methylbenzenes are linear as shown in Fig. 3. The linearity introduces an additional problem, that of defining the direction in which the extrapolation should be made. McDonald's suggestion concerning the reason for the variation with coverage would necessitate extrapolation to $f=1$, while the alternate possibility offered here would require an extrapolation to $f=0$.

[6] W. K. Hall (unpublished data).

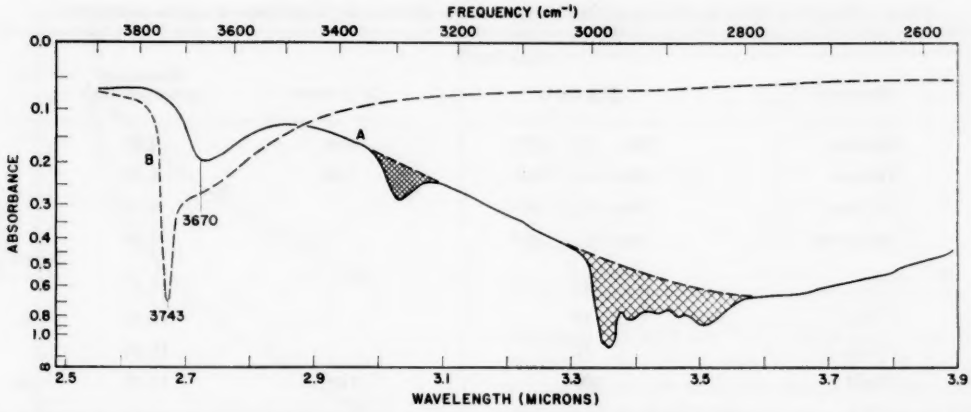

FIG. 2. Interaction of diethylamine with surface silanol hydroxyl groups. (A) 21 mm of diethylamine adsorbed on the Cabosil wafer; (B) wafer degassed at 450°C prior to the diethylamine adsorption. Cross-hatched areas are absorption bands of the diethylamine.

Both extrapolations were performed. The resulting $\Delta\nu_{OH}$ values are tabulated in Table I. The absolute magnitudes are different, but since the $\Delta\nu_{OH}$ vs f curves are nearly parallel, the relative shifts seem to be preserved. There is no basis for eliminating either of the extrapolations. The measurements of other workers, where available, are also listed in Table I.

The chloromethane data were obtained before the importance of coverage was fully realized and are not extensive enough for the construction of a plot similar to Fig. 3. However, most of the data were taken at low f values, i. e., between $f=0.1$ and 0.2. Therefore, because of the near parallelism of the plots for the methylbenzenes, it is felt that the shifts obtained at low coverage for the chloromethanes should provide a reasonable representation of the relative strengths of interaction with the surface silanol OH group. The lowest observed $\Delta\nu_{OH}$ values are given in Table I.

The shapes of the hydrogen bonded OH bands are given for both sets of compounds in Fig. 4. They were mechanically separated using the assumption that the groups producing the 3692-cm^{-1} band do not interact with the adsorbate at low surface coverage and therefore have constant intensity. The resulting symmetrical shape of the bands in Fig. 4 lends support to this assumption.

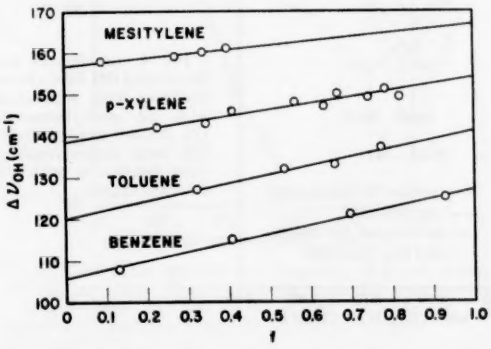

FIG. 3. Dependence of the frequency shifts of the methylbenzenes upon the degree of coverage.

The nature of the interaction between surface silanol groups and adsorbate molecules which causes the shift in the OH stretching frequency is hydrogen bonding.[1-5] The proton acceptor in a hydrogen bonded system generally has a nonbonded lone electron pair through which the interaction is established.[7] Recently, the similarity between the frequency shift of the OH stretching vibration due to hydrogen bonding and that which occurs in the stretching frequency of halogen molecules involved in charge-transfer interactions has been pointed out.[8-10] These authors classify hydrogen bonding as a special case under general charge-transfer interactions.[11] If this is the case, then the strength of the interaction of a series of donor molecules with a given acceptor should be related to the ionization potential of the donors.[12,13] Since the frequency shift is a measure of the strength of the interaction,[14,15] a plot of the adsorbate ionization potential (I) vs the frequency shift should reflect this relationship. Figures 5 and 6 are plots of $\Delta\nu_{OH}$ vs I for the two series, methylbenzenes and chloromethanes. In Fig. 5, both sets of frequency shifts are plotted for the methylbenzePhotoiones, nization potentials were

[7] L. Paoloni, J. Chem. Phys. **30,** 1045 (1959).
[8] W. B. Person, R. E. Humphrey, W. A. Deskin, and A. I. Popov, J. Am. Chem. Soc. **80,** 2049 (1958).
[9] W. B. Person, R. E. Humphrey, and A. I. Popov, J. Am. Chem. Soc. **81,** 273 (1959).
[10] W. B. Person, R. E. Erickson, and R. E. Buckles, J. Am. Chem. Soc. **82,** 29 (1960).
[11] R. S. Mulliken, J. Am. Chem. Soc. **74,** 811 (1952).
[12] H. McConnell, J. S. Ham, and J. R. Platt, J. Chem. Phys. **21,** 66 (1953).
[13] S. H. Hastings, J. L. Franklin, J. C. Schiller, and F. A. Matsen, J. Am. Chem. Soc. **75,** 2900 (1953).
[14] R. M. Badger, and S. H. Bauer, J. Chem. Phys. **5,** 839 (1937).
[15] R. M. Badger, J. Chem. Phys. **8,** 288 (1940).

TABLE I. Frequency shifts of the surface silanol OH stretching vibration in the presence of various adsorbates.

Adsorbate	$\Delta\nu_{OH}$ (cm^{-1}) This work		$\Delta\nu_{OH}$ (cm^{-1}) Other work	Ionization potential[f] (ev)
Benzene	106[a]	127[b]	110[c]	9.25
Toluene	120[a]	141[b]	120[d]	8.82
p-Xylene	139[a]	154[b]		8.45
Mesitylene	156[a]	166[b]		8.39
CCl_4	40			11.47
$CHCl_3$	48			11.42
CH_2Cl_2	72			11.35
CH_3Cl	106		110[e]	11.28

[a] These values obtained by extrapolation to $f=0$.
[b] These values obtained by extrapolation to $f=1$.
[c] Reference 2.
[d] A. N. Sidorv, Doklady Akad. Nauk S.S.S.R. **95**, 1235 (1954).
[e] Reference 4.
[f] References 16 and 17.

used for the correlation.[16,17] It should be pointed out that the correlation between I and $\Delta\nu_{OH}$ is not the same for both series, that is, one cannot make a single plot of all the low coverage data. However, it is doubtful whether this could be expected since there are two different types of donor electrons involved in the interactions; viz., the aromatic pi electrons in one case and probably the chlorine lone pair electrons in the other.

These correlations provide evidence that the hydrogen bonding interaction between surface silanol groups and the methylbenzene or chloromethane adsorbate molecules is of the charge-transfer type with the adsorbate molecules acting as the electron donors and the surface silanol OH's acting as the electron acceptors. The shift to lower frequency of the surface silanol OH stretching vibration is then presumably the result of an increase in charge in the OH bond.

In order to provide a clearer picture of the nature of the interaction, the frequency shifts of a typical carbinol, *t*-butyl alcohol, interacting with the same methylbenzene series were measured. Table II is a tabulation of the $\Delta\nu_{OH}$ values, and Fig. 7 is a plot of $\Delta\nu_{OH}$ vs ionization potential. A comparison with the results given in Table I and Fig. 5 is quite informative. The magnitudes of the shifts of surface silanol OH are roughly four times as large as the corresponding carbinol shifts. In fact, there is essentially a linear relationship between the carbinol $\Delta\nu_{OH}$ and each of the surface silanol $\Delta\nu_{OH}$ sets.

It is interesting to discuss the frequency of the free,

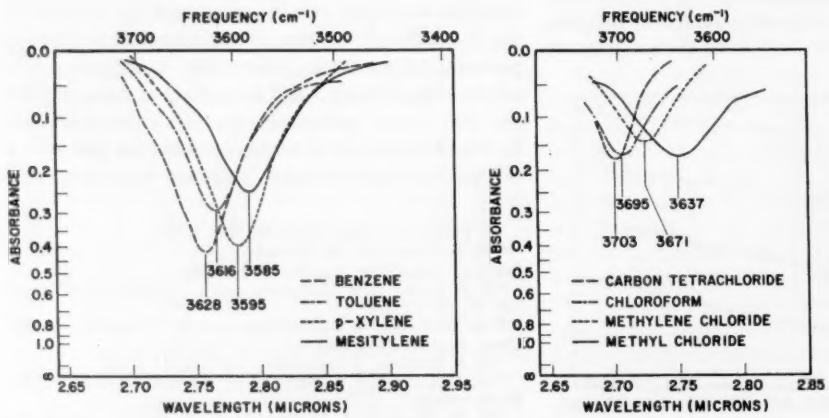

FIG. 4. (a) Bonded surface silanol OH band shapes resulting from interaction with the methylbenzenes. (b) Bonded surface silanol OH band shapes resulting from interaction with the chloromethanes.

[16] K. Watanabe, J. Chem. Phys. **26**, 542 (1957).
[17] W. C. Price, R. Bralsford, P. V. Harris, and R. G. Ridley, Spectrochim. Acta **14**, 45 (1959).

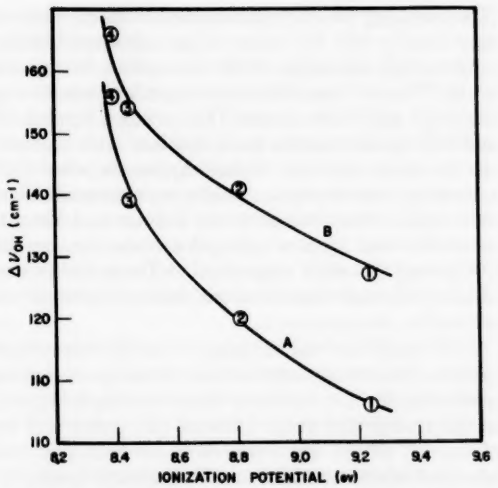

FIG. 5. Correlation between the frequency shifts of surface silanol OH stretching vibration and the ionization potentials of the methylbenzene adsorbates. (1) benzene; (2) toluene; (3) *p*-xylene; (4) mesitylene.

i.e., nonhydrogen bonded, surface silanol groups in the light of the above considerations. The frequency of the free OH stretching vibration of surface silanol groups is higher (3743 cm^{-1}) than that observed (in nonpolar solvents) in molecular silanols[18] (~3684 cm^{-1})[19] or

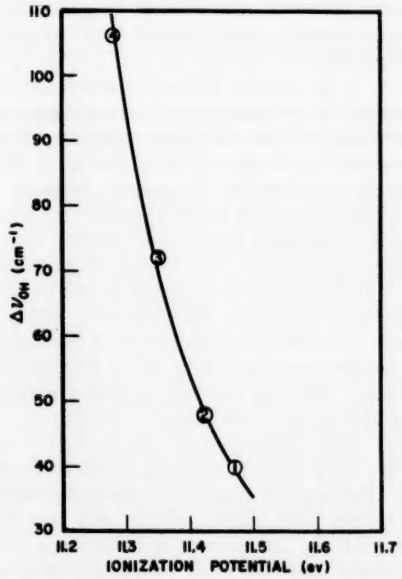

FIG. 6. Correlation between the frequency shifts of surface silanol OH stretching vibration and the ionization potentials of the chloromethane adsorbates. (1) carbon tetrachloride; (2) chloroform; (3) methylene chloride; (4) methyl chloride.

[18] The term molecular sinanol denotes the SiOH group in individual molecules such as in *t*-butyl silanol.

[19] R. West and R. H. Baney, J. Am. Chem. Soc. **81,** 6145 (1959).

TABLE II. Frequency shifts of the OH stretching vibration of *t*-butyl alcohol produced by interaction with the methylbenzenes.

Donor	ν_{OH} (cm^{-1})	$\Delta\nu_{OH}$ (cm^{-1})
CCl_4	3618	...
Benzene	3591	27
Toluene	3587	31
p-Xylene	3578	40
Mesitylene	3574	44

carbinols (~3614 cm^{-1}).[19,20] West and Baney[19] have suggested that an increased positive character of the proton causes the molecular silanol OH stretching frequency to be higher than that in carbinols. There is considerable experimental evidence, both chemical and physical, which indicates that the proton in molecular silanols has a stronger positive character than a carbinol proton.[19] The increased positive charge on the proton is thought to be the result of pi bonding between one of the unshared electron pairs on the oxygen and an unoccupied *d* orbital of the silicon which produces a shift in the OH bonding electrons toward the oxygen.[19] Overlap integral calculations[22] have shown this type of bonding to be probable, especially when the *d* orbitals are ultimate orbitals as in silicon. The experimental Si—O and Si—X, where X is a halogen, bond distances are

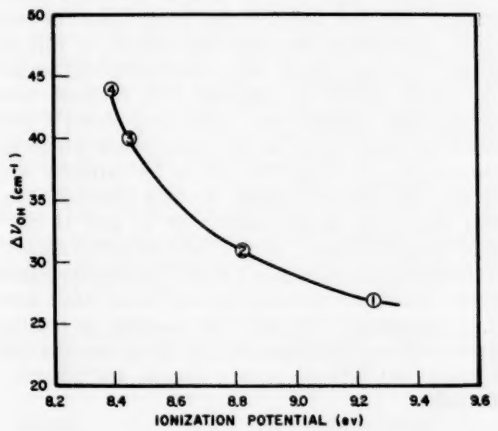

FIG. 7. Correlation between the frequency shifts of the OH stretching vibration in *t*-butyl alcohol and the ionization potentials of the interacting methylbenzenes. (1) benzene; (2) toluene; (3) *p*-xylene; (4) mesitylene.

[20] This frequency is the average of the values reported by West and Baney[19] for four carbinols which were identical, except for the replacement of C by Si, to the four silanols which were used to determine the silanol OH stretching frequency. The value lies within the range 3610–3630 given by Jones and Sandorfy.[21]

[21] R. N. Jones and C. Sandorfy, *Technique of Organic Chemistry* (Interscience Publishers, Inc., New York, 1956), Vol. 9, p. 417.

[22] D. P. Craig, A. Maccoll, R. S. Nyholm, L. E. Orgel, and L. E. Sutton, J. Chem. Soc. **1954,** 332.

shorter than those calculated using the covalent radii, thus indicating that these bonds have a partial double bond character.[22]

The difference between the frequency of the stretching vibration in surface silanol groups and carbinol groups is approximately twice that observed between molecular silanol and carbinol groups. Thus, the protons in surface silanol groups must have an even greater positive character than those in molecular silanol groups. A possible explanation is that there is increased delocalization of the oxygen lone pair electrons through pi bonding with the vacant *d* orbitals of both the bonded silicon atom of the surface silanol group and an adjacent nonbonded silicon atom. This delocalization can be described by the resonance

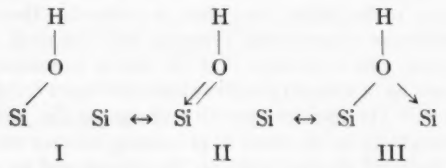

In molecular silanols only structures I and II are important, while in surface silanols there is in addition to I and II, a possible contribution from III. This increased delocalization of the lone pair electrons of oxygen would cause a larger shift of the bonding electrons toward the oxygen of the OH in surface silanol groups thereby makin the proton more positive than in molecular silanol groups. Thus, the surface silanol group should be more acidic than either the molecular silanol or carbinol groups. The much larger $\Delta\nu_{OH}$ values observed for surface silanol groups as compared with carbinols have already been pointed out. West and Baney[19] have shown the $\Delta\nu_{OH}$ values for molecular silanol groups are also considerably larger than those for carbinols with the same donors. For example, the $\Delta\nu_{OH}$ values observed with mesitylene as the donor were 47 and 71 cm^{-1}, respectively, for *t*-butyl alcohol[17] and trimethyl silanol,[17] as compared to a minimum 156 cm^{-1} for surface silanol groups. Thus, the observed ν_{OH} and $\Delta\nu_{OH}$ values seem to be consistent with both the possible pi bonding between silicon and oxygen and the charge-transfer type of interaction between surface silanols and adsorbate molecules.

Intensities

Yates and Folman[4,5] have measured the optical densities of the perturbed surface silanol OH stretching, and the CH and NH stretching vibrations of ammonia, acetone, and methyl chloride molecules adsorbed on the surface of porous glass. They find that the optical densities of the hydrogen bonded surface silanol OH vibration vary linearly with the volume of gas adsorbed. However, when ammonia is the adsorbate, the straight line does not go through the origin as it does with methyl chloride. On the other hand, the optical density of the 3730-cm^{-1} NH stretching vibration of adsorbed ammonia does not vary linearly with the volume of gas adsorbed, but does pass through the origin, while the optical density plot of the 2970-cm^{-1} band of methyl chloride passes through the origin and is also linear. The hydrogen bonded OH and NH optical density plots obtained with ammonia the adsorbate exhibit marked hysteresis when both adsorption and desorption points are measured. These observations were interpreted by Folman and Yates to mean that two types of adsorption sites exist, one the OH group, the other unspecified.[4,5] These results were obtained through the use of simultaneous spectral and adsorption measurements.

McDonald[3] has shown, using a Cabosil-water vapor system, that the apparent amount (from spectral measurements) of water adsorbed when the sample is placed in the undispersed beam between the source and entrance slit of the spectrometer is one-fourth of that adsorbed when the same sample is placed in the dispersed beam between the exit slit and the detector. This difference is due to heating of the sample by the absorbed radiation.[3]

The nature of the double beam infrared spectrophotometer used in this work was such that the dispersed sample beam could not be physically separated from the dispersed reference beam. Therefore, all spectral measurements were necessarily made in the undispersed sample beam. In the light of McDonald's findings, it was decided to measure relative intensities from spectral data alone, rather than to attempt quantitative intensity measurements which require both spectral and adsorption data.

Since it is the relative intensities which are sought, and because the interaction with the surface is weak, the intensities of the adsorbate molecule vibrations were assumed to be directly proportional to those of comparable vibrations in the gaseous molecule. Most of the current theories of infrared solvent effects express the difference between gaseous and solution intensities as a function of the refractive indices of the solute and solvent.[23] It is therefore felt that the intensities of physically adsorbed molecules will be directly proportional to the solution intensities since a series of molecules such as the alkylbenzenes have very nearly identical refractive indices. Thus, the constant of proportionality for each member of the series should be roughly the same. However, small differences in the constants are expected due to the effect of the weak interaction with the surface. Therefore, the integrated absorption coefficient for the carbon tetrachloride solution was used in conjunction with the area under the absorbance curve of the adsorbate (over the same wavelength interval) to calculate the apparent surface concentration in the form of a product of the concentration (C) times the path length (L). Plots of CL vs f for each of the alkylben-

[22] A. D. Buckingham, Proc. Roy. Soc. (London) **A248**, 169 (1958) and references therein.

zenes should be a series of lines of different slope passing through the origin.

The values of f, the fraction of free surface OH groups which are interacting, were calculated by considering the free band, i.e., the 3743-cm^{-1} band in Fig. 1, to be symmetrical and making the assumption that the 3692-cm^{-1} band did not change in intensity. The latter assumption made it possible to subtract out the contribution to the area from the 3692-cm^{-1} band. Thus, the f values were calculated as the ratio of the difference between the initial area under the 3743-cm^{-1} band and the area resulting after each adsorption to the initial area.

It is surprising that the plots of CL vs f for the alkylbenzenes are superimposed upon one another within experimental error as shown in Fig. 8. This implies that the interaction with the surface silanol groups, because it is relatively weak, has practically no effect on the vibrational intensities of the adsorbate molecules.

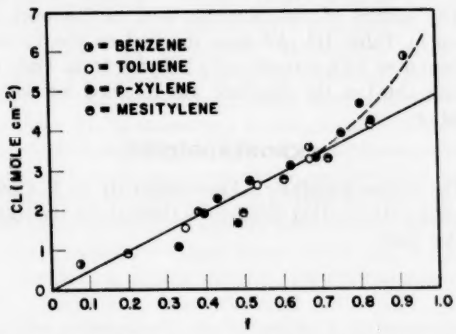

FIG. 8. Relationship between the relative surface concentration of the methylbenzene adsorbates and the fraction of surface silanol OH groups which are interacting.

The relationship between f and CL is essentially linear. However, there seems to be some curvature at the higher values of f. The data in that region are too scanty to allow a judgment as to whether the curvature is real or a result of experimental errors. The values of f used for the plot of $\Delta\nu_{OH}$ vs f in Fig. 3 were obtained from the smooth curve of Fig. 8.

In the light of the findings of Folman and Yates,[4,5] the fact that the curve of Fig. 8 passes through the origin seems significant. Apparently, the intensities of the CH stretching vibrations of the methylbenzenes adsorbed on amorphous silica exhibit the same behavior as the intensity of the CH stretching vibration of CH_3Cl adsorbed on porous glass. Further comment cannot be made until more quantitative intensity data are available.

Experimental

The spectra were measured on a Perkin-Elmer model 21 spectrophotometer which was equipped with a lithium fluoride prism. The atmospheric water vapor

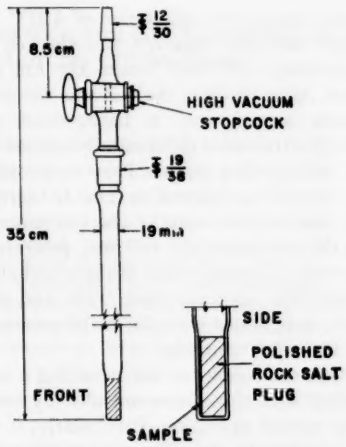

FIG. 9. Quartz cell for measuring the spectra of adsorbed molecules.

bands were used for calibration. The cell, which was constructed of quartz, had an end section of square crosssection approximately 10×10 mm on the inside. Details are given in Fig. 9. A polished rock salt plug approximately 9.0×9.0×25 mm fits into this end section. The amorphous silica (Cabosil) sample was a rectangular section approximately 9×23 mm cut from a 1-in. diameter pressed disk. The thickness of the disks were 0.1–0.2 mm. They were prepared by pressing Cabosil powder in an ordinary KBr pellet press at a pressure of 1000–2000 psi. The rectangular silica sample was inserted between the rock salt plug and quartz cell body. This technique provided a cell of very short optical path length (0.5–1.0 mm). Consequently, there was negligible absorption by gaseous molecules at the pressures used in these experiments.

The technique used for measuring a spectrum was as follows. The cell was attached to the vacuum system and evacuated to a pressure of 10^{-4} mm Hg. Roughly one-half an atmosphere of O_2 was admitted and

TABLE III. Source of the chemicals used in this work.

Chemical	Source
Benzene	Baker analyzed reagent
Toluene	Phillips pure grade
p-Xylene	Phillips pure grade
Mesitylene	API standard sample
Carbon tetrachloride	Fisher "certified reagent"
Chloroform	Fisher "spectro-analyzed"
Methylene chloride	Fisher "spectro-analyzed"
Methyl chloride	Matheson Company
t-Butyl alcohol	Eastman Kodak white label

the cell was heated to a maximum of 450°C for 1 hr. The oxygen was then removed and the cell pumped at approximately $10^{-5}-10^{-6}$ mm Hg for an additional hour. After cooling, the cell was removed from the vacuum system and a background spectrum (from 2.0–3.9 μ) recorded differentially against a similar cell which had no silica sample. Prior to recording each spectrum, the cell was allowed to come to thermal equilibrium in the sample beam of the instrument. After obtaining the spectrum, the cell was returned to the vacuum system, pumped, a dose of the adsorbate added, and the spectrum again recorded. This, and all subsequent doses, were added with the initial pressure in the system at $10^{-3}-10^{-4}$ mm Hg.

The instrument conditions for recording a spectrum were identical with those recommended by the manufacturer for normal operation. Particularly, it was unnecessary to widen the slits. The computed spectral slitwidths were approximately 4.0 cm^{-1} in the 3700 cm^{-1} region and 2.4 cm^{-1} in the 2950 cm^{-1} region.

The spectra were recorded using an expanded wavelength scale of 20 cm/μ for the chloromethanes and 80 cm/μ for the methylbenzenes. The spectra were scanned at a rate approximately 15 min/μ. The areas of bands were measured directly on an automatic table-top integrator which has previously been described.[24] The integration was carried out over the entire multiple-band system in the CH stretching region to avoid separation problems. Beer's law plots for each of the methylbenzenes in carbon tetrachloride were linear.

The spectra of tertiary butyl alcohol interacting with each of the methylbenzenes were measured in carbon tetrachloride solution. The alcohol concentration (approximately 0.01 M) was such that no self-association was detectable. The aromatic concentration was approximately 1 M. Each spectrum was recorded differentially against an equal concentration of a carbon tetrachloride solution of the corresponding methylbenzene using matched 10-mm quartz cells. The frequency shifts were measured from the frequency of the free OH band in the carbon tetrachloride solution. Thus, it was necessary to make the assumption that the interaction between the carbon tetrachloride and the carbinol was small and constant and, therefore, negligible. The frequency shifts were measured by assuming the residual unbonded OH to be symmetrical and mechanically separating the bands by replotting.

The sources of the chemicals used in this work are given in Table III. All were distilled on the vacuum system over P_2O_5 through a P_2O_5 drying train. Only the middle third of the distillate was retained for the adsorption.

ACKNOWLEDGMENT

The author gratefully acknowledges Dr. G. F. Crable for many stimulating discussions throughout the course of this work.

[24] R. H. Hughes and R. J. Martin, Symposium on Composition of Petroleum Oils, Special Publication No. 224 ASTM.

Long-Range Nuclear Magnetic Shielding in Molecules and the Anisotropy in the Magnetic Susceptibility of a Carbon-Carbon Single Bond

JEREMY I. MUSHER

Lyman Laboratory, Harvard University, Cambridge 38, Massachusetts

(Received February 9, 1961)

A method is discussed for obtaining quantitative measurements of long-range NMR shielding effects in molecules based on the theory of Ramsey as extended by McConnell. These effects are shown to arise principally from the diamagnetic part of the magnetic susceptibility of the individual bonds when the origin of coordinates is taken at the geometric center of the bond. Application is made to saturated hydrocarbon alcohols for which the only long-range shielding contributions come from tetrahedral carbon-carbon bonds. From high-resolution NMR measurements of tertiary protons on carbocyclic molecules the existence of these effects is verified and the magnitude of the magnetic anisotropy on the individual bonds causing such effects is determined.

1. INTRODUCTION

RECENTLY several authors have been interested in the information available from studies of nonlocal or "long-range" contributions to the magnetic shielding of a nucleus. In particular, McConnell[1] adapted Ramsey's expression[2,3] to give the shielding contribution for a "long-range" bond and showed how this was dependent on the anisotropy in the magnetic susceptibility of the bond. McConnell[1] and Pople[4] have studied benzene and acetylene, respectively, and have indicated how the unusual chemical shifts of their protons can be attributed to calculated magnetic anisotropies. Bothner-By and Naar-Colin[5,6] and Narasimhan and Rogers[7] have studied the reverse problem: the determination of bond anisotropies from chemical shift data (and available calculations), the former for a carbon-carbon bond and the latter for a carbonyl bond. The latter paper, which we first heard of after this work was completed, is the more extensive attempt to give quantitative experimental susceptibility anisotropies. However, these authors could not obtain conclusive results because of the relative closeness of the "long-range" carbonyl bond to the protons which it shielded. The current interest in long-range shielding contributions is emphasized by the inclusion of a chapter on "diamagnetic anisotropy" in Jackman's recent book on NMR.[8]

In this paper we study the variation of the shielding of a proton through a series of nearly identical molecules as a function of the change in the long-range molecular configuration. From the protons' relative chemical shifts and the known molecular geometries we determine the anisotropy in the magnetic susceptibility of a carbon-carbon single bond based on McConnell's dipolar expansion. In doing this we show experimentally that long-range shielding does exist and that it is correctly explained to lowest order by the McConnell expression.

2. THEORY

Ramsey[2,3] has derived an expression for the magnetic shielding of a nucleus in a molecule due to contributions from all the electrons of the molecule. The shielding tensor $\boldsymbol{\sigma}_N$ is defined by

$$\mathbf{H}_{\text{eff}}{}^N = (\mathbf{1} - \boldsymbol{\sigma}_N) \cdot \mathbf{H}_{\text{ext}}, \tag{1}$$

which relates the effective magnetic field at nucleus N to the externally applied static field. If the nuclei of a given molecule are in a fixed orientation λ, and if $|\, n \,\rangle$ are the complete set of total electronic wave functions for all orientations of the system while $|\, o\lambda \,\rangle$ is in the ground-state wave function for the orientation λ, then $\boldsymbol{\sigma}^\lambda$ is given by[2]

$$\begin{aligned}\boldsymbol{\sigma}^\lambda = (e^2/2mc^2)\, \langle 0\lambda \mid \sum_k \{ \mathbf{1}[\mathbf{r}_k{}^0 - \mathbf{R}_{kl}] \cdot \mathbf{r}_k{}^0 \\ - [\mathbf{r}_k{}^0 - \mathbf{R}_{kl}]\mathbf{r}_k{}^0 \} / \mathbf{r}_k{}^{03} \mid 0\lambda \,\rangle \\ - 4\ \mathrm{Re} \sum_n (E_n - E_0)^{-1} \langle 0\lambda \mid \sum_k \mathbf{m}_{k0}{}^0 / \mathbf{r}_k{}^{03} \mid n \,\rangle \\ \times \langle n \mid \sum_k \mathbf{m}_{kl}{}^0 \mid 0\lambda \,\rangle, \end{aligned} \tag{2}$$

where we have dropped the subscript N. The $\mathbf{r}_k{}^0$ denotes the radius vector of the kth electron from nucleus N as the origin, the $\mathbf{R}_{kl}$'s are arbitrary gauge-dependent factors,

$$\mathbf{m}_{k0} = -(e\hbar/2mci)\, \mathbf{r}_k{}^0 \times \boldsymbol{\nabla}_k$$

$$\mathbf{m}_{kl} = -(e\hbar/2mci)[\mathbf{r}_k{}^0 - \mathbf{R}_{kl}] \times \boldsymbol{\nabla}_k,$$

* This work was supported in part by a fellowship, CF-9935, from the National Cancer Institute, Public Health Service, and by the joint program of the Office of Naval Research and the U. S. Atomic Energy Commission.

[1] H. M. McConnell, J. Chem. Phys. **27,** 226 (1957).
[2] N. F. Ramsey, Phys. Rev. **78,** 699 (1950).
[3] N. F. Ramsey, Phys. Rev. **86,** 243 (1952).
[4] J. A. Pople, Proc. Roy. Soc. (London) **A239,** 541, 550 (1957).
[5] A. A. Bothner-By and C. Naar-Colin, J. Am. Chem. Soc. **80,** 1728 (1958).
[6] A. A. Bothner-By and C. Naar-Colin, Ann. N. Y. Acad. Sci. **70,** 833 (1958).
[7] P. T. Narasimhan and M. T. Rogers, J. Phys. Chem. **63,** 1388 (1959).
[8] L. M. Jackman, *Applications of Nuclear Magnetic Resonance Spectroscopy in Organic Chemistry* (Pergamon Press, New York, 1959).

m denotes the mass of the electron, and the sum is over all the k electrons of the molecule. The first term is often called the Lamb term since it reduces to the value calculated by Lamb for single atoms, and is also called the diamagnetic term. The second term has been called the high-frequency or paramagnetic term. For the same reason that the two terms contributing to the magnetic susceptibility are not uniquely separable[9] the same is true of the terms contributing to $\mathfrak{d}^\lambda$. We shall, however, assign the gauge and the coordinate system in such a way as to simplify the expression for $\mathfrak{d}^\lambda$ and consider it to be a sum of a Lamb term $\mathfrak{d}_\lambda{}^L$ and a high-frequency term $\mathfrak{d}_\lambda{}^{HF}$ defined within that gauge. In the case of distant electrons, these two shielding terms can be shown to arise from the interaction of $\mathfrak{y}$, the magnetic moment of N with an induced diamagnetic moment and with an induced paramagnetic moment, respectively. These moments, which are, respectively, of negative and positive sign (with respect to $\mathbf{H}_{ext}$) result from the scalar product of $\mathbf{H}_{ext}$ with the diamagnetic and second-order paramagnetic terms[10] of the magnetic susceptibility χ^D and χ^P. $\mathfrak{d}_\lambda{}^L$ and $\mathfrak{d}_\lambda{}^{HF}$, however, can be of either sign corresponding to different orientations of the susceptibility tensor (relative to $\mathfrak{y}$) which in the axially symmetric case (again for distant electrons) is a dipole and transforms as $P_2(\cos\theta)$. Thus we do not call $\mathfrak{d}_\lambda{}^L$ diamagnetic nor do we call $\mathfrak{d}_\lambda{}^{HF}$ paramagnetic.

We consider a proton N located in a rigid organic molecule containing A other nuclei[11] $\{a\}$ and S electrons $\{s\}$ and neglect any effects from electrons located on other molecules, i.e., all solvent effects are neglected. We now subdivide the collection of electrons $\{s\}$ into those tightly bound to nucleus N, $\{s_N\}$, those tightly bound to the A other nuclei $\{a\}$,

$$\sum_{a=1}^{A}\{s_a\}$$

and those remaining, $\{s_B\}$. The use of the term "tightly bound" follows Ramsey[3] and signifies that for these electrons the potential is approximately spherically symmetric about the nucleus in question and that the density of these electrons at any other nucleus is small. If the molecule under study is a saturated hydrocarbon all those electrons not tightly bound to a nucleus are involved in bonding. To a certain approximation, two electrons may be assigned to each bond with very small overlap existing between electrons on different bonds. The electrons $\{s_B\}$ may therefore be exhaustively assigned pairwise to two-element sets $\{s_f\}$ for all the F single bonds $\{f\}$ in the hydrocarbon so that

$$\{s_B\}=\sum_{f=1}^{F}\{s_f\}.$$

We now define the gauge for all the electrons except those in $\{s_B\}$ such that when $k\in\{s_a\}$, $\mathbf{R}_{kl}=\mathbf{R}_a$, the radius vector for the nucleus a, and when $k\in\{s_N\}$, $\mathbf{R}_{kl}=0$. By doing this we eliminate the terms of $\mathfrak{d}_\lambda{}^{HF}$ arising from all the tightly bound electrons[3] (or we transfer whatever contribution they might have made into that of a spherically symmetric distribution about the $\mathbf{R}_a$ and $\mathbf{R}_N=0$ as the origins); $\mathfrak{d}^\lambda$ reduces to

$$\mathfrak{d}^\lambda=\mathfrak{d}_\lambda{}^L\{s_N\}+\sum_{a=1}^{A}\mathfrak{d}_\lambda{}^L\{s_a\}+\sum_{f=1}^{F}(\mathfrak{d}_\lambda{}'^L\{s_F\}+\mathfrak{d}_\lambda{}'^{HF}\{s_f\}). \tag{3}$$

It should be noted that the separation of $\mathfrak{d}_\lambda{}'^{HF}\{s_B\}$ into $\sum_f\mathfrak{d}_\lambda{}'^{HF}\{s_f\}$ which is the sum of the contributions of individual bonds depends on the validity of the assumption that these electrons do not have appreciable overlap, or are in a sense, therefore, "tightly bound" to the respective bonds, for otherwise there would be cross terms between the $\mathbf{m}_{k0}{}^0$'s from electrons involved in different bonds. This property of additivity for the contributions from the individual bonds is somewhat justified by the work of Pascal on magnetic susceptibilities[12] and should be valid in all types of bonds except where conjugation or ring currents are possible[13] Thus the only cross terms in $\mathfrak{d}_\lambda{}'^{HF}$ will arise from the pair of electrons in each bond f

$$\mathfrak{d}_\lambda{}'^{HF}\{s_f\}=\mathfrak{d}_\lambda{}'^{HF}(1_f,2_f)=-4\,\mathrm{Re}\sum_n(E_n-E_0)^{-1}$$
$$\times\{\langle 0f\lambda\,|\,\mathbf{m}_{1_f}{}^0/r_{1_f}{}^{03}+\mathbf{m}_{2_f}{}^0/r_{2_f}{}^{03}\,|\,nf\rangle$$
$$\times\langle nf\,|\,\mathbf{m}_{1_f}{}^0+\mathbf{m}_{2_f}{}^0\,|\,0f\lambda\rangle\}, \tag{4}$$

where there is still an arbitrariness in the gauge of the vector potential and the ground- and excited-state wave functions refer only to the two electron system of $\{s_f\}$. For the pair of electrons in each bond f we define the gauge such that $\mathbf{R}_{kl}=0$ for $k\in\{s_f\}$ for all $f\in\{f\}$. We now transfer our vectors $\mathbf{r}^0$ and $\mathbf{m}^0$ to the coordinate system of the electrical center of gravity 0_f, a distance $\mathbf{R}_f$ from nucleus N of that bond. We define the radius and angular momentum operators without the superscript zero for these electrons as referring to

[9] As is shown by Van Vleck[10] the separation of the magnetic moment (or the susceptibility) into diamagnetic and paramagnetic terms is not unique since it depends on the coordinate system and hence the gauge employed; the sum of the two terms is of course the same in any gauge or coordinate system. Such assignments of these terms however are in fact instructive in that they provide useful classical analogs despite their nonuniqueness. The two terms can be of the same order of magnitude despite the perturbation theory nomenclature.

[10] J. H. Van Vleck, *The Theory of Electric and Magnetic Susceptibilities* (Oxford University Press, New York, 1932).

[11] The notation $\{x\}$ is an abbreviation for the set or collection of X elements $\{x_1, x_2, \cdots x_X\}$. The sum of sets

$$\sum_{i=1}^{I}\{x_i\}$$

signifies the set of all the elements belonging to all the I sets $\{x_i\}$. $k\epsilon\{s\}$ means that k is an element of the set $\{s\}$. $\{f\}\subset\{g\}$ means that all elements of $\{f\}$ are elements of $\{g\}$.

[12] A. Pacault, Rev. Sci. **86**, 38 (1948).

[13] Although ring currents are in principle possible through the overlap of sp^3 bonds around a saturated cyclohexane ring we have assumed that such effects are negligible. Their existence could be observed by the nonconsistency of the $\Delta\chi$ determined here with a $\Delta\chi$ determined from noncyclic or multicyclic systems.

0_f as origin

$$\mathbf{r}_k^0=\mathbf{r}_k+\mathbf{R}_f$$

$$\mathbf{m}_{k0}^0=\mathbf{m}_{k1}^0=\mathbf{m}_k-(eh/2mci)\mathbf{R}_f\times\nabla_k, \qquad (5)$$

for $k \in \{s_f\}$. It should be noted that this is not the same as setting the gauge $\mathbf{R}_{kl}=\mathbf{R}_f$ for $k \in \{s_f\}$. However this transformation does amount to transferring any contribution from the spherically symmetric (about 0_f) part of the electron distribution within the bond into the $\mathfrak{d}_\lambda^L$ term as well as providing a convenient origin from which to discuss our localized electron pairs.

Following McConnell[1] we consider a bond or electron pair to be at "long range" from N when $(r_k^0)^{-3}$ for $k \in \{s_f\}$ can be adequately approximated by the expansion in $|\mathbf{r}_k|/|\mathbf{R}_f|$ about the origin 0_f,

$$1/(r_k^0)^3=(1/R_f^3)-[(3\mathbf{r}_k\cdot\mathbf{R}_f)/R_f^5]-\tfrac{3}{2}(r_k^2/R_f^5)+\tfrac{15}{2}[(\mathbf{r}_k\cdot\mathbf{R}_f)^2/R_f^7], \qquad (6)$$

and we furthermore for simplicity assume all bonds separated by two bonds from N to satisfy this criterion and take note of the error involved in the few cases for which errors propogated by this assumption might not be small. We then let $\{s_{SR}\}$ be the electrons on the four tetrahedral bonds of the carbon on which the proton is located and let their total shielding contribution be $\mathfrak{d}^\lambda\{s_{SR}\}$, where we do not differentiate between $\mathfrak{d}^L$ and $\mathfrak{d}^{HF}$. By our definition then, this includes all short-range or non-long-range bonds. (This would also include in the case of a fluorine atom the high-frequency term, which here is strictly paramagnetic, arising from the fluorine's bonding p electron and its other four p electrons none of which is "tightly bound.") Following McConnell's calculation *to the lowest order in* $1/R_f$ we get the contribution from each bond f to the shielding tensor which corresponds to the effective field at N due to a dipole of susceptibility χ at R_f;

$$\mathfrak{d}^\lambda\{s_f\}=\mathfrak{d}_\lambda^L\{s_f\}+\mathfrak{d}_\lambda^{HF}\{s_f\}=\frac{2\chi_\lambda^f}{R_f^5}\cdot\left[\frac{\mathbf{1}R_f^2-3\mathbf{R}_f\mathbf{R}_f}{2}\right], \qquad (7)$$

where χ_λ^f is the magnetic susceptibility tensor for an orientation λ given by

$$\chi_\lambda^f=\chi_\lambda\{s_f\}=\chi_\lambda(1_f,2_f)=\chi_\lambda^{Df}+\chi_\lambda^{Pf}$$
$$=-\tfrac{1}{2}(e^2/2mc^2)\langle 0\lambda f|\sum_{k=1_f,2_f}\mathbf{1}r_k^2-\mathbf{r}_k\mathbf{r}_k|0\lambda f\rangle$$
$$+2\sum_n(E_n-E_0)^{-1}\langle 0\lambda f|\sum_{k=1_f,2_f}\mathbf{m}_k|nf\rangle\times\langle nf|\sum_{k=1_f,2_f}\mathbf{m}_k|0\lambda f\rangle. \qquad (8)$$

Thus now the shielding from a single bond is formally divided into terms arising explicitly from the diamagnetic and paramagnetic contributions to the magnetic susceptibility as defined about the (arbitrary) center of gravity of the electron distribution of the bond as an origin.

The total shielding $\mathfrak{d}^\lambda$ is now reduced to a sum of five terms where the primed summation excludes the bonds whose electrons are in $\{s_{SR}\}$

$$\mathfrak{d}^\lambda=\mathfrak{d}_\lambda^L\{s_N\}+\mathfrak{d}_\lambda\{s_{SR}\}+\sum_{a=1}^{A}\mathfrak{d}_\lambda^L\{s_a\}+\sum_{f=1}^{A}{}'(\text{dipole field of }\chi_\lambda^{Df})+\sum_{f=1}^{F}{}'(\text{dipole field of }\chi_\lambda^{Pf}). \qquad (9)$$

Since we are interested in nuclear shieldings in molecules in the liquid or gas phase (of small correlation time τ_c), we now average over all orientations λ of $\mathbf{\mu}\cdot\mathfrak{d}^\lambda\cdot\mathbf{H}$ and get the zz component of the average value of $\mathfrak{d}^\lambda$, i.e., the average value of the zz component of $\mathfrak{d}^\lambda$, and call this just the scalar $\sigma=\langle\sigma_{zz}{}^\lambda\rangle_{\lambda\lambda}$. It is easy to show that the contributions from all the $\mathfrak{d}^L\{s_a\}$ will be zero[3] as will any spherically symmetric (about 0_f) portion of all $\mathfrak{d}^L\{s_f\}=$(dipole field of χ^{Df}) and $\mathfrak{d}^{HF}\{s_f\}=$(dipole field of χ^{Pf}). The contribution of $\langle\sigma_{zz\lambda}{}^L\{s_N\}\rangle_{\lambda\lambda}$ is just the atomic Lamb term and equals zero for a bare proton. Hence Eq. (9) gives for the total scalar shielding when averaged over all orientations

$$\sigma\equiv\langle\sigma_{zz}{}^\lambda\rangle_{\lambda\lambda}=\sigma\{s_{SR}\}+\sum_f{}'\sigma^L\{s_f\}+\sum_f{}'\sigma^{HF}\{s_f\}, \qquad (10)$$

or the sum of the scalar shielding from short-range bonds with the sum of the scalar terms for all long-range bonds in the molecule.

In our study we consider protons in organic molecules containing only C—C, C—H, C—O, and OH bonds. The sums in (10) can be reduced to sums over the subset $\{g\} \subset \{f\}$ containing G bonds, where $\{f\}-\{g\}$ is the set of all bonds either "short range" or involving a hydrogen atom. (The $\{f\}$ is the set of *all* bonds in the molecule.) As is pointed out by Pople[4] the contribution of $\sigma^{HF}\{s_f\}$ for f involving a hydrogen atom should be small since it depends on the p state contributions to the hydrogenic electron wave function.[14] This is, however, an approximation of limited validity since, for example, in the hydrogen molecule[2] the contribution is rather significant. Thus very close C—H (or O—H) bonds should not be entirely neglected—at 2.5 A by analogy with the H_2 molecule the high frequency contribution should be $\sim 0.02\times10^{-6}$. The argument is the same for σ^L for the hydrogen electron involved in the bond. We will assume that σ^L is also small for the carbon bonding electron although a treatment of atomic susceptibilities instead of bond

[14] This depends on the legitimacy of the one-electron approximation. If we consider the lowest excited state to be a p^* carbon state and an s hydrogen state then the matrix elements will be of the form $\langle p^*+s|\mathbf{m}|p+s\rangle$ which will only have nonzero contributions from $\langle p^*|\mathbf{m}|p\rangle$. For a C—C bond, on the other hand the matrix element will be $\langle p^*+p|\mathbf{m}|p+p\rangle$ which will have four times as many nonzero terms and the shielding is proportional to the matrix elements squared.

TABLE I. $f(R, \theta)$ for specific bonds and protons on a decalin molecule.

C—C bond-g[a]	$f(R,\theta)_g{}^N=(1-3\cos^2\theta_g{}^N)/3R_g{}^{N3}$ N equatorial[b]	N axial[b]
C2—C3	-0.0184×10^{24}	0.0134×10^{24}
C3—C4	0.0048	0.0067
C7—C8 (3eq methyl-C-*i*-propyl)	−0.0025	−0.0010
C8—C9	0.0013	0.0019
C2—Ceq methyl[c]	0.0134	0.0134
C2—Cax methyl	0.0134	−0.0183
C3—Ceq methyl (C3—C7)	−0.0039	−0.0133
C3—Cax methyl	0.0052	0.0208
C4—Ceq methyl (C4—C1O)	−0.0056	−0.0046
C4—Cax methyl	0.0044	−0.0010
4eq C-C-*i*-propyl[d] (C10—C9)	0.0001	−0.0009
4eq C-C-*t*-butyl[e]	0.0019	0.0033
2eq C-C-*i*-propyl	0.0208 −0.0133	0.0056 −0.0133
2eq C-C-*t*-butyl[e]	0.0052	0.0208

[a] Considering structure numbered
[b] Protons at C-1 position.
[c] Signifies bond between 2-C and C of 2-equatorial methyl substituent.
[d] Assuming staggered configuration with neither methyl axial. Values given for each CH—CH_3 bond.
[e] Assuming staggered configuration for axial methyl. For total *t*-butyl contribution add to two *i*-propyl and C4-Ceq methyl bonds.

susceptibilities would properly take this term into account. However, had we considered atomic susceptibilities, such that all sp^3 electrons were identical, no dipolar effect would have been observed since a charge distribution of tetrahedral symmetry has no dipole field. This is so because each proton "sees" only a collection of differently oriented tetrahedral carbon atoms and a collection of (spherically symmetric) hydrogen atoms. The fact that a dipolar effect (below) is observed serves as justification of the neglect of σ^L for the carbon electron used in bonding with the hydrogen. Within the limits of these approximations

$$\sigma=\sigma\{s_{SR}\}+\sum_{g\in\{g\}}\sigma\{s_g\}. \tag{11}$$

In the case of hydrocarbons, Eq. (11) includes the sum of the shielding from short-range bonds and the shielding from all the long-range C—C bonds in the molecule. In this treatment we can take no further advantage of the separation of $\sigma\{s_g\}$ into Lamb and high-frequency parts and hence we no longer distinguish between them.[15]

We will consider specifically the case in which all the protons have similar immediate environments—one C—O and two C—C short-range bonds—so that $\sigma\{s_{SR}\}$ will be the same for all of them. (This involves the neglect of "inductive effects.") The differences between the shieldings in different molecules will then depend only on the anisotropic part of the susceptibility χ_g. Thus the relative shielding σ^* is

$$\sigma^*=\sum_g\sigma\{s_g\}=\sum_g\langle\sigma_{\lambda zz}\{s_g\}\rangle_{Av\lambda}$$
$$=\sum_g\langle(\chi_{\lambda zz}{}^g/R_g{}^3)-[3(\chi_\lambda{}^g\cdot\mathbf{R}_g\mathbf{R}_g)_{zz}/R_g{}^5]\rangle_{Av\lambda}, \tag{12}$$

where $\chi_\lambda{}^g$ is given by Eq. (8) and z is the direction of the applied magnetic field H_{ext}. We shall not however call this phenomenon which contributes to the shielding "diamagnetic anisotropy"[8] nor shall we reverse the sign of the χ's based on this appellation as has been done in the recent literature.[5,6,8]

In principle we can calculate σ_g for any bond based on approximate wave functions,[16] although the fact that the second derivatives of the wave functions are involved might make such calculations very sensitive to the specific choice of wave function. We do not include any such calculations in the present study although comparison of the results of these calculations with the experimental values could provide a sensitive check on the wave functions employed.

We shall consider (as does McConnell[1]) that our bonds are axially symmetric and attempt to observe experimentally the difference between the longitudinal and the transverse components of the magnetic susceptibility. The contribution to the scalar shielding σ from an axially symmetric bond g is of the form

$$\sigma\{s_g\}=(\Delta\chi^g/3R_g{}^3)(1-3\cos^2\theta_g), \tag{13}$$

where θ_g is the angle between $\mathbf{R}_g$ and the symmetry axis of the bond (usually the bond axis itself). The scalar $\Delta\chi^g$ is given by

$$\Delta\chi^g\equiv\chi_L{}^g-\chi_T{}^g, \tag{14}$$

where the scalars χ_L and χ_T are the λ averages of the susceptibility components parallel and perpendicular

[15] I am grateful to Professor C. P. Slichter for several illuminating discussions on this point and on the general problem of the chemical shift. As he rightfully points out it is only when atomic susceptibilities are discussed that separations of the related shielding into Lamb terms and high-frequency terms are useful. In fact, as he suggests, it is generally preferable to treat atoms rather than bonds just because such a separation is possible. However, as we mention above, we would then have to consider the sp^3 electrons involved in different bonds as having different susceptibilities—as they can be looked at as being in different but unknown crystal fields—and thus we can take no advantage of our knowledge of unbonded sp^3 wave functions in determining σ^L and σ^{HF}. Our approach considering bond susceptibilities is, in a sense, justified by the recent work of O. Sinanoğlu [Proc. Natl. Acad. Sci. (to be published)].

[16] For such a calculation on electric polarizabilities, see H. C. Bolton, Trans. Faraday Soc. **50**, 1261 (1954).

to the symmetry axis and are the appropriate combination of terms (from the appropriate excited states) from the quantum-mechanical form of χ^g. Thus our relative scalar shielding at nucleus N reduces to

$$\sigma^* = \langle \sigma_{zz}{}^{*\lambda} \rangle_{\lambda\lambda} = \sum_g (\Delta\chi^g/3R_g{}^3)(1-3\cos^2\theta_g), \quad (15)$$

where again $\{g\}$ represents the set of all bonds in the molecule not "short range" nor containing hydrogen. We shall use this expression below to derive from experimental values of σ^* a value for $\Delta\chi$ for an average carbon-carbon single bond.

3. PROCEDURE AND RESULTS

We wish now to demonstrate experimentally the existence of these long-range contributions to the shielding of a proton (σ_g) in a molecule containing no double or triple bonds or ring currents. At the same time we demonstrate the existence and determine the magnitude of a definite anisotropy in the magnetic susceptibility ($\Delta\chi$) of an average carbon-carbon single bond from which such long-range contributions originate. The argument requires a number of qualifications. We shall first present the argument concisely and then proceed with a detailed account including all the qualifications.

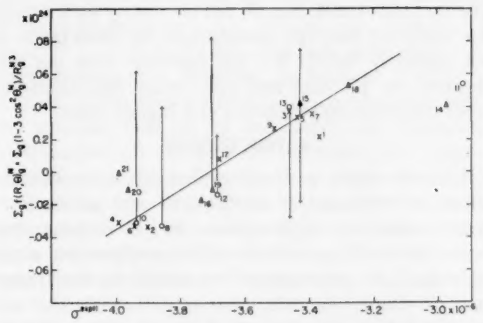

FIG. 1. Plot of $\Sigma_g F(R, \theta)$ vs experimental shielding σ_{exptl} given in units of 10^{-6} relative to internal hexamethyldisiloxane. Points denoted by (X) are those of highest validity (see text).

TABLE II. Angular part of shielding contributions and experimental chemical shifts.

No.[a]	Molecule	$\Sigma_g F(R,\theta)$[b]	σ_{exptl}[c]
1	10-methyl-*trans*-decal-*cis*-2-ol	0.0214	−3.367
2	10-methyl-*trans*-decal-*trans*-2-ol	−0.0334	−3.900
3	*trans*-4-*t*-butylcyclohexanol	0.0371	−3.457
4	*cis*-4-*t*-butylcyclohexanol	−0.0307	−3.987
5	*trans*-4-*i*-propylcyclohexanol	0.0338	−3.433
6	*cis*-4-*i*-propylcyclohexanol	−0.0326	−3.942
7	*trans*-4-methylcyclohexanol	0.0356	−3.388
8	*cis*-4-methylcyclohexanol	−0.0328 (0.0392)	−3.855
9	*cis*-3-methylcyclohexanol	0.0269	−3.505
10	*trans*-3-methylcyclohexanol	−0.0311 (0.0610)	−3.937
11	*trans*-2-methylcyclohexanol	0.0536	−2.917
12	*cis*-2-methylcyclohexanol	−0.0138 (0.0219)	−3.683
13	cyclohexanol	0.0402 (−0.0272)	−3.457
14	2,5-dimethylcyclohexanol-eee[d]	0.0403	−2.970
15	2,5-dimethylcyclohexanol-eae	0.0744 (−0.0177)	−3.425
16	2,5-dimethylcyclohexanol-eea	−0.0177	−3.735
17	2,5-dimethylcyclohexanol-aee	0.0086	−3.677
18	menthol (2-*i*-propyl-5-methylcyclohexanol-eee)	0.0533[e]	−3.275
19	isomenthol (aea)	−0.0106 (0.0819[e])	−3.700
20	neomenthol (eea)	−0.0106	−3.963
21	neoisomenthol (eaa)	−0.0015	−3.992

[a] Numbering as used in Fig. 1.
[b] Value for principal conformation in units of 10^{24} cm^{-3}. Numbers in ( ) corresponds to value for less favorable conformation.
[c] In units of 10^{-6} with respect to internal hexamethyldisiloxane.
[d] Refers to favored conformation of 2-methyl (*i*-propyl), 5-methyl, and 1-hydroxyl respectively thus defining these isomers.
[e] Assuming the *i*-propyl conformation which does not give 1,3-diaxial-methyl-OH interaction.

Table II are plotted in Fig. 1 with $\sigma_N{}^{\text{exptl}}$ as the abscissa and $\sum_g f(R, \theta)_g{}^N$ as the ordinate. A marked linear dependence of these points is found enabling us to conclude that such long-range bonds do contribute to the shielding and that there is an anisotropy in the magnetic susceptibility of the average carbon-carbon single bond. Drawing the line of "best fit" through these points we obtain from its slope the value of

$$\Delta\chi^{C-C} \equiv \chi_L{}^{C-C} - \chi_T{}^{C-C} = 8.3 \pm 1.0 \times 10^{-30} \text{ cm}^3 \text{ molecule}^{-1}$$
$$= 5.0 \pm 0.6 \times 10^{-6} \text{ cm}^3 \text{ mole}^{-1}.$$

All our molecules have identical $\sigma\{s_{SR}\}$ and contain only long-range C—C bonds and bonds containing hydrogen. We can therefore deal with the relative shielding σ^* of Eq. (15), and henceforth we will drop the asterisk. The molecules are assumed to be in the liquid state and the summation is over all long-range C—C bonds g which are assumed to be axially symmetric with magnetic anisotropies of $\Delta\chi^g$. If all C—C bonds in the molecule have the same $\Delta\chi^g$, Eq. (15) becomes

$$\sigma_N = \Delta\chi^{C-C} \sum_g f(R, \theta)_g{}^N. \quad (16)$$

Thus from the calculated values of $\sum_g f(R, \theta)_g{}^N$ and the experimentally observed values of σ_N we can determine $\Delta\chi^{C-C}$. In Table I are listed $f(R, \theta)_g{}^N$ for specific bonds g and nuclei N on a decalin structure and in

The fact that these data do not lie exactly on a straight line indicates that the assumptions we have made are not perfectly valid. We feel however that our conclusions are justified and give every indication that other contributing effects are of a higher order.

4. DISCUSSION

There are many qualitative references to the shielding effects of ethylenes,[8,17] acetylenes[18] and aromatics,[1,19] and theoretical explanations for deviations from expected shieldings as observed in acetylene and simple hydrides,[4] in polynuclear benzenoid hydrocarbons[20] and in simple fluoride compounds[21] with the only complete discussion presented for the H_2 molecule.[2] In all except the last, only relative contributions are examined in order either to justify apparent anomalies in the expected position of resonance or to show the direction and magnitude of the shift of a given series of compounds relative to the position of a single compound. We shall proceed along somewhat similar lines and instead of calculating the total shielding for a given proton we shall determine that part of the shielding arising from bonds separated by at least two bonds from the proton.

NMR shielding contributions to protons from carbon-carbon single bonds are much smaller than from double or triple bonds or from aromatic rings because of the severe localization of charge imposed by the usual sp^3 hybrid bond structure. The problem of contributions to the shielding from C—C single bonds is not only difficult because of their smaller magnitude, however, but because the hindered rotation about the bonds requires information about the populations in the different conformations before an attempt can be made to estimate the contributions to the shielding from the respective distant bonds. Substituted cyclohexanes and decalins provide examples of saturated compounds in fixed conformations—or in two fixed conformations—and we have obtained a series of such molecules of known geometry differing slightly from one another which prove ideal for comparative measurements. The molecules we have chosen are some alkylcyclohexanols and two decalols for which only C—C bonds have to be considered. This is because the hydroxyl group always has the same orientation relative to the proton studied—the one on the same carbon as the OH—and its effect is therefore constant throughout the series. As has been shown[17,22,23] the resonance of this proton lies considerably to low applied field from all the methyl and methylene protons in these molecules and thus can be readily distinguished and its position easily measured relative to an internal standard.

A given cyclohexane molecule possesses two distinct possible geometric structures, called conformations,[24] in equilibrium with each other with an energy barrier low enough so that rapid ring inversion, which occurs by means of simultaneous rotation about all the C—C bonds, can take place at room temperature. Such a molecule possesses two types of substituents (or protons): those perpendicular to the pseudo-plane of the chair (the usual ring structure, appearing as a zig-zag, or chair from end on) called axial (a) and those skew to the ring called equatorial (e). When the ring inverts all axial substituents become equatorial and all equatorial substituents become axial. The molecule is generally in the conformation of lower energy when it has the greater number of substituents equatorial.

For example, the molecule $C_6H_{11}X$ can exist in either of the two possible conformations:

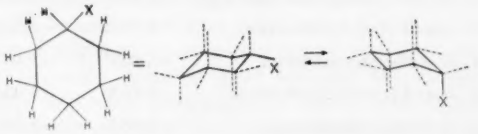

where the equilibrium ratio depends on the nature of the substituent X. If X=H obviously the ratios are 1:1. These structures are based on the assumption that a carbon atom forms four bonds situated at the corners of a regular tetrahedron and that the boat form

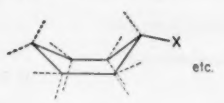

which is the other geometrically possible strainless structure for a six-carbon ring, does not exist to any appreciable extent. All deviations from tetrahedral bond angles are assumed negligible although undoubtedly such deviations exist and must contribute to the spread of the experimental points.

Various attempts have been made to estimate the energy difference in monosubstituted cyclohexanes between the conformation with the substituent axial and the conformation with the substituent equatorial.[25] From these it is possible to assert that all (non*gem*) alkylcyclohexanols ($RC_6H_{10}OH$) in the equilibrium equatorial-equatorial$\rightleftarrows$axial-axial (ee$\rightleftarrows$aa) for the two substituents exist in the conformation ee virtually 100% of the time. The *t*-butyl and *i*-propyl-cyclo-

[17] J. N. Shoolery and M. T. Rogers, J. Am. Chem. Soc. **80,** 5121 (1958).
[18] J. V. Hatton and R. E. Richards, Trans. Faraday Soc. **56,** 315 (1960).
[19] J. S. Waugh and R. W. Fessenden, J. Am. Chem. Soc. **79,** 846 (1957).
[20] H. J. Bernstein, W. G. Schneider, and J. A. Pople, Proc. Roy. Soc. (London) **A236,** 515 (1956).
[21] A. Saika and C. P. Slichter, J. Chem. Phys. **22,** 26 (1954).
[22] R. U. Lemieux, R. K. Kullnig, H. J. Bernstein, and W. G. Schneider, J. Am. Chem. Soc. **80,** 6098 (1958).
[23] J. I. Musher, J. Am. Chem. Soc. **83,** 1146 (1961).
[24] See, for example, W. G. Dauben and K. S. Pitzer, *Steric Effects in Organic Chemistry* (John Wiley & Sons, Inc., New York, 1956).
[25] For example, S. Winstein and N. J. Holness, J. Am. Chem. Soc. **77,** 5562 (1955).

hexanols in the equilibrium ea⇄ae exist in the conformation with the alkyl group equatorial and the OH axial virtually 100% of the time and the methylcyclohexanols in this equilibrium are in the conformation with the methyl group equatorial better than 90% of the time. For cyclohexanol one of the estimates places it in the conformation with the OH equatorial 81±7% of the time.[25] These ratios will vary slightly with solvent and with concentration.

We are interested in these determinations because the long-range contributions to the shielding for a given proton will in general be quite different in the two conformations[8,17,22,23] and in the absence of precise data on their relative populations we would have no way of determining how to weight appropriately the contributions from each. We thus want to consider primarily molecules in a single conformation and at least be aware of the error involved due to a possible admixture of the energetically unfavorable conformation. The *trans*-decalols do not impose the same problem since they are rigid structures. This is also true of many steroid molecules, on which some experimental results are available, which are neglected, however, since all such molecules contain functional groups whose shielding effects we cannot yet account for. Nevertheless in principle they admit the same interpretation we shall make here for the cyclohexanes and decalins.

We have determined $f(R,\theta)_g{}^N=(1-3\cos^2\theta_g{}^N)/3R_g{}^{N3}$ for N both an equatorial and an axial proton and for the C—C bonds occurring in the molecules we had available for study assuming preservation of ordinary bond angles and distances. These values are listed in Table I where θ and R are determined from the geometric center of the C—C bond (or the electrical center of gravity of the C—C bond dipole) and the center of nucleus N. The terms $f(R,\ \theta)_{\text{C2–Cax}}{}^e$, $f(R,\ \theta)_{\text{C2–Ceq}}{}^e$, and $f(R,\ \theta)_{\text{C2–Ceq}}{}^a$ will be slightly in error because of the inadequacy of the point-dipole approximation. The contributions of $f(R,\theta)$ for the isopropyl methyl groups are based on the assumption of the 100% *trans* conformation for the two tertiary hydrogens. This should be the preferred conformation since it places the two methyl groups skew (or equatorial) to the pseudo-plane of the ring and avoids placing a methyl group in an energetically unfavorable "axial" position. For the *t*-butyl contribution this "axial" methyl group is necessary if a staggered system is to be maintained. These assumptions might lead to small error in the 1,4-disubstituted compounds which should be canceled out when only isomeric pairs are considered.

We consider now the total relative shielding for any molecule to be the sum of the shielding contributions from each long-range C—C bond in the molecule. The effects of C—H bonds will be small and the contributions from cross terms between matrix elements from electrons involved in different bonds will also be small. We assume now that all C—C bonds have the same $\Delta\chi$ so that we can withdraw $\Delta\chi$ outside of the summation for σ, i.e., that $\sigma_N=\sum_g f(R,\theta)_g{}^N\Delta\chi^g=\Delta\chi^{\text{C–C}}\sum_g f(R,\theta)_g{}^N$ [Eq. (16)]. In general all C—C bonds will have a different $\Delta\chi$ because of effects of different substituents on each of the carbons, but in the limiting case of an infinitely long single-chain hydrocarbon all the $\Delta\chi$'s will be equal. The bonds in our molecules differ from those in single-chain hydrocarbons by the substitution of one or two methyl groups for hydrogens or the substitution of a hydrogen for a carbon thus ending the chain. We would expect only the immediate environment to effect the local C—C electronic wave functions and examination of Pascal's constants shows that the type of substitutions mentioned above has little effect on the "atomic" susceptibilities. Thus Eq. (16) seems reasonable.

In Table II the sums $\sum_g f(R,\theta)_g{}^N$ for N the tertiary proton adjacent to the OH group in a series of molecules for which the predominant conformations are assumed, are tabulated, as well as the experimental shielding $\sigma_N{}^{\text{expt}}$ in units of 10^{-6} relative to internal hexamethyldisiloxane for these molecules.[26] The values from Table II of $\sum_g f(R,\theta)_g{}^N$ and $\sigma_N{}^{\text{expt}}$ are plotted in Fig. 1 where each point is numbered according to the numbering in the table. Those points marked by (×) are considered of greatest validity, those by (△) are all except one of the 2,5-dimethylcyclohexanols and the menthols, and those by (○) the remainder.

We now proceed to comment on the validity of $\sum f(R,\theta)$ for the various molecules. Those denoted by (×) are all virtually 100% in a single conformation[27] or definitely rigid and involve no bonds for which the point-dipole approximation is seriously in error and are therefore considered the most valid.

Molecules 8, 10, 12, and 13 cannot reasonably be considered 100% in one conformation and for these we have plotted along the same abcissa $\sum f(R,\theta)$ for the energetically unfavorable conformation noting it by (+). For these compounds we would expect the true $\sum f(R,\theta)$ to be a weighted average of the values for each conformation heavily weighted in the direction of the energetically favorable one. From the figure this can be seen to be a valid qualitative observation. In

[26] The experimental procedure has been discussed earlier[23] and some of the data were presented at that time. All of these compounds were studied in CCl_4 solution in order to eliminate effects of different solvents and the standard deviations of the shift values are 0.008×10^{-6}. Since these peaks, which are unresolved spin-spin multiplets, are virtually symmetrical the geometrical center and the position of maximum peak height give the same value for the shifts. Effects of the solvent have been assumed to be negligible since all the molecules should interact with the solvent molecules—which are themselves magnetically isotropic—in virtually an identical manner thus giving a constant effect over the series. The concentrations are on the order of 5–10 mole % and the effect of variation of concentration of such solutes in CCl_4 is small[28]: the tertiary proton peak in cyclohexanol is constant within experimental error from 2.5–20 mole % in CCl_4. Peak positions of such compounds measured in CS_2 solution appear 0.016–0.032×10⁻⁶ to higher field from their positions in CCl_4 solution.

[27] This refers to ring conformation. See the discussion above for the *t*-butyl and *i*-propyl conformations.

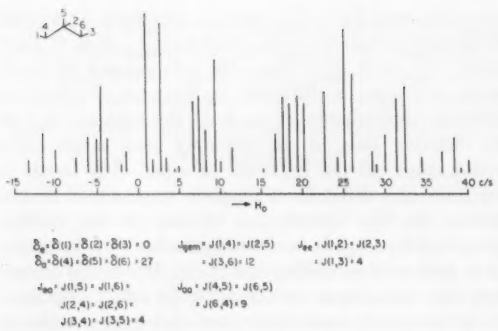
-15 -10 -5 0 5 10 15 20 25 30 35 40 c/s
H_0
$\delta_a = \delta(1) = \delta(2) = \delta(3) = 0$
$\delta_e = \delta(4) = \delta(5) = \delta(6) = 27$
$J_{gem} = J(1,4) = J(2,5) = J(3,6) = 12$
$J_{ee} = J(1,2) = J(2,3) = J(1,3) = 4$
$J_{ae} = J(1,5) = J(1,6) = J(2,4) = J(2,6) = J(3,4) = J(3,5) = 4$
$J_{aa} = J(4,5) = J(6,5) = J(6,4) = 9$

FIG. 2. Calculated spectrum of six-spin proto-cyclohexane system. Many of the 792 calculated transitions were of zero intensity to three decimal places, and those overlapping within a quarter of a cycle are drawn as a single line. Allowing for Lorentzian line shapes these would still show fine structure about the two peak maxima. This was not reported in the literature for cyclohexane[29] and its absence is attributed to the broadening due to coupling with the increased number of spins.[32] The δ's and J's are respectively chemical shifts and coupling constants in cps.

principle, were the line of best fit precisely valid, we could calculate for these molecules the percentages in each conformation. When we do this we find 89, 97, and 79 for the percentages in the favorable conformation of cyclohexanol, *cis*-4-methylcyclohexanol and *trans*-3-methylcyclohexanol. However at this time the errors are too great to make the determination significant. This implies a temperature-dependent chemical shift which could be used to determine these equilibria more accurately.

In those denoted by ($\triangle$) and the *cis*- and *trans*-2-methylcyclohexanols (11 and 12) the point-dipole approximation is poor for one of the bonds. Isomenthol (19) is considered to be principally in the conformation with the isopropyl group axial which can be shown to be of lower energy[28] than the other conformation. The 2,5-dimethylcyclohexanol-eae-aea (15) which is noted by ($\blacktriangle$) is not an experimental point but is the weighted mean between the two possible conformations (+), based on the observation that the ΔE between the two conformations is only one-half that of cyclohexanol itself or about 250 cal/mole. In 20 and 21 there is some interaction in the isopropyl methyl groups which causes the nonequivalence of the six methyl protons as shown by their complex NMR spectrum. This interaction which is probably with the OH group and is accidentally degenerate in the other two isomers indicates there *are* preferred orientations of the isopropyl group as we have already assumed. The preferred orientations we have chosen are consistent with the respective degeneracy and nondegeneracy in the methyl proton shifts for the different isomers. Because the error in the point-dipole approximation and in the neglect of C—H bonds cannot be resolved analytically; however, it is difficult to interpret the validity of our calculations for these molecules.

We look now at the line of best fit drawn for the most valid points ($\times$) and take its slope for the experimental value of $\Delta\chi$ for an average carbon-carbon single bond: $\Delta\chi^{C-C}=8.3\pm1.0\times10^{-30}$ cm^3 molecule$^{-1}=5.0\pm0.6\times10^{-6}$ cm^3 mole^{-1}, where the estimate of error is based on the variation in slopes *considering each of the three most valid pairs of isomers*; the 4-*t*-butylcyclohexanols, 4-*i*-propyl cyclohexanols, and 10-methyl-*trans*-decalols-2 give 7.8, 7.6, and 9.3×10^{-30} cm^3 molecule^{-1} for their respective slopes. Furthermore, most of the other points lie rather close to this line, and the evidence appears good that we are justified in drawing the relevant conclusions: (a) there is a definite contribution to the shielding from long-range carbon-carbon single bonds in the form of an effective field at the nucleus N of a pair of point dipoles located parallel and perpendicular to each C—C axis, the perpendicular chosen in the plane of R_g^N, and (b) there is a definite anisotropy in the magnetic susceptibility such that the longitudinal susceptibility is greater than the transverse susceptibility (or that χ_L is paramagnetic relative to χ_T), and it is this anisotropy which makes the dipoles of (a) of different strengths, thus providing a net or observable effect in molecules rapidly reorienting relative to the applied magnetic field.

The positive sign of $\Delta\chi$ indicates that the diamagnetic susceptibility perpendicular to the axis of symmetry χ_T^D must be considerably greater *in magnitude* than χ_L^D. This is so because in an axially symmetric system $\chi_L^P=0$ and only $\chi_T^P(>0)\neq0$. Therefore, for $\Delta\chi=\chi_L-\chi_T=\chi_L^D-\chi_T^D-\chi_T^P>0$, $|\chi_T^D|$ must be greater than $|\chi_L^D|$ by an amount equal to $\Delta\chi+\chi_T^P$. Thus in the case of a carbon-carbon single bond it is the *diamagnetic part* of the susceptibility that makes the major contribution to the shielding of a distant proton. This is reasonable on the grounds of greater bond cross section perpendicular to the bond than along it. However, the sign of $\Delta\chi$ could not have been determined without recourse either to experiment or to the calculation of χ_T^P because of the lack of knowledge of the relative magnitudes of χ_T^D and χ_T^P.

5. COMMENTS

A. The measurement of the $\Delta\chi$ for a carbon-carbon single bond by this method accomplishes what would be very difficult to do by any other known method. The ideal experiment for measuring the susceptibility of the C—C bond in both the transverse and longitudinal directions would be to freeze ethane in a crystal in which all C—C bonds were parallel and such that all molecules were sufficiently far apart to eliminate nuclear dipole fields and then performing the magnetic susceptibility measurements. By using the experimental value of $\Delta\chi$ and the quantum-mechanical expression for $\Delta\chi$, the validity of different possible wave functions for the bond can be determined.

[28] J. I. Musher (unpublished results).

B. At this point a few comments must be made on the previous attempt in the literature to obtain this magnetic anisotropy. In two papers Bothner-By and Naar-Colin[5,6] discuss such phenomena, and in the second of these they calculate a value of $\Delta\chi = 5.5\times10^{-6}$ cm^3 molecule^{-1} $= 3.3\times10^{-6}$ cm^3 mole^{-1} for a carbon-carbon single bond. They base this on the chemical shift difference between the methylene protons of cyclohexane and cyclopentane. They assume that (1) cyclopentane is planar and (2) there are no contributions from the bonds further away than the γ carbon. These allow for a certain margin of error, however, as can be seen by the comparison with the data from a long-chain hydrocarbon in the same paper. Based on their $\Delta\chi$ they show that this long-chain hydrocarbon is 80% in the energetically unfavorable *gauche* conformation. We therefore are not surprised to find a large difference between the value they have obtained for $\Delta\chi$ and ours.

We, however, believe that a major contribution to this chemical shift difference comes from "hybridization," etc. Thus, for example, data from cyclopentanols can probably not be placed directly on the plot of Fig. 1.

C. In regard to the relationship[5] between the anisotropy in the magnetic susceptibility and the anisotropy in the electric polarizability for C—C bonds as derived from Kerr constant work ($b_T/b_L = 1/3.9$), there is no reasoning connecting the relative signs of the two phenomena. The first comes *in part* from matrix elements $\sum_{i,j} m_{i_{0n}} m_{j_{0n}}$ while the second comes from matrix elements $\sum_{i,j} P_{i_{0n}} P_{j_{0n}}$. Hence there is no dependence of one on the other, and, although an anisotropy in one would in general require an anisotropy in the other, there is no way of comparing relative magnitudes or signs except by considering the explicit molecular or bond wave functions.

D. Jensen *et al.*[29] have studied cyclohexane itself at low temperatures and find two broad overlapping peaks whose centers are separated by 27.3 cps at 60 Mc/sec. This separation is then considered to be the chemical shift difference between axial and equatorial protons and is used for a determination of $\Delta F^{\ddagger}$ at a single temperature for the chair-chair inversion. On the basis of the $\Delta\chi$ above, however, we predict 33 ± 4 cps for this chemical shift difference. The apparent discrepancy is explained by the fact that the maxima of broad resonance multiplets for strongly coupled systems are not, in general, separated by exactly the chemical shift difference between the coupled nuclei. In Fig. 2 we show the calculated spectrum[30] of a spin-spin cyclopropane system for which the two protons on each carbon have been treated as axial and equatorial, respectively, and separated by 27 cps and coupled around the ring using typical cyclohexane *gem*, *trans*, and *gauche* coupling constants.[31] From this spectrum we observe that the peak maxima are separated by only 23.5 cps whereas $\delta_{ae} = 27$ cps. This is because the spectrum is not that of superposed ABB_2' and BAA_2' as would naively be expected, but one of type $AA'A''BB'B''$ where the A's and the B's each have the same chemical shift but none of the six protons are magnetically equivalent. A calculation for the twelve proton spectrum of cyclohexane undoubtedly would show an analogous effect, although with increased coupling the entire spectrum would be even more broadened so that probably little fine structure of the individual peaks would be observed.[32] If now we use the calculated ratio of δ_{apparent} to δ_{true} to give us an idea of the correct δ_{ae} from Jensen's data we get $\delta_{ae} \sim$ 31.5 cps, which is within the range of our experimental error. This does not change these authors' measurements of $\Delta F^{\ddagger}$.

E. Guy and Tillieu[33,34] have calculated by a variation method the two susceptibilities of such a C—C single bond. They obtain $\Delta\chi = 1.31\times10^{-6}$ cm^3 mole^{-1}, which agrees in sign with our experimental results but is decidedly different in magnitude. We have not had time in which to explore the implications of this discrepancy as well as a similar one for ethylenic[35] and acetylenic bonds. They are rather surprising in view of the very close agreement of these authors' calculated *total* susceptibilities with the experimental values. If the agreement is not illusory, i.e., if the calculation is not insensitive to the variation function chosen nor is there an error involved, then apparently the anisotropic high-frequency terms (for the vector potential $\mathbf{A} = \frac{1}{2}\mathbf{H}\times\mathbf{r}$) are almost smoothed out isotropically by the

[29] F. R. Jensen, D. S. Noyce, C. S. Sederholm, and A. J. Berlin, J. Am. Chem. Soc. **82,** 1256 (1960).

[30] These calculations were performed on the IBM 704 at the MIT Computation Center. The author is grateful to Dr. A. A. Bothner-By for the use of his machine program.

[31] Coupling constants are similar to those in reference 22. This work was completed before the more recent determinations of these coupling constants by the author [J. Chem. Phys. **34,** 594 (1961)]. The difference in magnitude—principally in $J_{\text{trans}} = J_{aa}$—should not greatly change the distribution of the spectral peaks.

[32] Such broadening is shown by machine calculations in the spectrum of a proton coupled to another proton which is in turn strongly coupled to other protons, even though these latter protons are not themselves coupled to the first proton.[28] It is, of course, this multiple coupling between protons which all have relatively similar chemical shifts that causes the inward shift of the peak maxima and the nonsymmetry about the peak maxima.

[33] J. Guy and J. Tillieu, J. Chem. Phys. **24,** 1117 (1956).

[34] J. Tillieu, Ann. phys. **2,** 471, 631 (1957).

[35] An interesting observation: we believe that they obtain the correct *anisotropy* for ethylenic C—C π bonds[36] in their discarded calculation which neglected the nodes in the wave function. The *total* susceptibility here, though, does not agree with experiment when combined with the results of their other calculations. They therefore refined the calculations and obtained the "incorrect" $\Delta\chi$ and the "correct" χ.

[36] That is to say, the bond is almost axially symmetric about the axis in the plane of the bond and perpendicular to it with $\Delta\chi = \chi_L - \chi_T < 0$. We will justify this statement later. Incidentally this makes us choose for the calculations of χ based on H_2NCHO the Table I of reference 7 or $\Delta\sigma < 0$ for the formamide protons instead of Table II or $\Delta\sigma > 0$ as chosen by these authors. This conclusion is also in agreement with the recent study[37] of $H_2N^{15}CHO$ if the deviation from planarity of the mean position of the amide protons is not great.

[37] B. Sunners, L. H. Piette, and W. G. Schneider, Can. J. Chem. **38,** 681 (1960).

variation method. We would like to thank Dr. A. D. McLachlan and Dr. M. R. Baker for having called our attention to this work after the manuscript had been completed.

F. An attempt was made to determine the $\Delta\chi$ for a carbon-fluorine bond utilizing the above method and the data of Tiers.[38] Tiers studied the F^{19} spectrum of perfluorocyclohexane at $-66°$ and found the chemical shift between the axial and equatorial fluorines to be 18×10^{-6}. This leads to the absurd value for $\Delta\chi=2\times10^{-4}$ cm^3 mole^{-1} or many times the total susceptibility.[39] We believe that the greater contribution to the shift comes from the distortion in the fluorine electrons rather than from the direct effect of the field at the fluorine nucleus due to the anisotropic susceptibilities of the distant C—F bonds. This distortion could be caused by the electric field set up at a fluorine atom by the electric dipole moments of the other C—F bonds and the charge imbalance on its own bond. Preliminary calculations indicate that this electric field effect can be of the observed magnitude.[28] This could be demonstrated by observing only a small chemical shift between the two fluorines in 4-*t*-butyl-1,1-difluorocyclohexane.

G. The plot of Fig. 1 can also be used for determination of molecular structure involving tertiary protons on hydroxyl-substituted carbons. If one calculates the geometric parameters for the different possible configurations and employs these parameters in conjunction with NMR data and the curve of Fig. 1, it should be possible: (1) to determine the conformations in six-membered and higher fused rings; (2) to determine the conformations in perhaps five- and four-membered rings; (3) to observe boat conformations in cyclo-Ci rings when they predominate; and (4) to determine in some special instances the location of the hydroxyl group on the ring. Other nonhydrocarbon substituents whose long-range effects have not been studied should be sufficiently removed (about 6 A) from the tertiary proton under scrutiny for such interpretations to be valid.

This method of structural determinations is, of course, completely general and not restricted to protons on hydroxyl-substituted carbons. For example, similar curves can easily be constructed for chlorine- and bromine-substituted carbons from Reeves and Strømme's[41] data from low-temperature measurements of chloro- and bromo-cyclohexane.

Note added in proof. See also the article by P. T. Narasimhan and M. T. Rogers, J. Chem. Phys. **31,** 1302 (1959). This gives a value of $\Delta\chi^{e-e}=5.6\times10^{-6}$ if C—H bonds are neglected (Dr. Narasimhan has corrected a typographical error for us) while studying mostly shorter range bonds. This is in rather good agreement with the value we have obtained from rather longer range bonds. We interpret this as indicating that "inductive effects" are not important, that the $\Delta\sigma_I$ of these authors is not relevant, and serving to confirm our statement of disbelief in the calculated anisotropies of Tillieu and Guy.[33] If our interpretation is correct then the concept of electronegativity contributions for hydrocarbon shifts must be re-evaluated. In particular there appears to be no need to invoke arguments of change in electron densities and hybridization to explain the differences in secondary and tertiary proton shifts[6] as in *cis*-bicyclo-3,3,0-octane [W. B. Moniz and J. A. Dixon, J. Am. Chem. Soc. **83,** 1671 (1961)]. Using our $\Delta\chi$ and their data we calculate $\Delta\sigma=0.60\times10^{-6}$ as compared with their rough experimental value of $\Delta\sigma=0.63\times10^{-6}$. The proximity of one of the bonds involved in this calculation makes the very close agreement fortuitous. A recent related paper by J. R. Cavanaugh and B. P. Dailey, J. Chem. Phys. **34,** 1099 (1961) also prefers to accept the Tillieu and Guy calculations for the magnetic anisotropy and calls the observed experimental shift the "C—C bond shift." We are hoping to measure the magnetic susceptibilities directly and hence explicitly confirm or disprove these calculations.

ACKNOWLEDGMENTS

The author is grateful to Dr. R. H. Baker, Dr. H. C. Brown, Dr. A. R. H. Cole, Dr. E. L. Eliel, and Dr. W. Hückel who very kindly provided the compounds used in this study. The author would also like to thank Professor J. S. Waugh for his critical comments on the manuscript.

[38] G. V. D. Tiers, Proc. Chem. Soc. **1960,** 389.

[39] A similar absurdity occurs if one uses the recent data[40] on C^{13} shifts in substituted ethanes.

[40] W. G. Schneider (private communication).

[41] L. W. Reeves and K. O. Strømme, Can. J. Chem. **38,** 1241 (1960).

Paramagnetic Defects in Irradiated NH_4ClO_4

TERRY COLE

Scientific Laboratory, Ford Motor Company, Dearborn, Michigan

(Received February 23, 1961)

Analysis of the electron magnetic resonance of x-ray damaged crystals of NH_4ClO_4 shows that the long-lived defects are NH_3^+ ions. Isotropic hyperfine splittings are found to be 54.6 Mc for nitrogen and 72.5 Mc for hydrogen. These radicals appear to be planar and execute restricted rotation at room temperature. A second transient defect is identified as ClO_3.

INTRODUCTION

IT is well known that ionizing radiation produces stable paramagnetic centers in a number of inorganic and organic solids.[1-5] In a previous paper[5] we have shown that $KClO_4$ upon irradiation at room temperature produces long-lived paramagnetic defects which were identified by EMR as ClO_2 molecules.

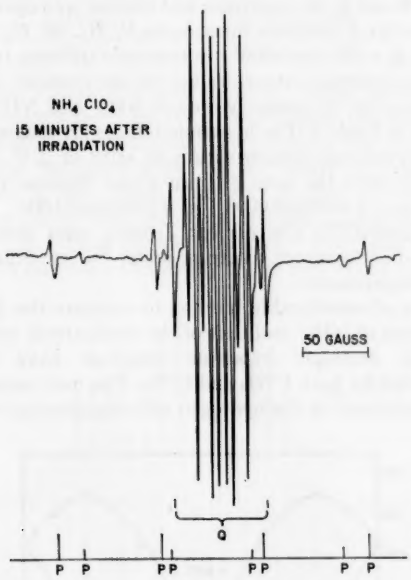

FIG. 1. EMR spectrum of irradiated NH_4ClO_4 single crystal. The first derivative of the spectrum is shown.

Subsequently it was found that many inorganic perchlorates produce stable defects with well-resolved hyperfine structure. This paper presents analysis of the two paramagnetic defects produced in ammonium perchlorate ClO_3 and NH_3^+.

[1] H. M. McConnell, C. Heller, T. Cole, and R. W. Fessenden, J. Am. Chem. Soc. **82**, 766 (1960).
[2] N. M. Atherton and D. H. Whiffen, Mol. Phys. **3**, 1 (1960).
[3] T. G. Castner and W. Kanzig, J. Phys. Chem. Solids **3**, 178 (1957).
[4] J. E. Wertz, P. Auzins, J. H. E. Griffiths, and J. W. Orton, Discussions Faraday Soc. **28**, 136 (1959).
[5] T. Cole, Proc. Natl. Acad. Sci. U. S. **46**, 506 (1960).

EXPERIMENTAL

Single crystals grown from aqueous solution of reagent-grade NH_4ClO_4 were irradiated $\frac{1}{2}$ to 3 hr at room temperature with a molybdenum target x-ray tube operating at 50 kv and 20 ma; crystals were 4 cm from the focal spot of the tube. ND_4ClO_4 crystals were grown from 99% ND_4ClO_4 prepared by triple exchange with excess D_2O (99.8%). Immediately after irradiation the crystals appeared yellow, becoming white and turbid after about 24 hr. Crystal axes were identified by means of precession camera photographs and were aligned for EMR observations with an optical goniometer.

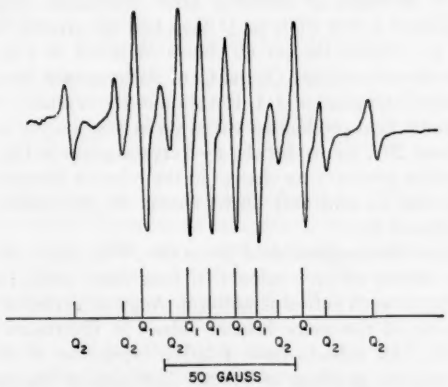

FIG. 2. EMR spectrum of the Q defect in NH_4ClO_4 which is identified as NH_3^+. The spectrum was taken 24 hr after irradiation.

Ammonium perchlorate is orthorhombic[6] (at room temperature) containing four molecules per unit cell; cell dimensions are $a=9.202$ A, $b=5.816$ A, $c=7.449$ A, and the space group is $Pnma$.

EMR spectra were taken with a conventional X-band spectrometer employing a TE_{01} mode cylindrical cavity and 100-kc field modulation. The polarizing magnetic field was continuously controlled and monitored by an NMR servo system. Low-temperature spectra were observed with an X-band superheterodyne spectrometer.

[6] R. W. G. Wyckoff, *Crystal Structure* (Interscience Publishers, Inc., New York, 1951), Vol. II, Chap. VIII, p. 23.

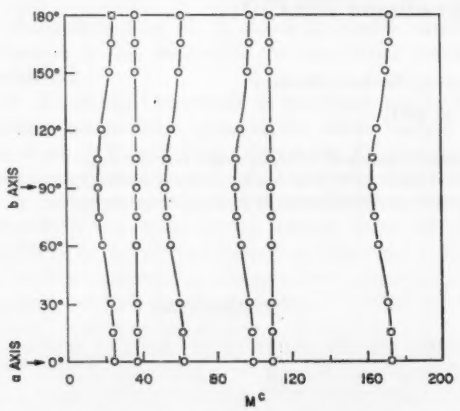

FIG. 3. Variation of the hyperfine splitting of the Q lines with the magnetic field lying in the (001) plane. Only the high-field half of the spectrum is shown.

RESULTS

A typical EMR spectrum of an irradiated crystal of NH_4ClO_4 is presented in Fig. 1; it consists of two sets of lines labeled P and Q. The two groups may be distinguished by the fact that at room temperature the set P decreases in intensity after irradiation with a half-life of 2–3 hr while set Q has a half-life greater than 100 hr. Within the set Q, shown in detail in Fig. 2, there are two subsets Q_1 and Q_2 of six lines each having relative intensities of 3:1. Rotation of the crystal in the magnetic field produces a variation in line spacing in Q of about 20% shown for the $a-b$ crystal plane in Fig. 3. Rotation produces no change in the relative intensities of Q_1 and Q_2 and only slight change in the center of gravity of Q.

When the magnetic field lies in the (001) plane the P lines consist of two subsets of four lines each. Line spacing in each subset is uniform. Angular variation in splitting of the more intense subset is illustrated in Fig. 4. The subsets have relative intensities of 3:1, and relative spacings of 1:0.83. Rotation of the field out of the (001) plane causes each of the lines of the set P to split into a doublet.

Irradiated ND_4ClO_4 also produces a resonance spectrum that can be divided into two sets of lines. One set is identical in all respects save linewidth to the set P described above. Figure 5 shows a typical spectrum of the second set. Radical concentrations were estimated to be approximately 10^{-3} mole percent.

ANALYSIS

A. NH_3^+

The spectrum of Fig. 2 can be decomposed into an equally spaced triplet of quarters, each quartet having relative intensities 1:3:3:1 as illustrated in Fig. 6. This spectrum will arise if the unpaired electron in the defect interacts with one nucleus of spin 1 and three equivalent nuclei of spin $\frac{1}{2}$. We are therefore led to assign the spectrum to the radical NH_3^+. Complete deuteration of this radical would change the 1:3:1 quartets to 1:3:6:7:6:3:1 septets with line spacings reduced by a factor of 6.514. Synthesizing this spectrum in Fig. 6 we find it in excellent agreement with the observed spectrum in Fig. 5. This analysis does not rule out the possibility of the radical-containing oxygen atom ($I=0$) but such a species as ONH_3^+ would not show the close agreement with π radical theory demonstrated below for NH_3^+. The NH_3^- would be paramagnetic; however mass spectrometric studies[7] of ammonia have found no evidence of NH_3^-.

Observed EMR spectra of NH_3^+ may be derived from the spin Hamiltonian

$$\mathcal{H}=-\beta\mathbf{S}\cdot\mathbf{g}\cdot\mathbf{B}_0+\mathbf{S}\cdot\sum_k\mathbf{A}_k\cdot\mathbf{I}_k, \qquad (1)$$

where β is the Bohr magneton, $\mathbf{B}_0$ the magnetic induction, $\mathbf{S}$ and $\mathbf{I}_k$ the electronic and nuclear spin operators (subscript k indicates nucleus $k=N$, H_i, or D_i, $i=1$, 2, 3), $\mathbf{g}$ is the electronic spectroscopic splitting tensor, $\mathbf{A}_k$ the hyperfine tensor. Values for the elements of the diagonalized hyperfine tensors in NH_3^+ and ND_3^+ are given in Table I. The hyperfine tensors are diagonal in the crystal axis system within an error of $\pm5°$. Both radicals have the same g tensor whose diagonal values are: $g_{aa}=2.0039\pm0.0003$, $g_{bb}=2.0034\pm0.0003$, $g_{cc}=2.0032\pm0.0003$. The nuclear Zeeman term does not affect the resonance spectrum under the conditions of these experiments.

It is of considerable interest to compare the EMR spectrum of NH_3^+ and that of the isoelectronic methyl radical. Isotropic hyperfine couplings have been measured for both $C^{13}H_3$ and $C^{12}H_3$. The most accurate determination[8] of the hydrogen splitting gives $a_C=64.5$

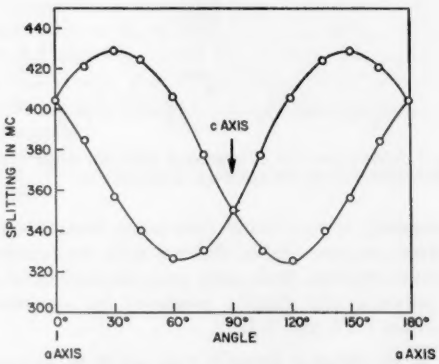

FIG. 4. Angular variation of the hyperfine splitting of the Cl^{35} defect when the magnetic field lies in the (010) plane.

[7] K. Schofer, and P. Conrad, Z. Physik **107,** 393 (1937).
[8] C. K. Jen, S. N. Foner, E. L. Cochran, and V. A. Bowers, Phys. Rev. **112,** 1169 (1959).

Mc while in $C^{13}H_3$ carbon and hydrogen splitting were found[9] to be in the ratio $a_C/a_H=1.68$. Combining the two results gives $a_C=109$ Mc.

Isotropic hyperfine couplings in NH_3^+ can be calculated from the formula

$$a_k=\tfrac{1}{3}|\mathrm{Tr}A_k|. \tag{2}$$

Using the components of $\mathbf{A}_k$ given in Table I gives $a_N=54.6\pm0.4$ Mc and $a_H=72.5\pm0.4$ Mc. We have here assumed that all of the components of $\mathbf{A}_N$ and $\mathbf{A}_C$ have the same relative sign.

If NH_3^+ is a planar π electron radical McConnell's[10] theory of indirect hyperfine interaction predicts that that a_H will proportional to $\rho(J/\epsilon)$, where ρ is the unpaired spin density of the cental atom ($\rho=1$ for NH_3^+ and CH_3), J is the $\sigma-\pi$ exchange integral and ϵ is the singlet-triplet excitation energy for the NH bond (Karplus[11] has shown this relation to be approximately correct even for small pyramidal distortions). From the experimental data we find,

$$\frac{a_H(CH_3)}{a_H(NH_3^+)}=0.89=\frac{J(CH_3)\epsilon(NH)}{J(NH_3^+)\epsilon(CH)}. \tag{3}$$

Isotropic hyperfine interaction for C^{13} is also accounted for in π radicals[10,12] by the $\sigma-\pi$ exchange polarization of the covalent sp^2 orbitals. To calculate the nitrogen splittings we must allow for the contraction of the orbitals of the central atom due to the increase in nuclear charge from carbon to nitrogen, as well as the change in nuclear magnetic moment. Using Hartree[13] $2s$ wave functions (since only the $2s$ part of the orbital has an appreciable value, $|\psi_{2s}|^2$ at the N nucleus) we find,

$$|\psi_{2s}(\mathrm{N})|^2/|\psi_{2s}(\mathrm{C})|^2=1.68. \tag{4}$$

We can now calculate a value for a_N/a_C;

$$a_N/a_C=\frac{\gamma_N\psi_{2s}(\mathrm{N})^2J(NH_3^+)\epsilon(CH)}{\gamma_C\psi_{2s}(\mathrm{C})^2J(CH_3)\epsilon(NH)}=0.545, \tag{5}$$

γ_N and γ_C are the magnetogyric ratios for N^{14} and C^{13}, respectively. Observed splittings have the ratio $a_N/a_C=0.502$. Such close agreement strongly supports the assumption that the defect is a π electron radical isoelectronic with the methyl radical. This is further evidence against NH_3^-. Some of the discrepancy in the splitting ratio may be due to the fact that our calculation ignores the effect of the ionic matrix on the molecular wave functions.

Further consideration of the orbitals of the nitrogen atom shows the effect of pyramidal distortion on the splittings in NH_3^+. We take as the unperturbed N orbitals three $sp^2\sigma$ orbitals in the $x-y$ plane each occupied by a pair of electrons and singly occupied $p_z\pi$ orbital normal to the molecular plane. From a consideration of the vector character[14] of p_x, p_y, and p_z it can be shown that a pyramidal distortion of the molecule will produce orbitals σ_i' and π' such that,

$$\pi'=\xi s+(1-\eta^2)^{\frac{1}{2}}\pi \tag{6}$$

$$\sigma_i'=(\tfrac{1}{3})^{\frac{1}{2}}(1-\xi^2)^{\frac{1}{2}}s+(\tfrac{2}{3})^{\frac{1}{2}}\tau_i+\eta\pi, \tag{7}$$

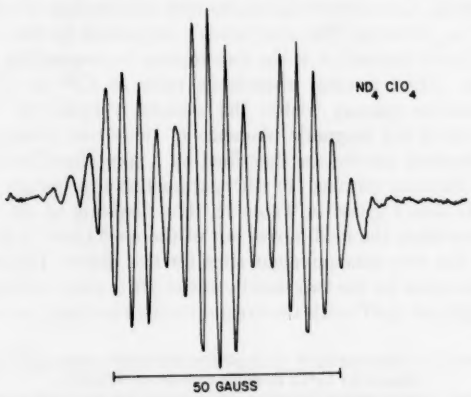

FIG. 5. EMR spectrum of ND_3^+ in ND_4ClO_4 24 hr after irradiation.

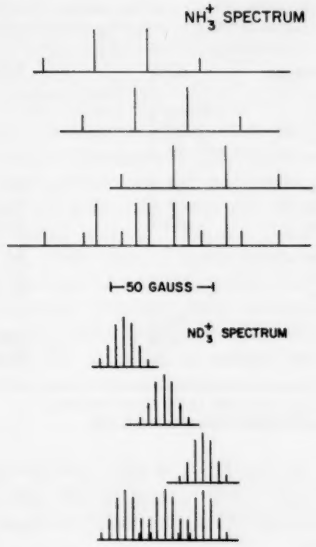

FIG. 6. Synthesis of the NH_3^+ spectrum from a triplet of quartets, and of the ND_3^+ spectrum from a triplet of septets.

[9] T. Cole, H. O. Pritchard, N. R. Davidson, and H. M. McConnell, Mol. Phys. **1**, 406 (1960).
[10] H. M. McConnell, J. Chem. Phys. **24**, 764 (1956); H. M. McConnell and D. B. Chesnut, *ibid.* **28**, 107 (1958).
[11] M. Karplus, J. Chem. Phys. **30**, 15 (1959).
[12] A. D. McLachlan, H. H. Dearman, and R. Lefebvre, J. Chem. Phys. **33**, 65 (1960).
[13] D. R. Hartree, *The Calculation of Atomic Structures* (John Wiley & Sons, Inc., New York, 1957), p. 167.
[14] H. Eyring, J. Walter, and G. E. Kimball, *Quantum Chemistry* (John Wiley & Sons, Inc., New York, 1944), p. 223.

TABLE I. Components of the hyperfine tensors[a] for NH_3^+ and ND_3^+ in single crystals of NH_4ClO_4 and ND_4ClO_4.

Tensor component	NH_3[b]	ND_3[b]
$A(H)_{aa}$	73.5	
$A(H)_{bb}$	72.3	
$A(H)_{cc}$	71.6	
$A(N)_{aa}$	61.8	59.5
$A(N)_{bb}$	53.3	51.7
$A(N)_{cc}$	48.7	46.8
$A(D)_{aa}$		11.3
$A(D)_{bb}$		11.3
$A(D)_{cc}$		11.3
a_H	72.5	
a_N	54.6	52.6
a_D		11.3

[a] The subscripts a, b, and c refer to the crystal cell axes.
[b] The standard deviation for all entries is ±0.4 Mc.

where τ_i are the set $\frac{1}{2}(-p_x+3p_y)$, $\frac{1}{2}(-p_x-3p_y)$, p_z. Coefficients ξ and η will depend on the bond angles. We assume that the σ_i' remains doubly occupied and π' singly occupied.

Normalization of the orbitals imposes the condition,

$$\xi^2-3\eta^2=0, \tag{8}$$

while the vector character of the p orbitals gives

$$\eta/(\eta^2+\tfrac{2}{3})^{\frac{1}{2}}=\sin\theta, \tag{9}$$

where θ is the angle between the σ_i' and the $x-y$ plane. Substituting (8) in (9) we find

$$\xi^2=2\tan^2\theta. \tag{10}$$

If the spin densities in the new orbitals are ρ_π and ρ_σ they will produce a nitrogen splitting

$$a_N=a_N(2s)[\xi^2\rho_\pi+(1-\xi^2)\rho_\sigma]. \tag{11}$$

The splitting $a_N(2s)$ of a nitrogen $2s$ atomic orbital containing a single electron is estimated from the Hartree wave function[13] to be 1550 Mc. From a_H we find that $\rho_\sigma=0.05$ and using $\rho_\pi=1.0$ gives $a_N=77$ Mc for the planar configuration and $a_N=441$ Mc for a pyramid with H—N—H bond angles of 109.5°. Therefore NH_3^+ must be very nearly planar.

Equation (11) also provides an explanation for the difference in a_N between NH_3^+ and ND_3^+ found in Table I. In the latter molecule the umbrella mode vibrations will be lowered in amplitude by a factor of $\sqrt{2}$ due to the substitution of deuterium thus giving a smaller value for $\langle\tan^2\theta\rangle_{Av}$ and so a smaller a_N.

Turning to the anisotropy of the hyperfine splitting there are two points to be made: first, on the basis of previous studies of radicals in single crystals two sets of lines[15] would be expected for NH_3^+ corresponding to the two magnetically nonequivalent positions in the unit cell for the parent NH_4^+; second, C^{13} and H splittings[16] in the radical $(COOH)_2C^{13}H$ are highly anisotropic (e.g., the C^{13} splitting varies from 23 to 215 Mc), a similar anisotropy is expected for rigidly oriented NH_3^+. It seems reasonable to conclude that the molecule is undergoing restricted rotation at room temperature which partially averages out the anisotropy of the hyperfine interaction. A similar case is that of the averaging of quadrupole coupling tensors by torsional vibration studied by Bayer.[17] In order to test this hypothesis several spectra were taken at 4.2°K. These spectra showed a marked increase in the number of lines and a strong angular dependence. An analysis of the low-temperature results has not been made; however, they indicate that there are at least two distinct low-temperature sites for the molecule.

A more detailed picture of the rotational motion requires a study of the temperature dependence of the resonance spectrum. However, from the room-temperature data we can state that the frequency of rotation must be rapid with respect to the hyperfine splitting frequencies. Otherwise the spectra would be poorly resolved with unsymmetric line shapes. Also the axis of rotation cannot coincide with the C_3 axis of the radical as such coincidence would produce a cylindrically symmetric A_N contrary to observed data.

B. The Chlorine Defect

We now turn to the transient species producing the lines labeled P in Fig. 1. The sets of four evenly spaced lines of equal intensity suggest that the unpaired electron in these defects interacts with one nucleus of spin $\frac{3}{2}$, i.e., chlorine. This conclusion is supported by the 3:1 relative intensities of the two subsets corresponding to the 3.06:1 natural abundance ratio of Cl^{35} to Cl^{37}. Relative spacing within the subsets is equal to the ratio of the magnetic moments of these two isotopes. Observed spectra are described by a spin Hamiltonian of the same form as (1) with parameters appropriate to this defect given in Table II. The doubling of the P lines when the field moves out of the $a-b$ plane is due to the two nonequivalent sites for this defect. Hyperfine z axes for the two sites lie in the (010) plane making angles of ±30° with the crystal c axis, the x and y axes

TABLE II. Components of the hyperfine and spectroscopic splitting tensors for $Cl^{35}O_2$ in single crystals of NH_4ClO_4.

Tensor component	Value in Mc
$A(Cl)_{xx}=A(Cl)_{yy}$	323±1
$A(Cl)_{zz}$	429±1
$g_{xx}=g_{yy}$	2.008
g_{zz}	2.007

[13] C. Heller and H. M. McConnell, J. Chem. Phys. **32**, 1535 (1960).
[16] T. Cole and C. Heller, J. Chem. Phys. **34**, 1085 (1961).
[17] H. Bayer, Z. Physik **130**, 227 (1951).

are arbitrary since the hyperfine tensor is cylindrically symmetric about z.

In making the identification of the chlorine defect we must choose among the possibilities ClO, ClO_2, ClO_3, and ClO_4. The ClO would possess electronic orbital angular momentum about the internuclear axis which would cause a deviation of the g factor from 2.00. A similar case is O_2^- dealt with by Kanzig and Cohen.[18] The ClO_2 is known to have hyperfine splittings[5,19] much smaller than those here observed. The ClO_4 would be expected to be of tetrahedral symmetry and produce an isotropic hyperfine interaction rather than one with cylindrical symmetry.

Since the hyperfine energy for the Cl nucleus in nearly 400 times the nuclear Zeeman energy it was not possible to determine the relative signs of the components of $\mathbf{A}(\mathrm{Cl})$ as has been done for proton hyperfine tensors[1] in oriented organic free radicals. If A_{zz} is of the same sign as A_{xx} and A_{yy} we find from Eq. (2) $a_{Cl}=376$ Mc; if the signs are opposite $a_{Cl}=75$ Mc. The former value corresponds to an unpaired electron with 64% 3s character; the latter to an unpaired electron with 13% 3s or 64% 4s character. The value used for Cl 3s splitting was obtained from the Hartree wave function[13] that for 4s was taken from the work of Kanzig.[3] In view of the considerable amount of s character for the unpaired electron in either case and the arguments presented for the shape of NH_3^+ it seems probable that ClO_3 is nonplanar. Walsh[20] has predicted a nonplanar structure for ClO_3 from molecular orbital theory.

Note added in proof. Das and Jukherjee [J. Chem. Phys. **33,** 1808 (1960)] have shown that polarization of the nitrogen 1s electrons produces a contribution to the hyperfine coupling which is negative in sign. Including this effect in the calculation of a_N gives a value of 60–65 Mc in better agreement with the value in Table I.

ACKNOWLEDGMENTS

The author wishes to thank Dr. J. Lambe of this laboratory for taking the low-temperature spectra and Dr. C. Heller for his enlightening discussions of this work.

[18] W. Kanzig and M. H. Cohen, Phys. Rev. Letters **3,** 509 (1959).

[19] J. E. Bennett and D. J. E. Ingram, Phil. Mag. **1,** 109 (1956).

[20] A. D. Walsh, J. Chem. Soc. **1953,** 2301.

Temperature-Dependent Chemical Shifts in the NMR Spectra of Gases*

L. PETRAKIS AND C. H. SEDERHOLM

Department of Chemistry, University of California, Berkeley 4, California

(Received February 16, 1961)

It is found that the chemical shifts of various gaseous compounds, using gaseous methane as a standard, vary with temperature. The slopes of chemical shift versus temperature at 50°C are tabulated for several compounds. This effect is ascribed to excitation of vibrational modes of the molecules, the protons in the excited molecules being differently shielded than the protons in the ground vibrational states. The data are interpreted to yield approximate chemical shifts associated with the excitation of various types of modes. NMR isotopic shifts are discussed on the basis of these data.

INTRODUCTION

RECENTLY, Gutowsky,[1] Tiers,[2] and Saunders[3] have reported several examples of an NMR chemical shift of proton and fluorine resonances resulting from an isotopic substitution in the vicinity of the nucleus under consideration. In all cases thus far reported, the resonance of the observed species moves to higher field, that is to greater magnetic shielding, when an atom in the immediate vicinity is replaced by a heavier isotope.

The observed chemical shift is an average of the chemical shifts associated with the possible molecular configurations, averaged over the molecular vibrations. Gutowsky[1] has suggested that the observed isotopic shifts come about, not as a result of perturbations of the electronic wave functions caused by the isotopic substitution, but as a result of changes in the dynamic state of the molecule. The altered effective mass for vibrations in which the substituted nucleus participates results in altered zero-point vibrational energies for these modes and thus in a change in the averaging process, producing an altered chemical shift. The chemical shifts are altered as a result of changes in effective mass for vibrations which are completely harmonic; however, the effect should be considerably larger if anharmonic vibrational modes are involved.

Gutowsky[1] has made a semiquantitative calculation of the chemical shift resulting from the change in the zero-point energy of the bending vibration of the CH_2 group, assuming this to be a harmonic oscillator. His calculation gives the proper direction for the shift and an order of magnitude agreement.

By measuring the chemical shift which accompanies the thermal excitation of vibrational modes in various molecules, we have attempted to investigate experimentally this explanation of the isotope effect. The shifts under consideration are approximately 0.001 cps/°C in magnitude while the temperature-dependent shifts due to solvent effects are usually orders of magnitude greater than this. Therefore, in order to avoid such temperature-dependent solvent effects this investigation was done entirely on gaseous samples.

EXPERIMENTAL

Gaseous methane was used as a reference because of the sharpness of its resonance, the large number of equivalent hydrogens per molecule, the ease of sample preparation, and its presumed temperature independence. This latter point will be discussed later.

The results, tabulated in Table I, were obtained using a Varian 60-Mc/sec spectrometer. The probe was equipped with a homemade variable temperature insert which readily controlled the temperature of the sample to ±2°C over the range 0°-100°C. Except for cyclobutane,[4] tetramethyltin,[5] and 2-butyne[5] the samples were made up from commercially available sources. For each substance a 5-mm thin-walled sample tube was made containing a mixture of the gaseous sample and gaseous methane, each if possible at a partial pressure of approximately 5 atm. The tubes were collapsed at a distance 5 cm from the bottom so that the entire gaseous sample could be thermostatted in the insert. The portion of the tube above the collapsed section provided a means of spinning the sample, which was found advantageous to the resolution even with gaseous samples.

The separation between the signals had to be measured to an accuracy of a few hundreths of a cycle per second. Such accuracy can be obtained using the wiggle-beat method, but this method is not applicable to signals which are widely separated. Therefore, the following method was used which results in a precision of approximately 0.02 to 0.10 cps depending upon the condition of the field and instrument. Basically the method is the sideband technique with modifications. A Hewlett Packard audio oscillator, model 200J, was modified by placing a gang of three 5–25 $\mu\mu$f condensers in parallel with the three variable condensers in the tuning section. The oscillator, so modified, was stable to ±1 part in 10^5,

* This research was supported in part by the U. S. Atomic Energy Commission.

[1] H. S. Gutowsky, J. Chem. Phys. **31,** 1683 (1959).

[2] G. V. D. Tiers, J. Am. Chem. Soc. **79,** 5585 (1957); J. Chem. Phys. **29,** 963 (1958); J. Phys. Chem. **64,** 373 (1960); J. Phys. Soc. Japan **15,** 270 (1960).

[3] M. Saunders, J. Plostnieks, P. S. Wharton, and H. H. Wasserman, J. Chem. Phys. **32,** 317 (1960).

[4] The sample of cyclobutane was kindly provided by Professor W. Gwinn of this department.

[5] The samples of tetramethyltin and 2-butyne were kindly provided by California Research Corporation, Richmond, California.

and the frequency could be changed by increments of 1 part in 10^5. The period of the modulating signal, rather than its frequency, was measured with a Hewlett Packard counter. This indirect technique allowed us to measure the frequency rapidly to better than 0.001 cps.

The frequency of the signal generator was adjusted so that one sideband of the methane signal was close to, but resolvable from, the signal due to the protons the shift of which was to be measured; and the amplitude of the sideband was adjusted so that the heights of the two peaks were equal. Then the sideband frequency was adjusted so that the two peaks were nearly superimposed. The resulting signal was recorded in both directions of sweep, along with the period of the audio-signal. The frequency of the audio signal was changed by approximately one or two parts per 10^6 and the entire process was repeated. In this manner, a record was made of a pair of peaks as a function of the audio frequency. By inspection of this record, it was quite easy to distinguish an envelope of these peaks. The amplitude of the signal increased from the starting point, went through a maximum, and then decreased. In this manner, the random fluctuations in the magnitude of the signal due to changes in the homogeneity of the field, changes in the scan rate, or noise could be disregarded. The audio signal corresponding to the maximum of the envelope was selected as representing the separation between the methane and sample resonances. This method was used unless the signals were very close together, approximately 5 cps, in which case it was assumed that the scan rate was linear with time over this time interval, and the separations were measured graphically using a sideband near the peak to be measured. In all cases, five or six independent measurements were made. In a typical case, the root-mean-square deviation of these individual measurements was 0.06 cps and the most probable error was 0.02 cps.

The chemical shifts from methane of 11 compounds were measured as a function of temperature. Usually, five measurements were made in the temperature range 25° to 100°C. To within the experimental accuracy, these points fell nearly on a straight line for each compound. The slopes of these lines at 50°C are tabulated in Table I. No attempt was made to estimate the curvature of the lines, but in several cases it was apparent that the absolute value of the slope was increasing with increasing temperature.

TABLE I. Temperature dependence of chemical shifts from methane.

Compound	$d(\nu_0\delta^{\text{methane}})/dT$ cps per °C	$\nu_0\delta^{\text{methane}}$ 25°C (cps)
CH_4	0.0000	0
HBr	0.0000±0.0005	−260.5
C_2H_6	0.0000±0.0005	−44.7
C_3H_6	−0.0080±0.0027	−3.9
C_4H_8	−0.0071±0.0009	−113.9
C_5H_{10}	−0.0035±0.0009	−86.9
$C(CH_3)_4$	−0.0061±0.0014	−49.2
$Si(CH_3)_4$	−0.0125±0.0015	−8.4
$Sn(CH_3)_4$	−0.0102±0.0025	−5.9
C_2H_2	−0.0087±0.0014	−80.1
CH_3CCCH_3	−0.0047±0.0008	−87.7
C_2H_4	+0.0038±0.0015	−310.6

DISCUSSION

The great majority of organic and inorganic compounds show proton resonances within a range of a few hundred cps at 60 Mc/sec. For example,[6] the chemical shift of HBr is 260 cps from CH_4. One would expect that the chemical shift brought about by the excitation of vibrational modes should be less than the chemical shift between protons in completely different molecules. On this basis, it seems very unlikely that the chemical shift of the upper vibrational state from the ground vibrational state in HBr should be more than 100 cps. Even if this number were 1000 cps, this would not invalidate the argument below. Let Δ be defined as the chemical shift of the upper vibrational state from the ground vibrational state. Assuming $|\Delta(\text{HBr})|<100$ cps and remembering that the vibrational frequency of HBr is 2559 cm^{-1}, one readily calculates that $|dv/dT|$ for HBr is less than 0.0001 cps per °C, where ν is the resonance frequency at 14 092 gauss. Throughout this discussion we assume in addition that in the gaseous phase there are only free unassociated molecules, and therefore, no other effect causes a dv/dT of comparable magnitude.

The linewidth of the signal from HBr is several cycles per second. For this reason measurements made using it as a standard are somewhat difficult. Therefore, methane was adopted as a secondary standard. It is apparent from Table I that methane is temperature independent with respect to HBr, and is therefore temperature independent on an absolute basis to within our experimental accuracy.

The NMR shifts of most of the compounds under consideration are indeed temperature dependent. In general, the resonance shifts to low field as the temperature is increased.

Let Δ_i be the shift associated with exciting the ith vibrational mode of a molecule, δ^0 the shift from methane of the ground vibrational state, ν_i the vibrational frequency associated with the ith vibrational mode, ν_0 the spectrometer frequency, and g_i the degeneracy of the ith mode. We can then write

$$\nu_0\delta=\frac{\nu_0\delta^0+\sum_i g_i \exp[-(h\nu_i/kT)](\Delta_i+\nu_0\delta^0)}{1+\sum_i g_i \exp[-(h\nu_i/kT)]}, \quad (1)$$

[6] W. G. Schneider, H. J. Berns'ein, and J. A. Pople, J. Chem. Phys. **28**, 601 (1958).

TABLE II. Average infrared vibrational frequencies for CH_2 bending modes in cyclic hydrocarbons.

Mode	Cyclopropane	Cyclobutane	Cyclopentane
CH_2 rock	1000 cm^{-1}	1050 cm^{-1}	1055 cm^{-1}
CH_2 wag	1050	1250	1250
CH_2 twist	870	1080	1100

where δ is the chemical shift from methane. When all of the vibrations with sizeable Δ's have ν's greater than 200 cm^{-1}, and when we are in the temperature range around 50°C, this can be simplified to

$$\nu_0\delta=\nu_0\delta^0+\sum_i g_i\Delta_i \exp[-(h\nu_i/kT)] \quad (2)$$

and

$$d\nu_0\delta/dT=\sum_i g_i\Delta_i(h\nu_i/kT^2)\exp[-(h\nu_i/kT)]. \quad (3)$$

That is, there is an additive contribution to $d\nu_0\delta/dT$ from each of the various modes of vibration.

The question of degeneracy is somewhat complicated by the following: Consider a single hydrogen atom vibrating against a carbon skeleton; there is a Δ associated with exciting this mode of vibration. Now consider two identical hydrogen atoms attached to the same carbon atom. In order to achieve the same observed chemical shift of the two hydrogen nuclei, one would have to excite both the symmetric and antisymmetric stretching modes. The Δ associated with either of these two modes would be approximately one-half the Δ associated with the stretching mode of a single hydrogen atom. Therefore, if one hopes to assign a given Δ to a given kind of vibrational mode, one must collect terms in the sum of Eq. (3) which deal with a given kind of vibration, e.g., CH_3 parallel deformations or CH_2 deformations, and consider this set of terms as a single contribution. One should then use an average of the individual vibrational frequencies, assign a degeneracy of one, and assign a Δ_{eff} to this average mode. In the case of a single group, Δ_{eff} is equal to the chemical shift brought about by exciting all of the modes of one kind in that group. These Δ_{eff}'s should not depend upon the symmetry of the molecule, but only upon the type of motion involved.

Over the temperature range studied it is impossible to gain much information about Δ_{eff} for any mode the frequency of which is above 2000 cm^{-1} since these modes are always so lightly populated that the term in the sum for dv/dT associated with them is less than our experimental error if $|\Delta_{eff}|<130$ cps. This seems reasonable in that all organic compounds have resonant frequencies in a range of approximately 600 cps at 60 Mc/sec. Therefore, although exciting such modes as the CH stretching mode is probably very effective in causing a chemical shift, the effect is too small to be measurable in the temperature range under consideration.

Methane. The bending modes in methane are at 1526 cm^{-1} and 1306 cm^{-1}. The temperature dependence of the chemical shift of methane is 0.0000 ± 0.0005 cps per °C. Since both of these modes only involve changing H—C—H bond angles, one would expect Δ_{eff} for these two modes to be of the same sign. This limits the Δ_{eff} for each of the bending modes in methane to less than 10 cps in absolute value.

Ethane. Again, the temperature dependence of the chemical shift in ethane is 0.0000 ± 0.0005 cps per °C. This may come about as an accidental, exact cancellation of two or more temperature-dependent terms of opposite sign, but this seems highly unlikely; particularly since a consistent picture can be presented by assuming all Δ_{eff} are negative except for modes involving delocalization of multiple bonds. It is therefore assumed that for ethane the individual terms in the sum of Eq. (3) do not cancel each other, but in fact are individually zero to within our experimental error. One then is led to the following limits on the absolute value of Δ_{eff} for the various vibrations in ethane: $|\Delta_{eff}|$ for CH_3 perpendicular deformation is less than 17 cps; for the CH_3 parallel deformation, it is less than 13 cps; for the CH_3 wag, it is less than 3 cps; and for the C–C stretch, it is less than 3 cps.

In Gutowsky's semiquantitative calculation[1] of the contribution of the H–C–H bends, a Δ_{eff} is predicted for these modes of approximately 2 cps. Using this calculated order of magnitude, it must now be assumed only that the contribution to the chemical shift due to the CH_3 wagging modes does not exactly cancel out the contribution from the C–C stretching mode. One would expect these two modes to result in quite different orders of magnitude. Therefore, this assumption seems very reasonable.

Cyclic compounds. In this series of compounds the temperature dependence of the chemical shift becomes smaller as the size of the ring is increased. This immediately implies that the low-lying ring deformation modes have very small Δ_{eff}'s since the larger the ring, the lower the ring mode frequencies become. By comparison with the bending modes in methane and ethane, and with the predictions of Gutowsky's calculation,[1] it seems unreasonable that the absolute value of Δ_{eff} for the CH_2 deformations should be greater than 10 cps. This would result in a negligible contribution to $d\nu_0\delta/dT$. In comparison with ethane again, $|\Delta_{eff}|$ for the C–C stretching modes is probably less than 3 cps which also gives a negligible contribution to $d\nu_0\delta/dT$. One must therefore look to the CH_2 bending modes for the cause of the temperature-dependent chemical shift. In Table II are tabulated the averages of these modes for the three compounds.

It can be seen that the CH_2 bending modes are the lowest in frequency in the cyclopropane and are the highest in cyclopentane. Thus if these modes all had the same magnitude of Δ_{eff} associated with them, this would result in the proper trend of temperature dependence of chemical shifts with ring size. If one assumes that the Δ_{eff}'s for the three modes in a given compound

are equal one calculates $\Delta_{eff}=-14$, -16, -9 cps for cyclopropane, cyclobutane, and cyclopentane, respectively. Although the experimental agreement is not good, it at least makes one believe that these are the modes which are mainly responsible for the temperature dependence, and that $\Delta_{eff}=-13$ cps is of the proper order of magnitude for these modes. Indeed, it is not surprising that Δ_{eff} varies somewhat within this series due to the change in electronic configuration in the CH bonds due to ring strain.

Tetrahedral compounds. Again by comparison with ethane one would expect the CH_3 perpendicular and parallel deformations, the CH_3 wags, and the skeletal stretching modes to contribute a negligible amount to $d\nu_0\delta/dT$. The torsional modes are so low in frequency that they must involve very small changes in the electronic structure. Therefore, their contribution to $d\nu_0\delta/dT$ is expected to be very small. This is in agreement with the observation for the low-lying ring modes in the cyclic compounds.

The temperature-dependent shift must therefore come about as a result of the skeletal bending modes. Making this assignment, one calculates for the skeletal bending modes $\Delta_{eff}=-6$, -11, -11 cps for tetramethylmethane, tetramethylsilane, and tetramethyltin, respectively. The near equality of these three values is reassuring considering the differences between the three molecules.

Multiple-bonded compounds. In acetylene both the CH stretch and the C≡C stretch are so high in frequency that even if $\Delta_{eff}=\pm 100$ cps for these modes, the observed temperature dependence would be negligible. The only modes left are the CH bending modes and these must account for -0.0083 cps per °C. This implies that Δ_{eff} for these bending modes is -17 cps which is quite high compared to the bending modes in the CH_3 group, and is even quite high compared to the bending modes in the CH_2 group. This is probably due to the proximity of the π electrons in the triple bond. These electrons will be responsible for the proton's being less shielded when it is off the figure axis of the molecule than when it is on.[7] Therefore, exciting the CH bending modes will cause the protons to spend a greater fraction of their time off the figure axis, thus moving their resonance downfield in excess of the shifts observed in the other CH bending modes cited above.

In 2-butyne, again assuming that the CH_3 deformation modes, the CH_3 rocking modes, and the C–C stretching modes contribute only a very small amount as in ethane, one must assign Δ_{eff}(skeletal modes)$=4.2$ cps. This seems a rather large effect compared to other shifts calculated for skeletal modes such as the C–C stretch. However, when one considers that again bending the molecule interferes with the π electrons, one can believe that 4.2 cps is not too large a Δ_{eff} for the skeletal bends.

[7] See the discussion of the effect of π electrons on protons in the vicinity: J. A. Pople, W. G. Schneider, and H. J. Bernstein, *High Resolution Nuclear Magnetic Resonance* (McGraw-Hill Book Company, Inc., New York, 1959), pp. 176–179.

TABLE III. Chemical shifts associated with excitation of vibrational modes.

Mode	Δ_{eff} (cps)
CH_2 rocks, wags, and twists	-13
Skeletal bending modes in tetramethyl compounds	-10
C—H bends in C≡C—H	-17
CH_2 twists in C=CH_2	$+36$

In ethylene, a positive shift is observed with increasing temperature. One can make a good estimate of the Δ_{eff}'s for the CH_2 modes from the cyclic compounds. Again, the frequency of the CH stretches and the C=C stretch are too high to show up as a temperature variation of the chemical shift. The CH_2 rocks and wags should have Δ_{eff}'s of about 20 cps taking into account the π electrons. All of these contributions combine to give a $d\nu_0\delta/dT$ of approximately -0.0070 cps per °C. The experimentally observed $d\nu_0\delta/dT$ of $+0.0038$ cps per °C varies from this by 0.0108 cps per °C. This large upfield shift must result from the twisting mode about the double bond. As this mode is activated, the double-bond character of the bond should be decreased and the electron density in the vicinity of the protons should be increased causing an upfield shift as observed. This interpretation is of course made with the naive assumption that greater electron density provides greater shielding which is not precisely true. On the basis of the above calculations Δ_{eff} for this twisting mode in ethylene is $+36$ cps. These results are summarized in Table III.

CONCLUSIONS

Exciting a vibrational mode in a molecule does in general cause chemical shifts of the protons which are in the vicinity of the excited mode. The magnitude of the investigated shifts range from 0 to 40 cps, and may be in either direction (to increased or decreased shielding).

The observed shifts due to isotopic substitution can be explained on the basis of the magnitude of the shifts reported here. For example, assuming shift is linearly connected with position in the potential well, if excitation of a CH_2 deformation mode from the ground state to the first excited state ($E=\frac{1}{2}h\nu$ to $\frac{3}{2}h\nu$) produces a shift of less than 13 cps, substitution then of D for H ($E=\frac{1}{2}h\nu$ to $\sqrt{3}/4h\nu$) should produce a shift of less than 0.2 cps at the deuterium and hydrogen atoms. This is less than, but of the order of magnitude of the observed shifts. The CH_2 rock, wag, and twist should each make a contribution of approximately the same magnitude as the one calculated above.

Gutowsky[1] in his explanation of the observed isotope shifts has attributed the entire effect to the CH_2 defor-

mation modes. However, the results of this work lead us to believe that one cannot hope to explain the observed isotopic shifts unless one also considers vibrational modes other than the CH_2 deformation. Although no quantitative information can be gained from this work on the shift associated with excitation of the C–H stretching mode, the fact that excitation of modes other than the CH_2 deformation produces large chemical shifts suggest that the C–H stretching modes may be very important in the explanation of isotopic shifts.

THE JOURNAL OF CHEMICAL PHYSICS VOLUME 35, NUMBER 4 OCTOBER, 1961

Nonresonant Dielectric Dispersion in Asymmetric Rotors*

JAMES E. BOGGS AND A. P. DEAM

Department of Chemistry and Electrical Engineering Research Laboratory, The University of Texas, Austin 12, Texas

(Received February 6, 1961)

Dielectric dispersion measurements at 400 Mc and 40.0°C are reported for CH_2=CHCl and CH_2=CF_2 in the gas phase. The results for these two molecules and earlier measurements on C_2H_3Cl are compared with theoretical expectations for nonresonant dispersion resulting from pressure-broadened transitions between asymmetry doublet levels.

INTRODUCTION

NONRESONANT dispersion and absorption in the microwave region have been the subject of numerous recent investigations. For symmetric top molecules, which have been most extensively studied, the phenomena are related to transitions between nearly degenerate levels which are, respectively, symmetric and antisymmetric with respect to inversion.[1–6] It has been shown[4,6–11] that certain asymmetric rotors also exhibit nonresonant dispersion and absorption, and the effects have been explained[3] in terms of transitions between the asymmetry doublet levels. It is the purpose of the present work to compare the theoretical predictions for asymmetric rotors with experimental results which have previously been reported for ethyl chloride[4,7] and with new measurements on vinyl chloride and 1,1-difluoroethylene.

EXPERIMENTAL METHODS AND RESULTS

The apparatus and experimental method used have been described previously.[4] The gases were analyzed mass spectrometrically and found to be free of significant quantities of impurities. Special care was taken to look for impurities which might themselves show dielectric dispersion. In calculating molar polarizations, the molar volume was taken as $RT/p-A$, where $A=0.388$ liters for CH_2=CHCl and 0.177 liters for CH_2=CF_2, both at 40.0°C.[12]

The measured molar polarizations at 40.0°C and 400 Mc are shown as a function of pressure in Fig. 1. The lines drawn through the experimental points are plots of the Cole-Cole equation

$$\frac{P-P_\infty}{P_0-P_\infty}=\frac{1+(p/p_M)^{\alpha-1}\sin(\alpha\pi/2)}{1+2(p/p_M)^{\alpha-1}\sin(\alpha\pi/2)+(p/p_M)^{2(\alpha-1)}},$$

where P_0 is the molar polarization at low frequency (or at high pressure), P_∞ is the molar polarization at frequencies above the dispersive region (or at low pressure), p_M is the pressure at the midpoint of the dispersion curve, and α is a measure of the distribution of linewidths.

The data for CH_2=CHCl at 40.0°C are well fitted by the Cole-Cole equation with $P_0=57.70$ cc, $P_\infty=54.00$ cc, $\alpha=0.03$, and the line-broadening constant $\Delta\nu/p=3.5$ Mc/mm. A value of 57.03 cc has previously been obtained for the static polarization P_0 by measurements at low frequency.[13]

The data for CH_2=CF_2 give values of $P_0=49.92$ cc, $P_\infty=47.70$ cc, $\alpha=0$, and $\Delta\nu/p=4.1$ Mc/mm. The static dielectric constant has not been previously measured in the gas phase, but Roberts and Edgell have determined the dipole moment as 1.37 debye from the

* This work has been supported by the Office of Naval Research.

[1] G. Birnbaum, J. Chem. Phys. **27,** 360 (1957).
[2] J. E. Boggs, J. Am. Chem. Soc. **80,** 4235 (1958).
[3] E. B. Wilson, Jr., J. Phys. Chem. **63,** 1339 (1959).
[4] J. E. Boggs and A. P. Deam, J. Phys. Chem. **64,** 248 (1960).
[5] A. A. Maryott, A. Estin, and G. Birnbaum, J. Chem. Phys. **32,** 1501 (1960).
[6] J. E. Boggs, A. P. Deam, and J. M. King, J. Chem. Phys. **33,** 1852 (1960).
[7] Krishnaji and G. P. Srivastava, Phys. Rev. **106,** 1186 (1957).
[8] J. E. Boggs, C. M. Crain, and J. E. Whiteford, J. Phys. Chem. **61,** 482 (1957).
[9] J. E. Boggs, J. E. Whiteford, and C. M. Thompson, J. Phys. Chem. **63,** 713 (1959).
[10] J. E. Boggs and H. C. Agnew, J. Phys. Chem. **63,** 1127 (1959).
[11] J. E. Boggs and A. P. Deam, J. Chem. Phys. **32,** 315 (1960)
[12] P. G. T. Fogg and J. D. Lambert, Proc. Roy. Soc. (London) **A232,** 537 (1955).
[13] J. A. C. Hugill, I. E. Coop, and L. E. Sutton, Trans. Faraday Soc. **34,** 1518 (1938).

microwave Stark effect.[14] Taking the distortion polarization as 12.3 cc (the sum of the electron group refractions plus 10%), our value of P_0 leads to a dipole moment of 1.39 debye.

DISCUSSION

A. Nearly Prolate Rotors

Vinyl chloride has rotational constants of $A=56\,121$ Mc and 56 281 Mc, $B=6030$ Mc and 5904 Mc, and $C=5445$ Mc for the Cl^{35} and Cl^{37} isotopes, respectively.[15] The molecule approaches a prolate rotor very closely, with Ray's asymmetry parameter $\kappa=-0.9769$ for $CH_2{=}CHCl^{35}$ and -0.9779 for $CH_2{=}CHCl^{37}$. Since vinyl chloride has the major component of its dipole moment along the least axis of inertia, it will be governed by a-type selection rules and the observed $\Delta J=0$ transitions will be at low frequencies where they should contribute to nonresonant dispersion. Calculation of some of the expected transition frequencies shows that some of the weaker transitions having low values of the quantum number K_{-1} fall above 400 Mc, but most of the strong transitions are far below. The latter should contribute to nonresonant dispersion, the higher frequency transitions appearing, if at all, as distortions of the shape of the dispersion curve. An examination of the tables of Schwendeman and Laurie[16] shows that the individual line intensities for a rotor with $\kappa=-0.977$ do not differ greatly from those for a prolate symmetric rotor.

For a symmetric rotor, the fraction of the orientation polarization associated with nonresonant polarization, $(P_0-P_\infty)/(P_0-P_D)$, is given[4] by

$$\frac{1}{\mu^2}\sum_{JK} f_{JK}\,|\,\mu_{JK}\,|^2,$$

the matrix elements being those appropriate for a $\Delta J=0$ transition. The same relationship should apply for a slightly asymmetric rotor to the extent that it can be approximated by a symmetric rotor model. If vinyl chloride is considered as a prolate symmetric rotor with $A=56\,121$ Mc and $B=C=5730$ Mc (the geometric mean of the actual B and C), the sum

$$\frac{1}{\mu^2}\sum_{JK} f_{JK}\,|\,\mu_{JK}\,|^2$$

can be evaluated by Birnbaum's closed-form expression as 0.103. The calculation is only moderately sensitive to the choice of B; if B is increased by 1%, the sum increases by 0.7%. The calculated value, however, corresponds to the entire dipole moment of the molecule rather than to the component of the dipole moment along the a axis which contributes to the nonresonant dispersion. The latter may be calculated,

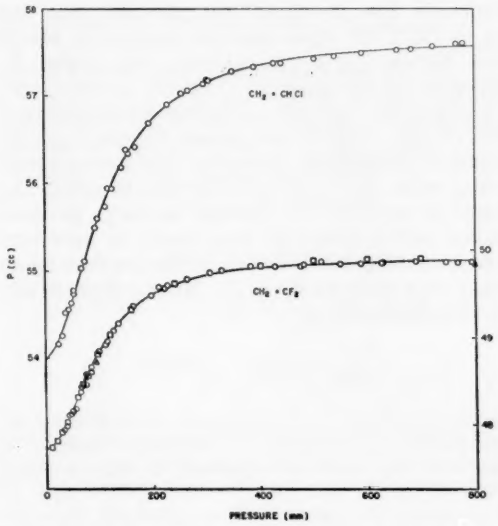

FIG. 1. Molar polarization as a function of gas pressure at 40.0°C and 400 Mc. The units on the left ordinate refer to $CH_2{=}CHCl$ and those on the right ordinate refer to $CH_2{=}CF_2$.

assuming the moment lies along the C—Cl bond which is inclined at an angle of approximately 20° from the a axis.[15] This leads to a value of $(\mu_a/\mu)^2=0.883$ and the corrected value of the sum over states is 0.091. Taking the distortion polarization of vinyl chloride as 17.2 cc (the molar refraction plus 10%), the value of $(P_0-P_\infty)/(P_0-P_D)$ calculated from our measurements is 0.091. The agreement between this value and the predicted value is better than would have been expected considering the approximations made.

Ethyl chloride is also a nearly prolate rotor with $A=30\,124$ Mc and 33 328 Mc, $B=5494$ and 5397 Mc, $C=4962$ Mc and 4812 Mc, and $\kappa=-0.9577$ and -0.9590 for $C_2H_5Cl^{35}$ and $C_2H_5Cl^{37}$, respectively.[17] If it is considered as a symmetric rotor with $A=30\,124$ Mc and $B=C=5220$ Mc, the calculated value of

$$\frac{1}{\mu^2}\sum_{JK} f_{JK}\,|\,\mu_{JK}\,|^2 \quad \text{is } 0.141.$$

The C—Cl bond forms an angle of 26° 42′ with the a axis,[18] so $(\mu_a/\mu)^2=0.798$, and the corrected value of the sum over states is 0.113. The previously reported dispersion measurements[4] lead to a value of

$$(P_0-P_\infty)/(P_0-P_D)$$

of 0.114, again in good agreement with expectation.

B. Difluoroethylene

The behavior of difluoroethylene is quite different. This molecule approaches the oblate rotor case with

[14] A. Roberts and W. F. Edgell, J. Chem. Phys. **17,** 742 (1949).
[15] J. H. Goldstein and J. K. Bragg, Phys. Rev. **75,** 1453 (1949).
[16] R. H. Schwendeman and V. W. Laurie, *Tables of Line Strengths* (Pergamon Press, New York, 1958).
[17] R. S. Wagner and B. P. Dailey, J. Chem. Phys. **22,** 1459 (1954).
[18] R. S. Wagner and B. P. Dailey, J. Chem. Phys. **26,** 1588 (1957).

$A=11\,002$ Mc, $B=10\,429$ Mc, $C=5346$ Mc, and $\kappa=+0.797$.[14] The dipole moment is along the axis of least moment, so a-type selection rules apply. An inspection of the expected Q-branch transition frequencies shows that only a relatively small number of lines of high J fall at low enough frequency to contribute to nonresonant dispersion. Our measurements give a value for $(P_0-P_\infty)/(P_0-P_D)$ of 0.059. The degree of asymmetry is perhaps too large for comparison with a symmetric rotor model to have very precise meaning, but if the calculations are done for an oblate rotor with $A=B=10\,712$ Mc and $C=5346$ Mc, the calculated value of

$$\frac{1}{\mu^2}\sum_{JK} f_{JK}\,|\,\mu_{JK}\,|^2 \quad \text{is } 0.429.$$

The dipole moment lies on the a axis. Even allowing for considerable inaccuracy in the calculated value, it is clear that the observed dispersion is only a small fraction of that which would be associated with all of the allowed $\Delta J=0$ transitions, as was predicted from the expected transition frequencies.

Presumably, one could calculate the intensity sum for the asymmetric rotors directly, without referring to a symmetric rotor analog as we have done here. The calculations would be very tedious, however, since the summation would need to be carried out to quite high J values, especially in the case of $CH_2=CF_2$ where these are the significant transitions. The calculations which have been reported[7] for C_2H_5Cl use a linewidth which does not agree with our experimental results or with other nonresonant widths for similar molecules.

ACKNOWLEDGMENT

The authors would like to express their appreciation to Professor E. Bright Wilson for his helpful discussions and suggestions.

THE JOURNAL OF CHEMICAL PHYSICS VOLUME 35, NUMBER 4 OCTOBER, 1961

Flame Propagation in Free-Radical-Containing Solids at Low Temperatures

A. L. BERLAD

Convair Scientific Research Laboratory, San Diego, California

(Received February 13, 1961)

A nonadiabatic theory of flames is formulated which describes the features of flame propagation in free radical containing cryogenic solids. This "cryogenic flame" theory is an extension of nonadiabatic flame theory associated with gaseous flames. The general features of cryogenic flames prescribed by the theory include: the characteristic propagation velocity of the reaction wave, the spatial structure of the composition and temperature fields, and the extinction limits associated with flame existence-nonexistence. Application of the formulation is illustrated for the case of flame propagation in N-atom-containing solid N_2.

INTRODUCTION

IT has been noted by Herzfeld and Bass[1] that flame propagation may occur in cryogenic solids which contain chemically reactive species. For the case of a medium consisting of solid nitrogen deposited at 4°K from a microwave discharge, the flame is experimentally observed as a green reaction front which propagates through the medium at a burning velocity u of about 2 cm/sec.[2,3]

Recently, a theory of flame propagation in solid nitrogen at low temperatures has been proposed by Reed and Herzfeld.[4] Good agreement between calculated and observed u values was obtained; however, this agreement must be considered to be fortuitous because of the flame-theoretical assumptions made. The compromising assumptions include a "reaction zone size," as well as a given *temperature "at" which* the reaction proceeds. Neither of these questionable assumptions need be made when a more complete formulation is considered.

It is the purpose of this paper to extend current nonadiabatic flame theory[5,6] to "cryogenic flame" systems. Given the thermophysical and kinetic properties of the reactive medium, the resulting formulation can be used to deduce the actual temperature and composition fields, the burning velocity and the extinction limits associated with a given flame system.[5,6] The theory may also be applied to deduce any unknown kinetic parameter if the burning velocity is known experimentally. Such application is demonstrated for

[1] C. M. Herzfeld and A. M. Bass, Sci. American **197**, 3 (March, 1957).

[2] W. Richardson, National Bureau of Standards.

[3] H. A. Papazian, Convair Scientific Research Laboratory, San Diego, California (private communication).

[4] S. G. Reed and C. M. Herzfeld, J. Chem. Phys. **32**, 1 (1960).

[5] A. L. Berlad and C. H. Yang, Combustion and Flame **4**, 325 (1960).

[6] C. H. Yang, Combustion and Flame (to be published).

the case of flame propagation through N-atom-containing solid N_2.

MATHEMATICAL MODEL

The basic, nonadiabatic flame model previously proposed[5,6] for gaseous flames may be modified to describe the condensed phase phenomenon. Thus, we take the reactive cryogenic medium to be contained within a cylinder of very great length and wall temperature T_u. Cylindrical annuli, plane parallel slabs, or other geometries can be treated equally well.[5,7] For the reaction B+B→B_2, one requires: The energy conservation equation is

$$(d/dx)\lambda(dT/dx)-cG(dT/dx)=-\Re\Delta H+l, \quad (1)$$

and the mass conservation equation is

$$(d/dx)D(d\beta/dx)-(G/\rho)(d\beta/dx)=\frac{\Re\Delta H}{\rho c(T_a-T_u)}, \quad (2)$$

where it is assumed that atom-atom recombination rates at walls are small (compared to reaction rates within the flame volume). The boundary conditions (b.c's) are (unburned, upstream medium)

$$T=T_u\{\beta=1, dT/dx=0\} \quad (3)$$

and (burned, downstream medium)

$$T=T_u\{d\beta/dx=0, dT/dx=0\}. \quad (4)$$

Boundary conditions (3) imply that the concentration of reactant B is not changing with time (unburned composition) as long as the medium is at $T=T_u$. Conditions (4) imply that at a far distance downstream from the flame, the medium eventually cools to the wall temperature T_u.

For the case where l is taken to be zero (adiabatic case), the downstream conditions (4), become

$$T=T_a\{d\beta/dx=0, dT/dx=0\}. \quad (5)$$

Existence of Flame Solutions—Extinction Limits

For the general nonadiabatic case, the problem is to find solutions to Eqs. (1) and (2), subject to conditions (3) and (4). Only certain particular values of G will permit such solutions.[5,6] The mass flow rate G of "unburned" crystal as seen by an observer traveling with the reaction wave, is the eigenvalue for the problem. In addition, relatively large values of the heat loss function l (wall quenching limit) and/or relatively small values of the mole fraction of reactive species f (inflammability limit) will prevent the existence of a solution (and thus the existence of the flame) for all values of G.[5] Thus, we demonstrate these flame extinction limits in a manner similar to that employed for gas phase flames.[5]

Make the transformation $\theta=(T-T_u)/(T_a-T_u)$ and approximate[5] θ by the Gaussian $\theta_m\exp(-x^2/2\sigma^2)$ and $T^3\exp(-E/RT)$ by $k_2\theta^q$, over the temperature range of interest. Then, integration of Eqs. (1) and (2), for $(D\rho c_p/\lambda)=0$ (a simplifying, but nonessential approximation), and a reaction rate of the form (see Appendix) $\Re=f_{N,u}{}^2C_1\beta^2T^3\exp(-E/RT)$, yields

$$\theta_m=\left\{1-\left[1+\frac{f_{N,u}{}^2C_1\Delta Hk_2\theta_m{}^q}{c(T_a-T_u)}\left(\frac{\pi}{2q}\right)^{\frac{1}{2}}\left(\frac{\sigma}{G}\right)\right]^{-1}\right\}$$
$$-(g\lambda/cd^2)(\tfrac{1}{2}\pi)^{\frac{1}{2}}\theta_m(\sigma/G)$$
$$-\frac{S(T_a-T_u)^3\epsilon}{\lambda}\left[\tfrac{1}{2}(\tfrac{1}{2}\pi)^{\frac{1}{2}}\theta_m{}^4+\frac{4T_u\theta_m{}^3}{T_a-T_u}(\tfrac{1}{6}\pi)^{\frac{1}{2}}\right.$$
$$\left.+\frac{3T_u{}^2}{(T_a-T_u)^2}(\pi)^{\frac{1}{2}}\theta_m{}^2\right](\sigma/G). \quad (6)$$

Note that the undetermined parameters, σ and G may be treated as a single parameter (σ/G). On the rhs of Eq. (6), the first term represents the integrated heat release in the range $\theta=0$ to $\theta=\theta_m$; the second and third terms represent integrated conduction and radiation losses, respectively, over the same range. If a flame (physically meaningful solution) is to exist, then Eq. (6) must be satisfied. Conversely, properties of the system which limit the permissable range of θ_m values are the key properties in the determination of extinction limits. In this connection, we note that θ_m and (σ/G) must always be positive. The second and third terms on the rhs of Eq. (6) are always negative. Consequently, a positive value of θ_m is precluded by either of the following:

(i) Sufficiently small, nonzero positive values of the concentration of reactive species (small $f_{N,u}$). This defines a "concentration limit."

(ii) Sufficiently large, finite positive values of the conduction heat loss term (large λ/d^2). This defines a "wall quenching limit." Note that even for physically large reactive media (small conduction losses) the ever-present radiation loss implies a lower limit on C_1, if a flame is to exist. As is the case for gas-phase flames, the existence of heat losses (no matter how small) limits the range of possible θ_m values.

"Cryogenic flames" experimentally display the properties implied by the above analysis, that is,

(a) there is a characteristic velocity associated with the reaction wave.

(b) flame extinction limits are observed. Experimentally, the steady-state wave propagation phenomenon is not observed for very low concentrations of reactive species and/or very small thicknesses of the reactive medium.

APPLICATION OF THEORETICAL MODEL TO FLAME PROPAGATION IN SOLID NITROGEN AT LOW TEMPERATURES

As noted earlier, given the necessary kinetic and thermophysical properties of the reactive medium, one may *simultaneously* deduce G, $T(x)$, $\beta(x)$ from

[7] A. L. Berlad and A. E. Potter, Jr., *Fifth Symposium on Combustion* (Reinhold Publishing Corporation, New York, 1955).

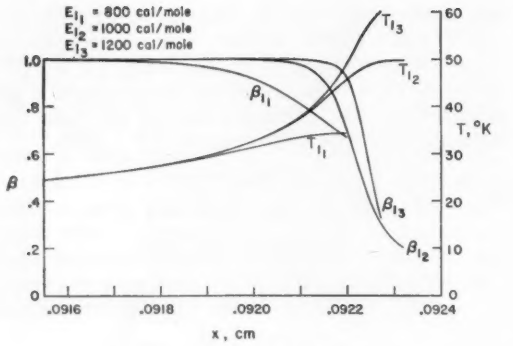

FIG. 1. Trial flame structures.

relations (1)–(4). For the case of N-atom-containing solid N_2, G values have been observed[2] and initial N-atom concentrations estimated.[8,9] Thermal conductivity[10] measurements have been made, and values for the heat capacity and the density are available.[11] An expression for the reaction rate may be derived from the work of Seitz[12] (see Appendix) and is given by

$$\mathfrak{R}=\frac{\rho f_N^2(kT)^3}{h^3\nu_s^2}\exp\left(-\frac{E_j}{RT}\right). \tag{7}$$

The diffusion coefficient (see Appendix) is given by

$$D=\frac{\delta^2(kT)^3}{h^3\alpha_s\nu_s^2}\exp\left(-\frac{E_j}{RT}\right). \tag{8}$$

At this point, we should note that significant uncertainties exist in the data available for $f_{N,u}$, λ, E_j, and ν_s. However, the parameter in greatest doubt is E_j. Moreover, the appearance of E_j, [Eq. (7)] in an exponential makes the solution of this problem very sensitive to the E_j value selected. On the other hand, experimentally observed u values do not vary considerably, either from experiment to experiment or from experimenter to experimenter. Inasmuch as variations of experimental conditions (apparatus geometry, $f_{N,u}$, etc.) must certainly have existed, we conclude that u is not very sensitive to these variations. This is indeed, the same observation which applies to gas phase flame systems.

It therefore is more useful to employ the experimentally determined u value to deduce E_j, rather than to make a precarious assumption for the value of E_j in order to deduce a u value.

Digital computation (IBM 7090) was employed, together with the following values of the thermophysical properties of the medium, in order to deduce E_j:

$T_u=10°\text{K}$, $T_a=60°\text{K}$
$(G/\rho_u)=2.0$ cm/sec
$\lambda = 6.46\times10^{-4}(20/T)^2$ cal/(cm·sec·°K)
$\alpha_s=12$, for all T
$f_{N,u}=3.45\times10^{-3}$ (associated with $T_a=60°\text{K}$)
$\nu_s=1.42\times10^{12}$ sec^{-1} (Debye frequency)
c_p, given by tabulated values of reference 13
$\Delta H=8{,}009.7$ cal/g
$\rho(T)=1.14-5.435\times10^{-3}T=[\text{g/cc}]$
$\delta=3.893_5\times10^{-8}$ cm.

Here (and in reference 4) T_u is estimated to be 10°K. This estimate provides for the experimental fact that heat-transfer effects cause the reactive medium to equilibrate at a temperature that is somewhat higher than that of the refrigerant (4°K). It is to be noted that the reaction rate is vanishingly small at 10°K (as well as at 4°K), thereby making the solution of the problem insensitive to modest errors made in estimating T_u. The thermophysical properties of the medium, together with $f_{N,u}$ (given above) imply $T_a=60°\text{K}$. The effect of different $f_{N,u}$ values (and correspondingly different T_a values) on the solution to the problem is discussed, later.

In order to employ digital integration techniques to the problem, the spatial regime for the integration must be finite. This may be assured in the following way. Take $\mathfrak{R}=0$ and $D=0$ at $T_u=10°\text{K}$. This then leads to an asymptotic solution of Eqs. (1) and (2) which permits replacement of the upstream boundary conditions [Eq. (3)] by the following initial conditions (i.c.'s), for $T_0=10.1°\text{K}$:

$$\left.\begin{aligned}&x_0=0;\ T_0=10.1°\text{K};\ (dT/dx)_0=(0.1)(cG/\lambda);\\&(d\beta/dx)_0=0;\ \beta_0=1\end{aligned}\right\}. \tag{9}$$

Flame theory calculations generally involve a quest for an eigenvalue, G, such that Eqs. (1)–(4) are satisfied. However, given an experimentally determined value of G, we may choose to determine E_j as the eigenvalue. As indicated earlier, the latter calculation appears to be a more useful one for the case under consideration. The digital computation is carried out in the following way:

(a) select a trial E value E_{mn}
(b) use the i.c.'s [Eq. (9)] and the conservation Eqs. (1) and (2) to determine trial temperature and composition profiles.
(c) for the near-adiabatic case, the correct trial E value will be recognized by the fact that the b.c.'s of Eq. (5) are satisfied by the resulting trial profiles for $T(x)$ and $\beta(x)$.

Three different trial E values result in the three sets of

[8] B. J. Fontana, J. Chem. Phys. **31,** 148 (1959).
[9] J. L. Jackson, J. Chem. Phys. **31,** 154, 722 (1959).
[10] H. M. Roder, National Bureau of Standards, Boulder, Colorado (private communication).
[11] *American Institute of Physics Handbook*, edited by D. E. Gray (McGraw-Hill Book Company, Inc., 1957).
[12] Frederick Seitz, *The Modern Theory of Solids* (McGraw-Hill Book Company, Inc., New York, 1940).
[13] W. F. Giaque and J. O. Clayton, J. Am. Chem. Soc. **55,** 4875 (1933).

T and β profiles shown in Fig. 1. Both T_{11} and T_{12} reach maxima far below $T=T_a=60°K$; T_{13} intersects $T_a=60°K$ with a very large $(dT/dx)_{13}$ value for a β_{13} of about 0.3. Obviously, none of these three trial E values is correct.

Figure 2 shows the $\mathfrak{R}(x)$, $T(x)$, $\beta(x)$ profiles resulting from two different trial E values of $E_{21}=1025$ and $E_{22}=1050$. Again, neither E_{21} nor E_{22} is correct. However, the resulting profiles show that the E value which will satisfy the conditions of Eq. (5) lies somewhere between $E=1025$ and $E=1050$. We therefore take $E=1038$ cal/mole to be the deduced E_j value which closely approximates the conditions of the problem.

The effect of different $f_{N,u}$ values on the deduced E value has been investigated. Thus, assumption of a 15% smaller value of $f_{N,u}$ leads to a deduced E value which is smaller by 9%. It is clear also that variations in the numerical values for λ, ν_s, G may effect the deduced flame structure and its associated, characteristic E value. Thus, should the value of $E_j \simeq 1$ kcal/mole need re-examination, on the basis of future reestimates of these parameters, the current theoretical formulation may easily be re-employed.

It is interesting to consider the effect that the kinetics of the crystalline-phase change in N_2 may have upon this calculation. It is known that there are two N_2 phases in equilibrium in the neighborhood of 35.6°K, and that there is a significant latent heat involved in the phase change.[14] Given the kinetic rate for the phase change, this effect may easily be incorporated in the above theory. Thus Eq. (1) would be rewritten

$$(d/dx)\lambda(dT/dx)-cG(dT/dx)=-\mathfrak{R}\Delta H+\mathfrak{R}_p\Delta H_p+l,$$

where $\mathfrak{R}_p=\mathfrak{R}_p(T,\gamma)$. In fact, given adequate independent knowledge of G, E, and the thermophysical properties of the medium, it appears possible to deduce $\mathfrak{R}_p$. At present, however, the rates implicit in $\mathfrak{R}_p$ are not known. The calculations which were performed in obtaining the curves of Figs. 1 and 2 involve the assumption that $\tau_p \geq 2\times10^{-4}$ sec, $u=2$ cm/sec, and a "reaction zone" of the order of 10^{-4} cm (Fig. 2) implies a phase change which affects only the "cooling" (downstream) side of the reaction wave. Thus, the phase change has virtually no affect on the calculated value of E.

However, very fast phase-transformation kinetics will affect the flame structure on the "hot" (upstream) side—and, therefore, the deduced E value. The effect of crystalline phase transformation rates on this and related phenomena is presently under investigation.

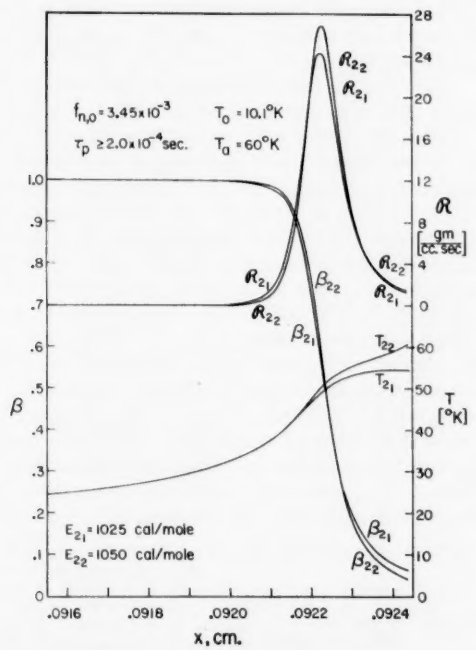

FIG. 2. Two trial flame structures which bracket the correct one.

NOMENCLATURE

B	Reactive atomic species
B_2	Diatomic species, reaction product
c	Heat capacity (cal)/(gm)(deg)
C_1	$(\rho k^3/h^3\nu_s^2)$
D	Diffusion coefficient (cm²)/(sec)
d	Cylinder diameter (cm)
E_j	Activation energy necessary for an interstitial atom to "jump" to a new equilibrium position in the solid
E_{mn}	Trial value of E, employed in the deduction of E_j
f_N	Mole fraction of N in N-atom containing solid N_2
$f_{N,u}$	Initial mole fraction of N in N-atom containing solid N_2
G	Characteristic (mass) burning rate, (g)/(cm²)(sec)
g	Geometric factor for conduction heat loss
h	Planck's constant
ΔH	Heat of "combustion" (cal/g)
ΔH_p	Crystalline phase change latent heat
k	Boltzmann constant
k_2	A constant
l	Heat loss function, l_c+l_r, (cal-cm^{-3}-sec^{-1})
l_c	Heat loss function, conduction $[\lambda g(T-T_u)/d^2]$
l_r	Heat loss function, radiation $[S\epsilon T^4]$
N	Numerical concentration of "inert" particles (cm^{-3})
q	A constant for a given, small range of T
R	Gas constant

[14] K. K. Kelley, Bulletin 477, Bureau of Mines (1950).

$\Re$	Chemical reaction rate in the solid (g)/(cm³) (sec)
$\Re_p$	Crystalline-phase change reaction rate in the solid (g)/(cm³) (sec)
S	Shape factor for radiation
T_a	Adiabatic flame temperature, °K
T_u	Initial temperature of the reactive solid, °K
u	G/ρ, burning velocity (cm/sec)
x	Spatial coordinate (cm)
α_s	Number of saddle points about a given free-radical equilibrium position
β	Free radical (species B) dimensionless concentration in solid inert ($f_N/f_{N,u}$)
γ	Parameter specifying crystalline phase
δ	Distance between crystal planes in the direction of diffusion (cm)
ϵ	Emissivity, effective
θ	$(T-T_u)/(T_a-T_u)$
θ_m	Maximum value of θ
λ	Thermal conductivity, cal/(cm) (°K) (sec)
ν_j	Jump frequency of a diffusing atom in an inert lattice (sec^{-1})
ν_s	Characteristic vibrational frequency of an interstitial atom (sec^{-1})
ρ	Density (g-cm^{-3})
σ	Shape modulus of Gaussian function
τ_p	Reaction time for phase change in N_2 crystal

ACKNOWLEDGMENT

It is a pleasure to acknowledge the invaluable contribution to the computational program of Miss Catherine D. Rozendaal, of the Convair Astronautics Digital Computer Laboratory.

APPENDIX

Reaction Rate and Diffusion Coefficient

The jump frequency for an interstitial atom B is given[12] by

$$\nu_j=(1/h^3)\left[(kT)^3/\alpha_s\nu_s^2\right]\exp(-E_j/RT). \quad \text{(A1)}$$

Thus, if one takes the probability of finding a similar, reactive particle at an adjacent site to be ($f_N\cdot\alpha_s$) and the number of jumps per cubic centimeter per second to be ($\nu_j f_N N$), then the number of molecules of B_2 produced per cubic centimeter per second is ($\nu_j f_N^2\alpha_s N$) and the reaction rate is given by

$$\Re=(\rho f_N^2/h^3)\left[(kT)^3/\nu_s^2\right]\exp(-E_j/RT). \quad \text{(A2)}$$

The diffusion coefficient associated with the interstitial atoms is given[12] by

$$D=(\delta^2/h^3\alpha_s)\left[(kT)^3/\nu_s^2\right]\exp(-E_j/RT) \quad \text{(A3)}$$

or

$$D=\delta^2\nu_j. \quad \text{(A4)}$$

Magnetic Susceptibility of Mercuric Oxide at Various Temperatures

H. MIKHAIL, Z. HANAFY,* AND T. M. SALEM*
Faculty of Science, Cairo University, Giza, Egypt

(Received October 24, 1960)

Mercuric oxide exists in two forms, the red and the yellow oxides. Magnetic susceptibility determinations showed no appreciable difference between the two oxides; the red one has a mass susceptibility of $(-0.221_7\pm 0.0002)\cdot 10^{-6}$ emu/g, while the yellow one has a slightly lower mass susceptibility of $(-0.216_8\pm 0.0002)\cdot 10^{-6}$ emu/g at room temperature (25°C).

The temperature variation of their mass susceptibility between room temperature (25°C) and about 300°C was also investigated. The general shape of the curve for the two oxides is essentially the same, namely, an increase in diamagnetism with rise in temperature followed by a mild drop and subsequently a sharp rise. The position of the peak occurs at about 50°C for the red oxide and at about 114°C for the yellow oxide. A tentative explanation of their behavior was given, based on impurity ionization.

1. INTRODUCTION

THE magnetic study of oxides of most elements needs an elaborate work in order to find out the rules governing their behavior. It is well known that free electrons play an important role in oxide semiconductors. From the magnetic susceptibility point of view, free electrons may be responsible for either a net paramagnetic or a net diamagnetic contribution.

Considering the oxides of the second group elements whose cations are all diamagnetic, the corresponding experimental diamagnetic value of oxygen ion in these compounds, based on pure ionic linkage,[1] differs widely from 18.90 in ZnO, 18.17 in CdO, and 13.75 in HgO. Moreover, the discrepancy for the oxygen ions is greatly manifested in the main group of the alkaline-earths metal oxides, as their values vary from −59.25 in CaO, 11.36 in SrO, and −103.70 in BaO. From this we see that the rule governing the value of the oxygen ion in these oxides is too complicated.

Mercury, in particular, has two mercuric oxides HgO, one being red and the other yellow, depending on the method of preparation. Both forms tend to be partially dissociated, even at ordinary temperatures and pressures if left for a long time. It is the aim of the present work to investigate whether the difference in color of the two oxides is associated with any difference in the temperature variation of their mass susceptibility. The mass susceptibility at 25°C of the yellow and red oxides are respectively $(-0.215_8\pm 0.0002)$ and $(-0.221_7\pm 0.0002)\cdot 10^{-6}$ emu/g as found by the present authors. Nevgi and Mathur[2] obtained a numerically slightly higher mass suceptibility for the yellow oxide $(-0.244\cdot 10^{-6})$ than the red oxide $(-0.243\cdot 10^{-6})$ at room temperature and they concluded that susceptibility values are not affected by particle size, to which, according to Zachariasen,[3] the color difference is probably due. Adolphe *et al.*[4] reported mass susceptibilities $(-0.206\pm 0.004)\cdot 10^{-6}$ and $(-203\pm 0.004)\cdot 10^{-6}$ for the yellow and red oxides, respectively, and they concluded that both oxides are identical rather than allotropic. From x-ray structure point of view, many workers[5] showed that the two forms of the mercury oxide were identically the same.

2. EXPERIMENTAL AND RESULTS

The Gouy method as adopted by one of the present authors in a previous work[6] was employed. The electromagnet used was oil cooled, and was capable of producing a field of 7000 gauss for a current of 10 amp in the coils. The air gap was about 1.5 cm, a distance which is quite sufficient for introducing a heating oven. The balance used was a Galilio-Sartorious. It had an air damping system and could read accurately to 10^{-4} of a gram with great ease. Two experimental tubes were used; one was silica of cross-sectional area 0.7852 cm² and the other was Monax tube of cross-sectional area 0.1965 cm.² Five sets of readings were taken corresponding to field currents of 10, 8, 6, and 4 amp. Such measurements were especially carried out in order to test and correct for any ferromagnetic impurity that may be present. Each set was a mean of eight readings. The mass susceptibility was calculated from the formula

$$\chi_s=(W/dW)\cdot(dS/S)\cdot 0.72 +0.029[1/\sigma-(W/S)(dS/dW)1/d], \quad (1)$$

where dS is the net force resulting from the material and dW is the net force resulting from a standardizing material (water). The mass susceptibility χ_s of the red HgO referred to water as standard $(-0.72\cdot 10^{-6})$ was found to be $(-0.221_7\pm 0.0002)\cdot 10^{-6}$ emu/g, while the

* Present address: The National Research Center, Dukki, Cairo, United Arab Republic.

[1] W. R. Angus, Proc. Roy. Soc. (London) **A136,** 569 (1932); J. C. Slater, Phys. Rev. **36,** 51 (1930); I.C.T. **6,** 354 (1929).

[2] M. B. Negvi and R. N. Mathur, Z. Physik. **100,** 613 (1936).

[3] W. Zachariasen, Z. physik. Chem. **128,** 421 (1927).

[4] A. Pacault and N. Pacault, Compt. rend. **218,** 671 (1944).

[5] K. Aurivillius, Acta Cryst. **4,** 685 (1956); G. R. Levi, Gazz. chim. ital. **54,** 709 (1924).

[6] H. Mikhail, Math. and Phys. Soc. Egypt **2,** No. 3 (1943); J. Chem. Soc. **1944,** 590; **1949,** 2927; J. Chem. Phys. **21,** 1004 (1935).

TABLE I. Magnetic susceptibility of HgO at various fields.

Field current	dW/W for distilled water	dS/S for red HgO	dS/s for yellow HgO	$\chi_s \cdot 10^6$ red HgO	$\chi_s \cdot 10^6$ yellow HgO
10 amp	$(0.0150/3.3448) = 4.485 \cdot 10^{-3}$	$(0.0227/16.9340) = 1.341 \cdot 10^{-3}$	$(0.0125/9.5158) \cdot 1.313 \cdot 10^{-3}$	-0.221_4	-0.216_8
8 amp	$(0.0119/3.3448) = 3.558 \cdot 10^{-3}$	$(0.0180/16.9340) = 1.063 \cdot 10^{-3}$	$(0.0099/9.5158) = 1.040 \cdot 10^{-3}$	-0.221_4	-0.216_6
6 amp	$(0.0077/3.3448) = 2.302 \cdot 10^{-3}$	$(0.0117/16.9340) = 0.6908 \cdot 10^{-3}$	$(0.0063/9.5158) = 0.662 \cdot 10^{-3}$	-0.222_4	-0.212_9
4 amp	$(0.0035/3.3448) = 1.047 \cdot 10^{-3}$	$(0.0053/16.9340) = 0.3130 \cdot 10^{-3}$	$(0.0029/9.5158) = 0.305 \cdot 10^{-3}$	-0.221_5	-0.216_0

TABLE II. Magnetic susceptibility of HgO using a different specimen tube.

10 amp	$(0.0526/10.8225) = 4.860 \cdot 10^{-3}$	$(0.08023/55.3959) = 1.4483 \cdot 10^{-3}$	$(0.04797/33.9250) = 1.414 \cdot 10^{-3}$	-0.221_1	-0.215_7

mass susceptibility for the yellow oxide was found to be $(-0.215_6 \pm 0.0002) \cdot 10^{-6}$ emu/g at 25°C.

Red mercuric oxide has been prepared by the action of heat on mercuric nitrate as follows.

Mercuric nitrate was prepared through the action of pure concentrated nitric acid, which is free from nitrogen oxides and distilled twice, on pure Merck mercury which has been twice distilled in vacuum. The $Hg(NO_3)_2 \cdot H_2O$ so formed was deposited after cooling and the precipitate with its solution was evaporated till dryness and then heated at 300°C until it was completely transferred into red HgO. Traces of HNO_3 were removed by slight alkali followed by distilled water and the sample was finally dried. A test for free nitrogen was done by the micro-Kjeldahl method, then the sample was examined spectroscopically for any other probable impurities.

The yellow HgO has been prepared at room temperature by the wet method from $HgCl_2$, which was prepared by the action of HCl on pure mercury, and caustic potash (B.D.H.). The filtrate was washed several times to free it from Cl ion and KOH, and is then dried between sheets of filter paper in absence of light and at ordinary temperatures. The sample was also tested spectroscopically for impurities.

Typical result are given for the values dW/W, dS/S as well as the corresponding susceptibilities at 25°C in Table I using a Monax glass tube as a container. A single typical result was given in Table II in the case of the silica tube corresponding to a field current of 10 amp. It should be mentioned that density of either oxide was taken to be 11.14 g/cc at room temperature (25°C).

Similar measurements were carried out at various temperatures on both the red and the yellow oxides using the Monax glass tube, and the results are represented graphically in Fig. 1 and 2. A noninductive tubular heating oven, whose temperature was measured by means of a copper-constantan thermocouple over the range between room temperature and about 300°C, was used. Appreciable decomposition of the sample takes place above about 200°C in the yellow oxide and above about 250°C in the red oxide.

3. DISCUSSION OF RESULTS

It is well established that free electrons in a semiconductor play an important role in the magnetic behavior. As was stated before, they may be responsible for either a net paramagnetic or a net diamagnetic contribution. Considering the problem more closely, allowance has to be made for the effective masses of the free electrons in the lattice. It is already known that electrons and holes in the conduction band in a semiconductor produce a diamagnetic (Landau) as well as a paramagnetic (Pauli) contribution resulting from their orbital and spin moments, respectively. The net electronic susceptibility per cubic centimeter (χ_e), based on classical statistics, is given by

$$\chi_e = (n\mu_B^2/kT)[(g/2)^2 - \tfrac{1}{3}(m/m^*)^2], \qquad (2)$$

where n is the carrier concentration, g the Landé factor, μ_B the effective Bohr magneton, m the free electron mass, and m^* the effective mass of the electron in the lattice. From Eq. (2) we see that the sign of χ_e depends on the value of m/m^*. If $m^* \simeq m$, this gives a paramagnetic contribution, while if m^* is less than 0.644 times the free mass m, then the diamagnetic contribution predominates. Thus, the effective mass of the free electrons decides the sign of χ_e. However, the magnitude of χ_e is highly sensitive to temperature variations through the exponential dependence of n on temperature, as might be noted from the equation for the carrier concentration in an intrinsic semiconductor, viz.,

$$n = 2(2\pi kT/h^2)^{\frac{3}{2}}(m_e \cdot m_h)^{3/4} \cdot \exp[-(E_g/2kT)] \qquad (3)$$

$$= AT^{\frac{3}{2}} \cdot \exp[-(E_g/2kT)], \qquad (4)$$

where m_e and m_h are respectively the masses of an electron and a hole, E_g is the energy gap width of the forbidden band, and A is a constant.

Equation (2), however, has to be modified when the semiconductor contains impurity centers. Assuming one type of impurity to be present, we should then write (n_1+n_2) instead of n, where n_1 is the intrinsic carrier concentration per cubic centimeter and has the temperature dependence given by Eqs. (3) or (4); n_2 is the number of electrons per cubic centimeter released by

thermal ionization of the impurity. Then, the electronic susceptibility (χ_e) becomes

$$\chi_e=(n_1+n_2)(\mu_B^2/kT)[(g/2)^2-\tfrac{1}{3}(m/m^*)^2]. \quad (5)$$

At low temperatures[7] (below saturation), n_2, according to the Wilson model of a semiconductor, is given by

$$n_2=(2N_d)^{\frac{1}{2}}(2\pi mkT/h^2)^{3/4}T^{3/4}\exp[-(E_d/2kT)], \quad (6)$$

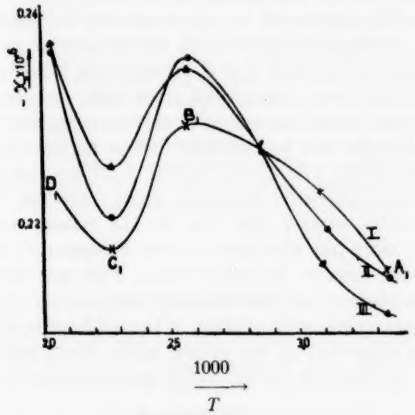

(a)

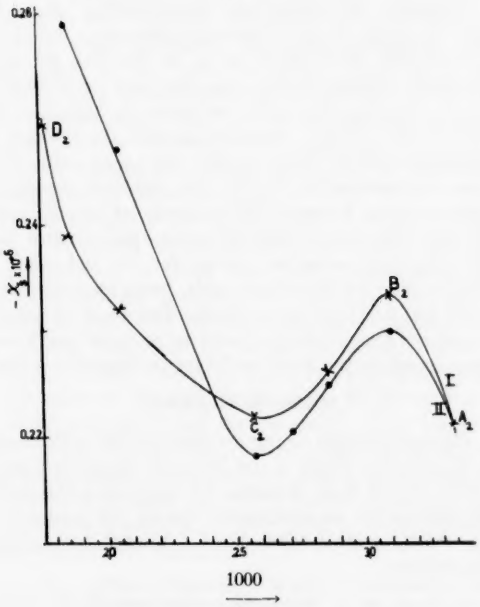

(b)

FIG. 1. (a) Variation of the magnetic susceptibility (x_s) in emu/g vs $1/T$, where T is the absolute temperature for the yellow oxide. (b) The same for red mercury oxide. Curve I for preheated samples. Curve II for a heat-treated sample. Curve III for the same sample after a second heat treatment.

[7] C. Kittel, *Introduction to Solid State Physics* (John Wiley & Sons, Inc., New York, 1957) 2nd ed., pp. 356 and 360.

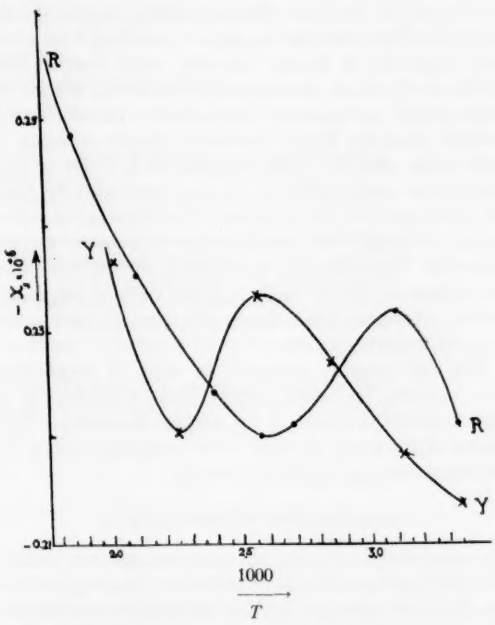

FIG. 2. Comparison of the temperature dependence of magnetic susceptibility (x_s) for the two mercuric oxides.

where N_d is the number of impurity atoms and E_d is the impurity gap width. At low temperatures, n_1 is too small and the temperature variation of the factor (n_1+n_2) is practically dominated by the change of n_2 since E_d is much smaller than E_g.

As the temperature is raised, a saturation stage is approached when the impurities become fully ionized and n_2 tends to N_d, assuming each impurity atom to give one free electron. At this stage, therefore, (n_1+n_2) is practically constant, and thus χ_e according to Eqs. (2) or (5) decreases roughly as $1/T$.

In the intrinsic range of temperature, electrons are increasingly liberated from the pure lattice when they acquire sufficient thermal energy to surmount the forbidden energy gap. The temperature variation of χ_e is now essentially controlled by n_1, and since n_1 increases exponentially with temperature, so χ_e increases numerically.

According to the above argument, we can interpret the different portions of the susceptibility versus temperature curves as follows. By referring to Figs. 1(a), 1(b), and 2, we see that:

1. The first portion AB of the curve, in which diamagnetism increases with rise of temperature, can be explained by the thermal release of electrons (n_2) from impurity centers at low temperatures. At the peak of the curves, the number of free electrons is approaching saturation.

2. The middle portion BC of the curve, where diamagnetism decreases with rise of temperature, may be

attributed to the fact that in view of saturation, the number of free electrons n_2 present resulting from localized impurity is nearly constant with temperature, while the intrinsic carrier concentration n_1, despite its exponential temperature dependence, remains much smaller than n_2. Thus, (n_1+n_2) is nearly constant in this range and χ_e varies roughly as $1/T$ for a nondegenerate semiconductor. As we have already seen, the peak starts in the red oxide earlier than in the yellow oxide, although both oxides show the same general behavior. This situation may arise if the impurity concentration in the red oxide is larger than in the yellow oxide, assuming both forms to contain the same type of impurity centers.

We may roughly estimate, in order of magnitude, the impurity ionization energy from a knowledge of the dielectric constant of the oxides. Assuming Bohr's model of the atom to apply to the impurity atoms, the ionization energy would be given by

$$E_i=13.6(m^*/m)(1/\epsilon^2). \tag{7}$$

At radio frequency and at temperatures low enough (−50°C) to freeze in the effect of any relaxing entities, the dielectric constant is about 9.0 for the two oxides.[8] By taking this value to represent also the optical dielectric constant, and taking m^*/m to be equal to 0.5, which is a reasonable estimate for a diamagnetic material, the ionization energy comes out to be near 0.06 ev.

A difference in the concentration of impurity centers in the two oxides is bound to make E_i slightly different in the two forms since the process is generally easier (E_i smaller) for larger concentration. In this way we may account for the observation that the peak in curve (Fig. 2) occurs for the red form at a temperature (50°C) lower than that for the yellow form (115°C).

3. The high-temperature portion CD of the curves may be considered as arising from the dominant action of the electrons which jump from the valence band to the conduction band and cross the forbidden gap. At this stage n_2 remains constant, but n_1 increases exponentially with temperature and dominates the factor (n_1+n_2), so that the net increase in (n_1+n_2) occurs at a higher rate than the increase in T.

The temperature dependence of electrical conductivity of the two forms of HgO in the range 100–250°C has been determined by the present authors and was found to be 1.18 ev for the red oxide and 1.02 ev for the yellow oxide. If we assume intrinsic conductivity in this range, we may take the forbidden gap width for the two oxides to be of the order of 1 ev, which is considerably greater than $E_d(=2E_i)$. In the portion CD, however, the energy of thermal agitation is large enough to make the temperature dependence of χ_e practically overwhelmed by the exponential increase of n_1.

The above argument explains the general behavior of the temperature dependence of the susceptibility in the two oxides. It should be noted that the diamagnetism of all temperature-independent factors such as the contribution of ion cores or of electrons in the filled valence band[9] has been disregarded since only temperature-dependent terms concern us in this investigation.

It remains now to comment further on the noncoincidence of the two curves in Fig. 2. If we accept the view that impurity ionization energy for the red is appreciably smaller than that for the yellow, we may expect more free electrons at room temperature in the red oxide than in the yellow oxide. This may account for the observation that the room temperature value of the diamagnetic susceptibility of the red form is slightly higher than that of the yellow oxide. The extent depends of course on the amount of impurity present.

4. CONCLUSION

Although the diamagnetic susceptibility values for the two oxides do not differ much from each other, the temperature dependence of χ_e in the two forms is markedly different. This behavior may be accounted for by assuming that in the red oxide the impurities are more easily ionized (possibly because the number of impurity atoms is larger) than in the yellow oxide. This view is supported by the fact that dielectric absorption measurements below room temperature clearly point out the existence of impurity centers and confirm that the impurity ionization energy for the red oxide is smaller than for the yellow oxide, being approximately 0.025 and 0.032 ev,[8] respectively. These last values are in order of magnitude in agreement with our rough estimate based on the Bohr model for the impurity atoms.

ACKNOWLEDGMENT

The authors wish to express their thanks to Professor A. R. Tourky, Head of the National Research Center of the United Arab Republic for suggesting the problem and for his encouragement during the progress of the work, and to Dr. Y. L. Yousef for helpful discussions.

[8] Y. L. Yousef (private communication).

[9] G. Busch and E. Mosser, Helv. Phys. Acta **32**, 24 (1959); **26**, 611 (1952).

THE JOURNAL OF CHEMICAL PHYSICS VOLUME 35, NUMBER 4 OCTOBER, 1961

First Excited $^1\Sigma_g^+$ State of the Hydrogen Molecule*

ERNEST R. DAVIDSON†
Chemistry Department, Indiana University, Bloomington, Indiana

(Received March 21, 1961)

A variation calculation on the first excited $^1\Sigma_g^+$ state of H_2 has been carried out using an expansion in elliptical coordinates. All results are reported in Hartree atomic units.

The potential function resulting from this calculation is characterized by having minima at $R=1.9$ and $R=4.3$ and a maximum at $R=3.3$.

The energy obtained at $R=1.9$ using a 20-term, open-shell, covalent-type wave function was -0.7162 as compared with the "experimental" value of -0.7181. Due to convergence difficulties, many more configurations are required to improve this result significantly. At $R=4.3$, on the other hand, the best result was obtained with an open-shell wave function including nine ionic terms and nine atomic terms. This result of -0.7007 is below the reported "experimental" value of -0.6935 because the two lowest $(2p\sigma)^2\ ^1\Sigma_g^+$ vibrational levels have not been found experimentally. The energy at the top of the barrier was computed to be -0.6844 and probably is as low as -0.6884.

The vibrational levels for this potential function have been computed by a numerical integration technique. The fact that these are in one-to-one correspondence with a combination of the experimental $1s2s$ and $(2p\sigma)^2$ levels indicates that both of these sets of levels belong to the first excited state.

I. INTRODUCTION

UNFORTUNATELY, as Dieke[1] has pointed out' the analysis of the emission spectrum of the hydrogen molecule is difficult because there are many lines but few easily discernible regularities or band systems. Also, those energy levels which have been assigned to this molecule show many irregularities not expected from qualitative quantum-mechanical considerations. These experimental difficulties make it apparent that a more accurate theoretical calculation on the higher energy levels of the hydrogen molecule is needed in order to verify the assignment of energy levels, to explain the irregularities, and to facilitate further analysis of the spectrum.

The first excited $^1\Sigma_g^+$ state is particularly interesting since it is readily accessible to theoretical calculation and supposedly is fairly well known experimentally. At the same time, however, the vibrational-rotational levels associated with this state show many irregularities in spacing which are not easily explained. Further, except for a recent paper by Kolos and Roothaan,[2] only rough estimates by Hylleraas[3] and by MacDonald[4] are available for predicting the potential curve for this state. Even the relatively precise results obtained by Kolos and Roothaan extend over only a short range of internuclear distance and give a poorer estimate of the energy than one would expect from a 40-term James and Collidge type function.

† Present address: Theoretical Chemistry Laboratory, University of Wisconsin, Madison, Wisconsin.

* Supported in part by the AFOSR and Indiana University and by the National Science Foundation. These calculations were carried out in the Indiana University Research Computing Center.

[1] G. H. Dieke, J. Mol. Spectroscopy **2,** 494 (1958).

[2] W. Kolos and C. C. J. Roothaan, Revs. Modern Phys. **32,** 219 (1960).

[3] E. Hylleraas, Z. Physik **71,** 739 (1931).

[4] J. K. L. MacDonald, Proc. Roy. Soc. (London) **A136,** 528 (1932).

II. QUALITATIVE PREDICTIONS

Most of the irregularities present in the excited $^1\Sigma_g^+$ states can easily be predicted from simple perturbation considerations although no one seems to have approached the problem in this way previously.

The electronic Hamiltonian for the hydrogen molecule is conventionally written in Hartree atomic units as

$$H=-\tfrac{1}{2}\nabla_1^2-\tfrac{1}{2}\nabla_2^2-r_{a1}^{-1}-r_{b1}^{-1}-r_{a2}^{-1}-r_{b2}^{-1}+r_{12}^{-1}. \quad (1)$$

If the r_{12}^{-1} term is treated as a perturbation, then for a fixed value of R the eigenfunctions of the unperturbed Hamiltonian can be written as

$$\Psi_{ij}^{(0)}=\begin{cases}\phi_i(1)\phi_i(2) & i=j\\ 2^{-\frac{1}{2}}[\phi_i(1)\phi_j(2)\pm\phi_j(1)\phi_i(2)] & i\neq j.\end{cases} \quad (2)$$

Here, the ϕ_i are the well-known wave functions for the hydrogen molecule positive ion. The electronic energy of the molecule, to this approximation, is given by

$$E_{ij}^{(0)}=E_i+E_j. \quad (3)$$

Since this can be done at every internuclear distance, the potential function $E_{ij}^{(0)}(R)$ is easily constructed from the $E_i(R)$. These latter potential functions have already been found for several states and a wide range of R by Bates.[5]

The results obtained for several of the $E_{ij}^{(0)}$ are shown in Fig. 1. The outstanding features of this plot are the numerous crossings and asymptotic degeneracies between states of the same symmetry. For instance, the $(2p\sigma_u)^2\ ^1\Sigma_g^+$ state is degenerate at large R with the $(1s\sigma_g)^2\ ^1\Sigma_g^+$ state and crosses the $1s\sigma_g 2s\sigma_g\ ^1\Sigma_g^+$ state, the $1s\sigma_g 3d\sigma_g\ ^1\Sigma_g^+$ state, etc.

If the effect of the r_{12}^{-1} perturbation term is included,

[5] D. R. Bates, Proc. Roy. Soc. (London) **A246,** 215 (1953).

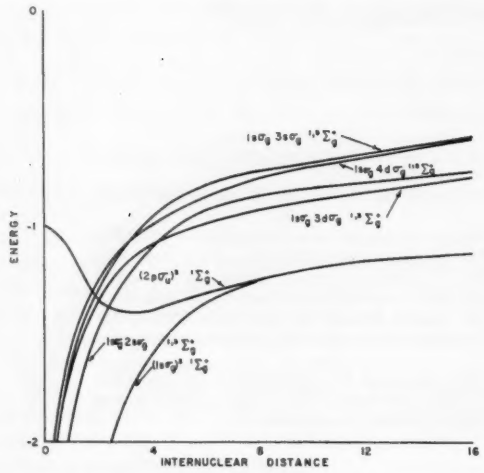

FIG. 1. A zeroth-order approximation to the electronic energy of H_2 as a function of distance.

all of the crossings between states of the same symmetry disappear and the Ψ^0 wave functions become mixed. Many of the degeneracies at large R are removed also. Thus, for example, the $(1s\sigma_g)^2$ and $(2p\sigma_u)^2$ states become mixed at large R to form the valence bond function $2^{-\frac{1}{2}}[1s_a(1)1s_b(2)+1s_b(1)1s_a(2)]$ and the ionic function $2^{-\frac{1}{2}}[1s_a(1)1s_a(2)+1s_b(1)1s_b(2)]$. The first-order correction for the first of these functions is zero while $E^{(1)}$ for the ionic function is $+\frac{5}{8}$.

From simple considerations of this type the potential curves $E_{ij}+1/R$ are easily sketched as shown in Fig. 2 for three of the $^1\Sigma_g^+$ states. As shown by this sketch, double minima in the higher potential curves should be expected. Also, there are more minima present than there are united atom states. It is for this reason that spectroscopists have been unable to establish a one-to-one correspondence between observed sequences of term levels and expected electronic states.

III. CALCULATION OF THE POTENTIAL CURVE

The linear variation method was used and the basis set was picked to minimize the second root of the secular equation at each value of R. The justification for this procedure is based on the extended variation theorem proved by Hylleraas and Undheim[6] and on the excited state convergence theorem proved by Shull and Lowdin.[7]

For values of R near the inner minimum it was expected that the wave function for the first excited $^1\Sigma_g^+$ state would be approximately of the open shell form $2^{-\frac{1}{2}}[1s\sigma_g(1)2s\sigma_g(2)+2s\sigma_g(1)1s\sigma_g(2)]$. It is known, however, that the $1s\sigma_g$ wave function for H_2^+ can be expressed accurately as a linear combination of a few functions of the type

$$f_i(n_i,j_i,\alpha)=N_i(2\pi)^{-\frac{1}{2}}(2/R)^{\frac{1}{2}}\xi^{n_i}\eta^{j_i}\exp(-\alpha\xi),$$

where ξ and η are the elliptical coordinates $(r_a+r_b)/R$ and $(r_a-r_b)/R$, respectively. Similarly, the $2s\sigma_g$ function can be expressed as a linear combination of a few functions of the type $\bar{f}_i=f_i(n_i,j_i,\bar{\alpha})$, where $\bar{\alpha}<\alpha$. Hence, it seems natural to attempt to expand the wave function Ψ for this excited state as a linear combination of configurations $\Phi_k(1,2)$ which are defined by

$$\Phi_k(1,2)=\sum_{i,j}\gamma_{i,j}{}^k[f_i(1)\bar{f}_j(2)+\bar{f}_j(1)f_i(2)]$$

with the $\gamma_{i,j}{}^k$ chosen so that Φ_k has the same symmetry properties as Ψ.

With a 20 configuration wave function, the optimum value of α at $R=2.0$ was found to be 1.4 and the optimum value of $\bar{\alpha}$ was found to be 0.55. The energy obtained with this function was -0.7159 at $R=1.9$ which compared favorably with the value of -0.71635 obtained by Kolos and Roothaan but was rather far from the experimental value of -0.7181. The optimum parameters for other distances and for two other excited states are given in Table I along with the corresponding energies.

A natural spin-orbital analysis of the wave function obtained at $R=1.9$ is shown in Table II. From these results, the best u and v functions were found such that $2^{-\frac{1}{2}}[v(1)u(2)+u(1)v(2)]$ was a good approximation to Ψ. From previous considerations, it was expected that v should resemble the $1s\sigma_g$ function and u should resemble the $2s\sigma_g$ function. As shown in Fig. 3, the v function is, in fact, quite similar to the $1s\sigma_g$ function. The primary difference between these two functions is that the v function is somewhat less diffuse than the $1s\sigma_g$ function. This increased electronic density between

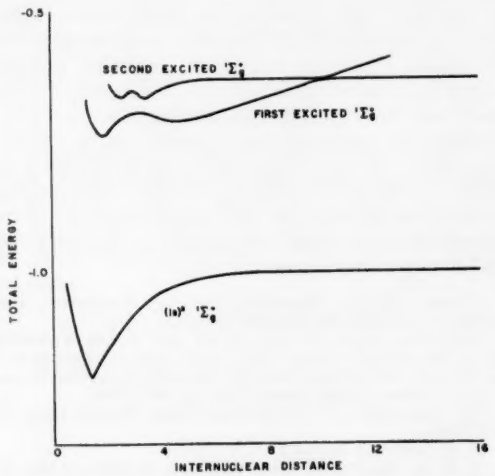

FIG. 2. A sketch of the potential curves for the first three $^1\Sigma_g^+$ states of H_2.

[6] E. A. Hylleraas and B. Undheim, Z. Physik **65**, 759 (1930).
[7] H. Shull and P.-O. Lowdin, Phys. Rev. **110**, 1466 (1958).

TABLE I. Parameters for open-shell calculation.

(A) 20 configurations

R	α_2	$\bar{\alpha}_2$	λ_2	α_3	$\bar{\alpha}_3$	λ_3	α_4	$\bar{\alpha}_4$	λ_4
2.0	1.4	0.55	−0.7156						
2.5	1.6	0.70	−0.7034						
3.0	1.8	0.85	−0.6863	1.6	0.70	−0.6290			
3.5	1.9	1.00	−0.6754	1.8	0.85	−0.6426	1.8	0.85	−0.5781
4.0	2.0	1.20	−0.6732	2.0	1.20	−0.6357	2.5	1.00	−0.5579
4.5				2.3	1.20	−0.6247	2.5	1.00	−0.5592

(B) 24 configurations, $\alpha=1.1$, $\bar{\alpha}=0.4$

R	λ_2	λ_3	λ_4
1.0	−0.5754	−0.4510	−0.3665
1.5	−0.6988	−0.6293	−0.6048
2.0		−0.6527	−0.6497
2.5		−0.6453	−0.6393
3.0			−0.6156

(C) Ionic calculation

R	α_2	λ_2	α_3	λ_3	α_4	λ_4
2.0	1.5	−0.6682	1.5	−0.4420	1.5	−0.2718
2.5	1.5	−0.6905	1.5	−0.5704	1.5	−0.4215
3.0	1.5	−0.6869	1.5	−0.6325	1.5	−0.4899
3.5	2.0	−0.6880	1.5	−0.6506	1.5	−0.5221
4.0	2.0	−0.6982	2.0	−0.6410	1.5	−0.5371
4.5	2.5	−0.7004	2.0	−0.6343	2.0	−0.5303

the nuclei in the v function is compensated for in the u function which is much more diffuse than the corresponding $2s\sigma_g$ function. Also, the singularities at the nuclei in the $2s\sigma_g$ function have been nearly removed in the u function by the shielding effect of the inner shell electrons.

As previously shown, for values of R near the outer minimum, the wave function for the first excited state should be approximately of the form $2^{-\frac{1}{2}}[1s_a(1)1s_a(2)+1s_b(1)1s_b(2)]$. It has been shown by Chandrasekhar,[8] that an open shell form $1s_a1s_a'$ is much more effective in representing H^- than is the closed shell form. Hence, the configurations were defined as before except that f_i was defined as

$$f_i(n_i,j_i,\alpha,\beta)N_i(2\pi)^{-\frac{1}{2}}(2/R)^{\frac{1}{2}}\xi^{n_i}\eta^{j_i}e^{-\alpha\xi}e^{-\beta\eta},$$

and $\bar{f}_i$ was defined as $f_i(n_i,j_i,\bar{\alpha},\bar{\beta})$. Since it was expected that the f_i should represent functions centered on the nuclei, β was set equal to α and $\bar{\beta}$ was set equal to $\bar{\alpha}$. A further simplification was arbitrarily introduced by setting $\bar{\alpha}=\frac{1}{2}\alpha$.

With a wave function consisting of nine ionic configurations and nine covalent configurations, a minimum energy of −0.70067 was obtained at $R=4.35$ and $\alpha=2.5$. The only experimentally determined sequence of term levels which corresponds to a minimum at this internuclear distance has previously been assigned to the $(2p\sigma_u)^2\,{}^1\Sigma_g^+$ state. An extrapolation from the experimental levels[1] indicates that the minimum energy of the potential curve for this state should be −0.6935. Dieke[9] has previously pointed out, however, that there is reason to believe the first two term levels of the sequence have not been observed experimentally. Hence, the result of −0.70067 is not necessarily too low to correspond to the experimental $(2p\sigma_u)^2\,{}^1\Sigma_g^+$ state.

A natural spin-orbital analysis of the wave function at $R=4.25$ provides further evidence for equating the $(2p\sigma_u)^2$ experimental "state" with the outer minimum in the first excited state. As shown in Table III, the dominant NSO is σ_u in symmetry so that to a first approximation the wave function is indeed the product of two odd functions.

The u and v functions found at the inner minimum cannot be defined as real functions at the outer minimum since the first two coefficients in the NSO expansion at $R=4.25$ have the same sign. Incidentally, this is the first known example for which this is true.[10] The significance of these coefficients having the same sign can best be understood from a consideration of the formula given by Shull[11] for the fraction of ionic character, I, of a bond in the case that one of the first two NSO's are σ_g in character and one σ_u. From this formula,

$$I=\tfrac{1}{2}+a_1a_2(a_1^2+a_2^2)^{-1},$$

it can be seen that the fraction of ionic character can only exceed $\frac{1}{2}$ if the signs of a_1 and a_2 are the same. For the wave function at $R=4.25$ the fraction ionic character given by this formula is 0.931 which indicates that

[8] S. Chandrasekhar, Astrophys. J. **100,** 176 (1944).

[9] G. H. Dieke, Phys. Rev. **76,** 50 (1949).

[10] H. Shull and P.-O. Lowdin, J. Chem. Phys. **30,** 617 (1959).

[11] H. Shull, J. Am. Chem. Soc. **82,** 1287 (1960).

TABLE II. Natural spin-orbital analysis at $R=1.9$.

A. Basis functions

$$\phi_k=(n, j, \alpha)=N_k(2\pi)^{-\frac{1}{2}}(2/R)^{\frac{1}{2}}\xi^n\eta^j e^{-\alpha\xi}$$

$$\chi_i=\sum_k b_{ik}\phi_k$$

k	ϕ_k	N_k	b_{1k}	b_{2k}	b_{3k}
1	(0, 0, 1.4)	3.7512622	0.4747	−0.4753	
2	(1, 0, 1.4)	2.1931496	0.1793	−0.1911	
3	(2, 0, 1.4)	1.0193643	−0.0714	−0.0079	
4	(0, 2, 1.4)	9.5768300	0.1095	−0.0823	
5	(0, 0, 0.55)	0.63191935	0.2973	0.2821	
6	(1, 0, 0.55)	0.18653265	0.0404	0.0818	
7	(2, 0, 0.55)	0.03703813	−0.8702	−0.9543	
8	(0, 2, 0.55)	1.4829275	0.0153	0.0085	
9	(0, 1, 1.4)	7.1018861			0.4085
10	(1, 1, 1.4)	4.0259230			0.1505
11	(0, 1, 0.55)	1.1315876			1.2162
12	(1, 1, 0.55)	0.32721795			−1.2538

B. Eigenvector coefficients

$$[N, M]=2^{-\frac{1}{2}}[\phi_N(1)\phi_M(2)+\phi_N(2)\phi_M(1)] \qquad N\neq M$$

$$[N, N]=\phi_N(1)\phi_N(2)$$

$$\Psi=\sum_{N,M} c_{N,M}[N, M]=\sum_i a_i\chi_i(1)\chi_i(2)$$

N, M	$c_{N,M}$	N, M	$c_{N,M}$	N, M	$c_{N,M}$
1, 5	1.0000	3, 5	−0.6419	9, 11	0.1959
1, 6	0.6256	3, 6	0.6673	9, 12	−0.1392
1, 7	−3.7166	3, 7	−0.0217	10, 11	0.2393
1, 8	0.1315	3, 8	0.4967	10, 12	−0.5627
2, 5	0.7787	4, 5	−0.2736		
2, 6	−0.6616	4, 6	−0.5627		
2, 7	−0.8761	4, 7	0.0114		
2, 8	−0.0073	4, 8	−0.2771		

C. Natural orbital coefficients

i	a_i	i	a_i	i	a_i
1	0.76193	5	−0.01540	9	0.00106
2	−0.64486	6	−0.00263	10	−0.00023
3	−0.05542	7	0.00169	11	−0.00002
4	0.01780	8	0.00158	12	0.00002

there is a very large probability for finding both electrons simultaneously at the same end of the molecule.

IV. TERM LEVELS

The vibrational and rotational term levels were computed from the potential curve given in Table IV by a numerical integration technique.[12] The direct comparison of these results with experiment is somewhat difficult, partly because the error remaining in the potential function is fairly large and partly because Dieke's classification of the term levels is not completely correct.

The theoretical results obtained[13] are presented in Table V along with the corresponding experimental values. In this table, p denotes the number of nodes in the vibrational wave function $S_{p,K}(R)$ for $K=0$. For $K\neq 0$, however, p denotes a probability density function $|S_{p,K}(R)|^2$ similar to the function $|S_{p,0}(R)|^2$ although possibly with a different number of nodes. The necessity for this distinction is best demonstrated by a careful study of the functions $S_{p,K}(R)$ shown in Fig. 4.

It is interesting to note that the difference between experiment and theory is nearly constant at 0.00398 ± 0.00030. Hence to a first approximation, the absolute error in the theoretical potential function is independent of R. Also, the "irregularities" in the experimental results are predicted by these theoretical results and are not due to higher-order interactions, omitted in the Born-Oppenheimer approximation, as Dieke[9] originally supposed.

The effect of variation of rotational quantum number is of considerable interest to spectroscopists. Table VI gives a comparison of the observed and predicted rotational divided differences

$$\Delta_{p,K}=(E_{p,K+1}-E_{p,K})/(K+1).$$

[12] E. Davidson, J. Chem. Phys. **34,** 1240 (1961).
[13] See also E. Davidson, J. Chem. Phys. **33,** 1577 (1960).

TABLE III. Natural spin orbital analysis at $R=4.25$.

A. Basis functions

$$\phi_k=(n, j, \alpha, \beta)=N_k(2\pi)^{-\frac{1}{2}}(2/R)^{\frac{1}{2}}\xi^n\eta^j e^{-\alpha\xi}e^{-\beta\eta}$$

$$\chi_i=\sum_k b_{ik}\phi_k$$

k	ϕ_k	N_k	b_{1k}	b_{2k}	b_{3k}
1	(0, 0, 2.5, 2.5)	5.5901699	0.3398	−0.3719	−0.6994
2	(0, 0, 2.5, −2.5)	5.5901699	−0.3398	−0.3719	−0.6994
3	(0, 1, 2.5, 2.5)	7.2167692	0.0549	0.0047	−0.3690
4	(0, 1, 2.5, −2.5)	7 2167692	0.0549	−0.0047	0.3690
5	(1, 0, 2.5, 2.5)	4.0770701	0.1010	−0.0427	−0.3383
6	(1, 0, 2.5, −2.5)	4.0770701	−0.1010	−0.0427	−0.3383
7	(0, 0, 1.25, 1.25)	1.9764235	0.1829	−0.1970	0.5382
8	(0, 0, 1.25, −1.25)	1.9764235	−0.1829	−0.1970	−0.5382
9	(0, 1, 1.25, 1.25)	2.9490201	−0.2072	−0.5686	0.8900
10	(0, 1, 1.25, −1.25)	2.9490201	−0.2072	0.5686	−0.8900
11	(1, 0, 1.25, 1.25)	1.0608719	−0.0099	−0.4122	0.4985
12	(1, 0, 1.25, −1.25)	1.0608719	0.0099	−0.4122	0.4985

B. Eigenvector coefficients

$$[N, M]=[\phi_N(1)\phi_M(2)+\phi_N(2)\phi_M(1)]+(-1)^{i_N+i_M}[\phi_{N+1}(1)\phi_{M+1}(2)+\phi_{N+1}(2)\phi_{M+1}(1), \quad M \text{ odd}$$

$$=[\phi_N(1)\phi_M(2)+\phi_N(2)\phi_M(1)]+(-1)^{i_N+i_M}[\phi_{N+1}(1)\phi_{M-1}(2)+\phi_{N+1}(2)\phi_{M-1}(1), \quad M \text{ even}$$

$$\Psi=\sum_{N,M} c_{N,M}[N, M]=\sum_i a_i\chi_i(1)\chi_i(2)$$

N, M	$c_{N,M}$	N, M	$c_{N,M}$	N, M	$c_{N,M}$
1, 7	−1.3823	3, 7	−1.0153	5, 7	0.8074
1, 9	−0.5774	3, 9	−0.3369	5, 9	0.5580
1, 11	0.9832	3, 11	0.4701	5, 11	−0.1626
1, 8	1.0000	3, 8	0.4617	5, 8	−0.3912
1, 10	−1.2894	3, 10	−0.5996	5, 10	−0.1565
1, 12	0.4489	3, 12	0.2590	5, 12	0.1605

C. Natural orbital coefficients

i	a_i	i	a_i	i	a_i
1	0.71324	5	−0.05282	9	0.00299
2	0.64872	6	−0.01527	10	0.00051
3	−0.25092	7	−0.00833	11	0.00034
4	−0.06600	8	0.00627	12	−0.00006

The difference between these two sets of numbers is less than 0.00003 in all cases except for $p=4$ and 5. The larger error in this case is due to the fact that $E_{5,0}-E_{4,0}$ is only 0.00087 theoretically but is 0.00127 experimentally. Thus, the theoretical results predict too much mixing of these two levels; and hence, $\Delta_{4,0}$ is too small and $\Delta_{5,0}$ is too large. In any case, since $\Delta_{4,0}>\Delta_{5,0}$, the amount of mixing must increase as K increases until $\Delta_{4,K}$ becomes less than $\Delta_{5,K}$. After this happens, the levels become unmixed as K is further increased. This effect is clearly demonstrated by both the experimental and theoretical results given in Table VI.

For $p=2$ and $p=3$, the small value of 0.00006 obtained for the divided differences indicates that the probability density is largely in the outer minimum. Hence, the emission transition to the $1s2p\sigma_u\,{}^1\Sigma_u^+$ state is nearly forbidden by the Franck-Condon principle. Any lines arising from these transitions should be so weak that these term levels would be difficult to

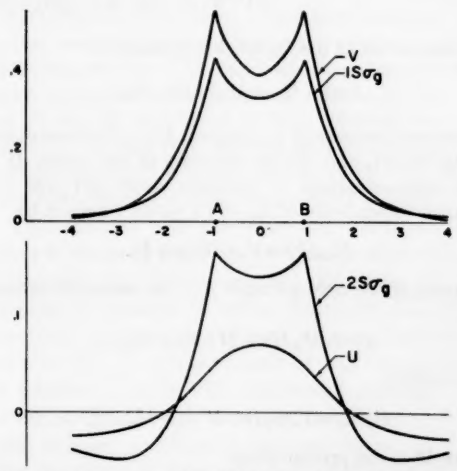

FIG. 3. A comparison along the internuclear axis of the u and v functions at $R=1.9$ with the wave functions for H_2^+.

TABLE IV. Summary of best results.

R	λ_2	R	λ_2	R	λ_2
0.5	0.1615	3.25	0.68443	5.5	−0.68983
1.0	−0.57543	3.5	−0.68797	6.0	−0.68214
1.5	−0.69882	3.75	−0.69441	6.5	−0.67483
1.8	−0.71508	4.0	−0.69825	7.0	−0.66761
1.9	−0.71618	4.25	−0.70049	7.5	−0.66054
2.0	−0.71587	4.5	−0.70035	8.0	−0.65393
2.5	−0.70339	4.75	−0.69914	10.0	−0.63192
3.0	−0.68683	5.0	−0.69685		

R	λ_3	λ_4
1.0	−0.4510	−0.3665
1.5	−0.6293	−0.6048
2.0	−0.6528	−0.6497
2.5	−0.6453	−0.6393
3.0	−0.6325	−0.6156
3.5	−0.6506	−0.5781
4.0	−0.6410	−0.5579
4.5	−0.6343	−0.5592

verify experimentally. It is probably for this reason that Dieke was unable to find these levels although he realized they were present.[9]

The variation of the term levels with the reduced mass of the molecule is also of interest to spectroscopists since six isotopic forms of the hydrogen molecule are known. In the equation

$$-kd^2S_{p,K}(R)/dR^2-kK(K+1)S_{p,K}(R)/R^2 +V(R)S_{p,K}(R)=E_{p,K}S_{p,K}(R)$$

for the motion of the nuclei, k is given by

$$k=m(M_A+M_B)/2M_AM_B,$$

where m is the mass of an electron, M_A is the mass of one of the nuclei, and M_B is the mass of the other. If V were approximately a parabola with $d^2V/dR^2=f^2$, then the dependence of $E_{p,0}$ on k would be given by

$$E_{n,0}(k)=V_e+fk^{\frac{1}{2}}(n+\tfrac{1}{2}).$$

In terms of the reduced mass μ of the molecule defined by

$$\mu=2(M_AM_B)/M(M_A+M_B),$$

this becomes

$$E_n(\mu)=V_e+f(m/M)^{\frac{1}{2}}(n+\tfrac{1}{2})\mu^{-\frac{1}{2}},$$

where M is the proton mass.

If the two minima could be considered separately, then the variation of E_p with μ for the potential function for the first excited $^1\Sigma_g^+$ state should either be

$$E_p(\mu)=V_A+f_A(m/M)^{\frac{1}{2}}\mu^{-\frac{1}{2}}(n+\tfrac{1}{2})$$

or

$$E_p(\mu)=V_B+f_B(m/M)^{\frac{1}{2}}\mu^{-\frac{1}{2}}(q+\tfrac{1}{2}),$$

where the subscripts A and B refer to the inner and outer minimum, respectively. Thus, on a plot of $E_p(\mu)$ against $\mu^{-\frac{1}{2}}$, two sets of straight lines should be evident,

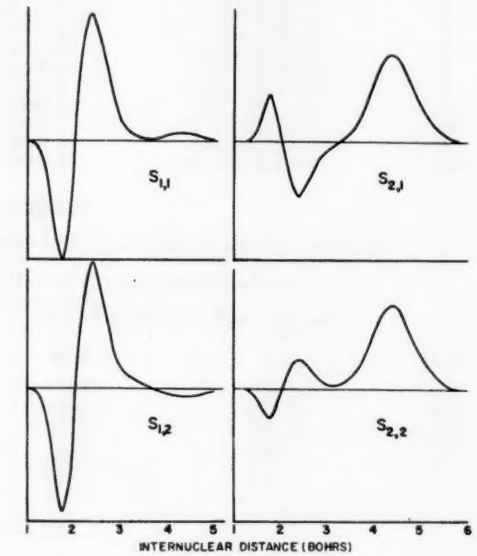

(a)

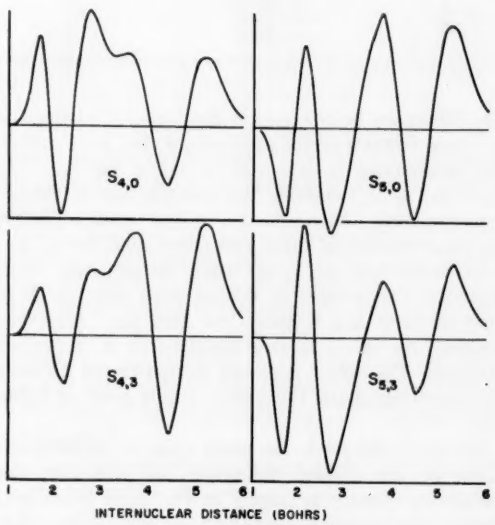

(b)

FIG. 4. Some vibrational eigenfunctions illustrating the need for distinguishing between the number of nodes and the shape of the probability distribution function.

TABLE V. Term levels[a] for H_2.

K / p	0	1	2	3	4	Source
0	−0.71277	−0.71248	−0.71190	−0.71104	−0.70991	$v=0$, $1s2s$
	−0.70986	−0.70959	−0.70905	−0.70825	−0.70718	theory
1	−0.70215	−0.70188	−0.70134	−0.70053	−0.69948	$v=1$, $1s2s$
	−0.69827	−0.69802	−0.69753	−0.69680	−0.69584	theory
2	−0.69791	−0.69785	−0.69775	−0.69758	−0.69735	theory
3	−0.69285	−0.69279	−0.69268	−0.69251	−0.69228	theory
4	−0.69274	−0.69253	−0.69215			$v=2$, $1s2s$
	−0.68857	−0.68843	−0.68819			theory
4				−0.69169	−0.69134	$v=0$, $(2p\sigma)^2$
				−0.68790	−0.68760	theory
5	−0.69147	−0.69138	−0.69118			$v=0$, $(2p\sigma)^2$
	−0.68770	−0.68758	−0.68728			theory
5				−0.69076	−0.69001	$v=2$, $1s2s$
				−0.68677	−0.68603	theory
6	−0.68741	−0.68733	−0.68718	−0.68696	−0.68667	$v=1$, $(2p\sigma)^2$
	−0.68373	−0.68365	−0.68351	−0.68329	−0.68299	theory
7	−0.68442	−0.68429	−0.68402	−0.68364		$v=3$, $1s2s$
	−0.68044	−0.68033	−0.68011	−0.67980	−0.67941	theory
8	−0.68178	−0.68166	−0.68143	−0.68106	−0.68056	$v=2$, $(2p\sigma)^2$
	−0.67762	−0.67751	−0.67728	−0.67693	−0.67648	theory
9	−0.67837	−0.67828	−0.67808	−0.67780	−0.67741	$v=3$, $(2p\sigma)^2$
	−0.67439	−0.67429	−0.67409	−0.67378	−0.67338	theory
10	−0.67513	−0.67502	−0.67480	−0.67449	−0.67408	$v=4$, $1s2s$
	−0.67111	−0.67101	−0.67082	−0.67052	−0.67013	theory
11	−0.67206	−0.67195	−0.67174	−0.67146		$v=4$, $(2p\sigma)^2$
	−0.66786	−0.66777	−0.66757	−0.66728	−0.66690	theory

[a] Experimental results were converted from Dieke's tables by the formula $E(\text{a.u.}) = -1.164557 + 4.5563309\times10^{-6}\,E(\text{cm}^{-1})$.

one set passing through V_A and one set passing through V_B for $\mu=0$. Near points at which a line from one set "crosses" a line from the other, however, the levels must perturb each other enough to prevent the crossing since the discrete solutions to the one-dimensional Sturm-Liouville problem are nondegenerate.

Figure 5 shows a plot of the actual variation of E with $\mu^{-\frac{1}{2}}$. These results are nearly what was expected. The lines do have slopes proportional to $(n+\frac{1}{2})$ although the A set of lines is appreciably curved. Also, it appears that, for E_p larger than the top of the potential barrier, $E_p=V_n+f_n(m/M)^{\frac{1}{2}}(n+\frac{1}{2})\mu^{-\frac{1}{2}}$, where V_n is intermediate between V_A and V_B, and f_n is between f_A and f_B.

Thus, it would seem that, relative to their variation with K and μ, the energy levels below the barrier can be uniquely classified as belonging either to one minimum or to the other. Those above the barrier all behave alike, however, and seem to correspond to some averaging parabolic type potential curve.

V. CONVERGENCE DIFFICULTIES

Although the potential curve thus far obtained is sufficiently accurate to explain the experimental results for this state, there is still an average difference of about 0.004 Hartrees between experiment and theory. In the neighborhood of the inner minimum, which is the range of R used to determine the correct configurations to include, the error is only 0.002, however. Thus, in this range the present results are nearly as good as those obtained by Kolos and Roothaan[2] with a much more elaborate wave function. The difficulty with the K and R calculation is fairly obvious since this state has an open-shell electron distribution, and they tried to describe it with a closed-shell function (that is, they have taken $\alpha=\bar{\alpha}$ throughout their calculation).

The difficulty with the wave function used in this paper is not so obvious, however, and a more thorough investigation of the convergence difficulties with this function is perhaps in order. Extensive calculations involving configurations of the $\sigma_g\sigma_g'$ type, showed that each of the six configurations of this type included in column A, Table VII, contributed more than 10^{-4} to the energy and that the additional eleven configurations included in column B each contributed more than 10^{-5}. In addition, there were at least 25 configurations which contributed more than 10^{-6}. The apparent energy

TABLE VI. Rotational divided differences for H_2.

$\Delta_{p,K}=(E_{p,K+1}-E_{p,K})/(K+1)$

p \ K	0	1	2	3	Source
0	0.00029	0.00029	0.00029	0.00028	experiment
	0.00027	0.00027	0.00027	0.00027	theory
1	0.00027	0.00027	0.00027	0.00026	experiment
	0.00025	0.00025	0.00024	0.00024	theory
2	0.00006	0.00006	0.00006	0.00006	theory
3	0.00006	0.00006	0.00006	0.00006	theory
4	0.00021	0.00019	0.00015	0.00009	experiment
	0.00014	0.00012	0.00010	0.00007	theory
5	0.00009	0.00010	0.00014	0.00019	experiment
	0.00012	0.00015	0.00017	0.00019	theory
6	0.00008	0.00008	0.00007	0.00007	experiment
	0.00008	0.00007	0.00008	0.00007	theory
7	0.00013	0.00013	0.00013		experiment
	0.00011	0.00011	0.00010	0.00010	theory
8	0.00012	0.00012	0.00012	0.00012	experiment
	0.00011	0.00012	0.00012	0.00012	theory
9	0.00009	0.00010	0.00009	0.00009	experiment
	0.00010	0.00010	0.00010	0.00010	theory
10	0.00011	0.00011	0.00010	0.00010	experiment
	0.00010	0.00010	0.00010	0.00010	theory
11	0.00011	0.00010	0.00009		experiment
	0.00009	0.00010	0.00010	0.00009	theory

limit using $\sigma_g\sigma_g'$ functions alone was -0.71362 ± 0.00005 as shown in Table VIII.

Next, the nonlinear parameters for the $\sigma_u\sigma_u'$ configurations were varied and were found to be optimum with

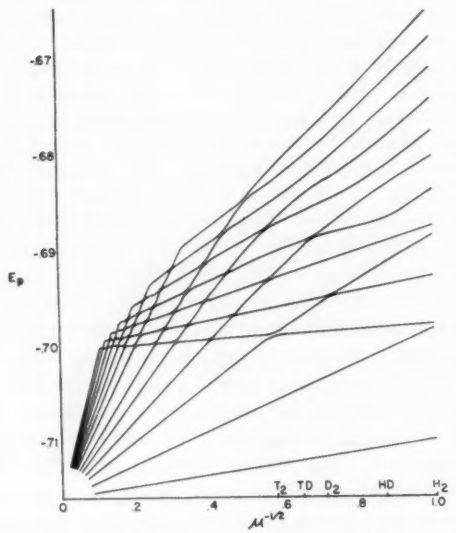

FIG. 5. The isotopic shift of the term levels as a function of the reduced mass μ of the nuclei.

TABLE VII. Approximate wave functions at $R=1.92$ with $\alpha(\sigma_g)=1.4$, $\bar{\alpha}(\sigma_g)=0.55$, $\alpha(\sigma_u)=1.4$, $\bar{\alpha}(\sigma_u)=0.75$, and $\alpha(\pi_u)=2.4$.

Energy	A -0.712337	B -0.716727
Configuration	Coefficient	
$(0,0,0)(\bar{0},\bar{0},\bar{0})$	1.00000	1.00000
$(0,0,0)(\bar{1},\bar{0},\bar{0})$	−0.04779	0.46044
$(0,0,0)(\bar{2},\bar{0},\bar{0})$	−2.82828	−3.22187
$(0,2,0)(\bar{0},\bar{0},\bar{0})$	0.47126	0.13077
$(0,2,0)(\bar{1},\bar{0},\bar{0})$	−0.40550	0.09744
$(0,2,0)(\bar{2},\bar{0},\bar{0})$	−0.28674	−0.56998
$(2,1,0)(\bar{0},\bar{1},\bar{0})$	−0.19629	−0.24029
$(2,1,0)(\bar{1},\bar{1},\bar{0})$	0.16237	0.21431
$(0,1,0)(\bar{0},\bar{1},\bar{0})$	−0.18874	−0.23263
$(0,1,0)(\bar{1},\bar{1},\bar{0})$	0.21740	0.26744
$(1,0,0)(\bar{0},\bar{2},\bar{0})$		0.11648
$(0,0,0)(\bar{0},\bar{2},\bar{0})$		−0.00734
$(1,0,0)(\bar{1},\bar{0},\bar{0})$		−0.86307
$(0,0,0)(\bar{3},\bar{0},\bar{0})$		0.04502
$(2,0,0)(\bar{0},\bar{2},\bar{0})$		−0.11647
$(1,0,0)(\bar{3},\bar{0},\bar{0})$		−0.21687
$(2,0,0)(\bar{1},\bar{0},\bar{0})$		0.25204
$(1,0,0)(1,0,0)$		0.20151
$(0,0,0)(0,2,0)$		0.10749
$(0,4,0)(\bar{0},\bar{0},\bar{0})$		0.05419
$(0,4,0)(\bar{1},\bar{0},\bar{0})$		−0.07273
$(0,0,1)(0,0,1)$		−0.07079
$(1,0,1)(0,0,1)$		0.05584
$(1,0,1)(1,0,1)$		−0.02829

$\alpha=1.4$ and $\bar{\alpha}=0.75$. An exhaustive study of these configurations revealed that the four included in calculation A were essential. No others contributed more than 2×10^{-5}, however, although there were 20 or more which contributed as much as 10^{-6}. When the π_u^2 and

TABLE VIII. Apparent energy convergence limits.

	$R=2$	$R=1.92$
$\sigma_g\sigma_g'$	-0.71305 ± 0.00005	-0.71362 ± 0.00005
$\sigma_u\sigma_u'$	-0.00320 ± 0.00005	-0.00297 ± 0.00005
π_u^2	-0.00076 ± 0.00005	-0.00076 ± 0.00005
π_g^2	-0.00009 ± 0.00005	-0.00009 ± 0.00005
Total	-0.7171 ± 0.0002	-0.7175 ± 0.0002

π_g^2 configurations were tried, it was found that three of the π_u^2 terms contributed more than 2×10^{-6}. Again it was found that there were many terms which contributed as much as 10^{-6}.

The apparent convergence limit obtained from this calculation is -0.7175 ± 0.0002 at $R=1.92$ which still differs appreciably from the experimental value of -0.7181. The best energy actually obtained, -0.71700, came out of a calculation using 18 $\sigma_g\sigma_g'$, 4 $\sigma_u\sigma_u'$, and 10 π_u^2 configurations. These results indicate that there are severe convergence difficulties with this choice of basis functions. In all probability, the source of this difficulty is that, as was previously mentioned, the outer-shell function is nearly a one-center function and has no singularities at the nuclei. All of the basis functions, however, have singularities at these points. Hence, many basis functions are required to represent the u function accurately. This difficulty could best be avoided by using two-center functions to represent v but one-center Gaussian-like functions to represent u. This, of course, would lead to three-center electron repulsion integrals; but, in spite of this trouble, it would probably be the easiest way to obtain an accurate energy for this state.

VI. CONCLUSIONS

This paper has attempted to give a rather complete description of the first excited $^1\Sigma_g^+$ state of the hydrogen molecule. The unusual potential curve obtained for this state leads to difficulties not only in describing the electronic wave function, because it varies greatly with internuclear distance, but also in predicting the vibrational term levels, since simple harmonic oscillator or Morse potential approximations are no longer sufficient.

Nevertheless, the term levels have been computed and found to include both the $1s2s$ and $(2p\sigma_u)^2\,^1\Sigma_g^+$ experimental series of levels, as well as two additional levels as yet unobserved. The wave function has also been computed and, although there are great convergence difficulties, it is possible to describe it fairly accurately. Thus, near the inner minimum the electrons lie in two shells. The inner of these shells is very similar to the lowest state of H_2^+ while the outer shell is a very diffuse one-center function. Near the outer minimum, the electron distribution corresponds very nearly to a symmetrical H^+H^- wave function.

ACKNOWLEDGMENTS

The authors wishes to thank Harrison Shull for many helpful suggestions and criticisms concerning this research. Thanks are also due Stanley Hagstrom for suggesting this problem and for allowing the use of several of his computer programs. The author also wishes to thank Darrell Ebbing and Basil Anex for the use of their computer programs.

APPENDIX 1. MATRIX ELEMENTS AT INNER MINIMUM

A. Normalization Constants (Table A.1)

$$f_i=N_i(2\pi)^{-\frac{1}{2}}(2/R)^{\frac{1}{2}}\xi^{n_i}\eta^{j_i}e^{-\alpha_i\xi}[(\xi^2-1)(1-\eta^2)]^{|m_i|/2}e^{im_i\phi}.$$

TABLE A.1. Normalization constants.

i	(n_i, j_i, m_i)	α_i	N_i
1	(0, 0, 0)	1.40	3.7512622
2	(1, 0, 0)	1.40	2.1931496
3	(2, 0, 0)	1.40	1.0193643
4	(0, 2, 0)	1.40	9.5768300
5	(0, 4, 0)	1.40	13.415938
6	(0, 0, 0)	0.55	0.63191935
7	(1, 0, 0)	0.55	0.18653265
8	(2, 0, 0)	0.55	0.03703813
9	(0, 2, 0)	0.55	1.4829275
10	(3, 0, 0)	0.55	0.0054270242
11	(2, 1, 0)	1.40	1.8264288
12	(0, 1, 0)	1.40	7.1018861
13	(0, 1, 0)	0.75	1.9609990
14	(1, 1, 0)	0.75	0.73007682
15	(0, 0, 1)	2.40	20.788323
16	(1, 0, 1)	2.40	12.459601

B. Overlap Integrals (Table A.2)

$$S_{i,j}=\int f_i^* f_j d\tau.$$

TABLE A.2. Overlap integrals.

i,j	$S_{i,j}$	i,j	$S_{i,j}$
1, 1	1.00000000	2, 9	0.63559896
1, 2	0.94971950	2, 10	0.15280217
1, 3	0.79500582	3, 3	1.00000000
1, 4	0.71228172	3, 4	0.60231026
1, 5	0.54872520	3, 5	0.47951732
1, 6	0.76731923	3, 6	0.96376289
1, 7	0.45144161	3, 7	0.77215740
1, 8	0.20787660	3, 8	0.48470553
1, 9	0.52806873	3, 9	0.70385845
1, 10	0.082672438	3, 10	0.25855210
2, 2	1.00000000	4, 4	1.00000000
2, 3	0.94026078	4, 5	0.95000594
2, 4	0.69814410	4, 6	0.57448214
2, 5	0.54716278	4, 7	0.34911750
2, 6	0.89412706	4, 8	0.16516074
2, 7	0.61207161	4, 9	0.76151567
2, 8	0.32986701	4, 10	0.067032669
5, 5	1.00000000	9, 9	1.00000000
5, 6	0.45458995	9, 10	0.35022114
5, 7	0.28081472	10, 10	1.00000000
5, 8	0.13459279	11, 11	1.00000000
5, 9	0.73565942	11, 12	0.80028655
5, 10	0.05514648	11, 13	0.98017460
6, 6	1.00000000	11, 14	0.93142814
6, 7	0.89584367	12, 12	1.00000000
6, 8	0.67266837	12, 13	0.88677944
6, 9	0.73182161	12, 14	0.64010506
6, 10	0.45502139	13, 13	1.00000000
7, 7	1.00000000	13, 14	0.91497068
7, 8	0.91666850	14, 14	1.00000000
7, 9	0.67235050	15, 15	1.00000000
7, 10	0.73793566	15, 16	0.97075849
8, 8	1.00000000	16, 16	1.00000000
8, 9	0.51297329		
8, 10	0.93612609		

C. Matrix Elements

If a configuration is defined by

$$\Phi_N = f_i^*(1)f_j(2) + f_j(1)f_i^*(2) + f_i(1)f_j^*(2) + f_j^*(1)f_i(2),$$

where N denotes the pair of indices (i, j), then the matrix elements given in Table A.3 may be defined as

$$S_{N,M} = \int d\tau_1 d\tau_2 f_i(1) f_j^*(2) \Phi_M(1, 2)$$

$$T_{N,M} = \int d\tau_1 d\tau_2 f_i(1) f_j^*(2)\, T\Phi_M(1, 2)$$

$$V_{N,M} = \int d\tau_1 d\tau_2 f_i(1) f_j^*(2)\, V\Phi_M(1, 2),$$

where $T = -\frac{1}{2}\nabla_1^2 - \frac{1}{2}\nabla_2^2$ evaluated at $R = 2$ and

$$V = -r_{a1}^{-1} - r_{a2}^{-1} - r_{b1}^{-1} - r_{b2}^{-1} + r_{12}^{-1}$$

evaluated at $R = 2$. If matrix elements for other values of R are desired these may be obtained from the equations

$$S_{N,M}(R) = S_{N,M}, \qquad V_{N,M}(R) = (2/R)\, V_{N,M},$$

$$T_{N,M}(R) = (4/R^2)\, T_{N,M}.$$

TABLE A.3. Matrix elements.

N, M	$T_{N,M}$	$V_{N,M}$	$S_{N,M}$
1, 1	2.0493121	−6.9046267	3.1775576
2, 1	1.3699629	−5.0558930	2.4844870
2, 2	1.2985339	−4.6503015	2.4075990
3, 1	0.8357604	−3.2225071	1.6643522
3, 2	1.1005125	−3.7787416	2.0210252
3, 3	1.1940318	−3.8256568	2.0864254
4, 1	1.6763001	−5.6706542	2.3061858
4, 2	1.1364467	−4.1779872	1.8119553
4, 3	0.7043069	−2.6776704	1.2117208
4, 4	4.2963203	−7.0431145	2.6600594
5, 1	1.1472821	−4.1759404	1.7948765
5, 2	1.0901999	−3.8628288	1.7397758
5, 3	0.9285587	−3.1527990	1.4549733
5, 4	3.5123650	−5.4912894	2.1928109
5, 5	3.7613269	−5.4093528	2.2437660
6, 1	0.7138861	−2.6759146	1.1971015
6, 2	0.9312159	−3.1523310	1.4509992
6, 3	1.0088041	−3.2019086	1.4932295
6, 4	2.4910075	−3.7033527	1.5351005
6, 5	3.3774036	−4.5986418	1.9486580
6, 6	3.6792933	−4.7903025	2.0545562
7, 1		0.2969468	
7, 2		0.1932574	
7, 3		0.0975791	
7, 4		0.4208799	
7, 5		0.2763809	
7, 6		0.1405772	
7, 7	4.1090717	−7.3730084	3.9214846
8, 1		0.2218579	
8, 2		0.1593520	
8, 3		0.0894236	
8, 4		0.3186268	
8, 5		0.2306160	
8, 6		0.1301843	
8, 7	3.0499823	−6.1343424	3.6558658
8, 8	2.6304809	−5.6089612	3.7351168
9, 1		0.3682647	
9, 2		0.2061906	
9, 3		0.0898026	
9, 4		0.5074426	
9, 5		0.2872719	
9, 6		0.1263323	
9, 7	4.6337298	−7.6666814	3.3389705
9, 8	2.9115897	−5.6044494	2.7193069
9, 9	7.1483720	−9.7907250	3.5727556
10, 1		0.2570976	
10, 2		0.1620129	
10, 3		0.0815412	
10, 4		0.3595367	
10, 5		0.2285609	
10, 6		0.1158092	
10, 7	3.7472606	−6.6009752	3.1164201
10, 8	2.6300662	−5.3169158	2.7929969
10, 9	5.0722152	−7.5139830	2.9652054
10, 10	4.3301450	−6.6727617	2.8194690
11, 1	1.2106432	−5.0077854	2.3343716
11, 2	0.8237257	−3.7900858	1.9235205
11, 3	0.4804090	−2.4370857	1.3227464
11, 4	2.3054219	−5.5382340	2.3836174
11, 5	1.5305518	−4.0455073	1.8709993
11, 6	0.8339072	−2.4906849	1.2186564
11, 7		0.4376334	
11, 8		0.3569751	
11, 9		0.4639492	
11, 10		0.3507244	
11, 11	1.9456250	−5.5841745	2.8079720
12, 1	1.5146772	−5.2310729	2.2740378
12, 2	1.0352834	−3.8589264	1.8214854
12, 3	0.6427638	−2.4764008	1.2454928
12, 4	2.4073888	−5.5891912	2.2111776
12, 5	1.4821974	−3.8959875	1.6453657
12, 6	0.8020774	−2.3614948	1.0473656
12, 7		0.3922524	
12, 8		0.2966950	
12, 9		0.4735771	
12, 10		0.3364542	
12, 11	2.0360552	−5.5832508	2.5707188
12, 12	2.4920724	−5.9883712	2.5577132
13, 1	0.9709359	−4.6826053	2.5088928
13, 2	0.9016014	−4.3145902	2.4520682
13, 3	0.7313645	−3.4537438	2.0389873
13, 4	0.8018628	−3.8789811	1.8751668
13, 5	0.7536726	−3.5906826	1.8236580
13, 6	0.6177115	−2.8852888	1.5102581
13, 7		0.2228355	
13, 8		0.1983662	
13, 9		0.2071589	
13, 10		0.1724117	
13, 11	0.7150553	−3.7647241	2.1227652
13, 12	0.7354294	−3.5802990	1.8509604

TABLE A.3.—*Continued.*

N, M	$T_{N,M}$	$V_{N,M}$	$S_{N,M}$	N, M	$T_{N,M}$	$V_{N,M}$	$S_{N,M}$
13, 13	0.8029750	−4.3551513	2.7492634	18, 3	0.4242017	−2.3893383	1.2531245
14, 1	0.5035028	−1.9430929	1.0369151	18, 4	1.6313949	−5.9678540	2.4969181
14, 2	0.8533495	−2.8432426	1.5505149	18, 5	0.8972920	−3.8524939	1.7092567
14, 3	1.1109320	−3.4523778	1.9066235	18, 6	0.3686192	−1.9767340	0.9211788
14, 4	0.4299179	−1.6214706	0.7510778	18, 7		0.3712203	
14, 5	0.7239073	−2.3797824	1.1117588	18, 8		0.2763961	
14, 6	0.9401423	−2.8961695	1.3614400	18, 9		0.4479483	
14, 7		0.0421191		18, 10		0.3110934	
14, 8		0.0431432		18, 11	1.3234577	−5.3929740	2.5423959
14, 9		0.0340553		18, 12	1.4773907	−5.5000101	2.4145629
14, 10		0.0365095		18, 13	0.9107722	−4.5245871	2.4482864
14, 11	0.2679550	−1.4513061	0.8266038	18, 14	0.1316858	−1.0620105	0.5804768
14, 12	0.3908714	−1.5010591	0.7877557	18, 15	1.0008262	−4.7226692	2.3905151
14, 13	0.5471456	−2.5484697	1.5396263	18, 16	0.0828477	−1.0108270	0.6112087
14, 14	1.1951927	−3.6120457	2.0136694	18, 17	0.6218101	−3.9042236	2.3020277
15, 1	0.8408429	−4.3642993	2.1814710	18, 18	2.3979118	−8.3754628	4.0000000
15, 2	0.5922132	−3.4716608	1.8845495	19, 1	2.0715400	−6.0781418	2.2420592
15, 3	0.3293527	−2.2902389	1.3275492	19, 2	0.9243054	−3.3919564	1.3413422
15, 4	2.0611838	−5.0421326	2.3494084	19, 3	0.3030966	−1.4875356	0.6264549
15, 5	1.5587330	−3.9733682	1.9859471	19, 4	4.0233958	−6.9591352	2.3530247
15, 6	0.9227107	−2.5666796	1.3561599	19, 5	2.0622966	−3.9018072	1.4002232
15, 7		0.4318114		19, 6	0.8228485	−1.7194153	0.6510352
15, 8		0.3809999		19, 7		0.4635230	
15, 9		0.3980478		19, 8		0.3043528	
15, 10		0.3236943		19, 9		0.6874702	
15, 11	1.6321611	−5.0593100	2.7752650	19, 10		0.4260335	
15, 12	1.4395579	−4.6927165	2.3333829	19, 11	2.6450819	−5.7673948	2.1837888
15, 13	0.6224758	−3.6740240	2.2459345	19, 12	3.2369485	−6.4102103	2.2752988
15, 14	0.1608956	−1.3610770	0.8299222	19, 13	0.6147365	−3.0170784	1.2934700
15, 15	1.6251513	−4.9725003	2.9908334	19, 14	0.0805149	−0.5680162	0.2518375
16, 1	0.3031618	−1.7143899	1.0121247	19, 15	1.8492004	−4.5602746	1.8469412
16, 2	0.5390589	−2.4841876	1.5028667	19, 16	0.0258895	−0.4968437	0.2427590
16, 3	0.7130841	−2.9882144	1.8326562	19, 17	0.2908957	−2.3536459	1.0989167
16, 4	0.2590294	−1.4328595	0.7552124	19, 18	2.2377526	−6.9792324	2.6521643
16, 5	0.4567502	−2.0819118	1.1124284	19, 19	6.2076771	−9.6945770	3.0146906
16, 6	0.6026189	−2.5094810	1.3513256	20, 1	1.3846066	−4.6912206	1.7950816
16, 7		0.0520439		20, 2	0.9446303	−3.4663670	1.4140931
16, 8		0.0571689		20, 3	0.5894965	−2.2272256	0.9447715
16, 9		0.0363277		20, 4	4.6367196	−6.6911884	2.4223195
16, 10		0.0402656		20, 5	3.8622980	−5.2939970	2.0247597
16, 11	0.2050696	−1.3955683	0.8946841	20, 6	2.7717550	−3.6147835	1.4327202
16, 12	0.2361272	−1.3251456	0.7703167	20, 7		0.4025949	
16, 13	0.4405216	−2.4450382	1.6629231	20, 8		0.3072082	
16, 14	0.7710014	−3.1076380	1.9247041	20, 9		0.4770544	
16, 15	0.1631707	−1.4164837	0.9872693	20, 10		0.3410838	
16, 16	0.6263650	−2.9261760	2.0466970	20, 11	2.3910682	−5.0990932	2.1163971
17, 1	0.5330041	−3.9086447	2.2945672	20, 12	2.4193872	−5.0916794	1.9321092
17, 2	0.4816129	−3.6506096	2.2871796	20, 13	0.6651991	−3.2218766	1.4825127
17, 3	0.3556466	−2.8919390	1.8951461	20, 14	0.3618766	−1.3512995	0.5839933
17, 4	0.4362842	−3.2467013	1.7520846	20, 15	2.2127235	−4.7021314	2.1198448
17, 5	0.3985531	−3.0444282	1.7437679	20, 16	0.2180961	−1.1949386	0.5965575
17, 6	0.2985799	−2.4196756	1.4426760	20, 17	0.3604774	−2.7000522	1.4004227
17, 7		0.2278419		20, 18	1.3427753	−4.9350292	1.9569323
17, 8		0.2193338		20, 19	4.1826788	−6.4629570	2.0883813
17, 9		0.1828966		20, 20	6.1439513	−6.8749839	−2.4133040
17, 10		0.1627528		21, 1	0.9576408	−3.4639095	1.3935856
17, 11	0.5187749	−3.3908125	2.1259932	21, 2	0.9109956	−3.2125542	1.3509933
17, 12	0.4056417	−2.9949721	1.7045471	21, 3	0.7776079	−2.6272990	1.1275198
17, 13	0.6036796	−4.0308687	2.8257528	21, 4	3.8656196	−5.2934370	2.0195242
17, 14	0.2395003	−2.0845498	1.4067686	21, 5	4.1791304	−5.2937292	2.0960865
17, 15	0.5600345	−3.5487460	2.4316800	21, 6	3.7682222	−4.5424313	1.8356584
17, 16	0.2879916	−2.2241094	1.7042088	21, 7		0.2657730	
17, 17	0.6241919	−4.0914558	3.1924542	21, 8		0.2233452	
18, 1	2.0098779	−7.2730896	3.3966796	21, 9		0.2718722	
18, 2	1.0772941	−4.6752448	2.3251853	21, 10		0.2179548	

TABLE A.3.—*Continued.*

N, M	$T_{N,M}$	$V_{N,M}$	$S_{N,M}$	N, M	$T_{N,M}$	$V_{N,M}$	$S_{N,M}$
21, 11	1.5838083	−3.6868769	1.6363229	23, 8		0.0600896	
21, 12	1.4616012	−3.4874204	1.4020859	23, 9		0.1239768	
21, 13	0.6285890	−2.9887252	1.4380830	23, 10		0.0783033	
21, 14	0.6076399	−1.9859196	0.8596386	23, 11		0.1365853	
21, 15	1.6880752	−3.6972148	1.7808972	23, 12		0.1414721	
21, 16	0.3831959	−1.7383212	0.8750491	23, 13		0.1760938	
21, 17	0.3309256	−2.5364019	1.3927010	23, 14		0.0206679	
21, 18	0.7471821	−3.1921648	1.3396112	23, 15		0.1114691	
21, 19	2.1914520	−3.6302632	1.2408836	23, 16		0.0210666	
21, 20	5.2413938	−5.5352702	2.0469985	23, 17		0.1457601	
21, 21	5.7353263	−5.6345123	2.1577138	23, 18		0.4396871	
22, 1		0.3556517		23, 19		0.2158133	
22, 2		0.0176107		23, 20		0.0833779	
22, 3		0.0630622		23, 21		0.0439980	
22, 4		0.1541104		23, 22	6.0966700	−4.0132142	1.9415170
22, 5		0.0770952		23, 23	5.5643201	−3.9078598	1.9423721
22, 6		0.0278877		24, 1		0.3447756	
22, 7		0.0866244		24, 2		0.1874520	
22, 8		0.0552249		24, 3		0.0743384	
22, 9		0.1294583		24, 4		0.1532409	
22, 10		0.0782935		24, 5		0.0841140	
22, 11		0.1330506		24, 6		0.0336593	
22, 12		0.1431285		24, 7		0.0962473	
22, 13		0.1656347		24, 8		0.0673966	
22, 14		0.0180751		24, 9		0.1217423	
22, 15		0.1041062		24, 10		0.0803469	
22, 16		0.0177275		24, 11		0.1431866	
22, 17		0.1313193		24, 12		0.1424212	
22, 18		0.4440949		24, 13		0.1912728	
22, 19		0.2314805		24, 14		0.0237456	
22, 20		0.0836982		24, 15		0.1220577	
22, 21		0.0421470		24, 16		0.0253250	
22, 22	6.9360396	−4.2402696	2.0000000	24, 17		0.1657039	
23, 1		0.3467775		24, 18		0.4440730	
23, 2		0.1800779		24, 19		0.2046074	
23, 3		0.0680182		24, 20		0.0846282	
23, 4		0.1522168		24, 21		0.0467310	
23, 5		0.0798252		24, 22	5.3004588	−3.7841906	1.8847441
23, 6		0.0304381		24, 23	5.0212074	−3.7866794	1.9415170
23, 7		0.0900075		24, 24	4.7203232	−3.7732604	2.0000000

APPENDIX 2. MATRIX ELEMENTS AT OUTER MINIMUM

A. Overlap Integrals (Table B.1)

The defining equation for the integrals is given in Appendix 1, Part B and the basis functions are defined in Table III.

TABLE B.1. Overlap integrals.

i, j	$S_{i,j}$	i, j	$S_{i,j}$
1, 1	1.00000000	4, 10	0.85915008
1, 2	0.096577240	4, 11	0.072698443
1, 3	−0.95531323	4, 12	0.58072691
1, 4	0.00000000	5, 5	1.00000000
1, 5	0.97729553	5, 6	0.090365822
1, 6	0.091403686	5, 7	0.89909686
1, 7	0.83805248	5, 8	0.23853073
1, 8	0.22762617	5, 9	−0.91199427
1, 9	−0.83905453	5, 10	−0.11416823
1, 10	−0.10629955	5, 11	0.76151016
1, 11	0.66170778	5, 12	0.19721072
1, 12	0.17555132	6, 6	1.00000000
2, 2	1.00000000	6, 7	0.23853073
2, 3	0.00000000	6, 8	0.89909686
2, 4	0.95531323	6, 9	0.11416823

Table B.1. (*continued*)

i, j	$S_{i,j}$	i, j	$S_{i,j}$
2, 5	0.091403686	6, 10	0.91199427
2, 6	0.97729553	6, 11	0.19721072
2, 7	0.22762617	6, 12	0.76151016
2, 8	0.83805248	7, 7	1.00000000
2, 9	0.10629955	7, 8	0.45830791
2, 10	0.83905453	7, 9	−0.83195627
2, 11	0.17555132	7, 10	0.00000000
2, 12	0.66170778	7, 11	0.94340165
3, 3	1.00000000	7, 12	0.42371251
3, 4	0.041175097	8, 8	1.00000000
3, 5	−0.94154477	8, 9	0.00000000
3, 6	0.00000000	8, 10	0.83195627
3, 7	−0.72595595	8, 11	0.42371251
3, 8	−0.091971124	8, 12	0.94340165
3, 9	0.85915008	9, 9	1.00000000
3, 10	0.13941775	9, 10	0.28935540
3, 11	−0.58072691	9, 11	−0.80090434
3, 12	−0.072698443	9, 12	0.00000000
4, 4	1.00000000	10, 10	1.00000000
4, 5	0.00000000	10, 11	0.00000000
4, 6	0.94154477	10, 12	0.80090434
4, 7	0.091971124	11, 11	1.00000000
4, 8	0.72595595	11, 12	0.44075565
4, 9	0.13941775	12, 12	1.00000000

B. Matrix Elements

The matrix elements as defined in Appendix 1, Part C are given in Table B.2 for the 18 configurations in the order listed in Table III.

TABLE B.2. Matrix elements.

N, M	$T_{N,M}$	$V_{N,M}$	$S_{N,M}$	N, M	$T_{N,M}$	$V_{N,M}$	$S_{N,M}$
1, 1	6.0960608	−6.5251516	1.7984078	11, 6	0.0476122	0.3389562	−0.0585711
2, 1	−6.1385892	5.6379744	−1.5109314	11, 7	0.0522177	−0.7931411	0.1879587
2, 2	7.8105894	−6.4748190	1.6873670	11, 8	1.7446567	−1.5426977	0.3841200
3, 1	4.8644670	−5.5229289	1.5788286	11, 9	−0.0660600	−0.6313199	0.1577614
3, 2	−4.8933687	4.7847556	−1.3374522	11, 10	6.1385892	−6.8571316	1.5109314
3, 3	4.3927842	−5.1124270	1.5112424	11, 11	7.8105894	−7.8615155	1.6873669
4, 1	−6.4359235	6.1031145	−1.5846375	12, 1	1.7279339	−2.8624273	0.8125669
4, 2	6.8857486	−5.7581251	1.4830566	12, 2	0.0324703	0.3840902	−0.1543070
4, 3	5.2364762	5.2075778	−1.4044718	12, 3	1.5833390	−2.6189086	0.7696602
4, 4	7.2907452	−6.0737328	1.5165999	12, 4	−1.7132488	2.2931698	−0.5978919
5, 1	6.4236440	−5.4070718	1.3941190	12, 5	−0.3184113	0.1556231	−0.0007331
5, 2	−8.6490871	6.7033573	−1.6910070	12, 6	−1.6549888	2.1353660	−0.5711122
5, 3	5.2079792	−4.6290842	1.2446482	12, 7	1.4885405	−2.7973425	0.8389353
5, 4	−7.5373276	5.7647658	−1.4428390	12, 8	0.0188685	0.3868226	−0.1577280
5, 5	9.9994205	−7.1934471	1.7694904	12, 9	1.3136723	−2.5208275	0.7863322
6, 1	−5.2637544	5.2076436	−1.3977604	12, 10	4.8644670	−6.2975115	1.5788286
6, 2	5.5548921	−4.8907325	1.3091458	12, 11	4.8933686	−5.7287311	1.3374522
6, 3	−4.8452590	4.8723049	−1.3523471	12, 12	4.3927841	−5.7429623	1.5112424
6, 4	6.0925789	−5.2375811	1.3542236	13, 1	−2.0697918	−2.7472479	−0.6801508
6, 5	−6.2095675	4.9519987	−1.2897005	13, 2	0.0474590	−0.1502966	0.0787257
6, 6	5.7665993	−4.9713436	1.3243807	13, 3	−1.7132488	2.3250109	−0.5978919
7, 1	5.4103999	−6.2798286	1.8269728	13, 4	2.2673658	−2.3534927	0.5506668
7, 2	−5.5419287	5.4584476	−1.5513785	13, 5	0.4179514	−0.4041830	0.0564500
7, 3	4.3957572	−5.4208983	1.6437869	13, 6	1.9829007	−2.0332044	0.4910538
7, 4	−5.7182670	5.8656182	−1.6161874	13, 7	−1.7542790	2.6229888	−0.6873712
7, 5	5.8000592	−5.2292675	1.4348916	13, 8	−0.0133863	−0.1563720	0.0795836
7, 6	−4.7471911	5.0955832	−1.4592154	13, 9	−1.4187374	2.2029744	−0.6028285
7, 7	4.9976810	−6.1761957	1.9066874	13, 10	−6.4359235	7.1371659	−1.5846375
8, 1	−5.5949015	5.4586924	−1.5421027	13, 11	−6.8857486	7.0239515	−1.4830566
8, 2	7.1365568	−6.2630483	1.7281963	13, 12	−5.2364762	6.0092279	−1.4044718
8, 3	−4.5643219	4.7337391	−1.4007054	13, 13	7.2907453	−7.1633425	1.5165999
8, 4	6.3118318	−5.5836308	1.5225278	14, 1	0.4199928	0.2020667	0.0000000
8, 5	−7.9326777	6.4926756	−1.7410018	14, 2	−2.3094522	2.0326094	−0.4847314
8, 6	5.2126738	−4.8484034	1.3808441	14, 3	0.3184113	0.1555211	0.0007331
8, 7	−5.2273159	5.3902587	−1.6246948	14, 4	−0.4179514	0.0372939	−0.0564500
8, 8	6.7496259	−6.1844633	1.8186201	14, 5	2.7079766	−2.4761618	0.5700920
9, 1	4.2080024	−5.2604794	1.5975249	14, 6	−0.2956043	0.0452448	−0.0514821
9, 2	−4.3101101	4.5769863	−1.3661516	14, 7	0.4226471	0.1968042	−0.0009960
9, 3	3.8273644	−4.9273115	1.5561000	14, 8	−2.0788817	1.9661450	−0.4976769
9, 4	−4.5433233	4.9514982	−1.4277254	14, 9	0.3173498	0.1533488	0.0000000
9, 5	4.5909296	−4.4204927	1.2754071	14, 10	−6.4236441	6.6880160	−1.3941190
9, 6	−4.2272325	4.6807246	−1.3981111	14, 11	−8.6490871	8.1784235	−1.6910070
9, 7	3.9880234	−5.2874622	1.7134030	14, 12	−5.2079791	5.6252074	−1.2446482
9, 8	−4.1915011	4.6288201	−1.4728820	14, 13	7.5373276	−7.1227240	1.4428390
9, 9	3.5350190	−4.8826343	1.6586190	14, 14	9.9994206	−8.7907151	1.7694904
10, 1	2.1777905	−3.4194844	0.9364105	15, 1	−1.7337759	2.3249141	−0.5930787
10, 2	0.0108542	0.4664742	−0.1822542	15, 2	−0.0476122	−0.1073539	0.0585711
10, 3	1.7279339	−2.8621423	0.8125669	15, 3	−1.6549888	2.1613595	−0.5711122
10, 4	−2.0697918	2.7050259	−0.6801508	15, 4	1.9829007	−2.0336885	0.4910538
10, 5	−0.4199928	0.2020667	0.0000000	15, 5	0.2956043	−0.3289546	0.0514821
10, 6	−1.7337759	2.2923381	−0.5930787	15, 6	1.9939464	−1.9464093	0.4840164
10, 7	1.8513125	−3.2777126	0.9438652	15, 7	−1.4814561	2.2554757	−0.6121476
10, 8	0.0087657	0.4547199	−0.1806106	15, 8	−0.0024685	−0.1238676	0.0632656
10, 9	1.4256366	−2.7219225	0.8159980	15, 9	−1.3761259	2.0671137	−0.5848774
10, 10	6.0960607	−7.5295130	1.7984077	15, 10	−5.2637543	6.0080091	−1.3977604
11, 1	−0.0108542	−0.8145183	0.1822542	15, 11	−5.5548921	5.8735313	−1.3091458
11, 2	1.9219524	−1.5884538	0.3711604	15, 12	−4.8452590	5.5273256	−1.3523471
11, 3	−0.0324703	−0.6506966	0.1543070	15, 13	6.0925789	−6.0853969	1.3542236
11, 4	0.0474590	0.4512175	−0.0787257	15, 14	6.2095675	−6.0111417	1.2897005
11, 5	−2.3094522	2.0970014	−0.4847314	15, 15	5.7665993	−5.6681209	1.3243806

TABLE B.2.—*Continued.*

N, M	$T_{N,M}$	$V_{N,M}$	$S_{N,M}$	N, M	$T_{N,M}$	$V_{N,M}$	$S_{N,M}$
16, 1	1.8513125	−3.2773253	0.9438652	17, 10	5.5949014	−6.6496447	1.5421027
16, 2	0.0522177	0.4552453	−0.1879587	17, 11	7.1365567	−7.6244761	1.7281963
16, 3	1.4885405	−2.7967369	0.8389363	17, 12	4.5643218	−5.6833051	1.4007054
16, 4	−1.7542790	2.5821131	−0.6873712	17, 13	−6.3118318	6.8256811	−1.5225278
16, 5	−0.4226471	0.1966656	0.0009960	17, 14	−7.9326777	7.9463165	−1.7410018
16, 6	−1.4814561	2.2230416	−0.6121476	17, 15	−5.2126738	5.8415400	−1.3808441
16, 7	1.6503482	−3.2141294	0.9775982	17, 16	5.2273159	−6.5869477	1.6246948
16, 8	0.0476891	0.4485046	−0.1900708	17, 17	6.7496259	−7.5571750	1.8186201
16, 9	1.2995054	−2.7268303	0.8679189	18, 1	1.4256366	−2.7219224	0.8159980
16, 10	5.4104000	−7.2584449	1.8269728	18, 2	0.0660600	0.3692686	−0.1577614
16, 11	5.5419287	−6.6514574	1.5513785	18, 3	1.3136723	−2.5206005	0.7863322
16, 12	4.3957572	−6.1980087	1.6437869	18, 4	−1.4187374	2.1717968	−0.6028285
16, 13	−5.7182669	6.8773338	−1.6161874	18, 5	−0.3173498	0.1533488	0.0000000
16, 14	−5.8000592	6.4871181	−1.4348916	18, 6	−1.3761259	2.0409796	−0.0000000
16, 15	−4.7471911	5.9017358	−1.4592154	18, 7	1.2995054	−2.7271387	0.8679189
16, 16	4.9976811	−7.1553344	1.9066874	18, 8	0.0506775	0.3767825	−0.1652892
17, 1	−0.0087657	−0.7923202	0.1806106	18, 9	1.1662172	−2.4969992	0.8314774
17, 2	1.7446567	−1.5418189	0.3841200	18, 10	4.2080025	−6.0246129	1.5975249
17, 3	−0.0188685	−0.6531088	0.1577280	18, 11	4.3101101	−5.5121262	1.3661516
17, 4	0.0133863	0.4500528	−0.0795836	18, 12	3.8273644	−5.5670993	1.5561000
17, 5	−2.0788817	2.0278818	−0.4976769	18, 13	−4.5433233	5.7456900	−1.4277254
17, 6	0.0024685	0.3565225	−0.0632656	18, 14	−4.5909296	5.4109439	−1.2754071
17, 7	−0.0476890	−0.7850171	0.1900708	18, 15	4.2272325	5.3481052	−1.3981111
17, 8	1.6335228	−1.5273668	0.4072311	18, 16	3.9880235	−6.0767467	1.7134030
17, 9	−0.0506775	−0.6461990	0.1652892	18, 17	4.1915011	−5.5973521	1.4728820
				18, 18	3.5350191	−5.5534131	1.6586190

THE JOURNAL OF CHEMICAL PHYSICS VOLUME 35, NUMBER 4 OCTOBER, 1961

Spectrum of NBr Excited in Active Nitrogen*

EARL R. V. MILTON AND H. B. DUNFORD
Department of Chemistry, University of Alberta, Edmonton, Canada
AND
A. E. DOUGLAS
Division of Pure Physics, National Research Council, Ottawa, Canada

(Received March 27, 1961)

The spectrum of NBr near 6000 A, excited by the action of active nitrogen on bromine, has been photographed at high dispersion and the rotational structure of the bands has been analyzed. The bands have been attributed to a $^1\Sigma^+ - {}^3\Sigma^-$ transition in which the $^3\Sigma^-$ state is the ground state of the molecule. Only two of the five possible branches were observed, both of them belonging to the $F_1(J=N+1)$ component of the $^3\Sigma^-$ state. The unusual structure of the bands is attributed to the fact that the coupling in the $^3\Sigma^-$ state is intermediate between Hund's case b and case c. The equilibrium internuclear distances are $r_e' = 1.731$ A and $r_e'' = 1.79 \pm 0.02$ A and the dissociation energy is estimated to be 67 ± 5 kcal. The emission spectrum is believed to be caused by the combination of $N(^4S)$ and $Br(^2P_{\frac{1}{2}})$ atoms into some unknown excited state of NBr which is induced, by wall collisions, into the $^1\Sigma^+$ state.

WHEN bromine is admitted into a stream of active nitrogen an orange flame is produced which has maximum intensity in the region of a glass wall. Elliott[1] photographed the spectrum of the flame at moderate dispersion and on the basis of a vibrational analysis, attributed it to a transition between two unknown states of NBr. This spectrum is the only known spectrum of the NBr molecule. The mechanism of flame excitation has been discussed recently.[2] The present paper reports the results of an analysis of the rotational fine structure of the spectrum and on the basis of these

* Presented at the American Chemical Society meeting, St. Louis, Missouri, March 30, 1961.

[1] A. Elliott, Proc. Roy. Soc. (London) **A169,** 469 (1939).

[2] E. R. V. Milton and H. B. Dunford, J. Chem. Phys. **34,** 51 (1961).

FIG. 1. 8′–6″ band of the NBr spectrum. The band is degraded to the violet.

results, gives a further discussion of the mechanism of flame excitation.

EXPERIMENTAL

The NBr spectrum was produced by admitting bromine vapor in equilibrium with liquid bromine at room temperature, through a pinhole leak, into a Pyrex glass tube about 1.5 m long and 2 cm in diameter containing active nitrogen. The latter was produced in a condensed discharge and pumped through the glass tube at a speed of 6 liters per second and a pressure of 1–2 mm. Under these conditions the orange flame could be observed down the entire length of the tube albeit only faintly in the downstream half. When the tube was viewed end-on, the intensity of the orange emission was observed to be at a maximum at the wall and to decrease gradually towards the center where it was replaced by the active nitrogen afterglow. A quartz window was sealed on the end of the reaction tube and the light passing through this window was focused on the slit of the spectrograph.

The spectrum was photographed with a 10-m concave grating spectrograph at a dispersion of 0.7 A/mm on Kodak 103a-F plates. Exposure times were from seven to ten hours with a slitwidth of 60 μ. Spectra of active nitrogen were obtained with 4 to 6-hr exposures from the same apparatus for comparison purposes. Lines from an iron hollow cathode lamp photographed in the second order were used as wavelength standards.

RESULTS

Bands identical with those described by Elliott[1] were obtained from the spectrum of the flame. The $v'-v''=2$ ($\Delta v=2$) sequence was obtained essentially free from overlapping by bands of active nitrogen. One such band is shown in Fig. 1. Bands from two other sequences, $\Delta v=1$ and 3, were also photographed but these were overlapped to a considerable extent by nitrogen bands. The wavenumbers of the lines of the 12 bands which have been measured are given in Tables I and II. Other sequences were too weak to photograph at high dispersion.

The band system consists of a number of double-headed bands and Elliott has shown that the two heads are due to the two equally abundant isotopic species NBr^{79} and NBr^{81}. The intensity distribution in the band system is somewhat unusual. Bands are observed with values of v' from two up to ten. Bands with $v'=9$ are very intense, those with $v'=10$ are much weaker and no bands with $v'>10$ are observed. Thus one must conclude either that there is some mechanism in the excitation process which can excite levels up to $v'=10$ but not beyond or that levels above $v'=10$ are predissociated.

The band heads have been measured and found to fit the equations

$$\nu_{\text{head}}=14787.3+785.5(v'+\tfrac{1}{2})-4.363(v'+\tfrac{1}{2})^2$$
$$-691.75(v''+\tfrac{1}{2})+4.720(v''+\tfrac{1}{2})^2 \qquad \text{for } NBr^{79} \quad (1)$$

and

$$\nu_{\text{head}}=14787.3+784.0(v'+\tfrac{1}{2})-4.344(v'+\tfrac{1}{2})^2$$
$$-690.45(v''+\tfrac{1}{2})+4.702(v''+\tfrac{1}{2})^2 \qquad \text{for } NBr^{81}. \quad (2)$$

From the constants in Eq. (1) and the usual equations for the vibrational isotope shift,[3] the wave number differences between the pairs of band heads were calculated. The calculated and observed vibrational isotope shift are shown in Table III. The good agreement between the two sets of values is excellent confirmation that the vibrational analysis is correct and that the bands are due to NBr. The rotational isotope effect is small and has been neglected in this calculation.

As can be seen in Fig. 1, each band consists of two branches which at first glance appear to be a P and an R branch. A closer inspection reveals that the lines of the two branches can not be represented by a single quadratic equation as is usually the case with a related P and R branch and, in fact, in the region near the apparent band origin the spacing between the lines of the P branch is only a little over half of that between lines of the R branch. We were thus forced to conclude that the bands are not due to a simple $\Sigma-\Sigma$ transition but are of a rather unusual type. An understanding of the nature of these bands is complicated by the fact that many lines of one branch are lost in the head. It was only after making a systematic search for common combination differences between bands having one vibrational state in common that it was possible to analyze these apparently very simple bands.

[3] G. Herzberg, *Spectra of Diatomic Molecules* (D. Van Nostrand Company, Inc., Princeton, New Jersey, 1950).

TABLE I. Vacuum wave numbers of the lines of the NBr^{79} bands (cm^{-1}).[a,b]

	9–6		8–5		9–7	
J	$R(J)$	$P(J)$	$R(J)$	$P(J)$	$R(J)$	$P(J)$
0						
1						
2	17 565.19*				16 939.35*	
3	66.35				40.61	
4	67.75		17 496.03*		41.95	
5	69.11		97.39*		43.34	
6	70.48*		98.76*		44.81*	
7	72.10*		500.27		46.42	
8	73.66		1.85*		48.09	
9	75.32		3.52		49.82*	
10	77.06		5.27		51.65*	16 933.26H
11	78.86		7.08*		53.56	33.46**
12	80.72	17 558.78H	8.93	17 486.85H	55.48	33.60**
13	82.61	58.96*	10.83	87.01*	57.49	33.87
14	84.58	59.22	12.79*	87.26*	59.56	34.20*
15	86.59	59.49	14.81	87.55*	61.68	34.57*
16	88.62	59.83	16.89*	87.79*	63.87	35.02*
17	90.72	60.16	18.96	88.16*	66.10	35.55*
18	92.85	60.55	21.10	88.51*	68.39	36.07*
19	95.04	61.01*	23.27	88.97*	70.71	36.64*
20	97.28	61.51	25.49	89.42*	73.12	37.35*
21	99.54	61.98	27.77	89.92*	75.54	37.98
22	601.83	62.61*	30.06	17 490.49*	78.00	38.73
23	4.18	63.18	32.34*		80.52	39.51*
24	6.48*	63.80	34.72*		83.10	40.34*
25	8.92*	64.45*	37.17*		85.71	41.24
26	11.40*	65.19	39.65*		88.37	42.13
27	17 613.89*	65.93	17 542.09*		91.07	43.08*
28		66.71*			93.76	44.13
29		67.51			16 996.60	45.17
30		68.36				46.27
31		17 569.29				47.41
32						48.54*
33						49.74
34						16 951.08

	8–6		7–5		6–4	
J	$R(J)$	$P(J)$	$R(J)$	$P(J)$	$R(J)$	$P(J)$
0						
1						
2	16 858.00		16 777.50			
3	59.22		78.73		16 698.97	
4	60.50		80.03		700.28*	
5	61.90		81.38		1.72	
6	63.42*		82.95		3.16**	
7	65.02		84.54**		4.82*	
8	66.61*		86.22*		6.84**	
9	68.44*		88.04*		8.27	
10	70.33*		89.78		10.09	
11	72.14	16 851.73H	91.67	16 771.14H	11.99	16 691.29H
12	74.10	51.93*	93.63	71.29*	13.94	91.49*
13	76.10	52.25*	95.64	71.66	15.95	91.77
14	78.15	52.60*	97.72	71.97*	18.03	92.06*
15	80.30	52.99	99.85	72.29	20.17*	92.36
16	82.48	53.36*	802.03*	72.69*	22.37	92.77*
17	84.72	53.86	4.26	73.16	24.61*	93.24
18	87.00	54.40*	6.57	73.68	26.88	93.72
19	89.34	54.94*	8.89	74.23*	29.22	94.28*
20	91.71	55.60*	11.26	74.85	31.57	94.87
21	94.13	56.29*	13.66	75.49	34.00	95.53*
22	96.61	56.94*	16.14	76.23	36.50	96.15
23	99.11	57.75*	18.67	76.92*	39.00	96.90*
24	901.70	58.56*	21.21	77.76*	41.58	97.75*
25	4.28	59.44	23.87	78.58*	44.15	98.48
26	16 906.95	60.34	26.48	79.43*	46.83	99.37
27		61.32*	16 829.18	16 780.37	16 749.47	700.28*
28		16 862.24				16 701.19
29						
30						

TABLE I.—*Continued.*

	5–3		8–7		7–6	
J	*R*(*J*)	*P*(*J*)	*R*(*J*)	*P*(*J*)	*R*(*J*)	*P*(*J*)
0						
1						
2						
3			16 233.22		16 143.24	
4			34.71		44.63*	
5	16 622.72		36.21		46.08	
6	24.20*		37.78		47.63	
7	25.90*		39.41		49.27	
8	27.49		41.15		51.03*	
9	29.25		42.96		52.85	16 135.91H
10	31.09		16 244.87*	16 226.19H	54.75	36.05*
11	32.98			26.55*	56.73	36.28
12	34.93	16 612.14H		26.84	58.77	36.51*
13	36.96	12.52		27.20*	16 160.89*	36.88
14	39.05*	12.84*		27.64		37.28
15	41.18	13.15		28.08*		37.78*
16	43.38	13.55*		28.67		38.30
17	45.59*	13.98		29.28		38.91
18	47.90	14.46		29.95*		39.56*
19	50.19*	15.00*		30.38		40.27*
20	52.59	15.53*		16 231.10		40.96**
21	55.02	16.18				41.79*
22	57.48	16.85				42.73
23	60.03	17.57*				43.64*
24	62.56	18.33				16 144.63*
25	16 665.17	19.12				
26		19.94*				
27		16 620.89				
28						
29						
30						

	5–4		4–3		3–2	
J	*R*(*J*)	*P*(*J*)	*R*(*J*)	*P*(*J*)	*R*(*J*)	*P*(*J*)
0						
1						
2			15 876.42*			
3	15 965.53		77.81		15 790.91*	
4	66.91		79.19*		92.12*	
5	68.34**		80.64		93.64	
6	69.93		82.20		95.20	
7	71.60		83.93*		96.81*	
8	73.35*		85.68		98.63*	
9	75.18		87.38**		800.51*	
10	77.08		89.37**		2.30*	15 783.08H
11	79.04*	15 958.03H	91.38*	15 870.23H	4.40	83.22*
12	81.09*	58.45**	93.48*	70.64*	6.46	83.50
13	83.23*	58.81	95.64*	70.98**	15 808.58	83.78*
14	85.46*	59.22*	97.74*	71.44**		84.14
15	87.76*	59.54*	900.02*	71.75		84.55
16	89.90*	60.17	2.35	72.23		85.00*
17	92.53*	60.70**	4.70	72.81*		85.59*
18	94.84	61.39*	7.12*	73.48**		86.17
19	97.33	62.05*	9.60	74.08		86.83
20	99.82	62.77	12.15	74.65*		87.53
21	16 002.28**	63.55*	15 914.74*	75.58*		88.31
22	5.09	64.40		76.22		89.00**
23	7.74	65.29*		77.23*		89.99
24	16 010.53	66.22**		78.20*		90.91*
25		67.24*		79.19*		15 792.12*
26		68.34**		80.23*		
27		69.44*		81.29*		
28		70.51		15 882.44		
29		15 971.78*				
30						

[a] *H*=head. One asterisk indicates that the line is overlapped—two asterisks, badly overlapped.
[b] 6′–5″ band was not read because of extensive overlap by active nitrogen spectrum.

TABLE II. Vacuum wave numbers of the lines of the NBr^{81} bands (cm^{-1}).

	9–6		8–5		9–7	
J	$R(J)$	$P(J)$	$R(J)$	$P(J)$	$R(J)$	$P(J)$
0						
1						
2	17 560.36*				16 935.55*	
3	61.62				36.83	
4	62.92		17 491.37*		38.18	
5	64.26		92.56*		39.51*	
6	65.71		94.00*		41.06	
7	67.25		95.40**		42.63	
8	68.82		97.10*		44.28*	
9	70.48*		98.76*		46.00*	
10	72.19*		500.51*		47.82	16 929.51H
11	73.99		2.31		49.74*	29.68**
12	75.85	17 553.99H	4.16	17 482.14H	51.65*	29.84*
13	77.74	54.18*	6.05	82.34*	53.63	30.14*
14	79.69	54.43*	8.08**	82.56*	55.70	30.46*
15	81.69	54.69*	10.03*	82.87**	57.83	30.82
16	83.74	55.05	12.06	83.09*	60.01*	31.29
17	85.83	55.38	14.15	83.44*	62.22	31.77
18	87.97	55.76	16.26*	83.82*	64.48	32.29
19	90.13	56.17*	18.45	84.24	66.82	32.88
20	92.33	56.69	20.65	84.69*	69.18	33.60**
21	94.61	57.20	22.89	85.17	71.60	34.20*
22	96.87	57.78	25.20	17 485.77*	74.10	35.02*
23	99.21	58.37	27.52		76.60	35.70*
24	601.57	58.96*	29.91		79.15	36.64*
25	3.98		32.34*		81.74	37.35*
26	6.48*	60.36*	34.72*		84.40	38.32
27	17 608.92*	61.01*	17 537.17*		87.09	39.35*
28		61.90			89.82	40.34*
29		62.61*			16 992.60	41.33*
30		63.51				42.46
31		17 564.45*				43.59
32						44.81*
33						46.00*
34						16 947.25

	8–6		7–5		6–4	
J	$R(J)$	$P(J)$	$R(J)$	$P(J)$	$R(J)$	$P(J)$
0						
1						
2	16 854.40*		16 773.95			
3	55.60*		75.20*		16 695.53*	
4	56.95*		76.49*		96.90*	
5	58.28		77.89*		98.34	
6	59.71		79.43*		99.80	
7	61.32		80.99		701.41	
8	62.99		82.67		3.16*	
9	64.73		84.45*		4.82*	
10	66.61*		86.20*		6.84**	
11	68.44*	16 848.10H	88.04*	16 767.65H	8.54*	16 687.92H
12	70.33*	48.30**	90.04	67.89*		88.17*
13	72.38	48.64*	92.06	68.15*	12.49	88.41*
14	74.40	48.98	94.11	68.46	14.55	88.66*
15	76.57	49.38*	96.24	68.77	16.69	89.00
16	78.74	49.77	98.41	69.19	18.86	89.37*
17	80.97	50.26	800.64	69.65*	21.09	89.84
18	83.24	50.76	2.92	70.18	23.36	90.33
19	85.57	51.30	5.25	70.71	25.69	90.87
20	87.95	51.93**	7.62	71.29*	28.06	91.49*
21	90.36	52.60*	10.05	71.97*	30.49	92.06*
22	92.82	53.36*	12.49	72.69*	32.93	92.77*
23	95.32	54.12	15.01	73.40	35.45	93.48
24	97.90	54.94	17.55	74.23*	38.00	94.28*
25	900.49	55.78	20.13	75.05	40.58	95.07
26	16 903.14	56.66	22.77	75.93	43.22	95.97
27		57.75*	16 825.44	16 776.84*	16 745.89	96.90*
28		16 858.56*				16 697.75*
29						
30						

TABLE II.—*Continued.*

	5–3		8–7		7–6	
J	*R*(*J*)	*P*(*J*)	*R*(*J*)	*P*(*J*)	*R*(*J*)	*P*(*J*)
0						
1						
2						
3			16 230.68*		16 140.96*	
4			32.11		42.19*	
5	16 619.41		33.60		43.64*	
6	20.89*		35.15		45.18	
7	22.54		36.74		46.81	
8	24.20*		38.50		48.54	
9	25.90*		40.33		50.35*	16 133.51H
10	27.75		16 242.24	16 223.63H	52.25*	33.63*
11	29.65			23.96*	54.34*	33.83*
12	31.62*	16 608.88H		24.25	56.26	34.12
13	33.62	9.27*		24.63	16 158.37	34.46
14	35.68	9.44		25.17*		34.87
15	37.82	9.88*		25.51		35.34*
16	40.00	10.27		26.19*		35.91**
17	42.23	10.71*		26.55*		36.51**
18	44.50	11.18*		27.20*		37.08*
19	46.82*	11.70*		27.74*		37.78*
20	49.22	12.14**		16 228.47		38.53*
21	51.62	12.84*				39.41*
22	54.07	13.55				40.27*
23	56.58	14.30				41.20*
24	59.12	15.00*				16 142.19*
25	16 661.71	15.82				
26		16.66*				
27		16 617.57				
28						
29						
30						

	5–4		4–3		3–2	
J	*R*(*J*)	*P*(*J*)	*R*(*J*)	*P*(*J*)	*R*(*J*)	*P*(*J*)
0						
1						
2			15 874.42*			
3	15 963.45*		75.86		15 789.00**	
4	64.77		77.23*		90.35*	
5	66.22**		78.65*		91.82	
6	67.77		80.23*		93.36	
7	69.44*		81.79*		95.04	
8	71.20		83.63*		96.81*	
9			85.46		98.63	
10	74.88		87.38**		800.51*	15 781.25H
11	76.89	15 955.91H	89.37**	15 868.23H	2.44*	81.44*
12	78.91*	56.36*	91.38*	68.60	4.56	81.69
13	81.09	56.69	93.48*	69.00	15 806.70	81.97
14	83.23*	57.11	95.86	69.35*		82.36
15	85.46*	57.54	97.96*	69.78		82.76
16	87.76*	58.03**	900.24			83.22*
17	90.12	58.45**	2.61	70.98*		83.78*
18	92.53*	59.22*	5.03	71.44*		84.35
19	95.04*	59.93*	7.38*	72.12		85.00*
20	97.55	60.70**	10.03*	72.81*		85.66*
21	16 000.17*	61.39*	12.62*	73.48*		86.49
22	2.77	62.32*	15 915.25	74.42		87.29
23	5.43*	63.16		75.28		88.13
24	16 008.23	64.09**		76.22		89.00**
25		65.11*		77.23*		15 790.35*
26		66.22**		78.20*		
27		67.24*		79.19*		
28		68.34**		15 880.42		
29		15 969.44*				
30						

TABLE III. Vibrational isotope shifts of the NBr bands (cm^{-1}).

$v'-v''$	Calculated	Observed from band heads
4–3	1.951	1.95
5–4	2.105	2.10
7–6	2.427	2.41
8–7	2.592	2.58
5–3	3.245	3.25
6–4	3.367	3.34
7–5	3.492	3.49
8–6	3.622	3.61
9–7	3.754	3.75
8–5	4.687	4.68
9–6	4.784	4.78

The combination differences for the upper state of each band were found to consist of a simple progression of numbers which could be represented by the equation

$$\Delta_2F(J)=4B(J+\tfrac{1}{2}), \qquad (3)$$

where J is an integer. This expression (with a small additional term to account for centrifugal stretching) is expected to fit the combination differences of a $^1\Sigma$ state or of one of a relatively few other states such as a 0 state or the F_2 component of a $^3\Sigma$ state. It was assumed tentatively that the upper state was a $^1\Sigma$ state and an attempt was made to identify the lower state.

With the numbering of the lines determined by the upper state combination differences and Eq. (3), the lower state combination differences were determined. It was found that these could not be fitted to Eq. (3) since $\Delta_2F''(J)/(J+\frac{1}{2})$ was not a constant. A detailed investigation of these unusual $\Delta_2F''(J)$ values was hampered by the fact that the lines of low J value for one of the branches are lost in the band head and hence the very interesting low values of $\Delta_2F(J)$ could not be determined. In order to overcome the difficulty it was assumed that the upper state combination differences, which as discussed above form a regular series, can be extrapolated accurately down to $J=1$. From these extrapolated upper state combination differences and the one branch which extends down to low J values, the lower state combination differences were determined down to about $J=3$. One such set of $\Delta_2F''(J)$ values is given in Table IV.

At this stage, from quite good upper state B values and rough estimates of the lower state B values, it became apparent that the two branches in each band are of types which can best be described as a Q and an S branch. Such pairs of branches are commonly observed in singlet-triplet transitions. As will be discussed further, below, it appears most probable that the ground state of NBr is a $^3\Sigma^-$ state and since the upper state of the observed bands behaves like a $^1\Sigma$ state it was tentatively assumed that the bands are due to a $^1\Sigma^+-{}^3\Sigma^+$ transition in which only the F_1 component of the $^3\Sigma^-$ state is observed. We shall now show that such a transition can account for the bands.

If, as usual, only electric dipole radiation need be considered, then the selection rules for a $^1\Sigma^+-{}^3\Sigma^-$ transition are $\Delta J=0, \pm1$ and positive rotational levels combine with negative but levels of the same sign do not. Following these selection rules Fig. 2 gives a schematic diagram of the possible branches in a $^1\Sigma^+-{}^3\Sigma^-$ transition. It can be seen that five branches are possible. Here we shall postulate that only the two branches terminating on the $F_1(J=N+1)$ levels occur and the possible reason for this will be discussed later. Thus the branches observed are the S-form R branch and the Q-form P branch shown in solid lines in Fig. 2. In this paper the transition will be referred to as a $^1\Sigma^+-{}^3\Sigma^-(F_1)$ transition.

Once having assumed that the bands arise from a $^1\Sigma^+-{}^3\Sigma^-$ transition, it is possible to evaluate the rotational constants. The upper electronic state presented no difficulty since, as discussed above, the combination differences form a regular progression. The B values were determined by plotting $\Delta_2F'(J)/(J+\frac{1}{2})$ against $(J+\frac{1}{2})^2$ in the usual manner.[3] The B values obtained in this way are given in Table V.

The evaluation of the constants for the lower state is

TABLE IV. Observed and calculated values of $\Delta_2F(J)$ in cm^{-1} for the $v=7$ level of the $^3\Sigma(F_1)$ state of NBr. The values in the columns marked "calculated (I)" and "calculated (II)" were obtained from Eq. (4) with the constants $B=0.414$, $\lambda=8.7$, $\gamma=-0.7$ cm^{-1} and $B=0.418$, $\lambda=10$, $\gamma=-0.025$ cm^{-1}, respectively.

J	$\Delta_2F(J)$ Observed	$\Delta_2F(J)$ Calculated (I)	$\Delta_2F(J)$ Calculated (II)
3	5.25	5.38	5.32
4	6.87	6.91	6.87
5	8.49	8.46	8.43
6	10.02	10.03	10.01
7	11.56	11.61	11.59
8	13.18	13.19	13.18
9	14.77	14.78	14.78
10	16.36	16.40	16.39
11	18.05	18.01	18.01
12	19.69	19.63	19.63
13	21.28	21.25	21.26
14	22.92	22.87	22.89
15	24.54	24.51	24.53
16	26.13	26.13	26.17
17	27.80	27.78	27.82
18	29.46	29.43	29.47

much more difficult. Schlapp[4] has given equations for the rotational levels of a $^3\Sigma$ state. For the F_1 levels the equation is

$$F_1(J)=B_vJ(J+1)+(2J+3)B_v-\lambda$$
$$-[(2J+1)^2B_v^2+\lambda^2-2\lambda B_v]^{\frac{1}{2}}+\gamma(J+1). \quad (4)$$

The rotational terms and hence the combination differences now depend on three constants B_v, λ, and γ. Since the relative values of the rotational energy levels are largely determined by the term $B_vJ(J+1)$ and there are two constants λ and γ to account for the difference between $F_1(J)$ and $B_vJ(J+1)$, it is very difficult to determine each of these independently. In Table IV the observed combination differences $\Delta_2F(J)$ for the $v=7$ level are compared with two sets of values calculated from Eq. (4) first using the constants $\lambda=8.7$, $\gamma=-0.7$, $B_7=0.414$ cm^{-1} and second with $\lambda=10$, $\gamma=-0.025$, $B_7=0.418$ cm^{-1}. It can be seen that the difference between the two calculated sets is small and each can be said to fit the observed set of levels within the experimental error. Thus it appears that the lower state levels can be fitted by Schlapp's equation, but we can obtain very little precise information about the rotational constants. Fortunately the values of B_v are not strongly dependent on the choice of λ so that in spite of very inaccurate values of λ and γ, reasonably good values of B_v may be obtained.

Using the values $\lambda=8.7$ cm^{-1} and $\gamma=-0.7$ cm^{-1}, the B value of the $v''=7$ and $v''=3$ levels were determined. Since it was found that the combination differences for the various vibrational levels of the lower states are linear functions of v, it was assumed that B is a linear function of v and that the B values for all the other observed lower state vibrational levels could be obtained by interpolation and extrapolation from the third and seventh levels. These values are listed in Table V. The constants of the NBr molecule are collected together in Table VI.

DISCUSSION

It has been shown above that the spectrum of NBr can be interpreted as one arising from a transition between a $^1\Sigma^+$ and the F_1 component of a $^3\Sigma^-$ state. This unusual type of transition raises a number of problems some of which will now be discussed.

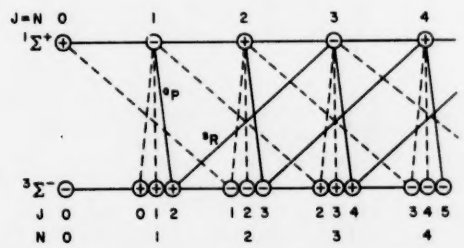

FIG. 2. Schematic diagram showing the five possible branches in the NBr spectrum. Solid lines indicate the two observed branches.

TABLE V. Rotation constants of the NBr^{79} molecule in cm^{-1}.

v	B_v'	B_v''
3	0.4599	0.430
4	0.4561	0.426[a]
5	0.4526	0.422[a]
6	0.4485	0.418[a]
7	0.4448	0.414
8	0.4411	0.410[a]
9	0.4371	0.406[a]

[a] Obtained from B_3 and B_7 by interpolation.

The outer electrons of the NBr molecule should have a configuration similar to that of S_2 or O_2. In these molecules the ground state configuration consists of a number of closed shells and two electrons in a π shell. This π^2 configuration gives $^3\Sigma^-$, $^1\Delta$, and $^1\Sigma$ states of which the $^3\Sigma^-$ is expected to be lowest and to form the ground state of the molecule. In oxygen the transition between the $^1\Sigma^+$ and $^3\Sigma^-$ states gives rise to the atmospheric absorption bands near 7600 A and it appears not at all unlikely that the NBr bands observed here arise from the same transition. Whereas the transition in the homonuclear molecules such as O_2 or S_2 is highly forbidden and can occur only through magnetic dipole radiation, in the heteronuclear molecule NBr it is much less forbidden and can occur through electric dipole radiation. Thus, from a consideration of the electron configuration of NBr, it seems reasonable that a $^1\Sigma^+-{}^3\Sigma^-$ transition should be observed.

The reason for the appearance of only two of the five possible branches in the $^1\Sigma-{}^3\Sigma$ transition is not clear but is is quite likely that it is related to the type of coupling between the electron spins and internuclear axis that exists in the $^3\Sigma$ state. In NBr we might expect the triplet spin splitting to be much greater than in oxygen or even sulfur. The observed value of $\lambda/B\sim25$ as opposed to $\lambda/B=1.4$ in oxygen shows this large spin splitting does indeed exist. With this large spin splitting the $^3\Sigma$ state may take on the characteristics of a Hund's case c state.[5] In this type of coupling the F_1 levels move away from the F_2 and F_3 to form an 0^+ while the F_2 and F_3 levels form a 1 state. The transition we have observed can then be described as a $^1\Sigma^+$ (or 0^+)-0^+ transition while the related $^1\Sigma^+$ (or 0^+)-1 transition has not been observed. Thus it is possible to find a characteristic of the F_1 levels which differentiates them from the F_2 and F_3 but the observation that the $^1\Sigma^+-0^+$ transition probability is much greater than the $^1\Sigma^+-1$ transition probability has no simple theoretical basis.

[4] R. Schlapp, Phys. Rev. **51**, 342 (1937).

[5] R. S. Mulliken, Revs. Modern Phys. **3**, 89 (1931).

TABLE VI. Constants of the NBr^{79} molecule in cm^{-1}.

State	T_e	ω_e	$\omega_e x_e$	B_e	α	r_e, A
$^1\Sigma^+$	14787.3[a]	785.5[b]	4.363[b]	0.4733	0.0152	1.729
$^3\Sigma^-$	0	691.75[b]	4.720[b]	0.444[c]	0.0040[c]	1.79[c]

[a] Measured from band heads with respect to the F_1 component of $^3\Sigma^-$.
[b] From band heads.
[c] The values are subject to large errors (see text).

Elliott[1] has reported some weaker bands which occur between the strong bands measured here. These bands are not observed in the much weaker, high-dispersion spectra which we have obtained.[6] It is quite possible that these bands are due to the F_2 and F_3 levels. The constants $\lambda=8.7, \gamma=-0.7$ do not place the heads of the F_2 and F_3 components of the bands at wavelengths of the weak heads reported by Elliott but it has been pointed out above that this value of λ is a very inaccurate one. It is indeed possible to choose a value of λ which is not inconsistent with the observed bands and which, at the same time allows the heads of the F_2 and F_3 components to account for a number of Elliott's weaker bands.

To summarize, the situation is that the observed bands can be accounted for if it is assumed that they are due to a $^1\Sigma^+-^3\Sigma^-(F_1)$ transition. It can not, however, be claimed that this assignment is unique, since bands from such a transition can never be distinguished experimentally from those of $^1\Sigma^--^3\Sigma^+$ transition, and here the rather unusual spectrum can be accounted for by even other types of transitions. The theoretical evidence that the ground state of NBr is a $^3\Sigma^-$ state and that a low-lying $^1\Sigma^+$ state should exist, gives strong support to the assignment of the bands to a $^1\Sigma^+-^3\Sigma^-(F_1)$ transition. Also, as will be discussed below, it appears reasonable that the method of excitation used here should give transitions involving the ground state of NBr. Thus while there is no simple direct proof that the bands are due to a $^1\Sigma^+-^3\Sigma^-(F_1)$ transition there is considerable indirect evidence to support this assignment.

Assuming that the observed bands are due to a $^1\Sigma^+-^3\Sigma^-(F_1)$ transition, we will now consider how they can be excited in active nitrogen and what information can be obtained regarding the dissociation energy of NBr. From the Wigner-Witmer correlation rules it follows that a ground-state bromine atom (^2P) and a ground-state nitrogen atom (^4S) can combine to give $^3\Sigma^-$, $^5\Sigma^-$, $^3\Pi$ and $^5\Pi$ states of the NBr molecule. The $^3\Sigma^-$ state which has been observed probably correlates with ground-state atoms but the $^1\Sigma^+$ state must correlate with some higher states of the separated atoms, probably $N(^2D)+Br(^2P)$. The energy levels of NBr must therefore be of the form shown in Fig. 3.

[6] On the most intense photograph of the NBr spectra which we obtained some additional faint lines were observed in the 9-7 and 8-6 bands. However, we have been unable to make any assignments to the lines.

It has been noted earlier that the vibrational levels of the $^1\Sigma^+$ state are populated up to the $v=10$ level but not beyond. There is kinetic evidence discussed in an earlier paper[2] which points quite strongly to the reactions

$$N(^4S)+Br(^2P_{\frac{1}{2}}) \xrightarrow{\text{wall}} NBr^*$$

$$NBr^* \rightarrow NBr+h\nu$$

being responsible for the observed emission. It therefore appears plausible that ground state atoms combine first to form an NBr molecule in one of the three states $^3\Pi$, $^5\Pi$, $^5\Sigma^-$ and that a transition to the $^1\Sigma^+$ state is wall induced. This mechanism is similar to that proposed for the recombination of nitrogen atoms in active nitrogen except for the wall effect. The combining atoms at room temperature can have only one or two kcal of kinetic energy and thus the $v=10$ level of the $^1\Sigma^+$ state, which is 63.4 kcal above the $v=0$ level of the ground state, cannot lie more than one or two kcal higher than the energy of the separated atoms. The sharp cutoff of the band system at $v=10$ seems to suggest that 63.4 kcal is in fact very close to the dissociation energy itself. The dissociation energy obtained by a long Birge-Sponer extrapolation of the $^3\Sigma$ state is 71.5 kcal. Since such extrapolations usually err on the high side, this value for the dissociation energy of the molecule agrees very well with the ~62-kcal lower limit obtained above. We therefore estimate the dissociation energy of NBr to be 67±5 kcal.

A more detailed mechanism which is in accord with

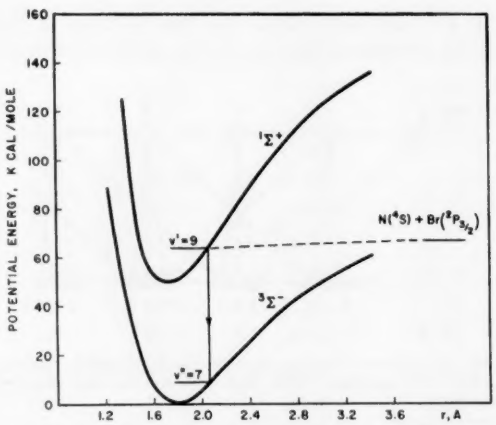

FIG. 3. Morse potential energy diagram for NBr.

the kinetic and spectroscopic observations is

$$N(^4S)+Br_2(^1\Sigma^+)\rightarrow NBr(^3\Sigma^-)+Br(^2P_{\frac{1}{2}})+21\text{ kcal}, \quad (5)$$

$$N(^4S)+NBr(^3\Sigma^-)\rightarrow N_2(^1\Sigma^+)+Br(^2P_{\frac{1}{2}})+158\text{ kcal}, \quad (6)$$

$$N(^4S)+Br(^2P_{\frac{1}{2}})\xrightarrow{\text{wall}}NBr(^3\Pi, {}^5\Pi, \text{or } {}^5\Sigma^-), \quad (7)$$

$$NBr(^3\Pi, {}^5\Pi \text{ or } {}^5\Sigma^-)\xrightarrow{\text{wall?}}NBr(^1\Sigma^+), \quad (8)$$

$$NBr(^1\Sigma^+)\rightarrow NBr(^3\Sigma^-)+h\nu. \quad (9)$$

If reaction (7) occurred as a gas phase process, the $^3\Pi$ state could radiate before diffusing to the wall, and either of the quintet states would dissociate in a single vibration since they involve no bonding electrons. However, there is no evidence to indicate whether the wall is important in reaction (8) which could occur very rapidly.

ACKNOWLEDGMENT

We wish to thank Dr. G. Herzberg for helpful advice.

THE JOURNAL OF CHEMICAL PHYSICS VOLUME 35, NUMBER 4 OCTOBER, 1961

Mean and Equilibrium Molecular Structures of Methane and Deuteromethane as Determined by Electron Diffraction* †

L. S. BARTELL, KOZO KUCHITSU, AND R. J. DENEUI

Institute for Atomic Research and Department of Chemistry, Iowa State University, Ames, Iowa

(Received February 20, 1961)

The structural parameters of methane and methane-d_4 were determined with the new rotating-sector electron diffraction apparatus of Iowa State University. The results demonstrated, for the first time by electron diffraction, the existence of isotope effects on structure. Mean internuclear distances were C—H = $1.106_8\pm0.001$ A, C—D = $1.102_7\pm0.001$ A, H···H = 1.811 ± 0.007 A and D···D = 1.805 ± 0.008 A. Mean amplitudes, reckoned from mean positions, were C—H = $0.075_1\pm0.002$ A, C—D = $0.066_3\pm0.002$ A, H···H = 0.120 ± 0.006 A, and D···D = 0.105 ± 0.006 A.

The isotope effects were just those expected for atoms of different mass vibrating in identical anharmonic force fields. Vibrational anharmonicity led to measurable phase shifts in the molecular diffraction patterns from which the asymmetry of the internuclear distribution functions could be determined. This allowed a direct experimental determination of the approximate equilibrium C—H and C—D bond lengths, giving 1.08_2 A. Somewhat more rigorous calculations of the correction from mean to equilibrium distances based on an anharmonic Urey-Bradley field led to equilibrium C—H and C—D bond lengths of 1.084_7 A and 1.086_3 A, respectively. Corresponding equilibrium bond lengths computed from the spectroscopic r_0 values of 1.094_0 A and 1.092_3 A, respectively, were 1.085_0 A and 1.085_6 A. The comparison clearly illustrates the appreciable difference between electron diffraction and spectroscopic methods in the manner of averaging over molecular motions, but also confirms the essential equivalence of molecular information derived, if suitable corrections are applied to each.

THE natural indeterminacy associated with atomic positions in molecules due to zero-point vibrational motions is of the order of 0.1 A. The experimental error in the best spectroscopic and electron diffraction structure determinations today is of the order of 0.001 A or less. It is clear, then, that the absolute significance of experimental structural parameters, in terms of thousandths of an angstrom unit, depends crucially upon the breadths and asymmetries of the vibrational wave functions and upon the manner of averaging over the molecular rotation-vibration states. Although the problem is relatively simple, in principle, for diatomic molecules, it is sufficiently complex for polyatomic molecules that in only a handful of cases have true equilibrium bond lengths been determined by spectroscopic methods. In no electron diffraction investigations heretofore have results been accurately reduced to equilibrium parameters, even though the diffraction averaging problem, being essentially a purely vibrational one, is simpler than the spectroscopic problem.

A really critical experimental comparison of the electron diffraction and spectroscopic methods, properly taking into account the different types of averaging over molecular motions, has never been made. It seemed desirable to undertake such a comparison, therefore, examining molecules in which zero-point effects are large. Molecules containing hydrogen atoms exhibit unusually large and asymmetric vibrational motions, and further, afford an opportunity for varying amplitudes by isotopic substitution. Methane and deuteromethane, then, present an especially favorable system for study.

PROCEDURE

Recording Diffraction Patterns

The electron diffraction apparatus used in this study was recently constructed at the Institute for Atomic Research of Iowa State University and has not yet been described in the literature. It is similar to the unit of the

* Contribution No. 973. Work was performed in the Ames Laboratory of the U. S. Atomic Energy Commission.

† Presented at the 138th Meeting of the American Chemical Society, New York, New York, September 12, 1960.

University of Michigan,[1] but was designed to fix the camera geometry more precisely and to give a greater range in scattering angle. A higher pumping speed allows clean diffraction patterns to be recorded beyond $s=60$ with continuous introduction of even noncondensable specimens. Research-grade methane (99.58%) obtained from the Phillips Petroleum Company and methane-d_4(99+%) obtained from Merck and Company Ltd. were used as samples. Diffraction photographs were taken on Kodak 4-×5-in. process plates using 40.00-kv electrons from a well-stabilized source and an r^3 sector of 48-mm radius. Camera distances were either 213.77 mm (long camera distance) or 107.22 mm (middle distance).[2]

Experimental conditions such as sample pressure and exposure time were carefully determined and controlled to reduce extraneous scattering. Typical values were as follows[3]: sample pressure 15 mm Hg, exposure 40 sec (at long distance); sample pressure 20 mm Hg, exposure 120 sec (at middle distance); electron beam current, 0.4 μa. Other experimental features closely resembled those described in previous papers.[1]

Four apparently flawless plates were selected for each camera distance, and optical densities ($D=0.25-0.7$) were measured on the Leeds and Northrup recording microphotometer of the University of Michigan.

Analysis of Data

The densities were converted to intensities using the equation,[4] $E=D(1+cD)$ with $c=0.05$,[5] and the intensities were processed by an IBM 650 digital computer.[6]

Imperfections in the sector shape were measured using diffraction photographs of argon, and corrections were applied to the data for methane. The molecular intensity taken at the long camera distance which covered the region from $s=3$ to $s=20$ agreed excellently, in the overlapping region, with that taken at the middle distance which covered $s=8$ to 40 or more. Intensities appeared sensitive to molecular scattering features to better than 0.1%. The indices of resolution

$$R=M_{\text{expt}}(s)/M_{\text{calc}}(s),$$

as measured directly from the patterns or as inferred from the radial distribution curves (see Table II), were approximately 100% for the middle distance patterns and 90% for the long distance patterns.[7] The radial distribution curves, computed with an artificial damping function $\exp(-0.0023s^2)$ were corrected for the integral termination ripple.[8] The asymmetry caused by anharmonic vibrations[9] was explicitly taken into account, and the molecular parameters were determined by the method of steepest ascents.[8] The resultant parameters were corrected for the failure of the Born approximation[10] influencing l, using the table of Ibers and Hoerni,[11] and for the effect of gas delocalization[7,12,13] on r_g.

Error Analysis

The net random and systematic errors influencing bond distances, other than those associated directly

[1] L. O. Brockway and L. S. Bartell, Rev. Sci. Instr. **25,** 569 (1954).

[2] A short distance of 68 mm is available for studying scattering at large s, but was unnecessary for methane, the molecular pattern of which damps rapidly.

[3] When the stopcock of a 5-liter flask in which the sample gas was contained at a pressure p was opened, and the gas was continuously admitted into the camera chamber through the fine specimen nozzle, the pressure of the chamber P reached its equilibrium value in less than 0.1 sec. It was found that P, as measured by a hot cathode ionization gauge, was roughly proportional to p^2 at small p, as expected if the gas on passing through the nozzle follows the equation for viscous flow. If p exceeded 25 mm Hg, the speed of the diffusion pumps fell rapidly and the undesirable effect of delocalized gas pressure grew disproportionally large. Care was taken then, to keep the pressure p under 20 mm Hg for such gases as CH_4 and CD_4 which are not condensed by liquid nitrogen.

[4] L. S. Bartell and L. O. Brockway, J. Appl. Phys. **24,** 656 (1953).

[5] The calibration constant c of the photographic emulsion was estimated by taking diffraction photographs of diatomic molecules, five plates in one run, under identical diffraction conditions except for slight (measured) differences in sample pressure p. They were exposed consecutively with exposure times t varied by varying the number of shots (each of constant time) per plate, and developed simultaneously. It was assumed that the scattered electron intensity E is proportional to the product pt. The densities D of maxima and minima were measured and plotted against E. In several series of experiments, it was shown that the intensity E is well represented by the form $E=D(1+cD)$ for D up to 1.2 within the limits of uncertainty of c, and that $c=0.05\pm 0.01$ for Kodak Process plates and D-11 developer regardless of the emulsion numbers used and of the aging of the developer during the period of experiment.

[6] R. A. Bonham and L. S. Bartell, J. Chem. Phys. **31,** 702 (1959).

[7] In our previous experience with the Michigan diffraction unit, evidence indicated that the failure to achieve $R=100\%$ was principally due to scattering by a background of uniformly delocalized gas sample in the diffraction chamber. In the present investigation it was decided to measure the contribution of this extraneous scattering directly. Gas was introduced into the diffraction camera through a baffled opening across the chamber from the nozzle, and was presumed to distribute itself uniformly. Diffraction photographs of the delocalized gas were taken at the steady-state pressure in the camera observed during the recording of the regular diffraction patterns. The resulting intensities suggested that the delocalized specimen was responsible for 5% of the intensity of regular patterns recorded at the middle distance, and for 12% to 14% at the long distance. The implication is that, if the total intensities were corrected for delocalized scattering, the resultant index of resolution would be about 107% of the maximum value anticipated. Whether this discrepancy is a result of hidden experimental errors in measurements involving delocalized gas or inadequacies in the conventional electron scattering theory is uncertain.

[8] L. S. Bartell and L. O. Brockway, J. Chem. Phys. **32,** 512 (1960).

[9] L. S. Bartell, J. Chem. Phys. **23,** 1219 (1955).

[10] R. Glauber and V. Schomaker, Phys. Rev. **89,** 667 (1953).

[11] J. A. Ibers and J. A. Hoerni, Acta Cryst. **7,** 405 (1954).

[12] L. S. Bartell, J. Appl. Phys. **31,** 252 (1960).

[13] As described in footnote 7, diffraction patterns were taken to correspond to the delocalized contribution to the total patterns. The resultant photographs exhibited weak molecular features which agreed well with the theoretical predictions [Eq. (6)] of reference 12. From the observed ratio of delocalized to localized scattering, the correction, Δr_s, to r_g due to gas spread was calculated.[12] The corrections ranged from -0.0010--0.0015 A. If the discrepancy noted in footnote 7 arises because of some nonrandom characteristic of the gas flow pattern in the experiments the corrections Δr_s may be too large. If it is the theoretical scattering formulas which are in error, it is probable that the Δr_s are correct but that the analyses for the experimental amplitudes l must be considered slighty uncertain.

with specimen spread or measurements of intensity, were estimated to be about 6 parts per 10 000. They are broken down in the first four lines of Table I. This uncertainty has been reduced about twofold in comparison with previous results reported from this laboratory, principally because of the greater precision in fixing the camera geometry. Only experience will provide a measure of the error in the present method of determining the correction for spread of gaseous sample.[13] The value listed in Table I was somewhat arbitrarily taken as $\frac{1}{4}$ of the correction, and represents the uncertainty in amount and distribution of the delocalized sample and the arbitrariness in estimating the atomic intensity at small s. Of several different methods for assessing random errors in intensity measurements, two are discussed below, one for the first time.

In principle an estimate of errors in intensities can be derived from a least-squares analysis of the radial distribution curve. This approach, described elsewhere,[6] gave standard errors for r(C–H) and r(C–D) of 0.0009 A and 0.0011 A, respectively. Since, as discussed in reference 6, it may be subject to hidden uncertainties, it seemed desirable to get a more direct measure of the uncertainties in intensity. This was done as follows.

From each set of four plates taken at a given camera distance, one was selected at random as a reference plate. The intensities I of each of the other three plates were subtracted from that of the reference, point by point at corresponding s values, and the standard deviation associated with the random scatter was calculated. This standard deviation was assumed to be $2^{\frac{1}{2}}$ times greater than the standard deviation $\sigma(I)$ corresponding to a given plate. For CH_4 the standard deviation was quite uniform from plate to plate, and $\sigma(I)/I$ was approximately 4.5×10^{-4} over the range of s except at small scattering angles where it rose to about 1×10^{-3} as the sector opening decreased to a narrow slit. For CD_4, $\sigma(I)/I$ was similarly uniform, with a value of about 5.0×10^{-4}. In addition to the random scatter there was a rapidly damped sinusoidal fluctuation in phase with the molecular pattern and about 1 or 2% of the amplitude of the pattern. It arose because the total exposures of the various plates were not identical. If this nonrandom contribution had been included with the random, the total $\sigma(I)/I$ would still have been less than 1×10^{-3}, except at small angles.

It is useful to derive a relationship between the standard deviation in intensity and the associated standard error in the positions of the peaks in the experimental radial distribution curve $f(r)$ from which the internuclear distances are determined. From the well-known relations

$$f(r)=\sum_i s_i\{\exp(-bs_i^2)\}M(s_i)\sin s_i r\quad\Delta s_i$$

$$\simeq f_m\exp\{-[r-r_0(1)]^2/2(2b+l^2)\},\qquad(1)$$

where

$$M(s)=[(I_{\text{tot}}/I_{\text{atom}})-1],$$

Table I. Estimated uncertainties in bond lengths, thousandths of an angstrom unit.

Source	(C—H)	{(C—H) − (C—D)}	(C—D)
Electron wavelength	0.2	0.0	0.2
Camera length	0.3	0.2	0.3
Magnetic disturbance due to sector race	0.2	0.0	0.2
Microphotometer radial scanning[a]	0.4	0.4	0.4
Gas spread correction	0.4[b]	0.4	0.3[b]
Intensity error as determined by			
random intensity scatter	0.3	0.4+	0.3
L. S. curve fit of $f(r)$ peak	0.3	...	0.6
fit of over-all $f(r)$ curve[c]	0.9	...	1.1
Estimated net	1.2	0.7[d]	1.3

[a] Determined several years ago, no opportunity for recent check.
[b] Arbitrarily taken as 1/4 of the correction.
[c] Includes errors not recognized in intensity scatter, such as errors in sector calibration function.
[d] This uncertainty is possibly a little too optimistic in view of the minor discrepancies of the diffraction r_e values (Table IV).

it is evident that the error δf_i in the $f(r)$ function due to an error δM_i in the reduced intensity, is

$$\delta f_i=(s_i\{\exp(-bs_i^2)\}\sin s_i r\quad\Delta s_i)\delta M_i.$$

If s_i is not too large (i.e., is below $\sim\pi/l$), the shift in the center of gravity of a peak in $f(r)$ due to δf_i is nearly the same as the shift δr_i in the position of the maximum. From Eq. (1), it follows that

$$\delta r_i=(2b+l^2)(\partial\delta f_i/\partial r)/f_m$$
$$=(2b+l^2)(s_i^2\{\exp(-bs_i^2)\}\cos s_i r\quad\Delta s_i\delta M_i)/f_m.$$

The standard error $\sigma_I(r)$ associated with the effect of random intensity errors on the position of the maximum of $f(r)$ is then

$$\sigma_I(r)=[(2b+l^2)/f_m]\{\sum[s_i^2\exp(-bs_i^2)\times\cos s_i r\quad\Delta s_i\delta M_i]^2\}^{\frac{1}{2}}$$
$$\simeq[(2b+l^2)/2^{\frac{1}{2}}f_m]\{\sum[\sigma(I)/I]_i^2\times[s_i^2\exp(-bs_i^2)\Delta s_i]^2\}^{\frac{1}{2}}\qquad(2)$$

if $\sigma(I)/I$ is more or less uniform over the range of s and if the errors δM_i are truly independent.

Although Eq. (2) is the equation used below to calculate $\sigma_I(r)$, it is helpful in the presentation to introduce a further approximation which does not lead to serious errors if the maximum value of s, namely s_M, is selected judiciously (e.g., $s_M\sim30$ for CH_4). If it is assumed that Δs_i is constant, and $s_i\{\exp(-bs_i^2)\}\sigma(I)/I=T$ where T is independent of s, then it is easy to show that

$$\sigma_I(r)=[(2b+l^2)/6^{\frac{1}{2}}f_m]Ts_M^{\frac{1}{2}}\Delta s_i^{\frac{1}{2}}.\qquad(3)$$

TABLE II. Structure of methane derived by least squares from radial distribution curve (in Å unit).

	CH_4		CD_4	
	C—H	H—H	C—D	D—D
$r_g(0)$[a]	1.106_8	1.811	1.102_7	1.805
$r_g(1)$[b]	1.101_4	1.803	1.098_6	1.801
$\sigma(r)$[c]	0.001_2	0.007	0.001_3	0.008
l(L. S.)[d]	0.076_4	0.119	0.068_3	0.104
$\sigma(l)$[c]	0.002	0.006	0.002	0.006
l^e	0.074_5	0.119	0.066_0	0.104
l_e(exp)[f]	0.078_1	0.123	0.068_4	0.106
l_e(calc)[g]	0.078_8	0.124_7	0.066_8	0.104_5
l(harm)[h]	0.078_0	0.128_2	0.066_0	0.107_4
R^i	102.5	98.1	101.2	97.5

[a] Center of gravity of nuclear probability curve, $P(r)$, referred to as r_g in recent literature and in the text.
[b] c.g. of R.D. curve, or c.g. of $P(r)/r$ curve.
[c] Standard errors.
[d] Mean amplitudes derived from L.S. analysis.
[e] Experimental mean amplitudes corrected for the failure of Born approximation.
[f] Experimental mean amplitudes reckoned from equilibrium position.
[g] Calculated l_e, reference 15.
[h] Mean amplitudes calculated by harmonic approximation, reference 15.
[i] Index of resolution of middle camera distance data in %, uncorrected for gas delocalization.

It is apparent that this general approach suffers the difficulty, in application to experiments, characteristic of error analyses in electron diffraction when based on intensity functions. The finer the subdivision Δs_i, the smaller *without limit* is $\sigma_I(r)$, so that it is possible to arrive at an unrealistically small standard error by taking sufficiently small subdivisions. The fundamental difficulty is that, as our diffraction data are measured at present, the errors in $M(s_i)$ are not truly independent if Δs_i is small. From the scattergrams from which $\sigma(I)$ was derived, clear nonrandom patterns were evident in places. The characteristic breadth of the patterns, as judged from plates that were read at intervals ranging from $\frac{1}{4}$ to $\frac{1}{8}$ s units, seemed to be appreciably less than 1 s unit. If the characteristic breadth of the nonrandom features id denoted by Δs_c, it is plausible to take Δs_c rather than Δs_i, in Eq. (3), to circumvent the foregoing difficulty.

Application of Eq. (2) to experimental data, for which Δs_i was taken as $\pi/10$ in calculating $f(r)$, gives

$$\sigma_I(r) = 0.0003_4 \text{ A for C—H, per plate}$$
$$= 0.0003_8 \text{ A for C—D, per plate}$$
$$\sim 0.0002 \text{ A for four plate average.}$$

If it is considered that $\Delta s_c/\Delta s_i$ is equal to or (probably) less than $10/\pi$, as judged above, then the appropriate standard error is equal to or less than $(10/\pi)^{\frac{1}{2}}$ times that based on Eq. (2). Accordingly, a value of 0.0003 A is reported for $\sigma_I(r)$ in Table I. It may be noted that this value is similar to that implied by the curve fitting of the C–H peak, but is appreciably smaller than the uncertainty implied by the spurious features discernible over the whole range of the $f(r)$ curve. This is presumably due to the fact that the radial distribution function makes evident errors in intensity that are reproduced in each diffraction plate, and hence escape detection in plots of intensity differences. The least optimistic of the alternatives was chosen for the net standard error reported in Tables I and II.

The standard errors of vibrational amplitudes were estimated principally from the least-squares fit of $f(r)$ as discussed elsewhere[9] and from an assumed uncertainty of up to 3% in indices of resolution. The contribution of random intensity scatter is negligible in comparison with the latter factor.

In the estimation of uncertainties, no consideration was given to possible errors in the standard approximations used to describe the scattering of fast electrons by molecules.

RESULTS

Mean Lengths and Amplitudes

As shown in Table II, the parameters of the hydride are significantly different from those of the deuteride, as is evident in the experimental radial distribution curves illustrated in Fig. 1. The mean bond length[14] r_g is clearly greater for C–H than for C–D, a result attributable to the larger amplitude of vibration of H atoms in the asymmetric force field of the molecule. The parameter most directly determined from the experimental radial distribution function is $r_g(1)$, the mean position of the $f(r)$ peak, rather than the position r_g of the true probability function. Since[9] $r_g(1)$ is smaller than r_g by l^2/r, the difference between positions of H and D radial distribution peaks is slightly less than the difference between the r_g's, as shown in Table II.

The mean amplitudes l obtained in this study are compared with those calculated from the vibrational wave function in which the anharmonicity of intramolecular vibrations has been taken into account.[15] It is important to make a clear distinction between various definitions of mean amplitudes, since differences of one from another sometimes exceed experimental errors. The value l obtained from the present least-squares fit of $f(r)$ by Gaussian peaks was, therefore, converted by an analytical procedure[16] to the root mean-square amplitude reckoned from the equilibrium position r_e.

[14] Referred to in Table II as $r_g(0)$, according to the notation of reference 9, to distinguish the parameter from $r_g(1)$, the center of gravity of the radial distribution function.
[15] K. Kuchitsu and L. S. Bartell (to be published). A preliminary report was given in abstract R7, Symposium on Molecular Structure and Spectroscopy, Columbus, Ohio, 1960.
[16] K. Kuchitsu and L. S. Bartell, J. Chem. Phys. (to be published).

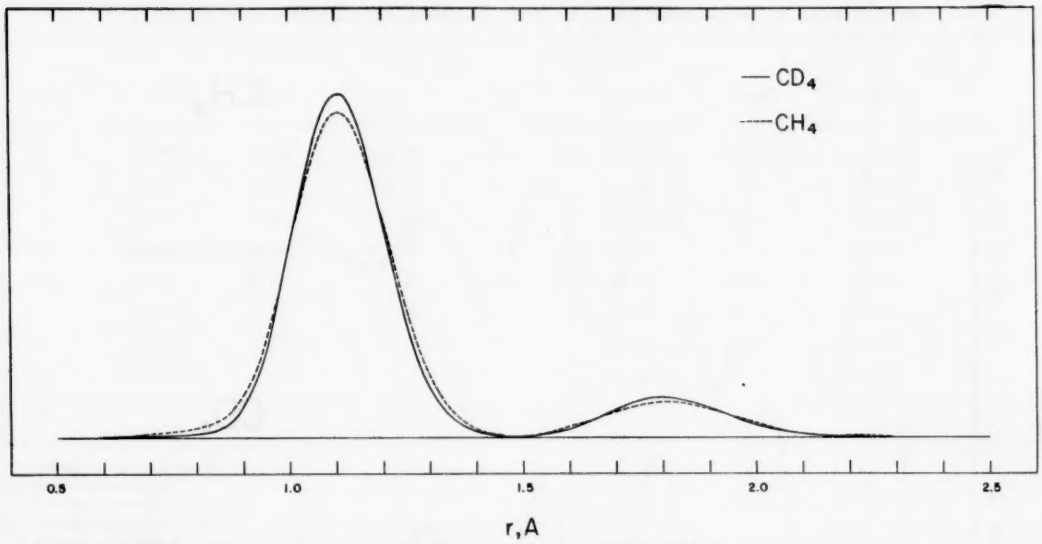

FIG. 1. Experimental radial distribution curves for CH_4 (dashed line) and CD_4 (solid line), broadened somewhat by an integral convergence factor. The mean lengths and amplitudes are slightly greater for CH_4 than for CD_4.

This parameter is variously denoted as l_e (reference 17), $\langle \Delta r^2 \rangle^{\frac{1}{2}}$ (reference 15), or u_e (reference 18). A useful alternative parameter, reckoned from the mean position, is l_g (reference 17), or u_a (reference 18). The difference between l_e^2 and l_g^2 is easily shown[18] to be $(r_g - r_e)^2$. The l_e(calc) listed in Table II, based on spectroscopic data, are taken from Table X of reference 15.

Excellent agreement is obtained between the experimental and calculated quantities. It may be noted, however, that no corrections have been made on the observed amplitudes for the effect of finite sample size which will make the corrected experimental amplitudes smaller by a few ten thousandths of an angstrom.[1] The calculated amplitudes, on the other hand, will be increased by a similar order of magnitude if the effect of the quartic and higher potential terms is properly taken into account.

Up to the present time, almost all calculations of mean amplitudes have been based on the approximation of harmonic vibrations and on the use of fundamental frequencies[19] (except H_2O and CO_2 by Retian).[18] The amplitudes l(harm) based on this approximation are, therefore, calculated[16] and listed in Table II for comparison. They are not very different from the more exact amplitudes l_e(calc) computed from normal frequencies by means of an anharmonic model.

Anharmonicity

Manifestations of asymmetry of stretching vibrations were clearly apparent in the present analysis. The experimental radial distribution peaks were plainly skewed, but when they were corrected for anharmonic effects by the use of Eq. (9) of reference 9, they could be fitted almost exactly by Gaussian curves. The C–H peak is shown in Fig. 2 as an example. From theoretical considerations,[15] it was possible to predict the distribution function for C–H and C–D bonds. The form

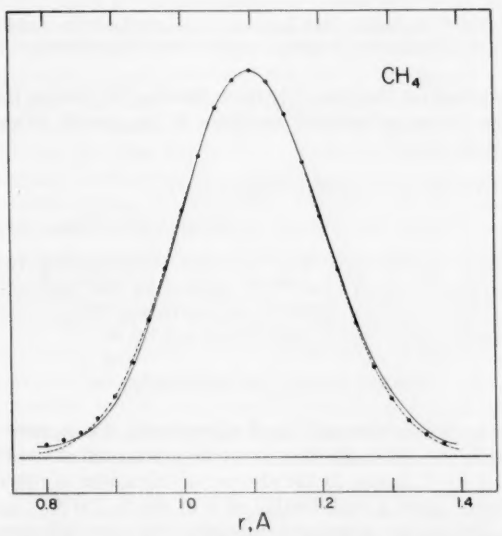

FIG. 2. Asymmetry of the C–H radial distribution peak. The original peak (solid line) is asymmetric because of the anharmonic vibrations. When the calculated asymmetric contribution is subtracted, the resulting points can be fitted by a Gaussian curve (dashed line). A recent small change in assumed index of resolution has given a slightly better fit than depicted.

[17] Y. Morino, Y. Nakamura, and T. Iijima, J. Chem. Phys. **32,** 643 (1960).
[18] A. Reitan, Acta Chem. Scand. **12,** 785 (1958).
[19] S. J. Cyvin, Kgl. Norske Videnskab. Selskabs, Skrifter No. 2 (1959).

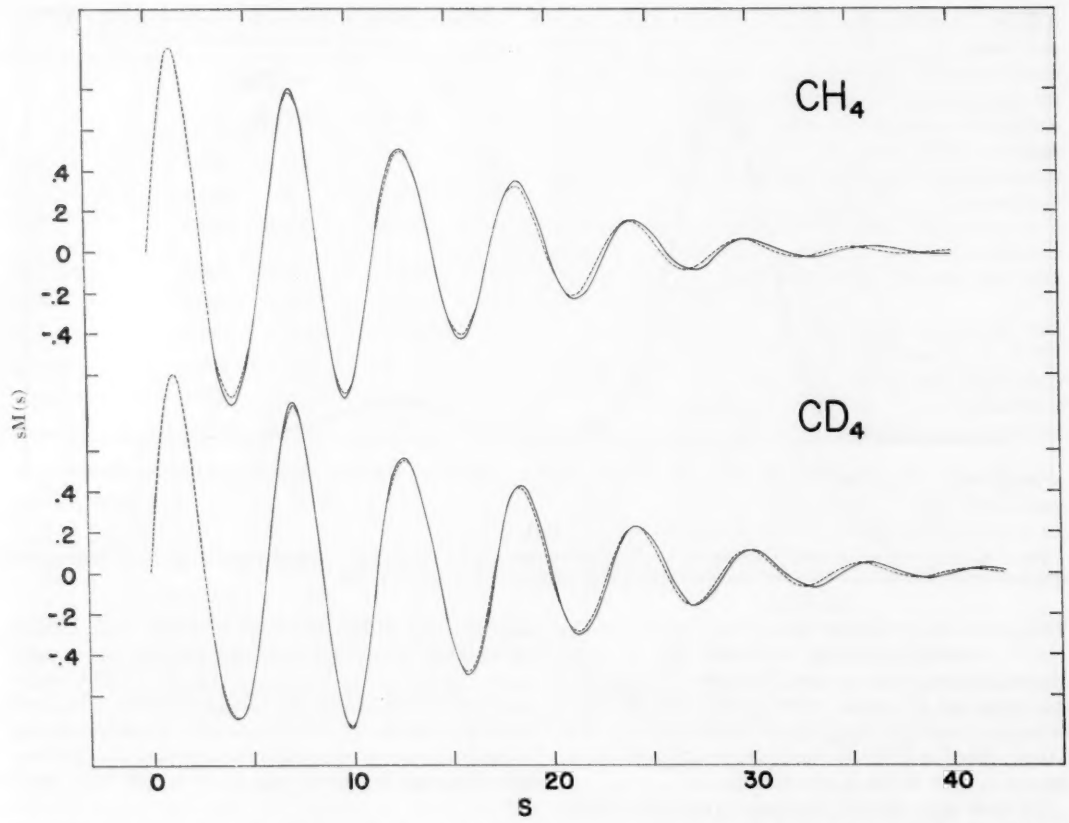

FIG. 3. Comparison of experimental intensity functions (solid lines) and functions calculated assuming harmonic vibrations (dashed lines). The observed frequency modulation of the experimental curves results from the anharmonicity of the molecular vibrations.

assumed for the present purpose was the distribution for the Morse anharmonic oscillator in its ground vibrational state.[20]

$$P(r)=K\exp\{-[(al_\alpha)^{-2}\exp(-a\Delta r)] +[a-(al_\alpha^2)^{-1}]\Delta r\}, \quad (4)$$

where $\Delta r=r-r_e$, a is a constant characterizing the asymmetry such that $P(r)$ approaches the harmonic oscillator distribution when a tends to zero. The parameter l_α can be shown to be related to l_e by [16]

$$l_e^2=l_\alpha^2+(15/4)l_\alpha^4+(45/32)l_\alpha^6+\cdots.$$

According to the analysis of reference 15, the asymmetry of the Morse-like bond stretching potential of C—H and C—D bonds, in the absence of vibrations of other bonds, gives a contribution to a of nearly 2.0 A^{-1}. In addition, the zero-point vibrations of the hydrogen atoms, through the agency of strong nonbonded repulsions, skew the distribution even further. The effective "dynamic" asymmetry constant can be computed from the moments, $\langle\Delta r^n\rangle$, calculated from the first-order perturbation vibrational wave functions of methane.[15] It was found, using $n=1$, 2, and 3, that the effective constant is $a\sim 2.6$ A^{-1}, 0.6 A^{-1} higher than the "static" stretching contribution.

The anharmonicity was also clearly shown in the frequency modulation of the molecular intensity curves. The molecular intensity function associated with an anharmonic oscillator can be expressed as[9,16]

$$M(s)=\sum c_i\exp(-l_i^2s^2/2)\{\sin s[r_g(1)+\phi(s)]\}/sr_e, \quad (5)$$

where i represents C–H (or C–D) and H···H (or D···D). For the Morse oscillator, the phase shift $s\phi(s)$ of $M(s)$ can be calculated from [16]

$$\phi(s)=-(al_\alpha^4s^2/6)-(a^2+r_e^{-2})(3a-2r_e^{-1})(l_\alpha^6s^2/6) +(a^3l_\alpha^8s^4/20)+\cdots. \quad (6)$$

In Fig. 3, the experimental curves are compared with the theoretical curves calculated using the r_g values derived from the experiments, but with $\phi(s)$ taken as zero. The effect of $\phi(s)$ is conspicuous. Theoretical curves calculated using $a=2.6$ A^{-1} for C–H and C–D

[20] P. M. Morse, Phys. Rev. **34**, 57 (1929).

TABLE III. Asymmetry parameter as determined from frequency modulation of diffraction pattern.

	CH_4				CD_4			
node	s_n[a]	Δs_n[b]	ϕ[c]	a[d]	s_n[a]	Δs_n[e]	ϕ	a
7	20.06	0.10_8	−0.59	2.8	20.06	0.05_9	−0.32	2.6
8	23.01	0.19_8	−0.95	3.3	23.01	0.13_7	−0.65	3.8
9	25.95	0.28_8	−1.22	3.4	25.93	0.19_9	−0.84	3.8
10	28.78	0.26_0	−0.95	2.4	28.80	0.21_0	−0.80	3.1
11	31.86	0.48_9	−1.69	3.3	31.64	0.18_5	−0.64	2.1
12	34.84	0.62	−1.96	3.2	34.63	0.31_6	−1.00	2.7
13	37.96	0.88_5	−2.57	3.6	37.66	0.49	−1.43	3.3
14	...	...	...	...	40.59	0.56	−1.52	3.1
Av.				$3.1_6 \pm 0.5$[f]				$3.0_5 \pm 0.5$

[a] Corrected for specimen spread.
[b] Assumes $r_g(1) = 1.1015$ A.
[c] Phase shift in 10^{-2} A.
[d] Asymmetry parameter in A^{-2}.
[e] Assumes $r_g(1) = 1.0986$ A.
[f] Includes uncertainty in l and $r_g(1)$.

are virtually indistinguishable from the experimental curves when plotted on the scale shown in Fig. 3. Since the H···H and D···D terms damp rapidly owing to large amplitudes of vibration, the $M(s)$ curve at moderate values of s exhibits features due principally to C—H or C—D terms. Consequently, it is possible to determine an experimental value of a directly from $M(s)$ by noting the difference Δs_n between positions of nodes of the experimental curve at s_n and nodes of a calculated curve with the same r_g value, but with $a=0$. From Eq. (3) it is seen that

$$\Delta s_n = -s_n \phi(s)/r_g(1), \tag{7}$$

from which a can be calculated by successive approximations using relation (6). Values of a so determined are recorded in Table III.[21] It is to be noted that the experimental a values for CH_4 and CH_4 agree satisfactorily with each other and with the theoretical estimate of a in view of the difficulty of the measurement.

The radial distribution curves in Fig. 1 show well-defined peaks of the H···H and D···D nonbonded distances. They are found to be only slightly asymmetric, and r_g and l were determined in the same way as for bonded distances,[22] taking $a \sim 1.2$ A^{-1}. The ratios of the nonbonded to the bonded distances r_g are almost equa to the tetrahedral value, $2(2/3)^{\frac{1}{2}}$.[23]

Equilibrium Bond Length

The center of gravity r_g obtained in the experiment is considered to be related to r_e in the following way:

$$r_g = (\psi | r_e + \Delta r | \psi) = r_e + \langle \Delta r \rangle, \tag{8}$$

where $\langle \Delta r \rangle$ is the instantaneous displacement of the bond length from r_e, averaged over the vibrational states. The displacement Δr can be expanded in terms of normal coordinates with the aid of the theory of normal vibrations.[24] The wave function ψ is that of a perturbed harmonic oscillator because the potential function includes higher than quadratic terms of the normal coordinates. Since there has been no experimental information regarding the cubic coefficients, which are the only important higher terms in the calculation of r_g, a method of estimating them was developed by expanding the Urey-Bradley field to the cubic power.[15] A normal coordinate analysis using the spectroscopic data of Jones and McDowell[25] led to the estimation of the potential, by the use of which a first-order perturbation calculation was carried out.[15] A minor correction for the centrifugal distortion was made to calculate r_g at room temperature. The result is shown in Table IV. It was confirmed that the experimental differ-

[21] It may seem contradictory that although the C–H length is greater than the C–D length, and positions of diffraction features are inversely proportional to bond distances, nevertheless the nodes listed in Table III for CH_4 are at consistently greater values of s than those for CD_4. The answer is, of course, that this apparent anomaly at moderate to large s results from the asymmetry of the distributions. In the lower s range not listed, the nodes for CH_4 are at smaller values of s than those for CD_4.

[22] The determination of r_g and l is quite insensitive to the value of a assumed, but it is reasonable to include a plausible asymmetry in the analysis, and better fits result.

[23] Strictly, it is the r_e values that should give this ratio, and according to the analysis of reference 15, the ratio of r_g's should deviate somewhat. The discrepancy is within the present experimental error, however.

[24] E. B. Wilson, Jr., J. C. Decius, and P. C. Cross, *Molecular Vibrations* (McGraw-Hill Book Company, Inc., New York, 1955).

[25] L. H. Jones and R. S. McDowell, J. Mol. Spectroscopy **3**, 632 (1959).

TABLE IV. Equilibrium bond lengths (in A unit).

Method		C—H(CH_4)	C—D(CD_4)
Electron diffraction	r_g(exp)[a]	1.106_8	1.102_7
	r_g-r_e(calc)[b]	0.022_1	0.016_4
	r_e	1.084_7	1.086_3
Spectroscopy	r_0(exp)[c]	1.094_0	1.092_3
	r_g-r_e(calc)[d]	0.013_1	0.009_8
	r_0-r_e(calc)[b]	0.009_0	0.006_7
	r_g	1.107_1	1.102_1
	r_e	1.085_0	1.085_6

[a] Present study.
[b] Reference 15. Uncertainties in estimated potential constants contribute an uncertainty in the correction of the order of 0.003 A.
[c] References 27 through 30.
[d] References 15, 31, and 32.

ence in r_g between C–H and C–D is caused by the effect of mass-sensitive intramolecular vibrations, there being no need for invoking a difference between intramolecular force fields to explain the isotope effect.

An alternative estimation of the equilibrium bond lengths is provided by the diffraction experiment itself. If the experimental asymmetry constant a is used in the expression for the shift $r_g-r_e\sim 3al^2/2+$ (minor centrifugal correction) anticipated for an anharmonic oscillator, the experimental r_e value for C–H and C–D becomes 1.08_2 A, with an apparent uncertainty of 0.004 A. The agreement with results calculated as described above is entirely satisfactory.

Since there has been no reliable value of r_e obtained from spectroscopic studies, a calculation was made to reduce the effective rotational constant B_0 to the equilibrium rotational constant B_e by the use of the method of Wilson and Howard,[26] and of Hecht,[27] using the cubic potential constants estimated in the above procedure.[15] Since there are several different experimental values of B_0, the latest and possibly the most reliable values[27–30] were selected to calculate r_0. As shown in reference 15, and independently by Laurie and Herschbach,[31] and Oka,[32] r_g may be computed from r_0 and the quadratic potential constants, even if the anharmonic constants are unknown. It was found, as shown in Table IV, that the mean and equilibrium bond lengths derived from the spectroscopic results are in good agreement with those derived from the present electron diffraction study.

[26] E. B. Wilson, Jr., and J. B. Howard, J. Chem. Phys. **4,** 260 (1936).
[27] K. T. Hecht, J. Mol. Spectroscopy **5,** 335 (1960).

CONCLUSION

Determined for the first time by electron diffraction were (a) an isotope effect on bond lengths and mean amplitudes of vibration, (b) an asymmetry of stretching vibrations, (c) values for equilibrium bond lengths, and (d) the precise relationship of electron diffraction bond lengths to spectroscopic bond lengths.

The isotope effects were just those expected for atoms of different mass vibrating in identical anharmonic molecular force fields. The vibrational asymmetry agreed well with that predicted by a new model for estimating cubic potential constants for molecules. The comparison between diffraction and spectroscopic bond lengths demonstrates the appreciable difference between the usual parameters reported for the two different experimental methods, but also confirms the essential equivalence of molecular information derived, if suitable corrections are applied.

ACKNOWLEDGMENTS

This research was supported in part (fellowship for K. K.) by a grant from the Petroleum Research Fund administered by the American Chemical Society. Grateful acknowledgment is hereby made to the donors of said fund. We are also greatly indebted to Professor L. O. Brockway and the University of Michigan for making available the recording microphotometer for this investigation.

[28] B. P. Stoicheff (private communication, 1960).
[29] M. A. Thomas and H. L. Welsh, Can. J. Phys. **38,** 1291 (1960).
[30] G. G. Sheppard and H. L. Welsh, J. Mol. Spectroscopy **1,** 277 (1957).
[31] V. W. Laurie and D. R. Herschbach, Abstracts 17 and 18, Meeting of the American Physical Society, Berkeley, California, December 30, 1960.
[32] T. Oka and Y. Morino, J. Mol. Spectroscopy (to be published).

Low-Resolution Analysis of the $n \rightarrow \pi^*$ (3000 A) Absorption Spectrum of *s*-Triazine†

J. S. BRINEN* AND LIONEL GOODMAN

Whitmore Chemical Laboratory, The Pennsylvania State University, University Park, Pennsylvania

(Received February 1, 1961)

The 3000-A absorption band of *s*-triazine has been examined under low resolution. The long wavelength portion of this band is assigned to the allowed $n \rightarrow \pi^*$ promotion $^1A_2'' \leftarrow {}^1A_1'$ with 0-0 band at 31 574±15 cm^{-1}. Evidence is presented for the onset of a second $n \rightarrow \pi^*$ transition at ~32 500 cm^{-1}. The observed sequence of states contradicts previous predictions based on approximate sp^2 hybridization, and indicates that in the excited states the n orbital has very little *s* character (~0.1).

INTRODUCTION

THE near-ultraviolet absorption spectrum of the 1,3,5 azine was first examined by Hirt, Halverson, and Schmitt[1] and was shown by these authors, through solvent shift, to be similar to the other 6-membered azines in that the lowest energy band at 3000 A (Fig. 1) is $n \rightarrow \pi^*$ in orbital characterization.

The spectral features of *s* triazine are strikingly different from those of the other azines.[2] The ratio of the extinction coefficients of the band onset and the band maximum is approximately 0.02 (Fig. 1). The bands in the vapor spectrum are not nearly as "sharp" as those of the other azines, and the blue region of the spectrum shows no structure at all.

The low-lying (n, π^*) states in *s*-triazine are of unusual interest because both the highest filled n and lowest vacant π^* orbitals are symmetry twofold degenerate. The sequence and spacing of the (n, π^*) states will then be governed by electron repulsion interactions in a manner analogous to the splitting of the (π, π^*) states in benzene.

The factors controlling the transition energies were discussed in a previous paper by the authors[3] (I). From group-theoretical considerations, three states are predicted: E'', A_1'', A_2'', the latter being allowed by a dipole transition from the ground state. Another E'' state arises by promoting an electron from the lowest-energy n orbital to the degenerate π^* orbitals, and is predicted to be slightly higher in energy than the aforementioned three states.

From the detailed calculations carried out in (I), it was concluded that: (1) all four states are grouped within 1 ev, hence the prediction was made that the 3000-A band contains all four transitions, (2) the lowest-energy transition is predicted to be forbidden ($E''MA_1'$) *provided the nonbonding orbitals are in sp^2 or approximately sp^2 hybridization in the excited states.*

In this paper we report the details and conclusions obtained by analyzing the 3000-A band under low-resolution absorption conditions. The conclusions of this analysis not only assign the sequence of transitions in the 3000-A band, but also yield considerable insight into the form of the nonbonding orbitals and the molecular geometry in the excited states.

EXPERIMENTAL

The solution spectra were measured in hydrocarbon solvents on a Beckman DU quartz spectrophotometer with an automatic recording accessory of Warren Electronics, Inc. For low- and high-temperature experiments, a quartz-windowed brass absorption cell of 2-cm optical path was kept at dry ice-acetone temperatures (193°K) or at 328°K (hot water) by a surrounding metal Dewar. The low-temperature spectra were obtained in methylcyclohexaneisopentane (1:4) solutions; the high-temperature spectra in cyclohexane. Room-temperature spectra, obtained in approximately $1 \times 10^{-3} M$ solutions, were measured in quartz absorption cells with optical paths of 2 cm. No special precautions were taken to obtain highly accurate molar extinction coefficients.

The vapor spectra were obtained on a modified Perkin-Elmer model 13 recording spectrophotometer using a fused silica prism and a Beckman hydrogen lamp. Single-pass operation with slits of 0.02—0.03 mm was used throughout. Wavelength calibration was carried out with a Westinghouse H-1/LB/C mercury discharge lamp immediately before and after obtaining the *s*-triazine spectra. The uncertainty in frequency is estimated as ±8 cm^{-1}. High-temperature vapor spectra (~60°C) were measured in an asbestos-insulated 10-cm quartz cell heated by Nichrome wire. A stopcock was fused to the top of the cell to prevent escape of vapor.

S-triazine was purified by vacuum sublimation. The solvents were purified by the procedures described by Potts,[4] except for the cyclohexane, which was Matheson, Coleman, and Bell spectro quality and used directly upon unsealing a fresh bottle.

† Supported by a grant from the National Science Foundation.

* This and the preceding paper (reference 3) comprise the doctoral dissertation of J. S. B., The Pennsylvania State University, February, 1961.

[1] R. C. Hirt, F. Halverson, and R. G. Schmitt, J. Chem. Phys. **22**, 1148 (1954).

[2] L. Goodman, J. Mol. Spectroscopy **6**, 109 (1961).

[3] J. S. Brinen and L. Goodman, J. Chem. Phys. **31**, 482 (1959).

[4] W. J. Potts, Jr., J. Chem. Phys. **20**, 809 (1952).

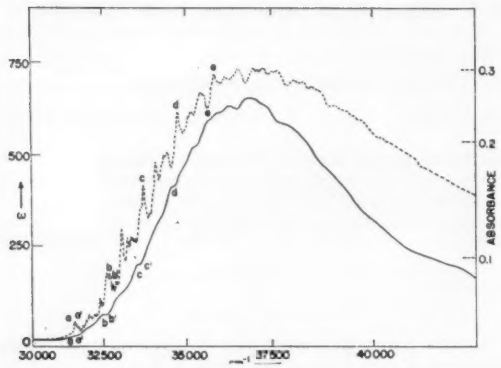

FIG. 1. Room temperature spectra of *s*-triazine:—solution;– – – vapor.

SOLUTION SPECTRUM

The solution spectrum is shown in Fig. 1 (at 300°K) and in greater detail in Fig. 2 (both at 200°K and at 300°K). The sharp vibrational peaks and fine structure of the vapor spectra (Fig. 1) are obscured in solution.

However, the principal progressions are present (depicted above), permitting a basic vibrational analysis.

The principal peaks, *a*, *b*, *c*, *d*, and *e* (Fig. 1) at 31 328, 32 436, 33 557, 34 638, and 35 714 cm^{-1} corresponding to the sharp vapor spectra are spaced 1108±50 cm^{-1} apart. This spacing agrees favorably with the totally symmetric ring-angular distortion vibration ν_{12} of 1132 cm^{-1} in the ground state, obtained from infrared and Raman data.[5-8] This and ν_{6a} are usually the most prominant vibrational modes in allowed azine $n\rightarrow\pi^*$ transitions and its prominence in the *s*-triazine absorption spectrum allows assignment of the sharp spectrum as the allowed electronic transition, $A_2''\leftarrow A_1'$. The other totally symmetric vibrations in *s*-triazine (3062 cm^{-1} CH stretch, 992 cm^{-1} ring breathing) are not prominent, consistent with their relative weakness in the $n\rightarrow\pi^*$ spectra of the other azines.[2]

The 0–0 band is assigned as the first weak peak (molar extinction coefficient ~15) at 31 328 cm^{-1}. The weakness of the 0–0 band is to be noted. The ratio ϵ_{0-0}/ϵ max in solution is unusually small (~1/50) and implies either Franck-Condon forbiddeness or the presence of other transitions in the absorption envelope, or both (*vide infra*).

The shoulders at 31 746 and 32 884 fit the series 0–*n* (1108)+0–1 (418). The 418 cm^{-1} vibration is assigned to the degenerate e'' vibration ($\nu_{16a,b}$) and has a ground state frequency of 341 cm^{-1}.[5] Another series 0–*n* (1108)+0–1 (677) fits the shoulders at 33 113, 34 247, 35 286, and 36 337 cm^{-1}, respectively. The 677-cm^{-1} frequency corresponds either to an a_2'' (ν_{11}) vibration (ground state 735 cm^{-1}) or to an e' (ν_{6a}) vibration (ground state 676 cm^{-1}). It is interesting to note that both e'' and a_2'' are nonplanar vibrations.

From the temperature variations of the solution spectra (Fig. 2), the positions of three "hot" bands a',b',c', were located at 31 407, 32 573, and 33 704 cm^{-1}, respectively. These appear just to the blue of the totally symmetric sequence, *a*,*b*,*c*. A consideration of the Boltzmann factor, which governs the population of the excited vibrational levels in the ground state, leads us to believe that the 341-cm^{-1} e'' ground state vibration is involved in the observed temperature-dependent sequence. For a vibrational energy in the vicinity of 400 cm^{-1}, the population would decrease by a factor of <3:1 in going from 300°K to 200°K (dry ice-acetone temperature), while for the same temperature change and a vibrational

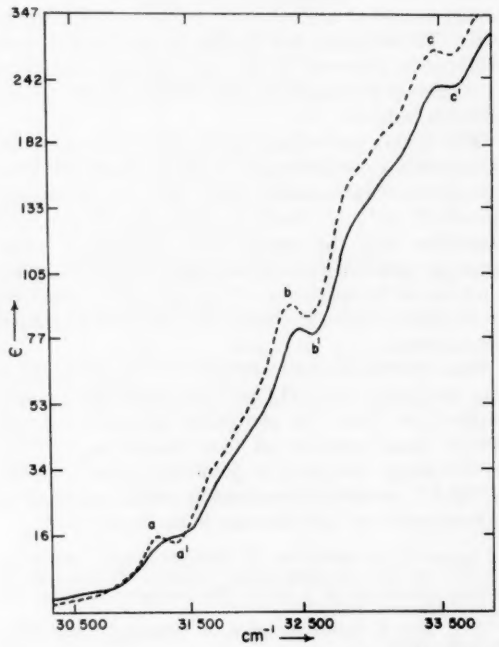

FIG. 2. Temperature dependence of the long wavelength region of the *s*-triazine solution spectrum [solvent: (1:4) methylcyclohexane-isopentane, concentration: $1.4\times10^{-3}M$]———300°K; ------200°K.

[5] J. E. Lancaster and N. B. Colthup, J. Chem. Phys. **22,** 1149 (1954).
[6] R. F. Stamm and J. E. Lancaster, J. Chem. Phys. **22,** 1280 (1954).
[7] J. Gobeau, E. L. Jahn, A. Kreutzberger, and C. Grundmann, J. Phys. Chem. **58,** 1078 (1954).
[8] S. Califano and B. Crawford, Jr., Spectrochim. Acta **16,** 900 (1960).

TABLE I. Solution data.

cm^{-1}	Band[a]	Assignment	ν_i[b]	D_{6h}	D_{3h}	ν''[c]	ν'[d]
31328	*a*	0–0					
Totally symmetric sequences (fundamentals)							
32436	*b*	1′–0	ν_{12}	b_{2u}	a_1'	1132	1106
33557	*c*	2′–0					
34638	*d*	3′–0					
35714	*e*	4′–0					
Nontotally symmetric sequences (fundamentals)							
31746	*f*	1′–0	$\nu_{16a,16b}$	e_{2u}	e''	341	418
Combination bands							
32884		(1′–0) ν_{12}+(1′–0) $\nu_{16a,b}$					
33113		(1′–0) ν_{12}+(1′–0) ν_{11} (or $\nu_{6a,b}$)	ν_{11}	a_{2u}	a_1''	735	677
33887		[(2′–0) ν_1′+(1′–0) ν_{11} (or $\nu_{6a,b}$)]	$\nu_{6a,b}$	e_{2g}	e'	676	677
34247		(2′–0) ν_{12}+(1′–0) ν_{12} (or $\nu_{6a,b}$)	ν_1	a_{1g}		992	937
34399		(2′–0) ν_{12}+(2′–0) $\nu_{16a,b}$					
35286		(3′–0) ν_{12}+(1′–0) ν_{11} (or $\nu_{6a,b}$)					
35971		[(4′–0) ν_{12}+(1′–0) $\nu_{16a,b}$]					
36337		(4′–0) ν_{12}+(1′–0) ν_{11} (or $\nu_{6a,b}$)					
Hot bands							
31407	*a*′	(1″–1′) $\nu_{16a,b}$					
32573	*b*′	(1′–0) ν_{12}+(1′–1″) $\nu_{16a,b}$					
33704	*c*′	(2′–0) ν_{12}+(1′–1″) $\nu_{16a,b}$					

[a] Letters corresponding to Figs. 1 and 2.
[b] The notation of R. C. Lord, A. L. Marston, and F. A. Miller, Spectrochim. Acta **9**, 113 (1957).
[c] Ground state vibrations from references 6–9.
[d] Excited state vibrations from this work.

energy of 700 cm^{-1} (corresponding to the e' or a_2'' vibration) the decrease in population would be >5:1.

The close proximity of the "cold" 1108-cm^{-1} sequence makes a quantitative estimation of the intensity change of the "hot" band difficult. Assuming approximate gaussian bands with half-width 150 cm^{-1} for both "cold" and "hot" bands, the intensity of the hot band is estimated to decrease by a factor ~2:1 in going from 300°K to 200°K. The decrease is certainly considerably less than 5:1, and thus favors the e'' vibration. The "hot" bands mentioned above fit the series 0–n (1108)—1–1′ (418−341), providing confirmation of the assigned value for $\nu_{16}'_{a,b}$ (418 cm^{-1}).

The assignment of the bands in the solution spectra are listed in Table I.

VAPOR SPECTRUM

The room-temperature vapor spectrum (Fig. 3) of *s*-triazine is quite complicated, and the assignment of the absorption band to one allowed transition is by no means clear-cut. The features present lead us to the conclusion that, even if more than one electronic transition is present, the lowest-energy transition is allowed.

This conclusion is based on the temperature independence of the band at 31 574±15 cm^{-1} (*a*, Figs. 3 and 4). This is the lowest energy band with appreciable intensity, and is the first band in the totally symmetric sequence (0–n)ν_{12}' (*a*, *b*, *c*, *d*, and *e*). Hence, it is assigned as the 0–0 transition. The corresponding band in solution (ϵ=14.9) is red shifted by 246 cm^{-1}.

A number of very weak bands (ϵ<1) (Fig. 4) were found to the red of the proposed 0–0 band. An attempt was made to observe the temperature dependence of these bands, but their intrinsic weakness prevented a conclusive result.

To circumstantiate the allowed assignment of the lowest-energy transition, Professor K. K. Innes very kindly examined for us the rotational structure of the bands at 3167 A (*a*) and 3119 A (*j*) with dispersions of 1.20 A/mm and 0.40 A/mm. Because of the weakness of the 3167-A band (the proposed 0–0 band), no fine structure was obtained. However, Innes observed a

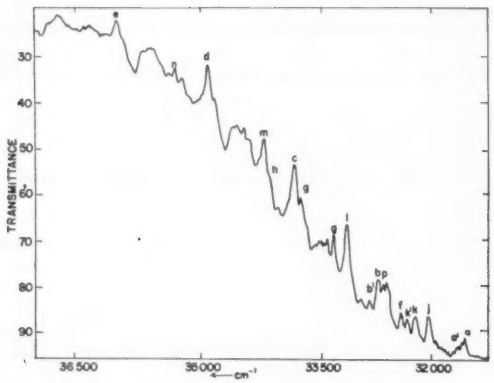

FIG. 3. Details of the long-wavelength region of the *s*-triazine vapor spectrum.

strong, sharp *Q* head, degraded toward the red. The presence of the *Q* branch is consistent with the assignment of the 3167-A band as the 0–0 transition. Both bands were observed to belong to a parallel band system; hence, the electronic transition moment is polarized perpendicular to the molecular plane, consistent with an allowed $n \rightarrow \pi$ promotion.[9]

By using this 0–0 band, two alternate possibilities allow assignment of most of the intense peaks in the vapor spectra. The ambiguity lies in assigning a numerical value to the a_1' upper-state ring-distortion vibration (1132 cm^{-1} in the ground state). From intensity considerations, the band at 32 744 cm^{-1} (*b*) is assigned as 0–1 of the a_1' ring-distortion vibration, assuming a value of ~1140 cm^{-1} for the upper-state vibration. A value of 1106 cm^{-1} for this vibration gives a better fit with the observed spectrum, but the weakness of the bands (*p*, *q*) leads us to sacrifice this fit so as to satisfy the intensity requirements.[10]

The next sharp band in the vapor spectrum is the one at 32 062 cm^{-1} (*j*). This band is 488 cm^{-1} to the blue of the proposed 0–0 band and is assigned as 0–1 of the e'' out of the plane vibration. This is the only band which showed rotational fine structure. The *Q*-head degradation toward the red indicates that one or both of the moments of inertia about the axes in the plane of the molecule is decreased during the electronic excitation and supports the view that the corresponding vibrational frequency increases in the excited state.[11]

Examination of the red region of the vapor spectrum at high temperature (~60°C) revealed a series of "hot" bands which fit the progression 0–*n* (a_1' 1132 cm^{-1} g sec)+1–1′ (341 cm^{-1} g sec) and are shown in Fig. 4 (*a*′ and *b*′). The probable assignments of the more intense bands in the vapor spectrum are tabulated in Table II. It is noted from Table II that we have assigned only roughly half of the many weak vibrational peaks; hence, the detailed analysis is far from final.

A striking feature of the vapor spectrum is the diffuseness of the bands as we go towards the blue region. This diffuseness has its onset approximately 1000 cm^{-1} to the blue of the 0–0 band (*a*) and is the probable cause for the lack of rotational structure in band (*k*). Approximately 5000 cm^{-1} to the blue of the 0–0 band (*a*) nearly all vibrational structure is blurred out. We assign the diffuse region to one or more of the other $n \rightarrow \pi^*$ transitions predicted in I (*vide infra*).

CONCLUSIONS OBTAINED FROM THE ANALYSIS

From the analysis presented in Secs. III and IV, the following conclusions may be drawn concerning the sequence and spacing of states in the 3000-A absorption band:

(1) The lowest-energy electronic transition is the sharp series allowed $^1A_2'' \leftarrow {}^1A_1'$ transition with the 0–0 band at 31 574 cm^{-1}.

(2) The onset of another electronic transition is probable at approximately 32 500 cm^{-1} (diffuse region). This transition is assigned to an intrinsically forbidden excitation made allowed vibronically, and therefore must be either $^1A_1'' \leftarrow {}^1A_1''$ or $^1E'' \leftarrow A_1'$ in symmetry.

(3) The prominent vibrations are the ring-distortion vibration, $\nu_{12}(a_1')$, and the nonplanar e'' vibrations,

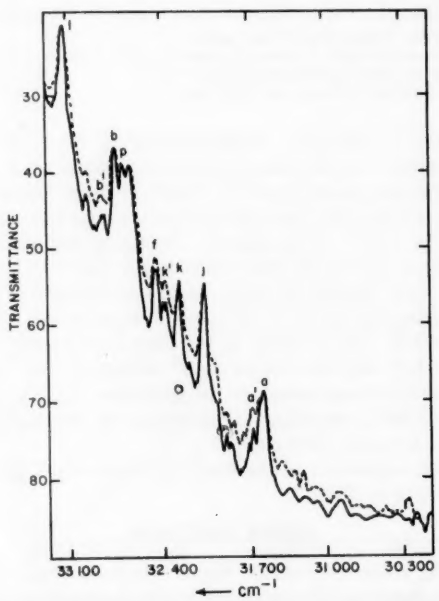

FIG. 4. Temperature dependence of the long wavelength region of the *s*-triazine vapor spectrum———300°K, – – – –~360°K.

[9] K. K. Innes, J. A. Merritt, W. C. Tincher, and S. G. Tilford, Nature **187**, 500 (1960).

[10] Use of $\nu_{12}' = 1106$ cm^{-1} allows assignment of two additional vibrational bands (32 680 and 33 778). However, the prominent bands *b* and *c* now become combination bands.)

[11] H. Sponer and E. Teller, Revs. Modern Phys. **13**, 75 (1941).

TABLE II. Vapor data.[g]

cm^{-1}	Band[a]	Strength[j]	Assignment[b]		D_{6h}	D_{2h}	ν'' [c]	ν' [d]	Δ[h]
31574	*a*	m	0–0						
31674	*a'*	w	(1′–1″) $\nu_{16a,b}$						
32062	*j*	m	1′–0	$\nu_{16a,b}$	e_{2u}	e''	341	488	−47
32258	*k*	m	1′–0	$\nu_{11}(\nu_{6a,b})$	$a_{2u}(e_{2g})$	$a_2''(e')$	735(676)	684	
32373	*k'*	w	(1′–0) $\nu_{11}(\nu_{6a,b})+(1'–1'')\ \nu_{16a,b}$						−25
32436[e]		w	1′–0	ν_1	a_{1g}	a_1'	992	862	
32632		m							
32680		w							
32744	*b*	s	1′–0	ν_{12}	b_{2u}	a_1'	1132	1140[f]	−30
32852	*b'*	w	(1′–0) $\nu_{12}+(1'–1'')\ \nu_{16a,b}$						−2
32976		w							
33162	*l*	s	(1′–0) $\nu_{12}+(1'–0)\ \nu_{16a,b}$						+40
33317	*g*	m	2′–0	ν_1	a_{1g}	a_1'			−19
33428		w							
33529		w							
33704		w							
33778		m							
33847	*c*	s	2′–0	ν_{12}	b_{2u}	a_1'			−7
33933		w							
34048		w							
34066		w							
34165	*h*	w	3′–0	ν_1	a_{1g}	a_1'			−5
34241	*m*	s	(2′–0) $\nu_{12}+(1'–0)\ \nu_{16a,b}$						+101
34412		w							
34459		w							
34544		w							
34620		w							
34825		m							
34910	*d*	s	3′–0	ν_{12}	b_{2u}	a_1'			+84
35050		w							
35249		w							
35305	*n*	w	(3′–0) $\nu_{12}+(1'–0)\ \nu_{16a,b}$						+177
35556		w							
35657		w							
35689		w							
35958	*e*	s	4′–0	ν_{12}	b_{2u}	a_1'			+180
36271		w							
36657		w							
37050		w							

[a] Letters corresponding to Figs. 1, 3, and 4.
[b] Notation of Lord, Marston, and Miller (see reference b, Table I).
[c] Ground state vibrations. See references 4–7.
[d] Excited state vibrations.
[e] Appears to be hot. This may be due to the effects of nearby hot bands.
[f] For discussion of ν_{12} assignment see text.
[g] R. C. Hirt and R. G. Schmitt (private communication) have obtained additional bands under higher resolution.
[h] $\Delta=\nu_{theor}-\nu_{exp}$
[j] s=strong, m=medium, w=weak

$\nu_{16a,b}$, depicted below. The presence of the e'' vibrations may mean a nonplanar excited state.

The presence of nonplanar vibrations together with the weak 0–0 band, but considerable oscillator strength for the entire band envelope, suggests that the geometry of the $^1A_2''$ excited state of *s*-triazine is changed from that of the ground state.

INTENSITIES

The oscillator strength of the 3000-A band (cyclohexane solution) has been measured by Mason[12] and is sizeable (0.021). We obtain from the isopentane solution spectra an oscillator strength of 0.018 in reasonable agreement with Mason's measurement.

The electronic factors which contribute to azine $n\rightarrow\pi^*$ transition intensities have been discussed by Goodman[2] in his recent review paper. In *s*-triazine the excited states are described to a good approximation, as discussed in I, by 2-configuration wave functions. The *A* states arise from conjugate pairs of the configurations $n_1\pi_2$ and $n_1\pi_2$ (where the closed-shell part has been dropped for brevity). The transition moment integrals $\mathbf{Q}_{ij}=\int n\ \mathbf{r}e\pi_j d\delta$ associated with the above configurations are computed to be sizeable: $Q_{12}=Q_{\bar{1}2}=0.121$ A using Slater orbitals.[2] The appreciable intensity of the allowed transition $A_2''\leftarrow A_1'$ is accounted for by the two configurational transition moments being in phase, whereas for the forbidden transition ($A_1''\leftarrow A_1'$) the transition moments are out of phase. The theoretical oscillator strength for the allowed transition is thus calculated to be appreciable, 0.014, but considerably less than the observed value.

The transition-moment integrals involving configurations making up the E'' states ($n_1\pi_2$, $n_1\pi_{\bar{2}}$, $n_0\pi_2$, and $n_0\pi_{\bar{2}}$) are small and exactly zero for D_{3h} symmetry consistant with $E''\nleftarrow A_1'$.

For a small perturbation of the excited state geometries away from D_{3h} symmetry, the exact cancellation of the two out-of-phase A_1'' transition moments is destroyed and the $A_1''\leftarrow A_1'$ transition is predicted to increase to significant magnitudes. No such mechanism exists for the E'' states. Their intensities are governed by the in-phase (lower-energy state for the case where the C.I. integral is <0) and out-of-phase (higher-energy state for C.I. integral <0) combination of small transition moments and these can only become appreciable for large distortions. Further discussion of the forbidden transition intensities would require consideration of borrowing effects such as those given by Pople and Sidman[13] and Albrecht[14] for other cases.

DISCUSSION

The predicted sequence of states obtained from our previous calculations (I) ($E''<A_2''$) is contradicted by the conclusions of this anlaysis. In order to dissect this contradiction, we have extended the calculations described in I to include higher-order configurational interaction.

The additional singly excited configurations of appropriate symmetry arise from promoting an *n* electron to π_3, the highest-energy π orbital. These are an A_2'' state ($n_0\rightarrow\pi_3$), and an E'' state ($n_{1,\bar{1}}\rightarrow\pi_3$). The additional stabilized than the E'' state (by $\sim$0.02 ev). Other configurations of appropriate symmetry are the doubly excited configurations involving simultaneous $\pi\rightarrow\pi^*$ and $n\rightarrow n^*$ excitation. Since these configurations are approximately 5–7 ev above the low-lying ones, and since these configurations include all the $n\rightarrow\pi^*$ symmetries, there is no reason to expect that higher-order C.I. can reverse the sequence of the low-lying states predicted in I.

The observed sequence of states may be taken as important evidence for major *n*-orbital rehybridization in *s*-triazine upon $n\rightarrow\pi$ excitation. This conclusion is consistent with the suggestion,[2] based on observed singlet-triplet intervals, that all azine $n\rightarrow\pi^*$ excited states have *n* orbital *s* characters in the vicinity of 0.1. Identical *n*-orbital hybridizations for all four low-lying states in *s*-triazine seems especially reasonable since the excited state charge distributions are very nearly identical.[3] The $n\rightarrow\pi^*$ C.I. integrals are quite sensitive to *n*-orbital hybridization, as shown in I (Fig. 4). For an excited state *n* orbital *s* character of $\sim$0.1 (all states) the A_2'' and the E'' states cross [including the effects of the higher lying $-(n,\pi^*)$ configurations], the A_1'' state becoming very slightly lower in energy.[15]

On using an *s* character of 0.10, the predicted S–T split is $\sim$0.5 ev. The lowest triplet level in *s*-triazine is predicted to be (n,π^*), both the $^3A_2''$ and $^3E''$ states being nearly degenerate and $\sim$0.2 ev below the lowest $\pi\rightarrow\pi^*$ triplet.[16] The 0–0 band of the S–T transition is calculated to be $\sim$27 500 cm^{-1}, in agreement with the onset of the T–S emission of *s*-triazine, observed by Paris, Hirt, and Schmitt,[17] of $\sim$26 500 cm^{-1}.

The very noticeable broadness of the vapor-spectrum bands as we go towards the blue region is consistent with the presence of a degenerate state. Jahn-Teller

[12] S. F. Mason, J. Chem. Soc. **1959**, 1240.

[13] J. A. Pople and J. W. Sidman, J. Chem. Phys. **27**, 1270 (1957).

[14] A. C. Albrecht, J. Chem. Phys. **33**, 156 (1960).

[15] The spacing is too small for unambiguity. An important facet is that the splitting of n_0 and $n_{1,\bar{1}}$ becomes important for small *s* characters.

[16] N. Mataga and K. Nishimoto, Z. physik Chem. **13**, 140 (1957).

[17] J. P. Paris, R. C. Hirt, and R. G. Schmitt, J. Chem. Phys. **34**, 1851 (1961).

splitting[18] of the E'' state during a nontotally symmetric vibration might cause diffuseness due to lack of time for quantization of the E'' state. This view would assign the diffuse region to the $E''\leftarrow A_1'$ transitions made allowed by the Jahn-Teller distortion.

The lack of sharpness in the spectra of pyrazine (although not nearly as diffuse as in *s*-triazine) may also be due to the Jahn-Teller effect. There are two nearly degenerate states, $^1B_{1u}$ and $^1B_{3g}$, whose near degeneracy may be removed by vibrational perturbation. Pyridazine, whose rotational structure is very sharp, lacks the presence of an $(n\pi^*)$ degeneracy, either symmetry generated or accidental.

At the present time, this view must be regarded as speculative, however, inasmuch as dissociative processes would also be consistent with the diffuse spectra. The dissociative mechanism would explain the blurring of both the vibrational and rotational bands as well as the weakness of the phosphorescence intensity. The emission intensity is proportional to the triplet-level population, which would be lowered as a result of a predissociative process, despite the relatively high extinction coefficient of the singlet-singlet absorption band maximum.

[18] H. A. Jahn and E. Teller, Proc. Roy. Soc. (London) **A161**, 220 (1937).

ACKNOWLEDGMENTS

The authors express their thanks to Professor K. K. Innes for obtaining the rotational spectra and for his critical interest, and to V. G. Krishna for numerous discussions and suggestions. They gratefully acknowledge generous gifts of *s*-triazine from Dr. R. C. Hirt and Dr. C. Grundmann.

THE JOURNAL OF CHEMICAL PHYSICS VOLUME 35, NUMBER 4 OCTOBER, 1961

Mechanism of the Mercury Photosensitized Decomposition of *n*-Butane

R. J. CVETANOVIĆ, W. E. FALCONER,* AND K. R. JENNINGS†
Division of Applied Chemistry, National Research Council, Ottawa 2, Canada
(Received March 30, 1961)

The results of further studies of the mercury photosensitized reactions at room temperature of *n*-butane and of its mixtures with nitrous oxide are reported. The importance of a self-scavenging process responsible for low quantum yields of hydrogen at finite conversions has been demonstrated by carrying out experiments at low conversions closely approaching initial conditions. The initial quantum yield of hydrogen has been determined relative to that of nitrogen from the mercury photosensitized decomposition of nitrous oxide. The mechanism of the self-scavenging process is discussed.

INTRODUCTION

THE two objectives of the present work have been (1) to obtain further information on the initial steps in the mercury photosensitized decomposition of *n*-butane and (2) to utilize this reaction to study the relative rates of reactions of hydrogen atoms. The latter will be reported in a separate publication[1] (referred to in the following as Part III). The former is a continuation of a recent work (referred to in the following as Part I) by one of the authors dealing primarily with a technique for determination of relative quenching cross sections in such processes.[2]

The quantum yield of nitrogen (ϕ_{N_2}) formed in mercury photosensitized decomposition of nitrous oxide in its mixtures with hydrocarbons (RH), or with other compounds which readily consume oxygen atoms, is well represented over an extensive experimental range by the empirical expression

$$1/\phi_{N_2}=\alpha[1+\beta(RH)/(N_2O)], \qquad (1)$$

where α and β are constant at not too low total pressure and at constant light intensity and partial pressure of mercury vapor.

Under such conditions, the following competing reactions have to be considered:

(1) $\mathrm{Hg}+h\nu\rightarrow\mathrm{Hg}^*$

(2) $\mathrm{Hg}^*+RH\rightarrow\mathrm{Hg}+R+\mathrm{H}$

(2′) $\mathrm{Hg}^*+RH\rightarrow\mathrm{Hg}'+RH$

(10) $\mathrm{Hg}^*+N_2O\rightarrow\mathrm{Hg}+N_2+O$

(10′) $\mathrm{Hg}^*+N_2O\rightarrow\mathrm{Hg}'+N_2O$

and

(f_1) $\mathrm{Hg}'+N_2O\rightarrow\mathrm{Hg}+N_2+O$

(f_2) $\mathrm{Hg}'+RH\rightarrow\mathrm{Hg}+R+\mathrm{H}$

(g_1) $\mathrm{Hg}'+N_2O$, (g_2) $\mathrm{Hg}'+RH$ $\rightarrow$ deactivation of Hg′ followed by dissipation of energy.

* National Research Council Summer Student 1958. Present address: University of Louvain, Louvain, Belgium.

† National Research Council Postdoctorate Fellow 1958–1960. Present address: Department of Chemistry, The University, Sheffield 10, England.

[1] K. R. Jennings and R. J. Cvetanović (to be published).

[2] R. J. Cvetanović, J. Chem. Phys. **23**, 1208 (1955).

Here Hg stands for Hg6($^1S_0$), Hg* for Hg6($^3P_1$), and Hg′ for Hg6($^3P_0$).

In as much as it is assumed that quenching to the metastable state Hg′ does not occur ($k_{10'}=k_{2'}=0$), the steady-state treatment leads to the simple expression

$$\frac{1}{\phi_{N_2}}=1+\frac{k_2}{k_{10}}\frac{(RH)}{(N_2O)}, \tag{2a}$$

i.e., in Eq. (1) $\alpha=1$ and $\beta=k_2/k_{10}$. In the more general case when reactions (10′) and (2′) are assumed to occur, the simple expression (2a) is again obtained provided $k_{g1}=k_{g2}=0$ and $k_{f2}/k_{f1}=k_2/k_{10}$. This case is, therefore, formally equivalent to the case when no quenching to the metastable state occurs. On the other hand, if "physical quenching" reactions (g_1) and (g_2) do occur (while $k_{f1}=0$), then the following somewhat more complex expression is obtained:

$$\frac{1}{\phi_{N_2}}=\frac{k_{10}+k_{10'}}{k_{10}}\left[1+\frac{k_2+k_{2'}}{k_{10}+k_{10'}}\frac{(RH)}{(N_2O)}\right]. \tag{2b}$$

In this case, therefore, $\beta=(k_2+k_2')/(k_{10}+k_{10'})$ and $\alpha=(k_{10}+k_{10'})/k_{10}$, i.e., here α is greater than unity.

In all these cases the constant β in Eq. (1) is identified with the ratio of the *over-all* quenching efficiencies, i.e., it includes quenching both to the ground state and to the metastable state of mercury, in as much as the latter occurs. β is therefore equivalent to the ratio of the over-all quenching efficiencies which may be inferred from measurements by standard physical methods. Application of Eq. (1) provides, therefore, a simple technique for determination of over-all quenching cross sections from chemical measurements and has been utilized for that purpose.[2–4]

In principle it is possible to establish, from the value of the intercept α, whether quenching to the metastable state of mercury occurs. Thus, from plots of Eq. (2b), the experimental value for $k_{10}/(k_{10}+k_{10'})$ is close to 0.8 suggesting about 20% quenching to the metastable state. However, this conclusion depends on the accuracy of the actinometric determinations of the amounts of light absorbed and is therefore rather unreliable.

Paraffins are frequently known to decompose in the mercury photosensitized reactions with quantum efficiencies well below unity. In view of this, *n*-butane and in particular its mixtures with nitrous oxide were investigated in some detail, as reported in Part I. The amount of hydrogen formed is a convenient measure of the extent of decomposition, and it was found that for n-C_4H_{10}/N_2O mixtures the following two relations hold:

$$1/\phi_{H_2}=\gamma[1+\delta(N_2O)/(n\text{-}C_4H_{10})] \tag{3}$$

and

$$R_{H_2}/R_{N_2}=\eta(n\text{-}C_4H_{10})/(N_2O), \tag{4}$$

both apparently independent of reaction temperature and the latter independent of mercury vapor concentration as well.

Since Eq. (3) is of the same form as Eq. (1), it was thought that δ might be equal to $1/\beta$. This was found to be the case. The value of $1/\gamma$ however was found to be 0.57 instead of unity, indicating, as anticipated, low quantum efficiency of hydrogen production, although subject again to the uncertainties of actinometric determinations. On the other hand, entirely independently of the actinometric accuracy, $1/\gamma$ was found to be considerably smaller than $1/\alpha$, both determined from the same experiments, i.e., with the same amounts of light absorbed. This meant that the primary quantum yield of hydrogen from *n*-butane was smaller than that of nitrogen from nitrous oxide. In fact, it was found that $\phi_{H_2}/\phi_{N_2}=0.72$ and this fraction represented an upper limit for ϕ_{H_2}. In agreement with this, the slope η from the plot of Eq. (4) was about 0.18 instead of 0.255, the value obtained for β.

At relatively high paraffin pressures, as used in these experiments, two possible causes of the low quantum yields of hydrogen have been variously considered[5,6]: (1) dissipation of energy by some kind of "physical quenching," and (2) partial self-scavenging of hydrogen atoms by the olefins formed in the process, involving in the case of *n*-butane the reactions

$$Hg^*+n\text{-}C_4H_{10}\rightarrow H+C_4H_9+Hg \tag{2}$$

$$H+n\text{-}C_4H_{10}\rightarrow H_2+C_4H_9 \tag{3}$$

$$C_4H_9+C_4H_9\rightarrow C_8H_{18} \tag{4}$$

$$C_4H_9+C_4H_9\rightarrow C_4H_8+C_4H_{10} \tag{5}$$

$$H+C_4H_8\rightarrow C_4H_9 \tag{6}$$

$$H+C_4H_8\rightarrow H_2+C_4H_7 \tag{7}$$

$$C_4H_9+C_4H_7\rightarrow C_8H_{16} \tag{8}$$

Scavenging of hydrogen atoms by reaction (6) can be of importance if $k_6\gg k_3$ and the ratio k_5/k_4 is not too small. At the time when the work reported in Part I was completed, the extent of disproportionation of butyl radicals was uncertain to the extent that it might have been assumed to be small by analogy with ethyl radicals. Also, the ratio k_6/k_3 would be expected to be most probably temperature dependent and the buildup of C_4H_8 to be time dependent. However, in contrast with this, the constants in Eqs. (3) and (4) were found experimentally to be temperature independent and a time independent rate of hydrogen production from *n*-butane had been reported in the literature.[7] In view of this, physical quenching ap-

[3] R. J. Cvetanović and L. C. Doyle, Can. J. Chem. **35**, 605 (1957).

[4] F. P. Fehlner and R. L. Strong, J. Phys. Chem. **64**, 1522 (1960).

[5] B. de B. Darwent and E. W. R. Steacie, Can. J. Research **B27**, 181 (1949); B. de B. Darwent, J. Chem. Phys. **18**, 1532 (1950); H. E. Gunning and E. W. R. Steacie, J. Chem. Phys. **14**, 544 (1946).

[6] P. W. Beck, D. V. Kniebes, and H. E. Gunning, J. Chem. Phys. **22**, 672 (1954).

[7] S. Bywater and E. W. R. Steacie, J. Chem. Phys. **19**, 172, 319 (1951).

peared to be the more readily acceptable explanation of the low yield of hydrogen and a mechanism involving quenching to the metastable state of mercury was therefore proposed in Part I. However, the study of the process was immediately continued, and a substantial increase in the rate of hydrogen production was found at lower conversions making the above explanation untenable and suggesting instead that self-scavenging played an important role.[8] At about the same time, R. A. Back had arrived independently at the same conclusion for the mercury photosensitized reaction of *n*-pentane[9]) and more recently of propane and ethane.[10]

The present paper reports the results of further studies of the mercury photosensitized reactions of *n*-butane and of its mixtures with nitrous oxide. The

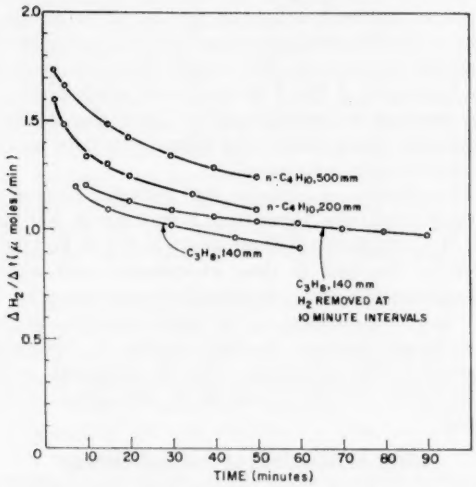

FIG. 1. Dependence of the integral rates of hydrogen formation on irradiation time (25±2°C. Reactor *A*. Full light intensity–approximately 2×10^{16} quanta/sec.)

occurrence of the self-scavenging reaction (6) appears to be well substantiated, and the assumption made in Part I that physical quenching occurs may now be eliminated, at least to a large extent and perhaps entirely. These results of course do not affect in any way the applicability of the technique outlined in Part I for determination of relative over-all quenching cross sections from the quantum yields of nitrogen. However, the attempt to separate the over-all quenching in the case of *n*-butane into quenching to the ground and to the metastable state of mercury is no longer valid.

EXPERIMENTAL

Two reaction systems were used: (*A*) A conventional static system of a total volume of 229 ml, with a

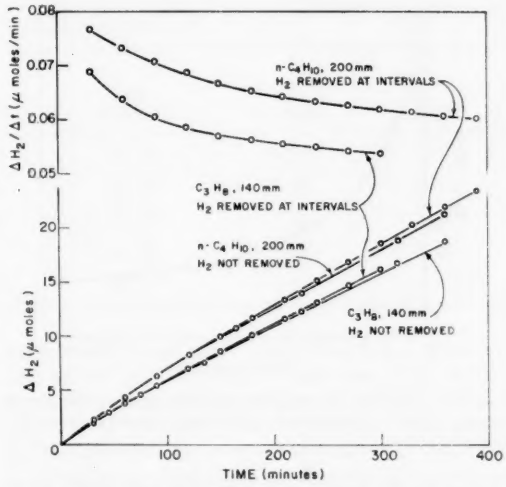

FIG. 2. Effect of irradiation time on hydrogen formation at reduced light intensity. Lower part of the figure gives the total amounts and upper part the integral rates of formation of hydrogen. (25±2°C. Reactor *A*. Light intensity approximately 1/20 of the full light intensity used for experiments in Fig. 1.)

cylindrical quartz reaction cell 5 cm in diameter and 10 cm long and provided with means for circulating the reactants prior to irradiation to ensure their complete mixing. This reaction system was essentially the same as described in Part I. (*B*) A circulating system of a total volume of 8.3 l into which the same quartz reaction cell as in *A* was incorporated and an all glass plunger-type circulating pump[11] with which the re-

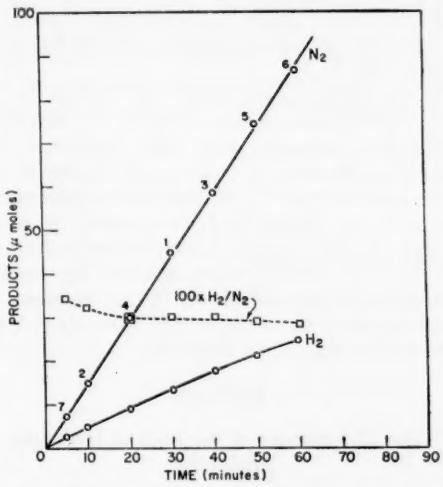

FIG. 3. Time dependence of N_2 and H_2 formation in a mixture of 100 mm N_2O and 200 mm *n*-C_4H_{10}. (25±2°C. Reactor *A* at full light intensity. The numbers on the N_2 plot give the order in which the experiments were performed.)

[8] R. J. Cvetanović, reported, in part, at the 1958 annual meeting of the Royal Society of Canada at Edmonton, Alberta.
[9] R. A. Back, Trans. Faraday Soc. **54,** 512 (1958).
[10] R. A. Back, Can. J. Chem. **37,** 1834 (1959).
[11] J. S. Watson, Can. J. Tech. **34,** 373 (1956).

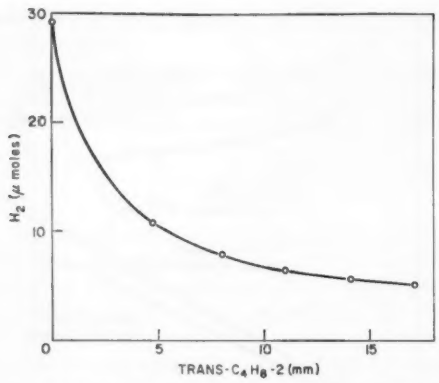

FIG. 4. The effect of *trans*-2-butene additions to 500 mm *n*-butane. (25±2°C. Reactor *A* at full light intensity. Irradiation time 20 min.)

actants in the quartz cell were renewed every 12–15 sec. Reactor *B* was used in order to approach closely the initial reaction conditions and yet produce enough product for quantitative analysis. With the large volume and the fast circulation employed the conversion of the butane was kept in this case down to 10^{-2}%. Reactor *B* and the procedure used with it are described more fully in Part III.

Mercury resonance radiation was supplied by two low-pressure mercury lamps placed one at each end of the quartz cell, at a distance of about 15 cm from the cell windows. The analysis system incorporated a LeRoy still,[12] a Toepler pump, a constant volume burette, and a copper oxide tube maintained at about 240°C for determination of carbon monoxide and of hydrogen when other noncondensable gases were present. The method of analysis is described in greater detail in Part I.

All the hydrocarbons used were Phillips research grade products and nitrous oxide was supplied by the Matheson Company, Ltd. The reactants were thoroughly degassed and bulb-to-bulb distilled *in vacuo* in the usual manner. In all experiments performed in reactor *B*, the butane used was purified by passage through two wash bottles of concentrated sulfuric acid and then over KOH pellets, followed by thorough degassing and bulb-to-bulb distillation *in vacuo*. The butene impurity was thus reduced from about 1 part in 2000 to less than 1 part in 20 000.

RESULTS

Time Dependence of the Rate of Hydrogen Production

Time dependence of the rates of hydrogen production has been studied in reactor *A*. Typical results obtained with 500 mm and 200 mm of *n*-butane, respectively, with full light intensity (approximately 2×10^{16} quanta/sec) are shown in Fig. 1. For comparison, a similar plot is given for experiments at various irradiation times of 140 mm of propane and also for a continuous experiment with 140 mm of propane in which hydrogen was removed at 10-min intervals and measured. The latter procedure was used to prevent competitive quenching by the accumulated hydrogen and the consequent decrease in the rate. In all cases integral rates are plotted.

In the experiments presented in Fig. 1, the light intensity was relatively high; and already at short exposure times, appreciable amounts of products were formed. Figure 2 shows the results of some experiments in which the light intensity was reduced (using neutral density filters) by a factor of 20. Experiments were performed with 200 mm of *n*-butane and 140 mm of propane, both with individual runs at various exposure times and with continuous runs in which hydrogen was removed at intervals. The integral rates are given in the upper part of Fig. 2 for the runs in which hydrogen was removed at intervals and it is seen that at short irradiation times these rates decrease rapidly as the irradiation time is increased.

The amounts of nitrogen and hydrogen formed at various irradiation times from a mixture of 200 mm n-C_4H_{10} and 100 mm N_2O are shown in Fig. 3. Full light intensity was used in these experiments; and within the experimental error, the rate of nitrogen formation is seen to be independent of the irradiation time in the investigated interval. A slight decline in hydrogen production with irradiation time is indicated, as is evident from the plot of the H_2/N_2 ratio given in the figure.

Effect of Additions of *trans*-2-Butene

Very small amounts of *trans*-2-butene added to 500 mm of *n*-butane strongly inhibit hydrogen production, as shown in Fig. 4. These experiments were carried out at constant irradiation time of 20 min and at full light intensity. Strong inhibiting effects are equally well observed by adding small amounts of ethylene or other olefins instead of *trans*-2-butene.

Experiments at Very Low Conversions

These experiments have been carried out in reactor *B* and with *n*-butane pretreated with concentrated sulphuric acid to remove the greatest part of olefin

TABLE I. Time dependence of H_2 formation in reactor *B*.

Run	n-C_4H_{10} (mm)	t°C	Irradiation time (min)	H_2 (μ moles)	$\Delta H_2/\Delta t$
4	301	24.5	10	18.8	1.88
2	299	25.8	20	37.0	1.85
3	302	24.9	20	37.5	1.87
5	300	23.6	30	55.6	1.85

[12] D. J. LeRoy, Can. J. Research, **B28,** 492 (1950).

TABLE II. Production of nitrogen and hydrogen in the mercury photosensitized reaction of mixtures of N_2O and n-C_4H_{10} at very low conversions. (Reactor *B*, 25±2°C, irradiation time 20 min.)

Run	N_2O (mm)	n-C_4H_{10} (mm)	$\frac{N_2O}{n\text{-}C_4H_{10}}$	ΔN_2 (μ moles)	ΔH_2 (μ moles)	H_2/N_2
A9	152.9	368.4	0.415	24.11	13.83	0.573
A4	184.6	351.4	0.527	26.58	11.78	0.443
A7	244.6	275.1	0.889	30.14	8.39	0.278
A3	286.5	231.5	1.24	32.48	6.59	0.203
A6	465.2	103.7	4.49	37.25	1.97	0.0530

impurity. That the initial conditions are closely approached in these experiments can be seen from Table I which shows little or no time dependence of the rate of hydrogen formation up to 30-min irradiation. In view of this, it was thought worthwhile to attempt to establish the quantum yield of hydrogen formation under these conditions. A value of 0.955 was obtained for the ratio of the yield of hydrogen from 300 mm n-C_4H_{10} to the yield of nitrogen from 500 mm N_2O containing 1% butene-1 (as oxygen atom scavenger), both irradiated for 20 min. After correcting the yield of N_2 from N_2O for the small amount of quenching by butene-1,[13] it is found that approximately $\phi_{H_2}/\phi_{N_2}=0.94$.

A more direct comparison of the ratio of the quantum yields is obtained from simultaneous reaction of mixtures of n-C_4H_{10} and N_2O. The data obtained in such a series of experiments are given in Table II. The ratio of the limiting values for R_{H_2} and R_{N_2} obtained by extrapolating the rate data to the pure n-C_4H_{10} and N_2O, respectively, is not much different from unity, although there is necessarily some uncertainty in such extrapolations. A plot of $1/R_{N_2}$ in accordance with Eq. (1) is given in Fig. 5 and the value of β is found to be 0.258, which is in excellent agreement with the value of 0.255 obtained in Part I. A plot of R_{H_2}/R_{N_2} in accordance with Eq. (4) is given in Fig. 6 with $\eta=0.241$, which represents a large increase from 0.18 obtained in Part I. The ratio η/β should be equal to ϕ_{H_2}/ϕ_{N_2} and this is, in the present case, again close to the value obtained for this ratio above. In assessing these results, however, it should be remembered that the values for hydrogen, analytically determined in these experiments by difference, are not as reliable as those for nitrogen. Thus, a plot of $1/R_{H_2}$ in accordance with Eq. (3) should give a value for δ such that $1/\delta=\beta$. A line satisfying this relation can be drawn reasonably well through the points, as shown in Fig. 7, although in view of the uncertainties in the slope and intercept of the plot it can only be said that such a relation would not be inconsistent with the experimental data.

The effect of pressure on the yield of hydrogen in experiments in reactor *B* is shown in Fig. 8 (curve I). The values are expressed as quantum yields relative to the quantum yield of nitrogen from N_2O taken as unity. Data obtained previously in Part I are plotted on the same scale for comparison (curve II). The much increased yield of hydrogen at the very low conversions used in the present work is evident, at first increasing with pressure but then levelling off and approaching that of nitrogen from N_2O at pressures higher than about 300 mm. In particular, there is no evidence in either of the two cases of a *decline* in the yield at higher pressures as commonly observed with olefins.

DISCUSSION

The results of the present work show that self-scavenging, as described by reactions (1)–(8) inclusive, is an important feature of the mercury photosensitized decomposition of *n*-butane. The "physical quenching" mechanism involving Hg $6(^3P_0)$ atoms postulated in Part I is not consistent with a time dependent rate of hydrogen formation and its pronounced increase at very low conversions. However, the system is kinetically complex and, in the following, it is proposed to test only the plausibility of the postulated reaction mechanism rather than attempt to relate quantitatively the

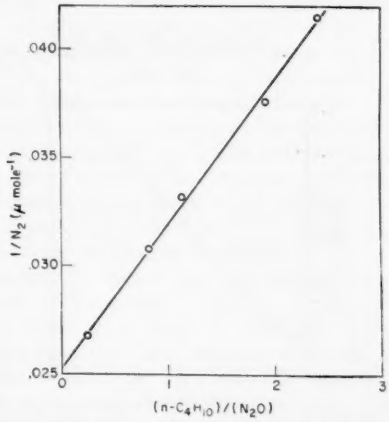

FIG. 5. Plot of the reciprocal rates of formation of nitrogen against $(n\text{-}C_4H_{10})/(N_2O)$ ratios. (Data taken from Table II.)

[13] Assumed to be twice as efficient as N_2O, as found for ethylene in Part I.

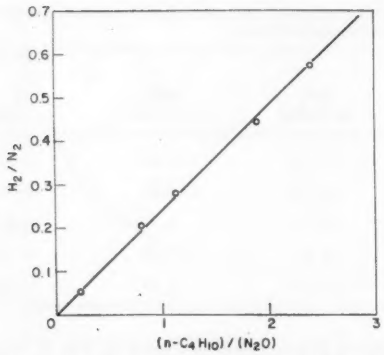

FIG. 6. Plot of R_{H_2}/R_{N_2} against $(n\text{-}C_4H_{10})/(N_2O)$ ratios. (Data taken from Table II.)

values of various rate constants. For this purpose some other reactions, such as

$$C_4H_9+C_4H_8\rightarrow C_8H_{17} \qquad (9)$$

and disproportionation of C_4H_9 and C_4H_7 radicals as well as mutual interaction of C_4H_7 radicals, are neglected as unimportant under the conditions employed in this work.

Writing RH for n-C_4H_{10}, Ol for C_4H_8 and ϕIa for the rate of reaction (2) it can be shown that

$$\frac{d(H_2)}{dt}=\phi\text{Ia}\frac{k_3(RH)+k_7(\text{Ol})}{k_3(RH)+(k_6+k_7)(\text{Ol})}. \qquad (5)$$

Equation (5) was integrated graphically by Back who thus obtained approximate values of the ratios of some of the rate constants in the case of n-pentane[9] and ethane and propane.[10] In the present work, it has been preferred to integrate this equation directly, although this leads to rather complex expressions. The following two equations can be derived:

$$(\text{Ol})=(\text{Ol})i+\frac{1+(k_5/k_4)+(k_7/k_6)[1+(2k_5/k_4)]}{1+k_5/k_4}(H_2)$$
$$-\frac{1+(k_7/k_6)[1+(2k_5/k_4)]}{1+k_5/k_4}(H_2^*) \qquad (6)$$

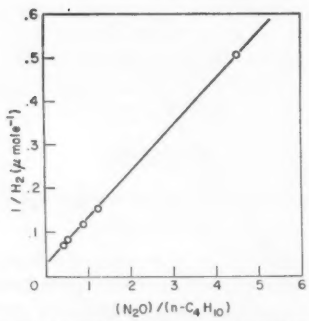

FIG. 7. Plot of the reciprocal rates of formation of hydrogen against $(N_2O)/(n\text{-}C_4H_{10})$ ratios. (Data taken from Table II. The straight line is drawn so as to satisfy the relation $1/\delta=\beta$.)

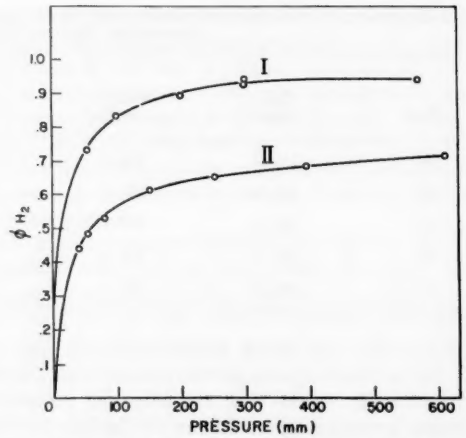

FIG. 8. The effect of pressure on quantum yields of hydrogen. (I) Obtained at very low conversions in present work (Reactor B; 25±2°C; irradiation time 20 min.) (II) Obtained at normal conversions (taken from Part I). ϕ_{H_2} is expressed relative to ϕ_{N_2} from nitrous oxide taken as unity.

and

$$f=\frac{1-\exp[-a(H_2')]}{a(H_2')}$$
$$=\frac{1+(k_4/k_5)+[k_7/(k_6+k_7)]}{1-\{1+(k_4/k_5)+[k_7/(k_6+k_7)]\}a(\text{Ol}i)}$$
$$\times\left(1-\frac{1+(k_7/k_6)(k_5/k_4)}{1+k_5/k_4}\frac{(H_2^*)}{(H_2')}\right), \qquad (7)$$

where (H_2^*) is the theoretical amount of H_2 which would be produced in the absence of any olefin im-

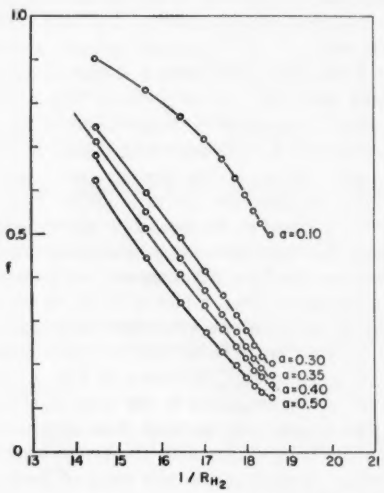

FIG. 9. Plot in accordance with Eq. (7) of the data presented in Fig. 2 for 200 mm of n-C_4H_{10} at reduced light intensity and with H_2 removed at intervals.

purity if loss of H atoms in reactions (6) and (7) did not occur $[(H_2^*)=\phi Ia\times t]$, (Oli) is the initial concentration of the olefin, and (H_2') and a stand, respectively, for

$$(H_2')=(H_2)+\frac{k_7}{k_6}\left[\frac{1+2k_5/k_4}{1+k_5/k_4}(H_2)-(H_2^*)\right] \quad (8)$$

and

$$a=\left(\frac{k_4}{k_5}+\frac{k_7}{k_6+k_7}\right)\left(\frac{k_6+k_7}{k_3}\right)\Big/\left(1+\frac{k_4}{k_5}+\frac{k_7}{k_6+k_7}\right)(RH). \quad (9)$$

Since, as shown in Part III, k_7 amounts only to a few percent of k_6, and k_5/k_4 is probably about unity, the difference between (H_2) and (H_2') is normally negligibly small. In view of this, there should be a value of a such that a plot of f against $1/(H_2)$ is linear. That this appears to be the case is shown in Fig. 9 for *n*-butane and in Fig. 10 for propane. The rate data from the upper part of Fig. 2 have been plotted in the two cases. There is evidently some latitude in the choice of the exact values of a corresponding to linear plots, but if the values of 0.11 and 0.35, respectively, are taken and assuming approximately $k_7/(k_6+k_7)=0.1$, it is found from intercepts that k_5/k_4 is 1.07 for *n*-butane and 0.54 for propane. For $(k_6+k_7)/k_3$, one then obtains 533 for *n*-butane and 920 for propane.

The values of the constants obtained from the plots in Figs. 9 and 10 appear to be of correct order of magnitude. A value of 445 has been found in Part III for k_6/k_3 for *trans*-2-butene and *n*-butane. The former is the olefin likely to be formed in greatest amount in the disproportionation reaction (5). The value of 920 for $(k_6+k_7)/k_3$ in the case of propane can be compared with a value of about 860 which can be inferred from a plot of the graphically integrated results obtained by Back with 300 mm of propane alone.[10] Recent estimates[14] of the k_5/k_4 values for *sec*-C_4H_9 radicals are 0.94 and 1.5 and for *iso*-C_3H_7 radicals 0.5 and 0.65. In the case of propane, Back finds for k_5/k_4 a value of 0.54 at 600 mm and 0.80 at 300 mm.

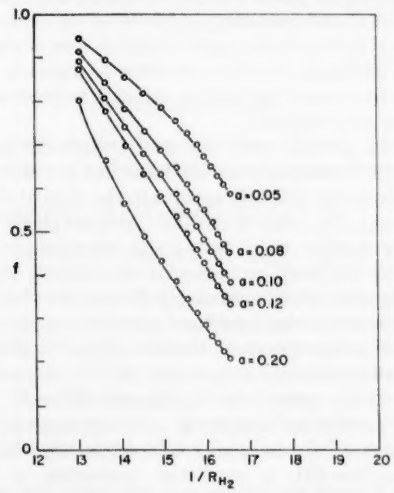

FIG. 10. Plot in accordance with Eq. (7) of the data presented in Fig. 2 for 140 mm of C_3H_8 at reduced light intensity and with H_2 removed at intervals.

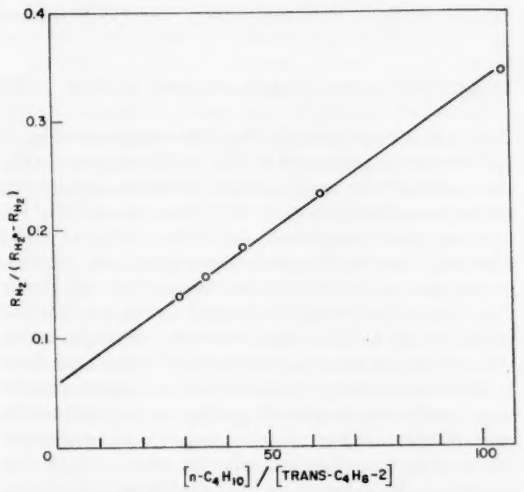

FIG. 11. Plot in accordance with Eq. (10) of the data presented in Fig. 4 for the effect of *trans*-2-butene additions to *n*-butane on R_{H_2}.

For several reasons a quantitative significance should not be attached to the values of rate constants obtained from plots in Figs. 9 and 10. In evaluating k_5/k_4 from the intercepts it was assumed that the initially present olefin impurity in *n*-butane was 1 part in 2000, as found approximately by gas chromatographic analysis, and no impurity was assumed in propane although the latter was not verified analytically. Furthermore, we have no ready explanation for the continuing slow decrease in the rate after the steady state should have been reached in the experiment with 140 mm propane at full light intensity in which hydrogen was removed at intervals, as shown in Fig. 1. A similar although less pronounced effect was observed with propane at reduced light intensity (Fig. 2) and in another experiment (not shown in the figures) in which both hydrogen and hexane were removed at intervals. An analogous behavior was found by Back with *n*-pentane[9] (although not with propane[10]) and was then ascribed to gradual decrease in the pressure of the paraffin.

Equation (7) should also be valid for the case of *n*-butane with various amounts of *trans*-2-butene initially added to it (Fig. 4). However, the rate of hydrogen formation then becomes drastically reduced and (H_2) is no longer approximately equal to (H_2'). On the other hand, it can be shown that, when the

[14] J. G. Calvert, Ann. Rev. Phys. Chem. **11**, 41 (1960).

product $a(\mathrm{Ol}i)$ is sufficiently large, Eq. (7) is reduced to

$$(\mathrm{H_2})/[(\mathrm{H_2}^*)-(\mathrm{H_2})]=k_7/k_6+k_3(R\mathrm{H})/k_6(\mathrm{Ol}i). \quad (10)$$

A plot in accordance with Eq. (10) is given in Fig. 11 for the results presented in Fig. 4. The values of $(\mathrm{H_2})$ are corrected for small amount of quenching by the olefin as explained in Part III. The value of $(\mathrm{H_2}^*)$ is approximately estimated from the value of $(\mathrm{H_2})$ obtained when no butene is added and from the time dependence of the rate just discussed. From the plot in Fig. 11, a value of 385 is obtained for $(k_6+k_7)/k_3$ and 0.058 for k_7/k_6. The plot, however, depends rather strongly on the value selected for $(\mathrm{H_2}^*)$ and since there is some uncertainty in this value we again consider these results only as providing a further support for the over-all plausibility of the considered mechanism rather than furnishing quantitative values of the rate constants. To achieve the latter objective, it is evidently necessary to work at very low conversions and this has been the procedure adopted in Part III to measure the relative rates of addition of hydrogen atoms to olefins.

The reaction scheme considered here can explain qualitatively all the features of the mercury photosensitized decomposition discussed in Part I. The previously observed time independence of the rate of hydrogen formation[7] was most likely due to a small olefin impurity initially present in the butane, perhaps coupled with some fortuitous cancellation of effects. However, in view of the complex nature of the process at finite conversions it is also necessary to try to explain why, in the case of $\mathrm{N_2O}/n\text{-}\mathrm{C_4H_{10}}$ mixtures, the very simple Eqs. (3) and (4) hold, as found in Part I (as well as in the present work at very low conversions). In this case, in addition to reactions (1)–(10), the following reactions have to be considered as well:

$$\mathrm{O}+\mathrm{C_4H_{10}}\rightarrow\mathrm{OH}+\mathrm{C_4H_9} \quad (11)$$

$$\mathrm{OH}+\mathrm{C_4H_{10}}\rightarrow\mathrm{H_2O}+\mathrm{C_4H_9} \quad (12)$$

$$\mathrm{O}+\mathrm{C_4H_8}\rightarrow\text{products}. \quad (13)$$

The following simplifying assumptions appear justifiable as a first approximation. (1) Reactions (7) and (8) can be neglected. (2) Steady-state concentration of olefin is attained. (3) Products of reaction (13) do not affect the concentrations of $\mathrm{C_4H_9}$ and $\mathrm{C_4H_8}$. Fortuitously, the values of the ratios k_6/k_3 and k_{13}/k_{11} are quite similar,[1,15] so that the following two simplifications can also be approximately made

$$\frac{1+k_6(\mathrm{Ol})/k_3(R\mathrm{H})}{1+k_{13}(\mathrm{Ol})/k_{11}(R\mathrm{H})}=1$$

and

$$\frac{1+k_{10}(\mathrm{N_2O})/k_2(R\mathrm{H})}{k_4k_6k_{11}/(k_4+k_5)k_3k_{13}+k_{10}(\mathrm{N_2O})/k_2(R\mathrm{H})}=1.$$

With these simplifications it is found, in agreement with the experimental results, that

$$1/\phi_{\mathrm{H_2}}=\sigma[1+k_{10}(\mathrm{N_2O})/k_2(R\mathrm{H})] \quad (11)$$

and

$$R_{\mathrm{H_2}}/R_{\mathrm{N_2}}=(1/\sigma)k_2(R\mathrm{H})/k_{10}(\mathrm{N_2O}), \quad (12)$$

where

$$\sigma=1+k_6k_{11}k_5/(k_4+k_5)k_3k_{13}.$$

Lack of temperature dependence in the plots of Eqs. (3) and (4) in Part I would suggest then that the temperature coefficients of the ratios k_6/k_3 and k_{13}/k_{11} may be similar. This, however, requires more extensive investigation.

As evident from Fig. 8, curve I, there is no decline in the rate with increasing pressure at very low conversions. Such a decline is observed in the case of olefins, where it indicates initial formation of a vibrationally excited triplet state capable of either decomposing or being collisionally deactivated.[16] It has been suggested[10] that the same may be true for paraffins but is normally not observed because of self-scavenging. Thus, in the case of propane, the extrapolated initial rate appeared to be smaller at 600 mm than at 300 mm, although the intrinsic uncertainty of such extrapolations was also pointed out.[10] The rates plotted in Fig. 8, curve I, can differ only very little from the initial rates, and there is evidently no indication of a collisional deactivation in the case of *n*-butane.

At pressures below about 100 mm, the rates begin to decline rapidly. Part of this decline is no doubt due to the fact that, at constant irradiation time, conversions are greater at lower butane pressures. This part has been calculated from Eq. (7) for the likely values of the ratios of rate constants and it appears that a large part of the decline in the rates at lower pressures is due to some other cause, perhaps an incomplete imprisonment of resonance radiation.

In the present work the initial quantum yield of hydrogen formation from *n*-butane has not been measured absolutely but only relative to the yield of nitrogen from $\mathrm{N_2O}$. The ratio of the two quantum yields is only slightly smaller than unity; and when allowance is made for the likely experimental uncertainty, and for a small amount of self-scavenging that occurs even at the very low conversions used and also for a small amount of inhibition by the residual olefin (1 part in 20 000 for experiments carried out in reactor *B*), the two quantum yields do not seem to be significantly different. Equations (7)–(9) can be used to calculate approximately these corrections. Assuming $k_4/k_5=1$, $k_7/(k_6+k_7)=0.1$, $(k_6+k_7)/k_3=470$, a combined correction of about 5% is obtained for experiments with 300 mm *n*-butane

[15] R. J. Cvetanović, J. Chem. Phys. **25**, 376 (1956); **30**, 19 (1959); Can. J. Chem. **38**, 1678 (1960).

[16] R. J. Cvetanović, H. E. Gunning, and E. W. R. Steacie, J. Chem. Phys. **31**, 573 (1959).

at 20-min irradiation, which within the experimental error brings the ϕ_{H_2}/ϕ_{N_2} ratio to unity.

The absolute values of these quantum yields remain uncertain. In Part I it was estimated that at room temperature ϕ_{N_2} is 0.78 on the basis of a value of 0.50 for ϕ_{H_2} from 200 mm *n*-butane.[7] Actually, it appears now that ϕ_{N_2} may be much closer to unity for the following reasons: (1) In Part I, R_{H_2} for 200 mm *n*-butane was measured in the time dependent region while the original actinometric determinations[7] were apparently done in the time independent region, i.e., under approximately steady-state conditions, presumably because of an appreciable olefin impurity initially present. It may be approximately estimated that a correction for this could increase ϕ_{N_2} by as much as 15–20%. (2) In the original actinometric determinations, complete absorption of resonance radiation by *n*-butane was assumed while under comparable conditions it is found[17] by direct measurement of light transmission that with a similar light source only about 95% of the incident radiation is absorbed in a reaction cell 10-cm long.

Although the sum of the two effects just discussed would tend to bring ϕ_{N_2} close to unity, it would be highly desirable to determine accurately the absolute value of this primary quantum yield by direct actinometric measurements. In the meantime, it may suffice to assume provisionally that ϕ_{N_2} is unity. On that basis, the primary quantum yield of hydrogen from *n*-butane is also unity. In as much as this is correct, the process is entirely explainable in terms of the reactions discussed in the present work and there is no need to postulate occurrence of physical quenching as was done in Part I. Under such conditions, either no quenching to the metastable state of mercury occurs or, if it does, then $k_{q1}=k_{q2}=0$ and $k_{f2}/k_{f1}=k_2/k_{10}$, which is a formally equivalent case as outlined in the Introduction. If, on the other hand, ϕ_{N_2} and ϕ_{H_2} are indeed smaller than unity, then there is a loss of light energy and the mechanism responsible for it is probably of physical nature.

[17] R. J. Cvetanović (unpublished results).

THE JOURNAL OF CHEMICAL PHYSICS VOLUME 35, NUMBER 4 OCTOBER, 1961

Relative Rates of Addition of Hydrogen Atoms to Olefines*

K. R. Jennings† and R. J. Cvetanović

Division of Applied Chemistry, National Research Council, Ottawa, Canada

(Received March 30, 1961)

Hydrogen atoms were produced by the mercury-photosensitized decomposition of *n*-butane at 435±5 mm pressure and at 23.5±1°C. By introducing known amounts of olefine, the rate of addition of hydrogen atoms to the olefine could be measured relative to the rate of abstraction from the *n*-butane by observing the fall in the rate of production of hydrogen. In this way, relative rates of addition to eight olefines were obtained, and the logarithms of the relative rate constants were found to correlate reasonably well with the atom localization energies of the olefines, but not with their maximum free valence.

INTRODUCTION

In terms of the transition-state theory, the rate constant of a chemical reaction may be expressed by

$$\text{Rate constant} = (kT/h)\cdot\exp(-\Delta F/RT)$$

$$= (kT/h)\exp(\Delta S/R)\cdot\exp(-\Delta H/RT), \quad (1)$$

where ΔF, ΔS, and ΔH are, respectively, the changes in free energy, entropy, and heat content involved in the formation of the transition-state complex from the reactants. It is the free energy of activation (ΔF) rather than the energy of activation (ΔH) which controls the rate of a reaction. Unfortunately, ΔF cannot be measured directly nor can it be calculated without making specific assumptions concerning the structure of the complex. This situation had led to a number of attempts being made to correlate relative reaction rates with physical properties of the reactants which are directly measureable or calculable.

This approach has been most successful in the case of the addition of atoms or radicals to unsaturated hydrocarbons. The reactivity of a number of polycyclic hydrocarbons towards CCl_3 radicals was found to correlate quite well with the maximum free valence F_r of the hydrocarbons.[1] Similar studies with CH_3 radicals have led to a correlation of the relative rate constants with the singlet-triplet excitation energy of the hydrocarbons.[2,3] Since many of the physical proper-

* Contribution No. 6491 from the National Research Council, Ottawa, Canada.

† Postdoctorate Fellow, 1958–60. Present address: Department of Chemistry, The University, Sheffield 10, England.

[1] E. C. Kooyman and E. Farenhorst, Trans. Faraday Soc. **49**, 58 (1953).

[2] M. Szwarc, J. Chem. Phys. **23**, 204 (1955).

[3] M. Levy and M. Szwarc, J. Am. Chem. Soc. **77**, 1949 (1955).

ties of polycyclic hydrocarbons are closely related, the relative rate constants of CH_3 addition can also be correlated with electron affinities,[4] free valence or atom localization energies,[5] or heats of reaction.[6]

Much of the experimental work has been carried out in solution, where solvation effects of varying magnitude could be a disturbing influence. Such effects may be eliminated by working in the gaseous phase, but until quite recently, very little work of this type had been reported. Melville and Robb[7] obtained a series of rate constants for the reaction of hydrogen atoms with a number of olefines at room temperature and at low pressures. Their results indicated that the reactivity of the double bond was not markedly dependent upon the amount of substitution, although the result for propylene was unexpectedly low. Darwent and Roberts,[8] using a totally different technique, obtained relative rates for the addition of hydrogen atoms to ethylene and propylene which did not support the low value for propylene. Relative rates of addition of oxygen atoms to a number of olefines have been recently obtained in this laboratory.[9] Correlations of the logarithms of the relative rate constants with such quantities as ionization potential, excitation energy, and bond order of the double bond illustrate the electrophilic nature of the oxygen atoms. The simple relationships between maximum free valence, atom localization energy, and singlet-triplet excitation energy found in polycyclic hydrocarbons[5] are not found in mono-olefines[10]; whereas the relative rates of *radical* addition may be correlated with the excitation energies of polycyclic hydrocarbons, the relative rates of the addition of *electrophilic* oxygen atoms correlate with the excitation energies of mono-olefines.

In view of the discrepancies in earlier results, the present work was undertaken with a view to obtaining a consistent set of relative rates for the addition of hydrogen atoms to mono-olefines and in the hope of finding similar correlations. Since hydrogen atoms are very small, complications due to steric factors should be minimized, and since the work was carried out in the gaseous phase, solvation effects were absent.

THEORY OF METHOD

The method used in the present work has to be discussed in the light of an earlier study of the mechanism of the mercury photosensitized decomposition of *n*-butane[11] (referred to in the following as Part I) and in particular of a recent extension of it[12] (referred in the following as Part II). For a paraffin (RH) such as *n*-butane, the important reactions in the presence of an olefine are

$$\mathrm{Hg}+h\nu\rightarrow\mathrm{Hg}^* \qquad \phi\mathrm{Ia}$$

$$R\mathrm{H}+\mathrm{Hg}^*\rightarrow R+\mathrm{H}+\mathrm{Hg} \qquad (q_1)$$

$$\mathrm{Olefine}+\mathrm{Hg}^*\rightarrow\mathrm{Deactivation\ or\ Products} \qquad (q_2)$$

$$\mathrm{H}+R\mathrm{H}\rightarrow\mathrm{H_2}+R \qquad (1)$$

$$\mathrm{H}+\mathrm{Olefine}\rightarrow R \qquad (2)$$

$$\mathrm{H}+\mathrm{Olefine}\rightarrow\mathrm{H_2}+R' \qquad (3)$$

$$R+R\rightarrow R_2 \qquad (4)$$

$$R+R\rightarrow R\mathrm{H}+\mathrm{Olefine} \qquad (5)$$

$$R+R'\rightarrow R\cdot R'. \qquad (6)$$

At sufficiently high pressures, the excited olefine molecules formed in the quenching reaction (q_2) are collisionally deactivated without decomposing.[13] If at the same time the work is restricted to very small conversions so that the buildup of olefine formed in the disproportionation reaction (5) can be neglected, the steady-state treatment leads to the following expression for the rate of formation of hydrogen:

$$R_{\mathrm{H_2}}=\left[1+1\Big/\left(\frac{k_1(R\mathrm{H})}{k_2(\mathrm{olefine})}+\frac{k_3}{k_2}\right)\right]^{-1}\cdot\frac{\phi\mathrm{Ia}}{1+[q_2(\mathrm{olefine})/q_1(R\mathrm{H})]}. \qquad (1)$$

Equation (1) can be rearranged into

$$f(\mathrm{H_2})=\frac{R_{\mathrm{H_2}}[1+q_2(\mathrm{olefine})/q_1(R\mathrm{H})]}{R_{\mathrm{H_2}}^*-R_{\mathrm{H_2}}[1+q_2(\mathrm{olefine})/q_1(R\mathrm{H})]}=\frac{k_3}{k_2}+\frac{k_1(R\mathrm{H})}{k_2(\mathrm{olefine})}. \qquad (2)$$

Here $R_{\mathrm{H_2}}^*$ stands for ϕIa and represents the rate of formation of hydrogen in the absence of an olefine (i.e., it is the limiting value of $R_{\mathrm{H_2}}$ at zero conversion obtained from *n*-butane containing no olefine impurity).

Equation (2) relates, in a simple manner, the decrease in hydrogen formation with increasing olefine/*n*-butane ratio as a result of competitive consumption of hydrogen atoms in reactions (1)–(3). However, in order to use this equation to obtain k_2/k_1 values for various olefines, it is necessary that (1) the initially present olefine impurity in the *n*-butane and (2) the olefine formed in reaction (5) are both sufficiently

[4] F. A. Matsen, J. Chem. Phys. **24,** 602 (1956).
[5] C. A. Coulson, J. Chem. Soc. **1955,** 1435.
[6] C. Walling, J. Phys. Chem. **64,** 116 (1960).
[7] H. W. Melville and J. C. Robb, Proc. Roy. Soc. (London) **A196,** 445, 466, 479, 494 (1949); **A202,** 181 (1950).
[8] B. de B. Darwent and R. Roberts, Discussions Faraday Soc. **14,** 55 (1953).
[9] R. J. Cvetanović, Can. J. Chem. **38,** 1678 (1960).
[10] S. Sato and R. J. Cvetanović, J. Am. Chem. Soc. **81,** 3223 (1959).
[11] R. J. Cvetanović, J. Chem. Phys. **23,** 1208 (1955).
[12] R. J. Cvetanovic, W. E. Falconer, and K. R. Jennings, J. Chem. Phys. **35,** 1225 (1961), preceding paper.
[13] R. J. Cvetanović, H. E. Gunning, and E. W. R. Steacie, J. Chem. Phys. **31,** 573 (1959).

small so that they cannot compete for hydrogen atoms with *n*-butane and the olefines added to it. In the present work, the residual olefine in the purified *n*-butane was less than 1 part in 20 000 and the conversion was kept down to 10^{-2}% and it can be readily calculated that any interference from these two causes was very small in the presence of added olefines. On the other hand, under the same conditions but in the absence of an added olefine, these effects cannot be entirely neglected. It was shown in Part II that, for the considered reaction scheme at finite conversions,

$$\frac{1-\exp[-a(H_2')]}{a(H_2')}=\frac{\left(1+\frac{k_4}{k_5}+\frac{k_3}{k_2+k_3}\right)}{1-\left(1+\frac{k_4}{k_5}+\frac{k_3}{k_2+k_3}\right)a(Ol_i)}\times\left[1-\frac{1+\frac{k_3}{k_2}\frac{k_5}{k_4}}{1+k_5/k_4}\frac{(H_2^*)}{(H_2')}\right], \quad (3)$$

where

$$(H_2')=(H_2)+\frac{k_3}{k_2}\left[\frac{1+2k_5/k_4}{1+k_5/k_4}(H_2)-(H_2^*)\right] \quad (4)$$

and

$$a=\left(\frac{k_4}{k_5}+\frac{k_3}{k_2+k_3}\right)\left[\frac{(k_2+k_3)}{k_1(RH)}\right]\left(1+\frac{k_4}{k_5}+\frac{k_3}{k_2+k_3}\right)^{-1}, \quad (5)$$

where (H_2) and (H_2^*) are the integral concentrations at any time t and (Ol_i) is the concentration of olefine impurity initially present [assumed to be the same olefine as formed by disproportionation in reaction (5)]. As zero reaction time is approached, it can be shown that approximately

$$\frac{R_{H_2^*}}{R_{H_2}}\approx 1+\frac{k_2+k_3}{k_1}\frac{(Ol_i)}{(RH)}. \quad (6)$$

Equation (6) can be used to assess approximately the difference Δ between the true $R_{H_2^*}$ and the smaller value experimentally found due to the effect of the residual olefine impurity alone. With $(k_2+k_3)/k_1$ of the order of 400 and an olefine impurity of 1 part in 20 000 Δ is about 2%. The effect of finite conversion alone and the combined effect of it and the olefine impurity can be calculated from Eq. (3) for given values of ratios of rate constants. Under conditions of the present work, the combined effect leads to a Δ of up to between about 3 and 4%. This introduces an error of up to about 10% into k_2/k_1 values, which can of course be approximately corrected by evaluating Δ and allowing for it. At the same time, as will be shown later, the *relative* values of k_2 for different olefines remain practically the same regardless of whether this correction is made or not.

A plot of $f(H_2)$ against the *n*-butane/olefine ratio should give a straight line of slope k_1/k_2 with k_3/k_2 as intercept. In the present work, the main emphasis has been on the determination of relative k_2 values for a number of olefines. Because of the long extrapolation, values of k_3/k_2 are subject to considerable error and in most cases have been found to be relatively small (less than about 0.1).

In evaluating $f(H_2)$ in Eq. (2), a value of 8.2 is assumed for q_2/q_1 for all olefines and *n*-butane. This value was obtained in Part I for ethylene and *n*-butane and it can be calculated from the quenching cross sections obtained by physical measurements[14] that the quenching efficiencies of various olefines are very similar. Since in the present work butane/olefine ratios higher than 200:1 were always used, quenching by the olefine was always less than about 4%, and any errors in applying this correction must remain very small.

EXPERIMENTAL

The reaction system had a volume of 8.3 l, and consisted of the quartz reaction cell of 200 ml, a circulating pump, a trap, and a buffer volume of several lengths of glass tubing of approximately 4-cm diameter. Using an all-glass circulating pump described previously[15] and consisting of two parallel plungers balanced on a glass arm, the reactants in the cell were renewed every 12–15 sec. The cell was illuminated from each end by a low-pressure mercury vapor lamp. The reaction system was isolated from the remainder of the apparatus by a mercury cutoff, since many of the reactants dissolve in tap grease. The volume of the system was determined by calibration against a standard volume.

Butane was admitted to the reaction system until the pressure was about 430 mm Hg, after which it was frozen down and pumped on. The butane was evaporated and frozen down several times, until no further noncondensible gas could be collected by means of a Toepler pump. The pressure of the butane was finally measured on a mercury manometer and corrected to 25°C.

Olefines were measured on a gas burette which was isolated from the reaction system and the remainder of the apparatus by two mercury cutoffs. This allowed the olefines to be transferred to the reaction system without coming into contact with stopcock grease.

The reactants were mixed by rapid warming of the condensed gases followed by freezing down and a final warming to room temperature; they were then allowed to circulate for a short time before the run began. The gases were irradiated for a period of 20 min, although preliminary runs were carried out irradiating for periods of 10 and 30 min. The amounts of hydrogen obtained when *n*-butane alone was irradiated for 10, 20, and 30 min are shown in Table I of Part II. Very

[14] B. de B. Darwent, M. K. Phibbs, and F. G. Hurtubise, J. Chem. Phys. **22**, 859 (1954).
[15] J. Watson, 7th International Combustion Symposium, 1958.

TABLE I. The values of $f(H_2)$ at various *n*-butane/olefine ratios.

		1	2	3	4	5	6	7
Ethylene								
$f(H_2)$		0.798	0.924	1.02	1.13	1.21	1.42	1.99
Ratio		299	384.5	397	418	515	627	683
Ratio/$f(H_2)$		375	416	389	370	426	442	343
$k_2=384$	$k_3/k_2=-0.019$							
Propylene								
$f(H_2)$		0.419	0.466	0.527	0.716	0.826	0.990	
Ratio		264	295	362	465	560	661	
$k_2=695$	$k_3/k_2=0.033$							
Butene-1								
$f(H_2)$		0.428	0.555	0.704	0.869	0.866	1.025	
Ratio		277	368	471	570	601	734	
$k_2=751$	$k_3/k_2=0.071$							
Isobutene								
$f(H_2)$		0.202	0.244	0.299	0.367	0.402	0.438	
Ratio		327	393	494	614	699	716	
$k_2=1755$	$k_3/k_2=0.017$							
cis-butene-2								
$f(H_2)$		0.849	1.011	1.118	1.331	1.463	1.669	
Ratio		249	315	360	404	451	513	
$k_2=314$	$k_3/k_2=0.023$							
trans-butene-2								
$f(H_2)$		0.656	0.696	0.956	1.303	1.405	1.424	1.476
Ratio		225	265	357	459	514	563	566
$k_2=400$	$k_3/k_2=0.076$							
Tetramethylethylene								
$f(H_2)$		0.456	0.630	0.647	0.851	1.005	1.165	
Ratio		278	364	397	539	591	655	
$k_2=560$	$k_3/k_2=-0.048$							
1:3-Butadiene								
$f(H_2)$		0.131	0.146	0.176	0.212	0.212	0.302	
Ratio		348	401	498	592	650	940	
$k_2=3505$	$k_3/k_2=0.033$							

little variation in the rate with time was found, so that it may be assumed that initial conditions are closely approached during a run of 20 min.

After the run, the gases were again frozen down and the solid pumped on. The pumping system consisted of two mercury vapor pumps and a trap immersed in liquid nitrogen, leading to a combined gas-burette Toepler pump. The pressure of hydrogen on a fixed volume was measured and corrected to 25°C. Any hydrocarbon carried over was removed by circulating the hydrogen through a trap immersed in liquid nitrogen, measuring the pressure once again. Occasional samples of hydrogen were combusted on copper oxide in order to test for the presence of methane. Non-combustible gases were always less than 0.5% of the hydrogen collected. Since ethylene has a slight vapor pressure at the temperature of liquid nitrogen, two further traps were introduced into the analytical pumping line when this gas was used. One of these was of conventional design, but the other was a "pump-down" trap capable of producing a temperature of −210°C, at which temperature ethylene has a negligible vapor pressure.

In calculating $f(H_2)$ values, $R_{H_2}{}^\circ$ had to be obtained in a separate run, and owing to variations in lamp output, pumping speed, and the possibility of polymer formation on the cell windows, this is likely to vary slightly. Consequently, blank runs were carried out very frequently, and average values of $R_{H_2}{}^\circ$ interpolated. Usually a slow drop in $R_{H_2}{}^\circ$ was found, amounting to less than 0.5% per run.

All runs were carried out at a temperature of 23.5± 1.0°C and at a pressure of 435±5 mm Hg. A number of runs were carried out at other pressures, but these were not used in the calculation of relative rates. In the absence of olefines, it was found in Part II that the rate of hydrogen production fell gradually when the pressure was reduced to less than 300 mm Hg. Between 300 mm and 600 mm Hg, hydrogen production was constant. Using butene-1 as the added olefine, two runs were carried out at 300 mm and two at 600 mm Hg. When $f(H_2)$ was plotted against the butane/olefine ratio, all four points fell on the same straight line as the six points obtained from runs carried out at 435 mm Hg. This would appear to indicate that the relative rates of the two competing reactions are independent of pressure between 300 mm and 600 mm Hg.

All reactants were Phillips research grade hydrocarbons. Olefines were purified by bulb-to-bulb distillation. A sample of *n*-butane was found by gas-liquid

TABLE II. Relative rate constants of the reactions of hydrogen atoms with olefines.

Olefine	Relative values of k_2[a]			k_2/k_1	k_3/k_2	
	$\Delta=0$ (1)	$\Delta=3.6\%$ (2)	$\Delta=5\%$ (3)	$\Delta=3.6\%$ (4)	$\Delta=0$ (5)	$\Delta=3.6\%$ (6)
C_2H_4	0.511	0.516	0.517	422	(−0.019)	(−0.001)
C_3H_6	0.925	0.924	0.924	756	0.033	0.045
C_4H_8—1	1.00	1.00	1.00	818	0.071	0.081
iso-C_4H_8	2.34	2.28	2.25	1863	0.017	0.020
cis-C_4H_8—2	0.418	0.433	0.439	354	0.023	0.066
trans-C_4H_8—2	0.533	0.544	0.549	445	0.076	0.117
$(CH_3)_2C{:}C(CH_3)_2$	0.746	0.749	0.753	613	(−0.048)	(−0.025)
1,3-C_4H_6	4.67	4.47	4.39	3660	0.033	0.032

[a] k_2 for C_4H_8—1 is taken as unity.

chromatography to contain 1 part in 2000 of butene. The butane was therefore passed through two wash bottles of concentrated sulfuric acid, then over KOH pellets to remove acid spray. In this way, the butene concentration was reduced to less than 1 part in 20 000. Enough butane for 4 or 5 runs was prepared in one batch and stored for use.

RESULTS

The experimental results are summarized in Table I, where $f(H_2)$ represents the function defined in Eq. (2), calculated without correcting R_{H_2} for finite conversion and residual olefine impurity, and "ratio" is n-C_4H_{10}/olefine. All slopes and intercepts were determined by applying the method of least squares and all values of k_2 are given in terms of an arbitrary value of $k_1=1$.

As mentioned earlier, Eq. (3) has been used to estimate the difference between R_{H_2} as obtained experimentally and the true value of this quantity, i.e., after correcting for the small residual olefine impurity and for the fact that although the conversions are kept very small they are nevertheless finite. These calculations are approximate because some assumptions have to be made regarding the values of the ratios of rate constants. Taking as the likely values under these conditions $k_5/k_4=1$, $(k_2+k_3)/k_1=470$, and $k_3/k_2=0.11$, it is found that the measured R_{H_2} is between about 2 and 4% smaller than the true value, depending on the extent to which the residual olefine impurity is less than 1 part in 20 000 (an upper limit corresponding to the analytical limit of detectability). In no case is this difference Δ likely to have been greater than 5%. To assess the effect of this, in addition to the values of k_2 given in Table I (i.e., at $\Delta=0$), the relative values of k_2 have been also determined by the mean least-square technique for values of Δ of 3.6 and 5%. The results are given in Table II where the value for 1-butene has been taken as unity in each case. It is seen that the relative values of k_2 for the various olefines are very little affected by the variation of Δ in this interval. On the other hand, the values of k_1, the rate constant for abstraction from n-butane, are more sensitive to variations in R_{H_2}. Thus, the relative value of k_1, taking again k_2 for 1-butene as unity, are 1/751, 1/818, and 1/843 for $\Delta=0$, 3.6, and 5%, respectively. The values at $\Delta=3.6\%$ are perhaps closest to the true values and they are listed in column (4) of Table II. The corresponding $f(H_2)$ plots for all the olefines studied except ethylene are given in Fig. 1.

The data for ethylene are less reliable than for the other olefines studied. The experiments with ethylene were carried out with an aluminum balancing arm in the circulating glass pump because in the later stages of this work the original glass balancing arm fractured and had to be replaced. As a result the pump was occasionally erratic in operation which led to an appreciable increase in the scatter of the points in the $f(H_2)$ plot. Since abstraction from ethylene should be negligible, the origin of this plot was also taken as a point in calculating by mean least squares the value of k_2/k_1 given in Table I. In this case, the value of k_2/k_1 can be calculated from each experimental point since when $k_3=0$, $k_2/k_1=(n\text{-butane})/f(H_2)\,(\text{olefine})$. The latter values are given in Table I for $\Delta=0$ and show the magnitude of the scatter. The mean of these values is 394 and the mean deviation is $\pm 7.3\%$.

In columns (5) and (6) of Table II are given the values of k_2/k_3 obtained from the intercepts of the $f(H_2)$ plots with $\Delta=0$ and $\Delta=3.6\%$, respectively. Because of large extrapolations, these values are uncertain, although their order of magnitude is probably correct. With $\Delta=3.6\%$, k_3/k_2 for ethylene is zero as would be expected. However, for tetramethyl ethylene a small negative value is obtained which is an error due to the large extrapolation.

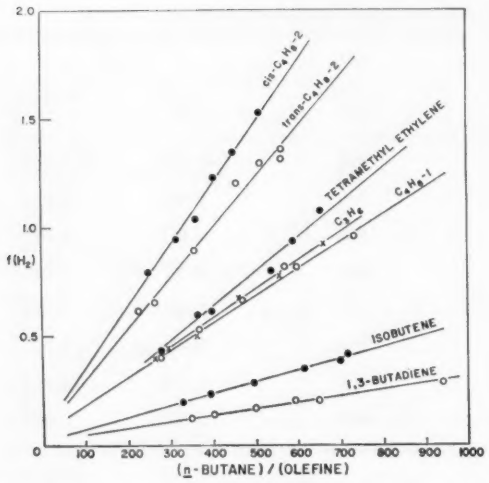

FIG. 1. Plots of the $f(H_2)$ values (calculated with $\Delta=3.6\%$) against *n*-butane to olefine ratios.

DISCUSSION

Using the molybdenum trioxide technique, Melville and Robb[7] obtained absolute rate constants for the rate of reaction of hydrogen atoms with an extensive series of olefines. In a later paper,[16] they corrected their values by allowing for the removal of the atoms by the silica window of the reaction cell, and the rate constants so obtained are given in Table III in units of cc mole^{-1} sec$^{-1}\times10^{-11}$. The results obtained in this work are also given, relative to *trans*-butene-2=6.3.

It is seen that there is no correlation whatever between the two sets of results, but there are a number of possible reasons for the differences. The difficult technique employed by Melville and Robb was designed to allow a determination of absolute reaction rates rather than relative rates, and consequently relative rates may not be as accurate as those determined by the more usual methods of gaseous-phase competitive reactions. Thus, a redetermination of the rates of reaction of hydrogen atoms with ethylene and propylene[16] gave values of 5.0 and 1.6 in the above units, in good agreement with the earlier absolute values, but changing the relative rates from 4.2 to 3.1. Other determinations of the relative rates of these two reactions, using quite different techniques, showed propylene to be rather more reactive than ethylene. Darwent and Roberts[8] found that propylene reacted 1.67 times as rapidly as ethylene, and Callear and Robb[17] obtained a value of 3.4. This led Bradley, Melville, and Robb[18] to redetermine this ratio directly using the molybdenum trioxide technique and a method utilizing mass spectrometry resulting in a value of 1.5 for the rate of reaction with propylene compared with the rate of reaction with ethylene. The value of 1.8 found for this ratio in the present work is therefore in good agreement with previous determinations.

The method of Melville and Robb does not distinguish between the addition to the olefine and abstraction of a hydrogen atom from it and the rate constants found are those for the total reaction. In the case of ethylene, abstraction is almost certainly negligible, but in the case of propylene, Darwent and Roberts[8] found that the rate of addition (k_2) was about six times the rate of abstraction (k_3). The values obtaned for k_3/k_2 in the present work indicate that abstraction may be even less important relative to addition of hydrogen atoms to olefins and corrections for abstraction are therefore unlikely to reduce the over-all rate constant by more than a few percent.

The use of the molybdenum oxide technique necessitates the use of low pressures, and most of the experiments were carried out at a pressure of about 6 mm Hg compared with a pressure of about 435 mm in the present work. Although it is difficult to predict the effect of variation of pressure, it is possible that the widely divergent results may be explained, at least partly, in terms of the "hot" radicals which are undoubtedly present at low pressures.[19]

As Back has pointed out,[20] the measurements of Melville and Robb may be somewhat in error since no allowance was made for the quenching of Hg* by the olefines. From the quenching cross sections for hydrogen[21] and olefines,[14] it appears that hydrogen is a more efficient quencher. However, the difference is not large; and since the hydrogen/olefine ratios used were often less than 10, some quenching by the added ole-

TABLE III. Comparison of k_2 values with the results of Melville and Robb.

	k_2 cc mole^{-1} sec$^{-1}\times10^{-11}$	
	Melville and Robb	This work
Ethylene	7.5	6.0
Propylene	1.8	10.7
Butene-1	...	11.6
Isobutene	5.7	26.4
cis-Butene-2	8.0	5.0
trans-Butene-2	6.3	6.3
Tetramethylethylene	4.8	8.7
Butadiene-1:3		51.8

[16] P. E. M. Allen, H. W. Melville, and J. C. Robb, Proc. Roy. Soc. (London) **A218,** 311 (1953).
[17] A. B. Callear and J. C. Robb, Trans. Faraday Soc. **51,** 638 (1955).
[18] J. N. Bradley, H. W. Melville, and J. C. Robb, Proc. Roy. Soc. (London) **A236,** 454 (1956).
[19] P. J. Boddy and J. C. Robb, Proc. Roy. Soc. (London) **A249,** 518 (1959); A. H. Turner and R. J. Cvetanović, Can. J. Chem. **37,** 1075 (1959).
[20] R. A. Back, Trans. Faraday Soc. **54,** 512 (1958).
[21] E. W. R. Steacie, Can. J. Research **B18,** 44 (1940).

fines did occur. In the present work, by using high butane/olefine ratios, quenching by olefines was kept low, and an approximate correction was made.

The reactions of hydrogen atoms with solid olefines at −195°C have recently been investigated by Klein and Scheer.[22] The atoms are formed by thermal dissociation of hydrogen on a heated nickel filament and then diffuse to the walls of the vessel where a thin layer of the olefine has been deposited. Several olefines, including propylene, 1-butene, and isobutene, react quite rapidly, whereas the reaction with 1,3-butadiene is very slow, and 1-hexene and *trans*-2-butene appear to be inert. The marked differences in rates of reaction are ascribed to differences in activation energies which will be relatively more important at low temperatures. Hardwick[23] has produced hydrogen atoms in the liquid phase by the radiolysis of *n*-hexane and preliminary results indicate that primary olefines are somewhat more reactive than secondary olefines, in keeping with the results found here.

Owing to the uncertainty of the absolute rate constants of reactions involving hydrogen atoms, it does not appear to be possible at present to assign absolute values for the reactions considered here. If one assumes a value of $k=6.3\times10^{11}$ cc mole^{-1} sec^{-1} for H+*trans*-2-butene, our values are given in the same units in Table III. If $k=5.7\times10^{11}$ cc mole^{-1} sec^{-1} for H+isobutene is taken as the standard, however, our values quoted in Table III would have to be divided by 4.8. It is clear that further work on the determination of absolute rate constants is desirable before the relative values can become absolute.

Since hydrogen atoms are expected to behave as typical free radicals and thus to resemble methyl

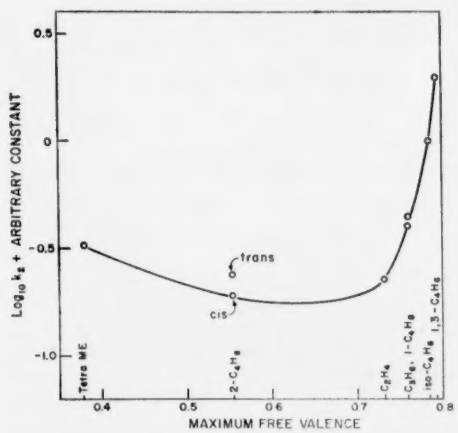

FIG. 2. Plot of $\log_{10} k_2$ against maximum free valence. (Maximum free valence values are taken from reference 10. Tetra ME= tetramethyl ethylene.)

[22] R. Klein and M. D. Scheer, J. Phys. Chem. **62,** 1011 (1958).
[23] T. J. Hardwick, J. Phys. Chem. (to be published).

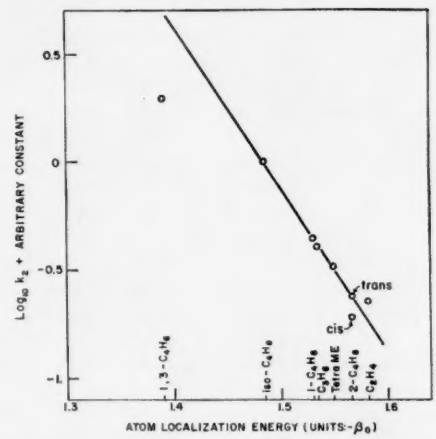

FIG. 3. Plot of $\log_{10} k_2$ against atom localization energy. (Atom localization energy values are taken from reference 10. Tetra ME=tetramethyl ethylene.)

radicals rather than oxygen atoms in their reactions with unsaturated hydrocarbons, it was thought possible that an approximate linear correlation might exist between the logarithms of the relative rate constants and the maximum free valence of the olefine. As may be seen from Fig. 2, however, no such correlation was found. When a similar plot is made against the atom localization energies E_{al} of the olefines, a fairly good correlation is found for the mono-olefines, as shown in Fig. 3, but 1,3-butadiene is only about 0.4 times as reactive as one would expect from the linear plot in Fig. 3. In the case of unsymmetrical olefines, the smaller of the two values of E_{al} was taken, and all values quoted are those given in reference 10. In assessing such correlations, however, it should be borne in mind that the values of theoretical quantities of this kind depend on the simplifying assumptions made in order to facilitate calculations. Using the values of E_{al} for ethylene, propylene, 2-butene, and 1,3-butadiene obtained by Pullman and Effinger[24,25] by allowing for differences in bond lengths, a roughly similar correlation is obtained but with the logarithm of k_2 for butadiene deviating somewhat in the direction opposite from that in Fig. 3. The values of E_{al} calculated by Binks and Szwarc[26] for ethylene, propylene, and isobutene correlate reasonably well, but the value for 1,3-butadiene would then require a k_2 for this compound very much larger than observed.

It has been suggested by Burkitt, Coulson, and Longuett-Higgins[27] that the atom localization energies rather than the maximum free valencies are probably

[24] B. Pullman and J. Effinger, Bull. soc. chim. France **1958,** 482.
[25] B. Pullman, J. chim. phys. **55,** 790 (1958).
[26] J. H. Binks and M. Szwarc, Proc. Chem. Soc. **1958,** 226.
[27] F. H. Burkitt, C. A. Coulson, and H. C. Longuett-Higgins, Trans. Faraday Soc. **47,** 553 (1951).

the more reliable measure of the reactivity of unsaturated compounds towards free radicals. This suggestion appears to be borne out by the present results for hydrogen atoms and olefines and is also supported by similar correlations for the reactions of methyl radicals with polycyclic hydrocarbons[24,26] and with a restricted group of mono-olefines.[26] With the latter, deviations from the correlations found for terminal olefines have been ascribed to steric hindrance in the case of internal olefines. A rough correlation with maximum free valences, on the other hand, was found for both terminal and internal olefines although this might have been to some extent fortuitous and has to be subjected to more rigorous test when more extensive experimental information becomes available.[10] The present work shows that there is no correlation with the maximum free valences in the case of hydrogen atom addition to olefins.

Further approximate features of correlations of this kind should be stressed. The free valence may be looked upon as a measure of the ease with which an incipient bond may be formed and therefore is concerned with the initial stages of the reaction prior to the formation of the transition-state complex.[28] The atom localization energy, on the other hand, is the energy required to localize completely a π electron on a particular atom in a conjugated system and represents an idealized condition which approximates the later stages of the reaction, subsequent to the formation of the transition-state complex. Thus, in either case, at best only approximate correlations may be expected. Furthermore, as mentioned earlier, there are serious mathematical limitations in theoretical calculations of this kind. For example, among other things, no distinction is made between the *cis*- and *trans*-isomers of internal olefines; although in the case of 2-butene, the *trans*-isomer is the more reactive towards both hydrogen and oxygen atoms, and towards methyl radicals.

An early suggestion of Evans that, in radical addition reactions to olefins, the changes in activation energies should be directly proportional to the changes in heats of reaction has been recently used by Walling[6] to correlate rates of methyl radical additions to some terminal olefines. For the rates of addition of hydrogen atoms to olefines determined in the present work, there is perhaps a very rough correlation of this kind for the mono-olefines; but the value for 1,3-butadiene is one to two powers of ten smaller than would be predicted on that basis. However, in view of the relatively small differences in reactivity and the appreciable uncertainty in the indirectly derived heats of reaction, no firm conclusions can be drawn.

In obtaining the plots in Figs. 2 and 3, no statistical factor of one-half has been applied to the rate constants for symmetrical olefines, as has been the usual practice in attempts to obtain similar correlations for methyl radicals. It is unlikely that this correction is generally justifiable. Its application in the present case would lead to a much poorer correlation.

Correlations of the type discussed here imply a constant pre-exponential factor in the Arrhenius rate equation for all the members of the reaction series, so that the logarithm of the rate constant is proportional to the energy of activation. Under such conditions, the linear correlation of atom localization energies with log$k$ values is equivalent to a correlation with the activation energies. In this connection, a determination of the relative energies and entropies of activation for this reaction series would be very desirable although it may be subject to considerable experimental difficulty in view of the relatively small differences in reactivity.

[28] R. D. Brown, J. Chem. Soc.; Quart. Revs. (London) **6**, 63 (1952).

THE JOURNAL OF CHEMICAL PHYSICS VOLUME 35, NUMBER 4 OCTOBER, 1961

Analysis of Polarized Crystal Spectra. The Spectrum of Cobalt(III) Acetylacetonate

T. S. PIPER*

William Albert Noyes Laboratory of Chemistry, University of Illinois, Urbana, Illinois

(Received April 13, 1961)

The analysis of broad bands in the polarized electronic spectra of transition metal ions in crystals is discussed. The band of cobalt(III) acetylacetonate due to the transition $^1T_1 \leftarrow {}^1A_1$ is found to be split by the trigonal field into components at 16 200 cm^{-1} ($^1A_2$) and at 17 000 cm^{-1} (^1E). The spectra indicate that the trigonal field of the free molecule is not appreciably distorted in the monoclinic crystal.

IN studies of electronic spectra of transition metal ions, it is advantageous to measure polarized spectra of molecules or complex ions in crystals. However, molecules of high symmetry are found more often than not in crystals at sites of lower symmetry. This note treats the problems involved in obtaining spectra of the broad spin-allowed bands, polarized with respect to molecular axes from polarized crystal spectra. As an illustration the crystal spectrum of cobalt(III) acetylacetonate is analyzed.

* Supported in part by a grant from the National Science Foundation.

ANALYSIS OF THE SPECTRA

Consider a molecule with an axis of symmetry threefold or higher and assume there is little distortion from this symmetry in the crystal whatever the site symmetry. Let the orientation of the molecular axis with respect to some convenient Cartesian coordinates (x, y, z) in the crystal be given by the polar angle ϑ measured from z, and the azimuthal angle φ measured in the xy plane from x. Furthermore, let the equation for the absorption of light in the crystal be written $I/I_0=10^{-a}$, where I_0 is the incident intensity, I the transmitted intensity, and a the absorbance. With the incident ray parallel to y, and polarized parallel ($\|$) or perpendicular ($\perp$) to the z axis, the fraction of light transmitted may be resolved into components parallel (π) and perpendicular (σ) to the molecular axis is given by

$$10^{-a_\parallel}=\cos^2\vartheta 10^{-a_\pi}+\sin^2\vartheta 10^{-a_\sigma}, \tag{1a}$$

$$10^{-a_\perp}=\sin^2\vartheta\cos^2\varphi 10^{-a_\pi}+(1-\sin^2\vartheta\cos^2\varphi)10^{-a_\sigma}. \tag{1b}$$

These equations may be solved for a_π and a_σ which are then plotted to obtain the band shapes.

CRYSTAL SPECTRA OF COBALT(III) ACETYLACETONATE

Crystals of monoclinic[1,2] aluminum acetylacetonate, containing about 1% of the cobalt acetylacetonate, are readily grown from acetone. The spectra[3] in Fig. 1 were measured with incident light perpendicular to the (001) and (100) faces, and polarized with respect to the b axis. The band near 6000 A is readily assigned to $^1T_1\leftarrow{}^1A_1$. The solution spectrum[4] is similar and the molar extinction coefficient is about 140. The transition $^1T_2\leftarrow{}^1A_1$ occurs near 3000 A in solution, and is seen as a uv tail in the crystal spectra. Absolute intensities in the crystal were not measured, however the values of a_σ (max) of the two crystal orientations are proportional to the thickness of the crystal within 5% error.

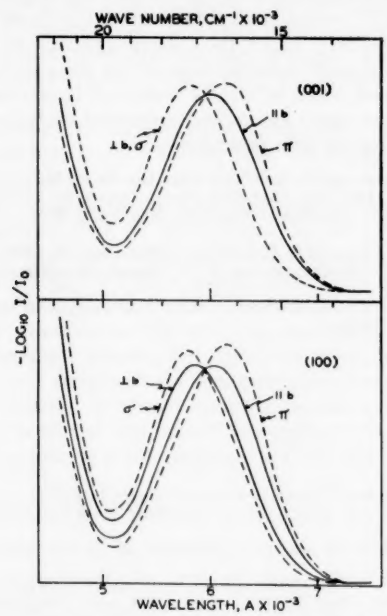

FIG. 1. Spectra of cobalt acetylacetonate (~1%) in aluminum acetylacetonate crystals about 2 mm thick. The measured spectra are the solid lines and the calculated spectra dashed, except that there is only one dashed curve for both the $\perp$ and σ (001) spectra.

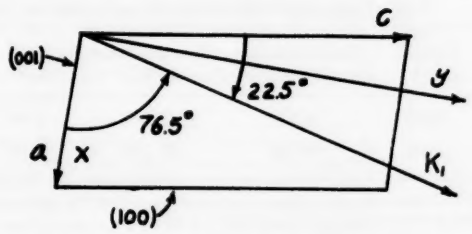

FIG. 2. Projections to scale on the ac plane. The projection of the molecular C_3 axis is parallel to K_1. The C_3 axis makes angles $\vartheta=\pm 31°$ to the b axis. In taking the (001) spectrum, the incident light is parallel to the y axis and is polarized with respect to the $z(b)$ axis.

A complete crystal structure of aluminum acetylacetonate has not been done. The space group[5] is $P2_1/c$, $\beta=98°50'$, and there are four molecules per unit cell (site symmetry 1). Singer[6] has measured the orientation of the molecular C_3 axis of chromium(III) acetylacetonate in this crystal by electron spin resonance. The C_3 axis has a projection on the ac plane parallel to the magnetic axis K_1 (Fig. 2). The C_3 axis makes a polar angle $\vartheta=\pm 31°$ with the b axis and therefore all the molecules are optically equivalent in the approximation of C_3 molecular symmetry. From Singer's data, $\vartheta=31°$ and $\varphi=76.5°$ for light incident on (001), and $\vartheta=31°$ and $\varphi=\pi-22.5°$ for light incident on (100). The reciprocal matrix of the coefficients of Eq. (1) is then calculated for each orientation.

$$(001):\quad \begin{pmatrix} 1.368 & -0.368 \\ -0.020 & 1.020 \end{pmatrix}$$

$$(100):\quad \begin{pmatrix} 1.522 & -0.522 \\ -0.447 & 1.447 \end{pmatrix}$$

The calculated π and σ spectra are plotted in Fig. 1. For the (001) spectrum, the first matrix above (second row) indicates that σ and $\perp$ spectra are sufficiently

[1] W. T. Astbury, Proc. Roy. Soc. (London) **A112,** 448 (1926).
[2] G. T. Morgan and H. D. K. Drew, J. Chem. Soc. **119,** 1059 (1921).
[3] The only previous spectra of crystals of trisacetylacetonates, is that of Cr by A. Chakravorty and S. Basu, J. Chem. Phys. **33,** 1266 (1960). These authors have not attempted to analyze the spectrum.
[4] K. Sone, J. Am. Chem. Soc. **75,** 5207 (1953).
[5] H. S. Jarrett, J. Chem. Phys. **27,** 1298 (1957).
[6] L. S. Singer, J. Chem. Phys. **23,** 379 (1955).

TABLE I. Data from the calculated π and σ spectra.

Crystal face	Band maximum, π cm^{-1}	Band maximum, σ cm^{-1}	$\epsilon_\sigma/\epsilon_\pi$[a]
(001)	16 250	17 100	0.99
(100)	16 200	17 200	0.97

[a] The molar extinction coefficient is defined by $I=I_0 10^{-\epsilon c l}$, where c is in moles/liter of crystal, and l is path length in cm.

similar to warrant a single curve for both. Data from the π and σ spectra are found in Table I.

DISCUSSION

The calculated π and σ spectra from the two different orientations of the crystal agree quite well, indicating that there is little breakdown of the trigonal symmetry in the monoclinic crystal. This observation is in agreement with Singer's data.[6] He found that the rhombic term in the spin Hamiltonian is small and certainly less than 10% of the axial term.

In an octahedral field the first excited state of Co(III) is $^1T_1$. The trigonal field resolves this level into $^1A_2$ and ^1E components. We identify the π and σ spectra respectively with these split components. This assignment assumes that the electronic selection rules are not broken down by vibrations. Support for this assumption is found in a comparison with the spectra of the trisoxalates.[7] Furthermore, we have observed the transition $^2E_a \leftarrow {}^2A_1$ of titanium(III) acetylacetonate[8] in this crystal at about 16 000 cm^{-1}. The band is nearly completely σ polarized as predicted by the electronic selection rules. In the spectrum of the trisoxalatocobaltate(III) ion, the next higher transition, $^1T_2 \leftarrow {}^1A_1$, is completely σ polarized as predicted by the electronic selection rules.[7] In the cobalt acetylacetonate note that the uv tail is strongly σ, polarized as expected.

We may get an approximation to the trigonal field parameter[9] K from the π and σ band maxima. The diagonal matrix elements of the trigonal field are readily calculated in the strong field representation, they are $-K(^1A_2)$ and $+\frac{1}{2}K(^1E)$. From the data in Table I, K is found to be $+600$ cm^{-1}.

This value of K may be in error by several hundred cm^{-1} since the vibrational progressions of the A and E components need not be the same. Calculation of K from band maxima receives some justification from an analysis of the ruby spectrum. By use of McClure's plot of the spectrum,[10] the calculated values of K are -360 and -490 cm^{-1} from the $^4T_2$ and $^4T_1$ bands, respectively. These may be compared to the more reliable value of -350 cm^{-1} obtained[9] from an analysis of the spin-forbidden transitions.

In conclusion, note that the sign of K found for the acetylacetonate is the opposite to that found for the oxalate ($K \sim -100$ cm^{-1}). The ionic model[11] predicts that if the radial parameters are unchanged, then the sign of K depends on the angle O-M-O within the chelate ring. K will have one sign if the angle is greater than 90° and the opposite sign if the angle is less than 90°. The radial parameters cannot be much different since the transition $^1T_1 \leftarrow {}^1A_1$ occurs at nearly the same wavenumber in both compounds. An indication of the bond angles may be obtained by a comparison to the corresponding chromium compounds. Although cobalt is slightly smaller than chromium and its bond angle may be slightly larger, the difference can not be large. The bond angle is found to be 93° in the acetylacetonate,[12] and about 83° in the oxalate.[13] It can be seen that these angles are in good agreement with the signs of the trigonal field parameters.

[7] T. S. Piper and R. L. Carlin, J. Chem. Phys. **33,** 608 (1960).
[8] R. L. Carlin and T. S. Piper (to be published shortly and to include crystal spectra of Ti(III) through Co(III) acetylacetonates).
[9] S. Sugano and Y. Tanabe, J. Phys. Soc. Japan **13,** 880 (1958).
[10] D. S. McClure, *Solid-State Physics*, edited by F. Seitz and D. Turnbull (Academic Press Inc., New York, 1959), Vol. IX, p. 488.
[11] T. S. Piper and R. L. Carlin, J. Chem. Phys. **33,** 1208 (1960).
[12] L. M. Shkol'nikova and E. A. Shugam, Kristallografiya **5,** 32 (1960).
[13] J. N. van Niekerk and F. R. L. Schoening, Acta Cryst. **5,** 196, 499 (1952).

NMR Fluorine-Fluorine Coupling Constants in Saturated Organic Compounds

L. PETRAKIS* AND C. H. SEDERHOLM

Department of Chemistry and Lawrence Radiation Laboratory, University of California, Berkeley 4, California

(Received February 8, 1961)

The spectra of several fluorine-substituted, saturated, organic compounds have been investigated. It has been found that the coupling constants between 1,2 fluorine atoms are usually near zero. The coupling constants between 1,3 fluorine atoms in a free chain are usually between 7 and 10 cps if all of the intermediate skeletal atoms are carbon atoms. If one of the intermediate skeletal atoms is a nitrogen atom, these coupling constants go up to between 10 and 17 cps. The coupling constants between 1,4 fluorine atoms are usually in the range 2–7 cps when a nitrogen atom is in the intermediate skeletal chain. Rings usually reduce all coupling constants below the above stated values.

Several exceptions are found to these generalizations. These generalizations with their exceptions lead the authors to believe that in the case of coupling between fluorine atoms, the main effect is not through-the-bonds, but rather a direct-through-space interaction. It is demonstrated that the restricted rotation about the carbon-carbon bonds has little to do with the near-zero coupling constants, but that these are readily explained on the basis of through-space coupling.

INTRODUCTION

IN 1956 Saika and Gutowsky[1] reported a near-zero coupling constant between the fluorine atoms on adjacent carbon atoms in the NMR spectrum of $CF_3CF_2N(CF_3)_2$. This appeared anomalous to them since fluorine-fluorine coupling constants were known to be large, and in particular, since the coupling constant between the fluorine atoms in the two nonequivalent perfluoromethyl groups was found to be 6 cps. Since that time, several other similar cases have been reported in the literature.[2–5] Furthermore, it has been generally assumed that the restrictions upon rotation are responsible for these near-zero coupling constants. This idea was presented in the literature by Crapo and Sederholm.[2]

The problem of the theoretical calculation of coupling constants between protons has been considered in the last few years by several authors,[6–8] who have extended Ramsey's[9] original treatment of the problem. It has been demonstrated that for the coupling between protons only the Fermi contact term contributes appreciably, and that magnetic dipolar and electron-orbital interaction may be neglected. On the other hand, not much real progress has been made in the theoretical prediction of F–F coupling constants, although a considerable number of such coupling constants have been determined experimentally. The most complete treatment of this problem is that of McConnell[6] who applied MO theory to the evaluation of the couplings in C_2F_4, and demonstrated that reasonable order of magnitude values could be obtained by considering contributions from magnetic dipolar and electron-orbital terms only. McConnell concluded that "nuclear spin coupling between pairs of nuclei other than protons presents a much more complex problem from a theoretical point of view. . .because, in general, both one-electron orbital and two-electron spin and orbital interactions make significant and sometimes comparable contributions to nuclear spin coupling." Karplus[7] arrived at a similar conclusion, although he suggested that electron-orbital and dipolar electron-spin terms often may be not very important. In this work we summarize and discuss the long-range coupling constants between fluorines for several organic compounds, and present a critical examination of the coupling mechanism which is generally assumed to proceed via the bonds.

EXPERIMENTAL AND INTERPRETATION

The spectra were run on a Varian spectrometer at 56.4 Mc/sec. All of the compounds listed gave first-order spectra with the exception of small second-order perturbations of some of the intensities. The samples were sufficiently pure so that no extraneous lines appeared. Coupling constants[10] are tabulated in Table I. The interpretation of all spectra was straightforward except for perfluorodiethylmethylamine,[11] compound 1. In this compound the multiplicity and overlap of lines made the interpretation somewhat complex. In Fig. 1 the observed spectrum is compared with the calculated spectrum based on the values of the coupling constants listed in Table I.

The spectrum of compound 2 consists of two lines, one containing seven equally spaced components, the other containing ten equally spaced components. Likewise, the spectrum of compound 3 consists of two lines, one containing five equally spaced components, the

* Present address: National Research Council, Ottawa, Canada.

[1] A. Saika and H. S. Gutowsky, J. Am. Chem. Soc. **78**, 4818 (1956).

[2] L. Crapo and C. H. Sederholm, J. Chem. Phys. **33**, 1583 (1960).

[3] C. A. Reilly, J. Chem. Phys. **25**, 604 (1956).

[4] G. Van Dyke Tiers, J. Am. Chem. Soc. **79**, 5585 (1957).

[5] J. A. Pople, W. G. Schneider, and H. J. Bernstein, *High Resolution Nuclear Magnetic Resonance* (McGraw-Hill Book Company, Inc., New York, 1959), p. 333.

[6] H. M. McConnell, J. Chem. Phys. **24**, 460 (1956).

[7] M. Karplus, J. Chem. Phys. **30**, 11 (1959); H. S. Gutowsky, M. Karplus, and D. M. Grant, *ibid.* **31**, 1278 (1959).

[8] M. J. Stephens, Proc. Roy. Soc. (London) **A243**, 274 (1957).

[9] N. Ramsey, Phys. Rev. **91**, 303 (1953).

[10] Most chemical shifts have been reported already by N. Muller, P. C. Lauterbur, and G. F. Svatos, J. Am. Chem. Soc. **79**, 1807 (1957).

[11] Henceforth all compounds will be referred to by their serial numbers listed in Table I.

TABLE I. Tabulation of coupling constants.

Serial number	Compound	Coupling constants (cps)
1	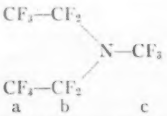	$J_{ab}=5.1$ $J_{ab'}=5.1$ $J_{ac}=6.8$ $J_{bc}=15.8$
2	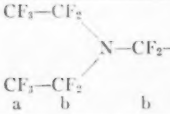	$J_{ab}=6.8$ $J_{ab'}=6.8$
3	$CF_3-CF_2-O-CF_2-CF_3$ a b b a	$J_{ab}=1.7$ $J_{ab'}=1.7$
4[a]	CF_3-CF_2-COOH a b	$J_{ab}=1.38$
5[b]	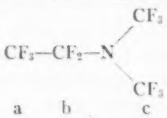	$J_{ab}\leq 1$ $J_{ac}=6$ $J_{bc}=16$
6	$CF_3-CF_2-CF_2-NF_2$ a b c d	$J_{ab}\leq 1$ $J_{ac}=8.6$ $J_{ad}=2.2$ $J_{bc}=1$ $J_{bd}=10.5$ $J_{cd}\leq 1$
7	$CF_3-CF_2-CF_2-COOH$ a b c	$J_{ab}\leq 1$ $J_{ac}=9.9$ $J_{bc}\leq 1$
8	$CF_3-CF_2-CF_2-COOCH_3$ a b c	$J_{ab}\leq 1$ $J_{ac}=9.0$ $J_{bc}\leq 1$
9	$CF_3-CF_2-CFClH$ a b c	$J_{ab}\leq 1$ $J_{ac}=10.8$ $J_{bb'}=270.4$ $J_{bc}=14.6$ $J_{b'c}=14.6$
10	$(CF_2)_3\equiv CF$ a b	$J_{ab}=4.0$
11	$CF_a-CF_2-CF_2H(D)$ a b c	$J_{ab}\leq 1$ $J_{ac}\leq 1$ $J_{bc}=4.0$–4.5
12	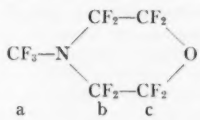	$J_{ab}=13.6$
13	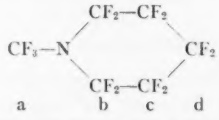	$J_{ab}=16.4$
14	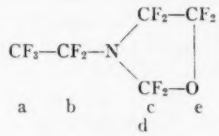	$J_{ab}\leq 1$ $J_{ac}=6.5$ $J_{ad}=6.5$ $J_{ae}\leq 1$ $J_{bc}=9.9$ $J_{bd}=9.9$ $J_{be}\leq 1$ $J_{cd}\leq 1$ $J_{ce}\leq 1$ $J_{de}=3.5$
15[c]	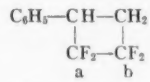	$J_{ab}\leq 1$ $J_{ab'}\leq 1$
16[d]	$CF_2Br-CFBrCl$ a c b	$J_{ab}=159$ $J_{ac}=13$ $J_{bc}=14$
17[e]	$CF_2Br-CFHCl$ a c b	$J_{ab}=175$ $J_{ac}=18$ $J_{bc}=18$

[a] See reference 3 in text. [b] See reference 1 in text. [c] See reference 5 in text. [d] See reference 17 in text. [e] See reference 18 in text.

other containing seven equally spaced components. Although very surprising, the analysis of these spectra was unambiguous and yielded the values of J listed in Table I.

DISCUSSION

The problem of F–F coupling, as pointed out already, is certainly more complicated than the corresponding coupling between protons due to the expected contributions to the coupling constant by the magnetic dipolar and electron-orbital terms in addition to the Fermi contact term. This is reasonable because atomic p orbitals centered on F atoms contribute greatly to the bonding, while the "p character" of atomic orbitals centered on protons is considered small.

Qualitatively, one can readily account for all F–F coupling constants in saturated compounds thus far investigated if one assumes that the major contribution to the coupling constants comes about as a result of a direct-through-space coupling rather than coupling through-the-bonds. Roberts *et al.*[12] have suggested a similar direct-through-space interaction to explain long-range H–F coupling constants. The large excursions of the p electrons in fluorine atoms make it reasonable to assume that such an effect could be significant in the case of F–F coupling constants and not significant in the case of H–H coupling constants. Similar arguments would apply to couplings between other atoms which have non-s electrons. Direct-through-space coupling of two nuclei A and B separated by two or more bonds may take place either through one-electron or through two-electron interaction. Physically, the one-electron part arises because nucleus A interacts magnetically with an electron, which in turn interacts with nucleus

[12] D. R. Davis, R. P. Lutz, and J. D. Roberts, J. Am. Chem. Soc. **83**, 246 (1961).

B (nuclear moment A: electron: nuclear moment B); the two-electron part arises because nucleus A induces a perturbation on a "local" electron, which interacts directly with an electron on nucleus B, which then interacts magnetically with nucleus B (nuclear moment A: electron 1: electron 2: nuclear moment B).

We first examine in detail the near-zero coupling constants. They appear in many cases between fluorine atoms on adjacent, saturated carbon atoms. These cases fall into two classes, one where relatively free rotation is allowed around the carbon-carbon bond, and another where rings limit the free rotation about the carbon-carbon bond. Near-zero coupling constants occur in both of these cases. However, there seems to be no set type of molecule which always yields a near-zero coupling constant. For instance, in compounds 1, 2, 3, and 4 the coupling constants between the CF_3 group and the adjacent CF_2 group are nonvanishing, whereas the coupling constants between the CF_3 group and the adjacent CF_2 group are nearly zero in a whole host of compounds. It has been assumed that the near-zero coupling constants come about as a result of averaging nonzero coupling constants over the three stable configurations with respect to rotation about the connecting carbon-carbon bond. Due to the common occurrence of this phenomenon, if this explanation is valid, one must assume that the coupling constant does not vary much from compound to compound but is only a function of the dihedral angle, as in the case of hydrogen (Karplus).[7] However, this would lead one to predict that the coupling constants in all compounds having the CF_3–CF_2 group would be nearly zero which is not the case. Hence, it appears that the near-zero coupling is not explained by any accidental, mutual cancellation of the coupling constants averaged over three staggered configurations.

In terms of the various contributions to the coupling constant, one might assume that these vanishing coupling constants are the result of mutually canceling interactions (one- and two-electron integrals of the same order of magnitude but of opposite sign). This, however, seems unreasonable because (1) the appearance of the near-zero couplings is rather widespread, and an accidental mutual cancellation, to better than 1 cps, of contributing interactions, each of which is probably several cps, seems highly unlikely; (2) this explanation does not account for the appearance of similar "anomalous" couplings in several other systems structurally unrelated to the perfluoro ethyl groups. For example, in lead tetraethyl[13] $J_{CH_2-Pb}=42$ cps but $J_{CH_3-Pb}=142$ cps. A more likely explanation of the anomalous coupling constants can be given, we feel, in terms of through-space-coupling. The near-zero coupling constants always occur between fluorine atoms on adjacent

[13] E. B. Baker, J. Chem. Phys. **26,** 960 (1957). For other related examples see P. T. Narasimham and M. T. Rogers, J. Am. Chem. Soc. **82,** 34 (1960); R. E. Dessy, T. J. Flautt, H. H. Jaffé, and G. F. Reynolds, J. Chem. Phys. **30,** 1422 (1959); G. J. Karabatsos, J. Am. Chem. Soc. **83,** 1230 (1961).

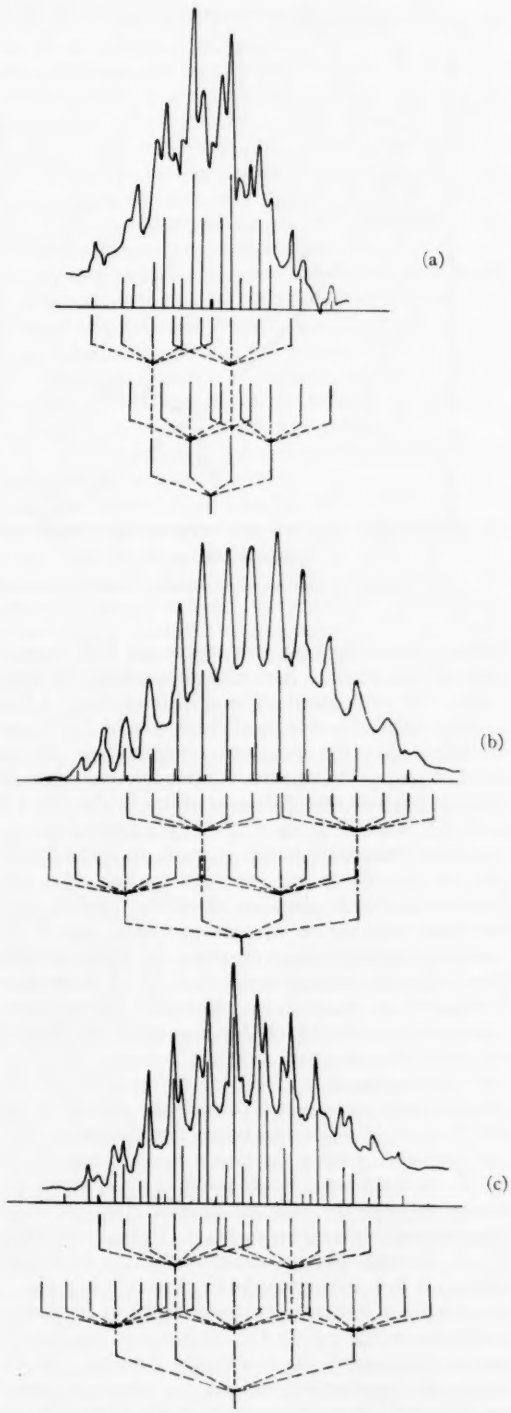

FIG. 1. Experimental and theoretical fluorine resonance spectrum of $(CF_3-CF_2)_2-N-CF_3$. (a) $C\underline{F}_3-CF_2-$. (b) $CF_3-C\underline{F}_2-$. (c) $C\underline{F}_3-N$.

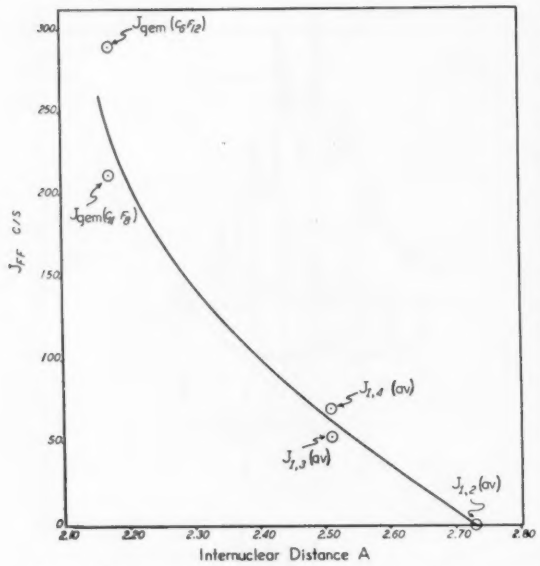

FIG. 2. Fluorine-fluorine coupling constant versus internuclear distance.

carbon atoms. Such fluorine atoms are held apart in space by the bonding. Assuming all bonding to be tetrahedral, the carbon-carbon bond distance to be 1.54 A and the carbon-fluorine bond distance to be 1.33 A, and assuming that the staggered configurations are the favored ones, the closest fluorine-fluorine approach between the two sets of fluorine atoms in the CF_3–CF_2 or R–CF_2–CF_2–R′ group is 2.73 A. We propose that the coupling through-the-bonds is small, in contradistinction to the case in the hydrogen analogs; that such through-the-bonds coupling diminishes rapidly with increasing number of intervening bonds; that in the case of coupling between fluorines the main contribution is directly-through-space; that 2.73 A is too great a distance to result in an observable through-space contribution; and that 2.73 A is just outside the distance at which through-space coupling becomes important. (It is reassuring to note that the distance at which the coupling approaches zero is equal to the sum of the van der Waals radii of the two interacting fluorine atoms.) One can then readily see that a small change in the C—C—R bond angle would result in closer stable distances between the adjacent fluorine atoms and thus in an observable coupling constant. This opening of the C—C—R angle can be brought about by steric hindrance, if R is sufficiently bulky. Figure 2 is a plot of the coupling constants between fluorines in various structural groups versus the internuclear distance between the magnetically interacting fluorines. For the structures involving free rotation, the constants plotted are "derived" from the observed coupling constants by considering all the staggered configurations that the two interacting groups may assume relative to each other. The internuclear distance between gem-fluorines in perfluoro cyclohexane assuming tetrahedral angles and normal bond distances is 2.17 A. The coupling[14] is 284 cps. For perfluoro cyclobutane, the gem-fluorine distance is again 2.17 A and the average coupling constant of several substituted cyclobutanes[15] is 211 cps. The near-zero coupling between 1,2 fluorine atoms which are separated by ~2.73 A in two of the three possible staggered configurations leads one to assign a value of zero to J for fluorine atoms separated by this distance. Next we consider the coupling constant between 1,3 fluorines (fluorines on skeletal atoms which are β to each other). In two of the nine possible staggered configurations of the –CF_2–CF_2–CF_2-group the 1,3 fluorines are closer to each other than the closest stable distance between 1,2 fluorines. Calculating on the basis of the staggered configurations and the above bond distances and angles, the 1,3 fluorine-fluorine distance in these two configurations[16] is 2.51 A.

The other seven configurations yield F–F distances which are greater than 2.73 A and correspond to zero coupling. We weight all nine of these possible configurations equally, although there may be some small barrier against the configurations which do not correspond to a zigzag carbon skeleton. On this basis, the coupling constant between 1,3 fluorine atoms should be $\frac{9}{2}\times(12)=54$ if *all* nine configurations were contributing equally to the coupling constant.

One may extend this calculation with less precision to the 1,4 fluorine coupling constants. These fluorine atoms are separated by five bonds and probably are essentially not coupled through the bonds. In as crude a calculation as this, one cannot hope to tell the difference between a nitrogen atom in the chain with 90° bond angles, and a carbon atom in the chain with 109½° bond angles. The calculation is again made for an all carbon chain with tetrahedral angles, but it should be about the same if a nitrogen takes the place of one of the chain carbon atoms. Again, taking the staggered configurations as the stable ones, there are 27 different relative positions for a pair of fluorines on the 1 and 4 carbon atoms. All of the distances between the fluorines are greater than 2.73 A except for four configurations in which the distances are 1.76 A (two cases) and 2.46 A (two cases). Certainly, the two configurations corresponding to the 1.76 A cannot exist as preferred configurations because of the close fluorine-fluorine approach. In order to increase this distance, one must rotate about some of the carbon-carbon bonds which should be relatively easy to do. It seems reasonable that rotation will occur about the carbon-carbon bonds until the fluorine atoms come to a distance of approximately 2.5 A, 0.2 A less than the van der Waals radii. This rotation lengthens the 2.46 A fluorine-fluorine distance to a distance

[14] J. Feeney and L. H. Sutcliffe, Trans. Faraday Soc. **56,** 1559 (1960).

[15] W. D. Phillips, J. Chem. Phys. **25,** 949 (1956).

[16] There is some evidence that these configurations are not the stable ones, but the structural data are not sufficient to warrant their use over the tetrahedral assumption. C. W. Bunn and G. R. Howells, Nature **174,** 549 (1954).

greater than 2.73 A and therefore these configurations can be neglected in the calculation. The two contributing configurations have a weight of 2/27, and therefore, the coupling constant for 1,4 fluorines should be $27(5.2)/2 \sim 70$ cps.

Thus, it appears that the coupling between two magnetic nuclei is a very sensitive function of the internuclear distance. Of course it would be naive to assume a complete, simple correlation between J_{FF} and internuclear distance D_{FF}, for one would be neglecting the obviously important dependence of J on other structural factors. For instance, the gem-fluorine-fluorine distances in the series C_3F_6, C_4F_8, and C_6F_{12} are nearly equal, and yet the geminal coupling constants vary by a factor of two in this series. On the other hand, through-space coupling is both useful and reasonable, particularly where non-*s* electrons are available. In this case one can certainly expect direct-through-space interaction to be more effective than the through-the-bonds "telegraphed" interaction which would require cooperative coupling of many bonding electrons.

Direct-through-space coupling is also capable of explaining why in compounds with the general formula CF_2X–CFYZ the two coupling constants between the gem-fluorines and the third fluorine atom are almost the same.[17,18] Nair and Roberts[19] have suggested that in all such cases there is a rapid interconversion among the three nonequivalent rotamers, but such rapid interconversion would not average the chemical shift between the gem-fluorines "unless the residence times of the molecule in each of the various rotational conformations are equal." Moreover, the observed chemical shifts and coupling constants would be the time-weighted averages over the three rotamers. In such a case, because of the relative magnitudes involved, the chemical shift is a much more sensitive function of the relative population of the rotamers. A change of a few percent in the population would result in a change in the chemical shift of several hundred cps, but only ~1-cps change in the coupling constant.

At room temperature the difference in depths of the three potential minima is probably small enough so that approximately equal population of the three rotational isomers is a good approximation. Direct-through-space coupling predicts a zero coupling constant between the *trans* fluorine atoms, but a small, constant Jg between *gauche* fluorine atoms. An almost equal population of the three rotational forms, while preserving the nonequivalence of the gem-fluorines, would result in almost equal coupling constants, as observed, equal to approximately $\frac{2}{3}Jg$.

In compound 5, the coupling constants are what would be expected on the basis of the model presented, the 1,2 fluorine atoms being coupled by less than one cycle, the 1,3 fluorine atoms being coupled by 16 cps, and the 1,4 fluorines being coupled by 6 cps in reasonable agreement with the calculated values. In compound 1 which is very similar to 5, the coupling constants are also similar except for the coupling between the 1,2 fluorine atoms. Here, that coupling has gone up to 5.1 cps. This might be expected from a model of the compound since there are a large number of atoms crowded around the central nitrogen atom. This tends to increase the C—C—N bond angle, thus throwing the 1,2 fluorine atoms closer to each other, and increasing the coupling constant. One might expect this effect to be more pronounced in compound 2 where another perfluoroethyl group is taking the place of perfluoromethyl, and indeed this is the case. Here, the 1,2 fluorine coupling constant has gone up to 6.8 cps which would imply a further increase in the C—C—N angle, as is expected.

In compound 3, the 1,2 coupling constant is again nonvanishing because of opening of the C—C—O bond angle due to steric hindrance between the two ends of the molecule. Note that here the 1,2 coupling constant is less than in compound 1 since the extra perfluoromethyl group is absent, thus not yielding as great an amount of steric hindrance. Also, the 1,4 coupling constant is about what it is in compound 6 and less than in compounds 1 and 2. A tertiary nitrogen in the chain certainly throws the 1,4 carbon atoms closer together than a secondary oxygen in the chain.

In compound 4 the coupling constant is small, but nonzero. This may come about through the bonds, although there may also be a small opening of the C—C—C bond angle due to the steric repulsion between the methyl group and the carboxyl group. Compound 7 gives results very similar to this with the 1,3 fluorine coupling constant being slightly less than the 1,3 fluorine coupling constants in compounds 1 and 5. This is what is expected since in compounds 1 and 5 an intermediate chain atom is a nitrogen atom with approximately 90° bond angles, whereas in this compound all intermediate chain atoms are carbon atoms with $109\frac{1}{2}°$ bond angles, thus throwing the 1,3 fluorine atoms further apart. It is not readily apparent why the 1,2 coupling constant in this compound is smaller than in compound 4; however, this difference is minor and the electronic structure has changed substantially in this area of the molecule. In compound 8 the coupling constants are very similar to compound 7. The decrease in the 1,3 fluorine atom interaction is reasonable since the added methyl group will interfere with the perfluoromethyl group, partially opening up the bond angle between the α, β, and γ carbon atoms, thus taking the 1,3 fluorine atoms further apart. Compound 6 gives very similar results. Again, it should be noted that the 1,3 fluorine atom coupling constant is smaller when all of the intermediate atoms are carbon atoms, than when one of them is a nitrogen atom.

Compound 9 again shows two different kinds of 1,2 coupling constants, a near-zero one which results from normal bond angles; and one which is equal to 14.6 cps

[17] J. J. Drysdale and W. D. Phillips, J. Am. Chem. Soc. **79**, 319 (1957).
[18] J. N. Shoolery and B. Crawford, Jr., J. Mol. Spectroscopy **1**, 270 (1957).
[19] P. M. Nair and J. D. Roberts, J. Am. Chem. Soc. **79**, 4565 (1957).

probably resulting from the steric repulsion between the Cl and I atoms and the adjacent CF_2 group, thus throwing the two sets of fluorine atoms closer together. The 1,3 coupling constant is quite normal. Compound 10 shows a large 1,2 coupling, again due to the steric repulsion of the three CF_3 groups, thus bringing each of them closer to the lone fluorine atom.

The spectra of compounds 11 were reported by Tiers[4] in connection with an isotopic substitution investigation. The two near-zero coupling constants were inferred from his paper. The near-zero coupling assigned to the 1,2 coupling is quite reasonable; however, on the basis of the other compounds we have investigated the near-zero coupling between the 1,3 fluorine atoms seems highly unlikely.

The spectra of compounds 12 and 13 are in general broad, and only a few coupling constants can be determined. These constants are consistent with coupling constants in similar compounds. Moreover, from the width of the unresolved peaks one can set an upper limit of about 6 cps on all other undetermined coupling constants. From our model, one would expect near-zero coupling constants for all pairs of fluorines except the 1,3 axial-axial fluorines. In one of the two canonical chair forms, these fluorines are closer than 2.73 A, and should give an observable coupling. However, a slight flattening of the ring would rapidly increase the internuclear distance to over 2.73 A corresponding to a near-zero coupling constant.

When the ring is reduced to five members such as in compound 14, fluorine atoms which are on adjacent carbon atoms are still not coupled, but fluorine atoms removed by one more bond are capable of getting closer together and therefore are slightly coupled. The 1,4 coupling constants across the nitrogen atom between the side chain and ring are quite normal. The 1,3 coupling constants across the nitrogen atom between the side chain and ring are somewhat smaller than usual, but the geometry of the strained ring system may keep these two sets of atoms further apart than they would be in an unrestrained linear chain. It is reassuring to note that the coupling constants across the nitrogen atom are the same to each of the two sets of ring fluorines which are adjacent to the nitrogen atom. This would be expected if it is indeed a through-space coupling since these two sets of atoms occupy similar positions in space with respect to the perfluoroethyl group. However, the electronic structure in the two N—C bonds should be somewhat different due to the asymmetrically placed oxygen atom, and hence if the coupling were through-the-bonds, one would expect a different coupling constant between the nonring fluorines and these two sets of ring fluorines.

In compound 15, the four-membered ring certainly holds the two sets of fluorine atoms far enough apart to yield a near-zero coupling constant which is observed. It is to be noted that in this case the fluorines are probably locked into the nearly eclipsed configuration, whereas in the six-membered rings, the fluorine atoms are restrained to two of the three staggered configurations. All of these cases result in near-zero coupling constants. It is hard to imagine any kind of function of J vs dihedral angle such that the average of the three staggered configurations would yield zero, the average over the two *gauche* staggered configurations would yield zero, and the value of the coupling constants corresponding to eclipsed and 120° would be zero, except for the trivial case where the coupling constant equals zero for all dihedral angles. Therefore, this set of examples implies again that averaging over various dihedral angles has little to do with the near-zero coupling constants.

In compounds 16 and 17, the 1,2 coupling constants are nonzero probably because of shortening of the fluorine-fluorine distance due to steric effect caused by the other halogens present.[20]

CONCLUSIONS

The coupling constants between fluorine atoms in saturated organic compounds can be explained if one assumes that coupling takes place primarily directly-through-space rather than through-the-bonds. Moreover, the coupling constant (other things being equal) seems to be a sensitive function of the internuclear distance between the magnetically interacting nuclei. The coupling constants between 1,2 fluorine atoms are usually nearly zero unless some shortening of the fluorine-fluorine distance occurs due to steric hindrance caused by neighboring groups. The coupling constants between 1,3 fluorine atoms in a free chain are usually between 7 and 10 cps if all the intermediate skeletal atoms are carbon atoms. If one of the intermediate atoms is a nitrogen atom, these coupling constants go up to the range 10–17 cps due to the smaller nitrogen bond angles. The coupling constants between 1,4 fluorine atoms are usually in the range 2—7 cps if a nitrogen atom is in the intermediate skeletal chain. Rings usually hold the molecules more firmly apart, reducing all of the coupling constants.

ACKNOWLEDGMENTS

This research was supported in part by the United States Atomic Energy Commission. The samples were for the most part obtained from Dr. Zeffert and Dr. Klapper of the Army Chemical Center. The samples of perfluorodiethylmethylamine and perfluorotriethylamine were obtained from Dr. Young of the University of Florida. The authors wish to express their appreciation to the above for their aid in this research.

[20] *Note added in proof.* In a private communication, R. K. Harris of University Chemistry Laboratories, Cambridge, England, has informed us of work he has recently completed which also supports through-space coupling. He has measured the *gauche* and *trans* coupling constants between fluorine atoms on substituted ethanes and found the *gauche* coupling constant to be several times the *trans* constant. In SF_5-OSO_2F, he has found the coupling constant between the equitorial fluorines and the lone fluorine to be an order of magnitude larger than the coupling constant between the axial fluorine and the lone fluorine.

THE JOURNAL OF CHEMICAL PHYSICS VOLUME 35, NUMBER 4 OCTOBER, 1961

On the Parameters Used in Semiempirical Molecular Orbital Theory for Conjugated Hydrocarbons*†

PETER G. LYKOS

Department of Chemistry, Carnegie Institute of Technology,‡ Pittsburgh 13, Pennsylvania, and Department of Chemistry, Illinois Institute of Technology, Chicago 16, Illinois

(Received January 11, 1961)

Within the π-electron approximation, formulas are displayed for some of the properties of the benzene molecule. The integrals which enter the formulas are treated as empirical parameters. The one-electron integrals are interpreted as being over-orthogonalized atomic orbitals consistent with the use of zero differential overlap for the two-electron integrals. An attempt is made to find one set of parameters which will simultaneously account for several properties of the benzene molecule. The resolution of benzene integrals into empirically evaluated components in a quantum mechanically well-defined way firstly provides a more critical test of the level of the π-electron approximation and secondly renders more sure the use of these parameter values for other molecules.

I. INTRODUCTION

THE semiempirical π-electron theory of the electronic structure and electronic spectra of complex unsaturated molecules, recently advanced by Pariser and Parr,[1] by now has proved remarkably successful in correlating and predicting various properties of various molecules.[2] The present paper is concerned with the values and interpretation of the empirical elements of their method.

Heretofore few attempts have been made to treat diverse molecular properties with any single consistent semiempirical scheme.[3] The first purpose of the present paper is to do just this with the Pariser-Parr method. An attempt will be made to show clearly what assumptions are usually made in applying the π-electron approximation to the calculation of various physical properties. A second purpose will be to understand in a more fundamental way the nature of the various theoretical parameters that enter the descriptions and to determine suitable semiempirical values for them. In order to facilitate such later redetermination of these parameters as may be necessary, the equations which determine them will be displayed in full.

In the present paper, after the method is briefly described, the benzene molecule is considered once more. First theoretical expressions are given for several of its physical properties, and then "best" parameter values are obtained by fitting the theoretical expressions to the experimental data.

II. PARISER-PARR METHOD APPLIED TO BENZENE

The Pariser-Parr method involves the use of the π-electron approximation, wherein it is assumed that certain properties of molecules such as benzene may be accounted for by explicit consideration of the π-electrons only. Mathematically expressed, an energy operator of the following form is assumed for the π-electrons of such a molecule:

$$H(1, 2, \cdots, n_\pi) = \sum_{\mu=1}^{n_\pi} \mathbf{H}_{\text{core}}(\mu) + \sum_{\mu>\nu=1}^{n_\pi} r_{\mu\nu}^{-1}. \qquad (1)$$

Use of Eq. (1) within a variational calculation is rigorously justified[4] provided one is willing to assume the following: (1) That the total wave functions for the molecular states of interest are antisymmetrized products of parts describing the σ electrons and parts describing the π electrons; (2) That the σ and π parts are orthogonal in the detailed sense that there is some set of orthonormal spin orbitals which can be partitioned into two subsets, the "sigma" orbitals and the "pi" orbitals; (3) That when the σ and π parts are expressed in terms of Slater determinants built from these orbitals, only the "sigma" orbitals enter the description of the σ parts and only the "pi" orbitals enter the description of the π parts; and (4) That the σ description is the same for all states of interest. Thus, *in principle*, the operators $\mathbf{H}_{\text{core}}(\mu)$ are well defined and are fixed for a fixed such "mean" σ description.

Wave functons for the various π-electron states are to be determined variationally; these are constructed in this method from the overlapping $2p\pi$ atomic orbitals χ_p (whatever their explicit form may be)[5] on the

* From part of a thesis submitted in partial fulfillment of the requirements of the degree Doctor of Philosophy at the Carnegie Institute of Technology, October 11, 1954.

† A preliminary version of this work was presented in the Carnegie Inst. Technol. Tech. Rept. on Research in Theoretical Chemistry (January 1, 1958).

‡ Supported in part by a research grant from the National Science Foundation to Carnegie Institute of Technology.

[1] R. Pariser and R. G. Parr, J. Chem. Phys. **21**, 466, 767 (1953).

[2] R. Pariser, J. Chem. Phys. **24**, 250; **25**, 1112 (1956).

[3] J. A. Pople, Trans. Faraday Soc. **49**, 1375 (1953); J. Phys. Chem. **61**, 6 (1957).

[4] P. G. Lykos and R. G. Parr, J. Chem. Phys. **24**, 1166; **25**, 1301 (1956).

[5] O. Sovers and W. Kaufmann, presented at the Sanibel Island Conference on Quantum Chemistry and Solid State Physics, January 2–13, 1961, and R. L. Miller of this laboratory are examining the extent to which atomic π orbitals are distorted in the $^2\pi_u$ state of H_2^+ in order to gain some insight into this problem. Preliminary results indicate that a significant amount of $d\pi$- and possibly higher $p\pi$ or $f\pi$-type orbitals mix with the $p\pi$-type orbitals.

TABLE I. Formulas, observed values, and calculated values for various properties of the benzene molecule.

Electronic excitation energy to lowest electronic state of following symmetries:	Core integrals	γ_{00}^{λ}	γ_{01}^{λ}	γ_{02}^{λ}	γ_{03}^{λ}	Calc (ev)	Obs (ev)
$^1B_{2u}$	$-2(\beta_{01}^{\lambda}-\beta_{03}^{\lambda})$	0	1/6	−1/2	1/3	—	4.91[a]
$^1B_{1u}$	$-2(\beta_{01}^{\lambda}-\beta_{03}^{\lambda})$	1/3	−5/6	7/6	−2/3	—	6.19[a]
$^1E_{1u}$	$-2(\beta_{01}^{\lambda}-\beta_{03}^{\lambda})$	1/6	2/3	−2/3	−1/6	—	7.02[a]
$^3B_{1u}$	$-2(\beta_{01}^{\lambda}-\beta_{03}^{\lambda})$	−1/3	1/2	−1/6	0	—	3.79[a]
$^3B_{2u}$	$-2(\beta_{01}^{\lambda}-\beta_{03}^{\lambda})$	0	1/6	−1/2	1/3	(4.91)	4.91
$^3E_{1u}$	$-2(\beta_{01}^{\lambda}-\beta_{03}^{\lambda})$	−1/6	1/3	−1/3	1/6	4.35	4.35
$2^{-\frac{1}{2}}(V_{1-2}\mid\mid V)_{03}$[b]	0	1	−5	5	−1	−0.81	b
E_K-E_N	$-2(\beta_{01}^{\lambda}-\beta_{03}^{\lambda})$	0	−1/6	0	1/6	4.56	3.56[c]
E^+-E_N	$-(\alpha^{\lambda}-\beta_{12}^{\lambda})$ $-(\beta_{01}^{\lambda}-\beta_{03}^{\lambda})$	−1/2	1/3	0	1/6	d	9.52
E^--E_N	$(\alpha^{\lambda}-\beta_{12}^{\lambda})$ $-(\beta_{01}^{\lambda}-\beta_{03}^{\lambda})$	1/2	1/3	0	1/6	d	0 to 1.7
$\chi_{\perp}-\chi_{\parallel}\approx\chi_{\perp}^{\pi}$	$-8\beta_{01}^{\lambda H}$[e]	0	0	0	0	f	54×10^{-6} erg/gauss

[a] Used to empirically fix $(\beta_{12}^{\lambda}-\beta_{14}^{\lambda})$, $(\gamma_{00}^{\lambda}-\gamma_{01}^{\lambda})$, $(\gamma_{00}^{\lambda}-\gamma_{02}^{\lambda})$, $(\gamma_{00}^{\lambda}-\gamma_{03}^{\lambda})$. See reference 1.
[b] This is a configuration interaction matrix element between two states corresponding to one-electron jumps and should be zero. See reference 10.
[c] "Best" estimate of vertical resonance energy of 3.17 ev was obtained from "theoretical" values of integrals, while 3.56 was based more on experiment and hence is more appropriate for an empirical fit. See reference 21.
[d] See text.
[e] The unit of diamagnetic susceptibility here is $(2\pi es/6hc)^2$.
[f] The best uncorrected calculated values are about 70% of the experimental result. See text.

several conjugated atoms taken in linear combination to form LCAO-MO's. For the case of benzene, these MO's are determined by symmetry conditions alone and from them many many-electron determinental wave functions can be formed and mixed by the linear variational method to give approximate molecular wave functions, and molecular properties can be computed as desired. This was what was done by Goeppert-Mayer and Sklar[6] in their classic treatment of the benzene spectrum. The various integrals which enter the calculations, namely the core integrals,

$$\alpha_p=\int\chi_p(1)\mathbf{H}_{\text{core}}(1)\chi_p(1)dv(1), \tag{2}$$

$$\beta_{pq}=\int\chi_p(1)\mathbf{H}_{\text{core}}(1)\chi_q(1)dv(1), \tag{3}$$

and the electronic repulsion integrals,

$$(pq\,|\,rs)=\iint\chi_p(1)\chi_q(1)(e^2/r_{12})\chi_r(2)\chi_s(2)dv(1)dv(2), \tag{4}$$

where determined "purely theoretically" by those authors.

However, the "pure theoretical" evaluation may be challenged. For the α_p and β_{pq}, the above-quoted "existence theorem" on the operator $\mathbf{H}_{\text{core}}(\mu)$ shows that these quantities rightly may be treated semiempirically until such time (yet far off) as *best possible* mean σ wave functions and *best possible* π distorted atom valence state orbitals are known. And for the $(pq\,|\,rs)$, one similarly feels that semiempirical interpretation may be better. These are features of the Pariser-Parr method.

In addition, one has the problem of the large number of the $(pq\,|\,rs)$ in a large molecule. Some means for handling or simplifying this bookkeeping is a must; one is provided in the Pariser-Parr method.

Preparatory to specifying just what this last device is, one may note that the molecular orbitals in benzene may be written in the form

$$\phi=6^{-\frac{1}{2}}\sum_{p=1}^{6}\omega^{jp}\lambda_p, \tag{5}$$

where $\omega=\exp(2\pi i/6)$ and where the λ_p are the *orthonormal* semilocalized orbitals of Löwdin[7,8]:

$$\lambda_p=\sum_q\chi_q S_{qp}^{-\frac{1}{2}}$$

[6] M. Goeppert-Mayer and A. Sklar, J. Chem. Phys. **6**, 645 (1938).

[7] P.-O. Löwdin, J. Chem. Phys. **18**, 365 (1950).
[8] B. C. Carlson and J. M. Keller, Phys. Rev. **105**, 102 (1957), have shown that the Löwdin orthogonalization corresponds to finding that orthogonalization which minimizes $\Sigma\int|\lambda_i-\chi_i|^2dv$, i.e., that gives orthogonal functions that best resemble the original nonorthogonal set of orbitals.

where $S_{pq}^{-\frac{1}{2}}$ is the pqth element of the inverse square root of the overlap matrix $\mathbf{S}$ and where

$$S_{pq}=\int \chi_p^* \chi_q dv. \tag{6}$$

These enter in this formulation in the integrals

$$\alpha_p^{\lambda}=\int \lambda_p(1)\mathbf{H}_{\text{core}}(1)\lambda_p(1)dv(1), \tag{7}$$

$$\beta_{pq}^{\lambda}=\int \lambda_p(1)\mathbf{H}_{\text{core}}(1)\lambda_q(1)dv(1), \tag{8}$$

$$(pq|rs)^{\lambda}=\iint \lambda_p(1)\lambda_q(1)(e^2/r_{12})\lambda_r(2)\lambda_s(2)dv(1)dv(2). \tag{9}$$

And one has the *exact* relation

$$S_{pq}^{\lambda}=\int \lambda_p(1)\lambda_q(1)dv(1)=\delta_{pq}. \tag{10}$$

But further, and this is how the problem of the superabundance of $(pq|rs)$ integrals gets simplified in the Pariser-Parr method, one finds by actual accurate calculations using Slater $2p_z$ orbitals (which are probably not the best orbitals to use but which may suffice for this purpose) that the integrals $(pq|rs)^{\lambda}$ are very small except those of the Coulomb type[9]

$$\gamma_{pq}^{\lambda}\equiv(pp|qq)^{\lambda}\approx(pp|qq). \tag{11}$$

It is assumed that the $(pq|rs)^{\lambda}$ save these are zero.[1] The results then are formulas containing α_p^{λ}, β_{pq}^{λ}, and γ_{pq}^{λ} as basic semiempirical quantities[10] everywhere, and with the assumption of zero differential overlap for the orthogonalized orbitals in the electronic repulsion terms.[11]

In assessing the ultraviolet absorption spectrum of benzene, Pariser and Parr stated that the β_{pq} were being neglected for non-neighbor atoms.[1] As a matter of fact, this simplification is unnecessary and will not be invoked here. There are really eight semiempirical parameters in the theoretical description of the benzene molecule in the Pariser-Parr method:

$$\alpha^{\lambda}\equiv\alpha_p^{\lambda},\ \beta_{01}^{\lambda},\ \beta_{02}^{\lambda},\ \beta_{03}^{\lambda};\qquad \gamma_{00}^{\lambda},\ \gamma_{01}^{\lambda},\ \gamma_{02}^{\lambda},\ \gamma_{03}^{\lambda}.$$

Table I gives formulas for a number of properties of benzene expressed in terms of these parameters. Brief remarks on the derivation of the various formulas and on the empirical evaluation of the parameters follow.

[9] R. McWeeney, Quart. Progr. Rept. Solid-State and Molecular Theory Group, M.I.T., January 15, 1954, p. 25.

[10] These can as well be labeled α_p, β_{pq}, and γ_{pq}, as has been done up to now with this method. It is important to recognize the true nature of these parameters, however, so superscripts are retained in the present paper.

[11] R. G. Parr, J. Chem. Phys. **20,** 1499 (1952).

Electronic Energy Levels

The molecular orbital wave function of the ground state of benzene is, in a standard notation,[12] $(0\bar{0}1\bar{1}-1-\bar{1})$, where the numbers indicate molecular orbitals, the bars indicate spin β, no bars indicate spin α, and the parentheses indicate an antisymmetrized and normalized product wave function (Slater determinant). The energy for this is, by the standard rules,[13]

$$\begin{aligned}E_N&=2I_0+2I_1+2I_{-1}+J_{00}+J_{11}+J_{-1-1}+4J_{01}-2K_{01}\\&\quad+4J_{0-1}-2K_{0-1}+4J_{1-1}-2K_{1-1}\\&=2I_0+4I_1+15J-4K_{01}-2K_{02}.\end{aligned} \tag{12}$$

Or, by using the expressions for the integrals over MO's in terms of integrals over Löwdin orbitals λ_p, one obtains

$$E_N=6\alpha^{\lambda}+8\beta_{01}^{\lambda}-2\beta_{03}^{\lambda}+(\tfrac{3}{2})\gamma_{00}^{\lambda}+(\tfrac{14}{3})\gamma_{01}^{\lambda}+6\gamma_{02}^{\lambda}+(\tfrac{17}{6})\gamma_{03}^{\lambda}. \tag{13}$$

In a similar fashion, one may write down directly the energy for any state function of benzene corresponding to any electron configuration. The assumption is made that the molecular states of interest are sufficiently well described by taking into account interactions among the ground-state configuration and all configurations derivable from it by excitation of one electron only. Doubly excited states of course may contribute but will nevertheless be ignored for now. On using these formulas,[12] one obtains the results in Table I for the energy *difference* between the ground state and several of the low-lying electronic energy states.

Two very important points should be observed in the expressions for the energy difference between electronic energy states. The first important point is that everywhere in the expressions for energy differences between electronic energy states the combinations $\beta_{12}^{\lambda}-\beta_{14}^{\lambda}$ appears. Thus, although they formally neglected non-nearest-neighbor β's, as a matter of fact, *Pariser and Parr's "nearest-neighbor β" for benzene is to be identified with difference $\beta_{12}^{\lambda}-\beta_{14}^{\lambda}$*, ($\alpha^{\lambda}$ and β_{13}^{λ} do not appear as a result of symmetry). The second important point is that everywhere in the expressions for the energy difference between electronic energy states, the sum of the coefficients of the several γ^{λ}'s is always zero. This means that the datum from which the γ^{λ}'s are measured may be chosen quite arbitrarily. Put another way, Pariser[14] suggested that the value of γ_{00} should be lowered from the "theoretical" value of 16.93 ev to an "empirical" value obtained from valence-state energy arguments of 11.08 ev. Parr suggested that γ_{03} should be evaluated using charged spheres. And a quadratic interpolation was made between those limiting values for γ_{01} and γ_{02}. However, the Pariser-

[12] R. G. Parr, J. Chem. Phys. **33,** 1184 (1960).

[13] H. Eyring, J. Walter, and G. E. Kimball, *Quantum Chemistry* (John Wiley & Sons, Inc., New York, 1944).

[14] R. Pariser, J. Chem. Phys. **21,** 568 (1953).

Parr theory applied to spectra depended for its success on *the selection of proper values for the differences between Coulomb repulsion integrals, not on their absolute values.*

In the expressions for the electronic excitation energies are implicit the following two assumptions: (1) that the LCAO-MO SCF approximation is adequate for the ground state; and (2) that limited configuration interaction using ground-state MO's provides an adequate description of the low-lying electronic energy states. Accordingly, the integrals over atomic orbitals (IOAO parameters) evaluated in this way will be averaged over the changes in the molecular core and the changes in electron correlation that will occur on excitation.[15] Thus, the IOAO parameter values obtained in this way, for example, will not necessarily be the best ones for describing the ground state within the LCAO-MO SCF framework. With regard to the experimental results, there is still uncertainty in the identification of some of the states used in Table I. Furthermore, even where the symmetry classification is known, the choice of which particular energy difference to be used for a Franck-Condon type vertical transition corrected for differences in zero-point vibrational energy is not entirely clear.[16] The choice made here leads to the results $\beta_{01}^{\lambda}-\beta_{03}^{\lambda}=-2.475$ ev, $\gamma_{00}^{\lambda}-\gamma_{01}^{\lambda}=4.215$ ev, $\gamma_{00}^{\lambda}-\gamma_{02}^{\lambda}=5.685$ ev, and $\gamma_{00}^{\lambda}-\gamma_{03}^{\lambda}=6.540$ ev.

Vertical Ionization Potential and Electron Affinity

For the ion $C_6H_6^+$, the wave function $(0\bar{0}\,1\,\bar{1}-1)$ may be assumed; for $C_6H_6^-$, $(0\bar{0}\,1\bar{1}-1-\bar{1}2)$ may be assumed. In specifying the ionization potential and electron affinity, the word vertical is used in the Franck-Condon sense where the nuclear configuration during these processes is taken to be the same as for neutral ground-state benzene. These processes are not necessarily vertical in the sense that the same orbitals, and hence parameters that depend on these orbitals, may be used here as for the ground state of neutral benzene. And in fact, the ground-state nuclear configuration of either of the two ions is likely to be rather different from that of benzene itself.[17] Since the number of electrons in the bound system changes, the expression for the associated energy change may contain $\alpha^{\lambda}-\beta_{02}^{\lambda}$ and/or γ_{00}^{λ} explicitly, even when the assumption is made once again that the same IOAO parameters may be used for benzene in its various low-lying states and for the benzene ions as well. The experimental results for the ionization potential of benzene range from 9.24–9.52 ev.[18] However, as regards the electron affinity of benzene, the isolated benzene negative ion has not been observed. It is usually considered that benzene has a negative electron affinity and its value has been estimated to be -0.54 ev by extrapolation using a semiempirical relationship for the family of catacondensed hydrocarbons.[19] Then it follows that

$$E_{+}-E_N=-(\alpha^{\lambda}-\beta_{02}^{\lambda})-(\beta_{01}^{\lambda}-\beta_{03}^{\lambda})-(\tfrac{1}{3})(\gamma_{00}^{\lambda}-\gamma_{02}^{\lambda})-(\tfrac{1}{6})(\gamma_{00}^{\lambda}-\gamma_{03}^{\lambda}) \quad (14)$$

$$E_{-}-E_N=(\alpha^{\lambda}-\beta_{02}^{\lambda})-(\beta_{01}^{\lambda}-\beta_{03}^{\lambda})-(\tfrac{1}{3})(\gamma_{00}^{\lambda}-\gamma_{01}^{\lambda})-(\tfrac{1}{6})(\gamma_{00}^{\lambda}-\gamma_{03}^{\lambda})+\gamma_{00}^{\lambda}. \quad (15)$$

If we adopt 9.52 ev as the vertical ionization potential and if we use the IOAO's obtained by fitting to the electron excitation energies, then we find $(\alpha^{\lambda}-\beta_{02}^{\lambda})=-9.54$ ev; i.e., for benzene in its ground state, $I.P.=-(\alpha^{\lambda}-\beta_{02}^{\lambda})$ very nearly. The expression for the electron affinity of benzene then leads to the following relationship: $\gamma_{00}^{\lambda}=9.56+(E_{-}-E_N)$. As $(E_{-}-E_N)$ is very likely nonnegative and perhaps as large as 1.7 ev, the range of empirical values for γ_{00}^{λ} is 9.56–11.3 ev.

Vertical Resonance Energy

One may arbitrarily require that each of three π-electron pairs in benzene is constrained to move between one of the three nearest-neighbor carbon atom pairs in the ring with no other change in the condition of the molecule. The π-electron energy of such a hypothetical state of the molecule may be computed and compared with the energy of the ground state. The energy difference between the ground state and that hypothetical state is what is termed the vertical resonance energy.

Such a hypothetical or "Kekule" state gives the energy

$$E_K(C_6H_6)=6\alpha^{\lambda}+6\beta_{01}^{\lambda}+(\tfrac{3}{2})\gamma_{00}^{\lambda}+(\tfrac{9}{2})\gamma_{01}^{\lambda}+6\gamma_{02}^{\lambda}+3\gamma_{03}^{\lambda}. \quad (16)$$

The assumption is made that the parameters α^{λ}, β^{λ}, and γ^{λ} have the same values for Kekule benzene as for normal benzene. Then the vertical resonance energy is completely determined by the same parameters which characterize the electronic excitation energies. The IOAO parameters to be used here, of course, should be ground-state parameters rather than parameters averaged over several low-lying electronic states. There seems to be no clear-cut way of recognizing this distinction and so we simply use the averaged parameters and obtain 4.56 ev.

Any comparison of a calculated vertical resonance energy with an experimentally or operationally defined number must take suitable cognizance of the energy difference between benzene in the hypothetical Kekule state and whatever real molecule, or collection of molecules, is used as a reference. There have been two comprehensive attempts to assess this difference. Mulliken and Parr[20] have presented an elaborate

[15] J. M. Parks and R. G. Parr, J. Chem. Phys. **32,** 1657 (1960).
[16] J. A. Petruska, Dissertation, University of Chicago (1960).
[17] L. C. Snyder, J. Chem. Phys. **33,** 619 (1960); Bull. Am. Phys. Soc. **6,** 165 (1961).
[18] J. D. Morrison and A. J. C. Nicholson, J. Chem. Phys. **20,** 1021 (1950); A. J. C. Nicholson, *ibid.* **29,** 1312 (1958).
[19] F. A. Matsen, J. Chem. Phys. **24,** 602 (1956); R. M. Hedges and F. A. Matsen, *ibid.* **28,** 950 (1958).
[20] R. S. Mulliken and R. G. Parr, J. Chem. Phys. **19,** 1271 (1951).

analysis of the problem where they defined a "standard" hydrocarbon based on an analysis of heats of formation of various hydrocarbons and considered two types of changes that occurred on relating a standard hydrocarbon to Kekule benzene. The first type of change was concerned with the compression or stretching of *standard* single and double bonds. The second type of change was concerned with second-order hyperconjugation energy which was introduced to account for the slight deviations in the assessment of heats of formation from formulas assuming the additivity of bond energies. They concluded that the vertical resonance energy of benzene should be about 3.17 ev.

More recently, Dewar and Schmeising[21] have made a remarkably successful analysis of bond lengths in hydrocarbons where the essential feature of their work is the assertion that the state of hybridization of the carbon atoms in a molecule is the important factor to recognize and, further, that the carbon atoms are remarkably insensitive to their environment. They further assumed that a Morse potential was an adequate representation of the potential in which any given bonded pair of nuclei moved. Using that model and heats of formation, bond lengths and force constants for a small number of hydrocarbons, they evolved a consistent set of Morse potential parameters for the various combinations of hybrid orbitals. Thus they conclude that σ compression strain is partially relieved in going from their "cyclohexatriene" (the reference compound) to benzene. They suggest that the resonance energy of benzene should be somewhere between 0.2–0.7 ev. Using their Morse potential function for a sp^2-sp^2 carbon-carbon σ bond, the change in energy involved in compressing such a bond from its equilibrium distance plus the stretch energy for an ethylenic double bond yields 0.89 ev for the compression energy going from their "cyclohexatriene" to Kekule benzene[22] and 2.1 ev for the vertical resonance energy.

Anisotropy of the Diamagnetic Susceptibility

A fairly elaborate nonempirical calculation of the diamagnetic anisotropy has already been made by Itoh *et al.*[23] However, the usual London-type approximation[24] was used there for simplifying integrals involving the vector potential in the integrand. Recently, the London approximation was modified and it was shown that the consistently low values of the diamagnetic anisotropy of benzene found by earlier workers could be substantially improved.[15] Within zero differential overlap, the expression for the diamagnetic anisotropy of benzene becomes

$$\Delta\chi=\chi_{\perp}-\chi_{\parallel}\approx\chi_{\perp}^{\pi}=-8\beta_{01}^{\lambda,H}(2\pi es/6hc)^2, \quad (17)$$

where e, h, and c are the charge on the electron, Planck's constant, and the velocity of light, respectively, and s is one-sixth the area of the regular hexagon defined by the six carbon nuclei in benzene. As the London approximation was invoked, we carry along the residual dependence on the magnetic field of the core integral; hence, the superscript H. All of the anisotropy is attributed to the relatively free π electrons. Once again, IOAO parameters characterizing the ground state should be used.

We have evaluated the difference $\beta_{01}^{\lambda}-\beta_{03}^{\lambda}(=-2.475$ ev) by fitting to the several low-lying electronic energy levels. The IOAO β_{01}^{H} equals $(1+f_{01})\beta_{01}$ where $(1+f_{01})$ is an *enhancement factor* for correcting the London approximation (which factor ranges over 1.145–1.334 if STO's with effective charge ranging over 3.18–2.00 are used[25]). Now $|\beta_{01}^{\lambda}|$ should be greater than 2.475 ev since $\beta_{01}^{\lambda}-\beta_{03}^{\lambda}=-2.475$ ev. Both the enhancement factor and the realization that what enters here is β_{01}^{λ} while the difference $(\beta_{01}^{\lambda}-\beta_{03}^{\lambda})$ enters elsewhere should lead to larger, and hence more nearly correct, estimates of $\Delta\chi$. The explicit form of the distorted valence-state π atomic orbital would be needed before this datum could be compared with the other properties of benzene.

To the extent to which they could be explicitly found the empirical values for the integrals over atomic orbitals for benzene obtained by the analysis presented in the foregoing are presented in Table II.

TABLE II. Empirical values for integrals over atomic orbitals for benzene.[a]

Integrals	Empirical values (ev)
Core	
$\alpha^{\lambda}-\beta_{02}^{\lambda}$	−9.54
$\beta_{01}^{\lambda}-\beta_{03}^{\lambda}$	−2.475
Electron Repulsion	
$\gamma_{00}^{\lambda}-\gamma_{01}^{\lambda}$	4.215
$\gamma_{00}^{\lambda}-\gamma_{02}^{\lambda}$	5.685
$\gamma_{00}^{\lambda}-\gamma_{03}^{\lambda}$	6.540
γ_{00}^{λ}	9.56−11.3

[a] The integral differences were evaluated using the electronic spectrum data except for $\alpha^{\lambda}-\beta_{02}^{\lambda}$ which was obtained using that data and the ionization potential and except for γ_{00}^{λ} which was estimated using the other parameters and an estimated range for the electron affinity of benzene. See the text for explanations of the symbols.

III. INTERPRETATION OF THE RESULTS

The theoretical values for the IOAO parameters depend on the assumed form of the distorted valence-

[21] M. J. S. Dewar and H. N. Schmeising, Tetrahedron **11**, 96 (1960).

[22] H. N. Schmeising extended his work (reference 21) for us and calculated the compressional energy for the change from his model of cyclohexatriene to Kekule benzene which result is 20.1 kcal/mole.

[23] T. Itoh, K. Ohno, and H. Yoshizumi, J. Phys. Soc. (Japan) **10**, 103 (1955).

[24] F. London, J. phys. radium **8**, 397 (1937).

[25] P. G. Lykos and R. G. Parr, J. Chem. Phys. **28**, 361 (1958).

state π AO's which in linear combination comprise the MO's. They also depend on the assumed σ many-electron wave function. In the past, whenever "theoretical" estimates of the IOAO parameters have been required, it has been customary to note that perhaps atomic SCF $2p\pi$ AO's for some carbon spectroscopic state or other should be used; however, for the sake of expediency, a Slater-type orbital (STO) with orbital exponent (3.18/2) or 3.25/2) was used instead.[26] The overlaps between two carbon SCF AO's over the range of internuclear distances appropriate for benzene have been calculated and were found to be quite different from the corresponding integrals calculated using STO's.[27] Accordingly, "theoretical" estimates of IOAO's obtained with such a crude representation of a distorted valence-state π AO should be used with caution, even where only semiquantitative estimates of the behavior of IOAO's with internuclear distance are required.

The electron repulsion integrals that were obtained within the assumption of zero differential overlap (ZDO) are interpreted as being integrals over Löwdin orthogonalized "atomic" orbitals. It is gratifying that the differences $\gamma_{00}^{\lambda}-\gamma_{0i}^{\lambda}$ are monotonically increasing with increasing internuclear distance. One would expect that γ_{00} should approach a valence-state value. Pariser's analysis leads to $\gamma_{00}=11.08$ ev; Julg's[28] analysis, which includes some additional correlation corrections, leads to $\gamma_{00}=9.87$ ev. Also, γ_{0i} should approach $1/R_{0i}$ for large R_{0i}. Within these restrictions we sought unsuccessfully a suitable empirical form for the γ_{0i} as a function of internuclear distance where we used a charged sphere-pair representation of a valence-state π orbital, were the sphere pair was not restricted to be tangent, and where nearest-neighbor orbitals could overlap. An attempt was made to use a single STO representation where the only parameter, the orbital exponent, was taken as a function of R_{0i}. This also was not adequate as the orbital exponent required by the empirical fit is lower for γ_{01} than for γ_{00} or γ_{02}. It would appear that the single STO or the charged sphere representations are too compact so that γ_{0i} approaches $1/R_{0i}$ behavior too quickly with increasing R_{0i}. Use of SCF AO's would tend to correct that trend. However, the question of whether or not hybrid electron repulsion integrals over orthogonalized SCF orbitals will be small needs to be examined.

The core integrals are also interpreted as being over Löwdin orthonormalized semilocalized orbitals.[29] Accordingly, those integrals depend on the geometry of the molecule in two ways: First, the operator $\mathbf{H}_{\text{core}}(\mu)$ contains potential terms resulting from every nucleus and every core electron; Second, the process of orthonormalization of the atomic orbitals actually corresponds to a transformation of the set of localized atomic orbitals to a set of many-center molecular orbitals of a particular kind.[8] Now although McWeeny has shown that in the special case of benzene the many center λ_i gave substantially the same Coulomb repulsion integrals as the corresponding χ_i,[9] it does not automatically follow that the same would be true for the core integrals. Therefore, before the benzene α and β parameter values may be carried over to other conjugated hydrocarbons, the dependence on molecular geometry should be examined.

In matrix notation we may relate the core integrals over λ to core integrals over χ as follows:

$$\mathbf{H}^{\lambda}=\mathbf{S}^{-\frac{1}{2}}\mathbf{H}\mathbf{S}^{-\frac{1}{2}}=\mathbf{S}^{-1}\mathbf{H}, \tag{18}$$

where

$$H_{ii}^{\lambda}\equiv\alpha^{\lambda}; \qquad H_{ii}\equiv\alpha$$
$$H_{ij}^{\lambda}\equiv\beta_{ij}^{\lambda}; \qquad H_{ij}\equiv\beta_{ij}. \tag{19}$$

The quantities of interest are the differences

$$\alpha^{\lambda}-\beta_{02}^{\lambda}=(S_{00}^{-1}-S_{02}^{-1})(\alpha-\beta_{02})+(S_{01}^{-1}-S_{03}^{-1})\times(\beta_{01}-\beta_{03}) \tag{20}$$

$$\beta_{01}^{\lambda}-\beta_{03}^{\lambda}=(S_{01}^{-1}-S_{03}^{-1})(\alpha-\beta_{02})+(S_{00}^{-1}-S_{02}^{-1})\times(\beta_{01}-\beta_{03}). \tag{21}$$

Because of the high symmetry of benzene, the unique elements of $\mathbf{S}^{-1}$ may be written down directly in terms of the unique elements of the overlap matrix itself[30], namely,

$$\begin{aligned} S_{ii}^{-1}&=6^{-1}(a+b+2c+2d)\\ S_{i,i+1}^{-1}&=6^{-1}(a-b+c-d)\\ S_{i,i+2}^{-1}&=6^{-1}(a+b-c-d)\\ S_{i,i+3}^{-1}&=6^{-1}(a-b-2c+2d), \end{aligned} \tag{22}$$

where

$$\begin{aligned} a^{-1}&=S_{ii}+2S_{i,i+1}+2S_{i,i+2}+S_{i,i+3}\\ b^{-1}&=S_{ii}-2S_{i,i+1}+2S_{i,i+2}-S_{i,i+3}\\ c^{-1}&=S_{ii}+S_{i,i+1}-S_{i,i+2}-S_{i,i+3}\\ d^{-1}&=S_{ii}-S_{i,i+1}-S_{i,i+2}+S_{i,i+3}. \end{aligned} \tag{23}$$

Thus, for a given overlap matrix, the differences $(\alpha-\beta_{02})$ and $(\beta_{01}-\beta_{03})$ are uniquely determined by the empirically evaluated differences $(\alpha^{\lambda}-\beta_{02}^{\lambda})$ and $(\beta_{01}^{\lambda}-\beta_{03}^{\lambda})$.

If we use STO's with orbital exponent (3.18/2) for the overlap integrals, we find

$$(\alpha-\beta_{02})=-9.76 \text{ ev} \quad (\beta_{01}-\beta_{03})=-4.68 \text{ ev}.$$

[26] F. A. Gray, I. G. Ross, and J. Yates, Australian J. Chem. **12,** 347 (1959).
[27] R. S. Mulliken, C. A. Rieke, D. Orloff, and H. Orloff, J. Chem. Phys. **17,** 1248 (1949).
[28] A. Julg, J. chim. phys. **55,** 413 (1958).
[29] R. McWeeney, Proc. Roy. Soc. (London) **A237,** 355 (1956); F. Peradejordi, Compt. rend. **243,** 276 (1956).

[30] The high symmetry of such a cyclic system permits the complete diagonalization of the overlap matrix and hence the direct calculation of the inverse square root of the overlap matrix. For an alternative procedure see P.-O. Löwdin, R. Pauncz, and J. de Heer, J. Math. Phys. **1,** 461 (1960).

If we use SCFAO's for the overlap integrals, we obtain

$$(\alpha-\beta_{02})=-8.29 \text{ ev}, \quad (\beta_{01}-\beta_{03})=-2.97 \text{ ev}.$$

Thus, the difference $(\alpha-\beta_{02})$ is relatively insensitive to the choice of $2p\pi$ AO's, but the difference $(\beta_{01}-\beta_{03})$ changes by almost 50%.

We could get absolute values for the α and β_{ij} IOAO's if the differences were to be reasonably well accommodated by assuming the $H_{ij}=-kS_{ij}$ where k is a constant. On this basis, we may obtain two k's according as SCFAO's or STO's are used to evaluate the overlap integrals. Thus, we obtain the following: On using STO's, we find $k=19.45$ ev, $\alpha=-10.54$ ev, $\beta_{01}=-5.02$ ev, $\beta_{02}=-0.78$ ev, $\beta_{03}=-0.34$ ev; on using SCFAO's, we find $k=15.79$ ev, $\alpha=-9.95$ ev, $\beta_{01}=-5.58$ ev, $\beta_{02}=-1.66$ ev, $\beta_{03}=-1.03$ ev. For either set of IOAO's, we find a fairly smooth behavior when the parameters are considered as a function of internuclear distance.

Alternatively, one might attempt to resolve $\mathbf{H}_{\text{core}}(\mu)$ in the manner of Goeppert-Mayer and Sklar[6] who essentially assumed a simple nonantisymmetrized valence-bond description of the core electrons, namely,

$$\mathbf{H}_{\text{core}}(\mu)=\mathbf{T}(\mu)+\sum_{i=1}^{n}\mathbf{U}_i(\mu) \tag{24}$$

$$[\mathbf{T}(\mu)+\mathbf{U}_p(\mu)]\chi_p(\mu)=W_{2p}\chi_p(\mu) \tag{25}$$

and

$$\mathbf{U}_q(\mu)=\mathbf{U}_q{}^*(\mu)-\int|\chi_q(\nu)|^2r_{\mu\nu}{}^{-1}dv(\nu), \tag{26}$$

where $\mathbf{U}_i(\mu)$ is the potential resulting from the ith carbon $+1$ ion in the core, $\chi_p(\mu)$ is assumed to be an eigenfunction of the corresponding atomic part of the operator, and $\mathbf{U}_q(\mu)$ is rewritten as a potential resulting from a neutral core atom, $\mathbf{U}_q{}^*(\mu)$, minus the average coulomb potential of the added electron,

$$\int|\chi_q(\nu)|^2r_{\mu\nu}{}^{-1}dv(\nu).$$

The integrals over the $\mathbf{U}_q{}^*(\mu)$ (penetration integrals) are usually assumed to be negligible.[31] The "eigenvalue" W_{2p} is identified with the negative of the vertical ionization potential for a π electron in the carbon atom in its distorted $sp^2\pi$ valence state. The value 11.2 ev has been used for $-W_{2p}$.[32] Here, in addition to the assumption of a particular core wave function, exchange has been neglected. Also, the assumption that the $\chi_p(\mu)$ are eigenfunctions of an atomic part of $\mathbf{H}_{\text{core}}(\mu)$ has been criticized recently.[33]

It is not clear at this time what resolution of $\mathbf{H}_{\text{core}}(\mu)$ would be most meaningful; however, the dependence of $\mathbf{H}_{\text{core}}(\mu)$, and hence of α and β_{ij}, on the geometry of the core must certainly be considered before those IOAO parameters found for one molecule are carried over to another molecule.

IV. CONCLUSION

The nature of the integrals over atomic orbitals that enter in a Pariser-Parr type approach to a π-electron system has been examined. The consequence of the use of zero differential overlap has been examined for the core integrals. The fact that a different set of IOAO's should be used for each state of the molecule has been recognized. Accordingly, empirically evaluated IOAO's found by handling several states simultaneously should be interpreted as parameter values *averaged* over the several states considered. It has been shown that a reasonable set of such averaged IOAO's can simultaneously account for several properties of the benzene molecule.

ACKNOWLEDGMENTS

Initiation of this work was made possible by an Allied Chemical and Dye Corporation Predoctoral Fellowship for the year 1953–54 while the author was at Carnegie Institute of Technology. The updating and completion of this work was made possible by a National Science Foundation Grant to Illinois Institute of Technology.

Many fruitful discussions and helpful suggestions by Professor Robert G. Parr are gratefully acknowledged.

[31] J. Kaufman and W. Koski, J. Am. Chem. Soc. **82,** 3262 (1960), report that the ionization potential of the methyl radical decreases by more than 2 ev when three methyl groups are substituted for the three hydrogens. This suggests that penetration effects are much more important than heretofore considered.

[32] I. J. Goldfarb and H. H. Jaffe, J. Chem. Phys. **30,** 1622 (1959).

[33] E. T. Stewart, J. Chem. Soc. **1959,** 70.

Anharmonicity in Unimolecular Reactions*

EVERETT THIELE AND DAVID J. WILSON

Department of Chemistry, University of Rochester, Rochester 20, New York

(Received March 9, 1961)

The in-line vibrations of a linear, symmetric, triatomic molecule having Morse bond-stretching potentials are studied numerically. The significance of the results for unimolecular rate theory is discussed. Harmonic and weakly anharmonic approximations appear to be inadequate.

INTRODUCTION

SINCE the recognition of the fundamental correctness of the Lindemann mechanism, theoretical advances in the description of unimolecular reactions have centered on obtaining and applying better descriptions of two energy-exchange processes: the intermolecular process leading to activation, and the intramolecular process leading to the dissociation (or isomerization) of the activated molecule.

In formulating the pressure-dependent rate k for a unimolecular reaction, most theories follow the arguments of Rice, Ramsperger and Kassel; these express k as the average over an equilibrium distribution of the quantity $[\omega k_r/(\omega+k_r)]$, where ω is an effective collisional frequency and k_r is the dissociation rate for molecules in the rth activated state.[1] In this formulation the problem of intermolecular energy transfer has been glossed over with the assumption of a strong collisional mechanism (see reference 2 for an alternative). It is also assumed, as Slater has recently pointed out,[1] that dissociation occurs randomly, with a probability $k_r\Delta t$ of occurring in the small time interval Δt.

In Kassel's theory it is assumed that k_r depends only on the total internal energy, and statistical arguments are employed to determine the functional form of this dependence.[3,4] Kassel's classical expression for k contains two parameters (the pre-exponential factor and s) which are not defined in terms of molecular properties and must be determined by comparison with rate data. Nevertheless, Kassel's theory provides a useful physical picture, which is especially important in interpreting the role played by molecular complexity in determining the pressure dependence of k.

Slater has taken a major step forward by using a detailed model for the intramolecular process leading to dissociation.[5–8]

Assuming that:

(I) Only vibrational motion is important in determining k_r,

(II) This vibrational motion is harmonic (i.e., subject to a normal mode analysis),

(III) Reaction occurs when a particular internal coordinate (a linear combination of the normal coordinates) known as the reaction coordinate becomes sufficiently extended,

Slater determines k_r as a function of the energy in each of the normal modes. Slater's classical expression for k is similar formally to Kassel's, but in theory permits the evaluation of all pertinent rate parameters except the high pressure activation energy (E_0). There exists a degree of arbitrariness in the selection of a reaction coordinate; however, this arbitrariness and the indeterminancy of E_0 both arise from an incomplete knowledge of the potential surface which describes the vibrations, rather than from an inexactness in the formulation of the theory.

Recently there has been an accumulation of evidence suggesting that Slater theory is inadequate.[9–11] The assumption that molecular vibrations are harmonic up to the point of dissociation is obviously an oversimplification.[12] It is the purpose of this paper to examine the seriousness of this simplification, and to take a more realistic look at the dissociation process by considering the classical vibrational motion of a system with two internal degrees of freedom and an anharmonic potential. Since anharmonicities are necessarily large in a system capable of dissociating, approximate methods which assume small deviations from the harmonic solution are inadequate, and we are forced to rely to a large extent on numerical integrations of the equations of motion.

MODEL AND EQUATIONS OF MOTION

Consider the longitudinal vibrations of a linear and symmetric triatomic molecule, which is schematically represented in Fig. 1.

Let $m_1=m_3=$mass of one of the outer atoms, $m_2=$mass of the central atom, and $r_i=$displacement from

* This work was supported by grants from the National Science Foundation and the Research Corporation.

[1] N. B. Slater, *Theory of Unimolecular Reactions* (Cornell University Press, Ithaca, New York, 1959), pp. 16–20.
[2] F. P. Buff and D. J. Wilson, J. Chem. Phys. **32**, 677 (1960).
[3] See reference 1, pp. 30, 31.
[4] L. S. Kassel, *Kinetics of Homogeneous Gas Reactions* (Chemical Catalogue Company, New York, 1932), pp. 95–104.
[5] N. B. Slater, Proc. Roy. Soc. (London) **A194**, 112 (1948).
[6] N. B. Slater, Phil. Trans. Roy. Soc. London **A246**, 57 (1953).
[7] N. B. Slater, Proc. Roy. Soc. (London) **A218**, 224 (1953).
[8] N. B. Slater, *Theory of Unimolecular Reactions* (Cornell University Press, Ithaca, New York, 1959), Chaps. 5, 7.
[9] E. Thiele and D. J. Wilson, Can. J. Chem. **37**, 1035 (1959).
[10] E. Thiele and D. J. Wilson, J. Phys. Chem. **64**, 473 (1960).
[11] J. P. Chessick, J. Am. Chem. Soc. **82**, 2277 (1960).
[12] See reference 8, p. 146.

the equilibrium bond distance. The internal kinetic energy (K.E.) of this system is:

$$\text{K.E.}=\frac{m_1(m_1+m_2)}{2m_1+m_2}\left(\frac{\dot{r}_1^2+\dot{r}_2^2}{2}\right)+\frac{m_1^2}{2m_1+m_2}\dot{r}_1\dot{r}_2. \quad (1)$$

We shall take for the potential energy (V) the following expression which is the sum of two Morse potentials, one for each bond:

$$V=D[1-e^{-ar_1}]^2+D[1-e^{-ar_2}]^2. \quad (2)$$

Here the parameters D and a have the same interpretation as in the one dimensional case. The potential surface described by Eq. (2) has been represented by a series of equipotentials in the ar_1-ar_2 plane in Fig. 2. All solutions for a total energy E_T less than D are bounded, and represent stable vibrations about the equilibrium configuration $r_1=r_2=0$. For values of E_T slightly greater than D, dissociation may occur, with, say r_1 increasing without limit while r_2 remains essentially zero. For $E_T\geq 2D$ all solutions are unbounded with the possibility of both r_1 and r_2 increasing without limit.

Tredgold[13] has obtained exact solutions to the equations of motion for a system which is superficially similar to that described above. In physical terms this has been accomplished by casting the problem in a form equivalent to a central field problem and using conservation of angular momentum to integrate the equations of motion. This approach requires the use of a rather artificial potential, which has circular equipotentials in the normal mode plane. It is our opinion that Tredgold's results could yield useful information concerning the interchange of vibrational and rotational energy in a diatomic molecule.

From Eqs. (1) and (2), Lagrange's equations of motion are

$$(d^2r_1/dt^2)+2aD[m_1^{-1}+m_2^{-1}][e^{-ar_1}-e^{-2ar_1}]-(2aD/m_2)[e^{-ar_2}-e^{-2ar_2}]=0;$$
$$(d^2r_2/dt^2)+2aD[m_1^{-1}+m_2^{-1}][e^{-ar_2}-e^{-2ar_2}](-2aD/m_2)[e^{-ar_1}-e^{-2ar_1}]=0. \quad (3)$$

Introducing the dimensionless variables

$$x_1=ar_1, \qquad x_2=ar_2, \qquad \tau=(2a^2D/m_2)^{\frac{1}{2}}t, \quad (4)$$

we have

$$\frac{d^2x_1}{d\tau^2}+\left(1+\frac{m_2}{m_1}\right)(e^{-x_1}-e^{-2x_1})-(e^{-x_2}-e^{-2x_2})=0$$

$$\frac{d^2x_2}{d\tau_2}+\left(1+\frac{m_2}{m_1}\right)(e^{-x_2}-e^{-2x_2})-(e^{-x_1}-e^{-2x_1})=0. \quad (5)$$

FIG. 1

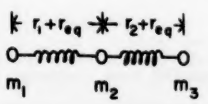

[13] R. H. Tredgold, Proc. Phys. Soc. (London) **A68**, 920 (1955).

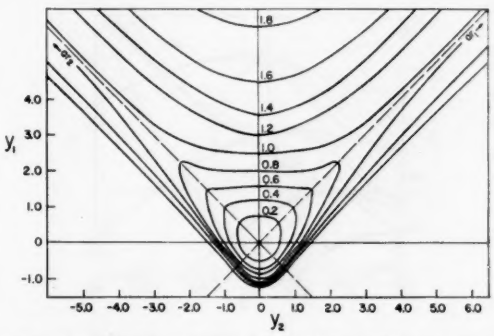

FIG. 2. Equipotentials for coupled Morse oscillators as calculated from Eq. (2).

(In all numerical calculations the factor m_2/m_1 was set equal to 3/4, corresponding to CO_2.)

LINEAR APPROXIMATION AND NORMAL MODES

As a basis for comparison with later work, let us consider the linear approximation to Eqs. (5). Expanding the exponentials, we have

$$(d^2x_1/d\tau_2)+[1+(m_2/m_1)]x_1-x_2=0;$$
$$(d^2x_2/d\tau^2)+[1+(m_2/m_1)]x_2-x_1=0. \quad (6)$$

The symmetry of the model allows us to write down a set of normal coordinates (y_i) immediately.

$$y_1=x_1+x_2, \qquad y_2=x_1-x_2. \quad (7)$$

We shall refer to y_1 as the symmetric mode, and y_2 as the antisymmetric mode.

The solutions to Eqs. (6) in terms of these normal modes are [14–15]

$$y_1=(2E_1)^{\frac{1}{2}}\sin[(m_2/m_1)^{\frac{1}{2}}\tau+\psi_1]; \quad (8)$$
$$y_2=(2E_2)^{\frac{1}{2}}\sin\{[2+(m_2/m_1)]^{\frac{1}{2}}\tau+\psi_2\}. \quad (9)$$

where E_1=energy of symmetric mode in units of D, and E_2=energy of antisymmetric mode in units of D. To this approximation E_1 and E_2 are constants of the motion. In the nonlinear problem E_1 and E_2 are of course no longer constant; however, we shall still find it useful to speak of the energy in a given normal mode at some instant of time.

Rewriting Eq. (5) in terms of the normal modes defined by (7), we have

$$(d^2y_1/d\tau^2)+(m_2/m_1)[e^{-\frac{1}{2}(y_1+y_2)}-e^{-(y_1+y_2)}+e^{-\frac{1}{2}(y_1-y_2)}-e^{-(y_1-y_2)}]=0; \quad (10)$$
$$(d^2y_2/d\tau^2)+[2+(m_2/m_1)][e^{-\frac{1}{2}(y_1+y_2)}-e^{-(y_1+y_2)}-e^{-\frac{1}{2}(y_1-y_2)}+e^{-(y_1-y_2)}]=0. \quad (11)$$

[14] H. Goldstein, *Classical Mechanics* (Addison-Wesley Publishing Company, Inc., Reading, Massachusetts, 1956), pp. 333–337.

[15] We use the term normal coordinates to mean any set of coordinates which diagonalizes the kinetic and potential energy in the harmonic approximation. It is often convenient to fix the normal coordinates by specifying that the kinetic energy matrix is the identity matrix; such a set of normal coordinates might be referred to as normalized normal coordinates.

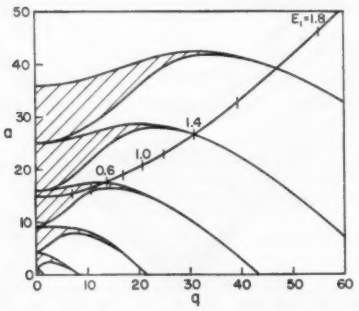

FIG. 3. Stability plot for Mathieu equation.

Equations (10) and (11) are then the exact differential equations governing the motion of the normal modes, the solutions of which form the basis for most of the remaining discussion.

PURE SYMMETRIC MODE

Consider the situation in which all the energy of the molecule is initially in the symmetric mode (i.e., $y_2=dy_2/d\tau=0$). Then both atoms are oscillating with equal amplitude away from or toward the stationary central atom. Physically it is clear that this situation will continue indefinitely. Assuming y_2 identically zero, we have from Eqs. (10) and (11),

$$(d^2y_1/d\tau^2)+(2m_2/m_1)[\exp(-\tfrac{1}{2}y_1)-\exp(-y_1)]=0; \quad (12)$$

$$d^2y_2/d\tau_2=0. \quad (13)$$

Equation (13) is written down to show that it is consistent with the assumption $y_2=0$. The nonexistence of a pure antisymmetric mode may be mathematically demonstrated by showing that the assumption $y_1=0$ leads to an inconsistent equation in $d^2y_1/d\tau^2$.

Equation (12) may be readily integrated by applying conservation of energy,[16] giving

$$y_1=2\log_e\left(\frac{(2E_1)^{\frac{1}{2}}}{2-E_1}\sin\left\{\left[\left(1-\frac{E_1}{2}\right)\frac{m_2}{m_1}\right]^{\frac{1}{2}}\tau+\psi_1\right\}+\frac{2}{2-E_1}\right). \quad (14)$$

This solution is valid for $E_1<2$. For $E_1\geq 2$ the solution is unbounded and corresponds to the simultaneous breaking of both bonds. The most important difference between the exact solution given by Eq. (14) and the harmonic solution given by (8) is the energy-dependent frequency term $[1-(E_1/2)]^{\frac{1}{2}}$. This dependence is characteristic of nonlinear oscillators,[17] and in this case shows that the frequency decreases with increasing energy.

We have thus obtained a specific solution to Eqs. (10) and (11) by picking a special set of initial conditions, such that the problem is reduced to that of a one-dimensional oscillator. This was possible only because of the symmetrical nature of the model, and in tself is of little value in drawing conclusions about coupled oscillators. A question of greater interest is: given a set of initial conditions which correspond to a small perturbation from the pure symmetric mode, will the antisymmetric mode remain small in amplitude? In other words, is the pure symmetric made orbitally stable?[18] We shall investigate this question using a standard technique of nonlinear mechanics[18] and then consider a numerical check of the results.

If y_2 is small so that the exponentials may be expanded in y_2 and only first power terms retained, Eqs. (10) and (11) reduce to

$$(d^2y_1/d\tau^2)+(2m_2/m_1)[\exp(-\tfrac{1}{2}y_1)-\exp(-y_1)]+O(y_2^2)=0; \quad (15)$$

$$(d^2y_2/d\tau^2)+[2+(m_2/m_1)][2\exp(-y_1)-\exp(-\tfrac{1}{2}y_1]y_2+O(y_2^2)=0. \quad (16)$$

Substituting the known solution to Eq. (15), given by Eq. (14), into (16), we have

$$(d^2y_2/d\tau^2)+[2+(m_2/m_1)]f(\tau)y_2=0 \quad (17)$$

$$f(\tau)=(2-E_1)[2(1-E_1)-A(\tau)]/[A(\tau)+2]^2$$

$$A(\tau)=(2E_1)^{\frac{1}{2}}\sin\{[(1-\tfrac{1}{2}E_1)(m_2/m_1)]^{\frac{1}{2}}\tau+\psi_1\}.$$

Equation (17) is an example of Hill's differential equation. It is linear, with the coefficient of y_2 a periodic function of the independent variable τ. Floquet's theorem[18,19] implies that there exist two linearly independent solutions to Eq. (17), y_2' and y_2'', which satisfy the relations

$$y_2'(\tau+\pi)=\sigma y_2'(\tau); \qquad y_2''(\tau+\pi)=\sigma^* y_2''(\tau);$$

where σ is a complex constant, and σ^* its complex conjugate. The general solution to Eq. (17), considered as a complex function of the real variable τ, is then bounded when $|\sigma|<1$ and unbounded when $|\sigma|>1$.

In order to avoid computational difficulties, we shall consider the approximation to Eq. (17), obtained by replacing $f(\tau)$ by the first two terms in its Fourier expansion;

$$f(\tau)\cong(1-\tfrac{1}{2}E_1)^{\frac{1}{2}}+b_1\cos\{[(1-\tfrac{1}{2}E_1)(m_2/m_1)]^{\frac{1}{2}}\tau\}$$

$$b_1=2(1-E_1)\left(\frac{2-E_1}{E_1}\right)^{\frac{1}{2}}+\frac{2(E_1-2)}{(2E_1)^{\frac{1}{2}}}. \quad (18)$$

The inconsequential phase angle ψ_1 has been set equal to $\pi/2$ in Eq. (17). Use of Eq. (18) and introduction of the new variable

$$\phi=\tfrac{1}{2}[(1-\tfrac{1}{2}E_1)(m_2/m_1)]^{\frac{1}{2}}\tau$$

[16] N. B. Slater, Nature **180,** 1352 (1957).

[17] N. W. McLachlan, *Theory of Vibrations* (Dover Publications, Inc., New York, 1951), Chap. 3.

[18] W. J. Cunningham, *Introduction to Non-Linear Analysis* (McGraw-Hill Book Company, Inc., New York, 1958), Chaps. 9, 10.

[19] E. T. Whittaker and G. N. Watson, *A Course of Modern Analysis* (University Press, Cambridge, 1952), pp. 412, 413.

causes this approximation to (17) to yield

$$(d^2y_2/d\phi^2)+(a-2q\cdot\cos 2\phi)y_2=0. \qquad (19)$$

$$a=4[1+(2m_1/m_2)][2/(2-E_1)]$$

$$q=4[1+(2m_1/m_2)]\left\{\left(\frac{2}{E_1}\right)^{\frac{1}{2}}-\frac{2(1-E_1)}{[E_1(2-E_1)]^{\frac{1}{2}}}\right\}.$$

Equation (19) is a special case of Hill's equation, the Mathieu equation. The boundedness of the solutions to the Mathieu equation as a function of the parameters a and q has been thoroughly investigated.[20] Figure 3 shows a portion of a stability plot for this equation. Points located within the shaded regions have values for a (plotted along ordinate) and q (plotted along abscissa) for which the general solution remains bounded. The solid line in Fig. 3 shows a and q plotted as functions of E_1, when $m_1/m_2=\frac{4}{3}$. From this plot we see that the value $E_1=0.6$ represents a critical energy (E_1^*). For $E_1<E_1^*=0.6$ the symmetric mode is orbitally stable; while for $E_1>E_1^*$ the symmetric mode is orbitally unstable. (In view of the approximation made, no importance is attached to the small stable regions indicated at $E_1=1.4$, etc.) E_1^* depends on the value of m_1/m_2 in a rather complicated manner. Physically it is clear that in the limit as $m_1/m_2\to 0$, the symmetric mode must be stable for all values of E_1. Ignoring rapid fluctuations of E_1^* as a function of m_1/m_2, one does find a definite trend in which E_1^* increases with decreasing values of m_1/m_2.

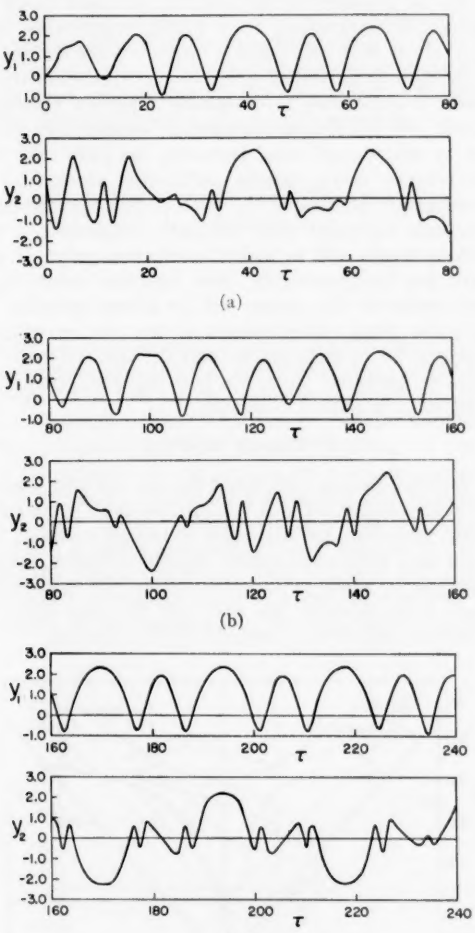

FIG. 4. (a) A run at $E_T=0.8375$ ($\tau=0$ to $\tau=80$). (b) A run at $E_T=0.8375$ ($\tau=80$ to $\tau=160$). (c) A run at $E_T=0.8375$ ($\tau=160$ to $\tau=240$).

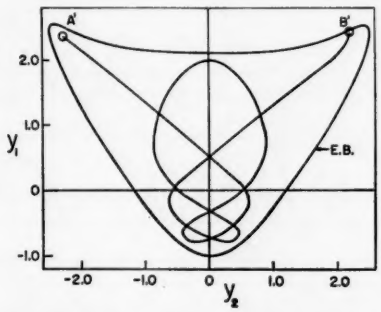

FIG. 5. Path of dissociating type of motion, $E_T=0.8375$. A' and B' are reflection points. The curve labeled E.B. is given by $V(y_1, y_2)=0.8375$.

The orbital stability of the symmetric mode was also tested by six numerical integrations[21] of Eqs. (10) and (11), at values of $E_T=0.3$, 0.5, 0.8375. In all cases the initial conditions were chosen such that the molecule was in its equilibrium configuration, with approximately 98.7% of the kinetic energy in the symmetric mode. The results of these runs corroborated the analysis based on the Mathieu equation. There are two further points of interest in connection with these runs. First it is observed that, in the runs with $E_T<0.6$, the amplitude of the antisymmetric mode can become appreciable (say $\frac{1}{4}$ of the amplitude of the symmetric mode when $E_T=0.5$) without a subsequent increase. This fact indicates that for $E_T<E_1^*$ there exists a large class of initial conditions for which the motion may be grossly characterized as almost symmetric. Secondly the runs at $E_T>0.6$, where the symmetric

[20] N. W. McLachlan, *Theory and Applications of Mathieu Functions* (Oxford Clarendon Press, London, 1947).

[21] All numerical integrations were carried out at the University of Rochester Computing Center using an IBM 650 computer. The method of Runga-Kutta-Gill[22] as incorporated in the Forder II B subroutine[23] was used. Successive points were calculated at intervals of $\Delta\tau=0.2$, with the value of the total energy used as a check on truncation errors. The maximum deviation between initial and final energy was 2.5% in the longest run to $\tau=240$ (Fig. 4). The error was substantially less in other runs.

[22] S. Gill, Proc. Camb. Phil. Soc. **47**, 96 (1951).

[23] T. A. Kennan and R. J. Winkelman, University of Rochester Computing Center, File Number 4.0.503, July 15, 1959.

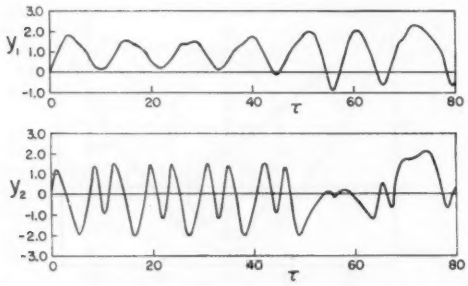

FIG. 6. 1–2 type of motion, followed by decay into dissociating type, for $E_T=0.8375$. Initial conditions: $E_1=0.209375$, $E_2=0.628125$.

mode is orbitally unstable, show a surprisingly rapid breakdown of this almost symmetric motion.

CONFIGURATION PLANE

In general we can consider the solutions $y_1=y_1(\tau)$ and $y_2=y_2(\tau)$ as tracing out a curve (or path of the system) in the y_1, y_2 configuration plane. A graph of this path, together with Fig. 2 (which shows the equipotentials in the y_1, y_2 plane), provides a compact picture which often makes the physical significance of a particular solution quite clear. B. Stevens[24] has given an interesting qualitative description of the paths traced out by a system of coupled nonlinear oscillators, based solely on a qualitative knowledge of the shape of the equipotentials.

It is well known[25] that it is possible to reduce Eqs. (10) and (11) to a single, second-order differential equation by making use of the fact that the independent variable τ does not enter explicitly into these equations, and also that a first integral, representing conservation of energy, is known. Carrying out this reduction gives the following differential equation for the path in the configuration plane:

$$-\frac{\partial V}{\partial y_1}+\left[\frac{2m_1+m_2}{m_1}\right]\frac{\partial V}{\partial y_2}\frac{dy_1}{dy_2}=\frac{d^2y_1}{dy_2^2}\frac{2[E_T-V(y_1,y_2)]}{\{(dy_1/dy_2)^2+[m_1/(2m_1+m_2)]\}},\quad(20)$$

where $V(y_1, y_2)$ is the potential [Eq. (2)] expressed in normal coordinates. The curve, given by

$$E_T-V(y_1,y_2)=0,\quad(21)$$

represents a boundary in the configuration plane which the path cannot cross because of conservation of energy. If the path reaches this energy boundary, then the rhs of Eq. (20) vanishes and we have

$$dy_1/dy_2=\left[\frac{m_1}{(2m_1+m_2)}\right]\frac{\partial V}{\partial y_1}\Big/\frac{\partial V}{\partial y_2}.\quad(22)$$

The term $(\partial V/\partial y_1)/(\partial V/\partial y_2)$ is simply the slope of the perpendicular to the energy boundary. Thus Eq. (22) expresses the fact that the path reaches the energy boundary only with a definite slope which is never equal to the slope of the energy boundary. In normalized normal coordinates the path is exactly perpendicular to the energy boundary. Hence, since the path cannot cross the energy barrier, it must end there. The end of the path will be called a perfect reflection point, since if we consider the motion of the system as represented by a point tracing out the path, this point will move up to the energy barrier, stop, and then retrace the same path in the opposite direction. It is clear that if the path has two perfect reflection points, then the motion of the system will be periodic.

In the consideration of particular solutions found by numerical integration, it is highly improbable that any given path will have a perfect reflection point. Indeed, with numerical integrations, truncation errors make it impossible to determine a perfect reflection point, even if it did exist in the exact solution for a given set of initial conditions. However, the path may approach the energy barrier sufficiently closely for a considerable portion of the path to be approximately retraced. The point where the path comes close to the energy barrier will be called a reflection point. If the path has two reasonably close reflection points then the motion of the system will be almost periodic, in that the gross characteristics of the motion will be repeated for at least several periods; this definition of "almost periodic" is much less stringent than the precise mathematical definition.

TYPES OF MOTION

We have already considered the one and only known periodic solution for this system; the pure symmetric mode. Also from the discussion of orbital stability, we know that there exist almost periodic solutions, corresponding to small perturbations from the symmetric mode when $E_1<0.6$. We shall say that this class of solutions exhibits the symmetric type of motion.

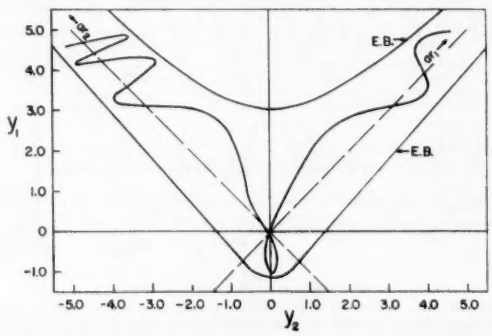

FIG. 7. A dissociation path for $E_T=1.2$, $T=28$. At the origin $E_1=1.1$ and $E_2=0.1$. The curve labeled E.B. is given by $V(y_1, y_2)=1.2$.

[24] B. Stevens, Can. J. Chem. **36**, 96 (1958).
[25] H. Poincare, *Les Methodes Nouvelles De La Mecanique Celeste* (Dover Publications, Inc., New York, 1957), Vol. I, pp. 7–9.

Let us now consider a run where the molecule was initially in its equilibrium configuration, with $E_1=0$ and $E_2=0.8375$. (In most runs the molecule was initially in its equilibrium configuration, at the origin of the configuration plane, and we adopted the convention of specifying initial conditions for these runs by giving E_1 and E_2 along with a plus or minus sign, indicating whether $dy_1/d\tau$ is initially positive or negative.) y_1 and y_2 are plotted as functions of τ for this run in Fig. 4. We observe first that there is no correspondence between the actual solution and the harmonic approximation, which for example predicts $y_1\equiv 0$. The solution from $\tau=140$ to $\tau=240$ is "almost periodic." The reflection points, corresponding to a near coincidence in the maxima or minima of y_1 and y_2 show up at $\tau=146$, 170, 194, 218. Furthermore, at these reflection points $y_1\cong\pm y_2$, which means that either r_1 or r_2 is close to zero, and practically all of the energy is localized in one bond. Making the assumption that all the energy remains in one bond, and solving for the corresponding hypothetical diatomic Morse oscillator with masses m_1+m_2 and m_1, we find

$$y_1=\log_e\left[\frac{(E_T)^{\frac{1}{2}}}{(1-E_T)}\sin\left\{\left[\frac{m_2}{m_1}\left(\frac{m_2+2m_1}{m_1+m_2}\right)(1-E_T)\right]^{\frac{1}{2}}\tau+\psi\right\}+\frac{1}{1-E_T}\right]. \quad (23)$$

Equation (23) accurately reproduces the peaks around each reflection point. For $E_T=0.8375$, the "amplitude" of Eq. (23) is 2.46, and the period 14.35, which agree with the observed values. This almost periodic solution is then characterized by a regular shuffling of almost all the energy from one bond to the other, and therefore will be said to exhibit the dissociating type of motion. The path in the configuration plane for this type of motion is highly symmetrical; it is plotted in Fig. 5, for the region $\tau=194$ to $\tau=217$. Other less perfect reflection points are found at $\tau=40$, 66, and 100. The motion in the region about these points is similar to

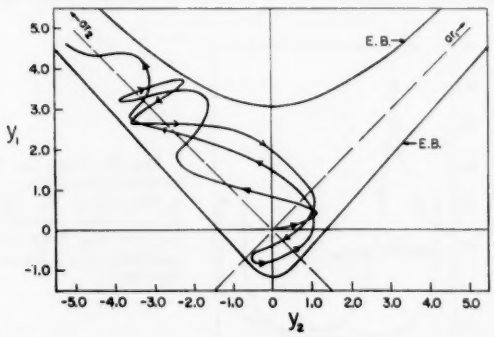

FIG. 8. A dissociation path for $E_T=1.2$, $T=66$. At the origin $E_1=0$ and $E_2=1.2$. The curve labeled E.B. is given by $V(y_1, y_2)=1.2$.

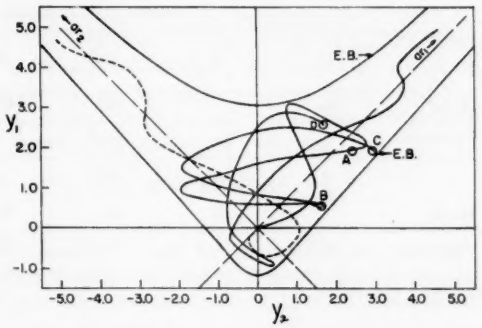

FIG. 9. A dissociation path for $E_T=1.2$, $T=63$. At the origin $E_1=0.4$ and $E_2=0.8$. The curve labeled E.B. is given by $V(y_1, y_2)=1.2$.

that about the reflection points in the almost periodic part of the solution, in that almost all the energy is localized in one bond, and will also be said to be of the dissociating type.

Let us now consider a run made with the initial conditions $E_1=0.1666$, +, $E_2=0.3333$. The motion is again almost periodic, with reflection points at both the maxima and minima of the symmetric mode. The antisymmetric mode oscillates at approximately twice the frequency of the symmetric mode, and for this reason will be said to exhibit the 1–2 type of motion. The path for this type of motion is similar in shape to the parabolic path which exists in the harmonic case when the frequencies are in the ratio 1:2. Because of the symmetry of the model, the 1–2 type motion exists also with its path reflected about the y_1 axis. Two other runs for $E_T=0.5$ were made. Both of these solutions were almost periodic, exhibiting only the 1–2 type of motion. In all these examples of the 1–2 type of motion, the path in the configuration plane for an entire run can be fairly accurately described as a slowly shifting parabola. All of the numerical solutions for $E_T=0.5$ can then be classified as either symmetric or 1–2 types of motion. This behavior supports the main conclusions of Stevens'[24] discussion of vibrational energy transfer, in the case where the total vibrational energy is insufficient to cause dissociation.

An example of the 1–2 type of motion for $E_T=0.8375$ is plotted in Fig. 6. This run was interesting in that it showed a decay of the 1–2 type of motion into the dissociating type. Returning to Fig. 4, we are now able to classify the motion qualitatively as 1–2 from $\tau=0$ to $\tau=16$; dissociating from $\tau=16$ to $\tau=114$; 1–2 from $\tau=114$ to $\tau=128$; and dissociating from $\tau=128$ to $\tau=240$. Five other runs were made at $E_T=0.8375$ and may be classified in terms of these two types of motion with about the same precision as was used in the above description of Fig. 4.

It is possible, then, to describe qualitatively the bounded particular solutions found in terms of three somewhat loosely defined types of motion, where, in the

TABLE I. Time lag between dissociations at $E_T=1.2$.

E_1	0	0.1	0.2	0.3	0.4	0.5	0.6	Hypothetical oscillator
T-Morse	66		83	145	63		21	17.6[a]
T-Harmonic	∞	∞	21.5	14.5	14.5	14.5	14.5	
E_1	0.7	0.8	0.9	1.0	1.1	1.2		
T-Morse		18	19	20	28	∞		
T-Harmonic	14.5	14.5	21.5	28.5	∞	∞		

[a] Computed from Eq. (24).

absence of more complete knowledge, initial conditions have taken on the secondary importance of only determining the type of motion first exhibited. Although this description is only qualitative, the approach to the problem through the consideration of periodic and almost periodic solutions may be capable of further analytical development.[26] In any event it is clear that systems with large anharmonicities exhibit properties far removed from the corresponding harmonic approximations.

DISSOCIATION

In applications to chemical kinetics, the behavior of the system when dissociation is possible ($E_T>1$) is of prime interest. A series of runs were made with $E_T=1.2$. The molecule was initially in its equilibrium configuration in each of these runs. By combining each run with a corresponding one in which the signs of the normal mode velocities ($dy_1/d\tau$ and $dy_2/d\tau$) have been reversed, we are able, by time reversal, to consider the two as one complete run from dissociation to dissociation (i.e., consider one of the two as a function of $-\tau$), a procedure which will prove convenient.

Dissociation is assumed to have occurred when one of the bonds reaches a critical extension $ar_i=\log(100)$, which makes the potential energy in that bond equal to 0.98. This value was chosen because we can be reasonably sure that, if a bond becomes so far extended, it will increase indefinitely, the subsequent motion being that of an atom moving almost freely away from a diatomic molecule. It should be pointed out that even with a complete knowledge of the potential surface, the choice of a "proper" dissociation criterion, applicable to the calculation of a rate constant, is not unambiguous, and depends ultimately on the mechanics of the collisional process.

Nine complete runs, from dissociation to dissociation, were computed. Using the terminology of the preceding section, we can describe five of these as examples of the dissociating type of motion, in which the energy localized in one bond is sufficient for dissociation to occur on the first extension of this bond. In Fig. 7 the configuration path for one of these is plotted. The oscillations about the r_1 or r_2 axis represent the vibrational motion of the unbroken bond. The time interval T between dissociations is determined essentially by the amount of energy remaining in the unbroken bond in the region of the critical extension. Using the unbounded solution for the hypothetical diatomic oscillator discussed in the previous section, and assuming that all the energy is localized in the breaking bond, we find the following expression for the minimum value of T:

$$T_{\min}=\frac{2}{(E_T-1)^{\frac{1}{2}}}\left[\frac{m_2(2m_1+m_2)}{m_1(m_1+m_2)}\right]^{\frac{1}{2}} \times\cosh^{-1}\left[\frac{1+(E_T-1)\exp(ar_i^*)}{(E_T)^{\frac{1}{2}}}\right], \quad 24)$$

where r_i^* is the critical bond extension.

An example of the dissociating type of motion in which the energy localized in one bond was insufficient to break that bond on the first extension is plotted in Fig. 8. In this case, since initially $dy_1/d\tau=0$, the remainder of the path is simply a reflection of that shown, and has been omitted for clarity.

An example of the 1–2 type of motion at $E_T=1.2$ is shown in Fig. 9. The dotted part of the curve resembles the first two examples. The solid path starting at the origin shows the system entering the 1–2 type of motion at the point A, following this through a poor reflection point at B, and up to the reflection point at C. The reflection point at C is so nearly perfect that the

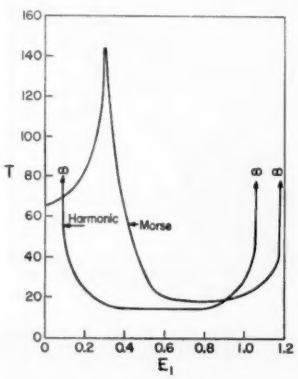

FIG. 10. Time lag T between dissociations as a function of E_1. The discontinuous harmonic function has been approximated by a continuous curve.

[26] See reference 25, p. 82.

system traces back a path almost identical with the incoming path up to the point D, where the system decays out of the 1–2 type of motion and subsequently dissociates along the r_1 axis. The remaining two dissociation runs are too long to be plotted in the configuration plane. These two runs showed no new qualitative features other than their unusual length.[27]

In Table I we list the values of T for all computed paths, as specified by E_1 and E_2 at the origin, for both the Morse and the harmonic models. In the harmonic case we have assumed dissociation when the potential energy (in units of D) in one bond equals 0.98. The T's are plotted as functions of E_1 in Fig. 10. Serious disagreement between the two models is found in the region of $E_1=0.3$, where the lifetime of excited molecules is much greater in the Morse case. The fact that both curves have broad minima at about the same value of T may be coincidental, since the value of this minimum is accounted for, in the Morse case, by the hypothetical diatomic oscillator approximation, Eq. (24), a concept which has no obvious analogy in the harmonic solutions.

In two cases ($E_1=0$ and $E_1=1.1$) we find the not too surprising result that dissociation has occurred in the Morse case, when it is impossible for the harmonic model. Noting that the only particular solution found in which dissociation does not occur is the special case of the pure symmetric mode, and recalling that the pure symmetric mode is orbitally unstable for $E_T>1$, we may reasonably speculate that for $E_T>1$, the set of initial conditions which do not lead to dissociation is of zero measure. The use of a requirement for dissociation which is less stringent than that given by the harmonic model, although still retaining the general framework of Slater theory, has been mentioned by Slater,[6] and discussed quantitatively by Gill and Laidler,[28] especially with regard to its effect at low pressures.

[27] Graphs of the results of all the calculations described in this paper are available on request.

CONCLUSIONS

We know that strong anharmonic forces are necessarily operative in any system which can dissociate, particularly when the path of this system in configuration space is moving in a region near which dissociation may occur. In view of the predominant effects of anharmonicity exhibited by the present model of a pair of coupled Morse oscillators, we feel that the use of normal modes in approximately describing a dissociation process, along with the extended concept of a gradual flow of energy among these normal modes, is of very doubtful validity. Indeed, in the present model the flow of energy is generally so rapid that normal modes are unrecognizable (see remark in reference 6).

On the basis of these limited results, it is difficult to see how the earlier form of Slater's treatment,[5–7] which was based on a completely harmonic model, can quantitatively describe unimolecular reactions. It is our opinion that a realistic theoretical description of the dissociation process must be based on a model in which the effects of anharmonicity play a leading role. The referee has pointed out, however (and we agree), the danger of generalizing from triatomic to complex polyatomic molecules.

[28] E. K. Gill and K. J. Laidler, Can. J. Chem. **36**, 1570 (1958).

Nuclear Contribution to the Heat Capacity of Terbium Metal*

E. C. HELTEMES AND C. A. SWENSON

Institute for Atomic Research and Department of Physics, Iowa State University, Ames, Iowa

(Received March 2, 1961)

The heat capacity of terbium metal has been measured between 0.25° and 1.0°K. The high temperature data can be expressed as $C=28R\times10^{-3}/T^2$ cal/mole-deg which is in excellent agreement with the paramagnetic resonance experiments of Baker and Bleaney on terbium ethyl sulfate. The data are compared with a Schottky formula for the heat capacity, assuming equal spacing between the nuclear hyperfine levels with an over-all spacing of $\Delta=0.45$°K, corresponding to the high temperature expression above. The agreement is within experimental error except at the very lowest temperatures obtained. The effective field at the nucleus of the terbium atom can be calculated and is found to be $H_{eff}=4\times10^6$ gauss.

THE low-temperature heat capacity of terbium metal has been measured by Kurti and Safrata[1] from 6° to 0.5°K, and by Stanton, Jennings and Spedding[2] from 4° to 1.4°K. Both measurements indicated an anomaly above 1.0°K, but of different magnitude and shape. This anomaly may well be associated with sample purity. The specific heat data below 1°K given by Kurti and Safrata showed a nuclear contribution which appeared to obey a T^{-2} law to 0.5°K. The objective of the present experiments, which used two cast samples of Ames Laboratory terbium metal similar to that used by Stanton, *et al.*, was first, to use a high purity sample to verify the results of Kurti and Safrata, and second, to extend these results to a lower temperature in an attempt to observe a departure from the T^{-2} dependence.

An ADL magnetic refrigerator, considerably modified, was used to cool the samples, and this established the lowest available temperature as 0.25°K. The heat reservoir of the magnetic refrigerator (also a piece of terbium metal) was connected by a copper rod to copper wires imbedded in a paramagnetic susceptibility thermometer (a sphere of powdered potassium chrome alum saturated with DC 550 silicone oil), which was in turn attached to the sample assembly by means of a superconducting lead switch.[3] This thermal switch, which was operated by a liquid-nitrogen-cooled solenoid, connected the susceptibility thermometer to the sample assembly, and enabled measurements to be made without having the susceptibility thermometer in thermal contact with the sample.

The sample assembly consisted of two thin pieces of terbium (0.0063 moles each for most of the runs), bolted and glued with GE 7031 adhesive to both sides of a thin copper strip, a manganin heater with superconducting niobium leads wound noninductively aroung the terbium, and similarly glued, and a 470 ohm (nominal) ½ watt "Old Speer" resistor mounted on the copper strip. The carbon resistor and the susceptibility thermometer were calibrated between 4° and 1°K using the T_{55E} scale, and the resistor data were fitted to an equation of the form $T_r=a\ln R(\ln R-b)^{-2}$. The term a varied slightly (one to three percent) from one run to the next, whereas b was roughly constant. Typical values were $a=0.0955$ and $b=2.715$. Paramagnetic susceptibility temperatures T_s were used to obtain corrections to the extrapolated temperatures T_r which were obtained from the above equation. The temperature difference, T_s-T_r, was less than 0.02° at all temperatures, but decreased rapidly

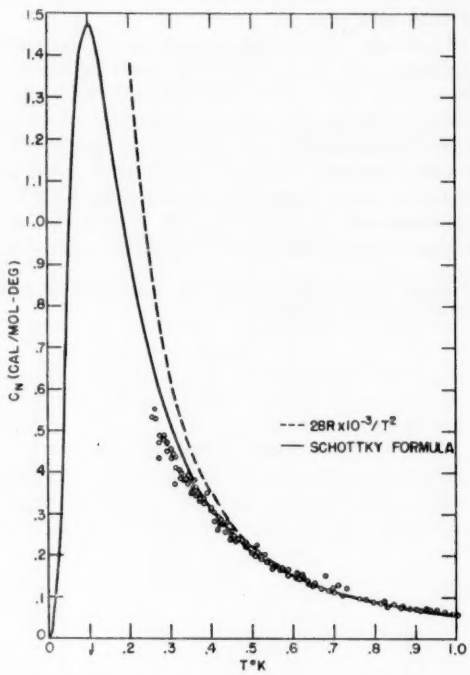

FIG. 1. The experimental data compared with Eqs. (1) and (2) with $A=28$ in Eq. (1).

* Contribution No. 998. Work performed in the Ames Laboratory of the U. S. Atomic Energy Commission.

[1] N. Kurti and R. S. Safrata, Phil. Mag. **3**, 780 (1958).

[2] R. M. Stanton, L. D. Jennings, and F. H. Spedding, J. Chem. Phys. **32**, 630 (1960).

[3] J. G. Daunt, Proc. Phys. Soc. (London) **A70**, 641 (1957).

below 0.5°K. This resulted in a fairly large correction to ΔT_r, the apparent temperature change for a given heat input, in this region. The carbon resistor temperatures were monitored on a 0–1 mv recording potentiometer which was attached to the galvanometer terminals of a Rubicon type B potentiometer. The procedure was, in most respects, the same as that used by Gaumer and Heer[4] in measuring the atomic heat of sodium metal.

The heat capacity contribution of the non-terbium part of the sample assembly was estimated as roughly four percent at 1°K, and was of much less significance at lower temperatures. The nuclear contribution C_N was obtained by subtracting from the data this correction and the values of Stanton, *et al.*, for the spin wave and electronic terms, while the lattice contribution was assumed to be negligible below 1°K. The results for C_N are shown in Fig. 1, where the high temperature data can be expressed as

$$C_N = A \times R \times 10^{-3}/T^2, \tag{1}$$

with $A = 28$ (± 1) (dashed line in Fig. 1). There is a small deviation near 1°K which may be due to the tail of the anomaly mentioned above. The experimental error above 0.5°K is estimated at about five percent, while at the lowest temperature it could be as large as 10 percent due to uncertainties in the temperature differences.

Kurti and Safrata reported $A = 25$ (± 1), while the paramagnetic resonance experiments of Baker and Bleaney[5] on terbium ethyl sulfate give $A = 28.2$ (± 0.6). Our experimental data agree within experimental error with Kurti and Safrata at their lowest temperature, 0.56°K, and also at 1°K if the same spin-wave correction term is used. Thus, the discrepancy in the values of A perhaps can be traced to the fact that they used too high a spin-wave correction, and that they should have observed deviations from Eq. (1) even at 0.56°K. The agreement between the resonance experiments in the dilute salts and the heat capacity measurements on the pure metal was excellent.

The nuclear specific heat of terbium arises from a splitting of the nuclear spin states into four hyperfine levels. This splitting arises from an effective field H_{eff} produced by the electronic spins in the $4f$ orbitals, interacting with the magnetic moment of the terbium nucleus, which has spin $I = \frac{3}{2}$.[5] The nuclear specific heat could be given by a formula of the Schottky type[6] if one assumed no direct nuclear spin-spin interaction and an equal spacing $\Delta/3$ between the four levels. Thus,

$$C_N = \frac{\Delta^2 R}{9k^2T^2}\left\{\frac{\exp(-\Delta/3kT)[1+\exp(-\Delta/3kT)]^4+4\exp(-\Delta/kT)}{[1+\exp(-\Delta/3kT)+\exp(-2\Delta/3kT)+\exp(-\Delta/kT)]^2}\right\}. \tag{2}$$

The specific heat as calculated from this equation is shown also in Fig. 1 (solid line), with $\Delta = 0.45$°K, corresponding to the high temperature value of $A = 28$. The disagreement between the calculated curve and the experimental data would seem to be slightly outside the experimental error at the lowest temperatures. Equation (2) would predict a maximum in the specific heat at about 0.1°K, with a value of C_N of the order of 1.5 cal/mol-deg. The value of Δ also allows one to use the magnetic moment of terbium as given by Baker and Bleaney[7] ($\mu = 1.52(\pm 0.08)$ nuclear magnetons) to calculate $H_{\text{eff}} = 4 \times 10^6$ gauss.

The authors are indebted to Dr. F. H. Spedding and Dr. A. H. Daane for kindly furnishing the high purity terbium metal which was used in this work.

Note added in proof. Recent NMR work on terbium metal [J. Herve' and P. Veillet, Compt. rend. **252,** 99 (1961)] has been called to our attention by Dr. N. Kurti, who also informed us of a theoretical explanation which was advanced by Bleaney and Hill (to be published) for the differences between the NMR data and those of reference 1. The latter authors have suggested that the electrical quadrupole interaction with the terbium nucleus is responsible for the departure of the specific heat curve from the Schottky curve of Fig. 1. The value of A [Eq. (1)] which can be derived from the NMR data (29.1) represents our data well down to 0.5°K when it is inserted into Eq. (2). The deviation below this temperature can be explained qualitatively by the quadrupole interaction, although the theory suggests that the influence of this interaction should be observable within our experimental precision at even higher temperatures. We are indebted to Dr. Kurti for his comments, and to Professor Bleaney and Dr. Hill for their suggestions and for communicating their results to us prior to publication.

[4] R. E. Gaumer and C. V. Heer, Phys. Rev. **118,** 955 (1960).
[5] J. M. Baker and B. Bleaney, Proc. Phys. Soc. (London) **A68,** 257 (1955).
[6] Charles Kittel, *Introduction to Solid State Physics* (John Wiley & Sons, Inc., New York, 1953), p. 136.
[7] J. M. Baker and B. Bleaney, Proc. Roy. Soc. (London) **A245,** 156 (1958).

Unperturbed Mean-Square End-to-End Distance of Polyethylene

C. A. J. HOEVE

Mellon Institute, Pittsburgh, Pennsylvania

(Received March 8, 1961)

It is shown that previous methods for calculating the mean-square end-to-end distance $\langle r_0^2 \rangle$ of polyethylene are invalid, since no account is taken of interactions between rotations around chain bonds. With the aid of recently developed matrix methods the value of $\langle r_0^2 \rangle / nl^2$ is calculated to be 6.75 at 160°C in excellent agreement with the results deduced from intrinsic viscosity measurements.

ALTHOUGH the concept of statistical chain element introduced by Kuhn[1] is basic to explanations of the general physical properties of polymers, a detailed insight in the conformations of the chains is required for an understanding of specific physical properties which are influenced by the chemical structure. At present elegant statistical mechanical methods[2–4] are available for calculating such experimentally accessible properties as chain dimensions which depend on the potentials associated with rotations around chain bonds. Polyethylene is one of the simplest molecules for which these potentials are sufficiently known and it is therefore interesting to apply the methods to this polymer and compare calculated and measured results.

Through the pioneering studies of Mizushima[5] and Pitzer[6] on normal paraffins it is known that three minima exist in the potential energy as function of the rotational angle φ around C—C bonds: one *trans* state ($\varphi = 0°$) and two symmetrically disposed *gauche* states ($\varphi = \pm 120°$). Furthermore, from spectral data an energy difference of 500 cal/mole[7,8] was obtained between *gauche* and *trans* states for normal paraffins higher than butane, in excellent agreement with the deductions from heat capacity measurements.[9] Electron diffraction data[10,11] further support this model and yield values of 1.53 A for the length l of a C—C bond and bond angles, $(180-\theta)°$, of 112° in the chain. Assuming these data also for polyethylene, we may calculate the mean-square end-to-end distance $\langle r^2_0 \rangle$ and its temperature dependence according to the following equation[12,13]

$$\langle r^2_0 \rangle / nl^2 = (1+\cos\theta)(1-\cos\theta)^{-1}(1+\langle\cos\varphi\rangle)(1-\cos\langle\varphi\rangle)^{-1}; \quad (1)$$

n is the number of chain bonds. The value -0.45 calculated for $d \ln\langle r^2_0 \rangle / d \ln T$ at 160°C is in good agreement with the value[14] -0.44 derived from stress-temperature measurements on cross-linked polyethylene. However, the value 3.34 calculated for $\langle r^2_0 \rangle / nl^2$ at 160°C does not accord with the value 6.55 deduced[15] from intrinsic viscosity measurements on polyethylene fractions. On reflection this difference between calculated and measured values is not surprising. Equation (1) was derived on the assumption of probabilities for *gauche* and *trans* states independent of the states of neighboring bonds. According to Pitzer[6] and Taylor,[13] however, two consecutive *gauche* states with opposite rotational angles should be highly improbable because of steric repulsions. It is the object of this paper to evaluate the effect of these steric interactions on the chain dimensions.

Let us consider that the energy of a *gauche* state following a *gauche* state with opposite rotational angle is ϵ cal/mole instead of 500 cal/mole for a *gauche* state preceded by a *gauche* state of the same sense or a *trans* state. According to previous methods[4] $\langle r^2_0 \rangle / nl^2$ is then given by

$$\langle r^2_0 \rangle / nl^2 = (001)[\mathbf{E}_3 + 2\mathbf{X}^*\mathbf{D}(\mathbf{E}_9 - \mathbf{S})^{-1}\mathbf{X}]\begin{bmatrix}0\\0\\1\end{bmatrix}, \quad (2)$$

where $\mathbf{E}_3$ and $\mathbf{E}_9$ are unit matrices of order 3 and 9, $\mathbf{D} = \text{diag.}\ (\mathbf{T}^{(1)}\mathbf{T}^{(2)}\mathbf{T}^{(3)})$, $\mathbf{S} = \lambda^{-1}\mathbf{W}\mathbf{D}$, $\xi^* = [\xi_1^*\xi_2^*\xi_3^*]$ is the eigenrow and ξ the eigenvector corresponding to the maximum eigenvalue λ of the matrix

[1] W. Kuhn, Kolloid-Z. **76,** 258 (1936); **87,** 3 (1939).
[2] M. V. Vol'kenstein, *Configurational Statistics of Polymer Chains* (Publishing House, Academy of Sciences, Moscow, U.S.S.R., 1959), Chap. 6.
[3] S. Lifson, J. Chem. Phys. **30,** 964 (1959).
[4] C. A. J. Hoeve, J. Chem. Phys. **32,** 888 (1960).
[5] S. Mizushima, *Structure of Molecules and Internal Rotation* (Academic Press, Inc., New York, 1954), Chap. 5.
[6] K. S. Pitzer, J. Chem. Phys. **8,** 711 (1940).
[7] N. J. Sheppard and G J. Szasz, J. Chem. Phys. **17,** 86 (1949).
[8] S. Mizushima and H. Okazaki, J. Am. Chem Soc. **71,** 3411 (1949).
[9] W. P. Person and G. C. Pimentel, J. Am. Chem. Soc. **75,** 532 (1953).
[10] K. Kuchitsu, Bull. Chem. Soc. Japan **32,** 748 (1959).
[11] R. A. Bonham and L. S Bartell, J. Am. Chem. Soc. **81,** 3491 (1959); R. A. Bonham, L. S. Bartell, and D. A. Kohl, *ibid.* **81,** 4765 (1959).
[12] H. Benoît, J. chim. phys. **44,** 18 (1947).
[13] W. J. Taylor, J. Chem. Phys. **16,** 257 (1948).
[14] A. Ciferri, C. A. J. Hoeve, and P. J. Flory, J. Am. Chem. Soc. **83,** 1015 (1961); P. J. Flory, C. A. J. Hoeve, and A. Ciferri. J. Polymer Sci. **34,** 337 (1959).
[15] Intrinsic viscosity data by P. M. Henry, J. Polymer Sci. **36,** 3 (1959); L. H. Tung, *ibid.* **36,** 287 (1959); and R. Chiang, *ibid.* **36,** 91 (1959). See also P. J. Flory, A. Ciferri, and R. Chiang, J. Am. Chem. Soc. **83,** 1023 (1961).

$[w_{ij}]$. $\xi^*\xi$ are assumed to be mutually normalized.[16] The $\mathbf{X}^*=[\xi_1^*\mathbf{E}_3\ \xi_2^*\mathbf{E}_3\ \xi_3^*\mathbf{E}_3]$ is a "row" vector with "elements" $\xi_1^*\mathbf{E}_3$ etc. and $\mathbf{X}$ is the corresponding "column" vector. $\mathbf{W}$ is a matrix with "elements" $w_{ij}\mathbf{E}_3$. In this case $w_{11}=w_{21}=w_{31}=1$, $w_{12}=w_{13}=w_{22}=w_{33}=\exp(-500/RT)$, $w_{23}=w_{32}=\exp(-\epsilon/RT)$. The $\mathbf{T}^{(1)}$, $\mathbf{T}^{(2)}$, and $\mathbf{T}^{(3)}$ are the transformation matrices corresponding to, respectively, *trans*, positive and negative *gauche* states, R is the gas constant and T is the absolute temperature.

Values of $\langle r^2_0\rangle/nl^2$ and $d\ln\langle r^2_0\rangle/d\ln T$ were calculated for $T=433$°K with the aid of an IBM 650 computer for values of w_{23} ranging from 0 to 0.3. The results are given in Table I. On plotting these results as continuous curves and assuming the experimentally obtained value[14] -0.44 for $d\ln\langle r^2_0\rangle/d\ln T$, we find that $w_{23}=0.052$, corresponding to $\epsilon=2560$ cal/mole. If the same value is used for w_{23}, $\langle r^2_0\rangle/nl^2$ is calculated to be 6.75, whereas the experimental value[15] is 6.55. Alternatively, we may evaluate w_{23} from the measured value of $\langle r^2_0\rangle/nl^2=6.55$ and calculate the temperature derivative using the resulting w_{23}. This procedure yields $w_{23}=0.072$, corresponding to $\epsilon=2280$ cal/mole and a calculated value of -0.48 for $d\ln\langle r^2_0\rangle/d\ln T$, as compared with -0.44 obtained experimentally. The agreement between calculated and measured results is excellent in both instances. As shown below, the calculated value of $\langle r^2_0\rangle/nl^2$ is more reliable than that of $d\ln\langle r^2_0\rangle/d\ln T$.

Experimental errors in $\langle r^2_0\rangle/nl^2$, mainly as a result of uncertainties in the second virial coefficients, may be as high as ten percent. An experimental error of the same magnitude is estimated for $d\ln\langle r^2_0\rangle/d\ln T$. Possible deficiencies in our knowledge of the potentials associated with bond rotation may affect the calculated values as follows. The angles of rotation in two consecutive *gauche* states with opposite rotational angles must be distorted from their normal values $\pm 120°$, since in this case the steric repulsions between two hydrogen atoms substituted on carbon atoms which are separated by three CH_2 groups must be intolerably large. Furthermore, differences in vibrational partition functions due to differences in shapes of the potential energy valleys have been neglected. However, this is probably a good approximation for states other than the highly strained state considered above. Although the calculated values of $d\ln\langle r^2_0\rangle/d\ln T$ may be somewhat in error as a result of these uncertainties, the value 6.75 calculated for $\langle r^2_0\rangle/nl^2$ is rather insensitive to distortions of these strained states and should be reliable. The excellent agreement between calculated and measured values of this quantity is an indication that interactions along the chain of still higher order than considered here must be relatively unimportant. This conclusion is corroborated by an examination of molecular models.

[16] It is to be noted that ξ^* is in general not the transpose ξ^T of ξ. Only for symmetric matrices $[w_{ij}]$ is $\xi^*=\xi^T$.

TABLE I. Calculated values of $\langle r_0^2\rangle/nl^2$ and $d\ln\langle r_0^2\rangle/d\ln T$ at 160°C.

w_{23}	ϵ(cal/mole)	$\langle r_0^2\rangle/nl^2$	$-d\ln\langle r_0^2\rangle/d\ln T$
0.30	1043	4.69	0.625
0.25	1201	5.03	0.631
0.20	1394	5.40	0.623
0.15	1643	5.81	0.595
0.10	1994	6.27	0.539
0.05	2594	6.77	0.438
0.00	∞	7.33	0.219

ACKNOWLEDGMENTS

The author thanks Dr. P. J. Flory for reading and criticizing the manuscript. Support by the Office of Naval Research is gratefully acknowledged.

Electron Density Distributions in ZnO Crystals*

GANESH P. MOHANTY† AND LEONID V. AZÁROFF

Metallurgical Engineering Department, Illinois Institute of Technology, Chicago, Illinois

(Received March 3, 1961)

Electron density distributions have been determined for two ZnO crystals that had been heated in Zn vapor and for an undoped crystal by very accurate measurements of their x-ray diffraction intensities. An examination of the difference between the electron densities of doped and undoped crystals shows that the doped crystals contain $15–60\times10^{19}$ atoms/cm^3 in the octahedral interstices. The incorporation of this large number of interstitial Zn atoms increases the axial ratio of the hexagonal unit cell from 1.6019 to 1.6025. The density of interstitials is approximately 1000 times greater than that calculated from the electrical conductivity of these crystals so that it must be concluded that most of the interstitial Zn atoms are electrically neutral. The presence of these interstitials explains why the time required to reach saturation for electrical conductivity is much greater in virgin crystals than in previously doped ones.

INTRODUCTION

ALTHOUGH the semiconductor properties of zinc oxide have been subjected to many investigations, the results obtained have not been easy to interpret because of the uncertainty regarding the relative importance of interstitial zinc atoms and oxygen vacancies in conduction processes.[1,2] As pointed out by Thomas,[3] chemical methods used to determine the amount of zinc present have limited value because they are equally affected by any other reducing agent present such as oxygen vacancies or impurities. Nevertheless it is generally agreed that *n*-type conductivity in semiconducting ZnO crystals is primarily due to interstitial zinc atoms although only indirect evidence for this has been presented so far. Recent electron density determinations for CdS have suggested that it may be possible to detect the presence of interstitial atoms in the so-called zincite or wurtzite-type structure by carefull x-ray diffraction measurements.[4] It was decided, therefore, to determine the electron density distribution in a ZnO crystal containing an excess of Zn atoms and to compare this to the distribution in a relatively pure crystal. The experimental and theoretical procedures used are described below. Interstitial zinc atoms were found to be present in the doped crystals in much larger amounts than those deduced from electrical conductivity measurements. Although most of the interstitial zinc atoms are apparently electrically neutral, their presence in such large numbers clearly supports the belief that interstitial zinc atoms and not oxygen vacancies are responsible for the observed conductivity. Moreover, it is now possible to understand a hitherto unexplained lack of reciprocity between the rate of diffusion of zinc atoms in and out of initially pure zinc oxide crystals.

X-RAY DIFFRACTION PROCEDURE

Three ZnO crystals grown at Bell Telephone Laboratories were used in this investigation. The crystals were transparent hexagonal prisms less than 0.01 cm in cross section. One crystal was in the as-grown condition and had a conductivity of 0.05 ohm^{-1} cm^{-1}. The other two crystals had been heated in a zinc vapor atmosphere[3] and had conductivities of the order of 5.0 ohm^{-1} cm^{-1}. The crystals were successively mounted in a special single-crystal diffractometer[5] equipped with a scintillation counter and the x-ray diffraction intensities of their *hk*0 reflections were measured using filtered Ag$K\alpha$ radiation. The intensities of the "pure" and one of the doped crystals were first measured at room temperature. Next, the *hk*0 intensities of the "pure" crystal and the other doped crystal were measured at -190°C using a liquid-nitrogen cryostat specially built for this purpose.[6] The reason for duplication of the measurements was, both, to check their reproducibility with two different doped crystals and to enhance the contribution from the expected small number of interstitial zinc atoms by decreasing their thermal vibrations. After correcting the measured intensities for absorption, extinction, anamolous scattering, and Lorentz-polarization effects, the internal consistency of the data was within $\pm2\%$ for all crystals investigated.

ELECTRON DENSITY MAPS

The experimentally determined intensities were converted to structure factors which were then used to synthesize electron density projections along the *c* axis with the aid of the IBM 704 computer at Argonne National Laboratory. The two maps of the projected electron density for the "pure" crystal contained two prominent maxima corresponding to the superposition

* This research was supported by the Office of Scientific Research of the U. S. Air Force.

† Now with Research and Development, A. O. Smith Company, Milwaukee, Wisconsin.

[1] G. Heiland, E. Mollwo, and F. Stöckmann, Advances in Solid State Phys. **8**, 191 (1959).

[2] D. G. Thomas, *Semiconductors* (Reinhold Publishing Corporation, New York, 1959), pp. 269–312.

[3] D. G. Thomas, J. Phys. Chem. Solids **3**, 229 (1957).

[4] Ganesh P. Mohanty and Leonid V. Azároff, Phys. Rev. **120**, 1224 (1960).

[5] M. J. Buerger, *Crystal-Structure Analysis* (John Wiley & Sons, Inc., New York, 1960), p. 120.

[6] A. E. Attard and Leonid V. Azároff, J. Sci. Instr. **37**, 238 (1960).

of pairs of zinc and oxygen atoms in this projection, and spurious background ripples. A very small peak also was present at the origin of the projected cell suggesting that the "pure" crystal may contain some interstitial Zn atoms. As expected, the low-temperature synthesis had higher and sharper maxima, as well as higher ripples in the immediate vicinity of the peak, caused primarily by the use of a finite number of terms in the Fourier series summation. The electron density maps of the two doped crystals were also similar to each other, except for detail, and resembled the maps of the "pure" crystal except for considerable increase in the size of the maximum located at the projected position of the octahedral interstices of the zincite structure. Although these peaks were clearly visible above the background ripples in the electron density, it was not possible to evaluate them directly because the x-ray diffraction intensities had been measured on a relative scale. The structure factors were next placed on an absolute scale, therefore, by using a modification of the Wilson[7] method in which $\ln(F_{obs}/F_{calc})$ was plotted against $\sin^2\theta/\lambda$. This, in turn, made it possible to compute a difference synthesis in which the electron density of the "pure" crystal was subtracted from that of the doped crystal according to the relation:

$$\Delta\rho=\rho_D-\rho_P=1/A\sum_h\sum_k(F_D-F_P)_{hk0}\cos 2\pi(hx+ky),$$

where A is the area of the projected unit cell and the subscripts D and P refer to the doped and pure crystals, respectively. Such a difference map not only has the advantage of showing off any differences between the electron densities of the two crystals, but it also does not suffer from series termination errors since the terms omitted in each series can be expected to cancel in the subtraction. It is important to realize that the above Fourier series is unlike the usual difference syntheses

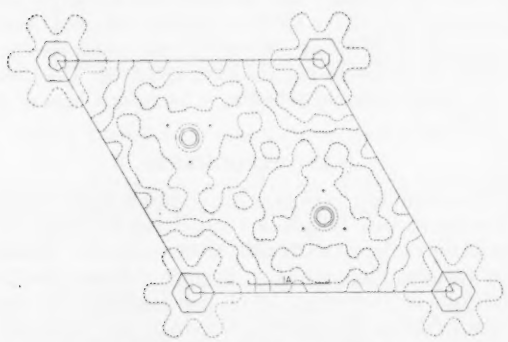

FIG. 1. Difference map of the c axis projection of ZnO obtained by subtracting the electron density of a "pure" crystal from that of a doped one. The zero contour is shown dashed, the solid contours are in equal steps of $1e/A^2$. The deepest negative depressions of $-1.1e/A^2$ are marked by crosses (in vicinity of atomic positions).

[7] A. J. C. Wilson, Nature **150**, 152 (1942).

TABLE I. Unit cell constants of a "pure" and doped ZnO crystal.

Crystal	a	c	c/a
"Pure"	$3.2494_0\pm0.00004$ A	5.2055 ± 0.0001 A	1.6019
Doped	$3.2491_9\pm0.00004$ A	5.2069 ± 0.0001 A	1.6025

used in crystal structure analysis in which the coefficients are differences between observed and calculated structure factors. Since the differences between two measured values are used in this work, any errors due to scaling, etc., are the same for both terms. Such errors, therefore, may introduce small uncertainties regarding the peak height of the final synthesis but do not affect its main features. As a final check of scaling errors, those reflections whose F_{obs} values did not fall on the straight-line logarithmic plot described above were omitted from another difference synthesis performed using room temperature data. The main features of this synthesis were sufficiently similar to those obtained using all the terms as to remove all doubts regarding the validity of the interpretations given below.

Difference maps were prepared using the room-temperature and liquid-nitrogen temperature data. Both maps were quite similar except for detail so that only the room-temperature map is shown in Fig. 1. As can be seen in this figure, the maxima occurring at the interstitial positions (corners of the unit cell shown) stand out quite clearly even in the room-temperature map. The two additional maxima at $\frac{1}{3}$, $\frac{2}{3}$ and $\frac{2}{3}$, $\frac{1}{3}$ represent small differences between the heights and shapes of the superimposed Zn and O peaks in the two crystals. The broken lines in Fig. 1 mark the zero contour separating negative and positive regions in the map. When the positive and negative regions lying within the projected areas of the two atoms (at $\frac{1}{3}$, $\frac{2}{3}$ and $\frac{2}{3}$, $\frac{1}{3}$) are integrated and summed, an excess negative density of 0.11 electrons obtains. Since this area contains the difference between the projected electron densities of the atoms in a doped and a pure crystal, the excess in negative density suggests that some of the zinc atoms in the doped crystal have been displaced from their correct sites (at $\frac{1}{3}$, $\frac{2}{3}$ and $\frac{2}{3}$, $\frac{1}{3}$) to the interstitial sites (at the corners of the projected cell in Fig. 1). The difference of -0.11 electrons is only slightly larger than the standard deviation of 0.10 electrons/A^2, however, so that no real significance can be attached to it.

The contours in the map shown in Fig. 1 are drawn in electron units so that is is possible to measure the volume of the origin peak and to calculate the number of interstitial zinc atoms present, on the average, in one unit cell. The volume of the origin peak corresponds to 0.942 electrons per unit cell of the doped crystal measured at room temperature. (Actually this number is a measure of the increase in electrons over any that may be present in these sites in the so-called pure crystal.) According to this calculation there are 6×10^{20} atoms/cc

in the interstices of the crystal studied at room temperature and 15×10^{19} atoms/cc in the one studied at liquid-nitrogen temperatures. Because the absolute scale determined by the Wilson method[7] is subject to small errors, however, these concentrations of interstitials should be regarded as order of magnitude estimates only. Nevertheless they clearly do not agree in magnitude with 10^{17} atoms/cc deduced by Thomas[8] for these crystals from electrical conductivity measurements.

UNIT CELL CHANGES

In view of the unexpectedly large amount of interstitial zinc atoms disclosed by the electron densities of the doped crystals, it was decided to check the specific gravity of both crystals. The unit cell constants for the "pure" and doped crystals were determined at room temperature using a special back-reflection Weissenberg camera.[9] The results are summarized in Table I. The calculated densities of both crystals are quite similar, 5.72 g/cm^3 and 5.73 g/cm^3 for the "pure" and doped crystals, respectively. The very small size of the actual crystals used prevented accurate measurement of their densities; that of the doped crystal was found to be $3\frac{1}{2}\%$ greater. Nevertheless the data in Table I clearly show the increase in the c/a ratio that may be expected for such a large number of interstitial zinc atoms. These values can be compared to those determined by Gray[10] who found that $a=3.2495\pm0.0002$ A and $c=5.2066\pm0.003$ A for a pale yellow ZnO crystal.

DISCUSSION

The electron density determinations described above, supported by the measured unit cell volume changes, clearly indicate that the actual number of interstitial zinc atoms present in a ZnO crystal doped by heating in a zinc vapor atmosphere is about 1000 times greater than the number deduced from conductivity measurements. Since there are no doubts regarding the accuracy of the latter, this means that the bulk of the interstitial zinc atoms are electrically neutral. It follows, therefore, that electrical conductivity measurements are not a wholly reliable indicator of the actual number of interstitial atoms present in ZnO crystals. This is probably also true of other crystals having the zincite structure because it contains continuous "tunnels" formed by adjacent octahedral voids whose total number just equals the number of zinc atoms in correctly occupied tetrahedral voids. In this regard it should be noted that the amount of interstitial zinc atoms present in the doped crystals analyzed above is just above the lower limit of detectability by the latest x-ray diffraction methods. For example, similar maxima were observed in the interstitial positions of isostructural CdS crystals doped with Cl additions,[4] however, they were too small to allow an equally unambiguous interpretation.

The large amount of interstitial zinc atoms introduced by the doping helps explain the anamolous behavior of ZnO crystals reported by Heiland, *et al.*[11] Suppose a previously doped ZnO crystal is annealed until all electrically active Zn atoms have diffused out of it. When such a crystal is again placed in a zinc vapor atmosphere at an elevated temperature, the time required to restore its conductivity is equal to the time required to remove the conductivity by annealing in air at the same temperature. A similar reciprocity exists between the growth in optical absorption and subsequent bleaching rates. If a virgin crystal is used, however, it takes about 1000 times longer to reach saturation at the same temperature than it does to anneal it. In view of the above reported results it appears that the initial doping requires a longer time period because a very large number of zinc atoms must enter interstitial sites before electrical conductivity reaches a saturation value. On the other hand, subsequent doping treatments can proceed more rapidly because the bulk of the interstitial atoms have been already incorporated in the crystal. Since these atoms are electrically neutral, their presence in the crystal does not directly affect the measured conductivity values.

The above discussion implies that the ionized zinc atoms diffuse more rapidly than the neutral ones. This is a reasonable assumption in view of the much smaller size of the ions (radius [12] of Zn^{+2} in octahedral sites is 0.74 A) relative to that of a neutral atom ($\sim$1.3 A). The stability of neutral atoms in the relatively large octahedral voids of the zincite structure is also attested to by the tendency of naturally occurring crystals to contain many interstitial atoms responsible for the deep red color of most zincite mineral specimens. It is of interest to cite in this connection an experiment performed by Thomas[13] who observed that a ZnO crystal heated in zinc above 800°C acquired a red color. After annealing it in air at 500°–600°C, the excess conductivity was removed but the color remained. The color was finally removed following a prolonged anneal at 900°C.

ACKNOWLEDGMENTS

We would like to express our gratitude to Dr. D. G. Thomas of Bell Telephone Laboratories for supplying us all the ZnO crystals used in this investigation. Thanks are also due Professor M. J. Buerger of Massachusetts Institute of Technology for making available to us the back-reflection Weissenberg camera in his laboratory and to Argonne National Laboratory for permitting us to use their IBM 704 computer.

[8] D. G. Thomas (private communication).
[9] M. J. Buerger, *X-Ray Crystallography* (John Wiley & Sons, Inc., New York, 1942), p. 436.
[10] T. J. Gray J. Am. Ceramic Soc. **37,** 534 (1954).
[11] G. Heiland, E. Mollwo, and F. Stockmann, Advances in Solid State Phys. **8,** 207 (1959).
[12] L. H. Ahrens, Geochim. et Cosmochim. Acta **2,** 155 (1952).
[13] D. G. Thomas, J. Phys. Chem. Solids **3,** 229 (1957).

Reversible Phase Transition of Phosphorus Pentoxide

I. B. JOHNS, H. E. ULMER, AND J. W. EDWARDS

Monsanto Chemical Company and Monsanto Research Corporation, Everett 49, Massachusetts

(Received March 28, 1961)

Measurements of volume change on compression of phosphorus pentoxide showed a reversible phase transition. Pressure-volume curves, obtained by a difference method, showed a marked hysteresis, the forward transition requiring from 1600 to 2700 kg/cm² greater pressure than the reverse, depending on the temperature. X-ray diffraction studies at high pressure confirmed the findings. The crystal form of the new modification has not yet been determined.

INTRODUCTION

IN the course of investigations on the effect of pressure on the conversion of phosphorus pentoxide from its chemically active *H* form to the less reactive *O* and *O'* forms, a new, reversible transformation was discovered. An effect of pressure on the rate of the transition between the known forms was expected because of their different densities: *H*, 2.30; *O*, 2.72; *O'*, 2.89 g/cm³.[1,2]

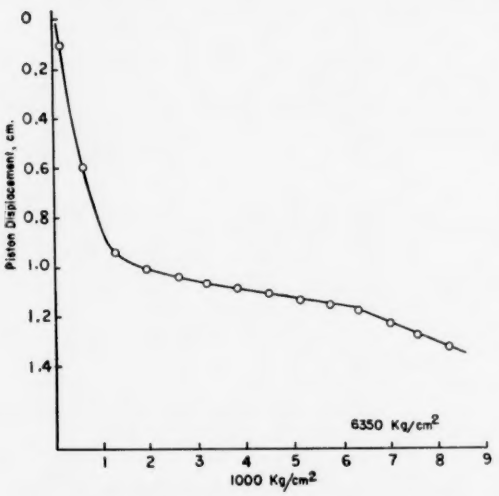

FIG. 1. Compression of phosphorous pentoxide at 215°C.

However, the transformation of the *H* for to the *O* and *O'* forms could not be effected by pressure.

EXPERIMENTAL

The initial study employed a steel bomb, 0.750 in. i.d., equipped with Bridgman plugs. A 15-g sample of *H*-form phosphorus pentoxide (analysis 0.15% water) was compacted into the bomb. The bomb was filled and closed while in a "dry box" under nitrogen dried with phosphorous pentoxide. The bomb was heated to 215°C by means of a temperature-controlled jacket. The upper, movable plug was forced in by a ram driven by a hydraulic press. Measurements of piston displacement vs force were made from which change in volume vs pressure were calculated. As is usual with powders, some time was required after each increase of pressure before the piston reached a steady position. The curve, Fig. 1, shows a definite change of slope at 6330 kg/cm². As will be seen later, this value, obtained without use of a fluid, is considerably too great.

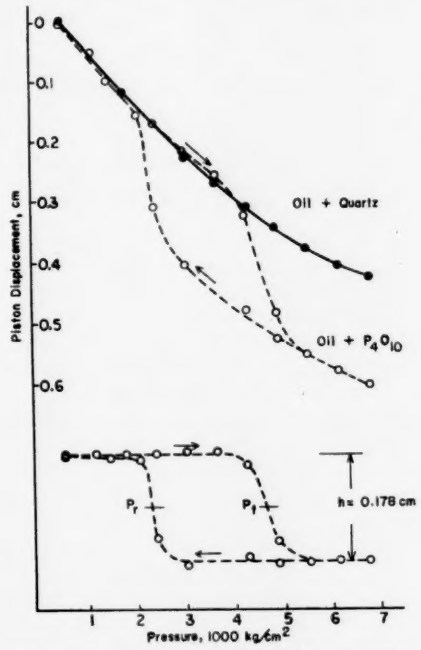

FIG. 2. Pressure-volume curve for P_4O_{10} at 150°C.

After the bomb had cooled while at maximum pressure, the position of the piston showed that the density of the charge was 2.52 g/cm². This decreased to 2.20 g/cm² on releasing the press. The upper plug was mova-

[1] W. L. Hill, G. T. Faust, and S. B. Hendricks, J. Am. Chem. Soc. **65**, 794 (1943).

[2] H. C. J. de Decker and C. H. MacGillavry, Rec. trav. chim. **60**, 153 (1941); H. C. J. de Decker, *ibid.* **60**, 413 (1941).

TABLE I. Transition pressures and volume changes of P_4O_{10}.

T °C	P_f, kg/cm²	P_r, kg/cm²	Δv, cm³
25	3910	1240	0.485
150	4600	2330	0.507
200	4720	2740	0.521
250	5180	3510	0.536

ble while the bomb was hot, indicating that the force was transmitted freely to the charge. After cooling, the plug moved jerkily. The product showed the same x-ray diffraction pattern as the original phosphorus pentoxide, indicating that complete reversion occurred when pressure was released.

Further studies were made in order to observe both the forward and reverse transformation and to determine the effect of temperature on the pressures at which they occur. Accurate pressure-volume curves for phosphorus pentoxide were obtained by a difference method in which the experimentally determined curve for piston displacement vs pressure for a mixture of P_4O_{10} in kerosene was compared with that for a mixture of the same volume of quartz sand in the same volume of kerosene. By this procedure, the bomb is filled to the same volume in each experiment and also contains the same amount of oil so that the difference between the two curves, taken at the same temperature, yields the difference between the curves for the two solids, the compressibility of the oil and the elastic deformations of bomb and piston being eliminated. The result is essentially the curve for P_4O_{10} alone since the compressibility of quartz is too small to be determined in the apparatus.

In Fig. 2 are shown the results of an experiment at 150°C. The solid curve gives the piston displacement vs pressure for 14.45 g silica sand in 4.5 g kerosene. The dotted curve was obtained with 13.0 g phosphorus pentoxide in 4.5 g kerosene. The volumes of the two solids are the same, within 0.2 cm³. The lower dotted curve gives the difference between the upper curves. The marked hysteresis in the transition is evident. This is remarkably reproducible. In one experiment the measurements were repeated around the curve four times with only slight shifts due to extrusion of the copper and lead gaskets in the Bridgman plugs. From the lower curve, the pressure was 4600 kg/cm² when the sample was half transformed in the forward direction and 2330 kg/cm² when half transformed in the reverse direction.

The volume change in the transition was calculated from the piston displacement, $\Delta h = 0.178$ cm, and the cross section of the bomb. In this experiment the change in volume of 13 g (5.652 cm³) phosphorus pentoxide was 0.507 cm³. This is a remarkably large change of volume. The density of the new form is calculated to be 2.53 g/cm³.

The curves for piston displacement vs pressure at 25°, 150°, 200°, and 250°C were determined. From these curves, the pressure for half-conversion in the forward P_f and reverse P_r directions and the volume change Δv in the transitions of 13.0 g phosphorus pentoxide were calculated. These data are given in Table I.

The following four conclusions can be drawn from these data. First, the volume change in the transition is larger the higher the temperature. Second, the pressure at which the forward transition occurs was affected much less by temperature than was the pressure at which the reverse transition occurs. Third, it is probable, from extrapolation of the data in Table I, that the new crystal modification would persist as a metastable form if the temperature were lowered to about −80°C before releasing the pressure. Fourth, it is probable that the hysteresis in the transition will disappear only at a temperature near 500°C, which is above the temperature of the *H–O* transition.

The new transition was confirmed by x-ray diffraction studies at high pressure. For this work, a beryllium pressure cell 1.27 cm o.d. and 1.9 cm long, with an axial hole 0.167 cm i.d., was fitted with steel pistons. The cell was filled with *H*-form phosphorus pentoxide wetted with oil. Force was applied to the pistons by means of a ram driven by a 2-in. diam air cylinder. Air pressure in the range from 0—100 psi yielded pressures in the cell from 1–6450 kg/cm².

With this instrument the diffraction pattern of the *H* form persisted until the pressure was raised above 4700 kg/cm² at 25°C, when the diffraction lines for the new form appeared. On reducing the pressure, the pattern of the new form persisted until the pressure reached 1272 kg/cm² when the pattern of the hexagonal form reappeared. This transition pressure is very near to that observed by the piston displacement method at 25°C, but such good agreement was not obtained for the forward transition.

Due to intense x-ray scattering by the polycrystalline beryllium cell, many of the lines in the diffraction patterns could not be observed. Accordingly, no conclusion can be drawn regarding the crystal form of the new modification. This must await further work with a cell of diamond or single-crystal beryllium.

CONCLUSIONS

High pressure causes a transformation of ordinary hexagonal phosphorus pentoxide to a new crystal modification which reverts to the hexagonal form when pressure is removed. There is a marked hysteresis in the transformation. The width of the hysteresis loop, on the pressure axis, decreases as temperature is raised. The transformation should be truly reversible at about 500°C, while the new modification should persist as a metastable form at one atmosphere and about −80°C.

Paramagnetism of Tetraphenanthroline Dihydroxyl Diferric Chloride*

NORMAN ELLIOTT

Chemistry Department, Brookhaven National Laboratory, Upton, Long Island, New York

(Received March 27, 1961)

The magnetic susceptibility of ferric *o*-phenanthroline has been measured and found to show abnormal temperature dependence. The results are explained in terms of an equilibrium between a singlet ground state and an excited triplet state of the dimer.

TETRAPHENANTHROLINE dihydroxyl diferric chloride, hereafter called ferric *o*-phenanthroline, was prepared by Gaines, Hammett, and Walden[1] in 1936. The authors reported a low magnetic moment, calculated from the room temperature susceptibility, and proposed a binuclear structure,

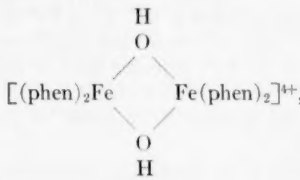

with magnetic interaction in Fe^{3+} pairs, to account for their observation. The susceptibility was redetermined in 1943 by Michaelis and Granick[2] however, and the moment was reported to be normal.

In the course of an investigation of the structural and magnetic properties of some chelates of the transition elements, ferric *o*-phenanthroline was prepared in this laboratory and its magnetic susceptibility measured as a function of temperature. The results are given in Table I and Fig. 1. A diamagnetic correction -273×10^{-6} has been made to the measured susceptibilities to obtain the data as presented. This was determined by measuring the molar susceptibility of *o*-phenanthroline, which was -106×10^{-6}, and adding to twice this value -40×10^{-6} for the two Cl^-, -13×10^{-6} for Fe, and -9×10^{-6} for the OH^- group.[3]

An "effective moment," obtained from the equation $\mu_{\text{eff}}=2.84(\chi_{\text{mol}}T)^{\frac{1}{2}}$ was also reported by Gaines, Hammett, and Walden[1] and by Michaelis and Granick.[2] These workers gave 1.4 and 2.4 Bohr magnetons, respectively, for the solid compound at 300°K. In this work, the value 1.6 Bohr magnetons was found. A reason for the different results is not known, but may be due to the possible existence of polymorphic structures.

The unusual temperature dependence of the magnetic susceptibility of ferric *o*-phenanthroline is similar to that of copper acetate,[4,5] and suggests that the ferric salt possesses a singlet ground state and a slightly higher triplet state. Since the Fe^{3+} ion has an odd number of electrons, normally five, a singlet or triplet state can be achieved if two Fe^{3+} ions combine in pairs, each Fe^{3+} being in a low-spin state with $s=\frac{1}{2}$, in agreement with the observed "effective moment" at room temperature.

Assuming ferric ions in low-spin states, interacting in pairs, the general equation for the magnetic susceptibility[6] reduces to the form

$$\chi=\frac{2g^2N\beta^2}{3kT}\left[1+\frac{1}{3}\exp\frac{W}{kT}\right]^{-1},$$

where g is the Landé factor, equal to 2 for electron spin only, and W is the singlet-triplet splitting energy.

TABLE I. Magnetic susceptibility vs temperature.

Temp °K	76°	177°	189°	245°
$\chi_{Fe}\times10^6$	373	952	985	1067
Temp °K	264°	297°	348°	391°
$\chi_{Fe}\times10^6$	1085	1105	1090	1075

The susceptibility data can be fitted quite well to this equation, taking $2g^2N\beta^2/3k=0.60$ and $W=344$ cm^{-1} (490°K). A temperature-independent term is also required to account for the residual susceptibility at low temperatures. The paramagnetic susceptibility is then given by the equation

$$\chi_{\text{mol Fe}}=\frac{0.60}{T}\left[1+\frac{1}{3}\exp\frac{490^\circ}{T}\right]^{-1}+360\times10^{-6}$$

and is plotted as the solid line in Fig. 1. The value of the g factor, 2.22, is approximately that observed in copper acetate, 2.17, while the temperature-independent magnetism, 360×10^{-6}, is six times larger.

So far as the author is aware, the only other compounds which show this type of magnetic behavior are

* Research performed under the auspices of the U. S. Atomic Energy Commission.

[1] A. Gaines, L. P. Hammett, and G. H. Walden, J. Am. Chem. Soc. **58,** 1668 (1936).

[2] L. Michaelis and S. Granick, J. Am. Chem. Soc. **65,** 481 (1943).

[3] P. W. Selwood, *Magnetochemistry* (Interscience Publishers, Inc., New York, 1943), p. 52.

[4] B. Bleaney and K. D. Bowers, Proc. Roy. Soc. (London) **A214,** 451 (1952).

[5] B. N. Figgis and R. L. Martin, J. Chem. Soc. **1956,** 3837.

[6] J. H. Van Vleck, *Electric and Magnetic Susceptibilities* (Oxford University Press, New York, 1932), p. 235.

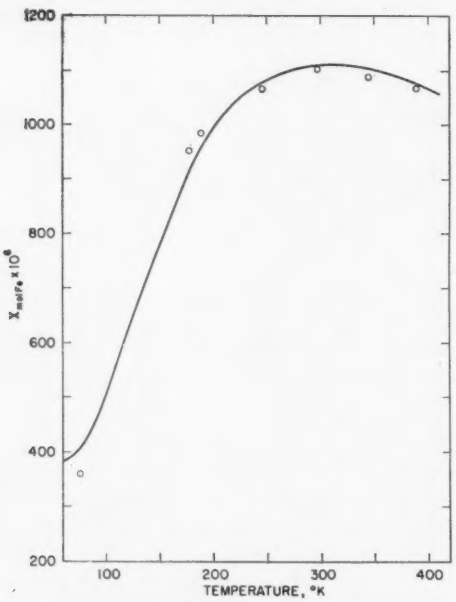

FIG. 1. Magnetic susceptibility of tetraphenanthroline dihydroxyl diferric chloride as a function of temperature. O, experimental susceptibility; —, calculated susceptibility.

the Cu II *n*-alkanoates.[7] These substances contain dimeric molecules with symmetry $D_{4h}-4/mm$, two Cu^{2+} ions lying on the fourfold axis, bridged by four carboxyl groups. A similar structure was considered for ferric *o*-phenanthroline with Fe^{3+} ion pairs on the fourfold axis and bridged by the nitrogen pairs of four phenanthroline molecules; but this structure was discarded for reasons of stereochemical hindrance. The configuration proposed by Gaines, Hammett, and Walden[1] appears to be the only one that is stereochemically stable.

[7] R. L. Martin and H. Waterman, J. Chem. Soc. **1957**, 2545.

In reasonably more detail, without the information that could only be supplied by an x-ray analysis, it may be assumed that the

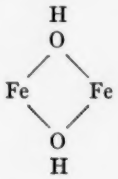

group is square. Using covalent radii taken from Pauling's tables,[8] 1.20 A for Fe^{3+} and 0.66 A for O^{2-}, the Fe^{3+} ions would be 2.63 A apart, approximately the same separation found for Cu^{2+} ions in copper acetate. This configuration of the magnetic group suggests that each O^{2-} is bonded to two Fe^{3+} ions by two p orbitals to form σ bonds at 90°. Each Fe^{3+} in turn has a $d_{x^2-y^2}$ orbital directed toward the ligand oxygens. The d_{xy} orbitals of the Fe^{3+} pairs are then in just the right orientation to form an Fe—Fe bond, each Fe d_{xy} orbital containing one electron as a result of the low-spin configuration.

The absence of a classically conjugated bridge in ferric *o*-phenanthroline, such as we find in copper acetate, does not rule out the possibility that the irons are coupled by an indirect exchange mechanism, for each oxygen has an unshaired electron pair which may be used in π bonding to the iron and bring about the magnetic coupling.

ACKNOWLEDGMENTS

The author wishes to thank Dr. David Christman, Dr. Stanley Seltzer, and Dr. Max Wolfsberg for their interest and help in this work.

[8] L. Pauling, *Nature of the Chemical Bond* (Cornell University Press, Ithaca, New York, 1948), Chap. V.

Band Structure and Transport of Holes and Electrons in Anthracene

OLIVER H. LEBLANC, JR.

General Electric Research Laboratory, Schenectady, New York

(Received March 13, 1961)

Previous mobility measurements indicate that the band approximation can be used to describe the behavior of injected holes and electrons in anthracene, and the present theoretical investigation appears to confirm this. The structures of the bands appropriate to a hole or electron are calculated with the tight binding approximation. Hückel linear combinations of Slater-type atomic orbitals are used for the molecular basis functions. Both bands are highly anisotropic and each is found to be approximately 0.56 kT wide at room temperature. Mobility tensors are derived using a simplified treatment of scattering which assumes isotropic scattering parameters. The calculated mobilities exhibit roughly the anisotropy that has been observed experimentally. Magnitudes of the scattering parameters are estimated from the observed mobilities, and these are found to be reasonable (e.g., free path>lattice distances).

INTRODUCTION

KEPLER[1] and LeBlanc[2] have measured the mobilities of electrons and holes injected in small numbers into an otherwise neutral anthracene crystal. Although the experimental information is not yet complete (the anisotropy of the mobility is not completely determined, for example), two facts have been clearly established: (1) The mobilities of both holes and electrons are of the order of 1 cm^2/v-sec at room temperature. (2) The mobilities vary with absolute temperature as T^{-n}, with $1<n<2$.

In a molecular crystal such as anthracene, the overlap of wave functions of adjacent molecules is small. It is, therefore, not clear *a priori* how the transport of an excess carrier will proceed in such a crystal. Since the overlap is small, the time required for resonance transfer of the excess carrier between adjacent neutral molecules will be relatively long. It might be so long, in fact, that transport could proceed more rapidly by phonon assisted "jumps" between nearest neighbors than by resonance transfer between them. Such a "jumping" process should lead to mobilities which increase strongly with increasing temperature, as is observed, for example, in the d bands in NiO.[3] This is not observed in anthracene.

The temperature dependence in anthracene, on the contrary, indicates that the effect (if any) of lattice phonons is to inhibit rather than promote transport. This suggests strongly that transport in anthracene can be treated in the usual band-approximation scheme. This approach uses as basis functions the Bloch momentum eigenfunctions of the perfect lattice. Crystal imperfections, phonon or other, are treated as perturbations that scatter the carriers among these perfect lattice states.

In order to be physically meaningful, such a band-approximation scheme must satisfy a stringent restriction imposed by the uncertainty principle.[4] One possible statement of this restriction is that the carrier mean-free path with respect to scattering must be larger than the lattice spacings. If this is not true, Bloch functions will be poor approximations to the carrier wave functions.

Applying this restriction in the formulation given by Fröhlich and Sewell[4] to anthracene, one finds that the observed mobilities are consistent with a band description only if the widths of the bands for holes and electrons are of the order of, or smaller than, kT at room temperature.

In this paper, we attempt to calculate directly the structure of the one-electron bands appropriate to excess holes and electrons in anthracene. The tight-binding approximation is used, with the best available approximate molecular wavefunctions as basis functions. Both bands are highly anisotropic, and each is found to have a width of $\approx 0.56kT$ at room temperature. The anisotropy should be relatively insensitive to variations in the approximate molecular wavefunctions used, whereas the bandwidths are very sensitive. The absolute accuracy of the calculated bandwidths is therefore not certain. The fact that they are found to be of the order of magnitude required by the uncertainty principle argument, however, indicates that the calculated values must be reasonably accurate.

Mobility tensors for holes and electrons are then derived from the band structures and a highly simplified treatment of scattering. It is assumed that scattering can be described in terms of an isotropic scattering parameter, and two possible cases are considered: (1) constant free time, and (2) constant free path. For either case, the mobility exhibits roughly the anisotropy that has been observed experimentally. Values of the scattering parameters are estimated from the reported mobilities,[1,2] and the results appear to be reasonable (e.g., free path $\approx$30–80 A).

[1] R. G. Kepler, Phys. Rev. **119**, 1226 (1960).
[2] O. H. LeBlanc, J. Chem. Phys. **33**, 626 (1960).
[3] F. J. Morin, Phys. Rev. **93**, 1195 (1954).
[4] H. Fröhlich and G. L. Sewell, Proc. Phys. Soc. (London) **74**, 643 (1959).

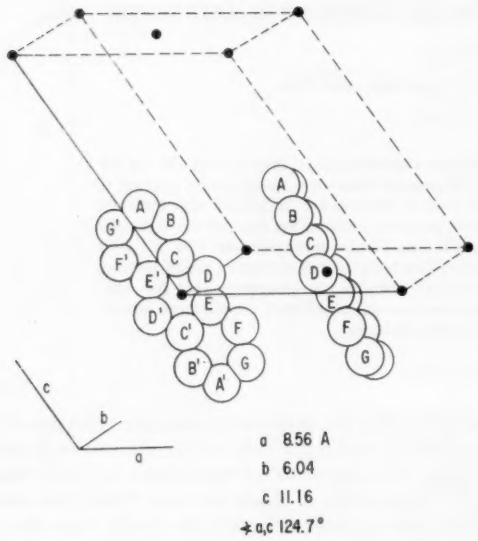

FIG. 1. Schematic representation of unit-cell geometry after reference 5. The two molecules in the cell make equal and opposite angles of 64° with the *ac* plane.

BAND STRUCTURE

The mobility measurements involve the injection of excess holes or electrons (one or the other, but not both simultaneously) in extremely small concentration (10^{10} cm^{-3} or smaller). At this dilution the interaction between the excess carriers is negligible, and the experimental results should be describable by a one-particle treatment. We therefore consider the case of only one excess hole or electron in an otherwise neutral crystal, each system being in its ground state. In what follows, the band containing the excess electron is called the "electron band," and that containing the excess hole is called the "hole band." This nomenclature, rather than the usual "conduction band" and "valence band," is adopted to emphasize the fact that we are considering the electronic states of two distinct systems rather than two states of the same system.

The anthracene crystal is monoclinic with two molecules per unit cell. The unit-cell structure is shown schematically in Fig. 1.[5] The molecule with geometrical center at (0, 0, 0) is transformed into that with center at ($a/2$, $b/2$, 0) by reflection in the *ac* plane followed by the indicated translations. Denote the unit-cell vectors by **a**, **b**, and **c**, and define new vectors $\boldsymbol{\alpha}=\frac{1}{2}(\mathbf{a}+\mathbf{b})$ and $\boldsymbol{\beta}=\frac{1}{2}(-\mathbf{a}+\mathbf{b})$. Then $\boldsymbol{\alpha}$, $\boldsymbol{\beta}$, and **c** connect the geometrical centers of nearest-neighbor molecules.

Because of the symmetry of the individual molecules and the symmetry of the lattice, interactions between molecules connected by $\boldsymbol{\alpha}$ are the same as interactions between those connected by $\boldsymbol{\beta}$. The Hamiltonian matrix is therefore identical to one describing a hypothetical crystal which is transformed into itself by the translations $\boldsymbol{\alpha}$, $\boldsymbol{\beta}$, and **c**, and which therefore contains one molecule per unit cell. The energy eigenfunctions in the anthracene crystal can therefore be constructed as one unique parametric function of the wave vector **k**, and the eigenvalues will thus be a single-valued function of **k**.

Since the interactions between molecules are small compared to the separations of the states of the isolated molecules, the tight binding approximation[6] can be used. One-electron crystal wave functions $\psi_{\mathbf{k}}$ are constructed from linear combinations of one-electron molecular wave functions ϕ_n,

$$\psi_{\mathbf{k}}(\mathbf{r})=\sum_{n=1}^{N}\exp(i\mathbf{k}\cdot\mathbf{r}_n)\phi_n(\mathbf{r}-\mathbf{r}_n). \tag{1}$$

Here $\mathbf{r}_n$ locates the geometrical center of molecule n, and the sum extends over the N molecules in the crystal. The molecular wave function ϕ_n is understood to be oriented in the crystal in the same way as is molecule n. Otherwise, ϕ_n is the same function for all n. In Eq. (1) and throughout the paper, the integrals $\int\phi_m^*\phi_n d\tau$ are neglected for $m\neq n$.

Application of periodic boundary conditions[6] defines an elementary cell in **k** space whose volume is given by the conditions

$$-\pi<\mathbf{k}\cdot\boldsymbol{\alpha},\ \mathbf{k}\cdot\boldsymbol{\beta},\ \mathbf{k}\cdot\mathbf{c}\leq+\pi. \tag{2}$$

The conditions (2) do not define the conventional Brillouin zone. But since the Brillouin zone is extremely complex in shape, and since there is a one to one correspondence between points in the Brillouin zone and points in the elementary cell defined by (2), it is convenient and justifiable to use (2) to set the limits on **k**.

In the case of the electron band, the wave function ϕ_n must describe the state where the excess electron is localized on molecule n. Therefore, ϕ_n for this case must be the one-electron wave function for the odd electron in the ground state of the isolated mononegative ion. The interaction between the excess electron and the remaining electrons and the nuclei in the crystal can be treated by the Hartree equation. The crystalline field is approximated by

$$V(\mathbf{r})=\sum_n V_n(\mathbf{r}-\mathbf{r}_n), \tag{3}$$

TABLE I. Intermolecular resonance integrals.

	(10^{-16} erg)	
	Electron	Hole
E_α	−31.1	−21.2
E_β	+19.3	−25.4
E_γ	+0.87	+5.02

[5] V. C. Sinclair, J. M. Robertson, and A. M. Mathieson, Acta Cryst. **3**, 251 (1950).

[6] F. Seitz, *Modern Theory of Solids* (McGraw-Hill Book Company, Inc., New York, 1940).

where V_n is the Hartree potential of an isolated neutral molecule.

The eigenvalue of ψ_n is then[6]

$$E(\mathbf{k}) = E_0 + E_1 + 2\sum_s E_s \cos\mathbf{k}\cdot\mathbf{r}_s, \tag{4}$$

where

$$E_0 = \int \phi_n[-(\hbar^2\Delta/2m) - eV_n]\phi_n d\tau, \tag{5}$$

$$E_1 = \sum_s{}' \int |\phi_n|^2 V_{n+s} d\tau, \qquad s \neq 0, \tag{6}$$

$$E_s = \int \phi_{n+s} V_{n+s} \phi_n d\tau, \tag{7}$$

and the lattice vectors $\mathbf{r}_s$ and $-\mathbf{r}_s$ are counted as one in the sum (4).

In the case of the hole band, exchange interactions between the $2N-1$ electrons in this band cannot be ignored. A Hartree-Fock treatment shows that the one-electron wave functions ϕ_n to be employed in (1) and (4) are those appropriate to an electron in the highest filled orbital of the neutral molecule. The energy of each electron in the band is found to be given by (4) except for the subtraction of one Hartree integral from E_0.

The structure of the bands is determined by the intermolecular resonance integrals E_s. To evaluate them we require functional forms for V_n and the appropriate ϕ_n. We use the approximation employed by Balk, de Bruijn, and Hoijtink in their detailed treatment of the anthracene mononegative ion.[7] V_n is a sum of 14

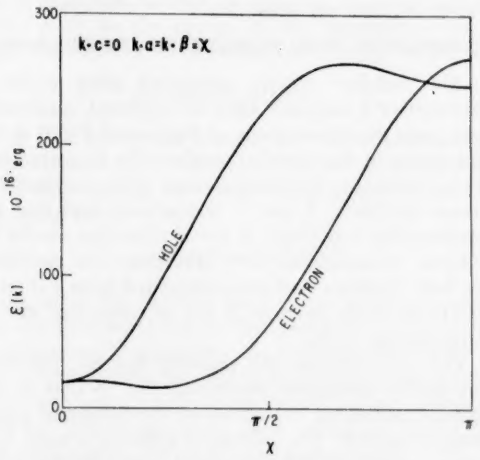

FIG. 2. Variation of $E(\mathbf{k})$ along [110] direction in Brillouin zone showing true maxima and minima. The origins of the energy scales are here arbitrarily chosen to make $E(0)$ the same for both bands.

[7] P. Balk, S. de Bruijn, and G. J. Hoijtink, Rec. trav. chim. **76**, 860 (1957).

TABLE II. Velocity components and mean square velocity.

	(10^{10} cm^2/sec^2)	
	Electron	Hole
$\langle v_a^2\rangle$	6.40	3.01
$\langle v_b^2\rangle$	5.65	5.80
$\langle v_{c'}^2\rangle$	(0.023)	0.760
$\langle v_a v_{c'}\rangle$	(−0.005)	−0.173
$\langle v^2\rangle$	12.07	9.57

Goeppert-Mayer and Sklar[8] neutral carbon-atom Hartree terms. The ϕ_n are Hückel[9] linear combinations of Slater type $2p_z$ atomic orbitals,[10] using for the electron and hole band, respectively, the Hückel coefficients for the lowest antibonding and highest bonding π orbitals.

With this approximation, each intermolecular resonance integral is a sum of many multicenter interatomic integrals. All interatomic integrals involving more than two centers are negligible. Of the remaining $14\times14=196$ two-center atomic integrals in each E_s, only those involving small interatomic distance are important. The calculation is straightforward, but tedious because of the complexities of the intermolecular geometry.[5] Details of the evaluation of the E_s are given in the Appendix.

The resonance integrals fall off rapidly with intermolecular distance, and only five nearest-neighbor interactions are found to be important. As stated above, the integral between molecules connected by $\boldsymbol{\alpha}$ is the same as that between molecules connected by $\boldsymbol{\beta}$, and we call them both E_α. The other significant terms are $E_b(\mathbf{r}_s=\mathbf{b})$ and $E_\gamma(\mathbf{r}_s=\mathbf{c}+\boldsymbol{\alpha}$, and $\mathbf{r}_s=\mathbf{c}-\boldsymbol{\beta})$. Interestingly enough, the integral between molecules connected by $\mathbf{c}$ is negligible, as is that between molecules connected by $\mathbf{a}$.

The one-electron energy for each band, less the constants E_0 and E_1, is given by

$$E(\mathbf{k}) = 2E_\alpha[\cos\mathbf{k}\cdot\boldsymbol{\alpha} + \cos\mathbf{k}\cdot\boldsymbol{\beta}] + 2E_b\cos\mathbf{k}\cdot(\boldsymbol{\alpha}+\boldsymbol{\beta}) + 2E_\gamma[\cos\mathbf{k}\cdot(\mathbf{c}+\boldsymbol{\alpha}) + \cos\mathbf{k}\cdot(\mathbf{c}-\boldsymbol{\beta})]. \tag{8}$$

The terms E_α, E_b, and E_γ for the electron and hole bands are listed in Table I. Except for the term E_γ for the electron band, the calculation of these quantities does not involve the cancellation of large atomic terms. Variations in the molecular wavefunctions used should not alter their relative sizes greatly, nor should averaging over the zero-point intermolecular vibrations.

The quantity E_γ for the electron band does involve the almost exact cancellation of two large interatomic integrals of opposite sign. This cancellation is nearly exact only when the molecules are in their equilib-

[8] M. Goeppert-Mayer and A. L. Sklar, J. Chem. Phys. **6**, 645 (1938).
[9] E. Hückel, Z. Physik **76**, 628 (1932).
[10] J. C. Slater, Phys. Rev. **36**, 57 (1930).

TABLE III. The velocity functions $\langle v_i v_j/|v|\rangle$.

	(10^5 cm/sec)	
ij	Electron	Hole
aa	1.41	0.81
bb	1.03	1.17
$c'c'$	(0.009)	0.19
ac'	(−0.003)	−0.03

rium lattice positions. Therefore, averaging over the zero-point lattice vibrations should increase the effective value of this term in the real crystal over that given in Table I. The effective value should probably be comparable to, but smaller than, E_γ for the hole band.

The true maxima and minima in $E(\mathbf{k})$ occur when $\mathbf{k}\cdot\mathbf{c}=0$ and $\mathbf{k}\cdot\boldsymbol{\alpha}=\mathbf{k}\cdot\boldsymbol{\beta}$, that is, for $\mathbf{k}$ parallel to $\mathbf{b}$. The contour of $E(\mathbf{k})$ for each band along this direction of $\mathbf{k}$ is shown in Fig. 2. The total width of each band is approximately 2.4×10^{-14} erg or $0.56kT$ at room temperature.

The possibility of further bandwidth reduction in the real crystal through lattice polarization can be investigated earily using a treatment of Sewell.[11] His equations for this effect in an ionic lattice can be modified for a rough estimate for a nonpolar lattice by replacing Z (the ionic charge) by $4\alpha/d^3$, where α is the molecular polarizability and d the lattice distance. Inserting reasonable values for these and the other parameters in his equations, one finds that the effect is negligible in anthracene.

MOBILITY TENSOR

We assume that carrier scattering can be described in terms of a relaxation time function $\tau(\mathbf{k})$.[12] We then consider two functional forms for $\tau(\mathbf{k})$, each involving one isotropic scattering parameter: (1) $\tau(\mathbf{k})=\tau_0$, constant free time; and (2) $\tau(\mathbf{k})\times|\mathbf{v}(\mathbf{k})|=\lambda$, constant free path. Here $\mathbf{v}(\mathbf{k})$ is the velocity associated with $\psi_\mathbf{k}$,

$$\hbar\mathbf{v}(\mathbf{k})=\partial E(\mathbf{k})/\partial\mathbf{k}. \tag{9}$$

The assumption of isotropic τ_0 or λ is obviously an oversimplification, since the scattering parameters should be anisotropic in the real crystal.

The mobility tensor is calculated in an orthogonal coordinate system whose axes are parallel to the $\mathbf{a}$ and $\mathbf{b}$ unit-cell vectors and the vector $\mathbf{c}'$ perpendicular to the ab plane. By symmetry, the b axis is a principal axis of the mobility tensor.

For constant free time τ_0, the components of the mobility tensor are

$$\mu_{ij}=e\tau_0\langle v_i v_j\rangle/kT, \tag{10}$$

where the v_i are the corresponding components of $\mathbf{v}(\mathbf{k})$, and the brackets indicate a statistical average over the band. Since the bands are $\approx0.56kT$ wide, the Boltzmann probability varies by a factor of only 1.7 over the band. The quantities $\langle v_i v_j\rangle$ are, therefore, virutally independent of temperature and are within a few percent of their maximum, infinite temperature values. We can therefore neglect the variation of the Boltzmann factor altogether, and the $\langle v_i v_i\rangle$ can then be evaluated in closed form.

The values so obtained are listed in Table II along with the mean square velocities, $\langle v^2\rangle=\langle v_a{}^2\rangle+\langle v_b{}^2\rangle+\langle v_{c'}{}^2\rangle$. The rms velocities are relatively small ($\approx10^5$ cm/sec), a corollary of the small bandwidths.

For constant free path λ, the components of the mobility tensor are

$$\mu_{ij}=e\lambda\langle v_i v_j/|\mathbf{v}(\mathbf{k})|\rangle/kT. \tag{11}$$

Once again we neglect the variation of the Boltzmann factor in computing the quantities in brackets, but even so they cannot be evaluated in closed form. In Table III we list values obtained with a three-dimensional Simpson's rule integration in which the integrands were evaluated at 125 points in $\mathbf{k}$ space [increments of $\pi/2$ in the variables in Eq. (2)]. The error in this integration procedure is such that the values given in Table III are too large and we estimate that they are too large by 50% or less in every case.

The small values of the quantities in Tables II and III for the ac' and $c'c'$ components for the electron band result from the small value of E_γ, which as we noted above is not reliable. These values probably should be comparable to, but smaller than, the corresponding values for the hole band.

COMPARISON WITH EXPERIMENT AND DISCUSSION

The mobility tensors calculated using either τ_0 constant or λ constant agree in a general, qualitative way with the observations of Mette and Pick[13] of the anisotropy of the electrical conductivity in anthracene. They found that the principal axes of the conductivity tensor are the a, b, and c' crystal axes, and that the conductivity is isotropic in the ab plane but smaller by a factor of about 5 in the c' direction. The mobilities for both electrons and holes calculated from Tables II or III are fairly isotropic in the ab plane and smaller perpendicular to it.

The anisotropy of the mobility has not yet been completely determined experimentally, so that no detailed quantitative evaluation of the calculated anisotropy is possible. The calculated mobility tensors with either τ_0 constant or λ constant do agree qualitatively, however, with the preliminary results given by Kepler.[1] He finds, as predicted, that the mobilities of both electrons and holes are larger in the ab plane than perpendicular to it. In contrast to Mette and Pick's results,

[11] G. L. Sewell, Phil. Mag. **3**, 1361 (1958).

[12] See for example, H. Jones, *Handbuch der Physik*, edited by S. Flügge (Springer-Verlag, Berlin, Germany, 1956), Vol. XIX, p. 227.

[13] H. Mette and H. Pick, Z. Physik **134**, 566 (1953).

Kepler also observes some anisotropy in the *ab* plane, as the present work would indicate should be present.

Estimates of the magnitude of τ_0 or λ can be made from the reported magnitudes of the mobilities. Kepler[1] gives values for holes and electrons, respectively, of 0.4 and 0.3 cm²/v sec in the c' axis and 1.3 and 2.0 cm²/v sec in one direction (otherwise unspecified) in the *ab* plane. LeBlanc[2] measured in the c' direction only and found 1.0 and 0.6 cm²/v sec for holes and electrons, respectively. The discrepancy between their results is probably indicative of the variation one might expect among different crystal samples. Comparison of Kepler's results with Tables II and III suggests the scattering parameters for holes and electrons are approximately equal, and we estimate from his mobilities: (1) $\tau_0 \approx 1\times10^{-12}$ sec, or (2) $\lambda \approx 30$ A. LeBlanc's value for the hole mobility gives the somewhat larger values (1) $\tau_0 \approx 2\times10^{-12}$ sec, or (2) $\lambda \approx 80$ A.

These values for the scattering parameters are reasonable. They indicate that the carriers travel, on the average, several lattice distances before being scattered, so that discussion of transport by means of the calculated band structures is credible.[4]

It is perhaps of some interest to try to estimate scattering parameters for phonon scattering directly from the band structure. In principle, this can be accomplished using the method of deformation potentials.[14] Unfortunately, however, this method has not been formulated heretofore in such a way as to be applicable to narrow bands. One, therefore, has to adopt the doubtful procedure of considering only those electrons or holes which are near the edges of their respective bands, and assuming that the wide-band formulation is applicable to these carriers.

Let $E(0)$ be the energy of the appropriate band edge. The deformation potential coefficient is defined as

$$E_D = dE(0)/d(\log V), \tag{12}$$

where V is the crystal volume, and the deformation is understood to leave the crystal symmetry unchanged. For a cubic crystal, the free path with respect to lattice scattering is[14]

$$\lambda_{ph} \approx \hbar^4/128(m^*)^2 E_D^2 \beta kT, \tag{13}$$

where m^* is the effective mass at the band edge, and β is the compressibility of the crystal. For both holes and electrons in anthracene, we estimate $E_D \approx 3\times10^{-14}$ erg and $m^* \approx 10^{-25}$ g. We find no data in the literature for β for anthracene, and use the value[15] for naphthalene, 18×10^{-6} atm^{-1}. Inserting these values in Eq. (13), one calculates $\lambda_{ph} \approx 50$ A at room temperature.

The λ_{ph} so estimated are of the same magnitude as the λ derived from the observed mobilities. However, the calculation of λ_{ph} is obviously very dubious, and we interpret the result only as a very preliminary indication that free paths of ≈ 50 A for lattice scattering are not inconsistent with the calculated band structure.

We therefore conclude that the calculated band structures should form a basis for understanding the behavior of excess holes and electrons in anthracene. A more realistic treatment of scattering than given here, however, will undoubtedly be indicated when more data are available on the anisotropy of the mobilities.

Lastly, it must be emphasized that the band structures are valid only for quite small concentrations of excess carriers. Use of one-electron functions presupposes that carrier interactions can be accounted for with a Hartree-Fock equation. The Bloch functions give suitable solutions only if the average carrier interaction energy is smaller than the bandwidth.[6] Given the small bandwidth calculated here, one finds that the band approximation fails for excess carrier concentrations greater than about 10^{14} cm^{-3}.

ACKNOWLEDGMENT

The author wishes to thank Dr. J. N. Murrell of Sheffield University for a letter describing a similar calculation in anthracene. He has calculated intermolecular overlap integrals and finds an anisotropy almost identical to that found here for the resonance integrals. Dr. Murrell's results will be published shortly.

APPENDIX: CALCULATION OF RESONANCE INTEGRALS

The molecular orbitals used are linear combinations of Slater-type atomic orbitals.

$$\phi_n = \sum_i C_{ni} u_i. \tag{A1}$$

The coefficients C_{ni} are determined from the secular equations given by Hückel[9] with overlap between the u_i neglected. The parameter used in the atomic orbitals is that given by Slater,[10]

$$u_i = (\alpha^5/\pi)^{\frac{1}{2}} r_i \cos\xi_i \exp(-\alpha r_i), \tag{A2}$$

with $\alpha = 1.64$ a.u. $= 3.08\times10^8$ cm^{-1}.

The potential function for the neutral molecule is taken as

$$V_n = \sum_i V_i, \tag{A3}$$

where V_i is the Goeppert-Mayer and Sklar[8] potential of carbon atom i. Using Slater-type orbitals, we find

$$V_i = -e^2 r_i^{-1}\{4+6(\alpha r_i)+4(\alpha r_i)^2+\tfrac{4}{3}(\alpha r_i)^3\} \times \exp(-2\alpha r_i). \tag{A4}$$

Neglecting three-center, or higher, interatomic integrals, each intermolecular integral is given by

$$\int \phi_m V_m \phi_n d\tau = \sum_{i,j} C_{mi} C_{nj} \int u_i V_i u_j d\tau. \tag{A5}$$

[14] W. Shockley, *Electrons and Holes in Semiconductors* (D. Van Nostrand Company, Inc., Princeton, New Jersey, 1950), p. 264.
[15] H. Essex, Z. anorg. u. allgem Chem. **88**, 189 (1914).

Let R_{ij} be the length of the radius vector joining atom i in molecule m and atom j in molecule n. Let θ_i and θ_j be the angles R_{ij} makes with the planes of molecules m and n, respectively. Finally, let η be the angle between the molecular planes. Then each atomic integral in (A5) is given by

$$(\alpha^5/\pi)\ \sin\theta_i \sin\theta_j S(t)+(\alpha^5/2\pi)\ \cos\theta_i \cos\theta_j C(t)\ \cos\eta, \tag{A6}$$

where $t=\alpha R_{ij}$, and

$$S(t)=\int r_i r_j \cos\xi_i \cos\xi_j V_i \exp[-\alpha(r_i+r_j)]d\tau, \tag{A7}$$

$$C(t)=\int r_i r_j \sin\xi_i \sin\xi_j V_i \exp[-\alpha(r_i+r_j)]d\tau. \tag{A8}$$

The integrals $S(t)$ and $C(t)$ can be evaluated in closed form. Sklar and Lydane[16] given an expression for $C(t)$ in terms of subsidiary integrals but do not evaluate the dependence on the argument explicitly. Both integrals have the form,

$$t^{-3}\{P_1(t)e^{-t}+P_2(t)e^{-2t}\}, \tag{A9}$$

where P_1 and P_2 are polynomials of low order. The smallest value of R_{ij} involved in each intermolecular interaction considered is as follows: E_α(3.60 A), E_b(3.75 A), E_γ(3.76 A). Therefore, $t>11.0$ for all distances of interest, and the second term in (A9) is negligible for both $S(t)$ and $C(t)$. For the terms in e^{-t} we find

$$(\alpha^5/\pi)\ S(t)=-e^2\alpha 2^{-7}t^{-3}\{1386+1386t+693t^2 -1696t^3+462t^4\}, \tag{A10}$$

$$(\alpha^5/2\pi)\ C(t)=-e^2\alpha 2^{-8}t^{-3}\{1386+1386t-2123t^2 +1072t^3\}. \tag{A11}$$

Since the atomic integrals decrease strongly with increasing R_{ij}, we find that two-figure accuracy in E_α, E_b, and E_γ can be obtained while neglecting all interactions between atoms more than 5 A apart. This limited the number of interatomic integral evaluations necessary to the values following (out of a possible 196 in each case): $E_\alpha(48)$, $E_b(23)$, $E_\gamma(6)$.

The signs of the resonance integrals are determined by the relative phases chosen for the ϕ_n in Eq. (1). We choose the phases such that $\phi_n(\mathbf{r}-\mathbf{r}_n)$ is transformed into $\phi_{n+\alpha}(\mathbf{r}-\mathbf{r}_n-\boldsymbol{\alpha})$ or $\phi_{n+\beta}(\mathbf{r}-\mathbf{r}_n-\boldsymbol{\beta})$ by (1) reflection in the ac plane passing through $\mathbf{r}_n$, followed by (2) translation by $\boldsymbol{\alpha}$ or $\boldsymbol{\beta}$.

[16] A. L. Sklar and R. H. Lydane, J. Chem. Phys. **7**, 374 (1939).

THE JOURNAL OF CHEMICAL PHYSICS VOLUME 35, NUMBER 4 OCTOBER, 1961

Extension of Stokes' Law for Ionic Motion to Include the Effect of Dielectric Relaxation*

RICHARD H. BOYD

Central Research Department, Experimental Station, E. I. du Pont de Nemours and Company, Wilmington, Delaware

(Received March 29, 1961)

The suggestion made by Fuoss that dielectric relaxation induced by ionic motion in polar solvents contributes to the frictional force experienced by the ion has been treated theoretically on a macroscopic basis analogous to the Stokes' law treatment of the conventional hydrodynamic friction. An equation previously proposed by Fuoss on a semiempirical basis results from this treatment. Experimental dielectric relaxation times are shown to lead to an effect of the proposed magnitude.

I. INTRODUCTION

THE starting point for discussing ionic mobility in solution at infinite dilution under the influence of an electric field has long been Stokes' law. That is, the ion is treated as a sphere moving in a continuous medium under the laws of classical hydrodynamics. Deviations from Stokes' law have been considered as due to breakdown of macroscopic hydrodynamics on a molecular scale and solvation effects.[1] Recently, Fuoss,[2] noticing the effect of dielectric constant on ionic mobility in mixed solvents, has made the important suggestion that dielectric relaxation in polar solvents induced by ionic movement gives rise to frictional resistance to that motion. He presents a semiempirical equation based on heuristic arguments for this effect. Specifically, Stokes' law for ionic motion

$$\lambda_0^{\pm}=\mathfrak{F}^2/(N6\pi\eta r_s) \tag{1}$$

(see Appendix for symbols) is modified to the following form:

$$\lambda_0^{\pm}=\frac{\mathfrak{F}^2}{N6\pi\eta(r+s/\epsilon_s)}, \tag{2}$$

where s is an empirical constant and ϵ_s the static dielectric constant.

The purpose of the present paper is to place this suggestion on a firmer basis by showing that (a) the effect of dielectric relaxation on ionic motion can be treated theoretically on a macroscopic basis in a straightforward manner consistent with Stokes' law itself and (b) the dielectric relaxation times for polar solvents are indeed such that they lead to effects of the magnitude proposed.

II. THEORETICAL TREATMENT

The ion is assumed to be a sphere of radius r moving in a continuous medium of viscosity η and static and high-frequency dielectric constants ϵ_s and ϵ_∞, respectively. The cylindrical coordinate system shown in Fig. 1 is used. It is assumed that the hydrodynamic disturbance of the solvent due to the ionic motion has no influence on the dielectric relaxation and vice versa. This should be a valid assumption since the net ionic motion in the field is a small perturbation on the random molecular motion in the fluid.[1] On this basis

$$f_S v+f_D v=F, \tag{3}$$

where f_S is the conventional hydrodynamic (Stokes' law) friction constant, f_D is the dielectric relaxation friction constant, v is the ionic velocity, and F is the force on the ion due to the electric field. The quantity f_D may be calculated from the rate of energy dissipation in the solvent due to dielectric relaxation induced by the ionic motion

$$\dot{W}=f_D v^2, \tag{4}$$

where $\dot{W}$ is the rate of dissipation of energy induced by one ion. $\dot{W}$ is calculated from the electric-field strength $\mathcal{E}$ and the displacement field D according to

$$\dot{W}=\int_v \dot{W}_v dV=(1/4\pi)\int_v [\mathcal{E}(dD/dt)]dV, \tag{5}$$

where $\dot{W}_v$ is the rate of energy dissipation per unit volume at a given point in the fluid.

The electric field is calculated under the assumptions that lead to the Debye equations[3] for dielectric relaxation. That is, the relaxation function is assumed to be exponential with a single relaxation time. Under the assumption of linear superposition of electric fields from previous time u,

$$D(t)=\int_{-\infty}^{t}\frac{d\mathcal{E}(u)}{du}\alpha(t-u)\,du+\epsilon_\infty\mathcal{E}, \tag{6}$$

where $\alpha(t-u)$ is the relaxation function and is assumed to be given by $\alpha(t-u)=(\epsilon_s-\epsilon_\infty)\{1-\exp[-(t-u)/\tau]\}$. This can be transformed into the following differential equation[3]:

$$\tau(dD/dt)+D=\tau\epsilon_\infty(d\mathcal{E}/dt)+\epsilon_s\mathcal{E}. \tag{7}$$

* Contribution No. 690.

[1] See, for instance, R. A. Robinson and R. H. Stokes, *Electrolyte Solutions* (Butterworths Scientific Publications, Ltd., London, 1959), Chap. 6, 2nd ed.

[2] R. M. Fuoss, Proc. Natl. Acad. Sci. U. S. **45**, 807 (1959).

[3] H. Frohlich, *Theory of Dielectrics* (Oxford University Press, London, 1958), Chap. III, 2nd ed.

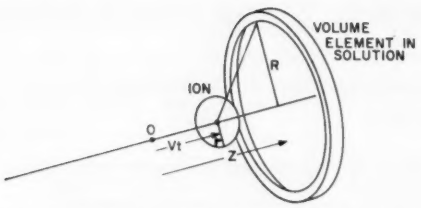

FIG. 1. Coordinate system for moving ion.

The displacement D is given by Coulomb's law as

$$D=e/[R^2+(Z-vt)^2] \tag{8}$$

(see Fig. 1 for coordinates) and

$$\frac{dD}{dt}=\frac{2e}{[R^2+(Z-vt)^2]^2}v(Z-vt). \tag{9}$$

Equation (7) can be integrated to

$$\mathcal{E}(t)=\int_{-\infty}^{t}\exp\left[-\frac{\epsilon_s}{\tau\epsilon_\infty}(t-u)\right]\frac{G(u)}{\tau\epsilon_\infty}du, \tag{10}$$

where

$$G(u)=\tau[dD(u)/dt]+D(u).$$

Explicit integration of Eq. (10) using Eqs. (8) and (9) leads to an expression for $\mathcal{E}$ which, with Eq. (9) for dD/dt can be used in Eq. (5) to compute $\dot{W}$. However, the integrations cannot be carried out rigorously in closed form. We now proceed to demonstrate a very close approximation to the desired result. The approximation is actually the condition that f_D be independent of the electric field. Equation (10) can be integrated by parts to give

$$\epsilon_s\mathcal{E}(t)=G(t)-\int_{-\infty}^{t}\exp\left[-\frac{\epsilon_s(t-u)}{\epsilon_\infty\tau}\right]\frac{dG(u)}{du}du. \tag{11}$$

The integral on the right is very small compared to $G(t)$ as may be shown by the following argument. To a first approximation

$$\exp[-\epsilon_s(t-u)/\epsilon_\infty\tau]$$

may be regarded as a unit step function at $u=t-\tau\epsilon_\infty/\epsilon_s$.[4] This leads to the following approximation:

$$\epsilon_s\mathcal{E}(t)\cong G(t-\tau\epsilon_\infty/\epsilon_s). \tag{12}$$

Examination of Eqs. (8) and (9) shows that if Z is much greater than $v\tau\epsilon_\infty/\epsilon_s$, then $G(t)$ will be very close to $G(t-\tau\epsilon_\infty/\epsilon_s)$. Since v is of the order of 10^{-3} to 10^{-4} cm/sec,[1] and τ of the order of 10^{-11} sec,[5] this is the case. In fact, if it were not, the dielectric relaxation friction constant would be field dependent. $\epsilon_s\mathcal{E}(t)=G(t)$ is used along with Eq. (9) and the ion is set at the origin by letting $t=0$, the nonvanishing contributions to Eq. (5) become

$$\dot{W}=\frac{e^2v^2\tau}{\pi\epsilon_s}\left[\int_{Z=-\tau}^{+\tau}\int_{R=(a^2-Z^2)^{\frac{1}{2}}}^{+\infty}\frac{Z^2 2\pi RdRdZ}{(R^2+Z^2)^4}+2\int_{Z=\tau}^{\infty}\int_{R=0}^{\infty}\frac{Z^2 2\pi RdRdZ}{(R^2+Z^2)^4}\right]$$

$$=\tfrac{4}{9}(e^2v^2\tau/\epsilon_s r^3). \tag{13}$$

Using Eq. (4) we obtain

$$f_D=\tfrac{4}{9}(e^2\tau/\epsilon_s r^3). \tag{14}$$

III. DISCUSSION

Equation (3), using the calculated dielectric relaxation friction constant [Eq. (14)], together with the Stokes' law friction constant leads to the following modified equation for the ionic conductance:

$$\lambda_0^{\pm}=\frac{\mathfrak{F}^2}{N[6\pi\eta r+\frac{4}{9}(e^2\tau/r^3\epsilon_s)]}. \tag{15}$$

It may be seen that, if the dielectric relaxation time τ is proportional to the solvent viscosity, this is essentially Fuoss' modified equation [Eq. (2)]. Thus the empirical

TABLE I. Comparison of calculated and experimental s values.[a]

Ion	Solvent	r	s_{exp}	s_{calc}
Bu_4N^+	ϕNO_2-CCl_4	5.0	15.0[a]	0.96
Br^-	...	1.95	23.5[a]	16.1
I^-	...	2.17	20.5[a]	11.6
NO_3^-	...	2.21	19.5[a]	11.2
Pi^-	...	3.59	13.0[a]	2.56
PCP^-	...	3.55	15.5[b]	2.68
PCP^-	acetone—CCl_4	3.55	1.8[b]	1.33

r = radius based on ionic radii (for Br^-, I^-) or molecular models (NO_3^-, Pi^-, PCP^-). Pi^- is picrate anion; PCP^- is pentacyanopropenide anion.

r for the nonspherical ions is taken as radius of sphere of equal volume.

$\tau(\phi NO_2)=40.9\times10^{-12}$ sec (25°C).[c]

$\eta(\phi NO_2)=1.81\times10^{-2}$ poise (25°C).[d]

$\tau(\phi NO_2)$ in $CCl_4=13.5\times10^{-12}$ sec[e]; 19.6×10^{-12} sec (25°C).[f]

$\eta(CCl_4)=0.904\times10^{-2}$ poise (25°C).[d]

τ(acetone) $=3.3\times10^{-12}$ sec (20°C).[g]

η(acetone) $=0.323\times10^{-2}$ poise (20°C).[d]

$(\tau/\eta)_{25°C}$ is assumed to equal $(\tau/\eta)_{20°C}$ for acetone.

[4] F. Schwarzl and A. J. Staverman, Physica **18**, 791 (1952).
[5] C. P. Smyth, *Dielectric Behavior and Structure* (McGraw-Hill Book Company, Inc., New York, 1955), Chap. IV.

[a] R. M. Fuoss, reference 2.
[b] R. H. Boyd, reference 6.
[c] G. L. Clark, J. Chem. Phys. **25**, 125 (1956).
[d] J. Timmermans, *Physico-Chemical Constants of Pure Organic Compounds* (Elsevier Publishing Company, Inc., New York, 1950).
[e] E. Fischer and R. Fessler, Z. Naturforsch. **8A**, 177 (1953).
[f] H. Hase, Z. Naturforsch. **8A**, 695 (1953).
[g] J. Calderwood and C. P. Smyth, J. Am. Chem. Soc. **78**, 1295 (1956).

slope s in Eq. (2) is given by the present macroscopic theory as

$$s=(1/6\pi)(\tau/\eta)\tfrac{4}{9}(e^2/r^3). \qquad (16)$$

Substitution of typical values of the parameters, $\tau=10^{-11}$ sec, $\eta=10^{-2}$ poise, $e=4.802\times10^{-10}$ esu, $r=3\times10^{-8}$ cm and $\epsilon_s=20$ shows that s/ϵ_s is of the order of 1×10^{-8} cm. This is comparable to the molecular radius r which it corrects in Eq. (2). Thus, dielectric relaxation times are of such a magnitude that the dielectric relaxation does contribute significantly to the frictional force experienced by the ion.

It is of interest to see how successful the present theory is in quantitatively predicting the observed effects in specific solvent systems and with particular ions.

Experimental values of s have been determined[2] by plotting values of r_s [Eq. (1)] versus $1/\epsilon_s$ in polar-nonpolar solvent mixtures. Equation (16) requires values of τ/η for each composition. In general, such values of τ have not been measured. However, a few values are available for pure polar solvents for which s has been measured in mixtures with nonpolar solvents. The assumption can be made that τ/η is independent of composition. For pure nitrobenzene, $(\tau/\eta)_{25°C}=2.70\times10^{-9}$; while in dilute solution in carbon tetrachloride, $\tau/\eta=1.0\times10^{-9}$ (see Table I for source of data). The above assumption is apparently not valid over the entire composition range; but for the range from pure polar to approximately half polar-half nonpolar for which s values can be calculated, the above assumption may be fairly reasonable.

Some qualitative remarks are in order. First, Eq. (16) shows that the s values should depend on the solvent system through the ratio τ/η. This can vary considerably from solvent to solvent, but there are apparently only two systems involving nonhydrogen-bonded solvents where both τ/η values and s are available for comparison. For pentacyanopropenide,[6] s has been measured in both acetone-carbon tetrachloride mixtures and nitrobenzene-carbon tetrachloride mixtures. The τ/η value for nitrobenzene is about twice that for acetone, but the s value is over eight times larger. Measurements of s have been made for a number of ions in acetonitrile, but no τ/η value seems to be available. In the present theory, the s value should depend on the ion only through the radius r (inversely proportional to r^3). Measurements on a number of anions in nitrobenzene-carbon tetrachloride mixtures[2] indicate that s does decrease with increasing r. However, such a correlation is not found for the quaternary alkyl ammonium cations[7] in acetonitrile-carbon tetrachloride.

Table I shows calculated values of s compared with experimental. The agreement for the smaller anions is not bad but is otherwise rather poor. This is not too surprising since the energy-dissipation rate depends on the inverse sixth power of the distance and is thus very sensitive to the immediate environment of the ion where a macroscopic theory would be expected to be least satisfactory.

[6] R. H. Boyd, J. Chys. Chem. (to be published).

APPENDIX. LIST OF SYMBOLS USED

$\lambda_0^{\pm}$ = equivalent conductance at infinite dilution for a monovalent anion or cation.
$\mathfrak{F}$ = Faraday of electricity.
N = Avogadro's number.
η = solvent viscosity (poise).
r = ionic radius (cm).
r_s = ionic radius from Stokes' law.
s = slope of plot of r_s vs $1/\epsilon_s$.
ϵ_s = static dielectric constant.
ϵ_∞ = high-frequency dielectric constant.
f_S = Stokes' law friction constant ($6\pi\eta r$).
f_D = dielectric relaxation friction constant.
v = ionic velocity (cm/sec).
F = force on ion due to electric field.
W = rate of energy dissipation by ion through dielectric relaxation in the solvent.
$\mathcal{E}$ = electric field (esu).
D = electric displacement (esu).
e = electronic charge (esu).
τ = dielectric relaxation time (sec).
t = time (sec).
u = previous time (sec).

[7] D. S. Berns and R. M. Fuoss, J. Am. Chem. Soc. **82**, 5585 (1960).

Statistical Computation of Reaction Probabilities. II*

F. T. WALL, L. A. HILLER, JR., AND J. MAZUR†

Noyes Chemical Laboratory, University of Illinois, Urbana, Illinois

(Received March 17, 1961)

With the use of a high-speed digital computer, additional numerical calculations have been carried out to investigate the probability of exchange attending collisions of hydrogen atoms with hydrogen molecules. The computations were based on classical mechanics, although the potential energy was assumed to be given by the London-Eyring-Polanyi formula. Initial conditions of the particles involved were chosen by a pseudorandom process, and most of the interactions proved to be of the type that failed to produce exchange. Out of more than 700 computations, however, it was found that 6 involved exchange under circumstances suggesting a reasonable explanation. Sample results are displayed in graphical form showing internuclear separations as functions of time. It appears from the results that molecules with little or no rotational energy are more likely to exchange with a colliding atom than are molecules with substantial amounts of rotational energy. This can be simply explained by the fact that a non-rotating molecule can be readily constrained by an oncoming atom to a colinear configuration for which the activation energy is a minimum.

A MATTER of considerable importance that has received a great deal of attention in recent years is that of reaction rates, and numerous investigators have contributed to this problem both experimentally and theoretically. From a theoretical point of view, the work of Eyring and co-workers on the semiempirical method for absolute reaction rates has proved most instructive and helpful. Nevertheless, the details necessary to describe even the simplest reactions have been difficult to obtain since, in the last analysis, the problem is quite involved and complex. The extensive researches in this field have been described systematically by Glasstone, Laidler, and Eyring,[1–5] and more recent work was discussed at a symposium on absolute reaction rates held at the University of Wisconsin in 1959, at which time a preliminary report of the present work was also given.[6]

Recently the present authors undertook the calculation of reaction probabilities for the simple system H_2+H by making computations on a high-speed digital computer.[7] The first work reported was concerned with colinear collisions, using classical equations of motion, and assuming the London-Eyring-Polanyi[4] form for the potential energy of the system. Several hundred calculations were made for collisions involving different energies, both for systems in which the molecule was initially vibrating and for those without initial vibrations. The results, although striking in some respects, were quantitatively uncertain because of deficiencies in the potential energy function. Nevertheless, some conclusions could be drawn; for example, it was found that initial vibration increased the probability of reaction and that the translational energy required for activation was diminished by a fraction of the vibrational energy.

The work reported in the present article is an extension of the earlier work, for it involves similar calculations, except that the systems were not restricted to colinear collisions. A pseudorandom selection of initial conditions was employed so that the molecule might initially possess different amounts of rotational, vibrational, and translational energy. Approximately 700 such calculations of three-dimensional collisions were carried out. Most of the collisions were of a glancing type that resulted only in a transfer of energy between the three categories mentioned above. As a matter of fact, out of all the 700 calculations, only six gave rise to exchange reactions, but these occurred under circumstances that appear to be significant.

CALCULATIONS

As indicated above, the calculations now reported were carried out for systems consisting of three hydrogen atoms not constrained to a line. The potential energy, assumed again to be of the London-Eyring-Polanyi type, is a function of the three internuclear separations r_{12}, r_{13}, and r_{23}, the atoms being designated by numerals 1, 2, and 3. The general system possesses, of course, nine coordinates and nine momenta, thus appearing to require the integration of 18 equations of motion in Hamiltonian form. The number of equations of motion can be reduced, however, from 18 to 12 by use of the integrals of motion of the center of gravity. This is accomplished by defining a new set of coordinates and momenta, as follows: The new coordinates are the Cartesian coordinates of atom 1 relative to atom 3, of atom 2 relative to atom 3, and the original coordinates

* The work here reported was supported in part by a grant-in-aid from the National Science Foundation.

† Present address: U. S. Department of Commerce, National Bureau of Standards, Washington 25, D. C.

[1] S. Glasstone, K. J. Laidler, and H. Eyring, *The Theory of Rate Processes* (McGraw-Hill Book Company, Inc., New York, 1941).

[2] J. O. Hirschfelder, H. Eyring, and B. Topley, J. Chem. Phys. **4**, 170 (1936).

[3] F. London, Z. Elektrochem. **35**, 552 (1929).

[4] H. Eyring and M. Polanyi, Z. physik. Chem. (Leipzig) **B12**, 279 (1931).

[5] H. Eyring, Chem. Revs. **10**, 103 (1932).

[6] Several of the papers from that symposium appear in the November issue of J. Chem. Phys. **31**, (1959).

[7] F. T. Wall, L. A. Hiller, and J. Mazur, J. Chem. Phys. **29**, 255 (1958).

of atom 3. The new momenta are the original three components of momentum of atom 1, the original three components of momentum of atom 2 and the three components of momentum of the whole system. This transformation of the equations of motion from the old to the new variables is a contact transformation, thus preserving the Hamiltonian form of these equations.[8] In the new Hamiltonian the three coordinates of atom 3 are absent. Moreover, the three components of the momentum of the system correspond to the integrals of the coordinates of atom 3 and therefore are constants. These can conveniently be set equal to zero; this implies only that the center of gravity is taken to be at rest.

The Hamiltonian for the system is, of course, given by

$$H=T(p_1\cdots p_6)+V(q_1\cdots q_6) \tag{1}$$

and the equations of motion are as follows:

$$\partial H/\partial p_i=\dot{q}_i \tag{2}$$

$$\partial H/\partial q_i=-\dot{p}_i. \tag{3}$$

It is clear that, given an initial set of coordinates and momenta, integration of Hamilton's equations will yield values of the coordinates and momenta at later times. A naive numerical integration plan could be carried out as follows: Using the first of Hamilton's equations, the change in a particular coordinate could be computed numerically by use of the equation

$$\Delta q_i=\dot{q}_i\Delta t. \tag{4}$$

Similarly, through use of the second of Hamilton's equations, a change in momentum could be calculated by use of the expression

$$\Delta p_i=\dot{p}_i\Delta t. \tag{5}$$

From the new coordinates and momenta, one then establishes a new Hamiltonian which is used for the next iterative cycle. Actually, our computer computations were carried out to a much higher order of accuracy than that implied by use of Eqs. (4) and (5). The Runge-Kutta-Gill[9] method was used, which gave an accuracy sufficient to maintain adequate constancy of the Hamiltonian and the total angular momenta.

TABLE I. Summary of run 3D17; No exchange.

	Initial	Final
T_{trans}	12.706 kcal/mole	14.848 kcal/mole
T_{rot}	3.176	0.060
H_{vib}	5.267	6.252
H_{total}	21.149	21.160
M_x	0 arbitrary units	0.0001 arbitrary units
M_y	5.5517	5.5516
M_z	−0.7783	−0.7781
	No. of iterative cycles 376	
	Impact parameter 0.160 A	

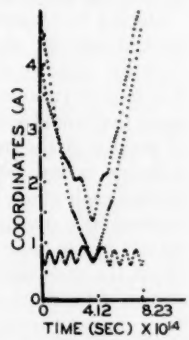

FIG. 1. Calculated internuclear separations vs time for run 3D17. Pertinent data given in Table I.

As pointed out earlier, the elimination of six coordinates and momenta that could be identified with motion of the center of gravity of the system, reduced the total number of equations from eighteen to twelve. In principle, the number could be further reduced, for example, by taking into account the fact that the Hamiltonian and the three angular momenta must be constant.[8] We found, however, that it was more convenient for computer computations to retain some redundant coordinates and momenta and to perform the numerical integrations for twelve quantities than it was to eliminate any more through use of constraints. Having made calculations for twelve coordinates and momenta, we were then able to check the accuracy of our numerical procedures by seeing how closely the total energy and the three total angular momenta remained constant. If, for any reason, changes in these quantities exceeded those expected from errors inherent in numerical integration or from roundoff, then the computation could be questioned. (Actually no serious errors were observed.)

The potential energy of diatomic hydrogen was represented by a Morse function using the following molecular parameters: dissociation energy, $D=108.5$ kcal/mole; equilibrium internuclear separation, $r_0=0.74$ A; harmonic vibrational frequency, $\nu_0=1.379\times10^{14}$/sec. The approximate activation energy calculated for the system is 11.78 kcal.

The time interval Δt associated with the increments for numerical integration, was taken to be 2.01×10^{-16} sec. This interval is short enough, compared to the natural period of vibration of a hydrogen molecule, to assure accurate computations, especially in light of our using a Runge-Kutta-Gill type of integration.

The initial conditions for each calculation were chosen by a pseudorandom process. No attempt was made to approximate the correct statistical weights through a

[8] For a discussion of the three-body problem see Chapter XIII of E. T. Whittaker, *Analytical Dynamics* (Cambridge University Press, New York, 1959).

[9] S. Gill, Proc. Cambridge Phil. Soc. **47**, 96 (1951).

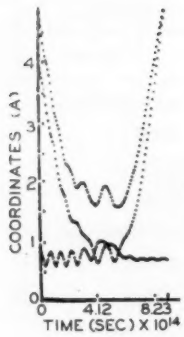

FIG. 2. Calculated internuclear separations vs time for run 2B5. Pertinent data given in Table II.

proper Monte Carlo method, but an element of randomness was introduced to obtain samples that might be studied subjectively. In all instances the initial configuration consisted of an atom about 5 A removed from the molecule. The momenta were more or less randomly chosen, subject to a given total energy. The numerical calculations were carried out by successive iteration and each set of computations was terminated when an atom was once again about 5 A removed from the molecule whether or not exchange occurred.

The computer output was in two forms, numeric and photographic. The numeric output consisted of initial and final coordinates and momenta, together with a count of the number of iterative cycles carried out. By examination of the initial and final coordinates, it was easy to ascertain whether or not reaction occurred. Moreover, by straightforward calculations, it was possible to calculate initial and final energies of translation, rotation, and vibration, as well as the changes thereof attending the collision. The numeric output, however, gave no indication of the details of the collision other than the time of interaction, which, of course, is proportional to the number of iterative cycles.

To gain an understanding of the detailed interactions, we also provided for a photographic output that depicted the entire collision process from beginning to end. The photographic representation was obtained by taking pictures of a cathode ray tube on which were displayed the three internuclear separations, r_{12}, r_{13}, and r_{23}, as functions of time. By observing the changes in these internuclear separations, as calculated by the machine and photographed from the cathode ray tube output, one could gain an understanding of the details of the interaction.

TABLE II. Summary of run 2B5; exchange occurred.

	Initial	Final
T_{trans}	14.889 kcal/mole	19.029 kcal/mole
T_{rot}	0	1.102
H_{vib}	5.267	0.051
H_{total}	20.156	20.182
M_x	0 arbitrary units	0.00015 arbitrary units
M_y	−4.9975	−4.9979
M_z	−6.6637	−6.6635
	No. of iterative cycles 468	
	Impact parameter 0.706 A	

RESULTS AND DISCUSSION

Typical results obtained from our calculations are illustrated in the figures and tables. Figures 1–8, which will be discussed in more detail below, display internuclear coordinates vs time for various collisions. In each instance, two of the internuclear separations, namely r_{12} and r_{13}, are initially large, and the third, r_{23}, is relatively short, corresponding to the internuclear separation of the molecule. When all three distances are less than about 2 A, one has the "activated complex." After an interaction period has elapsed, one of the three atoms flies away from the other two, as shown by the marked increase in two of the internuclear separations. In most instances, for which we carried out calculations, no reaction occurred; the figures here reproduced are not all typical, since several were chosen to illustrate atypical features.

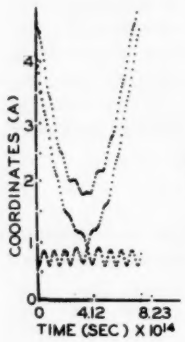

FIG. 3. Calculated internuclear separations vs time for run 2A1. $H_{total}=20.97$ kcal; exchange occurred.

Hoping to establish a quantitative basis for possible correlations, we also computed for each collision a quantity that we shall call the "impact parameter." The impact parameter is defined as the minimum distance that would occur between the atom and the center of gravity of the molecule, if both the atom and the molecule moved with uniform velocities without perturbing each other. In other words, assuming the atom to move with constant velocity relative to the center of gravity of the molecule, the perpendicular distance between the molecular center of gravity and the line of motion of the atom is the impact parameter. Obviously, if the impact parameter is large, we would expect little chance of reaction. On the other hand, if the impact parameter is small, we might expect that reaction could occur. Actually, a small impact parameter does not

guarantee reaction, although it is quite clear that a large one will assure no reaction.

Figure 1 displays a particular kind of collision which, in our recording system, was designated run 3D17. The upper curves initially denote r_{12} and r_{13}, whereas the lowest curve represents r_{23}, the internuclear separation of the original molecule. Examination of the figure will disclose that the molecule was initially vibrating (as shown by the oscillatory character of the lowest curve) and also rotating (as evidenced by the crossing of the two upper curves). When the atom collided with the molecule, however, it did so in a manner suggesting an approximately symmetric type vibration of a triatomic linear molecule. This is clear from the fact that the two lower curves are practically superimposed (at about 4×10^{-14} sec.), while the third internuclear separation is almost equal to twice the other two. The figure discloses further that, immediately following the compression of the triatomic complex, the system dissociated,

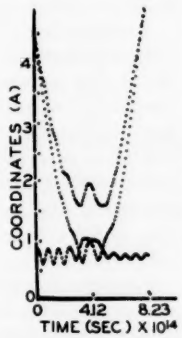

FIG. 4. Calculated internuclear separations vs time for run 3D14. $H_{\text{total}}=22.05$ kcal; exchange occurred.

leaving the molecule with a slight increase of vibrational energy as shown by the increased amplitude. At the same time, the rotational energy appears to be lost, inferred from the fact that the r_{12} and r_{13} curves do not cross after the collision. One cannot tell from the figure whether reaction did or did not occur, but the numerical output of the machine disclosed that no exchange took place.

A summary of the initial and final conditions for run 3D17 is given in Table I. It will be seen from the table that the molecule did, in fact, have a large amount of rotational energy to begin with, but that it lost most of that rotational energy in the course of the collision. The difference was made up by increases in the translational and vibrational energies. Examination of Table I will also give an idea with regard to the accuracy of the computations. Initially, the total Hamiltonian was 21.149 kcal, whereas at the end it was calculated to be 21.160 kcal. The difference measures accumulative errors resulting from imperfect numerical integration and rounding off in the computations. A further test of the accuracy of the method is given by comparing the angular momenta before and after collision. It will be seen that

FIG. 5. Calculated internuclear separations vs time for run 2B16. $H_{\text{total}}=21.12$ kcal; initial $T_{\text{rot}}=4.06$ kcal; impact parameter=0.568 A; no exchange.

the angular momenta, M_x, M_y, and M_z, are quite constant, which further suggests that the computation was reliable. Incidentally, the units employed for the angular momenta in Table I were quite arbitrarily chosen, by using atomic masses with velocities in the cgs system, and then shifting the decimal point to give a convenient tabular representation. Because only comparisons are involved, and no direct computations were made using these angular momenta, no difficulties attend this arbitrary representation. Finally, it should be pointed out that for run 3D17 the impact parameter was equal to 0.160 A. This small value for the impact parameter suggests that reaction could well have occurred. Since reaction did not occur, it is evident that the magnitude of the impact parameter alone is not sufficient to determine whether or not reaction occurs. A total of 376 iterative cycles were carried out for the calculations, that is to say, 12 differential equations were each solved 376 times by the numerical procedures described earlier.

In Fig. 2 we have displayed a collision which, in our notation, was designated run 2B5. Examination of the figure will disclose that the molecule was initially not rotating, although it was vibrating. The interaction occurring immediately after 4×10^{-14} sec was quite lacking in symmetry, and it is clear that exchange occurred. The new molecule, however, had little vibrational energy but apparently picked up some rotational energy. The details of the initial and final conditions are shown in Table II, in which data similar in kind to

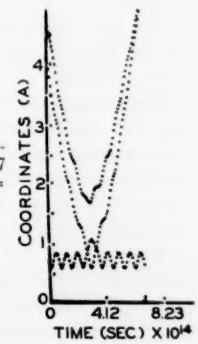

FIG. 6. Calculated internuclear separations vs time for run 2B13. $H_{\text{total}}=20.87$ kcal; initial $T_{\text{rot}}=0$; impact parameter=0.259 A; no exchange.

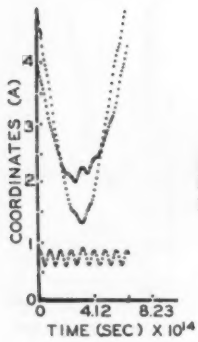

FIG. 7. Calculated internuclear separations vs time for run 2B3. $H_{total}=21.05$ kcal; initial $T_{rot}=2.35$ kcal; impact parameter=0.072 A; no exchange.

that of Table I are presented. Although, in this instance, the impact parameter was 0.706 A, a rather large quantity, reaction did occur. A total of 468 iterative cycles were involved in the computation.

Figure 3 illustrates another collision in which reaction quickly occurred with little change in vibrational energy, although some rotational energy was gained. Here too, the impact parameter was 0.704 A, a rather large quantity. The period of close interaction was marked by antisymmetric motions that led directly to exchange. Figure 4 illustrates still another reaction with exchange occurring. In this instance vibrational energy was lost, but rotational energy was gained, when the exchange took place. The impact parameter in this instance was 0.396 A.

Figures 5–7 display several quite typical interactions that did not lead to exchange. Figure 5 shows the type of interaction that occurs when an atom approaches a rapidly rotating molecule. Under such circumstances, the atom does not get close to the center of the molecule, and exchange is most unlikely. Figure 6 discloses an interaction that resembled an antisymmetric vibration stage of triatomic compression. Notwithstanding what appeared to be a favorable approach, no exchange occurred. Figure 7 illustrates another interaction of a molecule, with an appreciable amount of rotational energy, that was never closely approached by the atom.

Figure 8 displays an interesting interaction that represents the longest-lived complex we encountered in our 700 calculations. The total number of iterative cycles was equal to 896. Although the system interacted for a relatively long time, 18×10^{-14} sec, the original free atom ultimately flew off so that no exchange occurred.

The range of total energies covered by the calculations was 15.9 to 22.2 kcal, with initial translational energies varying from 7.6 to 15.9 kcal. As mentioned earlier, only six out of more than 700 calculations indicated exchange. Of the six that corresponded to reaction, the one with the lowest total energy had an impact parameter of 0.281 A and a total energy of 17.4 kcal. (The reader will recall that the calculated activation energy equals 11.78 kcal.) Of this total energy, 11.4 kcal was translational, and 6.0 kcal was identified with vibration; initially the molecule had zero rotational energy. This total energy, 17.4 kcal, is somewhat larger than the lowest exchange figure, 16.9 kcal, found earlier for colinear collisions with molecules possessing zero point vibrational energy of 6.2 kcal.[7] The pseudorandom process employed in the present calculations did not strike a colinear interaction of the type found before, but the two sets of calculations are fully compatible.

From the results described above, it should not be inferred that the reaction probability is six out of 700 or that the specific reaction rate can be calculated from such figures alone. Obviously the geometry of the approach and the definition of a collision must be taken into account. An involved analysis is necessary to take into account the proper weights to be attached to the various sample collisions considered in the pseudo-Monte Carlo calculations. At this time we will make no attempt to calculate a specific reaction rate constant because of the paucity of information. However, we will turn to a discussion of subjective conclusions that can be drawn from a careful study of the data.

Examination of the conditions that obtained before those collisions that resulted in exchange disclosed one factor that appeared most relevant. Four of the six "reactions" occurred when the original molecule had zero rotational energy, whereas the other two involved rotational energies of about 0.9 kcal/mole. Since our pseudorandom process for choosing initial conditions resulted in trials with rotational energies ranging from zero to 5.0 kcal/mole, it appears clear that low rotational energies favor reaction.

A reasonable explanation of the relationship between rotational energy and reaction probability is readily forthcoming. When an atom approaches a molecule, the mutual interaction is such that a minimum in potential energy is realized when the triatomic system is colinear. If the molecule has a substantial amount of rotational energy, it will not likely be constrained to a colinear configuration with the atom; classically, it will favor

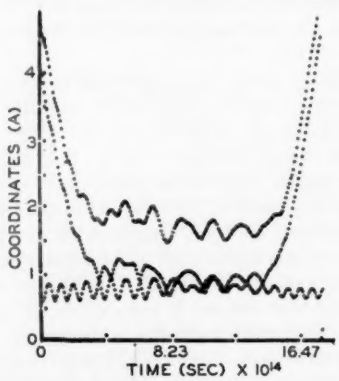

FIG. 8. Calculated internuclear separations vs time for run 5B13. $H_{total}=17.89$ kcal; initial $T_{rot}=0$; impact parameter=0.259 A; no exchange.

an aspect perpendicular to the line of motion of the atom over one that is colinear. If an atom approaches a molecule in a perpendicular fashion, it is less likely to react because the activation energy is higher. On the other hand, a nonrotating molecule can be lined up in colinear fashion with the atom, thus giving rise to a configuration with a minimum of activation energy and, hence, an increased probability for reaction. Therefore, it is reasonable to conclude that low rotational states are more favorable to exchange reactions than are higher states. In this connection, it was also observed that all six collisions resulting in reaction were accompanied by an increase in rotational energy of the final molecule, as compared to the initial molecule. (Obviously the opposite could not be true for those four that started with zero rotational energy, but the other two conceivably could have been accompanied by decreases.) Other collisions, involving initial rotational energies in the middle of the range studied, were as likely to be accompanied by increases of rotational energy as with decreases.

The effect of vibrational energy is also worth noting. Unlike the situation in colinear collisions, an increase in vibrational energy did not appear to increase the probability of reaction. However, we observed that five out of the six reacting collisions were accompanied by a diminution in vibrational energy. This suggests that a molecule initially with little rotational energy and some vibrational energy will react to give an exchanged molecule with less vibrational energy but with an increase in rotational energy. This appears to be the most general conclusion that can be drawn from what is, admittedly, fragmentary data. Although our statistics are limited, they nonetheless serve to suggest explanations of this kind.

It appears from the work so far completed that a full Monte Carlo analysis of various factors would be prohibitively time consuming. Nevertheless, we hope to study a few of the features involved without attempting, in the foreseeable future, what could be regarded as a complete analysis.

THE JOURNAL OF CHEMICAL PHYSICS VOLUME 35, NUMBER 4 OCTOBER, 1961

Zeeman Effect of the Nuclear Quadrupole Resonance Spectrum in Crystalline Powder

YONEZO MORINO AND MASAHARU TOYAMA

Department of Chemistry, Faculty of Science, The University of Tokyo, Tokyo, Japan

(Received March 6, 1961)

The Zeeman effect of the nuclear quadrupole resonance spectrum for spin $I=\frac{3}{2}$ in crystalline powder has been studied. Theoretical considerations have predicted that, in a nonaxial electric field gradient, the absorption line should be broadened with a characteristic envelope by a weak static magnetic field. When a radio-frequency (rf) field is applied parallel to the static field, one pair of sharp minima should be produced on the envelope at the frequencies shifted by $\pm\gamma H/2\pi$ from the unperturbed quadrupole resonance line, and two pairs of sharp maxima at $\pm(1-\eta)\gamma H/2\pi$ and at $\pm(1+\eta)\gamma H/2\pi$. Resonance spectra of Cl^{35} nuclei in *p*-dichlorobenzene and cyanuryl chloride have clearly displayed the predicted shape of envelopes on a recorder at room temperature. Analysis of them has resulted in determining the asymmetry parameters of electric field gradients with considerable accuracy; $0.07_0\pm0.01$ for the α-modification of *p*-dichlorobenzene, and 0.22 ± 0.03 for ν_1 line, and 0.23 ± 0.04 for ν_2 line of cyanuryl chloride.

INTRODUCTION

THE Zeeman study of nuclear quadrupole resonance spectra usually has been confined to single crystals. It is quite likely that in a crystalline powder the Zeeman pattern would be diffused out into the noise level, exhibiting no noteworthy feature. This presumption has been based on the consideration that the Zeeman splitting depends on the orientation of the field relative to each crystallite disposed at random in the sample. Recently one of the authors made a calculation of the transition probabilities between the nuclear quadrupole energy levels perturbed by a weak static magnetic field.[1] This calculation, together with the related experiments,[2,3] revealed a characteristic angular dependence of the two pairs of the Zeeman components resulting from the transitions $|m|=\frac{1}{2}\rightleftarrows\frac{3}{2}$ in a nucleus with a half-integral spin. When the static field is parallel to the principal xy plane of the electric field gradient (chosen as $|q_{xx}|\leqq|q_{yy}|\leqq|q_{zz}|$), the transitions corresponding to the inner pair of the Zeeman components are induced by the x component of the radio-frequency (rf) field, while those to the outer pair are induced by the y component. The inner or the outer pair of components in this case, therefore, disappears, depending upon whether the rf field is parallel to the principal y

[1] M. Toyama, J. Phys. Soc. Japan **14**, 1727 (1959).

[2] Y. Morino, T. Chiba, T. Shimozawa, and M. Toyama, J. Phys. Soc. Japan **13**, 869 (1958).

[3] F. J. Adrian, J. Chem. Phys. **29**, 1381 (1958).

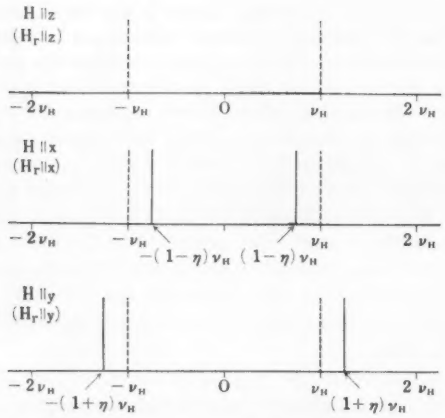

FIG. 1. Schematic illustration of the Zeeman effect of a nuclear quadrupole resonance line in a nucleus of spin $I=\frac{3}{2}$ by a weak static magnetic field parallel to the three principal axes of the electric field gradient. The dotted lines show the Zeeman components which are not observed when the rf field is applied parallel to the static field.

axis or to the x axis, and corresponding to it the remaining pair of the components becomes stronger.

This behavior of the Zeeman components is caused by the zeroth-order effect of the asymmetry of the electric field gradient. In the Zeeman study of a single crystal, this fact has provided us with a successful way for determining the location of the principal x and y axes in a slightly asymmetric field gradient.[4,5] In crystalline powder, a considerable effect of the asymmetry is expected to manifest itself upon the envelope shape of the absorption line broadened by the weak static field. The purpose of the present study is to investigate this change in line shape in crystalline powder for the spin $I=\frac{3}{2}$, and to establish a method for determining the asymmetry parameter η of the electric field gradient, without using a single crystal.

A similar circumstance is also revealed as a fine structure of the nuclear magnetic resonance spectrum. The situation has been discussed by Pound[6] for the axially symmetric case, and by Cohen and Reif[7] for the non-axial case. The results of their studies, specialized for the spin $I=\frac{3}{2}$, are summarized as follows. The magnetic resonance line, except the component caused by the transition $m=\frac{1}{2}\rightleftarrows-\frac{1}{2}$, should be broadened by the quadrupole interaction into the shape with one pair of sharp maximum peaks at the positions shifted by $\Delta\nu_1=\pm\frac{1}{4}(1-\eta)eQq_{zz}/h$ from the unperturbed Larmor frequency, and with two pairs of nicks at $\Delta\nu=\pm\frac{1}{4}(1+\eta)eQq_{zz}/h$ and at $\Delta\nu_3=\pm\frac{1}{4}eQq_{zz}/h$. In practice, however, because of the sensitivity of the detector, it is difficult to measure accurately the positions of the nicks. Only two peaks corresponding to $\Delta\nu_1$ were distinctly observed by Hon and Bray.[8] Thus this method is not applicable to determine the asymmetry parameter independently of the quadrupole coupling constant eQq_{zz}.

This article will begin with a qualitative discussion of the contribution of the asymmetry to the envelope shape of nuclear quadrupole resonance spectrum. It will provide us with, not only a forecast of the quantitative development in the later sections, but also an establishment of the applicability of the new method.

PRELIMINARY CONSIDERATION

The effect of the asymmetry of the electric field gradient on the Zeeman components is most remarkable when the static magnetic field is applied parallel to the principal xy plane. When the asymmetry parameter, defined by $\eta=(q_{xx}-q_{yy})/q_{zz}$, is small, two pairs of the Zeeman components for $I=\frac{3}{2}$ in these directions are located at, or close to, the splitting frequencies $\pm\nu_H$

$$\nu_H=|\gamma H/2\pi|, \tag{1}$$

where H is the strength of the static magnetic field and γ the gyromagnetic ratio of the resonating nuclei. The change in the line shape in a crystalline powder with static field is therefore expected to occur most distinctly in the vicinity of $\pm\nu_H$. If a first-order approximation is admitted for H and η, it is easily shown that we have no lines at $\pm\nu_H$ except for the three cases: $H\parallel z$, $H\parallel x$, and $H\parallel y$ (see Fig. 1). In this section there will be a discussion of how the Zeeman components appear or vanish in these cases, relative to the orientation of the rf field to the static field.

First we shall consider the system to which the rf field H_r is applied parallel to the static field. The transitions in the nuclear quadrupole resonance are, in general, induced by the component of the rf field, perpendicular to the principal z axis, within the approximation to the first order of η. When $H\parallel z$, the absorption spectrum itself is not observed, because the rf field is also parallel to the z axis. When $H\parallel x$ (i.e., $Hi\parallel x$), the outer pair of the Zeeman components should be located at the splitting frequencies $\pm\nu_H$, and the inner pair at $\pm(1-\eta)\nu_H$. However, with $Hi\parallel x$ only the transitions corresponding to the inner pair are allowed, and we have only a pair of strong lines at $\mathrm{M}(1-\eta)\nu_H$. When $H\parallel y$ (i.e., $Hi\parallel y$), the inner pair should be located at $\pm\nu_H$, and the outer pair at $\pm(1+\eta)\nu_H$. Here again no component is actually observed at $\pm\nu_H$, because only the transitions corresponding to the outer pair are allowed in this case. Consequently, when the external fields, H and H_r, are parallel to each other, no component comes to the positions of splitting frequencies $\pm\nu_H$, whereas the intensities of the components at $\pm(1-\eta)\nu_H$ and at

[4] Y. Morino and M. Toyama, J. Phys. Soc. Japan **15**, 288 (1960).
[5] Y. Morino, T. Shimozawa, M. Toyama, and K. Ito (to be published).
[6] R. V. Pound, Phys. Rev. **79**, 685 (1950).
[7] M. H. Cohen and F. Reif, Solid State Phys. **5**, 321 (1957).
[8] L. F. Hon and P. J. Bray, Phys. Rev. **110**, 624 (1958).

$\pm(1+\eta)\nu_H$ increase by the same amount as the decrease at $\pm\nu_H$. In a crystalline powder this situation will produce a pair of sharp minima at $\pm\nu_H$, and two pairs of sharp maxima at $\pm(1-\eta)\nu_H$ and at $\pm(1+\eta)\nu_H$ on the envelope of the absorption line. The Zeeman effect on crystalline powder will therefore provide a possibility for determining the asymmetry parameter and the gyromagnetic ratio.

These situations of the Zeeman components will be reversed in the system to which the external fields, H and H_r, are applied in the directions perpendicular to each other. When $H \parallel z$, a pair of strong components should be produced at $\pm\nu_H$, because in this case the rf field lies in the principal xy plane. When $H \parallel x$, the rf field is parallel to the yz plane, so that the transitions corresponding to the inner pair are forbidden. The Zeeman components, therefore, are not observed at $\pm(1-\eta)\nu_H$, but at $\pm\nu_H$. Similar discussion shows that when $H \parallel y$ the Zeeman components diminish to zero intensity at $\pm(1+\eta)\nu_H$ and appear at $\pm\nu_H$. The envelope shape in the vicinity of $\pm\nu_H$ is then strongly affected by the Zeeman components coming from the nuclei whose z axis is parallel or nearly parallel to the static field the Zeeman components coming from the nuclei whose z axis is parallel or nearly parallel to the static field, the perturbation by the asymmetry, in this case, being of second order.

The envelope shape in any other case may be approximated by a superposition of these two extreme cases, parallel and perpendicular, if the asymmetry parameter is sufficiently small. Therefore, the line shape is expected to be the most sensitive to the asymmetry of the field gradient in the parallel case: two pairs of maximum peaks at $\pm(1-\eta)\nu_H$ and at $\pm(1+\eta)\nu_H$. Hence it seems desirable to study the parallel case for the purpose of determining the asymmetry parameter.

CALCULATION OF THE ENVELOPE SHAPE

The system to be treated in this section is that of equivalent nuclei with spin $I=\frac{3}{2}$ in a crystalline powder sample. It is placed under the influence of a weak static magnetic field and an rf field, applied parallel to each other. For treating the system, we shall accept the following assumptions:

(1) The sample consists of a large number of single crystals orientated at random.

(2) The external fields are homogeneous over the entire sample.

(3) The absorption line in the absence of a static field is so sharp that it may be expressed by a δ function.

The calculation of the envelope shape will be treated by the first-order perturbation method; it willbe made for the frequency to the first order of the strength of the static field and for the intensity to the zeroth order. This approximation implies a Zeeman pattern symmetric with respect to the frequency of the pure quadrupole resonance. The effect of the linewidth will be discussed at the end of this section.

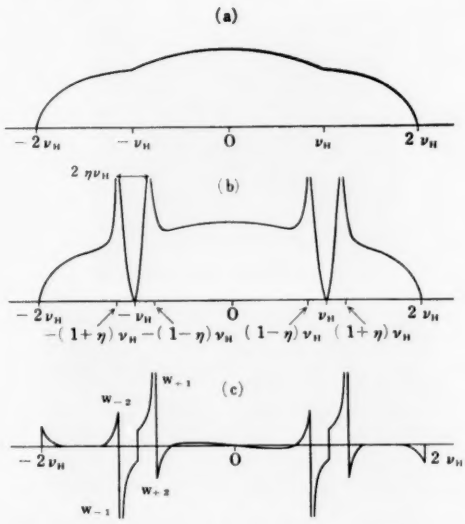

FIG. 2. Predicted envelope shape for $I=\frac{3}{2}$ in the parallel external fields $H_r \parallel H$ when the original line width is neglected. (a) Axially symmetric case ($\eta=0$), (b) slightly asymmetric case, and (c) the derivative form of (b).

A. Axially Symmetric Case

In the parallel external fields, the splitting frequency and the intensity of each Zeeman component, for the spin $\frac{3}{2}$ in the axial case ($\eta=0$), are expressed simply as follows[1]:

$$|\nu_\pm(\theta,\varphi)| = \tfrac{1}{2}\nu_H |[4-3\cos^2\theta]^{\frac{1}{2}} \mp 3|\cos\theta||, \tag{2}$$

and

$$P_\pm(\theta,\varphi) = \frac{3}{8}\sin^2\theta\left[1\pm\frac{|\cos\theta|}{(4-3\cos^2\theta)^{\frac{1}{2}}}\right]. \tag{3}$$

Here θ and φ denote the polar coordinates of the external fields taken with respect to the principal axes of each nucleus. The splitting frequency $\nu_\pm(\theta,\varphi)$ is measured from the position of the pure quadrupole resonance line, and the intensity $P_\pm(\theta,\varphi)$ is measured in an artibrary scale. The $+$ and $-$ signs in the suffices of ν and P indicate the inner and the outer pairs of the Zeeman components, respectively.

Under the accepted assumptions, the shape function for the envelope of the absorption line, broadened by the static field, is expressed by the following integral form:

$$I(\nu)d\nu = (N/4\pi)\iint_{\nu}^{\nu+d\nu} P(\theta,\varphi)\sin\theta d\theta d\varphi, \tag{4}$$

where N is a normalization constant. In the present case $I(\nu)$ is easily calculated by inserting Eqs. (2) and

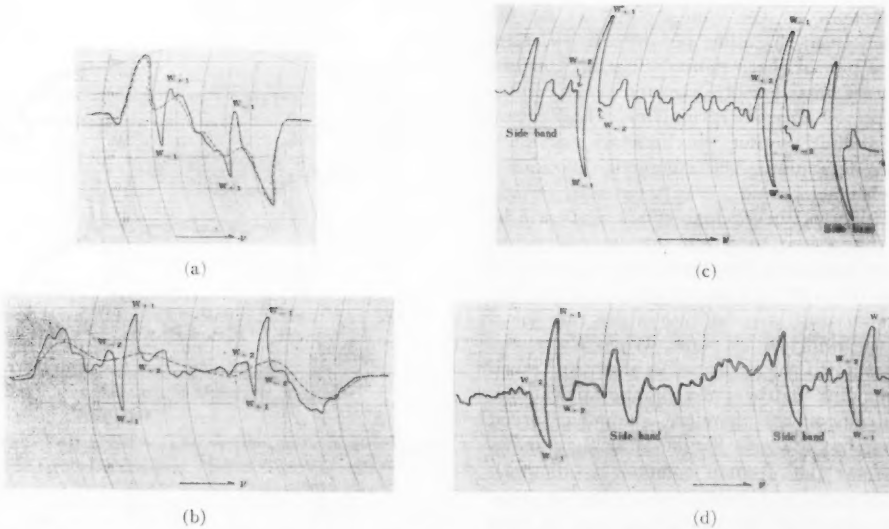

(a) (c)

(b) (d)

FIG. 3. Observed envelope shape of the Cl^{35} resonance spectrum for $H_r \parallel H$ in the α' modification of p-dichlorobenzene at the room temperature in various strength of the applied static field. The electric current operating the Helmholtz coil is (a) 150 mA, (b) 300 mA, (c) 450 mA, or (d) 700 mA. The dotted curves indicate the derivative curves for $\eta=0$.

(3) into Eq. (4),

$$I(\nu)=N/(12\nu_H)\cdot(4-f^2) \quad \text{for} \quad |f|\leqq 1 \tag{5}$$

and

$$I(\nu)=N/(24\nu_H)\cdot[(4-f^2)+|f|\{3(4-f^2)\}^{\frac{1}{2}}] \quad \text{for} \quad 1<|f|\leqq 2, \tag{5'}$$

where $f=\nu/\nu_H$. The envelope shape predicted by these equations is illustrated in Fig. 2(a). There are no gaps and no sharp peaks but only a pair of nicks at $\nu=\pm\nu_H$.

B. Nonaxial Case

Let us consider here only a slightly asymmetric case, because the general treatment of the envelope shape in a nonaxial case is complicated. An approximate calculation will be employed for the frequency to the first order of η and for the intensity to the zeroth order. The envelope shape is then approximated in most part by the result for the axially symmetric case. The correction due to the asymmetry will be made only in the vicinity of $\nu=\pm\nu_H$, where the noticeable effect of the asymmetry is brought about by the static field parallel to the principal xy plane.

Now, in the vicinity of the principal xy plane, i.e., $\theta\cong\pi/2$, $\cos\theta$ can also be treated to the same order of the approximation as the asymmetry parameter. The splitting frequency and the intensity of each Zeeman component for the spin $\frac{3}{2}$ is then reduced in this small region to the following forms[1]:

$$|\nu_\pm(\theta,\varphi)|=\nu_H|E_M(\tfrac{1}{2})\mp E_M(\tfrac{3}{2})| \tag{6}$$

and

$$P_\pm(\theta,\varphi)\cong\tfrac{3}{8}\left[1\pm\tfrac{1}{2}\eta\cdot\frac{\cos 2\varphi}{E_M(\frac{1}{2})\cdot E_M(\frac{3}{2})}\right], \tag{7}$$

where $E_M(\frac{1}{2})$ and $E_M(\frac{3}{2})$ denote the splittings of the quadrupole energy levels measured in the unit of $|\gamma\hbar H|$, i.e.,

$$E_M(\tfrac{1}{2})\cong 1-\tfrac{1}{2}\eta\cos 2\varphi \tag{8}$$

and

$$E_M(\tfrac{3}{2})\cong\tfrac{1}{2}[\eta^2+9\cos^2\theta]^{\frac{1}{2}}. \tag{8'}$$

The scale of $P_\pm(\theta,\varphi)$ is the same as that employed in Eq. (3).

According to Eqs. (6)–(8'), the shape function of the envelope (4) is converted into the explicit form:

$$I(\nu)=(N/2\pi\nu_H)[|\epsilon|/(1+|\epsilon|)]\times F\{(\pi/2),[2|\epsilon|/(1+|\epsilon|)]\} \tag{9}$$

where

$$\epsilon=(|f|-1)/\eta=(|\nu|-\nu_H)/\eta\nu_H \tag{10}$$

and

$$F(\phi,k)=\int_0^\phi\frac{dx}{(1-k^2\sin^2 x)^{\frac{1}{2}}} \tag{11}$$

The qualitative property of the shape function can easily be seen from the equation. $I(\nu)$ is symmetric with respect to $\epsilon=0$, or to $\nu=\pm\nu_H$. It converges except for the points $\epsilon=\pm 1$, i.e., $|\nu|=(1\pm\eta)\nu_H$ where it diverges to infinity. When $\epsilon\to\infty$ ($|\nu|\to\infty$), $I(\nu)$ tends asymtotically to $(N/4\nu_H)(1+1/4\epsilon^2)$, and when $\epsilon\to 0$, ($|\nu|\to\nu_H$), it tends to $N|\epsilon|/4\nu_H$. If this correction is made to the envelope shape for $\eta=0$, an approximate curve for $\eta\ll 1$ is obtained; it is illustrated in Fig. 2(b).

As discussed in the previous section, the envelope exhibits two pairs of sharp peaks at $|\nu|=(1\pm\eta)\nu_H$ and one pair of sharp minima at $|\nu|=\nu_H$, by which the envelope is completely divided into three parts: the central part coming from the inner components and two side parts coming from the outer components. In the narrow band detection scheme, the absorption line is usually recorded as a derivative form by slow passage. The envelope shape in this case is shown in Fig. 2(c). The spacing of the two adjacent deflections gives $2\eta\nu_H$. For convenience in later discussions, the wings of each deflection shall be denoted by $w_{\pm1}$ or $w_{\pm2}$ as shown in the figure.

The actual absorption line in the nuclear quadrupole resonance has a considerable linewidth which comes from spin-spin interaction, thermal motions of the lattice, and other sources. In fact, the envelope shape to be observed should be modified by the original line shape $g(\nu)$, i.e.,

$$\bar{I}(\nu)=\int_{-2\nu_H}^{2\nu_H} I(\nu')\,g(\nu-\nu')\,d\nu'. \tag{12}$$

By this modification the singularity which appears at $|\nu|=(1\pm\eta)\nu_H$ on the envelope derived above is eliminated and converted into a pair of sharp peaks. However, the deflection due to the asymmetry of the electric field gradient is fairly smooth if the applied static field is weak. A simple consideration will now be made to show what conditions should be required for observing the deflections under the influence of the linewidth.

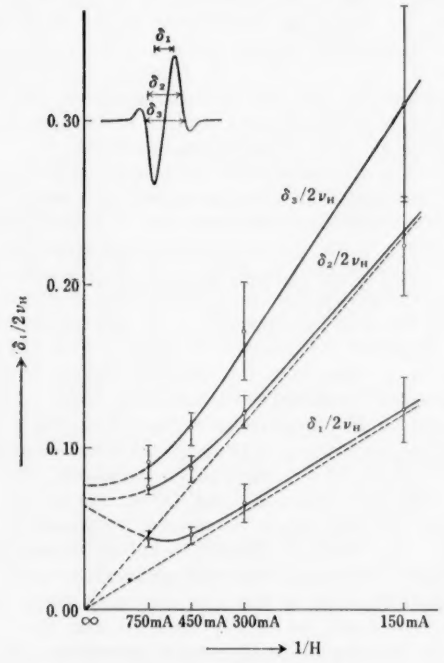

FIG. 4. Plot of $\delta_i/2\nu_H$ vs $1/H$ for the Cl^{35} resonance spectrum in the α modification of p-dichlorobenzene.

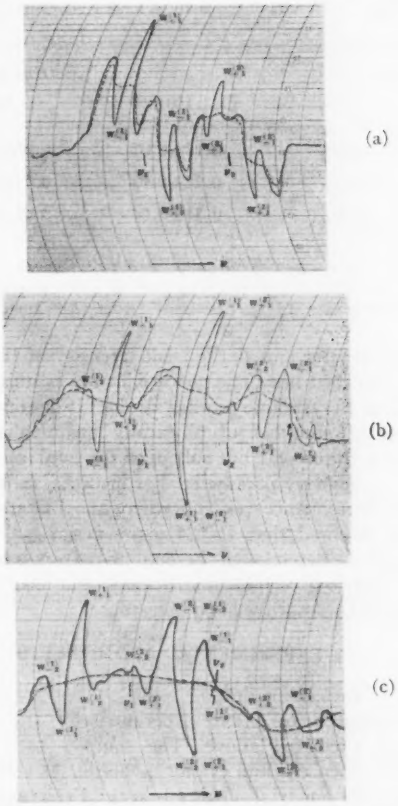

FIG. 5. Observed envelope shape of the Cl^{35} resonance spectrum for $H_r \parallel H$ in cyanuryl chloride at room temperature in various strengths of the applied static field. The electric current operating the Helmholtz coil is (a) 100 mA, (b) 200 mA, or (c) 300 mA. The wings resulting from lines ν_1 and ν_2 are discriminated with the superscripts (1) and (2), respectively. The dotted curves indicate the derivative curves for $\eta=0$.

First it is necessary to apply a field strong enough to give a splitting by the asymmetry greater than the line width $\Delta\nu$. Since the splitting due to η is in the order of magnitude of $\eta\nu_H=\eta|\gamma H/2\pi|$, this condition is expressed as

$$H\gtrsim 2\pi\Delta\nu/\eta|\gamma|. \tag{13}$$

A strong static field, however, decreases the intensity of the envelope by broadening. If the static field of the strength given by Eq. (13) is applied, the total broadening of the absorption line becomes $4\nu_H\gtrsim(4/\eta)\Delta\nu$. The peak intensity of the envelope decreases to where it is comparable to or weaker than $\eta/4$ times of that of the original line. It is essential, therefore, that

$$I_{\min}\lesssim(\eta/4)I_0, \tag{14}$$

where $I_{\min}$ is the minimum intensity detectable by the

TABLE I. Results of the analysis for the envelope shape of the Cl^{35} resonance spectrum in the α modification of p-dichlorobenzene at the room temperature.

	Current operating the Helmholtz coil (in mA)				
	150	300	450	750	∞
$\delta_1/2\nu_H$	0.12 ± 0.02	0.066 ± 0.012	0.046 ± 0.005	0.044 ± 0.005	$0.06_4\pm0.02$
$\delta_2/2\nu_H$	0.22 ± 0.03	0.122 ± 0.010	0.086 ± 0.007	0.076 ± 0.005	$0.06_9\pm0.02$
$\delta_3/2\nu_H$	0.31 ± 0.06	$0.17_1\pm0.03$	0.111 ± 0.010	0.091 ± 0.010	$0.07_7\pm0.02$
	$\langle\delta/2\nu_H\rangle_\infty=0.07_0\pm0.01$[a]				

[a] Average value of $\delta_i/2\nu_H$'s extrapolated to the infinite strength of the static field.

spectrometer and I_0 the peak intensity of the original unperturbed line. The condition (14) is unique in the case of a crystalline powder sample: It does not depend upon the number of physically inequivalent lattice sites in the crystal, but only upon the total intensity and the asymmetry parameter. For instance, in the case of the Cl^{35} resonance spectrum where $\Delta\nu=1$ kc and $\eta=0.10$, it is required that $H\gtrsim 24$ gauss and $I_{\min}\lesssim(1/40)I_0$. Hence the detection of the Zeeman pattern is impossible by ordinary oscilloscopic display, but could be performed by a narrow band detector.

EXPERIMENTAL AND RESULTS

Cl^{35} nuclear quadrupole resonance spectra have been investigated to prove experimentally the envelope shape predicted above. The samples used were p-dichlorobenzene and cyanuryl chloride as the standard cases of nonaxial field gradient. Each sample was prepared from the commercial product by purification and, if necessary, by grinding for satisfying the assumption (1) proposed in the previous section.

The magnet used for Zeeman study was the Helmholtz coil described in the previous paper.[2] It furnished a homogeneous static field of 108 gauss/ampere at the center of the magnet. About 10 g of crystalline powder sample were put in a cylindrical glass ampule with a diameter of about 1.5 cm. The rf coil was wound closely around the ampule and set to be coaxial at the center of the Helmholtz coil, so as to supply an rf field parallel to the static field. The absorption signals were detected by a self-quenched super-regenerative oscillator-detector of Dean's type with a frequency modulation of 230 cps. The detected signals were suitably amplified by an audio-amplifier and by a twin-T tuned amplifier and then recorded automatically through a phase-sensitive detector in a derivative form. The sweep rate was 1.5 kc/min. The quench frequency was 35 to 40 kc. The strength of the applied static field was 10 to 80 gauss. All the experiments were carried out at the room temperature.

The homogeneity of the static field was confirmed, but that of the rf field was not guaranteed. The fluctuation of the amplitude of the rf field, however, seems to have no significant influence on the envelope shape. It is necessary only to keep the rf field parallel to the static field. This condition, in practice, would be fulfilled fairly well within the accuracy of the intensity measurement. A justification follows from the fact that the deviation from the parallel direction takes place near the wall of the ampule, where the amplitude of the rf field is very small.

A. p-Dichlorobenzene

The observations were made for the Cl^{35} absorption line of the α modification whose frequency was measured to be 34.262 Mc at 26°C.[9] Typical charts of the observed Zeeman patterns are shown in Fig. 3. When the static field was relatively weak [see Fig. 3(a)], an intense background was observed with the shape corresponding to the derivative of the curve in Fig. 2(a). By increasing the strength of the static field, this background was smoothed out, and the deflections due to η appeared distinctly. However, in each chart, the wings $w_{\pm 2}$ were not so clearly observed. An interpretation for this fact will be given in the Appendix in terms of the effect of the original linewidth.

For the determination of the asymmetry parameter, it is necessary to measure the separation of each pair of adjacent deflections corresponding to $2\eta\nu_H$. However, by virtue of the original linewidth, the deflections observed are broadened and moreover, their locations are somewhat shifted from the ideal positions, as will be seen from Fig. 6 in the Appendix. It is difficult, therefore, to determine the points corresponding to $\pm(1+\eta)\nu_H$ and $\pm(1-\eta)\nu_H$ from the observed curves. Then we attempted to measure the following three spacings in order to find the separation $2\eta\nu_H$: (1) δ_1, the spacing between the extrema of two adjacent wings denoted by $w_{\pm 1}$; (2) δ_2, the spacing between the middle points of the adjacent deflections; and (3) δ_3, the spacing between the points where the adjacent deflections cut the zero level, which was actually found by subtracting a smooth background from each observed curve. If the original unperturbed line were extremely sharp, these spacings should be exactly $2\eta\nu_H$, so that the ratios $\delta_i/2\nu_H$ should give the asymmetry parameter η. In the

[9] T. C. Wang, C. H. Townes, A. L. Shawlow, and A. N. Holden, Phys. Rev. **86**, 809 (1952).

present analysis, these ratios were measured in various field strengths and extrapolated to the infinite field strength by assuming the first-order Zeeman effect over all the strength of the static field. Since in the infinite field strength the original linewidth can be neglected in comparison with $2\eta\nu_H$, the ratios should converge to η by this extrapolation. The validity of the assumption accepted here is easily seen by considering the fact that the static field, which is very weak compared with the resonance frequency, is enough to make the separation $2\eta\nu_H$ overcome the linewidth.

Figure 4 illustrates the process of the extrapolation actually employed. When the static field is weak compared with $2\pi\Delta\nu/\eta\gamma$, the linewidth is far larger than $2\eta\nu_H$, while the adjacent deflections should be shifted by the linewidth apart from each other. The spacing of them, therefore, should be comparable with the original linewidth, and hardly be affected by the change in the field strength. In this region the ratios $\delta_i/2\nu_H$'s are asymtotically proportional to the inverse of the static field; in particular, the asymtote of $\delta_1/2\nu_H$ is given by $\Delta\nu/2\nu_H$. On the other hand, when the static field is comparatively strong, the dominant part of the spacing comes from the separation by η. Especially δ_3 approaches to $2\eta\nu_H$ with an increase in field strength, while δ_1 approaches to $(2\eta\nu_H-\Delta\nu)$. Thus, by the extrapolation, the ratio $\delta_1/2\nu_H$ should converge to η along the curve $(\eta-\Delta\nu/2\nu_H)$ and $\delta_3/2\nu_H$ to η along $\{\eta+O[(\Delta\nu/2\nu_H)^2]\}$, whereas $\delta_2/2\nu_H$ should converge to η through the intermediate passage between them. The ratios $\delta_i/2\nu_H$ at each field strength and the extrapolated values are listed in Table I with the standard deviations which resulted from several observations.

From the extrapolated ratios, the asymmetry parameter of the electric field gradient at the Cl^{35} nuclei in the α modification of p-dichlorobenzene is found to be

TABLE II. Results of the analysis for the envelope shape of the Cl^{35} resonance spectrum in cyanuryl chloride at the room temperature.

	Current operating the Helmholtz coil (in mA)			
	100	200	300	∞
ν_1 line				
$\delta_1/2\nu_H$	0.18±0.03	0.15±0.02	0.15±0.02	0.19±0.05
$\delta_2/2\nu_H$	0.43±0.06	0.27±0.03	0.25±0.02	0.24±0.05
$\delta_3/2\nu_H$	...	0.35±0.05	0.31±0.04	0.25±0.10
ν_2 line				
$\delta_1/2\nu_H$	**0.19±0.03**	0.16±0.03	0.15±0.02	0.19±0.06
$\delta_2/2\nu_H$	**0.42±0.06**	0.27±0.03	0.26±0.03	0.24±0.06
$\delta_3/2\nu_H$	...	0.33±0.05	0.30±0.05	0.27±0.10
	ν_1 line; $\langle\delta/2\nu_H\rangle_\infty=0.22\pm0.03$			
	ν_2 line; $\langle\delta/2\nu_H\rangle_\infty=0.23\pm0.04$			

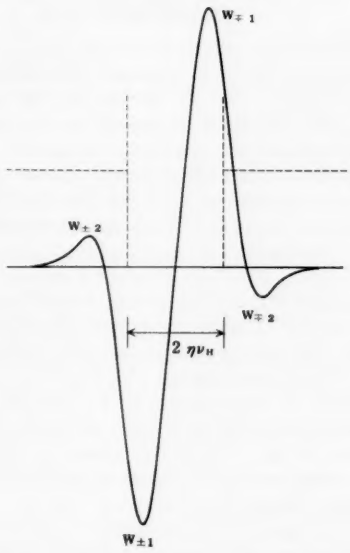

FIG. 6. A model of derivative envelope for $I=\frac{3}{2}$ in the vicinity of $|\nu|=\nu_H$, modified by a Gaussian distribution function with the line width $\Delta\nu=\eta\nu_H$, the dotted line indicating the unmodified model assumed by Eq. (15).

$0.07_0\pm0.01$ at room temperature. This value should be compared either with 0.08±0.02 by Dean[10] or with 0.05±0.02 by Ogawa and Ohi,[11] both of them having been obtained from the Zeeman study of single crystals.

B. Cyanuryl Chloride

In cyanuryl chloride, two distinct Cl^{35} absorption lines with the width of ca. 1 kc have been observed at 294°K at $\nu_1=36.300$ Mc and at $\nu_2=36.317$ Mc with the intensity ratio 2:1.[2,12] The envelope shapes observed for various strengths of the static field are presented in Fig. 5. Since the two absorption lines are close to each other, the deflections resulting from the two lines overlap each other when the static field is strong. The wings $w_{\pm2}$ were not so well observed in this case, either. An analysis similar to the case of p-dichlorobenzene gave the results summarized in Table II. The asymmetry parameters obtained are 0.22±0.03 for ν_1 and 0.23±0.04 for ν_2, which should be compared with those from the Zeeman studies of single crystals; 0.23±0.03 for ν_1 and 0.26±0.03 for ν_2 by Morino *et al.*,[2] or 0.24±0.01 for both lines by Adrian.[3]

[10] C. Dean, Phys. Rev. **86,** 607 (1952).
[11] S. Ogawa and K. Ohi, J. Phys. Soc. Japan **15,** 1064 (1960).
[12] H. Negita and S. Satou, J. Chem. Phys. **27,** 602 (1957). In cyanuryl chloride it has been reported that the two Cl^{35} absorption lines coalesced at 77°K to one line at 36.771 Mc [see footnote 2 and also P. J. Bray *et al.*, J. Chem. Phys. **28,** 99 (1958)]. Reinvestigation in the present study has, however, resolved two lines at 77°K, ν_1 at 36.770 Mc and ν_2 at 36.738 Mc. In earlier works the ν_2 line escaped our attention perhaps by an accidental coalescence with the first side band of the ν_1 line.

CONCLUSION

The asymmetry parameter of the electric field gradient at the nucleus offers important information on the nature of chemical bonds. In the case of spin $I \geqq 2$ or $I=1$, this important parameter can be determined from the quadrupole resonance frequencies without studying the Zeeman effect. In the case of spin $I=\frac{3}{2}$, it has been obtained only by the Zeeman study of a single crystal. The present study has developed another successful method for obtaining η by the measurement of the Zeeman effect on crystalline powder. Experiments on the Cl^{35} resonance spectra of *p*-dichlorobenzene and of cyanuryl chloride have revealed that the method gives the asymmetry parameters with an accuracy comparable to those obtained with single crystals. Since the intensity of the envelope is inversely proportional to the strength of the static field, the method requires a detector of high sensitivity. However, the present method, compared with the former, offers a number of advantages, discussed below.

In the first place the new method requires no single crystal. The preparation of a large single crystal is the most serious difficulty and has hampered the Zeeman study on the nuclear quadrupole resonance spectrum. Secondly the method is free from the tedious procedure of measuring the orientation of the crystal axes: for example, it is not necessary to locate the no-splitting locus or the principal *xy* plane, but only to set the rf field parallel to the static field. The experimental procedure is, therefore, far simpler.

It is really difficult to set the rf coil exactly at a desired direction. However, even if the external fields deviate from the parallel orientation, the deviation does not bring about a large uncertainty in the determination of the asymmetry parameter. The lack of coincidence of the directions does not shift the positions of the maximum peaks at $\pm(1-\eta)\nu_H$ and $\pm(1+\eta)\nu_H$, but merely decreases their intensities. The dominant part of the experimental error in the single crystal method comes from uncertainty in the location of the directions relative to the crystal axes.

Finally the new method makes it possible to study the Zeeman pattern at low temperatures where the absorption line is, in general, very strong. In a single crystal such a study is scarcely possible for two reasons: (1) It is difficult to obtain a large single crystal at low temperatures and (2) It takes a long time for the determination of the relative orientation, so that the crystal must be kept at low and constant temperature for a long time.

ACKNOWLEDGMENT

The authors wish to thank the Ministry of Education of Japan for aid in this investigation.

APPENDIX

The Modified Envelope Shape

Suppose, for brevity, that the envelope shape, ignoring the original linewidth, is represented by a simple model instead of Eq. (9); in terms of ϵ,

$$I(\epsilon)=N/(4\nu_H)[f(\epsilon)+\delta(|\epsilon|-1)], \tag{15}$$

where

$$f(\epsilon)=\begin{cases}1 & \text{for} \quad |\epsilon|\geqq 1,\\ 0 & \text{for} \quad |\epsilon|<1.\end{cases} \tag{15'}$$

A modified envelope shape in the vicinity of $|\nu|=\nu_H$ is easily derived from Eqs. (12) and (15) to the following derivative form:

$$[d\bar{I}(\epsilon)]/(d\epsilon)=N/(4\nu_H)[\xi(1-\epsilon)-\xi(1+\epsilon)], \tag{16}$$

where

$$\xi(\epsilon)=\frac{1}{\Delta\epsilon(2\pi)^{\frac{1}{2}}}[1+\epsilon/(\Delta\epsilon)^2]\exp[-\tfrac{1}{2}(\epsilon/\Delta\epsilon)^2]. \tag{16'}$$

In this derivation it has been assumed that the shape of the unperturbed line can be fitted with a Gaussian distribution function with the linewidth $\Delta\epsilon$ between the derivative extrema. Figure 6 illustrates the modified envelope shape for $\Delta\epsilon=1$, i.e., $\Delta\nu=\eta\nu_H$. The intensity of the wings $w_{\pm 2}$ is far weaker than that of $w_{\pm 1}$. This indicates a reason for why the wings $w_{\pm 2}$ have neither clearly been resolved in the investigations of *p*-dichlorobenzene nor of cyanuryl chloride.

Structural Effects in the Vapor Pressures of Isotopic Molecules. O^{18} and N^{15} Substitution in N_2O*

JACOB BIGELEISEN AND SLOBODAN V. RIBNIKAR†

Chemistry Department, Brookhaven National Laboratory, Upton, Long Island, New York

(Received March 17, 1961)

The relative vapor pressure ratios of the isotopic N_2O molecules have been determined by distillation in a column under total reflux. It is shown that the vapor pressures are in the sequence

$$N^{14}N^{14}O^{16} > N^{14}N^{15}O^{16} > N^{15}N^{14}O^{16} > N^{14}N^{14}O^{18}.$$

The absolute vapor pressure ratios have been determined from the kinetic behavior of the column and the decrease in separation by production from the column.

Theoretical calculations of the relative vapor pressure ratios can be made from the atomic masses and the random structure of liquid N_2O. The calculated relative isotope effects are in good agreement with experiment. The absolute value of $\ln P_{N^{14}N^{14}O^{16}}/P_{N^{14}N^{15}O^{16}}$ is calculated from the specific heat of N_2O to be 8.2×10^{-4} at 184°K, in good agreement with the experimental value $7.8\pm1.4\times10^{-4}$. The difference in vapor pressures of the isotopic isomers $N^{14}N^{15}O^{16}$ and $N^{15}N^{14}O^{16}$ is attributed to hindered rotation of the molecule in the liquid.

INTRODUCTION

EXPERIMENTS in recent years on the vapor pressures and triple points of the isotopic H_2,[1] CO,[2] NO,[3] CH_4[2,4–6] molecules *inter alia* have shown conclusively that the quantum effects in equilibria between a gas and the condensed system cannot be expressed solely in terms of the molecular weight of the gas. In the case of monatomic systems, the atomic weight is the only mass involved, and a quantitative description of such systems can be given in terms of the first- and higher-order quantum corrections[7–10] for pseudo-Boltzmann statistics. In the case of polyatomic molecules, there are contributions to the quantum effects from the rotation of molecule, from the coupling of translation with rotation of the molecule in the condensed phase[11,12] as well as coupling between these motions and the internal vibrations of the molecule. In addition, the internal vibrations are perturbed by the fields of the surrounding molecules. A theory has been developed by one of us[13] which includes the contributions of all of these effects to the vapor pressure ratio of isotopic molecules. The theory shows that through powers of $(\hbar/kT)^2$, which is valid to values of $\epsilon/kT<12\sqrt{2}$, the vapor pressure ratio of isotopic molecules depends on the reciprocal mass of the isotopic *atoms* times an energy parameter for the particular atom. The theory leads directly to the rule of the geometric mean in the vapor pressure and formally accounts for the behavior of such systems as CO, NO, CH_4, etc. It has been applied in detail to the vapor pressure ratio, heats of sublimation, and triple points of N^{15} and O^{18} substitution in NO, including double substitution.[14] The theoretical calculations were found to give quantitative agreement with experiment.

The molecule NNO offers an interesting possibility for further tests of the theory. One can investigate N^{15} and O^{18} substitution and there are two nonequivalent positions for the N^{15} substitution. The central nitrogen is virtually at the center of gravity of the molecule. The ratio of the moments of inertia of $N^{14}N^{14}O^{16}/N^{14}N^{15}O^{16}$ has been determined by microwave spectroscopy[15] to be 0.999932. Thus, comparison of $N^{15}N^{14}O^{16}$ with $N^{14}N^{15}O^{16}$ should give information on the role of rotation of the molecule on the vapor pressure ratio. If there are no further contributions from the internal vibrations, the comparison of $N^{14}N^{14}O^{16}$ with $N^{14}N^{14}O^{18}$ should be directly related to the differences between $N^{14}N^{14}O^{16}$, $N^{15}N^{14}O^{16}$, and $N^{14}N^{15}O^{16}$.

EXPERIMENTAL METHOD

Just at the time that the present experiments were in the stage of detailed planning Kuhn, Narten, and Thürkauf[16] reported the results of some Rayleigh distillations on N_2O. The distillation was performed

* Research carried out under the auspices of the U. S. Atomic Energy Commission.

† Permanent address: Boris Kidrich Institute of Nuclear Sciences, Belgrade, Yugoslavia.

[1] J. Bigeleisen and E. C. Kerr, J. Chem. Phys. **23,** 2442 (1955).

[2] T. F. Johns, *Proceedings of the International Symposium on Isotope Separation,* edited by J. Kistemaker, J. Bigeleisen, and A. O. C. Nier (North-Holland Publishing Company, Amsterdam, 1958), pp. 74–101.

[3] K. Clusius, K. Schleich, and M. Vecchi, Helv. Chim. Acta **42,** 2654 (1959).

[4] K. Clusius and H. H. Bühler, Z. Naturforsch. **9a,** 776 (1954).

[5] G. T. Armstrong, F. G. Brickwedde, and R. B. Scott, J. Research Natl. Bur. Standards **55,** 39 (1955).

[6] K. Clusius, F. Endtinger, and K. Schleich, Helv. Chim. Acta **43,** 1267 (1960).

[7] F. A. Lindemann, Phil. Mag. **38,** 173 (1919).

[8] K. F. Herzfeld and E. Teller, Phys. Rev. **54,** 912 (1938).

[9] J. de Boer, Physica **14,** 139 (1948).

[10] J. Bigeleisen and E. Roth, J. Chem. Phys. **35,** 68 (1961).

[11] A. Babloyantz, J. Mol. Phys. **2,** 39 (1959).

[12] H. H. Friedmann (private communication).

[13] J. Bigeleisen, J. Chem. Phys. **34,** 1485 (1961).

[14] J. Bigeleisen, J. Chem. Phys. **33,** 1775 (1960).

[15] D. K. Coles and R. H. Hughes, Phys. Rev. **76,** 178 (1949).

[16] W. Kuhn, A. Narten, and M. Thürkauf, Helv. Chim. Acta **42,** 1433 (1959).

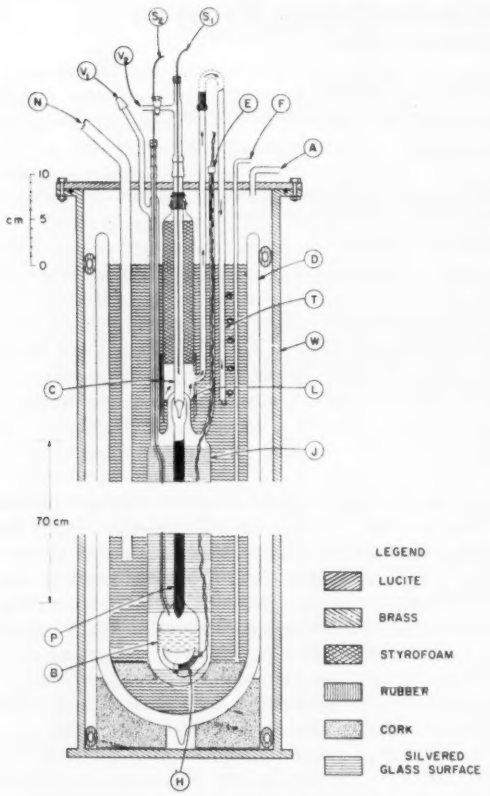

FIG. 1. Distillation column.

with material of natural abundance and no distinction was made between $N^{15}N^{14}O^{16}$ and $N^{14}N^{15}O^{16}$. Both of these molecules give the same parent ion in a mass spectrometer, which was the basis of the analytical method used by Kuhn, Narten, and Thürkauf. These workers found $\ln 2P_{N^{14}N^{14}O^{16}}/(P_{N^{14}N^{15}O^{16}}+P_{N^{15}N^{14}O^{16}})$ to be $11.6\pm0.3\times10^{-4}$ and $\ln P_{N^{14}N^{14}O^{16}}/P_{N^{14}N^{14}O^{18}}$ to be $18\pm2\times10^{-4}$. It is clear from their results that the experiments must be designed to give a precision of the order of 5×10^{-4} in the vapor pressure even if a qualitative difference between $N^{15}N^{14}O^{16}$ and $N^{14}N^{15}O^{16}$ is to be observed. A precision and accuracy one order of magnitude better than this is attainable by manometric methods with samples isotopically and chemically pure at a pressure of 1000 mm. Samples of $N^{15}N^{14}O^{16}$ and $N^{14}N^{15}O^{16}$ of the required isotopic purity can be prepared by the decomposition of appropriately labeled[17–19] samples of NH_4NO_3. The chemical purification would require both chemical treatment and finally fractionation in an efficient column with small hold up.

If a distillation column is operated under a number of appropriately controlled conditions, the theory of the column as developed by Cohen[20] and others[21,22] permits one to obtain both relative and absolute values of ϵ_j, defined as $\ln P'/P_j$. The analysis of mixtures of $N^{14}N^{14}O^{16}$, $N^{15}N^{14}O^{16}$, $N^{14}N^{15}O^{16}$, and $N^{14}N^{14}O^{18}$ has been described previously.[18] We have, therefore, chosen to use a column to measure the vapor pressure ratios of the singly labeled isotopic N_2O molecules.

If a quantity of N_2O of natural isotopic composition is brought to equilibrium under total reflux in a column having approximately 100 theoretical plates and with a negligible hold up in the column and in the condenser, none of the N^{15} or O^{18} species will be enriched (or depleted) in the condenser by more than a factor of 1.2. The mol fraction of $N^{14}N^{14}O^{16}$ is essentially 0.99 in the column, the boiler and the condenser at all times. Each of the components $N^{15}N^{14}O^{16}$, $N^{14}N^{15}O^{16}$, and $N^{14}N^{14}O^{18}$ is being fractionated against the major component as a two component mixture. At equilibrium the separation of the j'th minor component is

$$q_j\equiv\frac{R_{j\infty}}{R_{j0}}=\frac{(N_j/N^{14}N^{14}O^{16})_\infty}{(N_j/N^{14}N^{14}O^{16})_0}=\exp(-\epsilon_j n)\cong N_{j\infty}/N_{j0} \quad (1)$$

and

$$\ln q_j/\ln q_k=\epsilon_j/\epsilon_K. \quad (2)$$

The quantities used in connection with the operation of a column are defined below.

We shall now show that Eq. (2) for the relative elementary separation factors holds at any time in the distillation because of the small enrichment. The enrichment at short time is given by[23]

$$q=N(n,t)/N_0=1+2\epsilon(t/\pi\lambda)^{\frac{1}{2}}M+\cdots[t<\lambda n^2/10]. \quad (3)$$

At long times[24]

$$q=N(n,t)/N_0=e^{\epsilon n}-(e^{\epsilon n}-1)A\exp(-Bt/\lambda n^2),\quad [t>\lambda n^2/10], \quad (4)$$

where R = mol ratio in the condenser, R_0 = mol ratio in the boiler, N = mol fraction in the condenser, N_0 = mol fraction in the boiler, n = number of theoretical plates in the column, ϵ_j = elementary separation parameter equal to $\ln P_{N^{14}N^{14}O^{16}}/P_j$, ϵ = an arbitrary elementary separation parameter, λ = a characteristic time of the

[17] W. S. Richardson and E. B. Wilson, Jr., J. Chem. Phys. **18,** 694 (1950).

[18] L. Friedman and J. Bigeleisen, J. Chem. Phys. **18,** 1325 (1950).

[19] J. Bigeleisen and L. Friedman, J. Chem. Phys. **18,** 1656 (1950).

[20] K. P. Cohen, *The Theory of Isotope Separation as Applied to the Large Scale Production of* U^{235} (McGraw-Hill Book Company, Inc., New York, 1951).

[21] I. Dostrovsky, J. Gillis, D. R. Llewellyn, and B. H. Vromen, J. Chem. Soc. **1952,** 3517.

[22] M. Benedict and T. H. Pigford, *Nuclear Chemical Engineering* (McGraw-Hill Book Company, Inc., New York, 1957), Chap. 10.

[23] See reference 20, Eq. (3.32). Note that Cohen uses ϵ for the "heads" separation factor minus unity. For the case where $\alpha-1\ll1$, which is our case, the heads separation factor $\beta-1=(\alpha-1)/2$ (cf. reference 22, pp. 380–90). Our ϵ is therefore 2ϵ (Cohen). Our $S_\infty=e^{\epsilon n}$, whereas Cohen's is appropriately $e^{2\epsilon n}$.

[24] Reference 20, Eq. (3.28).

column$=2h$, h=holdup per unit flow (or average process time) per theoretical plate (sec), M=a confluent hypergeometric function (tabulated by Cohen,[20] p. 52), A=a function of the equilibrium enrichment and the ratio of the holdup in the condenser to that in the column (cf. Cohen,[20] pp. 46–48), and B=a function of the equilibrium enrichment and the ratio of the holdup in the condenser to that in the column (cf. Cohen,[20] pp. 46–48). We now consider the number of theoretical plates in the column as a function of the time of operation and write

$$q=1+\epsilon n(t)=\exp[\epsilon n(t)]. \tag{5}$$

From Eq. (3), at short time,

$$n_j(t)=2(t/\pi\lambda)^{\frac{1}{2}}M_j; \tag{6}$$

and from Eq. (4), at long time,

$$n_j(t)=n_\infty[1-A_j\exp(-B_jt/\lambda n^2)]. \tag{7}$$

Under the conditions under which Eq. (3) is applicable, the quantity $\epsilon^2t/\lambda<\epsilon^2n^2/10$. For a column with 100 plates and $\epsilon<2\times10^{-3}$, ϵ^2t/λ is restricted to values between 0 and 0.04. Between these values of ϵ^2t/λ, M varies between 1.000 and 1.0125. The ratio $n_j(t)/n_k(t)$ does not vary by more than one per cent. The relationship $\epsilon_j/\epsilon_K=\ln q_j/\ln q_K$ is good to one per cent at times smaller than $\lambda n^2/10$. At $t>\lambda n^2/10$,

$$\frac{n_j(t)}{n_k(t)}=\frac{1-A_j\exp(-B_jt/\lambda n^2)}{1-A_k\exp(-B_kt/\lambda n^2)}. \tag{8}$$

For values of $\epsilon n<0.2$, A is close to unity and varies by at most 1% over a wide range of values of the ratio of the holdup in the condenser to that in the column. B on the other hand varies by about 5% over the same range. The ratio $n_j(t)/n_k(t)$ is unity to within 5% at $\infty>t>\lambda n^2/10$. Therefore, within 5%, the relative ϵ's can be calculated from the equilibrium Equation (2).

Once the relative ϵ's have been determined, the absolute value of only one need be measured. Additional absolute values serve as a further check of the method. The absolute value of ϵ can be determined either by following the build up of enrichment in the column under total reflux or by the change in the separation performed by the column by a finite production. A convenient method for the determination of ϵ from column production operation has been described by Dostrovsky, Gillis, Llewellyn, and Vromen.[21] We have followed their procedure. Absolute values of ϵ can also be calculated by the following procedure from the build up of enrichment in the column. If there is no parasitic reflux in the column $\lambda=2H/Ln$, where H is the total holdup in the column and L is the boil up rate. Both of these can be determined experimentally. One can determine ϵ^2n from the measured separation at short times using the equation[23]

$$q=1+2\epsilon(t/\pi\lambda)^{\frac{1}{2}}M+\epsilon^2t/2\lambda. \tag{9}$$

The quantity ϵ^2n is then divided by ϵn, determined from q_∞, to give ϵ. The long time behavior of the column can be written

$$q_t-q_\infty=-A(q_\infty-1)e^{-pt}. \tag{10}$$

A semilog plot gives $p=BL/2Hn$, which can be combined with q_∞ to give ϵ.

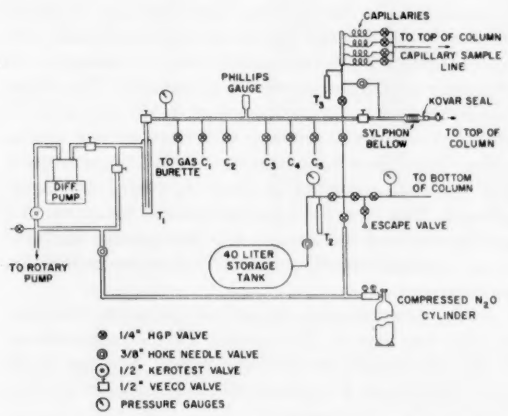

FIG. 2. Sampling and gas handling system.

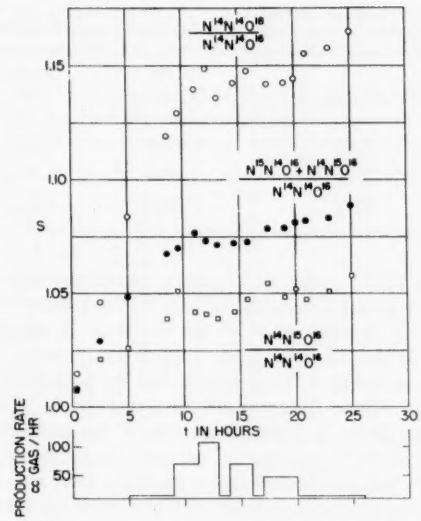

FIG. 3. Separation in the column as a function of time and production (distillation No. 10).

EXPERIMENTAL PROCEDURE

The distillation column used was constructed with slight modifications from the design used by Clusius and Schleich[25] for the distillation of NO. This design has a very versatile condenser, which can be maintained at constant temperature over a wide temperature

[25] K. Clusius and K. Schleich, Helv. Chim. Acta **42**, 234 (1959).

TABLE I. Isotopic composition $\langle N^{15} \rangle$ of the N_2O in the boiler corrected for production and holdup in the column. ($V_0 = 40$ cc.)

V_p in cc liquid	R_B/R_0 (found)	R_B/R_0 (calc)
0.26	1.0032	1.0030
1.16	1.0050	1.0044
1.52	1.0052	1.0055

range. It is capable of excellent operation even when the refrigeration is supplied from a source much colder than the freezing point of the distillate. A schematic cross section of the column used in the present study is shown in Fig. 1. The boiler B and the packed section of the column P are both insulated by a silvered vacuum jacket J. The column tube P was also silvered on its outside. In some of the early experiments, the column was unsilvered and a stainless steel radiation shield was placed concentric with but inside the vacuum jacket. This proved to be less efficient than the silvered arrangement, which gave smaller plate heights. The entire column was submerged in liquid nitrogen, which did not have direct contact with the condenser. Following the method of Clusius and Schleich, the position of the level of the liquid nitrogen in the condenser head L is adjusted by moving the leveling tube T in a vertical direction by a screw mechanism (not shown). The packed section was of 1.0-cm diam and 70-cm length. It was filled with Nichrome "Heli-pak" (Podbelniak Co. #2916) packing in the form of flattened spirals 0.035×0.070×0.070 in. The boiler had a capacity of 50 cc and was heated electrically by the heater H wound on the side arm. Electrical leads to the heater passed through the seal E. The jacket was pumped continuously through the tube V_1. Provision was made to introduce helium at V_1 to cool the packing and load the column. When the column was in operation at low heat input, the jacket pressure was 10^{-6} mm Hg. Samples of N_2O were taken from the condenser and boiler sections by the capillary silver tubes S_1 and S_2, respectively. The Dewar, inside which the column was mounted, had an unsilvered window for observation. The Dewar in turn was mounted inside a brass vessel equipped with lucite windows according to a design by Johnston.[26] Both the windows and the lucite cover were sealed to the vessel by O-ring seals.

The gas handling system is shown in Fig. 2. The N_2O used was taken from a cylinder of compressed gas furnished by the Matheson Company. It was subjected to a bulb to bulb distillation from which the first and last fractions were discarded. For some of the experiments a batch of N_2O was purified in the distillation column. Both samples of N_2O gave identical results. The purified gas was stored in the 40-liter storage tank.

The column was most successfully loaded in the following manner. Both the column and the jacket were first evacuated. The jacket was then cooled by filling the Dewar with liquid nitrogen to a level slightly below the condenser section. Helium was then admitted to the jacket to a pressure of the order of 1 mm. The purified gas from the storage tank was transferred to the vessel T_2, where it was liquefied and maintained at a pressure slightly above one atmosphere. From the trap T_2, the gas was condensed into the column. Practically all of the gas crystallized on the column packing. When the transfer was complete, the jacket was evacuated and heat was supplied to the boiler. The N_2O melted slowly and most of the liquid drained to the boiler. This method of loading led to good wetting of the packing and the plate height of the column loaded in this fashion was found to be smaller than that experienced by direct condensation into the boiler, followed by an initial operation at high boil up rate. After the N_2O had melted, the liquid-nitrogen level in the Dewar was raised and the level of tube T was adjusted to give the desired cooling rate. The level of the liquid nitrogen in the Dewar was maintained manually. Variations of the order of an inch in the liquid-nitrogen level in the Dewar had practically no influence on the cooling rate to the condenser. The pressure inside the column could be held constant to ±30 mm Hg over periods of the order of 24 hours. The reflux in the condenser, measured by counting the drop rate, was constant to 5%. In general, the column was operated at a pressure between 700–760 mm Hg. The temperature of investigation is therefore 184.0± 0.6°K.[27] No significant variation in ϵ is to be expected in this small temperature interval.

Since the isotopic composition of the material in the boiler changes slowly, it was sampled less frequently than the condenser section. In the first few distillations, a rough sampling procedure for the condenser section was used in which material in the condenser section was expanded into an evacuated volume. In the later experiments, controlled sampling was introduced to minimize perturbations in the column. Gas from the condenser section flowed through the silver capillary S_1 and then either through a precision needle valve or through a set of copper capillaries connected in parallel. The copper capillaries had a transmittance of 4–120 cc (N.T.P.) of N_2O/hr under a pressure difference of one atmosphere. They gave very reproducible withdrawal rates. The gas was collected in trap T_3 cooled by liquid nitrogen. The size of the gas sample was measured in a gas burette and the sample was isotopically analyzed on a Consolidated-Nier (21–201) isotope ratio mass spectrometer.

In the determination of the isotope ratios, the mass 44 peak was kept at 20-v output for the measurement of the 45/44 and 46/(44+45) ratios. For the 31/30 ratio, the output of the mass 30 peak was kept at 10 v.

[26] H. L. Johnston, Rev. Sci. Instr. **23**, 569 (1952).

[27] R. W. Blue and W. F. Giauque, J. Am. Chem. Soc. **57**, 991 (1935).

TABLE II. Separation of the isotopic N_2O molecules in a packed column.

Dist No.	Boil-up[a] rate (cc/hr)	Production[a] rate (cc/hr)	Reflux ratio	Time from start (hr)	$(S_0-1)\times10^3$ [b]	$(S_{<N^{15}>}-1)\times10^3$ [c]	$(S_{N^{14}N^{15}O^{16}}-1)\times10^3$ [d]	Remarks
1	~45	0	∞	1.5	35	13	5.1	Metal radiation shield
2	49	0	∞	5.0	23.7	14.9	8.7	
	49	0	∞	5.2	25.3	14.8	8.4	
3	82	0	∞	7.5	25.8	11.2	11.8	
	82	0	∞	19	24.7	11.9	12.7	
	82	0	∞	31	24.8	12.6	9.1	
	41	0	∞	51	31.9	20.4	13.4	
5	27	0	∞	2	30.9	18.1	15.7	
	27	0	∞	4	34.6	19.5	15.9	
	16	0	∞	7.5	37.6	19.9	16.0	
	16	0	∞	11	43.2	21.9	14.8	
6	14	0	∞	6.5	37.1	17.8	13.1	
	14	0	∞	11	40.8	18.1	14.1	
7	17	0	∞	1.5	47.8	23.7	15.0	Repacked
	17	0	∞	4.5	51.2	27.8	15.4	
	17	0	∞	6.5	51.7	25.3	14.4	
8	16	0.006	2700	4.7	71.8	38.5	16.2	Silvered jacket
	16	0.006	2700	6.5	76.6	41.5	...	
	16	0.090	180	7.4	87.8	48.4	23.3	
	16	0.090	180	9.0	85.0	48.6	26.2	
	16	0.21	76	9.7	88.0	50.5	28.6	
	16	0.21	76	10.5	86.1	45.5	28.6	
9	8	0.006	1300	7.0	70.4	33.3	22.1	
	8	0.060	130	9.8	85.3	44.1	23.3	
	8	0.021	380	10.6	74.9	39.0	29.5	
	8	0.021	380	11.1	77.6	41.6	29.4	
10	15.5	0	∞	0.4	14.4	7.8	7.1	Proper flooding
	15.5	0	∞	2.5	45.9	29.0	21.1	
	15.5	0	∞	5.0	83.5	48.3	25.7	
	15.5	0.006	2600	8.5	119.0	67.2	38.6	
	15.5	0.12	130	9.5	129.2	69.6	50.7	
	15.5	0.12	130	11.0	139.7	76.7	41.6	
	15.5	0.20	77	12.0	148.7	73.0	40.8	
	15.5	0.20	77	13.0	135.9	71.2	38.7	
	15.5	0.12	130	14.5	142.2	71.9	41.6	
	15.5	0.12	130	15.7	147.5	72.4	47.1	
	15.5	0.07	220	17.5	141.9	78.4	54.2	
	15.5	0.07	220	19.0	142.2	78.5	48.0	
	15.5	0.07	220	20.0	144.0	80.9	51.8	
	15.5	0.006	2600	20.9	155.4	81.7	47.1	
	15.5	0.006	2600	23.0	157.8	82.9	50.6	
	15.5	0.006	2600	25.0	164.8	88.2	57.7	
11	14	0.015	930	0.5	10.4	3.7	4.1	
	14	0.015	930	2.5	41.2	21.2	17.7	
	14	0.015	930	4.0	58.2	26.5	19.9	
	14	0.015	930	6.0	64.3	35.7	24.7	
	14	0.015	930	9.2	90.7	47.0	34.7	
	14	0.015	930	11.0	102.0	50.7	36.4	
	14	0.015	930	14.0	119.0	56.9	32.3	
	14	0.015	930	17.0	134.6	64.2	45.3	
	14	0.015	930	19.5	141.9	70.3	48.0	
	14	0.015	930	23.0	145.9	75.6	50.7	
	14	0.015	930	24.0	147.6	75.3	55.5	

[a] Boil up and production rates in cc liquid N_2O/hr.

[b] $S_0=\left(\frac{N^{14}N^{14}O^{18}}{N^{14}N^{14}O^{16}}\right)_B \Big/ \left(\frac{N^{14}N^{14}O^{18}}{N^{14}N^{14}O^{16}}\right)_T$.

[c] $S_{<N^{15}>}=\left(\frac{N^{15}N^{14}O^{16}+N^{14}N^{15}O^{16}}{N^{14}N^{14}O^{16}}\right)_B \Big/ \left(\frac{N^{15}N^{14}O^{16}+N^{14}N^{15}O^{16}}{N^{14}N^{14}O^{16}}\right)_T$.

[d] $S_{N^{14}N^{15}O^{16}}=\left(\frac{N^{14}N^{15}O^{16}}{N^{14}N^{14}O^{16}}\right)_B \Big/ \left(\frac{N^{14}N^{15}O^{16}}{N^{14}N^{14}O^{16}}\right)_T = \left(\frac{N^{15}O^{16+}}{N^{14}O^{16+}}\right)_B^{0.925} \Big/ \left(\frac{N^{15}O^{16+}}{N^{14}O^{16+}}\right)_T^{0.925}$.

TABLE III. Relative elementary separation parameters for the isotopic N_2O molecules.

$\epsilon_j \equiv \ln[(N^{14}N^{14}O^{16}/N_2O)_{j\ \text{vapor}}/(N^{14}N^{14}O^{16}/N_2O)_{j\ \text{liquid}}]$

Isotopic Species	Exptl	Theoret
$\epsilon_{N^{14}N^{14}O^{18}}/\epsilon_{N^{15}N^{14}O^{16}}$	1.38±0.07	1.46
$\epsilon_{N^{15}N^{14}O^{16}}/\epsilon_{N^{14}N^{15}O^{16}}$	2.10±0.10	1.67
$\epsilon_{N_2O^{18}}/\langle\epsilon_{N^{18}}\rangle$	1.88±0.04	1.82
$\langle\epsilon_{N^{15}}\rangle/\epsilon_{N^{14}N^{15}O^{16}}$	1.55±0.07	1.33

The ratio $N^{14}N^{14}O^{18}/N^{14}N^{14}O^{16}$ was obtained from the 46/44+45 and 45/44 ratios by the procedure given previously.[18] The $(N^{14}N^{15}O^{16}+N^{15}N^{14}O^{16})/N^{14}N^{14}O^{16}$ ratio was obtained from the 45/44 ratio after correction for O^{17}. Account was taken of the enrichment of O^{17} in the column by the assumption that the elemental separation parameter for O^{17} is one-half that of O^{18}. The enrichment of O^{17} was then calculated from the measured O^{18} enrichment. The $N^{14}N^{15}O^{16}/N^{14}N^{14}O^{16}$ ratio was determined from the 31/30 ratio after a similar correction for O^{17}. The effect of rearrangement of $N^{14}N^{15}O^{16}$ and $N^{15}N^{14}O^{16}$ on electron impact was measured in an enriched sample containing 7.5% of N^{15} in the end position, and found to be 7.5%, in agreement with the value of 7% measured earlier.[18] It can be shown that the measured separation factor has to be corrected for this effect, i.e., $S_{\text{true}} \cong (S)_{\text{meas}}^{1-a}$, where a is the degree of rearrangement.

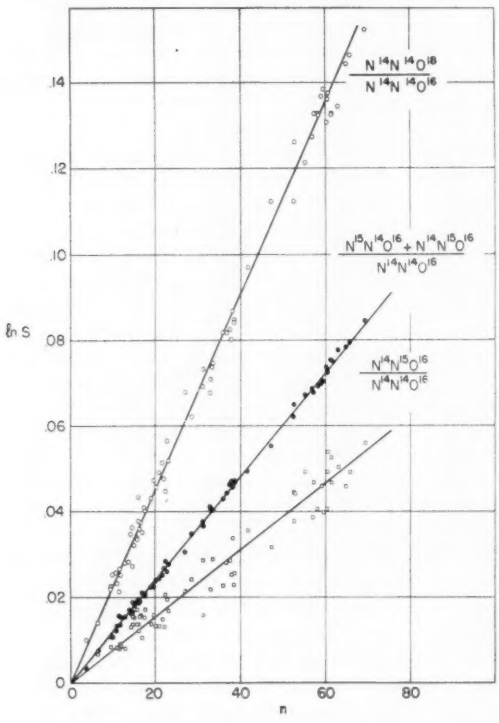

FIG. 4. Separation of the isotopic N_2O molecules in the column as a function of the number of plates.

EXPERIMENTAL RESULTS

Ten different distillation runs were carried out. Between the individual distillations, various changes were made in the column assembly, such as changes in the packing density, a change in the radiation shield, and changes in the sampling procedure. One experiment (No. 4) was abandoned *ab initio* when the gas sample was found to contain traces of water. The separation observed in distillation experiment No. 10 is shown in Fig. 3. For the purposes of reporting the experimental data, we define a separation $S_j = 1/q_j$. This definition gives a separation in the column greater than unity with positive values of ϵ_j. The $N^{14}N^{14}O^{16}$ is the most volatile of the isotopic N_2O molecules. We note from Fig. 3 that $\epsilon_{N^{14}N^{14}O^{18}}$ is larger than $\epsilon_{\langle N^{15}\rangle}$ in accord with the findings of Kuhn, Narten, and Thürkauf.[16] In accord with the theory of the column, production from the column lowers the overall separation. Of most interest is the fact that $\epsilon_{N^{14}N^{15}O^{16}}$ is significantly lower than $\epsilon_{\langle N^{15}\rangle}$. The difference in the over-all separation S of $N^{14}N^{15}O^{16}$ and $\langle N^{15}\rangle$ follows the dynamic behavior of the column.

TABLE IV. Kinetics of a packed column distillation of nitrous oxide (distillation No. 11).

Boil-up rate	16.5 g/hr		
Column holdup	3.56 g		
λ	$0.43/n$		
Steady-state separation		$\ln S_{O^{18}\infty}$ 0.170	$\ln S_{<N^{15}>}$ 0.089
Condenser to column		O^{18}	$\langle N^{15}\rangle$
holdup ratio $K/\lambda n$		0.06±0.01	0.05±0.01
Cohen kinetic parameters	A.	0.88	0.87
	B.	2.03	2.10
Slope of $\ln(S_\infty - S_t)$ vs t		0.064	0.066
Number of plates n		74	74
Separation parameter ϵ		23×10^{-4}	12×10^{-4}
Slope of S_t vs $t^{\frac{1}{2}}$		0.0321	0.0165
Number of plates from $t^{\frac{1}{2}}$ slope		83	88
Separation parameter ϵ		20.5×10^{-4}	10.3×10^{-4}

A correction was applied to the original data for the finite amount of material in the boiler. The dynamic holdup in the column packing was measured in a number of independent ways and found to be 2.9 cc of liquid N_2O under the range of operating conditions in the column. The amount of N_2O in the boiler was in the range 15–40 cc. The material balance equation gives

$$\sum V_P R_P + V_B R_B + V_H R_H \cong V_0 R_0. \qquad (11)$$

where V and R are, respectively, volumes and isotope ratios. The approximation introduced is the use of the isotope ratio rather than mol fraction. The subscripts P, B, H, and 0 refer, respectively, to product, boiler, column holdup, and starting material. We now assume that at any point Z in the column

$$R_Z = R_B \exp(-\epsilon n Z/l), \tag{12}$$

where $R_T/R_B = e^{-\epsilon n}$, l is the length of the column, and R_T is the isotope ratio at the top of the column. The mean concentration of the holdup in the column is

$$R_H = \frac{R_B}{l}\int_0^l \exp(-\epsilon n Z/l)\,dZ = \frac{R_B}{\epsilon n}(1-e^{-\epsilon n}) \tag{13}$$

$$= R_B(1-\tfrac{1}{2}\epsilon n).$$

The composition of the boiler R_B is then

$$R_B = \frac{V_0 R_0 - \sum V_P R_P}{V_B + V_H(1-\tfrac{1}{2}\epsilon n)}. \tag{14}$$

To a first approximation, $\epsilon n \simeq \ln(R_0/R_T)$. Equation (14) was verified experimentally and a comparison between calculation and experiment is given in Table I.

A summary of the column operation data is given in Table II. The $S_{\langle N^{15}\rangle}$ and $S_{N^{14}N^{15}O^{16}}$ data have been corrected for O^{17}. The isotopic composition of the material in the boiler was computed from Eq. (14). The ratios of the elementary separation parameters are obtained from the column data, Eq. (2), and the definition of $S_j = 1/q_j$,

$$\epsilon_j/\epsilon_k = \ln S_j/\ln S_k. \tag{15}$$

We show now that

$$2\langle\epsilon_{N^{15}}\rangle \cong \epsilon_{N^{15}N^{14}O^{16}} + \epsilon_{N^{14}N^{15}O^{16}} \tag{16}$$

even when $(N^{15}N^{14}O^{16}/N^{14}N^{14}O^{16})_0$ differs by a small amount from $(N^{14}N^{15}O^{16}/N^{14}N^{14}O^{16})_0$. The individual

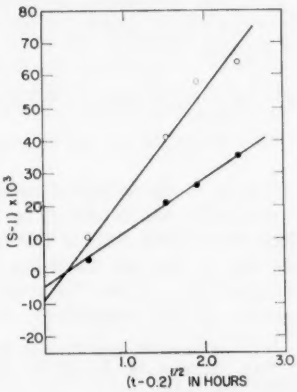

FIG. 5. Separation of $N^{14}N^{14}O^{18}$, ⊙; and $\langle N^{15}\rangle$, ●; in the column at short times.

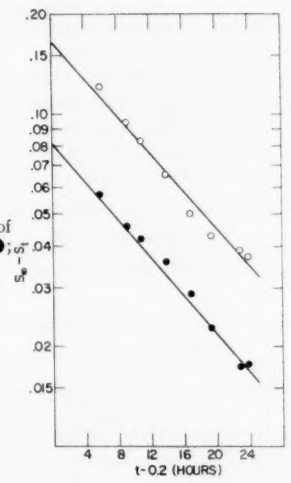

FIG. 6. Separation of $N^{14}N^{14}O^{18}$, ⊙; and $\langle N^{15}\rangle$, ●; in the column at $t>4$ hr.

and average N^{15} separations are

$$\langle S\rangle = \exp(\langle\epsilon\rangle n) = \frac{(R_{N^{14}N^{15}O^{16}} + R_{N^{15}N^{14}O^{16}})_B}{(R_{N^{14}N^{15}O^{16}} + R_{N^{15}N^{14}O^{16}})_T}, \tag{17}$$

$$S_{N^{14}N^{15}O^{16}} = \exp(\langle\epsilon_{N^{14}N^{15}O^{16}}\rangle n)$$

$$= (R_{N^{14}N^{15}O^{16}})_B/(R_{N^{14}N^{15}O^{16}})_T, \tag{18}$$

$$S_{N^{15}N^{14}O^{16}} = \exp(\epsilon_{N^{15}N^{14}O^{16}} n)$$

$$= (R_{N^{15}N^{14}O^{16}})_B/(R_{N^{15}N^{14}O^{16}})_T. \tag{19}$$

Let

$$(R_{N^{14}N^{15}O^{16}})_B/(R_{N^{15}N^{14}O^{16}})_B = 1+\delta, \tag{20}$$

then

$$2\langle\epsilon\rangle - \epsilon_{N^{15}N^{14}O^{16}} - \epsilon_{N^{14}N^{15}O^{16}} + \tfrac{1}{2}\delta(\epsilon_{N^{15}N^{14}O^{16}} - \epsilon_{N^{14}N^{15}O^{16}})$$
$$+\tfrac{1}{2}n(1-\tfrac{1}{2}\delta)[(\langle\epsilon\rangle - \epsilon_{N^{15}N^{14}O^{16}})^2 + (\langle\epsilon\rangle - \epsilon_{N^{14}N^{15}O^{16}})^2] = 0. \tag{21}$$

From Eq. (21) it follows that

$$2\langle\epsilon\rangle = \epsilon_{N^{15}N^{14}O^{16}} + \epsilon_{N^{14}N^{15}O^{16}} \tag{22}$$

to within one per cent in ϵ, even when δ is of the order of 10^{-2}, $n=100$, and $\langle\epsilon\rangle - \epsilon_{N^{15}N^{14}O^{16}} \sim 10^{-3}$.

The relative ϵ's are given in Table III and discussed in the next section. The ϵ ratios were weighted in proportion to the value of the individual $\ln S$ points. Since $\ln S$ is always positive,

$$\epsilon_i/\epsilon_j = \sum_a w_a(\ln S_i)_a / \sum_a w_a(\ln S_j)_a, \tag{23}$$

where w_a is the weighting factor for each measurement. The variance of the individual measurements was tested by the Chauvenet criterion and five of the fifty-seven determinations given in Table II, which are in themselves averages of several analyses, were rejected in obtaining the weighted ϵ ratios. The validity of Eq. (15) and the consistency of the data are shown in Fig. 4. We assume $\epsilon_{\langle N^{15}\rangle}$ to be exactly 12×10^{-4}, in

TABLE V. Absolute values of elementary separation parameters for the isotopic N_2O molecules ($\epsilon \times 10^4$).

Isotopic species	Experiment	$t^{\frac{1}{2}}$ plot	$\exp(-Bt/\lambda n^2)$ plot	Production data	Weighted mean ϵ (95% C.I.)
$N^{14}N^{14}O^{18}$	10	24±7		19±6	
	11	20.5±3	23±3		$22\pm2\times10^{-4}$
	Kuhn, Narten, and Thürkauf				$18\pm5\times10^{-4}$
$\frac{(N^{15}N^{14}O^{16}+N^{14}N^{15}O^{16})}{2}$	10	15±3		13±5	
	11	10.3±2	12±2		$12\pm2\times10^{-4}$
	Kuhn, Narten, and Thürkauf				$11.6\pm0.6\times10^{-4}$
$N^{14}N^{15}O^{16}$					$7.8\pm1.4\times10^{-4}$
$N^{15}N^{14}O^{16}$					$16.2\pm2.8\times10^{-4}$

agreement with the value determined by Kuhn, Narten, and Thürkauf and our absolute measurement to be described presently. Another choice of $\epsilon_{\langle N^{15}\rangle}$ will not change the ϵ ratios. This leads to $(n_a)_{\langle N^{15}\rangle}$ from each $(\ln S_a)_{N^{15}}$. A corresponding value of n_a is calculated from the O^{18} data using $\epsilon_{N^{14}N^{14}O^{18}}$ exactly $(1.88)(12)\times10^{-4}$. An average n_a is calculated by weighting $(n_a)_{\langle N^{15}\rangle}$ and $(n_a)_{O^{18}}$ in the ratio 2:1, the relative precision of the $\langle N^{15}\rangle$ and O^{18} measurements. The plots of $\log S_{\langle N^{15}\rangle}$, $\log S_{N^{14}N^{14}O^{18}}$, and $\log S_{N^{14}N^{15}O^{16}}$ against n are all straight lines through the origin, with relative slopes given by the values in Table III. Through the use of the column and precision isotope ratio measurements, the relative ϵ's of the isotopic N_2O molecules, which have ϵ's of the order 10^{-3}, have been determined with an accuracy of 5%.

The absolute ϵ's were determined from the data in distillation experiments 10 and 11. The experimental data for the kinetics of the column with no production in distillation No. 11 are given in Table IV. Cohen has shown that if the finite but small size of the condenser in a column is taken into consideration, Eq. (3) becomes

$$q(n,t)=1+2\epsilon(t/\pi\lambda)^{\frac{1}{2}}-\epsilon K/\lambda. \tag{24}$$

A plot of the short time separations is given in Fig. 5. The observed time has been corrected for the time of sampling. The ratio of the O^{18} and $\langle N^{15}\rangle$ intercepts and slopes are in the ratio of the ϵ's. The number of plates for O^{18} and $\langle N^{15}\rangle$, 83 and 88, respectively, are within 6% of one another, which is as good as can be expected. The values of the ratio of the holdup in the condenser to that in the packing $K/\lambda n$, determined from the O^{18} and $\langle N^{15}\rangle$ intercepts, agree within experimental error with independent estimates. For the operation of the column at $t>\lambda n^2/10$, the slopes of the $\log(S_\infty-S_t)$ vs t plots in Fig. 6 give 74 plates for both O^{18} and $\langle N^{15}\rangle$. The discrepancy with the short time behavior may be a consequence of the fact that packed columns are frequently more efficient at short times. This is presumably due to the gradual drying of the packing.

A summary of all the absolute ϵ values is given in Table V. Our results for $\epsilon_{N^{14}N^{14}O^{18}}$ and $\epsilon_{\langle N^{15}\rangle}$ are in good agreement with the data of Kuhn, Narten, and Thürkauf.[16]

THEORY OF THE ELEMENTARY SEPARATION PARAMETERS

When the vapor in equilibrium with a liquid or a solid is an ideal gas, the separation factor $\alpha=R_c/R_v$, where R_v and R_c are the isotope ratios in the vapor and condensed states, respectively, is related to the vapor pressure ratio by the equation

$$\ln\alpha_j=\epsilon_j=\ln P_{N^{14}N^{14}O^{16}}/P_j. \tag{25}$$

If one accounts for the gas imperfection and the finite volume of the condensed phase, then[28]

$$\epsilon_j=(\ln P_{N^{14}N^{14}O^{16}}/P_j)(1+BP-PV_c/RT) \tag{26}$$

and[29]

$$\epsilon_j=\ln f_{cj}-\ln f_j. \tag{27}$$

The quantities f_c and f are reduced molecular isotope partition function ratios.[13] The elementary separation parameter ϵ is directly related to the difference in the quantum effects in the condensed and gaseous states.

The theory of isotope effects in condensed systems containing polyatomic molecules has been developed recently.[13] It is shown (cf. reference 13, Eqs. 3.13 and 3.25) that

$$\epsilon_j=\ln f_{cj}-\ln f_j=(24N)^{-1}(\hbar/kT)^2\sum_i^{3N}(\mu_j'-\mu_j)(a_{jj}-b_{jj})_i+0(\hbar^4T^{-4}), \tag{28}$$

where μ_j is the reciprocal mass the jth atom which is isotopically substituted. The convention adopted is that the primed atom is the light one. The quantities a_{jj} and b_{jj} are the Cartesian force constants for the displacement of the j'th atom in the condensed and gaseous phases, respectively. If we write $k_j=a_{jj}-b_{jj}$,

[28] Cf. reference 10. Eqs. (8) and (9).
[29] Cf. reference 13, Eq. (2.17). Equation (27) follows from (2.17) and (2.11).

hen to order $(\hbar/kT)^2$,

$$\epsilon_j/\epsilon_l = \frac{(\mu_j'-\mu_j)k_j}{(\mu_l'-\mu_l)k_l}. \quad (29)$$

From Eq. (29) we obtain

$$\epsilon_{N^{15}N^{14}O^{16}}/\epsilon_{N^{14}N^{15}O^{16}} = k_{\text{end } N}/k_{\text{middle } N} \quad (30)$$

and

$$\epsilon_{N^{14}N^{14}O^{18}}/\epsilon_{N^{15}N^{14}O^{16}} = 1.46k_O/k_{\text{end } N}. \quad (31)$$

The N_2O molecule is linear with a small dipole moment (0.17 d). It is very similar to CO_2, with which it is isosteric. The molecules have the same molecular weight, overall molecular size, crystal structures, lattice constants, and very similar vibrational spectra in their gross features. In fact, the molecules form mixed crystals.[30] It is, therefore, not surprising that Blue and Giauque[27] attributed the entropy defect of 1.14 eu (obtained from thermal measurements on the solid at low temperature) to end for end random orientation of the N_2O molecules in the crystal lattice. This hypothesis has now been confirmed by recent neutron-diffraction studies by Dr. W. C. Hamilton[31] of this Laboratory. If we assume that there are but minor changes in the intramolecular force constants on condensation, the random structure for N_2O and its similarity to CO_2 lead to $k_O = k_{\text{end } N}$. Therefore, just as in the case of NO[14], $\epsilon_{N^{14}N^{14}O^{18}}/\epsilon_{N^{15}N^{14}O^{16}}$ is calculated to be 1.46.

We now consider the ratio $k_{\text{end } N}/k_{\text{middle } N}$. The middle nitrogen is virtually at the center of gravity of the molecule[15] and the sole contribution to $k_{\text{middle } N}$ arises from the potential which restricts the translation of the molecule (again we neglect contributions from changes in the intramolecular forces). There is the same contribution to $k_{\text{end } N}$ from the translation of the molecule, but $k_{\text{end } N}$ also has a contribution from the rotation of the molecule. In a linear molecule subject to an isotropic force, $k_{\text{trans+rot}}/k_{\text{trans}}$ is equal to $\frac{5}{3}$, just the ratio of the number of degrees of freedom. Thus, on this model, we calculate $\epsilon_{N^{15}N^{14}O^{16}}/\epsilon_{N^{14}N^{15}O^{16}}$ to be $\frac{5}{3}$. The calculated ϵ ratios are compared with the experimental ratios in Table III. The theoretical ϵ ratios are in good agreement with the experimental ones. The difference between $N^{15}N^{14}O^{16}$ and $N^{14}N^{15}O^{16}$ is somewhat larger than can be accounted for by an orientation-independent potential.

[30] L. Vegard, Z. Physik **71**, 465 (1931).
[31] W. C. Hamilton and M. Petrie, J. Phys. Chem. (to be published).

We need but calculate the absolute value of $\epsilon_{N^{14}N^{15}O^{16}}$. Theoretical values for the ϵ's for the other isotopic species can be obtained from this ϵ and the theoretical ratios given in Table III. To calculate $\epsilon_{N^{14}N^{15}O^{16}}$ we make use of the Debye $\theta = 127°$ K determined from the low-temperature heat capacity of N_2O.[27] Only the motion of the lattice points contributes to the Debye θ and it is, therefore, appropriate for the calculation of $\epsilon_{N^{14}N^{15}O^{16}}$. We write

$$(hc/k)^2 \sum_{\text{lattice}} \nu^2 = 9/5N\theta_D^2 = N(2\mu_N+\mu_O)(k_{\text{trans}})(\hbar c/k)^2,$$

$$k_{\text{middle } N} = 8.77\theta_D^2 \cdot (k/\hbar c)^2.$$

This value of $k_{\text{middle } N}$ leads to

$$\epsilon_{N^{14}N^{15}O^{16}} = \frac{8.77}{24}\left(\frac{1}{14}-\frac{1}{15}\right)(\theta_D/T)^2$$

$$= 8.2\times10^{-4} \text{ at } 184° \text{ K},$$

compared with the experimental value of $7.8\pm1.4\times10^{-4}$. The absolute ϵ's are thus calculated in adequate agreement with the experimental ones given in Table V.

CONCLUSIONS

Both relative and absolute values for the vapor pressure ratios of the O^{18} and N^{15} isotopic molecules have been measured by distillation in a packed column. A search has been made for a difference in the vapor pressures of the isomers $N^{15}N^{14}O^{16}$ and $N^{14}N^{15}O^{16}$. It is shown that the $N^{14}N^{15}O^{16}$ is the more volatile species and has a vapor pressure 0.07% larger than $N^{15}N^{14}O^{16}$ at 184° K.

The vapor pressures of the isotopic N_2O molecules can be accounted for in terms of the known random structure in the liquid and solid. The difference in vapor pressures of $N^{14}N^{15}O^{16}$ and $N^{15}N^{14}O^{16}$ arises from the hindered rotation of the molecule. The contribution to the difference in vapor pressures of the isotopic N_2O molecules from the restricted translation, "lattice vibrations," is calculated from the specific heat of solid $N^{14}N^{14}O^{16}$ in good agreement with the experimental data. The quantitative agreement between the calculated and experimental relative and absolute vapor pressure ratios for this series of four isotopic molecules adds further support to Bigeleisen's theory of quantum corrections in a condensed system of polyatomic molecules.

ACKNOWLEDGMENTS

We wish to thank Ernest Leadbeater for his assistance in the operation of the column and Theodore H. Middleton for the isotopic analyses.

THE JOURNAL OF CHEMICAL PHYSICS VOLUME 35, NUMBER 4 OCTOBER, 1961

Equilibrium Degrees of Crystallization Predicted for "Single Pass" and Folded Chain Crystallite Models

R.-J. ROE, K. J. SMITH, JR., AND W. R. KRIGBAUM

Department of Chemistry, Duke University, Durham, North Carolina

(Received March 24, 1961)

The free energy change for the crystallization of a bulk polymer consists of two parts: the "single crystal" term exhibited by low molecular weight compounds, and that arising from the deformation produced in the intervening amorphous chains as crystallization proceeds. The latter term limits the degree of crystallinity which can be achieved in a polymeric material at a given temperature. Beginning with an initially unstretched, isotropic sample, the entropy change associated with the deformation of the amorphous chains is calculated for two models, in which the chain either passes through a crystallite once and departs, or folds back and forth within the crystallite several times before re-entering the amorphous region. The folded chain morphology imposes less strain upon the amorphous chains, and hence results in the development of higher degrees of crystallinity from the original isotropic melt. The folded chain model, in which the amorphous portions are represented by flexibly linked chains, gives good agreement with the observed equilibrium degrees of crystallinity, for high molecular weight fractions of polyethylene, over a considerable temperature range. An approximate treatment is also given for the molecular weight dependence of crystallinity at a fixed temperature.

LOW molecular weight compounds form crystals which are very large in comparison with molecular dimensions. While macroscopic single crystals of some polymeric materials have been grown from dilute solutions, crystallization of bulk polymers results in the formation of regions of three-dimensional order (crystallites) which are considerably smaller than the length of a molecule. Hence, a particular molecule may pass through several crystalline and amorphous areas. The free energy change associated with the crystallization of bulk polymers therefore consists of two parts: the "single crystal" term corresponding to the transfer of units from a disordered, amorphous region to the ordered crystalline domain and, secondly, that arising from the deformations produced in the intervening amorphous regions as crystallization proceeds. Crystallization ceases when the latter term offsets the former.

This paper is concerned with an estimation of the magnitude of the strain imposed on the amorphous chains, through consideration of appropriate models. It appears from x-ray data that the arrangement of the molecular chains in the crystallites differs from one polymer type to the next. For this reason two models are examined in Sec. I. In one of these the chain is assumed to make a single pass through the crystallite, while in the second model the chain is permitted to fold back and forth several times within the crystallite before re-entering the amorphous domain. Consideration of the total free energy change leads to relationships between the equilibrium degree of crystallization, temperature, and molecular weight. Our attention will be confined to the crystallization of initially isotropic and undeformed samples; we intend to examine the effect of deformation prior to crystallization in a subsequent paper. In Sec. II the predictions based upon these models will be compared with each other, and with experimental data for polyethylene.

I. THEORY

A. Single Pass Crystallization with Longitudinal Growth

Gaussian Chain

The polymer molecule is represented by an equivalent, flexibly linked chain. Two links of the chain are assumed to enter crystal nuclei separated by a distance r_N, and the intervening links are then numbered 1, 2, $\cdots N$, beginning at one nucleus and terminating at the second. Two links, i and k, are chosen such that $t=|k-i|=N-n$. For a fixed r_N, the mean-square distance between links i and k may be obtained through use of the theorem on multivariate Gaussian distributions, given by Fixman,[1]

$$\langle r_t^2\rangle=\int_0^\infty r_t^2[P(r_N, r_t)/P(r_N)]dr_t,$$

where

$$P(r_N, r_t)=(3/2\pi b^2)^3(nt)^{-\frac{3}{2}}$$
$$\times \exp\{-(3/2ntb^2)[tr_N^2-2tr_Nr_t+Nr_t^2]\},$$

b being the length of one equivalent link. The integration yields

$$\langle r_t^2\rangle=(nt/N)b^2+(t/N)^2r_N^2. \quad (1)$$

We now permit the n links, in the portions between links 1 and i and k to N, to enter the two growing crystallites (see Fig. 1). If S_f is the entropy of fusion of a single link from a perfect crystal, then the "single crystal" contribution to the entropy change for the crystallization of n links is simply $-nS_f$. As a result of this process, additional restraints will be placed on the remaining amorphous chain of $(N-n)$ links, lead-

[1] M. Fixman, J. Chem. Phys. **23**, 1656 (1955).

ing to a deformation entropy ΔS_D. The total entropy change for the crystallization ΔS_T is therefore given by $\Delta S_T = -n S_f + \Delta S_D$.

For the calculation of ΔS_D, we require the mean-square distance between links i and k after crystallization $\langle r_c^2 \rangle$. Using spherical coordinates, as shown in Fig. 1, we obtain

$$r_c^2 = r_N^2 - 2r_N(l_1 \cos\theta_1 + l_2 \cos\theta_2) + l_1^2 + l_2^2 + 2l_1 l_2(\cos\theta_1 \cos\theta_2 + \sin\theta_1 \sin\theta_2 \cos\varphi).$$

Setting $l_1 = l_2 = nb/2$, and averaging over all orientations of the two crystallites, yields

$$\langle r_c^2 \rangle = r_N^2 - 2r_N nb\langle\cos\theta\rangle + (n^2b^2/2)[1 + \langle\cos\theta\rangle^2 + \langle\sin\theta\rangle^2\langle\cos\varphi\rangle].$$

If the angular distribution of the crystallites is assumed to be the same as that governing any link, so that $\langle\cos\varphi\rangle = 0$ and $\langle\cos\theta\rangle = r_N/Nb$,

$$\langle r_c^2 \rangle = n^2b^2/2 + (1 - 2n/N + n^2/2N^2) r_N^2. \quad (2)$$

Finally, we may average the result over the distribution of r_N values for a fixed N. Because the chain is Gaussian before crystallization, $\langle r_N^2 \rangle = Nb^2$.

The entropy of a Gaussian chain of $(N-n)$ links having a displacement length r is

$$s(r) = \text{const} - (\tfrac{3}{2}k)[r^2/(N-n)b^2]. \quad (3)$$

If Gaussian statistics still prevail for the remaining amorphous chains after crystallization, ΔS_D is simply $-(\tfrac{3}{2}k)[\langle r_c^2 \rangle - \langle r_t^2 \rangle]/(N-n)b^2$. Hence, the entropy change caused by the deformation of the remaining amorphous chain from r_t to r_c is

$$\Delta S_D = -(\tfrac{3}{2}k)[n/(N-n)][(n/2)(1+1/N) - 1]. \quad (4)$$

The total free energy change for the crystallization of n units then becomes

$$\Delta F = -n(\Delta H_f - T\Delta S_f) - T\Delta S_D, \quad (5)$$

where ΔH_f and ΔS_f are the heat and entropy changes

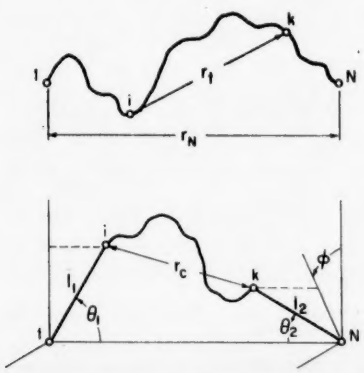

FIG. 1. The "single pass" crystallite model.

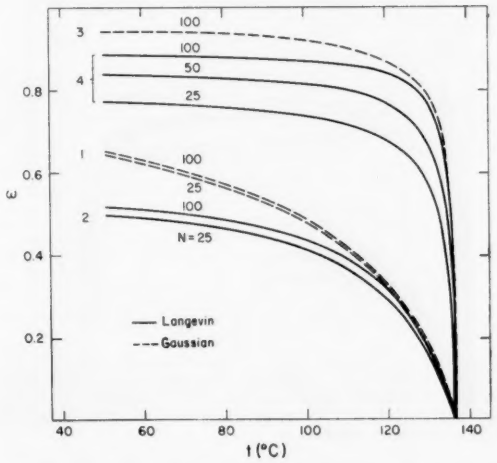

FIG. 2. Comparison of the equilibrium degrees of crystallinity ω for polyethylene as predicted, using the "single pass" and folded chain models.

associated with the fusion of one equivalent link from a perfect crystal. For simplicity we assume the molecular weight to be very large, so that further crystallization of the chain ends may be neglected. Thus, the degree of crystallization is simply n/N. Upon setting

$$(\partial\Delta F/\partial n)_{N,T} = 0,$$

the equilibrium degree of crystallization ω is found to be

$$\omega = 1 - \left(\frac{3N-3}{4NA+3N+3}\right)^{\frac{1}{2}} \cong 1 - \left(\frac{3}{4A+3}\right)^{\frac{1}{2}}, \quad (6)$$

where

$$A = (\Delta H_f/R)(1/T - 1/T_M^\circ), \quad (7)$$

and T_M° is the melting point of a large, perfect crystal.

If the orientation of the crystallites is assumed to be perfectly random, so that $\langle\cos\theta\rangle = 0$, the square root term in Eq. (6) is replaced by $[(3N+6)/N(4A+3)]^{\frac{1}{2}}$. This result will be nearly the same as that given above, so long as $N \gg 1$.

Inverse Langevin Chain

Since the remaining amorphous chains are near full extension, the departure from Gaussian statistics may well be important. The analog of Eq. (3) for a flexibly jointed chain is

$$s(r) = \text{const} - k(N-n)\{[r/(N-n)b]\beta + \ln(\beta/\sinh\beta)\}, \quad (3')$$

where β is the inverse Langevin function,

$$\beta = \mathfrak{L}^{-1}[r/(N-n)b].$$

Following the same procedure as before, we obtain for

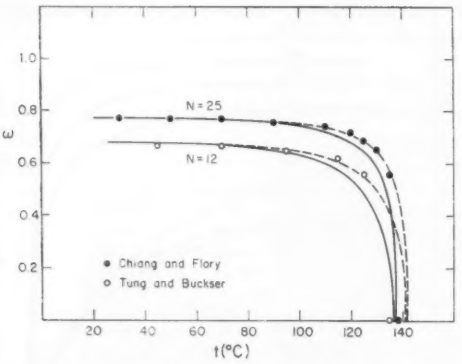

FIG. 3. Equilibrium degrees of crystallinity predicted, using the folded, flexibly jointed chain model, compared with the experimental data of Chiang and Flory[4] and Tung and Buckser[6] for polyethylene fractions.

this distribution,

$$\Delta S_D = k(N-n)\left[r_t\beta_t/(N-n)b + \ln(\beta_t/\sinh\beta_t) - r_c\beta_c/(N-n)b - \ln(\beta_c/\sinh\beta_c)\right], \quad (4')$$

where

$$\beta_t = \mathfrak{L}^{-1}\{1/[N(1-\omega)]^{\frac{1}{2}}\},$$

$$\beta_c = \mathfrak{L}^{-1}\left\{\left[\frac{1-2\omega+(N+1)\omega^2/2}{N}\right]^{\frac{1}{2}}\left(\frac{1}{1-\omega}\right)\right\}.$$

Upon setting $(\partial\Delta F/\partial n)_{N,T}=0$ there is obtained

$$A = \ln[(\sinh\beta_c)/\beta_c] - \ln[(\sinh\beta_t)/\beta_t] + \frac{[(N+1)\omega-2]\beta_c}{\{2N[(N+1)\omega^2-4\omega+2]\}^{\frac{1}{2}}} + \frac{\beta_t}{2\{N(1-\omega)\}^{\frac{1}{2}}}. \quad (6')$$

The first term in the expansion of the second logarithmic term exactly cancels the fourth term in Eq. (6′), so that, to a very good approximation,

$$A = \ln[(\sinh\beta_c)/\beta_c] + \frac{[(N+1)\omega-2]\beta_c}{\{2N[(N+1)\omega^2-4\omega+2]\}^{\frac{1}{2}}}. \quad (6a')$$

Values of ω may be calculated graphically from Eq. (6a′).

B. Folded Chain Crystallization

Gaussian Chain

We again adopt the model described above, but allow the $n/2$ links to enter each crystallite by folding back and forth several times, so that $r_c \cong r_N$. Since r_t is again given by Eq. (1), the assumption of Gaussian statistics for the remaining amorphous chains leads to

$$\Delta S_D = -(\tfrac{3}{2}k)[n/(N-n)]. \quad (4f)$$

If the energy required to form the folds is neglected, in comparison with that liberated upon crystallizing the n links, the equilibrium degree of crystallization for this model is given by

$$\omega = 1-(3/2AN)^{\frac{1}{2}}. \quad (6f)$$

Inverse Langevin Chain

The analog of Eq. (4f) for an inverse Langevin distribution is

$$\Delta S_D = k(N-n)\left[\beta_t/(N-n)^{\frac{1}{2}} + \ln(\beta_t/\sinh\beta_t) - \beta_c' N^{\frac{1}{2}}/(N-n) - \ln(\beta_c'/\sinh\beta_c')\right], \quad (4f')$$

where

$$\beta_c' = \mathfrak{L}^{-1}[1/N^{\frac{1}{2}}(1-\omega)].$$

Upon setting $(\partial\Delta F/\partial n)_{N,T}=0$ we find

$$A = \ln[(\sinh\beta_c')/\beta_c'] - \ln[(\sinh\beta_t)/\beta_t] + \beta_t/2[N(1-\omega)]^{\frac{1}{2}}. \quad (6f')$$

Once again the first order terms in β_t cancel, so that a good approximation is furnished by

$$A = \ln[(\sinh\beta_c')/\beta_c']. \quad (6fa')$$

II. COMPARISON WITH EXPERIMENT

Single Pass and Folded Chain Models

The results of calculations for the case of polyethylene, based upon the above models, are compared in Fig. 2, in which the predicted equilibrium degree of crystallization ω appears plotted against temperature. According to Quinn and Mandelkern,[2] the heat of fusion per CH_2 unit is 940 cal/mole, and $t_M^\circ = 137°C$. We estimate a statistical link to consist of approximately 20 CH_2 units. Dashed curves 1 were obtained for the "single pass" Gaussian chain model when $N=100$ or 25, while full curves 2 represent the corresponding cases for freely jointed chains. The divergence at lower temperatures indicates increasing departures of the amorphous chains from Gaussian behavior as crystallization proceeds. Dashed curve 3 and full curves 4 were calculated according to the folded chain Gaussian and inverse Langevin models, respectively. Here ω depends more strongly upon the concentration of nuclei through the parameter N. Comparison of curves 1 and 3, or 2 and 4, reveals that the "single pass" morphology imposes greater strains upon the intervening amorphous chains, and therefore results in considerably lower ω values than the folded chain model. Experimental evidence[3] indicates that polyethylene single crystals form from solution by a chain folding mechanism. From the consideration given above, one should also expect chain folding to play a dominant role in the crystallization of polyethylene from an isotropic melt.

[2] F. A. Quinn, Jr., and L. Mandelkern, J. Am. Chem. Soc. **80**, 3178 (1958).

[3] P. H. Till, Jr., J. Polymer Sci. **24**, 301 (1957); A. Keller, Phil. Mag. **2**, 1171 (1957); E. W. Fischer, Z. Naturforsch. **12a**, 753 (1957).

Comparison with Polyethylene Data

The filled circles in Fig. 3 represent the experimental data of Chiang and Flory[4] for a high molecular weight fraction ($M=490\,000$) of Marlex polyethylene. The full curve indicates values calculated according to Eq. (6fa′) for the folded, flexibly jointed model chain. We again assume 20 CH_2 units per equivalent link, so that $\Delta H_f=18\,800$ cal/mole as before, but in the present case we take $t_M°=138.5°C$, as reported for this sample. The value $N=25$ was chosen to fit the ω values at the lowest temperature. The agreement is rather good, but the predicted ω values just below the melting point are too low. Although 138.5° is the highest melting point reported for polyethylene, Chiang and Flory suggest that, due to the difficulty of attaining equilibrium very close to $t_M°$, the true crystal melting point may be a few degrees higher. This possibility would shift our calculated curve to the right, removing some of the discrepancy. As an illustration the dashed curve in Fig. 3 has been calculating assuming $t_M°=143°C$.

Tung and Buckser[5] have also reported data for several fractions of low pressure polyethylene. The ω values reported for their fraction of highest molecular weight ($M=118\,000$) are, in general, in good agreement with those of Chiang and Flory, although the observed melting point is somewhat lower (135°). This agreement is only apparent, however, because the two sets of authors have used quite different expressions for the specific volume of the crystalline phase. We have no basis for judging the correctness of these two relations. For the purpose of comparison, the open circles in Fig. 3 indicate ω values calculated from the dilatometric data of Tung and Buckser, with use of the conversion relation of Chiang and Flory. The curves were calculated assuming $N=12$, and $t_M°=138.5°$ (full curve), or 143° (dashed curve). If the relation of Tung and Buckser had been used throughout, both curves would be moved upward, requiring larger N values. In either event, a lower N value would be required to fit the latter set of data. This is quite reasonable, for the sample of Chiang and Flory was crystallized at a high temperature, 131.3°, whereas that of Tung and Buckser was crystallized at a low temperature. The nuclei density would therefore be expected to be considerably larger in the latter sample.

The treatment given in Sec. I involved the implicit assumption that all of the nuclei form simultaneously at the beginning of the process, so that N remains constant while the crystallite size (n) varies. One can also imagine the degree of crystallinity to change by an alteration in the number of crystalline runs per chain (variable N), the average length of a run (n) remaining constant. A combination of these two processes represents a third possibility. If F_σ represents the free energy

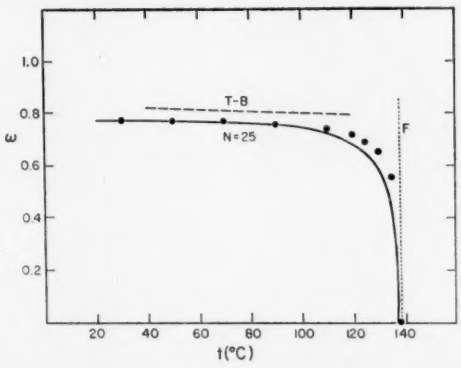

FIG. 4. Theoretical ω values calculated using the treatments of Flory[6] (curve F), Tung and Buckser[5] (curve T–B), and the present treatment (full curve), compared with experimental data for Chiang and Flory[4] for polyethylene.

of a portion of a polymer chain consisting of σ equivalent links ($\sigma \gg N$), the completely amorphous polymer as a reference state, then for an infinitesimal isothermal process

$$dF_\sigma=(\partial F_\sigma/\partial N)_{n,T}dN+(\partial F_\sigma/\partial n)_{N,T}dn. \tag{8}$$

Here F_σ is related to ΔF as given in Sec. I by

$$F_\sigma=(\sigma/N)\Delta F. \tag{9}$$

The condition for equilibrium is $dF_\sigma=0$. If N is maintained constant, the equilibrium condition employed in Sec. I is recovered from Eqs. (8) and (9). On the other hand, for a process with constant n, the equilibrium condition becomes

$$[\partial(\Delta F/N)/\partial N]_{n,T}=0. \tag{10}$$

The variation of ω with temperature, calculated for either the single pass or folded chain model, with employment of condition (10), is almost indistinguishable from that deduced above.

Equation (8) is insufficient to define the equilibrium state for the most general case in which both N and n are permitted to vary. However, since quite similar results are obtained when either N or n is treated as the only variable, it appears that essentially the same relationship between ω and T would result in this third case as well. In this connection it is interesting to note that if N and n are varied in such a manner that ω remains constant, (i.e., $dN=\omega dn$), then

$$(\partial F_\sigma/\partial n)_{\omega,T}=\omega\sigma[\partial(\Delta F/N)\partial N]_{n,T}+(\sigma/N)(\partial\Delta F/\partial n)_{N,T}.$$

Substitution for ΔF reveals that $(\partial F_\sigma/\partial n)_\omega<0$, which agrees with the observation that the size of the individual crystallites increases upon annealing.

[4] R. Chiang and P. J. Flory, J. Am. Chem. Soc. (to be published).
[5] L. H. Tung and S. Buckser, J. Phys. Chem. **62**, 1530 (1958).

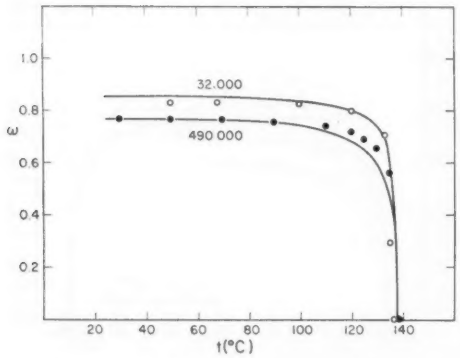

FIG. 5. A test of the predicted dependence of crystallinity upon molecular weight.

Comparison with Other Treatments

Various aspects of equilibrium crystallization of polymers were considered several years ago by Flory.[6] His assumption that the intervening amorphous chains were unstrained resulted in the prediction that most of the fusion should occur quite sharply within a few degrees of $t_M°$, as indicated by the dotted curve in Fig. 4 marked F. The entropy of deformation of the amorphous chains was included in an earlier treatment, by Flory, of crystallization induced by stretching[7]; however, the simplifying assumption that the crystallites are oriented along the draw axis renders the result invalid for low draw ratios, so that no comparison with the present treament is possible.

Tung and Buckser[5] have given a treatment which bears formal resemblance to that presented here. They have employed a simplified "single pass" model of Alfrey and Mark,[8] which is obtained upon setting the angles θ_1, θ_2, and φ (shown in Fig. 1) all equal to zero. This corresponds to a state of perfect crystallite alignment, and puts the intervening amorphous chains under compression as crystallization progresses, whereas, they would come under tension if the alignment were more random. Tung and Buckser obtained reasonable agreement with the experimental data at lower temperatures, as shown by the dashed line designated $T-B$ in Fig. 4, using two adjustable parameters corresponding to our N and r_N. They obtained higher ω values than those shown for our single pass model in Fig. 2 by allowing all of the chain ends to crystallize completely. This assumption does not appear warranted for "single pass" crystallization. Finally, their treatment fails for temperatures near $t_M°$, apparently because of the neglect of the single crystal entropy of fusion in their formulation of the free energy.

As indicated above, we believe the folded chain model is more realistic for polyethylene. Our treatment contains only one adjustable parameter, because $\langle r_N \rangle$ can be expressed in terms of N. It clearly offers the best representation of the experimental data over the entire temperature range.

Molecular Weight Dependence of ω

It is observed experimentally that, for polyethylene, at a given temperature, the equilibrium degree of crystallinity increases as the molecular weight decreases. Tung and Buckser[5] have advanced the suggestion that this arises from the complete crystallization of the free chain ends. Their model assumes that the nucleated units are spaced uniformly along the chain. A somewhat more realistic model would involve a random distribution of nucleated units along the chain.

We consider a sample containing a large number of polymer molecules, each consisting of x repeating units, and designate by ρ the probability that any unit has been nucleated. The probability that none of the x units in a particular chain has nucleated is given by $\exp(-\rho x)$, and this is also the fraction f_0 of all units which occur in molecules bearing no nucleated units

$$f_0 = \exp(-\rho x). \tag{11}$$

Beginning at one end of a chain, number the repeating units 0, 1, 2, $\cdots x-1$. The probability that the first nucleated unit encountered is the jth is $\rho \exp(-\rho j)$; thus the fraction f_j of all units contained in chain ends having exactly j units preceding a nucleated unit is $f_j = (\rho j/x) \exp(-\rho j)$. The fraction of all units found in chain ends having one unit nucleated f_E is obtained upon summing f_j over all possible values of j and multiplying by two, because each chain has two ends; thus,

$$f_E = (2\rho/x)\int_0^x j \exp(-\rho j)\,dj = (2/\rho x) \times[1-(1+\rho x)\exp(-\rho x)]. \tag{12}$$

The fraction of all units found in chain segments bounded on the two ends by nucleated units, f_B is $1-f_0-f_E$, or

$$f_B = 1-(2/\rho x)+(1+2/\rho x)\exp(-\rho x). \tag{13}$$

Let ω_∞ be the equilibrium degree of crystallinity for a sample of infinite molecular weight. In this case, of course, the crystallization of chain ends can be neglected. We assume that the fraction f_B of units in segments bounded at both ends by nuclei crystallize to degree ω_∞, and that the fraction f_E of units nucleated at one end only crystallize 100%; whereas the fraction f_0 of units in chains bearing no nuclei do not crystallize at all. The equilibrium degree of crystallization for chains having x units ω_x then becomes $f_B\omega_\infty + f_E$. Substitution from Eqs. (12) and (13) gives

$$\omega_x = \omega_\infty + (1-\omega_\infty)(2/\rho x)[1-\exp(-\rho x)] - \exp(-\rho x)(2-\omega_\infty). \tag{14}$$

[6] P. J. Flory, J. Chem. Phys. **17**, 224 (1949).
[7] P. J. Flory, J. Chem. Phys. **15**, 397 (1947).
[8] T. Alfrey and H. Mark, J. Phys. Chem. **46**, 112 (1942).

To return to the notation used in Sec. I, let there be on the average r chain segments, consisting of N equivalent links (bounded by two nucleated units) per chain. If there are s repeating units in one equivalent link, then the probability that any unit has nucleated (ρ) is given by

$$\rho=1/Ns=r/x; \tag{15}$$

thus $\rho x=r$, and Eq. (14) may be written

$$\omega_x=\omega_\infty+(1-\omega_\infty)(2/r)(1-e^{-r})-e^{-r}(2-\omega_\infty). \tag{16}$$

The assumption of Tung and Buckser,[5] that all chain ends crystallize completely, is represented by

$$\omega_x=\omega_\infty+(1-\omega_\infty)(2/r). \tag{17}$$

Hence, our relationship yields the same result for large r (high molecular weight). The ω_x values for lower r values calculated according to Eq. (16) will be smaller than these using the expression of Tung and Buckser. Figure 5 illustrates the experimental data of Chiang and Flory for two polyethylene fractions, having molecular weights 490 000 and 32 000. The full curves were calculated according to Eq. (16), with the same values used before, $N=25$ and $s=20$. For the lower molecular-weight fraction, the predicted degree of crystallinity is somewhat too large at the lowest temperatures studied. One is tempted to rationalize this discrepancy as being created because of incomplete crystallization of the dangling chain ends. On the other hand, Eq. (16) predicts that ω_x should pass through a maximum and decrease again, as the molecular weight is lowered still further. This predicted decrease arises from the increasing frequency of chains which bear no nucleated units for lower molecular weights. No such decrease was observed by Tung and Buckser, who examined molecular weights ranging down to 700. This may indicate that the density of nuclei (and hence ρ) is dependent upon molecular weight. Since the treatment leading to Eq. (16) assumed ρ to be independent of molecular weight, the agreement with experimental data shown in Fig. 5 is rather surprising.

ACKNOWLEDGMENTS

This work was partially supported by the Allegany Ballistics Laboratory, an establishment owned by the United States Navy and operated by Hercules Powder Company. W.R.K. gratefully acknowledges a Research Fellowship from the Alfred P. Sloan Foundation.

THE JOURNAL OF CHEMICAL PHYSICS VOLUME 35, NUMBER 4 OCTOBER, 1961

Theoretical Interpretation of Carbon-13 Hyperfine Interactions in Electron Spin Resonance Spectra*

MARTIN KARPLUS†

Department of Chemistry and Watson Scientific Computing Laboratory, Columbia University, New York 27, New York

AND

GEORGE K. FRAENKEL

Department of Chemistry, Columbia University, New York 27, New York

(Received March 16, 1961)

A quantitative theory of the isotropic electron-nuclear spin interactions of carbon 13 in pi-electron radicals is presented and applied to the hyperfine splittings observed in the electron spin resonance spectra of these substances. The splittings arise from sigma-pi interactions which polarize both the 1*s* and 2*s* electrons. The 1*s*-orbital spin polarization is shown to contribute a term of negative sign with a magnitude comparable to that from the 2*s* electrons. For an sp^2 hybridized carbon atom that is bonded to three atoms, X_i $(i=1, 2, 3)$, the hyperfine constant a^C has the form

$$a^C=(S^C+\sum_{i=1}^{3}Q_{CX_i}{}^C)\rho^\pi+\sum_{i=1}^{3}Q_{X_iC}{}^C\rho_i{}^\pi,$$

where ρ^π and $\rho_i{}^\pi$ $(i=1, 2, 3)$ are the pi-electron spin densities on atoms C and X_i, respectively. The contribution of the 1*s* electrons is determined by S^C and that of the 2*s* electrons by the Q's, where $Q_{BC}{}^A$ is the sigma-pi parameter for the nucleus of atom A resulting from the interaction between the bond BC and the pi-electron spin density on atom B. Calculations for a planar CHC_2 fragment model yield $S^C=-12.7$ gauss, $Q_{CH}{}^C=19.5$ gauss, $Q_{CC'}{}^C=14.4$ gauss, and $Q_{C'C}{}^C=-13.9$ gauss.

The theory predicts both the magnitude and sign of the hyperfine splittings and is readily applied to a variety of compounds. Excellent agreement is obtained with the available experimental data. For the methyl radical, the measured C^{13} splitting is shown to be consistent with a planar model and limits the deviation from planarity to $\lesssim 5°$. The theory provides a useful criterion for the validity of approximate wave functions that is illustrated by a comparison of various theoretical treatments for the naphthalene negative ion and triphenylmethyl. The sigma-pi interaction parameters are shown to depend on the bond length, the type of hybridization (including the angles between sigma bonds), and on the nature of the bonding atoms. For pi-electron systems, the results demonstrate that the magnitude of the sigma-pi exchange energy is a small fraction of the total energy. It is also noted that the proton parameter $Q_{CH}{}^H$ is somewhat larger in CHC_2 than in CH_3, which suggests a theoretical justification for some of the variation in the experimental "$Q_{CH}{}^H$" required to fit measured proton splittings. The form of the theory is readily extended to the treatment of hyperfine splittings from nuclei other than C^{13}.

I. INTRODUCTION

THE solution Zeeman spectra obtained by ESR techniques for a variety of neutral and ion radicals are a source of detailed information about their electronic structure. Although much of the past work has been concerned with the proton hyperfine splittings observed in these spectra, more recent investigations have also been devoted to an examination of the hyperfine interactions of the nuclei of many-electron atoms (e.g., C^{13} and N^{14}). The effects of the nuclei and electrons of such atoms are the primary concern of this paper.

In most of the radicals studied, the unpaired electron is localized in a pi system (to zero order) and the observed hyperfine splitting arises from sigma-pi interaction terms in the molecular Hamiltonian. For proton coupling, it has been shown by McConnell[1] and others[2,3] that these interactions can be treated by perturbation theory. There results an approximate, but simple and useful, relationship between the measured proton splitting and the unpaired electron spin density in the pi orbital of the carbon atom to which the proton is attached.

The availability of carbon-13 hyperfine splitting data for simple systems such as the methyl radical, as well as for a number of aromatic molecules, offers an approach to the understanding of the electron distributions that can supplement the proton work. McLachlan, Dearman, and Lefebvre[2] have pointed out in their discussion of sigma-pi exchange terms for the proton hyperfine interaction that an analogous formulation should be valid for carbon. They presented a simplified model which is not adequate for a detailed treatment of the hyperfine spectra.[4] Tuttle,[5] and Reitz, Dravnieks, and Wertz[6] noted some empirical correlations between the experimental spectra and the pi-electron spin distribution, but did not provide a theoretical analysis of the terms involved.

In this paper we attempt a detailed interpretation of

* This research was supported in part by the U. S. Air Force through the Office of Scientific Research. Acknowledgment is also made to the donors of The Petroleum Research Fund, administered by the American Chemical Society, for partial support of this research.

† Alfred P. Sloan Foundation Fellow.

[1] H. M. McConnell, J. Chem. Phys. **24,** 633, 764 (1956); H. M. McConnell and H. H. Dearman, *ibid.* **28,** 51 (1958); H. M. McConnell and D. B. Chesnut, *ibid.* **28,** 107 (1958), and other papers cited therein.

[2] A. D. McLachlan, H. H. Dearman, and R. Lefebvre, J. Chem. Phys. **33,** 65 (1960).

[3] S. Aono, Progr. Theoret. Phys. (Kyoto) **21,** 779 (1959).

[4] Reference 2 contains an unfortunate numerical error. If one uses the assumptions of McLachlan, *et al.*,[2] the quantity called Q_2 defined by them is actually found to be equal to -67.9 instead of -6.9 as quoted; this considerably alters their predictions.

[5] T. R. Tuttle, Jr., J. Chem. Phys. **32,** 1579 (1960).

[6] D. C. Reitz, F. Dravnieks, and J. E. Wertz, J. Chem. Phys. **33,** 1880 (1960).

the carbon-13 hyperfine splittings. Because the electronic environment of a carbon nucleus is considerably more complicated that that of a proton, a variety of interactions have to be included. As is well known, the 2*s* electrons make an important contribution to the hyperfine constant. We find that another significant contribution arises from the sigma-pi exchange terms with the 1*s* electrons. In addition, the neighboring atoms on which unpaired spin density is present have to be considered. In Sec. II, an estimate of the sigma-pi interactions is made by the use of model systems for which the required atomic and molecular integrals can be evaluated. The resulting expressions for the hyperfine interaction are applied to the radical species for which experimental data are available: the methyl and malonic acid radicals are discussed in Sec. III, and a number of aromatic molecules are treated in Sec. IV. The conclusions are presented in Sec. V.

II. THEORETICAL ANALYSIS

To estimate the various contributions to the carbon-13 isotropic hyperfine interaction, we consider a carbon atom with sp^2 hybridization and perform calculations on appropriate model compounds. A variation-perturbation approach is employed in which the zero-order function has a single unpaired electron in a pi orbital and all other electrons paired in sigma atomic orbitals or bonds. Since the isotropic electron-nuclear spin interaction term in the hyperfine Hamiltonian has the form, at high magnetic fields,[7]

$$\mathcal{H}_{hf}=\xi\sum_k\delta(\mathbf{r}_{kN})\,S_{kz}I_{Nz}, \tag{2.1}$$

where

$$\xi=8\pi\beta_e\beta_N g_e g_N/3$$

(in standard notation), a nonzero interaction constant requires net unpaired spin density at the nucleus. As has been shown for protons,[1–3] this arises from mixing of the sigma and pi electrons through the exchange terms in the molecular Hamiltonian. For carbon, both 1*s*- and 2*s*-orbital mixing has to be included to obtain a realistic estimate of the hyperfine interaction. Since the sigma-pi exchange terms are small, separate perturbation treatments can be performed for the 1*s* orbital and for the 2*s* orbital.

Carbon Atom 2*s* Contribution

The 2*s* contribution to the carbon-13 hyperfine splitting is estimated by a valence bond approach similar to that used previously for proton interactions.[1,8] We write the ground-state function Ψ in the form

$$\Psi=\sum_i\mu_i\phi_i, \tag{2.2}$$

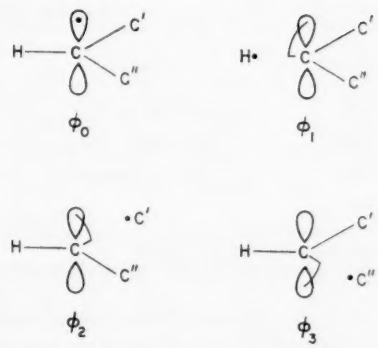

FIG. 1. Valence-bond structures for the CHC_2 fragment. The dot (·) represents the unpaired electron and the lines correspond to bonds. The diagram ϕ_0 is the doublet structure with perfect pairing of the sigma bonds and the ϕ_i ($i=1, 2, 3$) are the excited doublets with one broken sigma bond.

where the ϕ_i are valence-bond structures with coefficients μ_i that are determined by solution of the appropriate secular equation. The function ϕ_0 is the zero-order doublet structure with perfect pairing of the sigma electrons, while the $\phi_i (i>0)$ are excited doublet structures with one of the sigma bonds involving a 2*s* hybrid orbital broken and replaced by a bond between the 2*s* hybrid and the pi orbital.

The hyperfine interaction constant a^N (in gauss) resulting from the wave function Ψ is given by

$$a^N=\frac{\langle\Psi|\mathcal{H}_{hf}|\Psi\rangle}{g_e\beta_e\langle S_z\rangle\langle I_z\rangle}=\frac{\xi}{g_e\beta_e\langle S_z\rangle}\sum_{i,j}\mu_i^*\mu_j \times\langle\phi_i|\sum_k\delta(\mathbf{r}_{kN})\,S_{kz}|\phi_j\rangle, \tag{2.3}$$

where $\langle S_z\rangle$ is the expectation value of the total spin of the radical ($\langle S_z\rangle=\pm\frac{1}{2}$). Expansion of the valence-bond structures ϕ_i in terms of hybridized atomic orbitals v_t yields

$$a^N=(\xi/g_e\beta_e)\sum_t\Gamma(t)\,|v_t(\mathbf{r}_N)|^2=(\xi/g_e\beta_e)\rho(\mathbf{r}_N), \tag{2.4}$$

where $\rho(\mathbf{r}_N)$ is the net unpaired spin density at the point $\mathbf{r}_N$. The quantity $\Gamma(t)$, the atomic-orbital spin polarization, is defined by the equation

$$\Gamma(t)=\sum_{i,j}\mu_i^*\mu_j\gamma_{ijt}S_{ij}, \tag{2.5}$$

where S_{ij} is the overlap integral between structures ϕ_i and ϕ_j, and the coefficient γ_{ijt} is zero for v_t not in the island containing the phantom orbital of the appropriate Pauling superposition diagram and is $+1(-1)$ if v_t is an odd (even) number of bonds from the phantom.[9a,b] No cross terms $v_s^*(\mathbf{r}_N)v_t(\mathbf{r}_N)$ appear in Eq. (2.4) because we neglect such overlap contributions for con-

[7] A. Abragam and M. H. L. Pryce, Proc. Roy. Soc. (London) **A205**, 135 (1951).
[8] M. Karplus, J. Chem. Phys. **30**, 15 (1959).
[9] (a) J. Schug, T. H. Brown, and M. Karplus, J. Chem. Phys. (to be published). (b) P. Brovetto and S. Ferroni, Nuovo cimento **5**, 142 (1957).

TABLE I. Atomic-orbital spin polarizations $\Gamma(t)$.[a]

Radical	$\Gamma(\sigma_{CH})$	$\Gamma(s_H)$	$\Gamma(\sigma_{CC'})$	$\Gamma(\sigma_{C'C})$
CH_2	$(2/9)[3\eta_0\eta_1+\eta_1^2]$	$-(2/9)[3\eta_0\eta_1-\eta_1^2]$[b]	...	...
CHC_2	$(2/3)[\sqrt{3}\eta_0\eta_1+\eta_1^2]$	$-(2/3)[\sqrt{3}\eta_0\eta_1-\eta_1^2]$	$(1/3)[(6)^{\frac{1}{2}}\eta_0\eta_2+\eta_2^2]$	$-(1/3)[(6)^{\frac{1}{2}}\eta_0\eta_2-\eta_2^2]$
CH	$(2/3)[\sqrt{3}\eta_0\eta_1+\eta_1^2]$	$-(2/3)[\sqrt{3}\eta_0\eta_1-\eta_1^2]$	...	...
C_2	...	...	$(2/3)[\sqrt{3}\eta_0\eta_1+\eta_1^2]$	$-(2/3)[\sqrt{3}\eta_0\eta_1-\eta_1^2]$

[a] $\Gamma(\pi)=(1/3)(4\eta_0^2-1)$ for all radicals listed.
[b] These results include some small second-order terms omitted in the equivalent (but somewhat differently formulated) work cited in reference 8.

sistency with the approximations involved in the conventional valence-bond calculation of the function Ψ.

As model systems we consider in detail the methyl radical and the CHC_2 radical fragment. The CHC_2 fragment is introduced for the calculation of carbon-13 interactions in aromatic radicals because it plays a role analogous to that of the CH fragment for proton splittings. We assume here that both CH_3 and CHC_2 are planar and can be treated as seven-electron systems with neglect of the 1s electrons. Formally, CHC_2 is derived from CH_3 by replacing two of the hydrogen 1s orbitals by carbon sigma orbitals with sp^2 hybridization, all other electrons and orbitals on the noncentral carbon atoms being neglected. Defining our notation with respect to CHC_2, we have the structures shown in Fig. 1, with ϕ_0 the usual perfect pairing structure. The hydrogen 1s orbital is designated by s_H, the pi orbital on carbon C by π, and the sp^2 sigma orbitals bonded to H, C′, and C″, by σ_{CH}, $\sigma_{CC'}$, and $\sigma_{CC''}$, respectively. The sp^2 sigma orbitals of carbons C′ and C″ bonding them to C are designated $\sigma_{C'C}$ and $\sigma_{C''C}$, respectively. In CH_3, the corresponding orbitals are used, except for $\sigma_{C'C}$ and $\sigma_{C''C}$, which are replaced by $s_{H'}$ and $s_{H''}$. For consistency, we use the symbols $\sigma_{CH'}$ and $\sigma_{CH''}$ in place of $\sigma_{CC'}$ and $\sigma_{CC''}$, respectively.

Noting the assumed C_{2v} symmetry of CHC_2, we can replace the ϕ_i by orthogonalized symmetry orbitals ψ_i. For the ground states, we require the linear combinations

$$\psi_0=\phi_0$$
$$\psi_1=3^{-\frac{1}{2}}(\phi_0-2\phi_1)$$
$$\psi_2=(\tfrac{2}{3})^{\frac{1}{2}}(\phi_0-\phi_2-\phi_3), \qquad (2.6)$$

with Eq. (2.2) replaced by

$$\Psi=\sum_j \eta_j\psi_j \qquad (2.7)$$

and a corresponding substitution in Eq. (2.5) for $\Gamma(t)$. In the methyl radical, the C_{3h} symmetry and resulting relationship between the functions ϕ_1, ϕ_2, and ϕ_3, leads to the orthogonal set

$$\psi_0=\phi_0$$
$$\psi_1=\phi_0-(\tfrac{2}{3})(\phi_1+\phi_2+\phi_3). \qquad (2.8)$$

With these functions [Eqs. (2.6) and (2.8)] and the modified version of Eq. (2.5), the atomic-orbital spin polarizations $\Gamma(t)$ for CH_3 and CHC_2 take the form given in Table I. This table also includes the formulas for the CH and C_2 fragments.[10]

To obtain numerical values for the $\Gamma(t)$ and a^N [Eq. (2.4)], the secular equation appropriate for each radical must be solved. This requires a knowledge of the atomic and molecular exchange integrals of which the Hamiltonian matrix elements are constituted.[11] For CH_3, the integrals (π, σ_{CH}), (π, s_H), (σ_{CH}, s_H), $(\sigma_{CH}, \sigma_{CH'})$, $(\sigma_{CH}, s_{H'})$, and $(s_H, s_{H'})$ are needed, where (A, B) represents the exchange integral

$$(A,B)=\int A(1)B(2)\mathfrak{IC}B(1)A(2)d\tau_1 d\tau_2, \qquad (2.9)$$

with $\mathfrak{IC}$ the effective two-electron Hamiltonian for the orbitals A and B. Table II lists empirical estimates which, except for (π, s_H), have been used for these integrals in previous work on hydrocarbons.[12] In a study of the methyl radical,[8] it was found that the proton hyperfine splitting a^H is particularly sensitive to the molecular integral (π, s_H), for which a number of values have been suggested.[12,13] Rather than arbitrarily selecting one of these, we evaluate (π, s_H) from the measured value of a^H in CH_3.[14,15] With the assumption that CH_3 is planar and $a^H=-23.0$ gauss, we find that $(\pi, s_H)=0.792$ ev, a value 6% larger than the figure of 0.745 calculated by Altmann.[13] From Table I and Eq. (2.4), it is evident that this choice of (π, s_H) is equivalent to using the experimental value of a^H to determine the ratio (η_1/η_0) for CH_3. For the CHC_2 fragment, a number of additional integrals are required [i.e., $(\pi, \sigma_{C'C})$, $(\sigma_{CC'}, \sigma_{C'C})$, $(\sigma_{CC'}, \sigma_{C''C})$]. The integral $(\sigma_{CC'}, \sigma_{C'C})$ was set equal to 85% of the estimated carbon-carbon bond energy for an sp^2-sp^2 bond of length 1.40

[10] For CH, the functions are of the form $\psi_0=\phi_0$ and $\psi_1=3^{-\frac{1}{2}}(\phi_0-2\phi_1)$. For C_2 they are of the form $\psi_0=\phi_0$ and $\psi_1=3^{-\frac{1}{2}}(\phi_0-2\phi_2)$.
[11] Coulomb integral terms can be ignored because they contribute equally to all the normalized valence-bond functions.
[12] J. H. Van Vleck, J. Chem. Phys. **1**, 219 (1933), as modified by recent data as discussed in reference 8.
[13] S. L. Altman, Proc. Roy. Soc. (London) **A210**, 327, 343 (1951).
[14] R. W. Fessenden (private communication).
[15] C. K. Jen, S. N. Foner, E. L. Cochran, and V. A. Bowers, Phys. Rev. **112**, 1169 (1958).

A.[16] For $(\pi, \sigma_{C'C})$, the calculated result of 0.877 ev was multiplied by the factor 1.063, the ratio of the corresponding empirically adjusted (π, s_H) integral to its computed value. Since no simple procedure for empirical evaluation of $(\sigma_{CC'}, \sigma_{C''C})$ could be found, its calculated value was used directly; however, this is not very important, as $(\sigma_{CC'}, \sigma_{C''C})$ is small and has little effect on the hyperfine splitting estimates. Values for these additional integrals are also listed in Table II.

Substitution of the integrals into the matrix elements and solution of the secular equations lead to the η_j coefficients for each of the radical fragments. The $\Gamma(t)$ were calculated from the numerical values of the η_j by the formulas for $\Gamma(t)$ given in Table I. The results for the $\Gamma(t)$ are listed in Table III. To utilize the $\Gamma(t)$ for estimating hyperfine splittings by means of Eq. (2.4), a knowledge of the $|\psi_t(\mathbf{r}_N)|^2$ is required. An atomic hydrogen 1*s* function was used for hydrogen and the Hartree-Fock orbitals calculated by Jucys[17] were employed for carbon. These yield 507.6 gauss for the proton hyperfine splitting from a single 1*s* electron and 1191 gauss for the carbon-13 splitting from an unpaired 2*s* electron. Consistent with the neglect of overlap, no orbital contraction nor neighboring atom contribution to the spin density at a nucleus is included.[18] From the $\Gamma(t)$ for the different model systems (Table III), there result the various hyperfine contributions listed in Table IV. Since each of the radicals has a single unpaired pi electron on a carbon atom (the central one in CHC_2), the results correspond directly to the Q symbol introduced by McConnell[1] and are tabulated as such. We use the notation Q_{BC}^{A}, where the superscript (A) indicates the nucleus being considered and the subscript (BC) the bond involved, with the first letter (B) designating the atom on which the pi electron is located; e.g., $Q_{C'C}^{C}$ represents the hyperfine splitting from the nucleus of carbon atom C due to the interaction through the bond CC′ with a pi-electron spin on carbon C′.

TABLE II. Atomic and molecular exchange integrals for hybridized oribitals (A, B).

(π, σ_{CH})	=	1.26 ev
(π, s_H)	=	0.792
(σ_{CH}, s_H)	=	−3.916
$(\sigma_{CH}, \sigma_{CH'})$	=	0.921
$(\sigma_{CH}, s_{H'})$	=	0.108
$(s_H, s_{H'})$	=	−0.813
$(\pi, \sigma_{CC'})$	=	1.26
$(\pi, \sigma_{C'C})$	=	0.932
$(\sigma_{CC'}, \sigma_{C'C})$	=	−3.481
$(\sigma_{CC'}, \sigma_{C''C})$	=	0.573

TABLE III. Atomic-orbital spin polarizations $\Gamma(t)$. Numerical values.

Radical	$\Gamma(\pi)$	$\Gamma(\sigma_{CH})$	$\Gamma(s_H)$	$\Gamma(\sigma_{CC'})$	$\Gamma(\sigma_{C'C})$
CH_3	0.99351	0.04747	−0.04531[a]	...	...
CHC_2	0.99513	0.04904	−0.04674	0.03638	−0.03510
CH	0.99776	0.04832	−0.04609[a]	...	...
C_2	0.99872	...	...	0.03639	−0.03512

[a] These results differ somewhat from those in the work cited in reference 8 because of small differences in the exchange integrals (see Table II) and, in the case of CH_3, because of the inclusion of certain second-order terms in the $\Gamma(t)$ (see Table I, reference b).

The approximate nature of the theory employed certainly does not warrant the inclusion of four significant figures for the values listed in Table IV. The precise results of the calculations have been given, however, to indicate the variation in the Q's from one fragment to another and to ensure consistency in the applications. Table IV shows that the various fragments have almost, but not exactly, identical values for the corresponding Q's. The similarity in the magnitudes obtained is reasonable because all of the sigma-pi interactions are sufficiently small so as to make first-order perturbation theory a good approximation. One interesting difference is that Q_{CH}^{H} is greater for CHC_2 than for CH_3. This suggests that the larger values of Q_{CH}^{H} required to fit the proton splittings in spectra of aromatic hydrocarbons[19] may arise through deviations from first-order perturbation theory. Another result that is probably significant is that $Q_{CC'}^{C} \neq -Q_{C'C}^{C}$, even though the absolute accuracy in the Q calculations

TABLE IV. Calculated hyperfine splittings (Q values).[a,b]

Radical	Q_{CH}^{H}	Q_{CH}^{C}	$Q_{CC'}^{C}$	$Q_{C'C}^{C}$
CH_3	[−23.00][c]	18.85	...	...
CHC_2	−23.72	19.47	14.44	−13.94
CH	−23.39	19.18	...	...
C_2	...	...	14.45	−13.94

[a] All values in gauss. The number of significant figures listed is not intended to indicate the accuracy of the results (see text).

[b] The contribution of 1*s* electrons is the same for all the radicals and is given by $S^{C} = -12.7$ gauss.

[c] Fitted value; see text.

[16] For the bond energy, the value for the central bond of butadiene ($E = 100$ kcal/mole) minus 3.25 kcal/mole "resonance energy" was used. Since the butadiene bond length is 1.48 A, a correction to 1.40 A with an estimated force constant of 5×10^5 d/cm was made.

[17] A. Jucys, Proc. Roy. Soc. (London) **A173,** 59 (1939); J. Phys. U.S.S.R. **11,** 49 (1947).

[18] Neighboring atom contributions are small in any case: for CH_3 inclusion of these terms would lead to a value of $a^{H} = -21.07$ gauss in contrast to the value of $a^{H} = -23.00$ gauss given here. Inclusion of neighboring atom contributions gives 56.25 gauss for the 2*s* contribution to the C^{13} splitting as compared to $3Q_{CH}^{C} = 56.54$ given here.

[19] A. D. McLachlan, Mol. Phys. **3,** 233 (1960).

is considerably less than the four figures listed arbitrarily in the table. In the applications given in the following sections, we use the Q's from the CHC_2 fragment model for all cases except the CH_3 radical itself.

Although C—H bonds are relatively constant in length, there is considerable variation in the C–C distance in different compounds. Since the molecular integrals involved in the sigma-pi interaction depend on the internuclear distance, some changes in the hyperfine splitting constants are to be expected. For the range in which first-order perturbation theory is valid, we can write

$$Q_{CC'}{}^{C} \propto [(\pi, \sigma_{CC'}) - (\pi, \sigma_{C'C})]/(\sigma_{CC'}, \sigma_{C'C}). \quad (2.10)$$

Here $(\pi, \sigma_{CC'})$ is an atomic integral, which is independent of internuclear distance, while the molecular integrals $(\pi, \sigma_{C'C})$ and $(\sigma_{CC'}, \sigma_{C'C})$ both decrease with increasing bond length. Since $(\pi, \sigma_{CC'}) > (\pi, \sigma_{C'C})$ we see that $Q_{CC'}{}^{C}$ would be expected to be *larger* for *longer* bonds. The exact magnitude of this effect depends critically on the bond-length dependence of the integral $(\pi, \sigma_{C'C})$, which we shall not attempt to present here. However, the alteration in Q that would result may have to be included in more refined treatments of the sigma-pi interaction, particularly if an attempt is made to include the effect of zero-point vibrations.

Another factor that has to be considered in treating general systems is the dependence of the Q values on the hybridization of the sigma orbitals. The Q's may be altered through changes in both $\Gamma(t)$ and $|v_t(\mathbf{r}_N)|^2$ as a function of hybridization. For an sp-hybrid bond, such as exists in acetylene, we have $Q_{CH}{}^{C} = 38.1$ gauss instead of the value of 19.2 gauss found for sp^2 hybridization. The effect is greater for $Q_{CH}{}^{C}$ than for $Q_{CH}{}^{H}$ [$Q_{CH}{}^{H} = -23.4$ gauss for sp^2 and -34.7 gauss for sp hybridization][20] because the density at the carbon nucleus, as well as the interaction integrals, is altered by the change in hybridization. Corresponding changes would have to be introduced for a complete treatment of hydrocarbons with sigma orbitals that are not equivalent sp^2 hybrids (e.g., the cyclopentadienyl radical).

Carbon Atom 1s Contribution

The 1s contribution to the pi-electron hyperfine splitting of first-row atoms in neutral or ion radicals has been ignored in previous studies.[2] From recent work[21] on the ^4P state of the nitrogen atom, there is some indication of the possible significance of the 1s terms. Das and Mukherjee[21] found there that the 1s and 2s contributions are of comparable magnitude but opposite sign. However, it is essential to realize that the effect in an isolated atom is considerably different from that in an atom participating in one or more bonds (see below). To estimate the 1s contribution for the radicals of interest here, we apply perturbation theory to a carbon atom in the appropriate bonding (or valence) state. The lowest doublet state of the carbon atom in CH_3 or CHC_2 can be written as a single determinant of the form

$$\Psi_0 = (9!)^{-\frac{1}{2}} |1s(1)\alpha(1)1s(2)\beta(2)\sigma_1(3)\alpha(3)\sigma_1(4)\beta(4) \times\sigma_2(5)\alpha(5)\sigma_2(6)\beta(6)\sigma_3(7)\alpha(7)\sigma_3(8)\beta(8)\pi(9)\alpha(9)|, \quad (2.11)$$

where 1s and π are carbon 1s and pi orbitals, and the $\sigma_i (i = 1, 2, 3)$ are bonding molecular orbitals of the form

$$\sigma_i = N\{3^{-\frac{1}{2}}[(2s) + \sqrt{2}(2p\sigma_i)] + \cdots\}. \quad (2.12)$$

The $2p\sigma_i$ orbital is directed along the bond σ_i and the dots represent orbitals of the neighboring atom. The latter do not need to be considered explicitly because their differential overlap with the carbon 1s orbital is negligible. We assume that the contribution of the 1s electrons to the hyperfine interaction arises primarily from their excitation to the antibonding $\sigma_i{}^*$ orbitals. For the excited states, we have

$$\Psi_i = (9!)^{-\frac{1}{2}} |\sigma_i{}^*(1)\alpha(1)1s(2)\beta(2)\sigma_1(3)\alpha(3) \cdots\sigma_3(8)\beta(8)\pi(9)\alpha(9)| \quad (2.13)$$

$$i = 1, 2, 3,$$

where $\sigma_i{}^*$ is

$$\sigma_i{}^* = N\{3^{-\frac{1}{2}}[(2s) + \sqrt{2}(2p\sigma_i)] - \cdots\} \quad (2.14)$$

Although the Ψ_i employed here are not true doublets ($S = \frac{1}{2}$), their use corresponds to a relatively unimportant approximation in the conventional unrestricted Hartree-Fock treatment[22]; within the limits of first-order perturbation theory, the Ψ_i give exactly the same result as would a calculation with true doublet functions. Introducing the Ψ_i into the standard perturbation equation, we obtain

$$S^{C} = -\frac{2}{g_e\beta_e\langle S_z\rangle} \sum_{i=1}^{3} \frac{\langle\Psi_0|\mathcal{H}'|\Psi_i\rangle\langle\Psi_i|\xi\sum_k\delta(\mathbf{r}_{Ck})S_{kz}|\Psi_0\rangle}{\Delta E_{0,i}}, \quad (2.15)$$

where S^{C} is used to indicate the 1s contribution to the hyperfine splitting resulting from an unpaired electron in the carbon pi orbital. The operator $\mathcal{H}'$ is the sigma-pi perturbation Hamiltonian[2,20] and $\Delta E_{0,i}$ represents the excitation energy from Ψ_0 to Ψ_i. Explicit evaluation of the matrix elements in Eq. (2.15) yields the expression

$$S^{C} = \frac{\langle 1s(1)\pi(2)|1/r_{12}|\pi(1)2s(2)\rangle\langle 1s|(\xi/g_e\beta_e)\delta(\mathbf{r}_C)|2s\rangle}{\Delta E_{0,i}}$$

$$= \Gamma(1s)\langle 1s|(\xi/g_e\beta_e)\delta(\mathbf{r}_C)|2s\rangle. \quad (2.16)$$

The various factors in Eq. (2.16) must be evaluated by

[20] M. Karplus, J. Chem. Phys. **33**, 1842 (1960).
[21] T. P. Das and A. Mukherjee, J. Chem. Phys. **33**, 1808 (1960).
[22] G. W. Pratt, Phys. Rev. **102**, 1303 (1956); V. Heine, *ibid.* **107**, 1002 (1957); M. H. Cohen, D. A. Goodings, and V. Heine, Proc. Phys. Soc. (London) **73**, 811 (1959).

approximate methods to complete the calculation of S^C. The denominator was estimated to be 10 a.u. by using the x-ray term values of carbon given by Slater.[23] To obtain the exchange integral

$$\langle 1s(1)\pi(2)\,|1/r_{12}|\,\pi(1)2s(2)\rangle,$$

the Hartree-Fock functions of Jucys[17] were employed. These were used in place of a simpler Slater function approximation because the integral is rather sensitive to the detailed form of the radial wave functions, the node in the $2s$ function leading to both positive and negative contributions to the integral from different regions of space. Numerical integration gives -2.325×10^{-2} a.u. The density at the nucleus of the product of $1s$ and $2s$ Hartree-Fock functions is equal to 13.61 a.u., which yields $\langle 1s\,|(\xi/g_e\beta_e)\delta(\mathbf{r}_C)\,|2s\rangle=5460$ gauss. With $\Gamma(1s)=-2.325\times 10^{-3}$, we have

$$S^C=-12.7 \text{ gauss}.^{23a} \tag{2.17}$$

The accuracy of this perturbation calculation of S^C is difficult to assess by theoretical means. The magnitude of the result is, however, in accord with the experimental data (see Secs. III and IV), and is close to the value obtained by a semiempirical analysis of the hyperfine splitting constants (see Sec. IV). A more reliable estimate could be obtained by a detailed variational calculation on an appropriate system as, for example, the methyl radical.

In contrast to the Q values, S^C should be relatively independent of the bonds to the carbon atom (e.g., CH vs CC) since the integrals appearing in Eq. (2.16) and the excitation energy $\Delta E_{0,i}$ are insensitive to the type of neighboring atom. The major dependence on bond type that does exist arises from the form of the molecular-orbital functions σ_i and σ_i^*. If the CX_i bonds are partly ionic, the orbitals σ_i and σ_i^* of Eqs. (2.12) and (2.14), respectively, can be written in the form

$$\sigma_i=N'\{3^{-\frac{1}{2}}[(2s)+\sqrt{2}(2p\sigma_i)]+(1+\epsilon)\psi_{X_i}\} \tag{2.12a}$$

and

$$\sigma_i^*=N'\{(1+\epsilon)3^{-\frac{1}{2}}[(2s)+\sqrt{2}(2p\sigma_i)]-\psi_{X_i}\}, \tag{2.14a}$$

where ψ_{X_i} is the bonding orbital on X_i, ϵ is the ionic contribution, and $N'=[1+(1+\epsilon)^2]^{-\frac{1}{2}}$. For $|\epsilon|\ll 1$, we find on substituting in Eq. (2.15) and comparing with Eq. (2.16) that

$$S^C(\epsilon)=(1-\epsilon^2/2\cdots)\,S^C(\epsilon=0),$$

that is, S^C has a quadratic dependence on ionic character. Since ϵ is expected to be small for hydrocarbons, S^C should be nearly constant in these systems.

To demonstrate the difference in the hyperfine interaction between an isolated atom and the bonded system considered here, we again make use of the perturbation approach. For the carbon atom in its $1s^22s^22p^2(^3P)$ ground state, an excitation of the $1s$ to the $3s$ orbital is required to obtain a perturbation function which yields an unpaired spin density at the nucleus. From Eqs. (2.15) and (2.16) the resulting hyperfine splitting per unpaired p electron is less than in the bonded case because

$$\langle 1s(1)\pi(2)\,|1/r_{12}|\,\pi(1)3s(2)\rangle < \langle 1s(1)\pi(2)\,|1/r_{12}|\,\pi(1)2s(2)\rangle,$$

$$\langle 1s\,|\delta(\mathbf{r}_C)\,|3s\rangle\rangle<(\langle 1s\,|\delta(\mathbf{r}_C)\,|2s\rangle,$$

and $\Delta E_{1s,3s}\gtrsim\Delta E_{1s,2s}$. The $2s\rightarrow 2p$ promotion which occurs in the bonding process partially "empties" the $2s$ orbital so as to permit it to participate in the $1s$ exchange perturbation. This leads to a significant increase in the $1s$ hyperfine contribution for the bonded state. A corresponding augmentation in the $2s$ term takes place as well; it has been implicitly included in the valence-bond calculations of this section.

III. APPLICATION TO SIMPLE SYSTEMS

The results of the previous section can be applied directly to the methyl and malonic acid radicals. For each of these compounds experimental values of both the carbon 13 and proton hyperfine splittings are available.

Since there is a single unpaired pi electron in CH_3, we can write the simple expression

$$a^C=S^C+3Q_{CH}{}^C \tag{3.1}$$

for the C^{13} splitting. Assuming that the radical is planar (see below)[8,24,25] we make use of $Q_{CH}{}^C=18.85$ gauss from Table IV and the value $S^C=-12.7$ gauss from Eq. (2.17). Substituting these numbers into Eq. (3.1), we obtain $a^C=+43.8$ gauss. This result is in excellent agreement with the experimental measurement of $|a^C|=41\pm 3$ gauss made on frozen CH_3 by Cole, *et al.*[25] In that investigation, the observed carbon-13 splitting was used as evidence for the planarity of the methyl radical. However, the lack of a detailed theoretical treatment prevented any estimate of the maximum deviation from the planar configuration that would be consistent with the experimental result. Extension of the present calculation to the nonplanar case is straightforward. With the assumption of complete orbital following, the wave functions given previously[8] can be used and we find that the carbon-13 splitting takes the form

$$a^C\cong S^C\Gamma(\pi)+1191[(1-2\cot^2\theta)\,\Gamma(\sigma_{CH})+2\cot^2\theta\Gamma(\pi)],$$

[23] J. C. Slater, *Quantum Theory of Atomic Structure* (McGraw-Hill Book Company, Inc., New York, 1960), Vol. I, p. 206.

[23a] *Note added in proof*: An analogous calculation has recently been performed by H. Ben Jemia and R. Lefebvre [J. chim. phys. **58**, 306 (1961)] for the CH radical. They find a value of -4.12 gauss which corresponds to -12.36 gauss for the CH_3 radical.

[24] G. Herzberg and J. Shoosmith, Can. J. Phys. **34**, 523 (1956).

[25] T. Cole, H. O. Pritchard, N. R. Davidson, and H. M. McConnell, Mol. Phys. **1**, 406 (1958).

TABLE V. Experimental and calculated C^{13} splittings.

Radical	Position	Exptl proton splitting[a] a_i^H (gauss)	Spin density ρ_i^π	Calc C^{13} splitting[b] a_i^C (gauss)	Exptl C^{13} splitting[c] a_i^C (gauss)
Methyl		−23.0[d]	1.000	43.8	±(41±3)[e]
Malonic Acid	0	−21.2[f]	0.892[g]	31.8[h]	33.0[i]
$(HO\overset{2}{O}C)_2\overset{1}{C}\overset{0}{H}$	1	...	∼0.0[h]	−12.4[h]	j
	2	...	∼0.05[h]	...	...
Naphthalene⊖	α	−4.95[k]	0.2087[g]	7.38	±7.1[l]
	β	−1.865[k]	0.0786[g]	−1.20	±1.2[m]
	γ	...	−0.0746[n]	−7.06	...
Benzene⊖		−3.75[o]	0.1667[p]	1.30[q]	(±2.4)[q,r]
Cyclooctatetraene⊖		−3.209[s]	0.1250[p]	0.97[q]	±1.3[t]
p-Benzosemiquinone ion					
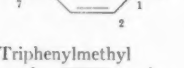	1	...	0.1072[v]	w	$\lvert a^C \rvert < 0.6$
	2	−2.368[u]	0.1071[v]	0.83[v]	±0.59[w,x]
	7	...	0.1786[v]	...	...
Triphenylmethyl	0	...	0.68[y,q]	26.2[q]	26[y,z]
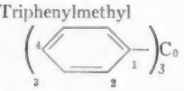	1	...	−0.1299[a']	...	...
	2	−2.53[b',z]	0.1067[g]	...	...
	3	+1.11[b',z]	−0.0468[g]	...	...
	4	−2.77[b',z]	0.1168[g]	...	...

[a] The sign given for the proton splitting is based on theoretical considerations except in the case of malonic acid where the sign has been experimentally determined.

[b] Computed from Eq. (4.2) with the ρ_i^π in column 4 and, except for the methyl radical, wth sigma-pi interaction parameters calculated for the CHC fragment. For the methyl radical, an explicit calculation of the parameters was made (see Sec. II).

[c] The sign of the experimental C^{13} splitting is unknown except in the cases where it is explicitly specified.

[d] From the work cited in reference 14 and 15.

[e] From the work cited in reference 25.

[f] From the work cited in references 26 and 27.

[g] Calculated from Eq. (4.4), and the data in the preceding column, with $Q_{CH}^H = -23.72$ gauss.

[h] See text, Sec. II.

[i] From the work cited in reference 27.

[j] See reference 29.

[k] S. I. Weissman (private communication).

[l] T. R. Tuttle, Jr., and S. I. Weissman, J. Chem. Phys. **25,** 189 (1956).

[m] From the work cited in reference 5.

[n] Obtained by taking $\Sigma\rho_i^\pi = 1$ and using the procedure of reference g.

[o] From the work cited in reference 31.

[p] From symmetry considerations.

[q] See text.

[r] Preliminary result obtained by F. Dravnieks, D. C. Reitz and J. E. Wertz (private communication).

[s] T. J. Katz and H. L. Strauss, J. Chem. Phys. **32,** 1873 (1960).

[t] From the work cited in references 37 and 38.

[u] B. Venkataraman, B. G. Segal, and G. K. Fraenkel, J. Chem. Phys. **30,** 1006 (1959).

[v] See work cited in reference 33 and comment in reference 34.

[w] From the work cited in reference 38.

[x] Reitz *et al.*[6] and A. van Roggen, J. Chem. Phys. **33,** 1589 (1960) have obtained a value of ∼0.6 gauss for a satellite splitting in the spectrum but were unable to determine whether it was attributable to the CH or CO carbon atom.

[y] See work cited in reference 30.

[z] These results are also in agreement with the work of P. B. Ayscough, A. P. McCoun, and R. Wilson, Proc. Chem. Soc. (London) **1961,** 16.

[a'] See reference n. The pi-density for the central carbon atom (0.68) was used as well as the pi densities at the other ring positions. The value of 0.68 was obtained by Adam and Weissman[30] from the linewidth of a dilute solid sample of the radical. Although they neglected the arisotropy arising from ρ_i^π, a rough calculation indicates the contribution from this source is of the order of only a gauss.

[b'] D. B. Chesnut and G. J. Sloan, J. Chem. Phys. **33,** 637 (1960). The assignment of the −2.53-gauss and 1.11 gauss splittings to the ortho and meta positions, respectively, and the assignment of signs of the a_i^H is based on theoretical considerations. See text and Table VII.

where θ is the angle between the direction of the π orbital and one of the CH bonds ($\theta = 90°$ for the planar case). The atomic-orbital spin polarizations do not vary significantly with angle for small deflections,[8] and an estimate of a^C can be made by using the $\Gamma(t)$ values in Table III. We find that $a^C \cong 61$ gauss for $\theta = 95°$ and $a^C \cong 114$ gauss for $\theta = 100°$. Since even the 95° result (5° bending) is 50% greater than the experimental result, the fact that the methyl radical is planar or nearly planar seems well substantiated. This conclusion is consistent with the previous work on the electronic absorption spectrum[24] and the proton hyperfine splittings.[8]

The malonic acid radical $[CH(COOH)_2]$ can be treated similarly. From the experimental value of the proton splitting ($a^H = -21.17$ gauss),[26,27] the unpaired pi-electron spin density on the central carbon atom is

[26] H. M. McConnell, C. Heller, T. Cole, and R. W. Fessenden, J. Am. Chem. Soc. **82,** 766 (1960).

[27] T. Cole and C. Heller, J. Chem. Phys. **34,** 1085 (1961).

estimated to be 0.89 by using the calculated $Q(Q_{CH}{}^{H} = -23.7$ gauss) for the CHC_2 fragment. Such a small amount of delocalization of the odd pi electron may result from nonplanarity in the structure of the radical, a nonplanarity that is suggested by the structure of the crystals of the parent compound, $CH_2(COOH)_2$, from which the radical is made by irradiation. The x-ray analysis shows that in the malonic acid crystals, both carboxyl groups are rotated out of the plane of the three carbons, one group being at 13° and the other at 90° to the CCC plane.[28] Neglecting the delocalized spin density, which would be expected to be primarily on the oxygen atoms, rather than on the noncentral carbon atoms, we have

$$a^{C}{}_{central} = 0.89(S^{C} + Q_{CH}{}^{C} + 2Q_{CC'}{}^{C}) = +31.8 \text{ gauss}, \tag{3.2}$$

where the values of $Q_{CC'}{}^{C}$ and $Q_{CH}{}^{C}$ for the CHC_2 fragment have been used. Comparison with the experimental value of +33.0 gauss,[27] of determined sign, shows excellent agreement. Assuming that there is zero unpaired spin on the noncentral carbon atoms and neglecting contributions from the oxygen atom, we can write a^{C} for the noncentral carbon atoms in the form

$$a^{C}{}_{noncentral} = (0.89)Q_{CC'}{}^{C'} = -12.4 \text{ gauss} \tag{3.3}$$

with $Q_{CC'}{}^{C'} = -13.9$ gauss, the value for the CHC_2 fragment. There is no polarization of a 1*s* orbital by the pi density on an adjacent carbon in the approximation used here. Also, rotation of the COOH group has no effect on the sigma-pi interaction involved in $Q_{CC'}{}^{C'}$ as long as the sp^2 hybridization remains unchanged. As yet there is no reliable experimental value for $a^{C}{}_{noncentral}$ that can be compared with the calculated result.[29] The spin polarization at the nuclei of the noncentral carbon atoms caused by pi-electron spin density on the oxygen atoms can be included by the methods of the following section; however, it undoubtedly represents a small contribution to the C^{13} splitting.

IV. APPLICATIONS TO AROMATIC SYSTEMS

Application of the calculations of Sec. II to aromatic radicals and other types of radicals with more than one pi electron requires an extension of the method. Since the molecules usually of interest contain localized sigma bonds, the radical-fragment results for the sigma-pi interaction parameters can be employed directly to evaluate the hyperfine splittings. Within the approximations of first-order perturbation theory, this is accomplished by considering separately the unpaired spin density in each pi orbital and adding its contribution to the sigma-electron spin polarization at the nucleus of interest.[1,2]

We consider a carbon atom C with sp^2 hybridization and pi-orbital spin polarization $\Gamma(\pi)$ [see Eq. (2.5)]. In accordance with conventional usage for pi-electron radicals, we shall use the term pi-orbital spin density and the symbol ρ^{π} in place of $\Gamma(\pi)$. The atom C is bonded to three other atoms, X_1, X_2, and X_3, with pi-electron spin density $\rho_i{}^{\pi}(i=1, 2, 3)$. The hyperfine contribution from the 2*s* orbital spin density at carbon atom C arising from spin polarization in the bond $C—X_i$ can then be written as

$$Q_{CX_i}{}^{C}\rho^{\pi} + Q_{X_iC}{}^{C}\rho_i{}^{\pi}. \tag{4.1}$$

Summing over all contributions, we find that the total splitting produced by the nucleus of carbon atom C has the form

$$a^{C} = (S^{C} + \sum_{i=1}^{3} Q_{CX_i}{}^{C})\rho^{\pi} + \sum_{i=1}^{3} Q_{X_iC}{}^{C}\rho_i{}^{\pi}. \tag{4.2}$$

The importance of including pi-electron densities on adjacent atoms, as in Eq. (4.2), was first pointed out by Weissman[30] some years ago, but a formulation of this suggestion was not given until the recent work of McLachlan, *et al.*[2] Equation (4.2) also contains the 1*s* contribution S^{C} since it was found to make a significant contribution in the calculation of Sec. II. In addition, Eq. (4.2) explicitly accounts for variations of the spin polarization in different bonds and for the possibility that the sigma-electron spin densities at opposite ends of a bond may not have the same magnitude, i.e., $|Q_{CX}{}^{C}| \neq |Q_{XC}{}^{C}|$. For carbon—carbon bonds, the results of Sec. II indicate that the difference $|Q_{CC'}{}^{C}| - |Q_{C'C}{}^{C}|$, which arises from second-order terms in the atomic-orbital spin polarizations $\Gamma(t)$, is only about 5% in typical cases. However, for a heteronuclear bond, such as a CO bond, a larger effect may be found. In particular, for this bond, the ratio of the Q's is, by first-order perturbation theory,

$$Q_{CO}{}^{C}/Q_{OC}{}^{C} = -[(\pi_C,\sigma_{CO}) - (\pi_C,\sigma_{OC})]/[(\pi_O,\sigma_{OC}) - (\pi_O,\sigma_{CO})]. \tag{4.3}$$

The notation for exchange integrals is based on the scheme used in Sec. II with the inclusion of the subscripts C and O to distinguish the carbon and oxygen pi orbitals. Since the atomic integrals (π_C,σ_{CO}) and (π_O,σ_{OC}) would not be expected to be equal, $Q_{CO}{}^{C}$ and $Q_{OC}{}^{C}$ may be different from each other.

From Eq. (4.2) it is evident that the theoretical evaluation of hyperfine splittings for carbon-13, as well as for the nuclei of other atoms in which the bonding is determined by *s* and *p* orbitals (e.g., N^{14}), requires a knowledge of the sigma-pi interaction parameters (the Q's and S) and the pi-electron spin densities $\rho_i{}^{\pi}$. For all the molecules to be treated here (except for

[28] J. A. Goedkoop and C. H. MacGillavry, Acta. Cryst. **10**, 125 (1957).

[29] Preliminary measurements of the C^{13} splitting in the C=O position by T. Cole (private communication) give a value in the range from 11 to 18 gauss.

[30] F. C. Adam and S. I. Weissman, J. Am. Chem. Soc. **80**, 2057 (1958).

TABLE VI. Naphthalene negative ion: theoretical spin densities and C^{13} splittings.

Method of obtaining spin density	Spin density			C^{13} splittings[a]			
	ρ_α^π	ρ_β^π	ρ_γ^π	a_α^C	a_β^C	a_γ^C	a_α^C/a_β^C
Valence bond[b]	0.187	0.072	−0.018	5.91	−1.04	−5.51	−5.68
Molecular orbital							
Hückel[c]	0.181	0.069	0.0	5.49	−1.03	−5.05	−5.36
Config. int.[d]	0.221	0.054	−0.050	7.82	−1.91	−7.00	−4.09
Approx. SCF (extended)[e]	0.211	0.055	−0.032	7.20	−1.75	−6.42	−4.11
Experimental (Q_{CH}^H = −23.72)	0.2087[f]	0.0786[f]	(−0.0746)[g]	±7.1[h]	±1.2[h]	(−7.06)[g]	±5.92[h]

[a] Computed using Eq. (4.2) with parameters for sigma-pi interaction calculated for CHC_2 fragment together with pi densities of columns 2–4.
[b] From work cited in reference 9a.
[c] From work cited in reference 39.
[d] From G. J. Hoijtink, Mol. Phys. **1,** 157 (1958).
[e] From work cited in reference 19.
[f] From experimental proton splittings; see Table V.
[g] Calculated from experimental proton splittings and $\Sigma\rho_i^\pi=1$.
[h] Experimental results cited in Table V.

the methyl radical discussed in the previous section), the CHC_2 fragment calculation of Sec. II is appropriate for determining the numerical values of S^C and the Q's. We have $S^C=-12.7$ gauss, $Q_{CH}{}^C=19.5$ gauss, $Q_{CC'}{}^C=14.4$ gauss, and $Q_{C'C}{}^C=-13.9$ gauss. With this set of theoretical parameters, together with the implicit assumption that their value is unaffected by variations in the sigma-bond framework and the pi-electron charge density, we require only the ρ_i^π values for each molecule in order to calculate the hyperfine splittings a^C from Eq. (4.2). If available, valence-bond or molecular-orbital wave functions can be used to determine the ρ_i^π. Alternatively, they can be estimated in some systems from the measured proton hyperfine splittings by use of the relationship[1]

$$\rho_i^\pi = a_i{}^H/Q_{CH}{}^H \tag{4.4}$$

with an appropriate choice of $Q_{CH}{}^H$. For most of the following we employ the ρ_i^π determined from the proton splittings since these are likely to provide the most significant test of Eq. (4.2) and its sigma-pi interaction parameters. In Eq. (4.4) we use $Q_{CH}{}^H=-23.72$ gauss, the value calculated in Sec. II for the CHC_2 fragment, although other estimates ranging from −22.5 gauss[31] to 24.2 gauss[32] have been suggested.

The results of the foregoing procedure, applied to the compounds for which C^{13} hyperfine splittings are available, are listed in Table V. For CH_3 and $CH(COOH)_2$, the spin density distribution has already been discussed in Sec. II. In the naphthalene negative ion, the proton splittings, together with the condition $\sum_{\text{all } i}\rho_i^\pi=1$, permit an evaluation of all the ρ_i^π. The symmetry of the benzene and cyclooctatetraene negative ions, as indicated by the proton splitting in the ESR spectra, requires that all ρ_i^π be equal when averaged over vibrations. With the condition $\sum_{\text{all } i}\rho_i^\pi=1$, this yields ρ_i^π values of $\frac{1}{6}$ and $\frac{1}{8}$ for the benzene and cyclooctatetraene negative ions, respectively. For the *p*-benzosemiquinone ion, the spin distribution is not completely determined by the proton splittings, and theoretical pi-electron densities must be used. A molecular-orbital calculation that has been adjusted to give fairly close agreement with the experimental proton splittings in a number of semiquinone ions[33,34] has been employed here to estimate the ρ_i^π. Finally, in triphenylmethyl a combination of the proton data for the rings and the anisotropic C^{13} splitting measured by Adam and Weissman[30] for the central carbon atom leads to the necessary ρ_i^π values.

Comparison of the results in Table V with the available experimental data shows excellent agreement, although the uncertainties in the theoretical treatment make it difficult to place any reliable *a priori* limits of error on the calculated values. It is of interest to note that the largest disagreements occur for the benzene and cyclooctatetraene negative ions. In both of these, considerable dynamical distortions (Jahn-Teller effect) of the symmetric state are expected.[35,36] Whether or not

[31] The value of $Q_{CH}{}^H=-22.5$ is based on the proton spectrum of the benzene negative ion as determined by T. R. Tuttle, Jr., and S. I. Weissman, J. Am. Chem. Soc. **80,** 5342 (1958).
[32] Based on a fit by McLachlan[19] to experimental hydrocarbon ion spectra of an approximate self-consistent field extended molecular-orbital theory.
[33] G. Vincow and G. K. Fraenkel, J. Chem. Phys. **34,** 1333 (1961), and G. Vincow, thesis, Columbia University, New York (1959).
[34] It is interesting to examine the change in pi-electron spin densities required to obtain an exact fit to the proton and C^{13} splittings. Taking $Q_{CH}{}^H=-23.72$ gauss (the molecular-orbital spin densities in Table V correspond to $Q_{CH}{}^H=-22.1$ gauss), one obtains $\rho_1^\pi=0.113$, $\rho_2^\pi=0.100$, and $\rho_7^\pi=0.187$. These values are well within the range of accuracy expected for the molecular-orbital calculations.
[35] H. M. McConnell and A. D. McLachlan, J. Chem. Phys. **34,** 1 (1961).
[36] L. C. Snyder, J. Chem. Phys. **33,** 619 (1960), and private communication.

TABLE VII. Triphenylmethyl: theoretical spin densities and C^{13} splittings.

Method of obtaining spin density	Angle of twist[b]	Spin density[a] ρ_0^π (central)	ρ_1^π	ρ_2^π (ortho)	ρ_3^π (meta)	ρ_4^π (para)	ρ_2^π/ρ_4^π	ρ_3^π/ρ_4^π	a_0^C (gauss)[c]
Valence bond[d]	0°	0.562	−0.228	0.200	−0.104	0.171	1.099	−0.571	26.7
	26.5°	0.646	−0.224	0.181	−0.096	0.171	1.058	−0.561	29.1
	45°	0.800	−0.191	0.135	−0.076	0.140	0.964	−0.543	32.5
Molecular orbital									
Hückel	0°	0.308	0.0	0.077	0.0	0.077	1.000	0.0	9.4
Approx. SCF (extended)[e]	0°	0.413	−0.045	0.114	−0.044	0.101	1.129	−0.435	14.5
	30°	0.516	−0.047	0.101	−0.041	0.087	1.161	−0.471	17.8
Experimental[f]		0.674[g]	−0.128[g]	0.107	−0.047	0.117	0.915	−0.402	[26.0]

[a] See Table V for labeling of positions.

[b] The angle of twist (ϕ) in the valence-bond calculation is such that $\cos^2\phi$ equals the ratio of the exchange integrals for rotated and parallel pi orbitals. For the molecular-orbital calculation, $\cos\phi$ is the ratio of the corresponding resonance integrals.

[c] Computed using Eq. (4.2) with parameters for sigma-pi interaction calculated for CHC_2 fragment together with pi densities from preceding columns of table.

[d] See work cited in reference 30 as well as T. H. Brown, D. H. Anderson, and H. S. Gutowsky, J. Chem. Phys. **33,** 720 (1960) and P. Brovetto and S. Ferroni, Nuovo cimento **5,** 142 (1957).

[e] See work cited in reference 19.

[f] The spin densities at the ortho, meta, and para positions are obtained from the experimental proton splittings by assuming $Q_{CH}{}^H = -23.72$ gauss, as in Table V. The spin densities at the 0 and 1 positions are obtained from the experimental isotropic C^{13} splitting by using Eq. (4.2), the ortho, the meta, and para spin densities, and the condition $\Sigma\rho_i{}^\pi = 1$.

[g] If the value of $\rho_0{}^\pi = 0.68$ determined by measurements of the anisotropic C^{13} splitting (see reference 30) is used, together with $a_0{}^C = 26.0$ gauss and Eq. (4.2), one obtains $\rho_1{}^\pi = -0.124$.

these distortions are sufficiently large to account for the discrepancies is difficult to estimate. Two contributing factors must be considered: the fluctuations in the pi-electron spin densities (as found by McConnell and McLachlan[35] for the benzene negative ion) and the variation of the Q's with vibration. Since an average must be taken over the product of the two factors, the result is a very sensitive function of the precise bond-length dependence of the Q's. The Jahn-Teller distortion in the cyclooctatetraene anion is expected to be smaller than in the benzene negative ion, but additional uncertainty exists in the interpretation of the carbon-13 splitting of the former because of ambiguities concerning its geometrical configuration.[37,38] In contrast to the carbon-13 interactions, the proton splitting should not be appreciably affected by the Jahn-Teller distortions. As $Q_{CH}{}^H$ is expected to be relatively independent of the carbon—carbon bond-length variation, $\langle a^H\rangle_{Av} = \langle Q_{CH}{}^H\rho^\pi\rangle_{Av} \cong Q_{CH}{}^H\langle\rho^\pi\rangle_{Av}$. Thus the agreement with the experimental value of a^H for the benzene negative ion is not surprising.

From the theory, not only the magnitude, but also the sign, of the hyperfine splittings are obtained. In the naphthalene negative ion, for example, the predictions are that the α position should be positive, but that both the β and γ positions should be negative. A very useful test of the theory would be provided by experimental determination of the signs of the splitting constants. This information can be obtained, in suitable cases, from the detailed analysis of ESR hyperfine spectra in solids or from the chemical shift in nuclear magnetic resonance spectra.

Evaluation of Molecular Wave Functions

Since we have seen that the formulas developed in this and the previous sections are adequate to account for the observed carbon-13 hyperfine splittings, it is of importance to examine the sensitivity of the results to the spin-density values. In particular, we compare some of the molecular-orbital and valence-bond calculations of spin densities to determine whether or not the carbon-13 splittings can be used as an effective criterion for the accuracy of molecular wave functions. The naphthalene negative ion and triphenylmethyl radical are discussed here because a variety of theoretical treatments are available for them. The results are presented in Tables VI and VII.

For the naphthalene negative ion (Table VI), none of the theoretical carbon splittings are in violent disagreement with observation. The valence-bond calculation with ionic structures[9a] and the single configuration Huckel calculation[39] give values very close to the measured carbon splitting ratio for the α and β position $[|a_\alpha{}^C/a_\beta{}^C| = 5.92]$, while the more refined molecular-orbital calculations[19] yield a value for the ratio $(a_\alpha{}^C/a_\beta{}^C)$ which is considerably farther from the experimental result. However, the actual magnitudes of the calculated splittings seem to be generally too small in the valence-bond and simple Huckel treatments, while they are somewhat too large in the two other molecular-orbital calculations. These differences are rather similar to those found in comparisons of the proton splittings[9]

[37] H. L. Strauss, T. J. Katz, and G. K. Fraenkel (to be published).

[38] H. L. Strauss and G. K. Fraenkel, J. Chem. Phys. (to be published).

[39] E. de Boer and S. I. Weissman, J. Am. Chem. Soc. **80,** 4549 (1958).

obtained from the various functions by use of Eq. (4.4) and confirm the need for better treatments of the spin distribution in the naphthalene negative ion. The numerical results in Table VI also indicate the importance of obtaining an experimental measurement of the carbon-13 splitting in the γ position.

For triphenylmethyl, Table VII shows that there is a rather wide range in the calculated results for the hyperfine splitting arising from the protons and the central carbon atom. Examination of the valence-bond calculations indicates that the ratios of the proton splittings are in rather good agreement with the measured ratios for all angles of twist listed, although a twist of greater than 45° appears to be required to reduce the calculated proton splittings sufficiently to coincide with experiment. The C^{13} splitting at the central carbon atom, however, shows best agreement for the planar configuration. This agreement for the C^{13} splitting arises partly from a cancellation of terms since the theoretical spin densities, particularly those at position 1 of the rings, differ considerably from the experimentally derived values. The molecular-orbital calculations in the SCF approximation give better results for the proton splittings but quite poor agreement with the C^{13} splitting at the central carbon atom. An improvement of the theories apparently requires corrections other than simple twisting of the benzene rings; again it would be very helpful to have available data for the C^{13} splittings in the ring positions.

Empirical Analysis of Hyperfine Constants

An empirical approach to the analysis of the hyperfine splittings may also be helpful, particularly for atoms other than carbon, because of the difficulty of obtaining relatively reliable atomic and molecular integrals for the evaluation of the sigma-pi interaction parameters. We indicate here only the possibilities of applying an empirical approach to CC and CH bonds. In order to reduce the number of parameters, we assume that $Q_{CC'}{}^{C}=-Q_{C'C}{}^{C}$. Using the $a_\alpha{}^{C}$ and $a_\beta{}^{C}$ values for the naphthalene negative ion with the spin densities determined from the proton splittings ($Q_{CH}{}^{H}=-23.72$) we obtain, from Eq. (4.2),

$$(S^{C}+Q_{CH}{}^{C}+2Q_{CC'}{}^{C})=34.3 \text{ gauss}. \qquad (4.5)$$

This should be compared with the value of 35.6 gauss determined by the calculations in Sec. II for the CHC_2 fragment. A variety of different semiempirical assumptions leads to rather similar results for the sum of the terms in Eq. (4.5), and the value of the sum is probably more certain than that of some of the individual parameters. The fit to the naphthalene negative ion data also gives $Q_{CC'}{}^{C}=-Q_{C'C}{}^{C}=13.6$ gauss, and $(S^{C}+Q_{CH}{}^{C})=7.2$ gauss. All these numerical values agree very closely with the calculated parameters and they can be used to treat satisfactorily carbon-13 splittings involving a carbon atom bonded as in CHC_2. For other types of bonding as, for example, at C_γ in naphthalene, a value of S^{C} is required. To estimate this number, we make use of the C^{13} splitting in the methyl radical together with the results derived from the naphthalene negative ion and obtain $S^{C}=-9.8$ gauss and $Q_{CH}{}^{C}=16.9$ gauss. The theoretical estimates of these parameters, $S^{C}=-12.7$ gauss and $Q_{CH}{}^{C}=19.5$ gauss, differ from the semiempirically determined quantities by a larger amount than is the case for any of the other parameters. The agreement is sufficiently good, however, to further buttress the reliability of the theoretical values and to demonstrate, as well, that an empirical approach can be fruitful.

Equation (4.2), which contains canceling terms of comparable magnitude but opposite sign, is extremely sensitive to the pi-electron spin densities and to the correctness of the sigma-pi interaction parameters. Because of these canceling terms, the careless application of Eq. (4.2) can lead to erroneous and misleading results. In any particular instance, due regard must be given to the numerical significance of the dominant terms, as can be seen from the following example. If we were to attempt to evaluate $Q_{CC'}{}^{C}$ (with the assumption that $Q_{CC'}{}^{C}=-Q_{C'C}{}^{C}$ and $Q_{CH}{}^{H}=-23.0$ gauss) by using the experimental C^{13} splittings for the central position of the malonic acid radical ($a_0{}^{C}=33.0$) and the α position of the naphthalene negative ion ($a_\alpha{}^{C}=7.1$), we would obtain an incorrect result. Employing the proton splittings (malonic acid, $a_0{}^{H}=-21.2$; naphthalene negative ion, $a_\alpha{}^{H}=-4.95$, $a_\beta{}^{H}=-1.865$) to calculate the pi densities, one obtains $Q_{CC'}{}^{C}=-Q_{C'C}{}^{C}=-55$ gauss instead of a number in the range of $Q_{CC'}{}^{C}=-Q_{C'C}{}^{C}\cong+14$ gauss. As indicated by inspection of the numerical significance of the terms, $a_\alpha{}^{C}$ in the naphthalene negative ion is not a suitable quantity for the evaluation of $Q_{CC'}{}^{C}$. On the other hand, if the experimental result for the β position ($a_\beta{}^{C}=-1.2$) is used in this calculation instead of $a_\alpha{}^{C}$, one obtains $Q_{CC'}{}^{C}=-Q_{C'C}{}^{C}=13.9$ gauss, in excellent agreement with our preceding estimates.

V. CONCLUSIONS

The major results of this paper are summarized by Eq. (4.2), which expresses the carbon-13 hyperfine splitting as a function of pi-orbital spin polarizations and sigma-pi interaction parameters (the Q's and S^{C}). The specific values found for the parameters by calculations on appropriate model systems demonstrate that (in contrast to the proton splittings) there is more than one term which makes a significant contribution. A very important factor is the hitherto neglected exchange polarization of the 1s electrons. It produces a large negative unpaired spin density at the nucleus that is proportional to the pi-orbital spin density on the atom containing the nucleus; that is, the 1s contribution can be written $S^{C}\rho^{\pi}$ where, from the atomic model, $S^{C}=-12.7$ gauss. Another term results from polarization by the pi-electron spin density of the three sigma

bonds of the sp^2-hybridized carbon atom. This contribution is positive and the theoretical estimate for a CH bond gives a splitting of $Q_{CH}{}^{C}\rho^{\pi}$ with $Q_{CH}{}^{C}=19.5$ gauss, while for a C—C′ sp^2 hybrid bond ($R=1.38$ A) the estimate of the splitting is $Q_{CC'}{}^{C}\rho^{\pi}$ with $Q_{CC'}{}^{C}=14.4$ gauss. Finally, there is the polarization of the bonds by pi-electron spin density on adjacent atoms. This is a negative contribution and the Q for a C—C′ bond ($R=$ 1.38 A) is nearly equal to $-Q_{CC'}{}^{C}$; more precisely, calculations for the splitting give $Q_{C'C}{}^{C}\rho_{C'}{}^{\pi}$ with $Q_{C'C}{}^{C}=-13.9$ gauss.

Equation (4.2) was tested by applying it to a series of radicals in which the spin distribution could be evaluated from structural considerations (e.g., a single pi electron, symmetry, or the known proton splittings). Comparison with the experimental measurements of carbon-13 splitting showed sufficient agreement to demonstrate the validity of the theory.

Since significant terms with positive and negative signs are present in Eq. (4.2), considerable cancellation can occur among the various contributions to the hyperfine splitting. The observed splitting for a nucleus in a complex molecule is, thus, very sensitive to the pi-electron spin distribution, and a comparison of experimental and calculated splittings can be used to measure the accuracy of the wave function. For systems such as the naphthalene negative ion and the triphenylmethyl radical that have been studied by molecular-orbital and valence-bond techniques, one finds considerable variation among the computed C^{13} splittings, as well as disagreement with the experimental measurements. There is an evident need for refinement in the theory of pi-electron distributions before the computed wave functions can be considered reliable.

Although the evaluation of the sigma-pi interaction parameters in terms of model systems involves a number of approximations, the method provides a useful guide to the significance of a variety of structural factors. The 1s interaction S^{C} is relatively insensitive to variations in the bonding because of the localization of the 1s orbitals. On the other hand, the 2s contributions (Q's) are affected strongly by the types of atoms comprising the bond (e.g., CH or CC′), by the hybridization of each of the orbitals involved, and by the bond length. These factors are particularly significant because the Q's depend, as shown in Eq. (4.3), on the difference between two integrals of nearly equal magnitude. As a result, in applying the theory to atoms that are differently situated from those discussed in this paper, consideration has to be given to changes in the electronic structure (an sp^2—sp^3 bond as in CH_2CH_2, variation in bond angles from 120° as in cyclopentadienyl radical, etc.).

An additional result of considerable interest is that the hyperfine interactions provide an excellent semiquantitative estimate of the validity of separating pi and sigma wave functions in the ground electronic states of pi-electron systems. The sigma-pi exchange energy for CH_3 is 0.060 ev while that for CHC_2 is 0.035 ev. Since the interaction parameters should be approximately valid for benzene itself, we estimate that in the ground state the sigma-pi exchange energy for all six pi-electrons is on the order of 0.2 ev. This quantity is only a small fraction of the total pi-electron energy, but may be significant in calculations of the excitation spectrum. Further studies from this viewpoint would be helpful in eludicating the electronic states of aromatic systems.

The method developed here for interpreting hyperfine splittings is applicable to all appropriately bonded elements in the first row of the Periodic Table; its formal extension to molecules containing more complex atoms is readily developed. Utilization of Eq. (4.2) for first-row atoms other than carbon requires either a determination of the appropriate exchange integrals or sufficient experimental data to permit empirical evaluation of the sigma-pi interaction parameters. Once the required parameters are available, the combination of the theoretical formulation with ESR measurements will provide a powerful tool for increasing our knowledge of the pi-electron spin distribution in a great variety of radical species.

Electrical Conductivity of Monocrystalline Cuprous Oxide

MICHAEL O'KEEFFE AND WALTER J. MOORE*

Chemical Laboratory, Indiana University, Bloomington, Indiana

(Received February 10, 1961)

The electrical conductivity σ of single crystals of cuprous oxide was measured from 25° to 1100°C and at oxygen pressures P_{O_2} from 10^{-5} to 760 mm. Except at very low P_{O_2} the σ at all T is due entirely to positive holes associated with native defects (cation vacancies). The different activation energies which occur in different temperature regions can be quantitatively interpreted on this basis. For example, in 1.4 mm O_2 and T above 750°C, $\sigma = 2.3 \times 10^3 \exp(-\epsilon_1/kT)$ with $\epsilon_1 = 0.625$ ev. This $\epsilon_1 = \epsilon_3 + (\Delta H/2)$, where ΔH is the heat of solution of an atom of oxygen and ϵ_3 is the activation energy for motion of positive holes in an electric field ($\epsilon_3 = 0.295$ ev and $\Delta H = 0.63$ ev). Polycrystalline cuprous oxide doped with beryllium displayed a conductivity consistent with an increase in vacancies and decrease in free positive holes due to incorporation of Be^{2+}.

CUPROUS oxide has become the prototype of oxides whose properties are governed by their departure from exact stoichiometry in the direction of excess oxygen. Recently Trivich[1] has reported a method for preparing thin sections of monocrystalline cuprous oxide. Ebisuzaki[2] in our laboratory has developed an alternative method for preparing single crystals of cuprous oxide by the oxidation of single crystals of copper. It has frequently been suggested, most recently by Apfel and Portis[3] on the basis of a comparison of dc and microwave conductivities, that the resistance of cuprous oxide at low temperatures is largely due to surface barriers of the type discussed by Slater[4] for lead sulfide. It is therefore desirable to base any fundamental analysis of the electrical properties of cuprous oxide on measurements made with single crystals of high purity.

Until recently the most reliable measurements of the temperature coefficient of conductivity of cuprous oxide were probably those of Anderson and Greenwood[5] and of Böttger,[6] who also give critical surveys of earlier work. Anderson and Greenwood established the existence of two conductivity regions, with high- and low-activation energies above and below 360°C, respectively. Böttger showed that at high temperatures the activation energy for conductivity is a function of oxygen pressure, being 0.62 ev for oxygen pressures greater than 2×10^{-3} mm, and increasing to about 0.95 ev at lower pressures. Böttger also showed that at high pressures the conductivity was proportional to $P_{O_2}^{1/7}$ as found earlier by Gunderman, Hauffe, and Wagner.[7]

All this work was done with various polycrystalline preparations of cuprous oxide. However, recently, Toth, Kilkson, and Trivich[1] described the preparation of single-crystal cuprous oxide and gave the results of measurements of high-temperature electrical conductivity. As this work overlaps ours, discussion will be deferred until after the results have been presented.

Measurements of thermoelectric power (Seebeck effect) have always shown cuprous oxide to be a hole conductor up to 1000°C. Anderson and Greenwood give accurate results and discuss earlier measurements.

Numerous measurements at room temperature have established the mobility of holes at about 50 $cm^2\ v^{-1}\ sec^{-1}$, though the mobility appears to depend on the prehistory of the sample. Typical results are given by Bloem[8] and by Nieke.[9] Schottky and Waibel[10] made measurements up to 750°C and found a reversal in the sign of the Hall coefficient around 500°C, implying electron conduction at higher temperatures.

From optical absorption studies Weichman[11] finds the band gap to vary linearly with the temperature from 2.0 ev at 0° to 1.45 ev at 900°C.

The amount of oxygen in excess of the stoichiometric ratio has been measured as a function of temperature and oxygen pressure by Wagner and Hammen[12] who find that the amount of oxygen in excess varies as $P_{O_2}^{1/5}$; from their results a heat of solution 0.63 ev per atom of oxygen may be calculated.[13] The melting point and the extent of the cuprous oxide field as a function of oxygen pressure have been measured by Smyth and Roberts.[14] Recent work on the heat of formation of copper oxides is due to Chiche.[15]

EXPERIMENTAL PROCEDURES

The crystals used in the experiments with pure cuprous oxide were all sections of the same crystal

* Work sponsored by the U. S. Atomic Energy Commission.

[1] R. S. Toth, R. Kilkson, and D. Trivich, J. Appl. Phys. **31,** 1117 (1960), Phys. Rev. **122,** 482 (1961).

[2] Y. Ebisuzaki, J. Appl. Phys. **32,** 2027 (1961).

[3] J. H. Apfel and A. M. Portis, J. Phys. Chem. Solids **15,** 33 (1960).

[4] J. C. Slater, Phys. Rev. **103,** 1631 (1956).

[5] J. S. Anderson and N. H. Greenwood, Proc. Roy. Soc. (London) **A215,** 353 (1952).

[6] O. Böttger, Ann. Physik **10,** 232 (1952).

[7] J. Gunderman, K. Hauffe, and C. Wagner, Z physik Chem. **B37,** 148 (1937).

[8] J. Bloem, Philips Research Repts. **13,** 167 (1958).

[9] H. Nieke, Ann. Physik **12,** 297 (1953).

[10] W. Schottky and F. Waibel, Physik Z. **36,** 912 (1935).

[11] F. L. Weichman, Phys. Rev. **177,** 998 (1960).

[12] C. Wagner and E. Hammen, Z. physik. Chem. **B40,** 197 (1938).

[13] W. J. Moore, J. Electrochem. Soc. **100,** 302 (1953).

[14] F. H. Smyth and H. S. Roberts, J. Am. Chem. Soc. **43,** 1061 (1921).

[15] P. Chiche, Ann. de Chim. **7,** 362 (1952).

(No. 6 prepared by Ebisuzaki by oxidation of a 99.999% Cu single crystal). The samples were mounted between cuprous oxide probes made by oxidation of thin copper wire welded to platinum wire. Each sample was about 7×3×0.5 mm.[3] The conductivity was measured by the four-probe method, the probes being about 1 mm apart. Potentials were measured with a Cary vibrating reed electrometer. The sample was supported solely by the probes and was surrounded by a mullite tube. Temperatures up to 1100°C and a pressure range of 10^{-5} to 760 mm of oxygen were attainable.

Cuprous oxide doped with beryllium was made by oxidizing 2 mm thick Johnson-Matthey copper containing 0.022 wt % beryllium in air at 1050°C for two days. Only two contacts were employed in this case; these were made by wrapping platinum wires around the ends of the sample prior to oxidation.

EXPERIMENTAL RESULTS

Equilibration Times

Early measurements established the existence of high- and low-temperature regions similar to those found by Anderson and Greenwood. The conductivity was found to be proportional to $P^{1/7}$ except at the lowest pressure. To obtain a measure of the rate of attainment of the new equilibrium after the ambient oxygen pressure was changed, we followed the time dependence of the conductivity at constant T when the P was reduced from 1 to 10^{-5} mm. If τ_T is the time taken for half the total conductivity change to occur at temperature T, and further if $\tau_T = \tau_0 \exp(E/kT)$ where E is the activation energy for vacancy diffusion (approximately 1.5 ev),[12] then the following values of τ_T were calculated from the value at 800°C.

T °C	450	650	750	800	890	990
τ_T (calc)	10^4	10^2	10	1.5	0.4	0.15 min
τ_T (obs)				1.5	0.5	0.25 min

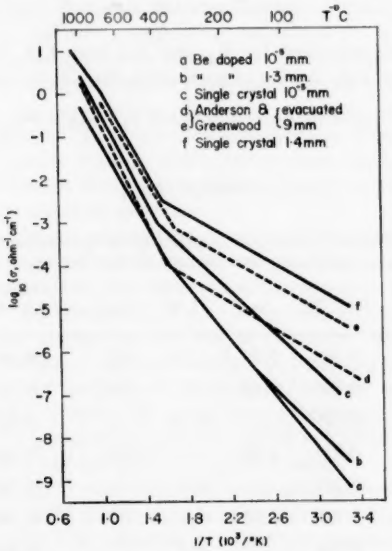
1000 600 400 200 100 T°C
a Be doped 10⁻⁵ mm
b " " 1·3 mm
c Single crystal 10⁻⁵ mm
d Anderson & Greenwood evacuated 9 mm
f Single crystal 1·4 mm
1/T (10³/°K)
0·6 1·0 1·4 1·8 2·2 2·6 3·0 3·4

FIG. 1. Temperature dependence of the conductivity of monocrystalline cuprous oxide, polycrystalline cuprous oxide doped with 0.022 wt % beryllium, and polycrystalline cuprous oxide as measured by Anderson and Greenwood.[5]

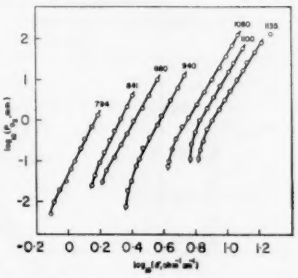

FIG. 2. Conductivity isotherms of monocrystalline cuprous oxide as a function of oxygen pressure.

Temperature Dependence of Conductivity

Once the sample had been equilibrated with an atmosphere at a sufficiently high temperature (900–1100°C) reproducible resistances were obtained on heating and cooling. In 1.4 mm O_2 the results can be described as follows:

$T > 750$°C

$$\sigma = 2.3\times10^{3} \exp(-\epsilon_1/kT)$$

$T < 750$°C

$$\sigma = 4.8\times10^{4} \exp(-\epsilon_2/kT) + 6.9\times10^{-1} \exp(-\epsilon_3/kT)$$

with $\epsilon_1 = 0.625$ ev, $\epsilon_2 = 0.91$ ev, and $\epsilon_3 = 0.295$ ev.

In a vacuum (i.e., $P < 10^{-5}$ mm) the conductivity below 1050°C is given by

$$\sigma = 1.6\times10^{4} \exp(-\epsilon_2'/kT) + 12 \exp(-\epsilon_3'/kT)$$

with $\epsilon_2' = 0.935$ ev and $\epsilon_2' = 0.51$ ev.

These results are in good agreement with those of Anderson and Greenwood (Fig. 1). The value of ϵ_1 (not observed by Anderson and Greenwood) is close to that found by Böttger.

Pressure Dependence of Conductivity

Figure 2 shows the results of a number of isotherms in which $\log_{10}\sigma$ is plotted against $\log_{10}P_{O_2}$. At high pressures a straight line is obtained with

$$m = \partial \log\sigma / \partial \log P \approx \tfrac{1}{7}.$$

If instead $\log(\sigma-\sigma_0)$ is plotted against $\log P$, where σ_0 is a constant found by trial, a straight line is obtained over the whole pressure range (see Fig. 3). In this case $m' = \partial \log(\sigma-\sigma_0)/\partial \log P \approx \frac{1}{5}$. The results are recorded in Table I, together with conductivity data at $P_{O_2} = 1$ mm.

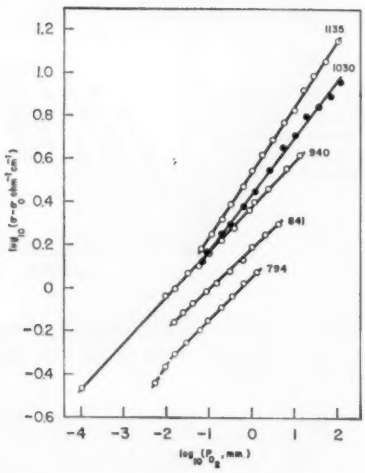

FIG. 3. Linear conductivity isotherms of cuprous oxide plotted as $\log(\sigma-\sigma_0)$ vs $\log P$.

Beryllium Doped Cuprous Oxide

Conductivity as a function of temperature was measured at two oxygen pressures. The results are plotted in Fig. 1. Although the results shown represent a number of runs, both heating and cooling, other nonreproducible results were obtained in which the conductivity was higher. This result may have been due either to exsolution of BeO or to the formation of a more conducting skin of pure Cu_2O on the surface, upon oxygen treatment. Above 140°C the conductivities of the sample at 10^{-5} mm and 1.3 mm O_2 were very nearly equal. Three distinct regions characterized by activation energies ϵ were observed

In 1.3 mm O_2,

$T>370$°C	370°C$>T>$240°C	240°C$>T>$20°C
ϵ 0.98 ev	0.61 ev	0.45 ev

In vacuum (10^{-5} mm) $T>370$°C

$T>370$°C	370°C$>T>$20°C
ϵ 0.98 ev	0.605 ev

Results of Trivich *et al.*

Where they overlap, the results of Trivich *et al.*, also obtained using single-crystal cuprous oxide, are in excellent agreement with those presented here. They restricted their measurements to the range of temperature and pressure in which Cu_2O is the stable phase. In the pressure range 10^{-2} to 10^{2} mm the activation energy was approximately 0.65 ev (to be compared with ϵ_1 above) increasing sharply to about 1.05 ev at pressures less than 10^{-2} mm (cf. ϵ_2' above).

Between 850 and 1000°C, Trivich found that the conductivity is proportional to $P_{O_2}^{1/7}$ with increasing deviation at lower pressures in agreement with the present results. Below 850°C and 10^{-3} mm the conductivity was observed to go through a minimum. This observation, the authors claim, shows that cuprous oxide becomes *n*-type at sufficiently low oxygen pressures.

DISCUSSION

If we consider first the pressure dependence of conductivity, the fact that the conductivity can be expressed as $\sigma-\sigma_0=kP_{O_2}^m$ might imply that the conductivity is composed of two parts, viz., $\sigma-\sigma_0$, respresenting the pressure dependent part and presumably due to hole conductivity, and σ_0 which is independent of both P and σ. However, it is hard to associate σ_0 with electronic conductivity, or even ionic conductivity, because the number of charge carriers contributing to σ_0 must vary in some way with impurity hole concentration. For this reason it is more likely that the relationship found merely illustrates the ease of obtaining straight lines from log-log plots.

An analysis of the pressure dependence of conductivity may be made as follows. We assume that the number of holes depends on a positive power of the pressure, i.e.,

$$N_{e^+}=kP^m. \tag{1}$$

The intrinsic ionization condition is

$$N_{e^+}N_{e^-}=k_i. \tag{2}$$

We also have in the absence of ionic conductivity

$$\sigma=N_{e^+}\mu^+e+N_{e^-}\mu^-e. \tag{3}$$

If we substitute for N_{e^-} and N_{e^+} from Eqs. (1) and (2) and take the log of both sides, Eq. (3) becomes

$$\ln\sigma=\ln(ke\mu^+)+m\ln P+\ln(1+\alpha P^{-2m}),$$

where

$$\alpha^{-1}=k^2\mu^+/k_i\mu^-,$$

TABLE I. Analysis of conductivity of cuprous oxide

T °C	$10^3/T$ °K	σ_0	$1/m$	$1/m'$	$\log_{10}\sigma$ ($P_{O_2}=1$ mm)
794	0.936	0.39	7.75	5.2	0.165
844	0.895	0.62	7.2	5.4	0.325
880	0.867	...	6.75	...	0.415
940	0.824	1.36	7.1	4.8	0.565
957	0.812	...	6.3	...	0.560
1050	0.755	2.92	6.6	3.7	0.740
1100	0.728	...	6.5	...	0.825
1135	0.710	4.80	6.1	3.4	0.915

so that, in terms of $\log P$,

$$\partial \ln\sigma/\partial \ln P = m \tanh(m \ln P - \tfrac{1}{2}\ln\alpha), \qquad (4)$$

since

$$\alpha^{-1}P^{2m} = N_{e^+}\mu^+/N_{e^-}\mu^-$$

$$\frac{\partial \ln\sigma}{\partial \ln P} = m\left(\frac{N_{e^+}\mu^+ - N_{e^-}\mu^-}{N_{e^+}\mu^+ + N_{e^-}\mu^-}\right). \qquad (5)$$

The present results are not sufficiently detailed to confirm the correctness of this approach by means of Eq. (4), but from Eq. (5) it can be said that over the range studied ($\partial \ln\sigma/\partial \ln P$, always positive), $N_{e^+}\mu^+ > N_{e^-}\mu^-$, so that the material is always p type. Further, in the region of constant $\partial \ln\sigma/\partial \ln P$, $N_{e^+}\mu^+ \gg N_{e^-}\mu^-$, so that in this region it is a good approximation to consider conduction to be entirely due to positive holes.

If we take the value of μ^+ at room temperature to be 50 $cm^2\ v^{-1}\ sec^{-1}$ and assume a $T^{-3/2}$ temperature dependence, we can estimate the number of holes present from Eq. (3). The number of vacancies has also been calculated from the data of Wagner and Hammen. Results for three temperatures at 1 mm are recorded in Table II.

These results are discussed further after a consideration of the activation energies.

Activation Energies

A reasonable interpretation of the activation energies ϵ_1, ϵ_2, and ϵ_3 found for the conductivity in 1.4 mm O_2 can now be given. On the assumption that at low temperatures there is a constant number of "frozen-in" vacancies and holes, $\epsilon_3 = 0.295$ ev represents the activation energy required to "dissociate" holes from their traps, the nature of which is left open for the present. Clearly any suggestions that grain boundaries are responsible for the observed resistances are disproved by the present results, which are in close agreement with the results obtained by Anderson and Greenwood with polycrystalline materials.

At the highest temperature cuprous oxide is in equilibrium with oxygen and the number of vacancies increases with temperature. The observed activation energy will therefore be composed of the activation energy for conduction proper plus the heat of formation of a vacancy (assuming that the number of holes is proportional to the number of vacancies). In other words, $\epsilon_1 = \epsilon_3 + \frac{1}{2}\Delta H$ (where ΔH is the heat of solution of an atom of oxygen) $= 0.295 + 0.315 = 0.61$ ev. This is in excellent agreement with the observed value.

In the region over which the activation energy is ϵ_2, the stable solid phase is no longer cuprous oxide but cupric oxide. The effective pressure will therefore be given by

$$P = P_0 \exp(-\Delta H'/kT)$$

TABLE II. Computation of number of positive holes in cuprous oxide.

T °C	μ^+	N_v	σ	N_e^+
1150	18	5×10^{19}	10	3.6×10^{18}
930	20	1.8×10^{18}	3.3	1×10^{18}
350	26	1.75×10^{15}[a]	2.5×10^{-3}	5.9×10^{14}
20	50	...	7.0×10^{-6}	8.8×10^{11}

[a] Corrected to the dissociation pressure of CuO at 350°C (10^{-8} mm) assuming N_v is proportional to $P^{1/8}$.

where $\Delta H'$ is the heat of the reaction,

$$4\ CuO \rightleftarrows 2Cu_2O + O_2.$$

From the data of Chiche the value of $\Delta H'$ at 900°C is calculated to be 2.82 ev. ϵ_2 will therefore be greater than ϵ_3 by $\Delta H/2 + \Delta H'/8$ where the number of vacancies depends on $P_{O_2}^{1/8}$. (See below.) The calculated value of ϵ_2 is then 0.96 ev. The observed value is sufficiently close to lend weight to this interpretation, particularly as in this temperature range complete equilibrium is not likely to be achieved.

Pressure Dependence

The problem of the pressure dependence of the conductivity cannot be regarded as solved. The conductivity at a given temperature is proportional to the number of free holes, which are in turn ionized from vacancies

$$V^+ \rightarrow V + e^+; \qquad (N_e + N_v)/N_{v^+} = c_1,$$

V^+ indicates a vacancy with its trapped hole at the Cu^+ site.

Vacancies are produced by the reaction

$$O_2 \rightarrow 2O = +4V^+; \qquad N_{v^+} = c_2 P_{O_2}{}^{\frac{1}{4}}.$$

In the absence of foreign atoms or ions and of intrinsic ionization,

$$N_{e^+} = N_v = N_{v^+}{}^{\frac{1}{4}} c_1{}^{\frac{1}{4}}$$
$$= (c_1 c_2)^{\frac{1}{4}} P_{O_2}{}^{1/8}.$$

On the other hand the excess of oxygen δ is proportional to the total number of vacancies. In atoms per cubic centimeter,

$$\delta = \tfrac{1}{2}(N_v + N_{v^+}),$$

if $N_v \gg N_{v^+}$,

$$\delta = \tfrac{1}{2} c_2 P_{O_2}{}^{\frac{1}{4}}.$$

This is the scheme originally proposed by Wagner.

However, the foregoing discussion has shown that the results can be interpreted if it is assumed that the number of free holes is directly proportional to the number of vacancies (see particularly the interpretation of ϵ_1 above). In other words, the holes are considered free of the vacancies and presumably trapped by some other process.

It is interesting to consider the analogous defect (the V-center) in the alkali halides. Electron-spin resonance measurements have shown[16] that in these materials the trapped hole is in the form of an X_2^- molecule-ion distinct from the vacancy; the activation energy for liberation of the hole is then to be associated with dissociation of the molecule-ion. It is of significance that in NaCl the electron mobility is of the order of 10^2 cm^2 v^{-1} sec^{-1};[17] hole mobility may be expected to be correspondingly large, so that the situation in Cu_2O may not be very different. It is possible that electron-spin resonance measurements will shed further light on this problem.

We must also consider that in high concentrations the effective orbit of a trapped positive hole may well be considerably larger than the distance between them, and will thus be under the influence of more than one "nucleus." For example, it has been calculated that $N_v+N_{v^+}=5\times10^{19}$ cm^{-3} at 1150°C in 1-mm O_2, corresponding to one vacancy and one trapped hole for 10^3 copper ions. The holes are therefore on the average only ten Cu-Cu distances apart. This should be compared with the value at 350°C of one vacancy for 3×10^7 copper ions or 300 Cu-Cu distances apart. Mott and Gurney[18] calculate that the mean free path of a positive hole in cuprous oxide at room temperature is 5 A so that at low temperatures the factor determining mobility will probably be lattice scattering. At higher vacancy concentrations, impurity scattering will become important and possibly predominant.

Comparison with Earlier Work

In the light of the above discussion it is now possible to explain some other measurements and observations. In particular, the Hall coefficient measured by Schottky and Waibel is explicable. The Hall coefficient is given by

$$R=-\frac{3\pi}{8e}\left[\frac{N_{e^-}\mu^{-2}-N_{e^+}\mu^{+2}}{(N_{e^-}\mu^{-}-N_{e^+}\mu^{+})^2}\right].$$

A typical value would be $\mu^-\sim10\mu^+$ so that the Hall coefficient should have a sign corresponding to electron conduction when $N_{e^-}>10^{-2}N_{e^+}$. It now appears likely that this situation can be achieved in a vacuum-treated sample such as Schottky and Waibel used.

The thermoelectric power, on the other hand, is given by

$$Q=-\frac{Q_1N_{e^+}\mu^{+}+Q_2N_{e^-}\mu^{-}}{N_{e^+}\mu^{+}+N_{e^-}\mu^{-}},$$

where Q_1 is the thermoelectric power associated with positive holes and Q_2 that associated with electrons. It has been shown that except possibly at very low oxygen pressures $N_{e^+}\mu^{+}>N_{e^-}\mu^{-}$ so that the thermoelectric power will normally indicate hole conduction. It remains difficult, however, to explain the observation of Anderson and Greenwood that the thermoelectric power decreased with increasing oxygen pressure. This effect is conceivably associated with the observation that the low-temperature activation energy for conductivity decreases with increasing extent of oxidation.

Beryllium-Doped Cuprous Oxide

Beryllium will almost certainly be incorporated into cuprous oxide as Be^{2+}. If a very small amount of Be^{2+} is put into oxygen-excess cuprous oxide, the beryllium can be considered as replacing Cu^{2+}, leaving the number of vacancies unchanged. Larger amounts of beryllium will be accompanied by one or two copper vacancies according to whether it goes in substitutionally or interstitially. Of course, equilibrium with the atmosphere is disturbed by this process, but qualitatively it can be said that Be^{2+} will increase the number of cation vacancies and reduce the number of free positive holes. The expected effect is therefore that the conductivity should become more nearly intrinsic.

For these reasons the 0.98 ev high-temperature process is thought to represent intrinsic conductivity. The identification of the low-temperature activation energies is rather more difficult, but gives support to the idea that as the number of holes decreases, the activation energy for impurity conduction increases. It is also necessary to bear in mind the possibility of such reactions as

$$Be^{2+}\rightarrow Be^{+}+e^{+}$$

which could conceivable be occurring in the 0.605 ev region.

CONCLUSIONS

The most important conclusion to be drawn from the present work is that at all temperatures the conductivity of cuprous oxide except at very low oxygen pressures is almost entirely due to positive holes associated with native defects (cation vacancies). The fact that there exist, nevertheless, different apparent activation energies associated with definite temperature ranges has now been satisfactorily explained.

We now need to obtain more definite information on the nature and concentration of the defects. It is hoped that this will be achieved by making simultaneous measurements of the Hall coefficient and conductivity as a function of pressure at high temperatures; and also by studying directly the departure from stoichiometry as a function of temperature and oxygen pressure. It is hoped, in particular, by these means to resolve the important problem of the dependence of the number of holes on oxygen pressure.

[16] W. Känzig, Phys. Rev. **99**, 1890 (1955); I. G. Castner and W. Känzig, J. Phys. Chem. Solids **3**, 178 (1957).
[17] A. Redfield, Phys. Rev. **91**, 244, 753 (1953).
[18] N. F. Mott and R. Gurney, *Electronic Processes in Ionic Crystals* (Oxford University Press, New York, 1942).

Molecular Orbitals in Some Boron Compounds

EMMETT B. MOORE, JR.
Boeing Scientific Research Laboratories, Seattle 24, Washington
AND
L. L. LOHR, JR. AND WILLIAM N. LIPSCOMB
Department of Chemistry, Harvard University, Cambridge 38, Massachusetts

(Received March 13, 1961)

An LCAO treatment of boron framework orbitals in $B_{10}H_{14}$ yields a charge distribution of $+0.05e$ on atoms 1 and 3, of $-0.25e$ on atoms 2 and 4, of $-0.03e$ on atoms 5, 7, 8, and 10, and of $+0.27e$ on atoms 6 and 9. When a charge of about $-0.2e$ is assigned to each bridge H atom, the order of reactivity agrees with that expected from the chemical behavior (neg 2,4<1,3<5,7,8,10<6,9 pos).

An LCAO investigation of boron orbitals in the B_5H_5 molecule of D_{5h} symmetry and with nine equal B—B distances indicates expected stability for the $B_5H_5^{-2}$ ion, but not for the neutral molecule. A simplified method of accounting for the molecular orbitals in icosahedral $B_{12}H_{12}^{-2}$ yields some conclusions concerning B_{11} hydrides and ions.

CHEMICAL evidence concerning electrophilic substitution[1] and D exchange[2] in the presence of $AlCl_3$ suggests on chemical grounds that atoms 2 and 4 of decaborane (Fig. 1) are most negative. Attack by various Lewis bases containing nitrogen, e.g., acetonitrile, has been shown[3] to occur at the 6, 9 positions, presumably most positive. The interpretation of chemical evidence concerning the charges on atoms 1, 3 and 5, 7, 8, 10 is not yet entirely clear,[2,4] but recent results concerning Friedel-Crafts alkylation[5,6] of decaborane, and nucleophilic substitution in decaborane, suggest[6,7] that the order of charge excess is (neg) 2, 4; <1, 3; <5, 7, 8, 10; <6, 9, (pos).

Localized three-center bonds[8] in decaborane give, on the other hand, charges of $-\frac{2}{3}$ on atoms 2 and 4, of 0 on atoms 1, 3, 6, and 9 and of $+\frac{1}{3}$ on atoms 5, 7, 8, and 10. In view of the observation that no localized bond theory of any sort correctly predicts charge distributions in molecules, it is remarkable and perhaps at least partly accidental that this approximation was successful at picking out the most negative boron atoms in decaborane. Of course, the order of the relative charges on the remaining, less charged, atoms was not correctly given in such a simplified theory. On the other hand, it may be hoped that a molecular orbital description of the charge distribution in decaborane would approximate the success that it has had in aromatic carbon compounds. In the present investigation, we shall consider only boron orbitals in the detailed molecular orbital calculations, but we shall modify our results by transfer of negative charge from the boron atoms to their bonded bridge hydrogen atoms. In B_2H_6 the bridge H atoms carry[9] about $0.2e$ of excess negative charge, and, accordingly, we assume a similar transfer of charge in the higher hydrides. For the molecular orbital discussion in such a large molecule as $B_{10}H_{14}$, we go no further in the present study than the one-electron LCAO treatment, which, so far, has been reasonably successful.

This LCAO method has shown even greater success in understanding and predicting stable polyhedral molecules and ions of boron hydrides and halides, as illustrated for the $B_{10}H_{10}^{-2}$ and $B_{12}H_{12}^{-2}$ ions.[8,10–12] Accordingly, an exploration of other polyhedral arrangements of possible stable boron halides was initiated some time ago. It was in the course of these molecular orbital studies that the simple polyhedral B_5H_5 arrangement of D_{5h} symmetry was found to have filled orbitals not for a neutral molecule but for a -2 ion. These results are, therefore, relevant to discussions of hydride ions, and are included here.

Thirdly, we present a simplified method of thinking of molecular orbitals in the polyhedral ions, somewhat similar to the method used[10] in $B_{10}H_{10}^{-2}$, so that we can discuss a possible B_{11} hydride or hydride ion in which the B_{11} arrangement is taken from an icosahedral B_{12} unit. It is precisely in this type of molecule or ion of very low symmetry, but nevertheless very compact geometrical arrangement, that the gap between localized bonds and molecular orbitals is difficult to bridge. Whether or not a given prediction, such as expected stability for $B_{11}H_{14}^-$, is eventually verified, the method of use of a subgroup of very low symmetry

[1] R. Schaeffer, J. Am. Chem. Soc. **79,** 2726 (1957).
[2] J. A. Dupont and M. F. Hawthorne, J. Am. Chem. Soc. **81,** 4998 (1959); Abstr. 138th Meeting Am. Chem. Soc., p. 46N, September (1960).
[3] J. Reddy and W. N. Lipscomb, J. Chem. Phys. **31,** 610 (1959).
[4] M. Hillman, J. Am. Chem. Soc. **82,** 1096 (1960).
[5] N. J. Blay, I. Dunstan, and R. L. Williams, J. Chem. Soc. **1960,** 430.
[6] R. L. Williams, I. Dunstan, and N. J. Blay, J. Chem. Soc. **1960,** 5006.
[7] I. Dunstan, R. L. Williams, and N. J. Blay, J. Chem. Soc. **1960,** 5012.
[8] W. H. Eberhardt, B. L. Crawford, Jr., and W. N. Lipscomb, J. Chem. Phys. **22,** 989 (1954).
[9] W. C. Hamilton, Proc. Roy. Soc. (London) **A235,** 395 (1956).
[10] W. N. Lipscomb, A. R. Pitochelli, and M. F. Hawthorne, J. Am. Chem. Soc. **81,** 5833 (1959).
[11] H. C. Longuet-Higgins and M. de V. Roberts, Proc. Roy. Soc. (London) **A230,** 110 (1955); **A224,** 336 (1954).
[12] J. A. Wunderlich and W. N. Lipscomb, J. Am. Chem. Soc. **82,** 4427 (1960).

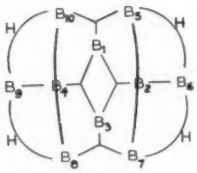

FIG. 1. Topological representation of the three-center bond approximation to the $B_{10}H_{14}$ structure. The terminal H atom on each B has been omitted.

for discussion of molecular orbitals in an ion as complicated as $B_{12}H_{12}^{-2}$ provides a greatly simplified explanation of the necessity for its -2 charge.

1. MOLECULAR ORBITALS IN $B_{10}H_{14}$[13]

A standard type of LCAO calculation was made. The secular equations[11] are

$$(\alpha_r - E)c_r + \sum_s{}'(\beta_{rs} - S_{rs}E)c_s = 0,$$

where

$$\alpha_r = \int \Phi_r H \Phi_r d\tau, \quad \beta_{rs} = \int \Phi_r H \Phi_s d\tau,$$

and

$$S_{rs} = \int \Phi_r \Phi_s d\tau.$$

Assuming that $\beta_{rs} = KS_{rs}$, the secular equations become

$$(\alpha_r - E)c_r + \sum_s{}'(K - E)S_{rs}c_s = 0. \qquad (1)$$

If we assume further that $\alpha_r = \alpha$, then

$$-xc_r + \sum_s{}'S_{rs}c_s = 0, \qquad (2)$$

where $'E = (\alpha + Kx)/(1+x)$.

Of the 44 electrons and 54 atomic orbitals available for bonding, 28 electrons and 32 atomic orbitals were assumed to be used in bonding the 10 terminal hydrogens and 4 bridge hydrogens, thus leaving 16 electrons and 22 orbitals for boron framework bonding. As indicated by a topological projection of the structure of the molecule (Fig. 2), tetrahedral hybrids of $2s$ and $2p$ orbitals were assumed[8] on atoms 1, 3, 5, 6, 7, 8, 9, and 10 and trigonal hybrids on atoms 2 and 4 (Fig. 2). The actual directions in space of these orbitals were altered slightly from the previous treatment[8] so that the hybrids on any given atom would be mutually orthogonal to a good approximation. All 63 boron-boron overlap integrals were computed throughout the molecule using Slater orbitals and angles between orbitals which were measured to the nearest five degrees on a scale model of symmetry C_{2v}. The secular determinant factors in the usual way into a 7×7 block of symmetry A_1, a 4×4 of A_2 symmetry, a 5×5 of B_1 symmetry, and a 6×6 of B_2 symmetry. The symmetry orbital overlap integrals S_{rs} were calculated, and then Eqs. (2) were solved. From these solutions, values of α_r were calculated,[8] thus allowing for modification[8] of α_r from various orbitals at atom r. The value of K was assumed to be -21 ev and Eqs. (1) were then solved. The final energies and wave functions are summarized in Table I. The symmetry orbitals, which are linear combinations of the hybrid orbitals, are given in Table II.

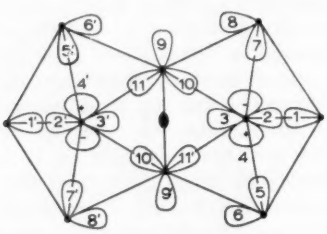

FIG. 2. Notation for hybrid orbitals of the B_{10} framework in $B_{10}H_{14}$. Orbitals which are designated with a prime in Table I are related by a twofold axis at the center of the molecule and out from the plane of the drawing.

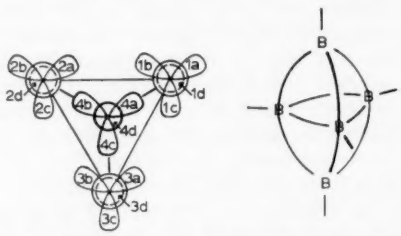

FIG. 3. (a) Hybrid orbitals in $B_5H_5^{-2}$. The tetrahedrally hybridized orbitals $5a$, $5b$, $5c$, $5d$ lie below the corresponding hybrids for atom 4. (b) Three-center bond approximation to the electronic structure of $B_5H_5^{-2}$.

There are eight bonding electron pairs for the boron framework, and hence a population analysis[9] of the first eight wave functions yields the following formal charges:

2, 4	5, 7, 8, 10	1, 3	6, 9
$-0.254e$	$-0.031e$	$+0.046e$	$+0.268e$.

On neglecting hybrid orbital moments by assuming that the excess charge is centered on the atom in question, we find a dipole moment of 3.6 debyes, in fortuitous agreement with the observed value of 3.52 debyes,[14] and more reasonable than the 6.2 debyes obtained[8] from the overlocalized three-center bond description. This calculated value would be decreased by assumption of $0.2e$ of negative charge on each bridge H atom, and increased by breakdown of the charge into individual orbital contributions, and would be decreased by electron-electron repulsions. We can only say at this stage that a large dipole moment is not unexpected on the basis of approximate theoretical arguments.

[13] A more complete discussion of the details of the $B_{10}H_{14}$ MO calculation appears in Boeing Scientific Research Laboratories Document D1-82-0085.

[14] A. W. Laubengayer and R. Bottei, J. Am. Chem. Soc. **74**, 1618 (1952).

TABLE I. Wave functions and energies of the molecular orbitals in the boron framework of $B_{10}H_{14}$.

E (ev)	
−16.593	$\Psi_{A_1}(1) = 0.177\Phi_1 + 0.141\Phi_2 + 0.195\Phi_3 + 0.263\Phi_4 + 0.281\Phi_5 + 0.160\Phi_6 + 0.210\Phi_7$
−14.034	$\Psi_{B_2}(1) = 0.323\Phi_{17} + 0.241\Phi_{18} + 0.144\Phi_{19} + 0.332\Phi_{20} + 0.034\Phi_{21} + 0.272\Phi_{22}$
−12.466	$\Psi_{B_1}(1) = 0.255\Phi_{12} + 0.206\Phi_{13} + 0.529\Phi_{14} - 0.326\Phi_{15} - 0.024\Phi_{16}$
−10.417	$\Psi_{A_1}(2) = 0.382\Phi_1 + 0.355\Phi_2 - 0.312\Phi_3 + 0.303\Phi_4 - 0.340\Phi_5 - 0.017\Phi_6 - 0.340\Phi_7$
−8.702	$\Psi_{A_2}(1) = 0.490\Phi_8 + 0.387\Phi_9 - 0.006\Phi_{10} - 0.291\Phi_{11}$
−8.170	$\Psi_{A_1}(3) = -0.042\Phi_1 + 0.040\Phi_2 - 0.238\Phi_3 - 0.269\Phi_4 + 0.636\Phi_5 + 0.392\Phi_6 - 0.501\Phi_7$
−7.721	$\Psi_{B_2}(2) = -0.323\Phi_{17} - 0.361\Phi_{18} + 0.373\Phi_{19} - 0.050\Phi_{20} + 0.115\Phi_{21} + 0.516\Phi_{22}$
−5.720	$\Psi_{B_1}(2) = 0.378\Phi_{12} + 0.592\Phi_{13} - 0.587\Phi_{14} + 0.065\Phi_{15} - 0.069\Phi_{16}$
6.425	$\Psi_{A_1}(4) = -0.633\Phi_1 - 0.218\Phi_2 + 0.232\Phi_3 + 0.762\Phi_4 - 0.515\Phi_5 + 0.585\Phi_6 - 0.391\Phi_7$
6.768	$\Psi_{A_2}(2) = 0.197\Phi_8 - 0.488\Phi_9 + 0.653\Phi_{10} - 0.315\Phi_{11}$
9.414	$\Psi_{B_2}(3) = 0.466\Phi_{17} + 0.125\Phi_{18} - 0.012\Phi_{19} - 0.646\Phi_{20} + 0.683\Phi_{21} - 0.008\Phi_{22}$
11.858	$\Psi_{B_1}(3) = 0.518\Phi_{12} - 0.346\Phi_{13} + 0.355\Phi_{14} + 0.610\Phi_{15} - 0.543\Phi_{16}$
36.831	$\Psi_{A_1}(5) = 1.124\Phi_1 - 0.939\Phi_2 + 0.806\Phi_3 - 0.127\Phi_4 - 0.188\Phi_5 + 0.021\Phi_6 - 0.788\Phi_7$
38.941	$\Psi_{B_1}(4) = 1.109\Phi_{12} - 0.779\Phi_{13} - 0.301\Phi_{14} + 0.000\Phi_{15} + 0.633\Phi_{16}$
39.717	$\Psi_{B_2}(4) = -0.906\Phi_{17} + 0.828\Phi_{18} - 0.792\Phi_{19} - 0.115\Phi_{20} + 0.132\Phi_{21} + 0.933\Phi_{22}$
55.530	$\Psi_{A_2}(3) = 1.133\Phi_8 - 0.152\Phi_9 + 0.188\Phi_{10} + 1.173\Phi_{11}$
63.246	$\Psi_{B_2}(5) = 1.096\Phi_{17} - 0.853\Phi_{18} - 0.819\Phi_{19} - 0.462\Phi_{20} - 0.457\Phi_{21} + 1.039\Phi_{22}$
112.261	$\Psi_{A_1}(6) = -0.172\Phi_1 - 1.014\Phi_2 - 0.909\Phi_3 + 1.809\Phi_4 + 1.492\Phi_5 - 1.252\Phi_6 - 0.304\Phi_7$
151.592	$\Psi_{A_2}(4) = -0.999\Phi_8 + 1.679\Phi_9 + 1.239\Phi_{10} + 0.611\Phi_{11}$
314.741	$\Psi_{B_1}(5) = -0.199\Phi_{12} + 1.551\Phi_{13} + 2.127\Phi_{14} + 2.546\Phi_{15} + 1.246\Phi_{16}$
298.898	$\Psi_{A_1}(7) = -1.182\Phi_1 + 1.740\Phi_2 + 2.391\Phi_3 + 0.001\Phi_4 + 0.866\Phi_5 - 1.886\Phi_6 - 2.195\Phi_7$
2919.20	$\Psi_{B_2}(6) = -0.922\Phi_{17} - 5.081\Phi_{18} - 4.464\Phi_{19} + 7.711\Phi_{20} + 4.211\Phi_{21} - 1.412\Phi_{22}$

The modification of the charge distribution by the $0.2e$ of negative charge on the bridge hydrogens then leads finally to the distribution

2, 4	1, 3	5, 7, 8, 10	6, 9
$-0.254e$	$+0.046e$	$+0.069e$	$+0.468e$,

which just agrees with the order found on chemical grounds. The asymmetry[15] of the hydrogen bridges, towards atoms 5, 7, 8, and 10, would make these atoms even more positive than indicated here, but we have no quantitative information on how the excess charge of the bridge hydrogen is to be distributed in an unsymmetrical hydrogen bridge. Perhaps this rough agreement with the chemical evidence should be as much as one can reasonably expect, but even so it does not seem completely reasonable that the charge on either atom 2 or 4 should be so different from the charge on either atom 1 or 3, either on chemical grounds[2,5,6] or on the basis of a free electron model.[16] Nevertheless, the model based upon delocalized molecular orbitals appears to be more reasonable than the model based upon localized three-center bonds, as we had hoped.

[15] E. B. Moore, Jr., R. E. Dickerson, and W. N. Lipscomb, J. Chem. Phys. **27**, 209 (1957).

[16] W. N. Lipscomb, J. Chem. Phys. **25**, 38 (1956).

2. MOLECULAR ORBITALS IN $B_5H_5^{-2}$ OF D_{3h} SYMMETRY

The polyhedral nature, the absence of bridge hydrogens, and the smaller number of orbitals all make the investigation of molecular orbitals of the trigonally symmetrical B_5H_5 group of atoms comparatively easier. Here, it is even reasonable to include the hybrid orbitals which point away from the center of the polyhedron towards H atoms, but, in the interest of reducing the number of parameters and the orders of the secular equations, the H orbitals themselves were omitted from the discussion. Accordingly, the $2s$, $2p_x$, $2p_y$, and $2p_z$ orbitals of the five B atoms were hybridized as sp^3 at the two apices, and sp^2 in the equatorial plane of the molecule for each of the other three B atoms (Fig. 3). The six B–B distances from the apical to the equatorial B atoms, and the three equatorial B–B distances, were all assumed to be equal to 1.70 A. All overlap integrals were evaluated from tabulated values of atomic overlap integrals based on orthogonalized Slater $2s$ and SCF $2p$ wave functions.[17] The symmetry orbitals listed in Table III correspond to the irreducible representations,

$$4A_1' + A_2' + 3A_2'' + 2E'' + 4E',$$

[17] R. S. Mulliken, J. Chem. Phys. **19**, 900 (1951).

TABLE II. Symmetry orbitals of $B_{10}H_{14}$.

$\Phi_1=N_1(1+1')$[a]	$\Phi_{12}=N_{12}(4-4')$
$\Phi_2=N_2(2+2')$	$\Phi_{13}=N_{13}(5-5'-7+7')$
$\Phi_3=N_3(3+3')$	$\Phi_{14}=N_{14}(6-6'-8+8')$
$\Phi_4=N_4(5+5'+7+7')$	$\Phi_{15}=N_{15}(9-9')$
$\Phi_5=N_5(6+6'+8+8')$	$\Phi_{16}=N_{16}(10-10'+11-11')$
$\Phi_6=N_6(9+9')$	
$\Phi_7=N_7(10+10'+11+11')$	$\Phi_{17}=N_{17}(1-1')$
	$\Phi_{18}=N_{18}(2-2')$
$\Phi_8=N_8(4+4')$	$\Phi_{19}=N_{19}(3-3')$
$\Phi_9=N_9(5+5'-7-7')$	$\Phi_{20}=N_{20}(5-5'+7-7')$
$\Phi_{10}=N_{10}(6+6'-8-8')$	$\Phi_{21}=N_{21}(6-6'+8-8')$
$\Phi_{11}=N_{11}(10+10'-11-11')$	$\Phi_{22}=N_{22}(10-10'-11+11')$

[a] Numbers in parentheses refer to hybrid atomic orbitals of Fig. 2. Values of $N_1\cdots N_{22}$ are, in order, 0.697, 0.695, 0.642, 0.416, 0.383, 0.651, 0.394, 0.719, 0.622, 0.765, 0.605; 0.696, 0.522, 0.424, 0.780, 0.800; 0.718, 0.719, 0.798, 0.503, 0.725, and 0.436.

of the symmetry group D_{3h}. The Coulomb integral[18] $\alpha(2s)$ was taken to be -15.63 ev, $\alpha(2p)$ to be -8.63 ev,[19] and it was assumed that $\beta_{rs}=KS_{rs}$, with K taken to be -21 ev. Solutions of the secular equations,

$$(\alpha_r-ES_{rr})c_r+\sum_s{}'(\beta_{rs}-ES_{rs})c_s=0, \qquad (3)$$

are listed in Table IV.

Neglecting the electrons in boron 1s orbitals and in B—H single bonds, the ion $B_5H_5^{-2}$ contains six pairs of electrons which fill the six lowest molecular orbitals. Of these six orbitals, three are symmetric and three are antisymmetric with respect to the plane h of D_{3h}. The molecular orbitals $\Psi_{A_1'^{(2)}}$, $\Psi_{A_1'^{(3)}}$, $\Psi_{A_2''^{(2)}}$, and $\Psi_{E'^{(3)}}$ consist largely of the symmetry orbitals Φ_1, Φ_4, Φ_6, and Φ_{15}, respectively, which point largely towards H atoms, and are of the correct symmetry to interact with them. Hence these orbitals will be considerably stabilized by interaction with hydrogen 1s orbitals to form B—H single bonds. The neutral molecule B_5H_5, which would contain five pairs of framework electrons, does not correspond to a closed-shell configuration, and hence would not be expected to be stable. On the other hand, the $B_5H_5^{+2}$ ion corresponds to a closed-shell configuration, but it would have a smaller binding energy than the expected $B_5H_5^{-2}$ ion.

A localized bond picture for the $B_5H_5^{-2}$ ion with D_{3h} symmetry can be drawn using three single B—B bonds in the horizontal plane h of the ion and three open three-center bonds[8] connecting the apical boron atoms [Fig. 3(b)]. Thus, this localized bond description also has three bonds which are symmetric and three which are antisymmetric with respect to the plane h of D_{3h}.

[18] The desirability of the use of different Coulomb integrals on 2s and 2p oribtals in LCAO calculations was first pointed out to us by R. Hoffmann of these Laboratories.

[19] R. S. Mulliken, J. Chem. Phys. **2**, 782 (1934).

The conclusion that $B_5H_5^{-2}$ is the stable species was tested further by examining the sensitivity to assumptions of various parameters. For example, the solutions of the secular equations (3) with $K=-13$ ev gave the same order of energy levels, although the bonding was only slight, as expected. Solutions were also obtained for the simplified secular equations

$$(\alpha_r-ES_{rr})c_r+\sum_s{}'\beta_{rs}c_s=0, \qquad (4)$$

in which $S_{rs}(r\neq s)$ was neglected except that it was retained in the relation $\beta_{rs}=KS_{rs}$. Neither this parameter variation nor the modified secular equations altered the conclusion that $B_5H_5^{-2}$ is the stable form of this aggregate of atoms.[20]

The secular equations (3) were also solved for the B_5H_5 molecule of tetragonal pyramidal (C_{4v}) symmetry assuming eight B–B distances to be 1.70 A. Overlap, Coulomb, and resonance integrals were evaluated as in the case of $B_5H_5^{-2}$ (D_{3h}). The molecular oribtals and energies in electron volts are A_1 at -18.35 (filled), E at -16.24 (filled), A_1 at -15.82 (filled), B_2 at

TABLE III. Symmetry orbitals of $B_5H_5^{-2}$.

A_1'	$\Phi_1=\sqrt{2}^{-1}(4d+5d)$
	$\Phi_2=(6)^{-\frac{1}{2}}(1b+1c+2a+2c+3a+3b)$
	$\Phi_3=(6)^{-\frac{1}{2}}(4a+4b+4c+5a+5b+5c)$
	$\Phi_4=\sqrt{3}^{-1}(1a+2b+3c)$
A_2'	$\Phi_5=(6)^{-\frac{1}{2}}(2a+3b+1c-2c-3a-1b)$
A_2''	$\Phi_6=\sqrt{2}^{-1}(4d-5d)$
	$\Phi_7=\sqrt{3}^{-1}(1d+2d+3d)$
	$\Phi_8=(6)^{-\frac{1}{2}}(4a+4b+4c-5a-5b-5c)$
E''	$\Phi_9^-=\sqrt{2}^{-1}(1d-2d)$
	$\Phi_{10}^+=(6)^{-\frac{1}{2}}(1d+2d)-(\frac{2}{3})^{\frac{1}{2}}(3d)$
	$\Phi_{11}^-=\frac{1}{2}(4b-5b+5c-4c)$
	$\Phi_{12}^+=\sqrt{3}^{-1}(4a-5a)+(2\sqrt{3})^{-1}(4b+4c-5b-5c)$
E'	$\Phi_{13}^-=\frac{1}{2}(4a-4b+5a-5b)$
	$\Phi_{14}^+=(2\sqrt{3})^{-1}(4a+4b+5a+5b)-\sqrt{3}^{-1}(4c+5c)$
	$\Phi_{15}^-=\sqrt{2}^{-1}(1a-2b)$
	$\Phi_{16}^+=(6)^{-\frac{1}{2}}(1a+2b)-(\frac{2}{3})^{\frac{1}{2}}(3c)$
	$\Phi_{17}^-=\frac{1}{2}(1b+1c-2c-2a)$
	$\Phi_{18}^+=(2\sqrt{3}^{-1})(1b+1c+2c+2a)-\sqrt{3}^{-1}(3a+3b)$
	$\Phi_{19}^-=(2\sqrt{2})^{-\frac{1}{2}}(1b-2a)+(\sqrt{3}/4)(2c+3b-1c-3a)$
	$\Phi_{20}^+=\frac{1}{2}(1b-1c-2c+2a)$

[20] *Note added in proof.* The title of a paper to be presented by R. E. Williams, C. D. Good, and I. Shapiro at the 140th Meeting of the American Chemical Society (Chemical and Engineering News, July 31, 1961, p. 94) suggests that a compound, $B_3C_2H_5$, isoelectronic with $B_5H_5^{-2}$ may have been discovered.

-13.71 (filled), A_1 at -12.61 (to H's), E at -9.79 (empty), A_1 at -8.99 (to H's), E at -6.70 (to H's), B_1 at -5.79 (to H's), B_1 at $+5.60$ (empty), E at $+11.31$ (empty), A_2 at $+16.74$ (empty), E at $+32.50$ (empty), A_1 at $+35.48$ (empty), and B_1 at $+66.15$ (empty). Stability is thus not indicated for a $B_5H_5^{-2}$ ion with C_{4v} symmetry, but possibly instead for a neutral B_5H_5 molecule containing five pairs of electrons in the boron framework. A more likely neutral molecular species would be B_5Cl_5 (C_{4v}), in which the boron framework is stabilized by back coordination of chlorine $2p$ electrons into the E level at -9.79 ev, the remaining molecular orbitals of negative energy being used in forming the B—Cl bonds.

3. POSSIBLE B_{11} COMPOUNDS BASED ON AN ICOSAHEDRAL FRAGMENT

In the molecular orbital study[10] of $B_{10}H_{10}^{-2}$ ion, a separation of orbitals of the 8 equatorial B atoms into those pointing towards the apices and those in the equatorial belt of the ion of D_{4d} symmetry was assumed. This separation is not based upon a symmetry argument, and hence is not exact, even in the one-electron approximation to the molecular orbitals. Nevertheless, if we assume tetrahedral hybrids about each equatorial B, with one towards its terminal H, one towards the apical B, and two essentially in the equatorial plane, we may expect not much interaction between the 16 equatorial orbitals of the 8 equatorial B atoms and the orbitals pointing towards the apices. Thus, the 16 equatorial orbitals were treated separately, and were found to accept five bonding pairs. The four orbitals pointing towards each apex B–H unit combine with the three orbitals of that unit to form three bonding levels, like the framework orbitals[8] of B_5H_9.

TABLE IV. Energies and wave functions[a] of boron molecular orbitals in B_5H_5.

E(ev)	
-18.31	$\Psi_{A_1'^{(1)}}=0.068\Phi_1-0.422\Phi_2+0.284\Phi_3+0.005\Phi_4$
-16.10	$\Psi_{E'^{(1)}}=-0.399\Phi_{13}-0.358\Phi_{15}-0.039\Phi_{17}+0.435\Phi_{19}$
-16.06	$\Psi_{A_2''^{(1)}}=0.246\Phi_6+0.507\Phi_7+0.324\Phi_8$
-11.71	$\Psi_{E''^{(1)}}=0.485\Phi_9+0.774\Phi_{11}$
-10.47	$\Psi_{E'^{(2)}}=0.317\Phi_{13}+0.503\Phi_{15}+0.346\Phi_{17}+0.754\Phi_{19}$
-9.81	$\Psi_{A_1'^{(2)}}=1.007\Phi_1+0.049\Phi_2+0.172\Phi_3+0.087\Phi_4$
-9.04	$\Psi_{A_1'^{(2)}}=-0.109\Phi_1-0.118\Phi_2+0.158\Phi_3+1.067\Phi_4$
-8.35	$\Psi_{A_2''^{(2)}}=1.011\Phi_6-0.256\Phi_7-0.302\Phi_8$
-5.82	$\Psi_{E'^{(2)}}=-0.732\Phi_{13}+0.861\Phi_{15}-0.448\Phi_{17}-0.043\Phi_{19}$
6.36	$\Psi_{A_2'^{(1)}}=1.653\Phi_5$
16.53	$\Psi_{E''^{(2)}}=1.442\Phi_9-1.052\Phi_{11}$
73.11	$\Psi_{A_2''^{(3)}}=0.302\Phi_6-1.493\Phi_7+2.484\Phi_8$
82.52	$\Psi_{A_1'^{(4)}}=0.290\Phi_1+1.824\Phi_2-2.479\Phi_3+0.624\Phi_4$
172.01	$\Psi_{E'^{(4)}}=1.791\Phi_{13}-0.304\Phi_{15}-3.798\Phi_{17}+1.146\Phi_{19}$

[a] Only one orbital of each pair of E' or E'' symmetry is listed for each energy. The other orbital has the same coefficients, and an index on each Φ increased by one. The $\Psi_{A_1'^{(1)}}$, $\Psi_{E'^{(1)}}$, $\Psi_{A_2''^{(1)}}$, and $\Psi_{E''^{(1)}}$ are filled in $B_5H_5^{-2}$, $\Psi_{A_1'^{(2)}}$, $\Psi_{A_1'^{(3)}}$, $\Psi_{A_2''^{(2)}}$, and $\Psi_{E'^{(2)}}$ are greatly stabilized further by interaction with the H atoms, while $\Psi_{E'^{(2)}}$ and all less stable orbitals are unfilled.

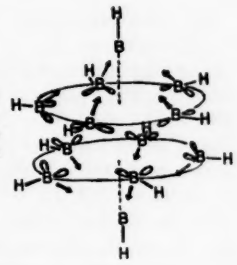

FIG. 4. Hybrid orbitals in $B_{12}H_{12}^{-2}$, showing equatorial orbitals of B as lobes, and orbitals from equatorial atoms towards apices as lines.

Now $B_{12}H_{12}^{-2}$, which has had a rather fuller discussion of its molecular orbitals elsewhere,[11] can be simplified in much the same way. Choose two opposite B atoms and regard them as apices (Fig. 4). The bonding of five equatorial B atoms to one of these apices is just like the bonding to the apex of hypothetical[21] $B_6H_{11}^+$, and requires three electron pairs. Bonding in the equatorial belt requires 7 electron pairs, since the ring is only slightly larger than that in $B_{10}H_{10}^{-2}$, and all molecular orbitals occur as doubly degenerate pairs except for the most stable totally symmetric orbital and the corresponding strongly antibonding one. Thus $7+3+3=13$ electron pairs are required for the framework bonding, as is already known from the more complete calculation. It may be added that the electron orbital ratio of $\frac{6}{8}$ for apex bonding is comparable with the ratio of 14/20, a condition which probably needs to be satisfied within reasonable limits in order that electron transfer from one set to the other does not occur.

It is now easy to see what the bonding would be if an apex atom is removed. Removal of one neutral :BH unit would leave $B_{11}H_{11}^{-2}$ with the five orbitals pointing towards the now vacant apex holding $6-2=4$ electrons. Now these five orbitals form one axially symmetric bonding molecular orbital and one degenerate pair requiring two more electrons. We could combine this set of orbitals with any sterically favorable group that would supply two more electrons in a σ, axially symmetric, orbital and a π pair. For example, we could use $(:N\text{–}H)^{+2}$ (with only 4 electrons) to make $B_{11}NH_{12}$, which might lose a proton to make $B_{11}NH_{11}^-$. Or we could use an $(H_3)^+$ group (σ and π) in a triangle perpendicular to the molecular axis to give $B_{11}H_{14}^-$, which is possibly more stable than $B_{11}H_{13}^{-2}$ which might require a direct B—B bond across the five-membered ring. A similar discussion of $B_{10}H_{10}^{-2}$ yields the $B_9H_{12}^-$ ion, in which the nine BH units are in C_{4v} symmetry, but combined by molecular orbitals to the triangle of H_3. However, a more promising structure for $B_9H_{12}^-$ is proposed in the following paper.

[21] W. N. Lipscomb, J. Chem. Phys. **28,** 170 (1958).

We close this section with a few comments on the LCAO's in the equatorial orbitals of $B_{12}H_{12}^{-2}$. Straightforward application of group theory to the 20 framework orbitals in the equator of $B_{12}H_{12}^{-2}$ yields the representation, in D_{5d}, $A_{1g}+A_{1u}+A_{2g}+A_{2u}+2E_{1g}+2E_{1u}+2E_{2g}+2E_{2u}$. Calculation of the energies in the Hückel approximation indicates that filled orbitals are A_{1g} at $H_0+2\beta$, E_{1g} at $H_0+1.45\beta$, E_{1u} at $H_0+1.40\beta$, and E_{2g} at $H_0+1.38\beta$; the unfilled orbitals are E_{2u} at $H_0+1.12\beta$, A_{2g} at H_0, A_{2u} at H_0, E_{2u} at $H_0-1.12\beta$, E_{2g} at $H_0-1.38\beta$, E_{1u} at $H_0-1.40\beta$, E_{1g} at $H_0-1.45\beta$, and A_{2g} at $H_0-2\beta$. Hence, all bonding levels above A_{1g} occur in pairs and an odd number of bonding electron pairs is required. The number 7 is reasonable in comparison with the corresponding number of 5 for equatorial bonding in $B_{10}H_{10}^{-2}$, and gives reasonable electron-orbital ratios as indicated above. For comparison with $B_{10}H_{10}^{-2}$ and $B_{12}H_{12}^{-2}$, we also mention $B_8H_8^{-2}$ of D_{2d} symmetry, assumed to have 18 equal B–B interactions. The 12 equatorial orbitals give the irreducible representations and energies, A_{1g} at $H_0+2\beta$ (filled), E_u at $H_0+\sqrt{3}\beta$ (filled), E_g at $H_0+\beta$ (back coordination from apical E_g), A_{1u} at H_0, A_{2u} at H_0, E_g at $H_0-\beta$, E_u at $H_0-\sqrt{3}\beta$, and A_{2g} at $H_0-2\beta$. The electron-orbital ratios are not as good for $B_8H_8^{-2}$ as for $B_{10}H_{10}^{-2}$ or $B_{12}H_{12}^{-2}$, but the indicated back coordination may stabilize this possible ion.

ACKNOWLEDGMENTS

The authors wish to acknowledge the assistance given by Arnold Rom and Dale Speakes in the solution of some of the secular equations on the IBM 704 and the assistance given by members of the Technical Support Group of Boeing Scientific Research Laboratories. In addition we wish to acknowledge the use of the IBM 709 Computer at the Massachusetts Institute of Technology for solutions of some of the secular equations. We also wish to thank the Office of Naval Research and the Office of Ordnance Research for support. One of us (L.L.L., Jr.) would like to thank the National Science Foundation for predoctoral fellowship support.

Molecular Structure of $B_9H_{13}(CH_3CN)$

FREDERICK E. WANG, PAUL G. SIMPSON, AND WILLIAM N. LIPSCOMB
Department of Chemistry, Harvard University, Cambridge 38, Massachusetts

(Received March 13, 1961)

A three-dimensional x-ray diffraction study of a single crystal of $B_9H_{13}(CH_3CN)$ has yielded the complete structure, including hydrogen atom positions. The nine boron atoms form an icosahedral fragment, like the arrangement in $B_{10}H_{14}$ with one boron atom missing. The structure is consistent with the present form of the topological theory of boron hydrides and ions in that it has two BH_2 groups, and is related to an anticipated $B_9H_{14}^-$ ion in the same way that $B_{10}H_{12}(CH_3CN)_2$ is related to $B_{10}H_{14}^{-2}$ ion. The crystals are monoclinic, in the space group $P2_1/m$, and have two molecules in a unit cell having parameters $a=5.64$, $b=9.22$, $c=9.81$ A and $\beta=90°\pm30$ min.

EVIDENCE of a simple degradative product of $B_{10}H_{12}(CH_3CN)_2$ by a solvolysis reaction was obtained first by Schaeffer,[1] and later by Fitch and Laubengayer[2] who suggested that the compound was an amine-stabilized B_9H_{11}. Hawthorne, Graybill, and Pitochelli[3] characterized this type of compound as $B_9H_{13}R$, where R is an electron pair donor, and prepared a number of amine derivatives as well as the $B_9H_{13}(CH_3CN)$ sample for the present study.

The expectation that degradation of the known[4] $B_{10}H_{12}R_2$ structure to $B_9H_{13}R$ involved loss of one R and its attached B led Hawthorne[5] to suggest that the B_9 arrangement was a fragment of the original B_{10} arrangement.

Then an application of the present form[6,7] of the topological theory of valence yielded the following deductions by one of us (W.N.L.) as outlined, in part, in reference 3 and in the lecture itself.[3] (1) This particular boron arrangement was deduced independently from the realization that the high-field doublet of the B^{11} nuclear magnetic resonance spectrum implied that three boron atoms were each joined to five other boron atoms. (2) The correct hydrogen atom arrangement, and the consequent bonding scheme, were then deduced to yield the correct structure, described below, having two bridge hydrogen atoms and two BH_2 groups.[8]

The present investigation of the molecular structure of $B_9H_{13}(CH_3CN)$ was carried out, first, to locate the boron atoms in order to find whether preservation of structural features extends to such degradation products, and, secondly, to locate the hydrogen atoms with reasonable certainty in order to distinguish clearly between possibly tautomeric structures which are or are not consistent with the present form of the valence theory of these compounds. As we shall show, the structure[9] of $B_9H_{13}(CH_3CN)$ is consistent with these valence principles. Hence, an extrapolation to possible structures for the $B_9H_{12}R^-$ type[3] of compound seems justifiable. We further suggest that $B_9H_{12}^-$ has C_s symmetry and topology 2621, and that a B_9H_{13} of C_s symmetry may be expected having 2702 for its bond topology.

STRUCTURE DETERMINATION

A preliminary unit cell and space group determination of $B_9H_{13}NH(C_2H_5)_2$ led to the data, $a=12.99\pm0.02$, $b=21.10\pm0.03$, $c=9.58\pm0.02$ A, Pbca and 8 molecules per cell. However, this study was abandoned in favor of the much simpler crystallographic problem presented by $B_9H_{13}(CH_3CN)$. Weissenberg photographs were taken of a single crystal of $B_9H_{13}(CH_3CN)$, with the use of Cu$K\alpha$ radiation, of the hKl levels for $0\leq K\leq 8$ and the Hkl levels for $0\leq H\leq 4$. The reciprocal lattice has symmetry C_{2h}, and the only systematic absences are those for OkO reflections when k is odd. Hence, the space group is either $P2_1$ or $P2_1/m$, but our later work indicated that $P2_1/m$ is the correct choice. Assumption of two molecules of $B_9H_{13}(CH_3CN)$ in the unit cell, which has parameters $a=5.639\pm0.007$ A, $b=9.220\pm0.008$ A, $c=9.813\pm0.020$ A, and $\beta=90°\pm30$ min, leads to a calculated density of 0.98 gm/cm^3 in agreement with the observed value of 0.99 gm/cm^3. Visual estimates of all intensities were made with the use of a standard scale prepared from timed exposures of reflections from the same single crystal. After correction for Lorentz and polarization factors, and correlation to a single scale, a total of 890 symmetry-independent observations were recorded.

[1] R. Schaeffer, J. Am. Chem. Soc. **79**, 1006 (1957); also private communication, December, 1958.
[2] S. J. Fitch and A. W. Laubengayer, J. Am. Chem. Soc. **80**, 5911 (1958).
[3] M. F. Hawthorne, B. M. Graybill, and A. R. Pitochelli, Abstr. 138th Meeting, Am. Chem. Soc. Paper 45N, September 11–16, 1960, New York, New York.
[4] J. Reddy and W. N. Lipscomb, J. Chem. Phys. **31**, 610 (1959).
[5] M. F. Hawthorne, private communication, January, 1959.
[6] R. E. Dickerson and W. N. Lipscomb, J. Chem. Phys. **27**, 212 (1957).
[7] W. N. Lipscomb, *Advances in Inorganic and Radiochemistry* (Academic Press Inc., New York, 1959) Vol. 1, p. 117.
[8] Actually, at the early stage of their first report[3] these deductions were incomplete, and hence the reported structure[3] with four bridge hydrogen atoms not only violates the topological rule which provides for no more than one bridge hydrogen atom to a boron atom joined to four other boron atoms, but it is also not in agreement with the x-ray evidence, described below.
[9] F. E. Wang, P. G. Simpson, and W. N. Lipscomb, J. Am. Chem. Soc. **83**, 491 (1961).

TABLE I. Observed structure factors×10. Range of h and value of k are indicated in parentheses; absence is indicated by a.

k = 0 (h,k,): (1-7,0,)71,23,79,80,40,24,8,(1-6,1,)
382,88,54,13,9,7,(0-5,2,)398,217,21,22,22,24(0-3,3,)
85,76,40,47,24(0-6,4,)227,85,81,50,35,a,29,(1-6,5,)
83,24,41,a,35,12,(0-6,6,)270,20,41,15,a,40,23,(0-5,7,)
85,19,a,11,27,(0-5,8,)115,50,14,a,14,6,(1-4,8,)43,22,
a,15,(0-3,10,)72,15,a,14,(1,11,)36,
k = 1 (h,k,): (0-7,0,)188,155,144,86,50,16,12,6,(0-
6,1,)269,72,59,40,45,55,9,(0-5,2,)82,73,25,34,6(0-3,3,)
331,84,60,7,58,a,21,(0-6,4,)129,160,47,77,11,16,8,
(0-6,5,)61,a,91,55,a,51,30,(0-6,6,)96,34,42,a,38,18,
12,(0-5,7,)15,28,a,a,a,26,(0-3,8,)51,15,14,10,(0-9,)
43,(0,11,)15,
k = 1 (h,k,): (1-4,0,)178,184,52,22,(1-7,1,)377,60,
21,a,a,a,7,(1-4,2,)40,a,13,62,(1-7,3,)110,49,8,32,84,
17,9,(1-6,4,)73,101,25,39,a,11,(1-6,5,)226,72,a,8,27,
18,(1-6,6,)19,127,31,14,24,13,(1-4,7,)119,a,16,18,
(2-5,8,)24,a,20,20,(2,11,)6,
k = 2 (h,k,): (0-7,0,)335,10,63,61,85,57,24,5,(0-7,1,)
65,44,29,113,21,19,24,33,(0-7,2,)68,69,42,37,12,21,17,
6,(0-6,3,)86,149,26,32,4,20,25,(0-6,4,)60,77,87,10,38,
27,7,(0-5,5,)36,76,60,a,a,a,23,(0-5,6,)36,53,32,54,16,
30,(0-3,7,)16,28,46,27,(0-5,8,)10,28,a,10,a,7,(0-2,9,)
51,a,12,(0-1,10,)23,15,(0,11,)7.
k = 2 (h,k,): (1-6,0,)36,152,76,12,18,27,(1-7,1,)142,
141,105,54,a,10,7,(1-7,2,)347,29,49,30,52,a,12,(1-6,3,)
73,140,59,42,21,10,(1-4,4,)135,55,23,23,(2-6,5,)8,108,
a,a,16,(1-6,6,)22,100,a,26,16,20,(2-3,7,)14,55,(1-4,8,)
76,a,12,8,(1-4,9,)26,50,a,17,(3,10,)18,(2,11,)11.
k = 3 (h,k,): (0-7,0,)141,a,121,41,29,28,26,31,(0-6,1,)
13,51,18,8,40,a,29,(0-7,2,)67,32,24,32,21,16,11,7,
(0-5,3,)71,90,28,50,38,19,(0-6,4,)32,67,60,59,5,a,22,
(0-5,5,)35,75,72,55,a,15,(0-6,6,)66,68,115,a,a,a,15,
(0-3,7,)44,64,18,11,(3,8,)13,(1-3,9,)13,a,22,
k = 3 (h,k,): (1-7,0,)79,58,63,108,a,26,9,(1-7,1,)
40,166,84,36,54,14,7,(1-4,2,)129,31,153,70,(1-6,3,)
64,245,a,37,33,22,(1-5,4,)84,48,104,24,21,(1-6,5,)
129,77,a,25,a,10,(1-4,6,)16,81,25,25,(1-5,7,)47,53,a,
a,16,(1-4,8,)30,a,59,21,(1-4,9,)33,66,17,13,(3,10)19,
k = 4 (h,k,): (0-6,0,)194,125,28,a,31,13,13,(0-5,1,)
45,143,40,11,27,25,(0-4,2,)77,56,23,40,54,(0-4,3,)66,a,
73,42,13,23,18,(0-4,4,)51,10,6,30,59,(0-5,5,)84,86,40,
18,6,42,(0-5,6,)64,44,38,40,34,12,(0-5,7,)37,59,9,14,
a,17,(0-4,8,)32,a,14,24,24,(1-2,9,)24,a,36,(1,10,)29,
k = 4 (h,k,): (1-6,0,)24,81,5,8,16,14,(1-6,1,)19,17,
36,21,a,27,(1-3,2,)17,71,97,(1-5,3,)51,22,45,103,10,
(1-6,4,)42,42,110,8,36,15,(2-5,5,)88,23,54,12,(1-5,6,)
72,31,46,a,13,(1-4,7,)14,24,33,(1-3,8,)20,27,40,(1-4,9,)
22,a,15,7,(2,10)10,
k = 5 (h,k,): (0-6,0,)175,125,72,9,72,7,13,(0-6,1,)
27,25,44,111,20,a,19,(0-6,2,)50,71,91,a,42,40,7,
(0-6,3,)47,51,46,97,25,a,18,(0-5,4,)67,67,40,30,27,
30,(0-6,5,)12,46,22,24,11,15,(0-4,6,)13,53,14,a,
12,(0-5,7,)24,27,10,43,a,16,(0-4,8,)20,34,43,a,53,
(0-3,9,)12,a,8,15,(2,10,)19,

k = 5 (h,k,): (1-7,0,)50,37,37,96,30,30,11,(1-6,1,)
59,25,63,29,48,26,(1-6,2,)54,16,49,17,49,22,(1-6,3,)
14,61,67,26,15,8,(2-6,4,)50,40,7,26,8,(1-3,5,)61,a,
a,(1-4,6,)17,27,a,24,(1-3,8,)18,a,22,(2-3,9,)12,10,
k = 6 (h,k,): (0-4,0,)137,76,31,10,20(0-2,1,)44,10,
13,(0-6,2,)78,a,88,14,a,a,11,(0-6,3,)145,143,a,25,
41,39,11,(0-5,4,)8,34,98,51,19,13,(0-4,5,)35,19,49,
30,24,(0-5,6,)31,a,28,30,a,18,(0-4,7,)14,14,a,a,16,
(0-2,8,)27,a,37,(1-2,9,)27,9,(0-1,10)13,10,(0,11,)6,
k = 6 (h,k,): (1-6,0,)26,37,69,28,18,7,(1-6,1,)75,18,a,
20,25,23,(1-6,2,)71,15,33,31,a,10,(1-6,3,)79,30,37,
61,a,19,(1-4,4,)92,16,45,28,(2-5,5,)46,26,a,29,(1-6,
6,)38,8,a,45,(1-5,7,)28,a,23,(1-3,8,)22,a,10,(1,9,)23,
k = 7 (h,k,): (0-6,0,)82,141,51,30,30,14,7,(0-5,1,)
64,7,76,45,a,11,(0-5,2,)84,50,44,30,20,31,(0-5,3,)31,
66,39,a,29,8,(0-5,4,)101,a,a,a,a,23,27,(0-4,5,)18,18,
42,a,19,(0-1,6,)16,51,(2-3,7,)26,14,(0-3,8,)30,10,18,
47,(0-2,9,)27,10,14,
k = 7 (h,k,): (1-6,0,)26,25,38,16,14,13,(1-5,1,)50,
81,20,12,18,(1-5,2,)116,24,a,34,13,(1-5,3,)32,52,29,
a,10,(1-5,4,)37,10,11,21,8,(4-5,5,)37,9,(1-5,6,)25,a,
21,(1-4,7,)20,a,a,20,(1-2,8,)50,12,(2,9,)25,
k = 8 (h,k,): (0-5,0,)21,12,16,(0-2,1,)140,a,38,
(0-5,2,)35,66,a,18,15,14,(0-5,3,)24,55,20,a,37,32,
(0-5,4,)11,65,27,34,31,16,(0-4,5,)113,45,a,39,10,
(0-4,6,)34,83,32,a,11,(0-2,7,)66,32,25,(0-1,8,)12,
53,(0,9,)14,
k = 8 (h,k,): (1-5,0,)45,20,a,7,23,(1-4,1,)40,a,14,
12,(1-5,2,)16,47,a,11,8,(1-5,3,)88,18,11,12,6,(3-4,4,)
9,20,(1-3,5,)59,12,27,(1-4,6,)34,26,a,25,(3,7,)10,
(1-2,8,)15,12,
k = 9 (h,k,): (1-5,0,)19,a,7,10,34,(0-5,1,)57,a,13,
10,16,7,(0-4,2,)42,a,a,13,18,(0-3,3,)50,a,25,35,
(0-4,4,)19,16,a,11,21,(0-2,5,)106,a,23,(1-3,6,)29,a,
25,(0-2,7,)49,a,9,(0,8,)12,
k = 9 (h,k,): (1-4,0,)79,44,45,25,(1-5,1,)18,13,30,
14,20,(1-4,2,)24,14,24,20,(2-3,3,)16,9,(1-2,4,)55,
15,(2-4,5,)31,a,15,(1-2,6,)34,8,(2,7,)13,
k = 10 (h,k,): (0-5,0,)26,15,10,15,(0-3,1,)17,10,
15,12,(0-2,2,)24,16,14,(0-3,3,)26,a,6,5,(1-4,4,)27,
(0-3,5,)46,16,12,44,(0-2,6,)11,a,24,(0,7,)9,
k = 10 (h,k,): (1-4,0,)39,28,54,25,(1-4,1,)37,59,
43,9,(1-4,2,)15,42,6,13,(1-4,3,)52,a,7,6,(2,4,)19,
(2-3,5,)27,10,
k = 11 (h,k,): (0-3,0,)16,a,49,17,(1-4,1,)35,25,21,
14,(2,2,)18,(0-3,3,)19,14,21,20,(0-2,4,)26,11,10,
(0-2,5,)17,a,8,
k = 11 (h,k,): (1-3,0,)21,8,46,(1-3,1,)8,a,5,(1-3,2,)
13,40,16,(1-3,3,)40,a,26,(1-2,4,)26,41,(1,5,)38,
k = 12 (h,k,): (0-2,0,)22,51,9,(0-2,1,)22,18,29,
(1,2,)19,(0-1,3,)6,5,
k = 12 (h,k,): (1-2,0,)12,7,(2,1,),(1,3,)9,

These data were multiplied by a single scale factor, determined by the usual statistical methods, and refined later by least-squares procedure. The three-dimensional Patterson function, sharpened by usual procedures, was then analyzed to give all boron, nitrogen, and carbon atoms. This analysis was reasonably straightforward. For example, the linear B—N≡C—CH_3 groups, excluding hydrogen atoms, were recognizable as lying in the mirror plane of the space group $P2_1/m$. Placement of these atoms then provided a starting point for analysis of vectors from these atoms to the other boron atoms. These additional vectors indicated that all boron, nitrogen, and carbon atoms satisfied the planar symmetry required for the molecule if the space group is $P2_1/m$, and this space group was later confirmed by the number and positions of hydrogen atoms and by the final detailed agreement of structure factors. Perhaps the only difficulty of the analysis was that the assumption of isotropic temperature factors for boron, nitrogen, and carbon atoms gave very poor agreement between observed and calculated structure factors in the early stages, and we therefore attempted to shift the molecule by one bond distance either way along the linear B—N≡C—CH_3 group, but without success. It was only when anisotropic temperature factors were introduced that the least squares refinement progressed to yield good agreement in spite of the preliminary omission of hydrogen atoms. At this stage, the value of $R=|\sum||F_0|-|F_c||/\sum|F_0|=0.21$ was found for the 782 strongest reflections, omitting the intense (110) reflection which, because of the platelike crystal shape, was quite narrow, unlike almost all other reflections on the photographs and unlike those on the intensity scale.

A series of three-dimensional difference electron density maps, in which all boron, nitrogen, and carbon

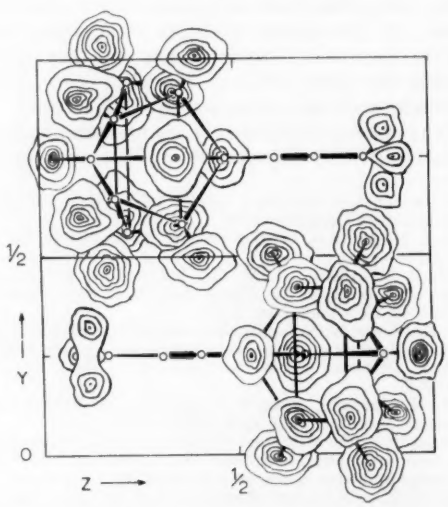

FIG. 1. Composite map from the three-dimensional electron density map from which B, C, and N have been subtracted. Contours are at 0, 10, 20, ···90 units where 105 units=1 electron/A³.

atoms were subtracted, then were computed first from the list of 782 reflections, excluding (110). In the first of these maps all hydrogen atoms except those of the CH_3 group were found, but lack of convergence and incomplete compensation at this stage for anisotropic thermal motion, as well as a few disturbing but obvious errors in the intensity list, produced a somewhat smeared electron density around H_8, and peaks about as high as those of hydrogen atoms between B_4 and $B_{4'}$, and between B_3 and B_6. This structure agreed with that found below for our final model, but we were unwilling to accept the over-all R value of 0.17 as representing the quality of the photographs. At this stage all calculations were set aside, and a complete and independent new set of observed reflections was carefully measured. However, the discrepancy for the (110) reflection remained such that $|F_{110}^{obs}| = 0.6\,|F_{110}^{calc}|$. We then came to the conclusion that this discrepancy was probably real, and possibly due to abnormal extinction and absorption associated with the particularly long path through the flat crystal for this particular reflection. Hence, this reflection was omitted from this list of 890 reflections (Table I) in all remaining calculations. The difference electron density map computed at this stage is shown in Fig. 1. All hydrogen atoms, even those of the CH_3 group, were clearly resolved. The lowest peaks which were not hydrogen atoms occurred at heights of 0.3 electrons/A^3, as compared with 0.3–0.4 electrons/A^3 for hydrogen atoms of the CH_3 group, and with 0.5–0.8 electrons/A^3 for all other hydrogen atoms.

The structure was refined by three-dimensional least squares procedures. Isotropic temperature factors were assumed at first on all atoms, including all hydrogen atoms except those on the CH_3 group, and the full matrix of all interactions was employed in the refinement. Then, anisotropic temperature factors were introduced for boron, nitrogen, and carbon atoms, but the isotropic thermal parameters on hydrogen atoms were kept fixed. Here, the full matrix was employed for all parameters except temperature factors of hydrogen. The final agreement factors are shown in Table II for various classes of reflection; final coordinates and thermal parameters are in Table III. Final bond distances and their standard deviations are shown in Table IV. Both the resolution of hydrogen atoms (Fig. 1) and the detailed agreement between F^{obs} and F^{calc} for all reflections are quite comparable with similar results[4] for $B_{10}H_{12}(CH_3CN)_2$. A drawing of the structure of $B_9H_{13}(CH_3CN)$ molecule is shown in Fig. 2.

TABLE II. Final Values of $R=\Sigma\,||F_o|-|F_c||/\Sigma|F_o|$.

hkl	
all	0.14
h even	0.16
k even	0.14
l even	0.13
$h+k$ even	0.14
$h+l$ even	0.14
$k+l$ even	0.14
$h+k+l$ even	0.14
$hk0$	0.11
$h0l$	0.13
$0kl$	0.16

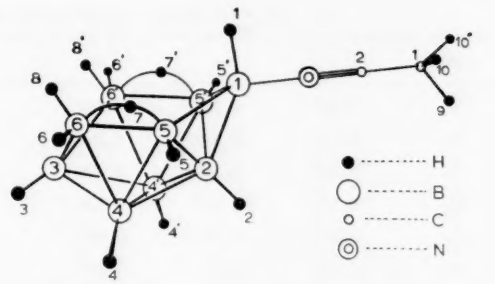

FIG. 2. Drawing of the molecular structure.

The many intermolecular contacts in the crystal have also been computed, but are not recorded here. All of these contacts are within normal van der Waals distances, including the H···H distances of 2.4 A between the hydrogen atoms of the CH_3 groups and neighboring hydrogen atoms. These contacts are normal only for the particular orientation of the CH_3 group about the C–CH_3 axis which occurs in the crystalline solid. We therefore suspect that this orientation is almost entirely an aspect of the molecular packing, rather than a property of an isolated $B_9H_{13}NCCH_3$ molecule.

DISCUSSION

The boron atoms are indeed arranged like nine of the ten boron atoms of the parent $B_{10}H_{12}(CH_3CN)_2$. Distances in the linear B—N≡C—CH_3 are very slightly, but systematically, less in the $B_9H_{13}R$ compound than in $B_{10}H_{12}R_2$. By far the largest changes in B–B contacts are the increases of B_3–B_6 by 0.13 A and B_4–B_6 by 0.07 A in the region of the BH_2 groups created when $B_9H_{13}R$ is formed from $B_{10}H_{12}R_2$. The results of both Fourier and least squares refinement clearly indicate the presence of these two BH_2 groups on atoms B_6 and $B_{6'}$, and two BHB bridges between B_5 and B_6 and between $B_{5'}$ and $B_{6'}$. An interesting, and completely objective, test of the positions of the two atoms H_8 and $H_{8'}$ was then made. When these atoms were placed into symmetrical bridge positions ($H_8\cdots H_{8'}=1.8$ A) between B_3 and B_6 and between B_3 and $B_{8'}$, respectively, they actually moved during the course of four consecutive three-dimensional least squares refinements 77% of the way towards the final positions in their re-

TABLE III. The final atomic coordinates[a] and their anisotropic temperature factors.

Atom	x	y	z	β_{11}[b]	β_{22}	β_{33}	β_{12}	β_{13}	β_{23}
C_1	0.987	0.250	0.169	733	138	76	0	26	0
C_2	0.111	0.250	0.296	514	95	72	0	26	0
N	0.209	0.250	0.396	466	97	81	0	46	0
B_1	0.341	0.250	0.529	389	110	71	0	25	0
B_2	0.142	0.250	0.664	285	125	80	0	19	0
B_3	0.481	0.250	0.869	411	118	92	0	13	0
B_4	0.236	0.151	0.808	429	108	71	25	32	11
$B_{4'}$	0.236	0.349	0.808						
B_5	0.296	0.087	0.640	465	101	87	16	24	12
$B_{5'}$	0.296	0.413	0.640						
B_6	0.507	0.070	0.783	431	159	104	70	19	27
$B_{6'}$	0.507	0.430	0.783						
H_1	0.542	0.250	0.527	4[b]	1	1			
H_2	0.976	0.250	0.644	3	1	1			
H_3	0.535	0.250	0.974	4	1	1			
H_5	0.800	0.016	0.403	6	2	2			
$H_{5'}$	0.800	0.484	0.403						
H_8	0.450	0.024	0.163	2	1	1			
$H_{8'}$	0.450	0.476	0.163						
H_7	0.509	0.077	0.645	8	4	3			
$H_{7'}$	0.509	0.423	0.645						
H_4	0.111	0.092	0.889	7	3	1			
$H_{4'}$	0.111	0.408	0.889						
H_6	0.693	0.098	0.784	7	2	1			
$H_{6'}$	0.693	0.402	0.784						
H_9	0.793	0.250	0.171						
H_{10}	0.010	0.175	0.116						
$H_{10'}$	0.010	0.325	0.116						

[a] Standard deviations of individual coordinates converted to A, average to ±0.006 A for B, N, and C, and ±0.04 A for H.

[b] Values of β_{ij} from the expression $\exp-(\beta_{11}h^2+\beta_{22}k^2+\beta_{33}l^2+2\beta_{12}hk+2\beta_{13}hl+2\beta_{23}kl)$ $\sin^2\theta/\lambda^2$ have been multiplied by 10^4 in the above listing. For H atoms isotropic thermal parameters B have been converted to equivalent anisotropic parameters, according to the expressions $\beta_{11}=B(a^*)^2/4$, $\beta_{12}=Ba^*b^*\cos\gamma^*/4$, etc., where the reciprocal lattice parameters have their usual meaning.

spective BH_2 groups. At the conclusion of all combined least squares and Fourier refinements, the distances $B_3\cdots H_8$ and $B_3\cdots H_{8'}$ became 2.07 A, and $H_8\cdots H_{8'}$ became 2.8 A.

The relevance of this detailed test of the positions of H_8 and H_8' is that the structure found in this study is consistent with the present topological theory[6,7] of boron hydrides and derivatives. This theory includes tautomerisms, such as those summarized in Fig. 3, as actual reactions expected to go toward BHB bridges in the neutral hydrides, and toward BH_2 groups in negative ions and amine derivatives in which additional formal negative charge is to be accommodated. This theory also includes conceptual substitutions, such as R for H^-, where R is an electron pair donor (for example, bonding in $B_9H_{14}^-$ and $B_9H_{13}R$ is the same), and also includes relations to hypothetical compounds, such as the probably nonexistent B_9H_{15} shown in Fig. 3, as well as other substitutions. Now, the impossibility of bonding of two bridge hydrogen atoms to a boron atom connected to four other nearest boron atoms was taken[6,7] as one of the structural principles of boron hydrides and their derivatives for three reasons: (1) this feature was not present among boron compounds of

known structure; (2) the two bridge hydrogen atoms are in a very crowded situation; and (3) a simple chemical process involving loss of H^+ and tautomerism to a BH_2 group (Fig. 3) is a probable transformation which preserves most of the valence and geometrical structure. It is apparent that the two BH_2 groups in $B_9H_{13}(CH_3CN)$, shown as structure II in Fig. 3, could conceivably transform by process T_2 into a form of $B_9H_{13}(CH_3CN)$ with four hydrogen bridges, but it does not do so, at least in its crystalline environment.

Secondly, the structure of B_9H_{15} shown in Fig. 3 violates this principle at three boron atoms, and hence is believed not to be a stable hydride. Nevertheless, the simple transformations T_1 and T_2, abstracted from the topological theory, when applied to this hypothetical structure of B_9H_{15} lead to structures which do satisfy the valency rules. Hence, it is useful to examine transformations, such as T_1 and T_2, even in hypothetical structures which are clearly unsatisfactory. The resulting application of these transformations to B_9H_{15} yields a unique prediction for $B_9H_{13}R$, provided only that the one R of the original $B_{10}H_{12}R_2$ remains attached at B_1. Unfortunately, a unique prediction of the structure of the $B_9H_{12}R^-$ type of compound cannot be made, even with the reasonable assumption that R is on B_1 (Fig. 3), because a tautomeric transformation of the type shown between structures IV and V is possible by process T_2. If, however, the donation of an electron pair to the boron framework by the R group favors the formation of several BH_2 groups, then structure V would be favored, but one BH_2 group is, probably, already present and hence structure IV or even some intermediate geometrical structure between those shown as IV and V may occur. Thus, our knowledge of the extent to which BH_2 groups are favored by electron donation to a boron framework would be increased if a structural study of a salt of $B_9H_{12}R^-$ were carried out.

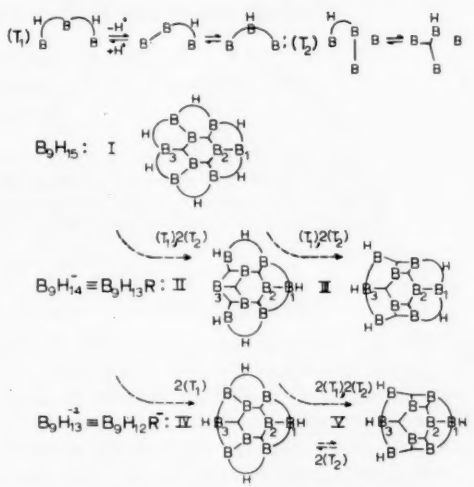

FIG. 3. Transformations T_1 and T_2 toward BH_2 groups in negative ions and amines, toward H bridges in neutral hydrides, and for transfer of protons around the periphery of a molecule or ion. The B_9H_{15} structure, which violates a topological rule, is purely hypothetical, and hence the curved arrows represent purely conceptual, but nevertheless useful, processes (not mechanisms) for predicting structures II, ···IV all of which satisfy the rules. Derivatives from $B_{10}H_{12}R_2$ have R attached at B_1, so that II is uniquely predicted for $B_9H_{13}R$, but III is also a possibility for $B_9H_{14}^-$. Likewise R is probably at B_1 in $B_9H_{12}R^-$, but structural possibilities are IV and V, related by process $2T_2$, or a stable intermediate between these two. Note that it is possible to place the two BH_2 groups of $B_9H_{13}^{-2}$ on any nonadjacent pair of B atoms, and hence corresponding $B_9H_{11}R_2$ derivatives may exist.

TABLE IV. Bond distances and standard deviations.

C_1C_2	1.426±0.011 A	Terminal hydrogens	
C_2N	1.126±0.008	B_1H_1	1.13±0.05 A
NB_1	1.507±0.010	B_2H_2	0.95±0.05
B_1B_2	1.731±0.011	B_3H_3	1.07±0.05
B_1B_5	1.865±0.006	$B_4H_4=B_{4'}H_{4'}$	1.18±0.03
B_2B_4	1.766±0.008	$B_5H_5=B_{5'}H_{5'}$	1.17±0.04
B_2H_5	1.745±0.007	$B_6H_6=B_{6'}H_{6'}$	1.10±0.04
B_3B_4	1.760±0.009	$B_6H_5=B_{6'}H_{5'}$	1.08±0.04
B_5B_6	1.842±0.008	Bridge hydrogen	
$B_4B_{4'}$	1.825±0.006	$B_5H_7=B_{5'}H_{7'}$	1.21±0.04
B_4B_5	1.785±0.011	$B_6H_7=B_{6'}H_{7'}$	1.35±0.04
B_4H_6	1.722±0.009	Methyl hydrogens	
B_3B_6	1.870±0.008	C_1H_9	1.09±0.04
		$C_1H_{10}=C_1H_{10'}$	0.84±0.08

Finally, it is not to be expected that the present form of the valence theory of boron hydrides is final, and hence a structural study of a $B_9H_{12}^-$ salt would be of great interest. Satisfactory structures are not so obvious for this ion, as they are for BiH_{12}^- ion, but two valence structures of topology 2621, both having the same atomic arrangement, have been found. Moreover, a structure, previously[6] overlooked, has been discovered for a B_9H_{13} having 2702 topology, its BH_2 groups in its mirror plane, and its boron arrangement like that in $B_9H_{13}(CH_3CN)$.

ACKNOWLEDGMENT

We wish to thank the office of Naval Research and the Office of Ordnance Research for support. We also thank Dr. M. F. Hawthorne for supplying us with the samples used in this study.

Refinement of the B_9H_{15} Structure and Test for Solid Solutions

PAUL G. SIMPSON AND WILLIAM N. LIPSCOMB
Department of Chemistry, Harvard University, Cambridge 38, Massachusetts

(Received March 13, 1961)

Refinement of the x-ray diffraction data for B_9H_{15} confirms the structure, establishes an x-ray criterion for crystal purity, and shows that the most difficult impurity to detect, namely, a possible B_8 hydride, is not present in amounts greater than about 5% or so. Taking all observations of the x-ray investigations together, we conclude that the B_9H_{15} single crystals were essentially pure.

INTRODUCTION

NO chemical analyses were possible for the B_9H_{15} samples on which the 374 independent x-ray diffraction maxima were obtained,[1,2] partly on account of the instability of the material, but also because these particular single crystals were very carefully grown over a period of hours from an impure melt. Some idea of the purity of the melt can be obtained from the $-19°$ to $-20°$ range of temperature over which about 20% of the sample was carefully formed into a single crystal. Assumption of an entropy of fusion of about 10 eu yields the result that the liquid was about 85 mole percent pure. An independent check of this percentage will become possible when the true melting point, as yet unknown, becomes available.

However, it is the purity of the crystal, not of the melt, which is relevant in this reinvestigation. Excluding H atoms, which contribute relatively little to the gross intensities, there are only 27 coordinates to be fixed, along with one thermal parameter for each of the 9 B atoms and a single over-all scale factor. Hence the problem is overdetermined by almost ten observations for each unknown, and the investigation of an additional parameter, such as the percentage of a likely impurity in the crystal, should yield at least the equivalent of a good chemical analysis of the crystal. Since an analysis of the percent composition of boron and hydrogen by current techniques cannot easily distinguish between the empirical formulas B_9H_{14}, B_9H_{15}, and B_9H_{16}, a determination by chemical means of the percentage of an impurity, such as B_8H_{14}, in a B_9H_{15} crystal is hopeless. We have carried out such an x-ray test of purity, and have further refined the structure of B_9H_{15} as described below.

X-RAY CRITERIA FOR PURITY

It seemed important from a structural chemical point of view to choose an impurity which would be chemically reasonable, and which would be the most difficult one to detect. Accordingly, a B_8 arrangement like that predicted[3] for all of the more stable B_8 hydrides was selected. This B_8 arrangement was allowed to coincide exactly with eight of the nine B atoms of B_9H_{15}. Moreover all of the H atoms of B_9H_{15} were allowed to remain in the structure. These last two assumptions have only the merit of simplicity, but they do render the test much more severe than it needs to be, since one cannot expect such exact coincidence for an impurity of slightly different shape, and since surely the hydrogen arrangements are somewhat different.

We now suggest the following criteria for comparison of models with different fractions of B_9 replaced by B_8. (1) Comparison of the values of

$$R_w=[\sum w(F_c^2-F_0^2)^2]^{\frac{1}{2}}(\sum wF_0^4)^{\frac{1}{2}},$$

where $w^{\frac{1}{2}}$ is inversely proportional to the assigned standard deviation[1] of the observed squared amplitude F_0^2. This criterion is most closely related to the sum of squares of residuals, minimized in the least-squares method. (2) Comparison of values of

$$R_F^2=\sum|F_0^2-F_c^2|/\sum F_0^2,$$

which is like the more usual criterion used in x-ray studies. (3) The number of reflections for which $F_c^2>2F_0^2$ or $F_c^2<\frac{1}{2}F_0^2$. (4) The behavior of the apparent mean-square amplitude of vibration of the one B atom (B_1) being replaced. (5) The residual electron density at the B atom (B_1) being replaced, in a three-dimensional electron density map from which the assumed structure is subtracted.

Before each of these criteria can be applied in a meaningful way, complete three-dimensional refinement to achieve the best possible fit of the observed data to each model, at each percentage of impurity, is required. Such a study was carried out, with results as summarized in Figs. 1–5, with one single isotropic temperature factor on each B atom and on each H atom. The refinement cycles using the full variance-covariance matrix converged very quickly, assuring us that the least-squares refinement was satisfactorily completed. The parameters that shift most markedly are the amplitude parameter of atom B_1 and the position and amplitude parameters of the two hydrogens directly bonded to it. As the form factor of atom B_1 is lowered the two hydrogens compensate by moving toward atom B_1 and lowering their apparent temperature factors until they

[1] R. E. Dickerson, P. J. Wheatley, P. A. Howell, W. N. Lipscomb, and R. Schaeffer, J. Chem. Phys. **25**, 606 (1956).
[2] R. E. Dickerson, P. J. Wheatley, P. A. Howell, and W. N. Lipscomb, J. Chem. Phys. **27**, 200 (1957).
[3] R. E. Dickerson and W. N. Lipscomb, J. Chem. Phys. **27**, 212 (1957).

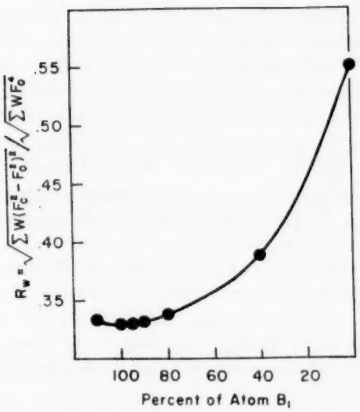

FIG. 1. Weighted reliability factors. All of the parameters were refined using individual isotropic temperature factors, and assuming the various percentages of boron atom 1. R_w values are 0.3324 at 110% of atom B_1, 0.3299 at 100%, 0.3301 at 95%, 0.3308 at 90%, 0.3386 at 80%, 0.3885 at 40%, and 0.5514 at 0%.

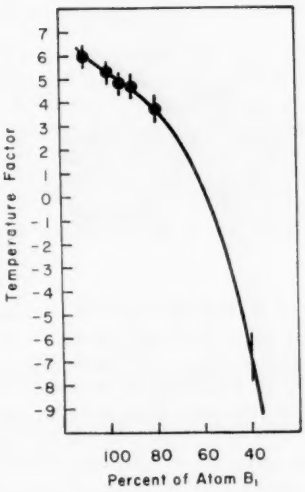

FIG. 3. Temperature factor of atom B_1. All of the parameters were refined using individual isotropic temperature factors, and assuming the various percentages of boron atom 1.

essentially coalesce when atom B_1 is completely removed. These compensations make the x-ray test very severe.

The best criterion is (1) (Fig. 1) essentially the weighted sum of squares of residuals which gives the purity as 99±3%, as described below. Criterion (5) (Fig. 4) is surprisingly insensitive, but the extremely low values of the residual electron density on the various difference maps at the location of B_1 illustrate the extent to which the apparent amplitude parameters and shifts in the position parameters have compensated for the impurity. This really is mainly a further verification that the least-squares refinement at each percentage of impurity has been satisfactorily completed. At 60% of impurity, corresponding to 40% of atom B_1, only 11% of one B atom shows up in this difference synthesis, because of this compensation. Best agreement is obtained for the pure crystal, but up to 30% of impurity is allowed if criterion (5) is used. Now criterion (4) is quite difficult to interpret in the absence of a complete rigid-body analysis of the thermal modes, not justified by our data. A reasonable value of 4.7±0.8 A^2 for the temperature factor constant B in the expression $\exp[-B\sin^2\theta/\lambda^2]$, was estimated by comparison of the values for the other atoms in the molecule (Fig. 5) in correlation with coordination number and hypothetical temperature-factor contours. According to criterion (4) the pure crystal is quite satisfactory, but this criterion does not distinguish up to 15 to 20% of impurity. Criterion (3) has the serious disadvantage of having a large intrinsic uncertainty, $\sigma=(npq)^{\frac{1}{2}}$, where p and q are probabilities of success and failure, respectively, in n trials. Because of this large standard deviation σ of the mean of successful events, we do con-

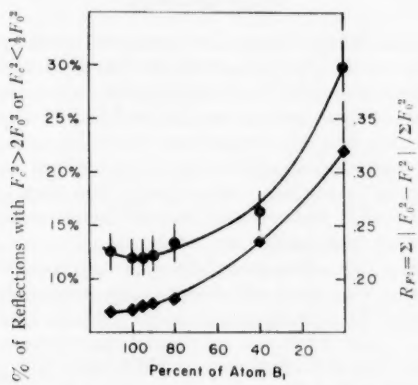

FIG. 2. R_{F^2} and percent of reflections with poor agreement. All of the parameters were refined using individual isotropic temperature factors, and assuming the various percentages of boron atom 1. The squares refer to R_{F^2} and the dots to the percentages.

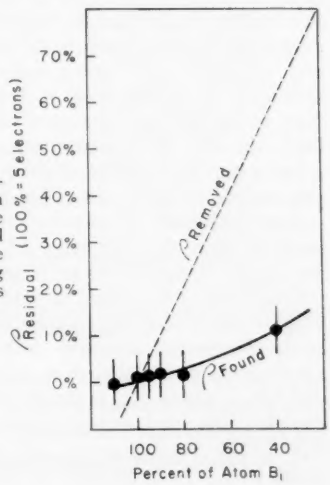

FIG. 4. Residual electron density at atom B_1. All parameters were refined using individual isotropic temperature factors, and assuming the various percentages of boron atom 1.

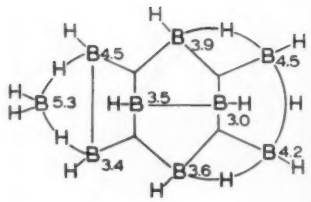

FIG. 5. Model of nonaborane showing individual temperature factors for the boron atoms. The temperature factors of the hydrogen atoms range between 11 and -6 A^2 using isotropic temperature factors for the boron atoms and 6 to -3 A^2 using anisotropic temperature factors on the B atoms. Atom B_1 is on the left.

sider it suggestive but not too significant that criterion (3) gives best agreement for 0 and 5% impurity, corresponding to 100 and 95% of B_1, respectively, in Fig. 2. Criterion (2) overemphasizes the large reflections, but does suggest better agreement for the lower percentages of impurity; in fact, the factor of 1.1 times the amplitude of scattering of atom B_1 gives even better agreement for criterion (2), but the dominating effect of the strong reflections causes us to doubt the significance of this detailed interpretation.

The basic difference between R_F^2 used in criterion (2) and R_w used in criterion (1) is the relative effect of strong and weak reflections. In

$$R_w=[\sum w(F_c^2-F_0^2)^2]^{\frac{1}{2}}/(\sum wF_0^4)^{\frac{1}{2}}$$

the weighting factors allow flexibility in the importance of strong and weak reflections while in

$$R_F^2=\sum|F_0^2-F_c^2|/\sum F_0^2$$

this effect is rigid, on the average proportional to F_0^2. Weighting factors $w=1/\sigma^2$ are introduced into R_w, which is minimized by least-squares refinement to take into account the standard deviation σ of the observed intensity F_0^2. If the standard deviations are taken to be proportional to the observed intensities F_0^2 then the relative effect of each reflection, strong or weak, is the same in determining the value of R_w. If, instead, constant absolute errors are assigned to all reflections the relative effect of a reflection will be on the average proportional to the square of its observed intensity F_0^4, and therefore the strong reflections will greatly dominate R_w. In the type of weighting scheme used here, an intermediate system of weights is chosen such that constant weights are assigned to all $F_0\leqslant F^*$, where a particular choice of F^* is justified below, and proportional weights are assigned to all $F_0>F^*$. In general, the final parameters will be somewhat dependent upon the particular F^* which a particular investigator assigns to his set of measurements.

Criterion (1) is devised to take the proper relative weights into account as follows. In the absence of directly determined standard deviations, constant absolute errors were assigned[4] to all reflections for which $F_0\leqslant 4F_{\min}$, where $F_{\min}$ is the lowest observed F in the complete list, and constant percentage errors were assigned to all F_0^2 for which $F_0\geqslant 4F_{\min}$. Both our methods of intensity measurements and comparison of final observed and calculated intensities in our earlier studies have led us to adopt a scheme of this kind as the best of the simple weighting procedures. Using these weighting factors criterion (1) gives best agreement for 99% purity, the value obtained from a plot of $\partial R_w/\partial(\%\text{ impurity})$, but is insensitive either way by about 3%. It should be noted that the position of the minimum is to some extent a function of the choice of F^*, here taken to be $4F_{\min}$. In summary of these last two statements regarding criterion (1), we feel that this is by far the best criterion, that it indicates that the crystal is pure B_9H_{15}, but that it is insensitive to impurities at least up to 3%, and probably up to about 5% or so.

[4] L. R. Lavine and W. N. Lipscomb, J. Chem. Phys. **22**, 614 (1954).

OTHER OBSERVATIONS RELATED TO CRYSTAL PURITY

We have no reason, on other grounds related to the x-ray data, to suspect even as much as 5% of impurity in the B_9H_{15} single crystals. The slow growth of the crystals, complete extinction in the polarizing microscope, the identity of relative x-ray intensities from several different single crystals grown from two different preparations, the absence of disorder streaks and diffuse reflections, the reasonable values of temperature factor constants ($B_B=3.9$ A^2 and $B_H=3.2$ A^2) in the original study,[2] the identity of peak heights of electron density, the low background of the three-dimensional map, the chemical reasonableness of the structure and the successful location of H atoms are all indications that no substantial amounts of impurity were present in the B_9H_{15} single crystals. The great sensitivity of the x-ray data to the details of the chemical structure is rather well illustrated by the rejection,[2] on the basis of the x-ray data alone, of a moleculer structure in which one H atom was misplaced by 1 A from its correct position.

FINAL RESULTS

No substantial changes have occurred in the molecular geometry of the B_9H_{15} molecule. The replacement of a single isotropic temperature factor for all B atoms and a single isotropic temperature factor for all H atoms by a separate isotropic temperature factor for each atom gives the results shown in Fig. 5. In addition a single parameter extinction correction in the form $F_0^2=F_c^2/(1+\alpha F_c^2)$ was averaged over the intense reflections to find the best value of the constant α.

A final three-dimensional-difference electron density map after refinement with isotropic temperature factors yielded no false peaks as high as one-half of a hydrogen atom, a result which is a substantial improvement over the previous difference map in which some false peaks were higher than H atom peaks.

The value of

$$R_F=\sum||F_0|-|F_c||/\sum|F_0|=0.155$$

of the previous study[2] has now been reduced to $R=0.124$ after refinement with isotropic temperature factors, and to $R=0.111$ after least-squares refinement in which anisotropic temperature parameters were introduced on the B atoms. The value of

$$r=\sum w(F_0^2-F_c^2)^2/\sum wF_0^4=0.134$$

of the previous study[2] was reduced to $r=0.109$ after isotropic refinement and $r=0.083$ after anisotropic refinement.

ACKNOWLEDGMENTS

All least-squares refinements were carried out with the use of W. R. Busing and H. A. Levy's program for the IBM 704, and the Fourier syntheses with use of W. G. Sly and D. P. Shoemaker's program. We wish to acknowledge support of this study by the Office of Naval Research and the Office of Ordnance Research. One of us (P.G.S.) wants to express his appreciation to the National Science Foundation for a graduate fellowship.

THE JOURNAL OF CHEMICAL PHYSICS VOLUME 35, NUMBER 4 OCTOBER, 1961

Effect of Pressure on the Low-Energy Absorption Peak of Several Phthalocyanines*

B. M. RIGGLEMAN AND H. G. DRICKAMER

Department of Chemistry and Chemical Engineering, University of Illinois, Urbana, Illinois

(Received March 20, 1961)

The effect of pressure has been measured on the intense low energy absorption peak in nine phthalocyanines in the solid state. In all cases the peak shifted to lower energies. The shifts were not large, but were very sensitive to the metal ion in the phthalocyanine. In general, the amount of shift was greater for ions having larger polarizability. The shift is attributed to perturbation of the excited π electron state due to dispersion interaction with metal ions in adjacent molecules.

THE effect of pressure has been measured on the low energy absorption peak of nine phthalocyanines. These include the metal-free material, and those containing Cu, Zu, Fe, Ni, Co, Cr, Sn, and Pb. The phthalocyanines were obtained from T. D. Smith of the E. I. duPont Company. The samples were run as very small crystallites diluted to 0.1% in NaCl because of the intense absorption of the peaks. The high-pressure optical system has been discussed elsewhere.[1,2]

The low energy absorption occurs always as a doublet, usually with one branch much more intense than the other. In the cases where the shifts of both parts of the doublet could be obtained they were essentially identical, as seen from the dotted curves in Fig. 1. The atmospheric-pressure-peak locations are shown in Table I.

Figure 1 shows the shift of six transition-metal ion phthalocyanines and the metal-free material to 50 kbar. Figure 2 shows shifts for the five compounds which could be measured to higher pressure. In every case a red shift is observed.

The transition is usually described as from the ground state to the first excited state of a π electron on the phthalocyanine ring, designated as $B_{1u}\rightarrow E_g$ by Basu.[3] The most striking result observed is that, while the pressure shifts are relatively modest, they are very sensitive to the metal ion involved.

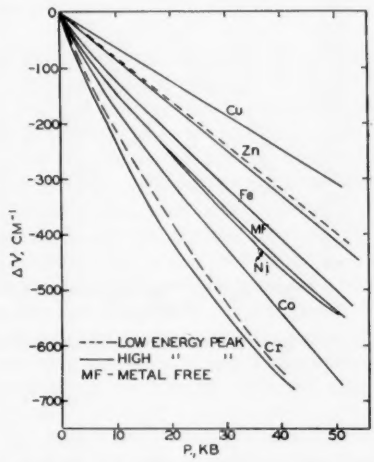

FIG. 1. Shift of peak vs pressure–low-pressure region–metal-free and transition metal phthalocyanines.

The phthalocyanine molecules crystallize in a parallel stack with adjacent stacks tilted with respect to each other.[4] It would seem reasonable to account for the red

* This work was supported in part by the U. S. Atomic Energy Commission.

[1] R. A. Fitch, T. E. Slykhouse, and H. G. Drickamer, J. Opt. Soc. Am. **47**, 1015 (1957).

[2] H. G. Drickamer, Rev. Sci. Instr. **32**, 212 (1961).

[3] S. Basu, Indian J. Phys. **37**, 511 (1954).

[4] J. Robertson, J. Chem. Soc. **1935**, 615.

TABLE I. Location of low energy peak at atmospheric pressure-phthalocyanines.

Phthalocyanines Metal free	ν_0 cm^{-1}
Cu^{++}	16 420
Zn^{++}	14 580
	15 900
Fe^{++}	15 200
Ni^{++}	16 330
Co^{++}	16 350
Cr^{++}	14 500
	15 950
Sn^{++}	13 920
Pb^{++}	14 050
Metal free	16 300

shift as a van der Waals' (dispersion) interaction between neighboring molecules, especially between the metal ion and the π electron states on the adjacent molecules. The excited state would consequently be lowered more in energy than the ground state.

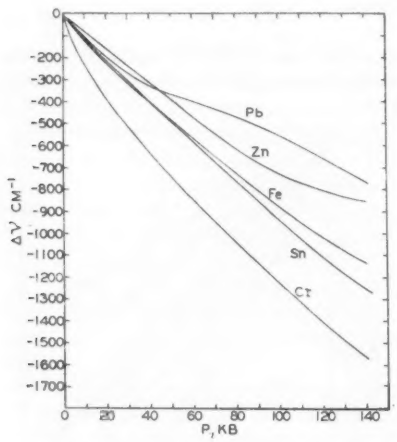

FIG. 2. Shift of peak vs pressure–compounds studied to 140 kbar.

Unfortunately, there are no very complete lists of polarizabilities for these plus-two ions. In any case, the polarizabilities of the ions in the phthalocyanine molecule need bear no quantitative relation to those of the free ion. However, Table II lists the molar refractions for four ions in aqueous solution.[5] The order is certainly qualitatively consistent with the shifts obtained in our work. Furthermore, it is reasonable that the Cr^{++} ion should be easily polarizable.

The reasons for the position of the metal-free phthalocyanine are not entirely clear cut. The H^+ ions have relatively low polarizability, but their small size may lead to a relatively large compressibility along the axis through the centers of the molecules.

Gutman[6] observed a slight red shift for phthalocyanine spectra with decreasing temperature. This is consistent with the red shift with increasing pressure observed in this work.

TABLE II. Molar refractions in aqueous solution.

Ion	Molar refraction cm^3/mole
Zn^{++}	0.29
Cu^{++}	0.39
Ni^{++}	0.67
Co^{++}	1.28

One further point of interest appears from the high-pressure data. The Pb^{++} and Sn^{++} phthalocyanines show nearly the same shift in the low-pressure region, which is not unreasonable. At higher pressures the Sn^{++} compound behaves in a manner consistent with the other phthalocyanines, but the shift levels off considerably in Pb^{++} phthalocyanines. The Pb^{++} ions have by far the largest ionic radius of any of the metals studied. It would appear that in the higher pressure region the compressibility along the axis through the centers of the molecules is limited by the size of the metal ion.

It should be noted that the peaks tended to broaden somewhat at high pressure, and the peak maximum lost intensity. There appeared, however, to be no significant change in total area under the curve.

[5] K. Fajana, Z. Physik **23,** 1 (1924).
[6] F. Gutman, J. Chem. Phys. **26,** 411 (1957).

Growth Rates of Zinc Crystals from the Vapor Phase

ROBERT L. PARKER* AND LAWRENCE M. KUSHNER
National Bureau of Standards, Washington 25, D. C.

(Received March 21, 1961)

The rate of growth of zinc crystals from the vapor phase has been studied as a function of the vapor supersaturation σ at a temperature of 390°C. The σ values ranged between 0.009 and 0.09. The rate R was found to vary approximately linearly with σ, permitting estimates to be made of the two parameters σ_1 and βC_0, appearing in the Burton, Cabrera, and Frank theory of crystal growth. The results indicate that surface nucleation was not operative in either the nucleation or the growth of these crystals.

INTRODUCTION

THERE are rather few quantitative measurements of the rate of growth of crystals from their vapor phase which enable one to determine the experimental parameters which occur in either the theory of surface nucleation[1] or in that of the screw dislocation model.[2] The former theory assumes that new layers must be started by the formation of two-dimensional nuclei on the surface of a completed layer, by spontaneous fluctuations in the surface density of adsorbed atoms ("adatoms"). A considerable vapor supersaturation is required to achieve such nucleation. The latter theory largely eliminates this nucleation barrier by the presence of a monatomic step on the crystal surface, due to the emergence of a screw dislocation there. The rate predictions of the two theories thus differ primarily at low supersaturations.

The work on polyatomic molecules, recently summarized by Bradley and Drury,[3] seems to favor the latter theory, but there are important discrepancies, as indicated by the work of Haward.[4] Furthermore, as Cabrera[5] has indicated, the theoretical calculations may not explicitly apply to growth by deposition of such molecules. The work of Hock and Neumann[6] on monatomic potassium vapor appears to be best described by the former theory, although this has been questioned by Sears.[7] Price's[8] study of cadmium crystals grown from the monatomic vapor but in the presence of a foreign gas, indicated that surface nucleation was operative in the nucleation of the crystals on a quartz substrate, but no nucleation barrier to their further growth was observed. More work on monatomic systems is necessary to help assess the quantitative validity of these theories.

In the present investigation, the growth rate of zinc crystals was studied as a function of the vapor supersaturation σ. This was done at low σ values, for the reason given above. Zinc was chosen because of its monatomic vapor,[9] its relatively high vapor pressure at convenient temperatures, and because of its availability in quite high purity (99.999+%).[10]

EXPERIMENTAL

The crystals are nucleated and grown in an evacuated, sealed Pyrex glass tube as shown in Fig. 1. The tungsten rod, sealed into one end of the tube, serves as a "cold tip" for nucleation and growth of the zinc crystals. The tube is prepared by sealing it with a Pyrex connecting tube, to a high vacuum system. After first outgassing the growth tube for 18 hr at 400°C, at a pressure of 1×10^{-6} mm Hg, an electric tubular furnace is placed over a portion of the connecting tube containing about 10 g of the zinc; this oven is then heated at 400°C until several grams of zinc metal distill into the cold growth tube. This distillation is also carried out at a residual gas pressure of 1×10^{-6} mm Hg, attained with a liquid nitrogen trap and an octoil-*S* diffusion pump. Then the growth tube is sealed off from the system. The tube thus prepared is placed in a strong temperature gradient so as to distill all the zinc into the end opposite the tungsten rod.

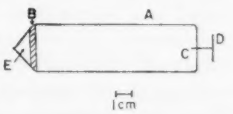

FIG. 1. Crystal growth vessel: A: Pyrex glass tube; B: zinc vapor source; C: 1-mm tungsten rod, sealed through Pyrex wall; D: nickel sheet 1.9 cm square, welded to tungsten rod; E: sealoff tip.

The rate measurements are performed by inserting the growth tube into the apparatus shown in Fig. 2. This arrangement provides for continuous weighing of the crystal as it grows in supersaturated vapor. To do

* This work is part of a thesis submitted in partial fulfillment of the requirements for the Ph.D. degree at the University of Maryland.

[1] R. Becker and W. Döring, Ann. Physik **24,** 719 (1935).

[2] W. K. Burton, N. Cabrera, and F. C. Frank, Trans. Roy. Soc. (London) **A243,** 299 (1951).

[3] R. S. Bradley and T. Drury, Trans. Faraday Soc. **55,** 1848 (1959).

[4] R. N. Haward, Trans. Faraday Soc. **35,** 1401 (1939).

[5] N. Cabrera, in *Growth and Perfection of Crystals*, edited by R. H. Doremus, B. W. Roberts, and D. Turnbull (John Wiley & Sons, Inc., New York, 1958), p. 324.

[6] F. Hock and K. Neumann, Z. phys. Chem. (Frankfurt) **2,** 241 (1954).

[7] G. W. Sears, J. Chem. Phys. **25,** 154 (1956).

[8] P. B. Price, Phil. Mag. **5,** 473 (1960).

[9] R. F. Barrow, P. G. Dodsworth, A. R. Downie, E. A. N. S. Jeffries, A. C. P. Pugh, F. J. Smith, and J. M. Swinstead, Trans. Faraday Soc. **51,** 1354 (1955).

[10] The zinc used was "Super Purity" Grade, from the New Jersey Zinc Company, New York, New York.

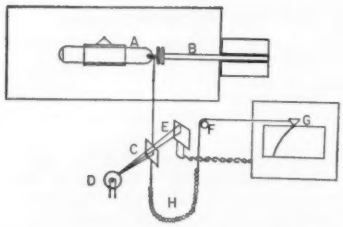

FIG. 2. Crystal growth apparatus: A: growth vessel; B: controlled heat leak; C: light-interrupting vane; D: light source; E: photocell; F: pulley for connecting wire; G: recorder pen; H: chain-weight.

this, the growth tube is mounted on a pivot above its center of gravity; as the crystal grows, the tube tilts. A fine wire leads vertically downward from the tube through the growth oven to a fine-link chain weight, as shown. As the tube tilts, the displacement of the wire is detected by the photocell system, which then, acting through an amplifier and servo-motor, adjusts the chain so as to rebalance the tube. The amount of chain-weight added is continuously recorded, and when calibrated gives the crystal weight versus time.

The proper temperature and supersaturation are provided by the large, well-controlled oven surrounding the growth tube. The entire tube, excepting the tungsten rod, is kept at a temperature T; the rod is maintained at a temperature $T_0 < T$ by the controlled heat leak shown. These temperatures are measured with calibrated chromel-alumel thermocouples, using a calibrated Leeds and Northrup type K-3 potentiometer. Since these thermocouples can not be in actual contact with the growth vessel without disturbing the weighing action, a temperature calibration run is necessary; additional thermocouples are placed firmly in contact with the growth vessel, enabling the necessary corrections to be made to the measured temperatures. The oven temperature fluctuations (in T) are limited to $\sim\pm 0.03$°C at 390°C. This degree of control is provided by a thermocouple-type controller, incorporating a dc potentiometer and low-drift amplifier detector. The over-all working accuracy for the difference $\Delta T = T - T_0$ is estimated to be $\sim\pm 0.1$°C.

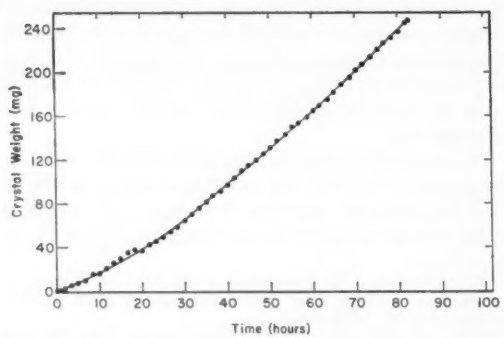

FIG. 3. Typical weight vs time curve, as obtained from apparatus in Fig. 2.

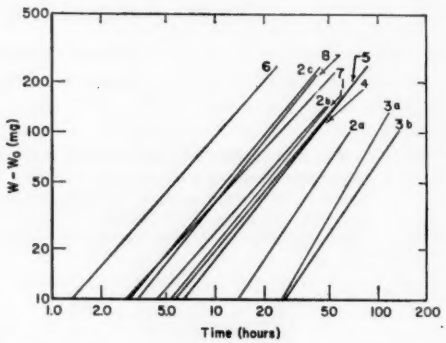

FIG. 4. Crystal weight vs time, log-log plots, for all growth runs.

The crystal is nucleated on the tungsten rod by gradually increasing ΔT from an initial negative value, to small positive values. Usually, the rate of increase is about 0.2°C in 8 hr. This slow rate of increase of supersaturation is necessary in order to prevent nucleation of many small crystals on the right-hand end of the tube. (Even with considerable care in this nucleation, growth occurred in several instances on the glass surface adjacent to the tungsten rod.) After nucleation occurs, as indicated by a weight increase, ΔT is adjusted to the desired value, and the weight versus time measurement proceeds, until a crystal weight of about 200 mg is achieved. The ΔT is then set equal to zero, and after cooling, the growth tube is removed. In order to perform the above experiment at various ΔT values, the crystal is evaporated back onto the source layer, and the above procedure repeated.

RESULTS

A typical weight versus time curve is given in Fig. 3, and in Fig. 4 are shown log-log plots of all the weight-time data, for various ΔT values. The temperatures, pressures, and supersaturations $\sigma = (p/p_0 - 1)$ for these experiments are given in Table I. Here p is the pressure

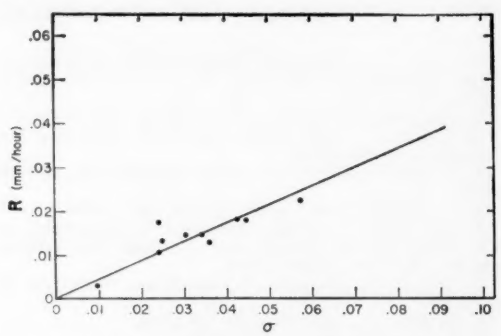

FIG. 5. Crystal growth rate R vs vapor supersaturation σ.

of the zinc vapor, and p_0 the equilibrium vapor pressure corresponding to the crystal temperature T_0. The vapor-pressure data for zinc were taken from Dushman.[11] The problem of converting a weight-time plot into a growth rate R (mm/hr) was attacked in the following way. Observing that the log-log plots are linear, one may write

$$W-W_0=at^n, \tag{1}$$

where W is the crystal weight in milligrams at time t, W_0 that at $t=0$, and determine a and n from the plot (Table II). Since the growth velocity R is a constant

TABLE I. Temperatures, pressures, and supersaturations in growth experiments.

Run No.	T, °C	ΔT,[a] °C	P,[b] μHg	ΔP, μHg	σ
1	390.4	0.9	59.69	1.81	0.031
2a	392.5	0.6_8	64.30	1.52	0.024
2b	392.3	0.9	63.86	2.06	0.033
2c	392.2	1.2	63.64	2.70	0.044
3a	394.0	0.6_7	67.79	1.59	0.024
3b	394.1	0.2_8	68.06	0.64	0.009
4	392.0	1.0	63.15	2.20	0.036
5	388.7	0.7	56.30	1.33	0.024
6	393.5	2.4	66.59	5.44	0.089
7	391.1	1.2	61.15	2.49	0.042
8	391.8	1.6	62.72	3.44	0.058

[a] A small correction due to crystal self-heating has been applied.
[b] The Knudsen flow correction was found to be negligible in this system.

in time in both the surface nucleation and the screw dislocation theories (for a given T and σ), one may write

$$dW/dt=R\rho A(t), \tag{2}$$

where ρ is the density of zinc, and $A(t)$ is the active surface area of the zinc crystal. Hence,

$$A(t)=kt^{n-1}, \tag{3}$$

where k is a constant. Except for curves 2b, 2c, and 3b, where the initial weight of the crystal is an appreciable part of the final weight, we require $A(t)=0$ at $t=0$, and to increase with time. A first estimate for k is obtained by assuming that the final crystal of weight W_f is in the form of a hemisphere, giving A_f, and hence

$$k=A_f/t_f^{n-1}, \tag{4}$$

and finally

$$R=na/\rho k. \tag{5}$$

Figure 5 presents the R values vs σ obtained in this way.

Probable contributions to inaccuracies in this method include the fact that the crystal is of course not hemispherical, but usually grows into the form of a truncated hexagonal pyramid of 10–20 mm² base area and 1–2 mm in height; and that at times, more than one nucleus is apparently formed, leading to a bi- or tri-crystal, with probable interactions between crystals of different orientation. Consequently, this method can be viewed as only giving an average growth velocity over the entire crystal surface; the primary growth mode clearly appears, however, to be the spreading of layers over the basal plane.

TABLE II. Values of n, a, and k.

Run No.	n	a	k	
1	1.20	1.306	15.5	
2a	1.47	0.207	2.46	
3a	1.72	0.038	0.883	
4	1.24	0.980	13.57	
5	1.19	1.250	15.81	
6	1.12	7.130	25.09	
7	1.06	3.326	27.20	
8	1.22	2.260	17.10	
a	n	a'	k	t_0
2b	1.11	1.923	20.6	19.2
2c	1.19	1.91	17.9	44
3b	1.44	0.036	2.46	277

[a] 2b, 2c, and 3b were treated by fitting $W=a'(t+t_0)^n$, hence $A=k(t+t_0)^{n-1}$, and k is determined as before, giving $R=na/\rho k$.

INTERPRETATION AND DISCUSSION

We first note that zinc crystals grow at supersaturations much less than the critical value $\sigma_c\approx 0.8$, which may be calculated for zinc from surface nucleation theory[12] as that supersaturation below which the growth rate drops essentially to zero ($\sim 1\mu$/month). Furthermore, the crystals nucleate onto the tungsten rod at $\sigma\approx 0.02$ to 0.03, which again is much lower than would be expected from surface nucleation theory.

The results of Fig. 5 may then be compared with the theory of Burton, Cabrera, and Frank. According to their rate expression,

$$R\approx\beta C_0 f(\sigma^2/\sigma_1)\tanh(\sigma_1/\sigma); \tag{6}$$

TABLE III. Experimental values of σ_1 and βC_0.

Reference	Substance	σ_1	βC_0
a	benzophenone	0.10	0.11 to 0.135
3	CBr_4 (cubic)	0.10	0.0075
	CBr_4 (monoclinic)	<0.0004	0.03 to 0.04
	I_2	0.10 to 0.135	0.29
Present	Zn	$\lesssim$0.009	0.08

[a] S. A. Kitchener and R. F. Strickland-Constable, Proc. Roy. Soc. (London) **A245**, 93 (1958).

[11] S. Dushman, *Vacuum Technique* (John Wiley & Sons, Inc., New York, 1949).

[12] G. W. Sears, Ann. N. Y. Acad. Sci. **65**, 388 (1957).

here $f=Mp_0/\rho N\phi$, $\phi=(2\pi mkT_0)^{\frac{1}{2}}$, where M = molecular weight of zinc, ρ = density, N = Avogadro's number, m = mass of one zinc atom, and k = Boltzmann's constant. R is proportional to σ^2 for $\sigma \ll \sigma_1$, and $R \propto \sigma$ for $\sigma \gg \sigma_1$. In the absence of any *a priori* knowledge of σ_1, the data in Fig. 5 were found to be best fitted by $R \propto \sigma$ and this is the line shown on this graph. This linear approximation is written

$$R=\beta C_0 f\sigma. \tag{7}$$

Hence, the quantity βC_0 can be found to be about 0.08, since f is known. Since no experiments were performed for $\sigma<0.009$, we can only set an upper limit to σ_1: $\sigma_1 \lesssim 0.009$. In Table III these values are compared with those obtained by two other investigators for polyatomic molecules; βC_0 and σ_1 are not available for the monatomic vapor studies of Price and of Hock and Neumann.

The quantity βC_0 obtained here is less than would be expected theoretically. It can be described as an over-all condensation coefficient. The quantity β may be written as the product of two factors β_1 and β_2 where $\beta=\beta_1\beta_2$ and where $0\leq\beta_1\leq 1$, $0\leq\beta_2\leq 1$. As Bradley and Drury[3] have pointed out, β_1 is the probability that an incoming atom adheres to the crystal surface at the time of collision from the vapor. This has recently been measured to be unity for zinc.[13] The second factor β_2 is less than unity if the exchange of atoms between the moving monatomic step on the crystal surface and the adsorbed "adatom" layer is not rapid enough to maintain zero "surface supersaturation" near the step. Burton, Cabrera, and Frank[2] stated that β_2 should probably be unity for monatomic substances; there appear to be no theoretical calculations of β_2. Finally, the factor C_0, $0\leq C_0\leq 1$, is less than unity if there is insufficient kink density in the step. An estimate of the kink density, following the method of Knacke and Stranski[14] for the calculation of the first- and second-neighbor energies, leads to one kink in about 20 lattice spacings along a step, which would imply $C_0\approx 1$.

Apart from these "condensation coefficient" factors, which are basically a measure of difficulties an atom might have in joining a step, there is the question of whether the step itself might be blocked or retarded in its motion, by impurities, for example. This situation was not considered in the theory of Burton, Cabrera, and Frank. Cabrera and Vermilyea[15] have given theoretical estimates for the decrease of step velocity for a given concentration of immobile adsorbed impurity centers in front of the moving step. The relative reduction in step velocity is

$$v/v_{\max}=(1-2r_cd^{\frac{1}{2}})^{\frac{1}{2}}, \tag{8}$$

where v is the step velocity in the presence of impurities, $v_{\max}$ is that without impurities, and d is the number/cm^2 of impurities just ahead of the step. The quantity r_c (the critical nucleus radius), is a measure of the maximum curvature a step may have for a given supersaturation, and is about 0.5×10^{-6} cm for $\sigma=0.09$; and about 0.5×10^{-5} cm at $\sigma=0.009$, in our experiments.

Of the three possible sources of impurities in the present experiments, namely, the residual gases at sealoff, impurities in the zinc source, and further outgassing of the Pyrex tube walls during the course of the experiments, simple estimates indicate that the first two can be neglected; the third appears more important. As Todd[16] has shown, even well-outgassed Pyrex will continue to give up water molecules by diffusion from the bulk of the material; this water is present in hydrated oxides in the glass. The volume V of water molecules emitted in a time t is

$$V=mt^{\frac{1}{2}}+s, \tag{9}$$

where s is the surface water (about one monolayer, removed completely in the initial outgassing). From Todd's "m" value for Pyrex at 390°C, one obtains under our outgassing and growth conditions about 13μg of water in the 1000 hr of operation. On the basis that these water molecules are apportioned uniformly in the total weight of zinc transferred during this time (about 5 g), one finds that the step velocity is probably not reduced more than 5% for $\sigma=0.09$, but may be significantly reduced at $\sigma=0.009$; the latter estimate requires, however, a more precise theoretical model than that given by the assumption of a regular "lattice" of surface-adsorbed impurities, as in the Cabrera-Vermilyea theory.

The present work thus supports the theory of Burton, Cabrera, and Frank, and has permitted estimates of the two theoretical parameters βC_0 and σ_1 for a monatomic system. No evidence of surface nucleation in either the nucleation of zinc on a foreign substrate, or in the further growth of the crystals, was found. In addition, the present work has indicated to what extent impurities might affect the observed parameters of the original theory.

[13] R. A. Rapp, J. P. Hirth, and G. M. Pound, J. Chem. Phys. **34**, 184 (1961).

[14] O. Knacke and I. N. Stranski, in *Progress in Metal Physics*, edited by B. Chalmers (Pergamon Press, New York, 1956), Vol. 6.

[15] N. Cabrera and D. Vermilyea, in *Growth and Perfection of Crystals*, edited by R. H. Doremus, B. W. Roberts, and D. Turnbull (John Wiley & Sons, Inc., New York, 1958).

[16] B. J. Todd, J. Appl. Phys. **26**, 1238 (1955).

Paramagnetic Resonance Spectra of Chromium III and Manganese IV Hexafluoride Ions: CrF_6^{3-} and MnF_6^{2-} * † ‡

LINDSAY HELMHOLZ, A. V. GUZZO, AND R. N. SANDERS
Chemistry Department, Washington University, St. Louis, Missouri

(Received March 15, 1961)

The paramagnetic resonance spectra of the ions CrF_6^{3-} and MnF_6^{2-} dilute solution in diamagnetic solids show fluorine hyperfine structure with both isotropic and anisotropic components. The anisotropic coupling constants are of the same order of magnitude as in the case of FeF_6^{3-}, but have the opposite sign indicating important contributions of π-bonding electrons. Accordingly, the previously estimated degree of σ bonding in FeF_6^{3-} is certainly too small, and estimates of the fluorine atomic orbital coefficients for the compound are made on the basis of the data presented here. The isotropic effects are to be understood in terms of configurational interactions. The isotropic coupling constants for the two ions have opposite signs and we are at present able to offer no rationalizations of this difference.

INTRODUCTION

THE paramagnetic resonance spectrum of the fluoroferrate ion FeF_6^{3-} in dilute solid solution has been discussed[1,2] in terms of the coefficients of the atomic orbitals making up the molecular orbitals occupied by the five unpaired electrons in this ion. This discussion led to the values of the coefficients of the individual fluorine $2s$ orbitals, $N_{e_g}^2a^2/3$, equal to 0.008 and for each of the fluorine p orbitals, $(N_{e_g}^2b^2/3 - N_{t_{2g}}^2c^2/4)$, equal to 0.035. In the expression for the p-orbital coefficient, the first term gives the $p\sigma$ contribution and the second the contribution of the $p\pi$ electrons. It has generally been assumed that $N_{e_g}^2$ and $N_{t_{2g}}^2$ have values close to unity and that $c^2/4$ is small compared to $b^2/3$, that is, σ bonding predominates. In order to investigate this latter point and to obtain some idea of the magnitude of the π-orbital contribution we have observed the spectra of CrF_6^{3-} and MnF_6^{2-} in dilute solid solution in K_2NaGaF_6 and Cs_2GeF_6, respectively. Each of these ions has three unpaired electrons, presumably in t_{2g} orbitals, and, if this is an exact description of the situation, $N_{e_g}^2a^2/3$ and $N_{e_g}^2b^2/3$ should be zero. The spectra indicate that the fluorine s contribution is not zero, but is much smaller than in the FeF_6^{3-} and that the anisotropic p contribution is of the same order of magnitude as FeF_6^{3-}. The sign of the p coupling constant, moreover, has been shown by Shulman and Knox[3] to be negative, whereas the value of A_p for FeF_6^{3-} is positive. Internal consistency of our data also indicates this difference in sign. This result indicates a considerable amount of π bonding, which in turn means the σ bonding in FeF_6^{3-} has been underestimated. Consequently, the extent of "covalency" must be considerable and assumptions mentioned above must be re-examined.

PROCEDURE

Solid solutions of CrF_6^{3-} and MnF_6^{2-} in the diamagnetic solids K_2NaGeF_6 and Cs_2GeF_6 were prepared by allowing concentrated HF solutions of the solvent solids with traces of the paramagnetic ions to evaporate slowly. This procedure yielded octahedra approximately 1–1.5 mm on an edge, with the cube faces more prominently developed in the case of the cesium salt. X-ray examination showed no evidence of deviation from the symmetry O_h for the environment of the chromium and manganese ions.[4] The metal to fluorine distances in these compounds are

Ga–F = 1.90 A (reference 4),
Ge–F = 1.77 A (reference 5),
Cr–F = 1.933 A (reference 3),
Mn–F = 1.74 A (reference 6).

The concentrations of paramagnetic ions were in the range of 1.0– to 0.1%.

The spectra were observed at 77°K or slightly below using the same techniques employed in reference 2.

The complex ions in the solid solvents used are all in parallel orientation. Figure 1 shows this orientation with respect to the crystal axes and the applied magnetic field; it is given by a single angular parameter α, the angle between the magnetic-field direction and the line between fluorine atoms 5 and 6. The rotation axis

* This work has been carried out with the assistance of the National Science Foundation.

† This report is abstracted from the theses submitted by A. V. Guzzo and R. N. Sanders in partial fulfillment of the requirements for the Degree of Doctor of Philosophy (A.V.G.) and Degree of Master of Arts (R.N.S.).

‡ Stanley Kirschner, "The paramagnetic resonance spectra of chromium III and manganese IV hexafluoride ions: CrF_6^{3-} and MnF_6^{2-}," from *Advances in the Chemistry of the Coordination Compounds*, (The Macmillan Company, New York, 1961).

[1] L. Helmholz, J. Chem. Phys. **31**, 172 (1959).

[2] L. Helmholz and A. V. Guzzo, J. Chem. Phys. **32**, 302 (1960).

[3] R. G. Shulman and K. Knox, Phys. Rev. Letters **4**, 603 (1960).

[4] A. V. Guzzo, thesis, Washington University, St. Louis, Missouri, 1960.

[5] J. L. Hoard and W. B. Vincent, J. Am. Chem. Soc. **61**, 2849 (1939).

[6] H. Bode and W. Wendt, Z. anorg. u. allgem. Chem. **269**, 165 (1952).

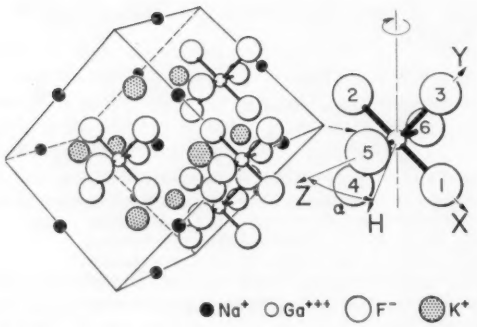

FIG. 1. A portion of the unit cell of K_2NaGaF_6 is shown with only the octahedra at the origin and three face centers. The octahedron at the right shows the central-atom coordinate system and the position of the axis of rotation of the crystal relative to the axes of the crystal and the octahedra. In the case of CrF_6^{3-}, it is assumed that the paramagnetic ion replaces the GaF_6^{3-} ion. The Cs_2GeF_6 structure is similar to this, differing only in that the sodium ions are absent and the potassium and GaF_6^{3-} ions are replaced by cesium and GeF_6^{2-} ions, respectively. The orientations are the same.

is taken in the $[\bar{1}10]$ direction referred to the axial system of the octahedron.

RESULTS

The spectra are shown in Figs. 2 and 3. They show anisotropic behavior but not such large fluorine hyperfine splittings as in the case of FeF_6^{3-}. The spectra can be accounted for on the basis of the energy levels of the following Hamiltonian:

$$\mathcal{H}=g\beta H\cdot S+A_s\sum_1^6 S\cdot I+A_p\{\sum_1^6 f_i(\alpha)\,S_zI_z$$

$$+f_i'(\alpha)\,S_zI_x+f_i''(\alpha)\,S_zI_y\}+B\sum_1^6 I_z,$$

to which a term $A_{s\mathrm{Mn}}S\cdot I_{\mathrm{Mn}}$ must be added for the MnF_6^{2-} case. The sums are taken over the six fluorine atoms. The last term gives the fluorine nuclear Zeeman energy. The coupling constants (A_s, A_p) have the same significance as in references 1 and 2, and the values of the $f(\alpha)$ are

$f(\alpha)=-\frac{1}{2}(3\cos^2\alpha-1)$	for atom	1–4
$f(\alpha)=+(3\cos^2\alpha-1)$		5–6
$f'(\alpha)=-\frac{3}{2}\sin\alpha$		1–2
$f'(\alpha)=+\frac{3}{2}\sin\alpha$		3–4
$f'(\alpha)=0$		5–6
$f''(\alpha)=-\frac{3}{2}\sin\alpha\cos\alpha$		1–2
$f''(\alpha)=-\frac{3}{2}\sin\alpha\cos\alpha$		3–4
$f''(\alpha)=-3\sin\alpha\cos\alpha$		5–6.

The magnetic axes for this evaluation of the function $f(\alpha)$ have been chosen with z along the field direction, x along the axis of rotation, and y perpendicular to these directions.

DISCUSSION OF THE SPECTRA

CrF_6^{3-}

For this case the [100] spectrum, which should be relatively simple since $f'(\alpha)$ and $f''(\alpha)$ are zero, is not particularly helpful since the resolution is very poor even at 77°K. Contributing to this difficulty is the fact that the $S=\frac{3}{2}\rightarrow S=\frac{1}{2}$ absorptions fall on top of the $S=-\frac{1}{2}\rightarrow S=\frac{1}{2}$ lines and are considerably less well resolved. It seems to be the case that the relaxation time for this particular orientation is shorter than for the other directions observed.

Using the [111] spectrum as a starting point, two sets of parameters appear to be possibilities: (1) $A_p=\pm6.7$, $A_s=\mp7.2$; (2) $A_p=\pm4.0$, $A_s=\pm1$. In order to decide between these, the derivative curves were calculated for the spectra in the three principal directions. Gaussian line shapes were used as is suggested by the FeF_6^{3-} spectra.[7] The comparison of the [100] spectra for the two possibilities leaves little doubt that the second set is the proper choice. The parameters were refined by adjusting them to give a reasonable fit between observed and calculated derivative curves for the [110] and [111] spectra. (Shown in Fig. 4.) The experimental data are not very satisfactory and we have not attempted to obtain a closer fit by varying the values of A_s and A_p and the Gaussian half-widths, but have attributed rather large limits of error to the parameters. The final "best" values are

$$A_s=\pm1.1\pm0.5$$

$$A_p=\pm4.5\pm1.0.$$

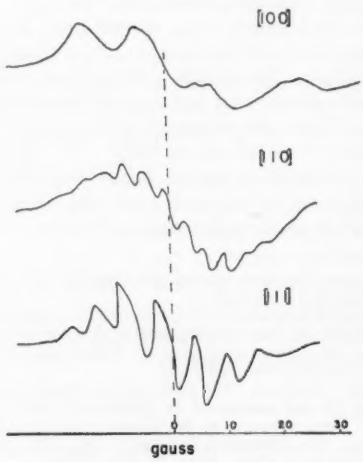

FIG. 2. The derivative curves for CrF_6^{3-} dissolved in K_2NaGaF_6 with the magnetic field in the indicated directions.

[7] S. Geschwind, Bell Telephone Laboratories (private communication).

MnF_6^{2-}

In this case, the [100] spectrum shows the best resolution and may be accounted for by the assumptions (1) $A_s=\pm 15 A_p=0$, or (2) $A_p=\pm 10 A_s=\mp 5$. The possibility, so far as positions of lines are concerned, $A_s=20A_p=5$, can be eliminated by intensity considerations. The overlaping of the spectra for the various values of I_{Mn} causes some trouble but the peaks at the extreme ends of the spectrum show the seven lines expected and the intensity relationships (the same for either choice) are qualitatively what is predicted. The choice between the two sets can be made readily from a consideration of the [111] spectrum which shows about twice as many lines as are observed when the magnetic field is in the [100] direction. The values $A_s=15$, $A_p=0$ are ruled out by this observation since they should give a spectrum identical with the [100] spectrum. The parameters were refined by adjusting them to give a better fit with the experimental line positions and intensities. The final values are

$$A_p=\mp 9.5\pm 1.0,$$

$$A_s=\pm 5.5\pm 1.0,$$

$$A_{sMn}=77.0\pm 1.0.$$

The improved resolution, observed in Fig. 3 with decreasing value of I_{Mn}, is caused by the second-order terms of the $S\cdot I_{Mn}$ term in the Hamiltonian. This results in a displacement of the $\frac{3}{2}\rightarrow\frac{1}{2}$ and $-\frac{1}{2}\rightarrow\frac{1}{2}$ spectra relative to one another by amounts which increase with I_{Mn}.

DISCUSSION OF RESULTS

CrF_6^{3-}

A discussion of the significance of these results depends on a decision as to the sign of the coupling constants, which can be obtained only indirectly from these data. Fortunately, the fluorine nuclear resonance in K_2NaCrF_6 has been investigated by Shulman and

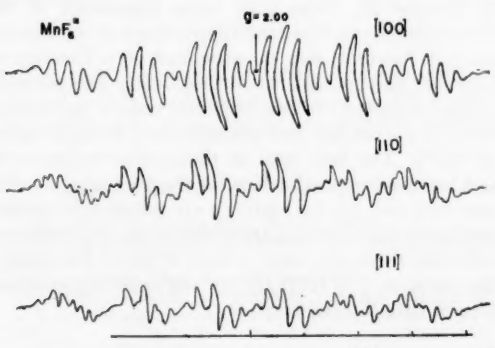

FIG. 3. The derivative curves for MnF_6^{2-} dissolved in Cs_2GeF_6 with the magnetic field in the indicated directions.

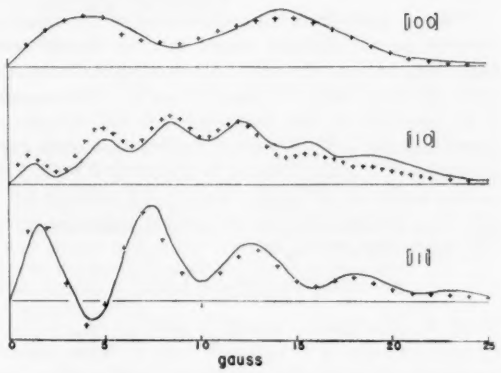

FIG. 4. The calculated and observed derivative curves for CrF_6^{3-}. The solid curves indicate the observed values and the crosses the calculated values of the derivatives at 1-gauss intervals for [100] and [111] and at 0.5-gauss intervals for the [110] spectra.

Knox[3] who find the values $A_\sigma-A_\pi=-7.2\pm 1.2$ and $A_s=-1.0\pm 0.5$. This value of $A_\sigma-A_\pi=-7.2$ does not include the direct dipolar interaction term, the last term in Eq. (1) below. If the value -7.2 is adjusted by the addition of this term, using our values for C and $N_{t_{2g}}^2$, the value of Shulman and Knox for the constant A_p is -4.3, to be compared with our value of -4.5. This agreement is well within the limits of error of our experiment and calculations.

Internal consistency of our data leads to a negative sign of A_p by the following argument: If A_p for the chromium salt were positive its value would be very closely equal to the direct dipolar contribution, the effect of the unpaired electrons on the central atom, and one would anticipate an increase of at most of 30% in going from CrF_6^{3-} to MnF_6^{2-}, whereas the effect of increased π overlap would tend to decrease this difference so that the overall effect would be a small one or perhaps even a decrease in the absolute value of A_p. The fact that the magnitude of A_p is more than twice as large for manganese as for chromium salt would thus be difficult to explain if the values were positive. We have consequently chosen the negative signs for A_p in the cases of both ions.

We have no simple explanation for the fact that the A_s parameters have opposite signs. That these quantities are not zero, as required by the simple molecular-orbital considerations, means that they result in all probability from contributions of higher-lying states through configurational interaction, and it is difficult to predict what these effects should be.

Assuming that the effect of configurational interaction on the molecular-orbital coefficients is small, the expression for A_p is

$$A_p=\tfrac{2}{5}\mu_N/3I_N\{-N_{t_{2g}}{}^2C^2/4\}\langle 1/r^3\rangle F_{2p}$$
$$+(\mu_N/I_N)C\cdot N_{t_{2g}}{}^2. \quad (1)$$

The first term gives the contribution of the unpaired electron on the fluorine atoms and the second term takes into account the direct interaction of the central atom electrons with the fluorine nuclei. The quantity C is discussed in the Appendix and has a value of approximately $0.75/R^3$ for the cases discussed here. The value of $N_{t_{2g}}$ is estimated by assuming it to be 1.00, with a value of the group overlap 0.1, solving for c, and then finding $N_{t_{2g}}$ by successive approximations. The expression for $N_{t_{2g}}$ is

$$N_{t_{2g}}=1/(1+c^2-2cG)^{\frac{1}{2}},$$

where G (the group overlap integral) $=\int d_{xy}\cdot\frac{1}{2}c(\pi_y{}^1-\pi_y{}^2+\pi_x{}^3-\pi_x{}^4)\,d\tau$. It is assumed, also, in these calculations that the molecular orbitals are antibonding. The values obtained are

CrF_6^{3-}	$N_{t_{2g}}{}^2(-c^2/4)$	$=-0.06\pm0.01$,
	$N_{t_{2g}}{}^2$	$=0.875$,
MnF_6^{2-}	$N_{t_{2g}}{}^2(-c^2/4)$	$=-0.095\pm0.01$,
	$N_{t_{2g}}{}^2$	$=0.735$,
FeF_6^{3-}	$N_{t_{2g}}{}^2(-c^2/4)$	$=-0.04\pm01$ (estimated),
	$N_{e_g}{}^2(+b^2/3)$	$=0.076$.

The value of $N_{t_{2g}}{}^2c^2/4$ for FeF_6^{3-} is estimated from the trend with bond distance and central atom charge and may be in error by 50%. Since the values of $N_{t_{2g}}{}^2$ are derived on the basis of the assumptions mentioned, limits of error for these quantities would have no real significance.

The values of the orbital coefficients are, at best, only of qualitative significance. The present data do not permit accurate determination of the parameters and, further, the nonzero values of A_s and $A_{s\,\mathrm{Mn}}$ indicate that configurational interaction must be important. It is difficult to say how this latter effect would influence the coupling constants A_p; but because of the qualitative correspondence between the experimental facts and the conclusions drawn from the simple molecular-orbital scheme, we are inclined to attribute no more than 20% of the magnitudes of the A_p's to this configurational interaction.

The relatively great importance of σ and π bonding in these fluoride complexes, indicated by our results, suggests that the energy separation of the antibonding eg and t_{2g} orbitals may be influenced to a considerable extent by the type of bonding. This energy difference is important, in turn, in the determination of the multiplicity of the ground states of complex ions of the transition elements, for example, the sextet state for FeF_6^{3-} and the doublet for $Fe(CN)_6^{3-}$. If the π bonding is limited for some reason—as in the cyanides because the π orbitals are already used, or as in the heavier elements because of increased interatomic distances—then the antibonding t_{2g} orbital may be an almost pure d function and have a lower energy than in the case strong π bonds are formed by the lower lying $d-\pi$ combination. The $eg-t_{2g}$ energy separation will then be larger, favoring the pairing of the valence electrons.

APPENDIX

The value of the direct dipolar interaction, the magnetic interaction of the electrons located on the central atom with the fluorine nuclei can be written in terms of the functions of α, $f(\alpha)$, $f'(\alpha)$, and $f''(\alpha)$ and the coordinates of the electron on the central atom, and R the interatomic distance. After integration over the central-atom φ coordinate, the expression becomes

$$f(\alpha)/(r')^3\{1-\tfrac{3}{2}(r/r')^2\sin^2\theta\},$$

when r is the distance from the central atom to the electron, and r' the distance from that electron to the fluorine nucleus in question. The angle θ is the angle between r and the line between the central atom and the fluorine atom being considered, and R the $X-F$ distance

$$(r')^2=(r^2+R^2-2rR\cos\theta).$$

What is desired, the quantity C of Eq. (1), is the function $f(\alpha)/(r')^3\{1-\frac{3}{2}(r/r')^2\sin^2\theta\}$ averaged over the central-atom d functions. The $f(\alpha)$ depends only on the angle of orientation of the crystal. The remainder of the expression is

$$\begin{aligned}(1/r'^3)\{1-\tfrac{3}{2}(r/r')\sin^2\theta\}&=(1/2r^3)(\partial^2/\partial h_1{}^2)\\&\quad\times\{1+(R/r)^2-(2R/r)\cos\theta\}^{-\frac{1}{2}}\\&=(1/2r^3)(\partial^2/\partial h_1{}^3)\{r/R\}\{1+(r/R)^2-2(r/R)\cos\theta\}^{-\frac{1}{2}},\end{aligned}\tag{2}$$

when $h_1=(R/r)$ and $h=(r/R)$. The second derivatives of the terms in brackets give series in h_1 and h with Legendre polynomials as coefficients. When multiplied by $\frac{1}{2}r^3=h_1{}^3/R^3$, these give series expansions of the desired functions. Since the θ dependence of the central-atom d functions can be expressed as a function of Legendre polynomials, the orthogonality and normalization properties of these functions reduce the calculations to a relatively few evaluations of average values of $(1/r^3)$. The first term in these series is just $1/R^3$ and is a good approximation for the Fe^{3+} case. For the case that only the $3d_{t_{2g}}$ orbitals are occupied, a calculation using orbitals which approximate the self-consistent field orbitals gives a value of $0.75/R^3$ for C. For FeF_6^{3-}, the value of C is $0.975/R^3$ for the same approximate type of radical wave function.

Quadrupole Coupling in Lithium Nitrate†

DAVID H. ANDERSON
Sandia Laboratory, Albuquerque, New Mexico

(Received March 6, 1961)

The value of the Li^7 quadrupole coupling constant in a single crystal of $LiNO_3$ has been found to be 35.5 ± 0.2 kc. It is expected that a reliable estimate of the quadrupole moment of Li^7 may be made with the observed coupling constant and the point-charge field gradient, because of the good agreement for Na^{23} in the case of the isomorphous crystal $NaNO_3$. The value found in this manner is ±0.069 b. The $LiNO_3$ crystal was γ irradiated to facilitate the measurements, and a γ-irradiated crystal of $NaNO_3$ was studied for comparison. It appears that the broadening of the Na^{23} satellite lines in the irradiated $NaNO_3$ results from a relaxation process and not from a wide distribution of static field gradients, and it is concluded that γ irradiation has little or no effect on the Li^7 coupling constant in $LiNO_3$. A precise knowledge of the Li^7 quadrupole moment would provide a test of the ionic model in $LiNO_3$.

INTRODUCTION

THE main objective of this paper is to attempt to estimate the nuclear electric quadrupole moment of Li^7 by a solid-state technique. The crystal studied was $LiNO_3$, which was chosen because of Bersohn's[1] apparent success in calculating the electric field gradient at the Na position in the isomorphous crystal $NaNO_3$. This calculation was based on an ionic model, which we will apply to $LiNO_3$. Similar ionic models have also been used by Bernheim and Gutowsky[2] to account for the pressure dependence of the Na^{23} quadrupole coupling in $NaNO_3$, and by Hewitt[3] who applied an extended ionic model to the magnitude and temperature dependence of the Nb^{93} quadrupole coupling in $KNbO_3$.

Previous attempts to arrive at the quadrupole moment of Li^7 using the known coupling constant of Li_2 and calculating the field gradient have been unsuccessful. The main reason is that the contribution of the nuclear charge to the field gradient is almost exactly canceled by the electron contribution. Thus, the magnitude and even the sign of the field gradient are uncertain.[4,5] It is hoped that this work will lead to a more reliable value of the quadrupole moment of Li^7, and, in addition, add information which will be of assistance in furthering our understanding of field gradients in ionic crystals.

THEORY

The crystal structure of $LiNO_3$ is isomorphous with that of $NaNO_3$,[6] and since the spin of Li^7 is $\frac{3}{2}$ we expect the quadrupole interaction to be completely analogous to the case of Na^{23} in $NaNO_3$, which was first studied by Pound.[7] (This assumes that the energy of the quadrupole interaction is much less than the Zeeman energy which proves to be the case.) In this case, with the symmetry axis of the crystal oriented at an angle θ to the magnetic field H_0 we therefore expect a three-line pattern consisting of a main center line at the normal frequency $\mu H_0/Ih$ plus two satellites given by

$$\nu_\pm=(\mu H_0/Ih)\pm(1/4h)e^2qQ(3\cos^2\theta-1). \quad (1)$$

In Eq. (1), μ, I, and Q are, respectively, the magnetic dipole moment, spin and electric quadrupole moment of the nucleus in question. Consequently, to obtain the coupling constant (e^2qQ/h) we merely measure the maximum separation between the satellites when H_0 is in the plane of the symmetry axis.

Having the coupling constant we then calculate the field gradient q which is, by convention, the zz component. To do this we use a point-charge model of the crystalline lattice and calculate the field gradient by direct summation.[1] Evaluation of the series was carried out on the Sandia Laboratory IBM 704 computer.[8]

Thus far we have not considered the effect of forces which polarize the electron charge cloud surrounding the nucleus, first discussed by Sternheimer and coworkers.[9] In the free ion the nucleus is usually "antishielded" due to the polarizing forces of the ionic charge and the nuclear quadrupole moment. In a solid the amount of "antishielding" may differ from the free-ion value due to the polarizing effects of external charges. Therefore to relate the experimental coupling constant $(\Delta\nu_{zz})$ to the field gradient we write

$$(e^2q/h)(1-\gamma_\infty)Q=\Delta\nu_{zz}. \quad (2)$$

Numerous papers have shown the importance of the antishielding factor $(1-\gamma_\infty)$ in quadrupole coupling. Although, at this time, it does not seem to be *generally*

† Work performed under the auspices of the U. S. Atomic Energy Commission.

[1] R. Bersohn, J. Chem. Phys. **29**, 326 (1958).
[2] R. A. Bernheim and H. S. Gutowsky, J. Chem. Phys. **32**, 1072 (1960).
[3] R. R. Hewitt, Phys. Rev. **121**, 45 (1961).
[4] E. G. Harris and M. A. Melkanoff, Phys. Rev. **90**, 585 (1953).
[5] R. M. Sternheimer and H. M. Foley, Phys. Rev. **92**, 1460 (1953).
[6] R. W. G. Wyckoff, *Crystal Structures* (Interscience Publishers, Inc., New York, 1957).
[7] R. V. Pound, Phys. Rev. **79**, 685 (1950).
[8] We are indebted to R. Bersohn for providing the IBM 704 program.
[9] See for example, R. M. Sternheimer and H. M. Foley, Phys. Rev. **102**, 731 (1956), and references cited therein.

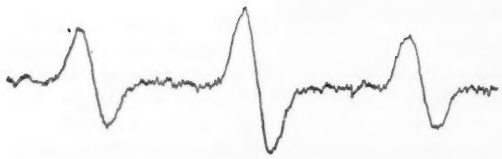

FIG. 1. The first derivative of the Li^7 resonance absorption in γ-irradiated $LiNO_3$ with H_0 approximately parallel to the hexagonal crystal axis. The lines are shown as a function of field with high field to the right and are slightly saturated.

valid to apply antishielding values, which are calculated from free-atom wave functions, to the consideration of quadrupole coupling in solids, it does seem apparent from recent work involving ultrasonic techniques[10,11] as well as the results of field gradient calculations,[3,12,13] that one can expect fairly good agreement between calculated and observed antishielding factors for positive ions. (For the smaller positive ions one might expect even better agreement because of low polarizabilities and the availability of more accurate wave functions.) For our specific application, if the calculated and observed $(1-\gamma_\infty)$ factors agree for Na^{23} in the case of $NaNO_3$, then we would expect similar agreement in the isomorphous $LiNO_3$ for Li^7. We actually obtain better agreement than Bersohn[1] due to a newer value[14] ($Q=+0.087\pm0.010$ b) of the quadrupole moment of Na^{23}. If we assume with Bersohn that the effective charge on the nitrogen atom is zero (this will be discussed later), use the calculated field gradient,[1] and the above value of the quadrupole moment, we find $(1-\gamma_\infty)_{\text{exp}}=5.52$ for Na^+ in $NaNO_3$. The agreement between this value and the calculated values of Das and Bersohn[15] (5.53), Sternheimer[16] (5.56), and Burns[17] (5.65) is very good. If this agreement is other than fortuitous, then we would expect the theoretical value of $(1-\gamma_\infty)$ for Li^+ to be applicable to Li^7 in $LiNO_3$.

EXPERIMENTAL PROCEDURE AND RESULTS

Our attempts at growing a single crystal of $LiNO_3$ from aqueous solution[7] at 65° were unsuccessful largely because of the difficulty of controlling the degree of supersaturation. Since $LiNO_3$ forms no methyl alcoholate[18] we tried growing the crystal from CH_3OH at room temperature but again failed. However, using reagent-grade $LiNO_3$ and absolute C_2H_5OH we isolated a single crystal about $1\times1\times0.5$ cm in size. This crystal was used for the coupling constant determination. (X-ray analysis gave the expected cell constants of $LiNO_3$.[19]) The $NaNO_3$ crystal used in the radiation studies, which will be discussed below, was grown from the melt and obtained from the Harshaw Chemical Company.

The nuclear magnetic resonance apparatus consisted of a Varian Associates wide-line rf unit (operated at about 16 Mc for the Li^7 spectra and about 11 Mc for Na^{23}), 12-in. electromagnet, and regulated power supply. Frequency measurements were made with a Hewlett-Packard 524-C frequency counter, having a stated accuracy of 5 parts in 10^8. To make the angular measurements the crystal was fastened to a rod which was concentric with an angular scale. The scale was attached to the top of the cross-coil probe and an indicator fixed to the rod. Thus, after aligning the crystal with respect to the indicator, angle readings could be made directly from the indicator and scale.

Our first measurements on the $LiNO_3$ crystal showed the long relaxation time observed previously.[7] This factor and the rather small size of the crystal prevented us from getting sufficiently good signal to noise ratios for accurate measurements. Irradiation had been used previously to reduce spin lattice relaxation times,[20,21] and therefore we exposed the $LiNO_3$ to approximately 5×10^8 rad of 1-Mev gamma rays. Figure 1 shows an example of a spectrum taken shortly after irradiation. (The signal was more and more easily saturated as the period from its irradiation time increased.) The peak-to-peak linewidth of the satellites and central line was about 3 kc ($\sim$1.8 gauss). Figure 2 shows the angular dependence of the satellite-satellite separation. Alignment was achieved by using the fact that the maximum separation was obtained when H_0 was parallel to the symmetry axis. From these measurements we found[22] $\Delta\nu_{zz}=35.5\pm0.2$ kc and $\Delta\nu_{xz}=\Delta\nu_{yy}=\Delta\nu_{zz}/2$.

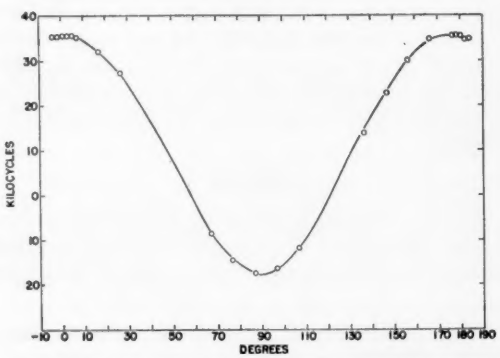

FIG. 2. The dependence of the Li^7 satellite-satellite separation in γ-irradiated $LiNO_3$ as a function of the angle (θ) between the crystal symmetry (Z) axis and the applied magnetic field (H_0).

[10] D. A. Jennings, W. H. Tantilla, and O. Kraus, Phys. Rev. **109**, 1059 (1958).
[11] D. S. Bolef and M. Menes, Phys. Rev. **114**, 1441 (1959).
[12] G. Burns, Phys. Rev. **115**, 357 (1959).
[13] E. G. Wilkner and T. P. Das, Phys. Rev. **109**, 360 (1958).
[14] See the discussion in reference 2.
[15] T. P. Das and R. Bersohn, Phys. Rev. **104**, 733 (1956).
[16] R. M. Sternheimer, Phys. Rev. **115**, 1198 (1959).
[17] G. Burns, J. Chem. Phys. **31**, 1253 (1959).
[18] M. M. Markowitz and R. Harris, J. Phys. Chem. **64**, 670 (1960).
[19] *Standard X-Ray Diffraction Powder Patterns*, National Bureau of Standards Circ. No. 539 (U. S. Dept. of Commerce, National Bureau of Standards, Washington, D. C.), Vol. 7.
[20] R. V. Pound, Phys. Rev. **81**, 156 (1951).
[21] J. F. Hon and P. J. Bray, Phys. Rev. **110**, 624 (1958).
[22] The coupling constant is about 10% smaller than that inferred from a powder pattern in reference 21.

Since the $LiNO_3$ crystal was irradiated prior to observation, we were interested in the specific effect that the radiation would produce on the observed spectra and in particular whether there would be any change of the quadrupole coupling constant. Not having a good nonirradiated crystal of $LiNO_3$ for comparison, we felt the next best substance would be $NaNO_3$. Before irradiation, we obtained the same results as Pound[7] and Eades *et al.*[23]; we found $\Delta\nu_{zz}=334.3\pm0.7$ kc, and the peak-to-peak linewidth of the components about 1.6 kc. By considerations similar to those of Andrew and Swanson[24] we found the Na^{23} relaxation in the $NaNO_3$ crystal to be quadrupolar (as expected), and the Li^7 relaxation in the γ-irradiated $LiNO_3$ crystal to be magnetic dipolar in origin. After irradiation to 5×10^8 rad (approximately 1-Mev γ rays) we obtained the spectrum shown in Fig. 3. (Only one satellite and the central component are shown; the other satellite was symmetrically placed.) The central line as shown is modulation broadened, but was observed to have approximately the same width as before irradiation. The satellites were much broader and weaker, the peak-to-peak linewidth being about 23 kc ($\sim$20 gauss), although broadened somewhat by the large modulation amplitudes utilized for observation. Using the crossover point of the derivative curves of the satellites for the measurement of the maximum separation we found $\Delta\nu_{zz}=339\pm2$ kc. In general, the line shapes of the satellites seemed to be rather asymmetric.

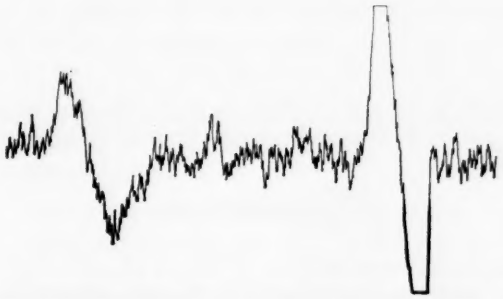

FIG. 3. The first derivative of the central line and one satellite from the Na^{23} resonance absorption in γ-irradiated $NaNO_3$. The lines, shown as a function of field with high field to the right, are modulation broadened and obtained at the position of maximum separation.

DISCUSSION AND CONCLUSIONS

First let us consider why the Na^{23} satellites are so broad in the γ-irradiated $NaNO_3$ crystal. Since the important defects are apparently NO_2 or NO_3 molecules and possibly F centers,[25] the breadth of the irradiated satellites might be ascribed to a wide distribution of static field gradients arising through both the charge and size effect.[26] Assuming that essentially the same defects are produced in γ-irradiated $LiNO_3$, this seems unlikely because then the irradiated $LiNO_3$ satellites would be expected to have a corresponding breadth. (The observed 3-kc width is about that expected from dipole-dipole interactions, but it is possible that radiation annealing is more important in $LiNO_3$ than $NaNO_3$.[27]) Since the $NaNO_3$ crystal has a quadrupolar relaxation mechanism and $LiNO_3$, magnetic dipolar, it seems probable that the Na^{23} satellite broadening is caused by the quadrupolar relaxation mechanism rather than the static field gradient distribution. Here, it may be the case that the diffusion of defects, which are introduced by the γ irradiation, may cause lifetime broadening of the satellites through the quadrupolar interaction.[28] The effect of the diffusion of defects should become small relative to the static field gradient effects at low temperatures, and the two effects could probably be separated by a study of the satellite width as a function of temperature.[28] The slight asymmetry in the satellite shape might be due to second-order quadrupole effects or, possibly, to a small static field gradient asymmetry.[28] This asymmetry could be studied by field- and angular-dependence measurements. However, the detailed consideration of the shape of the Na^{23} satellite in γ-irradiated $NaNO_3$ is not our main concern in this report.

From our results and the above considerations we also conclude that there is little, if any, change in the quadrupole coupling constant of Li^7 in $LiNO_3$ produced by the γ irradiation. It is true that a small change (1.5%) is noted in the Na^{23} coupling in $NaNO_3$. Here, however, the satellites were probably broadened by the quadrupolar relaxation mechanism, and were apparently somewhat asymmetric. The change in coupling is interpreted as arising from the change in crossover point of the derivative curve which results from the asymmetry. In the case of $LiNO_3$ the Li^7 relaxation is magnetic dipolar and no broadening of the satellites is observed. The decrease in spin lattice relaxation time of Li^7 in the irradiated $LiNO_3$ is attributed to the large dipole-dipole coupling between the paramagnetic centers and the Li^7 nuclei.

Let us now turn to an evaluation of the quadrupole moment of Li^7 through Eq. (2). From our experiment $\Delta\nu_{zz}=35.5\pm0.2$ kc, and we choose $(1-\gamma_\infty)=0.744$ based upon good wave functions for Li^+.[15,29] Using recently determined rhombohedral cell constants for $LiNO_3$[19] ($a=5.638$, $\alpha=48$ deg 7.8 min) the field gradient at the Li position was calculated with the IBM 704

[23] R. G. Eades, D. G. Hughes, and E. R. Andrew, Proc. Phys. Soc. (London) **71**, 1019 (1958).
[24] E. R. Andrew and K. M. Swanson, Proc. Phys. Soc. (London) **70**, 436 (1957).
[25] W. B. Ard, Jr., J. Chem. Phys. **23**, 1967 (1955).
[26] See for example T. P. Das and E. L. Hahn, Solid State Phys. Suppl. **1**, 205 (1958).
[27] J. F. Hon and P. J. Bray, J. Phys. Chem. Solids **11**, 144 (1959).
[28] M. H. Cohen and F. Reif, Solid State **Phys. 5,** 321 (1957).
[29] A. Dalgarno, W. D. Davison, and A. L. **Stewart**, Proc. Roy. Soc. (London) **A257,** 115 (1960).

program developed by Bersohn.[1] We find that

$$q=\frac{3.5497-7.3697Z_N}{a^3}.$$

If, as in the case of $NaNO_3$, we let the effective charge (Z_N) on the nitrogen be zero, we arrive at the following equation:

$$e^2/h\frac{(3.5497)}{(5.638\times10^{-8})^3}(0.744)Q(\mathrm{Li}^7)=\pm35.5\times10^3$$

and $Q(\mathrm{Li}^7)=\pm0.069$ b.

From this determination we, of course, get no information regarding the sign of Q. (In principle one might be able to determine the sign by working at very low temperatures.) Unfortunately, as is well known, the field gradient is quite sensitive to the x-ray-determined structural parameters. (In the case of $LiNO_3$, the unit cell coordinates were determined in 1928, when the determinations were considerably less accurate than today.) To show this, the field gradient was calculated for $u=0.262\pm0.01$, where u is the parameter which represents the various positions of the oxygen atoms in the unit cell. (The structure[6] of $LiNO_3$ is such that only the oxygen position is uncertain from the recent cell constant determination.[19]) Allowing the old value of $u=0.262$ to vary by ±0.01 (about ±0.06 A) is a reasonable method, therefore, to estimate the range of $Q(L_i^7)$ due to structural uncertainty. We find

$$Q(\mathrm{Li}^7)=\pm0.093\text{ b }(u=0.272),$$

$$Q(\mathrm{Li}^7)=\pm0.056\text{ b }(u=0.252).$$

Thus, a 4% change in the oxygen position can lead to a 30% change in the value of the calculated quadrupole moment.

Some comment is warranted on the assignment of zero charge to the nitrogen atoms in both the nitrate crystals. As noted by Bersohn[1] there is some theoretical justification for this (Pauling's hypothesis of neutrality), but the state of affairs is still rather unsatisfactory. For example, in $NaNO_3$, knowing the coupling constant and quadrupole moment one would like to be able to determine *both* Z_N and $(1-\gamma_\infty)$ uniquely. As pointed out by Bersohn[1] and Bernheim and Gutowsky,[2] this is not possible here because the data are insufficient. But if more information were available for a given crystal, e.g., if $\eta\neq0$, or if two coupling constants were known, then one could possibly make such a unique assignment. For the application to $LiNO_3$ we observe that agreement is obtained in the case of $NaNO_3$ if $Z_N=0$ and therefore similar results may be expected for $LiNO_3$.

Some recent work[3,12] has included the contribution of induced ionic dipole moments to the electric field gradient. In the former study[3] supplemental information was utilized; the latter study[12] involved the diatomic alkali halide gases, intrinsically a simpler system than a crystalline solid. In our case, the calculation would be more difficult. However, unless the agreement in the case of $NaNO_3$ is coincidental, the induced dipole effect should be small. Qualitatively, this may be expected for the following reasons: The largest contribution to the electric field gradient at the Na^+ (or Li^+) ion from induced moments would probably be expected from the induced dipoles of the nearby nitrate ions which lie on the symmetry (Z) axis with the Na^+ (or Li^+) ions. However, the Z components of these dipoles which would be induced by the alkali ions exactly cancel each other because of the crystalline symmetry. Therefore, any large effect upon the field gradient by induced dipoles seems unlikely.

Let us now compare our value (±0.069 b) of the quadrupole moment of Li^7 with other recent evaluations. Harris and Melkanoff[4] used an 18-term James function for the field gradient calculation in Li_2 and arrived at $Q=-0.042$ b. They noted the extreme sensitivity of the field gradient to the wave function, however, and concluded that the magnitude was still in doubt but that the sign was probably negative. A wave function, which predicts a dissociation energy quite close to the experimental value, has been used by Mannari and Arai[30] to calculate the field gradient in Li_2. Neglecting shielding effects (which would increase the field gradient by about 15%) they find $Q=-0.025$ b. Both of the above determinations use the value of $+0.060$ Mc[31] for the quadrupole coupling in Li_2. Since this value was obtained from the half-width of an unresolved line, the quadrupole coupling in Li_2 is rather uncertain. By considering induced dipole effects in the lithium halide gases, Burns[12] arrived at $Q=-0.016$ b. This value is in agreement with various estimates of about -0.02 b from nuclear-shell theory.[32]

Thus, our value for Q seems somewhat high in comparison to the most recent determinations. In terms of the theoretical model used here, we observe that allowing the nitrogen atom to have an effective positive charge would *lower* the field gradient and raise the calculated quadrupole moment. (Allowing the nitrogen atom to have an effective negative charge is physically unreasonable.) It is possible that a detailed treatment of induced dipoles will increase the field gradient, thereby lowering the calculated quadrupole moment. However, we see that in order for our calculated value to be about 0.02 b, the field gradient would have to increase by almost a factor of four. Such a relatively large effect from induced dipoles (or higher moments) would not be expected.

Finally, the possibility exists that the ionic model, even including the contributions of higher induced moments, is not adequate for the calculation of field gradients in ionic crystals. At present, there is not

[30] I. Mannari and T. Arai, J. Chem. Phys. **28,** 28 (1958).
[31] R. A. Logan, R. E. Coté, and P. Kusch, Phys. Rev. **86,** 280 (1952).
[32] See for example R. J. Blin-Stoyle, Revs. Modern Phys. **28,** 75 (1956).

enough information to allow a general statement to be made. To test the ionic model in the special case of $LiNO_3$ a precise determination of the quadrupole moment of Li^7 would be desirable. Because of the sensitivity of the field gradient to the wave function, as well as the question of the accuracy of the experimental coupling constant, the determination of Q from Li_2 is unsatisfactory. In the lithium halide gases, the internuclear distances are relatively small and ionic distortions can be expected. These distortions are not taken into account in an ionic model and may have a significant effect on the field gradient. A determination based upon the molecular-beam measurement of the coupling constant in LiH, which is not planned in this laboratory, appears to be promising.[33] Here, the charge asymmetry would probably lead to a resolvable coupling and, the fact that the molecule has only four electrons should allow an accurate wave function to be obtained. Also, if LiD were studied with a molecular-beam technique, a check on the accuracy of the wave function would be available since the quadrupole moment of D^2 is quite accurately known.

ACKNOWLEDGMENTS

The author would like to express his appreciation to Dr. R. Bersohn and Dr. R. A. Berheim for discussions which led to this work. We would also like to thank A. Brouillard for experimental assistance, Mrs. D. Martin for helping with the computations, and E. Graeber for performing the x-ray analysis.

[33] *Note added in proof*: A recent communication [S. L. Kahalas and R. K. Nesbet, Phys. Rev. Letters **6**, 549 (1961)] describes the determination of $Q(Li^7)$ from the Li^7 quadrupole coupling in LiH and the calculated field gradient. The value obtained was -0.0356 b with an estimated error of less than 10%. Although our estimate (0.069 b) is within a factor of 2 of this value, the agreement is not as good as in the case of $NaNO_3$. (This result is still dependent, of course, on an accurate knowledge of the crystal structure; a more accurate determination is desirable for $LiNO_3$.) In order to improve the calculation of the field gradient in $LiNO_3$, the distribution of charge in the NO_3^- ion should be examined more critically. Probably the weakest point in our procedure is the idealization of NO_3^- ion by simple point charges. A more realistic model would consider the moments of the charge distribution of the ion, which, however, would involve considerably more complex calculations.

THE JOURNAL OF CHEMICAL PHYSICS VOLUME 35, NUMBER 4 OCTOBER, 1961

Tetrafluoromethane: P–V–T and Intermolecular Potential Energy Relations*

D. R. Douslin, R. H. Harrison, R. T. Moore, and J. P. McCullough

Thermodynamics Laboratory, Bartlesville Petroleum Research Center, Bureau of Mines, U. S. Department of the Interior, Bartlesville, Oklahoma

(Received March 16, 1961)

Measurements of the gas compressibility of tetrafluoromethane were made in the region, 0–350°, 15–394 atm. From these results, values of the compressibility factor $Z=PV/RT$, the second, third, and fourth virial coefficients, and the parameters of the Beattie-Bridgeman and Benedict-Webb-Rubin equations of state were derived. The virial coefficients were correlated by the Lennard-Jones (12, 6), Lennard-Jones (28, 7), Stockmayer, and Kihara intermolecular potential energy functions, and numerical values for the molecular parameters were obtained. One of the first tests of the theoretical fourth virial coefficient of the Lennard-Jones (12, 6) potential was made using the experimental fourth virial coefficients of tetrafluoromethane.

THE pressure-volume-temperature properties of hydrocarbons, fluorocarbons, and mixtures of hydrocarbons and fluorocarbons are determined by the Bureau of Mines as part of an extensive program for evaluating the chemical thermodynamic properties of these and other materials over a wide range of temperatures and pressures. Because of its structural simplicity and high thermal stability, tetrafluoromethane is a compound of exceptional interest in the theoretical and correlational phases of these studies.

The most extensive previous experimental work on the gas compressibility of tetrafluoromethane was reported, for pressures below 50 atm, by MacCormack and Schneider.[1] Experimental values for the second virial coefficient, obtained from unpublished measurements by W. J. McManamey (University of Sydney), were given by Hamann and Lambert[2] in a theoretical treatment of tetrafluoromethane as a quasi-spherical molecule. Cawood and Patterson[3] reported a value for the second virial coefficient of tetrafluoromethane at 21°.

The present measurements covered a temperature range from 0 to 350° at pressures up to 394 atm. These data were used to derive the parameters of two closed

* Contribution No. 102.

[1] K. E. MacCormack and W. G. Schneider, J. Chem. Phys. **19**, 845 (1951).

[2] S. D. Hamann and J. A. Lambert, Australian J. Chem. **7**, 1 (1954).

[3] W. Cawood and H. S. Patterson, Phil. Trans. Roy. Soc. London **A236**, 77 (1937).

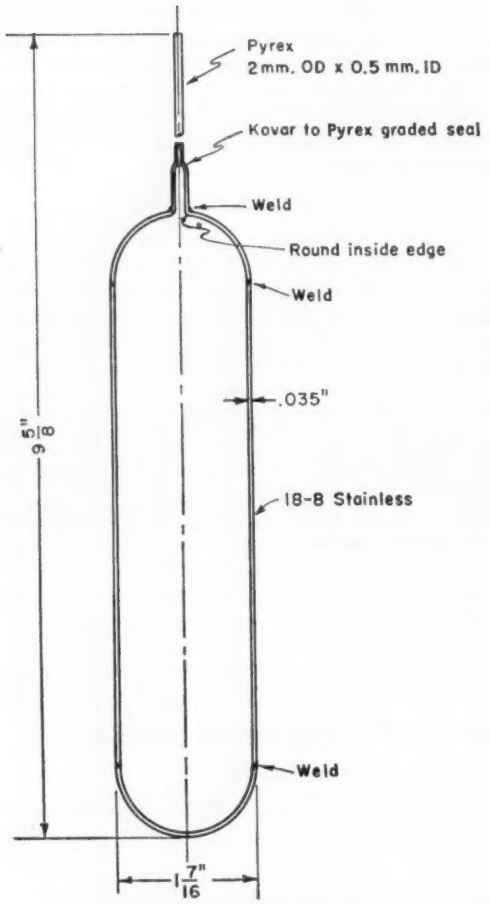

FIG. 1. Stainless-steel liner for P–V–T bomb.

equations of state and of the virial equation of state through the fourth virial. They provided the experimental data needed for one of the first tests of the theoretical fourth virial coefficient based on the Lennard-Jones (12, 6) potential.

EXPERIMENTAL

Method

The compressibility apparatus was the same, except for the sample liner, as in previous work on fluorobenzene[4] and perfluorocyclobutane.[5] In principle, the method used is similar to Beattie's.[6] Therefore, only a description of the sample liner used in the P–V–T bomb and other experimental details that relate specifically to the tetrafluoromethane measurements will be added. Because the sample exerted about 16.5-atm pressure in the liner at room temperature, a stainless-steel sample liner (Fig. 1) was used instead of the Pyrex liner described in previously reported work. A new blank-run calibration was made because of the small dimensional differences in the two liners and the differences in the thermal expansion and compressibility of Pyrex and stainless steel. All parts of the compressibility apparatus were individually calibrated by methods described previously. Corrections applied to the pressure measurement for the effect of pressure on the piston and cylinder of the dead-weight gauge were based on the values for a 0.05-in.^{2} piston given by Dadson.[7] The maximum correction was 0.02% at 400 atm.

In previous work, the small amount of mercury vapor in the sample space was calculated as an equivalent volume loss D_2 of liquid mercury based on the assumption that the mercury vapor behaved as a perfect gas regardless of the total pressure of the system. A closer approximation to the true value of D_2 is believed to be obtained from the formula

$$D_2=[200.6n_1/d_t][p_{Hg}/(P_T-p_{Hg})],$$

which is based on the assumption that mercury vapor exhibits the same nonideality as the sample. In this formula, n_1 is the number of moles of sample, d_t is the density of liquid mercury at the temperature t of the system, p_{Hg} is the vapor pressure of mercury adjusted for the Poynting effect, and P_T is the total pressure on the system. The maximum D_2 correction to the volume was 0.03% at 350° and a sample density of 0.75 mole liter^{-1}.

The over-all error in the compressibility measurements was estimated to vary from 0.03% at the lowest temperature and pressure to almost 0.3% at the highest temperature and pressure.

Material

The sample of tetrafluoromethane was supplied through the courtesy of Dr. R. C. McHarness, Kinetic Sales Service Laboratory, E. I. duPont de Nemours & Company. Although the infrared analysis received with the sample showed no detectable impurities, mass-spectrometer[8] analyses indicated 0.07% max CF_2H_2, 0.05% max CFH_3, 0.03% CO_2, and 0.06 to 0.16% F_2 on a molal basis. The sample was further purified by vapor transfer, at cylinder pressure, over Ascarite and

[4] D. R. Douslin, R. T. Moore, J. P. Dawson, and G. Waddington, J. Am. Chem. Soc. **80**, 2031 (1958).
[5] D. R. Douslin, R. T. Moore, and G. Waddington, J. Phys. Chem. **63**, 1959 (1959).
[6] J. A. Beattie, Proc. Am. Acad. Arts Sci. U. S. **69**, 389 (1934).

[7] R. S. Dadson, "The accurate measurement of high pressures and the precise calibration of pressure balances," The Institution of Mechanical Engineers and the International Union of Pure and Applied Chemistry, Joint Conference on Thermodynamic and Transport Properties of Fluids, July 10–12 (1957). Published by the Institution of Mechanical Engineers, 1 Birdcage Walk, London 3WI.
[8] The mass-spectrometer analyses were made by B. H. Eccleston, N. G. Foster, and R. Kendall of the Petroleum Research Center, Bureau of Mines, Bartlesville, Oklahoma, and by G. U. Dineen and G. L. Cook, Petroleum Research Center, Bureau of Mines, Laramie, Wyoming.

Anhydrone to remove any traces of carbon dioxide, fluorine, and water present, and was then distilled in a 100-plate Podbielniak Heligrid column. The first and last fractions, each equal to about 5% of the total sample distilled, were rejected. A mass-spectrometer analysis of the center fraction from the distillation showed 0.02% max CF_2H_2, 0.02% max CFH_3, and no water or carbon dioxide. These percentages of impurity are estimated maximum amounts and may be large by a factor of two. The amount of free fluorine remained unchanged and, therefore, must have been formed in the ionization chamber of the spectrometer. From the last analysis, the purity of the sample of tetrafluoromethane used for the gas-compressibility measurements was at least 99.96%. A portion of the center cut was vapor transferred to the stainless-steel liner of the compressibility apparatus, and noncondensibles were removed by an outgassing procedure (i.e., freezing with liquid air, evacuating to 10^{-5} mm or less, and melting) carried through three complete cycles. The gas-compressibility measurements were made on a single sample that weighed 8.4874±0.0003 g, and was calculated to be 0.096457 mole.[9] The maximum percentage of impurities, given above, was assumed in the calculation of the number of moles of sample. Had the impurities been ignored, the calculated moles of sample would have been smaller by about 0.02%.

Physical Constants

The temperature of the compressibility bomb was measured to within 0.001° with a platinum resistance thermometer that had been calibrated by the National Bureau of Standards in terms of the International Temperature Scale[10] [T, °K=t, °C(Int., 1948)+273.16]. The more recent definition of the absolute acale, 0°C=273.15°K, was not used in the work on tetrafluoromethane. Measurements of the ice-point resistance of the thermometer made at the beginning and end of the experimental work showed no significant change.

The liter was chosen as the unit of volume in the equation of state correlations and in calculations of the compressibility factor, but the virial coefficients were calculated in volume units of cubic centimeters (1 cm^3=0.9999720×10^{-3} liter) to facilitate comparison with theory. Therefore, these two values of the gas constant were used as appropriate: R=0.0820544 liter atm deg^{-1} $mole^{-1}$, and R=82.0567 cm^3 atm deg^{-1} $mole^{-1}$.[11]

COMPRESSIBILITY

To eliminate the need for cross plotting in the correlational work, the compressibility measurements were taken at even values of temperature and density. Significant errors that otherwise would be introduced by graph paper were thus eliminated, and the full precision of the measurements was retained in the correlated results. The pressure, density, and temperature (Table I) are unsmoothed values. For each isotherm, beginning at lowest temperature, the pressure was measured first at the minimum density 0.75 mole $liter^{-1}$. After measurements at the maximum density, the initial pressure measurement was repeated to check for leakage of mercury or decomposition of the sample. The results of the check measurements at 0.75 mole $liter^{-1}$, column 5, agree with the initial values within the calculated reproducibility of the measurements, except for the 30° isotherm, for which the deviation is 0.003 atm.

An over-all check for stability of the tetrafluoromethane sample was made by repeating the 100° and 0.75 mole $liter^{-1}$ point after the investigation was completed. The final observed pressure was only 0.005 atm higher than the initial, indicating that neither the sample nor the system had changed significantly.

The tabulated values of pressure were corrected for the weight of the sample,[12] and for the partial pressure of mercury vapor,[13] adjusted at each pressure for the Poynting effect. The correction for mercury vapor did not include the van der Waals interaction of mercury vapor with tetrafluoromethane, which cannot be calculated accurately at present. However, the compressibility measurements are reported in sufficient detail so that the correction can be made when a reliable method for calculating it becomes available. In any case, the inaccuracy introduced by the neglect of the mercury-interaction correction is probably not great for tetrafluoromethane in the region of these measurements and is covered by the over-all accuracy uncertainty stated in the Experimental section.

EQUATIONS OF STATE

Parameters for the Beattie-Bridgeman (B-B)[14] and the Benedict-Webb-Rubin (B-W-R)[15] equations of state (Table II) were derived from the unsmoothed experimental values of Table I. The differences between observed and calculated pressures are listed for each point to make clear the ranges over which the equations are valid. Extrapolation of either equation to densities greater than the range of experimental values used to evaluate the parameters is not recommended for the reasons given by Beattie *et al.*[16]

[9] Based on the atomic weights, H=1.008, C=12.010, and F=19.00, E. Wichers, J. Am. Chem. Soc. **74,** 2447 (1952).

[10] H. F. Stimson, Am. J. Phys. **23,** 614 (1955).

[11] F. D. Rossini, F. T. Gucker, Jr., H. L. Johnston, L. Pauling, and G. W. Vinal, J. Am. Chem. Soc. **74,** 2699 (1952).

[12] The pressure equivalent of the weight of the sample, which was subtracted from the pressure that was read, varied from 0.005 atm at the lowest pressure to 0.0008 atm at the highest pressure. The correction varies because the shape of the top of the cell liner (Fig. 1) is that of a hemisphere instead of a right cylinder.

[13] Reference 4 contains a list of the selected values of the vapor pressure of mercury and a description of the way the mercury-vapor corrections were calculated and applied.

[14] J. A. Beattie and O. C. Bridgeman, Proc. Am. Acad. Arts. Sci. U. S. **63,** 229 (1928).

[15] M. Benedict, G. B. Webb, and L. C. Rubin, J. Chem. Phys. **8,** 334 (1940); **10,** 747 (1942).

[16] J. A. Beattie, C. Hadlock, and N. Poffenberger, J. Chem. Phys. **3,** 93 (1935).

TABLE I. The compressibility of tetrafluoromethane and the deviations obtained with the Benedict-Webb-Rubin, and Beattie-Bridgeman equations of state.

			Density, mole liter^{-1}												
t, °C (Int.)			0.75	0.75[a]	1.0	1.5	2.0	2.5	3.0	3.5	4.0	4.5	5.0	5.5	6.0
			Pressure, normal atmospheres[b]												
0.00	Obs		15.480	15.478	20.086	28.559	36.149	42.974	49.150	54.804	60.039	64.967	69.704	74.369	79.050
	Obs-Calc	B-W-R	+0.100		+0.166	+0.325	+0.498	+0.653	+0.752	+0.778	+0.694	+0.482	+0.146	−0.287	−0.810
		B-B	−0.003		−0.007	−0.015	−0.018	−0.011	+0.010	+0.060	+0.137	+0.242	+0.387	+0.588	+0.830
25	Obs		17.194	17.196	22.453	32.339	41.486	50.000	58.012	65.628	72.967	80.130	87.251	94.473	101.908
	Obs-Calc	B-W-R	+0.036		+0.063	+0.018	+0.169	+0.190	+0.182	+0.116	−0.015	−0.236	−0.530	−0.860	−1.218
		B-B	+0.031		+0.053	+0.097	+0.141	+0.164	+0.176	+0.160	+0.118	+0.029	−0.090	−0.208	−0.331
30	Obs		17.538	17.535	22.923	33.087	42.538	51.387	59.764	67.756	75.520	83.129	90.736	98.470	106.456
	Obs-calc	B-W-R	+0.030		+0.047	+0.085	+0.114	+0.117	+0.094	+0.002	−0.131	−0.353	−0.630	−0.944	−1.279
		B-B	+0.039		+0.063	+0.116	+0.163	+0.191	+0.204	+0.166	+0.111	−0.008	−0.158	−0.326	−0.506
50	Obs		18.898	18.899	24.792	36.057	46.720	56.893	66.701	76.251	85.656	95.045	104.587	114.393	124.621
	Obs-Calc	B-W-R	0.000		−0.005	−0.024	−0.061	−0.122	−0.207	−0.332	−0.511	−0.736	−0.964	−1.207	−1.434
		B-B	+0.060		+0.096	+0.174	+0.244	+0.284	+0.287	+0.228	+0.089	−0.128	−0.383	−0.656	−1.021
75	Obs		20.591	20.590	27.116	39.749	51.903	63.709	75.279	86.735	98.206	109.825	121.755	134.178	147.212
	Obs-Calc	B-W-R	−0.021		−0.043	−0.100	−0.193	−0.308	−0.451	−0.622	−0.817	−1.033	−1.239	−1.393	−1.528
		B-B	+0.084		+0.132	+0.243	+0.332	+0.384	+0.372	+0.276	+0.087	−0.202	−0.565	−0.955	−1.391
100	Obs		22.275	22.275	29.426	43.412	57.049	70.468	83.789	97.142	110.662	124.512	138.840	153.853	169.728
	Obs-Calc	B-W-R	−0.032		−0.062	−0.136	−0.255	−0.401	−0.573	−0.767	−0.976	−1.173	−1.355	−1.470	−1.516
		B-B	+0.100		+0.159	+0.297	+0.407	+0.468	+0.451	+0.337	+0.112	−0.208	−0.621	−1.066	−1.512
125	Obs		23.952	23.953	31.725	47.047	62.155	77.175	92.224	107.462	123.034	139.086	155.832	173.413	192.127
	Obs-Calc	B-W-R	−0.034		−0.065	−0.148	−0.273	−0.430	−0.626	−0.830	−1.034	−1.236	−1.379	−1.497	−1.484
		B-B	+0.113		+0.181	+0.334	+0.462	+0.533	+0.505	+0.381	+0.149	−0.200	−0.607	−1.085	−1.491
150	Obs		25.625	25.626	34.021	50.671	67.233	83.830	100.617	117.715	135.322	153.553	172.699	192.863	214.330
	Obs-Calc	B-W-R	−0.030		−0.053	−0.133	−0.256	−0.423	−0.611	−0.832	−1.035	−1.260	−1.389	−1.505	−1.542
		B-B	+0.123		+0.201	+0.366	+0.504	+0.570	+0.552	+0.409	+0.171	−0.207	−0.601	−1.066	−1.483
175	Obs		27.296	27.296	36.304	54.274	72.282	90.460	108.963	127.937	147.553	168.020	189.528	212.277	236.618
	Obs-Calc	B-W-R	−0.018		−0.039	−0.106	−0.217	−0.373	−0.556	−0.764	−0.983	−1.171	−1.325	−1.449	−1.432
		B-B	+0.132		+0.212	+0.385	+0.529	+0.600	+0.582	+0.446	+0.194	−0.140	−0.535	−0.960	−1.237
200	Obs		28.964	28.965	38.585	57.868	77.316	97.066	117.270	138.103	159.733	182.364	206.259	231.582	258.762
	Obs-Calc	B-W-R	−0.002		−0.014	−0.064	−0.156	−0.292	−0.471	−0.671	−0.893	−1.113	−1.270	−1.423	−1.401
		B-B	+0.141		+0.223	+0.339	+0.547	+0.622	+0.594	+0.461	+0.207	−0.139	−0.495	−0.884	−1.025
225	Obs		30.627	30.629	40.860	61.455	82.331	103.639	125.550	148.221	171.872	196.686	222.912	250.816	280.728
	Obs-Calc	B-W-R	+0.014		+0.016	−0.009	−0.080	−0.200	−0.357	−0.562	−0.774	−1.005	−1.223	−1.404	−1.495
		B-B	+0.144		+0.231	+0.411	+0.555	+0.623	+0.600	+0.453	+0.219	−0.109	−0.466	−0.771	−0.880
250	Obs		32.289	32.291	43.132	65.034	87.334	110.200	133.807	158.325	183.973	210.974	239.569	270.100	302.842
	Obs-Calc	B-W-R	+0.036		+0.049	+0.055	+0.009	−0.084	−0.222	−0.414	−0.634	−0.871	−1.114	−1.282	−1.398
		B-B	+0.148		+0.236	+0.418	+0.556	+0.622	+0.596	+0.454	+0.221	−0.074	−0.383	−0.557	−0.514

TABLE I.—*Continued.*

			Density, mole liter^{-1}												
			0.75	0.75[a]	1.0	1.5	2.0	2.5	3.0	3.5	4.0	4.5	5.0	5.5	6.0
			Pressure, normal atmospheres[b]												
275	Obs		33.949	33.951	45.398	68.596	92.326	116.738	142.032	168.391	196.014	225.145	256.087	289.161	324.652
	Obs-Calc	B-W-R	+0.058		+0.083	+0.115	+0.109	+0.038	−0.081	−0.260	−0.508	−0.805	−1.097	−1.342	−1.569
		B-B	+0.150		+0.236	+0.411	+0.551	+0.606	+0.573	+0.434	+0.186	−0.127	−0.402	−0.520	−0.392
300	Obs		35.609	35.609	47.661	72.165	97.306	123.266	150.212	178.382	207.995	239.280	272.536	308.116	346.323
	Obs-Calc	B-W-R	+0.083		+0.120	+0.192	+0.215	+0.176	+0.046	−0.146	−0.402	−0.735	−1.110	−1.470	−1.851
		B-B	+0.152		+0.234	+0.411	+0.539	+0.587	+0.516	+0.354	+0.113	−0.187	−0.453	−0.539	−0.350
325	Obs		37.266	37.264	49.924	75.723	102.278	129.773	158.415	188.385	219.957	253.412	288.853	327.091	368.163
	Obs-Calc	B-W-R	+0.108		+0.160	+0.287	+0.326	+0.312	+0.220	+0.010	−0.283	−0.633	−1.221	−1.551	−1.939
		B-B	+0.152		+0.233	+0.404	+0.521	+0.552	+0.488	+0.296	+0.033	−0.233	−0.615	−0.515	−0.110
350	Obs		38.921	38.922	52.187	79.273	107.240	136.267	166.576	198.378	231.925	267.505	305.438	346.066	389.660
	Obs-Calc	B-W-R	+0.134		+0.206	+0.345	+0.441	+0.453	+0.375	+0.181	−0.130	−0.543	−1.020	−1.605	−2.349
		B-B	+0.151		+0.233	+0.390	+0.498	+0.510	+0.428	+0.241	−0.022	−0.293	−0.474	−0.444	−0.152
Av. dev., %		B-W-R	0.17		0.22	0.29	0.34	0.39	0.42	0.44	0.50	0.57	0.63	0.70	0.77
		B-B	0.38		0.46	0.55	0.56	0.51	0.41	0.27	0.11	0.11	0.28	0.41	0.48

			Density, mole liter^{-1}											
t, °C (Int.)			6.5	7.0	7.5	8.0	8.5	9.0	9.5	10.0	10.5	11.0	11.5	12.0	12.5
			Pressure, normal atmospheres[b]												
0.00	Obs		83.903	89.061	94.676	100.960	108.149	116.575	126.561	138.458	152.884	170.481	192.000	218.629	251.029
	Obs-Calc	B-W-R	−1.328	−1.784	−2.065	−2.102	−1.823	−1.162	−0.205	+0.816	+1.714	+2.059	+1.221	−1.341	−7.089
		B-B	+1.170	+1.640	+2.297	+3.258	+4.662	+6.755							
25	Obs		109.726	118.131	127.244	137.455	148.916	162.056	177.339	195.101	216.126	241.054	270.777	306.072	342.263
	Obs-Calc	B-W-R	−1.539	−1.743	−1.814	−1.586	−1.154	−0.455	+0.470	+1.274	+1.837	+1.639	+0.111	−3.770	−10.852
		B-B	−0.401	−0.324	−0.092	+0.578	+1.731	+3.690							
30	Obs		114.879	123.929	133.791	144.774	157.077	171.140	187.469	206.428	228.708	254.939	286.356	323.269	367.430
	Obs-Calc	B-W-R	−1.561	−1.733	−1.728	−1.474	−0.963	−0.354	+0.554	+1.349	+1.805	+1.374	−0.185	−4.373	−11.619
		B-B	−0.628	−0.613	−0.393	+0.233	+1.352	+3.298							
50	Obs		135.468	147.186	159.922	174.093	189.908	207.791	228.320	251.970	279.425	311.330	348.658	392.619	
	Obs-Calc	B-W-R	−1.587	−1.585	−1.437	−1.016	−0.435	+0.289	+1.145	+1.845	+2.091	+1.291	−1.109	−5.755	
		B-B	−1.298	−1.393	−1.282	−0.667	+0.540	+2.646							
75	Obs		161.150	176.143	192.482	210.584	230.884	253.472	279.421	308.736	342.440	381.498			
	Obs-Calc	B-W-R	−1.519	−1.428	−1.164	−0.660	+0.141	+0.820	+1.794	+2.233	+2.114	+1.100			
		B-B	−1.714	−1.906	−1.807	−1.134	+0.420	+2.816							
100	Obs		186.712	205.075	225.134	247.200	271.743	299.330	330.350	365.751					
	Obs-Calc	B-W-R	−1.441	−1.226	−0.791	−0.226	+0.507	+1.412	+2.161	+2.809					
		B-B	−1.853	−1.964	−1.669	−0.798	+0.978	+4.089							

TABLE I.—*Continued.*

			Density, mole liter^{-1}												
			6.5	7.0	7.5	8.0	8.5	9.0	9.5	10.0	10.5	11.0	11.5	12.0	12.5
			Pressure, normal atmospheres[b]												
125	Obs		212.147	233.889	257.529	283.630	312.493	344.771	381.244						
	Obs-Calc	B-W-R	−1.392	−1.086	−0.667	−0.015	+0.694	+1.498	+2.410						
		B-B	−1.803	−1.756	−1.327	−0.101	+2.072	+5.698							
150	Obs		237.418	262.452	289.777	319.795	353.276	390.238							
	Obs-Calc	B-W-R	−1.430	−1.157	−0.684	−0.096	+0.860	+1.542							
		B-B	−1.692	−1.529	−0.808	+0.712	+3.644	+7.851							
175	Obs		262.764	291.064	322.043	356.107	393.701								
	Obs-Calc	B-W-R	−1.334	−1.147	−0.680	−0.053	+0.625								
		B-B	−1.320	−1.028	−0.004	+1.990	+5.234								
200	Obs		287.988	319.607	354.291	392.333									
	Obs-Calc	B-W-R	−1.312	−1.178	−0.701	−0.113									
		B-B	−0.936	−0.436	+0.971	+3.403									
225	Obs		312.999	348.121	386.496										
	Obs-Calc	B-W-R	−1.466	−1.218	−0.740										
		B-B	−0.627	+0.298	+2.111										
250	Obs		338.173	376.424											
	Obs-Calc	B-W-R	−1.425	−1.452											
		B-B	−0.066	+0.927											
275	Obs		362.875												
	Obs-Calc	B-W-R	−1.830												
		B-B	+0.095												
300	Obs		387.599												
	Obs-Calc	B-W-R	−2.193												
		B-B	+0.352												
325	Obs														
	Obs-Calc	B-W-R													
		B-B													
350	Obs														
	Obs-Calc	B-W-R													
		B-B													
Av. dev., %		B-W-R	0.82	0.81	0.71	0.53	0.46	0.41	0.45	0.69	0.82	0.62	0.27	1.17	3.03
		B-B	0.57	0.65	0.63	0.67	1.13	2.18							

[a] Check measurements.

[b] The pressures are tabulated to the nearest 0.001 atm to retain the maximum internal consistency in line with the precision of the measurements. The over-all estimated accuracy of the compressibility measurements is given in the Experimental section.

Isothermal plots of the compressibility factor $Z=PV/RT$, calculated from the data of Table I, are shown in Fig. 2.

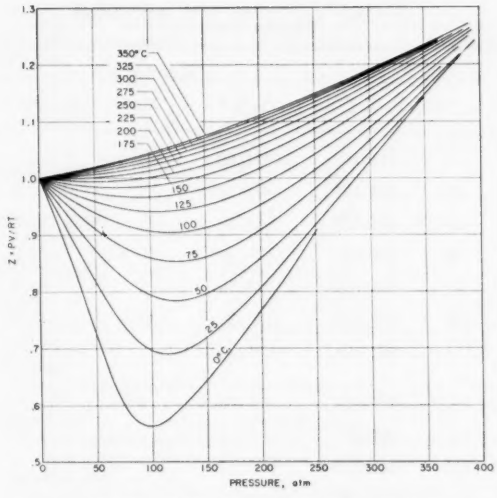

FIG. 2. Compressibility factor for tetrafluoromethane.

VIRIAL COEFFICIENTS

From statistical-thermodynamic theory, the pressure-volume-temperature relationships of a real gas can be represented in virial form [Eq. (1)] which is an infinite series of terms in regularly increasing powers of inverse volume, with temperature-dependent coefficients;

$$PV=RT(1+B/V+C/V^2+D/V^3+E/V^4+\cdots). \quad (1)$$

The quantities B_v, C_v, and D_v, defined by Eqs. (2), (3), and (4), were calculated

$$B_v=(PV/RT-1)V; \qquad B=\lim_{p\to 0}B_v \quad (2)$$

$$C_v=[(PV/RT-1)V-B]V; \qquad C=\lim_{p\to 0}C_v \quad (3)$$

$$D_v=\{[(PV/RT-1)V-B]V-C\}V; \qquad D=\lim_{p\to 0}D_v \quad (4)$$

from the unsmoothed experimental values of P, V, and T (Table I) and extrapolated to zero density to obtain B, C, and D, Tables III and IV. For comparison, other investigators' results for B are included in Table III. An analytical solution of a polynomial approximation to the virial equation would yield values of the virial coefficients that are slightly different from those reported here.

From Eqs. (3) and (4), C_v is seen to depend on the value of B, and D_v to depend on both B and C. The shapes of the C_v curves are so sensitive to the value chosen for B that they provide excellent criteria for extrapolating the B_v curves to zero density. As shown in Fig. 3, a small deviation from the "correct" value of B results in unreasonably large positive or negative curvature in the plots of C_v at low densities. Thus, the values of B were selected so that the C_v plots had a small, nearly constant curvature at low densities. Similarly, the values of C were selected using the D_v plots as guides.

These plots of B_v, C_v, and D_v provide an excellent visual test of the quality of the compressibility values. Their shapes also are sensitive to small errors in the calculated number of moles of sample. For example, neglect of the 0.04 mole % impurities in calculating the number of moles of tetrafluoromethane causes changes in the curvature and intercepts of the B_v, C_v, and D_v plots. In fact, uncertainties in the mass and purity of the sample cause a systematic uncertainty in values of B estimated to be between 0.1 and 0.7 cm^3 mole^{-1}. In comparison, uncertainties in the measurements of P, V, and T cause an uncertainty in B of only about 0.2 cm^3 mole^{-1}.

Because the major errors are systematic, the precision of the B values is at least one order of magnitude higher than the absolute accuracy. For this reason, the values of B are tabulated, on the thermodynamic temperature scale,[17] to 0.05 cm^3 mole^{-1} to allow for rounding-off to the nearest 0.1 cm^3 mole^{-1} when comparing the differences between experimental and calculated values.

TABLE II. Equations of state for tetrafluoromethane.[a]

Beattie-Bridgeman equation

$$P=[RT(1-\epsilon)/V^2][V+B]-A/V^2$$

$A=A_0(1-a/V)$;	$B=B_0(1-b/V)$;	$\epsilon=c/VT^3$
$A_0=4.3753$	$B_0=0.09683$	$c=25\times10^4$
$a=0.02161$	$b=-0.04222$	$R=0.0820544$

Benedict-Webb-Rubin equation

$$P=RT/V+(B_0RT-A_0-C_0/T^2)/V^2+(bRT-a)/V^3+\alpha a/V^6+[c(1+\gamma/V^2)\exp(-\gamma/V^2)]/V^3T^2$$

$A_0=1.86000$	$a=0.398530$	$\alpha=0.000250000$
$B_0=0.0552000$	$b=0.0121147$	$\gamma=0.0125000$
$C_0=0.154500\times10^6$	$c=0.0243300\times10^6$	$R=0.0820544$

[a] Units: normal atm, liter mole^{-1}, °K.

INTERMOLECULAR POTENTIAL ENERGY FUNCTIONS

Second Virial Coefficient

The Lennard-Jones (12, 6) and (28, 7) potentials have no orientational dependence. Thus they seem to be reasonable choices for theoretical correlations of the temperature dependence of the second virial coefficient of tetrafluoromethane. The Lennard-Jones (28, 7) potential was first suggested by Hamann and Lambert,[2] who showed that the corresponding states relationship

[17] J. A. Beattie, *Temperature, Its Measurement and Control in Science and Industry* (Reinhold Publishing Corporation, New York, 1955), Vol. II, Chap. 5.

TABLE III. The second virial coefficient of tetrafluoromethane.

		B, cm³ mole⁻¹		
t, °C	T, °K (Th.)	B.M.[a]	M&S[b]	M[c]
0	273.160	−111.00	−111.0	...
25	298.153	−88.30	...	...
30	303.152	−84.40	...	...
50	323.151	−70.40	−70.4	−72.4
75	348.153	−55.70	...	−56.1
100	373.160	−43.50	−43.1	−43.9
125	398.170	−33.20	...	−30.1 &31.1
150	423.183	−24.40	−26.0	...
175	448.197	−16.80	...	...
200	473.213	−10.10	...	..
225	498.229	−4.25	...	...
250	523.245	+1.00	+1.2	...
275	548.260	5.60	...	...
300	573.274	9.80	9.3	...
325	598.285	13.60	...	...
350	623.295	17.05	...	...

[a] Bureau of Mines, this research.
[b] MacCormack and Schneider (1951).[1]
[c] McManamey, as reported by Hamann and Lambert (1954).[2]

TABLE IV. Third and fourth virial coefficients of tetrafluoromethane.

t, °C	C, cm⁶ mole⁻² ×10⁻²	D, cm⁹ mole⁻³ ×10⁻⁴
0	71.0	0.5
25	60.7	2.1
30	59.0	2.7
50	53.8	3.8
75	48.7	4.9
100	44.9	6.4
125	42.1	8.0
150	39.8	9.7
175	38.1	11.4
200	36.6	12.8
225	35.4	14.3
250	34.4	15.8
275	33.5	17.5
300	32.5	19.5
325	31.8	21.0
350	31.0	22.3

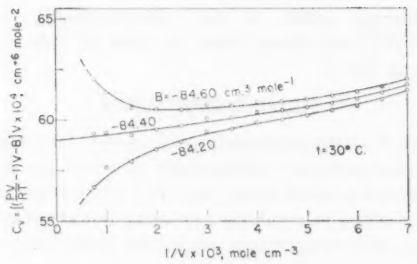

FIG. 3. The effect on C_v of a small error in B.

of the critical properties of the quasi-spherical gases tetrafluoromethane, silicon tetrafluoride, sulfur hexafluoride, and neopentane could be correlated better by the (28, 7) potential than by the (12, 6) potential. Except for neopentane, however, Hamann and Lambert were unable to prove that the (28, 7) potential was superior to the (12, 6) potential for correlating the second virial coefficient. That the (28, 7) potential is indeed clearly superior to the (12, 6) potential for correlating the second virial coefficient of tetrafluoromethane is shown in Table V, which lists deviations of observed and calculated values of B. Further evidence for the superiority of the (28, 7) potential for quasi-spherical molecules is shown by the correlations of the second virial coefficient of perfluorocyclobutane (Table VI) although perfluorocyclobutane does not conform as well

TABLE V. Comparison of experimental and theoretical second virial coefficients of tetrafluoromethane.

	$B_{obs-calc}$,[a] cm³ mole⁻¹			
t, °C	L-J (12, 6)	L-J (28, 7)	Stockmayer	Kihara
0	−3.6	0.0	−0.5	−0.4
25	−1.3	+0.1	+0.2	0.0
30	−1.3	+0.1	+0.1	0.0
50	−0.6	+0.1	+0.1	0.0
75	0.0	0.0	+0.1	0.0
100	+0.5	−0.2	+0.1	+0.3
125	+0.7	−0.1	+0.1	0.0
150	+0.6	0.0	0.0	0.0
175	+0.4	0.0	0.0	0.0
200	+0.5	−0.3	0.0	0.0
225	+0.6	0.0	0.0	0.0
250	+0.3	0.0	+0.1	+0.1
275	+0.2	+0.1	0.0	0.0
300	0.0	−0.1	+0.1	+0.1
325	0.0	0.0	+0.2	+0.2
350	−0.1	+0.2	+0.2	+0.2

[a] Observed values given in Table III.

as tetrafluoromethane or neopentane to the quasi-spherical approximation.

Both Stockmayer's[5,18] and Kihara's[5,19,20] potentials provided excellent correlations of the second virial coefficient of tetrafluoromethane, columns 4 and 5, (Table V) even though they are based on quite different molecular models and the orientational dipole parameter l of Stockmayer's potential is used empirically. The Stockmayer and Kihara correlations indicate that, in the temperature range of these measurements, a precision of at least 0.01 cm³ mole⁻¹ in the second virial coefficient of tetrafluoromethane will be required for a definitive test of a three-parameter potential energy function.

TABLE VI. Comparison of observed and calculated second virial coefficient of perfluorocyclobutane.

	$B_{obs-calc}$,[a] cm³ mole⁻¹	
t, °C	L-J (12, 6)[b]	L-J (28, 7)[c]
100	−17	−4
115.22	−10	+1
125	−5	+2
150	−5	+3
175	+2	+3
200	+4	+4
225	+4	+4
250	+4	+2
275	+3	+1
300	+1	0
325	0	0
350	−2	−1

[a] Observed values taken from Table VII, reference 5.
[b] θ=222.6°K; b_0=437.52 cm³ mole⁻¹.
[c] θ=464.8°K; b_0=310.10 cm³ mole⁻¹.

The spread in the values of the parameters shown in Table VII, particularly the θ's, is an indication of major differences in the potential functions. These differences are not as evident in the calculated or theoretical second virial coefficient values because the parameters were adjusted to give the best possible representation of the experimental results. The distances r_0's between molecular centers at the potential minimum of the Lennard-Jones (28, 7), Stockmayer and Kihara potentials are in fair agreement with the value 4.7 A calculated by Hamann and Lambert[2] from electron-diffraction measurements on tetrafluoromethane.

Third Virial Coefficient

As a means of testing potential energy functions, the third virial coefficient has not been particularly useful, largely because experimental values of the third virial coefficient are difficult to determine accurately, and the integrals in the theoretical equations are extremely difficult and laborious to evaluate. As a result, extensive tabulations of the theoretical third virial coefficient for the Lennard-Jones (12, 6) and Stockmayer potentials have appeared in the literature only in the last decade. Hamann and Lambert[2] give theoretical values for the third virial coefficient function of the Lennard-Jones (28, 7) potential at only two values of T/θ, both of which are outside the range of the tetrafluoromethane measurements. No tabulations for the Kihara potential are published. Consequently, comparisons of the observed third virial coefficient of tetrafluoromethane with theory (Fig. 4) are necessarily limited to the Lennard-Jones (12, 6) and the Stockmayer potentials. Theoretical values for the Lennard-Jones (12, 6) potential calculated by Boys and Shavitt[21] by the Gaussian function method are shown as the dashed line. The experimental

TABLE VII. Potential energy function parameters evaluated from the experimental second virial coefficient of tetrafluoromethane.[a]

Potential function	θ, °K	b_0, cm³ mole⁻¹	r_0, A	l	p[b]
Lennard-Jones (12, 6)	152.1	131.31	5.28	...	...
Lennard-Jones (28, 7)	313.1	97.72	4.55	...	...
Stockmayer[c]	139.0	120.23	4.84[d]	0.50	...
Kihara	291.1	90.37	4.66	...	0.69

[a] The parameters were evaluated by the method of superimposed logarithmic plots.
[b] The parameter p was defined, reference 5, for the spherical hard-core model, as the ratio of the shortest distance ρ between the surfaces of the cores to the distance r between their centers; $p=\rho/r$ at $\partial U(r)/\partial r=0$.
[c] The parameters of the Stockmayer potential are not directly comparable to the other parameters because of the effect of the orientational term on the potential energy.
[d] The value of r_0 for the Stockmayer potential was calculated at $g=2$, the position of the molecules for maximum orientational interaction.

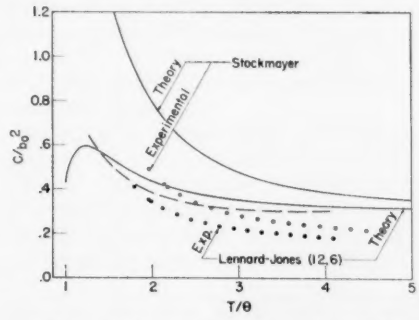

FIG. 4. Third virial coefficient of tetrafluoromethane. The dashed line represents the theoretical Lennard-Jones (12, 6) values as calculated from the Gaussian function method by Boys and Shavitt.[21]

[18] W. H. Stockmayer, J. Chem. Phys. **9,** 398 (1941).
[19] T. Kihara, Revs. Modern Phys. **25,** 831 (1953).
[20] Values of $F(\theta K)$ for θ/T from 0.01 to 7.00 in steps of 0.01 are given by J. F. Connolly and G. A. Kandalic, Phys. Fluids **2,** 463 (1960), and Documentation Institute, Library of Congress, Document No. 6307.
[21] S. F. Boys and I. Shavitt, Proc. Roy. Soc. (London) **A254,** 487 (1960).

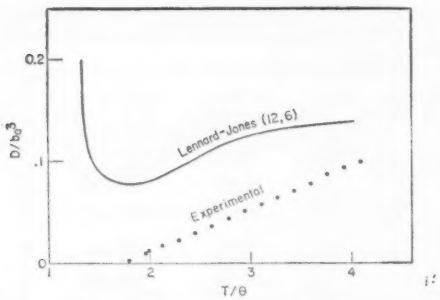

FIG. 5. The fourth virial coefficient of tetrafluoromethane.

values of C were taken from Table IV, and the parameters b_0 and θ were taken from Table VII. The agreement with theory is poor, probably because the parameters, as derived from the second virial coefficient, are essentially empirical. Also, the third virial coefficient is more sensitive to the shape of the potential field, and emphasizes the integral of the potential function at smaller values of the separation of the molecules.

Fourth Virial Coefficient

A calculation by Boys and Shavitt[21] of the fourth virial coefficient based on the Lennard-Jones (12, 6) potential is compared in Fig. 5 with the experimental values obtained for tetrafluoromethane. The experimental values of D were taken from Table IV, and the parameters b_0 and θ (Table VII) were obtained from the second virial coefficient correlation. The fact that the experimental values are positive and follow the upward temperature trend predicted by the theory is considered to be more significant than the lack of agreement in the absolute values. Because a systematic error of only 0.01% in number of moles of sample could account for most of the difference shown, the agreement is considered to be satisfactory.

Energy Levels of $PrCl_3$*

JACK S. MARGOLIS
Atomics International, Canoga Park, California

(Received March 13, 1961)

A review of the spectra of the Pr^{3+} ion in $PrCl_3$ is presented and the spectra are reanalyzed by means of a more complete Hamiltonian than has been previously used. This new Hamiltonian includes a complete calculation of the crystalline field interaction for a field of D_{3h} symmetry, and the first-order calculation of the orbit-orbit, mutual spin-orbit, and spin-spin interactions, as well as the usual spin-orbit and mutual electrostatic interactions. The multiplet splitting and crystalline field splitting are treated separately according to a least-squares procedure; the standard deviation of the center of gravity of the multiplets is 200 cm^{-1} without the orbit-orbit interaction and 105 cm^{-1} with the orbit-orbit interaction. The values of F_2, F_4, F_6, ζ, and α are 305.4, 51.88, 5.321, 729.5, —, cm^{-1}, respectively, in the first case, and 307.9, 50.23, 5.033, 755.1, −0.6542, cm^{-1}, respectively, in the second case. The standard deviation of the calculation for 40 of the crystalline field levels is 7 cm^{-1}. If the deviation of the $^1D_2$ levels, which fit the calculation particularly badly, are not included, the standard deviation is then only 4 cm^{-1}. The values of the crystalline field parameters are: $A_{20}\langle r^2\rangle=47.26$, $A_{40}\langle r^4\rangle=-40.58$, $A_{60}\langle r^6\rangle=39.62$, $A_{66}\langle r^6\rangle=26.67$ cm^{-1}.

INTRODUCTION

THE spectra of the salts of trivalent praeseodymium are typical of those of most other rare-earth salts. These spectra are composed of closely spaced groups of sharp lines which are widely spaced from each other. The groups of lines are usually spread out over an energy interval of several hundred cm^{-1} or less, and they are separated from each other by energies of, perhaps, an order of magnitude greater. The accepted explanation for the appearance of these spectra is that they arise from transitions between levels of the f^n configuration, where n is the number of the ion in the rare-earth series. The usual $(2J+1)$-fold degeneracy of the terms of such configurations is reduced to some extent by the action of the crystalline field. This crystalline field interaction is about an order of magnitude smaller than the spin-orbit interaction for the rare earths in most salts, and the transitions from the ground levels to the excited crystalline field levels are what give rise to the groups of closely spaced lines in the spectra. The lines are sharp because the $4f$ electrons are protected, more or less, from the influence of the lattice by the polarization of the $5s^2$ and $5p^6$ closed shells.

In the early days of the spectroscopy of the rare-earth salts, attention was paid only to the labeling of the levels of the rare-earth ions with their LSJ quantum numbers. The crystalline field splitting was not considered in the calculations of the energy levels, nor were the individual crystalline field levels identified experimentally. The first attempts to label the crystalline field levels by their appropriate quantum numbers, that met with fair success, were made by Hellwege and Hellwege.[1] They analyzed the spectra of $Pr_2Zn_3(NO_3)_2$ and $Pr_2Mg_3(NO_3)_2$ and deduced the symmetry of the lattice site of the Pr^{3+} ion to be C_{3v} in these salts; they also gave the crystal quantum number of about 10 of the levels. Later, Sayre, Sancier, and Freed[2] made an analysis of the spectra of $PrCl_3$ in which they identified many more levels of the Pr^{3+} ion. Their identifications were criticized and used by Judd[3] in a paper in which he made the following sort of calculations: He first deduced a set of intermediate coupling wave functions for the terms of Pr^{3+} by assuming a hydrogenic form for the radial wave function of the $4f$ electrons. This fixed the ratio of the Slater integrals F_k. He then adjusted the value of F_2 and the spin-orbit parameter ζ in order to fit the observed term splitting. Then, armed with a set of intermediate coupling eigenvectors, he proceeded to calculate the expectation value of the crystalline field in this basis. He did not use the full set of crystalline field parameters, but reduced them by one. This was accomplished by using the ratio (A_{60}/A_{66}) calculated by Wong.[4] Judd's criticism was later substantiated by the experimental results of Dieke and Sarup[5] who were able to take the fluorescence spectra of $PrCl_3$ and thereby provided identification for some of the levels missing from the SSF study. A calculation of the term energies of Pr^{3+} and also Tm^{3+}, which is the conjugate of Pr^{3+}, has been made by Runciman and Wybourne[6] who applied an $\alpha L(L+1)$ correction, about which more will be said later.

Although much attention is being paid these days to calculations of the crystalline field splitting of free ion levels, very few attempts have been made to apply the theory in a complete manner by computing the complete matrices of the crystalline field. That is to say, the applications of the theory to rare-earth spectra have usually

* This work was submitted as partial fulfillment of the requirements for the Ph.D. degree at the University of California at Los Angeles, 1960. It was partially supported by funds from the office of ordnance research.

[1] A. M. and K. H. Hellwege, Z. Physik **130,** 549 (1951).

[2] E. V. Sayre, K. M. Sancier, and S. Freed, J. Chem. Phys. **23,** 2060 (1955); **23,** 2066 (1955); **29,** 242 (1958). These authors shall be referred to as SSF in subsequent references.

[3] B. R. Judd, Proc. Roy. Soc. (London) **A241,** 414 (1957).

[4] C. A. Hutchison and E. Wong, J. Chem. Phys. **29,** 754 (1958).

[5] G. H. Dieke and R. Sarup, J. Chem. Phys. **29,** 741 (1958).

[6] W. A. Runciman and B. G. Wybourne, J. Chem. Phys. **31,** 1149 (1959).

TABLE I. These are the $|J, M\rangle$ basis functions for the irreducible representations of D_{3h}.

$^1\Gamma_1$:	$\|0,0\rangle$; $\|2,0\rangle$; $\|4,0\rangle$; $\frac{1}{2}[\|6,6\rangle+\|6,-6\rangle]+(\frac{1}{2})^{\frac{1}{2}}\|6,0\rangle$; $\frac{1}{2}[\|6,6\rangle+\|6,-6\rangle]-(\frac{1}{2})^{\frac{1}{2}}\|6,0\rangle$
$^1\Gamma_2$:	$\|1,0\rangle$; $\|3,0\rangle$; $\|5,0\rangle$; $(\frac{1}{2})^{\frac{1}{2}}[\|6,6\rangle-\|6,-6\rangle]$
$^1\Gamma_3$:	$(\frac{1}{2})^{\frac{1}{2}}[\|3,3\rangle-\|3-3\rangle]$; $(\frac{1}{2})^{\frac{1}{2}}[\|,4,3\rangle+\|4,-3\rangle]$; $(\frac{1}{2})^{\frac{1}{2}}[\|,5,3\rangle-\|5,-3\rangle]$; $(\frac{1}{2})^{\frac{1}{2}}[\|6,3\rangle+\|6,-3\rangle]$
$^1\Gamma_4$:	$(\frac{1}{2})^{\frac{1}{2}}[\|3,3\rangle+\|3,-3\rangle]$; $(\frac{1}{2})^{\frac{1}{2}}[\|4,3\rangle-\|4,-3\rangle]$; $(\frac{1}{2})^{\frac{1}{2}}[\|5,3\rangle+\|5,-3\rangle]$; $(\frac{1}{2})^{\frac{1}{2}}[\|6,3\rangle-\|6,-3\rangle]$
$^2\Gamma_5$:	$\|2,\pm2\rangle$; $\|3,\pm2\rangle$; $\|4,\pm2\rangle$; $\|5,\pm2\rangle$; $\|6,\pm2\rangle$; $\|4,\mp4\rangle$; $\|5,\mp4\rangle$; $\|6,\mp4\rangle$
$^2\Gamma_6$:	$\|1,\pm1\rangle$; $\|2,\pm1\rangle$; $\|3,\pm1\rangle$; $\|4,\pm1\rangle$; $\|5,\pm1\rangle$; $\|6,\pm1\rangle$; $\|5,\mp5\rangle$; $\|6,\mp5\rangle$

been made only to first order in the crystalline field. It should be mentioned, however, that extensions to crystalline field theory have been made in other ways, for example, by Jarret[7] who has shown how exchange interactions can be included.

The spectra of praseodymium salts are probably the most thoroughly studied of any of the rare earth and their spectra are undoubtedly the most satisfactorily understood. Slightly more than one-half of the 91 levels of the Pr^{3+} ion in the crystalline field of $PrCl_3$ have been identified and labeled, although somewhat ambiguously in some cases, according to their $LSJ\mu$[8] quantum numbers. In view of the thoroughness of the analysis of the Pr^{3+} levels, it was thought to be an appropriate time for a more extensive calculation to be made. For this purpose, the complete secular determinant of the f^2 configuration in a crystalline field has been written down and solved numerically.

This has been done with the thought of discovering the limits of validity of the usual crystalline field theory as applied to the rare earths, and of determining the necessity for corrections to this theory. To this purpose, the orbit-orbit interaction between the two f electrons was included into the calculations. This will be discussed later on.

CALCULATIONS

The calculations of the matrix elements were made by using the usual vector coupling methods. These do not always give results identical to the Racah tensor method of calculation since the vector methods allow for an arbitrariness in the choice of phase for the wave functions. For the proper choice of phase and the values of the electrostatic, spin-orbit, and reduced matrix elements of the crystalline field, the paper by Satten and Margolis[9] should be consulted.

[7] H. S. Jarret, J. Chem. Phys. **31,** 1579 (1959).

[8] The crystalline field quantum number μ is often used in place of the irreducible representation label to identify the crystalline field levels. It is defined and discussed by K. H. Hellwege, Ann. Physik **6,** 4, 95 (1948).

[9] R. A. Satten and J. S. Margolis, J. Chem. Phys. **32,** 573 (1960).

The point group symmetry at a Pr^{3+} lattice is C_{3h}. The normalization of the crystalline field potential is chosen so as to correspond to the one used by Judd. The terms which appear in the potential are:

$$V_{\text{cryst}}=A_{20}r^2T_{20}+A_{40}r^4T_{40}+A_{60}r^6T_{60}+A_{66}r^6(T_{66}+T_{6-6})+iB_{66}r^6(T_{66}-T_{6-6}).$$

The A_{LM} are regarded as empirical parameters which are adjusted to match the observed splitting of the levels. The T_{LM} are spherical tensor operators which transform like the spherical harmonics Y_{LM}. In order to simplify the diagonalization of the Hamiltonian, by dealing with only real matrices, the term in the interaction which has imaginary matrix elements, $iB_{66}(T_{66}-T_{6-6})$, was left out. This is equivalent to increasing the symmetry of the Pr^{3+} site to D_{3h} (the potential used by Judd has this symmetry). However, according to the crystal structure proposed by Zachariasen,[10] the nearest neighbors of the Pr^{3+} ion are nine Cl^- ions arranged in a D_{3h} symmetry, thus lending weight to the use of this symmetry in the potential. In any case, if we restrict ourselves to only 2×2 matrices, the eigenvalues of the Hamiltonian are the same whether we write the interactions as $A_{66}(T_{66}+T_{6-6})+iB_{66}(T_{66}-T_{6-6})$ or as $[A_{66}^2+B_{66}^2]^{\frac{1}{2}}(T_{66}+T_{6-6})$. This is not true for secular equations higher than second degree, but we expect first-order theory to be quite good in this case. Accordingly, since the local symmetry about the Pr^{3+} ion is so nearly D_{3h}, and since the results of the deviation from this symmetry effectively appear only in higher than first order, it was not thought necessary to include the B_{66} term explicitly. The value reported for $A_{66}\langle r^6\rangle$ is more reasonably, but not exactly, that for $[A_{66}^2+B_{66}^2]^{\frac{1}{2}}$, where B_{66} is much less than A_{66}. Furthermore, reduction from D_{3h} to C_{3h} symmetry will not reduce the degeneracy of any of the crystalline field levels; in a C_{3h} field the doubly degenerate levels of D_{3h} are Kramers' doublets and retain their twofold degen-

TABLE II. This is the character table for D_{3h}. The character for $(\sigma_hC_3^2)$, which is not necessary to specify the operations of the D_{3h} group, is included in order to facilitate the decomposition of the irreducible representation of D_{3h} into those of C_{3h}. Following the notation of Wilson, Decius, and Cross, *Molecular Vibrations* (McGraw-Hill Book Company, Inc., New York, 1955), the decomposition is $^1\Gamma_1$ and $^1\Gamma_2$ go into A', $^1\Gamma_3$ and $^1\Gamma_4$ go into A'', $^2\Gamma_5$ goes into E', and $^2\Gamma_6$ goes into E''.

	E	$2C_3$	$3C_2$	σ_h	$2S_3$	$3\sigma_v$	$(\sigma_hC_3^2)$
$^1\Gamma_1$	1	1	1	1	1	1	1
$^1\Gamma_2$	1	1	−1	1	1	−1	1
$^1\Gamma_3$	1	1	−1	−1	−1	1	−1
$^1\Gamma_4$	1	1	1	−1	−1	−1	−1
$^2\Gamma_5$	2	−1	0	2	−1	0	−1
$^2\Gamma_6$	2	−1	0	−2	1	0	1

[10] X. Zachariasen, Acta Cryst. **1,** 266 (1948).

eracy even though C_{3h} has no two-dimensional irreducible representations. The $|JM\rangle$ basis functions for the six irreducible representations of the D_{3h} group are listed in Table I. The character table for D_{3h} is put in Table II. The selection rules for electric dipole transitions are contained in Fig. 1.

The secular determinant for the levels of Pr^{3+} in a D_{3h} potential can be reduced to one 12×12, one 5×5, two 7×7's, two identical 16×16's, and two identical 14×14's by the usual group theoretical techniques.

The intermediate coupling parameters, which determine the energies of the $|LSJ\rangle$ terms, were determined separately from the crystalline field parameters, which determine the splitting of the levels of the $|LSJ\rangle$ terms. The intermediate coupling parameters were obtained by fitting them, according to an iterative "least squares" procedure, to the centers of gravity of the empirical levels. In the cases where all of the levels of a given $|LSJ\rangle$ term had not been found experimentally, its center of gravity was estimated by calculating where the missing levels would be. This was done by using a preliminary estimate of the crystalline field parameters.

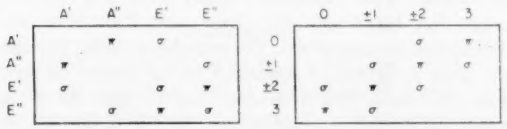

FIG. 1. The selection rule charts. The identification $A'\leftrightarrow\mu=0$; $A''\leftrightarrow\mu=3$; $E'\leftrightarrow\mu=\pm2$; and $E''\leftrightarrow\mu=\pm1$ should be made.

These centers of gravity were further corrected for higher-order shifts in the crystalline field by again calculating the crystalline field levels in first order and then subtracting the difference between the first-order and "exact" levels from the empirical ones. The center of gravity of the ground term was put at zero for these calculations, and so this energy was subtracted from all the other levels as well.

The electrostatic Slater integrals, F_2, F_4, F_6, and the spin-orbit parameter ζ were adjusted separately to fit the corrected centers of gravity. The results are given in Tables III and IV. This analysis was begun for the purpose of testing the limits of the theory, and it was thought to be interesting to include another interaction into the Hamiltonian; because it has been used by other investigators with some measure of success, which indicates its importance for understanding atomic energy level structure, this interaction was chosen to be the orbit-orbit interaction. It has been used by Trees[11] and others[12] to explain some of the features of the spectra of the transition group elements; also, Runciman and Wybourne[5] have applied this type of correction term to

[11] R. E. Trees, Phys. Rev. **84**, 1089 (1951); **83**, 756 (1951).
[12] D. R. Layzer, Special Rept. No. 23, Harvard University, May 2, 1950; C. W. Ufford and H. B. Callen, Phys. Rev. **110**, 1352 (1958).

TABLE III. The matrix elements of the orbit-orbit interaction. The effects of the spin-spin and mutual spin-orbit interactions are included here. The total is computed according to the weights $M^{(2)}/M^{(0)}=0.6090$ and $M^{(4)}/M^{(0)}=0.4276$.

Term	$M^{(0)}$	$M^{(2)}$	$M^{(4)}$	Total
$^1S_0$	672	224	102	852
$^3P_0$	616	138	−69.5	670
$^3P_1$	616	104	−39.8	663
$^3P_2$	615	101	−37.4	660
$^1D_2$	504	−37.3	−42.4	463
$^3F_2$	337	−107	44.2	291
$^3F_3$	337	−114	58.9	303
$^3F_4$	337	−113	48.4	289
$^1G_4$	112	−37.3	−26.2	78.0
$^3H_4$	−174	114	6.00	−101
$^3H_5$	−170	108	7.87	−101
$^3H_6$	−162	114	6.81	−90.1
$^1I_6$	−504	−37.3	−0.771	−527

the levels of Pr^{3+} and Tm^{3+}. However, not all of these investigators have used the orbit-orbit interaction in its exact form. That is to say, they have used an interaction of the form

$$\sum_{i<j}\alpha(\mathbf{r})\mathbf{l}_i\cdot\mathbf{l}_j.$$

This is, however, only one term in an expansion of the correct form of the orbit-orbit interaction. The reason that the interaction must have a more complicated form

TABLE IV. The centers of gravity of the LSJ terms. These have been corrected for displacements due to the crystalline field.

State	Exp	Calc ($\alpha=0$)	Calc ($\alpha\neq0$)	Calc $[\alpha L(L+1)]$
$^1S_0$	... cm^{-1}	50 673 cm^{-1}	49 484 cm^{-1}	49 974 cm^{-1}
$^3P_0$	20 373	20 407	20 356	20 402
$^3P_1$	20 924	20 984	20 975	21 011
$^3P_2$	22 130	22 211	22 233	22 266
$^1D_2$	16 640	16 973	16 701	16 738
$^3F_2$	4823	4735	4591	4571
$^3F_3$	6220	6088	5997	5980
$^3F_4$	6670	6774	6639	6639
$^1G_4$	9773	10 002	9828	9870
$^3H_4$	0	0	0	0
$^3H_5$	2112	2026	2112	2107
$^3H_6$	4295	4167	4320	4318
$^1I_6$	21 395	20 896	21 299	21 237
σ		200	105	127

TABLE V. The intermediate coupling parameters for which the results in Table IV were obtained.

	$\alpha=0$	$\alpha\neq 0$	$\alpha L(L+1)$
F_2	305.4 cm^{-1}	307.9 cm^{-1}	308.0 cm^{-1}
F_4	51.88	50.23	50.92
F_6	5.321	5.033	5.115
ζ	729.5	755.1	753.9
α	...	−0.6542	14.77

than the one above is that the argument of α involves the mutual separation of the electrons i and j, and not their individual separations from the nucleus. The correct form for the orbit-orbit interaction, calculated in a basis of states of the l^n configuration is in the author's dissertation[13] and can also be found in the papers by Horie[14] and Yanagawa.[15] The interaction is found to depend on three independent parameters, $M^{(0)}$, $M^{(2)}$, $M^{(4)}$, which can be expressed in terms of certain radial integrals. Instead of dealing with three independent parameters, it was found convenient to express $M^{(2)}$ and $M^{(4)}$ in terms of $M^{(0)}$. This was done by evaluating the appropriate radial integrals using hydrogenic wave functions.

$$M^{(k)}=\frac{\alpha^2}{4}\iint\frac{r_<^k}{r_>^{k+3}}R_{nl}(r_<)^2R_{nl}(r_>)^2d^3r_<d^3r_>.$$

These integrals are similar to the ordinary Slater integrals which, when evaluated according to the semi-empirical method employed here, have approximately the correct hydrogenic ratio. The ratios are for $4f$ electrons

$$M^{(2)}/M^{(0)}=0.6090, \qquad M^{(4)}/M^{(0)}=0.4276.$$

It turns out that the spin-spin and mutual spin-orbit interactions depend on the same parameters and so these were also included in the calculations. The orbit-orbit interaction gives the largest contribution to the energy and so the sum of these three are given the collective name orbit-orbit interaction. Also, of the three terms in the orbit-orbit interaction, it is the $M^{(0)}$ one which gives the largest contribution. It can be shown that this has the form

$$\begin{aligned}(j_1j_2LM\,|\,U_1^{(1)}\cdot U_2^{(1)}\,|\,j_1'j_2'L'M')&\\ =A(j_1j_2j_1'j_2')W(j_1'j_2'j_1j_2;Lk)&\\ =A(j_1j_2j_1'j_2')(-)^{2j_1-L-1}[(2j_1-1)!/(2j_1+2)!]&\\ \times\{-2[L(L+1)-2j_1(j_1+1)]\},&\end{aligned}$$

where A does not depend on L and W is the usual Racah coefficient. This expression, then, gives the $L(L+1)$ correction term used by Trees and Runciman and Wybourne, among others. The remaining terms, though, do cause a significant deviation of the correction term from this form. The first-order matrix elements of the entire orbit-orbit interaction are given in Table III. In Tables IV and V, are given a comparison of results obtained by using the complete and partial forms of the orbit-orbit interaction.

Once the intermediate coupling parameters are established, it is possible to do the least squares analysis for the crystalline field parameters. It is necessary that the intermediate coupling values are known first because the crystalline field splitting of the $|\,LSJ\rangle$ levels depend strongly on the mixing between states of different L and S but the same J. This mixing depends directly on the value of ζ and so it must be determined accurately if the crystalline field splitting calculations are to be done accurately. However, in calculating the least-squares values of the crystalline field parameters, it is necessary to replace the electrostatic energy by a single number for each $|\,LSJ\rangle$ term, which is adjusted so as to cause the center of gravity of the calculated levels to coincide with that of the empirical levels. It is necessary to resort to this stratagem since the intermediate coupling calculations cannot remove a standard deviation of about

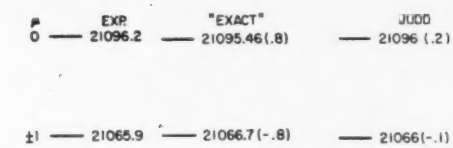

FIG. 2(a). The levels of $^3P_1$. The numbers in the brackets are the difference between the experimental and calculated energies.

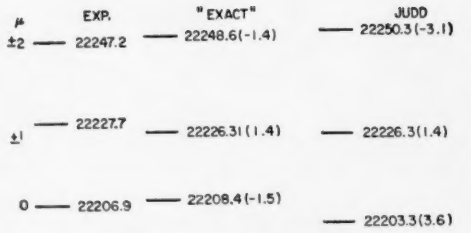

FIG. 2(b). The levels of $^3P_2$.

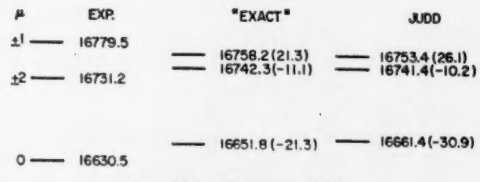

FIG. 2(c). The levels of $^1D_2$.

[13] J. S. Margolis, Ph.D. dissertation, University of California at Los Angeles, June, 1960.
[14] H. Horie, Progr. Theoret. Phys. (Kyoto) **10**, 296 (1953).
[15] S. Yanagawa, J. Phys. Soc. Japan **10**, 1029 (1955).

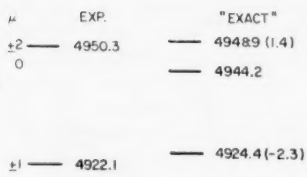

FIG. 2(d). The levels of $^3F_2$.

100 cm^{-1} in the centers of gravity of the $|LSJ\rangle$ levels. If the crystalline field parameters are adjusted according to the least-squares procedure with this standard deviation remaining in the centers of gravity, they will try to adjust themselves to remove it, and they will not adjust themselves so as to reproduce the observed splitting.

The results of the crystalline field calculations are given in Figs. 2(a)–2(k). The numbers under the column labeled Judd are not the ones calculated by him; his numbers have been adjusted so that the center of gravity of his levels agrees with the center of gravity of the empirical levels which was calculated as described above.

DISCUSSION

^3P Multiplet

Only the A_{20} and A_{40} crystalline field terms are effective in splitting the levels of this multiplet; there are three energy differences to compute and so the values of these parameters are over determined. The ^3P levels were used to obtain the initial estimate of these parameters. All of the levels of the ^3P multiplet were found by both SSF and DS, and their identifications are in substantial agreement. The calculated values of the crystalline field levels are compared to the experimental values and to Judd's calculations. The agreement is quite good; in fact, the deviations are smaller than the deviations of the values obtained by SSF and DS from their spectra.

$^1D_2$ Term

Again, both SSF and DS found all of the levels of this term in their spectra and are in agreement on the assignment of crystal quantum numbers to them. The agreement between the empirical levels and the calculated ones is the worst of any of the terms in the spectra both

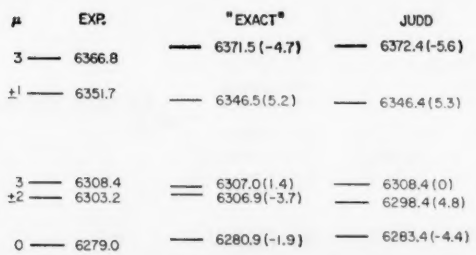

FIG. 2(e). The levels of $^3F_3$.

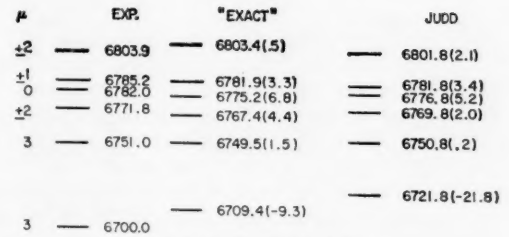

FIG. 2(f). The levels of $^3F_4$.

for Judd's first-order calculations and the calculations done here; however, the ordering of the levels is at least correct in both calculational schemes. The reduced matrix elements of the crystalline field for this term depend strongly on the mixing with the other $J=2$ states, and it is possible that the deviations here are due to configuration interaction modifying the intermediate coupling states. Judd's suggestion that it might be due to mixing with the $^1I_6$ term must be ruled out as this term has been found by DS and is much too far away in energy to be effective in causing the deviations; the crystalline field interaction of the $^1D_2$ levels with those of $^1I_6$ produces an energy shift of less than 1 cm^{-1} in these levels.

^3F Multiplet

Only the $\mu=\pm1$, ±2 levels of $^3F_2$ were found by DS, and none were found by SSF. The missing $\mu=0$ level is predicted to be between them; it is strange that it was not observed since transitions to this level from both the ground level (σ) and the first excited level (π) are allowed. The nonoccurrence of allowed transitions occurs also in the $^3F_4$ spectra where transitions to one of the $\mu=\pm2$ levels apparently does not occur, and in the $^1I_6$ spectra where many lines do not appear. It may be that these lines are so broadened or so weak that they are not detectable; it is not possible to use a selection rule on spin to explain the nonappearance of the transitions, as may be possible with the $^1I_6$ spectra. The agreement of the calculations with the empirical levels is very good, and probably within the experimental error.

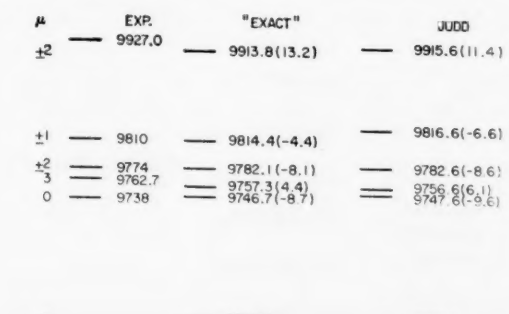

FIG. 2(g). The levels of $^1G_4$.

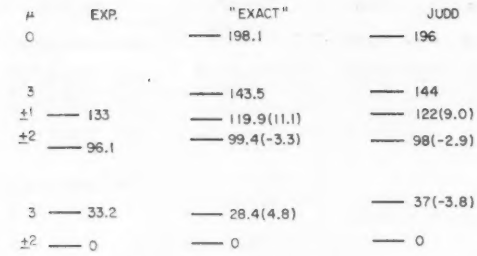

FIG. 2(h). The levels of $^3H_4$.

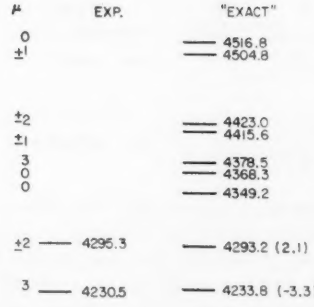

FIG. 2(j). The levels of $^3H_6$.

Individually, SSF and DS were not able to find all of the levels of the $^3F_3$ term, however, collectively this was accomplished. The levels at 6308 and 6352 cm^{-1} were not identified unambiguously in the DS spectra, and the calculations were used to remove the ambiguity in their labeling. The disagreements between the energies assigned to the levels by SSF and DS seem to be quite large, and, in several cases, amount to 4 or 5 cm^{-1}, which is close to the standard deviation of the calculations. However, there does not seem to be any confusion as to the ordering of the levels. SSF place two $\mu=3$ levels at 6296 and 6292 cm^{-1}. These designations are rejected on the theoretical grounds that the splitting between the two $\mu=3$ levels must be approximately twice the expectation value of the $A_{66}\langle r^6\rangle$ parameter for these levels. (See also Judd.) Fortunately, DS have found a $\mu=3$ level at 6366.8 cm^{-1} which agrees with the calculations. The agreement of the calculations is not so good as with the other terms, but it still is about the same as the agreement between the SSF and DS assignments.

The levels at 6800 cm^{-1} were identified by SSF as $^3F_2$, but DS found enough extra levels to verify Judd's designation of $^3F_4$ for these levels. Essentially, all of the $^3F_4$ levels are identified. The $\mu=\pm2$ level at 6773 cm^{-1} is common to both SSF and DS spectra. The SSF designations for the $\mu=0$, ±1, ±2 levels at 6782, 6785, and 6773 cm^{-1}, respectively, and the DS designations for the rest were used in this analysis. The agreement with the calculations is not too good, and, again, this may be due to the strong sensitivity of the reduced matrix elements to mixing with other states of the same J.

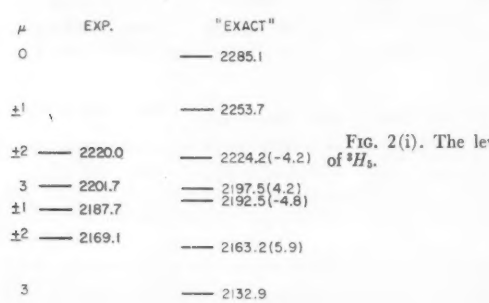

FIG. 2(i). The levels of $^3H_5$.

$^1G_4$ Term

Only one $\mu=3$ term is missing from the experimentally identified levels, and this is predicted to lie approximately 150 cm^{-1} below the rest; electric dipole transitions to $\mu=3$ states from the three lowest ground levels are forbidden, and so, if it appears at all, it should be very weak at low temperatures. In fitting the levels, only the $\mu=3$ level at 9762.7 cm^{-1} of DS was used; all the other levels are those found by SSF. The $\mu=\pm2$ level at 9927 cm^{-1} originally was thought to be a vibronic transition by SSF. Judd's calculations caused them to re-examine their spectra and make this new designation. As is the case with the $^3F_4$ levels, the mean square deviation of the calculations is probably higher than the experimental error (5.7 cm^{-1} for $^3F_4$ and 8.4 cm^{-1} for $^1G_4$). The mixing of the $^1G_4$ and $^3F_4$ levels by the spin-orbit interaction is very thorough, and so it is not surprising that if the $^3F_4$ levels do not fit well, the $^1G_4$ do not either.

^3H Multiplet

The $^3H_4$ term is the ground term for Pr^{3+} and, as expected, there is good agreement between SSF and DS as to its levels. However, as with the other $J=4$ states, the agreement here of the calculations with the empirical levels is not outstanding.

The designations of the levels of the $^3H_5$ term were guessed at by the simple expedient of using an initial

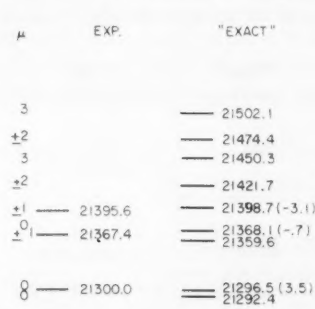

FIG. 2(k). The levels of $^1I_6$.

estimate of the crystalline field and adjusting the center of gravity of the calculated levels until they best matched the experimental ones. In this way, the ambiguity in the DS spectra of the levels at 2134.5, 2187.7, 2201.7, and 2222.0 cm^{-1} was resolved. The level at 2115.4 cm^{-1}, found by DS, does not fit into the calculations at all. It is a weak line, and possibly might be vibronic in origin. There is no other way to arrange the energy levels to obtain such satisfactory agreement with experiment, and so the present designations are retained.

Only two of the levels of the $^3H_6$ term found by DS can be made to fit the calculations, namely those at 4230.9 and 4295.4 cm^{-1}. These may be made to be the upper $\mu=\pm 2$, 3, or the lower $\mu=\pm 2$, 3 pair. However, by choosing them to be the lower pair, the center of gravity of the $^3H_6$ term agrees much more closely with the calculations.

$^1I_6$ Term

DS finds three levels for this term. The lower one of these, they find, is split in a magnetic field with a rather large splitting factor. The polarization of the lines indicates that this level should have the designation $\mu=0$; however, the levels with $\mu=0$ are nondegenerate and cannot be split in a magnetic field. The calculations show that two $\mu=0$ states should appear quite close to each other in the $^1I_6$ level structure; these can be coupled by the magnetic field, and if they are close enough to each other, will have a very nearly linear zeeman effect with the large splitting factor observed. The separation of these $\mu=0$ terms is calculated to be 4 cm^{-1}.

SUMMARY

The energy levels of Pr^{3+} in $PrCl_3$ have been calculated in the approximation that they arise from an f^2 configuration; the complete secular determinant of the crystalline field, spin-orbit, and mutual electrostatic interact ion has been written down and solved. The standard deviation for 40 levels is 7.0 cm^{-1} compared to a standard deviation of 10.3 cm^{-1} for 27 levels for Judd's first-order calculations. A further improvement in the calculations was made by including the small orbit-orbit, spin-spin, and mutual spin-orbit interaction between the two $4f$ electrons of the Pr ion. The use of these interactions reduced the standard deviation of the calculations of the centers of gravity of the LSJ terms of Pr^{3+} from 200 to 105 cm^{-1}.

The next step in the calculations would be to account for either configuration interaction in the Pr^{3+} ion or for the effects of bonding with the other atoms in the crystal, or for both. This would involve extremely extensive calculations and was not carried out. It appears that only in this way can the deviations of the calculations be removed, there apparently being no other interactions of just two $4f$ electrons large enough to explain the discrepancies.

ACKNOWLEDGMENTS

The numerical calculations in this paper were all carried out on the IBM 709 digital computer of the Western Data Processing Center at UCLA.

The author would also like to express his gratitude to Professor R. A. Satten with whom he had many useful discussions concerning this work.

Molecular Structure of Propylene

DAVID R. LIDE, JR.
National Bureau of Standards, Washington 25, D. C.
AND
DANIEL CHRISTENSEN
Chemical Laboratory of the University of Copenhagen, Copenhagen, Denmark

(Received March 21, 1961)

The microwave spectra of seven isotopic species of propylene have been studied in order to obtain an accurate molecular structure. The complete r_s (substitution) structure has been calculated. The more important parameters are: $r(C{=}C) = 1.336 \pm 0.004$ A, $r(C{-}C) = 1.501 \pm 0.004$ A, $\angle CCC = 124.3° \pm 0.3°$. The structure is compared with those of related molecules. It is concluded that no difference can be detected in the double-bond lengths in ethylene, propylene, and the vinyl halides. The CC single-bond length in propylene is indistinguishable from that in acetaldehyde and other acetyl compounds, and is 0.025 A shorter than the CC distance in saturated hydrocarbons. In the $=CH_2$ group in propylene, the CH bond *trans* to the methyl group appears slightly shorter than the *cis* CH bond; a similar effect occurs in the vinyl halides.

INTRODUCTION

THE microwave spectra of ordinary propylene and of one isotopic species have been reported previously.[1] While this investigation was chiefly concerned with internal rotation, some rough information was obtained on the molecular structure. However, it was necessary to assume the hydrogen parameters, and the stated uncertainty in the carbon-carbon distances was about ±0.02 A. Recently, there has been considerable debate[2–4] over the importance of conjugation and hyperconjugation in unsaturated hydrocarbons, as reflected in (among other things) the length of carbon-carbon bonds. Since the propylene molecule is frequently cited as one of the simplest examples of hyperconjugation, it is desirable to have a more precise structure for it. We have now obtained the microwave spectra of seven additional isotopic species of propylene, from which the complete molecular structure has been determined.

EXPERIMENTAL

All of the propylene species which were studied involved a single isotopic substitution, of either C^{13} or D, on the ordinary molecule, $C_3{}^{12}H_6$. For simplicity we shall designate each species by giving the position of the substituted atom, using the numbering of Fig. 1. Thus the H_1 species will refer to *cis* $CH_3CH{=}CHD$, and so on.

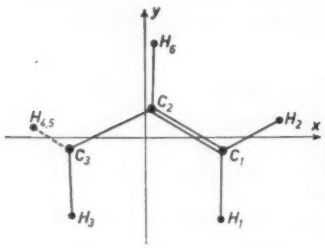

FIG. 1. Numbering of the atoms in propylene: x and y are principal axes; the z axis is perpendicular to the paper; $H_{4,5}$ is the projection of the out-of-plane hydrogen atoms.

The spectra of the C_1 and C_3 species were measured in natural abundance. The C_2 spectrum, which is reported in reference 1, was studied in an enriched sample. A deuterated sample containing a mixture of the H_1 and H_2 species was obtained commercially. A sample of $CH_2DCH{=}CH_2$, which provides the H_3 and $H_{4,5}$ species, was very kindly provided by Dr. D. R. Herschbach. Measurements on these species have already been made[5] for the purpose of establishing the conformation of the methyl group; however, somewhat higher accuracy is desirable for a quantitative structure determination, and we have accordingly remeasured the spectra.

2-D-propylene was prepared by zinc-dust reduction of 2-bromopropylene. This reaction gives very poor yield (≈1%), but the method is convenient for preparation of the very small amounts needed for microwave work. 15.5g of dioxane was added to the mixture of D_2O and CH_3COOD resulting from the reaction between 5.5-g D_2O and 16.3-g $(CH_3CO)_2O$. 15-g Zn dust and 6.8-g CH_3CBrCH_2 were introduced and the mixture was refluxed for 5 hours at 80°–90°C with mechanical stirring. Atmospheric moisture was excluded, and the temperature of the reflux condenser was kept at 10°C. The volatile reaction products were collected in a trap cooled with liquid nitrogen. After cooling the reaction flask was flushed with dry nitrogen. The crude product obtained was distilled *in vacuo* and finally purified by gas-chromatography; the amount of purified material was 0.0004 moles (gas). The mass spectrum showed only the presence of C_3H_5D and C_3H_6 (estimated ratio 2:1) and indicated the D atom to be placed at one of the double-bonded C atoms.

[1] D. R. Lide and D. E. Mann, J. Chem. Phys. **27,** 868 (1957).
[2] M. J. S. Dewar and A. N. Schmeising, Tetrahedron **5,** 166 (1959).
[3] R. S. Mulliken, Tetrahedron **5,** 253 (1959); **6,** 68 (1959).
[4] B. Bak and L. Hansen-Nygaard, J. Chem. Phys. **33,** 418 (1960).
[5] D. R. Herschbach and L. C. Krisher, J. Chem. Phys. **28,** 728 (1958).

TABLE I. Frequencies for propylene species (in Mc).

Species	Obs frequency (ν_A or peak) $1_{11}\rightarrow 2_{12}$	$1_{01}\rightarrow 2_{02}$	$1_{10}\rightarrow 2_{11}$	Corrected frequency $1_{11}\rightarrow 2_{12}$	$1_{01}\rightarrow 2_{02}$	$1_{10}\rightarrow 2_{11}$
Unsub.	33707.81	34851.52	36050.21	33707.75	34851.34	36049.97
C_1	32841.16	33933.42	35076.09[a]	32840.87	33933.38	35075.84
C_2	33625.62	34793.38	36019.84	33625.56	33793.21	36019.62
C_3	32847.20	33937.14	35077.02	32846.89	33937.09	35076.80
H_1	32229.17	33499.06	34850.14	32229.05	33499.03	34849.94
H_2	31174.64	32160.37	33186.35	31174.59	32160.34	33186.16
H_3	32364.93	33626.41	34966.94		same as obs frequency[b]	
$H_{4,5}$	31813.36	32735.34	33695.17		same as obs frequency	
H_6	32813.39	34223.64	35742.81	32813.30	34223.61	35742.64

[a] Not resolved from ν_E of the C_3 species.
[b] Torsional corrections are negligible for the H_3 and $H_{4,5}$ species.

ASSIGNMENT OF SPECTRA

The three $J=1\rightarrow 2$ transitions, which fall in the 30–36 kMc region, were measured for each isotopic species. Each transition is split into two components, designated as A and E, as a result of internal rotation, but not all of the doublets were resolved under the present experimental conditions. The observed frequencies of the A components (or, in the case of unresolved doublets, the peak frequency) are listed in Table I. The splittings $\nu_E-\nu_A$ are given in Table II for the transitions where they could be measured. The frequency measurements were accurate to at least 0.05 Mc, except for the C_1 and C_3 species, where the uncertainty may be as large as 0.10 Mc.

While the assignment of lines in the enriched isotopic samples is straightforward, some difficulty was encountered with the C_1 and C_3 species. Since these were studied in natural abundance, there is no direct way of distinguishing the lines of the two species. Furthermore, their rotational constants are so similar that the two spectra fall very close together; for the $1_{10}\rightarrow 2_{11}$ transition, in fact, the A component of one species is unresolved from the E component of the other. Fortunately, the observed lines can be sorted uniquely into two triplet patterns ($1_{11}\rightarrow 2_{12}$, $1_{01}\rightarrow 2_{02}$, and $1_{10}\rightarrow 2_{11}$) by requiring that the isotope shifts in the moments of inertia follow a rigid-rotor behavior. There are still two ways of assigning these two rigid-rotor spectra to the isotopic species C_1 and C_3. The coordinates of the carbon atoms were calculated for each assignment and combined with the coordinates of the various hydrogen atoms, which are obtained without ambiguity from the deuterated species. One choice was found to give a reasonable structure for the molecule (e.g., all CH distances in the range 1.08−1.10 A), while the other choice led to totally unacceptable CH distances. The assignment of lines to the C_1 and C_3 species is therefore firmly established.

TORSIONAL CORRECTIONS

In order to obtain accurate ground-state moments of inertia, it is necessary to correct the observed frequencies for the effect of internal rotation. These corrections are discussed in detail in reference 1. The torsional contribution to the frequency may be divided into two parts. The first of these can be absorbed, to a high approximation, into the effective rotational constants of the molecule, while the second produces deviations from a rigid-rotor pattern (and consequently a splitting into A and E components). In the original work on propylene,[1] both corrections were applied. The resulting moments of inertia (Table III of reference 1) have therefore been corrected for the contribution of one mode of vibration, the methyl torsion, but still contain contributions from the other 20 normal modes. Such a partial correction for rotation-vibration interactions does not seem desirable when the moments are to be used for a structure determination, since the structure will not be strictly comparable with those of other molecules obtained from simple "ground-state" moments. Accordingly, we have corrected only for those torsional contributions which lead to deviations from rigid-rotor behavior. The spectra of ordinary propylene and of the C_2 species have been treated in the same manner in order to obtain a consistent set of moments for all species. These moments differ slightly from the values in reference 1.

The correction which we require is designated by H_1 in reference 1 and is given explicitly in Eqs. (7) and (9) of that reference. The procedure adopted was to calculate first an approximate molecular structure from the observed ν_A frequencies. The inertial constants for each isotopic species were then calculated from this structure and used, together with the torsional barrier height of ordinary propylene (1978 cal/mole), to calculate the corrections H_1 for each species. These calculated corrections were applied to the observed ν_A

TABLE II. Torsional splittings ($\nu_E - \nu_A$).

Species	$1_{11} \rightarrow 2_{12}$ obs	$1_{11} \rightarrow 2_{12}$ calc	$1_{10} \rightarrow 2_{11}$ obs	$1_{10} \rightarrow 2_{11}$ calc
C_1	...[a]	0.46 Mc	−0.92	−0.90
C_2	...[a]	0.50	−0.93	−0.92
H_1	...	0.11	−0.45	−0.49
H_2	0.54	0.57	−0.89	−0.94
H_6	...	0.08	−0.44	−0.41

[a] Resolution was limited to about 0.7 Mc for the C_1 and C_2 species because of the necessity of working at high pressures.

frequencies to give the set of "corrected frequencies" included in Table I. The corrected frequencies were then fitted to a rigid-rotor formula to obtain the ground-state moments which were used for the final structure calculation. A recycling of the entire procedure gave no significant changes.

The moments of inertia obtained in this way are listed in Table III. The quantity $I_a+I_b-I_c$, which should be the same for all species except $H_{4,5}$, is also given. The agreement is well within the estimated experimental uncertainty.

The calculation of torsional corrections to the ν_A frequencies also yields the splittings $\nu_E-\nu_A$. The calculated splittings are compared with the observed in Table II. The close agreement provides some check on both the accuracy of the measurements and the method of handling the torsional corrections. It will be noted that the splittings are quite sensitive to isotopic substitution.

STRUCTURE CALCULATION

We shall describe the propylene molecule by a coordinate system xyz which coincides with the principal axis system of ordinary propylene (see Fig. 1); x, y, z are identified with a, b, c, respectively. The coordinates of each atom may be determined from the isotope shifts in the moments of the appropriate species, as described by Kraitchman[6] and Costain.[7] Since the experimental values of I_a are not sufficiently accurate, we are forced to use the rigid-rotor relation $\Delta I_a=\Delta I_c-\Delta I_b$. However, the experimental I_a must be used for the $H_{4,5}$ species, since isotopic substitution destroys the symmetry plane of the molecule.

The "substitution coordinates" (r_s) obtained in this way are listed in Table IV. They appear to be valid coordinates, with the exception of $x(C_2)$ and $y(H_{4,5})$. The central carbon atom is so close to the y axis that the substitution coordinate which one obtains (0.081 A) is probably unreliable. We have therefore calculated this coordinate from the first moment condition, $\sum m_i x_i=0$, which gives $x(C_2)=0.106$ A. In the case of $H_{4,5}$, the experimental uncertainty in ΔI_a is so large that the y coordinate is essentially undetermined.

TABLE III. Principal moments of inertia (in amu A²).[a]

Species	I_a	I_b	I_c	$I_a+I_b-I_c$
Unsub.	10.97[b]	54.3274	62.1491	3.15
C_1	10.99	55.8701	63.7424	3.12
C_2	11.16	54.3339	62.3563	3.14
C_3	10.95	55.8725	63.7252	3.10
H_1	12.57	55.9210	65.4015	3.09
H_2	11.01	59.1404	67.0270	3.12
H_3	12.47	55.7551	65.0956	3.13
$H_{4,5}$	11.68	58.3820	65.4993	4.56
H_6	13.25	54.3475	64.5044	3.09

[a] The conversion factor used was 505.531 (kMc)(amu A²).
[b] The experimental uncertainty in all I_a values is about ±0.05 amu A².

TABLE IV. Coordinates of propylene atoms (in A).

Atom	x	y	z
C_1	1.2538[a]	−0.2312[b]	0
C_2	0.1060[b,c]	0.4525[b]	0
C_3	−1.2550[a]	−0.1810[b]	0
H_1	1.2486[a]	−1.3226[a]	0
H_2	2.2110[a]	0.2708[b]	0
H_3	−1.1838[b]	−1.2633[b]	0
H_4	−1.8315[d]	0.14[e]	0.8775[f]
H_5	−1.8315[d]	0.14[e]	−0.8775[f]
H_6	0.1391[b]	1.5416[a]	0

[a] Estimated uncertainty ±0.001 A.
[b] Estimated uncertainty ±0.002 A.
[c] Calculated from first moment; substitution coordinate is 0.0812.
[d] Estimated uncertainty ±0.005 A.
[e] Mean of values from first moment and product of inertia; estimated uncertainty ±0.02 A.
[f] Estimated uncertainty ±0.01 A.

TABLE V. Structure of propylene.

$r(C_1=C_2)=1.336\pm0.004$ A	$r(C_1-H_1)=1.091\pm0.003$
$r(C_2-C_3)=1.501\pm0.004$	$r(C_1-H_2)=1.081\pm0.003$
	$r(C_2-H_6)=1.090\pm0.003$
$\angle H_1C_1H_2=118.0°\pm0.3°$	$\angle C_1C_2C_3=124.3°\pm0.3°$
$\angle H_1C_1C_2=120.5°\pm0.3°$	$\angle H_6C_2C_3=116.7°\pm0.3°$
$\angle H_2C_1C_2=121.5°\pm0.3°$	$\angle H_6C_2C_1=119.0°\pm0.3°$
Methyl group	
$r(C_3-H_3)=1.085\pm0.004$	$\angle H_3C_3H_4=109.0°\pm1.3°$
$r(C_3-H_{4,5})=1.098\pm0.014$	$\angle H_4C_3H_5=106.2°\pm1.8°$
$\angle H_3C_3C_2=111.2°\pm0.3°$	

[6] J. Kraitchman, Am. J. Phys. **21**, 17 (1953).
[7] C. C. Costain, J. Chem. Phys. **29**, 864 (1958).

However, it may be obtained from either the first moment condition, $\sum m_i y_i = 0$, or the product condition, $\sum m_i x_i y_i = 0$. The two calculations give 0.147 A and 0.131 A, respectively, with an uncertainty of 0.01–0.02 A in each case. We have adopted a value of 0.14± 0.02 A.

Table IV also includes an estimate of the uncertainty in each coordinate. These figures are somewhat arbitrary but have been made large enough to cover any errors from the frequency measurements, as well as the uncertainty introduced by the use of the relation $\Delta I_a = \Delta I_c - \Delta I_b$. The uncertainty from this source was estimated by analogy with the propane molecule, which has rather similar geometry. Here it was possible to measure all three moments with high accuracy, and the coordinates were found to vary slightly with the manner in which the rigid-rotor relations were introduced.[8]

The interatomic distances and angles obtained from the Cartesian coordinates are given in Table V. The uncertainties in these parameters have been carried through from the estimated uncertainties in Table IV. The limits of error which we have specified are felt to be conservative, with the possible exception of the parameters describing the methyl group. Here the large amplitude of the torsional oscillation may lead to larger, but not easily predictable, uncertainties.[8]

The moments of inertia of ordinary propylene calculated from the present structure are 10.927, 54.159, and 61.981 amu A^2. The observed I_b and I_c are each 0.168 amu A^2, or about 0.3%, larger than the calculated values. This difference may be compared with 0.5–0.6% in propane[8] and isobutane.[9]

DISCUSSION

When making a detailed comparison of the propylene structure with that of related molecules, we must take into account the possible difference in meaning of structural parameters determined by different experimental methods. The structure obtained here is essentially a substitution (r_s) structure, although the use of the center-of-mass relation introduces a slight ambiguity. It has been pointed out[9] that r_s values of the C–C distance in saturated hydrocarbons appear to be systematically lower by 0.005–0.010 A than the electron diffraction (r_g) determinations. It is also well-known[7] that r_0 structures determined from spectroscopic data may differ from r_s structures by many times the strictly experimental uncertainty. Therefore, we shall restrict ourselves as far as possible to comparisons between r_s structures.

The C=C double-bond length in propylene is found to be 1.336±0.004 A. If hyperconjugation is important in propylene, one expects, in principle, a lengthening of the double bond, relative to ethylene, although the most recent theoretical estimates[3] suggest that this increase should be small. The C=C distance in ethylene has been reported as 1.334±0.002 A by electron diffraction[10] (r_g), 1.339±0.002 A from the rotational Raman spectrum,[11] and 1.337±0.003 A from the infrared spectrum.[12] The infrared value is a mixed r_s and r_0 parameter, since it was obtained from the ground-state moments of C_2H_4 and C_2D_4. The isotope shifts in the moments fix the r_s coordinates of the H atoms, but the total moment must be used to locate the C atom. If we take into account the fact that moments calculated from r_s coordinates of simple hydrocarbons such as propylene and propane are 0.3–0.6% smaller than the actual ground-state moments, we may estimate the r_s value of the C=C distance in ethylene as 1.330–1.335 A. We conclude, then, that within the accuracy available at present, no difference can be detected between the double-bond length in propylene and ethylene. If there is any lengthening in propylene, it is almost certainly less than 0.010 A.

The C=C distance in propylene is also indistinguishable, within the stated limits of error, from the r_s values in vinyl chloride[13] (1.332±0.002 A), vinyl fluoride[14] (1.329±0.006 A), and vinyl cyanide[15] (1.339 A). A somewhat larger value, 1.347±0.003 A, has been reported in vinyl silane.[16] The difference between propylene and vinyl silane may be experimentally significant.

The C—C single-bond in propylene has the same length as in acetyl fluoride[17] (1.503±0.003 A), acetyl cyanide[18] (1.490±0.010 A), and acetaldehyde[19] (1.500± 0.005 A). On the other hand, r_s values for the C—C bond in saturated hydrocarbons[8,9] fall at 1.526±0.002 A, or about 0.025 A higher. A difference in the length of (sp^3)—(sp^2) and (sp^3)—(sp^3) bonds has long been recognized, but previous estimates, based on less accurate bond distances, were about twice as large as that found here.

The bond angles at the C_2 atom are slightly distorted from the values in ethylene,[12,20] where $\angle HCH = 117.4° \pm 1°$. Thus $\angle H_6C_2C_1$ in propylene is about 2° smaller, and $\angle CCC$ about 3° larger than the corresponding angle in ethylene. Rather larger distortions

[8] D. R. Lide, J. Chem. Phys. **33,** 1514 (1960).
[9] D. R. Lide, J. Chem. Phys. **33,** 1519 (1960).
[10] L. S. Bartell and R. A. Bonham, J. Chem. Phys. **27,** 1414 (1957).
[11] J. M. Dowling and B. P. Stoicheff, Can. J. Phys. **37,** 703 (1959).
[12] H. C. Allen and E. K. Plyler, J. Am. Chem. Soc. **80,** 2673 (1958).
[13] D. Kivelson, E. B. Wilson, and D. R. Lide, J. Chem. Phys. **32,** 205 (1960).
[14] D. R. Lide and D. Christensen, Spectrochim. Acta **17,** 665 (1961).
[15] C. C. Costain and B. P. Stoicheff, J. Chem. Phys. **30,** 777 (1959).
[16] J. M. O'Reilly and L. Pierce, J. Chem. Phys. **34, 1176** (1961).
[17] L. Pierce and L. C. Krisher, J. Chem. Phys. **31,** 875 (1959).
[18] L. C. Krisher and E. B. Wilson, J. Chem. Phys. **31,** 882 (1959).
[19] R. W. Kilb, C. C. Lin, and E. B. Wilson, J. Chem. Phys. **26,** 1695 (1957). This is an r_0 structure, but a recalculation shows that r_s for the CC bond probably does not differ from r_0 by more than 0.005 A.
[20] It may be shown that the $\angle HCH$ and r_{CH} given in reference 12 differ insignificantly from r_s values. See also reference 11.

TABLE VI. Comparison of C—H parameters in $H_2C{=}CHX$ compounds.[a]

	$X=H$[b]	CH_3[c]	F[d]	Cl[e]
$r(C_1—H_1)$	1.086±0.003 A	1.091±0.003	1.087±0.002	1.090±0.005
$r(C_1—H_2)$	1.086	1.081±0.003	1.077±0.003	1.078±0.005
$\measuredangle H_1C_1C_2$	121.3°±1°	120.5°±0.3°	120.9°±0.3°	121.0°±0.5°
$\measuredangle H_2C_1C_2$	121.3°	121.5°±0.3°	119.0°±0.3°	119.5°±0.5°
$r(C_2—H_6)$	1.086	1.090±0.003	1.082±0.004	1.079±0.005
$\measuredangle H_6C_2C_1$	121.3°	119.0±0.3°	129.2°±1°	123.8°±0.5°

[a] Atoms are labeled as in Fig. 1.
[b] References 12, 20
[c] This investigation.
[d] Reference 14.
[e] Reference 13.

are found in the vinyl halides,[13,14] but it is difficult to see any pattern in these changes. The C_2–H_6 distance appears to be slightly longer in propylene than in the vinyl halides (see Table VI).

The structure of the $=CH_2$ group in propylene has been determined with high accuracy and with no restrictive assumptions.[21] The result is compared in Table VI with the r_s structures for ethylene[20] and the vinyl halides. The bond ($C_1—H_1$), which is *cis* to the substituent, is seen to be consistently longer by about 0.010 A than the *trans* ($C_1—H_2$) bond. The mean length of the two bonds is 1.086, 1.082, and 1.084 A in propylene, vinyl fluoride, and vinyl chloride, respectively, which compares with 1.086 A in ethylene. While the observed difference in *cis* and *trans* CH bond lengths is not a great deal larger than the estimated uncertainty, its appearance in all three molecules leads us to believe that it is a real effect, and that it provides evidence that the *trans* CH bond is probably a little stronger than the *cis*.

The $H_1C_1C_2$ angle (*cis* to the substituent) is very close to the ethylene angle in all three molecules, but $\measuredangle H_2C_1C_2$ in the vinyl halides is about 2° smaller. In propylene, the *trans* angle appears 1.0° larger than the *cis* angle, which is probably experimentally significant.

The structure of the methyl group in propylene is poorly determined, largely because of the difficulty in locating the out-of-plane hydrogen atoms. The two distinct CH distances and HCH angles agree within the rather large experimental error. The two nonbonded HH distances are 1.755 A and 1.776 A, with an uncertainty of about 0.02 A in each; the corresponding distance in propane is 1.763 A. All of the present data can therefore be satisfied by an axially symmetric methyl group with r (CH) = 1.090 A and $\measuredangle$ HCH = 107.7°.

The one feature of the methyl structure which is fairly well fixed is the orientation of the plane defined by the three H atoms. The normal to this plane makes and angle of 24.8°±0.5° with the x axis, while the corresponding angle for the line joining C_3 to C_2 is 25.0±0.3°. Within an accuracy of 1°, therefore, the methyl axis coincides with the C—C bond.

In the determination of the barrier to internal rotation in propylene,[1] a value of 3.103 amu A² was used for the moment of inertia of the methyl group about its symmetry axis. With the best methyl structure found here, this moment becomes 3.123 amu A², with an uncertainty of at least 1%. There is no need, therefore, to correct the barrier height of reference 1, and the uncertainty quoted there still seems a reasonable one.

[21] Even the planarity of the vinyl group has been experimentally confirmed, since any deviation would destroy the C_s symmetry of propylene and lead to a splitting of the lines of the *asy* (CH_2D)$CHCH_2$ species (designated here as $H_{4,5}$). This is an extremely sensitive test for planarity.

ACKNOWLEDGMENTS

One of us (D.R.L.) is grateful to the National Science Foundation for a Senior Postdoctoral Fellowship under which a part of this research was conducted and to the Chemical Laboratory of the University of Copenhagen for its hospitality during this period. The second author (D.C.) is indebted to the Scandinavian-American Foundation for a grant making possible his visit to the National Bureau of Standards. We are also grateful to Dr. R. E. Ferguson for his assistance with the purification and analysis of the CH_3CD: CH_2 sample.

Ionization Cross Sections near Threshold by Electron Impact

R. E. Fox

Westinghouse Research Laboratories, Pittsburgh 35, Pennsylvania

(Received April 5, 1961)

Ionization curves near threshold have been taken with a mass spectrometer employing a monoenergetic electron beam. These curves have been fitted to previously published data from total ionization experiments in order to obtain absolute cross sections for the threshold energy region. Curves for helium, neon, argon, mercury, carbon monoxide, and nitrogen are given.

IN recent years a technique has been developed whereby ionization by electron impact can be studied by essentially monoenergetic electrons.[1,2] With this technique it has been possible to study in detail the shapes of the ionization efficiency curves near threshold of a number of gases.[3–6] Since these studies were performed with a mass spectrometer, only the relative shapes of the ionization efficiency curves could be obtained.

The ionization efficiencies (P_i) of several gases have been measured by a number of investigators.[7–9] These measurements have in general been made with instruments which could not make a mass analysis of the ions. In the early experiments the electron beam possessed an appreciable spread in electron energy. For this reason the curves obtained are not accurate in the vicinity of the ionization threshold. The notable exception to this is the work of Nottingham on the ionization efficiency of mercury vapor in which a magnetic analyzer was used to select electrons with narrow energy range from the larger energy distribution.

The ionization efficiency (P_i)[10] is defined as the number of ions formed per incident electron per centimeter path per millimeter pressure. A more convenient unit for many calculations is the ionization cross section Q_i. The cross section Q_i in square centimeters is related to the ionization efficiency P_i by the expression

$$Q_i = P_i/(3.55\times10^{16})$$

at 25°C.

In order to establish the ionization efficiency curves taken with the mass spectrometer near threshold on an absolute basis of ionization cross section, it is necessary to choose an energy range in which the present data on the shapes of the curves overlaps those of the ionization efficiency measurements.[11] The energy at which the value of P_i is selected to establish the cross-section scale should be sufficiently removed from the ionization threshold to be large compared to the energy spread of the electron beam used to determine the efficiency data.

Figure 1 gives the ionization cross section for helium. The value of Q_i is determined by taking the value of P_i as obtained by Smith[7] at 30-ev electron energy and converting by the above relation.

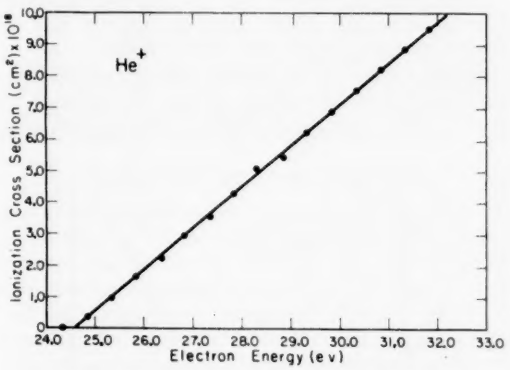

FIG. 1. The ionization efficiency curve for He^+.

Where the ionization proceeds linearly with energy (E) from threshold it is convenient to evaluate the slopes of the ionization efficiency curves $(\Delta Q_i)/\Delta E$ which are listed in Table I. It is seen from this table that the slope for helium is 1.3×10^{-18} cm²/ev in the energy range near threshold.

Figure 2 gives the ionization cross section for neon as a function of electron energy. The cross-section scale is determined by calibrating with the value for the ionization efficiency as obtained by Smith[7] at an electron energy of 30 ev. The slope of the curve is 1.6×10^{-18} cm²/ev. This slope includes ionization to both the

[1] R. E. Fox, W. M. Hickam, T. Kjeldaas, Jr., and D. J. Grove, Phys. Rev. **84,** 859 (1951).
[2] R. E. Fox, W. M. Hickam, D. J. Grove, and T. Kjeldaas, Jr., Rev. Sci. Instr. **26,** 1101 (1955).
[3] R. E. Fox, W. M. Hickam, and T. Kjeldaas, Jr., Phys. Rev. **89,** 555 (1953).
[4] W. M. Hickam, Phys. Rev. **95,** 703 (1954).
[5] R. E. Fox and W. M. Hickam, J. Chem. Phys. **22,** 2059 (1954).
[6] W. M. Hickam, R. E. Fox, and T. Kjeldaas, Jr., Phys. Rev. **96,** 63 (1954).
[7] P. T. Smith, Phys. Rev. **36,** 1293 (1930).
[8] W. B. Nottingham, Phys. Rev. **55,** 203 (1939).
[9] J. T. Tate and P. T. Smith, Phys. Rev. **39,** 270 (1932).
[10] Called E_i by Smith and Nottingham (references 7 and 8).
[11] Although the curves of P. T. Smith showed considerable curvature at the ionization threshold, due to the electron energy spread, they were linear in the region of the energy at which comparison is made to the present curves.

TABLE I.

Gas	Ionization potential (ev)	Energy used to establish the Q_i scale (ev)	$\Delta Q_i/\Delta E$ cm²/ev $\times 10^{18}$
Helium	24.58	30.0[7]	1.3
Neon	21.56	30.0[7]	1.6
Argon $^2P_{\frac{1}{2}}$	15.76	16.5[7]	13 (?)
Argon $^2P_{\frac{3}{2}}$	15.94	16.5[7]	18
Mercury[a]	10.43	11.4[8]	22.8
Mercury[b]	10.43	11.4	10.9
CO^+ $X\,^2\Sigma^+$	14.01	20.0[9]	5.7
$A\,^2\Pi$	16.53	20.0	0.9
$B\,^2\Sigma^+$	19.67	20.0	1.4 (?)
N_2^+ $X\,^2\Sigma^+$	15.58	20.0[9]	3.5 (3.1)
$A\,^2\Pi_g$	16.94	20.0	0.9 (1.4)
$B\,^2\Sigma_u^+$	18.75	20.0	2.0

[a] Initial rise of hump.
[b] At 1 ev above ionization onset.

$^2P_{\frac{1}{2}}$ and $^2P_{\frac{3}{2}}$ states of the ion.[12] This separation in neon is only 0.1 ev and hence cannot be resolved with the present energy spread in the electron beam.

Figure 3 shows the ionization cross section for argon as a function of the electron energy. The break in the curve is due to ionization of the doublet ground states

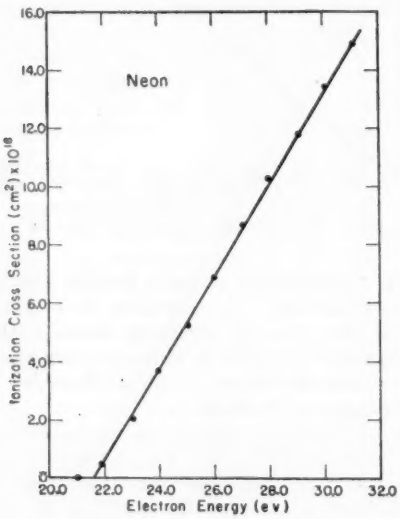

FIG. 2. The ionization efficiency curve for Ne^+.

[12] For a discussion of ionization to the doublet ground states of the rare gas ions see reference 3. For values of the energy separation of these states see Landolt and Bornstein, *Zahlenwerte und Functionen* (Springer-Verlag, Berlin, 1950), Vol. 1, Part I or C. E. Moore, *Atomic Energy Levels*, Natl. Bur. Standards Circ. No. 467 (U. S. Government Printing Office, Washington, D. C., 1952).

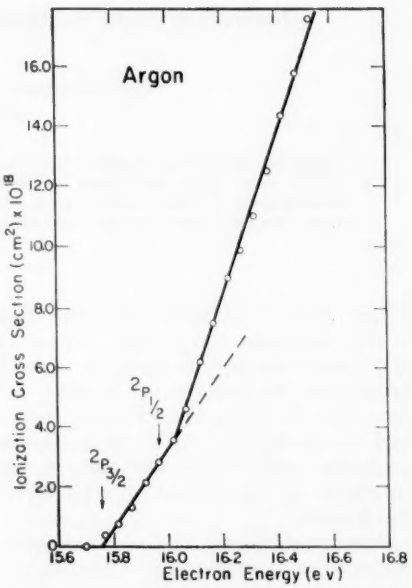

FIG. 3. The ionization efficiency curve for Ar^+ near threshold. The arrows indicate the doublet ground states determined from spectroscopic data.

($^2P_{\frac{1}{2}}$ and $^2P_{\frac{3}{2}}$) of the ion. The spectroscopic value for the energy separation of these states is 0.18 ev. With an energy spread of about 0.06 ev in the electron beam this separation is very difficult to measure. The average of 4 runs gives a value of 0.2 ± 0.1 ev. Since few data points are possible in this small energy region the determination of a slope for the $^2P_{\frac{1}{2}}$ state is extremely difficult and the value of 13×10^{-18} cm²/ev is only approximate. A value of 18×10^{-18} cm²/ev is obtained for the slope of the $^2P_{\frac{3}{2}}$ state. The Q_i scale for this curve is calibrated from the P_i value at 16.5 ev as measured by Smith.[7] Since this point is less than 1 v from the ionization potential there is probably appreciable error due to the spread in energy of the electron beam employed by Smith.

Figure 4 shows the ionization cross section of mercury vapor as a function of electron energy. The shape of

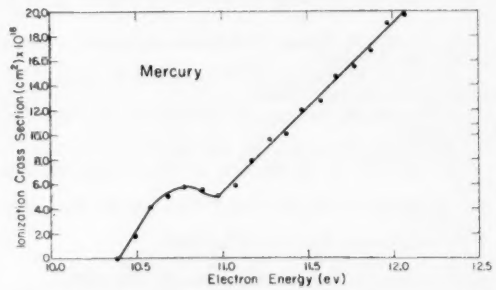

FIG. 4. The ionization efficiency curve for Hg^+ near threshold.

the curve is essentially the same as that obtained by Nottingham[8] and the Q_i scale is based on the P_i value obtained by him at 11.4 ev. This value is only 1 ev above the ionization threshold, but since Nottingham's data were taken with an electron beam in which 50% of the electrons were within an energy spread of 0.15 ev, the error in P_i due to the electron energy spread should be small. The presence of the "hump" in the curve near threshold makes it difficult to quote a value for the slope of the ionization curve near threshold. The initial slope of the hump is 22.8×10^{-18} cm²/ev while the slope at 1 v above threshold is 10.9×10^{-18} cm²/ev.

Figure 5 shows the ionization cross section of nitrogen as a function of electron energy. The break in the curve is due to ionization of the excited state of the ion.[5,13,14]

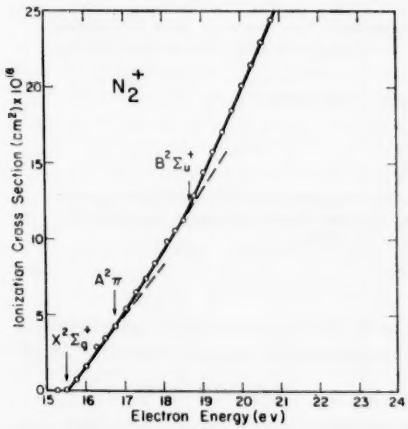

FIG. 5. The ionization efficiency curve for N_2^+. The arrows indicate the designated energy states of the ion determined from spectroscopic data.

The Q_i scale is calibrated with the value of P_i at 20 ev obtained by Tate and Smith.[9] This point is only about 4.5 ev above the ionization threshold and hence there may be a small uncertainty due to the electron energy spread in Tate and Smith's experiment. The slopes for ionization to the $X\,^2\Sigma_g^+$ ground state, $A\,^2\pi$ and $B\,^2\Sigma_u^+$ excited states are 3.5×10^{-18}, 0.9×10^{-18}, and 2.0×10^{-18} cm²/ev, respectively.

There has been some question concerning the shape of N_2^+ curve in the region of the first few volts above threshold. The curve obtained by Clarke[14] showed a nonlinearity in the region of 16.5 ev which was not observed by other investigators.[5,13] Schulz[15] studied N_2^+ with a total-ionization tube employing an RPD electron gun. He obtained a curve in substantial agreement with that obtained by Clarke.

[13] D. C. Frost and C. A. McDowell, Proc. Roy. Soc. (London) **A232**, 227 (1955).
[14] E. M. Clarke, Can. J. Phys. **32**, 764 (1954).
[15] G. J. Schulz (private communication).

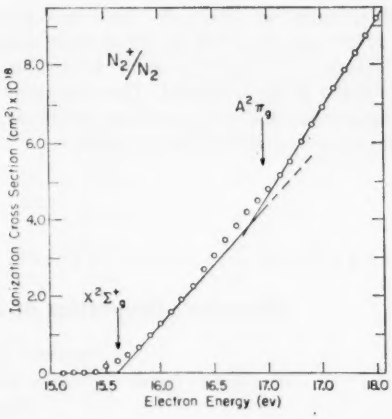

FIG. 6. The ionization efficiency curve for N_2^+ near threshold. The spectroscopically determined energy levels are indicated.

A study of the initial portion of the N_2^+ curve in greater detail is shown in Fig. 6. This curve taken with the mass spectrometer previously described,[2] is calibrated by a comparison with the data of Fig. 5. The slopes for ionization to the $X\,^2\Sigma_g^+$ ground state and the $A\,^2\pi_g$ excited state are 3.1 and 1.4×10^{-18} cm²/ev, respectively. The departure from linearity in the region of 16.5 ev is attributed to an additional ionization process such as autoionization. The curve is in substantial agreement with those observed by Clarke and Schulz.

In the case of carbon monoxide shown in Fig. 7, the Q_i scale is established by using the value of P_i at 20 ev obtained by Tate and Smith. This point is 6 v above the ionization threshold, and hence any error resulting from the electron energy spread should be smaller than that for nitrogen. In a comparison with nitrogen it is seen that the slope for the $X\,^2\Sigma$ ground state is considerably larger for CO whereas the slopes for each of

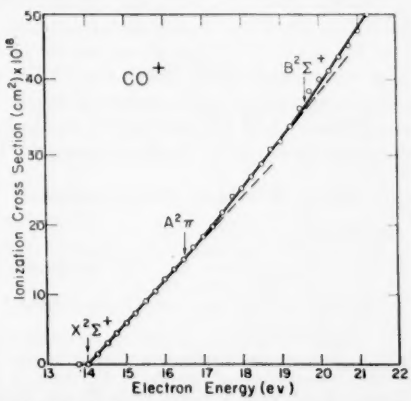

FIG. 7. The ionization efficiency curve for CO^+. The spectroscopically determined energy levels are indicated by arrows.

the excited states are essentially the same. The slope for the $B\,^2\Sigma^+$ state in CO is in considerable doubt due to the deviation from linearity of the data points in the vicinity of the $B\,^2\Sigma^+$ threshold. This deviation is observed for a wide variety of operating conditions and is not believed to be instrumental in origin.

The data for the shapes of the following curves has been previously published; helium,[6] mercury,[4] nitrogen,[5] and carbon monoxide.[5] The curves for argon and neon represent new data taken in collaboration with W. M. Hickam, and the data of Fig. 6 were taken in collaboration with R. K. Curran.

THE JOURNAL OF CHEMICAL PHYSICS VOLUME 35, NUMBER 4 OCTOBER, 1961

Electrical Properties of Nonstoichiometric Uranium Dioxide

S. Aronson,* J. E. Rulli, and B. E. Schaner†
Westinghouse Electric Corporation, Bettis Atomic Power Laboratory, Pittsburgh, Pennsylvania
(Received April 17, 1961)

Electrical conductivity and thermoelectric power measurements have been made on nonstoichiometric UO_2 at temperatures of 500–1150°C. The conductivity data in the single phase UO_{2+x} region can be represented by the equation

$$\sigma(\text{ohm cm})^{-1}=(3.8\times10^6)/T(2x)\,(1-2x)\,\exp[(-0.30\pm0.03\text{ ev})/kT].$$

An approximate equation for the thermoelectric power Q, is

$$Q=(k/e)\ln(1-2x/2x).$$

The electrical measurements confirm the ionic theory of nonstoichiometry in UO_2, postulated on the basis of thermodynamic evidence. Nonstoichiometric UO_2 is a relatively simple ionic solid in which activated electronic hole transfer occurs between U^{5+} and U^{4+} ions in the lattice.

INTRODUCTION

ELECTRICAL properties of uranium dioxide have been studied by a number of investigators in the past few decades.[1–3] Although much information has been accumulated, a coherent theory to account for the electrical behavior of nonstoichiometric uranium dioxide has not been developed. The experimental studies have been hampered by a lack of information on the nature of the nonstoichiometry in UO_2 and the phase relationships in the uranium-oxygen system.

The present study of electrical conductivity and thermoelectric power was undertaken in an attempt to correlate the electrical properties of nonstoichiometric UO_2 with its thermodynamic properties.[4–6] The results of the electrical measurements confirm the ionic theory of nonstoichiometry in UO_2 postulated on the basis of the thermodynamic data. Nonstoichiometric UO_2 is found to be a relatively simple ionic solid in which electronic hole transfer occurs between U^{5+} and U^{4+} ions.

EXPERIMENTAL

The nonstoichiometric uranium dioxide samples used in this study were high density (98–99% of the theoretical density), sintered plates of dimensions 3.8×0.6×0.1 cm. The average grain size was about 60μ. The plates were selected from a group of plates originally prepared for a metallographic study of the phase relationships in the region UO_2 to U_4O_9. Details of the preparation of these samples and their microstructures are presented in the metallographic study.[7] The compositions of the samples used for the electrical measurements were in the range of $UO_{2.001}$ to $UO_{2.23}$.

A simple dc current-potential method was employed for the electrical conductivity measurements. A UO_{2+x} plate was laid horizontally on platinum strips placed 3 cm apart on a flat quartz block. The strips served as the current contacts. The potential probes, in the form of platinum knife-edges set 1.50 cm apart, were pressed against the sample. A thermocouple (Pt, Pt−10% Rh) was placed adjacent to the center of the plate. A Leeds and Northrup K-3 potentiometer was used for the potential measurements. Current was measured with a calibrated ammeter. The currents used were generally in the range of 1–10 ma. Power was supplied by a storage

* Present address: Brookhaven National Laboratory, Upton, New York.
† Deceased.
[1] J. J. Katz and E. Rabinowitch, *The Chemistry of Uranium*, National Nuclear Energy Series, Div. VIII (McGraw-Hill Book Company, Inc., New York, 1951), Vol. 5.
[2] R. K. Willardson, J. W. Moody, and H. L. Goering, J. Inorg. & Nucl. Chem. **6**, 19 (1958).
[3] M. J. Brabers, *Proceedings of the Second United Nations International Conference on the Peaceful Uses of Atomic Energy, Geneva*, **1958** (United Nations, Geneva, 1958), Vol. 6, p. 122.
[4] S. Aronson and J. Belle, J. Chem. Phys. **29**, 151 (1958).
[5] S. Aronson and J. C. Clayton, J. Chem. Phys. **32**, 749 (1960).
[6] S. Aronson and J. C. Clayton, J. Chem. Phys. **35**, 1055 (1961).
[7] B. E. Schaner, J. Nuclear Materials **2**, 110 (1960).

battery. The conductivity cell was enclosed in a vertical, clear-quartz tube through which a slow stream of helium, dried over magnesium perchlorate, was passed. Temperatures as high as 1200°C were obtained by use of a vertical, resistance-wound tube furnace.

The cell used for the measurement of thermoelectric power is shown in Fig. 1. Diagonal placement of the sample was found to be convenient. Short lengths of 50-mil platinum wire were used as the potential contacts. They were laid in parallel about 2 cm apart across a raised platform (not shown in Fig. 1) at the top of the lavite holder. The UO_{2+x} plate was laid on these wires. The lavite weight was then pressed against the sample to insure good electrical contact. The lavite weight was grooved at the bottom and fitted over the sample to thermally insulate the edges of the sample. Two Pt, Pt−10% Rh thermocouples emerged from a central cylindrical hole in the lavite holder. The thermocouple beads were placed in contact with the potential wires upon which the sample rested. A temperature gradient was supplied either by the natural temperature gradient of the external resistance furnace or by supplying current to the small, internal, cylindrical heater shown in Fig. 1. The potential difference between the two potential leads, and the thermocouple voltages, were measured with a K-3 potentiometer. By combining the effects of the external furnace and the internal heater, it was possible to vary and reverse the temperature gradient on the sample. Temperature gradients of 5-15°C were employed. The measurements were made in an atmosphere of slowly flowing helium gas.

The oxygen contents of the uranium oxide samples were determined from the weight gains on the samples upon oxidation from $UO_{2.000}$.[7] After the electrical measurements were concluded, oxygen contents were again determined by chemical analyses for U^{6+} and U^{4+} ions. The O/U atomic ratios calculated from the weight gains were in reasonable agreement (±0.005) with the O/U atomic ratios determined from the chemical analyses. The compositions reported are in most cases average values from the weight gain and chemical analysis data. In the case of the samples of lowest oxygen content, the O/U atomic ratios, 2.001 and 2.002, were determined from the chemical analyses only, since the samples were used after sintering in hydrogen[7] without an oxidation step. These lowest compositions have an estimated accuracy of ±0.002 in the O/U atomic ratio.

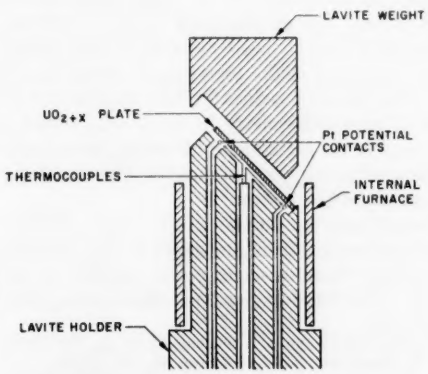

FIG. 1. Schematic of thermoelectric power cell.

TABLE I. Data on the electrical conductivity of nonstoichiometric uranium dioxide.

O/U ratio	Activation energy (ev)	Specific conductivity at 1100°C (1/ohm-cm)	Temperature of phase transition (°C)
2.001	[0.33][a]	0.28	
2.002	[0.36]	0.46	
2.021	0.30	6.8	
2.028	0.29	11.0	
2.031	0.30	9.9	
2.058	0.28	19.6	
2.063	0.29	23.3	
2.102	0.29	31.6	525
2.108	0.29	36.8	
2.139	0.31	44.4	645
2.143	0.30	45.4	655
2.178	0.32	53.7	960
2.180	0.31	52.0	975
2.194	(0.31)[b]	54.2	1040
2.207	(0.35)	55.1	1055
2.212	(0.30)	53.0	1075
2.229	(0.33)	55.7	1100
2.234	(0.30)	54.6	1095

[a] The values of the activation energy in brackets are less certain than the other values because of slow oxidation of the sample during a run.

[b] The values of the activation energy in parentheses are less certain than the other values because the range of measurement was approximately 100°C in each case.

RESULTS

The results of the electrical conductivity measurements are summarized in Table I. An equation which adequately represents the data in the single phase UO_{2+x} region is

$$\sigma=(3.8\times10^{6})/T(2x)(1-2x)\exp[(-0.30\pm0.03)/kT]. \quad (1)$$

σ(ohm cm)$^{-1}$ is the specific conductivity, T(°K) is the temperature, 0.30 ev is the activation energy, and x is the fractional value in the compositional formula UO_{2+x}. The choice of Eq. (1) is based on theoretical considerations which are presented in the following discussion. Some typical plots of $\log\sigma T$ versus $1/T$ are

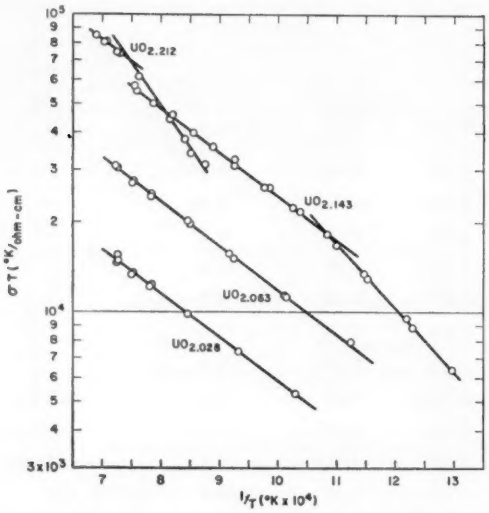

FIG. 2. Typical plots of $\log\sigma T$ versus $1/T$ for UO_{2+x}.

shown in Fig. 2. The conductivity data at 700° and 1100°C are compared with Eq. (1) in Fig. 3. A complete temperature cycle covering the approximate temperature range of 600–1100°C was made in each run. In some cases, measurements were made at temperatures down to 400°C and up to 1200°C. The measurements were stable and reproducible. At O/U atom ratios below 2.06, however, slight oxidation occurred during a run which tended to lower the measured resistances. The effect of the oxidation on the calculated activation energies was small, except possibly in the case of the two samples with the lowest oxygen contents. The effects of reversal of polarity and variations in applied voltage on the conductivity were negligible.

Breaks in the plots of $\log\sigma T$ vs $1/T$ were observed on several of the samples. These breaks correspond to a transition from a single phase UO_{2+x} region to a two phase, $UO_{2+x}-U_4O_{9-y}$ region. The temperatures of the phase transitions are shown in Table I. The accuracies of these temperature values are estimated to be ±15°C, from examination of the $\log\sigma T$ versus $1/T$ plots. A comparison of the phase boundary data obtained in this study with other studies[7–10] is shown in Fig. 4. It is observed that the conductivity data are in agreement with the metallographic data of Schaner[7] at temperatures below 900°C. At higher temperatures, however, the conductivity results deviate from the metallographic results. This is surprising because the two sets of data were obtained on samples from the same group of uranium oxide plates. The conductivity data at temperatures above 900°C are in good agreement with results obtained in studies of the pressures of oxygen in equilibrium with uranium oxides.[9,10] The existence of a large range of nonstoichiometry in the U_4O_{9-y} region which was found in the metallographic study, is not confirmed by the conductivity measurements. The reason for this discrepancy is not known.

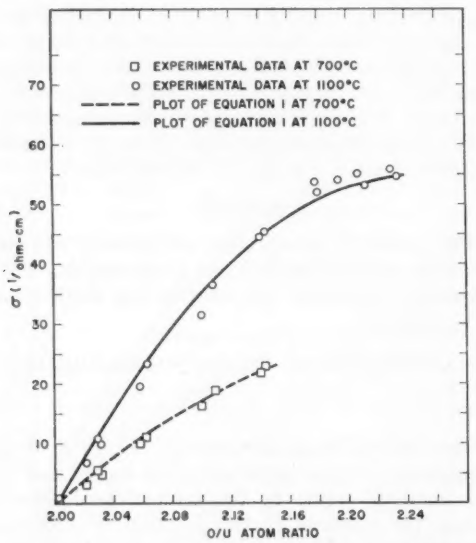
EXPERIMENTAL DATA AT 700°C
EXPERIMENTAL DATA AT 1100°C
PLOT OF EQUATION I AT 700°C
PLOT OF EQUATION I AT 1100°C
σ ($1/\Omega$-cm)
O/U ATOM RATIO

FIG. 3. Comparison of the conductivity data at 700°C and 1100°C with Eq. 1.

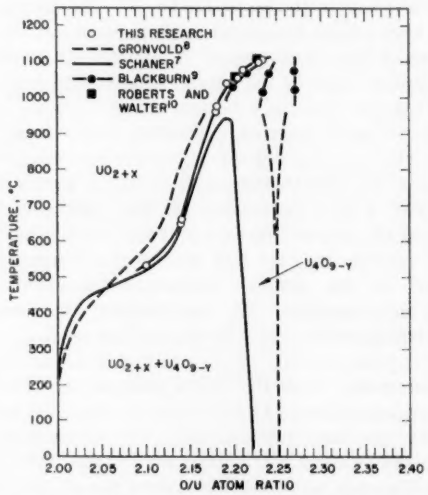

FIG. 4. Comparison of data on the phase relationships in the UO_{2+x} region.

Typical plots of thermoelectric power (TEP) as a function of temperature are shown in Fig. 5. A positive sign of the thermoelectric power signifies a positive voltage at the cold junction. It is observed that the TEP

[8] F. Gronvold, J. Inorg. & Nuclear Chem. **1,** 359 (1955).
[9] P. E. Blackburn, J. Phys. Chem. **62,** 897 (1958).
[10] L. E. J. Roberts and A. J. Walter, United Kingdom Atomic Energy Authority Report, AERE–R 3345, May, 1960.

decreases with increasing oxygen content. The dependence of TEP on temperature was variable. This may be, at least partly, due to experimental factors such as errors in the measurement of sample temperatures at the potential contacts and oxidation at low O/U ratios. Variations in TEP as high as 10% were obtained by reversal of the temperature gradient at temperatures near 1100°C. At lower temperatures the variation in TEP with changes in the temperature gradient was much lower. For the above reasons attention is not focused here on the temperature dependence of the thermoelectric power. The TEP data are summarized in Fig. 6. The limits of the values shown in Fig. 6 represent the range of TEP for each run in the single-phase UO_{2+x} region. An equation which has been found to be applicable to the TEP data is

$$Q=(k/e)\ \ln(1-2x/2x). \qquad (2)$$

Q is the thermoelectric power, k is Boltzmann's constant, and e is the electronic charge. The relevance of Eq. (2) is considered in the following discussion.

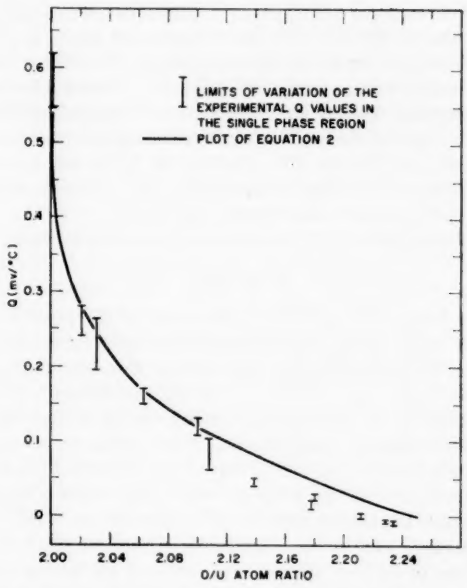

FIG. 6. Comparison of the thermoelectric power data with Eq. 2.

DISCUSSION

Studies of the thermodynamic properties of urania-base solid solutions[4-6] have indicated that nonstoichiometric uranium dioxide can be treated as a relatively simple ionic solid containing U^{4+} and U^{5+} cations, and lattice and interstitial O^{--} anions. The electrical properties of nonstoichiometric uranium dioxide are primarily electronic in nature, as discussed in the following. The electrical properties can be accounted for on the basis of the ionic mechanism, if it is assumed that electronic transfer occurs between U^{4+} and U^{5+} ions. The treatment is similar to that of Heikes and Johnson[11] and Van Houten[12] on lithium-substituted transition-metal oxides and that of Jonker[13] on cobalt ferrite. Possible reasons for the occurrence of activated electronic jumps between ions are discussed by these investigators.

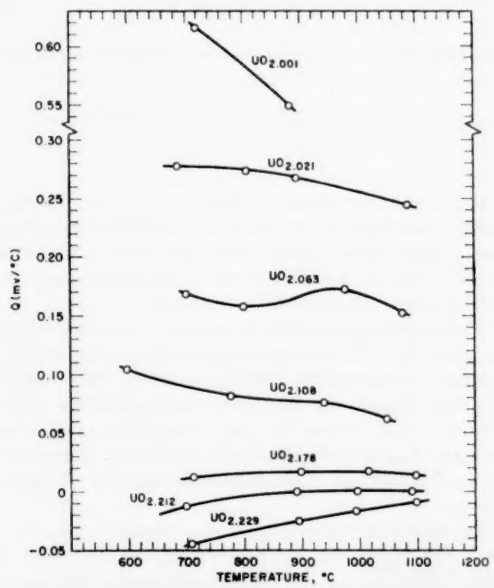

FIG. 5. Typical plots of thermoelectric power for UO_{2+x}.

In discussing the electrical properties of UO_{2+x}, each U^{4+} ion may be considered as a site for one electron which can jump to a U^{5+} ion. An equivalent treatment is to consider U^{5+} ions as sites for holes which can jump to U^{4+} ions. The latter approach is arbitrarily chosen for this discussion. The holes are treated as discrete, localized, entities in a manner similar to ions. An equation for the specific electrical conductivity similar to that of Heikes and Johnson[11] can be written

$$\sigma=Ce^2a^2\nu NP1/T\ \exp[-E/kT]. \qquad (3)$$

C is a constant containing geometric and entropy factors, e is the charge on a hole, a is the jump distance for a hole, ν is the vibrational frequency associated with the movement of holes, N is the number of holes per unit volume, E is the activation energy for a jump, and P is the probability that a hole, upon attempting to jump, will find an acceptor site (a uranium ion) unoccupied.

Eq. (1) which is of the same form as Eq. (3), was chosen on the basis of the above mechanism. The num-

[11] R. R. Heikes and W. D. Johnson, J. Chem. Phys. **26**, 582 (1957).
[12] S. Van Houten, J. Phys. Chem. Solids **17**, 7 (1960).
[13] G. H. Jonker, J. Phys. Chem. Solids **9**, 165 (1959).

ber of holes per unit volume N is assumed equal to the number of U^{5+} ions per unit volume and hence, is proportional to $2x$ in the formula UO_{2+x}. The factor 2 is included to indicate that $2U^{5+}$ ions are formed when an interstitial oxygen ion is introduced. The probability P, is equal to the fraction of the uranium ions which are present as U^{4+} ions. P is equal to $(1-2x)$ in Eq. (1). It is observed in Figs. 2 and 3 that Eq. (1) is in good accord with the conductivity data.

The mobility μ of the holes may be obtained from

$$\mu=\sigma/NeP. \tag{4}$$

The factor P is included to account for the possibility that an acceptor uranium ion is already occupied by a hole. The mobilities calculated from Eqs. (1) and (4) range from 0.021 cm^2/V sec at 600°C to 0.055 cm°/V sec at 1100°C. An order of magnitude estimate of the vibrational frequency v may be obtained by assuming a value of unity for the factor C in Eq. (3). A value of 3.9A, the stitution in Eq. (1), is 5×10^{13} sec^{-1}. This value is in the range of the atomic vibrational frequencies, as would be expected, and is in reasonable agreement with the values of 10^{-11} to 10^{-14} sec^{-1} calculated by Heikes and Johnson,[11] Van Houten,[12] and Jonker[13] for their systems.

It is assumed that the electrical conductivity in UO_{2+x} is primarily electronic. This assumption is supported by much experimental evidence. The activation energies for electrical conductivity[1-3] are much smaller than the activation energies for oxygen and uranium ion self diffusion in uranium dioxide.[14-16] Estimates of the ionic and electronic transport numbers, such as that made by Belle[14] on the basis of oxygen-diffusion and electrical-conductivity data, indicate that the ionic contribution to the electrical conductivity is very small. A direct check on the primacy of electronic conduction was made by measurements with emf cells of the form Ni, NiO | $UO_{2.001}$ | FeO, Fe and Pt, $UO_{2.18}$ | $UO_{2.10}$ | $UO_{2.02}$, Pt. The uranium oxide components were sections of the conductivity plates. The emf values at 1000–1100°C were less than 1 mv. These data indicate that the ionic transport numbers in UO_{2+x} are low.[4,17] The experiments were not sufficiently quantitative for an accurate determination of the ionic and electronic transport numbers.

Heikes and Johnson[11] have discussed the effect of using sintered bodies rather than single crystals for conductivity measurements. In the present study an attempt was made to minimize the extraneous effects of grain structure by using large-grained (60μ) samples having little porosity. Although the grain structure may have some effect on the measured conductivity values, it probably has little effect on the activation energy as is discussed by Heikes and Johnson.[11] Probably the grain structure does not significantly affect the variation of conductivity with oxygen content, since the data are in reasonable agreement with Eq. 1.

The thermoelectric power data which are summarized in Figs. 5 and 6, can be explained on the basis of the proposed mechanism. Jonker[13] and Van Houten[12] have treated the thermoelectric power data obtained in their studies on the basis of an energy level description similar to that commonly applied to semiconductors. Heikes[18] has discussed the thermoelectric power of localized electronic defects in some detail from a thermodynamic point of view. In these treatments, first an expression is obtained for the Peltier coefficient. An expression for the thermoelectric power is then obtained from the Kelvin relationship between the Peltier and the Seebeck effects.

Howard and Lidiard[19] and Haga[20] have treated the thermoelectric power of ionic solids from the standpoint of irreversible thermodynamics. Although these latter workers have discussed ionic conduction only, their treatment appears to be applicable to conduction by localized electronic defects as well. Their approach is utilized in the discussion which follows. The treatment has the advantage that an expression for the thermoelectric power is obtained directly without recourse to the Kelvin relationship.

The thermoelectric power Q of the UO_{2+x} cell may be related to the electrochemical potential of holes, γ_h, by the relationship

$$eQ=-d\gamma_h/dT. \tag{5}$$

The effect on Q of the platinum electrodes is neglected. Furthermore,

$$d\gamma_h/dT=e\,\mathrm{grad}V/\mathrm{grad}T+\partial\mu_h/\partial T=-eEdX/dT-\bar{S}_h, \tag{6}$$

$\mathrm{grad}V$ is the potential gradient, μ_h is the chemical potential of holes, E is the electric field intensity, $\bar{S}_h$ is the entropy change produced by the addition of a hole to a U^{4+} ion, and dX/dT is the reciprocal of the temperature gradient along the UO_{2+x} sample.

The entropy term may be resolved into two terms, $\bar{S}_{conf}$ and $\bar{S}_{add}$. $\bar{S}_{conf}$ is the change in the configurational entropy of the system resulting from the introduction of a hole. $\bar{S}_{add}$ is the additional entropy change which includes such factors as the change in vibrational entropy. $\bar{S}_{conf}$ is easily obtained by using the Boltzmann expression for the configurational entropy of holes,

[14] J. Belle, *Proceedings of the Second United Nations International Conference on the Peaceful Uses of Atomic Energy, Geneva*, **1958** (United Nations, Geneva, 1958), Vol. 6, p. 569.
[15] A. B. Auskern and J. Belle, J. Nuclear Materials **3**, 267 (1961).
[16] A. B. Auskern and J. Belle, J. Nuclear Materials **3**, 311 (1961).
[17] C. Wagner, *International Committee of Electrochemical Thermodynamics and Kinetics, Proceedings of the Seventh Meeting* (Butterworths Scientific Publications, Ltd., London, 1957), Chap. 85, p. 361.
[18] R. R. Heikes, *Theory of the Electron Transport Properties of the 4f Electrons in Rare Earth Compounds* (Conference on the Rare Earths, 1960).
[19] R. E. Howard and A. B. Lidiard, Phil. Mag. **2**, 1462 (1957).
[20] E. Haga, J. Phys. Soc. Japan **13**, 1091 (1958).

$S_h = k \ln W_h$. W_h is the number of equivalent ways of arranging the holes on the uranium cations.

$$\bar{S}_h = dS_h/dN_h = kd/dT\,[\ln N_c!/N_h!(N_c-N_h)!]$$
$$= k \ln(N_c - N_h/N_h) = k \ln N_{U+4}/N_{U+5}. \quad (7)$$

N_h, the number of holes in the lattice, is equal to the number of U^{5+} ions, N_{U+5}. N_c is the number of uranium cations. Sterling's approximation for the factorial terms has been used to obtain the final expression. The expression for the field intensity E, in Eq. (6), is obtained using the appropriate equation from irreversible thermodynamics.[20]

$$i_h = 0 = eD_h([-dN_h/dx]+[eN_hE/kT]$$
$$-[N_hQ_h^*/kT^2]dT/dx). \quad (8)$$

j_h is the current density of holes, Q_h^* is the heat of transport for holes, and D_h is the diffusion coefficient.

The final expression for the thermoelectric power, obtained from Eqs. (5), (7), and (8), is

$$Q = (k/e)\ln[N_{U+4}/N_{U+5}]+\bar{S}_{add}/e+Q_h^*/eT)$$
$$+(kT/e)(d \ln N_{U+5}/dT). \quad (9)$$

The first term in Eq. (9) is equivalent to Eq. (2). The agreement between the experimental data and Eq. 2, shown in Fig. 6, is fairly good. The first term in Eq. (9) is thus, of primary importance. The small difference between the plot of Eq. (2) and the data may be attributed to the other terms in Eq. (9) and to the contribution to the thermoelectric power of the platinum electrodes. Because of possible errors in the experimental procedures and the variability of the TEP values with temperature, which is discussed above, modifications of Eq. (2) are not considered further.

Expressions for the thermoelectric power of UO_{2+x} can also be obtained using the treatments of Jonker[13] and Van Houten[12] and that of Heikes.[18] The expression obtained in each case contains the first term in Eq. (9). The heat of transport and entropy terms appear to be similar in the various treatments, but are not identical. The exact relationships among these quantities remains to be determined. A term involving the change in concentration of holes, similar to the last term in Eq. (9), does not appear in the other treatments. It is not clear that the assumption that a gradient of holes does not exist is theoretically justified. A rigorous treatment of thermoelectric power relating the various points of view would certainly be of value.

It would be advantageous at this point to compare the electrical data with previous information on the electrical properties of UO_{2+x}. Since most of the previous work was done on the assumption that UO_{2+x} is a classical semiconductor involving a band structure, the equation $\sigma = \sigma_0 \exp[-E/2kT]$ was generally used. Support for a band picture was given by Hartmann who measured the Hall coefficient for UO_2.[21] His data showed that UO_2 is a p-type semiconductor. Hartmann's results on UO_2 can be interpreted to give a free-carrier concentrations of 10^{16} holes per cm^3, and a mobility of 10 $cm^2/V(sec)$ at room temperature. It should be noted that the present data give plots of $\ln\sigma$ versus $1/T$ which are as linear as the plots of $\ln\sigma T$ versus $1/T$.[21a] The dependence of the electrical conductivity on temperature cannot therefore distinguish between a band picture and a mechanism of localized jumps. However, the nature of the variation of conductivity and thermoelectric power with oxygen content and the constancy of the activation energy for electrical conductivity, are strong evidence in support of the mechanism presented here. It would be difficult to obtain a simple explanation of the electrical data on the basis of a band picture especially considering the gross nature of the nonstoichiometry in UO_2. Gruen[22] has suggested a mechanism of localized electronic jumps in UO_2 similar to that discussed above. Additional measurements of the Hall coefficient in uranium dioxide may be of value in clarifying the results of Hartmann.[21] The density of Hartmann's samples, about 6.5 g/cc, is surprisingly low. A need for Hall-coefficient data on carefully fabricated and well characterized uranium oxide samples is indicated.

There is qualitative agreement between the electrical data in this research and in other investigations in several respects. A number of investigators have observed an increase in electrical conductivity with increasing oxygen content.[1–3] The activation energy in UO_{2+x}, calculated from the equation

$$\sigma = \sigma_0 \exp[-E/2kT],$$

is 0.40 ev. This value is in qualitative agreement with values obtained by other workers.[1–3,22] The results of Willardson *et al.* on the thermoelectric power of UO_{2+x}[2] are complex probably due to the presence of nonequilibrium phases. At low oxygen contents, however, they observe p-type behavior in agreement with the present work.

The electrical measurements support the contention that U^{5+} ions rather than U^{6+} ions are present in UO_{2+x}. The approach of the specific conductivity towards a maximum value in the composition range $UO_{2.18}$ to $UO_{2.23}$, which is observed in Fig. 3, is accounted for in Eqs. (1) and (3), on the assumption that U^{5+} ions are present. A treatment for U^{6+} ions, similar to that of Eq. (3), would be in reasonable agreement with

[21] W. Hartmann, Z. Physik **102,** 709 (1936).

[21a] *Note added in proof.* Electrical conductivity measurements have recently been made on nonstoichiometric urania-zirconia solid solutions by R. Wolfe and J. Belle at the Bettis Atomic Power Laboratory. The data are better fitted by $\ln\sigma$ vs $1/T$ plots than by $\ln\sigma T$ vs $1/T$ plots. These data indicate that Eq. (3) may require modification. The results do not, however, affect the validity of the mechanism for electron movement proposed in this paper.

[22] D. M. Gruen, J. Am. Chem. Soc. **76,** 2117 (1954).

the experimental data at O/U atomic ratios lower than 2.18. It would however, predict a larger variation in conductivity in the composition range $UO_{2.18}$ to $UO_{2.23}$ than is observed experimentally. The thermoelectric power data are in better agreement with Eq. (2) (see Fig. 6) throughout the composition range studied, than they would be with a similar equation based on the presence of U^{6+} ions rather than U^{5+} ions.

The proposal that U^{5+} ions are present in UO_{2+x} is in agreement with thermodynamic data on nonstoichiometric urania and urania-thoria solid solutions[5] as mentioned above. The thermodynamic properties of nonstoichiometric urania-thoria were found to be very similar to those of nonstoichiometric urania. The same theory of nonstoichiometry applies to both materials.[5] Conclusions drawn from studies on urania-thoria solid solutions should therefore be applicable to urania as well. Results of x-ray[23] and magnetic susceptibility[24] studies on nonstoichiometric urania-thoria solid solutions, indicate that U^{5+} ions are present. These studies therefore, support the proposal that U^{5+} ions also occur in UO_{2+x}. However, direct magnetic susceptibility data on UO_{2+x}, indicate that U^{6+} ions rather than U^{5+} ions are present.[25] The reason for this discrepancy is not known.

In summary, it may be stated that UO_{2+x} is a relatively simple ionic solid, containing U^{5+} cations in lattice positions and O^{--} anions in interstitial positions. Electrical conduction occurs by an activated transfer of electronic holes from U^{5+} ions to U^{4+} ions. The activation energy is 0.30 ev. The thermoelectric power arises primarily from the temperature dependence of the chemical potential of the holes.

ACKNOWLEDGMENTS

The authors are grateful to the U.S. Atomic Energy Commission and the Westinghouse Electric Corporation for permission to publish this paper.

The authors wish to thank Dr. J. Belle for his aid in initiating this research and for his many helpful discussions. They also wish to thank Dr. R. R. Heikes, of the Westinghouse Research Laboratories, for the stimulation resulting from making his paper[18] available to them.

[23] J. S. Anderson, D. N. Edgington, L. E. J. Roberts, and E. Wait, J. Chem. Soc. **1954,** 3324 (1954).

[24] J. K. Dawson and L. E. J. Roberts, J. Chem. Soc. **1956,** 78 (1956).

[25] J. K. Dawson and M. W. Lister, J. Chem. Soc. **1950,** 2181 (1950).

Mean Lifetime of the Lowest Excited Singlet State of Benzene*

J. W. DONOVAN AND A. B. F. DUNCAN
Department of Chemistry, University of Rochester, Rochester, New York

(Received March 15, 1961)

The lifetime of the first excited $^1B_{2u}$ state of benzene has been determined from measurement of decay of fluorescence in the vapor phase. High-frequency electrical excitation, rather then optical excitation was used. The pressure dependence of the lifetime has been studied under different conditions. The lifetime extrapolated to zero pressure is 0.59 μsec. The pressure dependence is interpreted by a mechanism of collisional deactivation.

INTRODUCTION

THE average lifetime of an excited electronic state is a quantity which is useful in several ways. The magnitude of the lifetime is frequently taken as a measure of the degree and nature of the forbiddenness of optical transitions between the excited and normal states of a molecule. Data on lifetimes are also useful in the interpretation of kinetic measurements of photochemical reactions. The lifetime obtained in a direct experimental measurement is usually a function of pressure, because of nonradiative processes, such as collision quenching and chemical decomposition. A more significant quantity is obtained by extrapolation to zero pressure of lifetimes obtained at a series of pressures. This extrapolated value is directly related to the optical transition probability between states of the molecule.

The lifetimes of excited states of only a few polyatomic molecules in the vapor phase have been determined directly. Among these are acetone,[1] biacetyl,[1] nitrogen dioxide,[2] sulfur dioxide,[3] acetophenone,[4] and the benzyl radical.[5] Because of theoretical interest in benzene, the lifetime of the molecule in the $^1B_{2u}$ state has been determined. Attempts to determine the lifetime of the fluorescent decay after optical excitation were unsuccessful,[4] because of the relatively short lifetime. Flash tubes with sufficiently high light output generally have decay times greater then 0.5 μsec, but excitation of benzene vapor by means of high-frequency discharge was found to give luminescence decay curves suitable for determining the lifetime.[6]

EXPERIMENTAL

The use of an electrodeless discharge for excitation of polyatomic molecules has been discussed in detail by Robinson.[7] The sample is not in contact with metal parts and chemical decomposition is minimized because the average energy of excitation usually does not rise above the lowest ionization potential of the molecule (9.24 ev in the case of benzene[8]). This method thus offers some advantages, at least for polyatomic molecules, over excitation produced by bombardment with electrons of much higher energy accelerated from a hot filament by means of grid control.[9]

The high-frequency excitation circuit was a very simple one, composed of a capacitor and the primary of a Tesla coil taken from a Cenco leak tester. The capacitor was charged to 500 to 1000 v by batteries, through an isolating resistor of 20 kohms. A wire from the secondary of the Tesla coil was wrapped around a quartz tube containing the vapor sample. When the circuit was activated manually, the luminescence for excited species with lifetime short compared to the period of the exciting signal (about 1 Mc) appeared as an approximately 10 μsec burst of sawtooth pulses. The observed rise time of each sawtooth appeared to be determined only by the time constant of the measuring circuit, but the decay time was characteristic of the lifetime of the excited species. For small values of the capacitor and large values of the voltage to which it was charged (approximately 0.03 μfd and 1000 v, respectively), the luminescence peaks appeared almost of equal height throughout the pulse and ceased suddenly. Under these conditions, an excited species of longer lifetime gives a luminescence output which appears as a ragged-topped square wave terminated by an exponential decay.

For the measurement of decay times of benzene, the fluorescence of the sample was observed by a 1P28 photomultiplier (135 v per stage). The output of the photomultiplier was fed into a DuMont 303 oscilloscope placed across a current measuring resistor which was selected to keep the time constant of the measuring circuit small.[10] The oscilloscope traces of the luminescence decay were photographed together with a timing trace. Fast scope speeds required the superposition of 5 to 100 traces to obtain sufficient density on the nega-

* Partial support of this work by the Office of Naval Research is gratefully acknowledged. Support is also acknowledged from the Shell Company Foundation, Inc.

[1] W. E. Kaskan and A. B. F. Duncan, J. Chem. Phys. **18,** 427 (1950).

[2] D. Neuberger and A. B. F. Duncan, J. Chem. Phys. **22,** 1693 (1954).

[3] K. Greenough and A. B. F. Duncan, J. Am. Chem. Soc. **83,** 555 (1961).

[4] D. L. Whitcomb, thesis, University of Rochester, 1957.

[5] H. Schüler and M. Stockburger, Spectrochim. Acta **15,** 981 (1959).

[6] H. Fischer, J. Opt. Soc. Am. **47,** 981 (1957) has designed an air-gap coaxial condenser lamp with a high intensity and a decay time as short as 0.13 μsec.

[7] G. W. Robinson, J. Chem. Phys. **22,** 1384 (1954).

[8] K. Watanabe, J. Chem. Phys. **26,** 542 (1957).

[9] R. G. Bennett and F. W. Dalby, J. Chem. Phys. **31,** 434 (1959).

[10] G. H. Dieke, H. Y. Loh, and H. M. Crosswhite, J. Opt. Soc. Am. **36,** 185 (1946).

tive. To determine the decay constant, 10 to 15 points separated by equal time intervals on the decay curves were used. The decays were found to be exponential.

The shortest lifetime observed with this apparatus was 0.05 μsec for the (0, 2) transition in the second positive system of N_2. This value agrees well with values for the (0, 0) and (0, 1) transition in the same system reported by Bennett and Dalby.[9] The rise time of the oscillograph was found to be about 0.02 μsec. The 1 μsec timing marks used for the decay curves were compared with a signal from an Electronic Instrument Company model 324 signal generator. The signal was adjusted to within 30 cycles of 1 Mc, with the aid of a Computer Measurements Corporation model 201B frequency-period counter.

The spectrum of the luminescence of benzene vapor at several centimeters pressure was obtained by operating the Tesla coil continuously and photographing the emission with a Hilger small quartz spectrograph. The spectrum appeared to be identical with that listed for benzene by Pearse and Gaydon.[11] No impurity bands were observed in the short exposure time (10 min operation of the Tesla coil) necessary for an exposure.

In measuring decay times, no difficulty was encountered with decomposition of the benzene. Provided that the excitation was limited to a reasonable time interval (0.001–0.01 sec) the decay times obtained from separate sawteeth on the same trace were identical within experimental error (about 5%), and succeeding traces taken on the same sample gave identical results. In addition, for several experiments at low pressures, the pressure of the sample was measured before and after excitation, by means of a McLeod gauge. No change in pressure was observed over periods of excitation well in excess of those used for decay measurements. With continued excitation, however, a pressure increase was observed. For less stable molecules, the apparatus could be changed to a flow system, with a consequent increase in the difficulty of determining the pressure of the vapor.

Reagent-grade benzene was allowed to stand, with shaking, for several days over reagent-grade concentrated sulfuric acid. The benzene was decanted into an all-Pyrex still, and the first fraction (containing a trace of water azeotrope) discarded. The middle fraction was collected in a dry atmosphere. This material was degassed by several cycles of freezing and pumping on the vacuum line before it was introduced into the apparatus.

EXPERIMENTAL RESULTS

The decay of fluorescence from the lowest $^1B_{2u}$ state of benzene was measured at a number of pressures in the range 8 to 750 μ Hg. First, the total fluorescence was examined through a Corning 9863 filter, which removed the visible radiation. Next, the fluorescence transmitted by a Farrand monochromator between 2620 and 2720 A was examined in the same way. From a study of this particular region we hoped to obtain a measure of the effect of pressure on lifetime associated with decay of molecules principally in the lowest vibrational level of the excited state. The reciprocal lifetime for the region 2620–2720 A will be referred to as k_A and the decay constant for the whole fluorescence as k_T. From a least-square analysis of the data (27 measurements of k_A, 4 measurements of k_T) we find that the data fit closely to the straight lines

$$k_A = 1.69 + 0.0207\ P, \tag{1a}$$

$$k_T = 1.70 + 0.00577\ P, \tag{1b}$$

where k_A, k_T and the intercepts are in microseconds^{-1}, and P is in microns Hg. The lifetimes at zero pressure (τ_0) are thus 0.592 and 0.588 μsec., or are identical within the experimental error.

DISCUSSION

There are two points of interest in the present results. The first is the relatively accurate and directly determined value of τ_0, the mean lifetime for the $^1B_{2u}$ state of benzene at zero pressure. This value should be related to the transition probability from the normal state to this excited state. The f number given by McClure[12] for this transition is 0.00147. A lifetime of $\tau_0 = 0.75$ μsec was calculated from this value, using the approximate relation of Mulliken,[13] with an average transition frequency of 40 100 cm^{-1}.

The second point is concerned with the different slopes of the curves, Eq. (1b) and (1a), which is evidently connected with differences in quenching of fluorescence in different parts of the spectrum. The fluorescence spectrum of benzene has been examined in detail by Ingold and Wilson[14] at "high pressure" (25 mm Hg) and at "low pressure" (0.01 mm). It is clear from the different intensity distributions which they obtained at the two pressures that as the pressure is increased, the region 2620–2720 A is actually enriched in transitions from the zero level (or at least the lowest level responsible for most of the intensity) relative to the transitions from all excited levels to the normal state. The experimental results on lifetimes can be understood on this basis.

Consider first a simplified model consisting of the lowest level of the excited state, one higher level and the vibrational levels of the normal state. Let the instantaneous concentrations in the lowest level of the excited state be A_1, of molecules in the higher level be A_2. Let τ_1, τ_2 be the lifetimes of the excited levels, k_1, k_2 be the rate constants for deactivation by collision from these levels to the normal state. Let a_{21}, a_{12} be, respectively, the constants associated with transitions by

[11] R. W. B. Pearse and A. G. Gaydon, *The Identification of Molecular Spectra* (John Wiley & Sons, New York, 1941), p. 69.

[12] D. S. McClure, J. Chem. Phys. **17**, 905 (1949).

[13] R. S. Mulliken, J. Chem. Phys. **7**, 14 (1939).

[14] C. K. Ingold and C. L. Wilson, J. Chem. Soc. (London) **1936**, 941, 955.

collision downward and upward between the two vibrational levels of the excited state. The appropriate differential equations for decay from the two levels are

$$-dA_1/dt=(\tau_1^{-1}+k_1P+a_{12}P)A_1-a_{21}PA_2 \quad (2a)$$

$$-dA_2/dt=-a_{12}PA_1+(\tau_2^{-1}+k_2P+a_{21}P)A_2. \quad (2b)$$

These equations are solved by conventional methods, with the assumptions that $\tau_2=\tau_1$ and $k_2=k_1$. The general solutions are of the form $A_i=c_{i_1}\exp(-\lambda_1 t)+c_{i_2}\exp(-\lambda_2 t)$, with $\lambda_1=\tau^{-1}+kP$ and $\lambda_2=\tau^{-1}+kP+(a_{12}+a_{21})P$. Measurement of the total fluorescence shows that the total intensity decays according to

$$-(dA_1/dt+dA_2/dt)=-dA_T/dt=k_T(A_1+A_2),$$

$$=(\tau^{-1}+kP)(A_1+A_2),$$

or

$$k_T=(\tau^{-1}+kP)=\lambda_1. \quad (3)$$

Experimental measurement of decay in the 2620–2720 A region gives, presumably, $-dA_1/dt=k_AA_1$. Comparison with (2a) shows that

$$k_AA_1=k_TA_1+a_{12}PA_1-a_{21}PA_2,$$

or

$$k_A-k_T=a_{12}P-a_{21}P(A_2/A_1). \quad (4)$$

After substitution of the general solutions for A_2 and A_1, introduction of the values of the constants determined from the usual boundary conditions, writing $A_1^0=xA_T^0$ (A_T^0 is the total initial concentration of excited molecules) and writing $a_{12}=ra_{21}$, Eq. (4) may be written in the form

$$k_A-k_T=\frac{a_{21}(P)(1+r)[rx-(1-x)]\exp(-\lambda_2 t)}{\exp(-\lambda_1 t)+[rx-(1-x)]\exp(-\lambda_2 t)} \quad (4a)$$

$$=\frac{a_{21}(P)(1+r)[x(1+r)-1]}{\exp[a_{21}P(1+r)t]+[x(1+r)-1]}. \quad (5)$$

It is evident that the denominator of (5) is always positive. The condition for (k_A-k_T) to be positive is thus $x>1/(1+r)$. The equilibrium value of r is $\exp(-\Delta E/kT)$, where ΔE is the difference in energy between the adjacent vibrational levels considered. If ν is about 200 cm^{-1}, then $(k_A-k_T)>0$, when $x>0.72$. If ΔE is smaller, which is more probable, then x can be smaller for a positive difference between k_A and k_T. It is believed that these fractional initial populations are not unreasonable. These results lead only to a qualitative conclusion that k_A may be greater that k_T, and so only qualitative justification of the experimental results is provided.

This model neglects, of course, cascade from vibrational levels higher than the second level. An n-level model would be difficult to treat exactly, and it is uncertain whether such a treatment should be attempted until more detailed experimental information on fluorescence decay becomes available. The complexity of the benzene spectrum suggests that this molecule is an interesting but not a very promising case for a detailed study of this nature.

ACKNOWLEDGMENTS

The authors wish to thank Leonard Braun of the Cyclotron Electronics Laboratory of this University for assistance with circuit problems and Dr. David Wilson for use of electronic equipment as well as for suggestions in regard to this work.

Analysis of the Spectra of Trivalent Promethium and Holmium

M. H. CROZIER AND W. A. RUNCIMAN*
Physics Department, University of Canterbury, Christchurch, New Zealand
(Received March 31, 1961)

The spin-orbit matrices for the f^4 configuration have been calculated and checked. These have been applied to the analysis of the solid-state spectra of trivalent promethium and holmium. A tentative energy-level scheme for promethium is obtained. In the case of holmium, all levels below 27 000 cm^{-1} have been identified, including two levels hitherto unreported in the solid state, at 25 900 cm^{-1} and 26 190 cm^{-1}, and a root mean-square deviation between calculated and observed energies of 96 cm^{-1} is achieved. Values of the Landé splitting factor g are predicted for the holmium levels.

INTRODUCTION

ONE of the problems in the analysis of the solid-state spectra of a trivalent rare earth ion is the identification of the free ion energy levels. Under the influence of the crystal field, each such level splits into a close group of levels having the original mean energy to first order.

By carrying out full intermediate coupling calculations within the $4f^n$ configurations, the observed spectra of the f^2 and f^{12} ions praseodymium and thulium,[1] and of the f^3 and f^{11} ions neodymium and erbium[2] have been analyzed. The present paper extends this work to the f^4 and f^{10} ions promethium and holmium.

In intermediate coupling, considerable mixing of the spin and orbital momenta S and L may occur, but the total angular momentum J remains a good quantum number. Thus, experimental assistance to the analysis can be given by the determination of J values from the splitting of levels for ion sites of given symmetry[3] in the crystal. If S and L are not too heavily mixed, the spin selection rule $\Delta S=0$ for allowed transitions, and the measured value of the Landé splitting factor

$$g(SLJ) = 1+[J(J+1)+S(S+1)-L(L+1)/2J(J+1)]$$

may help to assign values of S and L. In this paper we shall find it convenient to use values of S and L to label states even when considerable mixing does occur.

For a particular ion, the energy levels are obtained by diagonalizing the combined matrices of the spin-orbit and electrostatic interactions. The electrostatic matrices required for f^4 and f^{10} are the same, and have been calculated by Reilly.[4] The spin-orbit matrices for the two configurations differ only in sign. We have calculated these, and they are given in Table I.

CALCULATION OF THE SPIN-ORBIT MATRICES

The requisite formulas have been given by Elliott *et al.*[5] following the methods of Racah.[6] The states are classified in the form $\langle f^n WU\alpha SLJM \mid$, where $W=(w_1w_2w_3)$ and $U=(u_1u_2)$ label irreducible representations of the group R_7 and its subgroup G_2. The additional quantum number α is needed only when in the reduction of U as a representation of the full rotation group R_3, the representation D_L occurs more than once. This arises only for $U=(31)$ and (40), which do not occur in f^4.

The dependence of the matrix elements on J may be extracted in the standard form[7]

$$\langle f^n WU\alpha SLJM \mid \textstyle\sum_i \mathbf{s}_i\cdot\mathbf{l}_i \mid f^n W'U'\alpha'S'L'J'M'\rangle = \delta(MM')\delta(JJ')(-1)^{S'+L+J+1} \bar{W}\begin{Bmatrix} S & S' & 1 \\ L' & L & J \end{Bmatrix} \langle f^n WU\alpha SL \,||\, V^{[11]} \,||\, f^n W'U'\alpha'S'L'\rangle,$$

where $\mathbf{V}^{[11]}$ is the double tensor operator $\sum_i \mathbf{s}_i^{[1]}\mathbf{l}_i^{[1]}$. Values of the $\bar{W}$ functions (6-j symbols) have been tabulated.[8]

Selection rules on the W and U quantum numbers have been described by McLellan.[9] It is also to be noted that when the identity representation occurs c times in the reduction of the direct products $W\times W'\times(110)$ or $U\times U'\times(11)$, then at most c sets of

$$\langle f^n WU\alpha SL \,||\, V^{[11]} \,||\, f^n W'U'\alpha'S'L'\rangle$$

having given W and W' or U and U', respectively, can be linearly independent. In the first case, only U, U', α, α', L, and L' vary within each set, and in the second only α, α', L, and L'. When $c=1$, the possible sets are seen to be proportional.

* Present address: National Magnet Laboratory, Massachusetts Institute of Technology, Cambridge 39, Massachusetts.

[1] W. A. Runciman and B. G. Wybourne, J. Chem. Phys. **31,** 1149 (1959).
[2] B. G. Wybourne, J. Chem. Phys. **32,** 639 (1960).
[3] H. Bethe, Ann. Physik **3,** 133 (1929); a summary has been given by W. A. Runciman, Phil. Mag. **1,** 1075 (1956).
[4] E. F. Reilly, Phys. Rev. **91,** 876 (1953).
[5] J. P. Elliott, B. R. Judd, and W. A. Runciman, Proc. Roy. Soc. (London) **A240,** 509 (1957).
[6] G. Racah, Phys. Rev. **62,** 438 (1942); **63,** 367 (1943); **76,** 1352 (1949).
[7] U. Fano and G. Racah, *Irreducible Tensorial Sets* (Academic Press Inc., New York, 1959), Eq. (15.6).
[8] M. Rotenberg, R. Bivins, N. Metropolis, and J. K. Wooten, *The 3-j and 6-j Symbols* (The Massachusetts Institute of Technology Press, 1959).
[9] A. G. McLellan, Proc. Phys. Soc. (London) **76,** 419 (1960).

TABLE I. The spin-orbit matrices for f^4. Since these are symmetric, elements above the diagonal have been omitted.

TABLE Ia.

$J=0$	^1S_a	^1S_b	^3P_a	^3P_b	^3P_c	^5D
(220) (22)^1S_a	0					
(000) (00)^1S_b	0	0				
(211) (11)^3P_a	$-(110)^{\frac{1}{2}}/10$	0	$-1/15$			
(211) (30)^3P_b	$(10)^{\frac{1}{2}}/2$	0	$-(11)^{\frac{1}{2}}/3$	$-1/3$		
(110) (11)^3P_c	$-(110)^{\frac{1}{2}}/5$	$-2(5)^{\frac{1}{2}}$	$1/5$	$(11)^{\frac{1}{2}}$	$-3/5$	
(111) (20)^5D	0	0	$-(3)^{\frac{1}{2}}/6$	$(33)^{\frac{1}{2}}/6$	$-2(3)^{\frac{1}{2}}$	$-3/2$

TABLE Ib.

$J=1$	^3P_a	^3P_b	^3P_c	^5D	^3D_a	^3D_b	^5F
(211) (11)^3P_a	$-1/30$						
(211) (30)^3P_b	$-(11)^{\frac{1}{2}}/6$	$-1/6$					
(110) (11)^3P_c	$1/10$	$(11)^{\frac{1}{2}}/2$	$-3/10$				
(111) (20)^5D	$-1/4$	$(11)^{\frac{1}{2}}/4$	-3	$-5/4$			
(211) (20)^3D_a	$5(21)^{\frac{1}{2}}/12$	$(231)^{\frac{1}{2}}/84$	0	$(21)^{\frac{1}{2}}/28$	$-5/28$		
(211) (21)^3D_b	0	$3(14)^{\frac{1}{2}}/7$	0	$(154)^{\frac{1}{2}}/14$	$-(66)^{\frac{1}{2}}/14$	$5/14$	
(111) (10)^5F	0	0	0	0	$6(7)^{\frac{1}{2}}/7$	$(462)^{\frac{1}{2}}/14$	-2

TABLE

$J=2$	^5S	^3P_a	^3P_b	$^3P_1$	^5D	^3D_a	^3D_b	^1D_a
$(111)(00)^5S$	0							
$(211)(11)^3P_a$	$\frac{6(5)^{\frac{1}{2}}}{5}$	$\frac{1}{30}$						
$(211)(30)^3P_b$	0	$\frac{(11)^{\frac{1}{2}}}{6}$	$\frac{1}{6}$					
$(110)(11)^3P_c$	$\frac{2(5)^{\frac{1}{2}}}{5}$	$\frac{-1}{10}$	$\frac{-(11)^{\frac{1}{2}}}{2}$	$\frac{3}{10}$				
$(111)(20)^5D$	0	$\frac{-(105)^{\frac{1}{2}}}{60}$	$\frac{(1155)^{\frac{1}{2}}}{60}$	$\frac{-(105)^{\frac{1}{2}}}{5}$	$\frac{-3}{4}$			
$(211)(20)^3D_a$	0	$\frac{(105)^{\frac{1}{2}}}{4}$	$\frac{(1155)^{\frac{1}{2}}}{140}$	0	$\frac{1}{4}$	$\frac{-1}{28}$		
$(211)(21)^3D_b$	0	0	$\frac{9(70)^{\frac{1}{2}}}{35}$	0	$\frac{(66)^{\frac{1}{2}}}{6}$	$\frac{-(66)^{\frac{1}{2}}}{42}$	$\frac{5}{42}$	
$(220)(20)^1D_a$	0	$\frac{37(42)^{\frac{1}{2}}}{120}$	$\frac{-(462)^{\frac{1}{2}}}{120}$	$\frac{-(42)^{\frac{1}{2}}}{20}$	0	$\frac{2(10)^{\frac{1}{2}}}{35}$	$\frac{8(165)^{\frac{1}{2}}}{105}$	0
$(220)(21)^1D_b$	0	0	0	0	0	$\frac{-6(11)^{\frac{1}{2}}}{7}$	$\frac{-19(6)^{\frac{1}{2}}}{42}$	0
$(220)(22)^1D_c$	0	$\frac{(1430)^{\frac{1}{2}}}{40}$	$\frac{(130)^{\frac{1}{2}}}{40}$	$\frac{(1430)^{\frac{1}{2}}}{20}$	0	0	0	0
$(200)(20)^1D_d$	0	$\frac{7(2)^{\frac{1}{2}}}{10}$	$\frac{-(22)^{\frac{1}{2}}}{10}$	$\frac{9(2)^{\frac{1}{2}}}{10}$	0	$\frac{-(210)^{\frac{1}{2}}}{35}$	$\frac{-4(385)^{\frac{1}{2}}}{35}$	0
$(111)(10)^5F$	0	0	0	0	0	$\frac{2(42)^{\frac{1}{2}}}{7}$	$\frac{(77)^{\frac{1}{2}}}{7}$	0
$(211)(10)^3F_a$	0	0	0	0	$\frac{-2(35)^{\frac{1}{2}}}{105}$	$\frac{-16(35)^{\frac{1}{2}}}{105}$	$\frac{-(2310)^{\frac{1}{2}}}{630}$	$\frac{-64(14)^{\frac{1}{2}}}{105}$
$(211)(21)^3F_b$	0	0	0	0	0	0	$\frac{-(14)^{\frac{1}{2}}}{3}$	0
$(211)(30)^3F_c$	0	0	0	0	$\frac{(5005)^{\frac{1}{2}}}{105}$	$\frac{-(5005)^{\frac{1}{2}}}{105}$	$\frac{-(2730)^{\frac{1}{2}}}{315}$	$\frac{-(2002)^{\frac{1}{2}}}{60}$
$(110)(10)^3F_d$	0	0	0	0	$\frac{-2(35)^{\frac{1}{2}}}{35}$	$\frac{-6(35)^{\frac{1}{2}}}{35}$	$\frac{2(2310)^{\frac{1}{2}}}{105}$	$\frac{-4(14)^{\frac{1}{2}}}{35}$
$(111)(20)^5G$	0	0	0	0	0	0	0	0

Ic.

^1D_b	^1D_c	^1D_d	^5F	^3F_a	^3F_b	^3F_c	^3F_d	^5G
0								
0	0							
0	0	0						
0	0	0	$\frac{-3}{2}$					
$\frac{(385)^{\frac{1}{2}}}{35}$	0	$\frac{2(6)^{\frac{1}{2}}}{15}$	$\frac{-(30)^{\frac{1}{2}}}{10}$	$\frac{23}{15}$				
$\frac{-(21)^{\frac{1}{2}}}{3}$	0	0	$\frac{(22)^{\frac{1}{2}}}{4}$	$\frac{(165)^{\frac{1}{2}}}{90}$	-2			
0	$\frac{-27(30)^{\frac{1}{2}}}{60}$	$\frac{-(858)^{\frac{1}{2}}}{15}$	0	0	$\frac{-(195)^{\frac{1}{2}}}{9}$	$\frac{-2}{3}$		
$\frac{-2(385)^{\frac{1}{2}}}{35}$	0	$\frac{-3(6)^{\frac{1}{2}}}{5}$	$\frac{(30)^{\frac{1}{2}}}{5}$	$\frac{-2}{5}$	$\frac{-2(165)^{\frac{1}{2}}}{15}$	0	$\frac{-6}{5}$	
0	0	0	0	$\frac{(2310)^{\frac{1}{2}}}{105}$	$\frac{(14)^{\frac{1}{2}}}{4}$	$\frac{(2730)^{\frac{1}{2}}}{21}$	$\frac{(2310)^{\frac{1}{2}}}{35}$	$\frac{-5}{2}$

TABLE

$J=3$	^5D	^3D_a	^3D_b	^5F	^3F_a	^3F_b
$(111)(20)^5D$	0					
$(211)(20)^3D_a$	$\frac{(14)^{\frac{1}{2}}}{14}$	$\frac{1}{14}$				
$(211)(21)^3D_b$	$\frac{2(231)^{\frac{1}{2}}}{21}$	$\frac{(66)^{\frac{1}{2}}}{21}$	$\frac{-5}{21}$			
$(111)(10)^5F$	0	$\frac{6(2)^{\frac{1}{2}}}{7}$	$\frac{(33)^{\frac{1}{2}}}{7}$	$\frac{-3}{4}$		
$(211)(10)^3F_a$	$\frac{-2(7)^{\frac{1}{2}}}{21}$	$\frac{-16(2)^{\frac{1}{2}}}{21}$	$\frac{-(33)^{\frac{1}{2}}}{63}$	$\frac{-3}{4}$	$\frac{23}{60}$	
$(211)(21)^3F_b$	0	0	$\frac{-2(5)^{\frac{1}{2}}}{3}$	$\frac{(165)^{\frac{1}{2}}}{8}$	$\frac{(165)^{\frac{1}{2}}}{360}$	$\frac{-1}{2}$
$(211)(30)^3F_c$	$\frac{(1001)^{\frac{1}{2}}}{21}$	$\frac{-(286)^{\frac{1}{2}}}{21}$	$\frac{-2(39)^{\frac{1}{2}}}{63}$	0	0	$\frac{-(195)^{\frac{1}{2}}}{36}$
$(110)(10)^3F_d$	$\frac{-2(7)^{\frac{1}{2}}}{7}$	$\frac{-6(2)^{\frac{1}{2}}}{7}$	$\frac{4(33)^{\frac{1}{2}}}{21}$	$\frac{3}{2}$	$\frac{-1}{10}$	$\frac{-(165)^{\frac{1}{2}}}{30}$
$(220)(21)^1F$	0	0	$\frac{(15)^{\frac{1}{2}}}{3}$	0	$\frac{(55)^{\frac{1}{2}}}{10}$	$\frac{(3)^{\frac{1}{2}}}{3}$
$(111)(20)^5G$	0	0	0	0	$\frac{(231)^{\frac{1}{2}}}{42}$	$\frac{(35)^{\frac{1}{2}}}{8}$
$(211)(20)^3G_a$	0	0	0	$\frac{-(55)^{\frac{1}{2}}}{14}$	$\frac{-4(55)^{\frac{1}{2}}}{35}$	$\frac{(3)^{\frac{1}{2}}}{8}$
$(211)(21)^3G_b$	0	0	0	$\frac{-5(39)^{\frac{1}{2}}}{56}$	$\frac{-(39)^{\frac{1}{2}}}{56}$	0
$(211)(30)^3G_c$	0	0	0	0	0	$\frac{-3(5)^{\frac{1}{2}}}{4}$

Id.

^5F_e	^5F_d	^1F	^5G	^3G_e	^3G_b	^3G_c
$\frac{-1}{6}$						
	$\frac{-3}{10}$					
0	$\frac{-(55)^{\frac{1}{2}}}{5}$	0				
$\frac{5(273)^{\frac{1}{2}}}{42}$	$\frac{(231)^{\frac{1}{2}}}{14}$	0	$\frac{-7}{4}$			
$\frac{(65)^{\frac{1}{2}}}{14}$	$\frac{-9(55)^{\frac{1}{2}}}{70}$	$\frac{-3}{2}$	$\frac{(105)^{\frac{1}{2}}}{28}$	$\frac{-5}{28}$		
$\frac{-5(33)^{\frac{1}{2}}}{28}$	$\frac{3(39)^{\frac{1}{2}}}{14}$	0	$\frac{(1001)^{\frac{1}{2}}}{56}$	$\frac{-(2145)^{\frac{1}{2}}}{168}$	$\frac{-73}{42}$	
0	0	0	$\frac{-(7)^{\frac{1}{2}}}{2}$	$\frac{(15)^{\frac{1}{2}}}{6}$	$\frac{(143)^{\frac{1}{2}}}{12}$	$\frac{-5}{6}$

TABLE

$J=4$	^5D	^5F	^3F_a	^3F_b	^3F_c	^3F_d	^5G	^3G_a
$(111)(20)^5D$	1							
$(111)(10)^5F$	0	$\frac{1}{4}$						
$(211)(10)^3F_a$	$\frac{-2(21)^{\frac{1}{2}}}{21}$	$\frac{-3}{4}$	$\frac{-23}{20}$					
$(211)(21)^3F_b$	0	$\frac{(165)^{\frac{1}{2}}}{8}$	$\frac{-(165)^{\frac{1}{2}}}{120}$	$\frac{3}{2}$				
$(211)(30)^3F_c$	$\frac{(3003)^{\frac{1}{2}}}{21}$	0	0	$\frac{(195)^{\frac{1}{2}}}{12}$	$\frac{1}{2}$			
$(110)(10)^3F_d$	$\frac{-2(21)^{\frac{1}{2}}}{7}$	$\frac{3}{2}$	$\frac{3}{10}$	$\frac{(165)^{\frac{1}{2}}}{10}$	0	$\frac{9}{10}$		
$(111)(20)^5G$	0	0	$\frac{11(7)^{\frac{1}{2}}}{126}$	$\frac{(1155)^{\frac{1}{2}}}{72}$	$\frac{5(1001)^{\frac{1}{2}}}{126}$	$\frac{11(7)^{\frac{1}{2}}}{42}$	$\frac{-3}{4}$	
$(211)(20)^3G_a$	0	$\frac{-(231)^{\frac{1}{2}}}{14}$	$\frac{-4(231)^{\frac{1}{2}}}{63}$	$\frac{(35)^{\frac{1}{2}}}{24}$	$\frac{5(273)^{\frac{1}{2}}}{126}$	$\frac{-(231)^{\frac{1}{2}}}{14}$	$\frac{(33)^{\frac{1}{2}}}{12}$	$\frac{-1}{28}$
$(211)(21)^3G_b$	0	$\frac{-3(455)^{\frac{1}{2}}}{56}$	$\frac{-(455)^{\frac{1}{2}}}{168}$	0	$\frac{-5(385)^{\frac{1}{2}}}{84}$	$\frac{(455)^{\frac{1}{2}}}{14}$	$\frac{11(65)^{\frac{1}{2}}}{120}$	$\frac{-(2145)^{\frac{1}{2}}}{840}$
$(211)(30)^3G_c$	0	0	0	$\frac{-5(21)^{\frac{1}{2}}}{12}$	0	0	$\frac{-7(55)^{\frac{1}{2}}}{30}$	$\frac{(15)^{\frac{1}{2}}}{30}$
$(220)(20)^1G_a$	0	0	$\frac{64(77)^{\frac{1}{2}}}{315}$	$\frac{-2(105)^{\frac{1}{2}}}{45}$	$\frac{-(91)^{\frac{1}{2}}}{18}$	$\frac{4(77)^{\frac{1}{2}}}{105}$	0	$\frac{4(3)^{\frac{1}{2}}}{21}$
$(220)(21)^1G_b$	0	0	$\frac{-(91)^{\frac{1}{2}}}{14}$	0	0	$\frac{(91)^{\frac{1}{2}}}{7}$	0	$\frac{-(429)^{\frac{1}{2}}}{14}$
$(220)(22)^1G_c$	0	0	0	0	$\frac{-5}{2}$	0	0	0
$(200)(20)^1G_d$	0	0	$\frac{-2(33)^{\frac{1}{2}}}{45}$	$\frac{7(5)^{\frac{1}{2}}}{15}$	$\frac{-2(39)^{\frac{1}{2}}}{9}$	$\frac{(33)^{\frac{1}{2}}}{5}$	0	$\frac{-2(7)^{\frac{1}{2}}}{7}$
$(211)(11)^3H_a$	0	0	0	0	0	0	$\frac{(770)^{\frac{1}{2}}}{495}$	$\frac{(210)^{\frac{1}{2}}}{9}$
$(211)(21)^3H_b$	0	0	0	0	0	0	$\frac{-7(715)^{\frac{1}{2}}}{495}$	$\frac{(195)^{\frac{1}{2}}}{45}$
$(211)(30)^3H_c$	0	0	0	0	0	0	$\frac{-(30030)^{\frac{1}{2}}}{495}$	$\frac{(910)^{\frac{1}{2}}}{105}$
$(110)(11)^3H_d$	0	0	0	0	0	0	$\frac{4(770)^{\frac{1}{2}}}{165}$	0
$(111)(20)^1I$	0	0	0	0	0	0	0	0

Ie.

^3G_b	^3G_c	^1G_a	^1G_b	^1G_c	^1G_d	^3H_a	^3H_b	^3H_c	^3H_d	^5I
$\frac{-73}{210}$										
$\frac{(143)^{\frac{1}{2}}}{60}$	$\frac{-1}{6}$									
$\frac{2(715)^{\frac{1}{2}}}{105}$	$\frac{-7(5)^{\frac{1}{2}}}{30}$	0								
$\frac{(5)^{\frac{1}{2}}}{35}$	0	0	0							
0	$\frac{(455)^{\frac{1}{2}}}{10}$	0	0	0						
$\frac{-(15015)^{\frac{1}{2}}}{105}$	$\frac{-2(105)^{\frac{1}{2}}}{15}$	0	0	0	0					
0	$\frac{-2(14)^{\frac{1}{2}}}{15}$	$\frac{-37(70)^{\frac{1}{2}}}{180}$	0	$\frac{-(130)^{\frac{1}{2}}}{20}$	$\frac{-7(30)^{\frac{1}{2}}}{45}$	$\frac{-1}{5}$				
$\frac{-2(11)^{\frac{1}{2}}}{5}$	$\frac{2(13)^{\frac{1}{2}}}{15}$	$\frac{4(65)^{\frac{1}{2}}}{45}$	$\frac{-(55)^{\frac{1}{2}}}{5}$	0	$\frac{-2(1365)^{\frac{1}{2}}}{45}$	0	$\frac{-1}{5}$			
$\frac{8(462)^{\frac{1}{2}}}{105}$	0	$\frac{(2730)^{\frac{1}{2}}}{180}$	0	$\frac{9(30)^{\frac{1}{2}}}{20}$	$\frac{(130)^{\frac{1}{2}}}{15}$	$\frac{-(39)^{\frac{1}{2}}}{15}$	$\frac{2(42)^{\frac{1}{2}}}{15}$	-1		
0	$\frac{2(14)^{\frac{1}{2}}}{5}$	$\frac{(70)^{\frac{1}{2}}}{30}$	0	$\frac{-(130)^{\frac{1}{2}}}{10}$	$\frac{-(30)^{\frac{1}{2}}}{5}$	$\frac{3}{5}$	0	$\frac{(39)^{\frac{1}{2}}}{5}$	$\frac{-9}{5}$	
0	0	0	0	0	0	$\frac{-(2145)^{\frac{1}{2}}}{330}$	$\frac{-(2310)^{\frac{1}{2}}}{33}$	$\frac{7(55)^{\frac{1}{2}}}{22}$	$\frac{-2(2145)^{\frac{1}{2}}}{55}$	$\frac{-7}{2}$

TABLE

$J=5$	^5F	^5G	^3G_a	^3G_b	^3G_c	^3H_a
$(111)(10)^5F$	$\frac{3}{2}$					
$(111)(20)^5G$	0	$\frac{1}{2}$				
$(211)(20)^3G_a$	$\frac{-(154)^{\frac{1}{2}}}{7}$	$\frac{(42)^{\frac{1}{2}}}{14}$	$\frac{1}{7}$			
$(211)(21)^3G_b$	$\frac{-(2730)^{\frac{1}{2}}}{28}$	$\frac{(10010)^{\frac{1}{2}}}{140}$	$\frac{(2145)^{\frac{1}{2}}}{210}$	$\frac{146}{105}$		
$(211)(30)^3G_c$	0	$\frac{-(70)^{\frac{1}{2}}}{5}$	$\frac{-2(15)^{\frac{1}{2}}}{15}$	$\frac{-(143)^{\frac{1}{2}}}{15}$	$\frac{2}{3}$	
$(211)(11)^3H_a$	0	$\frac{(330)^{\frac{1}{2}}}{165}$	$\frac{(385)^{\frac{1}{2}}}{11}$	0	$\frac{-2(231)^{\frac{1}{2}}}{55}$	$\frac{-1}{30}$
$(211)21)^3H_b$	0	$\frac{-(15015)^{\frac{1}{2}}}{165}$	$\frac{(1430)^{\frac{1}{2}}}{110}$	$\frac{-3(6)^{\frac{1}{2}}}{5}$	$\frac{(858)^{\frac{1}{2}}}{55}$	0
$(211)(30)^3H_c$	0	$\frac{-(1430)^{\frac{1}{2}}}{55}$	$\frac{(15015)^{\frac{1}{2}}}{385}$	$\frac{24(7)^{\frac{1}{2}}}{35}$	0	$\frac{-(39)^{\frac{1}{2}}}{90}$
$(110)(11)^3H_d$	0	$\frac{4(330)^{\frac{1}{2}}}{55}$	0	0	$\frac{6(231)^{\frac{1}{2}}}{55}$	$\frac{1}{10}$
$(220)(21)^1H_a$	0	0	$\frac{(429)^{\frac{1}{2}}}{11}$	$\frac{3(5)^{\frac{1}{2}}}{5}$	0	0
$(220)(22)^1H_b$	0	0	0	0	$\frac{-3(330)^{\frac{1}{2}}}{55}$	$\frac{(70)^{\frac{1}{2}}}{10}$
$(111)(20)^5I$	0	0	0	0	0	$\frac{-(5005)^{\frac{1}{2}}}{660}$
$(211)(20)^3I_a$	0	0	0	0	0	$\frac{5(1001)^{\frac{1}{2}}}{132}$
$(211)(30)^3I_b$	0	0	0	0	0	$\frac{-(3003)^{\frac{1}{2}}}{99}$

II.

^5H_b	^3H_c	^3H_d	^1H_a	^1H_b	^5I	^3I_a	^3I_b
$\frac{-1}{30}$							
$\frac{(42)^{\frac{1}{2}}}{45}$	$\frac{-1}{6}$						
0	$\frac{(39)^{\frac{1}{2}}}{30}$	$\frac{-3}{10}$					
$\frac{-3(30)^{\frac{1}{2}}}{10}$	0	0	0				
0	$\frac{(2730)^{\frac{1}{2}}}{30}$	$\frac{(70)^{\frac{1}{2}}}{5}$	0	0			
$\frac{-7(110)^{\frac{1}{2}}}{66}$	$\frac{7(1155)^{\frac{1}{2}}}{132}$	$\frac{-(5005)^{\frac{1}{2}}}{55}$	0	0	$\frac{-9}{4}$		
$\frac{-5(22)^{\frac{1}{2}}}{66}$	$\frac{5(231)^{\frac{1}{2}}}{132}$	0	$\frac{2(165)^{\frac{1}{2}}}{11}$	0	$\frac{(5)^{\frac{1}{2}}}{4}$	$\frac{-1}{4}$	
$\frac{-10(66)^{\frac{1}{2}}}{99}$	0	$\frac{(3003)^{\frac{1}{2}}}{33}$	0	$\frac{-(4290)^{\frac{1}{2}}}{66}$	$\frac{-(15)^{\frac{1}{2}}}{6}$	$\frac{(3)^{\frac{1}{2}}}{6}$	$\frac{-7}{6}$

TABLE

$J=6$	^5G	^3H_a	^3H_b	^3H_c	^3H_d	^5I
$(111)(20)^5G$	2					
$(211)(11)^3H_a$	$\frac{(33)^{\frac{1}{2}}}{3}$	$\frac{1}{6}$				
$(211)(21)^3H_b$	$\frac{-(6006)^{\frac{1}{2}}}{66}$	0	$\frac{1}{6}$			
$(211)(30)^3H_c$	$\frac{-(143)^{\frac{1}{2}}}{11}$	$\frac{(39)^{\frac{1}{2}}}{18}$	$\frac{-(42)^{\frac{1}{2}}}{9}$	$\frac{5}{6}$		
$(110)(11)^3H_d$	$\frac{4(33)^{\frac{1}{2}}}{11}$	$\frac{-1}{2}$	0	$\frac{-(39)^{\frac{1}{2}}}{6}$	$\frac{3}{2}$	
$(111)(20)^5I$	0	$\frac{-(77)^{\frac{1}{2}}}{132}$	$\frac{-35(286)^{\frac{1}{2}}}{858}$	$\frac{35(3003)^{\frac{1}{2}}}{1716}$	$\frac{-(77)^{\frac{1}{2}}}{11}$	$\frac{-3}{4}$
$(211)(20)^3I_a$	0	$\frac{7(5)^{\frac{1}{2}}}{12}$	$\frac{-(910)^{\frac{1}{2}}}{78}$	$\frac{7(195)^{\frac{1}{2}}}{156}$	0	$\frac{(385)^{\frac{1}{2}}}{28}$
$(211)(30)^3I_b$	0	$\frac{-7(15)^{\frac{1}{2}}}{45}$	$\frac{-2(2730)^{\frac{1}{2}}}{117}$	0	$\frac{7(15)^{\frac{1}{2}}}{15}$	$\frac{-(1155)^{\frac{1}{2}}}{42}$
$(220)(20)^1I_a$	0	$\frac{37(14)^{\frac{1}{2}}}{120}$	$\frac{8(13)^{\frac{1}{2}}}{39}$	$\frac{-7(546)^{\frac{1}{2}}}{312}$	$\frac{-(14)^{\frac{1}{2}}}{20}$	0
$(220)(22)^1I_b$	0	$\frac{(34)^{\frac{1}{2}}}{8}$	0	$\frac{-5(1326)^{\frac{1}{2}}}{312}$	$\frac{(34)^{\frac{1}{2}}}{4}$	0
$(200)(20)^1I_c$	0	$\frac{7(6)^{\frac{1}{2}}}{30}$	$\frac{-4(273)^{\frac{1}{2}}}{39}$	$\frac{-7(26)^{\frac{1}{2}}}{26}$	$\frac{3(6)^{\frac{1}{2}}}{10}$	0
$(211)(21)^3K_a$	0	0	0	0	0	$\frac{2(3003)^{\frac{1}{2}}}{273}$
$(211)(30)^3K_b$	0	0	0	0	0	$\frac{-(51051)^{\frac{1}{2}}}{273}$

Ig.

^3I_a	^3I_b	^1I_a	^1I_b	^1I_c	^3K_a	^3K_b
$\frac{-1}{28}$						
$\frac{(3)^{\frac{1}{2}}}{42}$	$\frac{-1}{6}$					
$\frac{2(70)^{\frac{1}{2}}}{35}$	$\frac{-(210)^{\frac{1}{2}}}{60}$	0				
0	$\frac{(510)^{\frac{1}{2}}}{12}$	0	0			
$\frac{-(30)^{\frac{1}{2}}}{5}$	$\frac{-(10)^{\frac{1}{2}}}{5}$	0	0	0		
$\frac{-2(195)^{\frac{1}{2}}}{91}$	$\frac{18(65)^{\frac{1}{2}}}{91}$	$\frac{-8(546)^{\frac{1}{2}}}{273}$	0	$\frac{4(26)^{\frac{1}{2}}}{13}$	$\frac{-29}{21}$	
$\frac{(3315)^{\frac{1}{2}}}{91}$	0	$\frac{(9282)^{\frac{1}{2}}}{156}$	$\frac{9(78)^{\frac{1}{2}}}{52}$	$\frac{(442)^{\frac{1}{2}}}{13}$	$\frac{4(17)^{\frac{1}{2}}}{21}$	$\frac{-4}{3}$

TABLE Ih.

$J=7$	^5I	^3I_a	^3I_b	^3K_a	^3K_b	^1K	^3L
$(111)(20)^5I$	1						
$(211)(20)^3I_a$	$\frac{(21)^{\frac{1}{2}}}{7}$	$\frac{3}{14}$					
$(211)(30)^3I_b$	$\frac{-2(7)^{\frac{1}{2}}}{7}$	$\frac{-(3)^{\frac{1}{2}}}{7}$	1				
$(211)(21)^3K_a$	$\frac{2(7)^{\frac{1}{2}}}{7}$	$\frac{-4(3)^{\frac{1}{2}}}{21}$	$\frac{12}{7}$	$\frac{-29}{168}$			
$(211)(30)^3K_b$	$\frac{-(119)^{\frac{1}{2}}}{7}$	$\frac{2(51)^{\frac{1}{2}}}{21}$	0	$\frac{(17)^{\frac{1}{2}}}{42}$	$\frac{-1}{6}$		
$(220)(21)^1K$	0	$\frac{-2(42)^{\frac{1}{2}}}{7}$	0	$\frac{-9(14)^{\frac{1}{2}}}{28}$	0	0	
$(211)(21)^3L$	0	0	0	$\frac{-(119)^{\frac{1}{2}}}{8}$	$\frac{(7)^{\frac{1}{2}}}{2}$	$\frac{-(34)^{\frac{1}{2}}}{4}$	$\frac{-15}{8}$

TABLE Ii.

$J=8$	^5I	^3K_a	^3K_b	^3L	^1L_a	^1L_b	^3M
$(111)(20)^5I$	3						
$(211)(21)^3K_a$	$\frac{2(3)^{\frac{1}{2}}}{3}$	$\frac{29}{24}$					
$(211)(30)^3K_b$	$\frac{-(51)}{3}$	$\frac{-(17)^{\frac{1}{2}}}{6}$	$\frac{7}{6}$				
$(211)(21)^3L$	0	$\frac{-3(15)^{\frac{1}{2}}}{8}$	$\frac{3(255)^{\frac{1}{2}}}{34}$	$\frac{-5}{24}$			
$(220)(21)^1L_a$	0	$\frac{(30)^{\frac{1}{2}}}{4}$	0	$\frac{-3(2)^{\frac{1}{2}}}{4}$	0		
$(220)(22)^1L_b$	0	0	$\frac{-(1938)^{\frac{1}{2}}}{17}$	0	0	0	
$(211)(30)^3M$	0	0	0	$\frac{4(323)^{\frac{1}{2}}}{51}$	0	$\frac{-3(170)^{\frac{1}{2}}}{17}$	$\frac{-5}{3}$

TABLE Ij.

$J=9$	^3L	^3M
$(211)(21)^3L$	$\frac{5}{3}$	
$(211)(30)^3M$	$\frac{2(5)^{\frac{1}{2}}}{3}$	$\frac{-1}{6}$

TABLE Ik.

$J=10$	^3M	^1N
$(211)(30)^3M$	$\frac{3}{2}$	
$(220)(22)^1N$	$\frac{(10)^{\frac{1}{2}}}{2}$	0

Since the orbital angular momentum operator $\mathbf{L}$ belongs to the same irreducible representations of R_7, G_2 and R_3, viz. $WUL=(110)(11)P$, its reduced matrix elements can be used as one of the independent sets when they do not vanish. Considering

$$\langle \beta L \,||\, L^{[1]} \,||\, \beta' L' \rangle = \delta(\beta\beta')\delta(LL')i[L(L+1)(2L+1)]^{\frac{1}{2}},$$

this means that in the first case, when $W=W'$, one independent set has elements of the form

$$\delta(UU')\delta(\alpha\alpha')\delta(LL')[L(L+1)(2L+1)]^{\frac{1}{2}}.$$

It then follows that in the second case there is an independent set with elements

$$\delta(\alpha\alpha')\delta(LL')[L(L+1)(2L+1)]^{\frac{1}{2}}$$

whenever $U=U'$.

These various results were used to obtain some of the matrix elements required from others already calculated for f^4. The complete matrices for f^3,[10] and the matrix elements connecting states of the two highest multiplicities of f^5 and f^6,[11] were also used. Additional relationships[12] between sets of reduced matrix elements have been calculated by Wybourne.

A sensitive check of the matrices was obtained by diagonalizing them numerically, it being possible to predict their eigenvalues by using the j-j coupling scheme. For f^n, the j-j configurations $(f_{5/2})^x(f_{7/2})^y$ where $x+y=n$, give rise to eigenvalues $\frac{1}{2}(-4x+3y)$, and the number of times which each such configuration occurs for given J can be determined.[13]

PARAMETERS

The electrostatic matrices depend on three parameters E^1, E^2, and E^3, and the spin-orbit matrices carry a further parameter ζ. The electrostatic parameters are not expected to deviate greatly from hydrogenic ratios,[5] and so this was made the basis of the initial calculations. Quite good values of E^3 and ζ could be found by interpolation from the values found for other rare-earth ions.[1,2,11] The assumption of hydrogenic ratios should be particularly satisfactory for states of predominantly maximum spin, since in the Russell-Saunders approximation their energies do not depend on E^1 and E^2.

TABLE II. Parameter values in units of cm^{-1}.

	E^1	E^2	E^3	ζ
Pm^{3+}	5080	26.64	513.6	1070
Ho^{3+}	6608	28.79	608.0	2163

[10] B. R. Judd and R. Loudon, Proc. Roy. Soc. (London) **A251**, 127 (1959).
[11] B. G. Wybourne, Ph.D. thesis, University of Canterbury, Christchurch, New Zealand, 1960.
[12] B. G. Wybourne, J. Chem. Phys. (to be published).
[13] Use E. U. Condon and G. H. Shortley, *The Theory of Atomic Spectra* (Cambridge University Press, New York, 1957), Table 2[10].

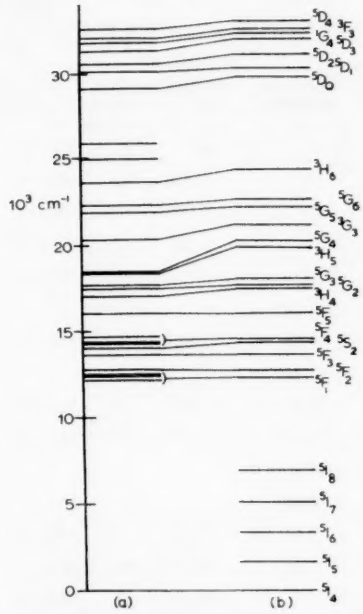

FIG. 1. Promethium: Tentative analysis of the solution spectrum. (a) Experimental band positions; (b) calculated energy levels for states exceeding 20% quintet character.

PROMETHIUM

The combined matrices of the spin-orbit and electrostatic interactions were diagonalized, using the estimated parameter values of Table II. The resultant energy levels are given in Table III. Since the solid-state results presently available[14] are rather limited, no reliable correlation of calculated and experimental energy levels was possible. However, by applying the spin selection rule to the solution spectra,[15] a tentative identification of all the states having more than 20% $S=2$ has been made. This is indicated in Fig. 1.

It would appear that Gruber and Conway[15] failed to observe the $^5I_8$ level, whose calculated energy lies within the range of their observations.

HOLMIUM

Here all levels below 25 000 cm^{-1} have previously been observed in the solid state[16–19] and the solution spectrum has been studied[20] as far as 42 000 cm^{-1}. We have found two further solid-state line groups at 25 900

[14] J. G. Conway and J. B. Gruber, J. Chem. Phys. **32**, 1586 (1960).
[15] J. B. Gruber and J. G. Conway, J. Inorg. & Nuclear Chem. **14**, 303 (1960); also G. W. Parker and P. M. Lantz, J. Am. Chem. Soc. **72**, 2834 (1950); W. F. Megger, B. F. Schribner, and W. R. Bozman, J. Research Natl. Bur. Standards **46**, 85 (1951); and D. S. Stewart, ANL-4812 (1956).
[16] H. Gobrecht, Ann. Phys. (5) **28**, 673 (1937).
[17] G. Rosenthal, Phys. Z. **40**, 5 (1959).
[18] H. Severin, Z. Physik. **125**, 455 (1949).
[19] H. G. Kahle, Z. Physik. **145**, 347 (1956).
[20] C. K. Jørgensen, Acta. Chem. Scand. **11**, 981 (1957).

TABLE III. Energy levels for Pm^{3+}.

Absorption band peak (cm^{-1})	Extinction coefficient	Calculated energy (cm^{-1})	SLJ label	SL composition of states
Ground level		0	$^5I_4$	97% ^5I
		1 586	$^5I_5$	98% ^5I
		3 305	$^5I_6$	99% ^5I
		5 101	$^5I_7$	97% ^5I
		6 934	$^5I_8$	95% ^5I
12 146	0.24			
12 412	0.74	12 288	$^5F_1$	94% ^5F
12 484	0.85			
12 781	1.54	12 731	$^5F_2$	91% ^5F
13 611	3.05	13 650	$^5F_3$	94% ^5F
13 982	0.36			
14 247	2.54			
14 327	2.14	14 369	$^5S_2$	92% ^5S
14 624	2.13	14 602	$^5F_4$	87% ^5F
		15 915	$^3K_6$	98% ^3K
15 972	0.45	16 016	$^5F_5$	90% ^5F
16 935	0.23	17 186	$^3K_7$	78% ^3K, 18% ^3L
17 391	0.64	17 473	$^3H_4$	47% ^3H, 20% ^3G, 15% ^5G
17 609	3.57	17 719	$^5G_2$	91% ^5G
18 262	3.33	18 095	$^5G_3$	71% ^5G, 25% ^3G
18 355	3.40			
		18 756	$^3K_8$	65% ^3K, 18% ^3L
		19 881	$^3H_5$	45% ^3H, 33% ^5G, 15% ^3G
20 272	1.41	20 274	$^5G_4$	71% ^5G, 25% ^3H,
		21 187	$^3G_3$	71% ^3G, 25% ^5G,
21 820	0.69	22 030	$^3D_2$	58% ^3D, 19% ^3P 10% ^1D
22 242	0.41	22 204	$^5G_5$	60% ^5G, 38% ^3H
		22 208	$^3L_7$	80% ^3L, 19% ^3K
		22 632	$^5G_6$	71% ^5G, 28% ^3H
		23 154	$^3D_1$	48% ^3D, 47% ^3P
23 663	0.20	23 353	$^3L_8$	55% ^3L, 23% ^3M 20% ^3K
		24 252	$^3G_4$	58% ^3G, 18% ^3H, 12% ^5G
		24 253	$^3L_9$	73% ^3L, 27% ^3M
		24 254	$^3M_8$	45% ^3M, 33% ^1L, 20% ^3L
		24 369	$^3H_6$	69% ^3H, 27% ^5G
		24 765	$^3D_3$	84% ^3D, 11% ^3F
24 910	0.51	24 849	$^3P_0$	100% ^3P
25 840	0.21	25 373	$^1D_2$	41% ^1D, 28% ^3P, 25% ^3F
		26 439	$^3F_4$	70% ^3F, 13% ^3G, 12% ^1G
		26 736	$^3G_6$	63% ^3G, 13% ^3H
		27 120	$^3P_1$	53% ^3P, 45% ^3D
		27 514	$^3I_5$	83% ^5I, 11% ^3G
		27 838	$^3M_9$	73% ^3M, 27% ^3L
		28 094	$^3F_2$	49% ^3F, 36% ^3P
		28 429	$^3M_{10}$	98% ^3M
		28 654	$^3F_3$	83% ^3F, 11% ^3D
		28 719	$^3I_6$	91% ^3I
29 070	0.39	29 128	$^3F_2$	82% ^3F
		29 221	$^3I_7$	93% ^3I
		29 319	$^1L_8$	56% ^1L, 28% ^3M
30 040	4.73	29 788	$^5D_0$	96% ^5D
30 480	4.96	30 318	$^5D_1$	97% ^5D
31 250	2.53	31 161	$^5D_2$	95% ^5D
31 720	0.31			
31 990	0.77	31 989	$^5D_3$	68% ^5D, 28% ^3F
		32 290	$^1G_4$	49% ^1G, 44% ^5D
32 530	0.32	32 552	$^3F_3$	72% ^3F, 24% ^5D
		32 864	$^1D_2$	52% ^1D, 20% ^3D, 19% ^3F
		32 930	$^3P_0$	92% ^3P
		33 019	$^5D_4$	38% ^5D, 30% ^1G, 28% ^1G
		34 442	$^1I_6$	59% ^1I, 36% ^3H
		35 337	$^3H_4$	75% ^3H, 9% ^1G, 10% ^3G
		35 979	$^3F_4$	90% ^3F
		35 983	$^3H_5$	60% ^3H, 38% ^1H
		36 362	$^1H_5$	38% ^1H, 31% ^3H, 23% ^3G
		36 962	$^1K_7$	92% ^1K
		38 013	$^3H_6$	62% ^3H, 36% ^1I
38 310	...	38 443	$^1D_2$	87% ^1D, 10% ^3F
		39 684	$^3G_4$	49% ^3G, 26% ^3P, 17% ^3H
		39 743	$^3G_5$	80% ^3G, 18% ^3F

TABLE IV. Energy levels for Ho^{3+}.

Experimental line groups		Calculated levels			
Label	Mean energy (cm^{-1})	Energy (cm^{-1})	SLJ label	SL composition	g
	Ground level	0	$^5I_8$	93% ^5I	1.241
	5 120	5 087	$^5I_7$	97% ^5I	1.174
A	8 590	8 647	$^5I_6$	95% ^5I	1.073
B	11 218	11 255	$^5I_5$	91% ^5I	0.914
C	13 319	13 349	$^5I_4$	90% ^5I	0.621
D	15 510	15 403	$^5F_5$	82% ^5F, 14% ^3G	1.358
E	18 554	mean { 18 221	$^5S_2$	75% S, 14% ^3P	1.830
		18 387 { 18 479	$^5F_4$	92% ^5F	1.337
F	20 650	20 568	$^5F_3$	91% ^5F	1.245
G	21 115	21 113	$^5F_2$	68% ^5F, 15% ^3D, 11% ^5S	1.124
H	21 400	21 321	$^3K_8$	72% ^3K, 12% ^3L	1.104
I	22 163	mean { 22 192	$^5G_6$	86% ^5G, 13% ^3H	1.309
		22 224 { 22 365	$^5F_1$	81% ^5F, 17% ^3D	0.107
K	23 980	24 104	$^5G_5$	50% ^5G, 30% ^3G, 11% ^5F	1.241
L	25 900	26 070	$^5G_4$	63% ^5G, 25% ^3G	1.129
M	26 190	26 195	$^3K_7$	83% ^3K, 11% ^3L	1.011
		28 040	$^5G_5'$	41% ^5G, 29% ^3H, 19% ^3G	1.165
		28 391	$^3H_6$	82% ^3H, 11% ^5G	1.174
		28 421	$^3L_9$	89% ^3L, 11% ^3M	1.100
		28 620	$^5G_2$	22% ^5G, 19% ^3F, 17% ^5F, 14% ^3D, 13% ^1D	0.904
		28 953	$^5G_3$	78% ^5G, 13% ^3F	0.941
		30 261	$^3K_6$	90% ^3K	0.877
		30 726	$^3F_4$	26% ^3F, 22% ^3H, 21% ^3G, 10% ^5D, 11% ^1G	1.074
		31 094	$^5G_2'$	50% ^5G, 15% ^3D, 10% ^3P	0.744
		33 296	$^3M_{10}$	98% ^3M	
		33 862	$^3L_8$	65% ^3L, 17% ^3M, 16% ^3K	
		33 921	$^3D_3$	78% ^3D	
		33 973	$^3P_1$	62% ^3P, 27% ^3D, 11% ^5F	
		35 125	$^5D_4$	31% ^5D, 24% ^5G, 18% ^3G, 17% ^3F	
		35 859	$^3F_3$	44% ^3F, 39% ^3G, 14% ^5D	
		36 267	$^1L_8$	53% ^1L, 26% ^3M, 18% ^3L	
		36 700	$^3P_0$	96% ^3P	
		36 745	$^3H_4$	28% ^3H, 25% ^1G, 20% ^5D, 17% ^3G	

Table IV (*continued*)

Experimental line groups		Calculated levels			
Label	Mean energy (cm^{-1})	Energy (cm^{-1})	SLJ label	SL composition	g
		36 802	$^3F_2$	53% ^3F, 17% ^5G, 11% ^1D	
		37 444	$^3H_5$	41% ^3H, 34% ^3G, 14% ^3I	
		37 673	$^3L_7$	73% ^3L, 13% ^{3}K, 10% ^1K	
		38 214	$^3I_7$	85% ^3I, 11% ^3L	
		38 521	$^3P_2$	49% ^3P, 20% ^1D, 12% ^3D, 10% ^5D	
		38 584	$^3M_9$	89% ^3M, 11% ^3L	
		39 215	$^3I_5$	58% ^3I, 25% ^3H, 13% ^1H	
		39 226	$^3F_4$	76% ^3F	
		39 654	$^3I_6$	84% ^3I	
		40 255	$^5D_3$	55% ^5D, 30% ^3G	
		40 424	$^5D_1$	40% ^5D, 32% ^3D, 23% ^3P	
		41 858	$^3F_4$	47% ^3F, 29% ^5D, 17% ^3H	
		42 051	$^5D_2$	76% ^5D	
		42 671	$^5D_0$	91% ^5D	
		43 115	$^3F_3'$	50% ^3F, 22% ^3G, 19% ^5D	
		43 361	$^5D_1$	56% ^5D, 25% ^3D, 17% ^3P	
		45 264	$^3M_8$	54% ^3M, 38% ^1L	
		45 314	$^3H_4'$	69% ^3H, 13% ^1G, 11% ^3G	
		45 680	$^3H_6'$	52% ^3H, 41% ^1I	
		46 212	$^1D_2$	50% ^1D, 21% ^3D, 21% ^3F	
		47 845	$^3H_5'$	59% ^3H, 23% ^3G, 16% ^3I	
		48 121	$^3F_3''$	79% ^3F	
		49 272	$^1H_5$	60% ^1H, 25% ^3H	
		49 454	$^3F_2'$	46% ^3F, 42% ^1D	

cm^{-1} and 26 190 cm^{-1}, in the absorption spectrum of $HoCl_3 \cdot 6H_2O$ at liquid nitrogen temperature. Jørgensen[20] reported one group of bands in this region.

By using estimated values of the parameters, the matrices were diagonalized, and their eigenvectors were used to determine the effect of small parameter variations on the corresponding energy levels by first-order perturbation theory.[21] Next, by reasoning discussed in detail below, a tentative identification of the observed levels was made, and improved parameters derived by the least squares procedure. This cycle was then repeated, starting with the improved parameters. The final parameters are given in Table II, and the resultant energies are compared with experiment in Table IV and Fig. 2.

[21] cf. R. E. Trees, J. Research Natl. Bur. Standards **55,** 335 (1955), Eqs. (3) and (4).

Group C and Lower Groups

These five levels have been recognized for some time as the ^5I multiplet, and obey Russell-Saunders coupling fairly well.[22]

Group D

This level is well isolated and was easily identified as $^5F_5$.

Groups E, F, G, and H

The initial calculations showed five fairly evenly spaced levels in this region in the order of increasing energy $^5S_2$, $^5F_4$, $^3K_5$, $^5F_3$, $^5F_2$. These were related to the observations by considering Kahle's[19] experimentally determined J values, viz., 7 for E, 3 for F, 1 for G, and 8 or 9 for H, and anticipating[1,2] that a departure

[22] B. R. Judd, Proc. Phys. Soc. (London) **A69,** 157 (1956).

from hydrogenic ratios would increase E^1, thereby shifting the predominantly triplet state up relative to the quintets. Thus, H was identified as $^3K_8$, G as $^5F_2$, and F as $^5F_3$, while E appeared to arise from $^5F_4$ and $^5S_2$, which are so close together that their individual line groups in the solid state are not recognizable. In the last case, the calculated energy used in the least squares adjustment was the $(2J+1)$-weighted mean

$$(5/14)(^5S_2)+(9/14)(^5F_4),$$

and double weight was assigned.

Group I

This was likewise identified as a merger of $^5F_1$ and $^5G_4$, the mean $\frac{3}{16}(^5F_1)+\frac{13}{16}(^5G_6)$ being used with double weight.

Group K

This well-isolated level appears to have $J=5$. The heavy mixing shown in its composition is a notable feature.

Groups L and M

The initial calculations showed the $^5G_4$ level to be in this region, and it was expected that $^3K_7$ (then some 1000 cm^{-1} lower) would lie here too with improved parameter values. Since our observations showed group M to be lower in intensity that group L, it was considered that this corresponded to a transition to $^3K_7$, which is spin forbidden in the Russell-Saunders approximation. By elimination, group L then arises from the $^5G_4$ level. Since the final parameter values do place $^3K_7$ above $^5G_4$, this seems quite satisfactory.

Higher Levels

Calculated positions of the higher levels are given in Table IV, but it does not appear profitable to attempt any analysis of the solution spectrum.[20]

ZEEMAN EFFECT

To assist the experimental verification of the holmium spectrum analysis, the value of the Landé splitting factor has been predicted for each level by using its eigenvector to determine the appropriate combination of Russell-Saunders values. These are given in the right-hand column of Table IV.

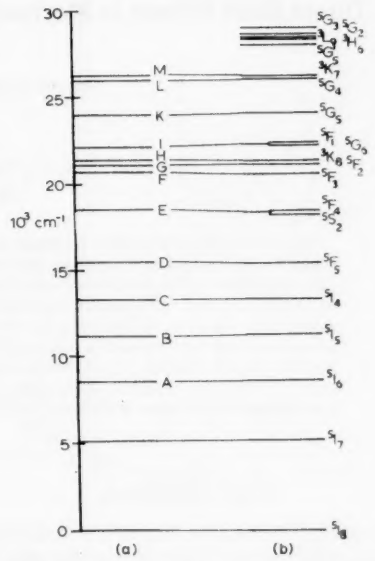

FIG. 2. Holmium: Analysis of the solid-state line groups. (a) Experimental energy levels; (b) calculated energy levels.

In the cases of groups E and I, where the crystal field produces appreciable mixing of free ion states, the selection rule $\Delta J=0, \pm 1$ allowed shows that a magnetic field will not add to this mixing in either case. It is therefore sufficient to quote g values for the individual free ion levels.

ACKNOWLEDGMENTS

We would like to thank Professor A. G. McLellan and Dr. B. R. Judd for indicating the significance of the Tables of $c[WW'(110)]$ and $c[UU'(11)]$.[9] The assistance of the staff of Sydney University in diagonalizing all the matrices on the Silliac computer is acknowledged. One of us (MHC) received assistance during this work from a Research Fund Fellowship awarded by the University of New Zealand.

THE JOURNAL OF CHEMICAL PHYSICS VOLUME 35, NUMBER 4 OCTOBER, 1961

Direct Field Effects in Electron Paramagnetic Resonance Hyperfine Spectra

JOHN A. WEIL*
Argonne National Laboratory, Argonne, Illinois
AND
JOHN H. ANDERSON†
Department of Physics, University of Pittsburgh, Pittsburgh, Pennsylvania

(Received March 9, 1961)

The electron paramagnetic resonance spectrum exhibiting hyperfine effects from one nucleus is discussed for the case when the nuclear spin interacts appreciably not only with the electron magnetic moment but also directly with the applied magnetic field. The predicted hyperfine structure consists, in general, of $2S(2I+1)^2$ lines. The angular dependence of the intensities and splittings is investigated; nodes in the splitting are found to be possible even when the eigenvalues of the hyperfine splitting tensor are nonzero. When the direct-field interaction is large, $2I+1$ principal hyperfine lines occur, flanked by weaker "outrider" lines. Another mechanism for producing outrider lines in high direct fields, the nuclear quadrupole interaction with an electric field gradient, is discussed. Magnetic resonance studies of color centers in germanium-doped quartz demonstrate some of the predicted effects.

I. INTRODUCTION

IN the analysis of electron magnetic resonance experiments, wide use has been made of the spin Hamiltonian

$$\mathcal{H}=\beta\mathbf{B}\cdot\mathbf{g}\cdot\mathbf{S}+\mathbf{S}\cdot\mathbf{A}\cdot\mathbf{I}+\mathbf{b}\cdot\mathbf{I}+\mathbf{I}\cdot\mathbf{Q}'\cdot\mathbf{I}. \quad (1)$$

The first term ($\mathcal{H}_g$) represents the direct effect of the external magnetic field $\mathbf{B}$ on the electron spin $\mathbf{S}$, the second term ($\mathcal{H}_A$) treats the interaction between $\mathbf{S}$ and a nuclear spin $\mathbf{I}$, while the last two terms ($\mathcal{H}_b$ and $\mathcal{H}_Q$) take into account the direct effect of $\mathbf{B}$ on $\mathbf{I}$ and the nuclear quadrupole interaction, respectively.

The elements of $\mathbf{A}$ are proportional to the free-electron g and to the nuclear g value (g_N), as well as to a function of the spatial distribution of the unpaired electron(s) relative to the nucleus. The vector $\mathbf{b}$ is proportional to $\mathbf{B}$, but is not necessarily equal to $-g_N\beta_N\mathbf{B}$ because other terms linear in $\mathbf{I}$ may also be present.[1] Analysis of $\mathcal{H}$ is usually carried out by perturbation techniques, assuming $\mathcal{H}_g\gg\mathcal{H}_A\gg\mathcal{H}_b$ and $\mathcal{H}_Q$. Bleaney[2] has treated this case when the tensors $\mathbf{g}$, $\mathbf{A}$, and $\mathbf{Q}'$ are simultaneously diagonal and are axially symmetric, and has calculated both the angular dependence of the spectral frequencies and the intensity of the absorptions.

In the course of an experimental investigation of anisotropic hyperfine structure in spin-resonance spectra of irradiated, germanium-doped quartz, we have observed zeros of the hyperfine splitting which, during rotation of $\mathbf{B}$ in certain planes, occur at angles separated by less than π. This will be shown to be inconsistent with the predictions of this approximation. Since the hyperfine splittings are quite small, it seemed to us that the direct action $\mathcal{H}_b$ of the external magnetic field might be responsible for the observed zeros. We find that, with removal of the restriction $\mathcal{H}_A\gg\mathcal{H}_b$, such zeros in the hyperfine splitting can indeed occur even if all principal values of $\mathbf{A}$ differ from zero, provided that these principal values do not all have the same sign. Furthermore, the usual selection rules are relaxed so that, in general, $2S(2I+1)^2$ transitions will occur. EPR studies of H atoms in irradiated solids have revealed the presence of such "quasiforbidden" lines.[3]

After completion of this work, we learned of the recent appearance of other papers dealing with the same type of hyperfine effects, in EPR spectra of fluorine atoms located around a central paramagnetic ion.[4,5a,5b] We believe that our presentation of the theory contains enough differences in detail to warrant retention of these portions of our results. Several interesting papers demonstrating such effects in irradiated organic substances have appeared recently,[6–8] and also contain discussions of the theory of these phenomena which to some extent run parallel to the work presented herein. Ludwig and Woodbury[9] also mention the existence of forbidden transitions when $\mathcal{H}_A\approx\mathcal{H}_b$.

* This work was performed under the auspices of the U. S. Atomic Energy Commission.
† This research was supported by the U. S. Air Force through the Air Force Office of Scientific Research of the Air Research and Development Command.

[1] Specifically, cross-product terms between $\beta\mathbf{B}\cdot(\mathbf{L}+2\mathbf{S})$ and $a\mathbf{I}\cdot(\mathbf{L}+\mathbf{S})$ will lead to a term of this nature, as has been observed in investigations reported by J. M. Baker, and B. Bleaney, Proc. Roy. Soc. (London) **245A,** 156 (1958), and by D. Halford C. A. Hutchison, and P. M. Llewellyn, Phys. Rev. **110,** 284 (1958).

[2] B. Bleaney, Phil. Mag. **42,** 441 (1951).

[3] G. T. Trammell, H. Zeldes, and R. Livingston, Phys. Rev. **110,** 630 (1958).

[4] J. M. Baker, W. Hayes, and M. C. M. O'Brien, Proc. Roy. Soc. (London) **254A,** 273 (1960).

[5a] A. M. Clogston, J. P. Gordon, V. Jaccarino, M. Reter, and L. R. Walker, Phys. Rev. **117,** 1222 (1960).

[5b] L. Helmholz and A. V. Guzzo, J. Chem. Phys. **32,** 302 (1960).

[6] N. M. Atherton and D. H. Whiffen, Mol. Phys. **3,** 1 (1960).

[7] I. Miyagawa and W. Gordy, J. Chem. Phys. **32,** 255 (1960).

[8] H. M. McConnell, C. Heller, T. Cole, and R. W. Fessenden, J. Am. Chem. Soc. **82,** 766 (1960).

[9] G. W. Ludwig and H. H. Woodbury, Bull. Am. Phys. Soc. **5,** 158 (1960).

The effects described in this paper will be observable in electron paramagnetic resonance (EPR) experiments at the magnetic fields **B** presently available ($\gtrsim 10^4$ gauss) when the hyperfine constant coupling the electron spin and the nuclear spin is small ($\gtrsim 1$ gauss), provided that the linewidth of the individual components is small enough for resolution to be possible. Anisotropy of **A** (and/or **g**) is also essential. Suitable small and anisotropic splittings are most likely to occur when the unpaired spin density is small at the given nucleus. Such is the situation in various polyatomic color centers in crystalline solids, in complexes containing suitable ligand atoms, and in organic free radicals.

Recent experiments[10] by N. W. Lord, in which double-resonance techniques were applied to the fluorine resonance of color centers in LiF, also require consideration of both $\mathcal{H}_A$ and $\mathcal{H}_b$.

In Sec. II, we discuss the hyperfine structure treating $\mathcal{H}_A$ and $\mathcal{H}_b$ on an equal footing. The quadrupole interaction $\mathcal{H}_Q$ is treated in Sec. III, in the approximation that it is small compared with $\mathcal{H}_A$ and $\mathcal{H}_b$. In Sec. IV, we discuss some experimental results for germanium-doped quartz.

II. JOINT ACTION OF ELECTRON SPIN AND EXTERNAL FIELD OF THE NUCLEUS

A. Effective Field Concept and Its Extension

In considerating a Hamiltonian of the form $\mathcal{H}_V = \mathbf{V}\cdot\mathbf{J}$, where **J** is an angular momentum operator and where **V** is independent of **J**, we shall speak of **V** as the field effective on **J**. If we select a basis of $2J+1$ states which are eigenstates of J^2 and $J_V \equiv \mathbf{V}\cdot\mathbf{J}/|\mathbf{V}|$ and do not depend on $|\mathbf{V}|$, then these are eigenstates simultaneously of $\mathcal{H}_V$. We shall speak of the direction of **V** as the quantization axis for **J**. The first three terms of the Hamiltonian [Eq. (1)] can be treated in this manner.

In the usual approximation $\mathcal{H}_Q \gg \mathcal{H}_A \gg \mathcal{H}_b$, taking $\mathcal{H}_Q = 0$, the representation for $\mathcal{H}$ is one in which both the electron spin and the nuclear spin are quantized along the respective "effective" fields acting on them. The field effective on the electron spin is not, in general, in the direction of **B**, because spin-orbit interaction couples the spin to the local electric field; instead, the direction of this effective field is given by the unit vector $\mathbf{u}_S$ parallel to $\beta\mathbf{B}\cdot\mathbf{g}$; here we neglect the alignment effect *on* the electron of the small nuclear magnetic moment.[11] Similarly, the effective field at the nucleus is not in the direction of **B**: First, because the electronic orbital motions also have magnetic effects on the nucleus, and are able to produce anisotropy of the hyperfine coupling tensor **A**; second, because the anisotropy of **g** causes the average direction of the aligned electron spin to differ from that of **B**. The direction of the field effective on the nucleus is given by

$$\mathbf{k}_M \equiv M\mathbf{K} \equiv M\sum_{ijk}(g_{jk}A_{ij}/g)\eta_k\mathbf{u}_i \qquad (2)$$

if we retain only that part of **S** in $\mathcal{H}_A$ which lies along $\mathbf{u}_S$, i.e., is diagonal (see footnote 11). Here M is the eigenvalue of the projection $\mathbf{u}_S\cdot\mathbf{S}$ of the electron spin operator along its axis of quantization; η_k is the direction cosine between **B** and the unit vector $\mathbf{u}_k$ along the kth axis of an arbitrary Cartesian set. The g value is given by

$$g = \{\sum_{j=1}^{3}(\sum_{k=1}^{3}g_{jk}\eta_k)^2\}^{\frac{1}{2}}. \qquad (3)$$

All square-root terms in our work are taken as nonnegative.

Turning now to the more general situation $\mathcal{H}_A \approx \mathcal{H}_b$, we again retain only that part of $\mathcal{H}_A + \mathcal{H}_b$ diagonal in **S**, which is just $(\mathbf{k}_M + \mathbf{b})\cdot\mathbf{I}$. We now extend the effective field concept by defining the vector $\mathbf{G}_M \equiv \mathbf{k}_M + \mathbf{b}$, which points along the quantization direction for **I**. That is to say, the nuclear quantization axis is determined by competition between the magnetic field supplied by the electron and the field applied externally. Thus, in general, it will differ from the direction of either of these fields (Fig. 1). An important new feature is now present, because the new effective field vectors $\mathbf{G}_M$, unlike the vectors $\mathbf{k}_M$, are not generally colinear for states differing in M and thus may differ

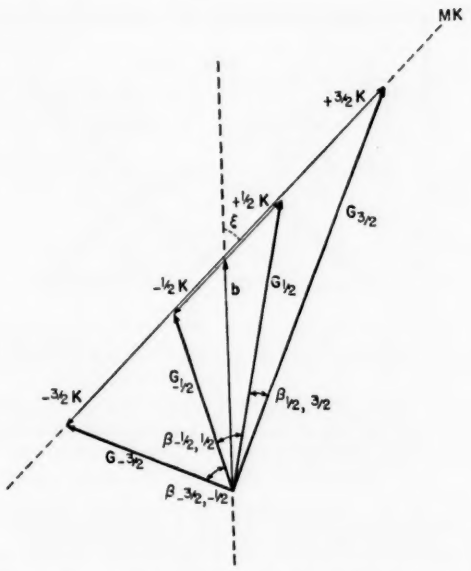

FIG. 1. The coupling of the direct-field contribution **b** and the electronic magnetic contribution $M\mathbf{K}$ to yield the effective field $\mathbf{G}_M$ at the nucleus, for $S = \frac{3}{2}$.

[10] N. W. Lord, Phys. Rev. Letters **1**, 170 (1958).

[11] More precisely, we neglect off-diagonal element of **S** occurring in $\mathcal{H}_A$; these lead to terms in the energies of the order $(|\langle m|\mathbf{A}\cdot\mathbf{I}|m'\rangle|^2/g\beta B)M$.

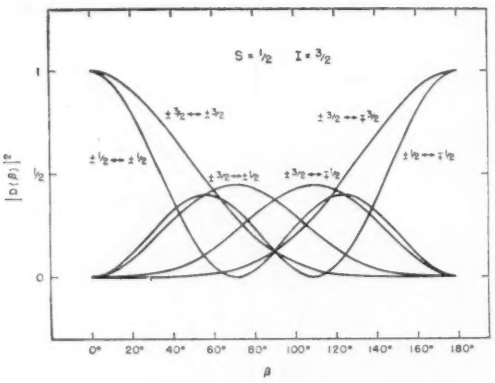

FIG. 2. The probabilities $|D_{mm'}(\beta)|^2$ for the transitions $m\rightarrow m'$, as a function of $\beta_{MM'}$, the angle between the effective fields at the nucleus for the lower and upper states of the electron spin. The situation is shown for $S=\frac{1}{2}$, $I=\frac{3}{2}$.

for the lower and upper states of a transition. Using the new quantization axis for $\mathbf{I}$, we obtain the energy

$$E(M, m)=g\beta BM+G_M m, \tag{4}$$

where the new hyperfine coupling constant G_M is the magnitude of $\mathbf{G}_M$ and is given by

$$G_M=\left\{\sum_i\left[\left(\sum_{jk}\frac{g_{jk}}{g}A_{ij}\eta_k M\right)+b_i\right]^2\right\}^{\frac{1}{2}}, \tag{5}$$

and where m is the eigenvalue of the projection $\mathbf{I}\cdot\mathbf{u}_N$ of the nuclear spin on the direction of the effective field $\mathbf{G}_M=G_M\mathbf{u}_N$. From Eq. (4), we see that the states occur with $2S+1$ equally spaced energy levels, each split further into $2I+1$ hyperfine levels. From Eq. (4) it is apparent that negative spin eigenvalues belong to states with lower energy than those with positive eigenvalues; this is a purely formal result, a consequence of the definition of m, $\mathbf{k}_M$, and $\mathbf{b}$.

The presence of the direct field term can manifest itself even if the hyperfine tensor $\mathbf{A}$ is isotropic. Here the vector

$$\mathbf{k}_M=AM\sum_{ik}(g_{ik}/g)\eta_k\mathbf{u}_i$$

[see Eq. (2)] becomes constant in length, although it retains its ability to vary its orientation relative to $\mathbf{u}_B$ when the latter changes direction. When $\mathcal{H}_A\gg\mathcal{H}_b$, isotropy of $\mathbf{A}$ does imply isotropy of the hyperfine energy $G_M m(\sim k_M m)$, despite anisotropy in $\mathbf{g}$, because the energy depends only on the length of $\mathbf{k}_M$ and of $\mathbf{I}$. However, when $\mathcal{H}_A\approx\mathcal{H}_b$, the energy depends on the length of $\mathbf{G}_M=\mathbf{k}_M+\mathbf{b}$, and $\mathbf{G}_M$ does change both in direction and also in length as the relative orientations of $\mathbf{k}_M$ and $\mathbf{b}$ vary.

B. Relative Intensities of Hyperfine Lines

The probability of each transition $M\rightarrow M'$ is proportional to the square of the electron transition moment $\langle M|\mathbf{S}\cdot\mathbf{B}_1|M'\rangle$, where $\mathbf{B}_1$ is the magnetic excitation field ($\mathbf{B}_1\perp\mathbf{B}$). Of the transitions between the energy levels obtained from Eq. (1) when $\mathcal{H}_g$ is dominant, only those having $M'=M\pm1$ are allowed, and these have relative probability given by the factor $[S(S+1)-M(M\pm1)]$.[2] When $\mathbf{g}$ is anisotropic, the intensities will depend on orientation.

In the EPR experiments involving nuclear effects, as considered in reference 2 and herein, B is assumed large enough so that the Larmor frequency $g\beta B/h$ of the electron is much greater than the nuclear Larmor frequency G_M/h. In this case of comparatively weak hyperfine coupling, the electron spin flips relative to the direction $\beta\mathbf{g}\cdot\mathbf{B}$ (with $\Delta M=\pm1$), whereas the nuclear spin cannot alter its orientation.[12] As a result, the hyperfine coupling energy will change during the transition. Furthermore, when M changes, the nucleus experiences a changed effective field, as shown in Fig. 1, and the *description* of its state using this new quantization axis will differ from that in the old frame, although the state itself is the same.

The angle between the new and the old quantization axes is given by

$$\cos\beta_{MM'}=[(\mathbf{G}_M\cdot\mathbf{G}_{M'})/G_M G_{M'}] \tag{6}$$

and is independent of m. The eigenstate $\chi_{m'}{}^I$ referred to $\mathbf{G}_{M'}$ may be expanded in the states $\psi_m{}^I$ referred to $\mathbf{G}_M$ using the notation of Rose[13]

$$\chi_{m'}{}^I=\sum_{m=-I}^{+I}D_{mm'}{}^I(\alpha\beta\gamma)\psi_m{}^I, \tag{7}$$

where $D_{mm'}{}^I(\alpha\beta\gamma)$ are the elements of the matrix representative of the three-dimensional rotation operator R, and where $\alpha\beta\gamma$ are the Euler angles defining the rotation; for our purposes, we set $\alpha=\gamma=0$ and take $\beta=\beta_{MM'}$. The relative transition probabilities $w_{Mm\rightarrow M'm'}$ between the states $\chi(M, m)$ and $\chi(M', m')$ are

$$w_{Mm\rightarrow M'm'}=|D_{mm'}{}^I(\beta_{MM'})|^2. \tag{8}$$

for given M and M'. Since transitions may now occur between any of the $2I+1$ old states and any of the $2I+1$ new states, a total of $(2I+1)^2$ hyperfine lines may occur for each transition $M\rightarrow M\pm1$. Figure 2 demonstrates the dependence of these transition probabilities on $\beta_{MM'}$ for the case $S=\frac{1}{2}$, $I=\frac{3}{2}$.

Near the limit $\mathcal{H}_A\gg\mathcal{H}_b$, the nuclear quantization axes $\mathbf{G}_M=M\mathbf{K}+\mathbf{b}$ are almost parallel to $M\mathbf{K}$. Hence they are nearly colinear ($\cos\beta_{MM'}=\pm1$) for all pairs of states. The selection rule obtained from the $|D_{mm'}{}^I|^2$ can now be written as $(M/|M|)m-(M'/|M'|)m'=0$, so that there will be $2I+1$ principal lines of equal

[12] Cases in which the coupling is sufficiently strong to turn over the nuclear spin during the transition have been observed. For instance, see C. A. Hutchison and B. Weinstock, J. Chem. Phys. **32**, 56 (1960).

[13] M. E. Rose, *Elementary Theory of Angular Momentum* (John Wiley & Sons, Inc., New York, 1957), p. 52.

intensity (for example, see Fig. 2); this rule is just the usual one of $\Delta m=0$ except when M and $M'=M\pm1$ are opposed in sign ($M=\mp\frac{1}{2}$). When $M=0$, $M\mathbf{K}$ will vanish in our approximation of $\mathcal{H}_g\gg\mathcal{H}_A$, so that the nucleus will be aligned by $\mathbf{b}$. Thus $\mathbf{G}_{M=0}$ will not, in general, be colinear with the other effective fields $\mathbf{G}_{M\neq0}$. Consequently, all $(2I+1)^2$ transitions between $M=0$ and $M=\pm1$ are allowed. Since, in the low-field approximation b is small, the frequencies of the extra lines will be very close to the "ordinary" lines predicted when $\mathcal{H}_b$ is ignored. One would expect the extra lines to manifest themselves in broadening the "ordinary" lines, if at all.

Near the limit $\mathcal{H}_b\gg\mathcal{H}_A$, $\mathbf{G}_M$ becomes fixed along $\mathbf{b}$ so that $\cos\beta_{MM'}=+1$. Here again only $2I+1$ transitions are allowed and occur with equal intensity, the correct selection rule being $\Delta m=0$. Of course, when $\mathcal{H}_A$ actually equals zero, these transitions will coincide and the hyperfine splitting will vanish.

In the intermediate range $\mathcal{H}_A\approx\mathcal{H}_b$, all $2S(2I+1)^2$ transitions are, in general, allowed, but their occurrence depends critically on the anisotropy of $\mathbf{A}$ and $\mathbf{g}$. Isotropy of both will cause $\mathbf{k}_M$ to be colinear with $\mathbf{b}$, again causing disappearance of the extra transitions.

C. The Hyperfine Spectrum

We define the *hyperfine transition energy* as

$$\Delta E_M'\equiv|\,G_Mm-G_{M+1}m'\,|\,. \tag{9}$$

The *hyperfine splitting* δ_M is defined herein as the absolute magnitude of the difference of the $\Delta E_M'$ for adjacent hyperfine lines arising from the same $M\rightleftarrows M+1$ transition. Neither of these quantities is easily discussed in complete generality because all $2I+1$ values of m' are allowed for a given m. However, they are tractable in several important special cases.

1. *The Hyperfine Spectrum When* $\mathcal{H}_A\gg\mathcal{H}_b$.

We can demonstrate easily that our method leads to the same result as Bleaney's,[2] by considering the case when b is small. Here Eq. (4) for the energies and Eq. (8) for the transition probabilities are unnecessarily inconvenient. Expanding the square root in Eq. (5), we obtain for the first order *hyperfine* energy

$$E'(M,m)=m[k_M+b\cos\xi_M+(b^2/2k_M)\sin^2\xi_M-(b^3/2k_M^2)\cos\xi_M\sin^2\xi_M+\cdots], \tag{10}$$

where $k_M=K\,|\,M\,|$ and where ξ_M is the angle between $\mathbf{k}_M$ and $\mathbf{b}$, given by

$$\cos\xi_M=(\mathbf{k}_M\cdot\mathbf{b}/k_Mb)=\sum_{ijk}\frac{M}{|\,M\,|}\frac{b_iA_{ij}g_{jk}\eta_k}{bKg}. \tag{11}$$

In this approximation, as discussed in the preceding section, the principal hyperfine transitions obey the selection rule

$$(M,m)\rightleftarrows\{M+1,[M(M+1)/|\,M(M+1)\,|\,]m\},$$

and we find

$$\Delta E_M'=\left|E'(M,m)-E'\left(M+1,\frac{M(M+1)}{|\,M(M+1)\,|}m\right)\right|$$
$$=m\left[(k_M/M)-\frac{b^2}{2(M+1)k_M}\sin^2\xi_M+\frac{b^3(2M+1)}{2(M+1)^2k_M^2}\cos\xi_M\sin^2\xi_M+\cdots\right], \tag{12}$$

valid for $M(M+1)\neq0$. The hyperfine splitting δ_M between members of the set of $2I+1$ principal lines is just the coefficient of m in Eq. (12). Setting b equal to zero in Eq. (12), we obtain Bleaney's first-order hyperfine correction.[2] Except for the transition $M=-\frac{1}{2}\rightleftarrows M'=+\frac{1}{2}$, the effect of the direct field is to decrease the splitting below the zero direct-field limit K.

The low direct-field approximation is sharply differentiated from the high direct-field approximation in the way zeros of the hyperfine splitting can occur and in the positions of quasi-forbidden lines which are allowed according to Eq. (8). The occurrence of zeros of the hyperfine splitting will be discussed in Sec. IIC3. We make a few remarks here on the quasi-forbidden lines. These lines increase in intensity as the anisotropy increases. The spectrum is, in general, complex. We shall not discuss it in detail. In the important case of the transitions $M=\frac{1}{2}\rightarrow M=-\frac{1}{2}$, inspection of Eq. (12) shows that the principal transitions $(-\frac{1}{2},\ I)\rightarrow(+\frac{1}{2},\ -I)$ and $(-\frac{1}{2},\ -I)\rightarrow(+\frac{1}{2},\ I)$ correspond to the maximum and minimum possible hyperfine transition energies $\Delta E_M'$, respectively. Quasi-forbidden transitions correspond, therefore, to values of $\Delta E_M'$ intermediate between the two extremes. Hence, near the limit $\mathcal{H}_A\gg\mathcal{H}_b$, all quasi-forbidden lines occur wholly within the set of $2I+1$ principal lines. They will tend either to superimpose on or to lie half-way between these strong lines. With other M values, the weak lines can occur either within or outside the strong multiplet; as $|\,M\,|$ increases, more and more of these lines will lie outside the strong multiplet. When M is integral, the quasi-forbidden lines will tend to lie equally-spaced with the allowed lines while, when M is half-integral, they will also be found to lie half-way between the strong lines.

Transitions to or from the state $M=0$ are not included in the discussion above. The expansion (10) is not valid for $M=0$. The direct field effect appears for these lines in first order. Furthermore, as shown in Sec. IIB, quasi-forbidden lines can become quite strong for such transitions if the anisotropy is large.

2. *The Hyperfine Spectrum When* $\mathcal{H}_b\gg\mathcal{H}_A$

It was shown in Sec. IIB that transitions for which $\Delta m=0$ are the strongly allowed ones near the limit $\mathcal{H}_b\gg\mathcal{H}_A$. If we expand Eq. (5) in this approximation,

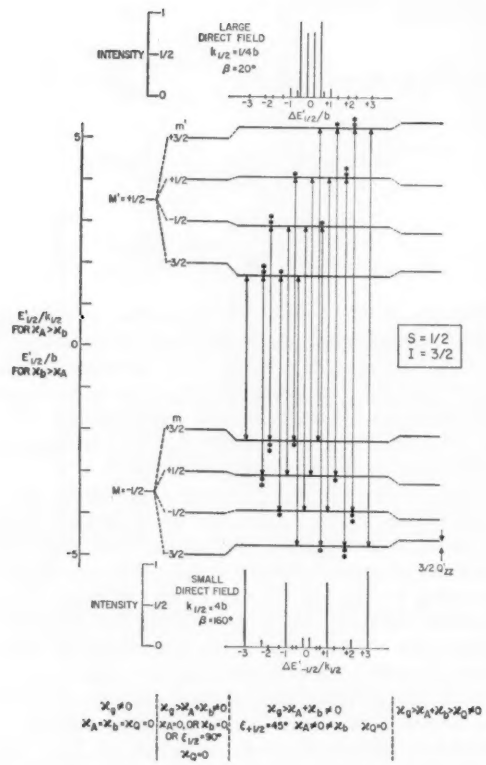

FIG. 3. The energy levels and EPR spectrum of the case $S=\frac{1}{2}$, $I=\frac{3}{2}$. The energy is symmetric in the variables k_M and b [$E=g\beta BM+G_Mm$, using $G_M=\{k_M^2+2k_Mb\cos\xi_M+b^2\}^{\frac{1}{2}}$], and hence a single level scheme can describe both. We portray the cases $k_M/b=4$ and $\frac{1}{4}$, with $\cos\xi_M=45°$. The former (low direct-field case) has lines as shown below the level scheme, where the relative intensities were obtained from Fig. 2. Similarly, the spectrum for the latter (high direct-field case) is presented above the energy levels. The quadrupole energy is added on the right. The quadrupole allowed transitions are starred for $\Delta m=\pm 1$ and double starred for $\Delta m=\pm 2$. In our quantization scheme, the former are more intense in the high direct-field case, while it is the latter which are more intense in the low direct-field case (see text, and compare with Bleaney[8]).

we obtain the hyperfine energy

$$E'(M,m)=m[b+k_M\cos\xi_M+(k_M^2/2b)\sin^2\xi_M-(k_M^3/2b^2)\cos\xi_M\sin^2\xi_M+\cdots] \quad (13)$$

and the hyperfine transition energy for the principal lines

$$\Delta E_M'=|E'(M,m)-E'(M+1,m)|=m\left[(k_M/M)\cos\xi_M+(k_M^2/2b)\frac{(2M+1)}{M^2}\sin^2\xi_M-(k_M^3/2b^2)\frac{(3M^2+3M+1)}{M^3}\cos\xi_M\sin^2\xi_M+\cdots\right], \quad (14)$$

both valid for all $M(\neq 0)$. Again the coefficient of m in Eq. (14) is the hyperfine splitting δ_M. This splitting is equal to or smaller than the zero-field splitting $k_M/M=K$ and tends toward independence of b as b increases. When only the first term of Eq. (14) is important, we see that δ_M vanishes not only when $k_M=0$ but also when $\cos\xi_M=0$. This is a special case of the more general conditions for vanishing of hyperfine splitting, to be discussed in Sec. IIC3.

As in the low direct-field approximation, the quasi-forbidden lines will be strongest when the anisotropy is large. These lines are expected, unlike the low direct-field case, to occur entirely *outside* the principal $2I+1$ lines for sufficiently large b/K. The justification for this statement is that the hyperfine transition energy $\Delta E'$ of a principal line is approximately mK; for a quasi-forbidden line $\Delta E'$ is approximately b [see Eq. (13)].

Figure 3 contains an energy level diagram and representation of the predicted spectra for $S=\frac{1}{2}$, $I=\frac{3}{2}$ in two special cases—one when $k_M=4b$ and the other when $k_M=\frac{1}{4}b$, while the angle ξ_M between $\mathbf{k}_{M=\frac{1}{2}}$ and $\mathbf{b}$ was arbitrarily picked to be 45°.

3. *Vanishing of Hyperfine Transition Energies and Splittings*

We wish to pay particular attention to the occurrence of orientations of the system at which zero hyperfine splitting occurs.

When $\mathbf{g}$ is isotropic, the hyperfine coupling constant K equals

$$\{\sum_{ijk}A_{ij}A_{ik}\eta_j\eta_k\}^{\frac{1}{2}};$$

in the principal axis system of $\mathbf{A}^2(=\tilde{\mathbf{A}}\cdot\mathbf{A})$, this becomes

$$K=\{\sum_i(\mathbf{A}^2)_{ii'}\eta_{i'}{}^2\}^{\frac{1}{2}}.$$

Since the $(\mathbf{A}^2)_{ii'}$ are non-negative and because $\sum_i\eta_i{}^2=1$, K can vanish only in the special case when one of these principal values (and thus the corresponding $A_{ii'}$) is zero while $\mathbf{u}_B$ points along the corresponding principal axis. (If two of the principal values vanish, K is zero everywhere in the plane spanned by the corresponding principal axes.) Thus any zeros in K occurring during the rotation of $\mathbf{u}_B$ in some arbitrary plane must occur only at orientations differing by π (or else everywhere in the plane). Exactly analogous considerations hold for the generalized hyperfine coupling energy G_M, taking the tensor in question to be $\mathbf{G}_M\cdot\mathbf{G}_M$, where $\mathbf{G}_M\equiv M(\mathbf{A}\cdot\mathbf{g}/g)+\mathbf{b}$ (with $\mathbf{b}=-g_N'\beta_NB\mathbf{T}$, where $\mathbf{T}$ is the unit tensor).

In the low direct-field case $\mathcal{H}_A\gg\mathcal{H}_b$, we have $\Delta E_M'\cong Km$ [Eq. (12)] and the hyperfine splitting is $\delta_M=K$. From the above, we see that zeros in $\Delta E_M'$ and δ_M are restricted to very special circumstances. However, in the general case, the transition energies $\Delta E_M'$ and splittings δ_M may vanish more often.

However, we see from Eq. (9) that $\Delta E_M'$ cannot vanish at all when m and m' have opposite signs (except

in the trivial case when both G_M and G_{M+1} vanish, which demands $K=b=0$). When m and m' have the same sign, the most important case is $m=m'\neq 0$. Here vanishing of $\Delta E_M'$ demands $G_M=G_{M+1}$, which in turn implies the condition

$$(2M+1)K^2+2\mathbf{K}\cdot\mathbf{b}=0. \tag{15}$$

Here also δ_M is simply equal to G_M-G_{M+1}. We see from Eq. (15) that $\Delta E_M'$ can be zero without the necessity that K be zero. For example, when the first term vanishes while $K\neq 0$ (i.e., $M=-\frac{1}{2}$), zeros occur when $\mathbf{K}\cdot\mathbf{b}=Kb\cos\xi_M=0$. Since $\mathbf{b}$ is proportional to $\mathbf{B}$, we can replace b_i by $b\eta_i$ in Eq. (11), and write the condition for zeros as

$$\sum_{ijk}A_{ij}g_{jk}\eta_i\eta_k=\sum_{ik}Z_{ik}\eta_i\eta_k=0 \tag{16}$$

where $\mathbf{Z}=\frac{1}{2}[\mathbf{A}\cdot\mathbf{g}+\mathbf{g}\cdot\mathbf{A}]$. This symmetrized (real) tensor can be diagonalized, so that the expression in Eq. (16) becomes $\sum_i Z_{ii}'\eta_i'^2$ in the principal axis system. Vanishing here does not require that any of the principal values be zero, but only that these occur with both signs. It also follows that orientations at which Eq. (16) is satisfied need not be separated by π.

Near the high direct-field limit $\mathcal{H}_b\gg\mathcal{H}_A$, the condition $\mathbf{K}\cdot\mathbf{b}=0$ for vanishing of $\Delta E_M'$ is general for any M (as discussed in Sec. IIC2). We shall describe in Sec. IV the observation of zero hyperfine splitting occurring at angles separated by less than π for a system with $S=\frac{1}{2}$ near this limit.

III. EFFECT OF THE NUCLEAR QUADRUPOLE MOMENT

We have shown that the direct-field effect in combination with large anisotropy can produce more than the usual $2I+1$ hyperfine lines. Another mechanism which can cause extra hyperfine lines is the interaction between the electric field gradient at the nucleus and the nuclear quadrupole moment, which may be present when $I\geq 1$. This mechanism is operative even if the hyperfine interaction is isotropic. For the low direct-field approximation $\mathcal{H}_A\gg\mathcal{H}_b$, $\mathcal{H}_Q$, Bleaney[2] has derived expressions for the positions and intensities of the quadrupole-allowed transitions when axial symmetry is present; the selection rules expressed in our quantization system (Sec. IIC1) are for $M\rightarrow M+1$ that $m'=[M(M+1)/|M(M+1)|](m\pm 1)$ and $m'=[M(M+1)/|M(M+1)|](m\pm 2)$. One aspect which will be of special interest here is that all the quadrupole lines for $M=-\frac{1}{2}\rightleftarrows M'=+\frac{1}{2}$ fall within the multiplet of the principal $2I+1$ lines for $\mathcal{H}_A\gg\mathcal{H}_b$.

When $\mathcal{H}_b$ and $\mathcal{H}_Q$ are no longer small compared with $\mathcal{H}_A$, the three agencies competing to align the nuclear spin cause the spectrum to be very complicated, i.e., realignment of the electron field $\mathbf{k}_M$ when the electron flips causes both the direct field $\mathbf{b}$ and the quadrupole field to act differently on the initial and final states. We shall not discuss this complex situation here, but shall limit ourselves to some remarks on the high direct-field approximation.

When $\mathcal{H}_b\gg\mathcal{H}_A$ and $\mathcal{H}_Q$, the selection rule in the absence of quadrupole effects is $\Delta m=0$. In general, introduction of $\mathcal{H}_Q$ causes mixing of nuclear states, so that now transitions in which m changes by ± 1 and ± 2 are also allowed, just as in the low direct-field case when $\mathcal{H}_Q\neq 0$. The first-order quadrupole correction to the energy (Eq. 4) is given by $\langle m|\mathcal{H}_Q|m\rangle$. The relative intensities of transitions between M and $M\pm 1$ near the high direct-field limit are, to first approximation, given by

$$w_{m\rightarrow m\pm n}=(K\cos\xi_M/nb^2)\,|\langle m|\mathcal{H}_Q|m\pm n\rangle|^2, \tag{17}$$

where $n=1$ or 2. In deriving Eq. (17), we have neglected all but the first two terms of the series expansion [Eq. (13)] for the energy, and we have assumed that $\mathbf{G}_M$ and $\mathbf{G}_{M\pm 1}$ have the same direction. The matrix elements are

$$\langle m|\mathcal{H}_Q|m\rangle=[3m^2-I(I+1)]\tfrac{1}{2}Q_{zz}' \tag{18a}$$

$$\langle m|\mathcal{H}_Q|m\pm 1\rangle=(2m\pm 1)[(I\pm m+1)(I\mp m)]^{\frac{1}{2}}\times\tfrac{1}{2}(Q_{xz}'\pm iQ_{yz}') \tag{18b}$$

$$\langle m|\mathcal{H}_Q|m\pm 2\rangle=[(I\pm m+1)(I\mp m)(I\mp m-1)(I\pm m+2)]^{\frac{1}{2}}\times\tfrac{1}{2}[\tfrac{1}{2}(Q_{xx}'-Q_{yy}')\pm iQ_{xy}'], \tag{18c}$$

where the Q_{ij}' are the elements of the tensor $\mathbf{Q}'$ in the coordinate system in which $\mathcal{H}_A+\mathcal{H}_b=\mathbf{G}_M\cdot\mathbf{I}$ is diagonal. Of the three eigenvalues of $\mathbf{Q}'$, the one having the largest magnitude is equal to $e^2qQ/[2I(2I-1)]$ in the usual nomenclature.[14] The transition probabilities in this case differ from those of the low direct-field case[2] only in that $(K\cos\xi_M/nb^2)^2$ occurs instead of the factor

$$[1/nKM(M\pm 1)]^2.$$

The quadrupole-allowed transitions $\Delta m=\pm 1$, ± 2 are indicated in Fig. 3 for the special case $S=\frac{1}{2}$, $I=\frac{3}{2}$. For $\mathcal{H}_b\gg\mathcal{H}_A$ and $\mathcal{H}_Q$, the $\Delta m=0$ lines occur as a central quartet. The quadrupole lines occur as outriders of this quartet, a feature different from that occurring in the approximation $\mathcal{H}_A\gg\mathcal{H}_b$, $\mathcal{H}_Q$, but similar to the case previously discussed for the direct-field allowed lines. However, the quadrupole outriders can exist even when $\mathbf{g}$ and $\mathbf{A}$ are isotropic, in contrast to the latter. The direct-field outrider lines ($\mathcal{H}_Q=0$) have maximum intensities relative to the central set of about $(A_{\|}-A_{\perp})^2/4b^2$. The quadrupole $\Delta m=\pm 1$ lines, on the other hand, are expected from Eq. (18b) to have maximum intensities of the order of $(Q_{zz}'K/b^2)^2$. Experimental observation of such lines is reported in the following section.

[14] M. H. Cohen and F. Reif, *Solid State Physics* (Academic Press, Inc., New York, 1957), Vol. 5.

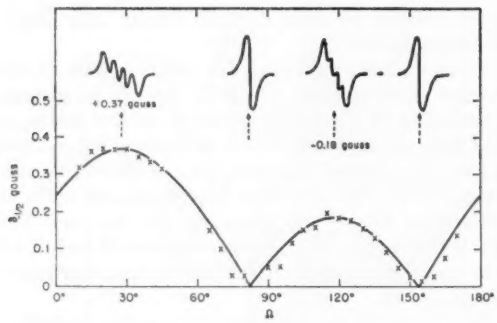

FIG. 4. The observed hyperfine splitting of one of the quartz C centers when a rotation ($\perp\mathbf{B}$) of the crystal is performed about a twofold symmetry axis. Spectra at special positions of the rotation angle Ω are also included. The angle $\Omega=0$ occurs when $\mathbf{B}$ is parallel to the crystal's threefold (c) axis.

IV. EXPERIMENTAL

While carrying out the analysis of the hyperfine lines in the 3-cm magnetic resonance spectra of the x-ray color centers in germanium-doped quartz,[15,16] we were confronted with the situation in which both the electron magnetic moment and the externally applied magnetic field polarize the nuclear spin. The EPR spectra at room temperature arise from two different color centers, A and C, each giving rise to three absorptions from symmetry-related sites. Furthermore, each of these six absorptions exhibits hyperfine structure which has been shown to arise from alkali ions.[15,16] With Na^{23} and Li^7, which have $I=\frac{3}{2}$, we in general observe four lines. The model suggested for the color center involved is that of an unpaired electron centered on an SiO_4 site, where germanium has replaced the silicon. The alkali ion is thought to reside nearby in one of the available open channels, and serves to furnish over-all charge neutrality. The unpaired spin density on the alkali ions is very small, leading to hyperfine splittings of less than 1 gauss. The nature of the difference between A and C is not yet quantitatively understood (but see reference 15).

In general, analysis of the spectra is rather complicated because of the strong superposition of the various lines (small g anisotropy). However, when the quartz single crystal is rotated about one of its three twofold symmetry axes with $\mathbf{B}$ perpendicular to this direction, the g values of two of the C centers are the same, whereas g for the third differs from this value. Since the resonance of the latter travels by itself during the rotation, with comparatively little overlap from A lines, it is possible to follow its behavior. Typical first derivative spectra and the hyperfine splittings $\delta_{-\frac{1}{2}}$ obtained for this rotation are shown in Fig. 4. For the unresolved or partially resolved spectra occurring at some of the angular positions, the splitting was estimated by subtracting the width of the individual component as obtained from the resolved spectra. This width was taken as 0.16 gauss between points of maximum slope. The data were obtained with a quartz crystal containing lithium as the dominant alkali ion.

Inspection of Fig. 4 reveals that $\delta_{-\frac{1}{2}}$ goes to zero twice within one quadrant, shown in Sec. IIC3 to be inconsistent with the theory treating only $\mathcal{H}_g+\mathcal{H}_A$. However, inclusion of $\mathcal{H}_b$ leads to an acceptable fit between these results and the theory. The magnitude of the direct field term $-g_N\beta_N\beta$ (e.g., 1.95 gauss for Li^7) is considerably larger than the observed hyperfine splitting. The splitting $\delta_{-\frac{1}{2}}$ for the main $2I+1$ transitions given by the selection rule $\Delta m=0$ is simply $G_{-\frac{1}{2}}-G_{+\frac{1}{2}}$. For the case $S=\frac{1}{2}$, if one ignores the small anisotropy in $\mathbf{g}$, this becomes

$$\delta_{-\frac{1}{2}}=\{(\tfrac{1}{2}A_{\max}+b)^2\cos^2(\Omega-28°)+(\tfrac{1}{2}A_{\min}+b)^2\sin^2(\Omega-28°)\}^{\frac{1}{2}}-\{(-\tfrac{1}{2}A_{\max}+b)^2\cos^2(\Omega-28°)+(-\tfrac{1}{2}A_{\min}+b)^2\sin^2(\Omega-28°)\}^{\frac{1}{2}}, \quad (19)$$

$$\approx|A_{\min}+(A_{\max}-A_{\min})\cos^2(\Omega-28°)| \quad (20)$$

where Ω is the angle measuring the rotation about the axis specified above ($\Omega=0°$ when $\mathbf{B}$ is parallel to the c axis of the crystal). The extrema in $\delta_{-\frac{1}{2}}$ are $|A_{\max}|$ and $|A_{\min}|$, respectively. The data can be well fitted by choosing $A_{\max}=+0.37$ gauss and $A_{\min}=-0.18$ gauss, as is evident from Fig. 4. The zeros in $\delta_{-\frac{1}{2}}$ occur at $\Omega_0=28°+\arctan(-A_{\max}/A_{\min})^{\frac{1}{2}}=83°$ and 153°. We note that the relative signs of $A_{\max}$ and $A_{\min}$ are obtained from the analysis. Since we deal with the situation close to the limit $\mathcal{H}_b\gg\mathcal{H}_A$, the splitting $\delta_{-\frac{1}{2}}$ becomes very insensitive to the choice of parameter b (taken here as 1.95 gauss).

We believe that the parameters $A_{\max}$ and $A_{\min}$ are close to being two of the principal values of $\mathbf{A}$. In support of this, although it has not yet been possible to arrive at the hyperfine tensor with accuracy, we find that choice of a third eigenvalue of $\sim+0.6$ gauss gives quite good agreement with the splitting of the C center at other orientations. We make a tentative identification with the principal $\mathbf{g}$ system: $A_1=-0.18\leftrightarrow g_1$, $A_2=+0.65\leftrightarrow g_2$, $A_3=+0.37\leftrightarrow g_3$ (see Table I of reference 15). However, it is not proved that $\mathbf{A}$ and $\mathbf{g}$ for this center really do possess coincident principal axes.

At some orientations, we have been able to detect very weak lines at the sides of the absorptions. These are most easily observable on the outside of the four-line hyperfine spectrum of the A center at some orientations (see Fig. 3 of reference 15). Since the A hyperfine structure is virtually isotropic ($\delta_{-\frac{1}{2}}\rightleftharpoons0.6$ gauss) in its g_1-g_3 plane (i.e. $\mathbf{B}\parallel$ twofold axis), the outrider lines observed here are not allowed by the theory using only $\mathcal{H}_A$ and $\mathcal{H}_b$. Because Na^{23} and Li^7 both have fairly large quadrupole moments, it seems likely that these are quadrupole-allowed transitions as discussed in

[15] J. H. Anderson and J. A. Weil, J. Chem. Phys. **31**, 427 (1959).
[16] J. A. Weil, A. H. Morris, and J. H. Anderson, Bull. Am. Phys. Soc. **4**, 416 (1959).

Sec. III. Detailed analysis of these and the other small peaks occurring, as well as of the broadening of some of the C lines at certain orientations, must await more elaborate experiments, which we hope to carry out.

ACKNOWLEDGMENT

We would like to thank Professor F. Keffer and Dr. G. Goodman for several helpful discussions on the contents of this paper. We thank the referee for calling our attention to references 3–5.

THE JOURNAL OF CHEMICAL PHYSICS VOLUME 35, NUMBER 4 OCTOBER, 1961

Calculations of the Coefficient of Viscosity and the Coefficients of Diffusion for Dissociating Hydrogen*

DAVID G. CLIFTON

University of California, Los Alamos Scientific Laboratory, Los Alamos, New Mexico

(Received April 6, 1961)

The kinetic theory of dilute monatomic gases and mixtures has been used to calculate some transport properties of dissociated hydrogen. The H_2—H_2 and H—H_2 interactions have been assumed to obey the modified Buckingham (exp-6) potential and the Lennard-Jones (12–6) potential, respectively, and the two H—H interaction potentials ($^1\Sigma_g$ and $^3\Sigma_u$) have been treated by the method of Hirschfelder and Eliason to obtain a weighted average rigid-sphere collision diameter. The coefficient of viscosity, the coefficient of diffusion in a binary mixture of the H—H_2 system, and the coefficients of self-diffusion for H atoms and H_2 molecules have been computed for temperatures from 1500° to 5000°K and pressures of 0.1, 0.5, 1, 2, 10, 50 and 100 atm.

THE equilibrium composition of dissociated hydrogen is a function of temperature and pressure. For the calculation of the viscosity of the equilibrated gas mixture, which consists of atoms and molecules, the gas can be treated as a binary mixture and the viscosity is therefore a function of pressure and temperature.

The coefficient of viscosity computations presented here are for dissociated hydrogen over the temperature range from 1500°K to 5000°K at the pressures of 0.1, 0.5, 1, 2, 10, 50, and 100 atm. The coefficient of diffusion in a binary mixture of the H–H_2 system, and the coefficients of self-diffusion for H and H_2 for the same temperature and pressure conditions have also been calculated.

The coefficient of viscosity of the binary mixture, η_{mix}, has been calculated using the equations given by Hirschfelder, Curtiss, and Bird[1] (hereafter referred to as MTGL). The notations are also to be found in MTGL. The coefficients of viscosity corresponding to the intereactions H_2–H_2, H–H, and H–H_2 (η_2, η_1, η_{12}, respectively) and the mole fractions of the species H and H_2 (x_1 and x_2, respectively) are used in this formulation of η_{mix}. The mole fractions of the species for any set of temperatures and pressures were calculated by solving the hydrogen dissociation equilibrium equation using the thermodynamic data from the National Bureau of Standards Series III Circular.[2]

The intermolecular potential of the H_2–H_2 interaction was assumed to obey the modified Buckingham (exp-6) potential[3] and the parameters utilized were those evaluated by Mason and Rice.[4] See reference 4 for the notations.

$$\alpha=14.0, \qquad r_m=3.337\ A, \qquad \epsilon/k=37.3°\text{K}.$$

The coefficient of viscosity of undissociated hydrogen was then calculated from the following expression which is given in reference 4 where the notations are explained.

$$[\eta_2]_3\times10^7 = 266.93(MT)^{\frac{1}{2}}f_\eta^{(3)}(\alpha, T^*)/r_m^2\Omega^{(2,2)*}(\alpha, T^*)\ \text{g/cm-sec}.$$

The method of Hirschfelder and Eliason[5] has been applied to the two potential energy curves ($^3\Sigma_u$ and $^1\Sigma_g$) for the H-H interactions, and the weighted average of the effective rigid-sphere collision diameters so obtained was then used to calculate a coefficient of viscosity corresponding to the H-H interaction. These potential energy curves have been established over a wide range of separations of the atoms by a combination

* Work done under the auspices of the U. S. Atomic Energy Commission.

[1] J. O. Hirschfelder, C. F. Curtiss, and R. B. Bird, *Molecular Theory of Gases and Liquids* (John Wiley and Sons, Inc., New York, 1954).

[2] F. D. Rossini *et al.*, *Selected Values of Chemical Thermodynamic Properties, Series III* (National Bureau of Standards Circular 500, Washington, 1952).

[3] E. A. Mason, J. Chem. Phys. **22**, 169 (1954).

[4] E. A. Mason and W. E. Rice, J. Chem. Phys. **22**, 522 (1954).

[5] J. O. Hirschfelder and M. A. Eliason, Ann. N. Y. Acad. Sci. **67**, 451 (1947).

TABLE I. Coefficient of viscosity for the interactions occurring in dissociated hydrogen (g/cm-sec).

T (°K)	$[\eta_2]_3\times10^7$ H_2—H_2	$[\eta_1]_1\times10^7$ H—H	$[\eta_{12}]_1\times10^7$ H—H_2
1000	2013	1458	1855
1500	2643	1963	2409
2000	3207	2417	2902
2500	3722	2858	3351
3000	4204	3276	3769
3200	4387	3443	3934
3500	4655	3685	4150
3700	4829	3847	4291
4000	5096	4109	4503
4200	5270	4264	4642
4500	5523	4498	4850
5000	5926	4942	5192
Method	Modified Buckingham (exp–6) potential	Hirschfelder and Eliason	Lennard-Jones (12–6) potential

of theoretical treatments and experimental spectroscopic data for normal $H_2(^1\Sigma_g)$. The data for these curves are in references 6–9. Hirschfelder and Eliason[5] demonstrate how one utilizes interaction potential curves of the inverse-power form to obtain effective rigid-sphere collision diameters which may then be employed to compute a coefficient of viscosity corresponding to this collision diameter. Their procedure has been followed here with one exception. Two interaction curves exist and has the *a priori* probability of interaction of the two curves are $\frac{3}{4}$ and $\frac{1}{4}$ for the $^3\Sigma_u$, and $^1\Sigma_g$, respectively; a weighted averaging of the effective rigid-sphere collision diameters squared was made.[10,11] The appropriate weighted average rigid-sphere collision diameter squared for the temperature under consideration and the following expression were then used to obtain the coefficient of viscosity corresponding to the H–H interaction.

$$[\eta_1]_1\times10^7=266.93(MT)^{\frac{1}{2}}/\sigma^2_{\text{rigid sphere}}\ \text{g/cm-sec}.$$

The coefficient of viscosity of a gas with particle interactions corresponding to the H–H_2 interactions was calculated using an "average" Lennard-Jones (12-6) potential function. Two limiting cases arise for the interaction of a hydrogen atom and a hydrogen molecule. The atom may approach the molecule perpendicular to the line of the nuclei ($\perp$) or the approach may be parallel to this line ($\parallel$). A quantum-mechanical calculation of the energy as a function of distance of separation for these two cases has been made by Margenau.[12] These values are also listed in MTGL. A plot of these calculated potential energy values was made for the two directions of approach and the necessary parameters to fit each of these curves to a Lennard-Jones (12-6) potential were taken from the plot. The results are

$$\epsilon/k(\perp)=37.9°\text{K}, \qquad \sigma_\perp=2.63\ \text{A},$$
$$\epsilon/k(\parallel)=23.5°\text{K}, \qquad \sigma_\parallel=3.00\ \text{A}.$$

To obtain a single "average" potential function for the H–H_2 interaction, and from a general consideration

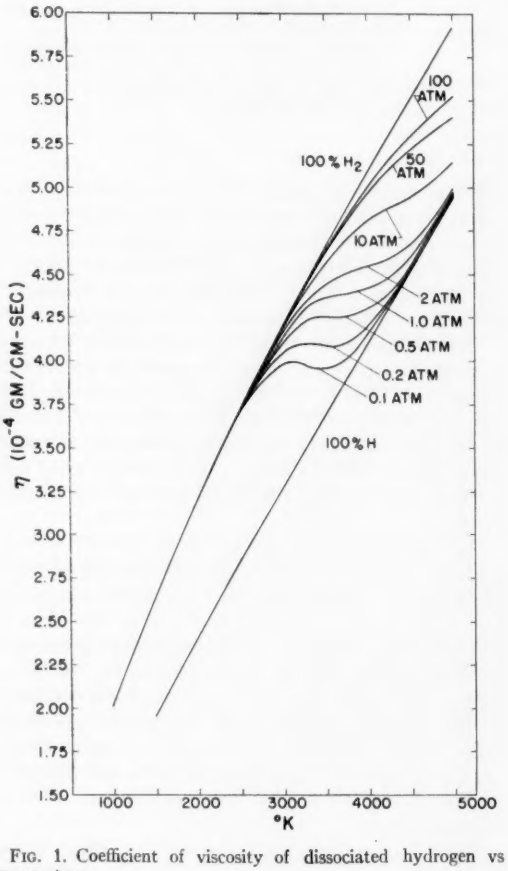

FIG. 1. Coefficient of viscosity of dissociated hydrogen vs temperature.

[6] R. Rydberg, Z. Physik **73,** 376 (1932); See also M. Beutler, Z. Physik Chem. **B27,** 287 (1934).

[7] A. Dalgarno and N. Lynn, Proc. Phys. Soc. (London) **A69,** 821 (1956).

[8] H. M. James, A. S. Coolidge, and R. D. Present, J. Chem. Phys. **4,** 187 and 193 (1936).

[9] J. O. Hirschfelder and J. W. Linnett, J. Chem. Phys. **18,** 130 (1950).

[10] D. D. Konowalow, J. O. Hirschfelder, and B. Linder, J. Chem. Phys. **31,** 1575 (1959); see also University of Wisconsin Theoretical Chemistry Laboratory Rept. WIS–AEC–22 (July 1959).

[11] E. E. Mason, J. T. Vanderslice, and J. M. Yos, Phys. Fluids **2,** 688 (1959); see also University of Maryland Institute of Molecular Physics Rept. IMP–NASA–9 (May, 1959).

[12] H. Margenau, Phys. Rev. **66,** 303 (1944).

TABLE II. Coefficient of viscosity of dissociating hydrogen.

	$\eta_{mix}\times10^7$ g/cm-sec							
T (°K)	0.1 atm	0.2 atm	0.5 atm	1 atm	2 atm	10 atm	50 atm	100 atm
1500	2643	2643	2643	2643	2643	2643	2643	2643
2000	3205	3206	3206	3206	3206	3207	3207	3207
2500	3695	3703	3711	3714	3717	3720	3721	3722
3000	3983	4049	4108	4137	4157	4182	4195	4196
3200	3995	4103	4208	4263	4301	4350	4371	4376
3500	3962	4089	4258	4365	4448	4564	4615	4627
3700	3997	4094	4259	4388	4502	4679	4763	4782
4000	4164	4210	4314	4426	4554	4815	4966	5004
4200	4293	4320	4387	4471	4585	4876	5079	5133
4500	4510	4521	4553	4600	4675	4949	5218	5300
5000	4945	4948	4957	4971	4997	5144	5412	5527

of the geometry of the system, the two sets of parameters above were averaged by weighting the perpendicular ($\perp$) approach two times and the parallel ($\parallel$) approach one time. Using these weights, an arithmetic average for the σ's and a geometric average for the ϵ/k's was made[1] and these results were obtained for the "average" Lennard-Jones (12-6) potential

$$\sigma_{12_{av}}=2.75 \text{ A}, \qquad (\epsilon_{12}/k)_{av}=32.27°\text{K}.$$

The coefficient of viscosity for the H–H_2 interaction was then obtained from the following expression which is given and explained in reference 1:

$$[\eta_{12}]_1\times10^7 = 266.93[2M_1M_2T/(M_1+M_2)]^{\frac{1}{2}}/\sigma_{12_{av}}{}^2\Omega_{12}{}^{(2,2)*}(T_{12}{}^*) \times \text{g/cm-sec}.$$

The computations for the coefficients of viscosity for these three systems are given in Table I.

The coefficient of viscosity of the mixture η_{mix} was calculated from $\eta_{mix}=(1+Z_\eta)/(X_\eta+Y_\eta)$ g/cm-sec, which is derived and explained in reference 1.

These values of η_{mix}, are given in Table II and Fig. 1. The appropriate values of $[\eta_1]_1$, $[\eta_2]_3$, and $[\eta_{12}]_1$ were taken from Table I, and the corresponding values of x_1 and x_2, which were obtained as described earlier, were used in the above expression as shown in reference 1.

In MTGL, the coefficient of diffusion in a binary mixture and the coefficients of self-diffusion are shown to be functions of the collision integrals and collision cross sections. Therefore, if one utilizes certain interaction potentials and parameters for viscosity calculations the diffusion coefficients consistent with this choice of potentials can be readily obtained.

The coefficient of diffusion in a binary mixture was calculated from equation 8.2-44 of MTGL where the parameters of the "average" Lennard-Jones (12-6) potential as explained above were used.

The coefficient of self-diffusion for the H_2–H_2 system was computed using the formula given by Mason and Rice[4] for a system that obeys the modified Buckingham (exp-6) potential and the potential parameters cited above.

The coefficient of self-diffusion for the H–H system was computed from the formula of MTGL for a system obeying the rigid-sphere type of potential. The effective rigid-sphere collision diameter for the H–H system was obtained by the method of Hirschfelder and Eliason[5] as applied to the two potential energy curves ($^3\Sigma_u$ and $^1\Sigma_g$) for the H–H interactions. In this method, the effective rigid-sphere collision diameter obtained for diffusion processes is different than the one obtained

TABLE III. Coefficients of diffusion.

T (°K)	$p[D_{12}]_1$ (atm cm²/sec)	$p[D_{11}]_1$ (atm cm²/sec)	$p[D_{22}]_1$ (atm cm²/sec)
1000	15.28	15.66	11.24
1500	29.88	31.70	22.34
2000	48.13	52.67	36.35
2500	69.64	78.60	53.01
3000	94.37	111.5	72.12
3200	105.5	125.3	80.43
3500	122.0	147.5	93.55
3700	133.4	164.1	102.7
4000	151.2	189.9	117.4
4200	163.6	208.6	127.6
4500	183.2	237.9	143.4
5000	217.9	291.9	171.4

for the viscosity calculations. For an explanation of this see reference 4. The two possible interaction curves were again taken into consideration in this self-diffusion calculation and were weighted and averaged as explained earlier. The results of the computations of the coefficients of diffusion are given in Table III.

Since the interaction potential functions which have been used here are generally defined by parameters fitted to low and moderate temperature data, some error can result from the use of these same potential forms at the higher temperatures. It has been shown[13,14] by scattering experiments that at very high temperatures, where the repulsive portion of the potential curves is important, the interaction potential curve is best represented by either a point center of repulsion model, $\phi(r)=d/r^s$ or the exponential repulsive potential $\phi=Ae^{-r/\rho}$, and the "extrapolation" of the exp-6 or the Lennard-Jones (12-6) potential to the high-temperature region results in considerable differences.[15,16]

Estimates of the errors introduced by this "extrapolation" are given. The H–H interaction curves are well known and an estimated error is about 10% in η_1 and 5% in D_{11} at 5000°K. In the case of the H_2–H_2 interaction (exp-6) the η_2 is low on the order of 12% and the D_{22} is low by about 18 to 20%.[15,16,17] The more serious errors occur in the H–H_2 interaction "extrapolation" since it is a 12-6 potential, and the errors here may be about 25% in the η_{12} and 40 to 60% in the D_{12}.[17]

The effect of these individual errors in the results for η_{mix} will vary due to the variation in composition. Since the H–H_2 interaction enters in as a mixing term only, the error in the final mixture is less than the rather large error due to this 12-6 extrapolation. The estimated uncertainty in the final η_{mix} values is of the order of 10 to 20% at 5000°K, and decreases at the lower temperatures.

ACKNOWLEDGMENT

The author wishes to gratefully acknowledge J. O. Hirschfelder for his suggestions and discussions about the treatment of the H–H and H–H_2 interactions and the use of weighted averages of these interactions. Gratitude is also extended to J. D. Rogers for bringing this problem to the author's attention and for many helpful comments and suggestions about the work and manuscript.

[13] R. E. Walker and A. A. Westenberg, J. Chem. Phys. **29,** 1147 (1958).
[14] I. Amdur and E. A. Mason, Phys. Fluids **1,** 370 (1958).
[15] I. Amdur and J. Ross, Combustion and Flame **2,** 412 (1958).
[16] R. E. Walker and A. A. Westenberg, J. Chem. Phys. **31,** 519 (1959).
[17] J. T. Vanderslice and E. A. Mason, J. Chem. Phys. **33,** 492 (1960).

THE JOURNAL OF CHEMICAL PHYSICS VOLUME 35, NUMBER 4 OCTOBER, 1961

Low-Temperature Chemisorption. III. Studies in the Field Emission Microscope

GERT EHRLICH AND F. G. HUDDA

General Electric Research Laboratory, Schenectady, New York

(Received March 2, 1961)

The dependence of adsorption upon surface structure has been examined with the field emission microscope. Nitrogen adatoms are found on all the planes of tungsten accessible to observation. Their rate of diffusion is fastest over the regions around the 111 pole; the barrier to migration over this area is only 20 kcal mole^{-1}, compared to 35 kcal mole^{-1} for diffusion over the sharply stepped region surrounding the 100 pole.

A strong structural effect is observed for the weakly bound α state of nitrogen, unstable at $T>400$°K. This state is concentrated on and around the (111). By contrast, nitrogen molecules held at 79°K in the γ state are distributed without pronounced specificity for surface structure. However, the absence of diffusion in both these states suggests that the nitrogen is held at isolated, discrete sites. The γ state on tungsten somewhat resembles nitrogen adsorbed on nickel; for this system chemisorption is lacking at room temperature, but at 79°K molecules are bound with an energy of at least 5.5 kcal mole^{-1}. At an even lower temperature, $T\sim20$°K, an additional binding state, consisting of nitrogen physically adsorbed on top of the chemisorbed layer, is observed on tungsten. Diffusion out of this state occurs at $T\sim40$°K with the formation of a sharp border, indicating immediate chemisorption of material spilling over the chemisorbed layer.

For the adsorption of carbon monoxide on tungsten no structural specificity appears in the field emission microscope. In addition to the primary chemisorbed state, the presence of weakly bound carbon monoxide is confirmed and it is shown that for neither state does dissociation occur. Both carbon monoxide and nitrogen lower the rate of electron emission from an initially clean tungsten surface. CO raises the work function by 0.5 ev at $T\sim300$°K. In the γ state nitrogen also causes an initial work function increase of 0.1 ev. Nitrogen adatoms, however, are found to lower the work function, in contrast with the results obtained for other dissociating gases, as well as with previous work function measurements on nitrogen itself.

ALTHOUGH an understanding of heterogeneous reactions starting from first principles still appears remote, progress can be made on a more empirical level, by unraveling the kinetics and energetics of the elementary reaction steps.[1] It is with this aim that we have examined several model systems.

Detailed information on the kinetic processes involved in the interaction of nitrogen and carbon monoxide with a tungsten surface, as obtained by flash desorption, has already been presented.[2] These studies revealed considerable complexity in the nature of the interactions as well as a significant dependence upon the structure of the surface. Our deductions about the type of binding involved and its variation with crystal structure have, however, been indirect and essentially macroscopic.

In order to supplement these rate studies and to apprehend structural effects on a more atomic scale, these interactions have been examined with the field emission microscope.[3] Three types of experiments will be reported.

(1) Measurements of the field dependence of electron emission. These yield the electron work function and therefore the change in the surface dipole layer due to the presence of the adsorbed gas. Since the extent to which the surface dipole is affected varies with the nature of the interaction, work function changes can be used to distinguish the presence of different states of binding.

(2) Observation of the relative emission intensity for different crystal faces during ad- and desorption. Both the number of adsorbed species as well as the change in emission per adsorbed entity may vary from site to site. Since these two effects cannot be measured separately, changes in intensity distribution over the emitter usually yield only qualitative information on the distribution of the surface phase.

(3) Observations on diffusion of adsorbed gas from a localized deposit. These outline the potential field acting on the adsorbed entity and can define structural effects without the interpretational difficulties of (2).

The behavior of both nitrogen and carbon monoxide on a tungsten field emitter will be examined; to establish the properties of a weakly chemisorbed molecular gas, we also touch briefly on the adsorption of nitrogen on nickel. However, our measurements are most extensive for the system nitrogen on tungsten. For this, a comparison of previous rate studies with the field emission observations, clearly defining the effects of surface structure on the properties of the adsorbed phase, will be carried out in a separate report.

I. EXPERIMENTAL TECHNIQUES

The equipment and procedures for routine observations with the field emission microscope are similar to those employed in studies on the adsorption of rare gases.[4] The techniques of forming tungsten emitters are standard. For nickel, observations have been made on 3-mil wire mounted on a 10-mil nickel support wire, without potential leads, and etched at 0.5–1.5-v ac in

[1] G. Ehrlich, J. Chem. Phys. **31,** 1111 (1959).
[2] G. Ehrlich, J. Chem. Phys. **34,** 29, 39 (1961).
[3] For general background material, see R. H. Good and E. W. Müller, *Handbuch der Physik*, edited by S. Flügge (Springer-Verlag, Berlin, Germany, 1956).
[4] G. Ehrlich and F. G. Hudda, J. Chem. Phys. **30, 493** (1959).

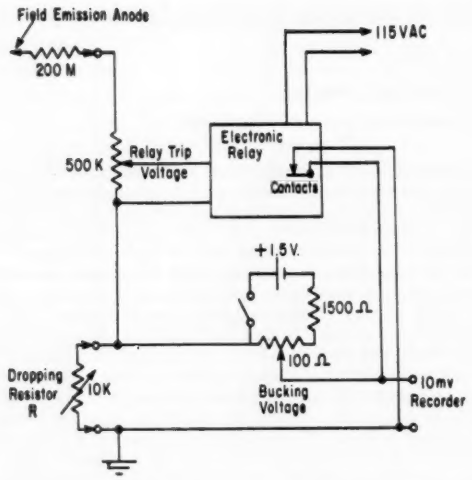

FIG. 1. Recording circuit for determination of field emission voltage. Electronic relay shorts recorder input when bucking voltage exceeds voltage across R.

concentrated HCl saturated with $KClO_4$.[5] In the present study, the exposure time for photographs of the emission patterns (taken uniformly at an emission of 2×10^{-7} amp) has been diminished by resorting to 3000 speed Polaroid film, type 47.

Improvements in experimental techniques have been made in the following areas:

A. Determination of Work Functions

Measurements of the current-voltage relation in field emission have in the past been so lengthy that work functions, derived from Fowler-Nordheim plots, have generally not been determined *during* the adsorption step itself.

In this study, work functions are rapidly determined by automatic recording of both the emission current and the applied voltage. The electron current (in the interval $5\times10^{-8}-2\times10^{-7}$ amp) is measured by a Keithley dc indicating amplifier, the output of which is displayed on a Speedomax G recorder. We employ another Speedomax to indicate the potential across a small portion (R in Fig. 1) of the current limiting resistor separating the anode from ground.

For points with a radius $r\sim1800$ A, field emission currents only become appreciable at anode potentials $V>2800$ v, and the voltage range covered in the Fowler-Nordheim plot therefore amounts to but a small fraction ($\sim7\%$) of this minimum potential. To measure changes in anode voltage more accurately, a part of the potential drop across the resistor R is therefore balanced out, using the circuit sketched in Fig. 1, so that a full-scale displacement on the recorder corresponds to $\Delta V\sim1000$ v. With these modifications, all data for a Fowler-Nordheim plot can be taken within 30 sec, with an average deviation of less than 0.5% in the slope. Significant work function measurements during the course of adsorption are therefore feasible.

B. Observation of Surface Migration

Shadowing the emitter with gas presents the primary problem in studying surface migration of the so-called permanent gases. This demands a directed gas source in the system, as well as provisions to trap excess gas that is not deposited on the field emission point.

These requirements have been met by the microscope shown in Fig. 2, in which localized deposits of any gas desired for study can be readily formed on one side of the field emission tip.[6] In this tube, patterned after one of Müller's low-temperature field ion microscopes,[7] the stem 1 bearing the field emitter assembly (point, supporting filaments, and potential leads for temperature determination) is developed into a Dewar vessel and is itself shielded by two separate, concentric Dewars (2 and 3) which are pierced on a level with the emitter tip. Through this opening a beam of gas can be shot at the emitter from a 5-mm tube (B) leading to the separately pumped gas handling system. The duration and intensity of this beam are regulated by a Granville-Phillips valve, type C(V).

In operation the second Dewar is cooled with liquid hydrogen and gas molecules not condensed on the field emission assembly are trapped on colliding with the glass walls. Provided the coolant in the emitter stem (1) has been properly chosen to bring the tip tem-

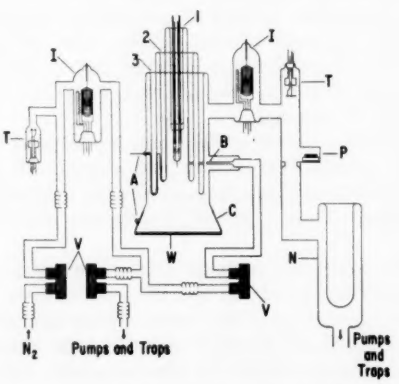

FIG. 2. Field emission microscope for surface diffusion studies: A, anode terminals; B, beam tube; C, tin oxide conductive coating; I, inverted ionization gauge; N, liquid nitrogen cooled trap; P, magnetically operated ground glass port; T, thermocouple gauge; V, Granville-Phillips valve; W, Willemite screen; 1, field emission stem, developed into Dewar; 2, trapping Dewar, filled with liquid hydrogen; 3, shielding Dewar, filled with liquid nitrogen.

[5] M. Benjamin and R. O. Jenkins, Proc. Roy. Soc. (London) **A176**, 262 (1940).

[6] For a different solution of this problem, see R. Gomer, J. Chem. Phys. **28**, 168 (1958).

[7] E. W. Müller, Ann. Physik [6. Folge] **20**, 315 (1957).

perature below that at which surface migration can occur, only one side of the emitter is coated with gas and the spreading of this deposit over the point can then be examined on raising the temperature.

This design incorporates several desirable features: (1) The microscope is continuously pumped, so that a variety of experiments can be carried out in it. (2) Only minimal amounts of liquid hydrogen (or helium) are required (70 cc for the central Dewar, and 150 cc for Dewar No. 2). (3) Surface diffusion of any gas which can be trapped on a liquid helium cooled surface can be studied merely by changing the gas bottle.

C. Gas Purity

In this and previous studies we have used assayed reagent-grade gas samples, in Pyrex containers provided by the Air Reduction Company. For nitrogen, the impurity content is listed as less than the mass spectrometric limit of 5 parts in 10^5, and this has been verified on our own mass spectrometer. During the initial stages of adsorption the impurities in the gas are therefore entirely unimportant.

However, at room temperature nitrogen covers only $\sim\frac{1}{2}$ of all the atom sites on the surface, and thereafter the sticking coefficient for nitrogen drops below 10^{-4}.[2] At such high surface concentrations, impurities present in the gas even at very low concentrations (such as 1 in 10^5) may successfully compete with nitrogen for sites,[8,9] thereby dictating the properties of the surface layer. For meaningful measurements at high nitrogen concentrations, the gas supply must therefore be cleaned further.

In our system this has been accomplished by evaporating a nickel film inside a bulb located between the gas bottle and the valve; this is done before opening the reservoir, but after the pressure has been reduced to $\sim 5\times10^{-10}$ mm. Once the breakoff seal is opened, the nitrogen is stored over this film. Nickel does not chemisorb nitrogen at room temperature, but it does bind CO, CO_2, H_2, O_2, and some hydrocarbons; residual impurities present in the gas should therefore be eliminated by selective adsorption on the nickel film. This point will be discussed in Sec. IIA2.

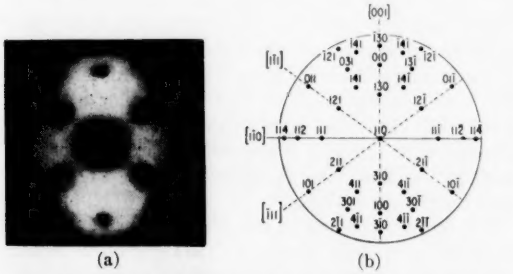

FIG. 3. (a) Field emission from clean W tip No. 68, 110 oriented. $r\sim2000$ A. (b) Orthographic projection of the cubic lattice, with orientation corresponding to the emission pattern in (a).

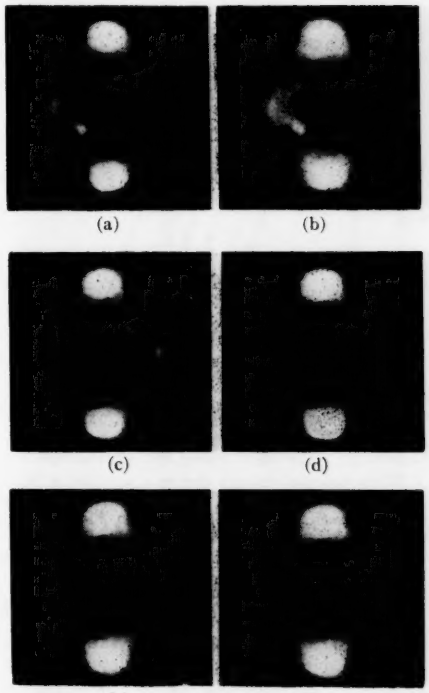

FIG. 4. Adsorption of nitrogen on W at $T=300°$K. Point No. 68. Applied voltage (V) for $i=5\times10^{-8}$ amp; V_0=voltage for clean emitter=2870 v; n=surface concentration in molecules cm^{-2}. (a) Adsorption interval $\Delta t=6$ min, $V=2940$ v, $n<60\times10^{12}$; (b) $\Delta t=10$, $V=2930$, $n<100\times10^{12}$; (c) $\Delta t=16$, $V=2960$; (d) $\Delta t=31$, $V=3010$; (e) $\Delta t=71$, $V=3060$; (f) $\Delta t=106$, $V=3090$; pressure $\sim8\times10^{-8}$ mm. Bright dot next to $12\bar{1}$ is a reflection arising in the photography.

II. NITROGEN ON TUNGSTEN

A. Room Temperature Observations

1. *Experimental Results*

Several interesting features have emerged from previous studies of the interaction of nitrogen with tungsten: (1) The rate of adsorption depends upon the structure of the surface on an atomic scale. (2) Compared with the number of tungsten atoms at the surface, only a limited quantity of nitrogen atoms can be taken up. (3) Two different states of binding, an atomically bound β state, as well as a considerably weaker α state are populated simultaneously at room temperature. The aim of our field emission observations has been to specify the extent to which different crystallographic features are involved in these effects.

The emission patterns in Figs. 3 and 4 illustrate the

[8] E. Greenhalgh, N. Slack, and B. M. W. Trapnell, Trans. Faraday Soc. **52,** 865 (1956).
[9] S. Wagener, J. Phys. Chem. **61,** 267 (1957).

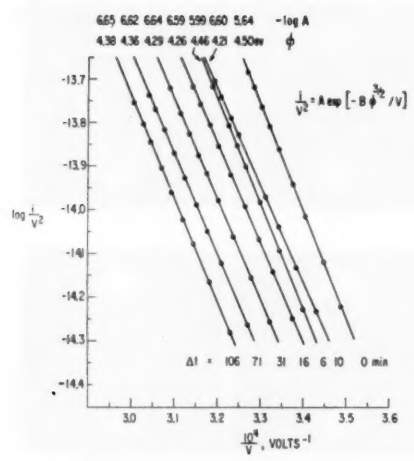

FIG. 5. Work function changes during adsorption of N_2 on W at $T=300°K$. Fowler-Nordheim (FN) plots taken at adsorption intervals (Δt) identical with photographs in Fig. 4. Emission current i in amperes, applied potential V in volts.

changes in the surface dipole layer when nitrogen adsorbs on an initially clean tungsten surface at $T=300°K$. A clean tungsten tip, in the 110 orientation standard throughout this report, is shown in Fig. 3, together with an orthographic projection of the cubic lattice identifying the various crystal planes. In Fig. 4 such a tungsten emitter was exposed to a low-pressure stream of nitrogen and the emission patterns were photographed as the gas layer built up. Upon adsorption of the first few molecules ($\sim 60\times10^{12}$ molecules cm^{-2}) the pattern changes significantly [Fig. 4(a)] as the regions around the 100 poles become more prominently emitting. At the same time the (111)'s, together with the immediate surroundings of the 211 planes become more sharply defined as the other regions around the 111 poles recede into darkness [Figs. 4(b), (c)]. With continuing adsorption of nitrogen [Figs. 4(d), (e)] the details in the 111 areas disappear and are superseded by a more uniform emission, still considerably less intense than that from the 100 regions. For these we have high emission extending from the 010 pole down to the 013 and 141 planes. This type of pattern is maintained even after further exposures to nitrogen pressures as high as 4×10^{-7} mm for more than 2 hr.

These changes in intensity distribution are accompanied by even more startling effects on the emission properties. As appears from the Fowler-Nordheim plots in Fig. 5 adsorption lowers the emission, and after the first few ($\sim$10) minutes the field current at constant applied voltage actually drops monotonically with increasing nitrogen coverage. On the other hand, the work function deduced from these plots initially diminishes from 4.50 to 4.21 ev and then rises slowly, reaching $\sim$4.4 ev at saturation.

These observations suggest that adsorption of nitrogen occurs on all of the crystal planes accessible to observation. This proviso excludes the 211 and 110 planes. For the clean point the work function of these planes is so high (4.70 and 5.99 ev, respectively)[10] that they are nonemitting and remain this way throughout the adsorption. Whatever the processes taking place on the (211) and (110), the emission from these densely packed planes is not increased to the level of their surroundings; this could conceivably arise from a complete absence of adsorption on them. We do know that adsorption takes place on the 100 pole and the regions around it up to the 111 zone line. These are the areas of strongest emission and therefore dictate the work function deduced from the Fowler-Nordheim plots. The lowest value of the average work function, $\phi=4.21$ ev, is below that of the work function of the most intensely emitting planes for clean tungsten (4.30 ev for the 116 plane). Adsorption of nitrogen therefore actually lowers the work function of the 100 region and we are not just dealing with the suppression of emission from higher work function planes. Following this line of thought, nitrogen must also have settled on and around the 111 poles, since even when the over-all work function has risen to 4.40 ev, the work function value of the clean (111), the emission from this region is less than that around the 100.

Most interesting are the changes in emission just *around* the (211) [Figs. 4(b)–(d)]. As already mentioned, our observations would be consistent with the possibility that nitrogen does not adsorb on the 211 and 110 planes. Both of these planes are fairly densely packed. In the (110) each tungsten atom has six nearest neighbors, as compared with eight in the interior. The 211 plane is made up of strings of tungsten atoms with either five or seven nearest neighbors, and one may conjecture that because of the high valence of nitrogen, adsorption on densely packed planes with only two or three free bonds is not feasible. However, it follows from Fig. 4(b) that adsorption does occur along the 111 zones. There the zone lines are comparable in intensity with the (100) and its surrounding areas, just as for the clean point on which the zone lines emit with just a little less intensity than the areas around (100). We have already decided that adsorption occurred around the (100) and we must therefore conclude that adsorption of nitrogen is responsible for the enhancement of the zone lines themselves, at the expense of their immediate environs.

The regions adjacent to the (211) can be envisioned as made up of short pieces of (110) planes, in which each tungsten atom has six nearest neighbors, with an occasional step in which each atom has only five immediate neighbors.[11] Since adsorption occurs on such planes, there appears to be no severe valence require-

[10] E. W. Müller, J. Appl. Phys. **26**, 732 (1955).

[11] Pictures of an atomic model showing this structure can, for example, be found in reference 4.

TABLE I. Work function changes for nitrogen on tungsten.

Investigator	Reference	$\Delta\Phi$ ev	T °K	p mm	Sample	Method
Bosworth and Rideal	12	1.38	90		Wire	Contact potential
Mignolet	18	0.50	293	$10^{-7}-2.5\times10^{-3}$	Film	Contact potential
		−0.44	77	10^{-6}	Film	Contact potential
		0.51	77	1.5×10^{-3}		
Suhrmann	29	0.22	293	8×10^{-5}	Film	Photoelectric
		−0.06	90	10^{-6}		
Eisinger	19	0.52	~300	5.6×10^{-9}	Ribbon	Photoelectric
		0.98		5.7×10^{-7}		
Ehrlich *et al.*	14	0.50	305	2×10^{-8}	Point cathode	Field emission
		−0.20	80	3.5×10^{-9}		
Becker	22	0.30	300	5×10^{-8}	Point cathode	Field emission
Jones and Pethica	17	0.54	300	10^{-6}	Ribbon	Contact potential

ment that excludes the occupation by nitrogen of densely packed planes having only three free bonds. We cannot examine adsorption on the (110) and (211) planes, however, and this is necessary to establish unequivocally the nature of the limitation on the number of adsorbed nitrogen atoms.

Both the strongly bound β state as well as the much weaker α may contribute to the pattern changes observed in Fig. 4. To resolve the contribution from these two we will resort to observations at higher temperatures, which will be presented later. Also, from room temperature measurements it is not at all clear what process determines the intensity distribution during adsorption, that is, whether the patterns are indicative of an equilibrium distribution of gas over the surface or of the kinetics of the adsorption process. This too remains to be established by higher temperature studies.

2. *Comparison with Previous Studies*

A number of investigators have reported on changes in the surface dipole during adsorption of nitrogen on tungsten. Their results are summarized in Table I. The earliest of these studies, by Bosworth and Rideal,[12] can probably be rejected because of the poorly developed vacuum techniques of that period. All of these investigations are in agreement, however, in indicating an increase in the work function after room temperature adsorption of nitrogen. More than that, measurements taken under recognizably good vacuum conditions all show an increase of the order of 0.5 ev at saturation.

The present study, on the contrary, suggests a diminution of 0.1 ev in the work function. An analogous discrepancy appears in the field-emission patterns. Pattern changes during adsorption of nitrogen have been reported by Brock,[13] but these do not have the characteristic features emphasized in Fig. 4. They lack the detailed intensity changes around the (111) and at saturation, emission occurs from a considerably greater fraction of the point, especially around the 110 pole.

The differences between this work and the results obtained in the past seem to stem from the presence of contaminants, presumably in the gas supply. Two factors conspire to make nitrogen particularly difficult in this respect. (1) As pointed out in Sec. IC, even when nitrogen adsorption stops at room temperature, other gases such as carbon monoxide, hydrogen, or oxygen may still adsorb on the surface. Only if these can be rigorously eliminated from the system will the results at saturation refer to nitrogen. Preliminary measurements were made in this Laboratory without passing the nitrogen over an evaporated nickel film. Emission patterns observed during the initial stages of the adsorption were similar to those in the present study. At saturation, however, the intensity distribution was quite different. Indeed, the saturation patterns, such as shown in Fig. 6, somewhat resembled those found for carbon monoxide (see Sec. IV).

In early studies[14] we also observed an initial diminution of the work function, followed, however, by an increase of 0.5 ev above the work function of the clean tungsten emitter. The emission properties at low concentrations *can* therefore be examined without gettering the nitrogen supply,[15] but difficulties will arise even in a thoroughly baked out system at high surface concentrations of nitrogen. (2) The work function of tungsten is changed only little by adsorption of nitrogen, compared with the changes brought about by oxygen, carbon monoxide, or hydrogen.[16] Even small residual quantities of these gases, present in a system because of improper preparation, will alter the work function behavior during the initial stages of nitrogen

[12] R. C. L. Bosworth and E. K. Rideal, Physica **4**, 925 (1937).
[13] E. G. Brock, Advances in Catalysis **11**, 452 (1957).
[14] G. Ehrlich, T. W. Hickmott, and F. G. Hudda, J. Chem. Phys. **28**, 506 (1958).
[15] We have been able to duplicate in a gettered system all the qualitative features of previous flash desorption measurements, although the original determinations were made without purification of the gas over nickel.
[16] A. Eberhagen, Fortschr. Physik **8**, 245 (1960).

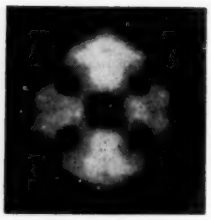

FIG. 6. Tungsten at $T=300°K$ saturated with nitrogen without special purification. Point No. 23. $i=5\times10^{-9}$ amp, $V_0=3200$ v. $\Delta t=$ 197 min, $V=4160$ v, $p\sim3\times10^{-8}$ mm.

adsorption, since they make a contribution to the overall work function out of proportion to their concentration.

This is also the only study in which the work function has been derived from Fowler-Nordheim plots and conceivably this high-field technique could itself be responsible for some of the differences observed. The work function derived from the slope of a Fowler-Nordheim plot is an intensity average, which favors those parts of the surface for which electron emission is high.[4] Contact potential measurements, on the contrary, give a true area average and this is also approached by measurements of the rate of electron emission at low fields.[16] Discrepancies between the values of the high- and low-field work function must therefore be expected if, on adsorption, the work function does not change uniformly for the entire surface.

It appears, however, that differences in the techniques of work function measurement or in the sample are *not* responsible for the discrepancies between the work function values reported here and those already in the literature. The saturation field emission pattern obtained with ordinary reagent nitrogen (Fig. 6) shows some differences from the clean tungsten point, but the intensity is uniform except for the close packed planes. Because of this uniformity we expect agreement between measurements on contaminated hemispherical single-crystal emitters and evaporated films and ribbons despite their structural differences, provided that the high-field technique is not in error. That the high field required for our observations does *not* cause significant perturbations is suggested by the excellent agreement between the preliminary field emission results (at saturation), taken without special precaution for cleaning the nitrogen, and the contact potential measurements of Jones and Pethica,[17] and of Mignolet,[18] as well as with the low-pressure photoelectric results of Eisinger.[19]

More than that, the differences in work function cannot be caused by differences in the sample. The present values refer primarily to the areas around the 100 poles which are, throughout the nitrogen adsorption, the most strongly emitting. These are precisely the planes exposed in tungsten ribbons for which rolling brings out grains with surfaces having normals between [100] and [211], yet on tungsten ribbons the work function increase has been reported as 0.5 ev.

3. *Adsorption and the Fowler-Nordheim Equation*

It is not just the disagreement with previous reports that makes the emission changes observed for the adsorption of nitrogen on tungsten unusual. As indicated in Fig. 5, the work function diminishes during the course of adsorption yet the total emission drops at higher coverages. The Fowler-Nordheim equation relates the emission density j to the work function ϕ and the applied field F through

$$j=(1.54\times10^{-6}F^2/\phi t^2)\exp(-6.83\times10^7(\phi v/F)\quad \text{amp cm}^{-2},\quad (1)$$

where both t and v are functions of $\chi=3.79\times10^{-4}(F^{\frac{1}{2}}/\phi)$, tabulated by Good and Müller.[3] From Eq. (1) we expect an increase in the emission on lowering the work function. This is illustrated in Fig. 7 in which the emission currents calculated from the FN relation are compared with the experimentally determined values at one stage of the adsorption process. The discrepancy with the experimental quantity amounts to a factor of 10, both for intermediate coverages (when the work function has dropped to 4.21 ev) and close to saturation (at $\phi=4.4$ ev, for example). The actual emitting area for the nitrogen covered point has, of course, diminished and this reduces the disagreement, but after correction for this effect the emission currents are still a factor of 5 below the FN values. This same behavior is seen even more dramatically when the adsorption is carried out at 79°K; under these conditions

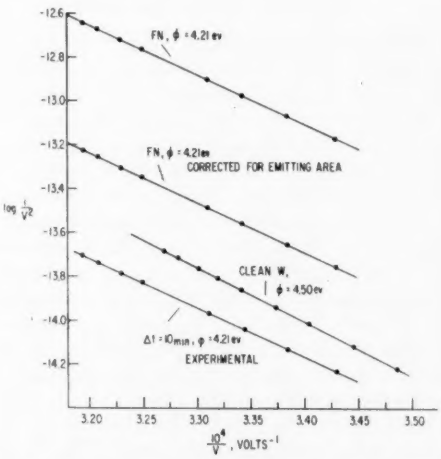

FIG. 7. Current voltage characteristics during N_2 adsorption. Comparison of experimental values with those calculated from Fowler-Nordheim (FN) relation, Eq. (1). FN currents obtained for work functions listed by fitting emission from clean surface to Eq. (1) using emitting area of 6×10^{-10} cm².

[17] P. L. Jones and B. A. Pethica, Proc. Roy. Soc. (London) **A256,** 454 (1960).
[18] J. C. P. Mignolet, Rec. trav. chim. **74,** 685 (1955).
[19] J. Eisinger, J. Chem. Phys. **28,** 165 (1958).

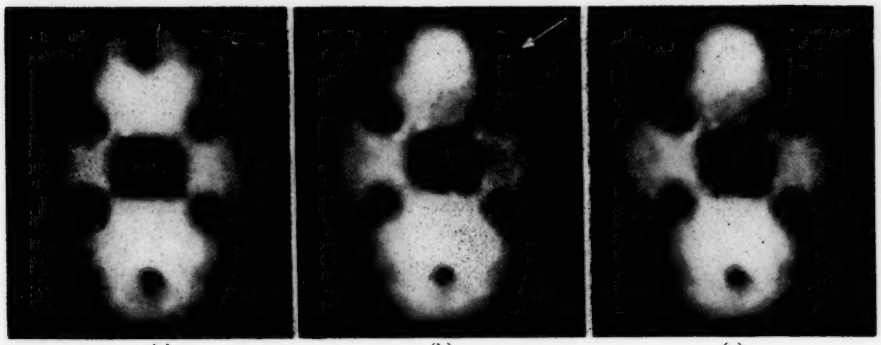

(a) (b) (c)

FIG. 8. Formation of localized nitrogen deposit on W at $T=290°K$, Point No. 34. $r\sim1300A$. (a) Clean W surface. (b) W surface after nitrogen deposition; arrow indicates direction of the N_2 beam. (c) Boundary formation at 111 zone lines after heating to $T\sim400°K$

the emitting area changes but little (as will be outlined in Sec. IID) yet the experimental emission currents are 2 orders of magnitude below the calculated one.

This failure of the Fowler-Nordheim equation is not surprising; the FN relation is based on a simple one-dimensional image force potential and does not account for the presence of discrete atoms on the surface which alter the shape of the barrier through which electrons tunnel. A very early attempt to remedy this defect was made by Stern, Gossling, and Fowler.[20] However, their estimates still depend on the assumption of a one-dimensional potential (ignoring image forces) which has been widened uniformly by the presence of the adsorbed layer, and are therefore somewhat arbitrary.

Although the cause of the failure of the Fowler-Nordheim equation will not be considered here, the disagreement we have found may raise some question about the validity of work function changes derived from field emission experiments. Even though the absolute emission intensity does not conform to the Fowler-Nordheim equation, serious errors are unlikely if the work function changes are derived from the field dependence of the emission current and not from the absolute current value. Provided the applied field is not too high, so that the thickness of the barrier still exceeds a few atomic diameters, the changes in the area under the potential curve with applied field are concentrated in those regions where the potential is linear in distance; the details of the barrier close to the surface thus will not affect the determination of the work function. This qualitative expectation is borne out by quantitative calculations for high-field tunneling through differently shaped potential hills, both with and without the inclusion of image forces.[21] These estimates differ appreciably in the absolute magnitude of the current. For all of them, however, the work function can be satisfactorily obtained from a plot of $\log i/V^2$ vs $1/V$.

Attempts have been made to derive work function changes during adsorption merely by observing the field emission current at a fixed applied voltage.[22] This procedure depends upon an accurate expression for the absolute emission intensity. Since the Fowler-Nordheim equation does not afford a good description of the emission from a nitrogen covered surface, work functions derived in this fashion may be suspect.

The point to be emphasized is that the field dependence of the emission current can yield reliable work functions. For nitrogen adsorbed on tungsten at room temperature, these work function changes are *negative* and nitrogen appears as the only diatomic gas so far studied which lowers the work function on dissociative chemisorption.

B. Surface Migration of Nitrogen on Tungsten

The key to the interpretation of changes in the emission patterns with temperature, as well as to the understanding of structural effects in adsorption, lies in the diffusion behavior of the adsorbed nitrogen. This has been examined by depositing nitrogen on one side of a tungsten field emission source in the apparatus of Fig. 2, and by observing the spreading of this deposit over the surface as the emitter is warmed.

1. Room Temperature Deposits

The deposition and first stages of spreading for nitrogen on a point initially at $T=290°K$ are shown in Fig. 8. The gas beam strikes the emitter along the 111 zone line at ~two o'clock. Some of the gas covers the 010 pole and a very small amount appears to penetrate over the $11\bar{1}$ pole toward the $1\bar{1}1$ zone line. This is material from the periphery of the beam, or else not accommodated to the substrate temperature.

[20] T. E. Stern, B. S. Gossling, and R. H. Fowler, Proc. Roy. Soc. (London) **A124,** 699 (1929).

[21] These are summarized by E. W. Müller, Ergeb. exakt. Naturw. **27,** 290 (1953).

[22] J. A. Becker, *Solid-State Physics,* edited by F. Seitz and D. Turnbull (Academic Press, Inc., New York, 1958), Vol. 7, p. 379.

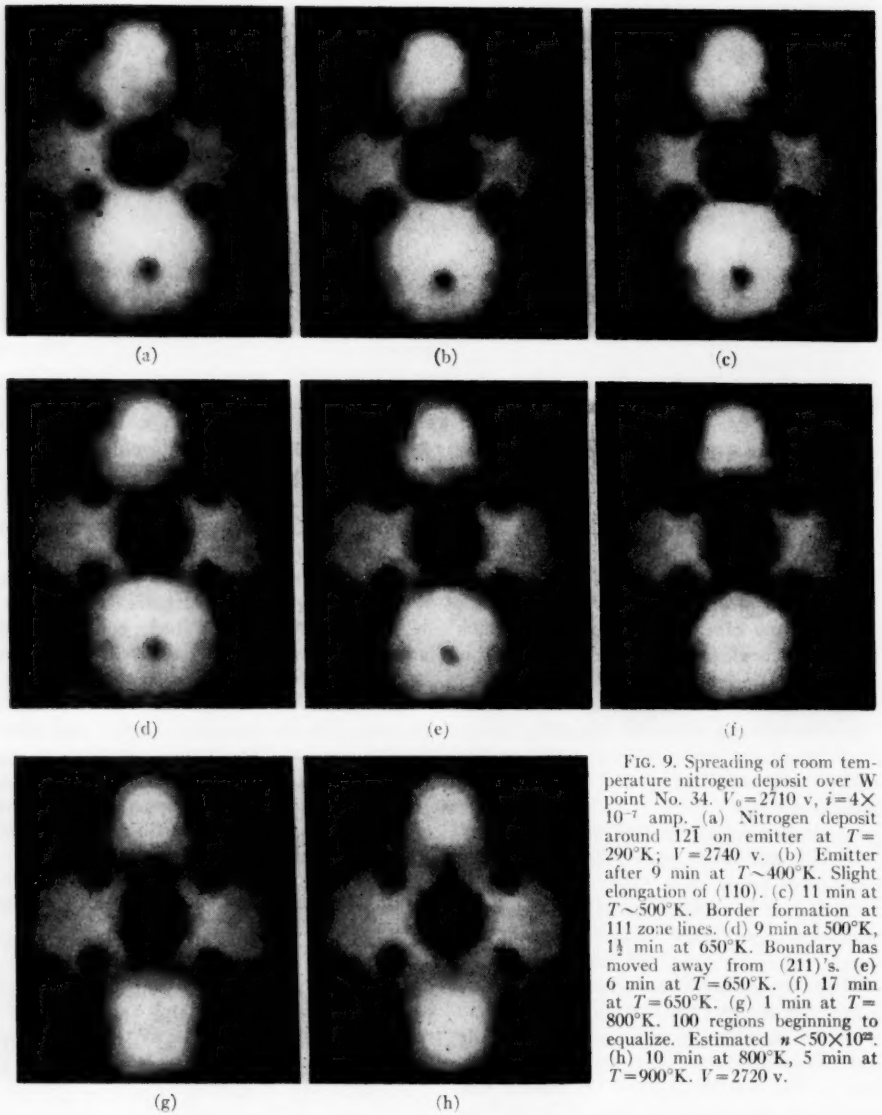

FIG. 9. Spreading of room temperature nitrogen deposit over W point No. 34. $V_0=2710$ v, $i=4\times10^{-7}$ amp. (a) Nitrogen deposit around $12\bar{1}$ on emitter at $T=290°K$; $V=2740$ v. (b) Emitter after 9 min at $T\sim400°K$. Slight elongation of (110). (c) 11 min at $T\sim500°K$. Border formation at 111 zone lines. (d) 9 min at 500°K, $1\frac{1}{2}$ min at 650°K. Boundary has moved away from (211)'s. (e) 6 min at $T=650°K$. (f) 17 min at $T=650°K$. (g) 1 min at $T=800°K$. 100 regions beginning to equalize. Estimated $n<50\times10^{12}$. (h) 10 min at 800°K, 5 min at $T=900°K$. $V=2720$ v.

The 111 pole, on the side opposite the beam impact area, remains entirely unchanged during the deposition, despite the fact that nitrogen is present on the adjacent 100 regions, and we form a well localized deposit under these conditions. A pronounced boundary does, however, form at the 111 zone lines once the point is heated to $T>400°K$, as in Fig. 8(c). It follows that nitrogen adsorbed at 290°K cannot diffuse over the tungsten surface, but that above 400°K migration begins in the vicinity of the 111 regions.

The diffusion of adsorbed material at higher temperatures is exhibited in more detail in Fig. 9. After formation of an initial deposit at 290°K (surface concentration $n<200\times10^{12}$ molecules cm^{-2}) the tip temperature was raised to 400°K. A slight elongation of the 110 is barely perceptible in Fig. 9(b). At $T\sim500°K$ [Fig. 9(c)], however, sharp boundaries have formed around the 100 poles coinciding with the zone lines, and the extent of the emitting caps surrounding the poles is diminished. At this temperature nitrogen therefore moves over the central 110 plane (or at least over its edges), as well as over the 111 zone lines. Diffusion must also take place over the 111 plane and its surroundings: These regions become dim at the expense of the (100)'s and there is no sharp boundary at the edge of the 110 plane.

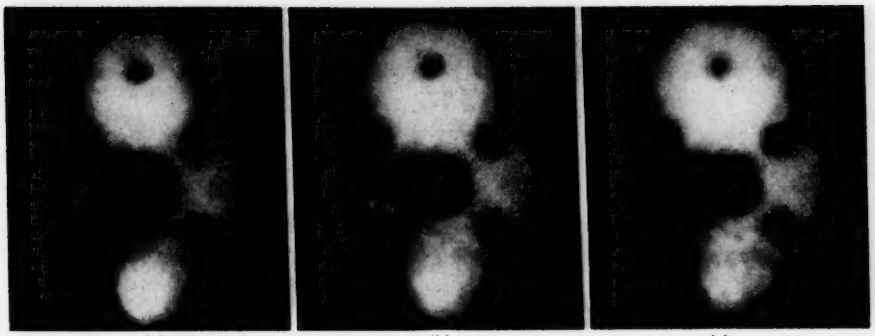

(a) (b) (c)

FIG. 10. Spreading from Nitrogen deposit at 77°K on W point No. 34. $V_0=2710$v. (a) Emitter at 77°K with nitrogen deposited around $12\bar{1}$. $V=2800$v. (b) Emitter after heating to $T\sim180$°K for ~9 min. Regions around $11\bar{1}$ and $12\bar{1}$ have become emitting. (c) Boundary formation around 100 region after heating to $T>350$°K, $V=2750$v. n after high temperature equilibration $<50\times10^{20}$.

On raising the temperature to 650°K, the edges of the emitting regions centered on the 100 poles pull back from the zone lines (d), and this trend continues as the point is maintained at this temperature (e, f) until the 100 pole itself becomes emitting and the region around it assumes a heart-shaped configuration. A complete equalization of the regions around the (100) and (010) is only achieved at $T\gg800$°K, as shown in Fig. 9(h). Estimates of the activation energy for migration have been made from the rate of advance of the boundary at a fixed temperature, assuming a jump frequency of 10^{12} sec^{-1}, as well as from the temperature dependence of the diffusion. For the low-temperature spreading over the 110 and 111 regions our observations suggest an activation barrier of ~20 kcal mole^{-1}, whereas the migration over the 100 regions at 650°K and above occurs across a potential barrier of ~35 kcal mole^{-1}. These two regions also differ in the *form* of the diffusion. In contrast to the spreading around the 100 poles, nitrogen moves across the area encompassed between the $[1\bar{1}1]$ and $[\bar{1}11]$ zone lines without a boundary. Around the (100), diffusing adatoms are rapidly immobilized in a distance small compared with the resolution of the microscope (~25 A), but such trapping does not occur around the (111). This suggests a considerably greater uniformity, on an atomic scale, of the binding sites in the latter regions.

2. *Low Temperature Deposits*

The behavior of nitrogen deposited at 77°K differs only slightly from that just outlined. The initial deposit shown in Fig. 10 is again localized. It is centered on the $(12\bar{1})$ and covers the (010), as well as the $(11\bar{1})$ and its immediate environment. Faint indications of change around the $(11\bar{1})$ are observable when the point is heated to ~130°K; these changes are complete at $T\sim180$°K. As can be seen in Fig. 10(b), the $(11\bar{1})$ becomes more strongly emitting, and the deposit around the $(12\bar{1})$ is surrounded by a clearly defined boundary, not apparent just after the initial deposit. Despite these changes, there is no indication of migration over the (110) or the (111). Diffusion with formation of sharp boundaries around the 100 regions [Fig. 10(c)] takes place only when the point is heated to $T>350$°K, in agreement with the room-temperature spreading experiments.[23] All this suggests that nitrogen in the γ state, which is formed in the initial deposit, is immobile at 77°K. At higher temperatures, where mobility is expected, the mean diffusion length x_s of γ nitrogen on the surface must be small by comparison with the dimensions of the planes of the emitter (<100 A); on heating, nitrogen in this state evaporates from the surface, or is converted into a more firmly bound state [Fig. 10(b)] rather than migrating away. x_s is related to the average jump distance l through

$$x_s=(l^2\tau_E/\tau_t)^{\frac{1}{2}},$$

where τ_E is the mean lifetime of the molecules on the surface, and τ_t the average time interval between jumps. Our observations therefore must mean that the ratio τ_E/τ_t is close to unity, and that the activation barriers to evaporation and diffusion are comparable.

At even lower temperatures we expect the participation of physically adsorbed nitrogen molecules in the diffusion process; this is confirmed by observation of nitrogen deposited on the tungsten emitter at 20°K. The number of gas molecules allowed to impinge on the point in Fig. 11(a) was larger than for the deposits at higher temperature, and the appearance of the nitrogen frozen on the surface is also quite different. The regions around (010), $(12\bar{1})$, and $(11\bar{1})$ are now essentially blacked out, and the boundaries of the deposit are sharply defined.[24] We have formed a many-layered structure at the point of impact of the gas beam, or at least within the range of those adsorbed

[23] This temperature is close to the instability range for a liquid nitrogen cooled filament and we therefore have not obtained a more accurate resistance-temperature calibration.

[24] Such boundary formation was first discussed by R. Gomer, R. Wortman, and R. Lundy, J. Chem. Phys. **26**, 1147 (1957).

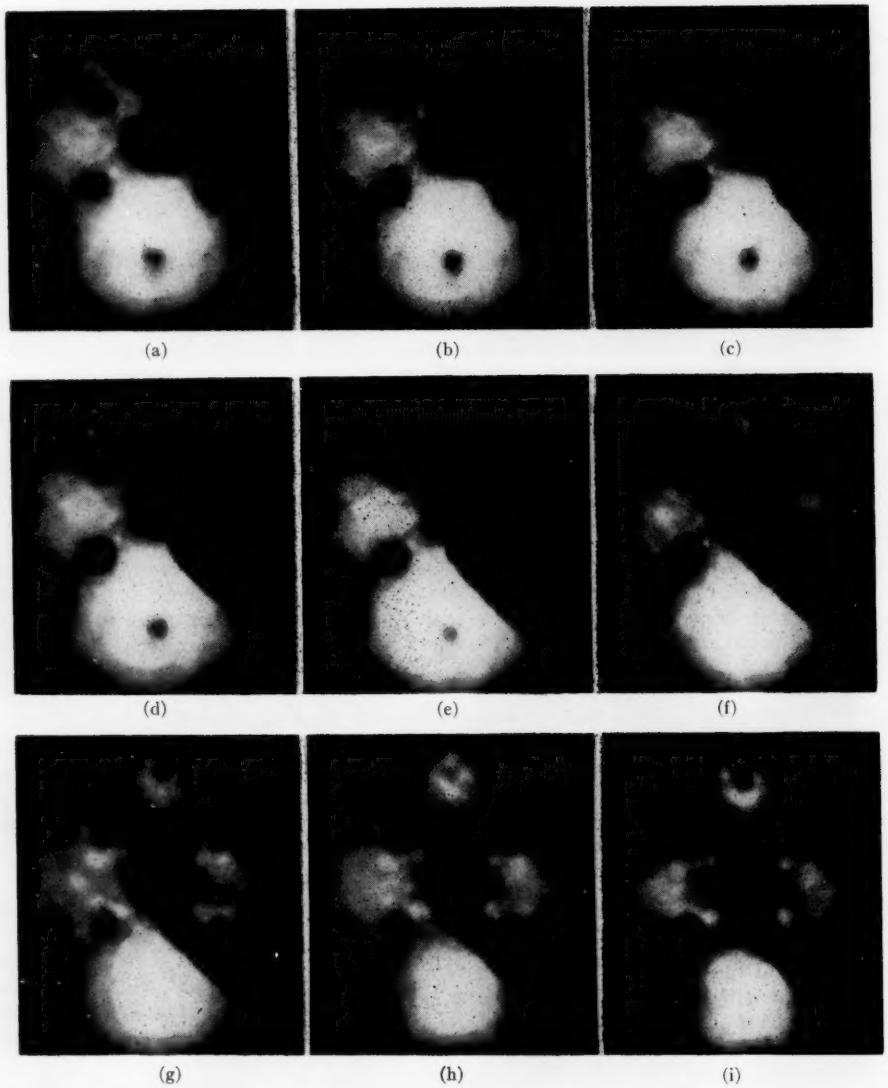

FIG. 11. Surface migration of nitrogen deposited at 20°K on W. Point No. 34. $V_0=2710$v. (a) Deposit at $T\sim20$°K, localized around (010), $(12\bar{1})$, and $(11\bar{1})$. $V=2850$v. (b) $T\sim40$°K for 1 min. Motion over regions around 010 and $11\bar{1}$. (c) 3 min at 40°K, 1 min at $T\sim45$°K. Boundary motion toward (100). (d) $T\sim45$°K for 1½ min. (e) $T=55$°K. Boundary advance toward (100) has stopped. (f) ~Room temperature for 1½ min (100) pole disappears (010) emerges. (g) ~Room temperature for ~1½ min. Room temperature form of (111)'s and (211)'s develops. (h) $T\sim700$°K for ~1 min. Boundary in 100 region begins to disappear, (111)'s and (211)'s change to high-temperature form. (i) $T\sim700$°K for ~1 min. Equalization of (100) and (010) poles starts. $V=2850$v. Estimated $n>100\times10^{12}$.

molecules which are incompletely accommodated to the surface temperature, and this thick nitrogen deposit prevents electron tunneling. The sharp boundary defining the limits of the deposit must result from rapid adsorption and immobilization on the metal surface of molecules falling from the top of this multilayer.

The crystal surface opposite the impact area of the beam remains unaffected during the formation of the nitrogen layer, indicating that at 20°K nitrogen physically adsorbed in a multilayer is immobile. Motion of the boundaries can be induced by heating the surface just a little. As shown in Fig. 11(b), the deposit extends over the 010 and $11\bar{1}$ regions even at $T\sim40$°K. This process, for which we estimate an activation energy of the order of 2 kcal mole^{-1}, continues until the advance of the boundary ceases, and cannot be started again by small temperature increases. This stage is reached in Fig. 11(e) at ~55°K. The

gradual emergence of the underlying 010 and $11\bar{1}$ regions (b–c), which previously had been effectively covered up, suggests exhaustion of the supply of nitrogen physically adsorbed on top of the primary layers.

At this same stage of spreading the 100 pole, which during formation of the initial deposit had changed very slightly, begins to emit with an intensity comparable to its immediate surroundings. This is caused by adsorption at, or in the vicinity of the pole, of material escaping from the sharp boundary. Changes in contrast on increasing the applied voltage as in Fig. 11 (d), (e) can be shown to be small. Since the sharp boundary remains in place and does not become diffuse, although the background emerges, it must be formed by strongly bound entities that do not diffuse at this temperature (55°K). Adsorption around the (100) therefore occurred from physically adsorbed molecules flying *over* the metal surface from the deposit and toward the vicinity of the pole.

This interpretation is buttressed by the further behavior of the adsorbed layer. On continued heating, the 100 pole completely disappears (f) as the emission from its surroundings becomes of equal intensity now after adsorption, despite an initial difference of 0.4 ev in work function on the clean emitter.[10] At the same time diffusion into the 111 region takes place (f to g). The temperature of this change is again uncertain since it takes place while the support wire is sweeping through the region of temperature instability. However, the sequence is that already observed for high-temperature deposits: After the spreading over the 111 region the nitrogen moves toward the (100), resulting in an ever decreasing emitting area there. The sharp boundary across the 100 region close to the $(21\bar{1})$, formed during the low-temperature spreading, maintains itself almost to the very end (h), proving that strongly chemisorbed material was responsible for it.

Despite the fact that most of the material spilling over was immediately immobilized and formed into a sharp boundary, some of the nitrogen physically adsorbed on top of the deposit traversed long distances (~400 A). A diffuse boundary would have formed, if the physically adsorbed molecules were able to traverse by random jumps, distances which are large by comparison with the resolution of the microscope (≒25 A). the physically adsorbed molecules were able to traverse by random jumps, distances which are large by comparison with the resolution of the microscope (≒25 A). The chemisorption of nitrogen around the (100) thus appears more like an evaporation phenomenon. Molecules from the multilayer, which do not have sufficient energy to evaporate completely, may still fly far away from the surface plane before falling back under the action of the (inhomogeneous) electric field applied during these observations.

Distinct stages in the diffusion of adsorbed nitrogen can be identified from these observations. Material deposited at 77°K and above spreads over the 110 and 111 regions at $T>400$°K, and over the region around the (100) at 650°K. Depletion of the low-temperature deposit, presumably by evaporation, does occur at even lower temperatures, starting at $T=130$°K. After condensation of a multilayer on tungsten at 20°K, spreading begins at $T\sim40$°K with the formation of sharply defined borders, together with some diffusion over the (100) without bordering.

The interpretation of this diffusion behavior in terms of the different binding states existing on the surface is quite unequivocal. Spreading from the deposit at 20°K involves the flow of nitrogen which is bound only at these low temperatures. Judging from the small activation energy this corresponds to physically adsorbed molecules on top of the layer bonded directly to the surface. The sharp boundary observed under these conditions is formed by nitrogen chemisorbed as atoms, that is, by nitrogen in the β state. This we deduce from the fact that the boundary is stable and essentially unchanging up to $T>600$°K, at which only this one β state has been isolated; the absence of any changes in the boundary eliminates conversion of one state to another in this range of temperatures.

The γ state, populated at 77°K, does not participate in diffusion—no spreading can be observed in the range 77°–400°K, which certainly defines the limits of stability of γ. The same applies to the α state. Diffusion occurs only at $T>400$°K, that is, at temperatures above those for which evolution of this state is rapid. No further changes on the 111 region occur over the next 400°K, so that we must assign the motion here to the atomically bound β state. Similarly it must be adatoms that migrate over the 100 region at $T>650$°K; no other state is stable here.

These diffusion measurements indicate a marked structural specificity in the interactions of nitrogen with a tungsten surface. They also suggest that both the α and γ states are held at isolated sites, for which the binding energy and the diffusion barrier are comparable.

C. Measurements at Elevated Temperatures

1. Adsorption

At room temperature chemisorption of nitrogen appears fairly general on the different crystal planes of tungsten. Our observations do not, however, distinguish the effects due to the two different states established by flash desorption. The α state, which is bound to the surface with an energy of ~20 kcal mole^{-1}, has been found to evolve at temperatures above $T=300$°K.[2] Nitrogen in the β state is dissociated and held as atoms with a binding energy of ~150 kcal per gram atom.[22,25] Evolution from this state, therefore, only occurs at an appreciable rate at $T>1000$°K.

[25] G. Ehrlich, J. Phys. Chem. **60**, 1388 (1956).

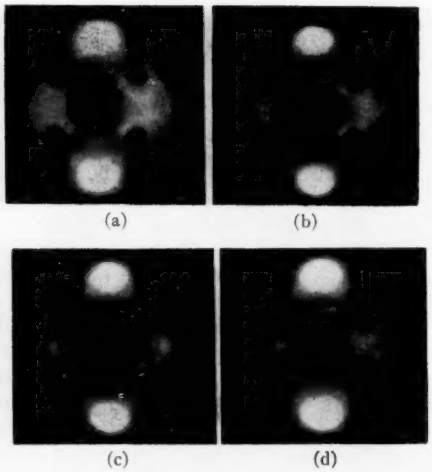

FIG. 12. Adsorption of nitrogen on tungsten at $T=370°K$. Point No. 68. $i=5\times10^{-8}$ amp, $V=2870$ v. (a) $\Delta t=5$ min, $V=2900$ v, $\phi=4.49$ ev; (b) $\Delta t=10$, $V=2880$, $\phi=4.24$; (c) $\Delta t=24$, $V=2940$, $\phi=4.30$; (d) $\Delta t=138$, $V=3040$, $\phi=4.42$, $p\sim6\times10^{-8}$ mm.

Since we have now established that diffusion of nitrogen, adsorbed at room temperature, only sets in at temperatures above 400°K we can hope to isolate the behavior of the α state by examining the adsorption in the range $300°<T<400°K$.

A sequence of emission patterns taken during the adsorption of nitrogen on tungsten maintained at 370°K is shown in Fig. 12. The general appearance of the point is much like that found during room temperature adsorption (Fig. 4), with one important exception. The sharply defined emission around the 111 and 211 planes, particularly along the 110 zone lines connecting the (111) and (211), is now lacking. This change in the appearance of the (111) during the initial stages of adsorption is made more apparent by heating a point to this temperature after adsorption has occurred at $T=300°K$, as indicated in Fig. 13.

The behavior of the work function during adsorption at 370°K is also similar to that already found at room temperature, and on raising the temperature from 300 to 370°K the emission properties are only slightly affected. This is expected, since differences in the field emission patterns taken at the two temperatures are centered on the 111 regions, which do not contribute strongly to the over-all emission. Our measurements therefore do not allow conclusions about the dipole moment of nitrogen in the α state, except for the qualitative statement that the polarization of this state should be of the same order of magnitude as that of the remaining adsorbed gas. The saturation pattern obtained at the higher temperature is no different from the one at 300°K, and on heating the latter no change in the intensity distribution is apparent. This is in conformity with our flash desorption measurements, which indicate a negligible concentration of nitrogen in the α state, amounting to only 2% of β at higher coverages.

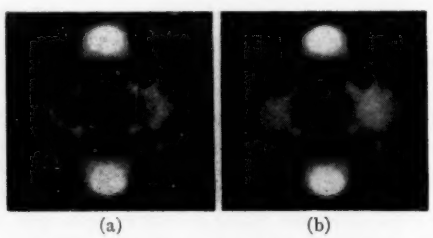

FIG. 13. Desorption of α state at $T=370°K$. Point No. 68. $i=5\times10^{-8}$ amp, $V_0=2900$ v. (a) $T=300°K$, $\Delta t=11$ min, $V=2930$ v. Adsorption at $p\sim6\times10^{-8}$ mm, $\phi=4.36$ ev. (b) Pattern a, after heating without further adsorption to $T=370°K$ for 2 min; $\phi=4.34$ ev.

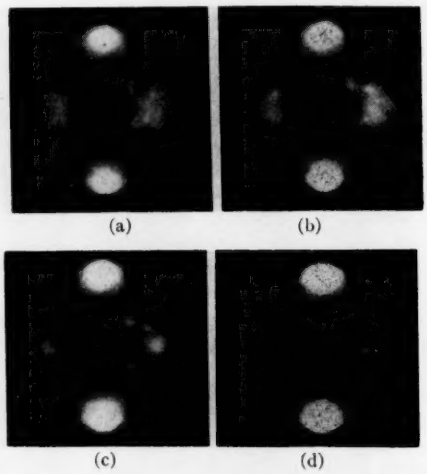

FIG. 14. Adsorption of nitrogen on tungsten at $T=560°K$. Point No. 68. $i=5\times10^{-8}$ amp, $V_0=2860$ v, $\phi=4.50$ ev. (a) $\Delta t=17$ min, $V=2850$, $\phi=4.28$; (b) $\Delta t=27\frac{1}{2}$, $V=2880$, $\phi=4.26$; (c) $\Delta t=62$, $V=2940$, $\phi=4.32$; (d) $\Delta t=235$, $V=2970$, $\phi=4.30$, $p\sim4\times10^{-8}$ mm.

The changes which occur on heating of the emission pattern (at low nitrogen concentrations) must be due to evaporation of nitrogen originally in the α state and therefore suggest that this state is formed preferentially on the regions around the (111). It is still possible that adsorption of nitrogen in the α state occurs on and around the (100) and just does not appreciably affect the emission there. However, flash desorption from rolled tungsten ribbons,[26] for which surface normals perpendicular to the (100) and its immediate neighbors were favored, revealed a significantly smaller α concentration than on wires of circular cross section. On wire samples, 111 planes are present and the enhancement in the α concentration on these samples

[26] T. W. Hickmott and G. Ehrlich, J. Phys. Chem. Solids **5**, 47 (1958).

supports the first interpretation. The combination of flash desorption and field emission observations therefore leads to the view that the α state of nitrogen is very sensitive to the surface structure and is concentrated around the 111 poles.

The course of the adsorption at even higher temperatures (such as in Fig. 14) is much the same. At 560°K the 111 region [Fig. 14(b)] shows even more pronounced changes from the room-temperature pattern than at 370°K; presumably surface diffusion has taken place in this area. At this temperature the concentration of α material should be negligibly small; from an analysis similar to that in Sec. IIA1, we can conclude that adsorption occurred on all of the exposed planes, again with the possible exception of the (110) and (211). We have now established that it is the nitrogen in the β state that adsorbs generally and without excluding any of the observable planes.

2. *Desorption and Surface Rearrangement*

The binding energy of nitrogen on tungsten is comparable to that of a tungsten atom to its own lattice, and it is therefore of interest to look for structural changes induced by adsorption. When a tungsten emitter saturated with nitrogen at room temperature is heated to higher and higher temperatures, the patterns (Fig. 15) do not coincide with those found during adsorption. This is expected, inasmuch as mobility of nitrogen atoms over all of the crystal regions becomes appreciable only for $T>650$°K. Only at these higher temperatures can we attain an equilibrium distribution rather than one dictated by the kinetics of adsorption.

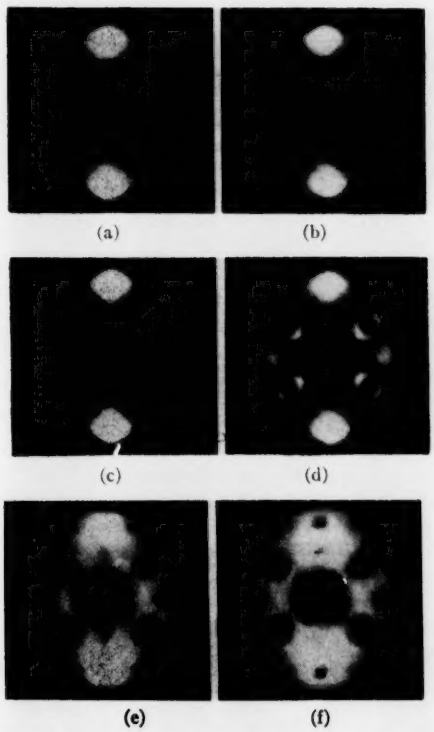

FIG. 15. Desorption of nitrogen from tungsten at elevated temperatures. Point No. 68, saturated with N_2 for 100 min at $p\sim2\times10^{-8}$ mm. $\phi=4.41$ ev. Desorption patterns obtained with emitter at $T=300$°K, after heating to temperature indicated for ~3 min. (a) $T=600$°K, $\phi=4.39$ ev; (b) 840°, 4.28; (c) 1025, 4.23; (d) 1150, 4.21; (e) 1300, 4.39; (f) 1390, 4.52.

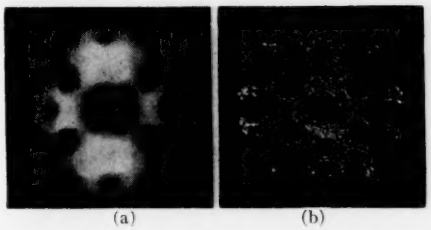

FIG. 16. Shape changes of clean tungsten point after high-temperature annealing. (a) Point No. 68 annealed at $T=1100$°K for 65 min. (b) Ion pattern of similarly shaped W point No. 56. $V=15.7\times10^3$ v, $p\sim10^{-3}$ mm He.

The most important changes when the point is heated above 1000°K occur around the 111 and 211 planes. As nitrogen is desorbed the over-all work function drops: After 3 min at $T=1150$°K [Fig. 15(d)] the 111 plane becomes emitting and the (211)'s are surrounded by a bright rim. On heating at still higher temperatures ($T\sim1300$°K) the nitrogen is almost completely eliminated and the intensity distribution over the emitter changes as indicated in Fig. 15(e) and (f). The 111 plane recedes into darkness and the zone lines through the 100 pole appear more sharply defined.

The extent to which we are witnessing a simple rearrangement of nitrogen adatoms is not clear from these observations. At $T>1000$°K, tungsten atoms in the surface layer have an appreciable mobility and these may rearrange themselves.[27] Such a rearrangement was deduced from flash desorption measurements for a tungsten filament heated at 1000°K in nitrogen.[2]

That a tungsten point does undergo shape changes at $T\sim1000$°K emerges from the observations contained in Fig. 16. There an emitter was heated for 1 hr at 1100°K and at pressures below 10^{-9} mm. Just as during the desorption sequence [Fig. 15(e)] the 111 planes have become dark, and we can now attribute this to an increase in the size of this plane at higher temperatures.[28] High-temperature annealing also brings out the 013 planes; changes in the structure of both the (130) and (111) can be made even more apparent in the ion microscope, as in Fig. 16(b).

The intensity distribution observed in Fig. 15(d) after heating to $T=1150$°K is the same as that obtained by prolonged annealing in nitrogen at a pressure

[27] E. W. Müller, Z. Physik **126**, 642 (1949).
[28] Such an effect was first reported by J. A. Becker, Bell System Tech. J. **30**, 907 (1951).

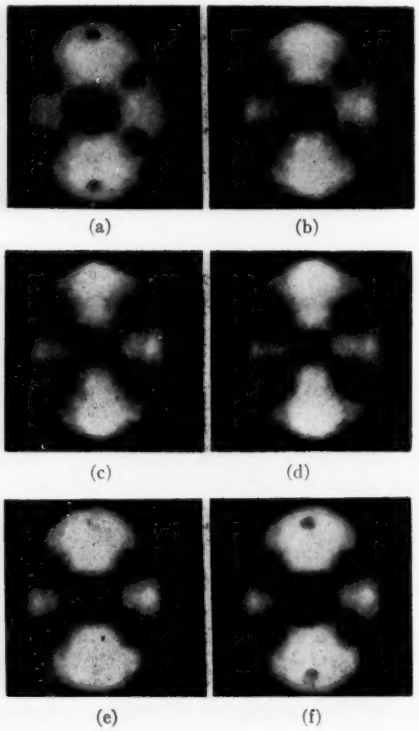

FIG. 17. Adsorption of nitrogen on tungsten at $T=79°K$. Point No. 68. $i=5\times10^{-8}$ amp, $V_0=2930$ v. (a) $\Delta t=5$ min, $V=2980$ v; (b) $\Delta t=20$, $V=3130$; (c) $\Delta t=32$, $V=3190$; (d) $\Delta t=61$, $V=3330$; (e) $\Delta t=91$, $V=3410$; (f) $\Delta t=131$, $V=3420$, $p\sim4\times10^{-9}$ mm.

of 2×10^{-7} mm. Just as when annealing without gas, we can therefore expect some surface rearrangement. If a simple redistribution of nitrogen atoms were sufficient to give the high-temperature pattern with its sharp, brightly emitting 111 plane and rings around the 211, then these effects should also be obtainable by allowing a nitrogen covered point to equilibrate at a lower temperature, at which the surface mobility of adatoms is rapid and the mobility of tungsten atoms negligible. We have annealed tips at just below 600°K for a series of nitrogen concentrations without, however, being able to reproduce the high-temperature effects of Fig. 15(d).

The differences in the emission pattern could conceivably still arise from a different distribution of nitrogen atoms at low and high temperatures, dictated by differences in the entropy of adatoms on different crystal regions. This is unlikely to be the main effect: We expect a rapid rearrangement to the low-temperature form on cooling the emitter, and this we do not observe experimentally. More than that, a rearrangement of the surface in the absence of nitrogen is definitely established and we therefore expect such a rearrangement in the presence of adsorbed material also. We cannot, however, conclude from the drastic pattern changes for a nitrogen covered tip at high temperatures that the rearrangement of the surface is more pronounced than for annealing in the absence of gas—it may be that small structural differences are pointed up by the adsorbed material.

D. Adsorption at Low Temperatures

Formation of an additional weakly bound state, designated γ, when nitrogen interacts with a tungsten surface maintained at 115°K was originally deduced from flash desorption. The presence of such a state at low temperatures is immediately confirmed by use of the field emission microscope. When a tungsten tip, brought close to saturation with nitrogen at room temperature and a pressure $p=5\times10^{-8}$ mm, is cooled to 79°K, further exposure to nitrogen profoundly changes the emission characteristics[29]: the work function drops by 0.2 ev from its room temperature value. The pre-exponential also diminishes, so that the current diminishes, so that the current diminishes and at the same time the emission becomes more uniform than at room temperature.

That the course of nitrogen adsorption is markedly different at low temperatures than at $T=300°K$ is borne out by field emission measurements with the tip entirely at 79°K. During adsorption on a liquid nitrogen cooled point, the appearance of the emission patterns (Fig. 17) changes much less than at the higher temperatures. The initial diminution of emission from the 111 plane is completely lacking. Instead the intensity of the 111 zone lines grows less and the 111 poles actually become more brightly emitting. The saturation pattern obtained by adsorption with tungsten maintained at 79°K throughout [Fig. 17(f)], does not differ appreciably from that formed by saturation at room temperatures prior to low-temperature adsorption.

The work function and pre-exponential show similar interesting and unexpected effects. As indicated in Fig. 18, the pre-exponential drops monotonically with increase in coverage over almost the entire accessible range. The work function, however, first rises by 0.1 ev and then drops below the value for clean tungsten, but only once much of the surface is filled. At saturation for $p\sim1\times10^{-7}$ mm, the slope of the Fowler-Nordheim plot yields a work function ~0.1 ev less than for clean tungsten; since the pre-exponential has also diminished with coverage, the voltage required to draw a constant test current (of 5×10^{-8} amp) rises monotonically. This diminution of the pre-exponential is not just due to a reduction of the gross emitting area. Figure 17 suggests that this area remains essentially unchanged, and it must be the structure of the ad-

[29] A further change in the work function during low temperature adsorption was noted in reference 18, and also by R. Suhrmann, Z. Elektrochem. **60,** 804 (1956).

sorbed layer which is responsible for the decrease in the transmission of electrons. The discrepancy between the field emission current experimentally observed and that calculated from the Fowler-Nordheim equation [Fig. 18(b)] amounts to a factor of 100; this strongly reinforces our caution about the applicability of this simplified relation to the calculation of absolute emission intensities during adsorption.

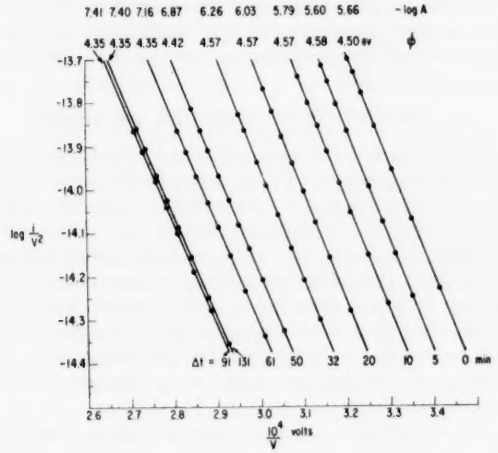

FIG. 18. (a) Work function changes during adsorption of nitrogen on W point No. 68 at $T=79°K$; FN plots taken at adsorption intervals (Δt) corresponding with those of Fig. 17. (b) Experimental current voltage characteristics after nitrogen adsorption at $T=79°K$, compared with values calculated from FN relation. Point No. 68.

From the emission patterns during adsorption it can be concluded that all observable planes are becoming populated with nitrogen, and that the additional γ state does not show any extreme structural selectivity. The initial rise in work function on low-temperature adsorption is therefore particularly significant. This rise, which takes place only for the first few molecules,

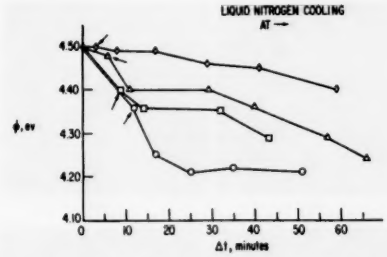

FIG. 19. Work function changes during nitrogen adsorption at 79°K on W point No. 68 partly covered at $T=300°K$. Start of liquid nitrogen cooling indicated by arrow.

is indicative of a unique behavior of the adsorbed nitrogen during the early stages, with an entirely different arrangement of the β state than that found at higher temperatures. This is also suggested by the fact that the work function of tungsten can be lowered by 0.35 ev if the emitter is first saturated at room temperature prior to liquid nitrogen adsorption, and only approximately 0.1 ev if adsorption is carried out entirely at 79°K. It is only the initial adsorption that is really different. If even very small amounts of nitrogen are added to a tungsten surface at 300°K, continuation of adsorption at 79°K only lowers the work function still more, and no increase is observed (Fig. 19).

This early stage of adsorption, which raises the work function, is again quite generally distributed and appears on all the observable planes (Fig. 17). Although the measurements reported so far do not permit a unique interpretation, it is clear from a comparison of Figs. 20 and 17 that the difference between the initial

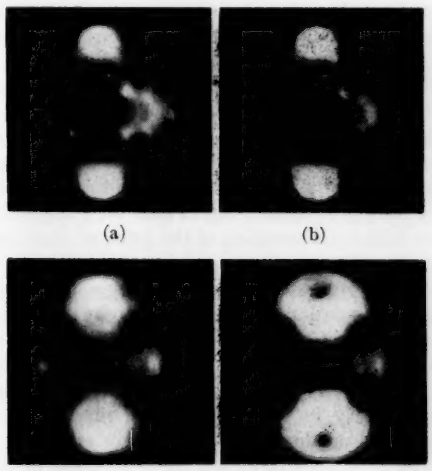

FIG. 20. Adsorption of nitrogen at 79°K on emitter partly covered at $T=300°K$. $i=5\times10^{-8}$ amp, $V_0=2990$ v, point No. 68. (a) $\Delta t=12$ min, $V=3050$ v, $T=300°K$; (b) $\Delta t=25$, $V=3060$, $T=79°K$; (c) $\Delta t=51$, $V=3190$; (d) $\Delta t=84$, $V=3330$, $p\sim8\times10^{-8}$ mm.

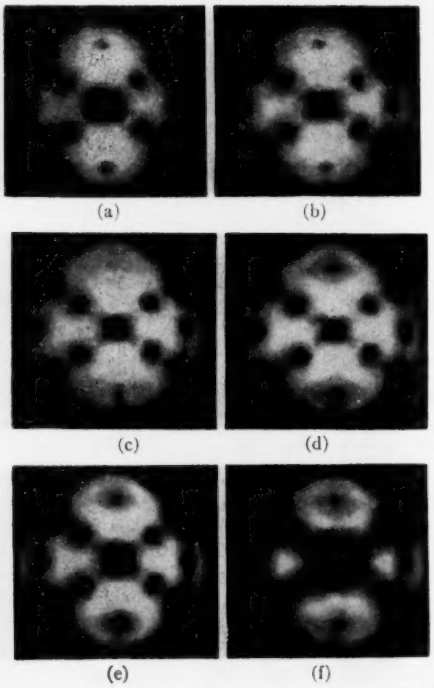

FIG. 21. Adsorption of nitrogen on tungsten at $T\sim20°K$. Point No. 23. $i=5\times10^{-9}$ amp, $V_0=3420$ v. (a) $\Delta t=14$ min, $V=3490$ v; (b) $\Delta t=23$, $V=3720$; (c) $\Delta t=32$, $V=3940$; (d) $\Delta t=43$, $V=4080$; (e) $\Delta t=63$, $V=4190$; (f) $\Delta t=111$, desorption by field, $p<2\times10^{-9}$ mm.

adsorption at room temperature and at 79°K is not due to gross effects such as preferential adsorption on one type of plane. Two possibilities must be considered. (1) On an atomic scale the adsorption of nitrogen in the β state occurs differently at low temperature than at high. This low-temperature layer forms unique sites for the formation of γ, sites which are different from those available on a room temperature layer of the β material. The increase in work function then results either from the differently arrayed β or else from the γ material. (2) At low temperatures only one state, γ, forms initially. Formation of the primary chemisorbed state β occurs only slowly and incompletely.

Flash desorption experiments[2] suggest the simultaneous population of β and γ, thereby favoring the first possibility. For the second model the weakly bound γ state would have to increase the work function when present alone on the surface, and this appears unlikely in view of our later observations for nitrogen adsorption on nickel. In any event, our observations demonstrate that the adsorption of N_2 on W at 79°K results in a singular arrangement of the gas on the substrate.

In the course of surface diffusion measurements, we have already identified the presence of yet another state of binding of nitrogen, which is important at even lower temperatures ($T\sim20°K$) and presumably consists of molecules held by van der Waals forces. Our observations of adsorption at $T=20°K$ are very preliminary. The emission patterns obtained, shown in Fig. 21, suggest a very uniform distribution of adsorbed material, the intensity distribution resembling that of a clean tungsten emitter. The work function changes are similar to those found at 79°K; apparently subsequent layers of nitrogen adsorbed on top of α and β are but weakly polarized. It is of interest, however, that at high coverages the field applied for emission becomes sufficiently strong to tear off the adsorbed layer [Fig. 21(f)].

III. ADSORPTION OF NITROGEN ON NICKEL

The increase in the work function when nitrogen adsorbs on tungsten at 79°K may conceivably stem from the presence of a single weakly bound state. Although a definitive test of this proposition by field emission is difficult, some indication of the emission properties of such a state should be obtainable by comparison with a system in which dissociative chemisorption does not occur, and only a weak, molecular state can exist. With this in mind, we have examined the interaction of nitrogen with nickel, for which strong chemisorption is reported lacking.

The emission from a clean nickel surface is shown in Fig. 22; here the intensity has been increased above that normal in our work to bring out the full symmetry of the pattern. At 300°K the pattern, as well as the emission characteristics remain unchanged, even when the nickel is immersed for 1 hr in a nitrogen atmosphere at $p=10^{-7}$ mm. Heating the support wire after this exposure does not result in any observable evolution of gas and we can, therefore, conclude that at these pressures nitrogen adsorbs on nickel at $T=300°K$ to less than 10^{12} molecules cm^{-2}.

This observation is in accord with previous reports on adsorption on nickel films[9,26,30–32]; in these the

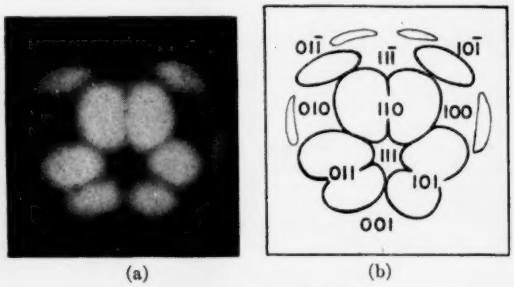

FIG. 22. Clean Ni tip. (a) Field emission pattern; $i=5.5\times10^{-8}$ amp, $V=9600$ v. (b) Orientation diagram of emitter in (a).

[30] R. Suhrmann and K. Schultz, Z. Naturforsch. **109,** 517 (1955).
[31] B. M. W. Trapnell, Proc. Roy. Soc. (London) **A218,** 566 (1953).
[32] O. Beeck, A. E. Smith, and A. Wheeler, Proc. Roy. Soc. (London) **A177,** 62 (1940).

vacuum conditions were not as well defined as in the present study and some doubt about the cleanliness of the surface may have persisted. For example, in low-energy diffraction studies employing ultra-high vacuum techniques, Germer[33] has recently observed the formation of crystalline films on the (111) face of nickel in the presence of N_2. Our own measurements, which show no adsorption at all under demonstrably clean conditions, confirm Germer's suspicion that diffraction patterns arose from contamination. This must pose a more severe problem than with tungsten, inasmuch as the nickel surface will selectively adsorb all the impurities likely to be present in an ultra-high vacuum system.

On lowering the emitter temperature to ~80°K, adsorption of nitrogen does, however, occur on the nickel surface, and the emission pattern changes as in Fig. 23. The zone lines, which for the clean point are very well defined, become almost indistinguishable after adsorption, and the size of the nonemitting areas generally diminishes. This is particularly noticeable around the central 111 plane. Only the 110 poles change in the opposite way—nitrogen adsorption lowers emission from these in contrast to their surroundings and they, therefore, become more prominent than for the clean pattern. The work function, derived from Fowler-Nordheim plots, diminishes slightly during adsorption, decreasing by less than 0.1 ev for the point saturated at $p=5\times10^{-7}$ mm. The pre-exponential again diminishes monotonically with increasing coverage so that the voltage necessary to maintain constant emission must be raised during a run, despite the lower work function.

Strong chemisorption of nitrogen is absent on nickel, and the drop in emission accompanied by a lowering in work function is therefore characteristic of the weakly bound nitrogen layer alone. From the stability of this layer at these temperatures and pressures we can estimate the *minimum* binding energy as ~5.5 kcal mole^{-1}, somewhat higher than the value to be expected for adsorption by dispersion forces alone. Nitrogen appears to be held to the nickel in a state resembling, in some respects at least, that of nitrogen on tungsten. Comparison of the emission properties of these two systems therefore seems justified, and lends support to the view that the increase in the work function observed for nitrogen adsorption on tungsten at $T=79$°K arises from the simultaneous adsorption of both atoms and molecules.

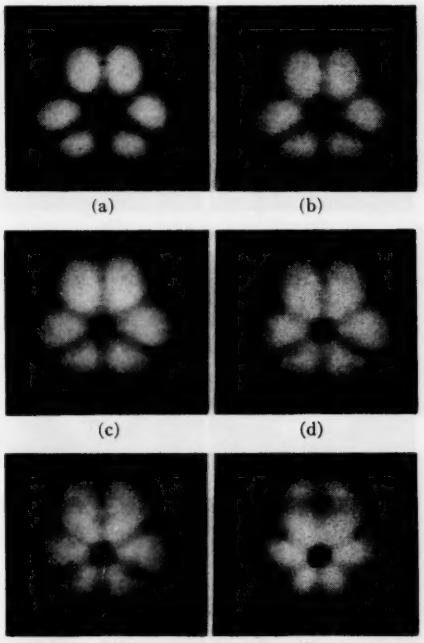

FIG. 23. Adsorption of nitrogen on Ni at 79°K. Point No. 45. (a) $\Delta t=0$ min, $\phi=4.75$ ev, $-\log A=6.04$; (b) $\Delta t=120$, $\phi=4.75$, $-\log A=6.50$; (c) $\Delta t=162$, $\phi=4.67$, $-\log A=6.93$; (d) $\Delta t=188$, $\phi=4.66$, $-\log A=7.11$; (e) $\Delta t=218$, $\phi=4.65$, $-\log A=7.30$; (f) $\Delta t=338$, $\phi=4.70$, $-\log A=7.30$; $p\sim1\times10^{-8}$ mm. Black spot bordering (111) is screen imperfection.

IV. ADSORPTION OF CARBON MONOXIDE ON TUNGSTEN

Just as with nitrogen, carbon monoxide can exist on a tungsten surface in different forms. By flash desorption four distinct states have been isolated in which carbon monoxide is bound to the surface as a molecule.[2] A weak state (α) with a binding energy of 20 kcal mole^{-1} forms once the surface has been substantially covered with a strongly chemisorbed material, designated β. The latter is itself held in three different forms, with desorption energies of the order of 50 kcal mole^{-1} and higher. Support for the presence of molecules in different levels can be deduced from changes in the emission distribution during adsorption.

A sequence of emission patterns for tungsten covered with increasing amounts of carbon monoxide[34] at room temperature is shown in Fig. 24. Initially the 111 zone lines darken [Fig. 24(b)] and a well defined region of high emission appears centered on the 100 poles (a and b). During the later stages of adsorption these features disappear. Continued adsorption results in the enhancement of the 111 poles (b and c); at saturation the point is fairly uniformly covered with carbon monoxide (e) and differs only slightly in appearance from the initial, clean pattern. Work function measurements were not carried out with the same accuracy as for nitrogen. However, for saturation at $p\sim4\times10^{-8}$ mm the work function increased by 0.5 ev and the pre-exponential diminished monotonically. We can con-

[33] L. H. Germer, E. J. Scheibner, and C. D. Hartman, Phil. Mag. [8] **5**, 222 (1960).

[34] Several studies of the interaction of carbon monoxide with tungsten by use of the field emission microscope have already been reported; we therefore note only briefly those of our findings that go beyond the subject matter covered elsewhere.

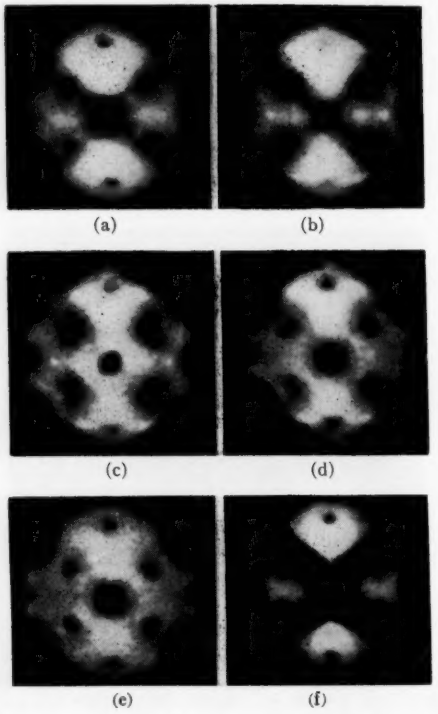

FIG. 24. Adsorption of CO on W at $T=300°K$. Point No. 7. $\phi_0=4.50$ ev, $-\log A_0=5.18$. (a) $\Delta t=7\frac{1}{2}$ min, $\phi=4.69$ ev, $-\log A=5.22$; (b) $\Delta t=24$, $\phi=4.89$, $-\log A=5.39$; (c) $\Delta t=48\frac{1}{4}$, $\phi=5.00$, $-\log A=6.16$; (d) $\Delta t=108$, $\phi=5.00$, $-\log A=6.82$; (e) $\Delta t=240$, $\phi=5.00$, $-\log A=6.94$; $p\sim4\times10^{-8}$ mm. (f) W point covered with CO after heating to $T\sim1000°K$. No carbon pattern is formed.

clude that adsorption of carbon monoxide occurs on all of the planes exposed on the point with the exception of the (110), which because of its high work function escapes observation.

Absorption with the emitter at a lower temperature, 80°K, and the gas still at 300°K is shown in Fig. 25. At this temperature carbon monoxide does not enhance the zone lines and even for the very early patterns the intensity distribution is uniform. The resemblance between the saturation pattern and that for clean tungsten is even stronger at 80° than at 300°K. The work function here increases by ~0.7 ev and the pre-exponential diminishes by ~2 orders of magnitude, when the point is saturated at $p\sim6\times10^{-9}$ mm and a temperature $T\sim80°K$.

The difference between the emission patterns during the early stages of adsorption at 80° and 300°K could again arise either from differences in the surface mobility and therefore in the arrangement of the primary chemisorbed layer, or else from the population of a second state at the lower temperature. Measurements by Gomer[35] and by Klein[36] suggest that such diffusion of the stable chemisorbed layer only occurs at $T>600°K$, and in our experiments adsorption therefore takes place into an immobile layer at both temperatures studied. The difference in the initial patterns around the 111 poles must be attributed to the presence of the α state, which at lower temperatures forms at lower coverages of the strongly bound β state. The effects of the carbon monoxide adsorbed in this α state upon electron emission are less specific to the crystal plane than those of β, and the differences between the 111 and 100 regions are diminished, or eliminated. Our observations in the field emission microscope are therefore in good agreement with the previous experiments which indicated the presence of a second, weakly bound, state of carbon monoxide (α), the onset of which shifted to lower coverages at lower adsorption temperatures. Unlike nitrogen, carbon monoxide adsorption at low temperatures does *not* result in the appearance of a new state, not observed at higher temperatures. The work function change at lower temperatures is larger than at higher temperatures, which is precisely what would be expected if under these conditions the surface concentration of the α state were increased above its 300°K value.

Flash desorption studies already indicated that carbon monoxide was not dissociated on the surface and this is also confirmed in the emission microscope. The patterns displayed so far have given no indication of the typical carbon configuration[3] that would be expected if dissociation occurred. After heating to 1000°K as in Fig. 24(f), these are still absent although we have formed a sharp boundary around the 100 regions. When the temperature of a surface saturated at $T\sim300°K$ is raised to 1400°K in $\sim5\times10^{-8}$ mm of

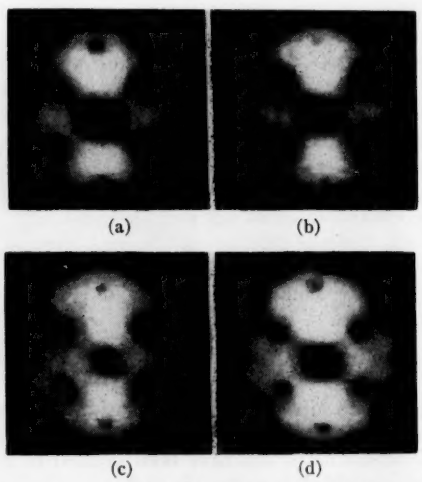

FIG. 25. Adsorption of CO on W at $T\sim80°K$. Point No. 7. $\phi_0=4.50$ ev, $-\log A=5.44$; (a) $\Delta t=61$ min, $\phi=4.56$ ev, $-\log A=5.60$; (b) $\Delta t=125$, $\phi=4.81$, $-\log A=5.96$; (c) $\Delta t=170$, $\phi=5.22$, $-\log A=6.54$; (d) $\Delta t=207$, $\phi=5.25$, $-\log A=7.57$, $p\sim4\times10^{-9}$ mm.

[35] R. Gomer, Discussions Faraday Soc. **28,** 23 (1959).
[36] R. Klein, J. Chem. Phys. **31,** 1306 (1959).

carbon monoxide, the emission picture again gives no indication of carbon formation. Evidently the carbon monoxide molecule does not lose its molecular identity on adsorption in any of its binding states, even at elevated temperatures.

V. SUMMARY

These observations on adsorption of nitrogen and carbon monoxide confirm and extend the conclusions previously derived from flash desorption. Such confirmation is important, since the latter technique rests upon examination of the rates of gas evolution from a surface, and conclusions about the adsorbed phase depend upon a detailed kinetic analysis. In the field emission microscope alterations in the surface properties by adsorption are observed more directly through changes in the rate of electron tunneling out of the metal.

The presence of nitrogen in a new state of binding, physically held to the surface by van der Waals forces, is demonstrated on a liquid hydrogen cooled field emitter. Changes in the emission properties of a tungsten surface exposed to nitrogen at various temperatures $T \geq 79°K$ also confirm the existence of nitrogen in states of low-binding energy, previously designated α and γ. Similar observations on the interaction of carbon monoxide with tungsten indicate contributions of at least two different binding states to this system, as well as the absence of dissociation into carbon and oxygen.

The emission microscope is uniquely adapted for exploring the effects of crystal structure upon surface kinetics and it is here that new insights have been attained. With the possible exception of the 211 and 110 planes, for which adsorption processes could not be followed, all planes on a tungsten crystal are found to participate in the atomic adsorption of nitrogen. No stringent limitation on the occupation of these planes by nitrogen adatoms is imposed because of the high valence of nitrogen. In an entirely similar fashion no structural specificity can be detected in the formation of the γ state of nitrogen, stable at low temperatures ($T \sim 79°K$). For carbon monoxide, the range of observations extends to all planes excepting only the (110), and here again none are excluded from the adsorption process.

A marked dependence in the behavior of the adsorbed nitrogen phase upon the structure of the tungsten surface has been observed for the α state. At the low pressure of our experiments this is stable only below $T \sim 400°K$, and shows a strong preference for the areas around the 111 plane, contained by the 111 zone lines. Study of boundary formation in the field emission microscope indicates that it is these same areas over which diffusion of nitrogen atoms occurs most rapidly. Motion of nitrogen adatoms over the 111 begins at $T > 400°K$. In contrast the diffusion over the regions beyond the 111 zone lines and toward 100 poles only sets in at $T > 650°K$. The activation barriers to surface migration over these two crystal regions are ~ 20 and ~ 35 kcal mole^{-1}, respectively, compared with an energy of ~ 150 kcal per gram atom which binds the nitrogen to the W surface.

These diffusion studies also show that nitrogen weakly held in the α and γ states does not have an appreciable diffusion lifetime in the temperature range of its stability. The activation energy for conversion to a more stable state, such as the atomically held β, or to evaporation must be comparable to the barrier that prevents hopping from one site to another. This type of behavior would be expected if nitrogen in these states were held on discrete, singular sites—a conclusion previously deduced from the fact that low-temperature evolution of nitrogen was observed in flash desorption without extensive conversion.[25]

Most unusual are the effects of adsorbed nitrogen upon the electron emission from tungsten. The formation of the weak γ state, in which nitrogen is held as molecules,[37] raises the work function, as does the α state of carbon monoxide. Atomically bound β nitrogen, however, does not conform to the pattern established for hydrogen and oxygen, which on chemisorption raise the work function. The presence of the atomic β state reduces the field emission current, but actually lowers the work function somewhat. Despite its very high binding energy to the surface (~ 150 kcal per gram atom), nitrogen thus appears as the only diatomic molecule which, when dissociated on tungsten, lowers the surface dipole moment.

[37] Or as atom pairs.

Molar Extinction Coefficients of Liquid O_3F_2, O_2F_2, and O_3 in the Visible Range*

A. D. KIRSHENBAUM AND A. G. STRENG
Research Institute, Temple University, Philadelphia, Pennsylvania

(Received March 13, 1961)

The absorption spectra for solutions of liquid O_3F_2, O_2F_2, and O_3 in a Freon mixture of $CClF_3$ and CCl_2F_2, and that of liquid O_3 in liquid O_2 were measured at 77°K and their molar extinction coefficients calculated. The effect of temperature on the molar extinction coefficient of liquid O_2F_2 in the Freon mix was studied.

IN our studies of the oxygen fluorides, O_2F_2, O_3F_2,[1,2] and O_4F_2,[3,4] it was necessary to know the molar extinction coefficients of liquid O_2F_2, O_3F_2, and O_3. A literature search showed that very little absorption data are available. The only data reported on O_2F_2 was that of Schumacher *et al.*[5] on gaseous O_2F_2 at -60°C. Recently, Maguire[6] presented a qualitative picture on the visible absorption of O_3F_2 dissolved in liquid oxygen. The only visible absorption data reported for ozone[7–10] are for gaseous O_3.

In these studies, the authors determined the molar extinction coefficients of liquid O_3F_2, O_2F_2, and O_3 dissolved in liquid O_2 and in an approximately 3:1 volume mixture of Freon 13 and Freon 12. The preparation and properties of O_3F_2 and O_2F_2 have been described previously.[1,2]

EXPERIMENTAL

Apparatus

A Beckman spectrophotometer, model DU, fitted with a special cell compartment to permit measurements at 77° to 175°K was used for the visible absorption data. The special compartment contained a silvered Pyrex glass Dewar flask with unsilvered strips for the passage of the light beam, similar to that reported by Alexander and Marvell,[11] Schoen, Kuentzel, and Broida,[12] and Caldin and Jackson.[13] The cells containing the solution and the solvent were placed inside the Dewar on a specially mounted holder which permitted their being placed into and removed out of the beam. The absorption cells were completely immersed in the coolant. The coolants used in these measurements were liquid nitrogen, Freon 12 (CCl_2F_2; mp 115°K), and Freon 13 ($CClF_3$; mp 92°K).

TABLE I.

Solvent	Molar extinction coefficient, cm^{-1} $mole^{-1}$ liter	
Freon mixture	2.81 at 570mμ	3.10 at 600mμ
Liquid O_2	1.44 at 560mμ	2 00 at 600mμ
Gaseous	1.23 at 575mμ	1.32 at 605mμ

Solvents

The solvents used were liquid oxygen and a mixture of Freon 12 and Freon 13. The mixture contained 23% by volume Freon 12 and 77% Freon 13. The liquid oxygen was used only with the liquid ozone, while the Freon mixture was used for all three (O_3, O_2F_2, and O_3F_2). The absorption spectra obtained were corrected for absorption by the refrigerants and solvents.

RESULTS

The visible absorption spectra were obtained for liquid O_3 dissolved in liquid O_2 and in the Freon 12 and 13 mixture. The coolant used was liquid N_2 (77°K). Both the liquid O_2 and Freon solutions were clear liquids at 77°K. The molar extinction coefficients were calculated, using the formula

$$D=\log_{10}(I_0/I)=AmCd.$$

The results obtained are compared in Fig. 1 with those reported for gaseous O_3 at 295°K (23°C). As can be seen, the molar extinction coefficient of O_3 is greatest when dissolved in the Freon mix as shown in Table I. The data show that the molar extinction coefficient of liquid ozone at 77°K is greater than that of gaseous ozone at 295°K.

The visible absorption spectra were obtained for

* This work was sponsored by the Office of Naval Research.

[1] A. D. Kirshenbaum and A. V. Grosse, J. Am. Chem. Soc. **81,** 1277 (1959).

[2] A. D. Kirshenbaum, A. V. Grosse, and J. G. Aston, J. Am. Chem. Soc. **81,** 6398 (1959).

[3] A. V. Grosse, A. G. Streng, and A. D. Kirshenbaum, J. Am. Chem. Soc. **83,** 1004 (1961).

[4] A. G. Streng and A. V. Grosse, "Addition and substitution products of oxygen fluorides," First Annual Progress Report for the Office of Naval Research, Research Institute, Temple University, Philadelphia, Pennsylvania, January 3, 1961.

[5] P. H. Brodersen, P. Frisch, and H. J. Schumacher, Z. physik. Chem. (Leipzig) **B37,** 25 (1937).

[6] R. G. Maguire, Air Tech. Rept. 60–287 (1960).

[7] E. C. Y. Inn and Y. Tanaka, J. Opt. Soc. Am. **43,** 870 (1953).

[8] Y. Tanaka, E. C. Y. Inn, and K. Watanabe, J. Chem. Phys. **21,** 1651 (1953).

[9] E. Vassy, Nature (Paris) **2985,** 245 (1936).

[10] C. E. Thorp, *Bibliography of Ozone Technology* (Armour Research Foundation, Illinois Institute of Technology, Chicago, Illinois, 1955), Vol. 2.

[11] E. R. Alexander and E. N. Marvell, J. Am. Chem. Soc. **72,** 3943 (1950).

[12] L. Y. Schoen, L. E. Kuentzel, and H. P. Broida, Rev. Sci. Instr. **29,** 633 (1958).

[13] E. F. Caldin and R. A. Jackson, J. Chem. Soc. **1960,** 2411.

TABLE II. Visible absorption spectra at 77°K in Freon mixture ($D = AmC^a d^b$).

Wavelength mμ	O_3		O_2F_2		O_3F_2	
	D	Am	D	Am	D	Am
350	...	...	1.76	13.13	0.814	18.76
360	...	...	1.89	14.10	...	...
365	...	...	...	...	0.765	17.63
380	...	...	1.58	11.79	0.720	16.59
400	...	...	1.075	8.02	0.735	16.94
420	...	...	0.690	5.15	0.750	17.28
430	...	...	...	...	0.750	17.28
450	...	...	0.338	2.52	0.660	15.21
470	...	...	0.166	1.24	0.575	13.25
480	...	...	...	...	0.605	13.94
500	0.027	0.27	0.084	0.63	0.519	11.96
540	0.162	1.61	...	...	0.238	5.48
570	0.269	2.68	...	...	...	...
580	0.260	2.59	0.032	0.24	0.086	1.98
600	0.315	3.14	0.014	0.10	0.005	0.12
625	0.198	1.97	0.009	0.07	0.005	0.12
650	0.123	1.22	0.012	0.09	0.005	0.12
675	0.071	0.71	...	...	0.005	0.12
700	0.037	0.37	0.014	0.10	0.000	0.00
725	0.037	0.37	...	...	...	...
750	0.009	0.09	...	...	0.005	0.12

[a] Concentration of O_3 in Freon mixture=0.1005 mole/liter. Concentration of O_2F_2 in Freon mixture=0.134 mole/liter solution. Concentration of O_3F_2 in Freon mixture=0.0434 mole/liter solution.
[b] d=1 cm.

liquid O_2F_2 and liquid O_3F_2 dissolved in the Freon mixture at 77°K. Their molar extinction coefficients are compared with those of liquid O_3 dissolved in the Freon mixture in Table II and Fig. 2. The maximum absorption for liquid O_3F_2 occurs in the region of 380 mμ to 430 mμ, the molar extinction coefficient being 17.0±0.5 cm^{-1} $mole^{-1}$ liter. Liquid O_2F_2 has its maximum at 360 mμ (14.0 cm^{-1} $mole^{-1}$ liter). Neither liquid O_3F_2 nor liquid O_2F_2 has any absorption at the wavelength that O_3 has at its maximum (3.1 cm^{-1} $mole^{-1}$ liter at 600 mμ).

The effect of temperature on the absorption of liquid O_2F_2 in the freon mixture was studied. It was observed that the higher the temperature, the greater the absorp-

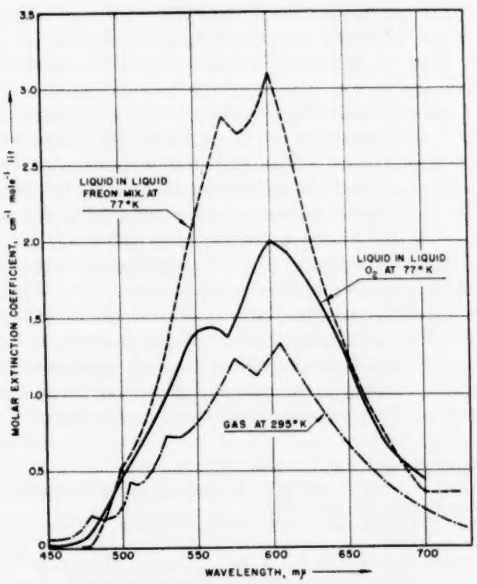
LIQUID IN LIQUID FREON MIX. AT 77°K
LIQUID IN LIQUID O₃ AT 77°K
GAS AT 295°K
MOLAR EXTINCTION COEFFICIENT, cm⁻¹ mole⁻¹ lit
WAVELENGTH, mμ

FIG. 1. Visible absorption spectra of O_3.

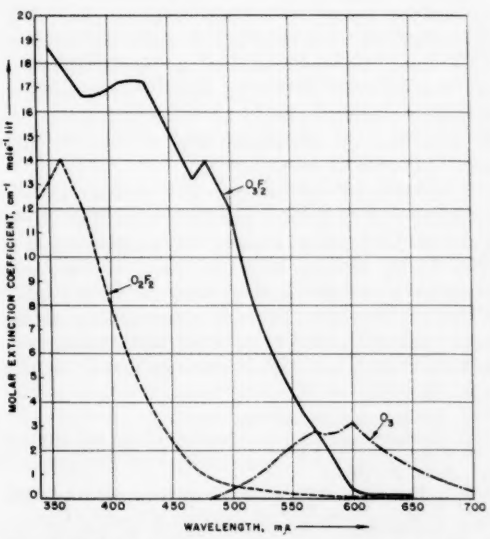

FIG. 2. Visible absorption spectra of O_3F_2, O_2F_2, and O_3 at 77°K in Freon 12+13 mixture.

tion. Its molar extinction coefficient at 360 mμ was 14.10 at 77°K, 15.27 at 140°K, and 15.65 cm^{-1} $mole^{-1}$ liter at 175°K. This agrees nicely with the color change of O_2F_2 with temperature (cherry-red liquid at 175°K and yellow-orange solid at 77°K).

ACKNOWLEDGMENT

The authors wish to thank Dr. A. V. Grosse for his helpful suggestions and the Office of Naval Research and Advanced Research Projects Agency for their support.

THE JOURNAL OF CHEMICAL PHYSICS VOLUME 35, NUMBER 4 OCTOBER, 1961

Solid State Photochemical Processes in Sodium Azide

G. J. KING, B. S. MILLER, F. F. CARLSON, AND R. C. MCMILLAN

Basic Research Group, U. S. Army Engineer Research and Development Laboratories, Fort Belvoir, Virginia

(Received January 5, 1961)

Some properties of vacancy color centers produced by ultraviolet light in NaN_3 at low temperature are studied by optical absorption and ESPR techniques. Thermal and optical bleaching experiments are discussed which allow one to correlate the optical bands with the ESPR data. The experiments are interpreted in terms of the de Boer model of the F center and the Seitz models of the F_2 and F_2^+ centers. Calculations based on the continuum models for these centers are made and are found to be in favorable agreement with the experimental data. A mechanism for the creation of vacancies and the subsequent formation of the color centers based on photolytic effects is proposed.

I. INTRODUCTION

SODIUM azide in its available pure state is a white microcrystalline powder. Clear, colorless crystalline platelets of the material may be grown, with some difficulty, from aqueous solution. The compound is an insulator, is diamagnetic,[1] and is highly ionic. It differs in thermal properties from alkali halide materials in that it decomposes[2] easily at temperatures well below its melting point (~598°K). Sodium azide is also photosensitive[3] and decomposes under uv irradiation according to the highly exothermic bimolecular chemical reaction $2N_3^- \rightarrow 3N_2 + 2e$, which creates an energy surplus of approximately 9 ev.[4] This reaction can also be produced by irradiation with x rays,[3,5] gamma rays,[6] and also by neutrons.[6]

Irradiation by the mercury 2537-A line at ~77°K produces a deep optical absorption band at 6100 A and a smaller band on the long wavelength shoulder at 7300 A. By analogy with the alkali halides,[7] these bands have been previously termed the F band and the R band, respectively. No band corresponding to the V band in alkali halides is observed when irradiation is performed with the 2537-A mercury line at ~77°K.[3] The optical bands at 6100 A and 7300 A become thermally unstable below ~298°K.

Electron spin resonances produced in sodium azide by uv irradiation have been reported previously.[8–10] Irradiation for short periods with an unfiltered mercury lamp at 573°K produces sodium metal colloids in sodium azide. The electron spin paramagnetic resonance (ESPR) of the conduction electrons of the colloidal sodium is easily observed.[8,9] Identification of the resonance as that from colloidal sodium has been corroborated by spectrophotometric means.[8]

Irradiation of sodium azide with a mercury uv lamp at 77°K, however, produces an ESPR absorption identified as an F center with resolved nuclear hyperfine interactions.[10] The difference in behavior of sodium azide at the two temperatures is attributed to the stability of photo-induced defect structure at 77°K. At the high temperature, which is only slightly below the melting point of sodium azide, thermal- and photodecomposition produce large quantities of nitrogen gas and allow remaining sodium atoms to migrate and form colloids. The process of thermal aggregation of metallic sodium in photolyzed azides has been compared to the development of photographic images.[11]

[1] G. J. King (unpublished data).
[2] W. E. Garner and D. J. B. Marke, J. Chem. Soc. **1936,** 657.
[3] J. Cunningham and F. C. Tompkins, Proc. Roy. Soc. (London) **A251,** 27 (1959).
[4] B. L. Evans and A. D. Yoffe, Chem. Revs. **59,** 515 (1959).
[5] H. G. Heal, Trans. Faraday Soc. **53,** Part 2, 210 (1957).
[6] H. Rosenwasser, R. W. Dreyfus, and P. W. Levy, J. Chem. Phys. **24,** 184 (1956).
[7] F. Seitz, Revs. Modern Phys. **26,** 7 (1954).
[8] B. S. Miller, J. Chem. Phys. **33,** 889 (1960).
[9] G. J. King, B. S. Miller, F. F. Carlson, and R. C. McMillan, J. Chem. Phys. **32,** 940 (1960).
[10] F. F. Carlson, G. J. King, and B. S. Miller, J. Chem. Phys. **33,** 1266 (1960).
[11] N. F Mott and R. W. Gurney, *Electronic Processes in Ionic Crystals* (Oxford University Press, New York, 1950), Chap. 8, p. 265.

II. EXPERIMENTAL PROCEDURES

Microcrystalline standards of sodium azide powder of very high purity were prepared by direct reaction of gaseous hydrazoic acid and pure sodium metal. The hydrazoic acid used in this procedure was prepared by the method of Kemp[12] in order to avoid sulfate contamination introduced into the hydrazoic acid during its production. In this manner, dry iron-free sodium azide is produced which shows a diamagnetic susceptibility of -17×10^{-6} cgs units per mole. Normal, chemically pure samples of sodium azide contain iron as a result of their manufacture and commonly show paramagnetic behavior. The impurities can usually be eliminated by multiple recrystallization of the material.

The crystals of sodium azide which were used for all optical measurements were grown from saturated aqueous solution. Until very recently, crystals suitable for optical experiments were obtained only with great difficulty. After an extensive investigation of environmental growth conditions, Kezer[13] has determined the parameters needed for successful production of large quantities of crystals of optical quality. These crystals are in the form of thin platelets which typically are $6\times6\times0.1$ mm in size. Careful selection procedures are required to avoid use of crystals exhibiting morphological disturbances such as twinning and stacking faults. These defects seriously interfere with optical measurements since the index of refraction of sodium azide is anisotropic. Occasionally a crystalline sample was crushed into a powder and its behavior compared to that of the pure dry powder in ESPR experiments.

The high-purity microcrystalline sodium azide samples were prepared for ESPR measurements in such a manner as to prevent contamination by contact with air or water. The azide was placed in a fused silica tube and the tube then evacuated to a pressure of 2×10^{-5} mm Hg. The fused silica tube was then sealed off with a torch. No microwave resonances were detected when such untreated samples were examined in the ESPR spectrometer. In some cases, to improve thermal contact for low-temperature experiments, the sample tubes were filled with helium gas to a pressure of about 0.5 mm Hg.

During the torching off of the sample, the azide in the tube is subjected to irradiation from the hot fused silica. By comparison with other sealing methods, no effect traceable to this irradiation was found. A small amount of sodium azide also decomposes near the sealoff point giving deposited sodium metal and pure nitrogen gas. The part of the tube covered by the sodium metal does not enter the sensing volume of the microwave cavity but does, however, serve as an effective getter for any residual active gases such as oxygen.

[12] M. D. Kemp, J. Chem. Educ. **37**, 142 (1960).
[13] O. F. Kezer (to be published).

Ultraviolet irradiation of the sealed sample through the fused silica tube was performed by using a Hanovia SH616A mercury vapor lamp placed approximately 5 cm from the sample. During the irradiation the sample was barely submerged in an open Dewar of liquid nitrogen. This rather crude arrangement permits optimum aperture conditions, results in efficient sample cooling, and the gas from the boiling nitrogen provides an optical path which transmits short-wavelength uv light.

The sample tube was periodically shaken to obtain mixing of the powder to assure good irradiation coverage. Approximately one hour of this treatment was sufficient to color the sample deep blue.

Irradiation with uv light at 195°K was accomplished by pressing the sample tube into dry ice powder in the Dewar instead of liquid nitrogen. In cases where optical bleaching of color centers was attempted, a Sylvania Blue Top type 300T8–½ tungsten projection lamp was used in conjunction with water heat filters and various suitable Corning glass filters.

All of the ESPR measurements were performed at 77°K. After appropriate sample treatment at a desired temperature, speedy transfer to a quick-sealing, low-temperature H_{102} cavity surrounded by a Styrofoam Dewar completed the preparation without allowing significant temperature change of the sample. The cavity had a quick-sealing entry port which allowed approximately three-fourths of the fused silica sample tube to extend beyond the limits of the cavity proper. The sample tube was approximately one-fourth filled (1 cc) with sodium azide. By proper mechanical treatment of the cavity the entire powdered sample could be shaken out of the sensitive volume of the cavity while the fused silica tube was held rigidly in its original position in the cavity. In this way, precise blank runs were obtained and any sample holder effects eliminated. Unless otherwise stated, in every case the optical and ESPR measurements were performed at 77°K.

The spectrometer used in these experiments consisted of a Varian type V4500 EPR spectrometer, a Varian regulated power supply type V2100A, and a 12-in. type 4012 high-resolution NMR magnet. A simple X band magic tee bridge with the AFC locked on to the sample cavity was employed for the majority of the measurements. Air-cooled VA201B klystrons, which are low noise and stable, were used for the majority of the measurements. Some high-power experiments were performed using a Varian type V58 klystron. The field of the magnet was modulated at 200 cps in most of the experiments.

Klystron frequencies were measured by means of a Hewlett-Packard type 540B frequency counter system and magnetic field strengths were determined by a proton magnetometer designed by Singer and John-

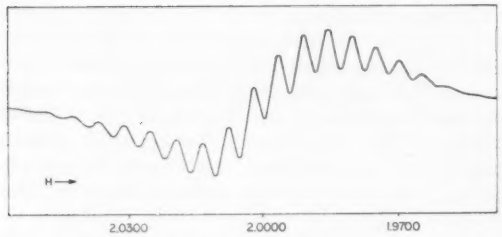

FIG. 1. The slope $d\chi''/dH$ of the ESPR absorption in sodium azide powder at high power. The spectroscopic splitting factor g is given for three points. Field modulation is 3 gauss at 200 cps. Temperature is ~77°K.

son.[14] This is an excellent instrument if moderate care is given to placement of components and shielding of the rf choke.

Optical measurements were performed using a Beckman DK-2 spectrophotometer which was equipped with a liquid-helium cryostat.[8] All optical measurements were transmission type and thin crystalline platelets of NaN_3 were used.

III. CORRELATION OF OPTICAL AND ESPR ABSORPTION BANDS

Initial experiments served to correlate the optical bands with the corresponding ESPR bands produced by uv irradiation at 77°K. Several criteria were used for deciding that a particular optical band and ESPR absorption were produced by the same defect center. It was required that the particular optical absorption to be related to an ESPR absorption must first show identical thermal and optical bleaching properties and that these properties should be unique to both of the absorptions. Another criterion was that, once a correlation was made, the optical band and the ESPR absorption should have separate and independent justifications within their own disciplines or techniques. That is, the F optical band should fit some optical model explaining its center wavelength with respect to other bands. The ESPR absorption for an F center should fit the symmetry properties and other reasonable requirements of an F-center spin resonance.

In the initial ESPR experiments, microcrystalline samples of sodium azide were irradiated for one hour with uv light at 77°K and then examined in the ESPR spectrometer. At sufficiently high power, a strong symmetric resonance with resolved hyperfine structure (Fig. 1) was observed, which previously[10] was ascribed to an F-center resonance.

Single crystal plates of sodium azide, given the same irradiation treatment and also kept at all times at 77°K, were found to exhibit optical absorption bands at 6100 and 7300A [Fig. 2(a)]. These two optical bands were the only two bands discernible after short-term (approximately 1 hr) irradiation at 77°K. Long duration (approximately 10 hours) uv irradiation at 77°K yielded other optical absorption bands which, however, were at least 100 times smaller than the 6100 A and 7300 A optical bands. These two optical bands were previously observed by Cunningham and Tompkins[9] in fresh crystals under the same general irradiation conditions. The ratio of the area of the 7300-A band to the area of the 6100-A band was found to be smaller in their experiment than in ours. This difference is possibly associated with the difference in the optical properties of the uv light sources used in the experiments. In our experiments it was found that the 7300-A optical band bleached rapidly at 195°K with the accompanying growth of the 6100–A band. The same thermal treatment given to the sample used in ESPR caused the F-center resonance to bleach and exposed a broad asymmetric absorption (Fig. 3) which was, in part, present before thermal bleaching (see below).

In addition to the thermal bleaching experiments, the 6100–A and 7300–A bands were irradiated with resonance radiation, as well as other wavelengths above the first absorption edge, in an attempt to bleach them optically. It was found, for irradiation with light within the 7300–A band alone, that the 7300–A band

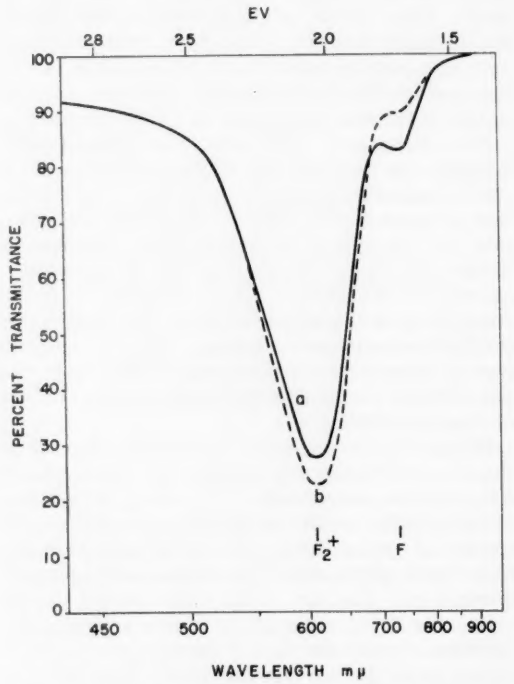

FIG. 2. (a) NaN_3 exposed to Hg vapor lamp for 15 min at 77°K. (b) After exposure to F-band light. Both curves measured at 77°K. The crossover point at 680 mμ is a point of constant absorption for this bleaching process.

[14] J. R. Singer and S. D. Johnson, Rev. Sci. Instr. **30,** 92 (1959).

bleached and the 6100–A band grew. The 6100–A band did not bleach with light of any wavelength between 3000 A and 10000 A. The ESPR absorption curve for the *F* center (Fig. 1) was found to have the identical optical bleaching properties to the 7300-A band.

The possibility of the presence of a second ESPR band lying under the *F*-center ESPR signal (Fig. 1) was then investigated, since the simultaneous presence of two optical bands possibly indicated the simultaneous presence of two separate ESPR signals. It was found that when the microwave power was reduced at least 15 db the symmetric *F*-center signal (Fig. 1) became distorted on the low magnetic field side (Fig. 4). Further reduction in power (20 db) produced an asymmetric resonance signal very similar to the bleached signal (Fig. 3). It was concluded that the sensitivity of shape to power is caused by the presence of a second ESPR center which saturates at less power than the *F* center and which is very asymmetric in its spin properties. Thus, a second center was found which was simultaneously present with the *F* center and which was asymmetric and possessed an unpaired spin. Further, by power desaturation it was demonstrated that the second ESPR center had the same ESPR character as the signal remaining after optical or thermal bleaching at 195°K. The ESPR powder data showed that the *F*-center resonance possessed a very large isotropic component since a large symmetric ESPR signal is observed in the powdered material. Questions concerning the actual mixing of the signals, e.g., how much of the envelope of the symmetric signal at high power actually belongs to the second more saturable asymmetric signal, could not be determined from the powder data. The reasons for this are that the spectrometer sensitivity to the individual signals is very much different because of linewidths and the non-isotropic behavior of the second center does not permit proper assessment of that center in the powdered material. Discussion of these aspects is deferred to Sec. VIII. For present purposes the ESPR information from powder samples is presumed to be sufficient.

One further correlation remained. The optical band at 6100 A bleached in the order of minutes at room temperature. The asymmetric ESPR band showed the same behavior and at the same time the blue color of the material disappeared. Optical bleaching could not be accomplished, as previously noted.

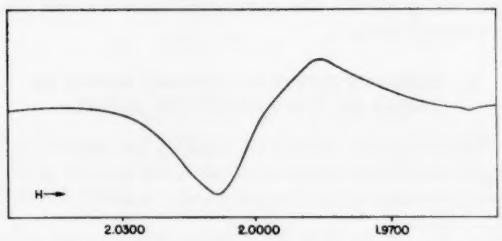

FIG. 3. The slope $d\chi''/dH$ of the ESPR absorption in sodium azide powder after thermal bleaching of the *F* center at 195°K. Data taken at 77°K. The spectroscopic splitting factor g is given for three points.

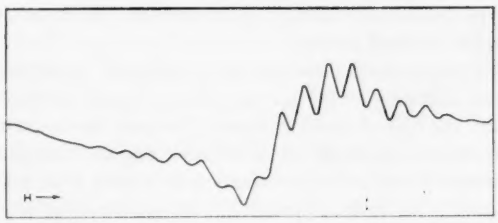

FIG. 4. The slope $d\chi''/dH$ of the ESPR absorption in sodium azide powder at reduced power (15 db). Other conditions are the same as in Fig. 1.

In summary, the 6100-A band (Fig. 2) is presumed to be caused by the same center which produces the broad ESPR signal (Fig. 3). The 7300-A band (Fig. 2) and the *F*-center resonance curve (Fig. 1) are presumed to be both produced by the *F* center.

IV. OTHER PROPERTIES OF THE BANDS

Irradiation at 77°K

The color centers produced by uv irradiation in NaN_3 at 77°K have some of the peculiarities of optical and thermal bleaching of color centers in alkali halides. The 7300-A *F* band is slightly unstable at 77°K, decaying roughly 20% in the first 24 hours. When bleached at 195°K, the process proceeds in several minutes to roughly 90% completion. The remaining *F* centers are "hard," a situation common to alkali halide *F* centers. These "hard" *F* centers can even tolerate several seconds of exposure to room temperature. Optical bleaching also presents the same behavior, some *F* centers showing "hard" behavior. The ESPR measurements agree in detail with all of the optical experiments in this connection.

It is presumed that outer surface effects may be responsible for some of the "hard" *F*-band behavior. At 77°K the first exciton absorption band is centered at 2400 A. All the output of our uv lamps which is effective in photolysis of NaN_3 is from 2537 A down to shorter wavelengths. The 50% transmission point in our crystals is approximately 2500 A. Thus, much of the short-wavelength incident light is absorbed on the surface. For this reason, proper comparison of the ESPR and optical data required running ESPR data on single crystals having the same approximate thickness as the optical samples. This work is included in Sec. VIII.

Optical bleaching of the 6100-A band does not occur, even after a three hour irradiation with a filtered 1-kw tungsten projection lamp (see also Sec. III). This resistance to optical bleaching is typical of coagulation-

type centers such as those responsible for the R and M bands in alkali halides.

During optical bleaching by F light at 77°K or thermal bleaching at 195°K, the 7300-A F band decreases and the 6100-A band increases. No other bands occur in crystals uv irradiated for one hour, and the bleaching process is entirely a two component system as is indicated by an isosbestic point. The ratio of area of growth of the 6100-A band to decrease of 7300-A band is roughly three. This permits the interpretations that the oscillator strength of the 6100-A band is greater than that of the 7300-A band or that one of the centers causing the 7300-A band decays into more than one of the centers causing the 6100-A band. A model which fits the optical observations (see Sec. VI) agrees with the former choice.

Irradiation at Helium Temperature

The optical bands at 6100 A and 7300 A were found to form with only slightly reduced efficiency at liquid-helium temperature. The optical bleaching of the 7300-A F band occurs readily at liquid-helium temperature also. While the optical bleach of the F band at 77°K is always accompanied by growth of the 6100-A band, at liquid-helium temperature, we found no growth at all of the 6100-A band when the F band was optically bleached. When the optically bleached sample was then raised to 77°K for 30 min and subsequently recooled to liquid-helium temperature, it was found that the 6100-A band had now grown (without any other changes in the absorption curve). The F band had not changed at all during the thermal treatment at 77°K.

A second, blank run, experiment was then performed which was identical in all respects to the previous experiment, except that no optical bleaching was attempted. In this case the band at 6100 A grew during thermal cycling at 77°K at the expense of the 7300-A band. Thus, the formation of the 6100-A band from the 7300-A band is primarily a thermal coagulation process. The optical bleaching at liquid-helium temperature removes an electron from the F-center vacancy but the liquid-helium temperature does not permit the vacancy to migrate. Apparently, the F center is definitely more stable at liquid-helium temperature than at 77°K, as is indicated by the thermal decay of the optical band. An important conclusion is, however, that coagulation of the F centers yields more of the centers responsible for the 6100-A band. Other conclusions are that some of the F centers formed at liquid-helium temperature are unstable at 77°K and the F vacancy is mobile at 77°K.

V. PRODUCTION OF ANION VACANCY TRAPS BY PHOTOCHEMICAL REACTIONS

In alkali halides, the production of an F band by uv light[15,16] may lead to the formation of auxiliary bands on the long wavelength side of the F band by coagulation of F centers or F-center vacancies. It appears that the formation of single vacancies in the initial stages of irradiation is favored since the F band is normally very much larger than R- or M-type bands. In sodium azide, assuming reasonable oscillator strengths, the formation of the F band as a primary band does not seem to occur since it is much smaller than the 6100-A band. This is in direct accord, however, with the chemical nature of the azide ion. A basic mode of photolytic decomposition available to sodium azide can be summarized by the bimolecular decomposition $2N_3 \rightarrow 3N_2$ which is exothermic in the amount of 9 ev.[4] This reaction produces sodium metal as the other product. The unimolecular decomposition of an azide ion by a ground-state process into N_2 and N is not favored by conservation rules.[4] In the event the excited state unimolecular interaction can be photolytically induced within the lattice, it is likely that the N atom or ion would interact with adjacent azide ions. This, in effect, accomplishes a bimolecular decomposition if the reaction $N+N_3^- \rightarrow 2N_2+e$ can then occur. If one assumes that adjacent azide ions in the lattice are induced to interact by the action of uv irradiation, then three N_2 gas molecules will be produced in the center of a considerable thermal spike. This process of interaction may be assisted by defects such as excitons, internal surfaces, and other imperfections. Since the N_2 molecule is small in comparison to the lattice dimensions of sodium azide, the probability is large that it will diffuse rapidly from the spike. This process requires that double anion vacancies be produced in preference to single anion vacancies. This agrees with a model adopted to fit the NaN_3 optical band structure, which assumes that the 6100-A band is formed by two vacancies with a trapped electron.

The occurrence of photo processes at low temperatures within the crystals is consistent with some previous studies[8,9] on sodium colloids but does not exclude external surface effects. The ESPR results are, however, primarily due to volume effects and not due to external surfaces.

VI. INTERPRETATION OF OPTICAL BANDS IN TERMS OF THE CONTINUUM MODEL

The location of the 6100-A band on the short wavelength side of the F optical band is the reverse of the usual behavior of the R-type bands in alkali halides.

---

[15] J. A. Cape, Phys. Rev. **122**, 18 (1962).

[16] P. W. M. Jacobs, 1959 International Symposium on Color Centers in Alkali Halides, Oregon State College, Corvallis, Oregon (unpublished).

On the basis of a continuum model[17,18] modified to fit the wavelength of the F-center optical band,[18] this behavior serves to point out the particular center responsible for the 6100-A band. The continuum model for R-type centers is based on the assumption that the optical transitions of the R-type centers in alkali halides can be interpreted in terms of the transitions of hydrogen molecules or molecule ions immersed in an effective dielectric continuum. According to this model, the only simple transition occurring on the short wavelength side of the F band is the $1s\sigma_g \rightarrow 2p\pi_u$ transition of the hydrogen molecule ion, or in the notation of Seitz, the F_2^+ center. In order to compare theoretical and experimental values, the effective dielectric parameter was assumed to be that demanded by the continuum theory to fit the F-center optical band position, $K=2.45$.

The crystal structure of sodium azide is rhombohedral (Fig. 5) and there are two likely vacancy pairs which can produce F_2^+ centers. An azide ion in sodium azide has six nearest neighbor sodium ions at a distance of 3.28 A from the center of the azide ion. These sodium ions are symmetrically placed about the azide ion in a roughly isotropic manner. The next nearest spherical shell of ions about the azide ion consists of 12 azide ions, if one considers not the center-to-center distances of the ions but the distance of closest approach. Sodium azide has a layer structure which separates the sodium and azide ions into parallel planes to which the [111] direction in the lattice is perpendicular. The separation of the center of each azide ion in the azide plane is 3.62 A, and since the internuclear axes of the ions are parallel, this is the minimum separation. The separation of the center of each azide ion from its nearest neighbor in the next azide plane is 5.46 A, but due to the length of the azide ions the actual minimum separation is only 3.42 A.

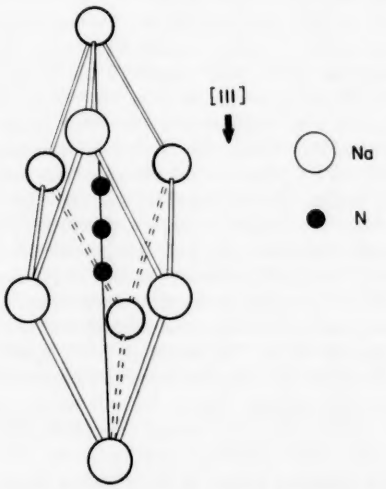

FIG. 5. Rhombohedral unit cell of sodium azide [see S. B. Hendricks and L. Pauling, J. Am. Chem. Soc. **47**, 2904 (1925)]. Magnetic field direction for ESPR single crystal measurements is shown. The light beam direction in optical measurements is also parallel to [111].

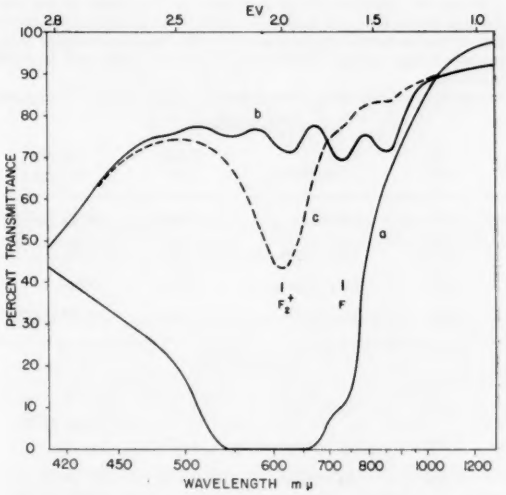

FIG. 6. (a) NaN_3 exposed to Hg vapor lamp for 18 hr at 77°K (b) Same crystal after thermal bleaching at 298°K for a few seconds. (c) Same crystal as (b) after exposure to filtered tungsten lamp. (All wavelengths greater than 420 mμ removed). Curves measured at 77°K.

In forming adjacent anion vacancies in sodium azide, the chemical reaction may involve the transport of a single N atom from the decayed azide radical site to the nearest azide ion. While the center-to-center separation of one possible vacancy pair is much larger than that of the other, the actual transport distances are nearly the same. Thus, two types of F_2^+ centers are to be expected. The 6100-A band was carefully investigated for structure by bleaching techniques and the two F_2^+ bands were found. The standard method was used to form the 7300-A and 6100-A bands except the irradiation lasted for 18 hr and very deep bands were formed [Fig. 6(a)]. The sample was then bleached by rapidly warming to 298°K and then immediately recooling to 77°K. The optical absorption curve then showed five distinct bands in the space covered by the 6100-A and 7300-A bands [Fig. 6(b)]. By using photoemission techniques (see below) it has been possible to show that the 5470-A band and the 6250-A band grow in a unique manner and merge into one band having an apparent center at 6100 A.

[17] R. Herman, M. C. Wallis, and R. F. Wallis, Phys. Rev. **103**, 87 (1956).

[18] B. S. Gourary and F. J. Adrian, in *Solid-State Physics*, edited by F. Seitz and D. Turnbull (Academic Press Inc., New York, 1960), Vol. 10, p. 127.

TABLE I. Predicted band positions on the basis of the continuum model for color centers in NaN_3. The internuclear separation of the vacancies is given in angstroms and the energies of the corresponding optical transitions in electron volts and in millimicrons.

R (A)	Transition	E calc ev	E obs ev (mμ)
	F_2^+ transitions		
3.62	$1s\sigma_g \rightarrow 2p\pi_u$	2.46	2.27 (547)
5.46	$1s\sigma_g \rightarrow 2p\pi_u$	1.97	1.97 (625)
3.62	$1s\sigma_g \rightarrow 2p\sigma_u$	0.84	None
5.46	$1s\sigma_g \rightarrow 2p\sigma_u$	0.41	0.49 (2520)
	F_2 transitions		
3.62	$^1\Sigma_g^+ \rightarrow {}^1\Sigma_u^+$	1.45	1.45 (850)
5.46	$^1\Sigma_g^+ \rightarrow {}^1\Sigma_u^+$	1.33	
3.62	$^1\Sigma_g^+ \rightarrow {}^1\Pi_u$	1.70	F band 1.70 (730)
5.46	$^1\Sigma_g^+ \rightarrow {}^1\Pi_u$	1.65	

Based on the assumption that the F-center band is at 7300 A, the continuum model predicts the bands given in Table I. The agreement of the observed data and the predictions of the simple theory are surprisingly good. The F_2^+ transitions for the 3.62-A separation are not in close agreement but this type of F_2^+ center is expected to show some asymmetric[19] character while the F_2^+ center for the 5.46-A separation is expected, from consideration of the lattice structure, to be symmetric. The predicted infrared band at 0.41 ev occurs in the molecular absorption bands of the azide ion. Investigation showed, however, that one of the bands at 0.49 ev occurred only when there was a high density of F_2^+ centers in the crystal and further this band bleached when the F_2^+ band was thermally bleached.

The continuum model also predicts four transitions for the F_2 centers. Two of these bands are superimposed. Some, but not all, of the "hard" character of the F centers may be due to this situation. The band at 4850 A is very weak and for the present is not identified.

The interpretation of the compound optical absorption band at 6100 A as one due to a single electron trapped at a double anion vacancy is further strengthened by the ESPR data. The ESPR resonance associated with the F_2^+ centers or 6100-A band is asymmetric on the powdered material and has a negative g-value shift from that of a free electron. The asymmetry of the resonance is produced by the anisotropic structure of the center and the anisotropic crystalline effects in sodium azide. The negative value of the g shift is in accord with the idea that the center is a trapped electron.

Presumably the preferential formation of the F_2^+ centers instead of the F_2 centers is connected with initial conditions during formation of the double vacancy. The relaxation of the lattice to accommodate the vacancies, and conditions such as precise location of lattice ions around the vacancies are presumed to be the determining processes. Once the conditions suitable for the existence of an F_2^+ center are established, the stability against capture of a second electron may be influenced by lattice polarization effects.

VII. PHOTOEMISSION EXPERIMENTS IN SODIUM AZIDE

Once a sodium azide crystal has been used for F-center experiments and then allowed to warm to room temperature, it is considered to be "old" since it contains large amounts of sodium metal.[3,8] This is seen as a large band centered at 3300 A due to atomic sodium. It is possible to bombard "old" sodium azide crystals with dense internal electron showers by irradiating the sample with a tungsten lamp, thus producing photoelectrons from the sodium metal. The tungsten lamp otherwise produces no vacancies in the crystal since the wavelengths are too long to be active. This property is used to investigate the stability of vacancies in sodium azide without perturbing the number of vacancies present.

The crystal discussed in the previous section and shown in Fig. 6(b) is considered to be an old crystal. During the short time (about 1 min) bleaching at 298°K the electrons in the color centers are thermally promoted from the vacancies and the vacancies are made mobile. When the crystal is immediately recooled to 77°K, the less mobile vacancies are trapped in the lattice. The absorption bands in Fig. 6(b) are only from the "hard" remnants which have managed to retain their electrons. The vacancies which have low mobility, being still present, can now retrap an electron if there is a sufficient density of electrons available. Irradiation with a tungsten lamp supplies the electrons. The growth of the F_2^+ bands at 5470 A and 6250 A into the 6100-A composite band can be studied in detail by this method. Figure 6(c) shows the condition of the crystal originally having the optical character of Fig. 6(b), after 2 hours of irradiation at 77°K with a filtered tungsten lamp. It is apparent from the regrowth of the F_2^+ bands that many double vacancies were trapped in the lattice. The double vacancies have low mobility and high stability in comparison to the single F vacancies. The apparent simultaneous bleaching of the 7300-A and 8500-A bands indicates that a large part of the 7300-A band in this experiment may not be due to hard F centers but rather to F_2 centers. The continuum model (see Table I) predicts bands near 7300 A and 8500 A for the four transitions of the

[19] V. Ya. Zevin, Soviet Phys.-JETP **36**(9), 81 (1959).

F_2 center. It is conceivable that these bands are produced by F centers which have coagulated in special sites and are bound. Capture of electrons to form F' centers may be responsible for the apparent bleaching.

At the present time, experiments are being conducted which use this method to measure directly the mobilities of the vacancies in sodium azide. It has been found that if the thermal bleaching of the sample lasts 12 hr at room temperature, that no amount of tungsten lamp irradiation will cause band growth at 77°K.

The most important conclusion of the experiment represented in Fig. 6 is that the double vacancies resulting in the F_2^+ bands do not result from coagulation of single vacancies but have an independent existence. The 12-hr thermal bleaching experiment, above, indicates also that none of these double vacancies are present in the crystal previous to uv irradiation at 77°K. The experiments do not preclude the formation of double vacancies by coagulation but statistically one would expect the F band then to be much larger than the F_2^+ bands. Presumably, the small band at 8500 A in Fig. 6(b) is a coagulation band, probably an F_2 band.

VIII. ESPR EXPERIMENTS ON SODIUM AZIDE SINGLE CRYSTALS

Most of the ESPR work was done on powders to allow a large number of experiments to be performed and yet conserve a small supply of good single crystals available for use. In addition, future work comparing normal sodium azide with nitrogen-15 tagged sodium azide was intended and growth of large crystals containing this material is very costly. The information found in single crystal ESPR experiments confirms the results and interpretations of the powder experiments.

Crystals selected for ESPR experiments were required to satisfy the same criteria as those for use in optical experiments. Particular attention was given to optical clarity and absence of twinning. This latter defect and related stacking faults produce temperature dependent variations in structure which result in spurious optical bands at low temperatures.

The supply of ten excellent crystals was selected from five large batches which were grown at different

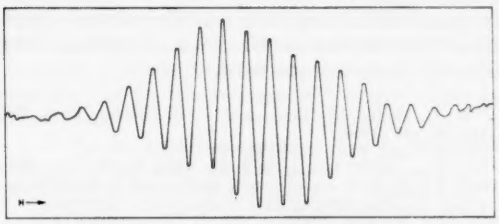

FIG. 7. The slope $d\chi''/dH$ of the ESPR absorption in a sodium azide single crystal. The field of the magnet is in the [111] crystal direction. The temperature is 77°K. Spin density approximately 10^{18} per cm^3.

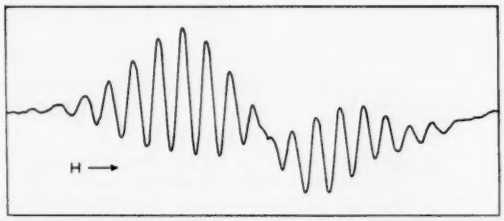

FIG. 8. The slope $d\chi''/dH$ of the ESPR absorption in sodium azide single crystal. The angle between the [111] direction and dc magnetic field is approximately 45°.

times. Each batch contained a minimum of 500 large (10×10×0.1 mm) crystals of good optical clarity. All ESPR measurements performed on crystals from this select sample agreed quantitatively in results.

The uv irradiation at 77°K of the sodium azide crystals was performed in the same manner as with the microcrystalline powders. In addition, the thermal and optical bleaching experiments were redone. In every case, the conclusions reached using the powdered material were supported by the data taken on crystals.

For a single crystal oriented with the dc magnetic field in the [111] direction (Fig. 5), the ESPR signal is almost entirely attributable to the hyperfine structure of the F center (Fig. 7). The line separation is approximately 9 gauss and the peak-to-peak-on-the-derivative linewidth is approximately 5 gauss. While the envelope of the ESPR trace changes shape markedly for other orientations, a set of lines having very closely the same line separation and linewidth as the F-center resonance can easily be found, regardless of crystal orientation (see Figs. 8 and 9). The close maintenance of the line spacing and linewidth of the F-center resonance hyperfine lines (Fig. 7) in all orientations is assurance that the large distortion of the resonance envelope in some orientations is produced by at least one other independent and separate center. At the same time this situation gives evidence of the isotropy of the F center, which reflects the good isotropy of the six sodium ions which form the first shell around the anion vacancy.

The distortion of the F-center resonance curve as shown in Figs. 8 and 9 is attributed here to the F_2^+ center. It was previously shown (Sec. III) that the 7300-A optical F band bleaches thermally at 195°K and F_2^+ centers remain. The corresponding ESPR experiment was performed to separate the F- and F_2^+-center resonances. The crystal was uv irradiated at 77°K and the ESPR curves were obtained as a function of angular orientation with respect to the dc magnetic field. The crystal was then bleached for 20 min at 195°K and orientational studies repeated under exactly the same conditions as in the previous experiment. A comparison of the ESPR traces for the same crystal and the same orientation before and after

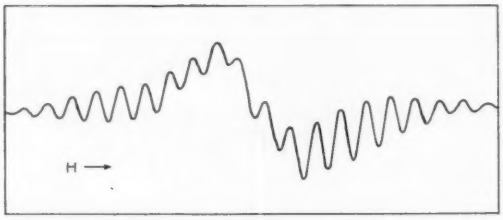

FIG. 9. The slope dX''/dH of the ESPR absorption in sodium azide single crystal. The angle between the [111] direction and the dc magnetic field is 90°. Temperature is 77°K.

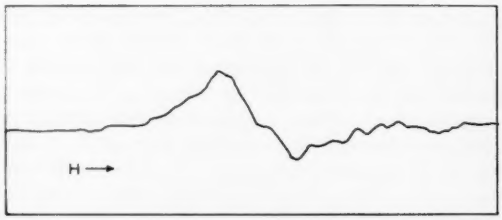

FIG. 10. The slope dX''/dH of the ESPR absorption in sodium azide single crystal after bleaching for 20 min at 195°K. The same crystal and orientation as in Fig. 9 and identical spectrometer settings. Temperature is 77°K.

bleaching is afforded by Figs. 9 and 10. The ESPR lines having the 9-gauss separation have bleached in Fig. 10, which is in agreement with the powder data (Figs. 1 and 3). It is apparent that the largest part of the shape of the envelope of Fig. 9 is supplied by the resonance shown in Fig. 10. Comparison of the bleached and unbleached signals for other orientations shows the same general result. Where the envelope of the series of lines with the 9-gauss separation appears strongly "modulated," the signal remaining after bleaching is strong and its over-all shape is that of the apparent modulation of the unbleached signal for the particular orientation. Figure 7 represents a relatively pure *F*-center ESPR signal. It was found that the F_2^+ signal corresponding to the orientation of Fig. 7 was sufficiently broad to preclude its simultaneous display when the spectrometer was set to display the narrow *F*-center hyperfine lines.

The central g value of the *F*-center resonance appears to be constant for all orientations of the crystal. It is difficult to make statements concerning the central g value of the resonance curve of the 195°K bleached crystals. It is apparent that these curves generally consist of at least two wide line resonances of from 30 to 50 gauss peak to peak and several other partly resolved narrow lines. The rather complicated ESPR behavior of the F_2^+ center is to be expected. Because the F_2^+ center will reflect the symmetry of the crystal, the magnitude of the hyperfine interactions should be dependent on crystal orientation with respect to the dc magnetic field. Because there are two sets of F_2^+ centers and also the crystal structure is complex there will generally be many sets of nonequivalent F_2^+ centers displayed for any given crystal orientation. This situation, in addition to the broad linewidths, will tend to suppress ESPR signals from the F_2^+ center.

The orientational studies clearly show that there are at least two separate centers present one of which, the *F* center, has an isotropic ESPR behavior and the other, an anisotropic behavior. Further, there is a direct correlation between the existence of the 7300-A optical band and the *F*-center ESPR band. In addition, the 6100-A optical band has a counterpart in an ESPR band which belongs to the center having anisotropic hyperfine interactions. It has not been possible using simple techniques to analyze the orientational anisotropy effects because of their complexity.

The appearance of an *F*-center ESPR signal with resolved hyperfine structure in sodium azide is rather surprising. That *F* centers can have resolved hyperfine structure has now been settled.[20–22] As an alternative hypothesis, it was thought possible that the hyperfine ESPR structure (Fig. 7) was due to nitrogen fragments. This hypothesis is rendered untenable by the data. The constancy of the hyperfine line spacing and linewidth for all orientations of the crystals demands a highly isotropic structure. Thus, any more complicated nitrogen fragment than N itself is precluded. However, the triplet nitrogen ESPR signal, with accompanying free-radical glow during decay, has recently been observed in x ray-irradiated sodium azide.[23]

It is difficult to imagine any different trapping site for nitrogen which here would give the number and intensity of lines observed. The weight of evidence obtained from single crystal data is thus very much in favor of the interpretation of the ESPR signals in terms of the de Boer *F* center and at least one other vacancy-type center.

ACKNOWLEDGMENTS

The work of M. D. Kemp in the difficult and hazardous preparation of the pure compound is gratefully acknowledged. The successful effort of O. F. Kezer in the production of large clear crystals has been of great value. The interest of Dr. Z. V. Harvalik, Group Director, is much appreciated.

[20] W. C. Holton, H. Blum, and C. P. Slichter, Phys. Rev. Letters **5,** 197 (1960).
[21] N. W. Lord, Phys. Rev. **105,** 756 (1957).
[22] H. Blum, W. C. Holton, Bull. Am. Phys. Soc. **6,** 112 (1961).
[23] G. J. King, F. F. Carlson, B. S. Miller, and R. C. McMillan, J. Chem. Phys. **34,** 1499 (1961).

Diffusion of Neon Isotopes in Fused Quartz

R. C. FRANK, D. E. SWETS, AND R. W. LEE
Research Laboratories, General Motors Corporation, Warren, Michigan

(Received April 21, 1961)

The diffusion of Ne^{20} and Ne^{22} through the walls of high-purity fused quartz hollow cylinders was studied using a mass spectrometer as a detecting device. The diffusion process was found to be relatively simple and fairly well described by Fick's laws. Diffusion coefficients and permeabilities were measured for both isotopes in the temperature range of 440° to 985°C. The D_0's for Ne^{20} and Ne^{22} were $(2.21\pm0.12)\times 10^{-4}$ cm²/sec and $(2.08\pm0.17)\times10^{-4}$ cm²/sec respectively. The activation energy for diffusion for Ne^{20} was 11 370±80 cal/g atom and the value for Ne^{22} was found to be statistically equivalent to this. The best estimate of the ratio of the D_0's was 1.05±0.01. Solubilities were calculated by dividing the permeabilities by the diffusion coefficients. The heats of solution for the two isotopes were the same and equal to −1950± 150 cal/g atom. The significance of the isotope effect in diffusion is discussed.

I. INTRODUCTION

THE existing information about the diffusion of neon in fused quartz is rather meager. T'sai and Hogness[1] made a study of the permeability of neon through fused quartz a number of years ago and more recently it was measured by Norton.[2] However, the diffusion coefficients were apparently never measured. Leiby and Chen[3] measured the permeability and diffusion coefficient of neon in Vycor, a commerical form of silica glass containing about 3% of impurities. Diffusion coefficients have considerable theoretical significance for determining solid state processes so it is desirable to know these as accurately as possible.

The relatively high natural abundance of a second stable isotope, Ne^{22}, makes neon an attractive element to use for studying isotope effects in diffusion. One of the tests which can be applied to a theory of the mechanism of diffusion is whether the theory correctly predicts the isotope effect. Some of the earlier semi-empirical formulations of D_0 such as the Langmuir-Dushman theory[4] did not clearly predict an isotope effect. Those theories of D_0 which are based on the transition state concept usually predict that the D_0 will vary as the reciprocal of the square root of the mass or reduced mass of the diffusing particles.[5–7] One recent theory based on an integration of the Liouville equation predicts that D_0 will vary as the reciprocal of the square of the mass.[8] Schoen has suggested that if a careful study were made of isotope effects it should be possible to determine whether a given diffusion process is interstitial or takes place by means of the interstitialcy (jumping of atoms between vacancy and interstitial positions) or by the vacancy mechanism.[9] This has has been recently reaffirmed by Tharmalingam and Lidiard.[10]

Earlier attempts to study the isotope effect in the diffusion of gases in fused quartz were made by Jones[11] with He^3 and He^4 and also in this laboratory with hydrogen and deuterium.[12] In the work to be reported here the permeabilities and diffusion coefficients of neon in fused quartz have been measured in the temperature range of 440° to 985°C using a mass spectrometer as a detecting device. From this the solubilities have also been computed. This was done for the two different isotopes, Ne^{20} and Ne^{22}, and the ratios of the diffusion coefficients and permeabilities have been calculated.

II. EXPERIMENTAL

The fused quartz diffusion specimens were hollow cylindrical specimens similar to those used in earlier work in this laboratory.[12,13] They were made from General Electric type 204 fused quartz. One of the diffusion specimens had a wall thickness of 1.37±0.03 mm. and the other two had a wall thickness of 1.08± 0.03 mm. Each of these diffusion specimens was sealed into a larger fused quartz tube in such a manner that it formed a boundary between two chambers. The inner chamber was connected by means of glass tubing to the ion source of a 60° sector field mass spectrometer. The outer chamber was connected to a gas manipulation system into which neon gas could be introduced at pressures up to or slightly above one atmosphere. The specimen was heated with a tube furnace and the temperature measured with a chromel-alumel thermocouple, ice bath, and potentiometer.

The gas used was research-grade neon obtained from the Matheson Company. Since the gas was al-

[1] L. S. T'sai and T. R. Hogness, J. Phys. Chem. **36,** 2595 (1932).
[2] F. J. Norton, J. Am. Ceram. Soc. **36,** 90 (1953).
[3] C. C. Leiby, Jr. and C. L. Chen, J. Appl. Phys. **31,** 268 (1960).
[4] S. Dushman and I. Langmuir, Phys. Rev. **20,** 113 (1922).
[5] A. E. Stearn and H. Eyring, J. Phys. Chem. **44,** 955 (1940).
[6] C. Wert and C. Zener, Phys. Rev. **76,** 1169 (1949).
[7] George H. Vineyard, J. Phys. Chem. Solids **3,** 121 (1957).
[8] I. Prigogine and Thor A. Bak, J. Chem. Phys. **31,** 1368 (1959).
[9] A. H. Schoen, Phys. Rev. Letters **1,** 138 (1958).
[10] K. Tharmalingam and A. B. Lidiard, Phil. Mag. Series 8, **4,** 899 (1959).
[11] W. M. Jones, J. Am. Chem. Soc. **75,** 3093 (1953).
[12] R. W. Lee, D. E. Swets, and R. C. Frank, J. Chem. Phys. (to be published).
[13] D. E. Swets, R. W. Lee, and R. C. Frank, J. Chem. Phys. **34,** 17 (1961).

TABLE I. Isotope abundance measurements.

Pressure (microns)	Ne^{22}/Ne^{20}
15.7	0.09928
15.7	0.09990
17.7	0.1019
8.	0.1005
8.	0.1009
8.	0.1030
12.	0.1021
12.	0.1017
12.	0.1002
51.	0.1021
51.	0.1019
51.	0.1024
	Average=0.1013±0.0008

ready very pure (~99.98%) no further attempt was made to purify it. Isotope abundance measurements were made using a conventional mass spectrometer gas sample system. A gold foil molecular flow leak was used and following the line of reasoning presented by Honig,[14] it is believed that the isotopic mixture which existed in the ion source was representative of that of the original mixture in the expansion volume of the sample system. For these particular measurements the strip chart recorder was replaced with a Rubicon potentiometer so that the output of the mass spectrometer could be measured more accurately. A sample of the gas from the original gas bottle was introduced into the expansion volume of the sample system and then as it flowed into the mass spectrometer through the gold foil leak, readings were taken alternatively on one neon peak and then the other. Only Ne^{20} and Ne^{22} were considered because the isotope abundance of Ne^{21} is too low (0.26%) to make it useful for diffusion studies. The isotope abundance measurements were made with several different gas pressures in the expansion volume with results shown in Table I. The isotope ratios appear to be independent of the pressure in the expansion volume indicating that molecular flow exists over the pressure range studied. The average isotope ratio Ne^{22}/Ne^{20} is slightly higher than that reported by Nier (0.09703±0.00040)[15] and conforms better to the results of Dibeler, Mohler, and Reese (0.10180± 0.00200).[16] However, since Nier calibrated his mass spectrometer with a synthetic argon isotope mixture it is possible that he was able to eliminate some mass discrimination effects that could not be eliminated here. In the permeability calculations the mass discrimination effect is probably eliminated automatically since the permeation rate and the isotope abundance measurements are made under essentially the same conditions and if the results of one set of measurements is divided by those of the other, any multiplying factors would be canceled.

The experimental procedure for the diffusion studies was essentially that used in the earlier work performed in this laboratory on helium,[13] hydrogen,[12] and deuterium[12] diffusion in fused quartz. A more detailed description of the methods of calculation described below are given in the earlier papers and are reviewed here only in order to make this paper self contained. At the beginning of each test the outer chamber was evacuated and then suddenly filled with about an atmosphere of the neon isotope mixture. The pressure was read with a mercury manometer and held constant. The mass spectrometer recorded the diffusion of neon through the fused quartz. When steady-state diffusion was attained, the gas was suddenly evacuated from the outer chamber and the mass spectrometer then recorded the evolution of the gas from the specimen.

The initial portion of the mass spectrometer record which is obtained when there is a high concentration of gas on the outside surface of the fused quartz can be integrated with a planimeter and the integral plotted against time. An extrapolation of the linear portion of this integral curve to the time axis gives an effective "time lag" which is related to the diffusion coefficient by

$$L=l^2/6D, \tag{1}$$

where L is the effective time lag, l is the thickness of the specimen, and D is the diffusion coefficient. Once the effective time lag has been measured from the replots of the mass spectrometer curves, the diffusion coefficient is easily obtained from Eq. (1). For reasons discussed in the earlier papers[12,13] this method is not as satisfactory as that involving the evolution or decay curves and therefore has been used mainly as a method of checking to make sure that the diffusion process is well behaved.

The mathematical description of the evolution process involves a rapidly converging series of exponentials.[13] Because of the rapid convergence of the series, the evolution curve can be described by a single exponential except for a small portion at the beginning. The time constant for this decay curve is obtained from

$$t_0=\frac{(t_2-t_1)}{\ln(h_1/h_2)}, \tag{2}$$

where h_1 and h_2 are two different mass spectrometer readings taken at t_1 and t_2 during the evolution period.

[14] R. E. Honig, J. Appl. Phys. **16,** 646 (1945).
[15] A. O. Nier, Phys. Rev. **79,** 450 (1950).
[16] V. H. Dibeler, F. L. Mohler, and R. M. Reese, J. Research Natl. Bur. Standards **38,** 617 (1947).

The time constant is related to the diffusion coefficient by the expression

$$t_0 = l^2/\pi^2 D. \tag{3}$$

The steady-state permeation rate into the mass spectrometer is described mathematically by

$$h_0 = (sADC_0/Fl)[(k-1)/\ln k], \tag{4}$$

where h_o is the steady-state mass spectrometer reading, A is the internal area of the specimen, k is the ratio of the external radius of the cylinder to the internal radius, C_0 is the concentration of gas atoms just inside the surface of the specimen, F is the conductance of the leak used to calibrate the mass spectrometer, and s is the sensitivity of the mass spectrometer for the particular gas being used. The permeability is defined as

$$P = DC_0 = (h_o Fl/sA)[\ln k/(k-1)] \tag{5}$$

When the gas pressure on the high-pressure side of the specimen is normalized to 1 atm, the C_0 is often called the solubility and is represented by S.

The temperature dependence of the permeabilities, P, the diffusion coefficients, D, and the solubilities, S, can usually be expressed by equations of the form

$$P = P_0^{-Q/RT}, \qquad D = D_0^{-E/RT}, \qquad S = S_0^{-H/RT},$$

where the P_0, D_0, and S_0 are constants, R is the gas constant, T is the absolute temperature, Q is the activation energy for permeation, E is the activation energy for diffusion, and H is the heat of solution. This behaviour is usually tested by plotting the logarithm of P, D, or S against $1/T$. If a straight line is obtained the above relationships are considered to hold.

The permeability is also a function of the gas pressure outside of the specimen and this can usually be expressed as $h_0 \propto p^x$. The x must be determined empirically for any gas-solid system and usually has values ranging from 0.5 to 1. In the case of helium in fused quartz it was found to be 0.95 ± 0.02. Some tests were also carried out in the present study to determine the value of x. This was done by measuring the permeation rate at four or five different pressures and plotting the permeation rate against the pressure on a log-log plot. For the case of neon permeation through fused quartz, x was found to be equal to unity within the limits of experimental error.

III. RESULTS

Permeabilities

During each test the isotope mixture was introduced into the outside chamber and as the isotopes diffused through the fused quartz into the mass spectrometer it was possible to focus alternately on each isotope and thereby obtain complete diffusion curves for both. The permeabilities for each isotope were calculated using Eq. (5) but it was necessary to correct for the fact that the pressure was not always exactly atmospheric and also for the existence of the opposite isotope. This was done using the formulas

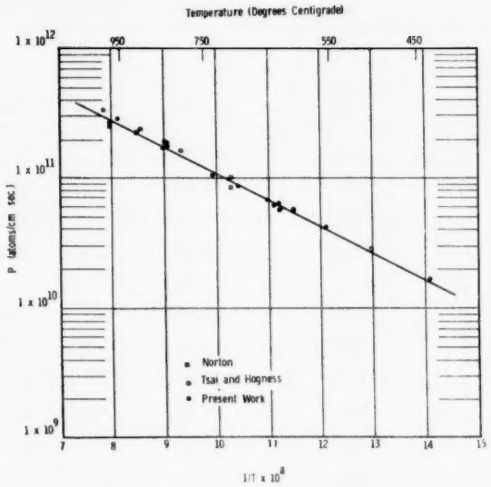

FIG. 1. Permeabilities P of Ne^{20} as a function of temperature.

$$h_{o20} = h_{20}(760/p)[1 + (Ne^{22}/Ne^{20})], \tag{6}$$

$$h_{o22} = h_{22}(760/p)[1 + (Ne^{20}/Ne^{22})], \tag{7}$$

where p is the total gas pressure used in the test in mm Hg, h_{20} and h_{22} are the mass spectrometer readings before the pressure correction, and h_{o20} and h_{o22} are corrected values to be used in Eq. (5) for calculating the permeabilities. The permeabilities for the two isotopes are listed in Table II. Since the permeabilities for the two isotopes are only slightly different it would be difficult to show curves of both on the same plot so in Fig. 1 we have plotted only the values for Ne^{20}. The results of T'sai and Hogness[1] and Norton[2] are plotted also and show very good agreement with the present work. The units of P are atoms/cm sec for a specimen 1 cm thick and 1 cm^2 in area and for a pressure differential of 760 mm Hg. These units are easily converted to the more conventional cc mm/sec cm^2 at 1 atm by multiplying by 3.73×10^{-19}. The data given in Table II was processed by a computer and least-mean-square curves were calculated for each of the two isotopes. The temperature dependence of the permeability of Ne^{20} in fused quartz is best represented by

$$P_{20} = 1.25 \times 10^{13} \exp\left[-\frac{9420 \text{ cal/g atom}}{RT}\right] \text{atoms/cm sec.} \tag{8}$$

TABLE II. Permeabilities and diffusion coefficients of neon isotopes in fused quartz.

Specimen	Temperature (°C)	$1/T\times10^4$	Permeabilities (10^{10} atoms/cm sec) Ne^{20}	Permeabilities (10^{10} atoms/cm sec) Ne^{22}	Diffusion coefficients (10^{-7} cm²/sec) Ne^{20}	Diffusion coefficients (10^{-7} cm²/sec) Ne^{22}
1	982	7.96	27.2	26.2	25.7	23.5
1	984	7.96	25.1	23.7	21.3	19.3
2	840	8.98	17.0	16.0	13.5	13.1
2	830	9.06	17.8	16.6	12.5	12.2
2	688	10.40	8.68	8.37	5.89	5.59
2	555	12.07	4.17	4.45	2.16	2.07
2	440	14.06	1.69	1.52	0.730	0.730
2	637	10.98	6.77	6.53	4.33	4.16
2	960	8.10	29.1	28.8	22.0	22.3
3	832	9.04	19.1	18.6	12.0	11.5
3	836	9.01	19.6	19.2	12.9	11.9
3	838	9.00	18.9	18.3	12.4	11.7
3	623	11.16	6.33	6.36	3.62	3.54
3	621	11.19	5.68	5.88	3.70	3.25
3	620	11.20	5.75	5.88	3.54	3.30
3	735	9.92	10.4	10.5	7.30	6.80
3	909	8.46	22.2	21.9	17.3	19.0
3	909	8.46	22.2	22.1	17.2	15.3
3	630	11.08	6.07	5.76	3.71	3.51

The temperature dependence of Ne^{22} is best represented by

$$P_{22}=1.20\times10^{13}\exp\left[-\frac{9390\text{ cal/g atom}}{RT}\right]\text{atoms/cm sec.} \tag{9}$$

Diffusion Coefficients

Both the time lag and decay methods were used to determine the diffusion coefficients and the results agreed quite well. However, as mentioned earlier, the decay values are considered slightly more accurate and are therefore listed in Table II. As was the case with the permeability values, the diffusion coefficients of the two isotopes are so nearly equal that only the results for Ne^{20} have been plotted in Fig. 2. From the figure it is seen that there is good agreement between points obtained from the three different specimens. The one value obtained by Leiby and Chen[3] for neon in Vycor is also plotted for comparison and the agreement is fairly good here, too.

The present data seems to be best fit by a single straight line indicating that there is probably only one activation energy involved. All of the data was processed by a computing machine and the least-mean-square line calculated for each isotope. The temperature dependence of the diffusion coefficients for Ne^{20} is best represented by

$$D_{20}=2.21\times10^{-4}\exp\left[-\frac{11\,370\text{ cal/g atom}}{RT}\right]\text{cm}^2/\text{sec.} \tag{10}$$

whereas the temperature dependence of the diffusion coefficients for Ne^{22} is best represented by

$$D_{22}=2.08\times10^{-4}\exp\left[-\frac{11\,340\text{ cal/g atom}}{RT}\right]\text{cm}^2/\text{sec.} \tag{11}$$

Although there was relatively good agreement between the time lag and decay values of the diffusion coefficients, the time lag values seemed to be consistently a few percent higher than the decay values. This effect was also reported in the earlier work on helium. Based on a number of tests at different pressures it was believed that the small difference in the

time lag and decay values was due to the fact that the first half of the transient curve is obtained while the sample is under pressure whereas the decay part of the curve is obtained while the chambers on both sides of the sample are evacuated.

It is felt that there is justification for defining a constant diffusion coefficient at a given temperature for the following reasons: (1) The diffusion coefficients calculated by the two methods are nearly equal, indicating that the diffusion process is relatively simple and the basic diffusion laws are fairly well obeyed; (2) The decay curves are simple exponentials except for a small portion near the end which represents only a few percent of the total gas evolved; (3) The effect of specimen thickness was just that predicted by the basic diffusion laws.

Solubility

It has been found that the diffusion of neon in fused quartz obeys the simple diffusion laws and, therefore, the solubility can be calculated using the equation

$$P=DS. \tag{12}$$

The solubility values for Ne^{20} have been plotted in Fig. 3. It is clear from the figure that the solubility decreases with increasing temperature and therefore the heat of solution is negative. This behavior is similar to that found for helium in fused quartz. The solubility values of Ne^{20} and Ne^{22} were also used to calculate least-mean-square lines for the two isotopes. The temperature dependence of the solubility of Ne^{20} is given by

$$S_{20}=5.59\times10^{16}\exp\left[-\frac{-1950\text{ cal/g atom}}{RT}\right]\text{atoms/cc}, \tag{13}$$

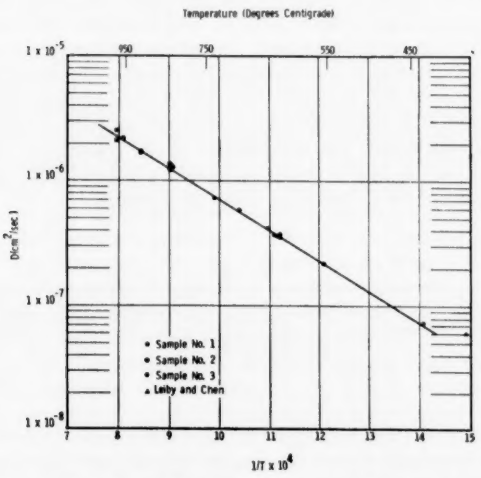

FIG. 2. Diffusion coefficients D of Ne^{20} as a function of temperature.

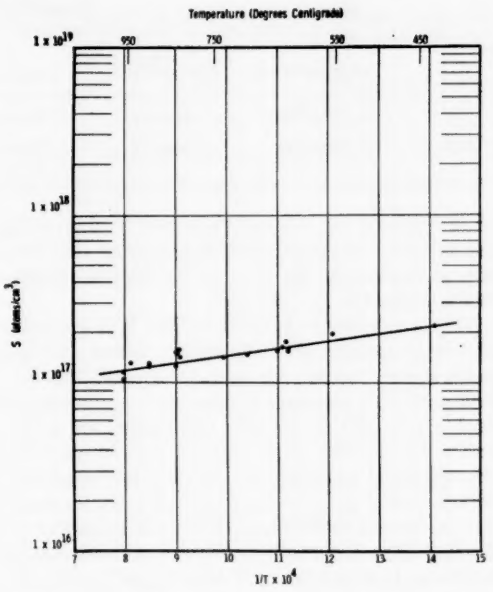

FIG. 3. Solubilities S of Ne^{20} as a function of temperature.

while that for Ne^{22} is given by

$$S_{22}=5.75\times10^{16}\exp\left[-\frac{-1950\text{ cal/g atom}}{RT}\right]\text{atoms/cc}. \tag{14}$$

Evaluation of Errors

In order to be able to decide how valuable the results of diffusion studies are, it is important to know how much error is involved in the reported values. The analysis of errors in diffusion data has been commonly ignored in published works. It therefore appears to be worthwhile to look at the analysis of errors in some detail.

In this type of experiment there are essentially two sources of error in the final results: (1) The lack of reproducibility of the actual measurements which is sometimes called the precision of the experiment, and (2) the uncertainty in all of the other parameters which are used to calculate the permeabilities and diffusion coefficients. These parameters are measured independently and their corresponding errors are evaluated independently. The error quoted for the activation energies is derived entirely from the first source of error, while that quoted for D_0, P_0, and S_0 must be derived from both sources of error. The errors in the ratio of the D_0's are derived only from the precision of the experiment since the multiplying factors are the same for both isotopes and cancel in the ratio. The error

TABLE III. Summary of results.

	E cal/g atom	D_0 (10^{-4} cm²/sec)	Q cal/g atom	P_0 (10^{13} atoms/cm sec)	H cal/g atom	S_0 (10^{18} atoms/cc)
Ne^{20}	11,370±80	2.21±0.12	9,420±140	1.25±0.17	−1,950±150	5.59±0.84
Ne^{22}	11,340±130	2.08±0.17	9,390±150	1.20±0.17	−1,950±170	5.75±0.92

in the ratio of the P_0's must not only be derived from the precision of the experiment but must also include the uncertainty of the value of the isotope abundance of the original isotope mixture.

In the treatment of diffusion data it is common to plot $\ln D$ against $1/T$. Therefore, before the least-mean-square curves are calculated and the errors evaluated, it is necessary to carry out a transformation. In the case of the diffusion coefficients, let $\ln D_i = y_i$ and $1/T_i = x_i$. The y's are plotted against the x's and the statistical treatment of the data is carried out in this system of coordinates. Similar transformations are also performed on the permeability and solubility data. Further discussion of the statistical methods described below can be found in any of several good textbooks on statistics.[17,18]

The standard deviation of the slope of the least-mean-square curve can be calculated using the equation

$$S_b = [(1-r^2)/(N-2)]^{\frac{1}{2}}(S_y/S_x). \qquad (15)$$

where N is the number of data points used to calculate the curve, S_y is the standard deviation of the dependent variable y, S_x is the standard deviation of the independent variable x, and r is the correlation coefficient.[19] Assuming a normal distribution, the probable error is just 0.675 times the standard deviation of the slope. This is the probable error in the slope and must be multiplied by the ideal gas constant R, to obtain the probable error of the activation energy.

In order to calculate the error in the D_0, P_0, and S_0 it is first necessary to determine how much of that error is due to the scatter of the data points. D_0 is normally found by extrapolating the least-mean-square curve to $1/T=0$ and since there is no actual data in this area the value obtained is affected by the uncertainty in the slope of the curve. Therefore the appropriate form of the standard deviation of this intercept is

$$S_a = S_y\{[(N-1)/(N-2)](1-r^2)[N^{-1} + \bar{x}^2/(N-1)S_x^2]\}. \qquad (16)$$

The parameters are as defined for Eq. (15) and $\bar{x}$ is the mean value of the independent variable. This calculation includes not only the scatter of the individual data points about a mean at a given value of x but also the uncertainty in the slope of the curve. The interpretation of this standard deviation is complicated by the fact that this is the standard deviation of x_0 which is equal to $\ln D_0$. Therefore the errors in the D_0 are not normally distributed and the antilog of $0.675 S_a$ can only be used as an estimate of the probable error. The diffusion coefficient measurements involve the thickness squared so it is necessary to add the error in the thickness to the precision of the other measurements. The errors are combined by the usual procedure of using the square root of the sum of the squares of the fractional errors as the fractional error of the products or quotients. The fractional error in the thickness $\Delta l/l$ is 0.03. In the case of the permeabilities it is necessary to combine the fractional errors in F_1, s, l, and A with the precision of the permeation rate measurements as obtained from Eq. (16). The fractional errors of these other parameters were independently estimated and have values of $\Delta l/l=0.03$, $\Delta A/A=0.05$, $\Delta F/F=0.02$, and $\Delta S/s=0.10$. All of the activation energies, D_0's, P_0's, and S_0's are listed in Table III along with their corresponding errors.

In the calculation of the ratio of the diffusion coefficients or the ratio of the permeabilities all of the multiplying factors cancel out and therefore the errors in these can be neglected. The errors involved then are only those of the precision of the experiment. Since the slopes of the curves for the two isotopes appear to be equal it is justifiable to ask whether they can be considered equal. The assumption of the equality of the two slopes can be tested by using a Student t test. The value of t is obtained by using the formula

$$t = \frac{b_1 - b_2}{\left[\dfrac{(S_{y_1}/S_{x_1})^2(N_1-2)(1-r_1^2)+(S_{y_2}/S_{x_2})^2(N_2-2)(1-r_2^2)}{(N_1+N_2-4)}\right]^{\frac{1}{2}}}, \qquad (17)$$

where the b's are the values of the slopes of the least-mean-square curves for the two isotopes and the other variables are the same as defined for Eq. (15). Substituting the appropriate values obtained from the

[17] W. J. Dixon and F. J. Massey, Jr., *Introduction to Statistical Analysis* (McGraw-Hill Book Company, Inc., New York, 1951), 1st ed., pp. 153–169.

[18] A. Hald, *Statistical Theory with Engineering Applications* (John Wiley & Sons, Inc., New York, 1952), pp. 522–546.

[19] The correlation coefficient is a measure of the strength of the relationship between two variables and is calculated by $r=(N\Sigma x_i y_i - \Sigma x_i \Sigma y_i)/[N(N-1)S_x S_y]$.

data, the t value is 0.039 for the diffusion coefficients and 0.033 for the permeabilities. These are very small compared to the values obtained from the t distribution even at very high confidence levels and therefore the hypothesis that the slopes are equal is accepted. If there is a real difference in slope between the two curves it cannot be detected with these data. The assumption of the equality of the slopes also implies that the ratio of the diffusion coefficients or of the permeabilities is independent of the temperature. Under these circumstances the best estimate of the ratio of the D_0's is the mean value of all of the ratios of the measured quantities. The ratios of the D's and P's are listed in Table IV and the mean values are listed below, along with the probable errors calculated using the formula

$$P.E.=0.675[\sum(x_i-\bar{x})^2/N(N-1)]^{\frac{1}{2}}, \qquad (18)$$

where the x's are now the individual ratios. These mean ratios are slightly different from the values which one would obtain by taking the ratios of the actual D_0 and P_0 values given in Eqs. (10), (11), (8), and (9), due to the small apparent differences in activation energy for the two isotopes. However the difference between these ratios and those calculated directly from the D_0's and P_0's are within the probable error.

TABLE IV. Ratios of the permeabilities and diffusion coefficients.

Specimen	Temperature (°C)	$1/T\times10^4$	P_{20}/P_{22}	D_{20}/D_{22}
1	982	7.96	1.04	1.09
1	984	7.96	1.06	1.10
2	840	8.98	1.06	1.03
2	830	9.06	1.07	1.02
2	688	10.40	1.04	1.05
2	555	12.07	0.94	1.04
2	440	14.06	1.11	1.00
2	637	10.98	1.04	1.04
2	960	8.10	1.01	0.99
3	832	9.04	1.03	1.04
3	836	9.01	1.02	1.08
3	838	9.00	1.03	1.06
3	623	11.16	1.00	1.02
3	621	11.19	0.97	1.14
3	620	11.20	0.98	1.07
3	735	9.92	0.99	1.07
3	909	8.46	1.01	0.91
3	909	8.46	1.00	1.12
3	630	11.08	1.05	1.06
Average			1.02±0.01	1.05±0.01

IV. DISCUSSION

In his study of the diffusion of helium isotopes in fused quartz Jones obtained the following results:

$$P_3/P_4=(1.170\pm0.004)\exp[-(57\pm2)/RT],$$

$$D_3/D_4=(1.167\pm0.005)\exp[-(51\pm3)/RT],$$

$$S_3/S_4=(1.003\pm0.003)\exp[-(6\pm2)/RT].$$

The ratio of the D_0 values is very close to the value 1.155, which would be expected if one assumed that the diffusion coefficients varied as the reciprocal of the square root of the mass. The same can be said for the P_0 values. Jones also indicated a higher activation energy for diffusion for the lighter He^3 isotope than for the heavier He^4 isotope although the difference is quite small. The interpretation of the results obtained earlier in our laboratory on the diffusion of hydrogen and deuterium in fused quartz[12] is complicated by the fact that the diffusing species are diatomic molecules which possess additional vibrational and rotational degrees of freedom. Furthermore the diffusion process itself was complicated by the fact that the hydrogen and deuterium reacted chemically with the lattice structure. It was found, however, that the diffusion coefficients for hydrogen were higher than those for deuterium in a ratio of 1.24 which is slightly smaller than that of the inverse-square-root of the mass (1.41). In the results obtained in the present work on the diffusion of neon in fused quartz, the ratio of the D_0 values was found to be 1.05±0.01 which again is very close to the ratio predicted from the inverse square root of the mass relationship (1.049). Therefore in general the results of studies of the diffusion of gaseous isotopes in fused quartz indicate substantial agreement with the predictions of the theories of diffusion based on the transition state concept. Furthermore it has been illustrated theoretically by Schoen[9] that when there is very little correlation between the directions of consecutive jumps of diffusing atoms, the isotope effect should be the inverse square root of the mass relationship. When there is a greater degree of correlation the isotope effect becomes very small. Since the isotope effect has been found in this work to be quite close to the inverse ratio of the square roots of the mass, and if this theory can be applied to neon in fused quartz, it would appear that a weak correlation between the jumps of the diffusing neon atoms is indicated. This suggests that the diffusion process is interstitial rather than by a vacancy mechanism.

Unfortunately in the case of fused quartz any considerations about the mechanism of diffusion must be

carried out rather cautiously. Most of the theories of diffusion apply principally to solids with the crystalline type of lattice structure, and it is quite clear that fused quartz does not have a crystalline lattice structure. The actual nature of the lattice structure is still somewhat controversial but the most popular model is that proposed by Zachariasen[20] and later modified slightly by the work of Warren.[21] In this model, the lattice structure is considered to be a random array of the basic silicon-oxygen tetrahedra but the degree of randomness is restricted by the fact that certain interatomic distances seem to be fixed.

In spite of the difficulties involved it is instructive to try to evaluate one of the most popular of the transition state theories, the Wert-Zener theory,[6] in terms of what is known about fused quartz in order to see specifically what problems are involved.

The Wert-Zener formulation of D_0 is essentially the following:

$$D_0 = n\alpha a^2 \nu \exp(-\Delta S/R), \tag{19}$$

where a is the lattice constant, n is the number of nearest neighbor interstitial positions, α is a numerical coefficient which depends on the location of the interstitial positions, ν is the frequency of vibration of the diffusing atom in the lattice site, R is the gas constant, and ΔS is the entropy of activation. The vibration frequency is generally taken to be just the classical frequency expressed by

$$\nu = (E/2m\lambda^2)^{\frac{1}{2}}, \tag{20}$$

where E is an energy which is usually assumed equal to the activation energy, m is the mass of the diffusing particle, and λ is the distance the atom jumps from one interstitial site to another. The entropy of activation is given by

$$\Delta S = -d\Delta G/dT, \tag{21}$$

where ΔG is the change in free energy at constant pressure and for isothermal changes is defined by

$$\Delta G = \Delta H - T\Delta S. \tag{22}$$

It can also be defined as the work necessary to move the diffusing particle from a potential energy minimum to the top of the potential barrier. Equation (21) can be rewritten as

$$\Delta S = -\Delta G_0 \frac{d(\Delta G/\Delta G_0)}{dT} \tag{23}$$

where ΔG_0 is the value of ΔG at absolute zero. Outside of the differential the ΔG_0 is approximated by E. In crystals and in metals in particular, the major part of the free energy change ΔG is believed to be associated with the straining of the lattice and therefore the temperature coefficient of $\Delta G/\Delta G_0$ can be approximated by the temperature coefficient of the shear modulus, $d(\mu/\mu_0)/dT$. The temperature coefficient of the shear modulus in nearly all crystals is negative and therefore the entropy of activation is positive

If Eq. (19) for D_0 is applied to the case of fused quartz and Eq. (20) used for the frequency, the ratios of the D_0's for two isotopes will be just the ratios of the reciprocals of the square roots of the two masses, if the activation energies are equal. However, in attempting to obtain the individual D_0's some problems are encountered. The activation energies are easily obtained from our experimental results and the mass of the neon atom can be obtained from published results of atomic mass measurements. Also an average lattice constant $\bar{a}$ and an average jumping distance $\bar{\lambda}$ can perhaps be estimated from a knowledge of the density and molecular weight of the fused quartz as well as from some of the x-ray diffraction results. However, the random nature of the lattice creates some uncertainty in n, the number of nearest neighbor interstitial positions as well as in α, which depends on the location of those interstitial positions.

Another interesting problem arises when an attempt is made to calculate the entropy of activation. In the temperature range in which the diffusion experiments are carried out the temperature coefficient of the shear modulus is positive for fused quartz.[22,23,24] This implies that the fused quartz lattice structure becomes more rigid instead of less rigid as the temperature is raised. That part of the entropy of activation which is associated with the strain energy must therefore be negative. Negative entropys of activation have been reported for substitutional diffusion in some metals[25] but they have been attributed to effects other than the variation of elastic modulus with temperature since the temperature coefficient of the elastic modulus is always negative in metals.

It is difficult to know exactly how the increase in rigidity with temperature affects the diffusion process unless the actual mechanism which produces this strange variation of the rigidity is known. Two possible explanations have been proposed. Babcock, Barber, and Fajans[26] proposed that the fused quartz lattice consists of two coexisting structures, one which predominates at high temperatures and one which pre-

[20] W. H. Zachariasen, J. Am. Chem. Soc. **54,** 3841 (1932).
[21] B. E. Warren, J. Appl. Phys. **8,** 645 (1937).
[22] F. Horton, Trans. Roy. Soc. (London) **A204,** 407 (1905).
[23] J. W. Marx and J. M. Sivertsen, J. Appl. Phys. **24,** 81 (1953).
[24] D. S. Hughes and Christian Maurette, J. Appl. Phys. **27,** 1184–86 (1956).
[25] G. J. Dienes, J. Appl. Phys. **21,** 1189 (1950).
[26] C. L. Babcock, S. W. Barber, and K. Fajans, Ind. Eng. Chem. **46,** 161 (1954).

dominates at low temperatures. Presumably the structure which predominates at high temperatures would have a higher rigidity and as the temperature was increased the rigidity of the fused quartz would appear to increase. Another explanation for the increase in rigidity with temperature has been proposed by Anderson and Bömmel.[27] It is based on the assumption that in going from the short-range order of the basic tetrahedra to the long range disorder of the lattice a slight warping of the silicon-oxygen bonds occurs. Under these circumstances the oxygen atoms can take two possible equilibrium positions and can oscillate between these positions. The increased rate of oscillation at high temperatures is believed to be the cause of the increase in the rigidity of the fused quartz. This viewpoint is supported by low temperature internal friction effects which take place in fused quartz.[27] In either of these two mechanisms it appears that raising the temperature would tend to obstruct diffusion and therefore one could expect the free energy to increase with temperature. If this is true the entropy of activation might be expected to be negative.

It is apparent that although the theories of diffusion based on the transition state concept predict the isotope effect, there are certain other aspects of these theories which are difficult to fit to the case of fused quartz. Notwithstanding, the unusual characteristics of this material provide interesting points of conjecture which should stimulate further research.

[27] O. L. Anderson and H. E. Bömmel, J. Am. Ceram. Soc. **38**, 125 (1955).

ACKNOWLEDGMENTS

The authors wish to acknowledge many helpful discussions with James Dallemand regarding the treatment of the errors. David Fry's interest and encouragement were a stimulating factor throughout the course of the experiments. Robert Williams kindly assisted with the operation of the mass spectrometer and with the data reduction.

Optical Absorption Spectra of Ni-Doped Oxide Systems. I.*

R. PAPPALARDO,† D. L. WOOD, AND R. C. LINARES, JR.
Bell Telephone Laboratories, Incorporated, Murray Hill, New Jersey

(Received March 30, 1961)

The optical absorption was studied at room temperature, at 78°, and at 4.2°K in the 2.6-μ to 0.2-μ region in single crystals of MgO, ZnO, $MgAl_2O_4$, and yttrium-gallium garnet doped with nickel. The absorptions found were correlated to electronic transitions within the 3*d*-shell using the formalism of the crystal-field theory. The value of the Dq and B parameters were derived for MgO:Ni ($Dq=-815$ cm^{-1}; $B=890$ cm^{-1}) and for ZnO:Ni where Ni is tetrahedrally coordinated ($Dq=405$ cm^{-1}; $B=795$ cm^{-1}). Interesting fine structure was found in the absorption spectra of MgO:Ni and its implications are discussed. An attempt is made to explain some of the fine structure of the absorptions in MgO and ZnO as due to spin-orbit effects. The observed spectra for MgO:Ni are used to infer the presence of Ni^{++} in octahedral coordination, both in the spinel and in the green phase of yttrium gallium garnet.

I. INTRODUCTION

THE present study was begun in order to try to

(a) check experimentally some predictions of the crystal-field theory concerning the energy-level scheme of iron-group ions surrounded by the same ligands (oxygens, in our case) arranged in different coordinations;

(b) determine from the optical absorption data of garnets and spinels the valency and site symmetry of impurity ions of the iron-group;

(c) find evidence of the contribution of lattice vibrations to the optical absorption of iron-group ions in centro-symmetric systems (e.g., MgO).

We report and discuss here optical absorption data at room temperature, 78°, and 4.2°K for Ni-doped single crystals of MgO, ZnO, $MgAl_2O_4$, yttrium-gallium garnets, and for Ni-doped germanium garnet powders. Our subsequent paper will be concerned with the corresponding data for the same systems doped with Co.

In greater detail the problems connected with the present study can be expressed as follows. With regard to the first point (a) above, the crystal-field theory predicts that the excited energy levels for $3d^n$-electronic systems in cubic symmetry (which is the easiest case to treat) will be determined, apart from the quantities B and C (Racah's parameters of electrostatic interaction which characterize interactions within the 3*d*-shell), by the sign and magnitude of the crystal-field parameter Dq, which is a measure of the interaction of the 3*d*-electrons with the rest of the lattice. The main contribution to the interaction arises from the nearest neighbors.[1–5] When the species of the nearest neighbors is kept constant (e.g., oxygen ions) but the number of the nearest neighbors changes, maintaining the cubic symmetry at the 3*d*-electron site, from six (octahedral coordination) to four (tetrahedral coordination) and to eight (body-centered cube coordination), then the scale factor Dq is predicted to vary when the ligand-ion distance is kept constant, according to the relation[5–7]

$$Dq_{\text{bcc}}=2Dq_{\text{tet}}=2(-4/9)Dq_{\text{oct}} \qquad (1)$$

(see Appendix I). This would imply a rather drastic change of the energy-level scheme and subsequently of the optical absorption in going from one type of coordination to another.

An immediate practical application of these differences in optical properties or iron-group ions in various cubic-symmetry coordinations, is the determination of the charge and site-symmetry of such ions when present in the garnet and spinel systems. The garnet systems possess very remarkable magnetic properties due to exchange interactions, via the intermediate oxygen ions, between iron-group ions. The strength of such interactions is dependent on the type of ions present, on their formal charge, and on the site they occupy, which can be sites possessing (predominantly) tetrahedral, octahedral, or dodecahedral[8] symmetry.[9] An analogous situation is found in the spinels where there are tetrahedral and octahedral sites available, indicated symbolically by ( ) and [ ], respectively. Information as to the site preference of the various ions in these systems can be obtained by means of x-ray investigations and by measurement of the magnetic

* Paper presented at the Thanksgiving Meeting of the American Physical Society, Chicago, November 1960.

† Visiting Scholar, 1959–60.

[1] F. E. Ilse and H. Hartmann, Z. Physik. Chem. **197,** 239 (1951).

[2] A. Abragam and M. H. L. Pryce, Proc. Roy. Soc. (London) **A205,** 135 (1951).

[3] L. E. Orgel, J. Chem. Soc. **4,** 4756 (1952); J. Chem. Phys. **23,** 1829 (1955).

[4] Y. Tanabe and S. Sugano, J. Phys. Soc. Japan **9,** 755–66 (1954).

[5] A. D. Liehr, J. Phys. Chem. **64,** 43 (1960), (also contains an extensive list of references on the subject).

[6] C. J. Ballhausen, Kgl. Danske Videnskab. Selskab., Mat.-fys. Medd. **29,** No. 4 (1954).

[7] R. Pappalardo, J. Mol. Spectroscopy **6,** 554 (1961).

[8] The eight oxygen ions nearest to the cations are located at the vertices of a distorted cube.

[9] S. Geller, R. M. Bozorth, C. E. Miller, and D. D. Davis, J. Phys. Chem. Solids **13,** 28 (1960).

properties of these systems.[10] On the other hand, on the basis of the crystal-field theory, one would expect that similar information could be obtained quite simply by studying the optical absorption of these systems in single crystals (especially if it is required to set up adequate reference spectra) and also in powders (by dissolving the powder sample in a KBr pellet or by studying its reflection spectrum).

Finally, the theory of electronic transition within the $3d$ shell in centro-symmetric systems postulates[11,12] that electric dipole transitions in such systems are only possible if there is a contamination of the even-parity $3d$ wavefunctions with odd-parity states, this mixing being caused by the odd-symmetry components of the electron-nuclear Hamiltonian in a Born-Oppenheimer expansion. In other words one would expect to find vibrational structure in the optical absorption of centro-symmetric systems. Two typical centro-symmetric systems are the divalent hexahydrated fluosilicate salts, and MgO when doped with divalent impurities. Actually vibrational structure was found in undiluted $NiSiF_6 \cdot 6H_2O$ at 20° and 4.2°K at the low-energy side of the absorption band in the 25 000 cm^{-1} region.[13] By the same token, similar structure should be present in the absorption band of MgO:Ni (and MgO:Co).

In studying the optical absorption of the oxide systems in question, considerable structure was found in the absorptions. In what follows we shall briefly try to correlate *some* of the observed structure to spin-orbit effects. For this purpose the spin-orbit splitting of the cubic-symmetry electronic terms has been calculated analytically and the results compared with the observed data.

II. EXPERIMENTAL

Most of the optical absorption properties were studied in the range of operation of the Cary model-14 Universal double-beam spectrophotometer, namely from 2.6 to $\sim 0.2\mu$, at room temperature, 78°, and 4.2°K. Some work was also done in the 2.5 to 15-μ region using the Perkin-Elmer model-21 infrared double-beam spectrophotometer. Since most of the samples had cubic symmetry or were grown in plates perpendicular to the optic axis, unpolarized light was used in the present work. The origin of the various samples will be mentioned while discussing the details of their absorption. The crystals used varied in thickness from a few tenths of a millimeter to a few millimeters, typical areas being 3×6 mm. For work at low temperatures a Pyrex cryostat was used, in which the samples were immersed in the coolant or in direct contact with it. For work at 78°K in the violet and uv region a quartz cryostat was used (we refer to a previous paper for more details on the experimental procedure).[14]

Uncertainty in the absolute wave numbers of sharp lines is estimated as ± 5 cm^{-1} in the 1-μ region. The uncertainty in the tabulated extinction coefficients is estimated as $\pm 10\%$ for absorptions of optical density of the order of 0.2. For stronger absorptions the uncertainty is due essentially to the process of extrapolating the background in the absence of the band. Details of the spectra are tabulated for convenience as follows. Besides wavelengths and frequency in cm^{-1}, we list the linear extinction coefficient from $I = I_0\, 10^{-\alpha x}$, with α in cm^{-1}, the width of the line at $\alpha = \frac{1}{2}\alpha_{max}$, and f-numbers of the absorptions (oscillator strengths). The oscillator strengths are a function of the area covered by the absorption bands and lines. When these are Gaussian-shaped, the area was obtained simply via the half-width, otherwise it was evaluated measuring the area directly.

III. MgO:Ni

(a) Observed Spectra

The optical absorption was studied at room temperature, 78°, and 4.2°K in a sample 4.4 mm thick. Spectra were also taken at room temperature and 78°K of a sample 17 mm thick which could not be fitted, owing to its large size, in the cryostat used for work at 4.2°K. The crystals were grown by Dr. Schupp, General Electric Lamp Research Division and were kindly made available to us by Dr. W. M. Walsh, Jr. of our Laboratories. The spectrochemical analysis, performed by Mr. E. K. Jaycox of our Laboratories, gave the content of Ni as 0.051% of total weight. The relative concentration of Mg to Ni ions was $Ni/Mg \simeq 3.5 \times 10^{-4}$, which indicates by the way the high sensitivity of the optical absorption method for detecting small amounts of Ni impurities. The absorption of MgO:Ni was also reported by W. Low,[15] but since the data were taken partly at room temperature and partly at 78°K using a sample more heavily concentrated than the ones we used, no structure was present in the spectra reported by this author. With the samples we used absorptions were found near 8500, 14 500 , and 25 000 cm^{-1}. The details of the various absorptions as follows. At room temperature a broad weak band is centered at 11 600 A (8620 cm^{-1}) and is detected only at high scanning speed. At 78°K the absorption in this region starts with two very sharp lines, A_1 and A_2 at 8002 and 8179 cm^{-1}, followed by a continuum (Fig. 1). The peaks of this continuum are more evident in a sample 1.7 cm thick and are located at 8440, 8560, 8850, and 9216 cm^{-1} (Fig. 2, Table I). In this thick sample and at 78°K, the two sharp lines A_1 and A_2, have half-widths of 9 and 8 cm^{-1}, respectively.

[10] S. Geller, J. Appl. Phys. Suppl. **31,** 30S (1960).
[11] J. H. Van Vleck, J. Phys. Chem. **41,** 67 (1937).
[12] J. H. Van Vleck, J. Chem. Phys. **7,** 472 (1939).
[13] R. Pappalardo, Nuovo cimento **6,** 392 (1957).
[14] R. Pappalardo and D. L. Wood, J. Chem. Phys. **33,** 1734 (1960).
[15] W. Low, Phys. Rev. **109,** 247 (1958).

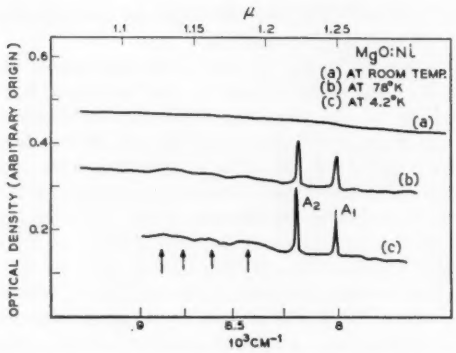

FIG. 1. Absorption spectrum of a single crystal of MgO:Ni in the 8500 cm^{-1} region: (a) At room temperature; (b) at 78°K; (c) at 4.2°K. Sample thickness 4.4 mm Ni 0.051% of total weight. Arrows indicate weaker and broader absorptions.

A considerable sharpening of these two lines is found when the sample 4.4 mm thick is cooled to 4.2°K. The half-widths are now 4.5 and 6 cm^{-1}, respectively, with a scanning speed of 25 A/sec. Probably the actual half-widths are even narrower on account of some instrumental broadening. Very little shift in the position of these two lines is found going from 78° to 4.2°K. The difference in frequency found was within the experimental error. The continuum shows a clearer structure at 4.2°K, but no new lines as sharp as A_1 and A_2 appear [Fig. 1(c)].

The second absorption is located in the 14 500 cm^{-1} region. At room temperature the absorption has a rather pronounced low-energy tail and reveals some weak structure [Fig. 3(a)]. This structure becomes more evident at 78°K. An initial doublet is followed by a continuum on which *four* peaks are superposed and possibly a few others of weaker intensity. For the purpose of detecting the weaker absorptions, it is better to consider the spectrum of the thicker sample where these lesser peaks are more pronounced (Fig. 4 and Table I). No spectacular changes are found cooling in the sample to 4.2°K [Fig. 3(c)].

The third absorption takes place in the blue region of the spectrum. At room temperature a very weak, flat

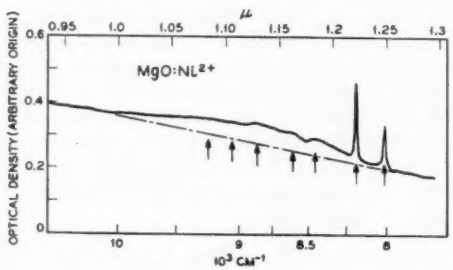

FIG. 2. Absorption in the 8500 cm^{-1} region of a MgO:Ni sample 1.7 cm thick, temperature 78°K.

TABLE I. MgO:Ni (0.051% of total weight; 4.4 mm thick) at temp. 78°K.

Absorption peaks	Wave-length in A	Wave number in cm^{-1}	Extinction coefficient α_{max} (cm^{-1})	Half-width at $\alpha=\frac{1}{2}\alpha_{max}$ (cm^{-1})	Oscillator strength
A_1	12 496	8002	0.14	12	2.6×10^{-7}
A_2	12 226	8179	0.24	11	4.0×10^{-7}
	11 900	8403	0.02		
	11 640	8591	0.02		
	a	a			
	7700 (?)	12 987 (?)	0.02		
B_1	7300	13 696	0.09	~80	1.1×10^{-6}
B_2	7180	13 927	0.08		
	b	b			
B_3	6785	14 738	0.11		
B_4	6680	14 970	0.1		
B_5	6585	15 186	0.13		
B_6	6490	15 408	0.12		
	6335	15 785	0.06		
C_1	4160	24 038	0.11		2.1×10^{-5} c
C_2	4120	24 272	0.22		
	4073	24 552	0.2		
	4000	25 000	0.22		

[a] In a sample 1.7 cm thick, two additional peaks are found at 8850 cm^{-1} and 9216 cm^{-1} (Fig. 2).

[b] Two weak absorptions are present in this region in a sample 1.7 cm thick. The additional peaks are located at 14.144 and 14.357 cm^{-1} (Fig. 1).

[c] At room temperature the same band has oscillator strength 3.1×10^{-5}.

absorption is found for the 4.4-mm sample in the 21 500 cm^{-1} region. This is followed by a bell-shaped band with peak at 24 690 cm^{-1} (Fig. 5). At 78°K the band already shows a complex structure. The absorption starts with two broad lines C_1 and C_2 at 24 040 and 24 270 cm^{-1}. Two more peaks are discernible followed by a continuum. This is more or less the pattern observed at 4.2°K except for the fine structure in the peak C_2 [Fig. 5(c), Table II].

(b) Assignment of Absorptions Bands to Transitions between Cubic-Field Terms

There is little doubt that the absorption is due to octahedrally coordinated Ni^{++}. For the assignment of

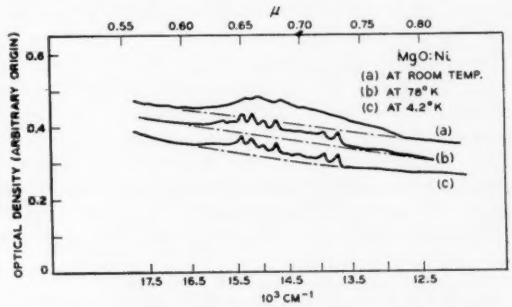

FIG. 3. Absorption in the 15 000 cm^{-1} region for MgO:Ni: (a) At room temperature; (b) at 78°K; (c) at 4.2°K. Sample thickness 4.4 mm.

the absorptions to cubic-symmetry levels we may use the results of the work by Jørgensen,[16] Tanabe and Sugano,[4] Low,[15] or Liehr and Ballhausen (LB).[17] We shall discuss first the present spectrum following the results of the calculations by Liehr and Ballhausen.[17] These authors treated simultaneously the effect of the Coulomb interaction, of the cubic crystal-field, and of the spin-orbit interaction, and plotted the resulting energy levels of Ni^{++} as a function of the crystal-field parameter Dq. As a suitable choice for the remaining parameters of spin-orbit coupling and electrostatic interaction they assumed

$$F_4=90\ \text{cm}^{-1}, \qquad F_2=14F_4,$$

and

$$\lambda=-275\ \text{cm}^{-1}, \tag{2}$$

with λ the spin-orbit constant in the $L-S$ scheme. The predicted positions of triplet levels (same multiplicity

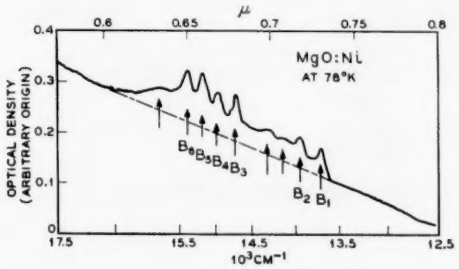

FIG. 4. Absorption at 78°K of a single crystal of MgO:Ni, thickness 1.7 cm.

as the ground-term $^3A_2$) is shown in Table III. Good agreement would be obtained for $Dq\simeq-850\ \text{cm}^{-1}$.

(c) First-Order Coupling Effects (First-Order)

The interesting and novel feature of the present spectra though, is the resolution into components of the intrasystem transitions which are usually observed as broad bands. This would in principle make it possible to discuss the fine structure observed as due to the combined effect on the cubic-field triplets of the spin-orbit coupling and the lattice vibrations associated with the electronic transitions. (In a centro-symmetric system such as MgO:Ni lattice vibrations are expected to be instrumental in making the electronic transitions possible.)

Because of the complexity of a detailed analysis of the contribution of lattice vibrations to the transition probabilities, we shall treat presently only the effect of

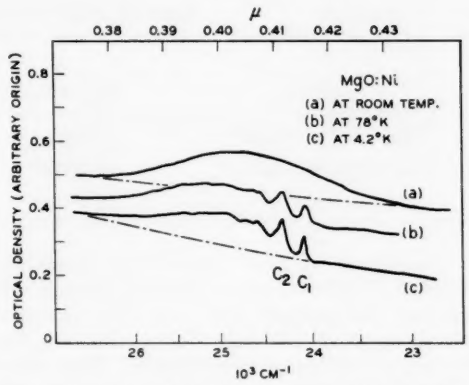

FIG. 5. Absorption of MgO:Ni (4.4 mm thick) in the 25 000 cm^{-1} region: (a) At room temperature; (b) at 78°K; (c) at 4.2°K.

spin-orbit coupling. We suppose for the sake of simplicity that, at least for the leading lines of each absorption group, the same lattice vibration modulates the electronic transitions from the ground level to the multiplet components of the excited terms. This simple model will then be compared with the observed data.

Liehr and Ballhausen[17] treated the effects of the spin-orbit coupling simultaneously with the consideration of the crystal-field effects and solved numerically the resulting secular equations. In an attempt to explain some of the fine structure of the Ni^{++} ion, we would be interested in expressing, analytically, the effect of the spin-orbit coupling on some of the excited electronic levels of Ni^{++}, especially regarding the rather controversial position of the $^1E_{1a}$ and $^3F_{1a}$ cubic-field terms.

TABLE II. MgO:Ni (sample 4.4 mm thick) at temp. 4.2°K.

Absorption peaks	Wave-length in A	Wave number in cm^{-1}	Extinction coefficient α_{max} (cm^{-1})	Half-width at $\alpha=\frac{1}{2}\alpha_{max}$ (cm^{-1})	Oscillator strength
A_1	12 485	8009.6	0.22	4.5	1.5×10^{-7}
A_2	12 215	8186.6	0.34	6	3.0×10^{-7}
	11 850	8438	0.045		
	11 600	8620	0.022		
	11 300	8849	0.022		
B_1	7300	13 698	0.1	85	1.3×10^{-6}
B_2	7180	13 927	0.08		
	6965	14 357	0.06		
	6870	14 556	0.056		
B_3	6785	14 738	0.11		10^{-5}
B_4	6677	14 976	0.1		
B_5	6585	15 186	0.13		
B_6	6485	15 420	0.11		
C_1	4154	24 073	0.18	52	1.4×10^{-6}
C_2	4119	24 277	0.22	116	3.8×10^{-6}
	4114	24 307			
	4079	24 515			
	4067	24 588	0.22		1.8×10^{-5}
	4010	24 937	0.22		

[16] C. K. Jørgensen, *Energy Levels of Complexes and Gaseous Ions* (J. Gjellerups Forlag, Kobenhavn, 1957); Rept. to the Xth Solvay Council, 1956.

[17] A. D. Liehr and C. J. Ballhausen, Ann. Phys. (N. Y.) **6**, 134 (1959); C. J. Ballhausen and A. D. Liehr, Mol. Phys. **2**, 123 (1959).

TABLE III. Triplet terms for Ni^{++} in octahedral symmetry.

Transitions	Theory (Liehr and Ballhausen)[17] $Dq=-800$ cm^{-1}	$Dq=-900$ cm^{-1}	Experiment	
$^3A_{2g}(d\epsilon^6d\gamma^2)\rightarrow{}^3F_2(d\epsilon^5d\gamma^3)$	7700 cm^{-1}	8700 cm^{-1}	8010 cm^{-1}	Group A
$\rightarrow{}^3{}_aF_1(d\epsilon^5d\gamma^3)$	12 500 cm^{-1}	14 000 cm^{-1}	13 670 cm^{-1}	Group B
$\rightarrow{}^3{}_bF_1(d\epsilon^4d\gamma^4)$	22 800 cm^{-1}	24 450 cm^{-1}	24 070 cm^{-1}	Group C

For this purpose we used Tanabe's and Kamimura's treatment[18] of spin-orbit effects for $3d^n$ systems in cubic symmetry. The excited terms[19] of Ni^{++} are both singlets (^1A, ^1E, ^1F, $^1F_2$) and triplets ($^3F_{1a}$, $^3F_{1a}$, $^3F_{2a}$) with respect to the spin-multiplicity. Then simple considerations of group-theory show, that in first-order (no mixing of cubic-field terms), the singlet levels will not be split, while the triplet levels will be split in a maximum of four levels. In fact the products[20] $D_S\times D_L$ of the cubic group representations will give[21]

$$\begin{aligned} &A_1\times\Gamma_i=\Gamma_i \\ &A_2\times F_1=\Gamma_5 \\ &F_1\times F_1=\Gamma_1+\Gamma_3+\Gamma_4+\Gamma_5 \\ &F_1\times F_2=\Gamma_2+\Gamma_3+\Gamma_4+\Gamma_5, \end{aligned} \tag{3}$$

since $S=0$ transforms as A_1, and $S=1$ as F_1. For the detailed calculation of the splitting directly in the cubic-symmetry basis Tanabe and Kamimura's tables were used.[18] The following energy-level splitting is found when interactions between different cubic-symmetry terms are neglected (Table IV). In the case of $^3F_1$ there are two cubic-symmetry terms characterized by the same transformation properties. After taking into account the coulomb mixing, one can write

$$|\,{}^3F_{1a}\rangle=\cos\theta'\,|\,{}^3F_1(d\epsilon^4d\gamma^4)\,\rangle-\sin\theta'\,|\,{}^3F_1(d\epsilon^5d\gamma^3)\,\rangle \tag{4}$$

$$|\,{}^3F_{1b}\rangle=\cos\theta\,|\,{}^3F_1(d\epsilon^4d\gamma^4)\,\rangle-\sin\theta\,|\,{}^3F_1(d\epsilon^5d\gamma^3)\,\rangle, \tag{5}$$

with

$$\tan2\theta=\frac{12B}{10Dq+9B},$$

$$\sin2\theta=-12B[225B^2+180BDq+100Dq^2]^{-\frac{1}{2}}, \tag{6}$$

$$\tan2\theta'=\frac{12B}{10Dq+9B},$$

$$\sin2\theta'=12B[225B^2+180BDq+100Dq^2]^{-\frac{1}{2}} \tag{7}$$

$$c_b=2\cos^2\theta-\sin^2\theta+2\sin2\theta, \tag{8}$$

with $Dq\simeq-850$ cm^{-1} for Ni^{++} in MgO. For $^3F_{1a}$ one has simply to use θ' instead of θ in (8) for $c_i(i=a,b)$. The splitting pattern is the same.

TABLE IV. Spin-orbit splitting of ^3F cubic-symmetry terms (first-order).

$^3F_2$	
$W_1=\zeta/2$	(single; symmetry properties: Γ_2)
$W_2=\zeta/4$	(threefold; Γ_5)
$W_3=-\zeta/4$	(fivefold; Γ_3 and Γ_4)
$^3{}_iF_1$	$(i=a,b)$
$W_1=(\zeta/4)c_i$	(fivefold; Γ_3 and Γ_5)
$W_2=(\zeta/4)c_i$	(threefold; Γ_4)
$W_3=-(\zeta/2)c_i$	(single; Γ_1)

(d) Direct Determination of Crystal-Field Parameters

Since the absorption we are considering shows considerable resolution, it will be convenient to determine directly from the observed spectrum the crystal-field parameters, which are usually obtained using the energy of the center of broad absorptions and neglecting spin-orbit effects. The value of Dq can be deduced quite easily since $^3F_2-{}^3A_2=10Dq$. If one adds the amount of the predicted spin-orbit coupling stabilization (Table III) of $^3F_2$ to the first line observed in the 8000 cm^{-1} region (line A_1, Fig. 1), one obtains $|\,Dq\,|=815$ cm^{-1}, which should be considered a good upper limit for Dq in case that lattice vibrational energy is associated with the electronic transistion. The ground-term shift due to spin-orbit coupling is neglected because it is only a second-order effect. By using similar considerations in the assignment of the absorption at 24 000 cm^{-1} to the $^3A_2\rightarrow{}^3F_{1b}$ transition, the value of the B parameter is deduced, $B=890$ cm^{-1}. With these values of the parameters

$$|\,Dq\,|=815\text{ cm}^{-1},\qquad B=890\text{ cm}^{-1}, \tag{9}$$

[18] Y. Tanabe and H. Kamimura, J. Phys. Soc. Japan **13**, 394 (1958).

[19] We intend for "term," a cubic-symmetry manifold labeled by the two quantum numbers S and Γ.

[20] H. Bethe, Ann. Phys. **3**, 181 (1929).

[21] Since various notations are used for cubic-group representations, we would like to remind the reader of the equivalence of the following symbols: Γ_1 and A_1; Γ_2 and A_2; Γ_3 and E; Γ_4, F_1 and T_1; Γ_5, F_2 and T_2. We shall try, whenever possible, to use Bethe notation[20] Γ_i for the cubic-symmetry representations of the total angular momentum space (product space of orbital angular momentum space and spin space).

the center of the $^3F_{1a}$ manifold is predicted (Fig. 6) at 13 560 cm^{-1} not far from the observed absorption which starts at 13 700 cm^{-1} (Fig. 3). In order to estimate the position of the singlet terms, we assume $C/B=4.4$. The only singlet level which we expect to see in the present highly dilute sample is the ^1E_a level, which is expected to have a strong spin-orbit mixing with $^3F_{1a}$. Using for the crystal-field parameters the set of values of Eq. (9) and $C=4.4B$, one can construct the predicted energy-level scheme (Fig. 6).

We are also interested, in the process of interpretation of the fine structure of the observed absorption, in the spin-orbit splitting constant c_i for $^3F_{1a}$ and $^3F_{1b}$ [Eq. (8)]. The wavefunctions for the corresponding states, Eqs. (4) to (7), are

$$|\,^3F_{1a}\rangle=-0.7023\,|\,d\epsilon^4d\gamma^4\rangle+0.7118\,|\,d\epsilon^5d\gamma^3\rangle,^{22} \quad (10)$$

$$|\,^3F_{1b}\rangle=0.7118\,|\,d\epsilon^4d\gamma^4\rangle+0.7023\,|\,d\epsilon^5d\gamma^3\rangle. \quad (11)$$

We add, for subsequent use in the discussion, the explicit form of ^1E_a

$$|\,^1E_a\rangle=0.171\,|\,d\epsilon^4d\gamma^4\rangle+0.9851\,|\,d\epsilon^6d\gamma^2\rangle. \quad (12)$$

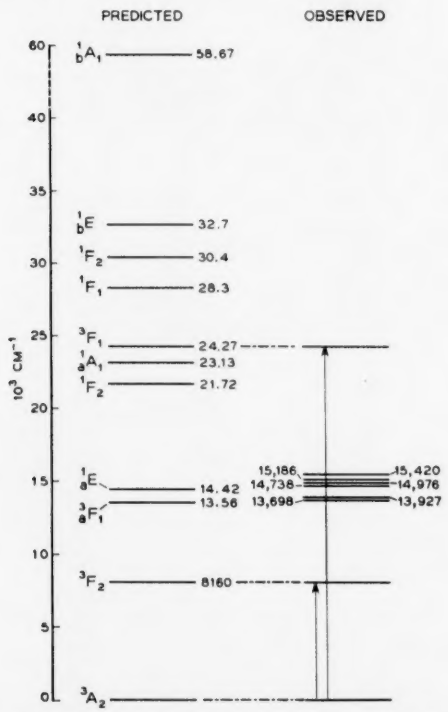

FIG. 6. MgO:Ni. Left: Predicted energy level scheme, assuming $|\,Dq\,|=815$ cm^{-1}; $B=890$ cm^{-1}; $C=4.4B$. Right: Observed absorptions. (Arrows indicate energy differences used in the calculation of the position of the cubic-field terms.) Intersystem combinations (from triplets to singlets) have low probability.

[22] The constants of Eq. (10) differ only by 5% from the analogous constants in the expression for $\Gamma_5(^3{}_aF_1)$ obtained from Liehr's and Ballhausen's calculation.

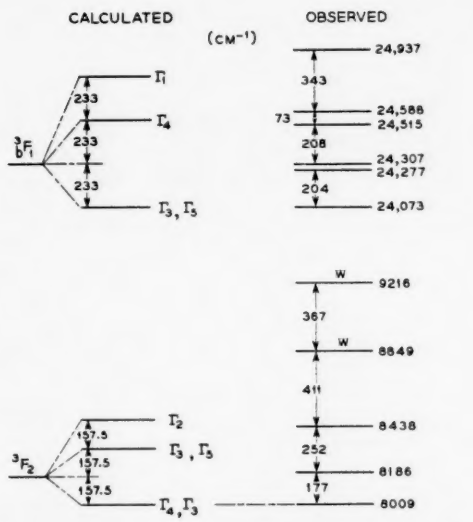

FIG. 7. MgO:Ni. Left: First-order splitting for $^3F_2$ and $^3{}_bF_1$, with the following choice of the parameters: $\zeta=630$ cm^{-1}; $|\,Dq\,|=815$ cm^{-1}; $B=890$ cm^{-1}. The separation from $^3F_2$ to $^3{}_bF_1$ is only schematic. Right: Observed absorption lines. (Those marked w are weak.)

The spin-orbit splitting constants for $^3F_{1a}$ and $^3F_{1b}$ are

$$c_b=-1.48, \qquad c_a=2.478. \quad (8b)$$

The predicted spin-orbit splitting scheme in first-order is given in Fig. 7.

(e) Second-Order Effects of Spin-Orbit Coupling

It was shown previously that in first order, some of the energy levels are accidentally degenerate in spin-orbit coupling (Fig. 7, Table IV). This accidental degeneracy will be removed when the mixing of different cubic-field terms by spin-orbit coupling is taken into account. Since the spin-orbit coupling operator is diagonal in J, nondiagonal matrix elements of spin-orbit will exist only between levels belonging to the same representations Γj of the total angular momentum space. In order to estimate the importance of this mixing of different terms, we shall concentrate on a specific case, namely that of the mixing of $^3F_{1a}$ and ^1E_a, which have only a representation in common, namely Γ_3 [see Eq. (3)]. In this case one would predict that the spin-orbit mixing of these two levels will leave unchanged the energy of the Γ_1, Γ_4, and Γ_5 multiplet components, while shifting the Γ_3 level belonging to $^3F_{1a}$, and thus lifting the accidental degeneracy of Γ_3 and Γ_5.

The relevant secular determinant (11×11) for such interaction has been constructed evaluating the matrix elements by means of Tanabe and Kamimura's formalism.[18,23] The matrix elements which characterize

[23] S. Sugano and Y. Tanabe, J. Phys. Soc. Japan **13**, 880 (1958).

TABLE V. Spin-orbit levels, inclusive of term mixing.

Transitions	Theory (Liehr and Ballhausen)[17] ($Dq=-900$ cm^{-1}, $\lambda=-275$ cm^{-1}, $F_4=90$ cm^{-1}) Energy	Separation	Experiment Energy	Separation
$\Gamma_5(^3A_2)\rightarrow\Gamma_2$[a]	8723		8009 (A_1)	
		163		177
$\rightarrow\Gamma_4$	8886		8186 (A_2)	
		336		252
$\rightarrow\Gamma_5$	9212		8438	
		142		
$\rightarrow\Gamma_2$	9354		8849	
			9216	

[a] The notation for the spin-multiplicity is no longer used because of the mixing of different cubic-field terms.

the mixing of the cubic-field terms $^3F_{1a}$ and ^1E_a are of the form

$$a_E\beta_F\langle{}^1E(d\epsilon^4d\gamma^4)\,|\,\mathbf{V}(1F_1)\,|\,{}^3F_1(d\epsilon^5d\gamma^3)\rangle + b_E\beta_F\langle{}^1E(d\epsilon^6d\gamma^2)\,|\,\mathbf{V}(1F_1)\,|\,{}^3F_1(d\epsilon^5d\gamma^3)\rangle, \quad (13)$$

when the wavefunctions of $^3F_{1a}$ and ^1E_a are expressed as

$$|\,{}^1E_a\rangle=a_E\,|\,{}^1E(d\epsilon^4d\gamma^4)\rangle+b_E\,|\,{}^1E(d\epsilon^6d\gamma^2)\rangle, \quad (14)$$

$$|\,{}^3F_{1a}\rangle=\alpha_F\,|\,{}^3F_1(d\epsilon^4d\gamma^4)\rangle+\beta_F\,|\,{}^3F_1(d\epsilon^5d\gamma^3)\rangle. \quad (15)$$

One finds after solving the (11×11) secular equation, that all the eigenvalues of the spin-orbit energy have the same value as for the first-order treatment of $^3F_{1a}$ and ^1E_a with the exception of two levels doubly degenerate which can only be Γ_3 levels, as predicted. In the simplest treatment, if one neglects the mixing of $^1E(d\epsilon^4d\gamma^4)$ in the term ^1E_a, Eq. (12), and similarly the mixing of $^3F_1(d\epsilon^4d\gamma^4)$ in $^3F_{1a}$, one obtains for the energy of the two Γ_3 multiplet components

$$W(\Gamma_3)=(3i\zeta/2)\left[(\delta/3i\zeta)-\tfrac{1}{12} \mp\left\{(\delta/3i\zeta)^2+\tfrac{1}{6}(\delta/3i\zeta)-\tfrac{65}{144}\right\}^{\frac{1}{2}}\right], \quad (16)$$

where δ is the energy difference of the cubic field terms $^3F_{1a}$ and ^1E_a. When the mixing of different subshell configurations is considered, then the eigenvalues of the spin-orbit energy will be accordingly modified by the presence of the mixing constants. Thus, neglecting the contribution from the product $a_E\beta_F$ and assuming $\delta=860$ cm^{-1} (from Fig. 6), $\zeta=630$ cm^{-1}, $c_a=2.48$, and one obtains the following eigenvalues of the spin-orbit energies of Γ_3 from the mixing of $^3F_{1a}$ and ^1E_a.

	2nd order	1st order	Difference (2nd order effect)	
$\Gamma_3(^1{}_aE)$	1124	860	+264	
				in cm^{-1} (17)
$\Gamma_3(^3{}_aF_1)$	125	390	−264	

(f) Comparison with Experiment

Group A (*8000* cm^{-1})

We shall first compare Liehr and Ballhausen's predictions with experiment.[17] These authors give the energy level scheme of Table V for the triplet manifold, assuming[24] $Dq=-900$ cm^{-1}, $\lambda=-275$ cm^{-1}, and $F_4=90$ cm^{-1}. The observed separation of the two sharp lines A_1 and A_2 (Fig. 1), corresponds quite well to the predicted energy separation of Γ_3 and Γ_4 of $^3F_2(d\epsilon^5d\gamma^3)$. Why only two such transitions are observed as narrow lines instead of the transitions to all available levels, is a question which can only be answered by considering in detail the transition probability of each of the various transitions.

It is rather interesting that the absorption in this region is in the form of sharp lines, even at 78°K, since no intersystem combinations are expected in this region and one can unambiguously associate these sharp lines to intrasystem combinations, for which a stronger dependence on the fluctuations of the crystal-field is expected.

The expressions for the first-order spin-orbit splitting, derived using Tanabe's and Kamimura's formalism, are then given in Fig. 7 and contrasted with the observed data. The agreement with experiment is poor. A comparison of the results of the first-order treatment with the energy differences of Table V shows a rather surprisingly large separation between the accidentally degenerate (first-order) $^3\Gamma_4$, $^3\Gamma_3$ levels when a second-order treatment is applied to the isolated $^3F_2$ term. While the predicted separation of these two levels according to Liehr and Ballhausen is in very good

TABLE VI. Spin-orbit levels inclusive of term mixing.

Transitions	Theory (Liehr and Ballhausen)[17] ($Dq=-900$ cm^{-1}, $\lambda=-275$ cm^{-1}, $F_4=90$ cm^{-1}) Energy (cm^{-1})	Separation (cm^{-1})	Experiment Energy (cm^{-1})	Separation (cm^{-1})
$\Gamma_5[^3A_{2g}(d\epsilon^5d\gamma^2)]$				
$\rightarrow\Gamma_3$[a]	12 338		12 987 (?)	
$\rightarrow\Gamma_1$	14 027		13 698 (B_1)	
		414		229
$\rightarrow\Gamma_4$	14 441		13 927 (B_2)	
		611		819
$\rightarrow\Gamma_5$	15 052		14 738 (B_3)	
		235		236
$\rightarrow\Gamma_2$	15 287		14 976 (B_4)	
			15 186 (B_5)	
			15 420 (B_6)	

[a] Essentially singlet level.

[24] Compare also with Eq. (18b).

agreement with the observed separation of the A_1, A_2 lines, a comparison with the spectra of MgO:Co should show whether this agreement is simply fortuitous, and the $A_1 \rightarrow A_2$ separation is due to lattice vibrational energies (see following article).

Group B ($at \sim 14\,500$ cm^{-1})

In this region spin-orbit coupling of the cubic-field terms $^3F_{1a}$ and ^1E_a is expected. Predicted (according to L.B.) and experimental energy separations are given in Table VI. We are mainly interested in the energy separation of the levels, since their absolute positions depend linearly on Dq and the Coulomb interaction parameters. There is a satisfactory agreement, although the observed group in question has more lines than predicted, unless vibrational contributions of the lattice are included. On the other hand the nature of the spin-orbit effects in this region depends rather markedly on the relative position of the cubic-field term ^1E_a and $^3F_{1a}$. If one were to use, instead of the choice[25] of Liehr and Ballhausen, one in which $B=890$ cm^{-1} and $C=4.4B$, then the relative separation of the two terms will be as indicated in Fig. 8. After the spin-orbit mixing of the two cubic-field terms is considered, one has a predicted pattern as given in the center column of Fig. 8 and which is rather similar to the observed pattern.

Group C ($\sim 24\,000$ cm^{-1})

In Table VII we compare again the Liehr and Ballhausen energy-level scheme with the observed narrow absorptions. Here also we are mainly interested not in the absolute energy of the levels, but in their energy separation. As for group A, the agreement is rather good for the energy separation of the leading

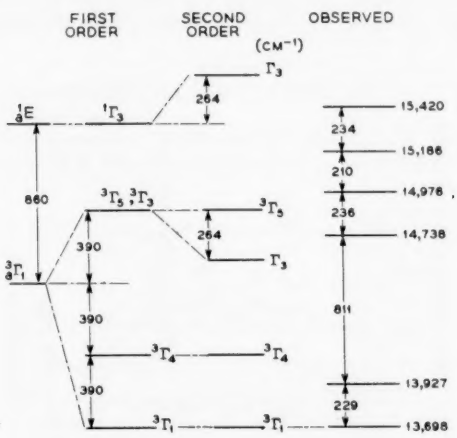

FIG. 8. MgO:Ni. Predicted spin-orbit coupling of $^3{}_aF_1$ and $^1{}_aE$ levels in first order (Left), and second order (Center). Right: Observed absorption lines.

[25] See also Eq. (18b).

TABLE VII. Spin-orbit levels inclusive of term mixing.

Transition	Theory[a] Energy	Theory[a] Separation	Experiment Energy	Experiment Separation
$\Gamma_5 \rightarrow \Gamma_3$	24 452		24 073 (C_1)	
		175		200
$\rightarrow \Gamma_5$	24 627		24 277	
			(C_2)	
$\rightarrow \Gamma_4$	24 703		24 307	
		192		208
$\rightarrow \Gamma_1$	24 895		24 515	
			24 588	
			24 937	

[a] See previous tables.

lines of the group. The predictions of the first-order treatment of spin-orbit effect are not in good agreement with experiment as can be seen in Fig. 7.

(g) Final Remarks

No attempt will be made in the present article to analyze the details of the vibrational contribution of the lattice to the electronic transitions. We think that there is strong evidence to show that this contribution is indeed present.

When the predictions of a simple spin-orbit treatment are compared with experiment, the energy separations of the line components in the absorption are in fair agreement with the predictions for the group ^1E_a and $^3F_{1a}$ in which the second-order effects of the spin-orbit coupling have been considered. The agreement is rather poor for the remaining multiplets whenever the treatment has been limited to first order. The agreement is improved for these groups when comparison is made of the observed data with the predictions by Liehr and Ballhausen, which give a complete treatment of second-order effects. Their predictions perhaps are not as good for the ^1E_a and $^3F_{1a}$ group where the over-all effects depend rather critically on the cubic-field separation of the two terms.

The two sharp lines A_1 and A_2 are unambiguously associated with an intrasystem transition ($^3A_2 \rightarrow {}^3F_2$) and can therefore be used as a very sensitive probe to study the nature of the crystal potential at the site of the Ni^{++} ion. Since the energy difference of the terms $^3F_2 - {}^3A_2$ depends *linearly* on Dq, and not via second-order effects as is the case with the usual sharp lines (Mn^{++}, Cr^{3+}, V^{++}) due to intersystem combinations,[26–28] one can expect rather large dependence on applied external pressure. In performing an experiment in which high pressures are applied isotropically, one should be able to observe large shift in the frequency of

[26] R. Pappalardo, Phil. Mag. **2,** 1397 (1958).
[27] S. Sugano and I. Tsujikawa, J. Phys. Soc. Japan **13,** 889 (1958).
[28] M. H. L. Pryce and W. A. Runciman, Discussions Faraday Soc. **26,** 34 (1958).

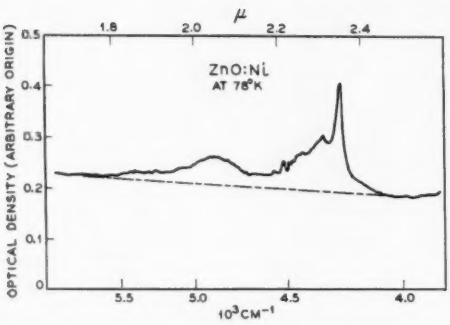

FIG. 9. Absorption of a single crystal of ZnO:Ni (0.11% Ni) at 78°K, in the 4500 cm^{-1} region. Sample thickness 0.008 in (~0.02 cm).

A_1 and A_2. Also when pressure is applied along definite directions, splitting and shifts in the line patterns should easily be observable. This sort of experiment should give results which can be easily correlated to internal parameters of the crystals, since elastic constants for MgO are fairly well known.

Another possible use of the lines would be as a probe for magnetic exchange effects. Assuming it might be possible to have a rather high concentration of another paramagnetic ion in the system, in principle it should be possible to observed optically effects due to magnetic coupling of neighboring ions on the sharp lines of Ni^{++}.

Finally, from a consideration of the energy level scheme of Ni^{++}, since the $^3F_2$ term to which line A_1 and A_2 belong is the lowest excited term and has a large energy separation from the ground state, one expects that it will fluoresce in the form of sharp lines. There is no need to emphasize the present interest in line fluorescence in a system optically isotropic, i.e., MgO doped with divalent ions. We believe that all these possibilities will deserve more experimental study of MgO:Ni in the future.

IV: ZnO:Ni

(a) Preparation of Samples

Single crystals of Ni-doped ZnO were grown[29] in the form of thin plates, from a PbF_2 flux, using a platinum crucible, and cooling the system from 1150° to 800°C at the rate of 5°C per hour.

From the melt, thin plates with the hexagonal zincite structure[30] were extracted, of average thickness 0.020 in., and most of them optically isotropic. Samples containing a nominal doping of 5% Ni proved optically too dense. Better results were obtained with a nominal doping of 0.5% Ni (of total weight). The resulting plates were of a light olive-green color. The Ni content was determined as 0.11% of total weight by Miss S. Vincent of these Laboratories using x-ray fluorescence techniques. The faces of the samples were accurately polished and the thickness of the samples used was 0.008 in. (i.e., ~0.02 cm).

(b) Absorption Spectra of ZnO:Ni

Preliminary work was performed by McClure[31] on mixed powders of ZnO and NiO, fired at high temperatures, and then diluted in KBr pellets. The resulting spectra gave indications of absorption bands in the same region where we had found considerable structure in the absorption. The following groups of absorptions were found in the samples investigated. In the ~4400 cm^{-1} region a group of lines is found first at 78°K and on lowering the temperature to 4.2°K, a new sharp line (A_1) appears, while the intensity of line A_2 is enhanced. The remaining absorption has a more complex structure than at 78°K (Figs. 9 and 10). A few isolated narrow absorptions are found at 78°K in the 8500 cm^{-1} region (Fig. 11). With the decrease in temperature, line B_0 disappears, while the intensity of B_1 is enhanced and its width decreased. Quite a few other lines appear at 4.2°K in this region.

A rather broad double band is present at ~13 000 cm^{-1}. No striking temperature changes are found in this absorption region (Fig. 12).

In the 15 500 cm^{-1} region a double band found at room temperature shows an interesting line structure at 78°K, in which a broad line D_0 is very intense and is followed by progressively weaker absorptions (Fig. 13). Then at 4.2°K line D_0 disappears and one can exclude the possibility that the disappearance is simply due to the general shift of the group, since actually the remaining lines of this group appear to be at practically the same frequencies.

At higher energy a strong edge absorption is present. Superposed on this band a rather strong subsidiary

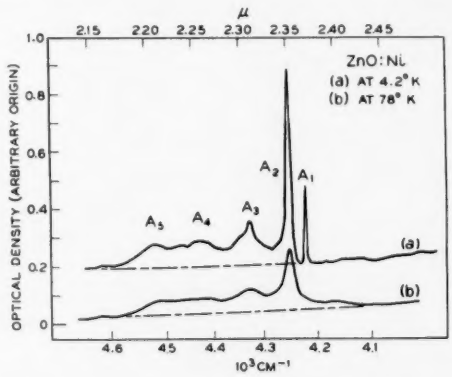

FIG. 10. Absorption of a ZnO:Ni single crystal (0.11% Ni) at 78°K and 4.2°K. Sample thickness 0.008 in. Note the appearance of line A_1 at 4.2°K.

[29] J. W. Nielsen and E. F. Dearborn, J. Phys. Chem. **64**, 1762 (1960).

[30] Landolt Bornstein, *Zahlenwerte und Funktionen I. Band* (Springer-Verlag, Berlin, Germany, 1955), Vol. 4.

[31] D. S. McClure, J. Phys. Chem. Solids **3**, 311 (1957).

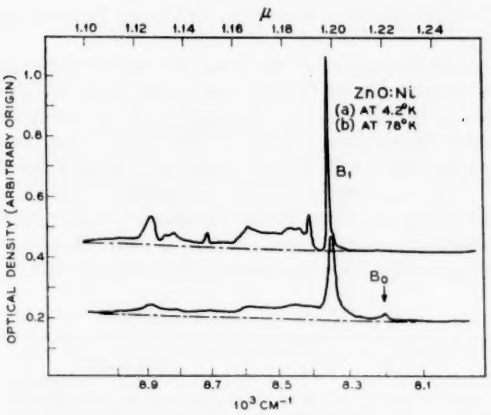

FIG. 11. Absorption lines of ZnO:Ni (0.008 in) at 78° and 4.2°K, in the 8500 cm^{-1} region. Note disappearance of line B_0 at 4.2°K).

absorption is found with center at $\sim$23 000 cm^{-1} (Fig. 14). Detailed information on all the absorptions, (namely; wave number of absorption peaks, extinction coefficients, ocillator strengths, etc.) is given in Tables VIII–X.

(c) Interpretation of the Spectrum of ZnO:Ni

In ZnO, the Ni^{++} impurity ions are expected to be present in sites possessing tetrahedral symmetry. The symmetry of the tetrahedral sites is rigorously cubic in the zinc-blende structure while a slight axial deformation is present in the hexagonal zincite structure.[30] The samples used had hexagonal structure. Using for preliminary consideration the value $Dq_{oct}\simeq -850$ cm^{-1} obtained in the case of MgO:Ni, one predicts for the cubic-field parameter in ZnO the value $Dq_{tet}=-4/9Dq_{oct}\simeq 380$ cm^{-1}, [according to Eq. (1)], while the parameters of electrostatic interaction and spin-orbit coupling should not be affected very much by the change in symmetry.

From Liehr and Ballhausen's[17] diagram we obtain the following energy-level scheme to be compared with

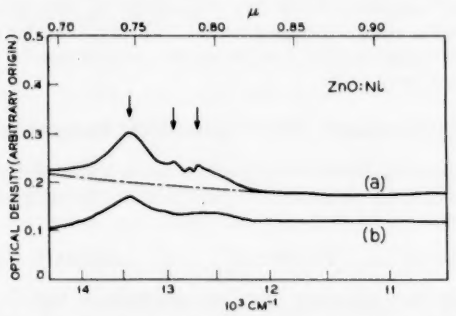

FIG. 12. Absorption of ZnO:Ni in the 13 500 cm^{-1} region: (a) At 4.2°K; (b) at 78°K.

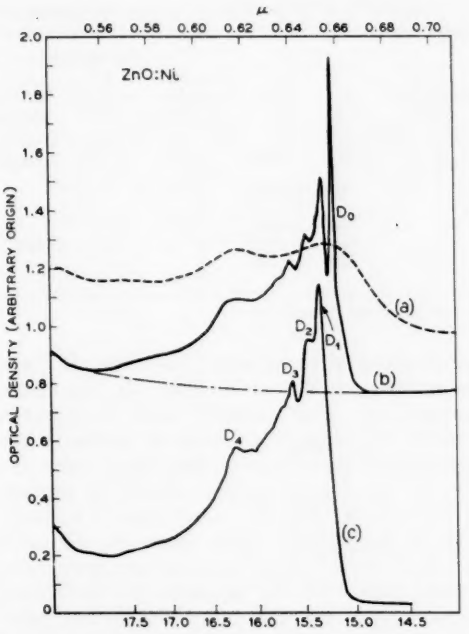

FIG. 13. Intense absorption of ZnO:Ni (0.008 in thick) at $\sim$15 500 cm^{-1}: (a) At room temperature; (b) at 78°K; (c) at 4.2°K. Note disappearance at 4.2°K of narrow absorption D_0.

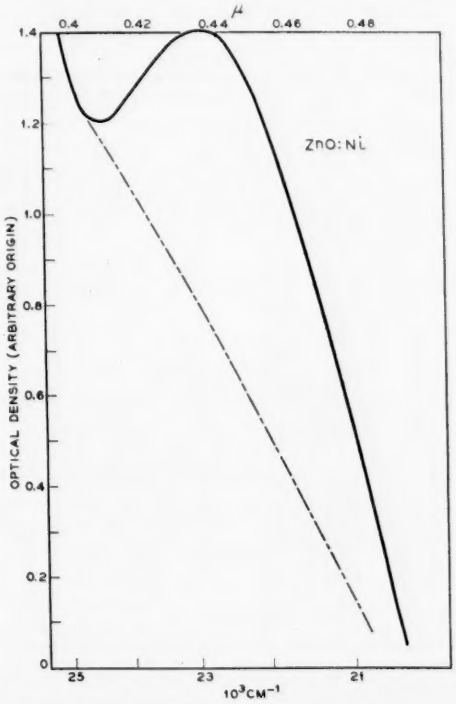

FIG. 14. Intense absorption superposed onto the strong edge absorption of the ZnO matrix; temperature 78°K.

TABLE VIII. ZnO:Ni[a] (0.02 cm) at room temperature.

Absorption peaks	λ in A	$\bar{\nu}$ in cm^{-1}	Extinction coefficient $\alpha_{max}(cm^{-1})$	Half-width at $\alpha=\frac{1}{2}\alpha_{max}$ (cm^{-1})	Oscillator strength
	11 920	8390	2.5		0.5×10^{-4}
	7420	13 480	0.75		
	6560	15 245	13.5		0.44×10^{-3}
	6160	16 233	11		
	5760	17 360	3		

[a] Dilution $(Ni/Zn)_{ions}=1.5\times10^{-3}$.

the experimental absorptions (Table XI). In the process of line identification in Table XI, the following considerations were implicitly used. In tetrahedral symmetry the absence of a center of symmetry makes the intrashell electric-dipole transitions parity allowable, so that the vibrational mixing of the states involved in the transition is not *a priori* necessary.[32] Then in the limit of cubic symmetry the product representation of the initial state and the dipole-moment operator (transformation properties Γ_5) must contain the cubic symmetry representation of the final state of the transition. For Ni^{++} in tetrahedral coordination, the ground level is Γ_1, and since $\Gamma_1\times\Gamma_5=\Gamma_5$ in the limit of cubic-symmetry, transitions to excited Γ_5 levels are expected to have greater intensity.

From an inspection of Table XI we can infer the preliminary conclusion that agreement with the predictions is very good for the position of the groups of triplet[33] levels (the position of their center of gravity depends only on B and Dq) while agreement is not as good for the singlet[33] levels (the energy of which is affected by the value of the parameter C). Liehr and Ballhausen assume for C/B, the free-ion theoretical value, namely 3.9, while generally the ratio is ~4.5.

TABLE IX. ZnO:Ni (0.02 cm) at 78°K.

Absorption peaks	λ in A	$\bar{\nu}$ in cm^{-1}	Extinction coefficient $\alpha_{max}(cm^{-1})$	Half-width at $\alpha=\frac{1}{2}\alpha_{max}$ (cm^{-1})	Oscillator strength
A_2	23 500	4255.3	11	35	1.8
A_3	23 090	4330.1	5	85	1.9
A_4	22 590	4426.7	3	100	1.35
	20 400	4902	2.5	300	3.4
	13 820	7235	2		
	(?)	(?)			
B_0	12 180	8210.2	1.5	35	0.23
B_1	11 980	8347.2	14	20	1.27
	11 840	8446	3		
	11 645	8587	2		0.1
	11 340	8818	1.5		
	11 255	8884	2.5		
	7890	12 674	1		
	7620[a]	13 123[a]	2		0.23
	7445	13 430	3.5		
	6620[a]	15 016[a]			
D_0	6580	15 197	54	50	12.8
D_1	6537	15 297	38		
D_2	6462	15 475	27.5		
D_3	6400	15 625	23		23
	6346	15 773			
D_4	6152	16 255	26		
	5800	17 240			
H	4630	22 935	38		73

[a] Shoulder.

TABLE X. ZnO:Ni (0.02 cm) at 4.2°K.

Absorption peaks	λ in A	$\bar{\nu}$ in cm^{-1}	Extinction coefficient $\alpha_{max}(cm^{-1})$	Half-width at $\alpha=\frac{1}{2}\alpha_{max}$ (cm^{-1})	Oscillator strength $f\times10^6$
A_1	23 690	4221.2	13.3	2.7	0.16
A_2	23 515	4252.6	34	9	1.3
A_3	23 100	4329	7.4		
	23 015	4345	5.4		2.1
A_4	22 600	4424.7	4.4		
A_5	22 100	4524.9	4.0		
B_1	11 976	8350	35	5.5	0.85
	11 896	8406.2	6.4	12	0.34
	11 840	8445.9	3.7		1.0
	11 650	8583.7	4.0		
	11 480	8711	2.0		
	11 340	8818	2.0		
	11 258	8882.6	4.9	45	1.0
	7885	12 682	2.2		
	7738	12 923	2.2		7.3
	7450	13 422	4.9		
D_1	6522	15 332	52.7		
D_2	6465	15 468	41.3		
D_3	6392.5	15 643	34		81
	6340	15 772.8	28		
D_4	6140	16 286	22.1		
	5780	17 300	4.0		
	[5060][a]	[17 860][a]			

[a] At this frequency $I_0/I=10$, namely optical density $D=1$.

Also, in the case of ZnO:Ni, we shall first try to derive the value of the crystal-field parameters from the observed data, and then try to interpret the fine structure of the observed spectrum by means of the spin-orbit coupling effects. We will adapt to the present case the results obtained for Ni^{++} in MgO and for the time being neglect low-symmetry components of the crystal potential.

(d) Derivation of the Crystal-Field Parameters

The parameters used by LB in the calculation of the energy-level scheme for Ni^{++} have the following values:

$$F_2=14F_4; \qquad F_4=90\ cm^{-1}; \qquad \lambda=-275\ cm^{-1}. \quad (18)$$

(λ is the spin-orbit coupling constant in the $L-S$

[32] C. J. Ballhausen and A. D. Liehr, J. Mol. Spectroscopy **2**, 342 (1958); errata, *ibid.* **4**, 190 (1960).

[33] Spin-multiplicity of parent term in strong-field limit.

TABLE XI. Ni^{++} in tetrahedral coordination.

Transitions	Theory (Liehr and Ballhausen)[17] Fig. 1 and Table I[a] $Dq=380$ cm^{-1}	$Dq=400$ cm^{-1}	Experiment (at 4.2°K)	
$\Gamma_1(^3F_1[de^4d\gamma^4])\rightarrow\Gamma_4(^3F_1[de^4d\gamma^4])$[b]	320 cm^{-1}	334 cm^{-1}	~150	
$\rightarrow\Gamma_2(^3F_1[de^4d\gamma^4])$	900	929		
$\rightarrow\Gamma_5(^3F_1[de^4d\gamma^4])$	1150	1122		
$\rightarrow\Gamma_4(^3F_2[de^5d\gamma^3])$	3950	4133		
		(79)		
$\rightarrow\Gamma_5(^3F_2[de^5d\gamma^3])$	4000	4212	4221 4252	
		(81)		(100)
$\rightarrow\Gamma_2(^3F_2[de^5d\gamma^3])$	4130	4293	4329 4352	
		(82)		(90)
$\rightarrow\Gamma_2(^3F_2[de^5d\gamma^3])$	4300	4475	4425 4524	
$\rightarrow\Gamma_5(^3A_2[de^5d\gamma^2])$	7900	8290	8350 (B_1)	
$\rightarrow\Gamma_5(^1F_2[de^4d\gamma^4])$	12 100 cm^{-1}	12 124 cm^{-1}	12 700	
$\rightarrow\Gamma_3(^1E[de^4d\gamma^4])$	12 600	12 657	~13 500	
$\rightarrow\Gamma_5(^3F_1[de^5d\gamma^3])$	15 450	15 587	15 332 (D_1)	
		(59)		(136)
$\rightarrow\Gamma_2(^3F_1[de^5d\gamma^3])$	15 520	15 646	15 468	
		(345)		(175)
$\rightarrow\Gamma_4(^3F_1[de^5d\gamma^3])$	15 800	15 991	15 643	
		(197)		(643)
$\rightarrow\Gamma_1(^3F_1[de^5d\gamma^3])$	16 100	16 188	16 286	
$\rightarrow\Gamma_5(^1F_2[de^5d\gamma^3])$	18 500	18 657		
$\rightarrow\Gamma_4(^1F_1[de^5d\gamma^3])$	20 100 cm^{-1}	20 236 cm^{-1}		
$\rightarrow\Gamma_1(^1A_1[de^4d\gamma^4])$	20 250	20 372		
$\rightarrow\Gamma_3(^1E[de^5d\gamma^2])$	21 600	21 994	22 900[c]	
$\rightarrow\Gamma_1(^1A_1[de^6d\gamma^2])$	43 800	44 004		

[a] The precise predicted values have been kindly made available by A. D. Liehr (private communication).
[b] The expression in round parenthesis indicates the parent term in the strong-field limit.
[c] At 78°K.

scheme.) The connection to Racah's[34] parameters is contained in the relations

$$A=F_0-49F_4; \qquad B=F_2-5F_4; \qquad C=35F_4. \tag{19}$$

In the particular case treated by LB

$$B=9F_4=810\text{ cm}^{-1}; \qquad C=35F_4=3.9B. \tag{18b}$$

We might now try to evaluate the B and Dq parameters directly from the observed absorptions by considering the position of two intrasystem transitions

$$^3F_{1a}\rightarrow{}^3F_2 \quad \text{observed energy} \quad 4400\text{ cm}^{-1}$$
$$^3F_{1a}\rightarrow{}^3F_{1b} \quad \text{observed energy} \quad \sim 15\,500\text{ cm}^{-1}. \tag{20}$$

[34] G. Racah, Phys. Rev. **62**, 438 (1960).

This enables one to find a preliminary set of values for Dq and B. These are only approximate values, as spin-orbit coupling effects have been neglected and as we shall see, they can be important for the ground state.

Now we are particularly interested in the amount of spin-orbit coupling stabilization of the ground state and in the spin-orbit splitting of the remaining ^3F cubic-symmetry terms. The constants c_a and c_b which determine the splitting of the $^3F_1$'s cubic-symmetry terms, depend on the values of the constant θ, which describe the mixing of the two $^3F_1$ terms due to Coulomb interaction [Eqs. (4)–(5)].

We substitute the preliminary value of Dq (positive!) and B, in $\tan 2\theta=12B/(10Dq+9B)$ and now we are able to have an estimate, via c_a and c_b, of the spin-orbit

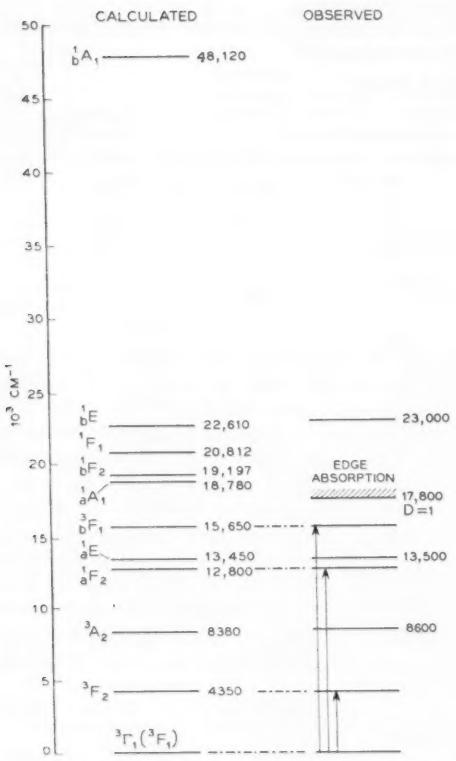

FIG. 15. ZnO:Ni. Left: Energy level scheme, assuming $B=795$ cm^{-1}; $Dq=405$ cm^{-1}; $C=4.36B$ and a ground-state stabilization (spin orbit) of 900 cm^{-1}. The energy plotted for the excited states corresponds to the center of gravity of each multiplet. Right: Observed energy differences. The energy separations indicated by the arrows have been used in the calculations to derive the values of the parameters Dq, B, and C. Transitions to singlet terms have low probability. Also indicated is the frequency at which the edge absorption has optical density *one* ($D=1$) over the background absorption.

splitting of $^3F_{1b}$. Then the B and Dq parameters are finally obtained, assuming a ground-state stabilization of $\sim$900 cm^{-1} (ζ is taken with the free-ion value of 630 cm^{-1}), and assuming the baricenter of the $^3F_2$ and $^3F_{1b}$ multiplets to be given approximately by the position of the first line of the corresponding group increased by the predicted half-width of the multiplet. In this way the following values are found for the pertinent parameters:

$$B=795 \text{ cm}^{-1}, \qquad Dq=405 \text{ cm}^{-1},$$

$$|\, Dq(\text{ZnO:Ni})/Dq(\text{MgO:Ni}) \,| = 405/815 = 0.497,^{35}$$

$$\times |\, Dq_{\text{tet}}/Dq_{\text{oct}} \,|_{\text{predict}} = 0.444. \quad (21)$$

These values are very close to those used in discussing Liehr and Ballhausen's energy-level scheme (Table XI), which accounts for the close agreement in the case of triplet terms. The energy value for $^3A_2$ is predicted as 8380 cm^{-1}. In Fig. 15 one can check how well experiment and theory agree. The values of the spin-orbit splitting constants obtained are

$$c_a=2.938, \qquad c_b=-1.94, \quad (22)$$

when the corresponding wavefunctions for $^3F_{1a}$ and $^3F_{1b}$ are expressed by

$$|\, ^3F_{1a}\rangle = 0.9385 \,|\, d\epsilon^4 d\gamma^4\rangle - 0.3453 \,|\, d\epsilon^5 d\gamma^3\rangle, \quad (23)$$

$$|\, ^3F_{1b}\rangle = +0.3453 \,|\, d\epsilon^4 d\gamma^4\rangle + 0.9385 \,|\, d\epsilon^5 d\gamma^3\rangle. \quad (24)$$

The remaining parameter C is obtained on the basis of the identification of the peak found at 12 800 cm^{-1} with the level $^1F_2$ (Fig. 12). The value $C=3470$ cm^{-1} is then obtained, so that $C/B=4.36$. Using Tanabe's and Sugano's energy matrices[4] and taking into account the spin-orbit stabilization of the ground state (Table IV), the required elements are known which enable us to set up the energy level scheme for ZnO:Ni. Both the calculated diagram and the observed absorption are given in Fig. 15.

(e) Spin-Orbit Splitting of Cubic-Symmetry Terms

As already mentioned in the case of MgO, we need consider, in a first-order treatment of spin-orbit coupling, only the ^3F cubic-symmetry multiplets. The details of the spin-orbit splitting for such levels are calculated once the values of ζ and c_a and c_b are given. The calculation is based on the considerations made in the case of MgO:Ni and the results of the first-order treatment are given in Fig. 16.

(f) Discussion of the Various Absorption Groups in ZnO:Ni Ground Manifold

In relation to the splitting of the $^3F_1$ ground term (Fig. 16) an attempt should be made to detect the band predicted at $\sim$1300 cm^{-1}, especially if a heavily doped sample is used, although in this region an absorption of the ZnO lattice is also present. In a sample containing a nominal 5% of Ni attempts made at room temperature to detect such a band were unsuccessful. On the other hand, according to Liehr and Ballhausen's diagrams,[17] a contribution from the level at $\sim$300 cm^{-1} above the lowest level in the ground-term manifold, ought to be discernible in the room-temperature spectrum and disappear at lower temperatures. At least in two bands we actually find some temperature effects, but only going from 78 to 4.2°K. The energy difference involved is $\sim$150 cm^{-1}. This could either be explained by postulating the existence of an electronic level at 150 cm^{-1} over the ground level, or by the existence of a vibrational mode contributiong to the transition to the excited level at 78°K. This would, from a rather general

[35] With regard to the change of R (ligand-cations distance) in the two coordinations, one may note that the Mg···O separation[30] in MgO is 2.10 A. The Zn···O separation in ZnO has the value 1.95 A when the parameter u is assumed to be $\sim$3/8. Or, conversely, the ionic radius for Mg^{2+} is estimated as 0.66 A, for Zn^{2+} as 0.74 A, and 0.69 A for Ni^{2+} (Ahrens[30]).

point of view, imply the existence of phonons of some 75 cm^{-1} in energy. It is interesting to note though, that no such thermal effects are found in ZnO:Co, where presumably a similar phonon energy should appear in the spectrum (see subsequent article). So the first hypothesis seems more justified.

Group A ($\sim$*4000* cm^{-1})

This group corresponds to the transition to the $^3F_2$ term (Fig. 15). Notice that in Fig. 10 a broad absorption located at $\sim$4900 cm^{-1} is missing, while it is shown in Fig. 9. The total width of the group at 4.2°K is $\sim$550 cm^{-1}.

The splitting due to the spin-orbit coupling should amount in first approximation to $\frac{3}{4}\zeta$. Taking[16] $\zeta_d=630$ cm^{-1}, one obtains 475 cm^{-1} for the predicted width of group A. From Table IV and Fig. 16, one sees that the first group of levels has degeneracy *five* in the first apprxoimation (Γ_5 and Γ_3), and that the separation from the next group, Γ_4, should be $\sim$300 cm^{-1}. If one takes the average positions of the lines A_1, A_2, A_3 and A_4, A_5, one sees that their separation is 250 cm^{-1}. The appearance of the sharp line A_1 at 4.2°K perhaps could be explained by assuming that the thermal deformation of the crystal enhances the noncubic components of the field at low temperatures and thus causes a splitting in those groups which are left degenerate by spin-orbit coupling even in second-order (Γ_3, Γ_4, Γ_5). The agreement of LB's calculations with the observed fine structure is quite good (Table XI).

Group B ($\sim$*8600* cm^{-1})

This group is due to the transition from the ground state to the cubic-field term $^3A_2(d\epsilon^6d\gamma^2)$. Although this is a triplet-triplet transition, its intensity is low. Since the ground term can be written as [Eq. (23)].

$$^3F_{1a}\{0.9385 \mid d\epsilon^4d\gamma^4\rangle - 0.3453 \mid d\epsilon^5d\gamma^3\rangle\}$$

and has predominantly the electronic configuration $d\epsilon^4d\gamma^4$, the transition to $^3A_2$ would imply a two-electron jump. This makes the transition probability low. Three remarks can be made concerning this group. First, if our assignment is correct, one can predict that $^3A_2$ will not be split in the first order by spin-orbit coupling. Even introducing low-symmetry components of the field, the maximum number of levels is raised to *three*. Figure 11 shows together with a single intense line, a very large number of weaker lines at 4.2°K. This seems to be evidence of vibrational contribution to the absorption. Second, in spin-orbit treatment, one multiplet component (Γ_5) is obtained from $^3A_2$ [see Eq. (3)]. It was noted previously that transitions to Γ_5 states have higher probability. Actually one intense line stands out in the absorption in this region (Fig. 11, Table XI).

The other interesting fact is the disappearance of line B_0 at 4.2°K. The separation $B_1 \rightarrow B_0$ is 137 cm^{-1}.

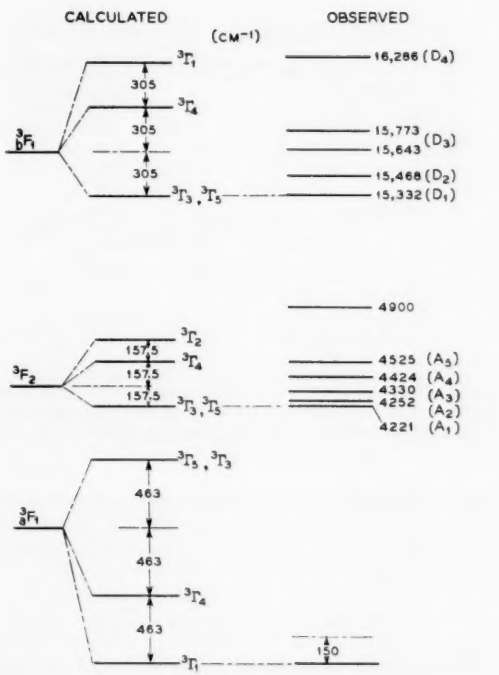

FIG. 16. ZnO:Ni. Left: Predicted spin-orbit splitting (in first order) of ^3F cubic-field terms, assuming $\zeta=630$ cm^{-1}; $B=795$ cm^{-1}; $C=4.36B$ and $Dq=405$ cm^{-1}. The separations of the cubic-symmetry terms $^3{}_aF_1 \rightarrow {}^3F_2$; $^3{}_aF_1 \rightarrow {}^3{}_bF_1$ are only schematic. Right: Observed energy separations.

We remark in passing that a similar effect for the group A is not excluded. The sensitivity of our instrumentation in that region is not high.

Group C ($\sim$*13 000* cm^{-1})

This is a weak absorption, not very well-resolved, and only slightly affected by cooling from 78° to 4.2°K. Two main peaks are located at 12 680 cm^{-1} (this followed by some fine structure at 4.2°K) and a more intense peak at 13 420 cm^{-1} (Fig. 12).

Liehr and Ballhausen's[17] diagram shows the presence of two singlet levels $^1F_2$ and ^1E in this region. There is a rather noticeable discrepancy between the predicted position of these two singlet levels and the experimental values (Table XI). The agreement can be improved if one remembers that the position of the singlet terms depends on the values of the C parameter of electrostatic interaction. Liehr and Ballhausen chose $C\simeq 3.9B$. A suitable value of the C parameter can be obtained using the experimental position of $^1F_2$, after allowing for the spin-orbit coupling stabilization of the ground state. We obtained for the parameter the value $C=$ 3500 $cm^{-1} \simeq 4.4B$.

If one then calculates the predicted energy of ^1E, one finds the value 13 150 cm^{-1}, which is in much better agreement with experiment (Fig. 15). However judging

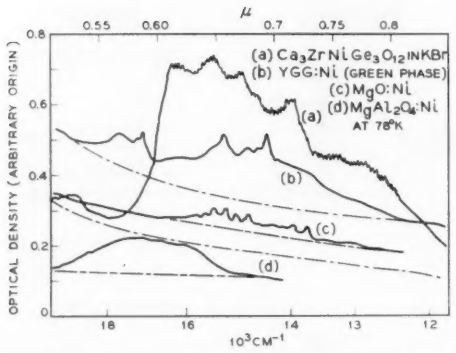

FIG. 17. Comparison of the absorption bands at 15 000 cm^{-1} and 78°K for different Ni-doped oxide systems: (a) $Ca_3ZrNiGe_3O_{12}$ in KBr pellet; (b) single crystal of nickel-doped yttrium gallium garnet (green phase); (c) single crystal of MgO:Ni; (d) single crystal of Ni-doped aluminum spinel.

by the dependence of the energy of these two singlet levels on the values of the cubic-field parameter Dq, one would expect narrower absorptions than are actually found.

Group D (~*15 500* cm^{-1})

The intense two-peaked band observed at room temperature (Fig. 13a) shows considerable sharpening at 78°K. The band starts with a very narrow intense band D_0 followed by weaker, broader peaks. This pattern is very similar to the absorption band of ZnO:Cu at 78°K.[7] At 4.2°K though, the intense narrow peak D_0 has disappeared. The separation $D_1 \rightarrow D_0$ is ~180 cm^{-1}, close to the analogous distance of the $B_0 \rightarrow B_1$ peaks in group B (Fig. 11, Tables IX and X). Probably this effect is due to the contribution of a level above the ground level, which ceases to be effective in absorption at 4.2°K.

Using Table IV we can estimate in first-order, the effect of the spin-orbit splitting. The constant c_b for the manifold in question.

$$^3F_{1b}\{+0.3453 \mid d\epsilon^4 d\gamma^4\rangle + 0.9385 \mid d\epsilon^5 d\gamma^3\rangle\},$$

is $c_b = -1.94$. The multiplet width should be ~950 cm^{-1}, the maximum degeneracy being concentrated in the low-lying components of the multiplet (Fig. 16). The separation of the peaks $D_0 \rightarrow D_4$ is actually about ~1000 cm^{-1}. The separations $D_2 \rightarrow D_1$ and $D_3 \rightarrow D_1$, though, are too small to be due to first-order effects of the spin-orbit coupling. However, we also found evidence in the preceding groups that the cubic-symmetry (accidental or not) degeneracy of the multiplet components appeared partially lifted. So it is perhaps tempting to explain the structure and width of this group mainly in terms of spin-orbit interaction, although there is no detailed agreement, even using LB's complete calculation (Table XI).

Group E (~*23 000* cm^{-1})

At 78°K a broad intense absorption is found at ~23 000 cm^{-1}, superposed on the strong edge absorption of the ZnO matrix. The high intensity of the band is perhaps associated with the mixing[36] of the level in question with the states involved in the electron-transfer mechanism of the ZnO lattice. Otherwise it would be hard to explain the presence of an intense absorption in a region where only singlet states are predicted by the theory. Actually, at least four singlet cubic-symmetry terms are expected in the region between the triplet manifold at 15 000 cm^{-1} and the present absorption. The highest of such singlet levels ^1E_b is predicted at 22 600 cm^{-1} (Fig. 15).

(g) Concluding Remarks

The predictions of the crystal-field theory for the position of the absorption bands for tetrahedrally coordinated Ni^{++} are in excellent agreement with the observed data, and Ballhausen's relation seems fairly well obeyed [see Eq. (21)]. The spectra of Ni^{++} tetrahedrally coordinated are drastically different, both in the frequency of the absorptions and in the shape of the bands, from the corresponding absorption spectra of octahedrally coordinated Ni^{++}, so that there will be no difficulty in discriminating between the two cases in systems possessing both octahedral and tetrahedral sites. Another factor which will help in differentiating the two cases is the different order of magnitude of the oscillator strength, which is much higher in ZnO. This high oscillator strength could be used analytically to detect concentrations of Ni at least 100 times lower than of the samples investigated, using for detection purposes down to Ni/Zn~10^{-5}, the intense and characteristic absorption band in the visible region.

Evidence of vibrational contribution to the absorption is found (group at 8000 cm^{-1}) although for noncentrosymmetric systems such as ZnO, the mechanism responsible for the electronic transitions is different[32] from that of MgO. A considerable number of fine structure lines is found in the absorption, including very sharp lines at 4.2°K. Undoubtedly even narrower lines are to be expected using thicker and more dilute samples.

In relation to the interpretation of the structure of the absorption, the spin-orbit splitting seems to be one of the predominant factors determining the width of the absorptions, but the greater complexity of the structure and the lower separation in energy of the individual line components (e.g., group A) suggests that the low-symmetry components of the crystal-field have an important effect in lifting the cubic-symmetry degeneracy of the twofold and threefold degenerate multiplet components Γ_3, Γ_4, and Γ_5.

[36] R. Englman, J. Chem. Phys. **32,** 299 (1960).

V. $MgAL_2O_4$:Ni

The samples studied (aluminum spinel No. 27) had thickness 0.496 cm. The color was a faint blue, with the coloration being more pronounced at the edges of the sample. At 78°K two bands of comparable intensity were found in absorption, a double-peaked absorption (16 025 and 17 240 cm^{-1}, Fig. 17d) and a band in the blue region of the spectrum, centered at 26 315 cm^{-1} (Fig. 18d, Table XII).

In the spinel structure two kinds of sites are available for the paramagnetic impurity ions, sites possessing tetrahedral symmetry and sites possessing octahedral symmetry.[30] A quick comparison of the absorption of the present spinel with the absorption spectrum of ZnO:Ni, leads one to exclude the presence of any significant amount of tetrahedrally coordinated Ni^{++}. On the contrary the spectrum is similar to the spectrum of $NiSiF_6 \cdot 6H_2O$ and MgO:Ni, especially regarding the double peaked absorption in the red region.[15,37]

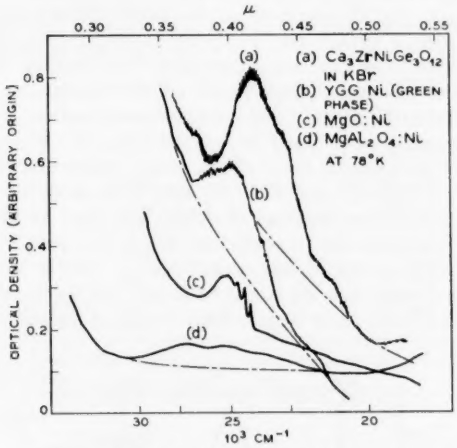

FIG. 18. Same as Fig. 17 in the 25 000 cm^{-1} region.

A closer comparison of the present spectra of the spinel and MgO:Ni reveals in the spinel a general shift of the absorption towards higher energies. How much this effect is due to a different strength of the crystal field in the two systems and how much it is due to the impurity content of the spinel, we cannot say for the time being. In fact a qualitative spectrochemical analysis has revealed that the main impurity ion in sample No. 27 is nickel (in the 0.01 to 0.3% range), but a comparable, though smaller amount of vanadium is also present.

Ni, V	0.01–0.3%
Ti, Si	<0.03%
Ca, Co	<0.005% (25)

[37] O. G. Holmes and D. S. McClure, J. Chem. Phys. **26,** 1686 (1957).

TABLE XII. $MgAl_2O_4$:Ni (sample 27) at 78°K (0.696 cm thick); Ni 0.01–0.3%.

Absorption peaks	λ in A	$\bar{\nu}$ in cm^{-1}	Extinction coefficient α_{max} (cm^{-1})	Half-width at $\alpha=\frac{1}{2}\alpha_{max}$ (cm^{-1})	Oscillator strength
	9300	10 750	0.05		
B	6260	16 025	0.18		
	5800	17 240	0.2		
C	3800	26 316	0.1		

As V^{3+} in octahedral coordination, this latter ion will absorb in a region which is near the Ni^{++} (octahedral) absorption. [In the vanadium alum two absorption bands are found[38] at 17 800 and 25 600 cm^{-1}). This may cause an apparent shift of the Ni^{++} (octahedral) bands.]

VI. NICKEL-DOPED YTTRIUM GALLIUM GARNET

Single crystals of yttrium gallium garnets doped with nickel, were grown from a PbO–PbF_2 flux by J. W. Nielsen of these Laboratories.[39] The melt, contained in a platinum crucible, was lowered in temperature from 1275° to 1000°C at the cooling rate of 1°C per hour. Two crystal phases are obtained, a green phase and a brown phase. In large single crystals the green phase is located at the center, while the brown phase occupies the periphery of the crystal. As one would expect, the absorption spectra of the two phases are drastically different.

(a) Green Phase

The spectrum of a green YGG:Ni, 0.232 cm thick, is shown in Figs. 17b and 18b and the details are given in

TABLE XIII. Yttrium gallium garnet (green phase, 0.16% Ni; 0.232 cm) at 78°K.

Absorption peaks	λ in A	$\bar{\nu}$ in cm^{-1}	Extinction coefficient α_{max} (cm^{-1})	Half-width at $\alpha=\frac{1}{2}\alpha_{max}$ (cm^{-1})	Oscillator strength $f\times10^4$
A	11 600	8620	0.13		
	7768	12 875	0.2		
	7325	13 651	0.5		
	6930	14 430	0.86		
	6770	14 770	0.6		
	6560	15 245	0.7		0.4
	6145	16 273	0.3		
	5870	17 035	0.5		
	5800	17 241	0.4		
	5650	17 700	0.4		
C	4200[a]	23 810[a]			0.25
	4000	25 000	0.85		

[a] Shoulder.

[38] H. Hartmann and H. L. Schläfer, Z. Naturforsch. **6a,** 754 (1951).

[39] J. W. Nielsen, J. Appl. Phys. **31,** 51S (1960).

TABLE XIV. YGG:Ni (brown phase, 0.22% Ni 0.53 cm thick).

Absorption peaks	λ in A	$\bar{\nu}$ in cm^{-1}	Extinction coefficient α_{max} (cm^{-1})	Half-width at $\alpha=\frac{1}{2}\alpha_{max}$ (cm^{-1})	Oscillator strength $f\times10^4$
78°K					
	11 300	8850	2	700	0.4
	9200	10 870	2	750	0.42
	8700	11 495	1.5		0.15
	8450	11 835	1.3		
	7600	13 160	0.4		
	6900	14 490	1.0		
	6500	15 385	1.0		
	[5150][a]	[19 420][a]			
Room Temperature					
	4300	23 255	15[b]		1.9

[a] Optical density *one* at this frequency.
[b] Sample 0.022 cm thick.

Table XIII. There is a rather weak absorption in the ~8000 cm^{-1} region, then a complex absorption showing fine structure in the 13 000 to 18 000 cm^{-1} region, and finally a band at 25 000 cm^{-1}. The absorption spectrum is typical of an octahedrally coordinated Ni^{++} ion. The spectrochemical analysis (Table XV) of the green phase, gave nickel as the main impurity in the amount of 0.16% of total weight (followed by Pb, in the range 0.01 to 0.3% of total weight). This allows us to evaluate the oscillator strength of the absorption, which is in the range of 10^{-4}. Divalent Ni present in the octahedral sites, usually occupied by Ga^{3+} ions, is presumably compensated by Pb^{4+}.

(b) Brown phase

The interpretation of the spectrum of this phase is not as simple as in the previous case. We looked at a crystal 0.053 cm thick. Absorption bands at 78°K are located at 8850 cm^{-1}, then a triple-peaked band at 11 100 cm^{-1}, and a flat absorption at 15 500 cm^{-1} at the threshold of a steeply rising edge-absorption (Fig. 19 and Table XIV). This edge absorption (located at mich higher energies in the green phase), is responsible for the brown coloration of the phase we are discussing. Using a thinner sample (0.0027 cm^{-1}) a band was found (Fig. 20) superposed on the edge absorption. The peak of this intense absorption, superposed on the continuum, is located at 23 250 cm^{-1} and is somewhat reminiscent of a comparable band found in ZnO:Ni (Fig. 14). When a first comparison is made of the present spectrum with that of MgO:Ni and ZnO:Ni, very little similarity is found with the spectrum of either. The band at 8850 cm^{-1} could be due to octahedral Ni^{++}. But then why isn't the corresponding absorption at 15 000 cm^{-1} more intense then the one at 8800 cm^{-1}, as is generally the case? Also there is apparently no sign of the absorp-

TABLE XV. Yttrium gallium garnet (run 760) spectrochemical analysis (qualitative).

Impurity content	Green phase	Brown phase
>10%	Y, Ga	Y, Ga
>1		
0.1–3.0	Ni	Ni
0.01–0.3	Pb	
<0.03	Sn	Al, Mg, Pb, Si, Pt
<0.005	Mg. Pt	Ca, Fe, In, Mn, Sn
<0.001	Al, Ca, Cr, Cu, Fe Mn, Si	Cr, Cu
	Spectrochemical Quantitative	
	0.16% Ni	0.24% Ni

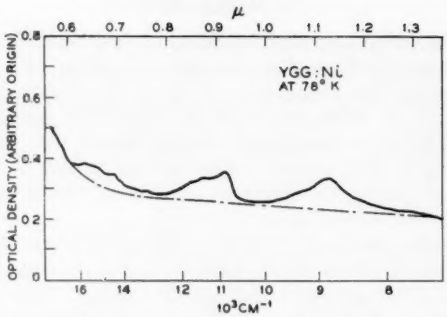

FIG. 19. Absorption spectrum at 78°K of a single crystal of Ni-doped yttrium gallium garnet (brown phase). At 16 000 cm^{-1} an intense edge absorption begins.

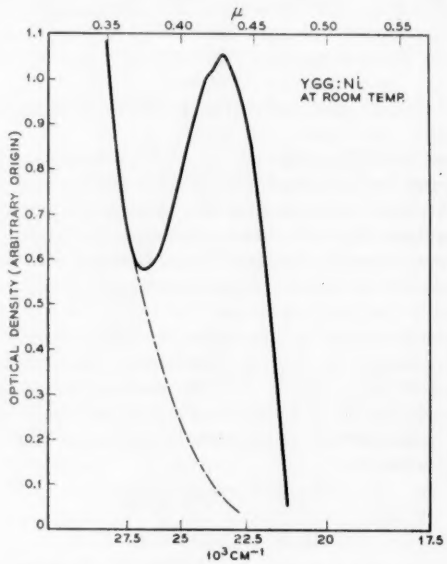

FIG. 20. Intense band superposed onto the edge absorption of a Ni-doped yttrium gallium garnet single crystal (brown phase; room temperature). Compare with Fig. 14 for ZnO:Ni.

tion of tetrahedral Ni. The possibility that the peculiar absorption observed is due to a different impurity had to be discarded after the analysis (Table XV) proved that Ni is the main impurity ion (0.24% of total weight) Another interesting thing revealed by the analysis, was that possible tetravalent ions such as Pb and Si, are present in much smaller amounts than in the green phase. In fact Pb and Si are in amounts less than 0.03% in the brown phase discussed (Table XV).

A possible explanation could involve the presence of Ni^{++} ions in sites possessing dodecahedral symmetry. In that case we can predict what kind of energy-level scheme will be characteristic of eight-coordinated Ni^{++}, using Liehr and Ballhausen's[17] calculations. Assuming for the B and C parameters Liehr and Ballhausen's choice [Eqs. (18), (19), and (18b)], and for Dq the typical value 800 cm^{-1}, the energy level scheme predicted for the body-centered cube approximation is given in Table XVI. As usual, the transitions between systems possessing the same spin-multiplicity will be more intense than electronic transitions between systems with different spin-multiplicity (apart from spin-orbit mixing which will only be important when multiplets of different spin have similar energies). The agreement between the energy-level scheme of Table XVI and the observed spectrum for the brown phase of YGG:Ni is not quite satisfactory (e.g., an intense band predicted at 18 700 cm^{-1} is missing). The only alternative left that would explain this spectrum, is to assume that Ni ions are present in some unusual valence states (Ni^{3+} or Ni^{4+}). This is justified perhaps by the very low content of tetravalent impurity ions in the crystal and by the requirement of the charge compensation in the crystal.

TABLE XVI. Energy level scheme for Ni^{++} in eight-coordinated or body-centered sites, from Liehr and Ballhausen[17] diagram, assuming $Dq=800$ cm^{-1}.

$^3\Gamma_1(^3F_1[de^3d\gamma^4])$[a] $\rightarrow {}^3\Gamma_3$, $^3\Gamma_5$[b]	1000 cm^{-1}
$\rightarrow {}^3\Gamma_5$, $^3\Gamma_3$, $^3\Gamma_2$, $^3\Gamma_4$	7800
$\rightarrow {}^1\Gamma_5$	12 200
$\rightarrow {}^1\Gamma_3$	12 800
$\rightarrow {}^1\Gamma_4$	15 400
$\rightarrow {}^3\Gamma_1$, $^3\Gamma_2$, $^3\Gamma_4$, $^3\Gamma_5$	18 700
$\rightarrow {}^1\Gamma_5$	21 500
$\rightarrow {}^1\Gamma_1$	22 600
$\rightarrow {}^1\Gamma_3$	28 800

[a] The expression in round parenthesis indicates the parent term in the strong-field limit.

[b] Superscripts indicate predominant spin-character and not exact multiplicity.

VII. NICKEL-DOPED GERMANIUM GARNETS

Optical absorption spectra were taken of two germanium garnets prepared in powder form by S. Geller and C. E. Miller of these Laboratories.[40] The KBr pellet technique was used to study the absorptions of these powders. Each KBr pellet contained about 10% in weight of the garnet and spectra were taken both at room temperature and at 78°K. For both $Ca_3TiNiGe_3O_{12}$ and $Ca_3ZrNiGe_3O_{12}$, absorptions were detected which are very similar to the absorption of Ni^{++} in octahedral coordination (Fig. 17a; Fig. 18a). Also the calculated oscillator strengths of the absorptions (Tables XVII, XVIII) are in good agreement with the values found for octahedral Ni^{++} in other systems. Thus the optical evidence for Ni^{++} in octahedral sites in the garnets, agrees with the conclusions reached by means of x-ray and magnetic investigation of garnets by Geller *et al.*[10]

TABLE XVII. $Ca_3TiNiGe_3O_{12}$ in KBr pellet (0.043 cm) at 78°K.

Absorption peaks	λ in A	$\bar{\nu}$ in cm^{-1}	Extinction coefficient[a] α_{max} (cm^{-1})	Half-width at $\alpha=\frac{1}{2}\alpha_{max}$ (cm^{-1})	Oscillator strength $f\times10^4$
	11 700	8547	4.6		
	8450	11 834	1		
	7450	13 422	9.3		
	6750	14 815	13.7		0.36
	6350	15 750	12.3		
	5600	17 860	5.6		

[a] Of KBr pellet.

VIII. CONCLUSION

The predictions of the crystal-field theory for Ni^{++} in tetrahedral and octahedral coordination have been experimentally verified and oscillator strengths evaluated for hexa- and tetra-coordinated Ni^{++}.

Very interesting narrow lines have been found in the spectra of both ZnO and MgO. In the case of MgO:Ni especially, the narrow absorption lines could be used as sensitive probes to explore crystal-field and magnetic effects at the Ni^{++} ions sites. (An application in the present article has been the precise determination of the Dq and B parameters for MgO:Ni.)

TABLE XVIII. $Ca_3ZrNiGe_3O_{12}$ in KBr pellet (0.07 cm thick) at 78°K.

Absorption peaks	λ in A	$\bar{\nu}$ in cm^{-1}	Extinction coefficient[a] α_{max} (cm^{-1})	Half-width at $\alpha=\frac{1}{2}\alpha_{max}$ (cm^{-1})	Oscillator strength $f\times10^4$
A	13 600	7353	2.3		0.17
	12 400	8064	3.3		
	11 400	8772	3.14		
B	7750	12 900	4		0.42
	7150	13 980	6.4		
	6450	15 267	7.43		
	5260	19 010	0.7		
C	4200	23 810	5		0.17

[a] Of KBr pellet.

[40] S. Geller and C. E. Miller, Acta Cryst. **13,** 179 (1960).

In first- or higher-orders the fine structure observed cannot be explained satisfactorily in terms of spin-orbit coupling effects *only*, but the contribution of lattice vibrations (for MgO) and low-symmetry components of the field (ZnO) should be treated simultaneously with the spin-orbit coupling. Considering the high symmetry of the MgO systems when doped with divalent ions, and the high number of individual components observed in absorption, a more refined treatment of the fine structure in MgO:Ni should prove particularly rewarding.

By using the spectra of ZnO:Ni and MgO:Ni as reference of the site-symmetry and valency of Ni, impurities in the spinels and garnets have been found. Octahedrally coordinated Ni^{++} is present in the aluminum spinel, in the germanium garnets, and in the green phase of yttrium gallium garnets. The interpretation of the spectrum of the brown phase of yttrium gallium garnets is still uncertain. A helpful step in this direction and also an interesting opportunity to check the crystal-field predictions for eight-coordinated iron-group ions, would be a study of the optical absorptions of such ions, present as impurities in the simple K_2O or Li_2O systems, in which the metallic ions are in a body-centered position, surrounded by a cube of oxygen ions.

Apart from the difficulty found in the case of the brown phase of yttrium gallium garnets, the simple study of the optical properties of these important systems has been shown to represent a powerful tool both in obtaining information on the effects of the lattice on the electrons of the impurity ions, and in exploring valence and coordination properties, which are ultimately associated with the origin of ferrimagnetic interactions in garnets and in spinels.

ACKNOWLEDGMENTS

The authors are grateful for the kind help and advice of the following members of the Bell Telephone Laboratories staff: A. D. Liehr for valuable discussions on the crystal-field and spin-orbit coupling theory and for important comments and criticism of the manuscript; S. Sugano for useful discussion on the spin-orbit coupling formalism; W. M. Walsh, Jr. for supplying the magnesium oxide samples; S. Geller for making available the germanium garnet powders and for useful information on the ionic site preference in garnets; E. K. Jaycox and D. L. Nash for the spectrochemical analysis of the samples; Miss S. Vincent for the x-ray determination of impurities in the ZnO samples; and J. P. Luongo and Miss D. M. Dodd for assistance in the spectrophotometric measurements.

APPENDIX

The relation $Dq_{tet}=-\frac{4}{9}Dq_{oct}$ has been introduced by C. J. Ballhausen.[6] The relation[5,7]

$$Dq_{bcc}=-\tfrac{8}{9}Dq_{oct} \tag{A1}$$

between the scale factor of the cubic field in the octahedral case and the body-centered cube case can be proved as follows. For eightfold coordination, a potential of cubic symmetry up to fourth-order terms in the $3d$-electron coordinates can be expressed as

$$V_{bcc}=\tfrac{7}{8}(Zee_{eff}/R^5)[35z^4-30z^2r^2+3r^4]$$
$$+\tfrac{35}{36}(Zee_{eff}/R^5)[(x+iy)^4+(x-iy)^4]. \tag{A2}$$

Then a simple calculation shows that:

$$\langle d\epsilon \mid V_{bcc} \mid d\epsilon\rangle=-\tfrac{16}{21}(Zee_{eff}/R^5)\langle r^4\rangle \tag{A3}$$

$$\langle d\gamma \mid V_{bcc} \mid d\gamma\rangle=\tfrac{8}{9}(Zee_{eff}/R^5)\langle r^4\rangle \tag{A4}$$

$$Dq_{bcc}=\langle d\gamma \mid V_{bcc} \mid d\gamma\rangle-\langle d\epsilon \mid V_{bcc} \mid d\epsilon\rangle$$
$$=\tfrac{40}{21}(Zee_{eff}/R^5)\langle r^4\rangle \tag{A5}$$

while for a potential of octahedral symmetry

$$\langle d\epsilon \mid V_{oct} \mid d\epsilon\rangle=\tfrac{2}{3}(Zee_{eff}/R_0^5)\langle r_0^4\rangle \tag{A6}$$

$$\langle d\gamma \mid V_{oct} \mid d\gamma\rangle=-(Zee_{eff}/R_0^5)\langle r_0^4\rangle \tag{A7}$$

$$Dq_{oct}=\langle d\gamma \mid V_{oct} \mid d\gamma\rangle-\langle d\epsilon \mid V_{oct} \mid d\epsilon\rangle$$
$$=-\tfrac{5}{3}(Zee_{eff}/R^5)\langle r^4\rangle. \tag{A8}$$

Then, if $\langle r_0^4\rangle/R_0^5=\langle r^4\rangle/R^5$,

$$Dq_{bcc}=-\tfrac{8}{9}Dq_{oct}. \tag{A9}$$

Thermal Diffusion Coefficient of Polystyrene in Toluene*

CECIL LEROY HERREN† AND JOE S. HAM
Department of Physics, A and M College of Texas, College Station, Texas

(Received April 10, 1961)

A moving boundary technique is used to measure the thermal diffusion coefficient for polystyrene in toluene as a function of molecular weight. An almost constant value of 1.5×10^{-7} cm²/mole/deg was obtained except below a molecular weight of 300 000 where a much smaller figure was found. This result agrees with the theory of Ham but disagrees with earlier measurements of Hoffman and Zimm.

A recently proposed theory[1] of the thermal diffusion process in dilute polymer solutions has reached the conclusion that the thermal diffusion coefficient D_T, in

$$\partial c/\partial t = -\nabla\cdot[D_0\nabla c + D_T c\nabla T] \qquad (1)$$

should be independent of the molecular weight of the polymer for sufficiently high molecular weights. The present note includes data that support this conclusion and gives results that are in qualitative agreement with the theory at lower molecular weights.

In our experiments, a triangular path interferometer[2] was used to observe the boundary between a solution of polystyrene in toluene and pure toluene while in a vertical thermal gradient. Conditions were such that there was no evidence of convection. Although the interferometer proved to be too unstable mechanically to follow the shape of the boundary, it could be used to follow its motion while in a thermal gradient. The rate of motion of this boundary after reaching steady state was measured and related to D_T.[3]

The two samples of polystyrene with molecular weights 82 000 and 267 000 were furnished by Dr. H. W. McCormick of Dow Chemical Company and had a ratio of weight-to-number average 1.08 and 1.04, respectively. Another sample was fractionated from commercial material and is the same as one used by Whitmore.[4] The sample whose molecular weight is about 10^6 was furnished by Dr. B. Zimm from the General Electric Laboratories and had been prepared so as to give close to a monodisperse molecular weight distribution.

A complication in the interpretation of these measurements is the marked concentration dependence of D_T.[3,4] In the usual experimental arrangement where the pure solvent is above the solution, the boundary maintains a sharpness, as a result of the nonlinearity, as the run proceeds. Under conditions where the nonlinearity does not aid in maintaining the boundary, the diffuseness made the measurements unreliable. Several runs with a finite concentration above the boundary confirm the idea that the more rapid motion in the more dilute solution sweeps material into the boundary region and that motion of the boundary is governed by the smallest diffusion coefficient (larger concentration).

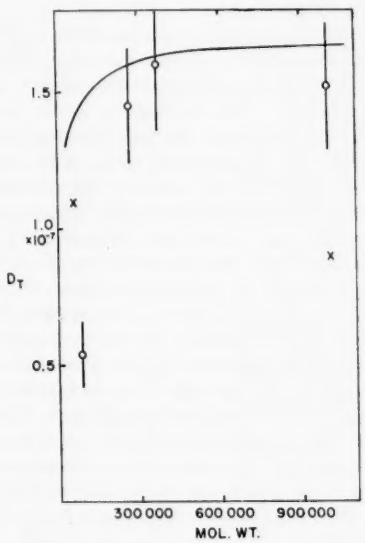

FIG. 1. The thermal diffusion coefficient D_T in cm²/sec/deg vs the molecular weight taken from the motion of the boundary between pure solvent and a solution whose concentration was 1 gm/dl. The circles are our experimental points with the uncertainties indicated. Each point represents data from several runs. The crosses are data from reference 3 using the same method although with different optical arrangements and different thermal gradients. The line is the theoretical curve based upon the theory of reference 1.

Figure 1 compares our measurements with those of Hoffman and Zimm and with theory. The difference between the magnitude of the effect we observed with that reported in the literature is not very surprising when one considers the different optical arrangement and other factors; although it is well outside of the errors in either set of measurements determined by

* This work was supported in part by the Robert A. Welch Foundation of Houston, Texas.
† Present address: Texaco, Inc., Bellaire, Texas.
[1] Joe S. Ham, J. Appl. Phys. **31**, 1853 (1960).
[2] P. Hariharan and D. Sen, J. Opt. Soc. Am. **49**, 1105 (1959).
[3] J. D. Hoffman and B. H. Zimm, J. Polymer Sci. **15**, 405 (1955).
[4] Frank C. Whitmore, J. Appl. Phys. **31**, 1858 (1960).

their reproducibility. Much more disturbing is the discrepancy in the lowest molecular weight sample in each study. Zimm and Hoffman found no decrease in D_T at molecular weights as low as 60 000, whereas we found a marked decrease below 300 000. In a private discussion with Dr. Hoffman, he has stated that the molecular weight fractionations used in the preparation of his samples were rough and that this might be the source of discrepancy.

The values observed in the low molecular-weight region are of interest because theory predicts a drop in estimates of the parameters occurring in this theory, the curve in Fig. 1 is obtained in almost quantitative agreement with the experimental data. The values used are $D_p=1.7\times10^{-4}$ $(MW)^{0.52}$ and $D_s=1.73\times10^{-5}$ cm^2/sec for the normal diffusion coefficient of polystyrene in toluene[5] and the self-diffusion coefficient of toluene.[6] The activation energies were taken to be $E_p=13\,000$ cal/mole and $E_s=2000$ cal/mole for the polymer and solvent respectively.[7] This is a remarkable agreement for such a simple theory.

In the past, a number of workers have used thermal diffusion columns to produce a molecular weight fractionation in polymer solutions.[8] The simple theory of column operation predicts that D_T is the parameter of primary importance in the fractionation process. It is suggested that this variation of D_T at low molecular weights is responsible for some of the fractionations observed in experiments with thermal diffusion columns. On the other hand, there exist measurements[8] which indicate that it may be the ratio D_T/D_0 that is the governing factor in the column operation. If the latter were true, one would expect the separation factor of the column would depend upon the molecular weight dependence of D_0 even for molecular weights so large that D_T no longer depends upon molecular weight. But if the column operation depends upon D_T and the molecular weight dependence found by our measurements is accepted, then the column should no longer be effective in separating molecular weights above 300 000. The experimental separation factor s^* shows a break similar in type although not quite as pronounced as that shown in the theoretical curve in Fig. 1. Thus, the experimental results of Langhammer using a column are consistent with theory and our data only if the effective separation parameter is associated with D_T rather than with D_T/D_0 as in his revision of the theory of the column operation.

The experimental data on thermal diffusion that have been reported in the literature have numerous self-contradictions.[1,4] These are probably due in part to the problems of concentration determination on small samples, the elimination of convective mixing and other experimental difficulties. In addition to these, there are also the difficulties of interpretation. It has been shown that D_T depends strongly upon the molecular weight and upon temperature.[4] In fact, it is only when these dependencies produce a nonlinearity that measurements could be made by the moving boundary technique. Thus, it is possible that some of the discrepancies between the values determined by different methods are real and are the result of linearization of the Eq. (1). Another type of difficulty that may have arisen results from the use of polydisperse samples. It is known that the dependency of the normal diffusion coefficient upon molecular weights in a polydisperse sample is complex, as there is considerable interference between different diffusing species. Presumably, a similar interference should occur in thermal diffusion.

The theory that has been developed[1] is sufficiently simple that it gives unambiguous predictions capable of experimental verification. At present, there is as much data in agreement with these predictions as against them. Although there is little promise contained in the theoretical predictions that thermal diffusion will have a practical utility, the problem of fractionating high molecular weight materials is so general that no avenue of approach should be unexplored. The development of commercial equipment that can make precise measurements on diffusion coefficients and the availability of almost monodisperse samples should permit reliable measurements of D_0 and D_T.

Note added in proof. G. Meyerhoff and K. Nachtigall reported at the International Symposium on Macromolecular Chemistry (Montreal, 1961) a study of the thermal diffusion of polymer solutions with a more refined optical system than that described here.

[5] V. N. Tsevetkov, Simpos. Inter. di Chem. Macro., Milano, 413, September, 1954.
[6] J. B. Lewis, J. Appl. Chem. (London) **5,** 228 (1955).
[7] A. H. Emery and H. B. Drickamer, J. Chem. Phys. **23,** 2252 (1955).
[8] G. Langhammer, H. Pfenning, and K. Quitzsh, Z. Elektrochem. **62,** 458 (1958); G. Langhammer and H. Forster, Z. physik. Chem. (Frankfurt) **15,** 212 (1958), and other references cited therein.

An EPR Study of the Tetrafluorohydrazine-Difluoramino Equilibrium

L. H. PIETTE
Varian Associates, Palo Alto, California
AND
F. A. JOHNSON, K. A. BOOMAN, AND CHARLES B. COLBURN
Rohm and Haas Company, Redstone Arsenal Research Division, Huntsville, Alabama

(Received April 13, 1961)

The EPR spectrum of the difluoramino radical (NF_2) was observed to be a single broad line at a pressure of 20–40 mm of N_2F_4 and a temperature of 340–435°K. The peak-to-peak linewidth was observed to be 104 gauss with a g value of 2.010. From the temperature dependence of the line amplitude, the ΔH of dissociation of N_2F_4 was calculated to be 19.3±1.0.

INTRODUCTION

JOHNSON and Colburn[1] have recently investigated the $N_2F_4 \rightleftarrows 2NF_2$ equilibrium by two methods: (1) measurement of the pressure-temperature relationships of the system at constant volume and (2) a spectrophotometric method based on the temperature dependence of the ultraviolet absorption of the difluoroamino radical. These methods gave a value of 20.8 kcal/mole for the N—N bond strength in tetrafluorohydrazine. We wish to report here the use of electron paramagnetic resonance (EPR) techniques in a study of this equilibrium.

EXPERIMENTAL

Tetrafluorohydrazine was prepared as described by Colburn and Kennedy.[2] It was purified by low temperature distillation and had a purity of >99% by mass spectral analysis.

EPR measurements were made using a Varian V 4500 spectrometer equipped with 100 kc field modulation. The temperature apparatus used for varying the temperature of the sample has been described elsewhere.[3] A Wheelco model 404 temperature controller was used to control the temperature to ±1°C.

Samples of N_2F_4 were introduced into a vacuum system at pressures from 2–4 mm. The gas was condensed from a volume of 5 cc with liquid nitrogen and sealed off in a quartz tube with a final volume of 0.5 cc giving a final pressure at room temperature of approximately 20–40 mm. The tubes were then placed in the spectrometer and the temperature varied from 342°K to 435°K. The peak-to-peak amplitude of the signal was measured at each temperature. This amplitude is directly proportional to the concentration of the radical specie contributing to the resonance line provided there is no change in line shape from one temperature to the next. No change in line shape was observed during an entire run. The amplitude of the line is also dependent upon the normal Boltzmann distribution of radicals in the lowest energy state. Since this distribution goes as $1/T$, it is necessary to correct the amplitudes of each line for the change in Boltzmann

TABLE I.

T	α	$2\log AT-\log(1-\alpha_T)$
342	0.021	1.106
353	0.033	1.283
365.5	0.051	1.432
376	0.074	1.564
386	0.101	1.695
397	0.147	1.858
406	0.173	1.958
417	0.229	2.092
426	0.277	2.198
434.5	0.325	2.311

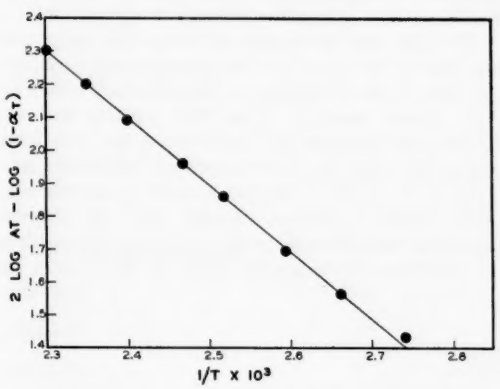

FIG. 1. The heat of dissociation of N_2F_4 from EPR data.

[1] F. A. Johnson and C. B. Colburn, J. Am. Chem. Soc. **83**, 3043 (1961).
[2] C. B. Colburn and A. Kennedy, J. Am. Chem. Soc. **80**, 5004 (1958).
[3] L. H. Piette and W. C. Landgraf, J. Chem. Phys. **32**, 1107 (1960).

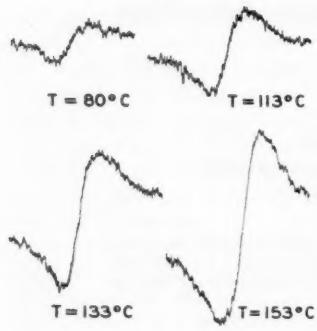

FIG. 2. The EPR signal of NF_2.

distribution. The relationship using the Boltzmann distribution correction between A (the signal amplitude) and the temperature is

$$2\ln AT = 2\ln C + \ln(N_2F_4)_T - \Delta E/RT, \qquad (1)$$

where A = signal amplitude, C = constant characteristic of the resonance absorption line of the radical observed, and $(N_2F_4)_T$ = concentration of N_2F_4 at temperature T. Since under the conditions of these experiments the degree of dissociation of N_2F_4 is not negligible, this must be corrected by using the extrapolated equilibrium constants Kp obtained from $(dp/dt)_v$ measurements.[1] The corrected form of the equation is then

$$2\log AT - \log(1-\alpha_T) = -\Delta E/2.3\,RT + C'$$

where α is the degree of dissociation of N_2F_4 at temperature T and 40 mm pressure.

RESULTS

Table I gives the results of the corrected experimental amplitude measurements. ΔE for dissociation is obtained directly from the slope of Fig. 1 and is 18.7 kcal/mole. The enthalpy change ΔH is found to be 19.3 kcal/mole from $\Delta H = \Delta E + RT^{\Delta\nu}$ where $\Delta\nu = 1$.

The EPR spectra of gases are very often quite complex due to the fact that the energy levels describing the spin states (assuming a Paschen-Back effect has taken place) contains terms that include not only nuclear spin-electron spin interactions but also interactions between the electron spin and molecular rotational levels of the molecule. In such a case the electronic moment, nuclear moment and the moment associated with molecular rotation are quantized along the direction of the applied field. In some cases the rotational couplings to electron spin can be very strong. The distinct lines resulting from such couplings however are very sensitive to pressure changes[4] and normally pressures above a few millimeters smear out the coupling to the extent that a single broad line is observed. Only a single broad line was observed in all of our runs on N_2F_4 and this is explained because of the high pressure and high temperatures used in the experiment. Figure 2 shows the spectra obtained at a variety of temperatures. The peak-to-peak linewidth was measured to be 104 gauss with a g value of 2.010. This large g value shift relative to DPPH (2.0036) is to be expected for systems capable of a strong spin orbit interaction as in fluoro compounds.[5]

TABLE II. Determination of heat of dissociation of N_2F_4.

Method	Value	Wt.
$(\Delta p/\Delta T)_v$[1]	19.85±0.5	4
EPR	19.3±1.0	2
μ. ν. spectra[1]	20.7±2.0	1
Weighted av	19.8±0.8 kcal/mole	

Recently Cochran *et al.*[6] reported the hyperfine splittings in NH_2 produced by ultraviolet irradiation of NH_3. Their results indicated that the coupling to the protons was approximately twice that of nitrogen, 23.9 compared to 10.3 gauss.

It has been shown in other systems such as irradiated teflon[7] and in fluoro substituted semiquinones[8] that the couplings by fluorine are in general greater than those by protons. Therefore it would be expected that the hyperfine interaction in NF_2 would be quite large thus accounting for the over-all linewidth of 104 gauss.

DISCUSSION

The N—N bond strength in tetrafluorohydrazine has now been evaluated by three methods (Table II) and the best value for the heat of dissociation of tetrafluorohydrazine is 19.8±0.8 kcal/mole.

[4] J. G. Castle and R. Beringer, Phys. Rev. **80,** 114 (1950); R. Beringer and J. G. Castle, Phys. Rev. **81,** 82 (1951).
[5] M. S. Blois, H. W. Brown and J. E. Maling, Technical Note, AFOSR-TN-60-716, Air Force Office of Scientific Research.
[6] E. L. Cochran, *Fourth International Symposium on Free Radical Stabilization* 1959 (D-I-I, National Bureau of Standards, Washington, D. C).
[7] H. N. Rexroad and W. Gordy, J. Chem. Phys. **30,** 399 (1959).
[8] D. H. Anderson, P. J. Frank, and H. S. Gutowsky, J. Chem. Phys. **32,** 1196 (1960).

Effect of Pressure on Crystal-Field Energy and Covalency in Octahedral Complexes of Ni^{2+}, Co^{2+}, and Mn^{2+} †

J. C. ZAHNER AND H. G. DRICKAMER
Department of Chemistry and Chemical Engineering, University of Illinois, Urbana, Illinois

(Received March 14, 1961)

The effect of pressure has been measured on the absorption spectra of $NiCl_2$, $NiBr_2$, $Ni(NH_3)_6Cl_2$, $CoCl_2$, $CoBr_2$, $MnCl_2$, and $MnBr_2$. The pressure shifts in every case correspond to increase in crystal field strength. To account for the shifts in a quantitative manner it is necessary to presume that the Racah parameter B decreases with increasing pressure. This can be interpreted as an increase in covalency at high pressure.

From the data on $MnCl_2$ and $MnBr_2$ it is possible to establish limitations on the possible range of values of the parameter ϵ introduced by Koide and Pryce to describe covalency in transition metal complexes.

THE effect of pressure has been measured on the optical absorption spectra of the chlorides and bromides of Ni^{2+}, Co^{2+}, and Mn^{2+}, as well as on $Ni(NH_3)_6Cl_2$. The types and sources of experimental material are summarized in Table I. The high-pressure optical techniques have been described elsewhere.[1,2]

The peaks which were observed are listed in Table II, in the abbreviated nomenclature used in this paper together with their normal assignments in group theoretical nomenclature. As will be discussed below, the assignment of the peak for Co-III can be made with considerable assurance based on the pressure shift. Peak III-Mn is really two transitions having the same crystal field energy, as discussed in a later section of the paper. The measurements on the high-energy peaks of $CoBr_2$ and $NiBr_2$ were limited by the red shift of the charge transfer peak.

Tanabe and Sugano[3] have developed equations for the energy of the transitions; as a function of the crystal field strength 10 Dq, and of the Racah parameters B and C.

For Ni^{++} the equations for the three transitions are

$$E(\text{I}-\text{Ni})=10Dq \tag{1}$$

$$E(\text{II}-\text{Ni})=15Dq+7.5B-6B[1+\mu]^{\frac{1}{2}} \tag{2}$$

$$E(\text{III}-\text{Ni})=15Dq+7.5B+6B[1+\mu]^{\frac{1}{2}}, \tag{3}$$

where

$$\mu=(10Dq-9B^2)/12B.$$

For all values of the parameters Dq and B in the range studied $\mu \ll 1$.

For Co^{++} the equations for the transitions studied are

$$E(\text{I}-\text{Co})=5Dq-7.5B+6B(1+\eta)^{\frac{1}{2}} \tag{4}$$

$$E(\text{II}-\text{Co})=15Dq-7.5B+6B(1+\eta)^{\frac{1}{2}} \tag{5}$$

$$E(\text{III}-\text{Co})=12B(1+\mu)^{\frac{1}{2}}$$

$$\eta=[(10Dq+9B)/12B]^2. \tag{6}$$

For Mn^{++} the energies of the transitions can be obtained from the following equations:

$$\begin{vmatrix} -10Dq+10B+6C-E & -(18)^{\frac{1}{2}}B & C \\ -(18)^{\frac{1}{2}}B & 9B+C-E & -18B \\ C & -(18)^{\frac{1}{2}}B & 10Dq+18B+6C-E \end{vmatrix}=0, \tag{7}$$

where the lowest root $E=\text{I}-\text{Mn}$;

$$\begin{vmatrix} -10Dq+18B+6C-E & 6^{\frac{1}{2}}B & 4B+3 \\ 6^{\frac{1}{2}}C & 13B+5C-E & -6^{\frac{1}{2}}B \\ 4B+C & -6^{\frac{1}{2}}B & 10Dq+18B+6C-E \end{vmatrix}=0, \tag{8}$$

where the lowest root $E=\text{II-Mn}$; the second lowest root $E=\text{IV-Mn}$.

$$E(\text{III-Mn})=10B+5C \tag{9}$$

$$E(\text{V-Mn})=17B+5C. \tag{10}$$

† This work was supported in part by the U. S. Atomic Energy Commission.

[1] R. A. Fitch, T. E. Slykhouse, and H. G. Drickamer, J. Opt. Soc. Am. **47**, 1015 (1957).
[2] H. G. Drickamer, Rev. Sci. Instr. **32**, 212 (1961).
[3] Y. Tanabe and S. Sugano, J. Phys. Soc. Japan **9**, 753, 766 (1954).

TABLE I. Materials investigated.

Compound	State investigated	Source or method of preparation
$NiCl_2$ $NiBr_2$	powder or approximately equal mixture of material and NaCl in powder form	Preparation from metal acetate hydrate and acetyl halide reagent-grade chemicals used.
$CoCl_2$ $CoBr_2$		
$MnCl_2$ $MnBr_2$	single crystal	R. Pappalardo, Bell Telephone Laboratories
$Ni(NH_3)_6Cl_2$	approx equal powder mixture with NaCl	Material prepared from $NiCl_2(H_2O)_6$ and ammonia using reagent grade chemicals

DISCUSSION

In the simplest crystal field theory one should be able to predict the energies of each transition from the crystal field strength Dq and the free ion value of B (or of B and C). This is almost never possible. It is frequently possible to establish a value of B and Dq which will fit all the peaks at atmospheric pressure. Table III shows these values (labeled Dq_0 and B_0) for Co^{++} and Ni^{++}.

It seems reasonable to assign the decrease in the value of B going from free ion to crystal to a spreading out of the metal ion charge cloud because of covalent interaction with the ligands. Another approach to covalency has been proposed by Koide and Pryce.[4] They presume that the d_ϵ orbitals which point at the ligands are involved in covalent interaction while the d_ξ orbitals are unaffected. Their formulation has been applied to Mn^{++} by Pappalardo[5] and by Stout[6] as well as the original authors. We have extended it also to Ni^{++}.

The effect of pressure on the crystal field and ionic parameters is discussed in the following paragraphs. Emphasis is placed on those factors which are relatively independent of the atmospheric pressure values of the Racah parameters as these are not well established. For each metal ion we discuss the change in crystal field strength assuming B is constant and equal to B_0; then the change in B (or B and C) with pressure is considered. In the final section of the paper we discuss the Koide and Pryce parameter ϵ.

TABLE II. Nomenclature for electronic transitions.

Nomenclature (this work)		Standard nomenclature
	Absorption peak	
Ni^{++}		
	I	$^3A_2(F) \rightarrow {}^3T_2(F)$
	II	$^3A_2(F) \rightarrow {}^3T_1(F)$
	III	$^3A_2(F) \rightarrow {}^3T_1(P)$
Co^{++}		
	I	$^4T_1(F) \rightarrow {}^4T_2(F)$
	II	$^4T_1(F) \rightarrow {}^4A_2(F)$
	III	$^4T_1(F) \rightarrow {}^4T_1(P)$
Mn^{++}		
	I	$^6A_1(S) \rightarrow {}^4T_1(G)$
	II	$^6A_1(S) \rightarrow {}^4T_2(G)$
	IIIa	$^6A_1(S) \rightarrow {}^4A_1(G)$
	IIIb	$^6A_1(S) \rightarrow {}^4E_g(G)$
	IV	$^4A_1(S) \rightarrow {}^4T_2(D)$
	V	$^4A_1(S) \rightarrow {}^4E_g(D)$

CHANGES OF Dq AND B

Equations (1)–(3) predict that, if the Racah parameter B is constant, peaks I-Ni, II-Ni, and III-Ni should show a large increase in energy (blue shift) with increasing crystal field strength (increasing pressure).

TABLE III. Atmospheric values of the parameters and peak energies used to determine them.

Material	B (free ion)	1 atm value in solids B_0	Dq_0
$Ni(NH_3)_6Cl_2$	1030	887	1090
$NiCl_2$	1030	823	755
$NiBr_2$	1030	730	728
$CoCl_2$	971	766	750
$CoBr_2$	971	713	697

	Absorption peaks[a]					
	Peak I		Peak II		Peak III	
	10^3 cm^{-1}		10^3 cm^{-1}		10^3 cm^{-1}	
	A	B	A	B	A	B
$Ni(NH_3)_6Cl_2$	10.9	10.9	17.85	17.49	28.52	28.52
$NiCl_2$	7.55	7.55	12.56	12.5	22.57	22.57
$NiBr_2$	7.28	7.28	12.0	12.0		
$CoCl_2$	6.58	6.58			17.1	17.1
$CoBr_2$	6.09	6.09			15.9	15.9

[a] Column A, experimental; Column B, calculated using Dq_0 and B_0.

[4] S. Koide and M. H. L. Pryce, Phil. Mag. **3,** 607 (1958).
[5] R. Pappalardo, J. Chem. Phys. **31,** 1050 (1959); **33,** 613 (1960).
[6] J. W. Stout, J. Chem. Phys. **31,** 709 (1959); **33,** 303 (1960).

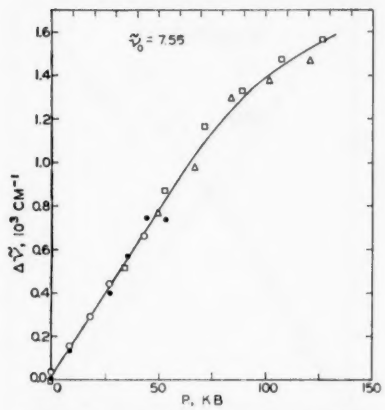

FIG 1. Pressure shift for I-Ni peak in $NiCl_2$.

Peaks II-Ni and III-Ni should shift roughly $1\frac{1}{2}$ times as fast as peak I-Ni. The experimental data for Ni^{++} are shown as the points and solid lines in Fig. 1-8. It can be seen that the data are in qualitative agreement with experiment. Since peak I-Ni depends on Dq only, it should be possible to predict the shifts of peaks II-Ni and III-Ni from peak I-N and B_0. The dotted lines in Fig. 2, 3, 5, 7, and 8 represent this calculation. The discrepancies are certainly larger than possible experimental error. The deviation is larger for peak III-Ni than for peak II-Ni. Since III-Ni is relatively sensitive to the value of B while II-Ni is quite insensitive, it would appear that B is decreasing with increasing pressure. It is possible to calculate meaningful values for B from peak III-Ni using Dq from peak I-Ni. Peak II-Ni is too insensitive to give significant values for B. The results for $NiCl_2$ and $Ni(NH_3)_6Cl_2$ are shown in Table IV together with results discussed below for $CoCl_2$, $MnCl_2$, and $MnBr_2$.

Within the accuracy of the data the calculated changes in B are of the same order for all complexes.

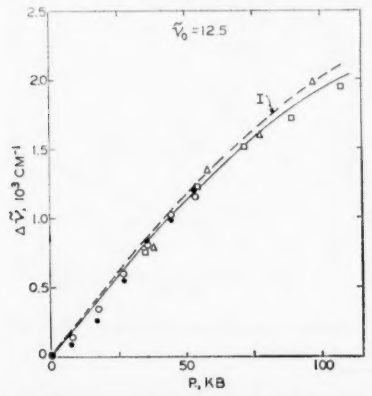

FIG. 2. Pressure shift for II-Ni peak in $NiCl_2$.

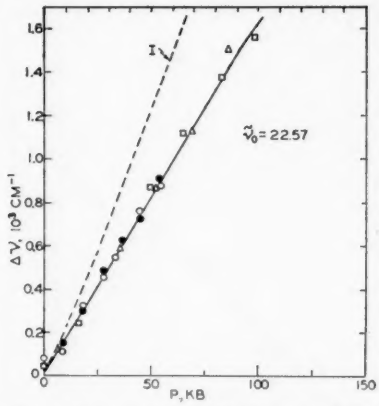

FIG. 3. Pressure shift for III-Ni peak in $NiCl_2$.

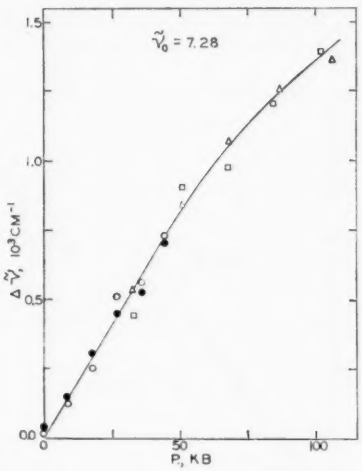

FIG. 4 Pressure shift for I-Ni peak in $NiBr_2$.

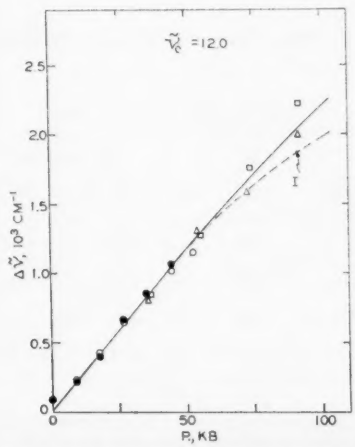

FIG. 5. Pressure shift for II-Ni peak in $NiBr_2$.

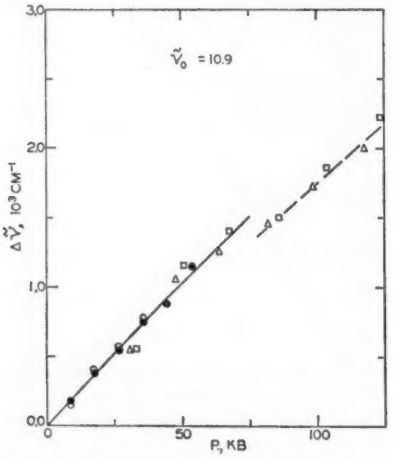

FIG. 6. Pressure shift for I-Ni peak in $Ni(NH_3)_6Cl_2$.

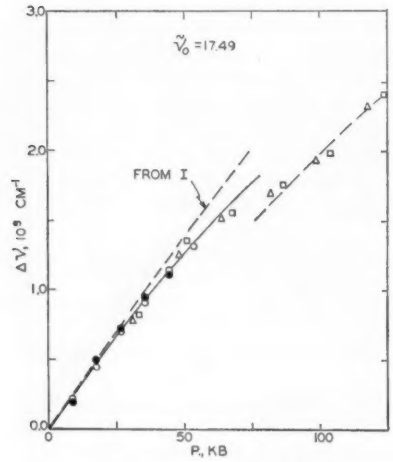

FIG. 7. Pressure shift for II-Ni peak in $^{\text{r}}Ni(NH_3)_6Cl_2$.

TABLE IV. Effect of pressure on B.

Substance	B_0 cm^{-1}	(B_P-B_0) cm^{-1} 25 kb	50 kb	75 kb	100 kb	150 kb
$CoCl_2$	766	−4	−8	...	−15	−21
$NiCl_2$	823	−4	−19	...	−29	
$Ni(NH_3)_6Cl_2$	887	−3	−11	−23		
$MnCl_2$	...[a]	−6	−12	...	−27.5	
$MnBr_2$	...[a]	−9	−18	...		

[a] B_0 is not needed for $MnCl_2$ and $MnBr_2$ as B_P-B_0 is obtained directly from the shifts.

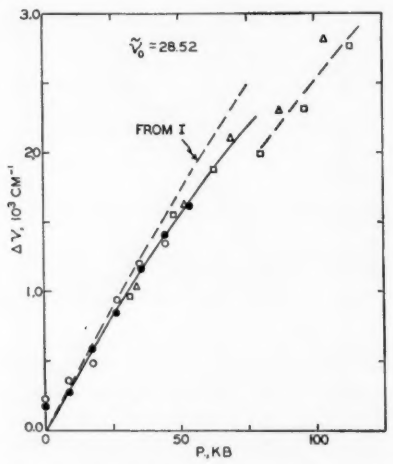

FIG. 8. Pressure shift for III-Ni peak in $Ni(NH_3)_6Cl_2$.

The $Ni(NH_3)_6Cl_2$ has a higher value of B_0 and shows a slightly smaller deviation of peak III when calculated for constant B. Just above 75 kbar there appears a small but consistent discontinuity in the shift for all three peaks of this compound. There also seemed to be some loss of light at this point. A first-order phase transition is possible, but cannot be proven.

It should be mentioned that our previous data on $Ni(NH_3)_6Cl_2$[7] indicated an increase of B with pressure. Since peak I was not obtained at that time the calculations were made from peaks II and III, which is not as accurate a procedure. Also, those data were among the first obtained on our optical apparatus, and the methods of operation and calculation were not well established.

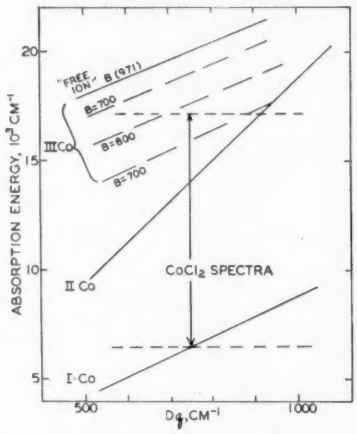

FIG. 9. Calculated energies for states in Co^{++} as a function of Dq and B.

[7] R. W. Parsons and H. G. Drickamer, J. Chem. Phys. **29**, 930 (1958).

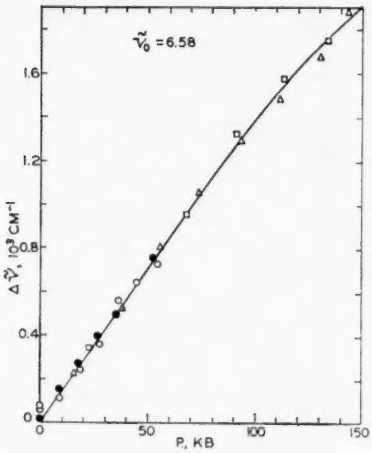

FIG. 10. Pressure shift for I-Co in $CoCl_2$.

Figure 9 shows the calculated change of energy of peaks I, II, and III for Co^{++} as a function of Dq and B. Peaks I and II are essentially independent of B, but peak III shows a definite B dependence. The solid lines and points in Figs. 10–13 show the measured shifts. Again large blue shifts are found, in qualitative agreement with theory. Fig. 14 shows the change in Dq with pressure as calculated from both peaks for $CoCl_2$. The dotted curves in Figs. 11 and 13 represent calculated shifts for peaks III-Co, using the value of Dq from peak I-Co and B_0. The discrepancies are larger than experimental error and can be represented as a decrease in B with pressure. The calculated decrease is shown for $CoCl_2$ in Table IV. It is of the same magnitude as that obtained for the Ni^{2+} complexes.

The dashed curve in Fig. 11 represents the calculated shift in this peak, if it is assigned to II-Co rather than III-Co. The discrepancy is clearly too large to be ac-

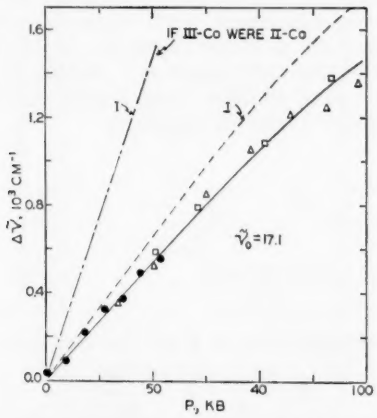

FIG. 11. Pressure shift for III-Co in $CoCl_2$.

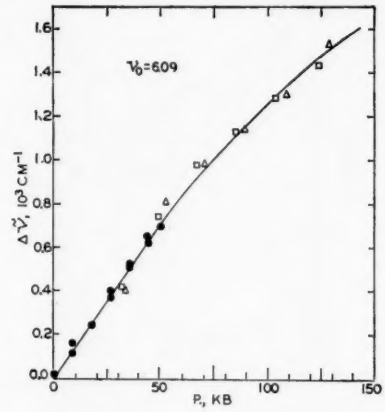

FIG. 12. Pressure shift for I-Co in $CoBr_2$.

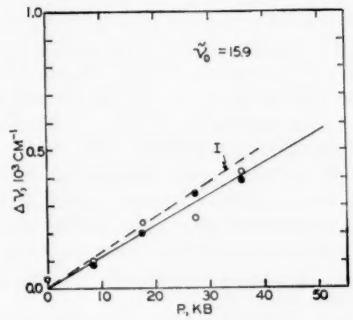

FIG. 13. Pressure shift for III-Co in $CoBr_2$.

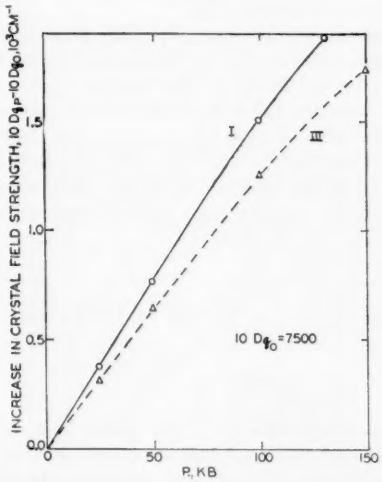

FIG. 14. Increase in crystal field strength with pressure—$CoCl_2$.

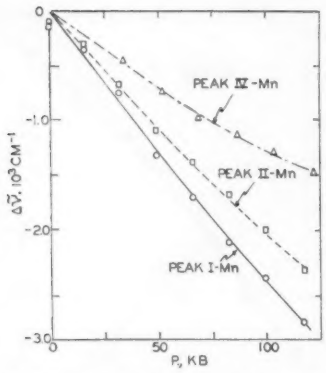

FIG. 15. Pressure shifts of peaks dependent on Dq in $MnCl_2$.

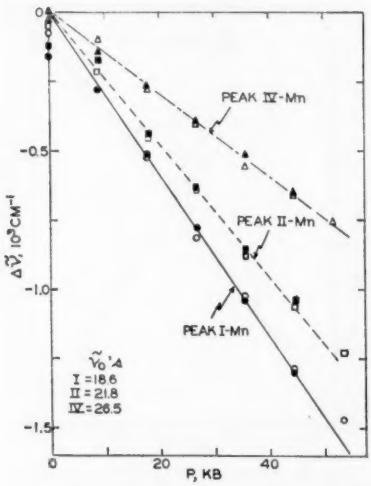

FIG. 16. Pressure shifts of peaks dependent on Dq in $MnBr_2$

counted for by any reasonable change in parameters and supports our assignment.

Equations (7) and (8) predict shifts for peaks Mn-I, Mn-II and Mn-IV which are complex functions of Dq, B, and C. For any reasonable values of B and C a large red shift is predicted for peaks I and II and a somewhat smaller red shift for peak IV. Figures 15 and 16 show the shifts of these peaks for $MnCl_2$ and $MnBr_2$. There is clearly qualitative agreement with theory. Unfortunately, the shifts are very sensitive to the absolute values of B and C, and the degree of quantitative agreement with experiment can be varied widely using values of these parameters within the accepted range at one atmosphere. No further discussion of these peaks is therefore offered.

From Eqs. (9) and (10) one can see that peaks III-Mn and V-Mn are independent of the crystal field energy, and should thus not shift with pressure if B and C are constant. Furthermore, the difference in energy of the two peaks equals $7B$.

Figures 17 and 18 show the shifts of peaks III-Mn and V-Mn with pressure for $MnCl_2$ and $MnBr_2$. Clearly B and C are not constant. The decrease in B, obtained directly from the difference in shift of the two peaks, is shown in Table IV. It is the same order as the changes for Ni^{++} and Co^{++}. While the difference between the change in B for $MnCl_2$ and $MnBr_2$ with pressure is rather small, it is reasonable that a larger decrease in B (greater increase in covalency) would be obtained with the more polarizable Br^- ion.

The change in the parameter C can be calculated from the equation

$$C_p - C_0 = \frac{1.7(\text{shift for III} - \text{Mn}) - \text{Shift for V} - \text{Mn}}{3.5}. \tag{11}$$

Figure 19 shows the decrease in B and C with pressure for $MnCl_2$ and $MnBr_2$. For values of $\gamma = C/B$ from 3–5 (the usual range postulated from atmospheric and free ion data) there would be a small increase in γ with increasing pressure.

ϵ AS A PRESSURE VARIABLE

From the pressure shifts of peaks Mn-III and Mn-V it is possible to obtain some useful results concerning the parameter ϵ. Peak III is really two peaks having the same crystal field energy. With the introduction of ϵ these peaks are no longer degenerate. In $MnCl_2$ and $MnBr_2$ they definitely appear as a doublet, but both peaks give identical shifts. Using Pappalardo's energy equations one obtains for these peaks

$$E'(\text{IIIa}) = (10+5\gamma)(1-\epsilon) \tag{12}$$

$$\begin{vmatrix} 13+5\gamma-\epsilon(4+2\gamma)-E' & -2\sqrt{3}(1-\epsilon) \\ -2\sqrt{3}(1-\epsilon) & 14+5\gamma-\epsilon(22+7\gamma)+\epsilon^2(8+2\gamma)-E' \end{vmatrix} = 0, \tag{13}$$

where $\gamma = C/B$, $E' = E/B$, the lower root of $E' = E'(\text{IIIb})$, and the second root $= E'(V)$. Let us define R as the relative shift of peak Mn-V to Mn-III with pressure. From the experimental data $R = 1.25$ in the 50-kbar region, both for $MnCl_2$ and $MnBr_2$.

The calculated value of R (for constant γ) is

$$R = \frac{\partial E'(\text{V})}{\partial \epsilon} \Big/ \frac{\partial E'(\text{III})}{\partial \epsilon}. \tag{14}$$

Here, for E' (III) one can use E' (IIIa), E' (IIIb)

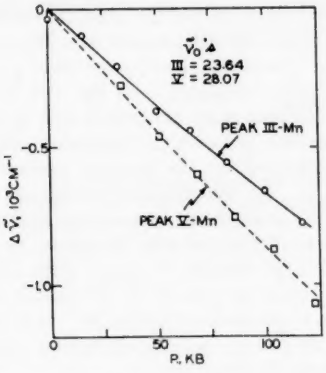

FIG. 17. Pressure shifts for peaks independent of Dq in $MnCl_2$

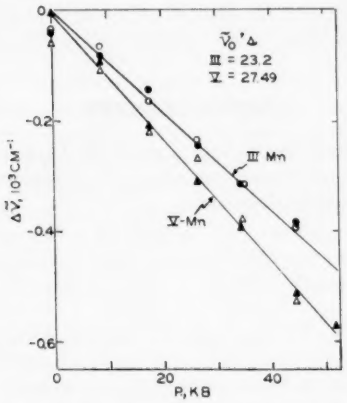

FIG. 18. Pressure shifts for peaks independent of Dq in $MnBr_2$.

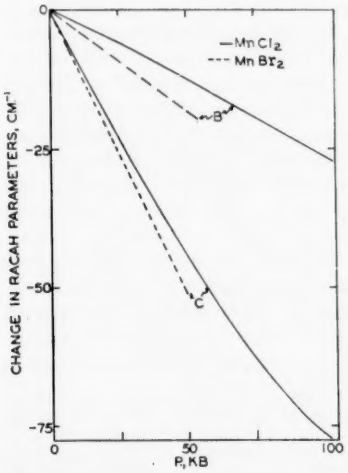

FIG. 19. Effect of pressure on the Racah parameters B and C—$MnCl_2$ and $MnBr_2$.

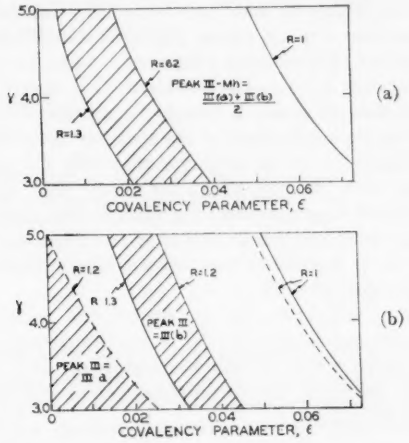

FIG. 20. (a) Allowed values of ϵ if peak III-Mn=½[IIIa)+IIIb)]. (b) Allowed values of ϵ if peak III-Mn=IIIa; if peak III-Mn=IIIb.

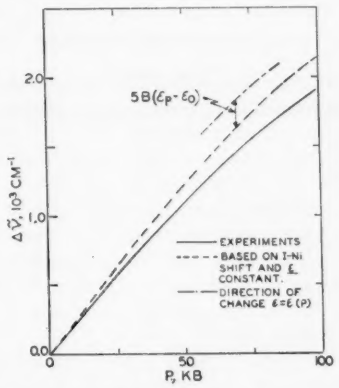

FIG. 21. The effect of the parameter ϵ in calculating shifts for peak II-Ni in $NiCl_2$.

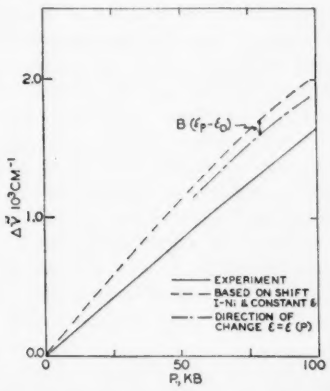

FIG. 22. The effect of the parameter ϵ in calculating shifts of peak III-Ni in $NiCl_2$.

or the average of these two values. The calculated R is a function of γ and ϵ only. Figure 20 shows the allowed values of ϵ for values of γ between 3–5 and for values of R between 1.2–1.3. The line for $R=1$ is clearly beyond experimental error. It should be stressed that these curves are independent of the absolute values of B and C. Clearly ϵ can be no larger than 0.04 for any fixed value of γ. It was shown by Stout[5] that values of $\epsilon=0.13$–0.15 are needed to account for the atmospheric peaks using the free ion value of B. Pappalardo[6] using a value of B obtained from the solid finds values of ϵ in the range 0.03–0.05.

It is relatively easy to correct the equations of Tanabe and Sugano for Ni^{++} for the parameter ϵ, if one keeps terms to only the first power in ϵ. The ϵ^2 terms introduce the Racah parameter A which cannot be evaluated

$$\text{I}-\text{Ni}=10Dq^*=10Dq+(A-8B)\epsilon \qquad (15)$$

$$\text{II}-\text{Ni}=15Dq^*+1.5B-3B\delta^*+5B\epsilon \qquad (16)$$

$$\text{III}-\text{Ni}=15Dq^*+13.5B+3B\delta^*-B\epsilon, \qquad (17)$$

where

$$\delta^*=[(10Dq^*-9B)/12B]^2\ll 1.$$

Peak I-Ni again determines Dq^*. From Eqs. (16) and (17), it can be seen that, if B is independent of pressure, the pressure shift (but not the absolute energy of the transition) should be independent of ϵ. Figures 21 and 22 show the experimental shifts for these peaks compared with shifts calculated from Dq^* and the free ion value of B. In both cases too large a shift is predicted. If ϵ increases with pressure the calculated shift of peak II-Ni is increased by an amount proportional to $5B(\epsilon_P-\epsilon_0)$, i.e., the discrepancy is increased. The shift of peak III-Ni is decreased by an amount proportional to $-B(\epsilon_P-\epsilon_0)$. While this is in the right direction, any change of ϵ large enough to correct peak III-Ni will give absurd results for peak II-Ni. Evidently, this form of correction is not satisfactory for Ni^{2+}. It is not possible to say at present whether including terms in ϵ^2 would improve this situation.

These results show the power of the high-pressure optical technique in the study of crystal-field phenomena, in the identification of the III-Co peak, in the understanding of the effect of interionic distance on the Racah parameter, and in understanding the covalency parameter ϵ.

ACKNOWLEDGMENTS

The authors would like to thank R. Pappalardo for the $MnCl_2$ and $MnBr_2$ crystals, and S. Sugano and T. S. Piper for helpful discussions.

Infrared Spectroscopic Study of the Photolysis of Methyl Azide and Methyl-d_3 Azide in Solid Argon and Carbon Dioxide*

DOLPHUS E. MILLIGAN
Mellon Institute, Pittsburgh 13, Pennsylvania

(Received April 3, 1961)

Experiments have been carried out on the photolysis of methyl azide and methyl-d_3 azide at high dilution in solid argon (4.2°K) and carbon dioxide (~50°K). Photolysis of these species in argon and carbon dioxide matrices results in the appearance of a number of new spectral features in the 3300–600 cm^{-1} region. The spectroscopic data for the photolysis products appear to be consistent with the identification of these species as methyleneimine (CH_2=NH) and methyleneimine-d_3 (CD_2=ND).

INTRODUCTION

STUDIES of the photolysis of methyl azide in rigid inert media were undertaken with the hope of producing the methylimino radical (CH_3N) under conditions suitable for infrared spectroscopic study. Although a literature search indicated that no previous photochemical studies had been carried out on methyl azide, we considered it quite likely that it would decompose by a free radical mechanism involving the methylimino radical and molecular nitrogen as the primary products. Our speculations on this point were guided largely by photochemical results obtained by Beckman and Dickinson[1] on the closely related molecule HN_3. According to these workers, the primary process in the photo-decomposition of hydrazoic acid involves the formation of an imino radical (NH) and molecular nitrogen.

Ultraviolet spectra of gaseous methyl azide recorded in this laboratory indicate two regions of absorption, a fairly weak and broad band centered at 2850 A which shows evidence of structure and a considerably stronger structureless band beginning near 2400 A and extending beyond 1900 A. Irradiation of the gaseous material with light falling within the short wavelength band is observed to result in the formation of nitrogen, ammonia and hexamethylene tetramine. These species have been observed by Leermakers[2] as products of the thermal decomposition of methyl azide in the temperature range 200–240°C. According to Leermakers, the thermal decomposition of methyl azide proceeds by a free radical mechanism involving a short-lived methylimino radical and nitrogen. He postulates that the CH_3N radical rearranges to methyleneimine, which polymerizes to hexamethylene tetramine and ammonia. The observation of the same principal products in the thermal and photochemical decomposition of methyl azide was interpreted to mean that the photolytic decomposition might likewise proceed through the intermediary of a short-lived methylimino radical. We considered it likely that the rearrangement reaction postulated in the gas phase might be partially, if not completely, quenched in the solid state due to rapid removal of the excess energy of the free radical species through collisions with the matrix material.

This paper presents the results of an infrared spectroscopic study of the photolysis of methyl azide and methyl-d_3 azide in solid argon and carbon dioxide matrices at 4.2 and 50°K, respectively.

EXPERIMENTAL

Methyl azide was prepared according to the procedure of Rice and Grelecki.[3] Methyl-d_3 azide was prepared in a similar manner using dimethyl-d_3 sulfate which was prepared by heating CD_3Br (99.5% deuterium) with Ag_2SO_4 in a sealed pyrex tube. The crude materials were dried over anhydrous magnesium perchlorate and purified further by several distillations.

Argon (Matheson) was purified by passing the gas through a cold trap immersed in a dry ice-acetone mixture (−80°C). Carbon dioxide (Matheson, bone dry) was used without further purification other than condensation at 77°K followed by pumping to remove noncondensable impurities. The gaseous mixtures of methyl azide with argon and with carbon dioxide were prepared by standard procedures. The mole ratios of matrix material to solute were varied from 200 to 500.

The low temperature cell used in these experiments was similar in design to one described previously by Becker and Pimentel.[4] The low temperature window (CsBr) was equipped with a copper-constantan thermocouple and was mounted in a copper block which communicated directly with the primary coolant. Thermal contact between the window and copper block was established by means of lead gaskets and screw pressure. A beryllium bronze lock washer was incorporated in the assembly in order to compensate for contraction with possible loss of thermal contact on cooling. This assembly was found to provide good

* This research was supported in part by the U. S. Air Force through the Air Force Office of Scientific Research of the Air Research and Development Command.

[1] A. O. Beckman and R. G. Dickinson, J. Am. Chem. Soc. **50,** 1870 (1928); **52,** 124 (1930).

[2] J. A. Leermakers, J. Am. Chem. Soc. **55,** 3098 (1933).

[3] F. O. Rice and C. J. Grelecki, J. Phys. Chem. **61,** 830 (1957).

[4] E. D. Becker and G. C. Pimentel, J. Chem. Phys. **25,** 224 (1956).

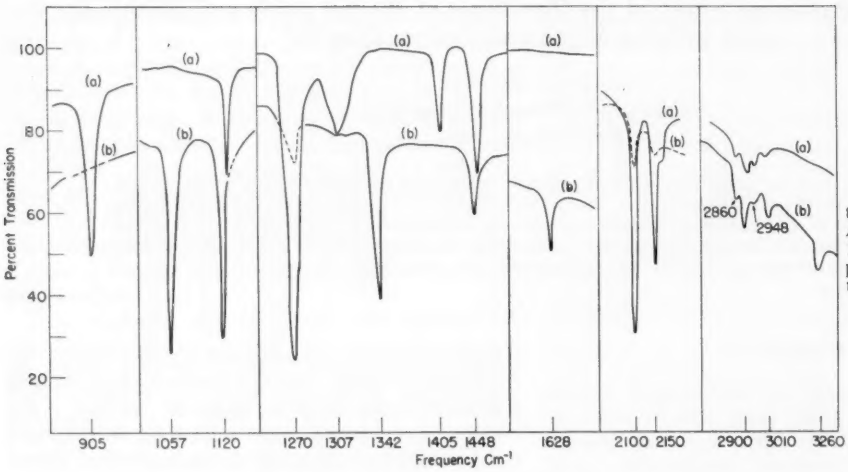

FIG. 1. Infrared Spectrum of CH_3N_3 in Solid Argon ($Ar/CH_3N_3=500$, $T=4.2°K$): (a)—before photolysis, (b)—after photolysis.

thermal contact between the window and block, as evidenced by the fact that upon cooling the cell the window reached the temperature of the primary coolant within a few minutes after the block had reached that temperature.

Sample depositions were carried out over periods ranging from 1 to 3 hr. The temperature of the sample window was observed periodically during deposition to insure that no significant warming of the deposit occurred.

Liquid helium was used as the primary coolant in experiments where argon was used as the matrix and sample deposition was carried out at 4.2°K. In experiments where carbon dioxide was used as the matrix, sample depositions were made in the temperature range 48–50°K. Temperatures in this range were obtained by pumping on solid nitrogen with a high speed pump (Welch 1397).

A medium pressure mercury lamp (G.E. AH–4) without the pyrex envelope was employed for irradiation of the deposits. The samples were irradiated through potassium bromide and barium fluoride windows. Identical results, as judged by the spectrum of the photolysis product, were obtained with both windows.

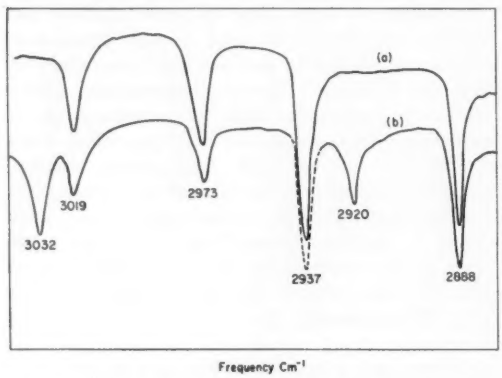

FIG. 2. Infrared Spectrum of CH_3N_3 in Solid Argon ($Ar/CH_3N_3=500$, $T=4.2°K$): (a)—before photolysis, (b)—after photolysis.

Infrared spectra were recorded on a Perkin-Elmer Model 13 infrared spectrometer equipped with NaCl and KBr prisms. The frequency accuracy is estimated to be ± 20 cm^{-1} at 3000 cm^{-1}, ± 5 cm^{-1} at 1600 cm^{-1} and ± 3 cm^{-1} below 1400 cm^{-1}. In several experiments a Perkin-Elmer Model 112G spectrometer, equipped with a Bausch and Lomb replica grating (75 lines/mm) blazed at 12 μ, was used. The frequency accuracy of this instrument is estimated to be ± 1 cm^{-1} both at 3000 cm^{-1} and at 1450 cm^{-1}.

RESULTS

Photolysis of CH_3N_3 in Solid Argon

Experiments were carried out on the photolysis of methyl azide in solid argon at mole ratios of argon to methyl azide of 250, 300, 400, and 500. The amount of gaseous mixture deposited in each of the experiments was adjusted to give approximately 30 micromoles of methyl azide. Essentially identical results were obtained in all of the experiments.

The infrared spectrum of methyl azide in solid argon at a mole ratio of argon to methyl azide of 500 is shown in the upper trace of Fig. 1. The spectral region near 3000 cm^{-1}, recorded on a grating instrument, is shown in the upper trace of Fig. 2. The frequencies of the fundamentals observed in solid argon, together with the frequencies reported for gaseous methyl azide,[5] are tabulated in Table I. The matrix spectrum of methyl azide is found to be in good agreement with the vapor spectrum except in the 3000 cm^{-1} region. It is possible

[5] E. Mantica and G. Zerbi, Gazz. Chim. Ital. **90**, 53 (1960).

that the lack of agreement here is due to difficulty in locating band centers in the vapor spectrum in this region. Quite possibly the absence of a band near 1035 cm^{-1} in the matrix spectrum is due to the low intensity of this band. As can be seen from Fig. 1, irradiation of solid solutions of argon and methyl azide with a medium pressure mercury lamp results in a decrease in the intensity of bands due to methyl azide and in the appearance of a number of new bands in the 3300–600 cm^{-1} region. These new bands are observed at 1057, 1120, 1342, 1448, 1628, 2900, 3010, and 3260 cm^{-1}. Under higher spectral resolution the 1057 cm^{-1} band is observed to split into two components, centered at 1057 and 1060 cm^{-1}.

The 3000 cm^{-1} region after photolysis is shown in considerably greater detail in the lower trace of Fig. 2. In this experiment spectra were recorded after irradiation for 15, 25, 45, and 60 min. At the end of an hour of irradiation the peak heights of the bands at 2937, 2973 and 3019 cm^{-1} were reduced to approximately twenty percent of their initial values, whereas the 2888 cm^{-1} band remained unchanged. New bands developed at 2920 and 3032 cm^{-1} and increased in intensity over the entire period of irradiation. The behavior of the 2888 cm^{-1} band suggests that it is associated with an impurity which does not photolyze under these conditions.

In several experiments, the behavior of the bands associated with the photolysis product was studied on diffusion in order to obtain information on the reactivity and stability of the species. When the irradiated deposits were allowed to warm up to about 45°K (where diffusion is known to occur in solid argon) and were recooled to 4.2°K, the bands which appear on photolysis were observed to broaden and to undergo a fifty per cent decrease in peak intensity. No additional bands were observed after diffusion, suggesting that the changes in spectral features are most likely due to formation of aggregates by the absorbing species.

A white solid is observed to remain on the sample window when the deposits are allowed to warm up to temperatures where the matrix material is lost. Spectra of this material recorded at room temperature are found to exhibit bands at 805, 1005, 1224, 1362, 1453, 2780, and 2940 cm^{-1}, in good agreement with the spectrum reported for hexamethylene tetramine.[6]

Photolysis of CD_3N_3 in Solid Argon

Experiments were performed on the photolysis of CD_3N_3 in solid argon at mole ratios of 200, 250, and 500. In the experiments involving mole ratios of 250 and 500 the amount of gaseous mixture was adjusted to give approximately 30 micromoles of CD_3N_3. In the 200 mole ratio experiment approximately 60 micromoles of CD_3N_3 were present.

[6] A. W. Baker, J. Phys. Chem. **61**, 450 (1957).

TABLE I. Infrared spectrum of methyl azide.

Assignment	Gas	Argon matrix	Carbon dioxide matrix
ν_{11}	3023	3019[a]	3018[a]
ν_1	3018	2973[a]	2983[a]
ν_2	2963	2937[a]	2935[a]
ν_3	2106	2100	2100
ν_{12}	1452	1448	1472 1460
ν_6	1417	1405	1425 1410
ν_7	1334	1307	1305
ν_4	1272	1270	1283 1270
ν_{13}	1140	1125	1123
ν_8	1035	...	...
ν_5	910	905	915
ν_{14}	666	660	...
ν_{10}	555	...	...
ν_9	259	...	...
ν_{15}	...	...	...

[a] Frequencies from grating spectra.

Irradiation of solid solutions of CD_3N_3 and argon results in the appearance of bands at 770, 818, 1067, 1087, 1570, and 2256 cm^{-1}. The spectrum of a typical deposit before and after photolysis is shown in Fig. 3. The presence of a band at 1087 cm^{-1} in the spectrum of the photolysis product is indicated by an apparent increase in the intensity of the band initially present at this frequency. Further evidence for the presence of this band is obtained in experiments which will be described later, involving the photolysis of CD_3N_3 in solid CO_2.

In the experiment carried out at a mole ratio of 200 more than 95% of the CD_3N_3 was decomposed. In addition to the features observed in the 250 and 500 mole ratio experiments, weak bands were observed at 2150 and 2420 cm^{-1}.

The behavior of the bands of the deuterated photolysis product on diffusion is found to parallel the behavior of the bands produced in the photolysis of CH_3N_3 in argon. Following each experiment a white solid remained on the sample window. The amount of this material was insufficient to allow detailed spectroscopic study. On the basis of the CH_3N_3 experiments it seems quite reasonable to assume that this material is the deuterated variety of hexamethylene tetramine.

Photolysis of CH_3N_3 and CD_3N_3 in Solid CO_2

Experiments were carried out on the photolysis of CH_3N_3 and CD_3N_3 in solid CO_2 at mole ratios of 200,

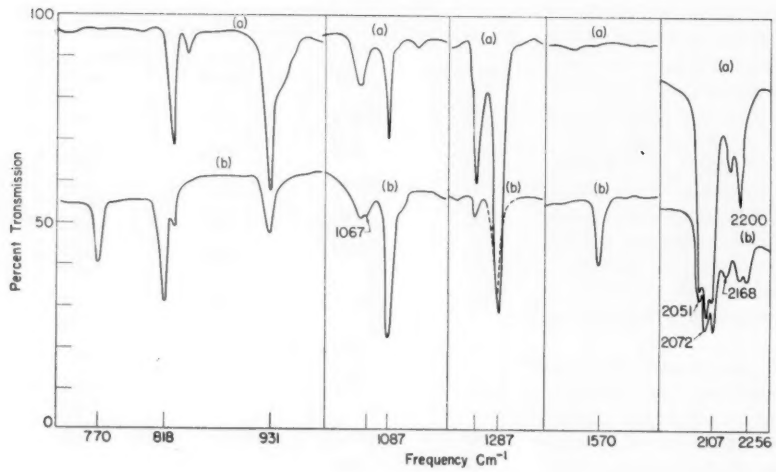

FIG. 3. Infrared Spectrum of CD_3N_3 in Solid Argon (Ar/CD_3N_3=500, T=4.2°K): (a)—before photolysis, (b)—after photolysis.

300 and 500. Spectra of CH_3N_3 and CD_3N_3 in solid CO_2 are shown in Figs. 4 and 5. The spectral region extending from 2000 to 2500 cm^{-1} is masked because of absorption by the matrix material and hence is not shown.

The spectrum of CH_3N_3 in solid CO_2 is found to differ somewhat from that in solid argon. There are small frequency shifts which are most likely due to a dielectric effect, and a number of bands which appeared as singlets in solid argon are present as well defined doublets in solid CO_2. These doublets do not appear to exhibit any dependence on concentration in the mole ratio range 200 to 500 and thus are probably not due to polymeric species. There appears to be no obvious explanation for this splitting. Possibly it results from multiple site occupancy by the solute species in the host (CO_2) lattice.

Irradiation of solid solutions of CH_3N_3 in CO_2 and of CD_3N_3 in CO_2 appears to result in the formation of the same products as are observed in the photolysis of these species in solid argon.[7] Spectra of the CH_3N_3 and CD_3N_3 photolysis products in solid CO_2 are shown in Figs. 4 and 5. The lowest frequency bands of the photolysis products appear to be the only bands significantly affected on going from argon to CO_2 as a matrix material. In solid argon the lowest frequency band of the CH_3N_3 photolysis product (1060 cm^{-1}) is a doublet under high resolution, with components centered at 1057 and 1060 cm^{-1}, whereas in solid CO_2 these bands are shifted to 1055 and 1078 cm^{-1}. Similarly, the lowest frequency band in the spectrum of deuterated photolysis product in argon (770 cm^{-1}), which is not resolved under the highest resolution obtainable (~1 cm^{-1}) in this region, appears to be split into two components centered at 784 and 788 cm^{-1} in solid CO_2.

In one experiment carried out at a mole ratio of CO_2 to methyl azide of 300, the spectral region extending from 2880 cm^{-1} to 3300 cm^{-1} was scanned on a grating instrument before and after photolysis. Before photolysis, bands are observed at 2888, 2934, 2983, and 3018 cm^{-1}. The 2934, 2983, and 3018 cm^{-1} bands decreased in intensity and eventually disappeared on photolysis, whereas the 2888 cm^{-1} band remained unchanged. New bands developed at 2922, 3048, and 3285 cm^{-1}. These results are in good agreement with those obtained using argon matrices.

DISCUSSION

The behavior of the bands which develop on photolysis of CH_3N_3 and CD_3N_3 in argon and in CO_2 clearly indicates that the species responsible for them are not free radicals. If these features are due to the methylimino radical or to other reactive free radical species, they are likely to be greatly reduced in intensity or to disappear completely when the deposits are permitted to diffuse. We might also expect to observe new bands after diffusion, due to free radical reactions. If the methylimino radical is present, we should expect to observe bands due to azomethane after diffusion. Ethane may also result if the dimerization of two methylimino radicals forms azomethane with energy in excess of the activation energy for its decomposition.

The absence of a concentration dependence of the bands of the photolysis product would appear to indicate that the species responsible for them are derived from single molecules of methyl azide. Of the various infrared active species that may be produced in the photolysis of CH_3N_3, HCN and methyleneimine (CH_2=NH) appear to be the most likely. HCN is not

[7] Experiments involving the photolysis of HN_3 and CH_2N_2 in solid CO_2 indicate that CO_2 is susceptible to attack by the NH and CH_2 free radicals. Moreover, experiments have shown that the isolation efficiency of CO_2 at 50°K is dependent on the nature of the solute species and hence that care should be exercised in the use of this material in matrix isolation experiments.

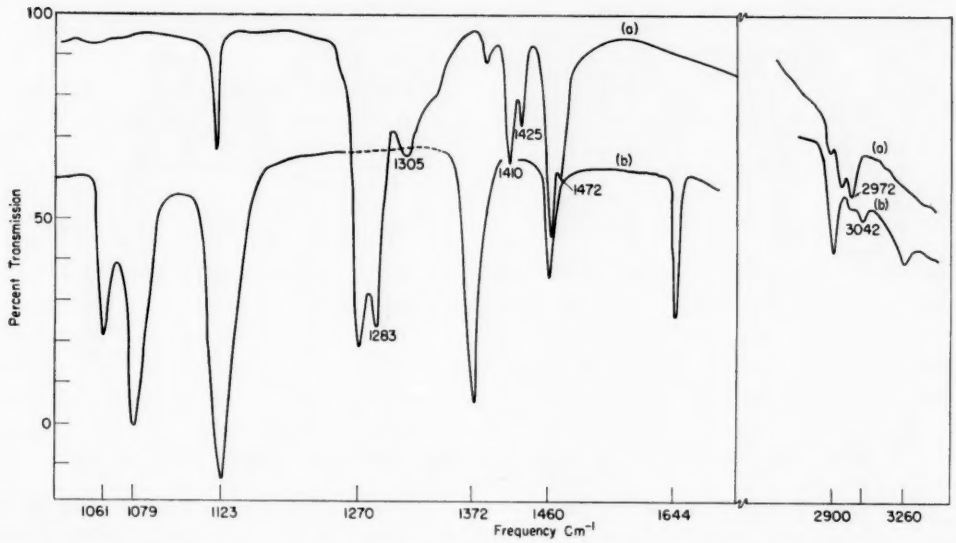

FIG. 4. Infrared Spectrum of CH_2N_2 in Solid Carbon Dioxide ($CO_2/CH_2N_2=250$, $T=50°K$). (a)—before photolysis, (b)—after photolysis.

present in spectroscopically detectable quantities; furthermore, the number of bands observed could hardly be explained solely on the basis of a triatomic species.

Pickard and Polly[8] have investigated the spectrum of a large number of ketimines of the general type $R_1R_2C{=}NH$, where R_1 and R_2 are alkyl or aryl substituents. These workers find that molecules of this type exhibit characteristic bands in the 3.12 and 6.05–6.15 μ regions associated with the N—H stretching and C=N stretching modes respectively. The CH_2N_2 photolysis product exhibits bands at 3250 and 1628 cm^{-1} in solid argon and at 3260 and 1644 cm^{-1} in solid CO_2. The assignment of these bands to NH and C=N stretching modes is strongly supported by data obtained for the deuterated photolysis product, which has bands at 2420 and 1570 cm^{-1} in solid argon and at 1585 cm^{-1} in solid CO_2. The 2400 cm^{-1} region in the CO_2 matrix experiments is obscured due to absorption by solid CO_2.

Methyleneimine is expected to be planar with no elements of symmetry other than the plane of the molecule. The vibrations are divided into two classes—those that are symmetric with respect to the plane of the molecule (A') and those that are antisymmetric with respect to the plane of the molecule (A''). Methyleneimine, along with many of the lower molecular weight ketimines, appears to exhibit a great tendency to polymerize. This species has often been postulated as a transient intermediate in the formaldehyde-ammonia reaction, which is known to yield hexamethylene tetramine. It should be possible to make some fairly reliable predictions of the spectrum of such a molecule on the basis of the infrared spectra of closely related molecules. Fortunately, the infrared spectrum of gaseous formaldoxime, one of the closer known relatives of methyleneimine, has been studied[9] in detail, and a complete vibrational assignment has been made. The frequencies and assignment of the fundamentals for formaldoxime and the bands observed in the spectrum of the CH_2N_2 and CD_2N_2 photolysis products in argon and in CO_2 are compared in Table II.

Methyleneimine should have at least two bands associated with CH stretching vibrations in the 3000 cm^{-1} region. In formaldoxime the symmetric and asymmetric carbon-hydrogen stretching vibrations have been assigned at 3098 and 2976 cm^{-1} respectively. Bands are observed at 3032 and 2920 cm^{-1} for the CH_2N_2 photolysis product in solid argon and at 3048 and 2922 cm^{-1} in solid CO_2. The assignment of these bands to vibrations involving hydrogen motion is favored by their absence in the spectrum of the deuterated photolysis product. These bands may be correlated with bands at 2150 and 2256 cm^{-1} in the spectrum of the deuterated photolysis product.

Bands due to the CH_2 and NH deformation vibrations of methyleneimine are expected in the 1300–1500 cm^{-1} region. The expectation that the NH deformation mode will give rise to absorption in this region is based on the range found for this vibration in aliphatic and aromatic secondary amines.[10] Pickard and Polly,[8]

[8] P. L. Pickard and G. W. Polly, J. Am. Chem. Soc. **76,** 5169 (1954).

[9] S. Califano and W. Luttke, Z. Physik. Chem. **6,** 83 (1956).

[10] L. J. Bellamy, *The Infra-red Spectra of Complex Molecules* (John Wiley & Sons, Inc., New York, 1958), pp. 256–257.

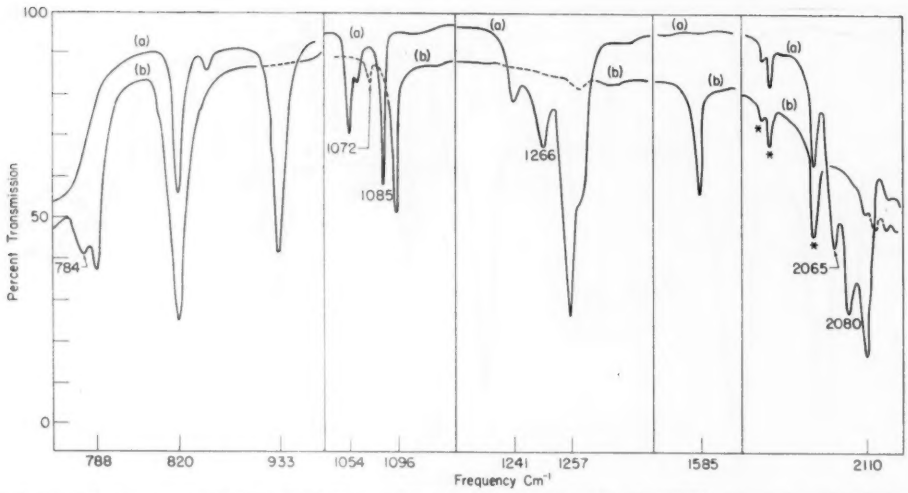

FIG. 5. Infrared Spectrum of CD_3N_3 in Solid Carbon Dioxide ($CO_2/CD_3N_3=250$, $T=50°K$): (a)—before photolysis, (b)—after photolysis.

studying a number of substituted ketimines with the —C═NH group, were apparently unable to identify the NH deformation mode. Possibly these workers did not detect absorption due to this vibration because of low intensity or because of masking by absorption due to the alkyl and aryl substituents.

Bands are observed at 1342 and 1453 cm^{-1} in the spectrum of CH_3N_3 in solid argon and at 1372 and 1460 cm^{-1} in solid CO_2. The deuterated photolysis product shows no evidence of absorption at these frequencies. Correspondingly, bands are observed at 1067 and 1087 cm^{-1} in solid argon and at 1072 and 1096 cm^{-1} in the spectrum of the deuterated product. The CH_3N_3 decomposition product does not absorb at these frequencies.

Since the NH deformation vibration generally leads to weak absorption,[10] the relative intensities suggest association of the more intense 1342 and 1087 cm^{-1} bands with the CH_2 and CD_2 deformation vibrations, respectively. Correlation of the 1453 cm^{-1} band and the 1067 cm^{-1} band must be regarded as doubtful. A product rule calculation using bond distances and angles for ethylene and the assignment given here for the in-plane vibrations indicates that absorption due to the ND deformation mode should be expected near 1200 cm^{-1}. The absence of a band in this region in the spectrum of the deuterated photolysis product can be accounted for on the basis of low intensity. This explanation is favored by the relatively low intensity of its counterpart in the spectrum of the hydrogenic material. The 1067 cm^{-1} band may be contributed by a partially deuterated species.

The CH_2 deformation mode of methyleneimine (1342 cm^{-1}) is assigned a frequency substantially lower than that found for this vibration in formaldoxime (1410 cm^{-1}). The lowering in frequency of this vibration in methyleneimine may be due to interaction with the NH deformation mode, which belongs to the same symmetry species.

Bands associated with the CH_2 wagging and rocking modes of methyleneimine are expected in the 1100–900 cm^{-1} region. These vibrations have been assigned to bands at 949 and 1154 cm^{-1}, respectively, in the spectrum of formaldoxime. Quite possibly the remaining fundamental of methyleneimine, the torsional mode, gives rise to absorption in the same spectral region as the wagging and rocking mode. In formaldoxime the CH_2 torsional mode has been assigned at 770 cm^{-1}, whereas in ethylene and ethylene-d_4, which are isoelectronic with methyleneimine, the torsional modes have been assigned[11] at 1027 and 726 cm^{-1}, respectively. Particularly on the basis of the data for ethylene, it does not appear entirely unreasonable to expect absorption due to the torsional mode of methyleneimine in the 1000 cm^{-1} region. Three bands are observed in the spectrum of the hydrogenic photolysis product in the 1150–1050 cm^{-1} region. These bands, at 1057, 1060, and 1120 cm^{-1} in solid argon and at 1055, 1078, and 1120 cm^{-1} in solid carbon dioxide, are absent in spectra of the deuterated photolysis product, indicating that they are associated with vibrations involving hydrogen motion. The deuterated photolysis product exhibits bands at 770 and 820 cm^{-1} in solid argon and at 784, 788, and 820 cm^{-1} in solid carbon dioxide.

On the basis of the vibrational assignment given for formaldoxime, we are tempted to assign the 1120 cm^{-1} band to the CH_2 rocking mode. Such an assignment would necessitate assigning the bands at 1057 and 1060 cm^{-1} to the wagging and torsional modes. The wagging and torsional modes belong to the same sym-

[11] R. L. Arnett and B. L. Crawford, Jr., J. Chem. Phys. **18**, 118 (1950).

TABLE II. Infrared spectra of formaldoxime and photolysis products of methyl and methyl-d_3 azide.

Assignment	Formaldoxime	CH_3N_3 Photolysis product-argon matrix	CH_3N_3 Photolysis product-carbon dioxide matrix	CD_3N_3 Photolysis product-argon matrix	CD_3N_3 Photolysis product-carbon dioxide matrix
OH stretch	3646	...	...	...	...
CH_2 symmetric stretch	3098	3032[a]	3048[a]	2256	...
CH_2 asymmetric stretch	2976	2920[a]	2922[a]	2150	...
C=N stretch	1642	1628	1644	1570	1585
CH_2 deformation	1410	1342	1372	1087	1096
OH deformation	1315	...	...	...	...
CH_2 rock	1154	1060	1079	770	788
CH_2 wag	949	1120	1123	818	820
NO stretch (NH stretch)	888	3260	3285[a]	2420	...
CH_2 torsion	770	1057	1061	770	784
C=N—O bend (NH deformation)	535	1448	1460	1067?	1072?
OH torsion	420	...	...	...	...

[a] Frequencies from grating spectra.

metry species and hence would hardly be expected to approximate each other so closely in frequency. Therefore, it seems somewhat more reasonable to assign the 1120 cm^{-1} band to the non-planar CH_2 wagging vibration and the two lower frequency bands to the torsional and rocking modes. Using the CO_2 matrix frequencies, 1120, 1055, 820, and 784 cm^{-1}, a frequency ratio of 0.54 is obtained. The theoretical product rule ratio calculated using bond distances and angles for ethylene is 0.59. Possibly, the lack of agreement arises from the assumption that the bond distances and angles of methyleneimine are not substantially different from those of ethylene.

On the whole, it appears that the spectra of the CH_3N_3 and CD_3N_3 photolysis products are in good agreement with spectra predicted for methyleneimine and methyleneimine-d_3. The appearance of NH and C=N stretching vibrations and the observation of the predicted number of infrared absorption bands give especially strong evidence for the presence of these molecules.

The formation of methyleneimine through the photolysis of methyl azide may involve either a short lived free radical (CH_3N) or an excited molecular species. Recent studies of the gas phase photolysis of this material by Darwent and Currie[12] indicate that the primary process involves the formation of the CH_3N radical and N_2 and that both of these species possess excess energy. These results favor the hypothesis that methyleneimine is formed by the rearrangement of a "hot" methylimino radical over an excited molecule mechanism.

CONCLUSIONS

Solid CO_2 at 50°K has proved a satisfactory matrix for studies of the photolysis of CH_3N_3 and CD_3N_3.

The photolysis of these species in solid argon and carbon dioxide results in the formation of methyleneimine and methyleneimine-d_3. Evidence has been obtained for the polymerization of methyleneimine to hexamethylene tetramine.

ACKNOWLEDGMENTS

The author wishes to thank Dr. M. E. Jacox and Dr. Robert M. Hexter for their interest in this work and for numerous helpful suggestions and criticisms.

[12] Private communications with Dr. B. de B. Darwent.

Nuclear Magnetic Resonance in $CuF_2 \cdot 2H_2O$ Single Crystals

R. G. SHULMAN AND B. J. WYLUDA
Bell Telephone Laboratories, Incorporated, Murray Hill, New Jersey

(Received April 27, 1961)

We have measured the hydrogen and fluorine nuclear magnetic resonance signals in single crystals of $CuF_2 \cdot 2H_2O$. The hyperfine interaction between the fluorine nucleus and the magnetic electrons has been separated into isotropic and anisotropic components which have been evaluated. The Néel temperature has been determined to be $10.92° \pm 0.2°$K in contrast to the maximum in the susceptibility which had been shown to occur at 26°K.

WE have made nuclear magnetic resonance measurements on the hydrogen and fluorine nuclei in single crystals of $CuF_2 \cdot 2H_2O$. These crystals were grown by slow evaporation of a water solution at 71.5°C by Dr. J. W. Nielsen as described previously.[1] The crystal structure has been determined by Geller and Bond[2] to be monoclinic in space group $C_{2h}(3)$–$I2/m$. The body-centered unit cell contains two formula units in which each Cu^{++} ion is coplanar with two fluoride ions 1.89 A away in the *ac* plane and two oxygens of the water at ± 1.93 A along the *b* axis. At 2.47 A distance lie two more fluoride ions in the *ac* plane which might be considered as completing the distorted octahedron around the copper. All fluorines have a short bond to one copper and a long bond to another. In the paramagnetic state measurements were made on both the hydrogen and fluorine nuclei. A single crystal was oriented and glued to a rod with proton free silica cement so that the *b* axis coincided with the rod axis. This was placed in the unsilvered tip of a glass Dewar and the tip was inserted into a Varian V-4210 rf probe. Figure 1 shows the frequencies satisfying the resonance condition as a magnetic field of constant amplitude was rotated in the *ac* plane. It can be seen that the fluorine shift is composed of temperature dependent isotropic and anisotropic components. The F^{19} resonance shift is similar to those previously observed[3] in transition element fluorides, and it arises from interactions between the nucleus and the magnetic electrons. We shall consider the dipole interactions and the hyperfine interactions separately. After subtracting the calculated dipole field, which contributed 6.2 gauss, from the measured anisotropy at 77°K, the residual direction-dependent shifts were used to calculate the anisotropic hyperfine interaction. The hyperfine interaction is described by a perturbing Hamiltonian $\mathbf{I} \cdot \mathbf{A} \cdot \mathbf{S}$. By using the previous[3–6] methods of analysis, we obtained preliminary values of $A_s = (86 \pm 6) \times 10^{-4}$ cm^{-1} and $A_a = (24 \pm 5) \times 10^{-4}$ cm^{-1} for the isotropic and anisotropic components of the hyperfine tensor. By converting these hyperfine interactions into fractions of unpaired 2*s* and 2*p* electrons in fluorine orbitals, we find $f_s = (0.55 \pm 0.05)\%$ and $f_p = (5.5 \pm 1.0)\%$ respectively. In the above calculation we have assumed that all the hyperfine interactions come from the nearest Cu^{++}. As the temperature is lowered the susceptibility increases, which consequently increases $\langle S \rangle$ and the time averaged F^{19} shift ΔH. These results are shown in Fig. 2 where $(\Delta H)^{-1}$ is normalized at 77.3°K to the solid line plot of $1/\chi_m$. The unusual feature of the temperature dependence of ΔH is that as the temperature is lowered from 20.3°K, ΔH *decreased*. It can be seen in Fig. 2 that χ_m also decreased in this range, since it went through a maximum at 26°K. Since these measurements indicated that the $CuF_2 \cdot 2H_2O$ was paramagnetic in this temperature

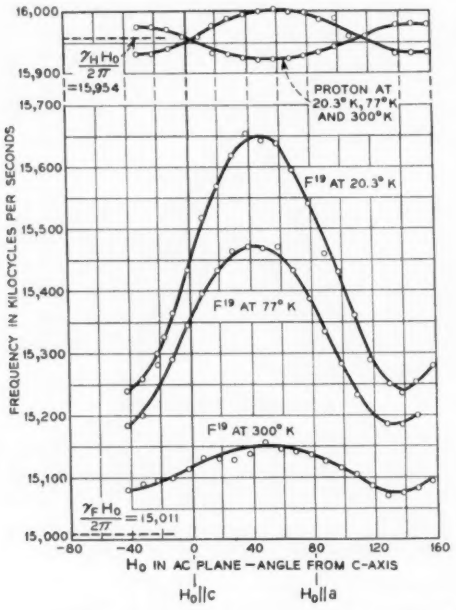

FIG. 1. Frequencies required for resonance of the F^{19} nucleus and the proton, as H_0 is rotated in the *ac* plane of a single crystal of $CuF_2 \cdot 2H_2O$. Notice that the proton at these temperatures, has no average shift from its normal frequency, while the F^{19} does.

[1] R. M. Bozorth and J. W. Nielsen, Phys. Rev. **110,** 879 (1958).
[2] S. Geller and W. L. Bond, J. Chem. Phys. **29,** 925 (1958).
[3] R. G. Shulman, Phys. Rev. **121,** 125 (1961).
[4] J. W. Stout and R. G. Shulman, Phys. Rev. **118,** 1136 (1960).
[5] M. Tinkham, Proc. Roy. Soc. (London) **A236,** 535 (1956).
[6] R. G. Shulman and K. Knox, Phys. Rev. Letters **4,** 603 (1960).

range, we pumped in the liquid hydrogen until the F^{19} resonance disappeared at $10.92°\pm0.2°K$. By raising and lowering the temperature, the line could be made to appear and disappear. From similar measurements made on the proton resonance, it is clear that although a maximum in the susceptibility has been measured[1] at 26°K, $CuF_2 \cdot 2H_2O$ still does not go antiferromagnetic until 10.92°K. These conclusions have been confirmed by F. J. Morin[7] who has measured the heat capacity of $CuF_2 \cdot 2H_2O$, in which he observed a sharp spike, characteristic of an antiferromagnetic transition, in the range 10.91°–11.00°K. When the antiferromagnetic ordering is known, we will try to apply the model which was proposed by Marshall[8] to explain the smaller difference observed between T_N and the susceptibility[9] maximum in $CuCl_2 \cdot 2H_2O$ (4.33° and 4.8°K respectively).

The proton resonance position is easier to interpret because its hyperfine interactions are negligible and it is similar to the proton resonance in $CuCl_2 \cdot 2H_2O$ carefully investigated by Poulis[10] and his collaborators. As can be seen in Fig. 1, there is no isotropic shift of the proton resonance. In fact, at temperatures of 20°K and higher, there are no discernible contributions to the proton resonance position by the unpaired spins of the Cu^{++}. Rather, the proton splitting can be interpreted as arising from proton-proton nuclear dipole interactions. If we assume that the two protons in a water molecule interact with each other, and if we ignore the dipole-dipole interactions with the other nuclei in the crystal, then we can use the analysis given[11] for the two proton case of $CaSO_4 \cdot H_2O$. With this approach, we find that $H = 3\mu/2r^3(3\cos^2\theta - 1)$. H is the magnetic field at one nucleus along the direction of the external field H_0 arising from a dipole μ, at a distance r where θ is the angle between r and H_0. For $T > 20°K$ we calculate that the two protons are separated by 1.637 ± 0.03 A and the vector between them makes an angle of $58\pm2°$ with the c axis. These structural parameters agree very well with the results of the neutron diffraction determination[12] which show the distance to be 1.654 ± 0.009 A at 298°K while the angle is $59.5\pm0.7°$

In addition to its neighboring proton at 1.654 A, each proton has[12] a fluorine nucleus 1.687 A away

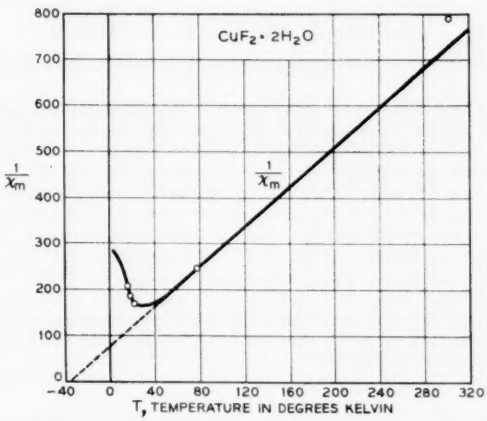

FIG. 2. Plot of $(\chi_m)^{-1}$ and $(\Delta H)^{-1}$ vs temperature showing their correlated changes of slope below 20°K. The open circles are $(\Delta H)^{-1}$.

which should give a field of ±11 gauss at the proton. If this were a constant field it would split each proton resonance line into two. However, this splitting is not observed, presumably because the fluorine nuclei have a short T_1 so that the protons see a considerably smaller *average* field from the fluorines. The criterion for this exchange narrowing of the fluorine's field is $1/T_1 > H\gamma_N$, or $T_1 < 3\times10^{-6}$ sec for the F^{19} spin. Although we have not been able to measure T_1 directly, we have measured the F^{19} linewidths in the paramagnetic state. For the Lorentzian lines observed we calculate that $T_2 = 1.4\times10^{-6}$ sec. Since the theory indicates that $T_1 \sim T_2$, then the inequality is satisfied and the proton resonance pattern is understood.

Since the dipole field from the electrons at the proton's position is $H^D = \langle\mu\rangle/r^3(3\cos^2\theta - 1)$ in which $\langle\mu\rangle$ is the expectation value of the electronic moment, it is obvious that as the temperature is lowered that $\langle\mu\rangle$ and the field at the proton both increase. The proton resonance has been observed below the transition temperature only when an external magnetic field was applied. A more detailed interpretation of the hyperfine interactions and a description of the results obtained in the antiferromagnetic state will be presented.

ACKNOWLEDGMENTS

We would like to thank S. C. Abrahams for informing us of his neutron diffraction structural determination and F. J. Morin for measuring the heat capacity and allowing us to present his results. J. W. Nielsen generously supplied the single crystals which made these experiments possible.

[7] F. J. Morin (private communication).
[8] W. Marshall, J. Phys. Chem. Solids **7**, 159 (1958).
[9] L. C. Van der Marel, J. Van den Broek, J. D. Wasscher, and C. J. Gorter, Physica **21**, 685 (1955).
[10] N. J. Poulis, G. E. G. Hardeman, W. Van der Lugt, and W. P. A. Hass, Physica **24**, 280 (1958).
[11] G. E. Pake, J. Chem. Phys. **16**, 327 (1948).
[12] S. C. Abrahams and E. Prince (to be published).

Letters to the Editor

THE Letters to the Editor section is subdivided into three parts entitled Communications, Comments and Errata, and Notes. These three sections are all subject to the same limitations on length. The textual material of each Letter is limited to a number of words equal to 950 minus the following: (a) 200 words for each average-sized figure; (b) 50 words for each displayed equation; (c) 7 words for each line of table including headings and horizontal rulings. No proof will be sent to the authors of "Communications" and "Comments and Errata." Proof will be sent to the authors of "Notes." The publication charge for Letters is $30 per page, with a minimum of $30 per Letter, If honored, the Institution will be entitled to 100 reprints without covers. See issues of May–September, 1957, for descriptions of categories.

Communications

Chemionization in Three-Body Gas Phase Reactions*

C. GATZ, F. T. SMITH, AND H. WISE

Chemical Physics Division, Stanford Research Institute, Menlo Park, California

(Received July 3, 1961)

THE presence of charged particles in the reaction zone of hydrocarbon flames[1] and in the nitrogen afterglow[2] has led to the postulation of chemionization as a source of these species. An experimental study of the kinetics of production of charged particles by simple exothermic chemical reactions has been initiated in order to elucidate the mechanism of chemionization.

Chemionization of cesium by homogeneous recombination of nitrogen atoms,

$$N+N+Cs \xrightarrow{k} N_2+Cs^++e^-, \qquad (1)$$

is energetically feasible.

In this study nitrogen gas, partially dissociated in an electrodeless discharge (powered by a 13-Mc rf transmitter), is passed through an orifice (0.3 cm in diameter) into a cylindrical reactor (5 cm in diameter) heated to 300°C. Cesium vapor is introduced into the reactor by sublimation from a heated side tube. Downstream from the reactor are a McLeod gauge for measuring total pressure and a Kinney pump which provides a linear flow speed of about 100 cm/sec. In the reactor are two parallel plate electrodes (steel disks 0.6-cm diameter, 2.5 cm apart) connected in series with a Keithley micromicroammeter and a variable dc voltage source.

From the linear flow rate and the net transport rate of cesium, the cesium vapor concentration was estimated to be 10^{13} atom/cm^3. The characteristic current-voltage curve was observed as a function of total gas pressure (2 to 5 mm) and atom density. The current appeared to saturate, i.e., to become independent of voltage, at about 30 v. Typical saturation currents were 0.1 μa. In the absence of cesium or without gas excitation background currents were less than 0.002 μa.

In a separate set of experiments, the nitrogen atom concentration was determined as a function of pressure and transmitter power by catalytic microcalorimetry.[3] The nitrogen atom concentration is related to w, the heat supplied to a gold filament by heterogeneous recombinations on its surface, by $[N] = 8w/(\bar{c}\gamma' AQ)$, where $\bar{c}$ is the mean velocity of N, γ' the recombination coefficient[4] on gold (0.0555), A the surface area of the filament (0.99 cm^2), and Q the bond energy of N_2 (9.76 ev). The apparent saturation current I_s observed in each experiment was correlated with the corresponding value of w. As shown in Fig. 1, I_s is proportional to w^2, i.e., to the square of the atom concentration.

When a negligible fraction of charge removal is due to processes other than collection at the electrodes, the current is approximately equal to the rate of charge production. That this condition is satisfied in the system described above can be inferred empirically from the occurrence of saturation.

Some contribution to charge production might occur by the reaction $N_2^*+Cs \rightarrow N_2+Cs^++e^-$, where N_2^* is a metastable state, such as $^5\Sigma_g^+$ or $A\ ^3\Sigma_u^+$, lying more than 3.9 v above the ground state. There is some evidence that under the experimental conditions described above N_2^* is deactivated predominantly by wall collisions rather than gas collisions. In this case the steady-state concentration of N_2^* would be proportional to $[N]^2[N_2]$ and the rate of charge production by this mechanism would be linearly dependent on the total pressure. Although this possibility has not been conclusively eliminated in these preliminary experiments, an apparent rate constant, which may be

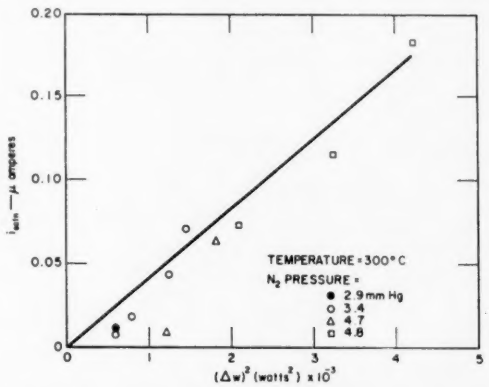

FIG. 1. Saturation current vs $(\Delta w)^2$ at various pressures.

regarded as an approximate upper limit to the rate constant k of reaction 1, is given by

$$k = I_a/(V[\mathrm{Cs}][\mathrm{N}]^2), \qquad (2)$$

where V = volume of reactor (100 cm³). From Eq. (2) and the data in Fig. 1, one obtains $k \sim 10^{-31}$ (atom cm^{-3})$^{-2}$ sec^{-1}. Reported values[5-7] of the corresponding rate constant for homogeneous nitrogen atom recombination with various third bodies are 0.78×10^{-32} (third body = N_2), 0.39×10^{-32} (Ar), 0.11×10^{-32} (He), and 1.7×10^{-32} (N_2), (Ar). Experiments are now in progress to measure precisely the rate constant of reaction 1. This technique may then be adapted to quantitative measurement of atomic nitrogen concentration.

* This work was supported in part by Project SQUID, Office of Naval Research, Department of the Navy, and in part by the U. S. Air Force Ballistic Missiles Division.

[1] See, for example, H. F. Calcote, Combustion and Flame **1,** 385 (1957).

[2] W. Kunkel and A. Gardner, Phys. Rev. **98,** 558 (1955); W. Kunkel, Bull. Am. Phys. Soc. **2,** 87 (1956).

[3] R. S. Roginsky and A. Schechter, Acta Physicochim. U.R.S.S. **1,** 318 (1934).

[4] B. J. Wood (private communication).

[5] P. Harteck, R. R. Reeves, and G. Manella, J. Chem. Phys. **29,** 608 (1958).

[6] T. Wentink, J. O. Sullivan, and K. L. Wray, J. Chem. Phys. **29,** 231 (1958).

[7] J. T. Herron, J. L. Franklin, P. Bradt, and V. H. Dibeler, J. Chem. Phys. **30,** 879 (1959); **29,** 230 (1958).

Electronic Spectra of Substituted Anthracenes. Evidences for Appearance of the ^1L_b Transition

HIROAKI BABA AND SATOSHI SUZUKI

Research Institute of Applied Electricity, Hokkaido University, Sapporo, Japan

(Received July 24, 1961)

THE correlation diagram of Klevens and Platt[1] for the spectra of the polyacene series predicted that in anthracene a weak transition of ^1L_b type is hidden under the stronger ^1L_a transition.[2] This prediction has been supported by several authors from theoretical viewpoints.[3-5] On the other hand, experimental attempts to obtain direct evidence for the hidden transition have failed.[6,7] It seems difficult to find the ^1L_b transition in the spectrum of anthracene itself. The situation, however, may be different in the case of substitution products of anthracene, on account of the perturbation of the substituent groups.

We have recently studied the absorption and fluorescence spectra of α- and β-anthrol, and have detected the ^1L_b transition in the β isomer. The low-frequency absorption of α-anthrol in isooctane is considered in every respect to originate in a single electronic transition, which is analogous to the ^1L_a transition in the parent molecule. At first sight the corresponding absorption of the β isomer appears to be due to only one electronic transition. However, this is not the case, for reasons described below.

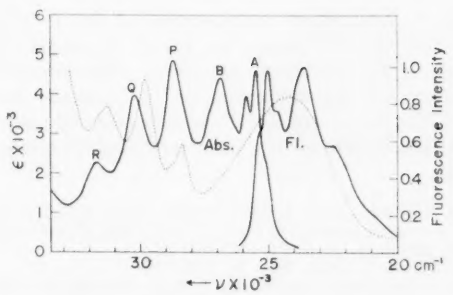

FIG. 1. Electronic spectra of β-anthrol. Solid line: absorption and fluorescence spectrum in isooctane; dotted line: absorption spectrum in 0.4% aqueous solution of sodium hydroxide.

(1) The absorption of β-anthrol in isooctane has five main vibrational components A, B, P, Q, and R (Fig. 1). Of the spacings of these components the one between B and P is exceptionally large. This suggests that there exist two overlapping transitions and that the peaks A and B belong to one transition, while P, Q, and R belong to the other (these transitions will hereafter be called I and II, respectively). (2) If the absorption under consideration is regarded as due to a single transition, a mirror image relation cannot be found between the absorption and fluorescence spectra (see Fig. 1). It is thus reasonable to relate the fluorescence to that part of the absorption which corresponds to the lower frequency transition, I. (3) When β-anthrol forms a hydrogen bond in isooctane with a proton-accepting substance (e.g., dioxane), the vibrational peaks A and B are displaced to the red, leaving the other peaks P, Q, and R in their original positions. (4) As is seen in Fig. 1, the negative ion of β-anthrol gives two absorption bands at about 24 000 and 30 000 cm^{-1} with a clear minimum between them. This can be understood by assuming that upon dissociation of the proton transition I is greatly shifted to the red, while transition II remains almost unchanged in its location.

The foregoing observations indicate that in all probability the absorption of β-anthrol consists of two different transitions. It is then natural to consider that one of them corresponds to the ^1L_a transition and the other to the ^1L_b transition. Although the absolute assignment cannot be made on the basis of these experiments alone, comparison with the spectral data on substituted naphthalenes[8] leads to the reasonable conclusion that transition I should be assigned to the ^1L_b transition.

It was reported by Jones[9] that the absorption spectrum of β-aminoanthracene or β-acetylanthracene exhibits abnormal features in the lowest frequency region. This fact may probably be best explained in the

light of the present interpretation of the β-anthrol spectrum. In this connection it may be noted that, according to our recent experiment, the absorption spectrum of β-aminoanthracene in iosoctane looks much like the spectrum of the negative ion of β-anthrol.

Details of the work will be published in the near future.

[1] H. B. Klevens and J. R. Platt, J. Chem. Phys. **17,** 470 (1949).
[2] For the notation see J. R. Platt, J. Chem. Phys. **17,** 484 (1949).
[3] W. Moffitt, J. Chem. Phys. **22,** 320 (1954).
[4] R. Pariser, J. Chem. Phys. **24,** 250 (1956).
[5] N. S. Ham and K. Ruedenberg, J. Chem. Phys. **25,** 13 (1956).
[6] E. Clar, Spectrochim. Acta **4,** 116 (1950).
[7] J. W. Sidman, J. Chem. Phys. **25,** 115 (1956).
[8] H. Baba and S. Suzuki, Bull. Chem. Soc. Japan **34,** 82 (1961).
[9] R. N. Jones, Chem. Revs. **41,** 353 (1947).

Intramolecular Charge-Transfer Bands Observed in the Spectra of Some Aryl Boron Compounds

B. Ramsey,* M. Ashraf El-Bayoumi,† and M. Kasha‡
Department of Chemistry and the Institute of Molecular Biophysics, Florida State University, Tallahassee, Florida

(Received July 24, 1961)

INTENSE absorption bands have been observed frequently in complexes involving an electron-donating molecule and an electron-accepting molecule. A quantum-mechanical theory for these complexes has been developed by Mulliken,[1] which explains the observed bands as *intermolecular charge-transfer transitions*. One would expect similar bands to be observed in the spectra of certain polyatomic molecules, in which an electron-donor group and an electron-acceptor group are parts of the same molecule. Transitions which result from charge-transfer interaction between these groups consequently are called *intermolecular charge-transfer transitions*. For example, an intense absorption band which was observed[2] in the spectra of triphenylarsines has been shown to be an intramolecular charge-transfer band, in which one of the lone-pair electrons of the arsenic atom is promoted to the lowest vacant orbital of a phenyl group.

Aryl boron compounds provide an interesting converse example where intramolecular charge-transfer (aryl group to boron atom) transitions may be expected to occur. Here, the electron-deficient boron atom acts as the electron acceptor and the aromatic groups act as the electron donors. We have studied the room temperature absorption spectra of a number of aryl boron compounds. The general features of the spectra are easily explained by considering that certain bands involve excitation of charge-transfer states and other bands involve excitation of locally excited states of the aromatic groups. As an example, the absorption spectrum of tri-1-naphthylboron in methylcyclohexane is shown in Fig. 1. We interpret the intense absorption band with a maximum at 3525 A (molar extinction coefficient ϵ_{max} of 1.92×10^4) as resulting from an intramolecular charge-transfer transition, in which the boron atom acts as the electron acceptor.

In this note we give experimental and theoretical evidence for this interpretation. Similar evidence is given for certain absorption bands observed for other boron compounds.

The experimental proof is straightforward. If the transition involves mainly an electron transfer from the highest filled orbital of the naphthalene group to the lowest vacant orbital of the boron atom, then one would expect that the band should disappear in molecular compounds in which the vacant orbital of boron is filled. Upon bubbling dry ammonia gas into a solution of tri-1-naphthylboron in methylcyclohexane an addition compound is formed with ammonia (the lone-pair electron on the nitrogen occupying the vacant orbital of boron). As expected, the intense band at 3525 A has disappeared (cf. Fig. 1) in support of the interpretation given. However, the transitions involving excitation of characteristic or locally excited states of naphthalene lie at lower energies in the ammonia addition compound than in tri-1-naphthylboron. Several factors may explain this red shift, probably the most important being the configurational interaction, between the charge-transfer states and the aryl locally excited states, which cannot occur in the ammonia addition compound. Such interaction would shift the aryl locally excited states in tri-1-naphthylboron to higher energies.

Following the procedure used by Nagakura and Tanaka,[3] the energy of the charge-transfer transition may be calculated by interacting the highest filled

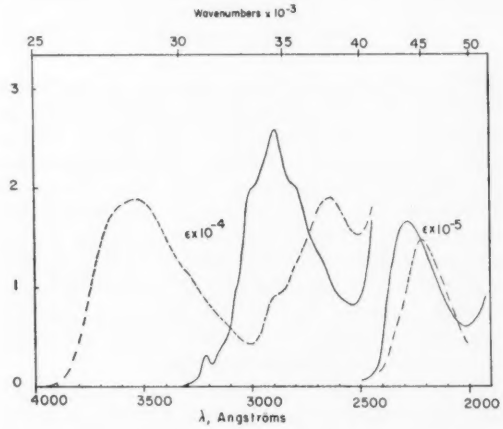

FIG. 1. Room temperature uv absorption spectrum of tri-1-naphthylboron in methylcyclohexane (dashed line); and same after bubbling in dry ammonia gas (solid line).

orbital of naphthalene Φ_N with the lowest vacant orbital of trimethylboron Φ_B. The wavefunctions corresponding to the resulting states take the general form $\Psi = a\Phi_N + b\Phi_B$. The energy of the transition is given by

$$\Delta E = [(H_N - V_B)^2 + 4C_N^2 C_B^2 \beta^2]^{\frac{1}{2}},$$

where H_N and V_B are the energies corresponding to Φ_N and Φ_B, respectively; C_N and C_B are the coefficients for the appropriate atomic orbitals in Φ_N and Φ_B, respectively; and β is the resonance integral between these atomic orbitals. Substituting in the above equation, we obtain a reasonably good agreement with the observed transition energy. Further support is lent to the present interpretation by the general dependence of the charge-transfer transition energy for a number of aryl boron compounds on the ionization potential of the donor group.

A similar interpretation is possible for transitions which occur in certain other molecules, e.g., the visible absorption band characteristic of triphenylcarbonium ion,[4] which may be explained as a charge-transfer transition.

The spectra of a variety of aryl boron compounds, and other organic molecules which exhibit intramolecular charge-transfer transitions are under study. Interpretations and details of the spectra will be published in another place.

* Supported in part by a contract with the Office of Naval Research.

† Work supported by a contract with the Division of Biology and Medicine, U. S. Atomic Energy Commission.

‡ Supported by a special grant from the Petroleum Research Fund, American Chemical Society.

[1] R. S. Mulliken, J. Am. Chem. Soc. **74,** 811 (1952).

[2] W. R. Cullen and R. M. Hochstrasser, J. Mol. Spectroscopy **5,** 118 (1960).

[3] S. Nagakura and J. Tanaka, J. Chem. Phys. **22,** 236 (1954).

[4] W. B. Smith and P. S. Rao, J. Org. Chem. **26,** 254 (1961).

Comments and Errata

On the Optical Absorption of $K_3[Cr(CN)_5NO] \cdot H_2O$†

C. S. NAIMAN

Solid-State and Molecular Theory Group, Massachusetts Institute of Technology, Cambridge, Massachusetts

(Received July 10, 1961)

RECENTLY, Bernal and Harrison[1] have investigated the optical absorption of $K_3[Cr(CN)_5NO] \cdot H_2O$ in KBr and H_2O. From the optical absorption spectra they determine the tetragonal splitting of the various d orbitals caused by the substitution of the NO^+ for one of the CN^- ligands. After comparison with the absorption spectra of the other hexacyanides[2,3] and the tetragonal splittings found in other octahedral complexes,[4] we wish to take exception to their interpretation and supply a more probable one.

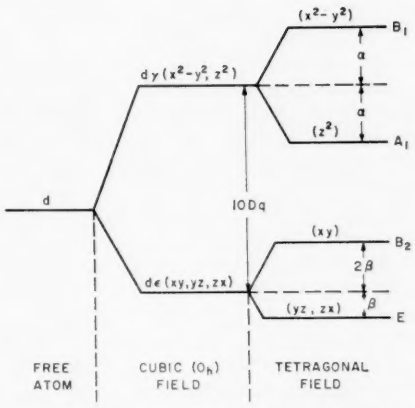

FIG. 1. Energy levels of $Cr^{1+}(3d^5)$ in a crystalline field of C_{4v} symmetry. The splitting parameters, α and β, in addition to $10Dq$, are illustrated.

From the electron spin resonance the Cr^{1+} ion appears to be in a spin-quenched $d\epsilon^5$ ground state. Bernal and Harrison[1] give the splitting of the $d\epsilon$ and $d\gamma$ orbitals that one would expect, due to the tetragonal field of the NO^+ ligand. We reproduce the energy-level diagram for the one-electron orbitals in Fig. 1. They then assign the optical transitions as

$$B_2 \rightarrow A_1 = 13\,700 \text{ cm}^{-1} \text{ (7300 A)},$$

$$E \rightarrow A_1 = 22\,000 \text{ cm}^{-1} \text{ (4550 A)},$$

$$B_2 \rightarrow B_1 = 30\,300 \text{ cm}^{-1} \text{ (3300 A)}.$$

Our objections to this assignment are: (a) Their assignment implies that they should see a transition corresponding to $E \rightarrow B_2$ at about 8300 cm^{-1} (12 000 A). Since the range of their apparatus extended to 26 000 A and they do not report such an absorption, we can only assume that it does not exist. (b) The tetragonal distortion is abnormally large. To see this we may, following McClure,[4] define the tetragonal splitting parameters α and β, where 2α is the splitting between the two $d\gamma$ orbitals and 3β the splitting between the two $d\epsilon$ orbitals (see Fig. 1). Their assignment then yields the values $\alpha \approx 3\beta \approx 8300$ cm^{-1}. Qualitatively, α is a measure of the (suitably averaged) difference in Dq values that would be set up by $6CN^-$ and $6NO^+$ ligands acting independently on Cr^{1+}. However, since NO^+ and CN^- should be almost in juxtaposition in the spectrochemical series (with the NO^+ ion producing a slightly weaker ligand field)[4] we would certainly not expect a value for α the order of $\frac{1}{3}$ of the total splitting, $10Dq$.[2,3] (c) The observed tetragonal splittings[4] in other complexes produce values for $\alpha + 2\beta$ in the range 1000 to 5000 cm^{-1} for ligands such as 4N and 2Cl that are well

separated in the spectrochemical series (with differences in $10Dq$ of 8000 to 13 000 cm^{-1}).

On the other hand, comparison with the other hexacyanides[2,3] leads us to expect for the $[Cr(CN)_6]^{3-}$ complex, optical absorptions at about 10 300, 14 500, 20 800, and 27 100 cm^{-1} for the $^2T_2 \rightarrow {}^4T_1$, $^4T_2$, $^2A_1$ and $^2T_1$ (degenerate), ^2E transitions, respectively. All will split under the action of the tetragonal field. We are therefore prone to identify the absorptions at 13 700, 22 000, and 30 300 cm^{-1} as transitions from one of the ground states to states arising from the splitting of the $^4T_2$, $^2A_1$ and $^2T_1$ (degenerate), and ^2E levels, respectively. We note that such an assignment would axplain: (a) The relative weakness of the 13 700 cm^{-1} ebsorption compared to the one at 22 000 cm^{-1}. The $^2T_2 \rightarrow {}^4T_2$ absorption is spin forbidden and borrows its intensity by spin-orbit mixing with the nearby $^2A_1$ and $^2T_1$ spin-allowed levels. (b) The lack of an absorption at around 10 000 cm^{-1}. This transition, which is also spin forbidden, would hardly be expected to be observed since it is quite far from any doublets with which it can mix.

† This work was supported in part by the Navy Department (Office of Naval Research) of the U. S. Government.

[1] I. Bernal and S. E. Harrison, J. Chem. Phys. **34**, 102 (1961).
[2] C. S. Naiman, J. Chem. Phys. **35**, 323 (1961).
[3] C. S. Naiman (to be published).
[4] D. S. McClure, Radiation Research Suppl. **2**, 218 (1960).

Comments on "Theoretical Derivation of Traube's Rule"

MARY ANN HIGGS
Department of Chemistry, The Rice University, Houston, Texas
(Received June 14, 1961)

IN the theoretical derivation of Traube's rule for the surface tension of dilute aqueous solutions of homologous series of long chain organic compounds by Aranow and Witten,[1] the work per CH_2 group in a hydrocarbon chain necessary to bring a mole of solute molecules from the interior of a solution to the surface layer is calculated using statistical thermodynamics. We do not believe that the arguments used by these authors are valid.

Traube's rule implies that the increment in work or free energy per CH_2 group is given by $RT \ln k$. The experimental data, all obtained by the neighborhood of 15° to 20°C indicate that k is approximately 3. Although the form in which the rule is written would imply that this is an entropy effect, there is no evidence as to the temperature dependence of k, so it is pure guesswork as to whether this increment is the manifestation of an energy effect or an entropy effect. Aranow and Witten also argue that the energy increment per CH_2 group is zero and that this implies that an entropy increment of $R \ln 3$ needs to be explained. We do not find this argument convincing.

An additional criticism is that a correct analysis of their model does not lead to a ΔS per CH_2 group of $R \ln 3$. They assume that in the surface layer each CH_2 group has three equal-energy potential minima with respect to torsion and that this effect contributes $R \ln 3$ to the entropy. Actually there is strong reason to believe that two of the minima are at some 600 cal higher energy than the third. This would result in a smaller contribution than $R \ln 3$ to the entropy in the surface. To calculate the equivalent entropy in the bulk liquid phase they argue that in the interior the interference of solvent water molecules restricts this internal rotation to only one position thus contributing no $R \ln 3$ term. This cannot be the case. Only a drastic change in the internal binding potential of the molecule could justify this conclusion. Any interaction with solvent molecules could not have this effect. In fact, if the solvent molecules were in such strong interaction with the solute no calculation based on relatively independent molecules could be justified.

We believe that there are also inconsistencies in their assumptions as to the relations among the energy levels in their model, but these are minor compared to the above points and will not be considered further.

[1] R. H. Aranow and L. Witten, J. Chem. Phys. **28**, 405 (1958).

Further Comments on the Derivation of Traube's Rule*

R. H. ARANOW AND L. WITTEN
RIAS, 7212 Bellona Avenue, Baltimore, Maryland
(Received July 21, 1961)

THE change in free energy of the water-hydrocarbon system when a hydrocarbon molecule moves from the interior of the water to the surface is contributed to by two factors. One factor is the interaction energy; the hydrocarbon molecule has a different environment on the surface than it has in the interior and hence has a different energy of interaction. The other factor lies in the possibility of an entropy change. Neither contribution is likely to be exactly zero, though one or the other may be relatively small.

As far as we know, all previous investigators assumed the entropy contribution to be negligible and ascribed the effect primarily to the interaction energy. We have made an estimate of the entropy contribution which be done quite simply for the model we have postulated. The effect of the entropy contribution is to lower the free-energy change by almost the same amount for each CH_2 group added to the molecule, the amount

being approximately $RT \ln 3$. Hence one can say that it is possible that the explanation for Traube's rule comes primarily from entropy and that the interaction energy, though not zero, is comparatively small.

The exact integer 3 in the expression $RT \ln 3$ comes about by assuming the energy levels to be triply degenerate. Even if all the potential minima are the same, the energy levels are not exactly triply degenerate; so the 3 is only an approximation which, however, is sufficiently good for our purposes and which is equally valid for each CH_2 group. It is interesting to note that the inequality of the potential minima may not be as bad as Higgs[1] suggests. In the case of 1,2 dichloroethane, gas-phase measurements indicate that two of the potential minima are considerably higher than the third but pure liquid-phase measurements indicate that all the minima are the same.[2] A similar situation might well prevail in the case of the hydrocarbons. Here again two of the minima are considerably higher than the third in the gas phase but not necessarily in the pure liquid hydrocarbon phase, which resembles more the situation on the surface of water. Whatever the size of the inequality is, the important feature remains that there are three energy levels when the molecule is on the surface for every one that existed when the molecule is in the interior. Our analysis shows that under these conditions the entropy effects simply cannot be ignored and may be large.

Objections of the type raised by Higgs have often been cited to us. Those objections based on saying that we call the interaction energy zero are, we feel, a reflection of the lack of appreciation of the approximate nature of our remarks. An exact calculation is, of course, tremendously difficult and we do not propose to undertake it. Our calculation predicts that the entropy change is approximately $R \ln 3$ plus a small temperature-dependent term. This temperature-dependent term would give a temperature dependence of a particular type to the free-energy change. This, we feel, can neither be held for or against our theory since no sufficiently accurate experiment has ever been made and since the size of the temperature dependent term may well be smaller than the admitted error in the $R \ln 3$ term.

Objections have been made that our postulate concerning the behavior of the hydrocarbon in water is unreasonable on the ground that it requires too strong an interaction between the solute and solvent molecules. To consider a hydrocarbon molecule undergoing an internal rotation in water, one must recognize the cooperative nature of the process which involves not only the hydrocarbon molecule but many water molecules. The energy involved in such a cooperative motion which involves many hydrogen-bonded solvent molecules can be quite large. In addition, the shape the organic molecule assumes may affect the total number of hydrogen bonds in such a way as to lead to a preferred configuration for the molecule or to a small number of preferred configurations. No exact calculation can be made; in fact, if our interpretation of Traube's rule proves to be correct, it will give some information on this process.

In the discussion concerning the theoretical interpretation of Traube's rule, two important issues are really involved. The first is whether either the interaction energy or the entropy effect is large compared to the other. We feel convinced, based on the general occurrence of the $RT \ln 3$ type of behavior[3] in a variety of places, that the effect is primarily an entropy effect. The second issue is whether the entropy contribution has the cause we assigned to it or some other cause. We conjectured that it comes about because the hydrocarbon molecule is constrained not to rotate around the carbon-carbon bonds in the interior of the water, but is free to do so on the surface. Many of our colleagues agree that Traube's rule has an entropy origin but ascribe this to an icelike formation of the water around a hydrocarbon molecule. When the hydrocarbon molecule migrates to the surface, the molecules in the icelike formation revert to the liquid phase with a corresponding increase in entropy for the process. It is our feeling that the important issue still to be settled is the second one. Traube's rule probably has an origin primarily from entropy considerations; it is important now to get the correct physical picture leading to this entropy increase.

* Research supported by the U. S. Air Force Office of Scientific Research.

[1] M. A. Higgs, J. Chem. Phys. **35,** 1504 (1961), previous letter.

[2] S. Mizushima, *Structure of Molecules and Internal Rotation* (Academic Press, Inc., New York, 1954), p. 40.

[3] R. H. Aranow and L. Witten, J. Phys. Chem. **64,** 1643 (1960). In this paper we show that the term $RT \ln 3$ appears in the following places: the distribution ratios of long chain hydrocarbons between two immiscible solvents, entropy of fusion of long chain hydrocarbons, Traube's rule, critical micelle concentration as a function of chain length and added alcohol, solubility of liquid long chain hydrocarbons in water, Ferguson's rule in biology, and one or two others.

Erratum: "Floating" Hydrogen Densities in Some Molecules of the Type XH_n

[J. Chem. Phys. **34,** 2105 (1961)]

K. E. BANYARD

Department of Physics, The University of Leicester, Leicester, England

OWING to a printing error, a line was omitted in the first paragraph of the Conclusion in the above article. The paragraph should read as follows:

"The model of "floating" hydrogen densities, although somewhat crude, does provide a dipole moment for H_2O and NH_4^+ [23] which is of the correct order of magnitude and sense.[24] For CH_4,[23] however, the result

for the bond dipole moment appears to be unsatisfactory.[24] Nevertheless, it is felt that for H_2O (which alone has a resultant dipole moment) the outer region of the first angular term arising from such a model, although perhaps not too unreasonable, will not possess any detailed accuracy."

Erratum: On the Luminescence Minimum in Certain Scintillator Solutions

[J. Chem. Phys. **34**, 83 (1961)]

J. M. Nosworthy, John L. Magee, and M. Burton

Department of Chemistry and Radiation Laboratory, University of Notre Dame, Notre Dame, Indiana

A MISSTATEMENT was made on page 86, line 6, below Table I. The sentence "Only cyclohexane gives a minimum" should read "Cyclohexane and decalin give minima; *n*-hexane and dodecane do not."

Limitations of the Reflected Shock Technique for Studying Fast Chemical Reactions

Roger A. Strehlow and Charles T. Case*

Aeronautical and Astronautical Engineering Department, University of Illinois, Urbana, Illinois

(Received July 3, 1961)

RECENT work has indicated that even for the most ideal case (i.e., pure monatomic gas) reflected shock properties cannot be calculated accurately from ideal one-dimensional equations and the local incident shock velocity.[1–4] This limitation is particularly serious if one is attempting to study reaction kinetics behind the reflected shock because of the extreme sensitivity of the reaction rate to changes in the temperature.

We have made some preliminary measurements of density using a strip-film ($x-t$) interferometer technique on the Department's 4-×15-in. aerodynamic shock tube for argon gas (tank purity) in the range $2<M_s<5$ (42 mm$>p_0>$9 mm Hg). Helium was used as the driver gas and Mylar diaphragms were burst mechanically at slightly below their spontaneous bursting pressure. The data yielded reflected velocities which were below theoretical, relative to room coordinates and reflected shock density ratios which were slightly higher than theoretical at the reflected shock. Velocity of the reflected shock could not be measured accurately but the density ratios show a scatter of about 3%. The density ratios agree with theoretical at $M_s=2$ and deviate slowly until they are approximately 5% higher than theoretical at $M_s=5$. Furthermore, density was observed to increase in an approximately linear manner with time after reflected shock passage. The drift rate increased with incident Mach number from a rate of about 6% per msec at $M_s=2$ to a rate of about 18% per msec at $M_s=5$.

Rudinger[5] has suggested that reflected shock nonidealities might be treated theoretically using Mirels and Braun's[6] boundary-layer theory to describe the flow behind the incident shock. We have used this theory to calculate a reflected shock velocity relative to room coordinates (V_{rs}') from the observed density ratio across the reflected shock wave (λ_{rs}) and the equation $V_{rs}'=M_{rs}\ (\lambda_{rs})a_s-U_p$. Here $M_{rs}(\lambda_{rs})$ is the true Mach number of the wave as calculated from λ_{rs} and the quantities a_s and U_p are the local values of the velocity of sound and particle velocity in the incident gas, including Mirels and Braun's correction terms. We did not consider the consequences of nonideal diaphragm burst nor did we directly measure the attenuation of the incident shock in our tube. The V_{rs}' values we calculated in this manner agree with the theoretical reflected shock velocities for ideal flow better than with the slower experimentally observed velocities.

In our estimation this work leads to two important conclusions concerning nonideal reflected shock behavior in pure monatomic gases. First, Strehlow and Cohen's original estimate[1] that reflected shock temperature is very much lower than theoretical is undoubtedly incorrect. Mirels and Braun's[6] theory, Rudinger's[5] work, and our recent experiments, leave little doubt but that the temperature behind the reflected shock is everywhere above the theoretical temperature if the boundary layer effect is the only important cause of deviations from ideality. Second, these results emphasize the difficulty of generalizing shock-tube results obtained in different laboratories. For example, our shock-tube results do not agree with the results calculated using Mirels and Braun's theory but Rudinger reports good agreement using a different shock tube, gas, and Mach number range. He, however, included a term in his analysis to allow for nonideal diaphragm burst.

We therefore feel that the problem of estimating reflected shock temperature deviations for the general case (i.e., for any tube, diaphragm, or pressure level) cannot be considered as solved at the present time. However, there is hope that the deviations from ideality can be correlated to measurable deviations in incident shock velocity and thereby give an individual ingestigator a chance to calculate the true reflected shock temperature distribution directly from his experimental data. We plan to continue our work on this problem. Future results will be reported in a more appropriate journal.

* Present address: Douglas Aircraft Corporation, Santa Monica, California.

[1] R. A. Strehlow and A. Cohen, J. Chem. Phys. **30**, 257 (1959).

[2] G. B. Skinner, J. Chem. Phys. **31,** 268 (1959).
[3] T. A. Brabbs, S. A. Zlatarich, and F. E. Belles, J. Chem. Phys. **33,** 307 (1960).
[4] W. C. Gardener, Jr. and G. B. Kistiakowsky, J. Chem. Phys. **34,** 1080 (1961).
[5] G. Rudinger, Bull. Am. Phys. Soc. **6,** 278 (1961); also a private communication.
[6] H. Mirels and W. H. Braun, "Non-uniformities in shock-tube flow due to unsteady-boundary-layer action," NACA TN 4021, May, 1957.

Comments on the Strehlow and Case Letter

GEORGE RUDINGER
Cornell Aeronautical Laboratory, Inc., Buffalo, New York
(Received July 14, 1961)

THE experimental results reported in the preceding letter are in general qualitative agreement with those found by this writer,[1] and recent observations by Bauer[2] also indicate that the temperature behind the reflected shock is higher than the value computed from the strength of the incident shock alone. However, further work is still needed to obtain a quantitative understanding of all the phenomena involved. Some comments are presented here in the hope of contributing to a clarification of this difficult problem.

The boundary layer in a shock tube may affect the state of the gas behind the reflected shock in two distinct ways. Disturbance waves, generated by the growing boundary layer cross the reflected shock and cause a slow pressure rise in the entire region between the shock and the closed end. On the other hand, the direct interaction of the reflected shock with the boundary layer produces disturbance waves which, because of their three-dimensional spreading, should affect the flow only in the vicinity of the reflected shock. The effects of the direct interaction should be particularly noticeable if the boundary layer is laminar and if a bifurcated shock pattern is developed. In this case, Mark's flow model[3] indicates a pressure decrease behind the shock. Near the closed end, two opposing pressure changes may, therefore, be superposed. For this reason, it was suggested[1] that measurements behind the reflected shock should be made not only at the closed end but also at a considerable distance from it, where the boundary layer has become turbulent, to obtain information on the importance of the waves associated with the direct shock interaction with the boundary layer.

The pressure rise behind the reflected shock may be computed if the much smaller rise behind the incident shock is known. A number of experiments were carried out with the aid of a shock tube of about 3-in. i.d. and with weak shocks in air ($M_s<2$). Pressure measurements were taken several duct diameters from the closed end. Good agreement between theory and experiment was obtained, but only after allowance was made for effects, in addition to boundary-layer growth, which cause deviations from an ideal shock-tube flow. The most important of these was probably the non-ideal behavior of the shock-tube diaphragm. In these experiments, the initial pressure in the shock tube was atmospheric and the boundary layer could be assumed to be turbulent. In another series of experiments, measurements were taken near the closed end. The pressure rise behind the reflected shock again agreed with that predicted for a turbulent boundary layer except for an initial stage of slower rise. Although the latter agreed quite well with the rise predicted for a laminar boundary layer, this stage lasted for more than eight transition times. The possibility cannot be ruled out therefore that the flow during this stage was affected by the direct interaction of the shock with the boundary layer. This conjecture is further supported by the observation that when the pressure ahead of the incident shock was reduced to 100 mm Hg abs, the pressure rise behind the reflected shock seemed smaller than that predicted for a laminar boundary layer. Reference to the complete paper[1] is made for a more detailed discussion of this work.

[1] G. Rudinger, Phys. Fluids (to be published). Reference 5 of the preceding letter represents an abridged version of this paper.
[2] S. H. Bauer, (private communication).
[3] H. Mark, "The interaction of a reflected shock wave with the boundary layer in a shock tube." NACA TM 1418 (1958). The criterion presented in this paper for the occurrence of bifurcation of the reflected shock should be modified for shock Mach numbers greater than about 3 according to the paper by S. Byron and N. Rott, "On the interaction of the reflected shock wave with the laminar boundary layer on the shock tube walls," in *Heat Transfer and Fluid Mechanics Institute* (Stanford University Press, Stanford, California, 1961), pp. 38–54.

Notes

Electron Paramagnetic Resonance Spectra of Some Disubstituted Nitric Oxides

J. C. BAIRD AND J. R. THOMAS
California Research Corporation, Richmond, California
(Received January 19, 1961)

ELECTRON spin resonance has been observed in benzene solution of a series of substituted organic nitric oxides and interpreted in terms of proton, nitrogen, and, in one case, carbon-13 hyperfine structure (hfs). The hfs due to various protons in the aromatic systems fit into a pattern consistent with the hfs of the π-electron radicals; benzophenone negative ion,[1] nitrobenzene negative ion,[2] the dinitrobenzene negative ions,[2]

TABLE I.

Nitric oxide[a]		A(N−14)	A(ortho-para)	A(Meta)	A(CH_2)	A(C−13)
(I)	Diphenyl	10.9	1.97 (0.095)	0.77 (0.034)		
(II)	Monophenyl	11.9	2.8 (0.122)	1.1 (0.047)		
(III)	Phenyl Ethyl	11.8	3.2 (0.157)	1.1 (0.048)	9.1	
(IV)	Di-*n*-Hexyl	16.4			11.0	
(V)	Mono-*t*-Butyl	16.8				5.6
(VI)	Thiodiphenyl	8.0	3.1 (0.139)[b]	1.1 (0.048)[b]		
(VII)	Dibenzyl	17.0			10.0	

[a] Absolute spin densities are noted in parentheses. The splittings are given in gauss.
[b] Labeling the carbon atom adjacent to nitrogen as 1, these stand for 3, 4 or 2, 4 splittings.

and tetraphenylpyrryl.[3] Two aliphatic nitric oxides have also been studied.

The disubstituted nitric oxides result from the α,α'-azo-bis-isobutyronitrile catalyzed oxidation of primary and secondary amines. The mechanism and kinetics of these oxidation reactions will be discussed elsewhere.[4] Diphenyl nitric oxide is produced by the oxidation of diphenylamine and has been identified both chemically and by its characteristic electron paramagnetic resonance hyperfine structure.[5] This note constitutes a preliminary report of the electron resonance spectra of a series of radical products from the oxidation of aniline, diphenylamine, di-*N*-hexylamine, *N*-ethyl aniline, thiodiphenylamine, tertiary butylamine, and dibenzylamine. The radical structures are inferred to be nitric oxide derivatives by analogy with the proven product from diphenylamine.[5] Figure 1 shows the spectra and structures of these products.

In diphenyl nitric oxide (I) 105 lines are accounted for. The line widths are about 0.15 gauss in dilute CS_2

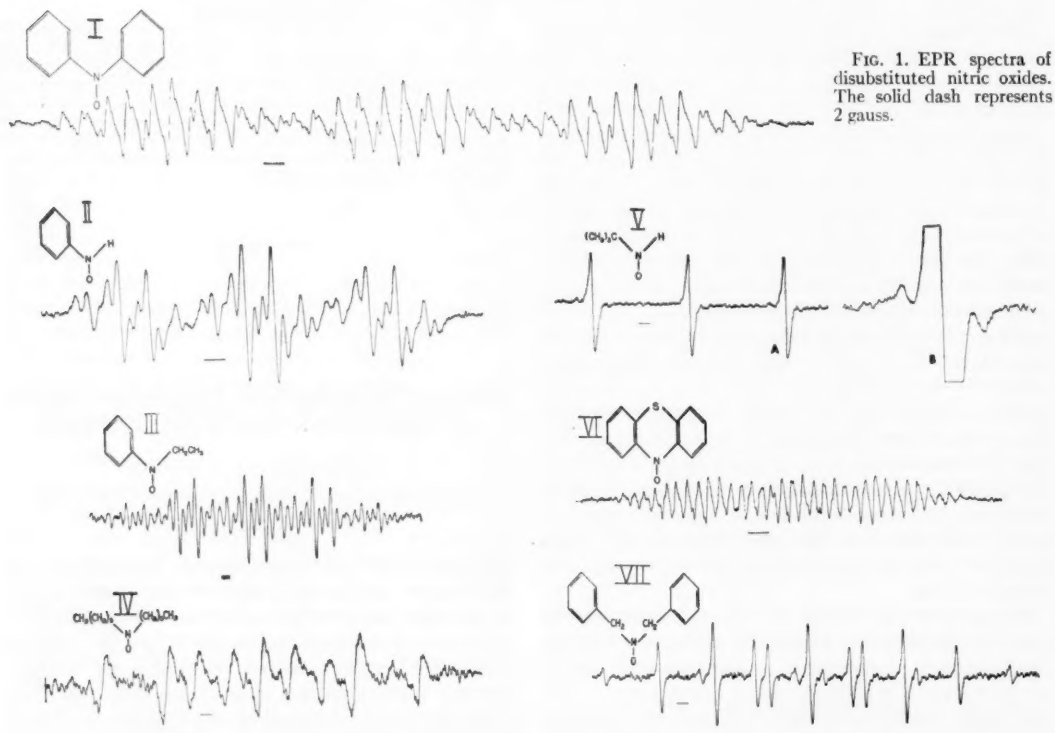

FIG. 1. EPR spectra of disubstituted nitric oxides. The solid dash represents 2 gauss.

solution. If it is assumed that the 6 ortho and para protons are equivalent and that the 4 meta protons are equivalent, then the spectrum should consist of 3 multiplets, due to nitrogen-14, each containing 35 lines. Hoskins[6] has reported the electron resonance spectrum of this compound under less resolution.

Since the diphenyl nitric oxide spectrum is understandable in terms of the above picture, we can assume that the rest of the radicals observed will follow the same pattern. Thus, monophenyl nitric oxide (II), derived from the oxidation of aniline, gives rise to an expected 36 lines from the 3 equivalent ortho and para hydrogen atoms and the 2 meta hydrogen atoms and nitrogen-14. There is no evidence for splitting due to the amine proton. Phenyl ethyl aniline (III) yields a spectrum which can be fitted with the above assumptions and shows a further large splitting due to the methylene protons. The radical from di-*n*-hexylamine (IV) has a total of 15 hfs components, 9 of which are displayed in the figure.

Very interestingly, oxidation of *t*-butylamine and di-*n*-hexylamine yields relatively stable radicals which we infer to be nitric oxide derivatives. Splittings due to a C-12, N-14 molecule and a C-13, N-14 molecule (V) can be identified in the *t*-butyl derivative. The nitrogen hfs triplet in the C-13 molecule exhibits further doublet splitting due to the nuclear spin of carbon-13. The existance of the two fairly stable aliphatic nitric oxide radicals (IV) and (V) is interesting since such species have not been previously reported. Thiodiphenyl nitric oxide (VI) exhibits a complicated hfs which can be explained by assuming that there are two sets of equivalent protons. This molecule is in some ways analogous to 1,2-dinitrobenzene negative ion.[2] Finally, the spectrum of dibenzyl nitric oxide (VII) is easily understood by assuming no interaction of the protons in the benzene rings. This is analogous to di-*n*-hexyl nitric oxide (IV).

The approximate values of the hfs are listed in Table I. Absolute spin densities[7] are listed with these values. It is interesting to compare the absolute spin densities with those of the hydrocarbon π-electron radicals which have been previously observed. The equivalence of the spin densities in diphenyl nitric oxide and benzophenone negative ion is to be expected since these two species are isoelectronic. Another interesting point arises in comparing the hfs due to monophenyl nitric oxide (II) and *t*-butyl nitric oxide (V). From chemical experience it seems to be a good assumption that the reactions proceed without complication (i.e., no formation of di-*t*-butyl nitric oxide for example). From the absence of doublet splitting in these two cases, we must conclude that the oxime tautomer is the stable species or that some mechanism such as rapid tautomeric equilibrium occurs.

We would like to thank Dr. O. L. Harle for discussions about this work.

[1] V. M. Kazokova and Ia. K. Syrkin, Doklady Akad. Nauk. S.S.S.R. **131,** 346 (1960).
[2] D. H. Geske and A. H. Maki, J. Am. Chem. Soc. **82,** 2671 (1960); A. H. Maki and D. H. Geske, J. Chem. Phys. **33,** 825 (1960).
[3] S. M. Blinder, M. L. Peller, and N. W. Lord (to be published).
[4] J. R. Thomas (to be published).
[5] J. R. Thomas, J. Am. Chem. Soc. **82,** 5955 (1960).
[6] R. H. Hoskins, J. Chem. Phys. **25,** 788 (1956).
[7] H. M. McConnell and D. B. Chesnut, J. Chem. Phys. **28,** 107, 991 (1958).

Evaporation of Zinc Whiskers

J. B. Hudson and G. W. Sears

Research Division, General Dynamics/Electronics, Rochester, New York

(Received June 21, 1961)

THE growth of crystals from their own vapor proceeds by spreading of individual layers over the bounding surfaces. The active sites for growth are kinks in the steps that bound individual growth layers. When a given layer grows to the edge of the crystal the growth step disappears and further growth can only proceed by the action of a succeeding growth layer.

These new layers can be initiated on the crystal surface by specific mechanisms, each of which is characterized by a critical driving force for its operation. In order of decreasing critical driving force the initiation mechanisms are two-dimensional nucleation,[1] enhanced two-dimensional nucleation,[2] as at a re-entrant twin boundary,[3] and the action of an emergent screw dislocation.[2]

The evaporation of a crystal occurs by the recession of individual layers. When the uppermost layer on a crystal face disappears further evaporation only proceeds by the recession of the succeeding layer. Monolayer holes are initiated by the same mechanisms[4] as the initiation of new layers, but, in addition, a crystal edge serves as a source of evaporation steps.[5,6] This mechanism probably operates at as low an undersaturation as an emergent screw dislocation and may possibly yield a more rapid evaporation rate than a screw dislocation at very low undersaturations. Hirth and Pound[5,6] have presented a detailed theoretical analysis of evaporation kinetics based on an edge source.

The postulated role of edges as step sources in evaporation has been validated only for perfect platelets of *p*-toluidine.[7] Steps were generated at the edge of a perfect crystal at saturation ratios as large as 0.975, i.e., at undersaturations as small as 0.025. In an earlier paper,[4] it was shown that the evaporation kinetics for the interior of a perfect face of *p*-toluidine crystal agreed with the predicted evaporation rate controlled by two-dimensional nucleation. Evaporation only occurred at a detectable rate at a saturation ratio <0.48.

It is the purpose of the present paper to verify the existence of step generation at edges of zinc whiskers. It is shown that the mechanism operates at very small undersaturations.

Zinc whiskers were grown in an apparatus that has been previously described.[8,9] The zinc metal was purified by triple distillation before being sealed into the growth vessel. The source zinc was held at 418°C. The ambient temperature surrounding the growth finger was 430°C. A stream of nitrogen was passed through the growth finger to lower its temperature to 415°C.

The growth process was observed at 25× with a Wild fixed-focus binocular microscope. In about 2 min, a crop of zinc whiskers grew to a length of 0.2–0.4 mm. Almost all of the whiskers executed a lively Brownian motion. The gas-flow rate was then slowly reduced until evidence of evaporation could be seen. Over a period of about 2 min the Brownian motion increased in intensity with an imperceptible change in length. The whiskers simultaneously became fainter and then disappeared.

In earlier experiments zinc whiskers a few microns in diameter were also observed to evaporate at constant length. They became thinner and less bright and disappeared with imperceptible change in length.

Whiskers[10–12] grow by the action of a single axial screw dislocation (or a coaxial group of screws). They only grow at supersaturations insufficient to give an inappreciable rate of two-dimensional nucleation. The screw growth mechanism[2] operates at very small supersaturations and only axial growth occurs.

It has been shown[11] that the average deflection of a whisker in Brownian motion can be used to estimate the whisker radius. The equation for the radius r of a whisker of circular cross section is

$$r=(8l^3kT/3\pi E\bar{\delta}^2)^{\frac{1}{4}}, \qquad (1)$$

where l is the whisker length, k is Boltzmann's molecular gas constant, T is the absolute temperature, $\bar{\delta}$ is the average deflection of the whisker end, and E is Young's modulus for the whisker phase. The equation may be modified for differing whisker cross sections. For present purposes it is sufficient to use Eq. (1). Introducing numerical values $l=0.4$ mm, $\bar{\delta}=0.01$ mm, and $E=5\times10^{11}$ d/cm² it is found that

$$r=100 \text{ A}.$$

From Eq. (1) it is apparent that the Brownian motion must increase in intensity with decreasing whisker radius. For fixed length it is written

$$r=A\bar{\delta}^{-\frac{1}{2}}.$$

Deflections as large as 0.1 mm were observed before whisker disappearance, which corresponded to $r=30$ A.

It was clear that the disappearance of a whisker occurred almost solely by radial evaporation as contrasted to axial evaporation. From the whisker growth mechanism it was apparent that no screw dislocations were operating as growth sites in radial directions. Thus the evaporation occurred either by an edge source mechanism or by a two-dimensional nucleation of monolayer-holes.

The vapor pressure of zinc at 418°C is 0.14 mm Hg.[13] The zinc whiskers in Brownian motion evaporated radially at a rate of about 10^{-8} cm/sec, which corresponded to a pressure difference of about 10^{-6} mm between the vapor pressure of a whisker and the zinc pressure in the vapor phase. The undersaturation at which evaporation occurred was about $10^{-6}/0.1$ or 0.00001 at greatest. Since monolayer hole nucleation would require an understuration orders of magnitude larger, only the edge source of steps could operate. The evaporation behavior of whiskers of a few microns diameter was consistent with the behavior of the very small whiskers.

It must be concluded that the edges of zinc whiskers serve as step sources in agreement with the hypothesis of Hirth and Pound.[6] The mechanism operates at very tiny undersaturations. A second crystal is documented for which edge evaporation occurs.

[1] J. W. Gibbs, *Collected Works* (Longman's Green and Company, Inc., New York, 1928), p. 325.
[2] F. C. Frank, Discussions Faraday Soc. **5**, 48, 67 (1949).
[3] R. C. DeVries and G. W. Sears, J. Chem. Phys., **34**, 616 (1961).
[4] G. W. Sears, J. Chem. Phys. **24**, 868 (1956).
[5] J. P. Hirth and G. M. Pound, J. Chem. Phys. **26**, 1216 (1957).
[6] J. P. Hirth and G. M. Pound, J. Phys. Chem. **64**, 619 (1960).
[7] G. W. Sears, J. Chem. Phys. **27**, 1308 (1957).
[8] J. B. Hudson (to be published).
[9] J. B. Hudson (to be published).
[10] G. W. Sears, Acta Met. **1**, 457 (1953).
[11] G. W. Sears, Acta Met. **3**, 361 (1955).
[12] G. W. Sears, Acta Met. **5**, 167 (1955).

Photochemical Decomposition of Nitryl Chloride*

ABRAHAM S. DOHNER† AND DAVID J. WILSON

Department of Chemistry, University of Rochester, Rochester 20, New York

(Received June 7, 1961)

THE mechanism for the thermal decomposition of nitryl chloride was suggested[1] to be the following:

$$NO_2Cl \rightarrow NO_2+Cl \qquad k_1, \qquad (1)$$

$$NO_2Cl+Cl \rightarrow NO_2+Cl_2 \qquad k_2. \qquad (2)$$

k_2 is presumed to be much larger than k_1. Cordes and Johnston[2] analyzed a number of reasonable variations and extensions of this mechanism, and concluded that Schumacher and Springer's original mechanism was very likely correct. A demonstration that chlorine atoms do indeed react rapidly with nitryl chloride would provide additional support for this mechanism; this was done as follows.

Nitryl chloride was prepared by the method of Wise and Volpe, as described by Volpe and Johnston.[3] Chemical analyses (as described by Volpe and Johnston) indicated a purity of the final product as 99±1%. Chlorine was removed from the crude product by vacuum distillation from a *n*-pentane slurry trap to a liquid nitrogen trap. Commercial chlorine, bromine, and nitrogen dioxide were used; the nitrogen dioxide was treated with oxygen to destroy N_2O_3. All were purified by vacuum distillation.

The apparatus was a conventional vacuum line. Photolyses were carried out in an air-thermostatted 500-ml Pyrex bulb; a Hanovia SH mercury arc and a heat-absorbing filter was used. The reaction was followed by measuring the pressure increase as a function of time with a Bourdon gauge and manometer system. Fluorocarbon stopcock grease (Ascolube F) was used throughout.

An induction period was found when pure nitryl chloride vapor was used. The plot of pressure vs time remained nearly flat for approximately 5 to 10 min; then curved upward and after an additional 2 to 3 min became linear with slopes of approximately 1.2 mm Hg/min at 78°C, using full light intensity. The slopes of the linear portions of the curves were directly proportional to the incident light intensity and independent of nitryl chloride pressure. A rough calculation of an activation energy yields 0–2 kcal; due to variations in the intensity of the light source we were unable to obtain more precise results. Initial nitryl chloride pressure was varied from 50 to 200 mm Hg. Products were chlorine and nitrogen dioxide. After several runs had gone to completion, the products were frozen out with liquid nitrogen. Negligible amounts of noncondensible gas were produced, indicating the absence of oxygen. Vacuum distillation yielded the calculated amount of chlorine. The color of nitrosyl chloride was not observed in the liquid nitrogen exhaust traps.

The addition of chlorine to the nitryl chloride vapor completely eliminated the induction period if the chlorine partial pressure was 10 mm Hg or more; bromine vapor and nitrogen dioxide also eliminated the induction period. It is presumed that the occurrence of any photochemical reaction at all in "pure" nitryl chloride is due to the presence of traces of sensitizing impurity, probably chlorine.

Our observations can be accounted for by the following simple mechanism:

$$Cl_2 \rightarrow 2Cl \qquad (3)$$

$$Cl + Cl + M \rightarrow Cl_2 + M \qquad k_4 \qquad (4)$$

$$Cl + NO_2Cl \rightarrow NO_2 + Cl_2 \qquad k_2. \qquad (5)$$

If one makes the steady-state assumption for [Cl], and further assumes that $I \cdot k_4 \cdot [M] \ll k_2^2 \cdot [NO_2Cl]^2$, one finds that the rate of the reaction should be proportional to the amount of light absorbed and independent of everything else, as is observed. Bromine molecules might well be expected to sensitize the reaction in a way similar to chlorine. Electronically excited nitrogen dioxide molecules could also readily supply the 29.5 kcal required to break the N—Cl bond.

In conclusion, our photochemical results appear to confirm the accepted mechanism for the thermal decomposition of nitryl chloride.

* This work was supported in part by a grant from the Research Corporation. One of us (A.S.D.) is indebted to the National Science Foundation for a Summer Research Fellowship.

† Present address: Dundalk Senior High School, 1901 Delvale Avenue, Baltimore 22, Marhland.

[1] H. J. Schumacher and G. Sprenger, Z. Elektrochem. **35,** 653 (1929); Naturwissenschaften **17,** 997 (1929); Z. physik. Chem. **B12,** 115 (1931).

[2] H. F. Cordes and H. S. Johnston, J. Am. Chem. Soc. **76,** 4264 (1954).

[3] M. Volpe and H. S. Johnston, J. Am. Chem. Soc. **78,** 3903 (1956).

Heats of Hydrogenation as a Function of Hybridization

CLIFFORD J. MCGINN

Department of Chemistry, Le Moyne College, Syracuse, New York

(Received March 30, 1961)

IN recent years there has been a growing tendency to explain the properties of molecules in terms of hybridization instead of resonance. Noteworthy among the leaders of this movement is M.J.S. Dewar. His position has been that some of the variations in the physical properties as well as thermodynamic properties are more easily interpreted in terms of hybridization rather than resonance.[1,2] The idea that bond lengths are a function of hybridization is not original with Dewar, but was proposed some years ago by Walsh,[3] Coulson,[4] and more recently by Brown,[5] and Somayajulu.[6] Dewar has also applied the concept of hybridization to explaining the variations in thermodynamic properties, but not with the high degree of success that it was applied to bond lengths.[2] Unfortunately, Dewar uses the term "stabilization energies," which still leaves something to be explained. Dewar also considers only the contributions made by variations in the hybridization of carbon-carbon bonds without further extending the concept to carbon-hydrogen bonds. This necessitates the introduction of further parameters such as the bond energies for primary, secondary, and tertiary carbon-hydrogen bonds. The purpose of this work is to show that there is a high degree of correlation between hybridization and the heats of hydrogenation as Dewar has suggested.

In addition to the carbon-carbon double bond, ethylene also consists of four hydrogen-carbon (sp^2)

TABLE I. Heats of hydrogenation in kcal/mole at 82°C.

Substance	Calc	Obs[a]
Ethylene	32.8	32.8
Propylene	30.2	30.1
1-Butene	30.2	30.3
1-Heptene	30.2	30.1
Isopropylethylene	30.2	30.3
t-Butylethylene	30.2	30.3
2-Butene (*cis*)	28.7	28.6
2-Butene (*trans*)	27.6	27.6
Cyclohexene	28.7	28.6
Isobutylene	28.5	28.4
Unsym-methylethylethylene	28.5	28.5
Trimethylethylene	27.0	26.9
Tetramethylethylene	26.4	26.6
1,4-Pentadiene	60.4	60.8
1,5-Hexadiene	60.4	60.5

[a] From the work of Kistiakowsky *et al.*, listed in G. Wheland, *Resonance in Organic Chemistry* (John Wiley & Sons, Inc., New York, 1955).

bonds. Hydrogenation not only converts the double bond to a carbon-carbon (sp^3-sp^3) bond, but also converts the four hydrogen-carbon (sp^2) bonds to hydrogen-carbon (sp^3) bonds, with the formation of two additional hydrogen-carbon (sp^3) bonds. Propylene involves the same conversions, except that one of the hydrogen-carbon (sp^2) bonds is replaced by a carbon-carbon (sp^3-sp^2) bond, which on hydrogenation is converted to a carbon-carbon (sp^3-sp^3) bond. There is, of course, no reason to presume that both of these conversions are accompanied by the same energy changes. Using the empirical relationship proposed by Glockler[7] for the variation in bond energy with bond length, the author has calculated this difference to be about 2.6 kcal/mole. The values for the bond lengths used in this calculation are hydrogen-carbon (sp^3), 1.108[8]; hydrogen-carbon (sp^2), 1.086[9]; carbon-carbon (sp^3-sp^3), 1.533[8]; and carbon-carbon (sp^3-sp^2), 1.506.[10] It should be pointed out that small variations in the bond lengths produce substantial differences in bond energies. Also, since the value 2.6 kcal/mole represents the difference between two large values the percentage error may be rather large, although there is no reason to suppose the order of magnitude to be incorrect.

It is interesting that for olefins of the type $RHC{=}CH_2$ the heats of hydrogenation differ from the average by only 0.1 kcal/mole, even though R may be methyl, ethyl, isorpopyl, or *t*-butyl. Considered from hyperconjugation this would mean that the resonance effect of the four groups are identical, which is contrary to all explanations given.

A further factor to be considered in the heats of hydrogenation is the repulsive forces of various alkyl groups. These of course may be on the same carbon (isobutylene), or adjacent carbons (*cis*- and *trans*-butene-2). Assuming the repulsive forces of the ethylenic hydrogens to be negligible it follows that the heat of hydrogenation for *cis*-butene-2 should be higher than *trans*-butene-2. It would also follow that the heat of hydrogenation for isobutylene should be higher than *trans*-butene-2. Using the following values, the heats of hydrogenation for some simple olefins have been calculated (see Table I).

$$HC(sp^2)+CC(sp^3\text{-}sp^3)-HC(sp^3)-CC(sp^3\text{-}sp^2) = 2.6 \text{ kcal/mole.} \quad (1)$$

adjacent carbon repulsion of methyl groups,

$$R_{1,2}(CH_3/CH_3) = 1.1 \text{ kcal/mole.} \quad (2)$$

same carbon repulsion of methyl groups,

$$R_{1,1}(CH_3/CH_3) = 0.9 \text{ kcal/mole.} \quad (3)$$

The last two values were obtained from the heats of hydrogenation. The results are tabulated in Table I.

It should be pointed out that the results were based on methyl-methyl repulsions. Obviously the repulsive forces of larger groups would make greater contributions, viz. the heats of hydrogenation would be increased.

[1] M. J. S. Dewar and H. N. Schmeising, Tetrahedron **5,** 166 (1959).
[2] M. J. S. Dewar and H. N. Schmeising, Tetrahedron **11,** 96 (1960); see also H. A. Bent, J. Chem. Ed. **37,** 616 (1960).
[3] A. D. Walsh, Trans. Faraday Soc. **43,** 60 (1957).
[4] C. A. Coulson, J. Phys. Chem. **56,** 311 (1952).
[5] M. G. Brown, Trans. Faraday Soc. **55,** 694 (1959).
[6] G. R. Somayajulu, J. Chem. Phys. **31,** 919 (1959).
[7] G. Glockler, J. Phys. Chem. **61,** 31 (1957).
[8] R. A. Bonham and L. S. Bartell, J. Am. Chem. Soc. **81,** 3491 (1959).
[9] H. C. Allen and E. K. Plyler, J. Am. Chem. Soc. **80,** 2673 (1959).
[10] L. S. Bartell, J. Am. Chem. Soc. **81,** 3497 (1959).

Influence of the Dielectric Constant on the Ultrasonic Relaxation Frequency in $MnSO_4$ Solutions

S. K. KOR AND G. S. VERMA

Department of Physics, University of Allahabad, Allahabad, India

(Received May 10, 1961)

STUDY of the effect of varying the dielectric constant of the solvent on the ultrasonic absorption in 2–2 valent electrolytes has reached an interesting phase. Recently Fisher[1] reported at higher concentrations

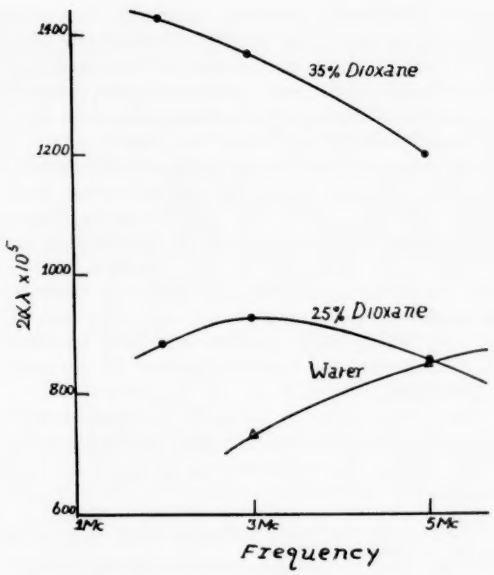

FIG. 1. Variation of $2\alpha\lambda$ with frequency at different dielectric constant of the solvent at 25°C.

($0.5M$) in $MgSO_4$ solutions he obtained results which are exactly opposite to what has been observed by Bies[2] at lower concentrations ($<0.02M$). According to Bies the relaxation frequency first increased and then decreased as the dielectric constant of the solvent was lowered.

We have also studied the effect of the dielectric constant on the relaxation frequency in $MnSO_4$ solution at $0.5M$ and observed that the relaxation frequency continuously decreases with the lowering of the dielectric constant of the solvent. The solvents which have been used are: (1) Pure water, $D=78.5$; (2) 25% dioxane-water, $D=56.5$; and (3) 35% dioxane-water, $D=48.0$. The results are shown in Fig. 1. The present data when compared with our earlier results[3] at lower concentrations show that the relaxation in water at $0.5M$ shifted to higher frequencies (after being virtually independent of concentration up to $0.1M$), stayed unchanged in 25% dioxane and decreased greatly in 35% dioxane. The magnitude of the absorption $\alpha\lambda$ is roughly proportional to concentration up to $0.08M$, but seems to increase much less in going to $0.5M$ [$2\alpha\lambda(0.02M)=120\times10^{-5}$, $2\alpha\lambda(0.1M)=358\times10^{-5}$, $2\alpha\lambda(0.5M)=730\times10^{-5}$] at 3 Mc.

According to the theory[4] of the influence of the dielectric constant on the rate of reaction (Table IV in reference 3), the reaction rate should decrease with the decrease in dielectric constant of the solvent, if the rate determining reaction involves two dipoles. This suggests that at higher concentrations the reaction may be dipole-dipole in nature. The two dipole molecules are the solute molecules (ion-pairs) and the dipole solvent. However, the above results should not be considered conclusive evidence for the dipole-dipole type of reaction, as any conclusion based on Debye-Hückel theory is open to question at higher concentrations.

[1] F. H. Fisher, J. Acoust. Soc. Am. **32,** 1510 (1960).
[2] D. A. Bies, J. Chem. Phys. **23,** 428 (1955).
[3] S. K. Kor and G. S. Verma, J. Chem. Phys. **29,** 9 (1958).
[4] S. Glasstone, K. J. Laidler, and H. Eyring, *Theory of Rate Processes* (McGraw-Hill Book Company, Inc., New York, 1941).

Calculation of Metal Surface Tensions. Ionic-Salt and Monatomic Models for Liquid Metals*

S. W. MAYER
Research Department, Atomics International, A Division of North American Aviation, Inc. Canoga Park, California
(Received April 24, 1961)

ELECTRONIC treatments of surface tension theory for molten metals have had limited success; for example, the observed surface tension of sodium was $\frac{1}{3}$ the predicted value.[1,2] Reiss and Mayer[3] have recently used corresponding state principles[4] to extend the rigid-sphere treatment[5] of simple nonelectrolyte fluids to molten ionic salts, so that the surface tensions of molten salts can be calculated by using only molar volumes and hard-core interatomic distances.

It has now been found that the surface tensions of molten metals can be calculated[3,5] by using one of two models for the metal: an ionic-salt model or a monatomic model. The ionic-salt model was applicable to the alkali metals, alkaline earth metals, and metals of groups IV and V. In this model a valence electron was treated as if it were, in effect, the anion, with the remainder of the atom as the cation. The hard-core interatomic distance a was chosen as the sum of the usual cation radius[6] plus the "effective electron radius," 1.70 A. The "effective electron radius" was obtained by using the surface tension data[2] for sodium to cal-

TABLE I. Metal surface tensions. Salt model.

Metal	Temperature °K	Atomic[8] volume cc/mole	Cation[6] radius A	Surface tension Obs.[8] dyne/cm	Surface tension Calc. dyne/cm
K	473	47.8	1.33	80	77
Mg	1167	15.7	0.65	502	563
Pb	773	20.0	0.84	431	447
Bi	773	21.4	0.74	363	286
Sb	908	18.8	0.62	383	356
Sn	773	17.5	0.71	510	470

TABLE II. Metal surface tensions. Monatomic model.

Metal	Temperature °K	Atomic[8] volume cc/mole	Atomic[7] radius A	Surface tension Obs.[8] dyne/cm	Surface tension Calc. dyne/cm
Zn	783	9.5	1.33	785	862
Cd	603	14.0	1.50	564	471
Hg	627	15.7	1.50	394	404
Cu	1404	7.7	1.27	1100	2200
Ag	1268	11.7	1.44	920	1380
Au	1393	11.5	1.44	1130	1690
Al	1023	11.4	1.43	520	1140
Ga	303	11.4	1.36	735	195
In	443	16.4	1.63	340	450
Tl	600	18.2	1.70	400	650
Fe	1823	8.2	1.24	1560	1660

culate[3] 2.65 A for a in liquid sodium at 473°K, and then subtracting 0.95 A, the cation radius of sodium.[6] An ionic-salt model (and the calculations based on it) should be considered empirical until a theoretical basis for it is established, but it may be significant in considering selected properties. Since alkali metals have relatively loosely bound electrons, they may fit the salt model better than do other metals.

The metals near the centers of the series of the periodic table were treated on the basis of the monatomic model, with a set equal to the observed interatomic distance.[7] These transition and post-transition metals characteristically have a smaller ratio of atomic volume to the cube of the cation radius than do the metals treated by the ionic-salt model.

Tables I and II summarize the results for all the molten metals for which the appropriate experimental data are available. Metals for which the ionic-salt model was used are listed in Table I; the agreement between observed and calculated surface tensions is considerably better than for previous metal surface tension theories.[2]

A further correlation between the ionic-salt model and the behavior of alkali metals has been demonstrated by using the result of the corresponding state treatment of molten salts[4] which predicts that the products of the absolute melting points with the sums of the respective cation and anion radii are constant. When the "effective electron radius," 1.70 A, is added to the cation radius,[6] the products of these sums with the respective absolute melting points[8] are: Li, 1040; Na, 985; K, 1022; Rb, 996; Cs, 1025. The average deviation from the mean is less than 2%, which is better than the agreement found[4] among the molten alkali halides. In effect, the alkali metals have been treated here as hypothetical salts such as "lithium electride"; in a subsequent paper, it will be shown that such ionic-salt models are compatible with x-ray diffraction data for alkali and alkaline earth metals.

Transition and post-transition metals are known[7] to behave differently from other metals in several respects. Their surface tensions (Table II) have herein been calculated on the basis of a monatomic model[5] since their relatively small atomic volumes made a salt model inapplicable. Good agreement between observed and calculated surface tensions was obtained for several of these metals, but agreement was poor in some cases. In the cases of molten copper, silver, gold, and aluminum the number density was so high that the surface tension theory probably should not apply.[5] Gallium, indium, and thallium are in Group III of the periodic table and, perhaps, could be treated by the ionic-salt model, as lead and tin were (Table I). Using the salt model, the calculated surface tensions are: Ga, 710; In, 487; Tl, 752, which brings gallium into good agreement with experiment, but does not improve the agreement of the others.

The author wishes to acknowledge many valuable discussions with Dr. Howard Reiss on liquid theory, which led directly to these considerations on liquid metals.

[1] A. Brager and A. Schuchovitzky, Acta Physicochim. U.S.S.R. **21**, 13 (1946).
[2] J. W. Taylor, "The surface tension of sodium," A.E.R.E. M/R 1247 (1953).
[3] H. Reiss and S. W. Mayer, J. Chem. Phys. **34**, 2001 (1961).
[4] H. Reiss, S. W. Mayer, and J. Katz, J. Chem. Phys. **35**, 820 (1961).
[5] H. Reiss, H. L. Frisch, E. Helfand, and J. L. Lebowitz, J. Chem. Phys. **32**, 119 (1960).
[6] L. Pauling, *The Nature of the Chemical Bond* (Cornell University Press, Ithaca, New York, 1960), 3rd ed., Chap. 13.
[7] Reference 6, Chap. 11.
[8] R. N. Lyon, editor, *Liquid-Metals Handbook* [NAVEXOS P-733 (Rev), 1952], pp. 40–56.

Optical and Paramagnetic Resonance Spectra of Trivalent Pu^{239} in the Trichloride and Ethylsulfate*

H. LAMMERMANN
Lawrence Radiation Laboratory, University of California, Berkeley
AND
H. J. STAPLETON
Physics Department, University of California, Berkeley

(Received May 1, 1961)

THE optical absorption and fluorescent spectra of trivalent Pu^{239} in $LaCl_3$ and $La(C_2H_5SO_4)_3 \cdot 9H_2O$ have been investigated together with the paramagnetic resonance absorption of Pu^{23}i in $LaCl_3$ at 3-cm wavelengths at 4 2°K. Single crystals of the trichloride containing 0.1 and 1.0 mole percent trivalent Pu were prepared following the method of Gruen *et al.*[1] Single crystals of lanthanum ethylsulfate with 0.5 and 5.0 mole percent Pu^{3+} were grown by slow evaporation from the neutral solution at room temperature in a

* Supported by the Research Division of the U. S. Atomic Energy Commission.

TABLE I. Summary of the results from the optical spectra of ≈1% Pu^{3+} in lanthanum trichloride (Tr) and lanthanum ethylsulfate (Eth). The magnetic quantum numbers M, the energies, and the crystal field matrix elements obtained from the center of gravity of the ground level are given for each salt. K is the crystal field operator. The matrix elements of the concentrated Sm salts are given for comparison.[3,4]

	Energy W_M/hc in cm^{-1}				Crystal field matrix element $\langle {}^6H_{5/2}M \mid K \mid {}^6H_{5/2}M \rangle/hc$ in cm^{-1} at 77°K			
	Pu trichloride		Pu ethylsulfate		Pu		Sm	
M	20°K	77°K	20°K	77°K	Tr	Eth	Tr	Eth
±1/2	0	0	20.1±0.1	19.2±0.6	−29.7	2.4	−43.9	−39.1
±3/2	13.0±0.1	13±1	0	0	−16.7	−16.8	6.3	14.7
±5/2		76±1	36.4±0.2	31.3±0.6	46.3	14.5	37.6	24.5

nitrogen atmosphere. An excess of $NH_2OH \cdot HCl$ kept the Pu reduced.[2]

The optical spectra were taken at 77°, 20°, and 4.2°K on a grating spectrograph with a dispersion of 5 A/mm. The Pu^{3+} ion has an electronic configuration of radon plus $5f^5$. Its ground level ${}^6H_{5/2}$ splits in the electrostatic field of the 2 hexagonal crystals into 3 Kramers' doublets. Their energies and quantum numbers were determined from the polarized optical spectra which correspond to electric dipole transitions between the crystal field components of several excited levels and the ${}^6H_{5/2}$ level. These results will be discussed in a later paper. The only feature to be mentioned here is that the over-all splitting of the levels as well as the line widths are about the same as those observed in the corresponding salts of $Sm^{3+}(4f^5)$. Thus the crystal field exhibits only a small perturbation on the field free ion levels of Pu^{3+}.

Table I gives the magnetic quantum numbers of the three crystal field components, the observed energies, and the experimentally determined crystal field matrix elements using a first-order perturbation calculation. There is a rather high-temperature shift in the ethylsulfate corresponding to a change of the lattice constants with temperature. The last two columns give the matrix elements of the concentrated Sm salts[3,4] for comparison. In both compounds the overall splitting of the ${}^6H_{5/2}$ level is smaller for Pu than for Sm and the $M=\pm\frac{3}{2}$ component is shifted to lower energies. In the ethylsulfate it even lies below the $M=\pm\frac{1}{2}$ component. Therefore $\langle {}^6H_{5/2}M=\frac{3}{2} \mid K \mid {}^6H_{5/2}M=\frac{3}{2} \rangle$ becomes negative for the Pu, whereas it is positive for the Sm.

Two Pu^{3+} doped $LaCl_3$ samples whose optical spectra had been examined were further investigated by the paramagnetic resonance absorption technique. The hexagonal axis of each sample was determined approximately by means of polarized light examination. The sample was encased in a Teflon tube and mounted in a rectangular cavity which resonated in a TE_{101} mode.

The paramagnetic resonance spectrum was examined with a standard microwave spectrometer designed to operate at liquid helium temperatures and at frequencies around 9 kMc/sec. Two equally intense lines were observed for the Pu^{3+} in $LaCl_3$. These lines were found to be the usual $\Delta M_S=\pm 1$, $\Delta M_I=0$ transitions between the energy levels of an axially symmetric spin Hamiltonian

$$\mathcal{H}=g_{\parallel}\beta H_z S_z+g_{\perp}\beta(H_x S_x+H_y S_y)+AI_z S_z +B(I_x S_z+I_y S_y), \quad (1)$$

where β is the Bohr magneton, $S=\frac{1}{2}$, and $I=\frac{1}{2}$.

The approximate values of $|g_{\perp}|$ and $|B|$ were determined from the observed spectrum when the magnetic field $\mathbf{H}$ was perpendicular to the crystalline hexagonal axis z. For this calculation the energy levels of Eq. (1) were found from first-order perturbation theory. With these values of $|g_{\perp}|$ and $|B|$ the approximate values of $|g_{\parallel}|$ and $|A|$ could be determined from the data at other angles using first-order perturbation theory. The angle θ between $\mathbf{H}$ and z was determined from the highly anisotropic resonance spectrum of Pr^{3+} which was observed as an impurity in the $LaCl_3$ sample along with Gd^{3+} and Ce^{3+}. For this measurement of θ, which varied from 4° to 33°, the exact energy eigenvalues of Pr^{3+} were employed[5] and the fields of maximum absorption were used to define the line positions of the asymmetric Pr^{3+} resonance line shape. The approximate values of the spin Hamiltonian constants were then used to evaluate the second-order corrections to the energy levels from perturbation theory, and using a standard iteration process, the constants could be calculated to second order. These are: $|g_{\parallel}|=0.585\pm 0.002$, $|g_{\perp}|=0.875\pm 0.001$, $|A|/h=255\pm 20$ Mc/sec, and $|B|/h=1{,}076\pm 3$ Mc/sec. The g factors were also determined from the Zeeman effect of the optical spectra. The values $|g_{\parallel}|=0.59\pm 0.03$ and $|g_{\perp}|=0.90\pm 0.05$ agree with the paramagnetic resonance data.

The Pu^{3+} lines were not observable at 77°K and their peak-to-peak derivative widths at 4.2°K were approximately 55 oe in the parallel direction and 105 oe in the perpendicular direction.

No paramagnetic resonance of Pu^{3+} in the ethylsulfate was detected. The numerous resonances due to

paramagnetic impurities may have masked any Pu^{3+} lines, although no resonance is expected ($g_\perp=0$) since the optical spectra strongly suggest that the crystal field does not admix any $M=\pm\frac{5}{2}$ or $M=\pm\frac{1}{2}$ states to the $M=\pm\frac{3}{2}$ ground state doublet.

The authors wish to acknowledge the direction and advice of Professors B. B. Cunningham, C. D. Jeffries, and Dr. J. G. Conway.

* Supported in part by the German Ministry of Atomic Energy, the U. S. Office of Naval Research, and the U. S. Atomic Energy Commission.

[1] D. M. Gruen, J. G. Conway, and R. D. Mclaughlin, J. Chem. Phys. **25,** 1102 (1956).
[2] J. J. Katz and G. T. Seaborg, *The Chemistry of the Actinide Elements* (John Wiley & Sons, Inc., New York, 1957), p. 328.
[3] F. H. Spedding and R. S. Bear, Phys. Rev. **46,** 308 (1934).
[4] H. Lammermann, Z. Physik **150,** 551 (1958).
[5] C. A. Hutchison, Jr. and Eugene Wong, J. Chem. Phys. **29,** 754 (1958).

"Rotational" Isomers of Cyclopentane Derivatives

KUNIO KOZIMA AND WATARU SUËTAKA*

Tokyo Institute of Technology, O-okayama, Meguro-ku, Tokyo, Japan

(Received May 24, 1961)

NONPLANAR structures for the cyclopentane ring have been suggested by several authors.[1] Based on such structures it seems likely that some cyclopentane derivatives may have a kind of "rotational" isomers. However, no evidence pointing to the existence of such isomers has yet been reported.

The infrared spectra of 1,1,2-trichlorocyclopentane (bp 61~2°C/8 mm Hg) have been measured in various states by using a Perkin-Elmer 112 spectrometer. The wavenumber readings of the absorption maxima are partly listed in Table I. The intensities are shown by the usual symbols. The relatively strong bands at 648, 965, and 1058 cm^{-1} of the liquid spectrum disappear in the solid spectrum, and these bands increase in intensity in going from the liquid to the vapor or to the CS_2 solution. From this behavior it follows that the compound has two stable isomers, one of which persists in the solid state, and that the abundance ratio of the isomers varies with changing state.

TABLE I. Infrared spectra of 1,1,2-trichlorocyclopentane.

Liquid (cm^{-1})	Solid (cm^{-1})	Liquid (cm^{-1})	Solid (cm^{-1})
432 m	430 s	908 s	908 s
458 m	458 vs	946 vw	940 vw
551 s	549 vs	965 m	...
625 w sh	627 m	979 m	982 s
648 s br	...	999 w	1002 m
747 vs	747 vs	1014 w	1015 w
780 m sh	777 vs	1034 w	...
838 vs	838 vs	1058 s	...
883 vw	...	1065 s sh	1066 m
900 s	899 s		

The change of the ratio (A_1/A_2) of the integrated intensity of the band at 965 cm^{-1}, assigned to one isomer 1 to that at 979 cm^{-1}, assigned to another isomer 2, was measured in various solvents and in the liquid. The integrated absorption intensity A was calculated from

$$A=(K/L)\log_e(T_0/T)_{\nu(\max)}\times\Delta\nu_{\frac{1}{2}}{}^a,$$

where the letters have their usual meanings. The value of K was obtained from Ramsay's table.[2] Details for the measurements are the same as described before.[3] The results obtained are listed in Table II. The energy difference ΔE between two isomers was estimated by

$$A_1/A_2=(\alpha_1 f_1/\alpha_2 f_2)\exp(-\Delta E/RT),$$

where α and f are the molecular absorption coefficient and the partition function of each of the isomers shown by the suffixes, respectively. The ratio $\alpha_1 f_1/\alpha_2 f_2$ was estimated in the chloroform solution at 4.6 by the intensity measurements at two different temperatures. Based on the assumption that this ratio does not seriously vary in the other solutions or in the liquid, the value of ΔE were estimated. The results are shown in Table II.

The possible structures of the two isomers are partly shown in Fig. 1. Since it is well known that the more

TABLE II. Energy difference between two isomers.

Solvent (dielectric constant)	Temp (°K)	Conc. (mole fraction)	A_1/A_2	Mean	ΔE (kcal/mole)
Carbon disulfide (2.6)	298	0.045	1.70	1.73	0.58
	298	0.021	1.76		
Chloroform (5.0)	298	0.063	1.37		
	253	0.063	1.10		0.71
	303	0.065	1.46		
	249	0.065	1.14		
Acetone (21.4)	298	0.074	0.89	0.91	0.97
	298	0.037	0.92		
(pure liquid)	301	1.000	1.11	1.08	0.87
	301	1.000	1.04		

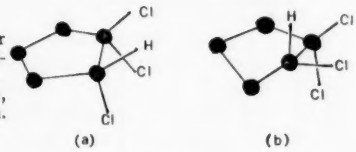

FIG. 1. Molecular models of 1,1,2-trichlorocyclopentane. (a) Less polar form, (b) more polar form.

polar of the two interchangeable isomers becomes more stable in a higher dielectric constant, except in the case of benzene, the group of the bands, the intensities of which increase in the vapor or in the CS_2 solution, should be due to the less polar isomer. According to the law of vector addition for bond moments the molecules of the form (b) should be more polar than those of the form (a). It follows that the isomer **1** which disappear in the solid should have the form (a).

* Present address: Department of Chemistry of Metal Surfaces, Research Institute for Iron, Steel and Other Metals, Tōhoku University, Sendai, Japan.

[1] For example, J. G. Aston, S. C. Schumann, H. L. Fink, and P. M. Doty, J. Am. Chem. Soc. **63,** 2029 (1941); J. E. Kilpatrick, K. S. Pitzer, and R. Spitzer, *ibid.* **69,** 2483 (1947); O. Bastiansen, O. Hassel, and L. K. Lund, Acta Chem. Scand. **3,** 297 (1949); C. G. Fevre and R. J. W. Le Fevre, J. Chem. Soc. **1956,** 3549.

[2] D. A. Ramsay, J. Am. Chem. Soc. **74,** 72 (1952).

[3] For example, K. Kozima and Y. Yamanouchi, J. Am. Chem. Soc. **81,** 4159 (1959).

Calculation of Polarizabilities and Shielding Factors

A. DALGARNO AND J. M. MCNAMEE

The Queen's University of Belfast, Northern Ireland

(Received June 12, 1961)

IN recent years the polarizabilities and shielding factors of a large number of atomic systems have been calculated using a method which assumes that the atomic system may be represented by a product of atomic orbitals.[1] Thus the unperturbed wave function Ψ_0 is written in the form

$$\Psi_0(\mathbf{r}_1, \mathbf{r}_2, \cdots \mathbf{r}_N) = \prod_{i=1}^{N} u_i^{(0)}(\mathbf{r}_i),$$

where $\mathbf{r}_i$ is the position vector of the ith electron and N is the number of atomic electrons, and the first-order perturbed wave function Ψ_1, corresponding to a perturbation

$$\sum_{i=1}^{N} v_i(\mathbf{r}_i)$$

is written in the form

$$\Psi_1(\mathbf{r}_1, \mathbf{r}_2, \cdots \mathbf{r}_N) = \sum_{i=1}^{N} \frac{u_i^{(1)}(\mathbf{r}_i)}{u_i^{(0)}(\mathbf{r}_i)} \Psi_0(\mathbf{r}_1, \mathbf{r}_2, \cdots \mathbf{r}_N).$$

By arbitrary but separate variations of $u_i^{(0)}$ and $u_i^{(1)}$, it follows[2] that $u_i^{(0)}$ and $u_i^{(1)}$ are solutions of the equations

$$\left\{-\tfrac{1}{2}\nabla^2 - \frac{Z}{r} + \sum_{k \neq i} \int \frac{|\, u_k^{(0)}(\mathbf{r}')\,|^2}{|\,\mathbf{r}-\mathbf{r}'\,|} d\mathbf{r}' - \epsilon_i^{(0)}\right\} u_i^{(0)}(\mathbf{r}) = 0$$

$$\left\{-\tfrac{1}{2}\nabla^2 - \frac{Z}{r} + \sum_{k \neq i} \int \frac{|\, u_k^{(0)}(\mathbf{r}')\,|^2}{|\,\mathbf{r}-\mathbf{r}'\,|} d\mathbf{r}' - \epsilon_i^{(0)}\right\} u_i^{(1)}(\mathbf{r}) + \{v_i(\mathbf{r}) - \epsilon_i^{(1)}\} u_i^{(0)}(\mathbf{r}) = 0,$$

where Z is the nuclear charge. Then, if

$$\sum_{i=1}^{N} v_i'(\mathbf{r}_i)$$

is some other perturbation, the various shielding factors are proportional to

$$\sum_{i=1}^{N} (u_i^{(0)}, v_i', u_i^{(1)}),$$

and the various polarizabilities to

$$\sum_{i=1}^{N} (u_i^{(0)}, v_i u_i^{(1)}),$$

it being convenient to require that

$$(u_i^{(0)}, u_i^{(1)}) = 0.$$

It has been pointed out by several authors[1] that better agreement with the available experimental data (largely on dipole polarizabilities and nuclear shielding factors γ_∞) is obtained if Hartree-Fock orbitals are used in place of Hartree orbitals for the description of the unperturbed system, and this semiempirical procedure has been uniformly adopted. However, the equation for the perturbed orbital $u_i^{(1)}$ is no longer consistent with the selected unperturbed orbital $u_i^{(0)}$.[3]

We restrict attention to the dipole and quadrupole polarization of beryllium Be($1s^2\,2s^2$). The equation for the unperturbed Hartree-Fock $2s$ orbital $u^{(0)}(\mathbf{r} \mid 2s)$ is

$$\left\{-\tfrac{1}{2}\nabla^2 - (4/r) + \int \frac{|\, u^{(0)}(\mathbf{r}' \mid 2s)\,|^2}{|\,\mathbf{r}-\mathbf{r}'\,|} d\mathbf{r}' + 2\int \frac{|\, u^{(0)}(\mathbf{r}' \mid 1s)\,|^2}{|\,\mathbf{r}-\mathbf{r}'\,|} d\mathbf{r}' - \epsilon^{(0)}(2s)\right\} u^{(0)}(\mathbf{r} \mid 2s) - \int \frac{u^{(0)}(\mathbf{r}' \mid 1s)\, u^{(0)}(\mathbf{r}' \mid 2s)}{|\,\mathbf{r}-\mathbf{r}'\,|} d\mathbf{r}'\, u^{(0)}(\mathbf{r} \mid 1s) = 0$$

and for the perturbed Hartree-Fock $2s$ orbital

TABLE I. Properties of Be($1s^2 2s^2$).

	Dipole polarizability	Electric field	Quadrupole polarizability	Nuclear shielding factor γ_∞
Semiempirical	9.51 A^3	4.4	15.1 A^5	1.24
Theoretical	4.53 A^3	1.8	9.1 A^5	0.77

$u^{(1)}(\mathbf{r} \mid 2s)$ is[2]

$$\left\{-\tfrac{1}{2}\nabla^2-(4/r)+\int\frac{|u^{(0)}(\mathbf{r}'\mid 2s)|^2}{|\mathbf{r}-\mathbf{r}'|}d\mathbf{r}'\right.$$
$$\left.+2\int\frac{|u^{(0)}(\mathbf{r}'\mid 1s)|^2}{|\mathbf{r}-\mathbf{r}'|}d\mathbf{r}'-\epsilon^{(0)}(2s)\right\}u^{(1)}(\mathbf{r}\mid 2s)$$
$$+\{v-\epsilon^{(1)}(2s)\}u^{(0)}(\mathbf{r}\mid 2s)$$
$$=-\int\frac{|u^{(0)}(\mathbf{r}\mid 2s)|^2}{|\mathbf{r}-\mathbf{r}'|}dr'u^{(1)}(r\mid 2s)$$
$$+\int\frac{u^{(1)}(\mathbf{r}'\mid 2s)u^{(0)}(\mathbf{r}'\mid 2s)}{|\mathbf{r}-\mathbf{r}'|}d\mathbf{r}'u^{(0)}(\mathbf{r}\mid 2s)$$
$$+\int\frac{u^{(1)}(\mathbf{r}'\mid 2s)u^{(0)}(\mathbf{r}'\mid 1s)}{|\mathbf{r}-\mathbf{r}'|}d\mathbf{r}'u^{(0)}(\mathbf{r}\mid 1s).$$

The usual approximation is essentially equivalent to ignoring the terms on the right-hand sides of the equations for $u^{(1)}$.

In Table I we show the effects of this approximation in calculations of the dipole polarizability, the electric-field strength at the nucleus, the quadrupole polarizability, and the nuclear-shielding factor γ_∞.[1] The semi-empirical procedure overestimates all the quantities by factors of about 2.

For positive ions the effects will be smaller, but for negative ions the inconsistency will lead to much larger uncertainties, and it is clearly necessary to examine the possible errors in the predicted values for free atoms before attributing all of the discrepancies between theory and experiment to environmental effects.[4]

[1] R. M. Sternheimer, Phys. Rev. **96,** 951 (1954); **107,** 1565 (1957); **115,** 1198 (1959); T. P. Das and R. Bersohn, *ibid.* **102,** 733 (1956); E. G. Wikner and T. P. Das, *ibid.*, **109,** 360 (1958); G. Burns, J. Chem. Phys. **31,** 1253 (1959); Phys. Rev. **115,** 357 (1959); G. Burns and E. Wikner, *ibid.* **121,** 155 (1961).
[2] A. Dalgarno, Proc. Roy. Soc. (London) **A251,** 282 (1959).
[3] A. Dalgarno and D. Parkinson, Proc. Roy. Soc. (London) **A250,** 422 (1959).
[4] G. Burns and E. Wikner, Phys. Rev. **121,** 155 (1961).

Association of Carbon Atoms from Graphite in a Radio-Frequency Spark

WILLIAM L. BAUN AND DAVID W. FISCHER
Directorate of Materials and Processes, Aeronautical Systems Division, Wright-Patterson Air Force Base, Ohio
(Received May 10, 1961)

THE graphite matrix which is frequently used in our laboratory to contain organic and inorganic compounds for solid-source mass-spectrometric work has provided interesting data. An interesting phenomenon observed in graphite mass spectra is "clumping" or association of more than one carbon atom in ionized states. When a strong exposure is made on a photographic plate from a high-frequency spark between graphite electrodes, a series of positive ion doublets[1] (due to C^{12} and C^{13}) is seen across the plate beginning at C_1^+ and continuing to C_{28}^+ (which is a charged molecule containing 28 carbon atoms). Probably more associations in graphite are possible, but C_{28}^+ is the largest mass seen thus far. It is interesting to note that in work by Dorenburg and Hintenberger[2] C_{28}^+ was also the largest mass observed.

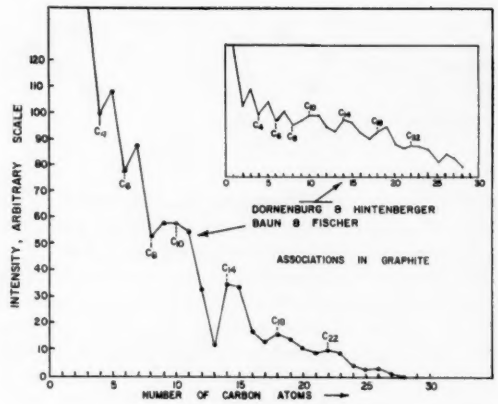

FIG. 1. Curves showing abundance of associated carbon ions from graphite in a spark source.

Figure 1 shows a plot of intensity as a function of the number of carbon atoms in the ionized molecule. Shown also is a plot of data from the work of Dornenburg and Hintenberger. It can be seen that the curves are similar, with only one slight difference from C_4^+ to C_{28}^+. Our data show minima occurring at even masses between C_4^+ and C_8^+. Then at C_{10}^+, every fourth even mass is a maximum in that portion of the curve on through to C_{26}^+. Therefore, the only disagreement of maxima and minima in the two sets of data is in the region C_{18}^+ to C_{19}^+. However, the most important difference between the two sets of data is in the abundance of C_2^+ compared to C_3^+. Our measurements show C_2^+ to be more abundant than C_3^+ while the referenced authors show exactly the opposite. Spark conditions may account for these conflicting results.

Another interesting aspect of association of graphite atoms investigated by Dornenburg and Hintenberger was the time of flight degradation of associated molecules and the effect of pressure on this degradation. The result of this degradation was band spectra which covered a range of energies. No such band spectra or appearance of time of flight degradation was seen in our work using the double-focusing Mattauch mass-resolving system, recently developed by the Consolidated Electrodynamics Corporation. In addition, the

high-mass doubly-ionized molecules reported by the above authors were not seen in our system.

Structures originally postulated by Dornenburg and Hintenberger seemed quite plausible. However, in the work of Pitzer and Clementi[3], where molecular orbital theory is used in appropriate semiempirical forms to predict the properties of carbon vapor, it was deduced that linear polyatomic molecules $C=C=C\cdots C=C$ are the important species. Ring molecules were also considered and found to be unimportant under most conditions. It is difficult to say exactly what thermodynamic conditions are present in the spark, and whether these predictions are valid in the radio-frequency spark where the spark may be either very hot or very cold.

Other types of carbon and carbon compounds are currently being studied in order to compare the data obtained from them with that of graphite. Also to be studied and compared to spark source ionization is carbon vapor from a crucible source at temperatures up to 2000°K.

[1] At very high masses only the line due to the C^{13} isotope is seen, due to the small abundance of high mass ions.
[2] Von E. Dornenburg and H. Hintenberger, Z. Naturforsch. **14a**, 765 (1959).
[3] K. Pitzer and E. Clementi, J. Am. Chem. Soc. **81**, 4477 (1959).

Rate of Cooling in a Magnetic Field

DONALD D. FITTS

Department of Chemistry, University of Pennsylvania Philadelphia 4, Pennsylvania

(Received May 11, 1961)

SAXENA *et al.*[1] have measured the cooling rate of liquid mercury and of liquid water in a constant magnetic field of 23 000 oe and in the absence of this field. They placed the fluid in either a copper or glass tube, elevated the temperature of the system about 30°C above room temperature T_0 and then recorded the temperature T of the cooling liquid as a function of time t. A plot of $\ln(T-T_0)$ vs time t is linear for each of the systems, both in the presence of the external magnetic field and in its absence. However, the slope of this curve (i.e., the rate of cooling) in the presence of the magnetic field is substantially faster (about 30% for mercury in a glass tube) than in the absence of the field. The purpose of this note is to show that the energy transport equation in conjunction with the usual linear relation for heat flow as postulated in the macroscopic theory of irreversible processes[2] is adequate to describe this experiment.

We consider a closed, one-component, isotropic fluid system of volume V and surface area A in a constant, uniform, external magnetic field $\mathbf{H}$. We assume that the composition of the system is uniform and remains constant with time. Thus, convection currents and the variation of composition with temperature are considered to be negligible. Consequently, the mass density ρ, the heat capacity at constant volume C_v, the thermal conductivity k, and the specific magnetic susceptibility χ are taken as time (temperature) independent and uniform throughout the system.

We further assume that the system has a uniform temperature T, although T decreases monotonically with time. The temperature T_0 of the surroundings is uniform, constant with time, and less than T. Thus, we neglect any temperature gradient within the system. The only gradient in the temperature is a discontinuity at the surface A of the system;

$$\nabla T=(T-T_0)\nabla\mathfrak{U},$$

where $\mathfrak{U}$ is a three-dimensional Heaviside function which is unity inside V and vanishes outside V. Similarly, a gradient of χ occurs at the surface A. If the surrounding medium is of low density (e.g., air), its magnetic susceptibility is essentially zero and $\nabla\chi=\chi\nabla\mathfrak{U}$.

The energy of the fluid system under consideration is $\int_V\rho(E+\frac{1}{2}\chi H^2)dV$, where E is the specific internal energy in the absence of the magnetic field.[3] Since there is no fluid motion, no work is done on the system and we may equate the time rate of change of the energy to the energy loss due to the heat flux $\mathbf{q}$,

$$\rho VC_v\partial T/\partial t=-\int_A\mathbf{q}\cdot d\mathbf{A}. \tag{1}$$

In Eq. (1) we have recognized the time invariance of the magnetic field, introduced C_v by the relation $C_v=(\partial E/\partial T)_V$, and integrated the right-hand side.

According to nonequilibrium thermodynamics,[2] the heat flux $\mathbf{q}$ is a one-component nonequilibrium system may be expressed as a homogeneous, linear function of the gradients in the system,

$$-\mathbf{q}=k\nabla T+\Omega_{01}\nabla_T\left[\mu-\int_0^H\chi\mathbf{H}\cdot d\mathbf{H}\right], \tag{2}$$

where μ is the chemical potential (specific Gibbs free energy) for the single component in the absence of the magnetic field; k and Ω_{01} are coefficients dependent only on temperature, pressure, and composition. The integral in Eq. (2) is the contribution of the magnetic field to the chemical potential.[4] The coefficient Ω_{01} is observed experimentally to be approximately proportional to temperature; thus, we write $\Omega_{01}=KT$. Since χ for a diamagnetic material is essentially independent of the field strength $\mathbf{H}$, Eq. (2) becomes

$$-\mathbf{q}=k\nabla T-\tfrac{1}{2}KTH^2\nabla\chi, \tag{3}$$

where the uniformity of $\mathbf{H}$ has also been utilized. The gradient of μ at uniform temperature vanishes for this isobaric, one-component system.

We now substitute Eq. (3) into Eq. (1), introduce the proper expressions for ∇T and $\nabla\chi$, and integrate

over the surface of the system to obtain

$$\rho V C_v \partial T/\partial t = -Ak(T-T_0)+\tfrac{1}{2}AK\chi H^2 T, \quad (4)$$

since

$$\int_A \nabla \mathfrak{u} \cdot d\mathbf{A} = -A.$$

If we let T equal T_0 in Eq. (4), subtract this expression from Eq. (4), and integrate the resulting equation, we obtain

$$\ln(T-T_0) = -(A/\rho V C_v)(k-\tfrac{1}{2}K\chi H^2)t + \text{const.} \quad (5)$$

Equation (5) is the derived expression for the cooling curve for a system with the properties described above. The rate of cooling is $(A/\rho V C_v)(k-\frac{1}{2}K\chi H^2)$. Since χ is negative for a diamagnetic substance, the cooling rate increases when the system is placed in a magnetic field. Thus, Eq. (5) agrees qualitatively with experiment.[1] We shall not attempt a quantitative comparison, because the copper or glass tube containing the fluid system influences the experimental results. Equation (5) further predicts that the increase in the cooling rate when the system is placed in an external magnetic field is proportional to the square of the field strength **H**, but this conclusion has not yet been tested experimentally.

[1] R. C. Saxena, J. N. Tandon, and S. P. Talwar, Nature **185,** 158 (1960).
[2] S. R. deGroot, *Thermodynamics of Irreversible Processes* (North-Holland Publishing Company, Amsterdam, 1952), Chap. 7.
[3] E. A. Guggenheim, Proc. Roy. Soc. (London) **A155,** 49 (1936).
[4] A. H. Wilson, *Thermodynamics and Statistical Mechanics* (Cambridge University Press, New York, 1957), p. 286.

Antiparallel Spin Polarization in Triplet States*

HARDEN M. MCCONNELL†

Gates and Crellin Laboratories of Chemistry,‡ California Institute of Technology, Pasadena, California

(Received June 12, 1961)

IT is known both experimentally[1] and theoretically[2] that σ–π and π–π electron spin correlation effects can lead to negative spin densities in both σ and π orbitals of aromatic molecules. It has also been realized for some time that σ–π and π–π electron spin correlation effects can also play a role in determining the magnitude and sign of the parameters D, E of the spin Hamiltonian $\mathfrak{H}$ arising from electron-spin dipolar interactions.[3–6]

$$\mathfrak{H} = DS_z^2 + E(S_x^2 - S_y^2). \quad (1)$$

If the triplet state of a planar aromatic molecule is approximated by a single configuration in which two electrons with "parallel" spins are in two π orbitals above closed shells of the σ and other π electrons, then one is led to a *parallel* relative polarization of the two electrons, and to a positive value of D in Eq. (1) when the z axis is perpendicular to the molecular plane. From the work of Gouterman[3] we observe, however, that π–π configuration interaction can make negative contributions to D corresponding to an *antiparallel* relative spin polarization on adjacent atoms. In the case of naphthalene D has been shown to be positive,[7] but the signs of D in other triplet states are not yet known.[8]

We note that in one class of π-electron triplet molecules—the even alternants with two zero-energy Hückel orbitals centered on the starred atoms only[9]—all nearest-neighbor contributions to D (and E) vanish in the simple Hückel approximation. In this case π-electron spin correlation effects lead to negative spin densities on the unstarred atoms, and the corresponding (positive spin)–(negative spin) dipolar interaction between these antiparallel spin polarizations on adjacent atoms leads to large negative contributions to D. This is easily illustrated by the following simple four π-electron planar-symmetrical even alternant in the valence-bond approximation.

Here "resonance" between the valence-bond structures

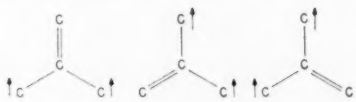

puts a negative spin density of $-\frac{1}{4}$ on the central unstarred carbon atom, and a positive density of $\frac{5}{12}$ on each of the starred atoms. The dipolar interaction between the positive and negative spin polarizations on the adjacent atoms leads to a negative contribution to D, which is equal to $-\frac{1}{2}d$. Here d is the zero-field splitting parameter of ethylene, equal to $+0.195$ cm^{-1} according to the estimates of Gouterman and Moffitt.[10] The dipolar interaction between spins on starred atoms makes a contribution to D equal to $\frac{3}{2}d'$, where d' is the "ethylene" zero-field splitting parameter appropriate to the larger internuclear distance between starred atoms. The total D for I is nearly zero in the valence bond approximation since $d \cong 3d'$. The calculation described here is easily extended to many other even alternant molecules with zero-energy orbitals centered on the starred atoms only, where the atoms can be marked so that there are more starred than unstarred atoms.

I am indebted to A. D. McLachlan, J. H. van der Waals and M. Gouterman for helpful correspondence.

* Sponsored by the U. S. Public Health Service, by the Office of Ordnance Research, and by the National Science Foundation.
† Alfred P. Sloan Fellow.

‡ Contribution No. 2715.

[1] H. M. McConnell, C. Heller, T. Cole, and R. W. Fessenden J. Am. Chem. Soc. **82,** 766 (1960); D. K. Ghosh and D. H. Whiffen, Mol. Phys. **2,** 285 (1959); M. E. Anderson, P. J. Zandstra, and T. R. Tuttle, J. Chem. Phys. **33,** 1591 (1960).
[2] See R. Lefebvre, H. H. Dearman, and H. M. McConnell, J. Chem. Phys. **32,** 176 (1960), and earlier references cited therein.
[3] M. Gouterman, J. Chem. Phys. **30,** 1369 (1959).
[4] R. McWeeny, J. Chem. Phys. **34,** 399, 1065 (1961).
[5] J. H. van der Waals (private communication).
[6] H. Sternlicht and H. M. McConnell (unpublished calculations).
[7] M. Klein (unpublished results).
[8] C. A. Hutchison and B. W. Mangum, J. Chem. Phys. **34,** 908 (1961); M. S. de Groot and J. H. van der Waals, Mol. Phys. **3,** 190 (1960).
[9] H. C. Longuet-Higgins, J. Chem. Phys. **18,** 265 (1950).
[10] M. Gouterman and W. Moffitt, J. Chem. Phys. **30,** 1107 (1959).

Paramagnetic Resonance of X-Irradiated CaF_2:Tm and of CaF_2:Yb

W. HAYES AND J. W. TWIDELL

The Clarendon Laboratory, Oxford, England

(Received June 26, 1961)

AN investigation of the effects of ionizing radiations on LiF and NaF containing divalent iron-group impurities has shown that electrons released during the irradiation were trapped by the impurities which are then observed in the singly charged state.[1-3] This work is now being extended to CaF_2 and other lattices containing lanthanide and actinide impurities; because of the previous absence of resonance data on thulium ions, measurements on CaF_2:Tm III are reported here and measurements on CaF_2:Yb IV are included for comparison.

When single crystals of CaF_2 containing trivalent rare-earth ions are grown by the Stockbarger method, the imputity ions enter the lattice substitutionally and charge compensation may be achieved by a F^- ion in the nearest interstitial site.[4,5] In some cases charge compensation is remote and the paramagnetic resonance spectrum shows the cubic symmetry of the CaF_2 lattice.[6]

When the X-band ESR spectrum of single crystals of CaF_2 containing 0.05% Tm was examined down to 20°K, no resonance was observed. The crystals were then x-irradiated at 77°K and the ESR spectrum investigated at 77°K without allowing the crystals to warm up. An isotropic spectrum with a two-line hyperfine structure was observed which may be fitted to the spin Hamiltonian

$$\mathcal{H}=g\beta H\cdot S+AI\cdot S,$$

with $I=\frac{1}{2}$, $S=\frac{1}{2}$, $g=3.453\pm0.003$, and $|A|=228\pm1G(368\pm2\times10^{-4}$ cm$^{-1})$; measurements at the K band agree with these results within the experimental error. The spectrum is assigned to ^{169}Tm III which is isoelectronic with Yb IV($4f^{13}\,{}^2F_{7/2}$). This result shows that the electrons were captured by Tm IV ions which must have been initially on cubic sites since it is unlikely that an associated charge-compensating defect, in particular F^- ions, would be mobile at 77°K. A machine calculation (unpublished) by M. J. M. Leask and W. P. Wolf of this laboratory shows that the ground state of Tm IV($4f^{12}$, $^3H_6$) in the cubic field of CaF_2 is nonmagnetic over a wide range of crystal-field parameters, and the fact that we do not observe a resonance from Tm IV is not surprising. Tm III ions were also observed after irradiation at room temperature with ionizing radiations and do not begin to decay rapidly until heated to about 550°C. We have also measured the g value of Yb IV at the X and K bands in the cubic field of CaF_2 and find $g=3.443\pm0.002$.

The ground configuration of Tm III and Yb IV consists of a single hole in a full $4f$ shell and only two terms $^2F_{5/2}$ and $^2F_{7/2}$ occur, with the latter lower. In the crystal field of CaF_2 the $J=\frac{7}{2}$ level splits into a doublet Γ_7 at $-18b_4-12b_6$, a quartet Γ_8 at $2b_4+16b_6$, and a doublet Γ_6 at $14b_4-20b_6$, where b_4 and b_6 are constants of the crystal field.[7] The $J=\frac{5}{2}$ level splits into a quartet $\Gamma_{8'}$ at $2b_{4'}$ and a doublet $\Gamma_{7'}$ at $-4b_{4'}$. The observed ground state is $\Gamma_7+\alpha\Gamma_{7'}$ where α is determined by the crystal field. The calculated g value is $3g_j-\Delta g$, where g_j is the Lande g value for the Γ_7 state and $\Delta g=-16\alpha/7\sqrt{3}$ is the first-order contribution to the g value arising from cross terms between Γ_7 and $\Gamma_{7'}$.

The measured g_j value for Tm I is[8] 1.14122 ± 0.00015 and since the g_j values for Tm III and Yb IV are not expected for our purposes to be significantly different from that for Tm I we compare our measured g values with $3g_j=3.423$ expected from the pure Γ_7 state. The difference between this g value and our measured g values indicates that the crystal field is larger than the estimate of Low,[9] whose measured g value for Yb IV is significantly different from ours, and this conclusion is supported by preliminary measurements on CaF_2:Yb in the infrared. It should also be mentioned that Γ_7 is admixed with Γ_8 by the dc magnetic field and the fact that our g values at the X and K bands agree within the experimental error indicates that the separation of these levels is at least 17 cm^{-1}.

The hyperfine interaction at $I\cdot J$ of ^{169}Tm I has been measured by Ritter[10] who finds $|a|=374.14$ Mc/sec, while our value for Tm III is $|a|=|A/3|=368$ Mc/sec. Values of $\langle r^{-3}\rangle$ for Tm I (10.51 a.u.) and for Tm IV (10.95 a.u.) have been given by Judd and Lindgren[11] and interpolating we find a value of 10.80 a.u. for Tm III. This would suggest that a for Tm III should be 3% larger than for Tm I whereas the observed value of 1.6% smaller. We have calculated the effect of the admixture of $\Gamma_{7'}$ on the hyperfine structure and find $A=A_0(1-\frac{7}{32}\Delta g)$, where A_0 is the hyperfine contribution from Γ_7. Since $\Delta g=0.030$ this admixture accounts only for 0.7% of the observed reduction of 4.6% in A

and the remainder may be due to the effect of core polarization and possible weak screening effects by the ligand electrons.

Neglecting these effects we may calculate a value of the nuclear moment of ^{169}Tm using the formula[12]

$$A/g=\frac{2\beta\beta_n\mu_n}{I}\langle r^{-3}\rangle\frac{\langle J\,||\,N\,||\,J\rangle}{\langle J\,||\,\Lambda\,||\,J\rangle},$$

where $\langle J\,||\,N\,||\,J\rangle=\frac{16}{21}$ and $\langle J\,||\,\Lambda\,||\,J\rangle=\frac{8}{7}$ and we find $|\mu_n|=0.24\pm0.01$ nm; our quoted error does not take account of possible errors in the calculated values[11] of $\langle r^{-3}\rangle$. Lindenberger[13] using optical measurements on Tm I finds $\mu_n=-0.20\pm0.02$ nm but Cabezas and Lindgren[8] using $\langle r^{-3}\rangle=10.5$ a.u. for Tm I calculate $\mu_n=-0.25$ nm from Lindenberger's data.

It is a pleasure to acknowledge helpful discussions on theoretical matters with Professor B. Bleaney. We are indebted to Dr. R. W. H. Stevenson of the University of Aberdeen for the crystals of CaF_2:Tm. The crystals of CaF_2:Yb were supplied by Mervyn Instruments Ltd.

[1] B. Bleaney and W. Hayes, Proc. Phys. Soc. (London) **B70,** 626 (1957).
[2] W. Hayes and D. A. Jones, Proc. Phys. Soc. (London) **71,** 503 (1958).
[3] W. Hayes, Discussions Faraday Soc. **26,** 58 (1958).
[4] B. Bleaney, P. M. Llewellyn, and D. A. Jones, Proc. Phys. Soc. (London) **B69,** 858 (1956).
[5] J. M. Baker, W. Hayes, and M. C. M. O'Brien, Proc. Roy. Soc. **A254,** 273 (1960).
[6] E. Friedman and W. Low, J. Chem. Phys. **33,** 1275 (1960).
[7] J. M. Baker, B. Bleaney, and W. Hayes, Proc. Roy. Soc. (London) **A247,** 141, (1958).
[8] A. Y. Cabezas and I. P. K. Lindgren, Phys. Rev. **120,** 920 (1960).
[9] W. Low, Phys. Rev. **118,** 1608 (1960).
[10] G. J. Ritter (private communication).
[11] B. R. Judd and I. P. K. Lindgren, Phys. Rev. **122,** 1802 (1961).
[12] R. J. Elliott and K. W. H. Stevens, Proc. Roy. Soc. (London) **A218,** 553 (1953).
[13] K. H. Lindenberger, Z. Physik **141,** 476 (1955).

Analysis of Complex NMR Spectra: Epichlorohydrin

C. A. Reilly and J. D. Swalen
Shell Development Company, Emeryville, California
(Received June 8, 1961)

In previous publications[1–3] the authors have developed an iterative method for calculating accurate parameters from high-resolution NMR spectra. In the present letter we illustrate the utility of the method by giving some preliminary values for the NMR parameters of epichlorohydrin (five nonequivalent protons).

Two FORTRAN programs, which greatly facilitate the calculations have been written for the IBM 7090 computer. Trial values of the shielding parameters and the spin-spin coupling constants are first entered and the main program (NMRIT) compiles the matrix of the spin Hamiltonian, diagonalizes it, and calculates the frequencies and intensities of the allowed transitions. The energy levels from which each transition originates are also indicated. With a judicious choice of these trial parameters an assignment of the observed spectrum is usually possible.[2]

A second program (NMRLS) utilizes the assignment of the observed transition frequencies to calculate numerical values for the spin energy levels and their precision by a least-squares technique. These energy levels, the initial trial parameters, and the observed frequencies are now used as input data for NMRIT. By an iterative process already described[2,3] NMRIT calculates new parameters, the process being continued until a predetermined convergence limit is reached, a serious divergence occurs, or a prescribed number of iterations is performed. At present the program allows for a maximum of ten iterations in any one calculation. The final values for the parameters, or extrapolations from them, may be used as initial values for further iterations, if desired.

The above programs have been used to advantage in analyzing the 60 Mc/sec and 40 Mc/sec NMR spectra of epichlorohydrin (these spectra have been published as Serial Nos. 3 and 4 of the API Catalogue). Values for the parameters are given below and are believed to be accurate to one or two units in the last place quoted. More precise values must await the availability of more precise experimental data.

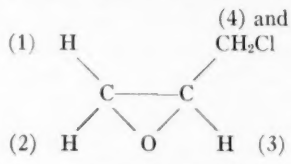

ppm from TMS

δ_1	2.65
δ_2	2.84
δ_3	3.20
δ_4	3.47
δ_5	3.74

	cps		cps		cps
$J_{12}=$	5.0	$J_{23}=$	4.0	$J_{34}=$	−6.6
$J_{13}=$	2.4	$J_{24}=$	0.6	$J_{35}=$	−4.0
$J_{14}=$	−0.2	$J_{25}=$	−0.1	$J_{45}=$	11.7
$J_{15}=$	−0.1				

It is noted that the two protons in the $-CH_2Cl$ group are magnetically nonequivalent because the rotational average of their parameters is different. This result would be expected even for rapid rotation about the bond connecting the $-CH_2Cl$ group to the rest of the molecule.[4] The large negative values for J_{34} and J_{35}

are unequivocal and somewhat surprising in view of Karplus' theoretical calculations.[5] However, because the pertinent bond angles are distorted from the tetrahedral value, the theoretical treatment given by Karplus may not apply.

[1] C. A. Reilly and J. D. Swalen, J. Chem. Phys. **32,** 1378 (1960).
[2] C. A. Reilly and J. D. Swalen, J. Chem. Phys. **34,** 980 (1961).
[3] J. D. Swalen and C. A. Reilly, J. Chem. Phys. **34,** 2122 (1961).
[4] J. A. Pople, Mol. Phys. **1,** 1 (1958).
[5] M. Karplus, J. Chem. Phys. **30,** 11 (1959).

Relation of Physical Behavior to Molecular Packing in Crosslinked Rubber

P. Mason
The Natural Rubber Producers' Research Association, Welwyn Garden City, England
(Received May 8, 1961)

THE physical consequences of crosslinking a polymer are, first, the establishment of the molecular network on which the equilibrium "rubber-like" elasticity depends; Flory has shown how the creation of this network leads to an increase in the internal pressure of the system,[1] so that crosslinking will be expected to produce a reduction in volume on this account alone.

Secondly, there is another, more localized, change in molecular packing resulting in a reduction in volume, an increase in the glass-transition temperature, and a shift of the mechanical and dielectric dispersion regions towards higher temperatures. Structural interpretation of these effects has hitherto been impeded by three difficulties: (i) the determination of crosslink density; (ii) the presence of the "foreign" atoms constituting the crosslink; and (iii) modifications to the polymer chains occurring during crosslinking.

A system is therefore being studied in which these difficulties are largely avoided. Purified natural rubber is heated with dicumyl peroxide for 1 hour at 140°C; the resulting crosslinks are direct covalent bonds between carbon atoms in neighboring chains. No "foreign" atoms are introduced, and there is substantially no modification of the rubber molecules. After extraction and drying, the equilibrium degree of swelling in *n*-decane is measured and used to obtain the crosslink density by reference to the original chemical determinations of Moore and Watson.[2] Measurements are then made of the specific volume at 20°C, the thermal expansion behavior and the dynamic mechanical behavior, both over a temperature range including the glass-rubber transition.

The specific volume at 20°C (v_x cc/g) is $v_0 = 1.103_8$ cc/g for the noncrosslinked material and falls to 1.015_9 cc/g at the highest level of crosslinking so far examined. The crosslink density (X crosslinks/g) could be estimated quantitatively up to about 2×10^{20}/g and within this range v_x decreases linearly with increasing X. Thus

$$v_x = v_0 - 0.0113\cdot10^{-20}X, \qquad (1)$$

from which the contraction can be expressed as 113 A^3 per crosslink, i.e., almost the average volume per monomeric unit, which is 124 A^3. Removal of the two hydrogen atoms in the formation of the crosslink accounts for 9 A^3, while the internal pressure contribution, calculated from Flory's theory, is approximately 2 A^3. Thus the major part of the contraction on crosslinking must be attributed to changes in local molecular packing rather than to the reduction in network entropy.

This remaining 102 A^3 can be further separated into occupied and free volume components. This is essentially the approach of Martin and Mandelkern,[3] using the Fox-Flory assumption of equal free volumes at the glass-transition point (T_g) together with the concept that the thermal expansion of the free volume is represented by the difference in expansion coefficients immediately above and below T_g. In the present experiments these coefficients both tend to decrease with increasing crosslinking, although there is considerable scatter. Taking smoothed values it is found that $\frac{1}{3}$ of the observed contraction at 20°C, i.e., 34 A^3, represents decrease in the free volume. Making the further reasonable assumption that the free volume increases from 0.025 at T_g to about 0.080 at 20°C, the 124 A^3 associated with each monomer represents approximately 10 A^3 free and 114 A^3 occupied volume. Each crosslink thus removes $\frac{1}{2}$ the occupied volume of a monomer together with free volume associated with 3 to four monomers.

Consideration of the packing around each crosslink is complicated by the presence of different structural types of crosslink. Each of the five carbon atoms in an isoprene monomer may in principle crosslink with any of the five in another monomer, so that 15 different crosslink types are possible, each with different packing characteristics. However, the relative proportions of these may be approximately estimated from chemical studies of the free-radical crosslinking mechanism.[4] Inspection of molecular models then indicates that the three most frequent types have similar structural effects, partly reducing the occupied volume of the two bonded monomers and partly increasing order and density in the near neighbors. The incidence of crosslink types may thus vary widely without affecting the constancy of the volume change per crosslink which forms a basic assumption in Fox and Loshaek's theoretical treatment.[5]

The effects of crosslinking on the glass-rubber transition are qualitatively the same whether the transition is followed by thermal expansion (at 1°C change per 4 min) or by mechanical relaxation (0.5

cps). As the crosslink density increases, each transition moves to higher temperatures and is spread out over a wider temperature range. Within the quantitative crosslinking range both T_g and the temperature of the dynamic loss maximum increase linearly with X. The change in either temperature is approximately 6°C for a crosslink density change of 10^{20}/g. This compares with 11°C for styrene-divinyl benzene copolymers[5,6] and 13°C for methyl methacrylate-ethylene glycol dimethacrylate copolymers,[7] the other two systems investigated in which the crosslinking complies with the requirements stated above. Crosslinking in these systems again involves the replacement of van der Waals' bonds by covalent bonds, the chemical environment being otherwise unchanged. The principal difference is that the crosslinks are quite large groups, and it is qualitatively reasonable that they could be twice as effective as simple carbon-carbon bonds in reducing local free volume and thereby increasing the transition temperatures.

This work forms part of the research program of the Board of The Natural Rubber Producers' Research Association.

[1] P. J. Flory, J. Chem. Phys. **18,** 112 (1950).
[2] C. G. Moore and W. F. Watson, J. Polymer Sci. **19,** 237 (1956).
[3] G. M. Martin and L. Mandelkern, J. Research Natl. Bur. Standards **62,** 141 (1959).
[4] J. L. Bolland, Quart. Revs. (London) **3,** 1 (1949).
[5] T. G. Fox and S. Loshaek, J. Polymer Sci. **15,** 371 (1955).
[6] K. Ueberreiter and G. Kanig, J. Chem. Phys. **18,** 399 (1950).
[7] S. Loshaek, J. Polymer Sci. **15,** 391 (1955).

Charge Exchange between Krypton Ions and Atoms

S. B. KARMOHAPATRO

Saha Institute of Nuclear Physics, Calcutta, India

(Received March 28, 1961)

BECAUSE of the spin multiplicities of the ions of the inert gases, the processes of charge exchange between these ions and their parent atoms show nonresonant character, similar to the ions in unlike gases. To investigate such reactions, we have measured the cross sections of the reaction $Kr^+ + Kr \rightarrow Kr + Kr^+$ in the energy range 3 to 7 kev.

The apparatus used in the experiment is basically a mass spectrometer and a collision chamber. The mass spectrometer has a two-direction-focusing magnetic analyzer which has already been described,[1] and a magnetic oscillation-type arc discharge ion source with radial extraction system. The instrument is set to receive the analyzed ion beam of Kr^+ at the collector. The beam current is 10^{-8} to 10^{-9} A at a resolving power ~45.

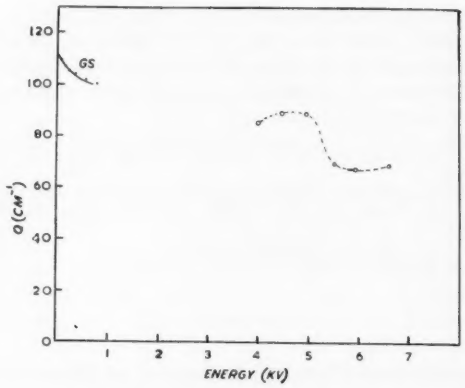

FIG. 1. Cross section (Q) vs energy (kv) curve for $Kr^+ + Kr \rightarrow Kr + Kr^+$. GS = Ghosh and Sheridan, 0 = present work.

The analyzed ion beam at the detector side passes through a 5-mm diam hole to the collision chamber. The collision chamber consists of two parallel electrodes for collection of charge exchange current, and a Faraday cylinder extended as a guard ring over the plate electrodes. The electrodes, kept at a potential difference 30 v, are connected to a vibrating reed electrometer to measure the charge exchange current I_x. The main ion current I_c to the Faraday cylinder is also measured with a vibrating reed electrometer. The cross section (Q) for the process $Kr^+ + Kr \rightarrow Kr + Kr^+$ in units cm^{-1} is calculated from the expression given by Ghosh and Sheridan,[2] $Q = [I_x]/[pl][I_x + I_c]$, where l = length of the surface on which charge exchange ions are collected, and p = pressure in mm Hg.

At sufficiently low pressures, the ratio $[I_x]/[I_x + I_c]$ is linearly dependent on pressure. This ratio for each energy value was measured at different pressures, ranging from 6×10^{-5} to 1×10^{-4} mm Hg. The slope of the p vs $[I_x]/[I_x + I_c]$ curves at $p = 8 \times 10^{-5}$ mm Hg for each energy value gives Q for that energy. The value of Q was thus obtained for different energies in the range 3 to 7 kev. The cross section (Q) as a function of energies (kv) for Kr^+ in krypton is shown in Fig. 1.

The pressure in the collision chamber was measured with an ion gauge and the ion-gauge pressure readings were converted to equivalent mm Hg pressure by use of a relative sensitivity factor for krypton, determined by Ghosh and Sheridan.[2]

Figure 1 also shows the charge exchange cross sections of krypton ions in krypton gas in the low-energy range, as measured by Ghosh and Sheridan[2]. No previous experimental data are known to have been reported for energies greater than 800 v.

The values obtained by us seem to be consistent with the work of Ghosh and Sheridan.[2] The indication of a minimum near ~5.5 kv shows that the reaction has a positive value of ΔE, the difference between the total energy of the initial and the final states.

From the empirical relation given by Hasted,[3] the energy V_{max} for maximum Q is obtained as $\log (V)_{max}{}^{\frac{1}{2}} = 1.09+1.01 \log \Delta E(M)^{\frac{1}{2}}$, where M is the mass of the ion; we have $V_{max} \sim 6$ kv for krypton ions in krypton when ΔE is considered to be equal to 0.68 ev, the energy difference between the spin doublet of Kr^+. The experimental V_{max} seems to be less than the above value. However, this may be compared with the experimental cross-sectional energy curves given by Gilbody and Hasted[4] for Ar^+ and Ne^+ in the parent gases with Q_{max} when the energy of the ions $\sim$150 and 10 ev, whereas the above empirical relation gives $\sim$200 and 25 ev, respectively.

Such discrepancies between the empirical and the experimental curves may be partly understood by assuming that the experimental curve is due to the superposed effects of the following reactions occurring to different extents:

$$Kr^+(^2P_{\frac{1}{2}})+Kr \rightarrow Kr+Kr^+(^2P_{\frac{1}{2}})+0.68 \text{ ev}; \quad \text{(i)}$$

$$Kr^+(^2P_{\frac{3}{2}})+Kr \rightarrow Kr+Kr^+(^2P_{\frac{1}{2}}); \quad \text{(ii)}$$

$$Kr^+(^2P_{\frac{3}{2}})+Kr \rightarrow Kr+Kr^+(^2P_{\frac{1}{2}})-0.68 \text{ ev}; \quad \text{(iii)}$$

and

$$Kr^+(^2P_{\frac{1}{2}})+Kr \rightarrow Kr+Kr^+(^2P_{\frac{3}{2}}). \quad \text{(iv)}$$

The experimental condition of the source and the collision chamber will determine the fractions of the above reactions, resulting in a spread to the value of V_{max}.

[1] S. B. Karmohapatro, Ind. J. Phys. **33,** 139 (1959).
[2] S. N. Ghosh and W. F. Sheridan, J. Chem. Phys. **26,** 480 (1957).
[3] J. B. Hasted, Proc. Roy. Soc. (London) **A227,** 466 (1955).
[4] H. B. Gilbody and J. B. Hasted, Proc. Roy. Soc. (London) **A238,** 334 (1957).

Crystal Splitting of the Anthracene 3800 A System

T. A. Claxton, D. P. Craig, and T. Thirunamachandran

William Ramsay and Ralph Forster Laboratories, University College, London

(Received June 16, 1961)

THE first measurement of the crystal splitting of this system[1] at 20°C gave 60 cm^{-1}. This was followed by others[2,3] giving either low values near 60 cm^{-1} or several times higher,[4] near 180 cm^{-1}. Brodin[5] suggested that the low values were found in experiments in which the absorbed light was not completely plane polarized, leading to a shift of the apparent maximum of the *b* polarized absorption maxima nearer to the *a* maximum. Lacey and Lyons[6] recently sought to avoid this by measuring the apparent splitting as a function of thickness and extrapolating to zero thickness, getting the still higher splitting of 330±40 cm^{-1} for the first absorption maximum.

TABLE I. Absorption maxima in anthracene crystal.

Band group	*a* component	*b* component	Splittings (exptl)	Splittings (calc)
A^0	25430 cm^{-1}	25240 cm^{-1}	190±10 cm^{-1}	195 cm^{-1}
A^1	26820	26680	140±10	133
A^2	28270	28190	80±25	79

New experiments have been made at liquid-helium temperature to try to resolve these differences. Thin crystals (0.11μ) were mounted on a fluorite disk, and the usual method of measurement[1] was varied by interposing a second polarizer between the crystal and Wollaston prism. This cuts down the unwanted component of polarized light by two or more orders of magnitude and so eliminates it as a complicating cause. Measurements of the absorption maxima in *a* and *b* directions in the *ab* face give the results in Table I for the first three absorption maxima and for the splitting, in general agreement with Wolf.[4] The last column gives values calculated by a method to be described later.

Although these values may still be slightly too low we do not think that the very large splitting found by the extrapolation method[6] can be real. It seems to be a result of nonlinearity in the curve of apparent splitting against crystal thickness, which leads to error when the curve is extrapolated linearly to zero thickness.

A theoretical interpretation of these results is as follows. There are now a number of pieces of evidence to show that, in the model using a point multipole representation of intermolecular effects, higher multipole interactions must be taken into account whenever, as in this instance, dipole coupling is small. These multipole quantities cannot be found from solution spectra and, if the results are sensitive to their inclusion, it may not be possible to relate solution and crystal spectra unambiguously. However, this reservation does not apply to the essential part of the argument given earlier[1] for the assignment of this transition to the short-axis polarized species $B_{1u}-A_g$ as based on the polarization ratio. This argument holds. The reason is that departures from the oriented-gas polarization ratio are second-order effects of crystalline interactions, corresponding to mixing of the transition with another at higher energies. Higher multipoles do not play a big part in this process, which depends mainly on the dipole transition moments, as determined from spectral intensities.

The crystal splittings on the other hand are first-order effects of interactions between molecules and are more sensitive to higher multipole terms. We have recalculated the splittings, vibrational intervals, and polarization ratios as determined both by the observed dipole transition moment, and by octupole transition moments selected from the range of possible values. The octupole components cannot be found accurately in

this way, because the dependence of splitting on them is rather weak; however, the best fit to the observed splittings is given by the values ($|r^3P_3{}^3 \sin 3\phi|$) = 20 A^3 and ($|r^3P_3{}^1 \sin\phi|$) = 2.4 A^3, the angle ϕ being measured in the molecular plane, from the long axis. Calculations based on these values are given in the last column of the table.

[1] D. P. Craig and P. C. Hobbins, J. Chem. Phys. **1955,** 539, 2309.
[2] J. Sidman, Phys. Rev. **102,** 96 (1956).
[3] J. Ferguson and W. G. Schneider, J. Chem. Phys. **28,** 761 (1958).
[4] H. C. Wolf, Z. Naturforsch **13a,** 414 (1958).
[5] M. S. Brodin (private communication), see reference 6.
[6] A. R. Lacey and L. E. Lyons, Proc. Chem. Soc. **1960,** 414.

Absorption Spectra of Anodic Tantalum Oxide Films

WENDELL M. GRAVEN

Aeronutronic, A Division of Ford Motor Company, Newport Beach, California

(Received May 19, 1961)

IN order to obtain additional information on optical and electronic properties of inorganic solids the ultraviolet absorption spectra of thin, anodically formed films of Ta_2O_5 have been determined. Oxide films were anodically formed on tantalum foil and made suitable for absorption measurements by removal of the supporting metal using a recently reported technique.[1]

Tantalum foil, 0.0005 in. thick, with a minimum purity of 99.9% was obtained from Fansteel Metallurgical Corporation. After preliminary cleaning with benzene and alcohol, and occasional etching with HF solution, the foil was placed in a Plexiglas holder which permitted one surface to be covered with an electrolytic solution. Buffered solutions of sodium borate-boric acid, sodium acetate-acetic acid, and ammonium citrate-citric acid were used alternately as electrolyte with no observable differences in the resulting films. Oxide layers of various thicknesses were obtained by application of suitable voltages between the foil and a platinum cathode, which was immersed in the electrolyte, with the use of a Hewlett-Packard variable voltage power supply.

After washing and drying the anodized foil, a section was transferred to a Plexiglas mount which served as a support for the free oxide film during the spectrophotometric measurements. An approximately 0.3-cm^2 area of the unanodized surface of the foil was covered with a dilute HF–HNO_3 solution, which was allowed to remain until the metal was dissolved and the film became transparent. This solution attacked the oxide also, but at a sufficiently slower rate so that complete removal of metal was possible for all except the thinnest films.

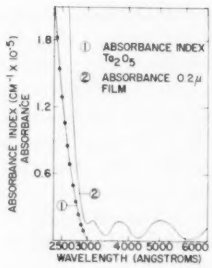

FIG. 1. Absorption spectrum of tantalum oxide film.

Absorption measurements for 25 films with formation voltages from 50 to 400 v were obtained with a Cary model 14 spectrophotometer.

Interference patterns of alternating maximum and minimum absorption were observed for each film. Film thicknesses were obtained from the slopes of plots of the product of the refractive index[2] and the wave number of successive maxima and minima vs their respective ordinal numbers.[3]

The observed proportionality of film thickness to formation voltage gave a thickness-voltage relation of 14.3 A/v, which agrees with the value of 15 A/v reported by Apker and Taft,[4] but is smaller than another reported value of 18.5 A/v.[5]

The absorption of a typical film obtained with a 150-v formation voltage is shown in Fig. 1. The long wavelength limit of absorption of approximately 2900 A is in agreement with a recently reported value of 2800 A for evaporated Ta_2O_5 layers,[6] as well as a reported value of 2850 A for the long wavelength limit of photosensitivity of oxide-coated tantalum electrodes and the observed abrupt cessation of interference phenomena at 4.6 ev.[4]

Absorbance indices (absorption coefficients), which are shown in Fig. 1, were obtained for the spectral region of 2900 to 2350 A from the slopes of plots of absorbance, corrected for reflection loss, vs film thickness for films ranging in thickness from 0.07 to 0.57 μ. There is an order-of-magnitude agreement between these results and the value of 7×10^5 cm^{-1}. which was estimated by Young from the variation of photocurrent with thickness for oxide-coated tantalum electrodes.[7]

[1] R. E. Salomon, W. M. Graven, and G. B. Adams, Jr., J. Chem. Phys. **32,** 310 (1960).
[2] J. T. Waber, G. E. Sturdy, E. M. Wise, and C. R. Tipton, Jr., J. Electrochem. Soc. **99,** 121 (1952).
[3] In a previous paper [W. M. Graven, R. E. Salomon, and G. B. Adams, J. Chem. Phys. **33,** 954 (1960)] Nb_2O_5 film thicknesses were calculated from interference data using a constant value of the refractive index. Subsequently, the optical dispersion of Nb_2O_5 has been reported [L. Young, Can. J. Chem. **38,** 1141 (1960)]. A recalculation using the improved method described for Ta_2O_5 films has resulted in a 10% decrease in the Nb_2O_5 film thicknesses. The reported absorbance indices are, therefore, increased accordingly and the corrected thickness-voltage relation is 27 A/v.
[4] L. Apker and E. A. Taft, Phys. Rev. **88,** 58 (1952).
[5] W. C. van Geel, C. A. Pistorius, and P. Winkel, Philips Research Repts. **13,** 265 (1958).
[6] W. P. Doyle, G. A. Lonergan, and D. C. Conlon, University College, Dublin, Tech. Rept. ASTIA No. 246651 (1960).
[7] L. Young, Trans. Faraday Soc. **50,** 153 (1954).

Isotope Size Effect in Van der Waals Radii and the Barrier to Rotation around the Carbon-Carbon Single Bond*

W. F. LIBBY

Department of Chemistry and Institute of Geophysics, University of California, Los Angeles, California

(Received April 17, 1961)

THE 2.85[1] kcal/mole barrier to internal rotation in ethane has had many explanations, but the possibility of using isotopic substitution to prove whether the extra stability of the staggered form is due to repulsive interference of the hydrogen atoms in the eclipsed state seems not to have been discussed. The isotope size effect[2-4] may afford an opportunity to check this possibility.

In the eclipsed form, ethane has $\frac{2}{3}\cdot 1.10+1.54$ or 2.27 A between the centers of the hydrogen atoms. This distance is appreciably less than twice the van der Walls radius for hydrogen, 1.2 A, as given by Pauling.[5] It therefore seems possible that steric interference is the cause of the barrier. Three times the root mean square of the amplitude of the bending motion of the C–H is $3(h\nu/2k)^{\frac{1}{2}}$ or 0.345 A for CH and 0.294 A for C–D and 0.224 A and 0.192 A, respectively, in the stretching mode. This means that the bound H atom has the shape of an oblate spheroid with the axial ratio $(r+0.224)/(r+0.345)$, where r (about 0.9 A) is the Van der Waals radius for an infinitely heavy hydrogen isotope. In any given direction the radius will lie between $r+0.224$ and $r+0.345$, depending on the direction. Now, if we suppose that of the 1.20 A of Van der Waals radius which Pauling[5] finds for protium between 0.224 and 0.345 A is this zero point amplitude, then the Van der Waals radius for D will be about 0.05 A less or only 1.15 A. In this case the barrier to internal rotation would be expected to be smaller if steric repulsion is the cause.

Kistiakowsky *et al.*[6] and Stitt[7] have shown, however, that the barrier to internal rotation in deutero ethane is the same as for protium ethane to within the experimental error of measurement by gaseous heat capacities, perhaps 10% of the barrier height. Similarly Lide,[8] using combination bands in the infrared found the following values:

$CH_3\cdot CH_3$, 3040 cal/mole; CH_3CD_3, 2880; CH_3CH_2D, 3310; CD_3CD_2H, 2560; CH_2DCH_2D, 2880; $(2h)$

CH_2D–CH_2D, 3050; CD_2H–CD_2H, 3090; (C_2) $(2h)$

CD_2H–CD_2H, 3470. (C_2)

Thus, we probably are justified in concluding that full deuteration of ethane does not reduce its barrier to less than 2.5 kcal/mole; whereas, the Van der Waals interaction would be expected to be reduced much more precipitously by the 0.05 A reduction in Van der Walls radius of each of the interacting hydrogen atoms. The sum of the two radii reductions is 0.10 A, which corresponds for most hydrocarbons to the compressions attained at about 30 000 atm pressure[9] at a mean total of about 3.0 kcal/mole of carbon of compressional work. It seems, therefore, that the lack of sensitivity of the barrier height to isotopic substitution is a strong argument that steric repulsion between hydrogens is not the principal cause of the barrier to hindered rotation—a conclusion deduced by others on other evidence.[10]

* This research was supported by the U. S. Air Force through the Air Force Office of Scientific Research of the Air Research and Development Command.

[1] K. S. Pitzer, Discussions Faraday Soc. **10,** 66 (1951).
[2] L. S. Bartell, Tetrahedron Letters, No. **6,** 13 (1960).
[3] K. T. Leffek, J. A. Llewellyn, and R. E. Robertson, Chemistry and Industry **1960,** 588.
[4] H. W. Joy and W. F. Libby, J. Chem. Phys. **33,** 1276 (1960). This paper took the root mean square of the vibrational amplitude as a measure of the size. This probably should be increased threefold to include 99.7% of the vibrations, since the root mean square includes only 67.43%. On the other hand, it calculated the difference in amplitudes as the square root of the difference of the average squares of the amplitudes for each isotope rather than as the difference of the square roots of the average squares. These two changes leave the results essentially unchanged.
[5] L. Pauling, *The Nature of the Chemical Bond* (Cornell University Press, Ithaca, New York, 1960), 3rd ed.
[6] G. B. Kistiakowsky, J. R. Lacher, and Fred Stitt, J. Chem. Phys. **7,** 289 (1939).
[7] Fred Stitt, J. Chem. Phys. **7,** 297 (1939).
[8] D. R. Lide, J. Chem. Phys. **29,** 1426 (1958).
[9] P. W. Bridgemen, Proc. Am. Acad. Arts Sci. **76,** 55 (1948).
[10] E. Bright Wilson, Jr., *Advances in Chemical Physics* (Interscience Publishers, Inc., New York, 1959), Vol. 2, p. 367.

Proton Resonance Shifts and Electron Susceptibilities in 1,3-Bisdiphenylene 2-Phenyl Allyl*

M. E. ANDERSON

North Texas State College, Denton, Texas

AND

R. S. RHODES AND G. E. PAKE

Stanford University, Stanford, California

(Received June 5, 1961)

IN substances in which the hyperfine coupling, $\hbar A\bar{I}\cdot\bar{S}$, between nuclei and electrons changes at a rate ω_e much greater than A, the nuclear resonance in an external magnetic field H_0, is not split, but is shifted by an amount proportional to the average value of the interaction.[1] In some free radicals the time dependence has its origin in the exchange interaction, $-2\hbar J\bar{S}_i\cdot\bar{S}_j$, between electron spins. For temperatures much greater than $\hbar J/k$ and fields much less than $\hbar J/u_0$ the effect of the exchange interaction upon a given spin $\bar{S}_i$ is well represented by letting the components of $\bar{S}_i$ have a

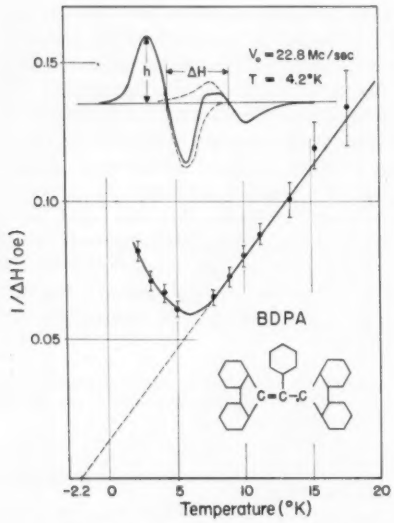

FIG. 1. Reciprocal of the Knight shift, ΔH, vs temperature. At fixed marginal oscillator frequency of 22.8 Mc/sec the static field is swept through proton resonance.

random time dependence characterized by the correlation function for spin $\frac{1}{2}$,

$$\langle S_{ix}(t)S_{ix}(t+\tau)\rangle=\tfrac{1}{2}\langle S_i^+(t)S_i^-(t+\tau)\rangle$$
$$=\tfrac{1}{2}\langle S_i^-(t)S_i^+(t+\tau)\rangle=\tfrac{1}{4}\exp(-\tfrac{1}{2}\omega_e^2\tau^2),$$

where $\omega_e^2=2J^2z$, and z is the number of nearest neighbors.[2] If $A/J\ll 1$, the proton resonance will be shifted by an amount $\gamma_p\Delta H=AI_z\langle S_z\rangle$. Since $\langle S_z\rangle$ is proportional to the static magnetic susceptibility of the unpaired electron, information concerning the electron susceptibility as well as the sign and magnitude of the hyperfine constant can be obtained from the nuclear resonance in such materials.[1,3]

We have measured the proton resonance shifts in polycrystalline samples of the organic free radical, 1,3-bisdiphenylene 2-phenyl allyl (BDPA),[4] and have obtained both the hyperfine constant and the temperature dependence of the electron susceptibility. At room and liquid nitrogen temperatures the spectrum is unresolved, but in the liquid helium range two components are observed (Fig. 1). At a fixed frequency of 22.8 Mc/sec the more intense component occurs at a field $H_0=\omega_0/\gamma_p$, the proton Larmor field. The other component is shifted upfield and occurs at $H=H_0+\Delta H$. The sign of the hyperfine constant A for these shifted protons is negative, i.e., the hyperfine field at the nuclei is opposed to the external field and the electron magnetization. Integration of the derivative spectrum and resolution into components gives a ratio of 68:32 for the intensities of the unshifted components. From ESR in BDPA in liquid solution Hausser reported a 9-line spectrum with relative intensities characteristic of a splitting by 8 equivalent unidentified protons.[5] If we tentatively identify these protons with the shifted component of the proton spectrum, we should expect the intensity of th iscomponent to be $8/(21+6)$ of the total intensity. (There is one molecule of benzene for every molecule of BDPA in the solid.[4]) The intensity ratio of unshifted to shifted components would then be $19/27:8/27=70:30$, well within the error in decomposition.

In order to obtain the magnitude of A one needs to know the temperature dependence of the electron susceptibility. In Fig. 1 the reciprocal of the Knight shift, ΔH, is plotted vs temperature. The temperatures above 4.2°K were obtained by assuming that the derivative peak amplitude h of the unshifted component is proportional to $1/T$. (The width of this component is constant.) The measurements were made by allowing the helium to evaporate and warming the sample by heating the surrounding gas. The sample remained at a given temperature long enough to permit recording the resonance. The temperature intercept of the extrapolated Curie-Weiss portion of the data gives a temperature $\theta=2.2\pm1.0$°K. Combining the 4.2°K splitting, $\Delta H=15\pm1$ oe, and the above value of θ we obtain $A=3.7\pm0.5$ Mc/sec or 1.3 ± 0.3 oe, compared to Hausser's result of 2.2 oe.

We see that, as in some other radicals, the hyperfine constants in liquids and solids do not differ greatly. The reason for their similarity, an explanation for small differences, and identification of the protons require further theoretical and experimental (e.g., deuteration) work.

Assuming J is of the order $k\theta/\hbar$, the value of J is consistent with that obtained from measurements of the specific heat and electron resonance linewidths.[6] It is also interesting that the shifted component broadens as the temperature decreases in the helium range. At room temperature the proton-proton dipole interaction appears to be the main source of line broadening. The contribution from the hyperfine interaction, of the order $A^2\omega_e^{-1}$, is small. However, as exchange ordering sets in, the rate of electrons spin fluctuation decreases and the hyperfine contribution to the width becomes more important. The shape of the shifted component is approximately Lorentzian, again suggesting that the hyperfine contribution is dominant. For temperatures down to 1.4°K the unshifted component does not change appreciably in width nor deviate from a short-tailed lineshape.

* Supported by the U. S. Air Force Office of Scientific Research.

[1] M. E. Anderson, G. E. Pake, and T. R. Tuttle, Jr., J. Chem. Phys. **33,** 1581 (1960).
[2] T. Moriya, Progr. Theoret. Phys. (Kyoto) **16,** 23 (1956).
[3] M. E. Anderson, P. J. Zandstra, and T. R. Tuttle, Jr., J. Chem. Phys. **33,** 1591 (1960).
[4] C. F. Koelsch, J. Am. Chem. Soc. **79,** 4439 (1957).
[5] K. H. Hausser, Z. Naturforsch. **14a,** 425 (1959).
[6] J. P. Goldsborough, M. Mandel, and G. E. Pake, *Proceedings of VII International Conference on Low Temperature Physics* (University of Toronto Press, Toronto, 1960), p. 235.

Approximate Mean-Square Amplitudes of Characteristic Two-Atom Vibrations*

C. J. G. RAW AND C. KUENZ

Department of Chemistry, Saint Louis University, St. Louis 4, Missouri

(Received May 25, 1961)

APPROXIMATE methods for calculating mean-square amplitudes of vibration have been veloped by Morino *et al.*[1] and by Cyvin.[2,3] In this note, we present a simpler approach to the problem of calculating mean-square amplitudes of two-atom characteristic vibrations, particularly in the range above 1200 cm^{-1}. Our aim is to avoid the detailed computation of the L-matrix elements, and the final expression involves only a knowledge of the appropriate vibration frequency and the stretching force constant.

The L matrix relates the internal coordinates R to the normal coordinates Q through the linear transformation $R=LQ$. The mean-square amplitude of vibration is defined by $\langle R_i^2\rangle=\sum_k L_{ik}^2\langle Q_k^2\rangle$. Here $\langle Q_k^2\rangle=(h/8\pi^2\nu_k)\coth[h\nu_k/2kT]$, where ν_k is the frequency of the normal vibration, h is Planck's constant, k is Boltzmann's constant, and T is the absolute temperature.[4] The method proposed here is based on the assumption that, for wave numbers greater than 1200 cm^{-1}, the hyperbolic cotangent differs very little from unity for temperatures near 298°K: $\coth[h\nu_k/2kT]=1$. Substituting this into the expression for $\langle Q_k^2\rangle$, we have $\langle Q_k^2\rangle=h/8\pi^2\nu_k=h\nu_k/2\lambda_k$, where $\lambda_k=4\pi^2\nu_k^2$ is the frequency parameter. From the definition of $\langle R_i^2\rangle$, it follows that $\langle R_i^2\rangle=\frac{1}{2}\sum_k L_{ik}^2 h\nu_k\lambda_k^{-1}$, or, in matrix notation, since $\langle R^2\rangle=L\langle Q^2\rangle L'$ (where L' is the transpose of L),

$$\langle R^2\rangle=\tfrac{1}{2}Lh\nu\Lambda^{-1}L', \qquad (1)$$

where Λ is the diagonal matrix with elements λ_k and ν is a diagonal matrix of the frequencies of vibration.

Assuming that the normal mode of vibration of frequency ν_k is a two-atom group vibration (i.e., a vibration that proceeds independently of the rest of the molecular framework), we can consider this vibration k to occur alone, all other frequencies of vibration being zero. It follows that there is only one nonzero element in the diagonal matrix ν. Likewise, the matrix Λ will be a zero matrix except for the single diagonal element $4\pi^2\nu_k^2$. Hence, Eq. (1) can be written in the form

$$\langle R_k^2\rangle=\tfrac{1}{2}h\nu_k L\Lambda^{-1}L'. \qquad (2)$$

It must be borne in mind that in Eq. (2) L is a zero matrix except for the kth row, L' is the transpose consisting entirely of zeros except for the kth column, and Λ^{-1} is a zero matrix except for the (k,k) diagonal element, which is equal to λ_k^{-1}.

Now, in general, $L\Lambda^{-1}L'=F^{-1}$, where F^{-1} is the inverse of the force constant matrix. In the case of the two-atom characteristic vibration considered here, the only nonzero force constant will be that corresponding to the group vibration ν_k; thus, $F^{-1}=1/F_{kk}$.

Equation (2) may be written as

$$\langle R_k^2\rangle=\tfrac{1}{2}(h\nu_k/F_{kk}). \qquad (3)$$

It is interesting to note that, according to Eq. (3), the mean-square amplitudes of vibration are temperature independent, as would be expected if the stretching frequencies are high.

In Table I, a comparison is made between the values of $\langle R_k^2\rangle^{\frac{1}{2}}$ calculated from Eq. (3) for some typical atom pairs in different molecules and those obtained from electron-diffraction and spectroscopic data. The approximate relation derived here [Eq. (3)] is clearly useful for those two-atom vibrations which can be

TABLE I. Root-mean-square amplitudes of characteristic atom-pair vibrations.

Atom pair	Molecule	Force constant (10^5 d cm^{-1})	Wave number (cm^{-1})	Eq. (7)	$\langle R_k^2\rangle^{\frac{1}{2}}$ (A) Spectroscopy	Electron diffraction
C—H	allene	5.07[a]	3030[a]	0.077	0.0772[a]	0.0772[b]
C—H	benzene	5.13[a]	3060[a]	0.077	0.0770[a]	0.072[c]
C—H	H_2CO	4.40[a]	2820[a]	0.080	0.0801[a]	...
C—H	$CH_2{=}CF_2$	4.8[d]	3060[d]	0.080	0.0767[d]	...
C—Cl	CCl_4	3.6[e]	797[e]	0.047	0.053[j]	0.041[e]
C=O	CO_2	15.6[e]	2349[e]	0.039	0.034[e]	0.034[e]
C=C	$CF_2{=}CF_2$	9.2[d]	1872[h]	0.045	0.039[d]	...
C=C	$CH_2{=}CF_2$	8.4[d]	1731[d]	0.045	0.049[d]	...
C=C	benzene	7.6[f]	1596[i]	0.046	0.0454[k]	0.0459[k]

[a] S. J. Cyvin, Acta Chem. Scand. **12**, 233 (1958).
[b] S. J. Cyvin, J. Chem. Phys. **29**, 583 (1958).
[c] I. L. Karle, J. Chem. Phys. **20**, 65 (1952).
[d] Y. Morino, K. Kuchitsu, and T. Shimanouchi, J. Chem. Phys. **20**, 726 (1952).
[e] I. L. Karle and J. Karle, J. Chem. Phys. **17**, 1052 (1949).
[f] J. W. Linnett, Quart. Revs. **1**, 73 (1947).
[g] L. J. Bellamy, *The Infrared Spectra of Complex Molecules* (John Wiley & Sons, Inc., New York, 1958), 2nd ed., pp. 57, 331.
[h] Y. Morino and K. Kuchitsu, J. Chem. Phys. **20**, 1809 (1952).
[i] G. Herzberg, *Infrared and Raman Spectra of Polyatomic Molecules* (D. Van Nostrand Company, Inc., Princeton, New Jersey, 1945), p. 366.
[j] D. A. Long and E. A. Siebold, Trans. Faraday Soc. **56**, 1105 (1960).
[k] O. Bastiansen and S. J. Cyvin, Nature **180**, 980 (1957).

classed as group vibrations, even at lower frequencies, although the hyperbolic cotangent term should be included for greater accuracy as its values would not then be approximately unity. Equation (3) also gives a useful check on the value of the stretching force constant, which should be of assistance in force constant calculations.

* This research was done as part of the National Science Foundation Undergraduate Research Participation Program in the Department of Chemistry of Saint Louis University.

[1] Y. Morino, K. Kuchitsu, A. Takahashi, and K. Maeda, J. Chem. Phys. **21,** 1927 (1953).
[2] S. J. Cyvin, Spectrochim. Acta **56,** (1959).
[3] S. J. Cyvin, Acta Chem. Scand. **12,** 233 (1958).
[4] R. W. James, Physik. Z. **33,** 737 (1932).

Substitution of a Catalytic Probe for a Tube of Infinite Length in Atom Recombination Experiments*

BERNARD J. WOOD AND A. BRUCE KING

Division of Chemical Physics, Stanford Research Institute, Menlo Park, California

(Received June 16, 1961)

IN a cylindrical tube of infinite length with an atom source at one end, the concentration of atoms[1] $n(x, \infty)$ at any cross section of the tube is given by[2,3]

$$n(x, \infty) = n(0, \infty) \exp[-(2/\delta)^{\frac{1}{2}} x/R], \qquad (1)$$

where $n(0, \infty)$ is the atom concentration at the source, x the axial distance from the source, and δ the diffusion Reynolds number[4] for the wall, equal to $4D_{ij}/\gamma c_i R$ in which γ is the recombination efficiency of atoms on the wall, c_i the mean velocity of the atoms, D_{ij} the diffusion coefficient for atoms through the gas, and R the radius of the tube. As a means of evaluating the recombination efficiency of atoms on a tube wall, this analysis has been applied in many instances to data derived from a system in which the heat flux into a movable probe of finite catalytic activity was employed as the measure of atom concentration $n(L, L)$ at various probe distances L from the source.

Under some conditions the introduction of a catalytic probe modifies the system to the extent that it may be analytically treated as a tube of finite length[3,5] whose walls may be different in recombination efficiency from that of the closure (probe). There are, in general, three distinct functions relating atom concentration to distance. The first, represented in Eq. (1), gives the atom concentration profile in an infinite tube. The second function[3] describes the atom concentration profile in a finite tube, relating $n(x, L)$ to x. The third is the experimental relation between the atom concentration at the probe and the probe position, i.e., $n(L, L)$ vs L. The functions of $n(x, \infty)$ vs x and $n(L, L)$ vs L are especially easily confused, because at large values of x and L, the slopes of these functions approach identical values.[3]

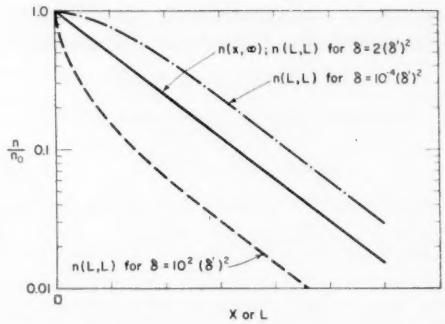

FIG. 1. Calculated[3] relative atom concentrations as functions of axial distance for tubes of infinite and finite length. (In this example $\delta = 100$.)

It is of interest to examine that condition when the net atom flux through a plane at $x = L$ in the infinite tube equals that to the surface of the closure at $x = L$, and the atom concentrations at $x = L$ are the same for both tubes, i.e., $F(L, \infty) = F(L, L)$ and $n(L, \infty) = n(L, L)$. From Eq. (1),

$$F(L, \infty) = -D_{ij}(d/dx)[n(L, \infty)]$$
$$= n(L, \infty)[(2/\delta)^{\frac{1}{2}}(D_{ij}/R)], \qquad (2)$$

and from the boundary condition for net atom flux on the closure of a finite tube,[3,4]

$$F(L, L) = n(L, L) D_{ij}/\delta' R, \qquad (3)$$

where δ' is the diffusion Reynolds number of the closure. By combining Eqs. (2) and (3), one obtains a relationship in dimensionless terms between the recombination efficiencies of wall and probe

$$\delta = 2(\delta')^2. \qquad (4)$$

The solid curve in Fig. 1 demonstrates the condition satisfying Eq. (4). The other curves illustrate the concentrations of atoms at the closure $n(L, L)$ when it is a more important sink for removal of atoms than the wall, i.e., when $\delta > 2(\delta')^2$, and, conversely, when $\delta < 2(\delta')^2$. For large values of L, all of the curves approach a constant slope which is identical to that for an infinitely long tube and which is governed only by the activity of the cylinder wall. Consequently, catalytic probe measurements taken at sufficient distances from the origin may be used to evaluate the wall activity. The effects of the presence of an active closure on absolute atom concentration, however, may be ignored only when Eq. (4) is satisfied.

* This work was supported, in part, by Project Squid, Office of Naval Research, Department of the Navy, and, in part, by the Division Research Committee, Physical and Life Sciences Divisions, Stanford Research Institute.

[1] In this notation for atom concentration the first argument refers to the axial position and the second to the tube length.
[2] W. V. Smith, J. Chem. Phys. **11,** 110 (1943).
[3] H. Wise and C. M. Ablow, J. Chem. Phys. **29,** 634 (1958).
[4] The correction for large values of probe activity [H. Motz and H. Wise, J. Chem. Phys. **32,** 1893 (1960)] has been neglected in this discussion.
[5] B. J. Wood and H. Wise J. Phys. Chem. (to be published).

Purification and Vapor Pressure of Nitric Oxide*

ERNEST E. HUGHES

National Bureau of Standards, Washington, D. C.

(Received May 10, 1961)

IN the course of a recent investigation it was necessary to measure the vapor pressure of nitric oxide in the range between 1 mm and 1μ of mercury. Reliable values have been published for pressures greater than 1 mm,[1] but there is some question about the few values reported below this pressure.[2] The method chosen to measure the vapor pressure is a modification of that reported by Tickner and Lossing.[3] A saturator is connected directly to a mass spectrometer whose response in terms of ion current per unit pressure of NO has been previously determined. The temperature of the saturator is slowly changed and the magnitude of the ion current, and consequently the pressure, is measured at different temperatures.

The saturator is shown in Fig. 1. The sample is first distilled into the saturator through the side arm which is then sealed off. The solid NO is melted and refrozen as a solid mass at the bottom of the inner tube. The quantity is sufficient to completely cover the thermocouple well. The outer jacket is filled with liquid oxygen previously cooled to liquid nitrogen temperature. The pressure in the outer jacket is reduced by vigorous pumping until the oxygen solidifies. The pump is stopped and the jacket vented. The oxygen is allowed to warm to its boiling point over a period of several hours. By cooling the outer jacket with liquid nitrogen to reduce heat intake, it is possible to maintain a warming rate of 2 to 4° per hr.

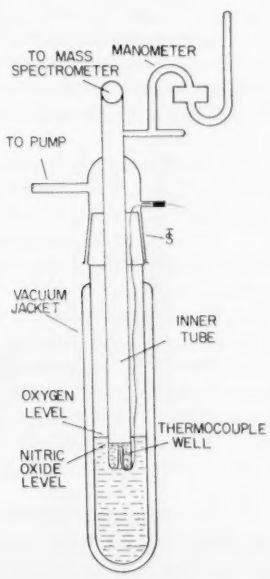

FIG. 1. Apparatus for measuring the vapor pressure of nitric oxide with a mass spectrometer.

The level of oxygen is about 1 cm above the level of NO. The total distance between the oxygen level and the bottom of the inner tube is no more than 3.5 cm. If the level of oxygen varies in either direction by a large amount erratic results are obtained, probably because of thermal gradients in the refrigerant.

It was possible to measure pressures up to 1 mm with the mass spectrometer. Above this pressure a mercury manometer with a cathetometer was used. The saturator functioned well up to a pressure of 10 mm. Above the temperature corresponding to this pressure, it was difficult to maintain equilibrium conditions.

Pure nitric oxide was prepared from cylinders of commercial nitric oxide. This grade of gas contains significant amount of other oxides of nitrogen and quantities of nitrogen. It was first purified by numerous distillations at the melting point of the solid (about $-160°$). Approximately twenty distillations were necessary to produce a product of high purity. Later it was found that a single passage of the gas through silica gel cooled to the temperature of dry ice was sufficient to remove all but nitric oxide and nitrogen. The nitrogen was separated easily by distillation at liquid nitrogen temperature.

The equation for the vapor pressure of the solid reported by Johnston and Giauque[1] for the range above 1 mm, fits the data of this investigation quite adequately for pressures as low as 10μ. Below this pressure the equation gives values which deviate slightly from the experimentally determined straight line but which are within the range of the observed values. The following straight line equation was found to fit the data over the whole range from 10 mm to 0.1μ:

$$\log_{10}P_{\text{mm}} = -(877.2/T) + 10.2368.$$

TABLE I. Vapor pressure of solid nitric oxide.

Pressure in mm Hg	Temperature in °C
10.	−178.2
5.0	−181.2
1.0	−187.5
0.5	−189.9
0.1	−195.1
0.05	−197.1
0.01	−201.5
0.005	−203.2
0.001	−206.9
0.0005	−208.3
(0.0001)	(−211.6)

There is much scatter of the data below 1μ and the use of this equation for pressures below 0.5μ is perhaps not justified. A summary of the data calculated using the equation is shown in Table I.

* This work was supported in part by the U. S. Public Health Service.

[1] H. L. Johnston and W. F. Giauque, J. Am. Chem. Soc. **51,** 3194 (1929).
[2] C. F. Mundell, Z. Phys. Chem. **85,** 462 (1913).
[3] A. W. Tickner and F. P. Lossing, J. Chem. Phys. **18,** 148 (1950).

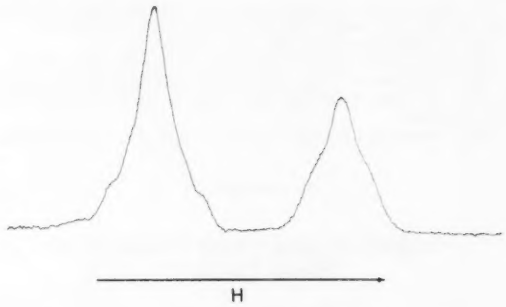

FIG. 2. B^{11} spectrum of B_4D_{10} (about 90% deuterated).

Absence of B^{10}—B^{11} Coupling in B_4H_{10}

JOHN S. RIGDEN, ROBERT C. HOPKINS, AND JOHN D. BALDESCHWIELER

Department of Chemistry, Harvard University, Cambridge 38, Massachusetts

(Received May 25, 1961)

THE general features of the B^{11} NMR spectrum of tetraborane[1] are consistent with the established structure of this molecule.[2,3] The spectrum includes a low-field triplet arising from coupling with the protons of the BH_2 groups, and a high-field doublet arising from coupling with the protons of the BH groups. Each feature of the BH_2 group resonance shows an apparent triplet structure that is just resolved.[1] This additional structure on the BH_2 resonance has been assigned to the coupling of each of the 2 and 4 boron atoms with two bridge protons.[4] Williams *et al.*,[1] also report a complex fine structure on the BH group resonance. They suggest that this may be a septet structure arising from B^{10}–B^{11} coupling between the central boron atoms (boron atoms 1 and 3).

The B^{11} spectrum of B_4H_{10} has been the only example reported of semiresolved boron-boron spin coupling in the boron hydrides. Furthermore, tetraborane is the only boron hydride which has only one single boron-boron bond uniting the boron framework. B_4H_{10} might thus be expected to be the most favorable example in which B^{10}–B^{11} coupling could be tested. Although internal rearrangement of the H atoms may be possible with the use of unsymmetrical intermediates,[5,6] this rearrangement has been shown to be slow.[7]

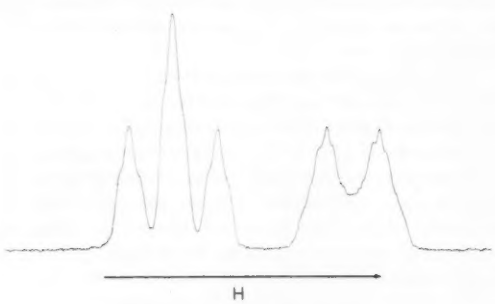

FIG. 1. B^{11} spectrum of B_4H_{10}.

It is possible to confirm the assignment of spin-spin coupling by nuclear magnetic double resonance.[8] If the fine structure is correctly assigned to B^{10}–B^{11} coupling, then irradiation at about the B^{10} resonance frequency should change the apperance of the fine structure in the B^{11} NMR spectrum. For a sufficiently large amplitude of the second radio-frequency field, the B^{10} fine structure should disappear.

The B^{11} NMR spectrum of B_4H_{10} at 15.1 Mc is shown in Fig. 1. In this spectrum, a septet structure on the BH doublet is not apparent. The structure on the BH group doublet is perhaps better described as a poorly resolved triplet. Upon double irradiation at the B^{10} resonance frequency, the structure on this group is not changed. Thus the fine structure cannot be assigned to B^{10}–B^{11} coupling between the 1 and 3 boron atoms. It is possible that interactions involving the quadrupole moments of both B^{10} and B^{11} could prevent the appearance of B^{10}–B^{11} coupling even when the boron atoms are bonded by a single bond.

The spectrum of B_4D_{10} (about 90% deuterated) is shown in Fig. 2. The shoulders at the base of both the boron 2 and 4, and boron 1 and 3 signals can be assigned to splitting of the B^{11} resonances by residual protons in the terminal positions. There is no fine structure on the central component of either feature in the spectrum. Thus the fine structre on the BH resonance is properly assigned to spin-spin coupling of boron atoms 1 and 3 with protons. The assignment of this structure to bridge proton coupling is consistent with the assignment of the fine structure on the BH_2 group to bridge proton coupling. The bridge protons actually are closer to the 1 and 3 boron atoms (1.33 A) than to the 2 and 4 borons (1.43 A).[6]

Helpful discussions with Professor W. N. Lipscomb, the assitance of Dr. Goji Kodama in the preparation of the tetraborane samples, and the financial support of

the National Science Foundation in this work are gratefully acknowledged.

[1] R. E. Williams, S. G. Gibbins, and I. Shapiro, J. Am. Chem. Soc. **81,** 6164 (1959).
[2] E. B. Moore, R. E. Dickerson, and W. N. Lipscomb, J. Chem. Phys. **27,** 209 (1957).
[3] C. E. Nordman and W. N. Lipscomb, J. Chem. Phys. **21,** 1856 (1953).
[4] The numbering of the atoms follows the convention given in reference 3.
[5] F. L. Hirshfeld, K. Eriks, R. E. Dickerson, E. L. Lippert, and W. N. Lipscomb, J. Chem. Phys. **28,** 56 (1958).
[6] W. N. Lipscomb, Advances in Inorg. Chem. and Radiochem. **1,** 119 (1959).
[7] J. E. Todd and W. S. Koski, J. Am. Chem. Soc. **81,** 2319 (1959).
[8] J. D. Baldeschwieler, J. Chem. Phys. **34,** 718 (1961).

Long-Range N^{14}—H^1 Nuclear-Resonance Coupling in Isonitriles*

I. D. KUNTZ, JR., P. VON R. SCHLEYER, AND A. ALLERHAND†

Frick Chemical Laboratory, Princeton University, Princeton, New Jersey

(Received May 29, 1961)

IN the course of routine measurements of the chemical shift of the hydrogens in *t*-butyl isonitrile, we observed splitting of the proton resonance. The triplet of approximately 1:1:1 intensity cannot result from proton-proton coupling. We believe this represents the first case of a resolvable long-range N^{14}-H^1 interaction.

Several other isonitriles have been examined and similar results obtained (Table I). Figure 1(a) shows the CH_3NC triplet, (b) the CH of $(CH_3)_2CHNC$, and (c) the CH_3 resonance of the same compound.

In most compounds containing nitrogen, even including some in which hydrogen is bonded directly to nitrogen, the electric field gradient about the N^{14} nucleus is

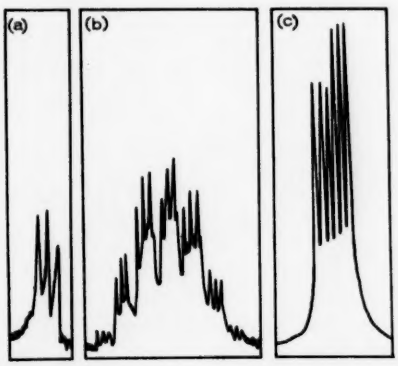

FIG. 1. The NMR spectra of isonitriles. (a) The methyl resonance of CH_3NC, (b) the CH resonance of $(CH_3)_2CHNC$, (c) the CH_3 resonance of $(CH_3)_2CHNC$ at decreased gain from (b).

TABLE I. Summary of the NMR spectra of isonitriles.[a]

Compound	$\tau \pm 0.02$	Multiplicity	J_{NH}cps ± 0.2	J_{HH}cps ± 0.2
$(CH_3)_3CNC$[b]	8.56	triplet	3.5	
CH_3NC[b]	7.15	triplet	2.7	
$C_6H_5CH_2NC$	5.72	triplet	1.3	
$(CH_3)_2CHNC$				
CH_3	8.55	tripled doublet	2.6	7.0
CH	6.13	tripled heptet	1.8	7.0
$CH_3(CH_2)_3NC$				
α-CH_2	6.70	tripled triplet shows splitting	2.0	6.7
β-CH_2				
$C_6H_{11}NC$[c]CH	6.42	broad peak		

[a] Varian 4300-B spectrometer; 40 Mc/sec; $SiMe_4$ internal standard.
[b] CCl_4 solutions; the other compounds were run neat.
[c] Cyclohexyl isonitrile.

sufficiently strong to decouple either partially or completely the N^{14} and H^1 spins through quadrupole relaxation.[1-4] The fact that splitting is observed with isonitriles indicates that the electric field gradient is unusually small and that the spin-lattice relaxation time of N^{14} must be comparable to the coupling constant.[2] The low electric field gradient must be due to the axial symmetry of the electron density near the nitrogen atom. The relaxation time for N^{14} T_n can be estimated from an equation due to Pople,[2] $\mathfrak{N}=10\pi T_n J$, where $\mathfrak{N}$ is a dimensionless parameter reflecting the degree of resolution of a proton multiplet (estimated roughly, to be 20 for the isonitriles). With $J_{NH}=2$ cps (Table I), T_n is about 0.3 sec. In contrast, T_n is only 0.02 sec for NH_3 which lacks axial symmetry.[2] From[2]

$$1/T_n = \tfrac{3}{8}\hbar^{-2}(eq)^2(eQ)^2\tau_c \qquad (1)$$

the difference of about 15 in T_n in going from NH_3 to the isonitriles corresponds approximately to a change of 225 in the electronic symmetry near the N^{14} nucleus.

A brief survey of other nitrogen containing molecules has been made to determine the generality of this long-range coupling. Data on amines, amides, nitroalkanes, and heterocyclic compounds has been available for some time.[3-5] These materials, of course, do not show such N^{14} splitting. The present examination of nitriles, *N*-oxides, and alkyl azides failed to reveal further examples of long-range coupling. If, as in isonitriles, J is less than 5 cps for these compounds, T_n must be small (<0.05 sec). This can be understood since the electronic symmetry around nitrogen is not axial in most of these functional groups. Nitriles resemble isonitriles[6] in being linear groups, but because of the lone-pair electrons on nitrogen, nitriles have a lower electronic symmetry than have isonitriles.

The NMR spectrum of isopropyl isonitrile is of particular interest since β coupling is stronger than α coupling, an effect noted in $Pb^{207}(C_2H_5)_4$[7] and more recently with

other magnetic nuclei.[8] The observed behavior of N^{14} corresponds with the analysis of such coupling given by Narasimhan and Rogers.[8]

We are indebted to Dr. David Grant and to Dr. James Shoolery for helpful suggestions.

* We acknowledge with appreciation support of this research by a grant from the National Science Foundation.

† Merck Foundation Fellow, 1960–1961.

[1] R. A. Ogg and J. D. Ray, J. Chem. Phys. **26,** 1515 (1957); J. A. Pople, W. G. Schneider, and H. J. Bernstein, *High Resolution Nuclear Magnetic Resonance* (McGraw-Hill Book Company, Inc., New York, 1959), pp. 214ff, p. 227.

[2] J. A. Pople, Mol. Phys. **1,** 168 (1958).

[3] J. D. Roberts, J. Am. Chem. Soc. **78,** 4495 (1956).

[4] L. M. Jackman, *Nuclear Magnetic Resonance Spectroscopy* (Pergamon Press, Inc., New York, 1959), p. 72ff.

[5] G. V. D. Tiers, "Characteristic NMR shielding values for hydrogen in organic structures" (unpublished).

[6] L. Pauling, *The Nature of the Chemical Bond* (Cornell University Press, Itahaca, New York, 1960), 3rd ed. p. 270; B. Bak, L. Hausen-Nygaard, and J. Rastrup-Andersen, J. Mol. Spectroscopy **2,** 54 (1958).

[7] E. B. Baker, J. Chem. Phys. **26,** 960 (1957).

[8] P. T. Narasimhan and M. T. Rogers, J. Chem. Phys. **31,** 1431 (1959); **34,** 1049 (1961).

A Shorter Method of Calculating Lennard-Jones (12-6) Potential Parameters from Gas Viscosity Data

W. A. Hawksworth

Department of Chemistry and Chemical Technology, University of Natal, Pietermaritzburg, Natal, South Africa

(Received May 8, 1961)

THE Lennard-Jones (12-6) potential model expresses the potential energy $\phi(r)$ as a function of the molecular separation r; and the two potential parameters, ϵ the maximum energy of attraction between two molecules, and σ the collision diameter for low energy head-on collisions: $\phi(r)=4\epsilon[(\sigma/r)^{12}-(\sigma/r)^{6}]$. These force constants can be calculated from the gas viscosity by making use of tables of reduced collision integrals for the Lennard-Jones model.[1] This method involves laborious trial and error approximations and it is therefore of some value to have a shorter, although similar, method of calculating the potential parameters.

The viscosity of a pure gas to the first approximation is given by

$$[\eta]_1\times10^7=\frac{266.93(MT)^{\frac{1}{2}}}{\sigma^2\Omega^{(2,2)*}(T^*)}, \qquad (1)$$

where η = viscosity in g/cm sec; T = temperature in °K; T^* = reduced temperature $=kT/\epsilon$; k = Boltzmann constant; M = molecular weight, σ = collision diameter in A; ϵ/k = potential parameter in °K; $\Omega^{(2,2)*}(T^*)$ = reduced collision integral at T^*.

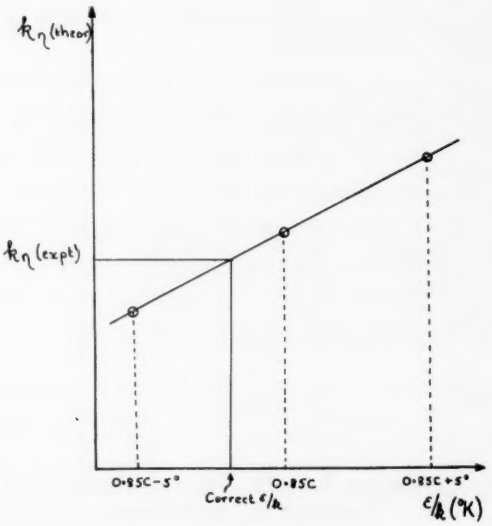

FIG. 1.

It is customary to define a quantity

$$k_\eta(\text{expt})=[\eta(T_2)/\eta(T_1)]_{\text{expt}}(T_1/T_2)^{\frac{1}{2}} \qquad (2)$$

and then ϵ/k is obtained by trial and error solution of the equation

$$k_\eta(\text{theor})=[\Omega^{(2,2)*}(T_1^*)/\Omega^{(2,2)*}(T_2^*)] \qquad (3)$$

The reduction of the temperature may be achieved by using critical temperature data or Raw's[2] approximate relationship $\epsilon/k=0.85C$, where C is Sutherland's constant, which is itself determined from the viscosity data. Each value of ϵ/k selected will thus yield a different solution $k_{\eta(\text{theor})}$. It has been found that a plot of $k_{\eta(\text{theor})}$ vs ϵ/k is linear for most gases. The following method of calculation for ϵ/k is thus proposed.

Since Raw's approximate relationship usually gives a value of ϵ/k within 10°K of the correct value, three values of $k_{\eta(\text{theor})}$ are calculated for the three values of ϵ/k: $(0.85C-5°)$, $(0.85C)$, and $(0.85C+5°)$. A graph is then drawn and the correct value of ϵ/k is found by interpolation (Fig. 1). By using Raw's relation the whole simplified method involves only a knowledge of the gas viscosity and not of any other properties such as critical data. The collision diameter σ may be found in the usual way by substitution in Eq. (1).

This method of calculation has been found to be entirely satisfactory and very convenient in practice, and can be adapted for higher approximations to the viscosity of a gas. This is usually unnecessary since most workers rarely claim an overall error of less than 1% in the experimental determination of the viscosity of a gas.

[1] J. Hirschfelder, C. Curtiss, and R. Bird, *Molecular Theory of Gases and Liquids* (John Wiley & Sons, Inc., New York, 1954).
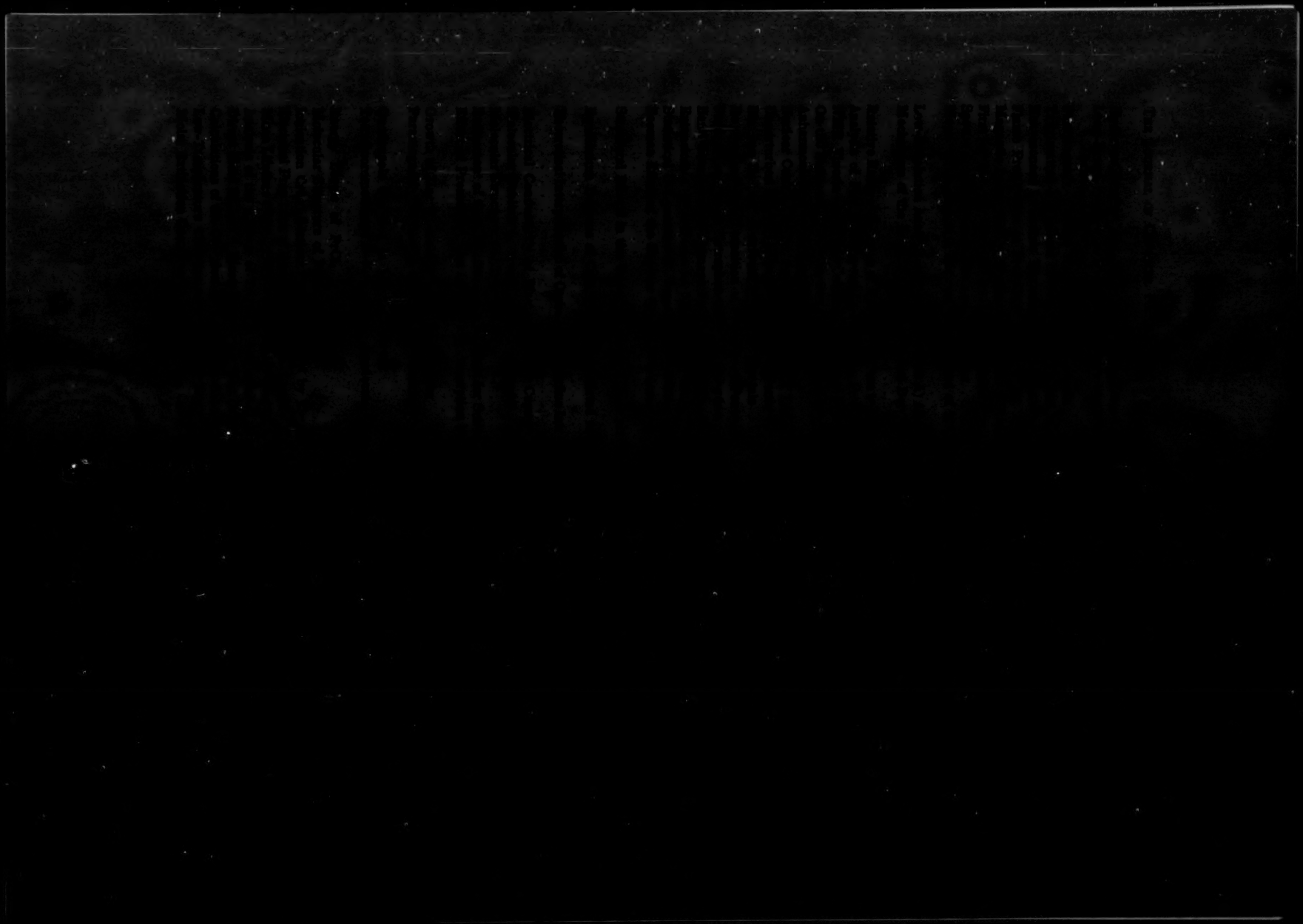
[2] C. J. G. Raw, J. S. African Chem. Inst. **7,** 96 (1954).